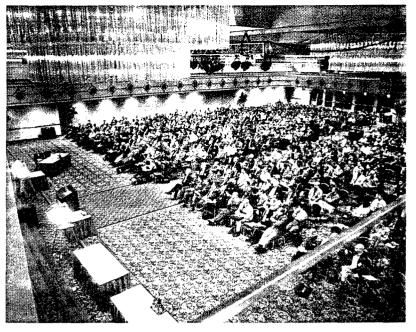
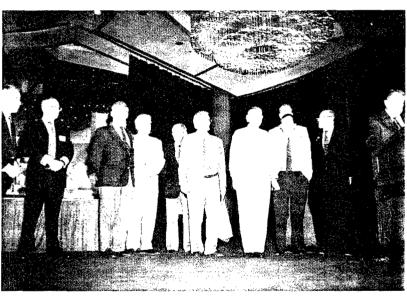
PROCEEDINGS OF THE 1999 PARTICLE ACCELERATOR CONFERENCE

PAGES 2259 - 2962













gati coll	hering and maintaining the data needed, a ection of information, including suggestion	information is estimated to average 1 hour and completing and reviewing the collection is for reducing this burden, to Washington 22-4302, and to the Office of Management a	of information. Send comments Headquarters Services, Directora	regarding this bur- te for Information	den estimate or any other aspect of this Operations and Reports, 1215 Jefferson
1.	AGENCY USE ONLY (Leave Blank)	2. REPORT DATE June 1999	3. REPORT TYPE AND DA Final; March 27- April 2		D
4.	TITLE AND SUBTITLE			5. FUNDING	NUMBERS
	Proceedings of the 1999 Particle	Accelerator Conference		G	
	Volumes 1 through 5				
6.	AUTHORS]	
	A. Luccio, W. MacKay - editors				
7.	PERFORMING ORGANIZATION N	IAME(S) AND ADDRESS(ES)		8. PERFORM	ING ORGANIZATION REPORT
	Brookhaven National Lab			NUMBER	
	P.O. Box 500				
	Upton, NY 11973				
9.	SPONSORING / MONITORING AC	GENCY NAME(S) AND ADDRESS(E	ES)	10. SPONSO	ORING / MONITORING AGENCY
	U.S. DOE			REPORT	NUMBER
	National Science Foundation				
	Office of Naval Research				
11.	SUPPLEMENTARY NOTES				
12a	a. DISTRIBUTION / AVAILABILITY	STATEMENT		12b. DISTRII	BUTION CODE
	Available to public		·		
			\		
				<u> </u>	
13.	ABSTRACT (Maximum 200 word: Papers for the eighteenth biennial Pa	's) article Accelerator conference, an inte	ernational forum on acceleator	science and teh	nology held March 27-April 2, 1999
	in New York City, organized by Broo	khaven National Lab.			
	·				
		·	•		
		•			
					l
14	SUBJECT TERMS				15. NUMBER OF PAGES
14.	SUBJECT TERIVIS				3779
					16. PRICE CODE
					10. PRICE CODE
	SECURITY CLASSIFICATION OF REPORT	18. SECURITY CLASSIFICATION OF THIS PAGE	19. SECURITY CLASSI OF ABSTRACT	FICATION	20. LIMITATION OF ABSTRACT
	Unclassified	Unclassified	Unclassified	1	UL
	ATTAINS STORES	OHOHOSHICU	VIII CC PIOLICU	4	

REPORT DOCUMENTATION PAGE

NSN 7540-01-280-5500

20000229017

298-102

Standard Form 298 (Rev. 2-89) Prescribed by ANSI Std. Z39-1

Form Approved

OMB No. 0704-0188





The American Physical Society

Proceeding of the 1999 Particle Accelerator Conference

(Editors: A. Luccio, W. MacKay)

Volume 4 of 5

Pages 2259 – 2962

DISTRIBUTION STATEMENT A
Approved for Public Release
Distribution Unlimited

Papers from the eighteenth biennial Particle Accelerator Conference, an international forum on accelerator science and technology held March 27 – April 2, 1999 in New York City, organized by Brookhaven National Laboratory. Sponsored by the Institute of Electrical and Electronics Engineers Nuclear and Plasma Sciences Society and the American Physical Society Division of Physics of Beams, and with support from the U.S. Department of Energy, the National Science Foundation, the Office of Naval Research, and Brookhaven Science Associates (BSA).

DTIC QUALITY INSPECTED 3

20000229 017

Proceedings of the 1999 IEEE Particle Accelerator Conference

Abstracting is permitted with credit to the source. Libraries are permitted to photocopy, beyond the limits of U.S. Copyright law for private use of patrons, those articles in this volume that carry a code at the bottom of the first page, provided the per-copy fee indicated in the code is paid through the copyright Clearance Center, 222 Rosewood Drive, Danvers, MA 01923. For other copying, reprint, or republication permission, write to the IEEE Copyright Manager, IEEE Service Center, 445 Hoes Lane, P.O. Box 1331, Piscataway, NJ 08855-1331. All rights reserved. Copyright ©1999 by the Institute of Electrical and Electronics Engineers, Inc.

IEEE Catalog Number: 99CH36366

Library of Congress Number: 88-647453

ISBN Softbound: 0-7803-5573-3 Casebound: 0-7803-5574-1 Microfiche: 0-7803-5575-X

CD-Rom: 0-7803-5576-8

Additional copies of this publication are available from:

IEEE Service Center 445 Hoes Lane Piscataway, NJ 08854-4150, USA

1-800-678-IEEE (1-800-678-4333)

1-732-981-1393

1-732-981-9667 (FAX)

e-mail: customer.service@ieee.org

VOLUME 4: CONTENTS

(A DETAILED TABLE CAN BE FOUND IN VOLUME 1)

Volume 4: POSTER, pp. 2259 - 2962

LOW- AND MEDIUM-ENERGY CIRCULAR ACCELERATORS	2259
SYNCHROTRON RADIATION FACILITIES	2304
FREE-ELECTRON LASERS	2450
ACCELERATOR APPLICATIONS	2513
RADIATION MONITORING AND SAFETY	2608
HIGH ENERGY HADRON ACCELERATORS AND COLLIDERS	2617
INSERTION DEVICES	
COMPUTER CODES	
BEAM DYNAMICS	2808
POST DEADLINE	2936

ACCELERATION OF COCKTAIL IONS AT THE JAERI AVF CYCLOTRON

M. Fukuda, K. Arakawa, S. Okumura, T. Nara, I. Ishibori, Y. Nakamura, W. Yokota, T. Agematsu, H. Tamura, JAERI, Takasaki, Gunma, Japan

Abstract

Ion species and energy of a cyclotron beam can be quickly changed using a cocktail acceleration technique. Cocktail beams of mass-to-charge (M/Q) ratio of 4 and 5 have been developed at the JAERI AVF cyclotron. Purity of the beam depends on the M/Q resolution of the cyclotron. The resolution has been estimated theoretically and experimentally. A radial spread of an internal beam bunch caused by phase slip of particles with a different M/Q value has been observed using a pulsed incident beam. For practical operation, some methods have been devised for avoiding intermixture of different ion species in a beam extracted from the cyclotron.

1 INTRODUCTION

Various ion species with a wide range of energy is available at the JAERI AVF cyclotron facilities [1] for research on materials science and biotechnology. Beam time required for the research ranges from several hours to a few days, relatively shorter than the use for nuclear physics. Frequent change of ion species and/or energy decreases the rate of cyclotron operation, because one through two hours are needed for changing and optimizing all the parameters of the whole cyclotron system. Fast change of the beam without loss of time is required for efficient use of the beam time.

The cocktail acceleration technique [2] is an optimum method for changing ion species and energy quickly. Different ion species having almost identical M/Q values produced by an ECR ion source are simultaneously injected into the cyclotron. The cyclotron parameters are optimized for one of the cocktail ions. The ion is fully accelerated under the isochronous condition given by

$$2\pi \frac{f_{RF}}{h} = \frac{Q}{M} \frac{B_0}{m_0 c^2}, \qquad (1)$$

where f_{RF} is an RF frequency, h a harmonic number, B_0 magnetic field for isochronism, m_0 unified atomic mass unit. Other ions with different M/Q values are gradually shifted an additional amount in phase, given by

$$\Delta \sin \phi = 2\pi h N \frac{\Delta (M/Q)}{M/Q}, \qquad (2)$$

where N is a turn number, and $\Delta \sin \phi$ is expressed as $(\sin \phi - \sin \phi_0)$, that is the change in phase from beginning of acceleration. The ions are phased out when the change in phase becomes +1 or -1. Other ion species can be extracted from the cyclotron by slightly changing the frequency by $\Delta f_{RF}/f_{RF}$ or the magnetic field by $\Delta B/B$ which is proportional to $\Delta (M/Q)/(M/Q)$. Changing of the frequency or the magnetic field is completed within a few minutes.

In addition the energy is approximately proportional to the mass of ions, which offers different linear energy transfer (LET) in a target material. Thus the cocktail beam has great merit in saving the beam time and in covering the wide range of LET.

2 M/Q RESOLUTION

In the development of a cocktail beam using $^{12}C^{3+}$, $^{16}O^{4+}$ and $^{20}Ne^{5+}$ ions, the $^{12}C^{3+}$ and $^{20}Ne^{5+}$ ions were observed in the beam optimized for the $^{16}O^{4+}$ ion [3]. A series of the M/Q=4 cocktail ions available at the JAERI AVF cyclotron are listed in Table 1 together with the M/Q difference from the nearest M/Q values. The M/Q difference of $^{12}C^{3+}$ and $^{20}Ne^{5+}$ ions from the $^{16}O^{4+}$ ion is 3.2×10^{-4} and 0.6×10^{-4} , respectively. The M/Q resolution of the cyclotron was estimated to investigate the intermixture of the different ion species.

Table 1: Parameters of the M/Q=4 cocktail ions

Ion	M/Q	$\Delta(M/Q)/(M/Q)$	E (MeV)	f _{RF} (MHz)
⁴ He ⁺	4.00210	6.6×10 ⁻⁴	25	11.9073
¹² C ³⁺	3.99947	3.2×10 ⁻⁴	75	11.9152
¹⁶ O ⁴⁺	3.99818	0.6×10 ⁻⁴	100	11.9190
²⁰ Ne ⁵⁺	3.99794	5.6×10 ⁻⁴	125	11.9197
⁴⁰ Ar ¹⁰⁺	3.99569	1,1×10 ⁻⁴	250	11.9264
⁸⁴ Kr ²¹⁺	3.99524	1,1×10	525	11.9278

2.1 Theoretical Estimation

The M/Q resolution defined by $R = I(M/Q)/\Delta(M/Q)I$ is equivalent to $If_{RF}/\Delta f_{RF}I$, which is given by differentiating the Eq. (1). The resolution can be estimated from a frequency range at which particles can reach to an extraction radius. Change in phase for the frequency shift $\Delta f_{RF}/f_{RF}$ with non-relativistic approximation is given by

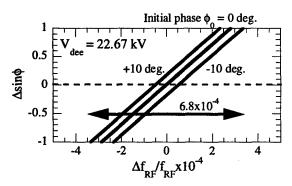


Figure 1: Dependence of the change in phase at the extraction radius on the frequency shift.

$$\Delta \sin \phi \approx 2\pi h \frac{\Delta f_{RF}}{f_{RF}} \frac{r^2}{2} \frac{mc^2}{\Delta E} \left(\frac{2\pi f_{RF}}{hc} \right)^2, \quad (3)$$

where r is a radius, ΔE the peak energy gain. Relation between the frequency shift and the change in phase at the extraction radius is shown in Fig.1. The $\Delta \sin \phi$ is approximately proportional to the frequency change. The frequency range for the beam with an initial phase width of 20 degrees RF is 6.8×10^{-4} . Assuming that a half width of the frequency range gives FWHM, the M/Q resolution is estimated at R=2900. The resolution for the extracted beam will be higher than this, since the beam is defined by acceptance of the extraction system [4].

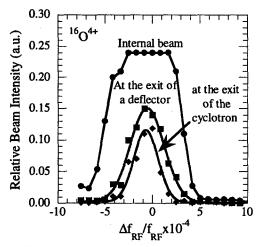
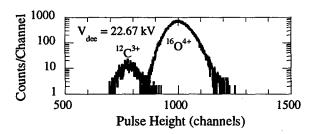


Figure 2: Dependence of the beam intensity on the frequency shift. The frequency shift range is estimated at 8.4×10^{-4} FWHM for the internal beam, 4.2×10^{-4} FWHM for the beam at the exit of the deflector and 3.0×10^{-4} FWHM for the beam extracted from the cyclotron.



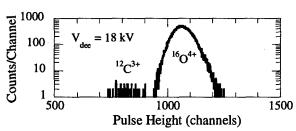


Figure 3: Pulse height spectra of the $^{12}\text{C}^{3+}$ and $^{16}\text{O}^{4+}$ cocktail beam obtained at dee voltages of 22.67 kV (upper) and 18 kV (lower). The yield ratio of the $^{12}\text{C}^{3+}$ ions to the $^{16}\text{O}^{4+}$ ions is 1.6×10^{-2} at 22.67 kV and 0.29×10^{-2} at 18 kV.

2.2 Experimental Estimation

Variation of beam intensity depending on the frequency shift is shown in Fig. 2. The width of the frequency shift for the internal beam just before extraction was 8.4×10^4 FWHM. In this measurement two sets of phase defining slits were placed at the position mostly evacuating from a beam. The phase width of the internal beam was larger than 20 degrees RF. The frequency range became a half at the exit of a deflector, and was further reduced to 3.0×10^4 FWHM after extracting from the cyclotron due to the acceptance of the extraction system. The resolution estimated from the frequency range is around 3300 that is insufficient for separating the $^{12}\text{C}^{3+}$ and $^{20}\text{Ne}^{5+}$ ions from the $^{16}\text{O}^{4+}$ beam.

2.3 Improvement of the Resolution

The amount of the change in phase is inversely proportional to the energy gain as given in Eq. (3). In order to separate the particles with different M/Q values before extraction, decrease in energy gain, that is increase in turn numbers, is required. Pulse height spectra of the $^{12}\text{C}^{3+}$ and $^{16}\text{O}^{4+}$ cocktail beam obtained by a plastic scintillator at a dee voltage of 22.67 kV and 18 kV are shown in Fig. 3. The yield ratio of the $^{12}\text{C}^{3+}$ to $^{16}\text{O}^{4+}$ went down to one fifth by simply changing the dee voltage. Careful optimization of parameters is required for further improvement of the resolution.

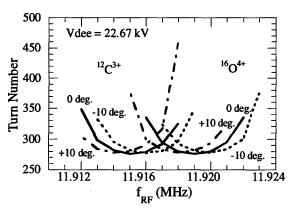


Figure 4: Increase in turn numbers for the ¹²C³⁺ and ¹⁶O⁴⁺ beams with an initial phase width of 20 degrees caused by the frequency shift.

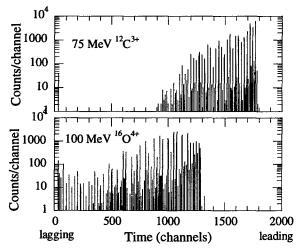


Figure 5: Beam pulses of the ¹²C³⁺ (upper) and ¹⁶O⁴⁺ (lower) ions at the optimum frequency of 19.916 MHz measured with a plastic scintillator.

3 TURN NUMBERS

The amount of change in phase for particles with different M/Q values is linearly increasing with turn numbers as given in the Eq. (2). The calculated turn numbers of the particles reaching to the extraction radius are shown in Fig. 4. The minimum turn number is obtained at the optimum frequency for each ion species.

An increment in turn numbers for the frequency shift of 2.5×10^4 ($\Delta f_{RF} = 3$ kHz) is around 60. The energy gain of the particles is gradually decreasing due to the drift of the beam phase caused by the frequency shift. The particles having lower energy stay in orbits at smaller radii, which causes radial spread of a beam bunch. The radial spread at the entrance of the deflector is larger than the aperture of the deflector. Thus the beam bunch is chopped by the deflector and extracted with multiple turns. Time spectra of the extracted beam at the optimum frequency for $^{12}C^{3+}$ are shown in Fig. 5. The beam was

pulsed before injection using a trapezoidal voltage chopper (P chopper) [5] so that the multiple turns could be observed. The ¹²C³⁺ ions were extracted first, and a pulse train of the ¹⁶O⁴⁺ ions appeared 41 turns later. The delay of the beam pulses was consistent with the calculation result shown in Fig. 4.

4 ELIMINATION OF IMPURITY IONS IN PRACTICAL OPERATION

In order to avoid intermixture of the different ion species in the extracted beam, a grouping of cocktail ions with sufficiently different M/Q values is required for the cocktail acceleration. The choice of the ion species for such grouping is, however, limited, which is lacking in variety for the use of multiple ion species.

Improvement of the M/Q resolution mentioned in the section 2.3 is an orthodox way for reducing the impurity ions. But additional time for parameter optimization might be necessary. This is contrary to the fast change of the beam.

For the practical operation, simplification of the ion species injected into the cyclotron is the easiest way for purification of the beam. In order to save the time for changing a gas supplied to the ECR ion source, the gas supplying system was modified. The capacity of gas pipes was minimized, and a nitrogen gas having an M/Q value far from 4 was used as a common support gas to save the time for purging in the pipes. As a result, the ion species can be changed within ten minutes.

The ⁸⁴Kr²¹⁺ beam contained some metallic ions coming from a plasma chamber of the ECR ion source, since the intensity of the ⁸⁴Kr²¹⁺ ions is low for our ECR ion source. Fortunately the krypton gas consists of some stable isotopes, and the M/Q values of the isotope ions is sufficiently different from the impurity ions. Optimizing the frequency to the isotope ions can purify the krypton beam.

- K. Arakawa, et al., Proc. 13th Int. Conf. On Cyclotron and Their Application, Vancouver, Canada, pp.119-122 (1992)
- [2] M.A. McMahan, et al., Nucl. Instr. and Meth. A253 (1986)1
- [3] M. Fukuda, et al., Proc. 11th Symposium on Accelerator Science and Technology, Harima Science Garden City, Japan, pp.139-141 (1997)
- [4] G. Ryckewaert, et al., Proc. 13th Int. Conf. On Cyclotron and Their Application, Vancouver, Canada, pp.737-740 (1992)
- [5] W. Yokota, et al., Rev. Sci. Instrum. 68 (1997) 1714

CONCEPTUAL DESIGN OF A 240 MeV SUPERFERRIC SEPARATED ORBIT CYCLOTRON *

O.Brovko, A.Butenko, A.Glazov, <u>I.Issinsky</u>*, V.Mikhailov, G.Khodzhibagiyan, A.Shabunov, A.Sukhanova, B. Vasilishin, JINR, Dubna, Moscow Region, 141980, Russia

Abstract

A conceptual design of the Separated Orbit Cyclotron (SOC) for the proton energy of 240 MeV based on the use of superferric magnets (dipoles and quadrupoles) is presented. Superconducting RF cavities are used as well. The beam intensity is determined by, but not limited to the 500µA available from the IBA "Cyclone-30" cyclotron to be used as the 30MeV injector. The electrical power draw of the helium refrigerator is 250kW.

1 INTRODUCTION

The separated orbit cyclotron (SOC) [1,2,3] has a number of attractive advantages over its classical analogues, the greater part of which are very high, close to 100%, coefficients of beam injection and extraction. This SOC's property allows one to deal with the acceleration of currents in the milliampere range at very small beam losses. In this way, the SOC more resembles a linear accelerator than a cyclotron.

By reason of the limited orbit separation determined by the achievable accelerating RF voltage, SOC-type accelerators can be practically constructed only by applying superconducting technology, namely, superferric magnets (dipoles and quadrupoles) of small outside transverse dimensions. Experience gained in the production and use of magnets of such a type [4], confirms their good operating quality. It is also reasonable to use superconducting cavities in the accelerating system.

This work was performed on contract from the HRIBF group at the Oak Ridge National Laboratory as part of their study for high-current drivers for the next generation radioactive beam facility. The conceptual design for the SOC has to meet requirements with the following main specifications: 1)The maximum proton energy should be between 200MeV and 250MeV depending on space. 2)Proton injection could be used with a 30MeV commercial cyclotron. The IBA model CYCLONE-30 at a maximum current of 500µA is accepted here. 3) The total internal beam loss and extraction beam losses must be less than 1.0%.

To research the conditions satisfying a stable motion of

particles without losses, a simulation program was developed. In the program, all main conditions of longitudinal and transversal motion were taken into consideration. According to the evaluated errors in the dipole and quadrupole alignment, the beam envelope, including orbit distortions, was computed. Its size lies within the limits of 42mm x 34mm and determines the aperture and outside dimensions of the magnets, the latter of which are equal to 96mm x 96mm.

2 LATTICE AND BEAM DYNAMICS

The SOC magnet system contains 240 bending-focusing periods with increasing length, divided into 16 sectors. At every turn, the beam traverses 16 periods, each consisting of two dipoles, defocusing and focusing quadrupoles and an accelerating RF cavity.

An isochronous condition is insured by the required length of the periods, which is achieved by combining bending angles in dipole pairs and straight parts of the equilibrium particle trajectory. Sufficient turn separation to clear magnet yokes is achieved by means of 16 accelerating cavities each with a maximum amplitude of 1.2MV. The total number of turns is 15, the final energy and radius are 240.9MeV and 3.526m, consequently. The last turn separation is equal to 97 mm.

Synchrotron motion in $(\Delta t, \Delta w)$ co-ordinates is presented in Fig.1 for a maximum energy spread Δw_m and bunch duration Δt_m at injection. The energy

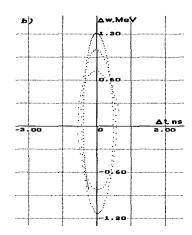


Figure 1: Synchrotron motion at $k_2=0.002$.

^{*}Work supported from Laboratory Director's Research and Development Funds from Oak Ridge National Laboratory, USA.

[#] Email: Issinsky@sunhe.jinr.ru

spread, increasing by the end of acceleration, is equal to 1.2MeV. During the acceleration, there are 2.5 synchrotron oscillations of the particles, and the maximum amplitude of these oscillations is 2.5 mm.

The focusing system of the accelerator represents a symmetric D-O-F-O structure. The dipole magnets are sectored and have zero edge angles. The length of each magnet was chosen so that all magnets had identical fields, equal to 1.4T. The values of the gradients in the defocusing and focusing quadrupole lenses are similar in all sectors and equal to G_D = -57.5T/m and G_F =53.5T/m.

Figure 2 shows a diagram of betatron oscillation resonances to 1-st. 2-nd and 3-rd orders.

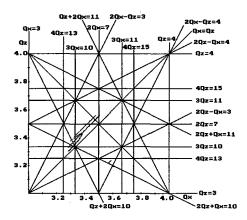


Figure 2: Diagram of betatron oscillation resonances.

A sextupole component of the dipole magnetic field with coefficient $k_2=0.002 \text{cm}^{-2}$ ($\Delta B=k_2Bx^2$) was taken into account. Nonlinearities in the quadrupole lenses were not considered because of their very high orders (fifth and more). In spite of crossing resonance lines, the motion is stable because the phase shift changes from sector to sector rather quickly.

Simulations including magnet alignment errors have been performed. Figure 3 shows tracking results in the

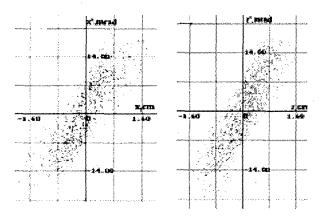


Figure 3: Phase diagram in the horizontal and vertical planes.

horizontal (x,x') and vertical (z,z') planes including misalignment errors to ± 0.4 mm, the $k_2=0.002$ cm⁻² sextupole coefficients. and initial conditions corresponding to emittance at injection $E_x=30\pi$ mm mrad and $E_z=20\pi$ mm mrad. Each point of the figures corresponds to the co-ordinates (x,x') at the focusing lens input and (z,z') at the defocusing lens input. It is seen that beam is well contained within the designed aperture of the magnets.

The acceleration of ions with q/A=1/2 in the SOC can be realised at a smaller ion acceleration rate (on the doubled harmonic) up to 46MeV/amu. In this case the injection energy should be 7.24MeV/amu.

3 SUPERFERRIC MAGNETS

The cross sections of the dipole and quadrupole magnets are presented in Figure 4. Their 2D magnetic fields have been calculated by the POISSON program for ARMCO steel. The investigations performed at the Laboratory of High Energies, JINR show a rather small difference of the saturation effects at helium and room temperature. The computed field distributions show a field inhomogeneity of about 1% in the dipoles and 3% in the quadrupoles.

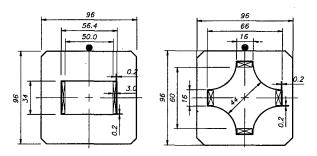


Figure 4: Cross section of the dipole and the quadrupole.

For quench protection reasons, the copper to superconductor ratio of the cable is chosen to be equal to 2:1. This helps to protect the magnet from small disturbances which can produce quenches. The width and thickness of the conductor containing 2970 NbTi filaments is 3.4mm and 1.4mm, respectively. It is insulated with double Capton and fiberglass epoxy layers for a total of 0.2mm thickness.

4 CRYOGENIC SYSTEM

The SOC cryogenic system consists of 16 sectors. Each sector contains 30 dipole and 30 quadrupole magnets with a cold iron yoke.

The equipment is mounted on the supporting sector platforms (Fig.5). Each of the platforms is fastened to the cryostat by suspension rods. The magnets are cooled in series by means of copper cooling tubes, which are soldered to a copper plate and mechanically attached to the iron yokes. Calculations show that the difference of temperatures between the cooling liquid and the s.c. winding is no larger than 0.2 K.

Indirect cooling of the windings is performed by a twophase helium flow. The mass vapour content of helium

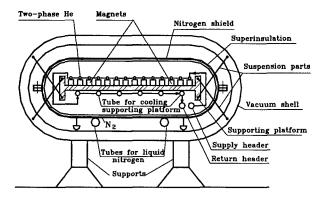


Figure 5: Cross section of the SOC

varies from 0 at the inlet of the sector to 0.9 at its outlet. Two-phase helium flow was chosen to cool the SOC on the basis of operating experience of the Nuclotron cryogenic system [4]. In comparison with two-phase helium, a single-phase coolant (liquid helium) leads to an increase of the helium flow through the magnet and to less efficient cooling. Experience has shown that instabilities in the flow distribution in parallel channels and large oscillations of vapour pressure and flow rate are not a problem with a two-phase helium system.

The cryogenic supply system is based on the TCF50 refrigerator with a 500W nominal capacity at 4.5 K.

The SOC has a common vacuum space for the beam and for cryogenic insulation. The operating pressure provided with cryosorbtion will be smaller than 1×10^{-7} Torr with hydrogen and helium being the major residual gases. No permanent pumps will be installed since none are required if helium leaks are kept small.

5 DESIGN OF THE ACCELERATOR FACILITIES

The SOC equipment is placed in the overall vacuum vessel. It is a ring chamber with an outside horizontal diameter of 9.0m and an oval cross section 0.7m x 3.5m in size (Fig.5). The vacuum chamber is assembled in sections corresponding to the number of sectors. The sectors are fastened by eight suspension rods inside the cylindrical parts. The length of the rods is chosen so that the middle of the platform remains in the initial horizontal plane with a sufficient accuracy after cooling down.

The operating position of the magnets at cryogenic temperature should be held within the limits from ±0.2mm to ±0.4mm relative to the equilibrium orbit. This problem could be solved in several ways: i) by defining the magnet positions through calculations of their expected displacement in the cold state; ii) by preliminary mapping of the footholds in the cold state of the support base on which the magnets are to be arranged afterwards; iii) by installing special windows for optical control of the magnet positions; iv) by adjusting the magnet position; v)by using beam diagnostics and correction systems.

To decrease cooling losses during SOC operation, the number of cryogenic current leads for supplying the magnets is reduced to a minimum: for instance all the dipoles are supplied with their current in series. In this case, the dipoles (formed in sector shape with different curvature radii) must have different lengths. To meet this requirement and to simplify fabrication, all the dipole magnet cores are made of identical stamped steel laminations. Steel laminations are welded or glued together on a mandril, the base dimensions of which correspond to the ones of the magnet gap (Fig.6). The mandril is flexible, and its curvature is adjusted for each dipole separately.

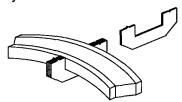


Figure 6: Steel laminations set on the mandril.

A similar mandril is used to fabricate the windings. This technology is used for quadrupole fabrication as well, with the difference of having no curvature and only four lengths.

6 CONCLUSION

From results of simulations, we can conclude that it is possible to accelerate beam with no additional corrections. In any case, provisions are made for horizontal and vertical correctors to compensate for coherent beam offsets.

In summary, the SOC concept is quite practical for high-current beam production in the few-hundred MeV range, and we strongly suggest that it should be further explored.

7 ACKNOWLEDGMENTS

The authors are grateful to Jose Alonso, Jerry Garrett and David Olsen for their support and attention to this work.

- [1]. F.M. Russell, ORNL. Nucl.Instr. and Meth., 23, 1963, p.229.
- [2] U.Trinks. Proc. of the Int. Conf. on Cyclotron. Vancouver, Canada, May 1992.
- [3] I.A.Shelaev. JINR Rapid Communications No.5[62]-93, p.16.
- [4] A.M.Baldin et.al., Proc. of the Cryog. Eng. Conf., Albuquerque, July 1993.

MAGNETIC FIELD CALCULATION FOR A 13 MEV PET CYCLOTRON*

W.Y. Yang, M. Yoon, S. Oh, Dept. of Physics, POSTECH, Korea, J.S.Chai, J.H. Ha, KCCH, Korea

Abstract

A design study of the main magnet for a 13 MeV cyclotron has been carried out in a joint collaboration between the Korea Cancer Center Hospital(KCCH) and POSTECH. A maximum energy of 13 MeV has been chosen to produce radio-isotopes such as ¹⁸F. There are four magnet sectors, each with radial-ridged shape. Maximum magnetic fields are 1.85T and 0.48T at hill and valley centers, respectively. The total size of the cyclotron is less than 2 m in diameter. The program TOSCA has been utilized for the field calculation and optimization. In this paper, we describe design parameters of the 13 MeV PET cyclotron, with emphasis on the magnetic field shape and the beam optics calculation.

1 INTRODUCTION

At the Korea Cancer Center Hospital (KCCH), design study of a 13 MeV cyclotron for Positron Emission Tomography (PET) has been in progress since 1997. The study has been carried out in a joint collaboration between KCCH and the Pohang University of Science and Technology (POSTECH).

The KCCH has played a leading role in Korea in radiation medicine as well as in the treatment and research of cancer, since it was established as the Radiological Research Institute in 1963 to promote the medical application of atomic energy in Korea. For neutron therapy and radiation treatment, a 50 MeV medical cyclotron, built by Scanditronix, was installed at the hospital in 1986. The cyclotron has provided an in-house source of radio-isotopes such as ²⁰¹Tl, ¹²³I, ⁶⁷Ga, etc, and in particular, the shorter-lived radioisotopes for diagnostic or clinical use. In addition to serving in-house duties, this cyclotron has also produced and supplied 15% of all cyclotron based radio-isotopes in Korea. This service has greatly contributed towards awareness of the potential benefits of nuclear medicine afforded by particle accelerators and evoked calls for similar services in other hospitals in Korea. So far only two hospitals have installed dedicated cyclotrons for PET (Positron Emission Tomography) applications, where the isotopes of interest are the four clinically significant positron emitters ¹⁵O, ¹³N, ¹¹C, and ¹⁸F in particular.

At the KCCH, increasing desire for an uninterrupted, reliable and timely supply of the isotopes to customers has prompted obtaining a dedicated 5-13 MeV cyclotron for PET applications and pursuing the purchase of another 30 MeV medical cyclotron in the very near future. A decision has been made to design the PET cyclotron in Korea. This

Email: moohyun@postech.ac.kr

will not only ease the problems associated with maintenance during operation but also keeps the door open for continuous upgrading of the machine in the future. The project is supported by the Ministry of Science and Technology (MOST) of the government, as a part of the 2^{nd} phase of the mid- and long-term nuclear energy research plan. The cyclotron construction project was officially started in April 1999 and is to be completed in three years.

In this paper, we introduce the major parameters of this 13 MeV PET cyclotron with particular emphasis on the magnetic field design and the equilibrium orbit calculation.

2 PARAMETERS

Table I shows major design parameters for the 13 MeV PET cyclotron. Maximum beam energy was chosen to be 13 MeV which is above the threshold energy for ¹⁸F production. A four-sector magnet structure is employed with radial-ridged shape. Hill angle is chosen to be 46 degree, but the effective hill angle seen by the beam increases slightly in radius because the vertex of the hill is not at the center of the cyclotron, as will be described later. For ion source, internal PIG source will be used. Though this will deteriorate the vacuum in the central region, it is more economical and simpler than adopting an external ion source. In order to provide an efficient vacuum conducting path in the central region of the cyclotron, there are four holes in the valley region.

Negatively charged hydrogen ions will be used for acceleration because extraction is much easier than for positively charged ions. Accelerating negative ions has also an advantage in that the maximum extracted energy can be varied easily by simply repositioning the stripping foil.

Magnetic fields at 13 MeV are 1.85 T and 0.48 T at the hill and valley centers, respectively. Maximum average magnetic field is about 1.2 T. Harmonic number is four, and therefore the radio frequency is about 72 MHz. Dee voltage is 40 kV. The energy gain per turn is given by

$$\Delta E = 4qV_{dee} \sin \frac{h\theta_{dee}}{2},\tag{1}$$

where V_{dee} is the dee voltage, h is the harmonic number and θ_{dee} is the dee angle. With V_{dee} =40 kV, h=4, θ_{dee} =43.6°, the energy gain per turn is ΔE =159 kV. The total number of turns to reach 13 MeV is therefore approximately 82.

This work is supported by Ministry of Science and Technology of Korean government

Table I: Main parameters of the 13 MeV PET cyclotron

Table 1. Wall parameters of the 13 MeV FET cyclotron					
Parameter	Unit	Value			
Maximum energy	MeV	13			
Beam species		Negative			
		hydrogen			
Number of sectors		4			
Ion source		Internal			
		negative PIG			
Hill angle	degrees	46.0			
Valley angle	degrees	44.0			
Maximum average					
magnetic field	T	1.2			
Harmonic number		4			
Radio-frequency	MHz	72			
Maximum average radius					
of a beam	cm	43			
Maximum orbit distance					
from the cyclotron center	cm	45			
Maximum magnetic field					
at the hill center	T	1.85			
Maximum magnetic field					
at the valley center	T	0.48			
Beam current	μ A	~20			

3 MAGNET SYSTEM

In the initial stage of the cyclotron design, major cyclotron parameters have been calculated by employing a simple first-order theory [1, 2] in beam optics, from which orbit radius, average magnetic field, fields at the hill and valley, focusing frequencies are determined as a function of beam energy. Fig. 1 shows the side view of the 13 MeV cyclotron. It shows that the height is approximately 93 cm and the diameter is 187 cm. For magnetic field calculation in the

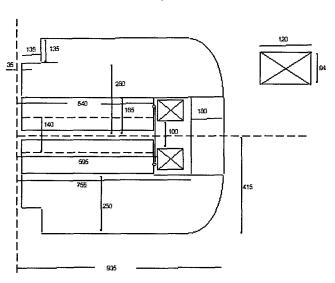


Figure 1: Side view of the 13 MeV cyclotron yoke and valley region, a two-dimensional program such as POISSON [3] has been utilized. Fig. 2 shows the two-dimensional plot of the magnetic field line in the yoke and

valley region, which is obtained with the help of POISSON program. Total current per each coil is 44,000 ampere-turns and the current density is about 3 A/mm².

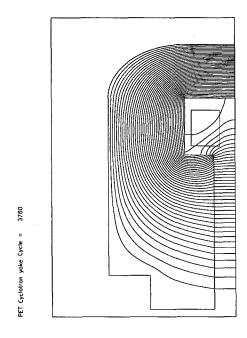


Figure 2: Magnetic field lines computed by POISSON

The OPERA-3D program was used to calculate the three-dimensional magnetic field. Fig. 3 shows the geometry of the cyclotron modeled by the OPERA-3D program. This figure shows four holes at the valley center. Presence of these holes distorts the field greatly. A step by step optimization of the magnet geometry is thus needed.

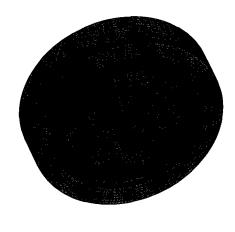


Figure 3: Cyclotron geometry modeled by OPERA-3D In order to maintain the isochronous field, we have em-

ployed a variable vertical gap along the radius in the hill region, rather than using conventional trim coils. This makes the cyclotron operation much simpler, avoiding complicated optimization procedure with trim coils. Simplicity in operation is very important for hospital-based cyclotron where resources for technical support are limited. When the vertical hill gap decreases in steps along the radius, the average magnetic field seen by an accelerating beam is increased in radius. We have been able to obtain a reasonable isochronism by adjusting the hill gaps. Difference in gap height at the minimum and maximum radius is about 6 mm. Fig. 4 shows the average magnetic field as a function of average beam radius. In this figure the average magnetic fields are the averaged fields along the equilibrium orbits. For given magnetic fields, equilibrium orbits are found by solving linearized equations of motion whose details will not be described here.

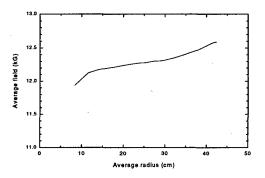


Figure 4: Average magnetic field for the 13 MeV cyclotron as a function of radius

Fig. 5 shows the frequency error due to the magnetic field given in Fig. 4. The vertical axis of this figure indicates $\omega_0/\omega-1$, where ω_0 is a fixed frequency which is basically the radio frequency and ω is the angular revolution frequency of a particle. From this figure, one can obtain the phase error of the particle using

$$\sin\phi(E) = \sin\phi_i + \frac{2\pi h}{qV} \int (\frac{\omega_0}{\omega} - 1)dE, \qquad (2)$$

where the integral extends from the initial energy E_i where $\phi = \phi_i$ to the given energy E. With the above equation applied to Fig. 5, we obtain the total phase excursion is within $\pm 15^{\circ}$.

Horizontal and vertical focusing frequencies (ν_r and ν_z) are also obtained from the equilibrium orbit calculation. Fig. 6 describes the excursion of ν_r and ν_z from injection to extraction radius. The lines in this figure represent $2\nu_y=1$, $\nu_x=3\nu_y, \nu_x=1, 3\nu_x+\nu_y=4, 3\nu_x=4, 3\nu_x-\nu_y=-4$ resonances. Therefore these are the structure(or perfect) resonances arising from the 4-fold symmetry of the magnet. It is seen that focusing frequencies are sufficiently away from the resonances.

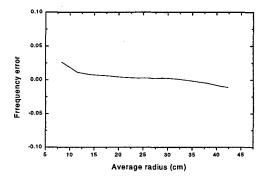


Figure 5: Frequency error as a function of radius for the 13 MeV cycl

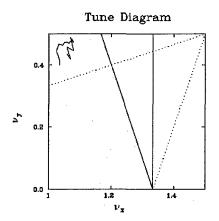


Figure 6: Tune diagram for the 13 MeV cyclotron

4 SUMMARY

In Korea, design studies for a 13 MeV PET cyclotron have been in progress. Currently, design of main magnets and the rf system are being carried out. When completed in 2002, this cyclotron will serve to produce short-lived radio-isotopes like ¹⁸F.

- M. Yoon, J.S.Chai, J.W.Kim, W.Y.Yang and S.Oh, Proceedings of the International Cyclotron Conference, Caen, France, 1998
- [2] S. Oh, W.Y. Yang, M. Yoon, J.S.Chai, J.H. Ha, J.W. Kim, Proceedings of the European Particle Accelerator Conference, Stockholm, Sweden, 1998
- [3] User's Guide for the POISSON/SUPERFISH Group of Codes, LA-UR-87-115, Los Alamos Accelerator Code Group

Studies on Single Turn Extraction for a Superconducting Cyclotron

J.-W. Kim, A. Goto, T. Mitsumoto, and Y. Yano Cyclotron Lab., RIKEN, Japan

Abstract

Feasibility of single turn extraction in a high-field separated sector cyclotron has been accessed. Three key requirements are: 1) larger last-turn separation than the beam width, 2) preservation of beam quality throughout the acceleration, and 3) phase space matching at injection. To enlarge separation of the last-turn orbital precession will be induced at the injection. Traversal of the ν_r =1.5 resonance can affect the radial beam width of light nuclei accelerating to the energy above 300 MeV/u. Tolerance to the gradient field of third harmonic, which causes the half-integer resonance in lowest order, was estimated to be 0.1 gauss/cm. The effects of vertical resonances were also evaluated, and the result was used in the yoke design. Moreover, longitudinal space charge forces were computed for a realistic charge distribution of beam on the estimation of the limiting current.

1 INTRODUCTION

A superconducting separated-sector cyclotron is to be built at RIKEN as the final stage energy-booster of the primary beam in the Radio Isotope Beam Factory (RIBF) [1]. A prototype sector magnet which is a 1/1 scale for the complete design verification, is scheduled to be complete this year [2]. The prototype contains a part of superconducting trim coils and a superconducting injection channel magnet to test the major cyclotron components under actual magnetic fields. The maximum fields in the extraction region of the sector magnet are plotted in Fig. 1 for some design particles.

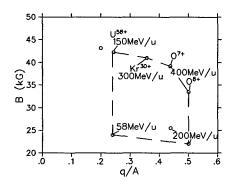


Figure 1: Maximum magnetic fields in the extraction region of the SRC for design nuclei.

To lessen beam induced damages extraction should be carried out without much losses. A larger last-turn separation than the radial beam spread and a preservation of beam quality are the prerequisites for single turn extraction. Orbit trackings have been performed for design nuclei using

isochronized magnetic fields which were obtained by leastsquare fittings with the main and trim coil fields calculated using TOSCA [3] at several different levels of excitations. The tune diagram of those nuclei is shown in Fig. 2.

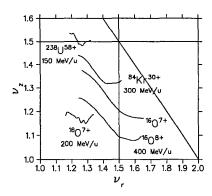


Figure 2: Tune diagram of the design nuclei in the SRC.

The six dimensional phase spaces of beam should be well matched with acceptance of each accelerator to avoid deterioration of beam qualities. The accelerator chain in the RIBF is shown in Fig. 3. We are particularly concerned with matching at the SRC. The transverse phase spaces need additional selection prior to the injection into the SRC. The design of the injection line is underway, and will be described elsewhere.

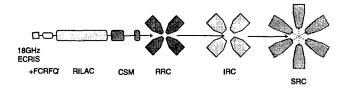


Figure 3: Accelerator chain of the primary beam in the RIBF.

2 ENHANCEMENT OF LAST-TURN SEPARATION

The radius-gain of a beam in cyclotron is given as below

$$\frac{\Delta r}{dn} = r \frac{\gamma}{\gamma + 1} \frac{\Delta E}{E} \frac{1}{\nu_r^2},\tag{1}$$

where γ is the relativistic factor, E is the kinetic energy of beam, and ΔE is the energy gain per turn. The main design particle is a light ion accelerating to the highest design energy 400 MeV/u because of its smallest turn separation. The radius gain of such an ion at the extraction is about 2-3 mm when a practical energy gain by rf cavities is used,

while the radial beam spread is about 4 mm when the beam emittance is 3.5 π mm·mrad. Hence, separation of the last-turn needs to be enlarged.

The major parameters which determine the turn separation are the energy gain and ν_r . In the initial design three cavities, which were symmetrically interspersed among six sectors, were chosen to be used because three unoccupied valleys can comfortably accommodate the flat-top cavity and electrostatic injection and extraction elements. But it was conceived afterward to be worthwhile to employ four cavities at the cost of the simple layout. Figure 4 shows the layouts of both schemes. The adoption of four cavities makes the beam injection more intricate and the placement of the components more congested, but benefits the limiting current by space charge forces. On the other hand, the location of the extraction radius is to be finalized in relation to the ν_r value, while maintaining the necessary field isochronism.

The main cavity is of a single-gap type, the maximum voltage is 600 kV in the extraction region at the power loss of 90 kW, and the voltage of the flat-top cavity is 200 kV at 30 kW [4].

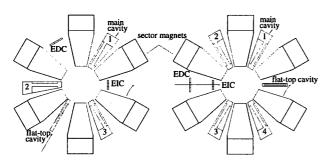


Figure 4: The SRC layouts with three or four cavities. Injection and extraction routes are indicated by arrows.

The last-turn separation is to be enhanced by off-centering at the injection. In usual compact cyclotrons, the orbital off-centering at the traverse of the radial resonance ν_r =1 would hurt beam qualities, but in high energy separated-sector cyclotrons the orbit can be off-centered from the point of injection. The orbit separation with precession can be written as [5]

$$\Delta r_p = \Delta r_c + A sin(2\pi \nu_r), \qquad (2)$$

where Δr_c is the radius-gain of a centered beam, which is the same as Δr of Eq. 1, and A is the amplitude of precession. Figure 5 shows the radius-gain as a function of energy gain when the O^{7+} beam is centered and off-centered. In fact, the radius-gain by three cavities may be sufficient to achieve the extraction efficiency over 99 % for the beam with current of $1p\mu A$ aimed at Phase I of the project [1] insofar as the beam quality is maintained. However, the four-cavity scheme is largely beneficial on the high current operation as demonstrated at the PSI proton cyclotron [6].

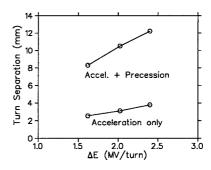


Figure 5: Last-turn separation of the 400 MeV/u O⁷⁺ beam when the beam is centered and off-centered at injection.

3 PRESERVATION OF BEAM QUALITY

3.1 Effects of resonances

Resonance traversal and approach, which affect beam qualities, have been investigated by workers for separated-sector cyclotrons [7]. We have performed similar studies using numerical methods for the SRC which exhibits a larger flutter field and thus stronger vertical focusing force than in existent separated-sector cyclotrons.

When the SRC accelerates light nuclei above 300 MeV/u, the ν_r =3/2 resonance is traversed. In the presence of the gradient field of third harmonic, the radial beam spread will increase above the resonance due to mismatching in eigen-ellipses across the resonance. Tolerance has been estimated, and is currently set to be 0.1 gauss/cm. Figure 6 shows a case of rather significant mismatch by the imposed gradient field of 0.7 gauss/cm. Orbital precession would then become less effective in enhancing separation of the last-turn.

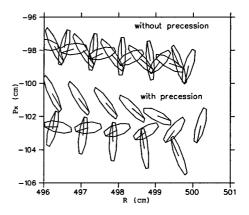


Figure 6: Phase space motion with and without precession near the extraction region. The third harmonic gradient field of 0.7 gauss/cm is imposed.

As shown on the tune diagram in Fig. 2, the ν_z =3/2 is traversed while the ν_z =1 is kept away. This tune arrangement is due to the fact that the integer imperfection resonance is more harmful than the half-integer one. The ν_z of the ions with q/A=0.5 is 1.07 under the design field at the energy around 390 MeV/u, and is 1.08 at 400 MeV/u. The first

harmonic B_r near the $\nu_z=1$, its presence being everywhere in the cyclotron, induces a vertically coherent oscillation whose amplitude (z_{eo}) is given if the smooth approximation is used by

$$z_{eo}(\omega t) = r \frac{\langle B_r \rangle}{\langle B_z \rangle} \frac{1}{\nu_z^2 - 1} cos(\omega t + \phi), \qquad (3)$$

where the bracket indicates an azimuthal average. Considering that the half height of the beam chamber is 3 cm, the first harmonic B_r should be kept much smaller than 10 gauss if the minimum ν_z is 1.07.

3.2 Space charge effects

Space charge forces, transversal and longitudinal, limit the beam current in a cyclotron [8]. The transversal space charge forces are usually crucial at the low energy end of the cyclotron chain, thus at the injection into the RRC, while the longitudinal space charge forces can limit the beam current throughout the chain. The transversal limiting current at the RRC is high in the range of tens of mA. Hence, the effects of longitudinal space charge forces have been mainly considered.

To compute the longitudinal space charge forces, the beam charge distribution should be known, but the actual charge distribution can be complicated especially when the orbits are in precession as seen in Fig. 6. The distribution has been measured for the Ti beam extracted from the RRC [9] as shown in Fig. 7. At the injection point of the SRC the charge distribution was obtained by ion tracking through the transport line which involves a buncher/debuncher for longitudinal phase space matching. The buncher is to be located in between the RRC and IRC.

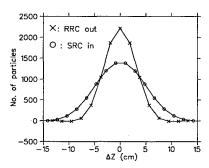


Figure 7: Charge distribution of beam extracted from the RRC as a function of bunch length, which is measured, and at the injection point of the SRC.

The Gordon formalism [10] was used to compute the electric fields of beam bunch as a function of azimuth. The formalism includes image charge effects due to the beam chamber. The electric field as a function of ϕ is given as

$$E_{\theta}(\phi) = 2F_0 G(\phi) \gamma^3, \tag{4}$$

where F_0 is the quantity having an electric field unit and $G(\phi)$ is a dimensionless field function specified by the geometric parameters. $G(\phi)$ was calculated for the SRC beam

with charge distribution of Fig. 7, and is plotted in Fig. 8. The beam height is assumed to be 6 mm with a rectangular charge distribution. Conducting planes are at $z=\pm 3$ cm.

The limiting current is defined as the current when the last-turn separation disappears due to the beam energy spreads induced by longitudinal space charge forces. The maximum electric field at 1 p μ A is about 25 V/m for the O⁷⁺ beam, and the limiting current is estimated to be 3 p μ A.

The dashed line in Fig. 8 indicates a correction of the space charge forces by controlling the relative rf phase between the main and flat-top cavities. If the charge distribution of actual beam has symmetry with respect to the central phase, such a correction is expected.

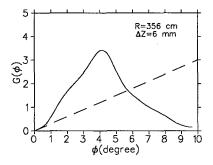


Figure 8: $G(\phi)$ as a function of phase angle assuming symmetric beam charge distribution w.r.t. the central phase. The dashed-line indicates a compensation of maximum E_{θ} .

4 CONCLUDING REMARKS

The number of rf cavity was increased from 3 to 4 for further enhancement of the last-turn separation at the cost of comfortable layout of the cyclotron components. The prototype magnet which is under construction will be used to gain experiences in alignments and thus to better estimate unwanted harmonic field components, as well as to test the performance of the sector-magnet. The longitudinal space charge forces have been approximately computed, so that continual efforts are required along with measurements.

- [1] Y. Yano et al., Proc. of 1997 Part. Accel. Conf., 930 (1997).
- [2] T. Kawaguchi et al., Proc. of 15th Int. Conf. of Cyclotron and Their Applications, in press (1998).
- [3] TOSCA is a product of Vector Fields, Oxford, England.
- [4] N. Sakamoto et al., Proc. of 15th Int. Conf. of Cyclotron and Their Applications, in press (1998).
- [5] W.M Schulte et al., IEEE Trans. on Nucl. Sci., NS-26, 2392 (1979).
- [6] Th. Stammbach et al., NIM B113, 1 (1996).
- [7] M.M. Gordon, Annals of Phys. 50, 571 (1968).
- [8] W. Joho, Proc. of 9th Int. Cyclotron Conf., 337 (1981).
- [9] H. Kumagai, Internal note, Linac Lab., RIKEN, (1998).
- [10] M.M. Gordon, Proc. of 5th Cyclotron Conf., 305 (1969).

MULTI-ORBIT SYNCHROTRON WITH FFAG FOCUSING FOR ACCELERATION OF HIGH INTENSITY HADRON BEAMS

R.Ueno, M.Matoba, *Kyusyu Univ., Fukuoka, Japan*T.Adachi, M.Fujieda, S.Ishi, K.Koba, S.Machida, <u>Y.Mori</u>, R.Muramatsu, C.Ohmori, I. Sakai, Y.Sato, T.Uesugi, K.Umezawa, Y.Yamamoto, M.Yoshii, *KEK-Tanashi, Tokyo, Japan*K.Noda, M.Kanazawa, S.Yamada, *NIRS, Chiba, Japan*

Abstract

Multi-orbit synchrotron(MOS) with fixed field alternating gradient(FFAG) focusing is attractive for acceleration of high intensity hadron beams because acceleration cycle could be increased. The magnetic field of MOS is static, therefore, the repetition rate of acceleration could be increased more than 10 times larger than that of ordinary rapid cycling synchrotron(RCS) if an efficient high voltage RF accelerating system becomes available. Recently, a new type of high gradient RF cavity (HGC) using high permeability magnetic alloy (MA) has been developed and MOS with FFAG focusing becomes very promising. In order to clarify the feasibility of rapid cycling MOS (RCMOS) experimentally, proof-of-principle (POP) machine, which accelerates protons up to 1MeV with 1kHz repetition, is under development. We have also made several designs on high intensity proton accelerators with RCMOS for various applications such as accelerator driven system(ADS) for energy breeder, spallation neutron source and proton driver for muon collider.

1 INTRODUCTION

High intensity medium energy (1GeV~10GeV) proton beams are required for many applications such as spallation neutron source, accelerator-driven system (ADS) for nuclear energy production, proton-driver for muon collider, etc. In these applications, large beam power of more than 1MW is requested. In order to realize such large beam power with ordinary proton synchrotron, rapid cycling of beam acceleration is inevitably. For example, an high intensity cyclotron with superconducting magnets has been discussed for ADS as a possible candidate for the cyclic accelerators. This is believed mostly because of the experience at the PSI cyclotron, which has obtained about more than 1MW beams so far. As for a synchrotron, it has been thought that it would be almost useless for ADS because the operation is a pulsed mode and the average beam current is small. The magnetic field is time varying according to beam acceleration in the synchrotron, the eddy-current power loss in the magnets becomes serious when the repetition rate of the accelerating cycle is increased and the magnetic field ramping exceeds more than 200T/sec. On the other hand, the accelerated particle number per pulse is limited by the space-charge effect. Practically, the maximum repetition of the rapid cycling synchrotron is limited to be less than 50Hz or so. Therefore, the maximum available beam power would be at most about 1MW[1]. However, the beam in the synchrotron is stable, because it is strongly focused in the transverse and longitudinal directions, and the instantaneous beam current in the ring becomes very large. Fixed-field alternating gradient (FFAG) synchrotron, thus, becomes attractive for this purpose.

Another issue is an electric power efficiency in operation of high intensity accelerator. For such large beam power accelerator, the electric power required for operation increases to an acceptable level if the electric power efficiency is small. The operational electric power efficiency of the accelerator is defined by the ratio of the total beam power to the total electric power requested for operation of the whole accelerator system. In order to make the ADS, for example, in a realistic manner, the electrical-power efficiency should be at least more than 30%. The beam power can be expressed by the product of the beam energy and the averaged beam current. The requested beam power for ADS would be at least 10MW. Since a beam energy of 1-3GeV is most practical for ADS if the accelerated particles are protons, the average beam current should be about 10mA. The accelerator comprises mainly the magnet and the rf accelerating systems. During operation, the 80-90% of the total electricity of the accelerator is dissipated for these two systems. The electric power consumed by the magnet system can be dramatically reduced by using a superconducting technique, and can become negligibly small. On the other hand, the electric power dissipated by the rf accelerating system would still be an issue even if a superconducting rf system is applied. The rf electric power for the accelerating cavity system is given by,

$$P = \frac{V^2}{R_s L} .$$

Here, V is the total rf voltage requested for beam acceleration, Rs the effective shunt impedance of the accelerating cavity per unit length and L the total length of the accelerator. In a linear accelerator, the total length of the accelerator should be kept small because of the site limitation and also to minimize the initial construction cost. Thus, a superconducting rf cavity system is inevitably essential in a linear accelerator system to reduce the total rf power requested for operation by increasing the effective shunt impedance. On the other hand, for a cyclic accelerator, such as cyclotron or synchrotron, the situation is more reluctant,

^{*}E-mail: Yoshiharu, Mori@kek.jp

because the cyclic accelerator is regarded as being a very long accelerator. More than 50% electric power efficiency seems to be possible in a cyclic accelerator, even if the normal conducting rf cavity is used.

2 MULTI-ORBIT SYNCHROTRON WITH FFAG FOCUSING

A multi-orbit synchrotron(MOS) using fixed-field alternating gradinet(FFAG) focusing seems to be very attractive for this purpose, because the repetition rate of the accelerating cycle could be raised ten times or more compared to that of the ordinary synchrotron. The idea of a MOS using a FFAG was proposed independently by Ohkawa[2], Symon[3] and Kolomensky[4] in the early 1950's, and electron-beam machines demonstrating this principle have been successfully built in the MURA project.[3] In MOS with FFAG focusing, where the magnetic field is constant in time, the shape of the magnetic field should be such that the betatron tunes for both the horizontal and vertical planes should be constant for all closed orbit, and departing from all of the dangerous resonance lines. The condition above is called "zero-chromaticity".

$$\frac{\partial}{\partial p} \left(\frac{K}{K_0} \right) \Big|_{\vartheta = const.} = 0, \quad \frac{\partial n}{\partial p} \Big|_{\vartheta = const.} = 0.$$

A magnetic field satisfying the scaling conditions described above must generally have the form,

$$B(r,\theta) = B_i \left(\frac{r_i}{r}\right)^n F\left(\theta - \zeta \ln \frac{r}{r_i}\right),$$

Table.1 Fundamental parameters of 1.5GeV FFAG synchrotron.

on.	
Injection Energy	0.25 GeV
Extraction Energy	1.5 GeV
Beam Intensity	5.5x10 ¹³ ppp
Repetition Rate	750Hz
Average Beam Current	6.6mA
No. of Sectors	16
Circumference Factor	2.68
Average Beam Radius	
injection	12.2m
extraction	13.4m
Magnetic Field	
injection	0.536T
extraction	1.5T
Field Index	10.5
Effective Field Index	3.9
Spiral Angle	64.6 deg
Fractional Angle	8.34 deg
Betatron oscillation tune	
horizontal	3.73
vertical	3.23
Transition Gamma	3.442
Max. RF Voltage	0.56MV
RF Frequency	2.39MHz~3.3 MHz

where ζ is a spiral angle. If ζ is zero, the magnetic field does not depend on θ , and the corresponding orbit points are distributed on a radial vector. The type of having this magnetic shape is called "radial sector". One the other hand, if θ behaves in a logarithmic manner, such as

$$\theta - \zeta \ln \frac{r}{r_i} = \text{const.},$$

the orbits remain geometrically similar, but move around the beam center towards larger radii. This type is called " spiral sector".

The MOS with FFAG focusing is very attractive for acceleration intense proton beams as described above and several proposals have been submited.[5][6] However, no practical proton-beam machine has been built so far. One of the most difficult technical issues to realize a high-repetition MOS is rf acceleration. The requested accelerating rf voltage per one turn is

$$\Delta V = 2\pi (1+n) \left(\frac{dr}{dt}\right) p.$$

Here, dr/dt is the orbit excursion rate. In the case of a1GeV MOS with the repetition rate of 1kHz, the requested rf voltage becomes almost 1MV. This is a rather difficult number if an ordinary ferrite-loaded rf cavity is applied, which

Design of magnet

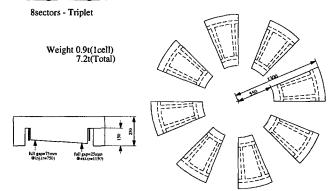
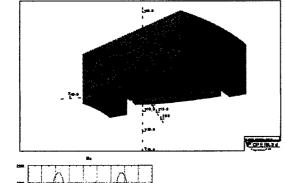


Fig.1 1MeV MOS proof-of-principle machie.

has been conventionally used for the proton synchrotron so far. In the ordinary ferrite-loaded rf cavity, the maximum accelerating field gradient is at most 10 kV/m or so. Therefore, more than 100m long straight sections are necessary for the rf cavities in the ring, although the total circumference of the 1GeV MOS would be less than 150m. Recently, a new type of high-gradient rf cavity using a high-permeability magnetic alloy has been developed at KEK for the JHF project, and a field gradient of 100kV/m has been successfully achieved. [7] Using this high-gradient cavity, the most difficult technical issue in realizing a high-repetition MOS can be solved.

A preliminary design of the 1.5GeV and 10MW beam power MOS with FFAG focusing has been carried out.[8] The fundamental parameters are listed in Table 1.



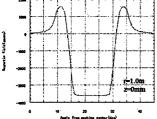


Fig.2 Magnetic field configuration calculated with OPERA-3D.

3 1-MeV AND 1-kHz POP MACHINE

In order to clarify the availability of very rapid cycling in MOS with FFAG focusing, we have been developing a small POP(proof-of-principle) machine. In this POP machine, the maximum energy is limited to 1MeV but the repetition rate of acceleration is 1kHz. The magnet configuration is a radial sector type and eight fold symmetry is chosen as shown in Fig.1. Each sector consists of three dipole magnets which form a triplet focusing configuration DFD(defocus-focus-defocus) and field index of each dipole magnet is 2.5, respectively. The maximum magnetic fields of the focusing and defocusing dipole magnets are 0.5T and 0.2 T, respectively. The magnetic field configurations in three dimensional directions are calculated with OPERA-3D (Fig. 2) and their results are used for beam tracking simulation. The average beam radius changes from 0.81m to 1.13m according to the increase of beam energy from 100keV to 1.1MeV. The half gap heights of the magnet at the radius of 0.75m and 1.15m are 73mm and 25 mm, respectively.

The betatron tunes for horizontal and vertical directions are varied with field index and the product of the magnetic field and the effective magnet length (Bl-product). The lines in Fig. 3 show the variations of the betatron tunes for both directions calculated with the SAD code. The design values of betatron tunes for horizontal and vertical directions are 2.25 and 1.35, respectively. The open squares and circles in Fig. 3 show the betatron tunes for two differ-

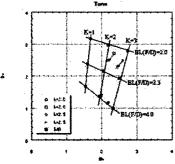


Fig. 3 Betarton tune diagra of 1MeV POP machine..

ent field indices of 2.5 and 2.0, respectively, which are obtained with beam tracking simulation for 3D magnetic field configurations presented in Fig. 2. The betatron tunes are slightly different from those estimated by SAD and change gradually during acceleration. The beam behaviors in the transverse direction obtained by beam tracking simulation are shown in Fig. 4. The rf frequency changes from

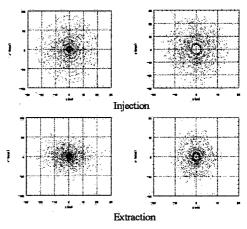


Fig. 4 Particle tracking simulation in transeverse direction.

0.85MHz to 2.05MHz. At the condition of the constant radial displacement as a function of time (dr/dt=const.), the rf voltage has to be increased from 1.1kV to 3.1kV. This rf voltage can be easily obtained by a magnetic alloy(MA) loaded rf cavity.[7] The longitudinal beam motions calculated by beam tracking simulation are shown in Fig.5.

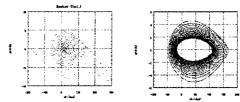


Fig.5 Particle tracking simulation in longitudinal direction.

4 SUMMARY

A 1.5GeV and 10MW multi-orbit proton synchrotron (MOS) with fixed field alternating gradient (FFAG) focusing has been designed. Although the repetition rate for accelerating cycle is rather high, 750 Hz, the required rf voltage is relatively small, only 580, because of its small ring size. A 1MeV POP(proof-of-principle) proton machine with 1kHz repetition is under development.

- [1] JHF Accelerator Design Study Report, KEK Report 97-16.
- [2] T.Ohkawa; Proc. of annual meeting of JPS (1953).
- [3] K.R.Symon et al.; Phys. Rev. 103 (1956) 1837.
- [4] A.A.Kolomensky et al.; ZhETF 33,298(1957).
- [5] R.L.Kustom et al.; IEEE, NS-32, 2672 (1985).
- [6] H.Sasaki; GEMINI Design Report, KEK-Report (1985).
- [7] Y. Mori, Proc. of EPAC98, Stockholm, 1998, page 299.
- [8] Y.Mori, Proc. of Thorium Fuel Cycle, Genshikaku Kenkyu, 43(1999)27.

NUMERICAL STUDIES OF A SECOND HARMONIC RF CAVITY FOR THE IPNS RCS*

J. C. Dooling*, F. R. Brumwell, G. E. McMichael, M. E. Middendorf, and R. A. Zolecki, ANL, Argonne, IL

Abstract

The Intense Pulsed Neutron Source (IPNS) Rapid Cycling Synchrotron (RCS) delivers 450-MeV protons in 70 ns pulses at 30 Hz to a heavy-metal target producing spallation neutrons for material science research. The average current extracted from the RCS is 15 µA with a peak intensity of 10 Amps. The large circulating currents in the RCS generate oscillations in the bunch which are presently controlled by modulating the phase of the two rf cavities. By adding second harmonic (SH) rf, the bunch length can be increased reducing the peak current. Simulations suggest that a 20-40 percent increase in extracted current should be achievable. The simulation program allows for phasing between fundamental and SH rf voltages. Initial studies to optimize phase indicate the need to maximize bucket area early in the acceleration cycle, whereas bunching factor is more significant later in the cycle.

1 INTRODUCTION

During the 1998 Fiscal Year, the Intense Pulsed Neutron Source (IPNS) conducted 354 experiments and was oversubscribed by almost a factor of two. IPNS is looking at several options to accommodate the demand for neutrons. One option is to increase the neutron flux available from the source by raising the incident proton beam current. Installing a second harmonic (SH) rf cavity in the RCS will increase the current limit of the synchrotron and decrease capture losses. The SH rf cavity should raise proton current to the target by 20-40 percent. Based upon this increase, IPNS could conduct an additional 100 experiments annually. Alternatively, higher current would improve the signal-to-noise ratio in collected data or provide better resolution for experiments.

SH rf was first proposed for the IPNS in the early 1980's but not pursued due to funding constraints and loss of personnel[1]. Elsewhere, ISIS is preparing to install a SH system which is expected to result in a 50 percent increase in current from their RCS[2,3].

2 MODELING

Several approaches are used to model capture and acceleration in the RCS. A longitudinal particle dynamics

code, CAPTURE_SPC[4,5](CAPT) is employed to study trapping and loss of injected beam including the effects of space charge. A predictor-corrector algorithm is used to independently compare phase-space area to that calculated with CAPT for the case of no space charge. Both analyses yield essentially identical results for the bucket phase-space area. The evolution of RCS bucket size during the acceleration cycle is shown in Figure 1.

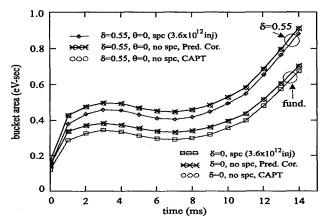


Figure 1: Evolution of stable phase-space in the RCS showing the effect of SH rf and space-charge

Longitudinal equations of motion for energy and phase may be written as,

$$\frac{\mathrm{d}}{\mathrm{dt}} \left[\frac{\Delta E}{\omega_{\mathrm{o}}} \right] = \frac{\mathrm{q}}{2\pi} \left[V(\phi, \theta) - V(\phi_{\mathrm{s}}, \theta) + V_{\mathrm{sc}}(\phi) \right] \tag{1}$$

$$\frac{\mathrm{d}}{\mathrm{d}t}\Delta\phi = \frac{\hbar\omega_0\eta}{\beta^2 E_s}\Delta E_s \tag{2}$$

where q is the charge, V is the amplitude of the rf voltage, φ is the phase of the bunch with respect to the rf, h is the harmonic number (h=1, in the IPNS RCS), ω_o is the cyclotron frequency, η is the slip factor, $\beta=v/c$, E is the total energy of the particle, and the subscript s refers to the synchronous particle. In the RCS β varies from 0.316 at injection to 0.737 at extraction corresponding to a frequency range of 2.21-5.14 MHz. Allowing for the presence of a second harmonic,

^{*}Work supported by U.S. DOE, Contract W-31-109-ENG-38

^{*}Email: jcdooling@anl.gov

$$V(\phi, \theta) = V[\sin(\phi) - \delta\sin(2\phi + \theta)]$$
 (3)

where δ is the ratio of second to first harmonic amplitudes and θ is phase shift. The space charge term may be expressed as,

$$V_{sc} = -q \frac{d\lambda(\phi)}{d\phi} \left[\frac{Rg_o}{2\varepsilon_o \gamma^2} - L\beta^2 c^2 \right] \frac{1}{R^2}$$
 (4)

where λ is line density, g_o is the capacitive coupling factor, and L is total inductance per turn. CAPT tracks particles using a leap-frog algorithm to achieve second-order accuracy. Figure 2 presents phase-space and separatrix results for the RCS with fundamental-only rf, 8 ms after injection. A gaussian energy spread is assumed at injection with $\Delta p/p=0.3$ percent, FWHM.

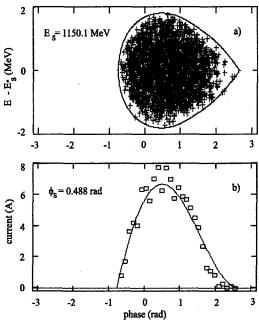


Figure 2: a) Bunch and phase-space from CAPT and b) current profiles from CAPT (\square) and HP (\longrightarrow) for fundamental-only rf at t=8 ms.

2.1 Bunch Factor

With proper phasing, SH rf raises the bunch factor (BF) by flattening the longitudinal current density profile. Reducing the peak current density is one method of delaying the onset of current-driven instabilities[6,7]. BF is defined as,

$$BF = \frac{1}{2\pi} \int_{\phi_1}^{\phi_2} \frac{I(\phi)}{I_{max}} d\phi$$
 (5)

The original implementation of CAPT has been modified to allow for variation in θ to optimize BF. In Figure 3, CAPT results are presented with δ =0.55 and θ =-1.072 rad,

which maximizes BF at 0.487; for the fundamental-only case shown in Fig. 2, BF=0.306. In both cases, the same rf voltage program is used.

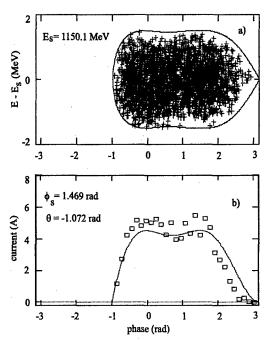


Figure 3: Same as Fig. 2 but with SH (δ =0.55) and θ to maximize BF.

2.2 θ and Losses

Modifying θ can help reduce acceleration losses. For the IPNS rf voltage program, the bucket tends to shrink until reaching a minimum near B max. CAPT predicts that after the initial trapping loss, particles continue to leave the bucket as the bunch is accelerated. The bunch fills the entire available phase-space after capture; therefore, any reduction in the bucket size will result in losses. The reduction in bucket size between 3 and 7 ms is evident in For a given δ , maximizing BF during the acceleration cycle by varying θ , results in a smaller stable phase-space area (bucket size) than with $\theta=0$. resulting loss can be seen in Figures 4 a) and b). Note that overall efficiency is improved relative to the θ profile where BF is maximized (θ_m) . However, to increase the current limit of the machine, θ should be varied to increase the BF. The simulation shows that it should be possible to adjust θ to maximize bucket size early in the cycle, then increase the BF to reduce the peak currents during the later stages of acceleration. One possible strategy is presented in Figure 5. The SH phase angle is kept at 0 until B max (8 ms, just after the minimum bucket size), then ramped to θ_m at t=10 ms. The BF is brought to its maximum value after B_{max} , where stable phasespace is increasing with time and, according to the analysis, acceleration losses cease.

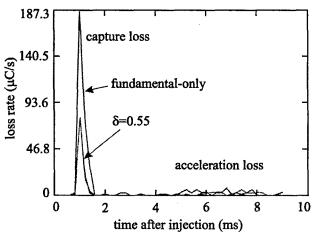


Figure 4a: Capture and acceleration losses

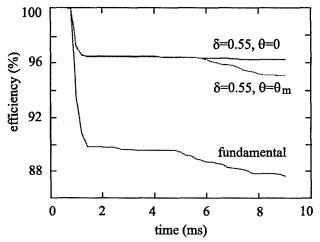


Figure 4b: Integrated loss rate for three rf cases: δ =0.55, θ =0; δ =0.55, θ = θ_m ; and fundamental rf only.

3 CURRENT LIMITS

Hoffman-Pedersen (HP) distributions[7] are used to examine current limits in the RCS. HP current profiles are shown in Figures 2 and 3 along with CAPT results. For the case of fundamental-only rf, peak current values at 8 ms are 6.7 A and 7.1 A from HP and CAPT, respectively; using SH rf with amplitude and phase as shown in Fig. 3, the peak currents are 4.5 A and 5.1 A. HP analysis indicates a microwave instability current limit for the machine in the range of 10-11 A. In the fundamental case just prior to extraction, peak current has risen to 10.8 A according to CAPT, in agreement with current-toroid measurements. With phased SH rf, near extraction time, calculations with CAPT predict a peak current of 7.8 A for the same injected charge.

Presently, the IPNS RCS is operating close to its current limit. By introducing SH rf with a third cavity, it should be possible to raise the current delivered to the target by 20-40 percent.

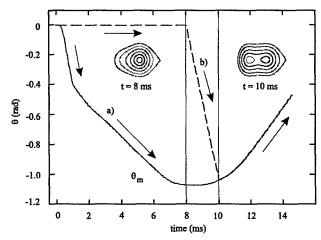


Figure 5: Phasing of the SH rf for a) maximum BF and b) better transmission (δ =0.55). Phase-space contours before and after the ramp are also shown.

- J. Norem, F. Brandeberry, and A. Rauchas, IEEE Trans. Nuc. Sci., 30(4), 3490(1983).
- [2] C. R. Prior, Proc. of the Twelfth Meeting of the International Collaboration on Advanced Neutron Sources, Abingdon, May 1993, RAL 94-025, Vol. II, p. A-11.
- [3] M. R. Harold, M. G. Glover, I. S. K. Gardner, and R. G. Bendal, "A Proposal to Improve the Performance of ISIS," ISIS Management Committee Report IMC/P16/96, 1996.
- [4] Y. Cho, E. Lessner, K. Symon, Proc. European Particle Accelerator Conf., p. 1228, (1994).
- [5] E. Lessner and K. Symon, Computational Accelerators Physics, Williamsburg, Virginia, September 1996, AIP Conf. Proc. 391, p.185 (1997).
- [6] P. Bramham, S. Hansen, A. Hofmann, E. Peschardt, IEEE Trans. Nuc. Sci., 24(3), 1490(1977).
- [7] A. Hofmann and F. Pedersen, IEEE Trans. Nuc. Sci., 26(3), 3526 (1979).

INJECTING RHIC FROM THE BROOKHAVEN TANDEM VAN DE GRAAFF*

J. Benjamin, C. Carlson, I. Feigenbaum, M. Manni, <u>D.B. Steski</u>, P. Thieberger AGS Department, BNL, Upton, NY, 11973, USA

Abstract

In preparation for the start of experiments using the Relativistic Heavy Ion Collider (RHIC) at Brookhaven National Laboratory (BNL), several significant upgrades and improvements were made at the Tandem Van de Graaff. Ion source developments have increased the beam current injected into the tandem, while improvements in foil manufacture and quality control have resulted in better transmission and longer lifetimes for the carbon stripper foils. An oscillating stripper foil chamber has been successfully operated in the high voltage terminal. These improvements have increased the amount of gold ions available from the tandem to $9x10^{\circ}$ ions per pulse, which is a factor of three increase in the last 3 years.

A second tandem Van de Graaff is presently being upgraded and connected to the tandem-to-booster transfer line. Once the upgrade is complete both tandems will have the ability to deliver ions to RHIC. It will also be possible for one tandem to inject RHIC while the other provides beam to a local target room, or to an application facility at the AGS Booster.

1 INTRODUCTION

The two MP Tandem Van de Graaffs (MP6 and MP7) at Brookhaven National Laboratory (BNL) began providing heavy ions to local target rooms in 1970. In 1986 a transfer line approximately 680 meters long allowed the tandems to directly inject heavy ions into the Alternating Gradient Synchrotron (AGS) for further acceleration. With the completion of the Booster Synchrotron in 1992 the transfer line was extended and gold ions could be accelerated in both the Booster and the AGS. In May of 1999, the Tandem Van de Graaffs will enter a new era when MP7 begins delivering gold ions for the Relativistic Heavy Ion Collider (RHIC).

The accelerating scheme for RHIC is shown in figure 1. Negative ions are produced by a cesium sputter ion source and then are accelerated to the terminal of the tandem. There the beam passes through a $2 \mu g/cm^2$ carbon stripper foil and is stripped to the +12 charge state. The gold ions are accelerated back to ground potential where they are stripped to the +31 or +32 charge state using an

object stripper foil approximately 13 μ g/cm² thick. This beam is then transported to the Booster where it is accelerated further, stripped, transferred to the AGS where it is again accelerated and stripped, and finally fills the two counter-rotating rings of RHIC.

RHIC ACCELERATION CONFIGURATION

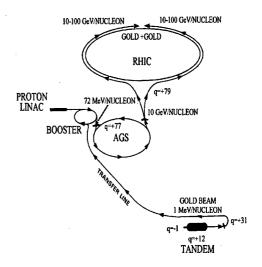


Figure 1: RHIC Acceleration Configuration

The Booster requires short pulses of high charge state beams at approximately 1MeV/nucleon. To achieve this the terminal of MP7 is run at 14 MV and the cesium sputter ion source is operated in a pulsed beam mode[1]. Pulsing the ion source allows several orders of magnitude higher instantaneous beam currents to be injected into the tandem than conventional DC operation without damage to the accelerator. The pulse length from the ion source can be as long as 2 msec however it is usually operated at between 500 usec and 1000 usec. For the AGS fixed target program the acceleration cycle typically calls for the tandem to deliver a pulse once every 3.5 sec. In the collider mode of operation the requirements are to deliver 4 pulses separated by 200 msec once every 3.5 sec for approximately 1 minute, until both rings of the collider are full[2]. The next request to fill the rings should occur on the order of 10 hours later.

^{*}This work performed under the auspices of the U.S. Department of Energy

^{*}Email: Steski@bnl.gov

The experience gained by injecting heavy ions into the AGS and the Booster has led to a number of improvements in the last few years. The improvements that have been made or are planned in the near future are discussed below.

hoped that further increases will be possible by reducing the space charge forces of the beam and by finding a more abundant negative molecule.

2 ION SOURCE IMPROVEMENTS

There has been a research and development effort for a number of years to improve the performance of the cesium sputter sources. The results of this effort can be clearly seen in figure 2, which shows the increase in peak beam intensity versus year. There has been a three-fold increase in the peak intensity available to the booster in the past three years. The increase has been mainly a result of efforts to reduce the large space charge forces experienced by the ion beam.

One of the methods used to reduce the space charge forces was to increase the energy of the ion beam. Beginning in 1996 the original General Ionix 860 [3] source was replaced by the Peabody Scientific PSX-120 [4] ion source. This allowed the ion source beam energy to be increased from 25 keV to 32 keV. The highest demonstrated current was 90.4 μ A of Au⁺³¹ when injecting at a beam energy of 35 keV. For a pulse length of 500 μ sec this corresponds to $9x10^9$ ions per pulse, which is double the intensity specified in the RHIC Design Manual[5].

Although limited research has been done at higher injection energies, it appears possible to deliver approximately 120 μ A of Au⁺³¹ or 12x10⁹ ions per pulse when using an extraction voltage of 50 kV. To operate reliably at 50 kV some minor modifications to the ion source will have to be made. The effects of these modifications on the beam optics of the ion source will have to be investigated.

Another improvement made was the insertion of an einzel immediately downstream of the ion source. First tried in 1997, this compensated for the blow up of the low energy ion beam and allowed higher beam currents to be transported to the entrance of the tandem.

There has also been a growing interest in accelerating uranium beams in RHIC. Unfortunately uranium does not form an abundant negative ion. Therefore the effort has concentrated in finding a suitable molecule that readily forms a negative ion. Preliminary results indicate that UO- is formed in sufficient quantity to provide usable beams. Using a uranium sputter target with a hole drilled in the middle to allow oxygen to be bled onto the surface and a unique pulsing scheme, a pulse with a peak intensity of 34 µA of UO- has been generated on the ion source test bench. Scaling this number to MP7 and using the efficiencies generated from the gold beam, this should generate a pulse with a peak intensity of 25 µA of U⁺³¹. For a 600 μsec pulse, that would be 3x10⁹ ions per pulse. Although this intensity is much less than the gold beam, it should be usable for RHIC. Because the research to produce a uranium beam for RHIC has just begun, it is

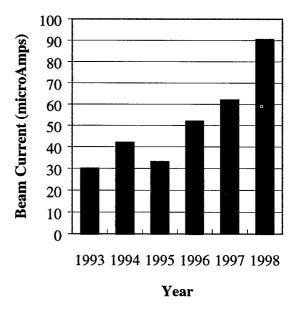


Figure 2: Peak Gold Intensity vs Year

3 IMPROVEMENTS IN STRIPPER FOILS

The thickness and lifetime of the carbon stripper foils have a profound effect on the quality and quantity of the ion beam delivered to the booster.

The thickness of the foils at the center terminal determines the transmission of the beam through the tandem. The thickness needs to be as close to $2 \,\mu g/cm^2$ as possible. To insure that the foils are of the proper thickness they are tested using an optical densitometer prior to being installed in the accelerator. A program is also under way to test the foils offline by looking at the energy lose through the carbon foils of a low energy Hebeam.

Once RHIC is operating with a beam survival of 10 hours, the lifetime of the terminal stripper foils will become less of a problem, as each foil will last for several days. However, during the setup phase, when high intensity pulses will be required every 3 seconds, the stripper foil lifetime will be very important. To improve the lifetime, an oscillating foil holder containing 300 foils has been installed in the terminal of MP7. The dimensions of the terminal foils were increased to 2.2 cm by 1 cm to allow for the 1.25 cm movement of the oscillator. The period of the oscillator was approximately 1 minute when it was first used during the 1998 heavy ion run. The average oscillating foil lifetime was approximately 6

hours, compared to the 2-hour lifetime of the stationary foils.

Although the object foils have a longer lifetime, an oscillating foil holder has also been installed at this position. The object foil oscillator is not operated continuously but rather is occasionally moved to a different spot. This has allowed object foils to last in excess of 24 hours.

4 MP6 UPGRADE AND THE INTERCONNECTING LINE

Presently the MP6 tandem Van de Graaff is undergoing the same upgrade as was completed on MP7[6] in the early 1980's. One of the major upgrades is to replace the existing accelerator tubes with longer tubes. Seven of the present 190 cm accelerator tubes have been replaced with 223 cm tubes, while the first tube has been replaced with a 244 cm tube of which the first 40 cm is half gradient. This has increased the active length of the tandem by 22% and will increase the maximum operating voltage.

Some of the other improvements to MP6 include more vacuum pumping along the accelerator tubes, the addition of 3 more pelletron chains for charging, and improved voltage dividers for the accelerator tubes and the support column. These improvements will make the two machines almost identical and allow MP6 to reach a terminal voltage of 14 MV reliably.

Once the upgrade is completed an inter-connecting line will bring the ion beam from MP6 to the existing MP7 beamlines. The interconnecting line consists of four 25-degree dipoles and one 90-degree dipole. The first two 25-degree dipoles will deflect the ion beam around MP7. If the beam is required in one of the local target rooms the 90-degree magnet will bend the beam into the existing image leg of MP7. However, if the beam is being used to inject RHIC then the other two 25-degree dipoles will deflect the beam into the MP7 object leg and into the tandem-to-booster transfer line.

The inter-connecting line will allow MP6 beam to be delivered to local target rooms at the same time that MP7 beam is being injected into RHIC. It will also allow the beams from MP6 to be diverted to RHIC if needed.

The fourth 25-degree dipole that is shared by the inter-connecting line and the MP7 object leg is a fast switching magnet. This will allow one beam to be delivered to RHIC from MP7 and then 3 seconds later a different species to be delivered to RHIC from MP6. This has uses for asymmetric ion species in RHIC with the same rigidity and will also allow different beams to be delivered to the Booster Application Facility.

5 CONCLUSIONS

The Brookhaven tandem Van de Graaffs have already surpassed the RHIC design specification and there are plans to increase the intensity further. The upgrade of MP6 and the interconnecting line are under construction and when completed will allow the target room user program to operate at the same time as RHIC. The tandems have proved themselves to be versatile reliable injectors for the AGS synchrotrons and with the number of recent improvements and upgrades they should prove to be just as reliable for RHIC.

- [1] Thieberger P., McKeown M., and Wegner H.E., IEEE transactions on Nuclear Science, NS-30 No. 4, 2746-2748, (1983)
- [2] RHIC Design Manual, http://www.agsrhichome.bnl.gov/NT-share/rhicdm/
- [3] Distributed by High Voltage Engineering Europa, P.O. Box 99 AB Amerfort, The Netherlands
- [4] Distributed by Peabody Scientific, Peabody, Ma, 01960, USA
- [5] RHIC Design Manual, http://www.agsrhichome.bnl.gov/NT-share/rhicdm/
- [6] Thieberger P., Nucl. Instr. And Meth. 220 (1984) 45-53

BARRIER CAVITIES IN THE BROOKHAVEN AGS*

M. Blaskiewicz[†], J.M. Brennan, T. Roser, K. Smith, R. Spitz, A. Zaltsman, BNL, Upton, NY 11973, USA M. Fujieda, Y. Iwashita, A. Noda, Kyoto University, Gokanosho, Uji, Kyoto 611, JP M. Yoshii, KEK, 1-1 Oho, Tsukuba 305, JP Y. Mori, C. Ohmori, Y. Sato, KEK - Tanashi, Tanashi 188, JP

Abstract

In collaboration with KEK two barrier cavities, each generating 40 kV per turn have been installed in the Brookhaven AGS. Machine studies are described and their implications for high intensity operations are discussed.

1 INTRODUCTION

During the 1998 high energy physics run the rf system in the AGS Booster ran with harmonic number h=1, and the AGS ran with h=6. This allowed for six Booster transfers per AGS cycle, even though the machine circumferences are in the ratio 1:4. Running the Booster with h=1 opened up the possibility of emittance conserving barrier bucket manipulations using two dedicated barrier cavities. The controls were set up to allow barrier cavity operation in a "pulse stealing" mode wherein the machine settings for the production cycle were changed to those appropriate for barrier operations for a few machine cycles and then switched back to the production cycle settings. This allowed for machine studies and hardware development over the entire run.

The principles of barrier cavity operation have been described elsewhere [1, 2, 3]. This paper focuses on hardware configurations and conclusions.

2 EXPERIMENTAL SETUP

The cavity and amplifier parameters are summarized in Table 1. As is clear from the table the two devices are quite different. The large R/Q of the cavity supplied by KEK allows the use of a small amplifier but requires beam loading compensation at moderate beam currents. The feedforward system is broad band with a full turn of delay[4]. The voltage waveforms without beam, corrected for uncompensated capacitive dividers, are shown in Figure 1. Dynamical implications are considered next.

Let T_0 and E_0 be the revolution period, and synchronous energy, respectively. Denote the arrival time of a proton as $nT_0 + \tau$ on the *n*th turn and let $\delta = E - E_0$ be its relative energy deviation. The proton equations of motion

Table 1: Cavity parameters

Parameter	BNL cavity	KEK cavity	
core material	ferrite	Finemet ¹	
gaps per cavity	4	4	
$f_{ m res}$	2.6MHz	1.1MHz	
R/Q per gap	180Ω	1500Ω	
Q	30	0.6	
coupling	single ended	push-pull	
amplifier rating	600 kW	30kW each	
beam loading correction	none	feed-forward	

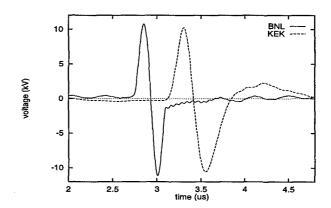


Figure 1: Gap voltage without beam over one AGS revolution period.

are derivable from the Hamiltonian

$$H(\tau,\delta) = \frac{\eta \delta^2}{2\beta^2 E_0} - q f_0 \int_0^\tau V(t') dt', \tag{1}$$

where η is the frequency slip factor, $\beta = v/c$, q is the proton charge, and f_0 is the revolution frequency. The equations of motion are $d\tau/dt = \partial H/\partial \delta$ and $d\delta/dt = -\partial H/\partial \tau$. The integral of the voltage waveform is proportional to the longitudinal potential well and the familiar pictures of introductory mechanics are applicable.

The voltage integrals without beam are shown in Figure 2. Protons are repelled from high potential regions and undergo stable oscillations in low potential regions. Measurements were made using low intensity small emittance injected bunches to map out the potential wells. It was found that potential in the off-pulse region of the BNL cavity is flatter than show in the figure, which is consistent with the

^{*} Work supported by US Department of Energy

[†] Email: mmb@bnl.gov

¹Trademark, Hitachi Metals, Ltd.

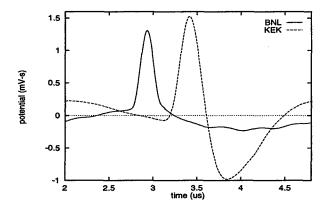


Figure 2: Integral of gap voltage without beam.

measured gap current for this cavity. The local minima in the KEK integral appear to be real.

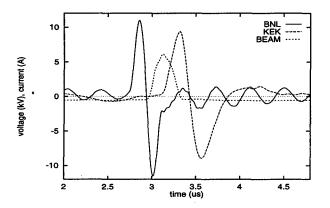


Figure 3: Gap voltage with beam and beam current. The feedforward on the KEK cavity is optimized.

Figure 3 shows the voltage waveforms of the BNL and KEK cavities along with the beam current. The oscillation in the BNL waveform is at the cavity resonant frequency with a decay rate consistent with the measured Q. The bunch contained 8.5×10^{12} protons; about the number required for the barrier cavity rf system to compete with the traditional rf system. Figure 4 shows the voltage integrals with beam.

3 MULTIPLE TRANSFERS

Controls for the barrier bucket system allowed multiple transfers, time dependent adjustment of the relative phase of the barriers, and amplitude modulation of the KEK waveform. Figure 5 shows a mountain range plot of cavity voltage used to accumulate five (5) Booster transfers. The BNL cavity was pulsed at the revolution frequency. The KEK cavity had a programmed delay and its amplitude was modulated to minimize emittance growth during coalescence. The first (bottom most) trace was taken about 100 ms after the first Booster transfer. There was 150 ms between transfers. Figure 6 shows the beam current for the same cycle as Figure 5. The ripples evident during de-

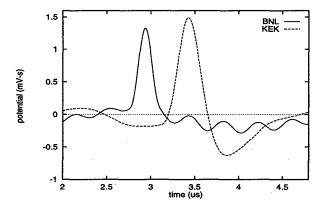


Figure 4: Integral of gap voltage with beam.

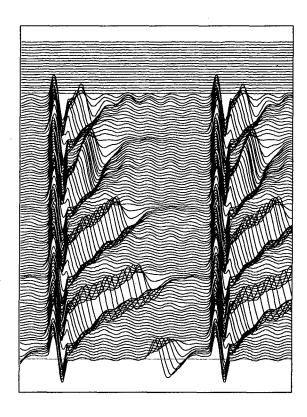


Figure 5: Mountain range plot of gap voltage for five transfers

bunching of the first transfer are due to the ripples in the BNL waveform, while the tendency for the beam to bunch toward later times is due to the asymmetry in the KEK waveform. After five transfers were accumulated the beam was rebunched slowly on h=6. The final emittance was $6\times6.7=40\mathrm{eV}$ -s, 2.8 times larger than the $5\times2.9=14\mathrm{eV}$ -s emittance of the Booster beam. Simulations predict $\lesssim10\%$ emittance growth due to rebunching and pseudo-Schottky scans were done to verify that the emittance was large before rebunching. Significant transition losses $\sim20\%$ occurred when the beam was accelerated[4].

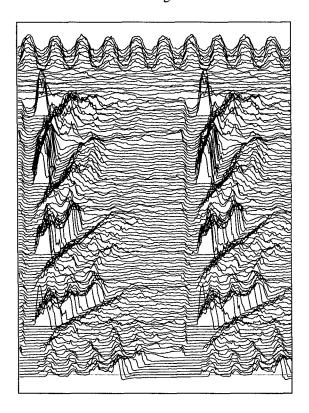


Figure 6: Mountain range plot of beam current for five transfers. A total of 3×10^{13} protons were accumulated.

4 CONCLUSIONS

The successful operation of a barrier bucket rf system appears to have several requirements. The barrier voltage pulses must closely approximate single periods of isolated sine waves. Overshoot and ripple will keep the beam from debunching or cause significant emittance growth during the process. The integral of the voltage as in Figures 2 and 4 may be more useful than the voltage itself. A well compensated voltage divider at the cavity is helpful.

Another key feature is the ability to modulate the amplitude of the barrier voltage. Rapidly turning off the waveform results in an emittance growth equal to the product of the width of the barrier and the energy spread of the stored beam.

For emittance conservation the barriers must form a matched bucket for the injected beam. This places constraints on the voltage and frequency that can be more severe than the momentum spread requirements of the debunched beam. Conversely, narrow barriers can place unacceptable constraints on the injection kicker magnet pulse, which was 800 ns in our case.

At moderate to high intensity the effects of beam loading become severe. For a low Q cavity a feedforward system is probably adequate but for high Q it is likely that some sort of feedback will be required. Since the barrier voltage is broad band there is no analogy to detuning in a harmonic rf system. To cancel the beam induced voltage the power amplifier must be able to deliver the full beam current per ac-

celerating gap. Let $\delta I = I_b - I_f$ be the difference between the beam current and feedback/feedforward current. In a linear system $\delta I(\omega) = T(\omega)I_b(\omega)$ where T is the transfer function for voltage correction. For an RLC resonator with steady state beam loading the mean square error in the integral of the voltage is given by

$$<\delta U^{2}> = 2\left(\frac{R}{Q\omega_{0}}\right)^{2}\sum_{n=1}^{\infty}\frac{|T(n\omega_{0})I_{b}(n\omega_{0})|^{2}}{(n/Q)^{2}+(n^{2}/h-h)^{2}},$$
(2)

where $h = \omega_r/\omega_0$ is the generalized harmonic number. The peak drive current needed to create a barrier voltage V is given by [2,3] $I_p = V(Q+1)/R$ which, for fixed I_p and V, implies $R/Q = V(1+1/Q)/I_p$.

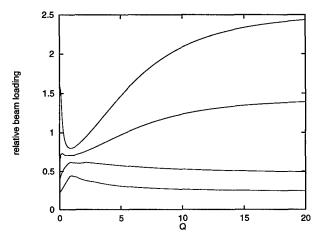


Figure 7: Sum in eq(2) with $T_n I_n = 1$ initially and then removing the largest 0,1,2, and 4 elements. The harmonic number was h = 7.5.

For perfect correction $T_n=0$ while $T_n=1$ for uncorrected lines. To illustrate the interplay of Q with feedback the elements of the sum in equation (2) were calculated with $T_nI_n=1$, and the value of R/Q was chosen so that the voltage and peak drive current were constant. The sum using all the elements was calculated as were sums with the largest 1,2, or 4 elements set to zero. Figure 7 shows the modified sums versus Q for the four conditions. The optimal value of Q increases with the number of lines corrected.

5 ACKNOWLEDGEMENTS

We thank the members of the AGS RF group and the KEK-Tanashi RF group for their great help. The expertise and dedication of the AGS operations staff were indispensible.

- [1] J.E. Griffin, C. Ankenbrandt, J.A. MacLachlan, A. Moretti, IEEE TNS, 30, p3502, 1983.
- [2] M. Blaskiewicz, AIP conf 377 p283 (1995).
- [3] M. Blaskiewicz, J.M. Brennan, EPAC96, p2373 (1996).
- [4] M. Fujieda et. al. these proceedings

A NEW SET OF MAGNETIC SEPTA IN THE CERN PS COMPLEX

J. Borburgh, M. Hourican, M. Thivent, PS Division, CERN, 1211 Geneva 23

Abstract

Over the last few years the CERN PS Complex has been upgraded to fulfill the requirements of two major projects: (i) - producing and transferring lead ions to the SPS for high energy physics experiments and (ii) raising the PSB to PS transfer energy from 1 to 1.4 GeV to generate the high brightness beam for the LHC. To cope with the tight demands imposed by these upgrades, ten magnetic septa, operating under vacuum in the PSB and the PS have been redesigned and progressively replaced. The new devices are bakeable, better suited to high vacuum operation and with higher performance. This paper reports the main characteristics and technological advantages of these magnets together with their present performance.

1 INTRODUCTION

Up to 1994 the yokes of the septa ejection magnets in the Proton Synchrotron ring were built of packets of laminations glued together with 'Araldite'. For reasons of life-time, lead ions require a better vacuum than could be achieved using the existing organic materials under vacuum. In the Booster, DC septa magnets, that were originally designed for 800 MeV beams, have been used for 1 GeV beams, since 1986, without modification. Because of the beam emittance requirements of the future LHC accelerator, the booster energy needs to be increased to 1.4 GeV as from 1999. The thermal limit of the DC magnets implied redesigning all Booster ejection and transfer septa. For reconstruction of these septa magnets, a single turn pulsed magnet approach has been adopted, which requires less energy hence less cooling power and therefore is less prone to erosion in the cooling circuits. To attain the required vacuum, the laminated yoke of these pulsed magnets must first be baked at 200 °C, despite the fact that these magnets are installed in non-bakeable accelerators. The connecting flanges of the magnet tanks should not exceed 50 °C when the magnets are being baked.

2 CONSTRUCTION DETAILS

To reach the objectives stated in the introduction, the entire conception of the magnets has been revised. In the following paragraphs, the most outstanding details will be described per component.

2.1 Vacuum Tanks

To reduce the risk of a leak developing during a bake out, cylindrical tanks have been fitted with circular UHV flanges for diameters <200 mm and 'Wheeler' flanges with copper seals for the bigger diameters (>375 mm). The connecting flanges of the tanks to the accelerator vacuum chamber are of a conical 'quick disconnect' type with aluminium seals, as standard in the CERN PS accelerators.

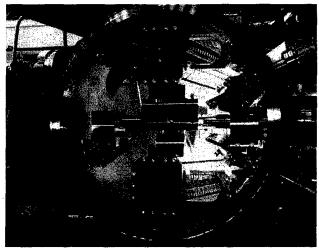


Figure 1: Vacuum Tank containing 2 ejection magnets

2.2 Magnet yoke

The new septa magnets, being of a pulsed type, are constructed with laminated yokes. Standard 0.35 mm thickness steel laminations with a 3% silicon content have been used, which are insulated on both sides with a 'Carlite' inorganic insulating coating. This solution provides a good inter-laminar resistance, and is still bakeable up to 200 °C. The laminated yoke is held together in a stainless steel support by ceramic coated endplates, while sitting on ceramic bars, to ensure the electrical insulation between the yoke and the support.

2.3 Coil

The single-turn coils have been made of 'OFHC' copper. The cooling circuit comprises two thin-walled stainless steel tubes embedded (and brazed) in pre-machined slots in the septum conductor. This reduces erosion of the cooling circuit due to the high water speeds of up to 10 m/s. To increase the mechanical strength of the 60 mm gap septa conductors, a 0.5 mm thick stainless steel plate

is brazed onto the outside of the septum conductor. To reduce the fringe field of the magnets, insulation has been eliminated between magnet yoke and septum conductor, while the return conductor of the coil is insulated with several layers of 0.06 mm and 0.12 mm thermally preformed 'Kapton' sheet, (see fig. 2)

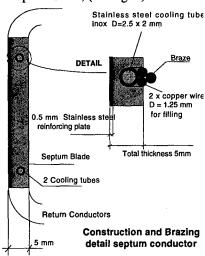


Figure 2: Cross section of septum conductor

2.4 Coil Springs

The complete magnet coil is held in the gap by clamping plates located outside of the magnet yoke. These insulated clamps retain the septum conductor in the gap, while a spring between the septum and rear conductor applies a mechanical force on the return conductor equal to the electromechanical force at the peak current.

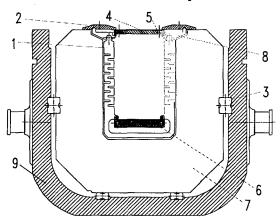


Figure 3: Cross section of magnet yoke assembly
[1. Damping Spring 2. Clamping Plate 3. Ceramic Support 4. Septum
Conductor 5. Cooling Tube 6. Rear Conductor 7. Lamination 8. Lever
9. Stainless Steel Support]

The springs, spaced every 45 mm, are made of beryllium copper (5% Be) suitably annealed to obtain the necessary modulus of elasticity, (see fig. 3)

2.5 Power Feedthrough

A water-cooled coaxial feedthrough, developed for use at 10 kA_{rms}, is used for all new pulsed septa magnets. The coaxial configuration provides the best possible symmetry in mechanical forces, (see fig. 4)

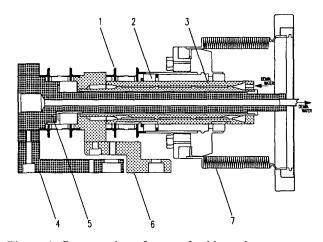


Figure 4: Cross section of power feedthrough

[1. Dilver / Stainless steel weld 2. Ceramic support 3. External conductor 4. Main connection 5. Central conductor 6. Main connection 7. Vacuum bellows]

2.6 Displacement system

All septa magnets can be moved remotely in the radial (or vertical, in the case of the septa in the transfer line) and angular directions, while their vacuum tanks remain fixed. A variable potentiometer, linked to the mechanical displacement system, provides a measurement of the position of the magnet inside the tank. The resolution of the radial and angular systems are 0.1 mm and 0.1 mrad, respectively. For the initial installation, the magnet tank is aligned in all directions. In the event of a failure, the entire vacuum tank with septum magnet can be replaced without the need for realignment.

2.7 Beam Screen

All septa magnet tanks (except transfer lines) are equipped with RF beam screens for the orbiting beam. These screens insure the continuity of the RF impedance of the vacuum tanks, to avoid unwanted harmonics during acceleration. The beam screens are made of perforated stainless steel sheet to improve vacuum pumping speed, and are linked with the connecting flanges of the tank by means of RF contacts.

2.8 Vacuum Equipment

The vacuum tanks are kept under vacuum with a dedicated set of ion pumps, additional pumping being provided by titanium sublimators for the tanks installed in the accelerator rings. In view of the large surface of the magnet laminations under vacuum, and the pressure level to be obtained, it is necessary to bake out the magnets

before commissioning. Standard off-the-shelf infra red lamps are used inside the vacuum tank, with reflectors of electro-polished stainless steel. By connecting two in series, the power consumption is reduced by a factor four, while their expected life time is dramatically increased. The temperature of the magnet is measured with ordinary Cu/Cn (Cn-Constantan) thermocouples, and the control and regulation utilises standard temperature regulators.

2.9 Calculations

For the first rough estimation of the septum magnet parameters, a program was used running under Microsoft Excel developed in the CERN/PS/SEPTA section. To finalise the cross sectional design of the magnet a finite element based program called 'FLUX2D' from Cedrat/Magsoft was used. The longitudinal design was determined using the finite element based program 'OPERA3D/TOSCA' from Vector Fields, using a model developed in house to simplify the magnet model without great loss of precision. For mechanical and thermal calculations the finite element program ANSYS from Swanson Analysis Systems was used, while the cooling requirements were checked with the CERN developed program TUBE, running under Microsoft Excel.

3 TECHNICAL SPECIFICATIONS

The technical specifications of all septa magnets are shown in Table 1.

4 RESULTS

Measurements of magnetic length of the septa confirm theoretical predictions to within 0.5% of the model. The fringe fields measured are less than 1/1000 of the gap field at a 50mm distance from the septum conductor, or better in case of the BESMH, (PSB Ejection) where a very low fringe field was required. After a bake out cycle, consisting of a quasi linear temperature increase of 200 °C over 12 hours, a 24 hour period at 200 °C, and an exponential temperature decrease of approximately 48 hours, a vacuum of $6x10^{-10}$ to $4x10^{-9}$ mbar is achieved. Since the bake out lamps are installed with reflectors, the connecting flanges of the vacuum tanks never exceed 50 °C, allowing the use of aluminium seals for connecting to the accelerator vacuum chambers.

5 CONCLUSIONS

The new set of septa magnets constructed as described in this article shows that it is possible to achieve a vacuum in the low 10° mbar range, even with laminated yokes under vacuum. In order to reach the low pressures specified, it is imperative to perform a pre-commissioning bakeout at 200 °C. The bakeout is performed using commercially available infra red lamps using less than nominal power avoiding excessive temperatures on the vacuum chamber connecting flanges.

The septa magnets for Booster ejection, beam transfer, and PS injection allow for 1.4 GeV operation without reaching thermal limits, since they are constructed as pulsed laminated magnets.

Table 1: Technical specifications of the septa magnet				
DECMU	DTCMV10	BTSMV20	DICMHA2	DI

	BESMH	BTSMV10	BTSMV20	PISMH42	PESMH16	PESMH58
L_{ea} (m)	0.95	1.00	1.00	0.57	2.18	0.81
$B_0(T)$	0.354	0.569	0.525	0.689	1.20	1.06
∫B.dl (T.m)	0.336	0.566	0.523	0.390	2.60	0.860
I (kA) single turn coil	7.0	27.3	25.2	33.1	28.5	21.1
E (GeV) protons	1.4	1.4	1.4	1.4	25.1	12
Deflection Angle (mrad)	47	79	73	55	30	20
Gap height (mm)	25	60	60	60	30	25
Gap width (mm)	89	116	116	116	65	65
Septum Thickness (mm)	3.8	5	5	5	3	3
Rear conductor thick (mm)	7.6	8.8	8.8	8.8	6.0	6.0
1/2 sine pulse width (ms)	3.1	3.1	3.1	3.2	3.5	2.8
Water flow (l/min.)	1.9	3.5	3.5	4.25	1.2	1.45
Year of installation	1998	1999	1997	1996	1994	1994

- J.Borburgh, "2 Dimensional Finite Element Calculations On Septum Magnets with "FLUX2D" and "Opera2D"", CERN Note PS/CA/Note 97-25
- [2]J.Borburgh, "3 Dimensional Finite Element Calculations On Septum Magnets with "Opera3D"", CERN Note PS/CA/Note 97-27
- [3]M.Hourican, "Remote Positioning System BTSMV20", CERN Note PS/CA/Note 97-02
- [4]J.Borburgh and M. Thivent, "SMH16-Flexible Stripline Failure Analysis with Ansy's", CERN Note PS/CA/Note 95-10

SPACE CHARGE EFFECT ON BETATRON OSCILLATIONS

K. M. Fung, C. M. Chu, W. C. Hsi, S. Y. Lee, Indiana University, Bloomington, IN L. Ahrens, G. Smith, N. Williams, Brookhaven National Laboratory, Upton, NY

Abstract

The transverse motion of the beam at the AGS was studied by analyzing the coherent beam signals, digitized at a 10ns interval, at various beam intensities. It was found that the coherent vertical tune shift of the centroid is consistent with the space charge model due to the image charge and current induced on the vacuum chamber wall. An enhanced linear coupling at a high intensity was also observed.

1 INTRODUCTION

The space charge effect is important for low and medium energy synchrotrons. The space charge force in high brightness beams can cause beam halo, beam envelope instability, beam emittance blow-up, collective beam instabilities, and more importantly beam loss. The space charge effect manifests itself in betatron and synchrotron tune shift, tune spreads, collective beam instability, etc.

The aim of this paper is to study the effect on betatron motion due to the space charge force. An initial excitation was given to the beam and then the sum and difference signals were measured (digitized) at different beam intensities below the threshold for instability. The coherent betatron motion was used to derive the betatron tune at different intensities. The coherent vertical tune shift of the centroid can then be obtained. The experimental data can be described by a model in which the beam induces image charge and current on the vacuum chamber wall whose electromagnetic field acts back on the beam.

The paper is organized as follows. In Sec. 2, we will discuss the experimental method which includes the excitation and measurement of the beam response and the observation of a few beam properties as a function of the beam intensity. In Sec. 3, we will give the details of data analysis, including a method to reduce the impact of longitudinal motion on the analysis of transverse motion. Finally, the conclusion will be given in Sec. 4.

2 EXPERIMENTAL METHOD

The AGS is a medium energy synchrotron with a circumference 807.12 m. The horizontal and vertical betatron tunes are about 8.8 and 8.9 respectively. It can be considered as a machine with 60 FODO cells and 12 superperiods. The injector for the AGS is the AGS booster whose circumference is 1/4 of the AGS ring. The single bunch beam intensity from the booster ranges from 1 to 20 ($\times 10^{12}$) protons. This experiment involves a single bunch injected from the AGS booster at 1.9 GeV kinetic energy.

To study the injection process with the space charge effect, we observe the betatron motion at the injection time.

Because of the intentional or unintentional offset between the injection orbit and the AGS closed orbit, betatron motion is induced. In other words, the excitation of the beam response is given in the form of an initial coherent transverse displacement. The sum and difference signals from a beam position monitor (BPM) was digitized at 10ns per channel. We recorded 50002 channels in each injection process. This corresponds to 175 turns with a revolution period $T_0=2848\mathrm{ns}$. The experiment was carried out for the beam intensities $N_\mathrm{B}=2.7,3.9,4,5.7,6.5,13(\times 10^{12})$ particles per bunch.

Fig. 1 shows a typical example of the sum signal for a beam intensity of 1.3×10^{13} particles. Since the signals were digitized at 10ns, the longitudinal profile has a resolution of 10ns and the total beam intensity can be obtained by integrating the sum signal. Since 175 turns corresponds to about 1/4 of the synchrotron period, the beam bunch is evidently more tightly bunched at the end of the data.

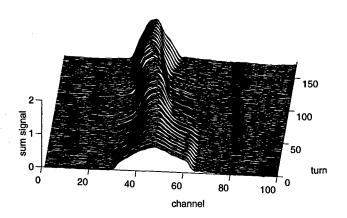


Figure 1: Evolution of the sum signal for $N_{\rm B}=1.3\times 10^{13}$. Note that bunch length decreases.

Fig. 2 (middle,bottom) shows that the peak intensity of the sum signal and the integrated sum signal appear to be a linear function of the beam intensity derived from a current transformer. This means that the beam intensity has not yet saturated so that the peak intensity still depends on the beam current. In other words, all the beam intensities for the experiment are below the threshold for instability. Therefore our study of the space charge effect is justified.

3 DATA ANALYSIS

The data processing steps consist of background removal, signal normalization and tune shift computation. For the first step, the noise is assumed to follow a Gaussian distri-

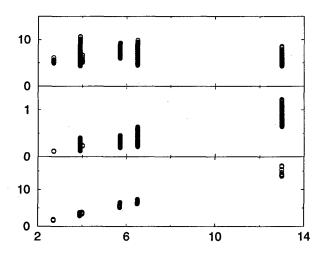


Figure 2: Beam properties at different intensities. The vertical width shows the fact that the beam properties vary with time. Horizontal axis shows intensity $N_{\rm B}(10^{12})$ measured by a current transformer. The top plot shows the rms bunch length in ns, the middle plot shows the peak of the sum signal (in arbitrary unit), and the bottom plot shows the integrated sum signal (in arbitrary unit).

bution characterized by σ and most of it could be removed by a cut at $\pm 3\sigma$. Let Σ and Δ be the sum and difference signals respectively. The normalized beam position signal is $y_n = \Delta/\Sigma$. The actual beam position is given by $40y_n$ mm, where the normalization factor 40 mm is the effective width of the BPM.

In order to study the transverse motion, we have to know the evolution of the transverse positions x and z. If the bunch length were independent of time, then we can follow the transverse motion of each channel turn by turn without ambiguity. However, Fig. 2 (top) shows that the bunch length changes with time and therefore following the channels directly can be ambiguous. One way of following the channels turn by turn is to identify the channels which are T_0 apart and use linear interpolation to estimate the signal between the digitized data. This method has two difficulties. Firstly, not all particles in the bunch have the nominal revolution period T_0 due to the momentum spread $\Delta p/p$. The change in period ΔT_0 is given by [1,2]

$$\frac{\Delta T_0}{T_0} = \eta \frac{\Delta p}{p} \tag{1}$$

where $\eta=1/\gamma_t^2-1/\gamma^2$ is the phase slip factor. Secondly, the synchrotron oscillation will affect T_0 . A much better way to follow the transverse motion is to focus on the centroid. The centroid is the channel which always divides the beam longitudinally into two portions with the same number of particles. This method does not require constant bunch length and it does not rely on the nominal revolution period T_0 at all. An additional advantage of this method is that it completely eliminates the effect of the rigid longitu-

dinal motion on the analysis of the transverse motion. This method can readily be generalized to include other channels. For example, we can select three channels in such a way that they always divide the beam longitudinally into four portions which contain the same number of particles. These channels represent the transverse motion of the head, the centroid and the tail of the beam. In general, we can label each channel by the fraction of the particles located in front of the channel. This labeling scheme combined with a linear interpolation between digitized data allows us to locate *any* channel longitudinally without ambiguity. For the above example, those three channels will be labeled as 25%, 50% and 75% respectively. The transverse motion for the above three channels is shown in Fig. 3.

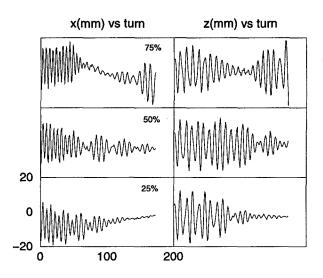


Figure 3: Betatron oscillations for $N_{\rm B}=1.3\times 10^{13}$. Left: horizontal motion. Right: vertical motion. Bottom to top: the head, the centroid and the tail of the beam.

Fig. 3 (left: top,bottom) shows that the horizontal motions of the channels 25% and 75% have opposite trends after the first 50 turns. This is related to a decrease in the bunch length which can be seen in Fig. 1 due essentially to a mismatched synchrotron phase space during the injection. The tune shift due to the coupling of transverse motion can also be seen. For the last step, we took the Fourier transform of the motion and look at the spectrum in Fig. 4.

The small peaks are due to the coupling of transverse motion while the large peak is the fractional part of the tune at a fixed intensity. Finally, the same analysis could be done for different beam intensities and the vertical tune of the centroid as a function of beam intensity is shown in Fig. 5.

The coherent tune shift is a result of the increase in intensity and it is given by [1, 2]

$$\Delta \nu_z = j \frac{eZ_\perp}{4\pi Rm \gamma \nu_z \omega^2} \hat{I}$$
 (2)

where Z_{\perp} is the transverse impedance, e is the proton charge, $\hat{I} = N_{\rm B} e/(\sqrt{2\pi}\sigma_t)$ is the peak current, σ_t is the

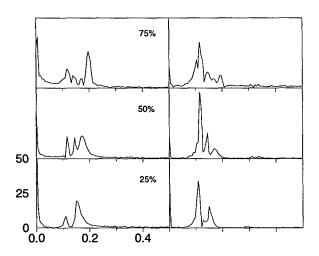


Figure 4: Amplitude of the Fourier transform of Fig. 3 versus fractional part of the tune. Left: horizontal. Right: vertical. Bottom to top: the head, the centroid and the tail of the beam. $N_{\rm B}=1.3\times10^{13}$.

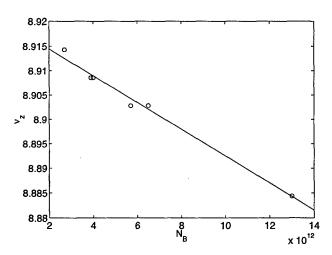


Figure 5: ν_z versus $N_{\rm B}$. Note the detuning due to the increase in the total number of proton $N_{\rm B}$ in a bunch. Circle: data for the vertical tune of the centroid(50%) as a function of the beam intensity. Line: a fit by Eq. 2. Value of the slope -2.739×10^{-15} can be used to find the effective beam pipe radius b.

rms bunch length, R is the mean radius of accelerator, m the mass of proton, $\gamma = 1/(1-\beta^2)^{1/2}$, $j^2 = -1$, ν_z is the vertical betatron tune, and ω is the revolution frequency. The most important contribution to Z_{\perp} is due to the induced charge and current on the beam pipe and it is given by [1,3]

$$Z_{\perp} = j \frac{Z_0 R}{\gamma^2 \beta^2 b^2} \tag{3}$$

where $Z_0 = \mu_0 c$ is the impedance of free space, b is the beam pipe radius. Since the resistive wall impedance ($\sim 10^5 \Omega/\text{m}$) is an order of magnitude smaller than Eq. 3 and

therefore it can be neglected. Using the slope of Fig. 5 and Eq. 2, b can be estimated and it is found to be about 3.4cm. The actual shape of the beam pipe varies. However, most of it is nearly elliptical with vertical half aperture of 3.89cm and horizontal half aperture of 8.66cm. Therefore, b has the same order of magnitude of a few centimeters as the actual beam pipe dimensions. Since the cross section of the actual beam pipe is not circular, b should be regarded as an effective size of the beam pipe.

4 CONCLUSION

The vertical betatron tune of the centroid decreased by 0.03 when the intensity increased from 2.7×10^{12} to 13×10^{12} . The reasonable value of b obtained by applying the circular beam pipe model indicates that the major source that caused the tune shift is the induced charge and current on the beam pipe. We also observed enhanced linear coupling at high space charge region (see the middle plots of Fig. 3).

- [1] S. Y. Lee, *Accelerator Physics*, (World Scientific, Singapore, 1999).
- [2] J. Gareyte, Beam Observation and the Nature of Instabilities, AIP Conf. Proc. 184, 343-429 (Fermilab Summer School 1987).
- [3] K. Y. Ng, Fields, Impedance and Structures, AIP Conf. Proc. 184, 472-524 (Fermilab Summer School 1987).

POLARIZED DEUTERONS AT THE NUCLOTRON

V.Anguelov, I.Issinsky, A.Kondratenko, A.Kovalenko, <u>V.Mikhailov</u>*, Yu.Pilipenko, Joint Institute for Nuclear Research, Dubna, Russia

Abstract

Started at the beginning of the 80th, the spin physics programme at the JINR Synchrophasotron is being continued succesfully. The next step of this programme is to accelerate of polarized beams at the Nuclotron. The first test run of polarized deuteron injection and acceleration has been carried out. The status and development of the polarized deuteron source, analysis of the depolarized effects in the linac, Nuclotron ring and beam injection/extraction transport lines are presented. Computer simulation of charge exchange injection into the accelerator is also considered.

1 INTRODUCTION

Polarized deuterons as the simplest nuclei with the well known spin structure are the best tool to study the inner nucleon structure at a distance of r < 0.5 fm, where quarkgluon degrees of freedom should manifest themselves. First spin experiments at the JINR synchrophasotron were carried out to study inclusive and binary reactions with vector and tensor polarized deuterons in 1981. After installing the Saclay-ANL proton polarized target on 1995, the spin program was supplemented by correlation experiments.

The scheme for acceleration of polarized deuterons at the Nuclotron accelerator facility [1] includes a cryogenic polarized deuteron source Polaris, a 5 MeV/u linac, a superconducting heavy ion synchrotron of a 6 GeV/u energy with 10 second spill slow extraction (under construction now), thin internal targets and a wide net of external beam lines. This scheme also allows one to generate high energy polarized neutron beams with well-determined characteristics.

Two principal problems of polarized particle acceleration are discussed in this paper. The first of them is to keep spin orientation during beam acceleration and transportation, the second one is to produce a high intensity of polarized ions sufficient for data taking in physics experiments...

2 DEPOLARIZATION OF THE BEAM

The spin vector of the every particle and beam

polarization change during deuteron acceleration and transportation. Let us denote Π as a beam polarization vector and S a unit vector, which shows the particle spin direction, then

$$\Pi = \langle S \rangle$$

angular brackets mean the average value of a particle distribution in the beam. If the S direction does not differ much from the one, determined by unit vector \mathbf{n} ($S = \mathbf{n} + \Delta S$), the depolarization degree D is determined by the dispersion of spin vector components transversal to \mathbf{n} :

$$D \approx 1/2[\langle (\Delta S_{tr})^2 \rangle - \langle \Delta S_{tr} \rangle^2];$$

where

$$\Delta S_{tr} = \Delta S - n(\Delta S n)$$

The dynamics of unit polarization 3-vector during its motion in external electric and magnetic fields is described by the Thomas quasi-classical equation:

$$dS/dz = \Omega \times S$$

where the derivative dS/dz goes with respect to the z-coordinate along the equilibrium particle trajectory, Ω is the rotation vector, which modulus is the Larmor frequency determined by the electromagnetic field structure. The analytical and numerical computation of this equation [2] allowed one to get the following results of beam depolarization in the linac, beam transport lines, beam acceleration and slow extraction.

In the injector of the Nuclotron, a 5 MeV/u Alvarez type linac, for equal transverse emmitances $\varepsilon_x = \varepsilon_y = 45\pi$ mm mrad and longitudinal motion equilibrium phase $\phi = 31.5^{\circ}$ the depolarization factor does not exceed 0.13%. The value $D \le 0.25\%$ for the same beam parameters in the the injection beam line. The injected beam is rotated in the vertical plane at angle 13° during beam transportation from linac to the Nuclotron. For polarization matching, it is necessary to turn polarization vector through the same angle in the channel entrance. A 13° rotation can be realized by the longitudinal field in the ion source solenoid. Otherwise, additional beam depolarization, due to coherent polarization rotation in the injection line, appears. Its value $D \approx \theta/2 \approx 2.5\%$.

Work supported by the Russian Foundation for Basic Research

^{*}Email:mikhail@sunhe.jinr.ru

It is known, that difficulties of beam polarization keeping in the accelerator ring are due to the crossing of spin resonances. Their perturbation conditions are determined by the relationship:

$$v = k_{\theta} + k_{x} Q_{x} + k_{y} Q_{y},$$

where /v/ is the number of spin precession per orbit revolution, k_{θ} , k_{x} , k_{y} - integer numbers and Q_{x} , Q_{y} - betatron tunes.

Table 1 shows possible spin resonances up to second order $(/k_x/ + /k_y/ \le 2)$ over a beam energy range from 5 MeV/u to 6 GeV/u and betatron tunes $Q_x \approx 6.8$, $Q_y \approx 6.85$. The results of computer simulations of resonance depolarization at a guide magnetic field velocity of dB/dt = 1 T/sec are shown in Table 1. The high lattice periodicity (32 cells and 8 superperiods) allowed to avoid an excitation of the most dangerous lattice resonances. The influences of magnetic field imperfections and correcting fields (normal and skew dipole, quadrupole, sextupole and octupole) are taken into account. Among non-perfection resonances in the Nuclotron, the most powerful one is v = -1 at an energy of 5.6 GeV/u. Its crossing is dangerous without taking special measures.

Table 1.Spin resonances at the acceleration

\mathbf{k}_{θ}	k _x	k,	ν	W _{kin} ,GeV/u	D, %
-7	0	1	-0.15	0.005	8
-7	1	0	-0.20	0.37	8
-14	0	2	-0.30	1.02	0.5
-14	1	1	-0.35	1.35	0.5
-14	2	0	-0.40	1.68	0.3
13	-2	0	-0.60	2.99	0.1
13	-1	-1	-0.65	3.32	0.1
13	0	-2	-0.70	3.65	0.1
6_	-1	0	-0.80	4.30	0.3
6	0	-1	-0.85	4.63	0.73
-1	01	1	-0.95	5.29	0.06
-1	0	0	-1.00	5.62	40

The task of beam polarization keeping under stationary conditions is appeared, when the spin and betatron tunes do not change much arises from a 10 second slow extraction. The beam depolarization degree under stationary conditions depends on closeness to spin resonance. A maximum effect appears when the particles are in the resonance band. In a real accelerator, it is very difficult to realize these resonance conditions exactly because of synchrotron modulation and betatron tune spread.

The data on beam depolarization for a 10 second spill duration of slow extraction are presented in Table 2.

The resonance v = -1 is dangerous for all the regimes.

The same situation occurs for experiments with an internal target.

Table 2. Spin resonances at the slow extraction

\mathbf{k}_{θ}	k _x	$\mathbf{k}_{_{\mathbf{v}}}$	ν	W _{kin} , GeV/u	D
-7	1	0	0.20	0.37	16
-14	1	1	-0.35	1.35	0.7
6	-1	0	-0.80	4.30	4
6	0	-1	-0.85	4.63	1.5
-1	0	0	-1.00	5.62	100

3 CRYOGENIC ION SOURCE POLARIS

About 20 years the Polaris [3] has been used to produce polarized deuterons at the Synchrophasotron. The source is based on the Stern-Gerlach atomic beam method and has the following features:

- magnetic fields are set by superconducting magnets operating in a persistent current state,
- cooling the dissociator, nozzle and skimmer is produced by a thermal contact with the cryostats,
- the source is very compact and requires power only for RF and control systems,

It is installed on a 700 kV terminal, and information exchange is performed by a fibre glass lines. Polarized deuterons are produced by exchange between polarized deuterium atoms and ions of hydrogen plasma $D^{0}\uparrow + H^{+} = D^{+}\uparrow + H^{0}$ and ionization $D^{0}\uparrow$ by plasma electrons. The beam current at the source entrance is equal to 200 $\mu A,$ the energy 15 KeV and the emittance 2.0π mm mrad.

A magnetic filter and cesium converter $(H^{+} \rightarrow H)$ is planed to install for $D^{+} \uparrow$ beam production at the charge exchange reaction $D^{0} \uparrow + H = D^{-} \uparrow + H^{0}$.

Polaris operates either in the vector or tensor polarization modes. The polarization sign can change pulse by pulse. To measure the beam polarization after acceleration in the 5 MeV/u linac, two types of low energy polarimeters with semiconductor detectors are used.

4 CHARGE-EXCHANGE INJECTION

The intensity of polarized deuterons at the Synchrophasotron is now equal to 5 10° particles per cycle due to multiturn injection. Without a special procedure, the intensity at the Nuclotron is approximately by an order lower because of single-turn injection into the latter. To increase the intensity of a polarized deuteron beam, three ways are considered at the Laboratory of High Energies:

- the formation of a particle short pulse comparable to the one revolution time in the new POLARIS ionizer,
- charge exchange $(D \uparrow \rightarrow D \uparrow^+)$ injection into the Nuclotron
- construction of a booster used to store and preaccelerate ions up to 200 MeV/u [4].

The last one is most effective and very useful for other ions, but it is the most expensive, of course. Below the second possibility of increasing the intensity, the charge exchange injection of polarized deuterons into the Nuclotron, is studied by computer simulations.

Injected beam parameters: deuteron energy 5 MeV/u,

emittance: $\varepsilon_x = 45.0\pi$ mm·mrad, $\varepsilon_y = 45.0\pi$ mm·mrad, relative momentum spread: $\Delta p/p = \pm 5.10^{-3}$.

To estimate the injection efficiency, a simple model of particle passage through matter was chosen. It includes elastic Coulomb scattering, ionization energy losses and energy struggling. We suppose to change the charge of every negative ion having passed through the stripper to the opposite one $(D\uparrow \to D\uparrow^*)$ for the first passage only, positive charge deuterons do not change their charge.

There are no perturbations and imperfections of the magnetic and electrical fields.

The following steps were undertaken using the computer program to simulate stripping injection into the Nuclotron:

- 1) to generate an injected beam particles at transverse deviation-angle (x,x'), (y,y') and relative momentum spread $\Delta p/p$, Gaussian distributed,
- 2) to add to the circulating beam,
- 3) Monte Carlo simulations of the processes in foil,
- 4) to compute particle emittances $\varepsilon_{x,y}$ and to remove particles with

 $\epsilon_{\rm x}>A_{\rm x},\,\epsilon_{\rm y}>A_{\rm y}$ and $\Delta p/p>\left(\Delta p/p\right)_{\rm mach}$, $A_{\rm x,y}$ =45 π mm mrad is the acceptance for particle with $\Delta p/p=5~10^3.$

Carbon was chosen as a stripping foil material.

All the calculations were carried out with the specially designed computer simulation code SINSIM - Monte Carlo object-oriented C++ program for Windows[5].

The growth of emittance and relative momentum spread was simulated by 100 macroparticle during 100-turn stripping injection. The intensity gain (I/I_o) during 100 turn stripping injection with the Nuclotron acceptance restriction is shown in Figure below.

This work is based on the preceding results for simulations of heavy ion stripping injection into synchrotrons [6], where. advantages to store ions with a small atom mass unit (up to carbon) by this method were shown.

5 CONCLUSION

The analytical and numerical simulations of the deuteron depolatization in the Linac, beam transport lines and Nuclotron showed the most resonanses not to be dangerous. The exception is the resonanse $\nu = -1$ at the energy of 5.62 GeV/u. Its crossing during acceleration time and and slow extraction near this energy are impossible without taking of special measures

We consider the possibility to get sufficient quantity of the polarized D in improved Polaris with optimism. At the charge exchange injection of D1 into the Nuclotron, it is possible to gain at least a factor of more than 10 for augmentation of the polarized deuteron intensity.

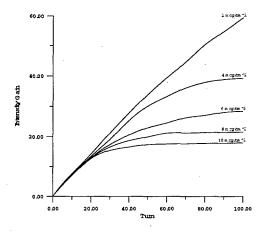


Figure. The intensity gain (I/I₀) during 100 turn stripping injection with the Nuclotron acceptance restriction.

6 REFERENCES

[1]Kovalenko A.D. Proc. 4-th European Part. Acc. Conf., London, 1994, vol. 1, p. 161.

[2]Issinsky I.B. et al. Proc. III Inter. Symp. Deuteron 95, Dubna,1996, p.169.

[3]A.A.Belushkina et al, In: High Energy Physics with Polarized Beams and Polarized Targets, Argone, 1978, AIP Conf. Proc. 51, 1979,p.351.

[4]I.B.Issinsky, V.A.Mikhailov. Conf. Record of 1991 IEEE Part. Acc. Conf., San-Francisko, vol. 5, p. 2886.

[5]B.Shorr, Programs for the Landau and the Vavilov Distribusions and the Corresponding Random Numbers, CERN Program Library, G110/G111(1974).

[6]V.Anguelov et al. Proc 4-th European Particle Acc. Conf., London, 1994, vol. 2. p. 1222.

ACCELERATION OF THE POLARIZED PROTON BEAM IN THE COOLER SYNCHROTRON COSY

A. Lehrach*, U. Bechstedt, J. Dietrich, R. Gebel, K. Henn, R. Maier, D. Prasuhn, A. Schnase, R. Stassen, H. Stockhorst, R. Tölle, Forschungszentrum Jülich, Germany

Abstract

A concept has been developed and realized to accelerate vertically polarized protons in the COoler SYnchrotron COSY at the Forschungszentrum Jülich up to the maximum momentum of 3300 MeV/c [1]. In addition, different Siberian snake schemes for COSY have been investigated to deliver a longitudinally polarized beam.

1 INTRODUCTION

The COoler SYnchrotron and storage ring COSY at the Forschungszentrum Jülich accelerates protons to momenta between $600\,\text{MeV/c}$ and $3300\,\text{MeV/c}$ [2]. At present the beam is used at four internal and three external target places. In addition, a polarized beam can be produced and accelerated at COSY. A colliding beams source, developed by a collaboration of the universities of Bonn, Erlangen, and Cologne is in operation [3]. The polarized H^- beam delivered by this source is pre-accelerated in a cyclotron to 295 MeV/c and injected via stripping injection into the COSY ring. The polarization of the circulating proton beam in COSY is measured continuously during acceleration with the internal EDDA detector [4].

2 DEPOLARIZING RESONANCES

For an ideal planar circular accelerator with a vertical guide field the particle spin vector precesses around the vertical axis. Thus the vertical beam polarization is preserved. The number of spin precessions per revolution of the beam in the ring is given by $\nu_{sp} = \gamma G$ [6], where G=1.7928 is the proton anomalous magnetic moment and γ is the Lorentz factor. During acceleration of a polarized beam, depolarizing resonances are crossed if the precession frequency γG of the spin is equal to the frequency of the encountered spin-perturbing magnetic fields. A strong-focusing synchrotron like COSY has two different types of strong depolarizing resonances, namely imperfection resonances caused by magnetic field errors and misalignments of the magnets and intrinsic resonances excited by horizontal fields due to the vertical focusing.

3 IMPERFECTION RESONANCES AT COSY

In the energy range of COSY, five imperfection resonances have to be crossed (Table 1). The resonance strength depends on the vertical closed orbit deviation. A spin flip occurs at all resonances, but the influence of synchrotron

Table 1: Resonance strength ϵ_r and ratio of preserved polarization P_f/P_i at imperfection resonances for a typical vertical orbit deviation y_{co}^{rms} , without considering synchrotron oscillation.

γG	E_{kin} (MeV)	P (MeV/c)	y_{co}^{rms} (mm)	$\epsilon_r \ (10^{-3})$	P_f/P_i
2	108.4	463.8	2.3	0.95	-1.00
3	631.8	1258.7	1.8	0.61	-0.88
4	1155.1	1871.2	1.6	0.96	-1.00
5	1678.5	2442.6	1.6	0.90	-1.00
6	2201.8	2996.4	1.4	0.46	-0.58

oscillation during resonance crossing cannot be neglected. At the first imperfection resonance, the calculated polarization with a typical momentum spread of $\Delta p/p = 1 \cdot 10^{-3}$ and a synchrotron tune of $\nu_s = 1 \cdot 10^{-3}$ is about P_f/P_i^1 = -0.60. At the other imperfection resonances, the effect is smaller, due to lower momentum spread and synchrotron tune at higher energies. Vertical correction dipoles or a partial snake can be used to preserve polarization at imperfection resonances by exciting adiabatic spin flips. Simulations indicate that an excitation of the vertical orbit by 1 mrad or a rotation angle of the spin in the partial snake of less than 1° is sufficient to cause a spin flip without depolarization. The vertical correcting dipoles in COSY are designed to increase the vertical orbit deviation by 1 mrad at maximum momentum. The solenoids of the electron cooler system inside COSY are available for use as a partial snake. They are able to rotate the spin around the longitudinal axis by about 8° at the maximum momentum of COSY.

4 INTRINSIC RESONANCES AT COSY

The number of intrinsic resonances depends on the superperiodicity P of the lattice, which is given by the number of identical periods of the accelerator. COSY is a synchrotron with a racetrack design consisting of two 180° arc sections connected by straight sections. The straight sections can be tuned as telescopes with 1:1 imaging, giving a 2π phase advance. Both arcs are composed of three unit cells which are each mirror-symmetrical. A half-cell has a QD-bend-QF-bend structure. When the betatron phase advance in the two straight sections of COSY is matched to 2π , these sections are optically transparent and only the arcs contribute to the strength of intrinsic resonances. One obtains for the

^{*}Email: lehrach@bnl.gov, present address: BNL, Upton, NY 11973

¹Ratio of beam polarization before (i) and after (f) crossing a depolarizing resonance.

resonance condition $\gamma G = k \cdot P \pm (\nu_y - 2)$, where k is an integer and ν_y is the vertical betatron tune. The magnetic structure in the arcs allows adjustment of the superperiodicity to P= 2 or 6. The corresponding intrinsic resonances in the momentum range of COSY are listed in Table 2.

Table 2: Resonance strengths ϵ_r of intrinsic resonances for a normalized emittance of 1π mm mrad and a vertical working point of 3.61 for different superperiodicities P.

\overline{P}	γG	E_{kin}	P	ϵ_r
		(MeV)	(MeV/c)	(10^{-3})
2	$6-\nu_y$	312.4	826.9	0.26
2	$0 + \nu_y$	950.7	1639.3	0.21
2,6	$8-\nu_y$	1358.8	2096.5	1.57
2	$2 + \nu_y$	1997.1	2781.2	0.53
2	$10 - \nu_y$	2405.2	3208.9	0.25

4.1 Optimizing the optics for polarized beam

To optimize the optics for a polarized beam, phase advances and betatron amplitudes have been determined along the ring. The measurements were done by exciting continuous betatron oscillations and observing the beam response with a network analyzer between a pair of beam position monitors. With the phase advance of the straight sections matched to 2π , the superperiodicity of the COSY lattice is determined by the arcs. The superperiodicity equals 6 if all unit cells operate with the same quadrupole settings. In this case only one intrinsic resonance $\gamma G = 8 - \nu_y$ occurs, but the transition crossing takes place at about 1600 MeV/c. To accelerate the beam to maximum momentum, the strength of the horizontally focusing quadrupoles in the inner unit cells is enhanced by about 40% to shift the transition energy above the maximum momentum. At the same time, the strength of the horizontally focusing quadrupoles in the outer unit cells is decreased by 20% to keep the betatron tunes constant. The superperiodicity of these beam optics is 2. Consequently, four additional intrinsic resonances are introduced (Table 2), which can be suppressed if the harmonics of the corresponding spin-perturbing fields are corrected. Theoretical studies of the COSY lattice revealed the possibility of suppressing the strength of intrinsic resonances using the vertically focusing quadrupoles in the inner unit. This has been confirmed by measurements with a polarized beam [7]. The new method avoids the drawbacks associated with the non-adiabatic nature of tune jumps, which otherwise would be necessary to preserve polarization at all intrinsic resonances at COSY.

4.2 Successful test of the tune jump system

A tune jump allows one to preserve polarization at intrinsic resonances by increasing the crossing speed significantly.

This is accomplished by abruptly changing the vertical betatron tune during resonance crossing in the range of microseconds. A magnet system consisting of two pulsed air core quadrupoles was developed. This system was designed to achieve polarization losses of less than 5% at the strongest intrinsic resonance, and less than 1% at all other intrinsic resonances in COSY [8]. To meet this goal, a vertical tune jump of 0.06 in $10\mu s$ was needed. Fig. 1 shows the polarization of the COSY beam measured during acceleration around the strongest intrinsic resonance $\gamma G = 8 - \nu_y$. This resonance excites a natural spin flip. The polarization loss depends on the vertical emittance of the beam. With a tune jump, the polarization was almost preserved. This tune jump method can be extended to all

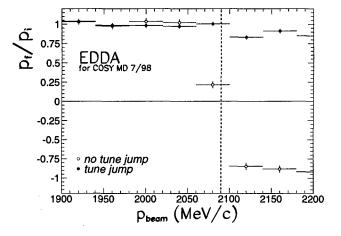


Figure 1: Ratio of preserved beam polarization P_f/P_i after crossing the strongest intrinsic resonance at 2090 MeV/c with and without tune jump measured during acceleration with the EDDA detector.

other intrinsic resonances because they are nearly a factor three weaker than the strongest resonance.

5 ACCELERATION OF THE POLARIZED BEAM

During the July 1998 running period, the polarized beam was accelerated to 2700 MeV/c. The spin was flipped at the imperfection resonances $\gamma G = 2, 3, 4$ and 5 using correcting dipoles. To avoid polarization losses at the first intrinsic resonance ($\gamma G = 6 - \nu_y$ at 827 MeV/c), the acceleration of the beam started with P=6 optics. At about 900 MeV/c, the COSY beam optics was then switched to superperiodicity P=2 to shift the transition energy. As expected, crossing $\gamma G = 0 + \nu_y$ at 1640 MeV/c led to polarization losses. After suppressing the strength of intrinsic resonances using the vertically focusing quadrupoles in the inner unit, the ratio of the preserved polarization at the second intrinsic resonance could be significantly increased. At the strongest intrinsic resonance, the polarization could be almost preserved using a tune jump. The measured polarization after this optimization for polarized beam is shown in Fig. 2. In the following running period in December 1998 we were

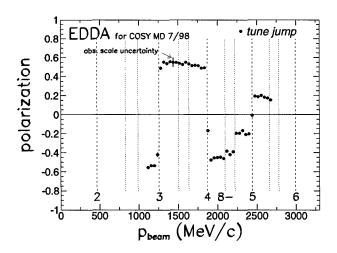


Figure 2: Beam polarization measured during acceleration with the EDDA detector in the momentum range between 1100 MeV/c and 2700 MeV/c.

able to preserve polarization at the maximum momentum of COSY.

6 SIBERIAN SNAKE FOR COSY

Siberian snakes are used to eliminate depolarizing resonances in circular accelerators. The spin is rotated by 180° in the snake, forcing the spin tune to be a half integer, independent of the beam energy [9]. To conserve the polarization using a Siberian snake with a solenoid field, the direction of the spin vector has to be longitudinal at the symmetry point of the snake, which is point in the accelerator opposite to the position of the snake. This can be achieved by turning on the snake after injection and ramping it until the rotation angle of the spin is 180°. During this process, the spin direction changes from vertical to longitudinal at the symmetry point, and the spin tune changes from $\nu_{sp} = \gamma G$ (without snake) to the nearest half-integer tune (180° snake). To avoid crossing depolarizing resonances, the snake can be turned on at half-integer spin tune. Then the spin tune is equal to a half integer for any snake strength. This condition is satisfied whenever the kinetic energy E_{kin} is given by $E_{kin} = 370 MeV + k \cdot 523 MeV$, where k is an integer. In the energy range of COSY, only a solenoid field is suitable. A solenoid field for 180° spin rotation rotates the transversal phase space by 32.2°. This can be compensated with two skewed quadrupole doublets. Different snake schemes for COSY have been investigated [1]. One possible magnet arrangement consists of four skewed quadrupoles, with a maximum gradient fields of 34.2 T/m and -32.2 T/m rotated by 21.5 and 15.2° in each doublet, and one solenoid lying in between. The required integral field strength for the solenoid is 12.4 Tm at 3300 MeV/c. Superconducting magnet technology has to be used to achieve an acceptable length of the snake. The total length of such a magnet system is 5.6 m, and it would fit into one of the straight sections of COSY.

7 CONCLUSION

Correction dipoles and the solenoids of the electron cooler acting as a partial snake were successfully used to preserve the polarization by exciting adiabatic spin flips. Both methods are available for all five imperfection resonances in the momentum range of COSY. With the standard optics of COSY, five intrinsic resonances are excited. Calculations predict, and measurements confirm, that some of these resonances can be suppressed by changing the optics during acceleration. A tune jump is necessary for the remaining intrinsic resonances. A magnet system consisting of two pulsed air core quadrupoles was developed and successfully used. Polarization measurements during acceleration confirm that the developed concept allows the acceleration of a vertically polarized proton beam up to the maximum momentum of COSY. The installation of a Siberian snake could also provide a longitudinally polarized beam in COSY.

8 ACKNOWLEDGEMENT

We are indebted to all members of the COSY team and the collaboration of the polarized source for their support. We are especially grateful to the EDDA collaboration for their sophisticated measurement of the beam polarization during acceleration.

- [1] A. Lehrach, Erarbeitung und Umsetzung eines Konzepts zur Beschleunigung polarisierter Protonen im Kühlersynchrotron COSY, PhD-thesis Universität Bonn (1997), Bericht des Forschungszentrums Jülich Juel-3501.
- [2] R. Maier, Cooler Synchrotron COSY Performance and Perspectives, Nucl. Inst. and Meth. A 390 (1997), 1.
- [3] P.D. Eversheim et al., The Polarized Ion-Source for COSY, 12th Int. Symp. on High-Energy Spin Physics, Amsterdam (1996), (published in World Scientific Singapore 1997, 306).
- [4] V. Schwarz et al., EDDA As Internal High-Energy Polarimeter, 13th Int. Symp. on High-Energy Spin Physics, Protvino (1998), (submitted to World Scientific Singapore).
- [5] A. Lehrach et al., Status of Polarized Beam at COSY, 12th Int. Symp. on High-Energy Spin Physics, Amsterdam (1996), (published in World Scientific Singapore 1997, 416).
- [6] V. Bargman, L. Michel, V.L. Telegdi, Phys. Rev. Lett. Vol.2 (1959), 435.
- [7] A. Lehrach et al., Suppressing Intrinsic Spin Harmonics at the Cooler Synchrotron COSY, submitted to Nucl. Inst. and Meth. section A (1999).
- [8] A. Lehrach et al., Tune jumping system for COSY, IKP Annual Report 1996, Bericht des Forschungszentrums Jülich Juel-3200, 263.
- [9] Ya.S. Derbenev and A.M. Kondratenko, Part. Accel. Vol.8 (1978), 115.

OPERATIONAL EXPERIENCE WITH THE ELECTROSTATIC STORAGE RING, ELISA

S. Pape Møller and U.V. Pedersen, ISA, Univ. Aarhus, DK-8000 Aarhus C, Denmark

Abstract

The design and initial operation of the first ion storage ring using electrostatic deflection and focusing elements was described in [1,2]. In the present contribution, the design will be only briefly described, and emphasis will be given to the operational experience with the storage ring. At the time of writing this contribution, different beams of both positive and negative atomic and molecular ions of masses ranging from 4 to 840 AMU's have been stored. The residual-gas pressure, which in the best cases has been below 10⁻¹¹ mBar, determines the lifetimes of low-intensity beams of stable ions. Lifetimes up to more than 30 seconds have been observed. Intensity-related losses of beam are observed when the number of injected particles is higher than a few times 10^s. These losses are not understood at present. Future research programs will be outlined, including storage of very heavy biomolecules.

1 INTRODUCTION

Research in low- and medium-energy atomic and nuclear physics has progressed tremendously with the introduction of small storage rings into these areas [3]. These storage rings for both light and heavy ions have evolved from the high-energy storage rings and use magnetic elements for deflection and focusing. The rings have circumferences larger than 40 m and rigidities larger than 2 Tm. In [1] it was proposed to construct a small storage ring using electrostatic devices for deflection and focusing. The design and first results from the commissioning of this electrostatic storage ring, ELISA, were described in [2].

The alternative storage device used to confine charged

particles for extended periods of time in a small volume of space is the electromagnetic trap [4], in which the confinement is provided by static (Penning trap) or varying (Paul trap) electromagnetic fields. In an ion trap, the ions have a vanishing average velocity as opposed to the energetic ions in a straight section of a storage ring. We also mention the recent development of a storage device consisting of two 180° electrostatic mirrors [5].

The layout of the ring is given in Fig. 1. The lattice consists of two 160° spherical electrostatic deflectors (SDEH), each having a 10° parallel-plate electrostatic

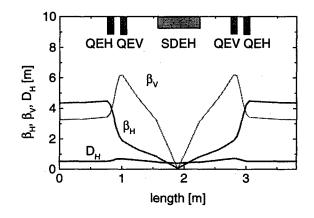


Figure 2: Lattice functions for ELISA.

deflector (DEH) and an electrostatic quadrupole doublet (QEH/V) on each side. The resulting lattice functions are shown in Fig. 2 and a very strong waist in the middle of the spherical bends, characteristic of this lattice, is seen. One of the main differences between electrostatic and

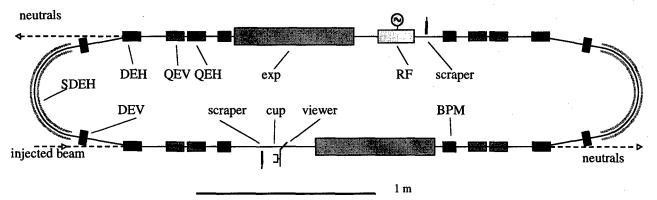


Figure 1: Layout of the ELISA storage ring. The abbreviations are explained in the text.

FYSSP@IFA.AU.DK

magnetic deflection is that the longitudinal energy is not conserved in the electrostatic case. This effect is actually what gives rise to the strong horizontal focusing in the 160° bends. Furthermore, such spherical deflection electrodes give rise to equally strong horizontal and vertical focusing. Closed-orbit correction can be performed with the four vertical correctors (DEV) and the four 10° bends.

Diagnostics of the injected beam can be made using the

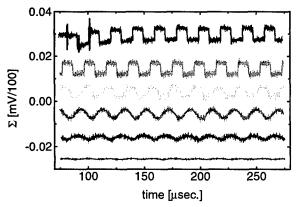


Figure 3: BPM sum signals from a chopped 22 keV N, beam. For details, see the text.

Faraday cup and the fluorescent-screen viewer, and the stored beam can be monitored with the four horizontal and four vertical beam-position monitor pick-ups. In addition, the two sets of scrapers can be used for beam size and position measurements. Finally, there are two ports for detection of ions having had a charge-changing collision in the straight sections. These neutralised ions are observed with a channel-plate detector with a fluorescent screen and provide a direct real-time observation of the projection of the circulating beam.

The high-voltage supplies are designed to allow storage of ions with kinetic energies less than 25 keV, and we stress here that this can be ions of almost any mass.

2 COMMISSIONING RESULTS

The first observations are made with the beam-position monitors, which provides both a Σ and a Δ signal reflecting the circulating intensity and the position of the beam, respectively. The Σ signals from a chopped 22 keV

 N_2^{+} beam consisting of around 5·10⁶ ions are shown in Fig. 3 at injection time and 1, 5, 15, 30 and 60 msec. later. Successive revolutions are clearly seen, and the signals show that there are no beam losses during the first many milliseconds. The de-bunching of the beam owing to the momentum spread is observed at late times.

When the beam has de-bunched, the intensity can not be measured with the pick-up's. The circulating intensity can, however, be monitored with the detectors at the end of the straight sections, since the number of neutralised ions is proportional to the circulating intensity and the residual-gas pressure. In fig. 4 is shown this neutral particle yield for four different injected currents of 1.5, 10, 44 and 140 nA of 22 keV O'. These currents correspond to 1.4·10⁵, 1·10⁶, 4.4·10⁶ and 1.4·10⁷ ions, respectively. The remaining beam is kicked out after 55 seconds, and the signal seen after this time corresponds to the background in the detector. An exponential decay is

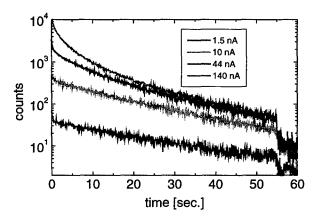


Figure 4: Neutral particle yield as function of time for four different injected currents of O.

observed for low currents, with a lifetime of 20 seconds. This lifetime is compatible with the electron detachment cross section for residual-gas collisions at a pressure of a few times 10⁻¹¹ mBar. Although the pressure is not known very accurately, increasing the pressure in ELISA has proven a lifetime dominated by the residual gas.

Cross sections for residual-gas interactions (electron capture and loss) are almost energy-independent at these low energies, which in turn means that storage times will scale inversely proportional to the velocity. We have measured the lifetimes of a O beam at 22 and 11 keV to 26 and 33 seconds, respectively, in accordance with this scaling. The longest lifetimes observed are a lifetime of 36 seconds for a 22 keV Xe⁺ beam.

A comparison of residual-gas dominated lifetimes of a positive and negative oxygen beam at 22 keV is made in Fig. 5. The lifetime of the positive beam is around 11 seconds, whereas the lifetime of the negative beam is around 26 seconds. This difference is explained by the electron-capture cross section of O^+ , which is

approximately a factor of 3 larger than the electrondetachment cross section of O at low energies. Both measurements are made with injected currents of around 1 nA and similar residual-gas pressures.

Since the residual-gas pressure determines the lifetimes of low-intensity beams, longer lifetimes can be obtained

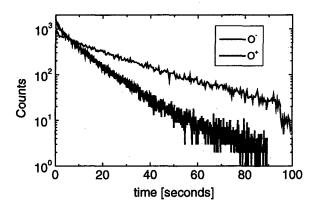


Figure 5: Comparison of lifetimes of O⁺ and O⁻ beams at 22 keV.

by reduction of this pressure. One possibility with a small ring like ELISA is the possibility to cool the whole ring, which in turn reduces the out-gassing of the vacuum chamber walls. This has been tried with a reduction of the pressure to a few times 10⁻¹² mBar. ELISA was cooled with liquid nitrogen, using the same insulation box as used during bake-out.

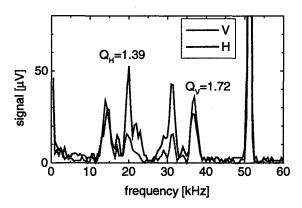


Figure 6: Betatron frequencies for a 22 keV CO⁺ beam in ELISA.

For larger currents, a reduction in the lifetime is seen in Fig. 4 at early times, corresponding to an intensity dependent lifetime. The origin of this effect is as yet unknown. Estimates of intra-beam scattering times give characteristic times of the order of hours, much longer than the characteristic times observed. Tune shifts are also too small (of the order of 0.001) to have a significant influence. Also intra-beam stripping, i.e. loss of ions due

to electron detachment in O-O collisions, can not explain the observations. Similar effects observed for positive beams corroborate this last statement. Measurements of beam profiles do not indicate a large emittance increase for the intense beams.

Looking at the lattice functions in Fig. 2 makes one focus on the very low beta-functions in the middle of the spherical deflectors, nominally equal to 0.1 and 0.02 m horizontally and vertically, respectively. It has been proposed [6] that the losses might be due to excitation of resonances by the strong envelope modulation. Although such an effect evidently exists, quantitative estimates of the influence are not yet available. A remedy for such an effect would be a modification of the lattice in order to make the lattice functions smoother. Such a modification is, however, not easy with a race-track configuration due to the strong focusing from electrostatic bends. One suggestion would be to replace the 160° spherical bend by two 80° cylindrical bends and a vertically focusing quadrupole, as suggested in [7].

Experience has shown that ELISA is rather sensitive to the betatron tunes. Measured tunes of a CO † beam are shown in Fig. 6. The tunes are measured by a FFT analysis of the Δ signal from a pick-up for a mis-steered chopped beam. The non-integer parts of the betatron frequencies are directly observed together with the revolution frequency at 52 kHz. In an electrostatic ring as ELISA, where the deflectors also are focusing, there is a strong coupling between the position and the tunes. This is a complication and a restriction in tuning the machine.

3 CONCLUSIONS AND OUTLOOK

The principle of an electrostatic storage ring has been proven to work and the first experiments studying the decay-properties of beams directly or by means of lasers are in progress. For these experiments, the intensity limitations observed are unimportant, as it also is for the planned study of stored bio-molecules. However, there are planned experiments aiming to study the interaction between stored ions and electrons, where higher intensities are required, and a solution to the intensity-problem will be sought.

- [1] S.P. Møller, Proc. 6'th European Particle Accelerator Conference, Stockholm 1998, p. 73.
- [2] S.P. Møller, Nucl. Instrum. Methods in Physics Research A 394 (1997) 281
- [3] S.P. Møller, Proc. 4'th European Particle Accelerator Conference, London 1994, p. 173
- [4] R.C. Thomson, Advances in atomic, molecular and optical physics **31** (1993) 63
- [5] M. Dahan et al, Rev. Sci. Instrum. 69 (1998) 76
- [6] Y. Senichev, private communication
- [7] T. Tanabe and I. Watanabe, private communication

SIMULATIONS OF RACETRACK MICROTRON FOR ACCELERATION OF PICOSECOND ELECTRON PULSE*

M. Washio*, R. Kuroda, Waseda University, 3-4-1 Okubo, Shinjuku, Tokyo J. Yang. T. Hori, F. Sakai, Sumitomo Heavy Industries Ltd.,1-1-2 Yato-cho, Tanashi, Tokyo

Abstract

Low emittance sub-picosecond electron pulses are expected to be used in a wide field, such as free electron laser, laser acceleration, femtosecond X-ray generation by inverse Compton scattering, and pulse radiolysis, etc. In order to produce the low emittance sub-picosecond electron pulses, we are developing a compact racetrack microtron (RTM) with a new 5 MeV injection system adopting an laser photo cathode RF gun [1]. The operation of RTM is kept under the steady state of beam loading for long pulse mode so far[2]. We have investigated for the first time by numerical simulation in the case of short- and single-pulse acceleration. As the results, RTM is also useful to accelerate a picosecond electron pulse under a transient state of beam loading. In the simulation, a picosecond electron pulse is accelerated to 139 MeV in RTM for the injection of about 5 MeV pulse with pulse length of 3 picoseconds, charge of 1 nC per pulse, and emittance of 1.8 mm mrad, which corresponds of output of the RF gun.

1 INTRODUCTION

Ultra-short and low emittance electron beams are indispensable tool for the physical chemistry investigation in ionisation and excitation processes of various kind of materials. Further, high quality X-ray beam with the pulse length of the pico- to femtosecond time region can be generated by the Inverse Compton Scattering process between high-brightness and short pulse laser light and the high quality electron beam [1-3].

One of the most powerful methods to generate the high quality electron beam is considered to apply a photo cathode RF gun system in the combination with racetrack Microtron (RTM). Recent rapid progress of the photo cathode RF gun system conducted by the collaboration among the BNL, KEK and SHI[4] promises us to generate suitable electron beams to inject into the RTM with desired beam parameters. In such a way, we can generate short pulse and very low emittance electron beam with the energy up to 150 MeV[5].

The design of RTM has been established and been demonstrated as the injectors of compact SR rings, AURORA-1 and-2[6]. The already-existing design is, however, optimized for the output beam having

somewhat long electron pulse length at around a few microseconds and relatively low peak current, 10mA at the maximum. When we apply the combination of RTM with photo cathode RF gun as the injection system, we have to investigate the behaviours of electron beams on the condition of transient beam loading and effect of chicane magnets for the 5MeV electron injection. The system configuration is shown in Fig. 1. The effects of space charge and synchrotron radiation while acceleration would next be taken into account.

In the first step of the simulation, we have calculated the output beam characteristics obtained from photo cathode RF gun using MAGIC code. In the second step, we have calculated the final beam characteristics as the output from RTM using a modified SUPERFISH code to treat the time dependent acceleration field.

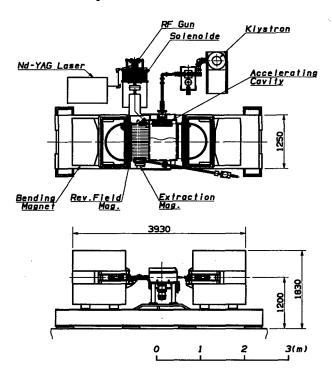


Figure 1 : Top view of 150-MeV RTM with RF gun injection system

2 RF GUN

RF gun using for our simulation is based on so-called BNL type, 1.6 cell s-band cavity structure. Fig 2 shows the typical emittance result obtained for the gun using the following parameters.

^{*}Work supported in part by the Grant for Special Project of Waseda University, No. 98A-901

^{*}Email: washiom@mn.waseda.ac.jp

• Input laser pulse length: 10ps

Laser beam spot size in diameter: 2.4mm
Acceleration Field Strength: 100MV/m

• Resonance Frequency : 2854.62MHz as a π mode

• Energy Gain: 4.9375 ±0.0225 MeV

• Electron Charge: 100 pC

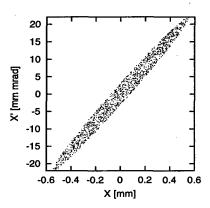


Figure 2: Normalized emittance of output beam from RF gun

The obtained normalized rms emittance is about 1.8mm mrad. with the pulse length of 3ps. This emittance value is not so small in the view point of RF gun characteristics. Better emittance can be obtained using other parameters by selecting the injection RF phase and laser light diameter, in the electron charge up to several hundreds of pC, however, acceptance of RTM is much limited and we selected the above parameters for the complete acceptance to RTM

3 MICROTRON

The major components of RTM are two 180 degree bending magnets placed on both end-sides with reverse field one in front of each, one s-band accelerating structure of 0.5 m long placed on the mid-portion of the first orbit near the injection point, and the RF gun as the injector. Here, except this new injection scheme, other sub-systems are precisely the same as the normal parameters of 150 MeV RTM. This means that the optimisation of parameters for high energy and low emittance electron injection does not carried out in this study. The principal parameters of RTM for the numerical calculation are shown in Table 1.

Circulating No.	23 laps
Energy Gain	6 MeV/lap
Bending Field	1.23 and 1.228 Tesla
Field Gradient	0.14 Tesla/m
Reverse Field	0.2919 and 0.2777 Tesla
Chicane Field	0.33 Tesla
RF Frequency	2856 MHz
Accelerating Gradient	15 MV/m
No. of Accelerating Cell	7 full + 2 half cells

Table 1: Parameters of RTM

4 SIMULATION RESULTS

For the simulation of single-bunch of 1nC, we have roughly estimated the stored energy in the acceleration cavity before and after the single-bunch acceleration. Originally, there is about 2 joules of stored energy in the cavity which consists of 7-full and 2-half cells of side coupled type. During the acceleration of 1nC electron bunch, it needs about 0.15 joule when accelerated to 150 MeV. Thus, about 7.5% of stored energy is taken away by the beam which enforces about 3.8% decline of electric field upon the cavity when no refill of RF power is assumed.

We have calculated the beam transmittance while circulating in RTM and the emittance after the acceleration are shown in Figs. 3 and 4 using the input parameters of Fig.2. Beam transmittance data shows that about 82 % of electrons are obtained at the acceleration energy to 139.55 MeV. The emittance data after the acceleration, we have obtained rms- εx , - εy are 0.12 and 0.037 π mm mrad., respectively. These are the smallest values which we have obtained by experiments and calculations[5], however, these are still larger than expected values.

The distribution of (E,ϕ) phase space of accelerated electrons within a bunch are shown in Fig. 5 (right) together with the histogram of energy distribution (left). From the figure, the beam energy after 23 laps of acceleration is read as 139.55 MeV and energy spread $\Delta E/E$ as ± 0.07 %. The phase distribution is more clearly shown in Fig.6, where the final distribution are demonstrated. The phase spread is compressed to 1.5 ° after the acceleration, about a half of the initial spread. It is equivalent to 1.5 psec pulse length. When acceleration is performed up to 151 MeV, we can get smaller energy spread down to ± 0.02 % of $\Delta E/E$.

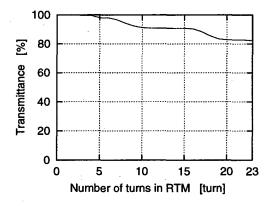


Figure 3: Beam transmittance in RTM

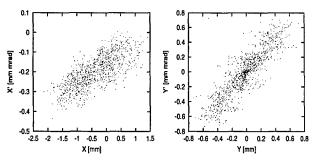


Figure 4 : Final emittance of output beam from RTM

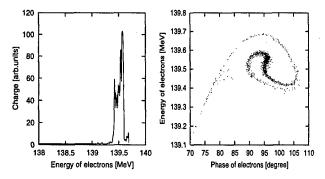


Figure 5: Final energy spectrum and (E,\$\phi\$) distribution of accelerated beam

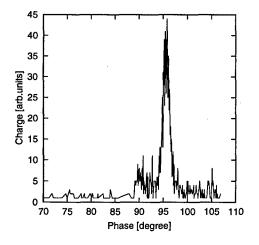


Figure 6: Final bunch length at 139.55MeV

5 CONCLUSION

It has been proved by numerical simulations that the acceleration of ultra-short single-bunch electron beam emitted from a photo cathode RF gun about 5 MeV was achieved. However, in the normal RTM parameter does not permit us conservation of normalized emittance. This may be considered that the reverse field of the first orbit is not perfectly arranged to get better εx . On the other hand, increase of εy may cause by lack of suitable lattice structures. Hence, we have two ways to upgrade the RTM for the acceleration of ultra-low emittance electron. One is to add focussing magnet for the conservation of

Ey and fine tuning of beam orbit at the reverse field. Other and better way is to be change the system at the first orbit to avoid the reverse magnet and the beam can accelerate through the achromatic orbit.

References

- [1] M. Washio et al., "Femtosecond X-ray Pulse Generation Using a Low Emittance Electron Beam and a High Power Laser", 7th China-Japan Bilateral Symp. On Radiation Chem. Oct. 28, Cengdu, China (1996)
- [2] M. Washio et al., "Femtosecond X-rays Produced by Inverse Compton Scattering between a Low Emittance Electron Beam and an Intense Laser Light", J. Surface Sci. Soc. Jpn., Vol.19 No.2 pp23-29 (1998)
- [3] J. Yang et al., "Evaluation of Femtosecond X-rays Produced be Inverse Compton Scattering under Linear and Nonlinear Interactions between a Low Emittance Electron Beam and an Intense Polarised Laser Light", Proc. EPAC'98 Stockholm, pp1082-1084 (1998)
- [4] F. Sakai et al., "Development of High Duty Operation RF Photoinjector", Proc. 11th Symposium on Accelerator Sci. and Technology, Harima, Japan pp473-475 (1997)
- [5] T. Hori et al., "Simulations of Ultra Short Single Bunch Operation on 150 MeV Microtron", Proc. Epac'98 Stockholm, pp517-519 (1998)
- [6] T. Hori et al., "AURORA-2: Compact Advanced SR Ring as an X-ray Source", 4th Int'l Conf. On SR Sources & 2nd Asian Forum on SR, Kyongju, Korea, pp148-158 (1995)

GENERATING HIGH-BRIGHTNESS ELECTRON BEAMS*

A.S. Alimov[‡], K. Halbach, E.A. Knapp, D.V. Kostin[†], G.A. Novikov[‡], V.I. Shvedunov^{‡§}, N.P. Sobenin[†], and W.P. Trower, World Physics Technologies, Blacksburg VA

Injection

Abstract

We have designed a compact <u>LIN</u>ear <u>AC</u>celerator injected pulsed <u>Race Track Microtron</u> to produce ~150 pC/bunch, 5π mm × mrad normalized transverse emittance, 5 ps bunch electron beams with energy selectable between 5 and 35 MeV in 2.5 MeV increments.

1 INTRODUCTION

Our proposed compact inexpensive electron source has advantages over a conventional LINAC but could be bunch charge limited [1]. Here we detail our design study of this system in which we investigated the injector, the RTM, and the injection/extraction line beam dynamics and obtained the Coherent Synchrotron Radiation and transverse Beam Blow Up bunch charge limits.

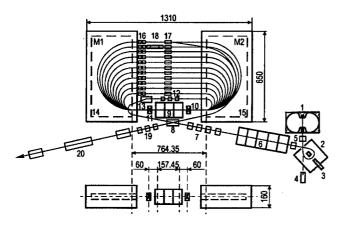


Figure 1: Electron source schematic

Our system, seen in Fig. 1 whose principal parameters are listed in Table 1, consists of (1) a Radio Frequency gun, (2) an α -magnet, (3) a slit, (4) a laser, (5) lenses, (6) the injector Accelerating Structure, (7,12,19) quadrupole triplets, (8,13) dipole magnets, (9) the RTM AS, (10,11) quadrupole singlets, (14,15) end dipole magnets, (16) correcting magnets, (17) extraction magnets, (18) a phase adjusting chicane, and (20) a bunch compressor. Our electron source has three important features: (a) Highenergy (5 MeV) injection provided by a thermionic RF gun, an α -magnet, and the injector AS; (b) Simple RTM optics and permanent magnet end dipoles; and (c) Beam

compression by simultaneously using the RTM AS, the end magnets, and an external chicane.

Table 1:	RTM	parameters	
Energy		5 MeV	
eam Energi	es	5 - 35 Me	٦

injection Energy	2 IME A
Output Beam Energies	5 - 35 MeV
Peak Beam Current	~30 - 100 A
Pulsed Beam Current	115 mA
Norm. Beam Emittance	$5 \pi \text{ mm} \times \text{mrad}$
Longitudinal Emittance	50 keV × deg
Beam Micro-pulse Length	5 - 1 ps
Beam Macro-pulse Length	5 μs
Pulse Repetition Rate	1 to 300 Hz
RF Frequency	2,856 MHz
RTM Dimensions	$130 \times 65 \times 16 \text{ cm}^3$
Pulsed RF Power	6 MW
End Magnet Field	0.5 T
End Magnet Weight	$2 \times 160 \text{ kg}$

2 INJECTOR

By separating the injector from the RTM, we can generate bunches using a variety of techniques and then optimize the RTM without concern for bunch formation. Our injection energy is high enough to suppress ordinary space charge effects and to simply solve the "first orbit" problem but sufficiently low so as to be economical. Injecting at 5 MeV is a reasonable compromise.

A conventional electron gun will not give us our injector bunch parameters, while a photocathode RF gun is too expensive. Thus, we will form bunches with a thermionic RF gun. To decrease/regulate the RTM beam loading, we can either operate the RF gun at the 4th subharmonic or alternatively at the 4th subharmonic or fundamental frequency using a preheated LaB₆ cathode gated by long pulses from an inexpensive laser [2]. The beam dynamics are unaffected for laser pulses whose length is comparable or greater than the RF period.

We study the beam dynamics in a single cavity 714 MHz RF gun (1) whose cavity length and RF field amplitude gives a 1.8 MeV maximum energy beam with a unique energy-phase correlated longitudinal phase space distribution. We then longitudinally prepare the 5 MeV injector bunches to match the RTM acceptance by a phase space transformation using an α-magnet (2) with an adjustable collimating slit (3) and a five cell standing

^{*}Work supported in part by DOE contract 50043-98-I.

Permanent address Electrical Engineering Department,

Moscow Engineering Physics Institute, Moscow, Russia.

[‡]Permanent address Institute of Nuclear Physics, Moscow

State University, Moscow, Russia.

Email: wptinc@naxs.net

wave AS (6). We transversely focus the injector beam with quadrupole triplets (5) placed at the α -magnet entrance and exit.

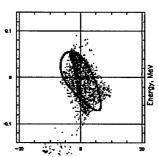


Figure 2: Longitudinal injector exit phase space

Figure 2 shows the longitudinal phase space at the injector exit matched to the RTM acceptance while Table 2 gives the bunch parameters at the injector exit [3,4].

Table 2: Injector exit bunch parameters

Tueste 2: Injector of	nt bundii paramotors
Qbeam	280 pC
Normalized $\langle \varepsilon_x \rangle$	18.4 mm \times mrad
Normalized $\langle \varepsilon_{y} \rangle$	20.3 mm \times mrad
$\langle W_{beam} \rangle$	5.0 MeV
ΔW_{beam}	± 56 keV
$arDelta arphi_{beam}$	± 3.6°
$\langle \mathcal{E}_L angle$	200 keV × deg

3 RTM

Our RTM has a 2.5 MeV synchronous energy gain per orbit and attains the 35 MeV maximum energy beam in 12 orbits. To maximize the longitudinal acceptance we chose the incremental number, v, to be 1 and so 0.5 T is the end magnet main field.

High-energy injection simplifies the RTM beam dynamics where we achieve focusing by quadrupole singlets installed at each end of the RTM AS as in Continuous Wave machines [5]. We optimize the quadrupole gradients and find matched transverse and longitudinal phase space ellipses parameters.

Our calculated bunch parameters at the RTM exit neglecting space charge effects, listed in Table 3, have transverse and longitudinal emittances slightly greater than our desired values. However, we have some excess bunch charge that we reduce by decreasing the α -magnet collimating slit width and thereby decrease the beam emittance.

Table 3: Bunch parameters at the RTM exit

Q _{beam}	230 pC
Normalized $\langle \mathcal{E}_x \rangle$	$12.97 \text{ mm} \times \text{mrad}$
Normalized $\langle \mathcal{E}_{v} \rangle$	$16.20 \text{ mm} \times \text{mrad}$
$\langle W_{beam} \rangle$	35.1 MeV
$\langle \Delta W_{beam} \rangle$	± 30 keV
$arDelta arphi_{beam}$	± 5°
$\langle arepsilon_{\it L} angle$	$102.8 \text{ keV} \times \text{deg}$

As in our 70 MeV RTM design [6], we use permanent magnet box-type end magnets [7] which in contrast to electromagnets require no power supply, cooling, or complicated control system and are more compact and weighs less. To compensate for beam defocusing, we form a reverse field at the magnet entrance with a second, opposite polarity, pole.

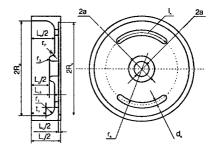


Figure 3: RTM accelerating structure

We use a standing wave on-axis coupled AS in both the injector and RTM. The three accelerating cell RTM AS, seen in Fig. 3, have $f_{\pi/2} = 2,856.04$ MHz, $r_{sh} = 72.7$ M Ω /m, $k_c = 7.0$ %, and Q = 14,530.

4 INJECTION AND EXTRACTION

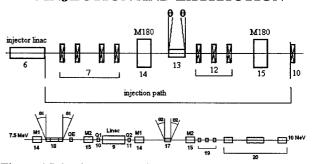


Figure 4 Injection (top) and extraction (bottom) paths

The injection path, shown in Fig. 4, provides a dispersion free beam which is transversely matched to the RTM acceptance.

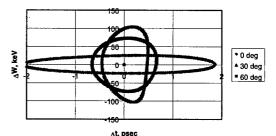


Figure 5: Extracted bunch longitudinal phase space

The extraction path provides a dispersion free extracted beam from any orbit after the 2nd whose bunches are simultaneously compressed. A three-magnet chicane installed at return path (18) shifts the extracted bunch phase by 15-60° on the penultimate orbit. On the final AS pass, the bunch gets an additional energy spread and then, between the end magnets, it is deflected by ~5°

horizontally by an extraction magnet (17), so that it enters end magnet M2 at nearly the same place as on its previous orbit. The bunch emerges at ~5° to the structure axis and is displaced by ~33 mm. After quadrupole focusing the bunch is compressed in a second three-magnet chicane (20). Fig. 5 shows the exiting longitudinal bunch phase space for three phase offsets.

5 PARASITIC PHENOMENA

Our high charge, short bunches and high pulsed current have never been obtained in a classical microtron or a RTM. Thus we must investigate CSR and regenerative transverse BBU, which can limit our accelerated bunch charge and pulsed current. CSR forces, which can increase the longitudinal and bending plane emittance from 3 to 5 times depending on the bunch length, δ_{z} [1,8], can be suppressed by decreasing the vacuum chamber height. A bunch circulating with radius R between two infinitely conducting plates separated by a distance of 2h radiates CSR power depending on the parameter $\Sigma = \delta / (2R\Delta^{3/2})$, where $\Delta = h/R$ [9]. Reducing h causes $\Sigma \approx 0.7$ to reduce the radiated CSR power by a factor of ten. Since CSR induced emittance growth is greatest in the 12th orbit, the emittance growth will also be reduced by an order of magnitude for $\delta_z \approx 0.5$ mm, $R \approx 25$ cm, and $h \approx 3$ mm. We will construct our vacuum chamber using the full 3 cm end magnet gap height into which we will place vertically movable plates so that we can experimentally investigate the CSR effects. In this way we hope to find a compromise between the beam losses and emittance growth.

Table 4: Main AS TM₁₁-like parasitic modes

			A		
N	f (MHz)	Q	$r_{\perp}(M\Omega)$	Pol.	Cell #
- 1	4862.16	22,657	1.25	X	1,3
2	4883.74	13,602	0.432	Y	1,3
3	4892.09	10,861	0.707	Y	2
4	4923.41	19,667	1.10	X	2

Regenerative transverse BBU has only been investigated in superconducting CW recirculating machines [10]. With our high pulsed current, we can reach the BBU threshold. The most dangerous RTM AS parasitic modes are TM₁₁-like and listed in Table 4.

The worst case steady state threshold BBU current is $I_t \bullet r'_{\perp} = 4E_z \lambda_r / [\pi \beta N \ln(W_e/W_i)],$

where r'_{\perp} is transverse shunt impedance per unit length, E_z is the accelerating field, the β -function is taken at the structure center, and Wi and W_e are injection and extraction energies [11]. For $E_z \approx 1.6 \times 10^7$ V/m, $\lambda_r \approx 0.061$ m, N=12, $\langle \beta \rangle \sim 3$ m, and injection and extraction energies of 5 and 35 MeV, respectively, $I_t \bullet r'_{\perp} \approx 0.018$ A×M Ω /m. For our RTM AS the maximum r'_{\perp} is ~ 15 M Ω /m and so $I_t \sim 1$ mA. However, our design calls for 115 mA so transverse BBU is important. Our computer simulations with both steady state and time dependent codes predict an I_t larger by an order of magnitude in the horizontal

plane and by two orders in the vertical plane. To increase our threshold BBU current above our desired 115 mA, we will damp the parasitic mode Qs by coupling them to external loads.

6 CONCLUSION

With our detailed design study and extensive computer simulations of a high charge/bunch low emittance 35 MeV electron source now complete, we are preparing to construct a prototype.

- A.A. Alimov, O.V. Chubarov, E.A. Knapp, V.I. Shvedunov, and W.P. Trower, "A Compact Race-Track Microtron as a Free Electron Laser Source", Nucl. Instrum. Meth. B139 (1998) 511.
- [2] P.G. O'Shea, J.A.Lancaster, J.M.J. Madey, R. Sachtschale, and C.R. Jones, "Single Bunch Injection System for an Electron Storage Ring Using a RF Photoinjector", in *Proc. 1997 Particle Accelerator Conf.*, M. Comyn, M.K. Craddock, M. Reiser, and J. Thomson, eds. (IEEE, Piscataway, 1998) p.2799.
- [3] PARMELA code, originally developed by K.R. Crandall.
- [4] V.G. Gevorkyan, A.B. Savitsky, M.A. Sotnikov, and V.I. Shvedunov, RTMTRACE code, VINITI deposit number 183-B89 (1989) (in Russian).
- [5] H.Herminghaus, A. Feder, K.-H. Kaiser, W. Manz and H.v.d. Schmitt, "The Design of a Cascaded 800 MeV Normal Conducting C.W. Race Track Microtron", Nucl. Instrum. Meth. 138 (1976) 1.
- [6] E.A. Knapp, A.W. Saunders, V.I. Shvedunov, N.P. Sobenin and W.P. Trower, "A Mobile Racetrack Microtron", Nucl. Instrum. Meth. B139 (1998) 517.
- [7] G.A. Novikov, O.V. Chubarov, K. Halbach, A.I. Karev, V.I. Shvedunov, and W.P. Trower, "Novel Race-Track Microtron End Magnets", Nucl. Instrum. Meth. B139 (1998) 527.
- [8] V.I. Shvedunov, H. Euteneuer, and K.-H. Kaiser, "Bunch Space Charge Limits in an RTM", in 1997 Particle Accelerator Conf., M. Comyn, M.K. Craddock, M. Reiser, and J. Thomson, eds. (IEEE, Piscataway, 1997) p.1902.
- [9] J.B. Murphy, S. Krinsky and R.L. Glukstern, "Longitudinal Wakefield for an Electron Moving on a Circular Orbit", Particle Accelerators, 57 (1997) 9.
- [10] P. Axel, L.S. Cardman, H.D. Graef, A.O. Hanson, R.A. Hoffswell, D. Jamnik, D.C. Sutton, R.H. Taylor, "Operating Experience with MUSL-2", IEEE Trans. Nucl. Sci. NS-26 (1979) 3143.
- [11] H. Herminghaus and H. Euteneuer, "Beam Blowup in Racetrack Microtron", Nucl. Instr. Meth. 163 (1979) 299.

OPERATION OF A LOW EMITTANCE LATTICE AT THE NSLS X-RAY RING*

E.B. Blum[#], R. Heese, R. Klaffky, S. Krinsky, BNL, Upton, NY J. Safranek, SSRL, SLAC, Stanford, CA

Abstract

The NSLS X-Ray Ring is now being operated with a low emittance lattice. The horizontal emittance was reduced to 45 nm-rad from 90 nm-rad at 2.584 GeV while maintaining a vertical emittance of 0.1 nm-rad. The electron beam life-time was unaffected by the emittance reduction because the decrease in the dispersion in the dipole magnets compensate for the higher bunch density in the Touschek effect. The lattice will also be implemented at 2.8 GeV after the strength of the focusing sextupoles is increased. The effect of low emittance operation on the synchrotron radiation users will be discussed.

1 INTRODUCTION

The NSLS X-Ray Ring has normally operated in a lattice with horizontal and vertical tunes of 9.14 and 6.20, respectively. The horizontal and vertical emittances were 90 nm-rad and 0.1 nm-rad. In the lattice design, the dispersion was constrained to be zero in the long straight sections. By relaxing this constraint, Safranek previously showed [1] that the horizontal emittance could be reduced to as little as 21 nm-rad with the same tunes at the cost of an excessive reduction in the dynamic aperture. He also obtained another lattice with a 38 nm-rad horizontal emittance and a dynamic aperture that was at least as big as the physical aperture everywhere in the ring. Unfortunately, the sextupole strength needed to correct the chromaticity of the 38 nm-rad lattice was greater than could be supplied by the existing sextupole magnets. Even so, a 50 mA electron beam could be stored before the onset of the head-tail instability.

To obtain a lower emittance without unreasonable increases in the sextupole strengths, a new lattice was developed with horizontal and vertical tunes of 9.83 and 5.71, respectively, producing a horizontal emittance of 45 nm-rad. The vertical emittance has remained unchanged at 0.1 nm-rad. Operating in this lattice required changes to the injection conditions and to the programs that are followed as the storage ring energy is ramped between the 750 MeV injection

energy and the 2.584 GeV operating energy. Currents as high as 500 mA have been stored using this lattice and 350 mA currents have been routinely stored for synchrotron radiation operations since September, 1998. The dramatic decrease in the beam size in the low emittance lattice is apparent from the digitized synchrotron radiation profiles in figure 1.



Figure 1: Digitized synchrotron radiation profiles in the original (left) and low emittance (right) lattices. The machine functions at the radiation source points are: (old) $\beta_x = 1.31 \text{m}$, $\beta y = 12.2 \text{ m}$; (new) $\beta_x = 1.04 \text{ m}$, $\beta y = 16.2 \text{ m}$.

2 LATTICE

The emittance ε_x of a storage ring is [2]

$$\varepsilon_{x} = \frac{CE^{2}}{\rho} \frac{\int_{D}^{\infty} \left(\beta_{x} \eta_{x}^{\prime 2} + 2\alpha_{x} \eta_{x} \eta_{x}^{\prime} + \gamma_{x} \eta_{x}^{2}\right) ds}{\int_{D}^{\infty} ds}, \quad (1)$$

where $C=1.47 \times 10^{-6}$ m/GeV², E is the ring energy, ρ is the dipole magnet bending radius, β_x is the horizontal beta function, η_x is the horizontal dispersion, $\alpha_x = -\beta'/2$, $\gamma_x = (1+\alpha_x^2)/\beta_x$, s is the longitudinal position around the ring, and the integrals are taken over all of the dipole magnets. The horizontal beam size at any point in the ring is

$$\sigma_X(s) = \sqrt{\varepsilon_X \beta_X(s) + \eta_Y^2 \sigma_F^2}, \qquad (2)$$

where σ_E is the energy spread

The NSLS X-Ray Ring was designed with a long straight section in each of the eight super-periods to provide space for injection components, RF cavities, wigglers and undulators for synchrotron radiation production. The original lattice was designed with zero dispersion in the long straight sections to minimize the beam size in the insertion devices by eliminating the second term in eqn. 2 and also to avoid any increase in the emittance from dispersion in the dipole field of a wiggler.

^{*}Work supported by the U.S Department of Energy under contract DE-AC02-98CH10086

^{*} Email: blum@bnl.gov

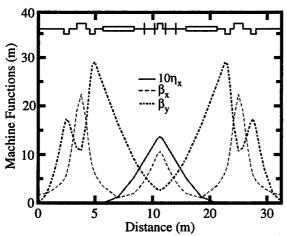


Figure 2. Machine functions in the original lattice.

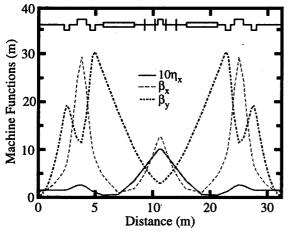


Figure 3. Machine functions in the low emittance lattice.

The properties of the X-Ray Ring lattice can be varied by adjusting the strengths of the four quadrupole families. Permitting non-zero dispersion in the long straight sections was found to reduce the emittance by lowering η_x and η_x' in the dipole magnets. The reduction in emittance more than compensated for the contribution to the beam size from straight section dispersion. The presence of dispersion in the wigglers located in the long straight sections did increase the emittance somewhat but the effect was small. A calculation shows that the dispersion in the 4.7 T, 5 pole superconducting wiggler increases the emittance from 43.3 to 45.6 nm-rad. Machine functions in the original and low emittance lattices are shown in figures 2 and 3.

To increase the dynamic aperture, a higher emittance lattice with weaker sextupoles but the same tunes as the low emittance lattice is used for injection at 750 MeV. When the storage ring is ramped from the injection energy to the 2.584 GeV operating energy, the lattice remains in the injection configuration until the ring energy reaches approximately 2.1 GeV. Then, the quadrupole k values are linearly interpolated from the

injection values to the low emittance values as the energy is increased from 2.1 to 2.584 GeV.

In the past, there has been a significant disagreement between the design and measured optics in the X-Ray Ring [3]. The discrepancy is mainly caused by the gradient errors produced by an orbit displacement in the sextupoles. The orbit error can not be easily corrected because the synchrotron radiation beamlines have been aligned to the displaced orbit. Instead, trim power supplies were connected to the quadrupole that is adjacent to the sextupoles in each of the eight superperiods. The trim current was determined by using the LOCO program [3] to find the quadrupole strengths that best restored the eight-fold periodicity of the measured orbit response matrix. This restored the machine functions to the design values.

An algorithm, sigycor, has been developed to correct the coupling of the horizontal and vertical betatron motion in the X-Ray Ring [4]. The algorithm uses the displacement in the vertical orbit with horizontal steering magnet field as a measure of the vertical coupling. The skew quadrupoles are then adjusted to minimize this coupling. The horizontal and vertical tunes were also varied to find where sigycor was most effective at minimizing the coupling. Following this procedure, a vertical emittance of approximately 0.1 nm-rad was achieved. This is the same as the vertical emittance obtained with the original optics.

3 ELECTRON BEAM LIFE-TIME

Two phenomena dominate the loss of electrons from the X-Ray Ring: the Touschek effect and scattering from the residual gas. The Touschek effect describes the loss of particles from the ring when their energy deviation exceeds the energy acceptance. The Touschek half-life is proportional to the volume of the electron bunch [5]. Consequently, an emittance reduction tends to decrease the Touschek life-time. However, the energy acceptance of the ring is determined by both the size of the RF bucket and the dispersion of the lattice. The reduced dispersion and momentum compaction ($\approx 50\%$ lower) of the low emittance lattice both contribute to an increase in the energy acceptance and may counteract the reduction in the bunch volume.

Particles are lost to gas scattering when the transverse or longitudinal momentum imparted to an electron by an interaction with a residual gas molecule carries the electron outside of the transverse or momentum acceptance of the ring [6]. The reduced dispersion in the low emittance lattice will again tend to increase the gas scattering life-time while the larger beta function in the quadrupole triplet will tend to decrease it.

Clearly, the competing factors that influence the Touschek effect and residual gas scattering make the

life-time of the low emittance lattice hard to predict but seem to counteract each other. The program ZAP [7] was used to calculate the life-time from these effects for both the original and low emittance design lattices. The calculations used an RF overvoltage of 1.4 and did not take the synchrotron radiation losses in the insertion devices into account. The results of these calculations are plotted as a function of beam current in figure 4. Also shown are measured life-times in both lattices. The points for the original lattice represent data collected during six days in July and August, 1998. The low emittance results were obtained during five days in October, 1998. The ZAP results closely resemble the data. The life-time in the low emittance lattice has proven to be slightly greater but not appreciably different than in the original.

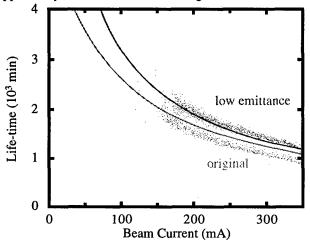


Figure 4: Measured and predicted life-times in the low emittance and original lattices.

4 EFFECT ON USERS

Most users are concerned only with the total flux of the synchrotron radiation and have not noticed any adverse effects from the low emittance lattice. The increase in life-time is an advantage but it is probably too small to notice. Certain users require tightly collimated x-ray beams and are more concerned with the brightness of the source than the flux. These users benefit greatly from the reduced emittance. Figure 5 compares energy spectra of the radiation produced by the X1 undulator in the forward direction. The two spectra were obtained from the low emittance and original lattices on successive 100 mA fills of the X-Ray Ring. The intensity of the first harmonic peak is approximately four times greater in the low emittance lattice.

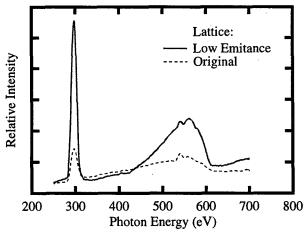


Figure 5: Photon energy spectra from the X1 undulator in the original and low emittance lattices. The beam current was 100 mA in both lattices.

5 CONCLUSIONS

The low emittance lattice has been successfully implemented in the NSLS X-Ray Ring at 2.584 GeV. The horizontal emittance was reduced to 46 from 90 nm-rad with the vertical emittance maintained at 0.1 nm-rad. Life-times are as good, or better than in the original lattice. The lattice will also be implemented at 2.8 GeV when a new power supply and cabling are obtained to increase the current in sextupole magnets.

6 ACKNOWLEDGEMENTS

The authors would like to thank Sue Wirick and Chris Jacobsen for measuring the radiation spectra shown in figure 5. They also thank Om Singh, Rich Biscardi, Yong Tang, Jim Murphy, and the rest of the NSLS staff for their help in implementing the low emittance lattice.

- J. Safranek, "A Low Emittance Lattice for the NSLS X-Ray Ring", proceedings of the 1997 Particle Accelerator Conference.
- [2] M. Sands, "The Physics of Electron Storage Rings: An Introduction", SLAC-121, Nov. 1970.
- [3] J. Safranek, "Beam-Based Modeling and Control of Storage Rings", proceedings of the 1997 Particle Accelerator Conference.
- [4] J. Safranek and S. Krinsky, "Plans to Increase Source Brightness of NSLS X-Ray Ring", Proceedings of the 1993 Particle Accelerator Conference, 1491-1493.
- [5] H. Bruck, Accelerateurs Circulaires de Particles, Presses Universitaires de France, Paris, 1966.
- [6] J. LeDuff, "Current and Density Limitations in Existing Electron Storage Rings", Nucl. Instrum. Meth. A239, 1985, p. 83.
- [7] M.S. Zisman, S. Chattopadhyay, and J.J. Bisognano, "Zap User's Manual", LBL-21270, 1986.

MEASUREMENT OF BEAM SIZE AT THE PHOTON FACTORY WITH THE SR INTERFEROMETER

M. Katoh and T. Mitsuhashi*

High Energy Accelerator Research Organization, Oho, Tsukuba, Ibaraki, 305-0801 Japan

Abstract

The beam size at the low emittance configuration of the Photon Factory was measured by the use of the SR interferometer. The spatial coherence of the visible SR beam was measured for both of the vertical and horizontal directions with the wavelengths at 500nm and 633nm. From the measured spatial coherence of the SR beam, the beam size measurements of 87.3 μ m in the vertical and 261.2 μ m in the horizontal were obtained. The observed horizontal beam size agreed with the designed beam size.

1. INTRODUCTION

The SR interferometer, which was developed by one of the authors, has good sensitivity for small beams. Since this method is based on the spatial coherence of th'e SR beam, it is suitable for measuring small electron beam sizes[1],[2][3]. The principle of object-profile measurement by means of the spatial coherency of the light is known as van Citterut-Zernike's theorem[4]. In this time, we measured both the vertical and the horizontal beam sizes at the high brilliant configuration of the Photon Factory. In the measurement of interferogram as a function of spatial frequency by the use of SR interferometer, we ordinary use the method which is scanning the double slit separation. In other hand, we can measure the spatial coherence by using the method which is scanning the wavelength. Using these two method together, we can measure the spatial coherence in wider spatial frequency region. In this time we measured the spatial coherence with different two wavelengths for the check of using these two methods.

2. SPATIAL COHERENCE AND BEAM SIZE

According to van Citterut-Zernike's theorem, the profile of an object is given by the Fourier Transform of the complex degree of spatial coherence at longer wavelengths such as visible light. Let f denote the beam profile as a function of position y_0 , and γ denote the complex degree of spatial coherence as a function of spatial frequency v. Then γ is given by the Fourier transform of f as

$$\gamma(v) = \int f(y_0) \exp\{-i2\pi v \cdot y_0\} dy_0 \qquad (1)$$

follows:

The interferogram which is observed with the SR interferometer (see Fig.1, below) $I(y_1)$ is given by,

$$I(y_1) = I_0 \left[\sin c \left(\frac{2\pi a}{\lambda R_1} y_1 \right) \right]^2 \cdot \left[1 + |\gamma(v)| \cos \left(\frac{2\pi D}{\lambda R_1} y_1 + \varphi \right) \right]$$
(2)

where a denotes the half of slit height of the double slit D, denotes the double slit separation, R_I denotes distance between the interferogram and the back principle point of objective lens of the interferometer, and φ denotes the phase of the interference fringe. The spatial frequency v is given by

$$v = \frac{2\pi}{\lambda R_0} D \tag{3}$$

where R_0 is distance between the object beam and the double slit. Two methods are available to measure the interferogram as a function of the spatial frequency, one is scanning double slit separation, and other is scanning the wavelength. Using equation (2), we can measure the degree of spatial coherence from the interferogram. Using equation (1), we can measure the beam profile by Fourier transform of the spatial coherence, and under the assumption of a Gaussian beam profile, we can measure the RMS beam size from the interferogram.

3. SR INTERFEROMETER

The SR interferometer is basically a wavefrontdivision-type two-beam interferometer using polarized quasi-monochromatic rays. A schematic drawing of the SR-interferometer is shown in Fig.1.

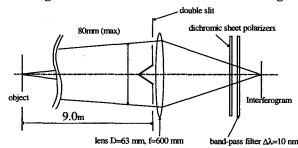


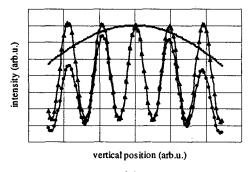
Fig.1 Outline of the SR interferometer.

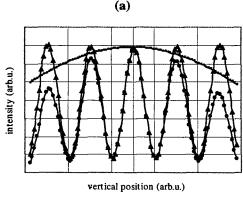
The double slit assembly is located in the front of the objective lens as close as possible(few mm). We use an aperture of 1(width) x 2(height) mm² for the double slit assembly. A diffraction limited doublet lens having a diameter of 63mm and a focusing length of f=600mm was used as an objective. A dichroic sheet polarization filter (extinction ratio: 10⁻⁴) and a band-pass filter of 10nm bandwidth was used to obtain a polarized quasi-monochromatic ray. The distance between source point and double slits of the SR interferometer is 9.03m.

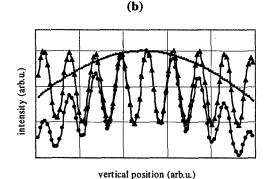
^{*} Email: mitsuhas@mail.kek.jp

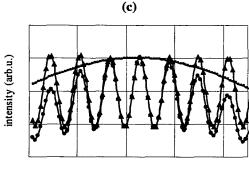
4.VERTICAL BEAM SIZE MEASUREMENT

4-1. Measurement of the absolute value (visibility) of the complex degree of spatial coherence in the vertical direction.









vertical position (arb.u.)
(d)

Fig. 2. Observed vertical interferograms. (a) D=7mm, λ =500nm, (b) D=7mm, λ =633nm, (c) D=12mm, λ =500nm, and (d) D=12mm λ =633nm.

The interferogram was measured by changing the double slit separations D between the two slits from 3mm to 22mm in 1.0mm steps at the two wavelengths of 500nm and 633nm. Four examples of observed interferograms are shown in Fig.2. From Fig.2, we can see that the contrast of the interference fringe is reduced when the double-slit separation is increased, due to the finite size of the beam.

4-2. Evaluation of vertical beam size from spatial coherence measurement.

The absolute value of the complex degree of spatial coherence is evaluated from the visibility of the observed interferogram. The results are shown in Fig. 3.

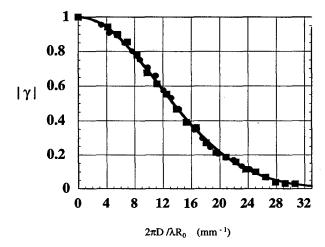


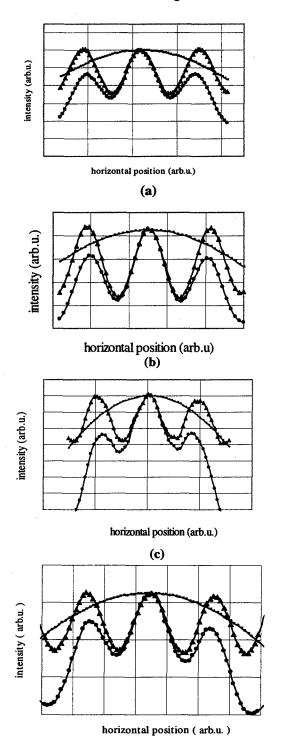
Fig.3. Absolute value of the complex degree of spatial coherence in the vertical direction. The round spots denotes the spatial coherence measured with λ =633nm, and the triangular spots denotes the spatial coherence measured with λ =500nm

From Fig.3, two results of the spatial coherence measured at wavelengths of 500nm and 633nm are agreed each other. Least-squares fitting of the spatial coherence by using a Gaussian beam profile is also shown in Fig.3. Since the result of fitting seems very good, we can conclude that the approximation of Gaussian profile to the beam profile is good enough. We can evaluate the RMS beam size from this fitting, and the result of the beam size is $87.3 \pm 0.4 \mu m$.

5. HORIZONTAL BEAM SIZE MEASUREMENT

5-1. Measurement of the absolute value (visibility) of complex degree of spatial coherence in the horizontal direction

The absolute value of the complex degree of spatial coherence for horizontal direction was measured in the same way as in the vertical direction, but with the double-slit rotated by 90°. Four examples of observed interferograms are shown in Fig. 4.



(d) Fig. 4. Observed horizontal interferograms. (a) D=5mm, $\lambda=500$ nm, (b) D=5mm, $\lambda=633$ nm, (c) D=7mm, $\lambda=633$ nm.

5-2.Result of Degree of Spatial Coherence and Horizontal Beam Size

The absolute value of the complex degree of coherence is evaluated from the visibility of the measured interferogram. The results are shown in Fig. 5.

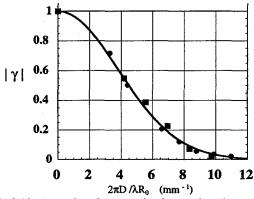


Fig.5. Absolute value of the complex degree of spatial coherence in the horizontal direction. The round spots denotes the spatial coherence measured with λ =633nm, and the triangular spots denotes the spatial coherence measured with λ =500nm

From Fig.5, two results of the spatial coherence measured at wavelengths of 500nm and 633nm are agreed each other. Least-squares fitting of the spatial coherence by using a gaussian beam profile including field depth effect is also shown in Fig.3. We can evaluate the RMS beam size from this fitting, and the result of the beam size is $261.2 \pm 2.6 \mu m$.

6. CONCLUSIONS

The vertical and horizontal beam sizes of the low emittance configuration of the Photon Factory were measured via SR interferometer. The two results of the spatial coherence measured at wavelengths of 500nm and 633nm are agreed each other. conclude the vertical beam size is 87.3 µm and the horizontal beam size is 261.2µm. The designed beam sizes are 263µm (using design values of energy spread and measured β and η -functions) in the horizontal and 110µm in the vertical (2% coupling is assumed). The observed beam size in the horizontal direction agreed with the estimated beam size. We achieved designed emittance in horizontal, and 1.26% coupling.

7. ACKNOWLEDGMENTS

The authors wish to thank to Mr. M. Shimoda for his help on data analysis. The authors also thank the Photon Factory operation group for their support.

8. REFERENCES

[1] T. Mitsuhashi, Proc of 1997 Particle Accelerator Conference, 766,(1997), Vancouver.

[2] T. Mitsuhashi, H. Iwasaki, Y. Yamamoto, T. Nakayama and D.Amano, Proc. 11th Symposium on Accelerator Science and Teqchnology 441 (1997).

[3] T. Mitsuhashi and T. Naitoh, Proc.of 6th European Particle Accelerator Conference 1565,(1998), Stockholm.

[4]M. Born and E. Wolf, "Principles of Optics, P459, Pergamon press. (1980).

A NEW PURIFICATION METHOD FOR SINGLE BUNCH OPERATION AT THE PHOTON FACTORY STORAGE RING

K.Haga, T.Honda, T.Kasuga, <u>T.Obina</u> and S.Sakanaka KEK, 1-1 Oho, Tsukuba, Ibaraki 305-0801 Japan

Abstract

Recently, the requests for single bunch operation of the Photon Factory 2.5GeV electron storage ring (PF-ring) have gradually increased and the requirements for the impurity, that is the rate of electrons in undesirable buckets to those in the main bunch, becomes severe. A purification method making use of the current dependence of the betatron tune has been applied up to present. However, after the reconstruction of the PF-ring toward low emittance optics[1], it requires a mastery skill to keep an impurity better than 10⁻⁵ and moreover the transversal motion of the main bunch excited by the method could affect experiments of SR users. In order to overcome the situation and improve the purity, a new single-bunch purification method, that is essentially a "selective RF knock-out (RFKO)", has been developed. The system worked stably during the users time and the typical impurity of 0.6×10^{-7} was achieved. Schematic description of the selective RFKO is shown in Fig.1, and related parameters of the PF-ring are shown in Table.1.

1 INTRODUCTION

Single bunch purity is very important for time resolved experiments such as Mössbauer spectroscopy, and the required impurity must be better than 1×10^{-6} - 10^{-7} . The typical impurity after the short bunch injection stays in the order of 10^{-3} - 10^{-4} ; consequently we must purity the spurious bunches in some method.

A transverse coupling impedance causes a shift in coherent betatron tune with the increase of the bunch current. Because the measured tune shift at the PF-ring was about -2x10⁴/mA, an RF knock-out (RFKO) tuned to the betatron frequency of the weak bunches can destroy the undesirable bunches with small currents but the main bunch with a larger current survives[2,3]. The frequency of RFKO and the aperture of a vertical scraper were adjusted preceded the users time, however, in some cases, it was difficult to keep the impurity better than 10.5 and we sometimes must re-configure such parameters. The difficulty is apparent after the reconstruction of the PFring because the non-linearity of the restoring forces becomes strong. Initial bunch current for SR users is about 60-70mA and the corresponding vertical tune shift is about 10-15kHz while the spread in the coherent tune is larger than the tune shift. Namely, the RFKO signal affects not only the spurious bunches but also the main bunch itself.

We developed a new purification method which is very simple and straightforward. An RFKO signal is modulated by a rectangular pulse train with a repetition of the revolution frequency of the beam. Since the pulse train has gaps with a width of the bunch spacing (about 2ns), only a selected bunch passing through the RFKO kicker on the gap timing can survive. In order to avoid effects of non-linearity of the restoring forces acting on the beam, the excitation frequency is frequency-modulated.

Table 1: Main parameters of PF ring

Parameters		unit
Energy	2.5	GeV
RF frequency	500.1	MHz
momentum compaction	0.061	
harmonic number	312	
emittance	36	nm rad
synchrotron frequency	23	kHz
betatron tune (vx/vy)	9.62/4.29	
RF voltage	1.7	MV
Radiation loss	400	keV

2 STSTEM DESCRIPTION

Figure 2 shows a block diagram of the system. A signal generator (MARCONI Inst., 2023) generates sinusoidal wave tuned to the vertical betatron resonant frequency, namely, $14\times f_{rev}+f_{\beta_y}\cong 22MHz$. Frequency modulation (maximum frequency deviation~100kHz, modulation

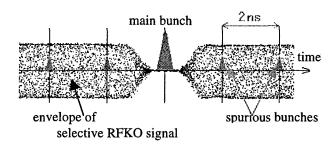


Figure 1: Schematic description of selective RFKO.

[†] Email: obina@mail.kek.jp

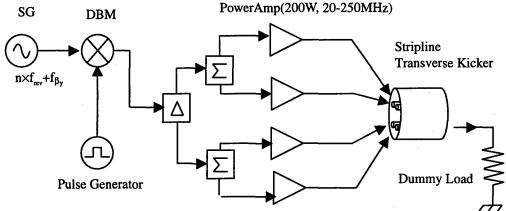


Figure 2: Block diagram of the system

frequency ~4Hz) is applied in order to avoid effects due to non-linearity of the restoring forces acting on the beam. A double balanced mixer (DBM) is used to turn the KO signal off during the period (~4ns) of passage of the main bunch. We tested several DBMs of several models in order to select a DBM which has excellent isolation between RF and LO port. The pulse generator HP8131A has a rise/fall time faster then the bunch spacing of 2ns, and an amplitude high enough to switch the DBM. The rise time of the pulse generator is faster than 200ps and the minimum pulse width is about 500ps with the amplitude of ± 5 V. A timing signal synchronized to the bunch revolution generated by dividing the RF acceleration signal by 312 (harmonic number) is used as the trigger of the pulse generator.

The output of the DBM is splitted by a 180° power splitter (mimi-curcuits), and splitted again with 0° power splitters in order to produce the signal which kick the beam only in vertical direction. The wide-band signal processing is required to maintain the fast rise time of the signal.

Power amplifiers (R&K A250-200-R) were previously used for the bunch-by-bunch feedback system during the high beam current study at the TRISTAN Accumulation Ring[4]. Its bandwidth and maximum power of 20-250MHz and 200W, respectively, are sufficient for our single bunch purification system. Four power amplifiers are connected to stripline electrodes of the transverse kicker. The output signals of the kicker electrodes are fed to the outside of the storage ring and used to adjust the timing of the pulse generator by observing the beam-induced signal and the RFKO signal simultaneously.

3 RESULTS

Figure 3 shows signals from button-type electrode when successive three bunches are injected (top) and removed except for the central bunch with the selective RFKO system (bottom). The pulse width was set to about 4ns and the opening of the vertical scraper was 7mm away from the centre of the beam.

A measurement of the bunch population is performed with a photon counting method using a PIN photodiode which has high sensitivity in X-ray region [5-7]. Figure 4 shows an example of photon counting measurement. The abscissa shows the time and the ordinate shows the counts of channels of MCA. Several spurious bunches are recognizable in every 2ns before the purification(top). It is clearly seen that the spurious bunches are removed with the purification procedure. The measured impurity of the 1st bunch (2ns behind the main bunch) was 8.3×10^{-5} and 5.6×10^{-7} before and after the purification, respectively. It took about 300 seconds to measure the impurity.

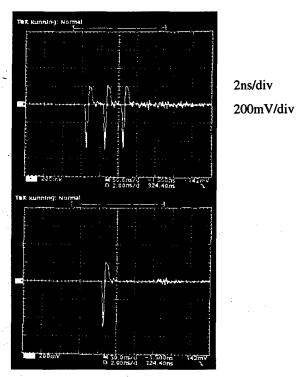


Figure 3: Successive three bunches are injected (top) and knocked-out except for the central bunch (bottom). (2ns/div, 200mV/div)

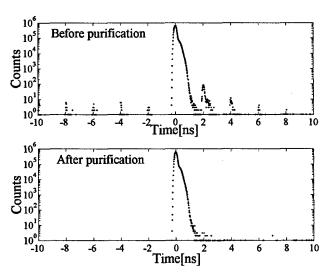


Figure 2: Bunch population measured with photon counting method before (top) and after (bottom) purification.

The rise time of the RFKO signal is fast enough, however, there are some ringing lasted for several nano seconds which can affect the main bunch. We decided the procedure of single bunch purification as shown below:

- Inject short bunches (about 70mA)
- Accelerates up to 3GeV to improve lifetime
- Increase H-V coupling to improve lifetime
- Remove leading bunches proceed the main bunch (for about 5sec)
- Remove trailing bunches after the main bunch (all time)

During the users time, we applied the purification system all the time because the impurity grows gradually without the purification. Some electrons thrown out from the main bunch are captured into the trailing buckets because there are openings of the separatrix due to the synchrotron radiation[8]. For example, an impurity of 4.6×10^{-5} was measured one hour after the stop of purification. Because there are no apertures toward the foregoing buckets, the purification of them are performed only once after injection. The vertical scraper is not used in the routine operation because we could accomplish the enough impurity without it.

A typical result impurity measurement during the users time is shown in Fig.5. In this case, the impurity is better then 10⁻⁷ behind the main bunch. There is a small bunch before the main bunch, however, can be overcome by optimising the purification procedure.

The pulse generator and signal generator are remotely controlled by GPIB via LAN-HPIB gateway. HP-VEE is used for an operator interface for its easy and rapid development environment. It was not necessary to

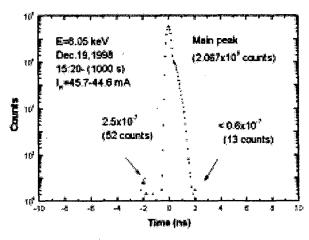


Figure 3: Typical impurity measurement during users time (courtesy of S. Kishimoto).

tune the system and to measure the impurity for every injection.

4 SUMMARY

We installed a new single bunch purification system at Photon Factory. An impurity of 2×10^6 - 0.6×10^7 was achieved during users time. The system works reliably and it becomes to an indispensable tool for single bunch operation. Several parameters (ex. FM modulation index, carrier frequency, clearing procedure) are not optimised yet. The impurity might be improved with the optimisation. We are installing the same system on the PF-AR (PF Advanced Ring).

The authors express their sincere thanks to Dr. S.Kishimoto for his great contribution for the X-ray photon counting system, and to Dr. Tobiyama who kindly provided the power amplifiers.

- [1] M. Katoh, et.al., "Operation of the Photon Factory with a High Brilliance Optics" EPAC'98 (1998)590
- [2] Photon Factory Activity Report #7 (1989) R-3
- [3] Photon Factory Activity Report #8 (1990) R-7
- [4] M.Tobiyama and E. Kikutani, "Study of Bunch by Bunch Feedback System in TRISTAN-AR", Proc. Particle Acc. Conf. (1997)2335
- [5] S. Kishimoto, Nucl. Instrum. and Methods, A309 (1991)603
- [6] S. Kishimoto, Nucl. Instrum. and Methods, A397 (1997)343
- [7] S. Kishimoto, Rev. Sci. Instrum. 69(1998)384
- [8] T.Obina, et.al, "Measurement of the longitudinal bunch structure in the Photon Factory positron storage ring with a photon counting system", Nucl. Instrum. and Methods A354(1995)204

ELETTRA STATUS AND DEVELOPMENT PLANS

C. J. Bocchetta*, S. Tazzari and R. P. Walker, on behalf of the ELETTRA team Sincrotrone Trieste, Trieste, Italy

Abstract

The present performance and upgrade projects of the ELETTRA light source are presented.

1 INTRODUCTION

The 2 GeV third generation light source ELETTRA has now completed more than 5 years of operation since the start of commissioning (October '93). ELETTRA currently operates for a relatively large number of hours per year, and with good efficiency. Far from being in a static operations phase however, a great deal of investment is being placed in the future growth and improvement of the facility including the construction of a number of new beamlines and insertion devices and a number of important machine development projects [1]. A major upgrade of the injection system is also under consideration.

2 STATUS AND ONGOING DEVELOPMENTS

2.1 Operations

At the end of 1998 ELETTRA completed five years of operation for Users. Over this period the facility operated for more than 27,000 hours of which more than 20,000 were dedicated to User experiments. 1998 concluded with a User uptime of 92.6% (93.6% excluding storms) bringing the overall five year up time to 93%. Last year the facility operated for the greatest number of hours, a total of 6528 of which 5256 were dedicated to User operation. The scheduled operations calendar for 1999 is less dense (6192 hours) and reflects the large number of installations to be performed on the machine. The more frequent shutdowns will be used for the installation of new front ends, vacuum chambers and insertion devices for new beamlines and for strategic upgrades to improve the performance of the accelerator. By the end of 1999 there will be 18 operational insertion device sections occupying eight of the eleven available straight sections. To date ELETTRA has eight beamlines fully operational, three are being commissioned of which one is fed by a bending magnet source. Eight additional beamlines are under construction of which four are bending magnet sources.

The accelerator which is normally run at 2.0 GeV is scheduled to operate at 2.4 GeV for 23% of its time

during the first semester of 1999. At this higher energy the current is limited to 120 mA to contain the thermal load on the vacuum chamber at acceptable values. The lifetime, strongly limited by the Touschek effect at the lower energies, is 52 hours at 100 mA compared to 32 at the same current at 2.0 GeV. ELETTRA is able to provide a maximum beam energy of 2.5 GeV.

2.2 Insertion Devices

The increased demand of the User community to have polarised radiation from insertion devices is being satisfied by the construction of new APPLE type undulators having four arrays of permanent magnets (NdFeB) [2]. By the end of November this year four of six planned undulators will be installed in the storage ring. Two of these with periods of 60 and 125 mm will be installed in one straight section separated by a chicane magnet, which enables two experimental stations to be operated simultaneously. The undulators of length about 2.2m are separated by a small dipole magnet that will provide a 2 mrad separation of the two photon beams.

One device has already been assembled and shows good agreement between measured field distributions and model calculations [3]. Traditional shimming techniques are not applicable in the elliptical undulator configuration and so new methods have had to be developed. Vertical block displacements were used to correct a phase independent quadrupole error. The optical phase error is a function of the field polarisation, but has been able to be compensated by groups of shims on two consecutive horizontally magnetized blocks. End coils compensate residual gap and phase dependent first and second field integrals.

In addition to the above mentioned undulators a wiggler has been approved and is under study for a second crystallography beamline. The main characteristics that are currently being studied are the length of the sections and end terminations that allow a better correction of field integrals.

Progress is being made with the compensation of residual closed orbit distortions of the electromagnetic elliptical wiggler (EEW) [4]. A dedicated digital feed-forward system compensates for the residual magnetic field errors by correcting the beam orbit with four coils (two per plane) powered by four independent power supplies. It is based on a DSP (Digital Signal Processor) system with A/D and D/A converters. The system samples the

^{*}email: carlo.bocchetta@elettra.trieste.it

horizontal and vertical currents provided by the EEW power supplies and computes the four correction currents. At present the computation is based on a pre-calibrated look-up table which minimizes the residual beam orbit distortion. The programmability of the DSP allows, however, to implement more sophisticated correction techniques.

2.3 New Vacuum Chambers

The installation of new insertion devices (ID's) providing horizontal, circular and vertical polarised synchrotron radiation has called for the development of new bending magnet vacuum chambers to account for the increased thermal load on the radiation slot. The chambers made of aluminium alloy AlMg-Mn (Peraluman) have high thermal conductivity and are greatly simplified compared to the original stainless steel types. The main differences being the absence of an internal NEG strip, and the removal of the photon beam stopper away from the chamber body. This has allowed a more compact form and minimised chamber deformation in addition to easing upgrades of the photon beam shutter whenever higher power densities are encountered from new insertion devices. The body has been constructed from two welded machined halves with an internal surface roughness of 0.2 um. Both Conflat and the rhomboidal VAT anticorodal flanges use diamond edged gaskets for aluminium to stainless steel connections.

In addition to the bending magnet chambers, extruded aluminium vacuum vessels are now being adopted for all future and some existing insertion devices. These ID chambers are pump-free with an elliptical cross-section that has a minimum internal aperture of 14 mm and an external dimension of 17 mm. These economical chambers are easy to manufacture and have cooling channels on either side. The same technique is also being adopted for those parts of the machine having a rhomboidal cross-section. In this case the extrusion is machined to the final exterior cross-section including cooling channels. Tapers to small aperture cross-sections, placed beneath lumped corrector magnets, are still made of stainless steel to reduce eddy current effects during operation of fast orbit feedbacks.

The first set of chambers (for bending magnet and insertion device) was installed in October last year.

2.4 SR-FEL Project

A storage ring FEL project was initiated in May 1998 under partial EC funding together with other European partners (CEA/LURE, CLRC-Daresbury, Univ. Dortmund, ENEA-Frascati and MAX-lab) [5]. All major equipment items are now under construction and are due for installation between August and October. First lasing attempts will be made towards the end of this year at 350 nm before proceeding towards shorter wavelengths (* 200 nm). Recent tests of ELETTRA performance in FEL

mode (1 GeV, 4-bunches) have given encouraging results that stable operation with 100 mA total current can be achieved with of the order 200 A peak current.

2.5 New Diagnostics

A new electron Beam Position Monitor (BPM) is presently under advanced design for the storage ring. The purpose of this system is to provide ultra-stable, at the μm level, position signals for a Local Feedback processor. The BPM has been designed for the low gap aluminium chambers mentioned above. In order to achieve the expected performance, two main developments have been undertaken: a mechanical design of a low gap BPM fitted with 14mm diameter buttons along with the relative support system and vacuum chamber interface and an electronic design that includes a new analogue front-end and a digital amplitude demodulator.

For maximum sensitivity in the vertical plane the buttons have been located close together with only 12mm center-to-center distance in the horizontal plane. Two bellows, either side of the BPM body, will isolate mechanical movement transmitted by the vacuum chamber. The support system will provide state-of-the-art short-term (vibrations) and long-term (thermal) stability to the monitor. Furthermore a monitoring of BPM motion at the sub- μ m level will be installed. Two such systems are presently under evaluation, one based on an opto-electronic micrometer, the second based on capacitive sensors.

The electronics of the BPM system is composed of the following blocks: an analog front-end, a digital receiver (AM demodulator) and a DSP processor. The main function of the front-end is to provide high-stability and resolution for the button signals with sufficient bandwidth for the Local Feedback to operate properly. Two frontend solutions are presently being designed: a 4-channel front-end, developed in collaboration with the Swiss Light Source, and a 4-to-1 multiplexed front-end, being developed in-house. In order to keep the gains matched on the four channels, a pilot frequency signal will be injected at the front-end inputs and the amplitudes of the four outputs will be kept equal by tuning each channel gain. The digital receiver block will provide x & y position signals by means of a state-of-the-art Digital Demodulator (Digital Down-Converter). Finally a DSP module will manage the data stream and provide filtered values to the central processor of the Local Feedback.

The BPM's will be installed in an ID straight of an existing beamline this summer. First tests with the new electronics are expected towards the end of the year.

In addition to new electron BPM's a new type of photon BPM is under development. This diagnostic is based on the energy analysis of emitted photo-electrons when an undulator photon beam strikes a blade. A prototype system based on two blades and hemispherical energy

analysers will be installed on a beamline at the end of this year [6].

A recently installed dual-sweep streak camera manufactured by Photonetics has been added to the arsenal of beam diagnostics. The device can operate in a syncroscan mode at 250 MHz, thereby allowing the observation of consecutive bunches spaced 2ns apart.

2.6 Third Harmonic Cavity

Progress has been made with the design of a third harmonic cavity to enhance beam lifetime. The decision to adopt a single super-conducting cavity has been taken, but the decision to go ahead awaits a final budgetary quotation and its approval. The structure of the cavity is a scaled version of the Soleil double cell system. It will operate at 1.5 GHz and the flange to flange length of the cryostat is approximately 1.1m. The cavity is idle and will provide a maximum voltage of 600 kV. Beam energy losses of a few Watts are easily replaced by the 500 MHz rf system. Taking into account static losses plus a safety margin a refrigerator of 40 W will be sufficient. The construction will be outsourced and a possible installation date is mid 2001. The improvement to the Touschek lifetime is of the order of a factor 3 to 3.5 at 2.0 GeV and 2 to 2.5 at 2.5 GeV.

2.7 Transverse Multibunch Feedback

A transverse multi-bunch feedback (one BPM and one kicker/plane) consisting of a wide-band bunch-by-bunch system is nearing completion [7]. The positions of the 432 bunches, separated by 2 ns, will be individually sampled and corrected. A prototype RF front-end module has been installed. The data is processed by digital electronics. Extensive filter simulations have been performed in a Matlab environment. Installation and first commissioning of the system is foreseen for the end of this year.

3 DEVELOPMENT PLANS

3.1 Short Insertion Devices

The beamline construction plan has already allocated ten insertion devices to the eleven possible long straight sections and the last remaining section will be allocated within the year. Attention is now turning therefore to the two short (1.2-1.5 m) sections in each achromat of the expanded Chasman-Green structure. Much of this space has already been put to good use by placing diagnostics and the rf cavities there, however even without moving existing diagnostics nine locations are available.

Machine operation with such devices has been studied and appears to be possible, with certain restrictions. Beam sizes and divergences are larger than for standard IDs and there is a greater sensitivity to energy spread variations. Linear optics effects on tunes, beta functions and dispersion are acceptable provided many high field devices are not installed. No further deterioration in

dynamic aperture is expected above that introduced by the existing devices. Effects on emittance are not great, but may limit the field of any high field tuneable devices to prevent intensity fluctuations on other beamlines. Flux and brightness calculations for representative devices indicate 20 times better flux from a wiggler and 200 to 300 times more brightness from an undulator compared to the bending magnet sources

In view of the strong interest in such sources a first bending magnet chamber is being constructed to allow the extraction of radiation at both 0° (ID) and 3.45° (bending magnet). This chamber will be in aluminium and is planned for installation in September. The ID itself is under study. With minor modifications a standard bending magnet front end will be adopted.

3.2 A New Injector

A decision has been taken to concentrate on a booster synchrotron as a possible new full-energy injector for ELETTRA. A design study is being carried out to be completed by the end of the year. The new injector would use a 100 MeV linac as a pre-injector. The 2.5 GeV booster placed on the inner side of the storage ring building can be constructed without major interference to the operation of the light source, up to the moment of connection. Studies are being performed to find the optimum lattice in terms of construction costs bearing in mind the requirement for top-up injection. An upgrade will also be performed of the storage ring injection elements. Use will be made as much as possible of existing equipment, for example the transfer line and parts of the existing linac.

- [1] C. J. Bocchetta and R.P. Walker, "Present Performance and Future Objectives at ELETTRA", Proc. EPAC 1998, p. 568.
- [2] B. Diviacco, et al., "Construction of elliptical undulators for ELETTRA", Proc. EPAC 1998, p. 2216.
- [3] B. Diviacco, et al., "Development of elliptical undulators for ELETTRA", this Conference.
- [4] R. P. Walker et al., "Construction and testing of an electromagnetic elliptical wiggler for ELETTRA", Proc. EPAC 1998, p. 2255.
- [5] R. P. Walker et al., Proc. 1998 Int. FEL Conf., to be published.
- [6] A. Galimberti, et al., "A new approach to photon beam position monitoring at ELETTRA", This Conference.
- [7] R. Bressanutti, et al., "Design considerations for the Elettra Transverse multi-bunch feedback", This Conference.

GAS INJECTION EXPERIMENT DURING ELETTRA OPERATION

E. Karantzoulis, J. Miertusova, F. Pradal, L. Tosi, G. Tromba, A. Vascotto Sincrotrone Trieste*, Italy

Abstract

Gas injection experiments have been performed to gain a better understanding of the effect of local vacuum conditions on beam lifetime and gas Bremsstrahlung. Various gases (H₂, N₂, Ar) were injected up to a pressure of 5e-6 mbar into the storage ring during machine operations, with various currents, energies, ID gaps and machine fillings. Results of lifetime and gamma dose rate measurements at different pressure conditions are presented and discussed.

1 LIFETIME DUE TO GAS DENSITY

The vacuum system of the ELETTRA storage ring has been designed to guarantee long lifetimes of stored beams i.e. at least ten hours with 300mA at 2 GeV. The total lifetime in an electron storage ring is mainly determined by: i) elastic and inelastic scattering on the residual gas molecules, ii) Touschek effect, i.e. scattering of electrons within the bunch, iii) trapping of charged particles in the beam potential and iv) quantum lifetime. In the ELETTRA synchrotron light source the total lifetime is Touschek dominated. For our purposes, the machine setting parameters, e.g. RF cavities temperatures, machine files, etc. are considered implicitly as constant parameters and are omitted in this work, as well as quantum effects which are only important for machines with extremely small apertures.

In this paper, we focus on lifetime measurements under different vacuum conditions. The higher the operating pressures the larger the cross sections of both the elastic and inelastic scattering and the probability of ion trapping can also increase in the presence of higher ion masses in the vacuum chamber.

The elastic scattering lifetime τ_{el} is usually expressed as:

$$\frac{1}{\tau_{elastic}} \sim \frac{Z^2 P}{E^2} (<\beta_x > \frac{\beta_{x0}}{A_{x0}^2} + <\beta_y > \frac{\beta_{y0}}{A_{y0}^2})$$
 (1)

where E is the beam energy, P is the pressure of a gas with atomic number Z around the ring, $<\beta_{X,y}>$ the average β -functions around the ring and $A_{(x,y)0}$ the limiting transverse half apertures.

*URL: www.elettra.trieste.it

The gas pressure varies with the total beam current I_t due to desorption effects as:

$$\langle P \rangle = \langle P_o \rangle + \langle \frac{dP}{dI_t} \rangle I_t \tag{2}$$

where <dP/dI_t> is the average gas desorption coefficient.

The inelastic beam-residual gas encounters give rise to Bremsstrahlung gamma rays causing a pressure dependent beam loss and the lifetime can be evaluated [2] by:

$$\tau_B = \frac{X_j}{cW\sum \rho_j}$$
⁽³⁾

where c is the relativistic electron velocity and W is the probability of the electron being lost from the machine per radiation length X traversing a material with density ρ_i. Both the radiation length as well as the material density can be expressed using the atomic weight A, the atomic number Z and the molecular partial pressures P; of the gas present in the vacuum chamber. The gas composition used to be represented by a hypothetical monatomic gas with Z = 4 to 5. As can be seen, to calculate the beam lifetime due to the gas density, the average values of pressures, atomic numbers, etc. are used to characterize the vacuum conditions in the chamber. However, the storage ring vacuum system is equipped with pumps located at a regular distance from each other and the pressure presents a parabolic distribution with minima at the pump location and the term average pressure is only used to evaluate the pressure between these two extremes. From the vacuum point of view, the operating pressure P in the ring is given by:

$$P = \frac{Q_T}{S} \tag{4}$$

where Q_T is the total gas load which is the sum of gas loads due to leakage (Q_L), out-gassing (Q_D), permeation (Q_P) and induced desorption (Q_I). The pumping speed S is a dynamic parameter which varies with pressure. Towards lower pressures the pumping speed exponentially diminishes in time and the real, or so called "effective" pumping speed (assuming the proper conductance of the pump's connection to the vacuum chamber) S_{ef} has to be taken into account [3]. All these vacuum parameters determining the operating pressure in the ring are strictly local values. The thermal and induced desorption as well as the permeation depends on the local degree of cleanliness and on the material quality of the vacuum chamber walls. If the storage ring is not perfectly tight the gas load from leakage is also rigorously localized.

The pressure in the ELETTRA storage ring is monitored by means of sputter-ion pump (SIPs) pressure readings [4]. In each of the 40 m long vacuum sectors, 25 SIPs are installed. Pressure profiles in all six vacuum sectors are displayed on the vacuum panels in the control room. From the pressure values P_i (N (=150) is the total number of pumps) the average pressure is calculated as:

$$\langle P \rangle = \sum_{i=1}^{N} P_i / N \tag{5}$$

Equation 5 is only an approximation and does not always reflect accurately the real vacuum conditions and to some extent the observed lifetime behavior. For example, in the case of a vacuum leak, a local pressure exceeding the normal operating pressure level by 2 to 3 orders of magnitude can be produced. In such cases a lifetime decrease is usually noticeable (a variation of about 30% less in most cases). However, the average pressure given from eq. 5 is affected only slightly and does not appear to fully explain the observed lifetime. To understand better the role of local pressure on the beam lifetime due to gas density the following experimental apparatus has therefore been installed in the ELETTRA.

2 EXPERIMENTAL APPARATUS

The drawing of the gas injection system allowing a local pressure increase in the storage ring is shown in fig. 1:

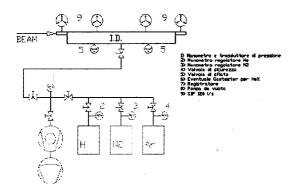


Fig. 1 - Experimental arrangement allowing gas injection into the ELETTRA storage ring

It is possible to inject through the dosing valve different gases (H₂, N₂, Ar) into the insertion device vacuum chamber ID_S3 and to create a local "pressure bump" up to 8e-6 mbar. In Fig. 2 many such bumps are shown obtained by regulating the gas flow. The average pressure values monitored during all the described experiments never exceeded 6e-9 mbar.

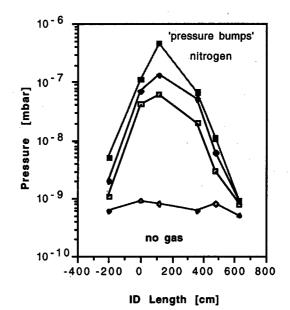


Fig. 2 - Pressure bumps created by nitrogen injection

3 RESULTS AND DISCUSSION

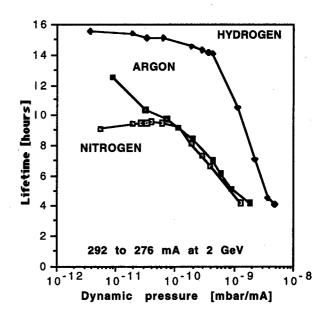


Fig. 3 - Total lifetime decrease caused by local dynamic pressure increase

Fig. 3 clearly shows that in the case of Ar, a minimum local pressure increase leads to an immediate lifetime reduction. This effect is less pronounced injecting nitrogen but at dynamic pressures higher than 1e-10 mbar/mA the lifetime decreases are the same for both argon and nitrogen. On the other hand the hydrogen 'pressure bump' causes a negligible lifetime decrease up to a local dynamic pressure of 1e-9 mbar/mA. It has been also observed that, switching off the SIPs, a uniform operating pressure varying from 3e-9 up to 7e-9 mbar was created in the

whole ring without any measurable change in lifetime whereas at the same average pressure (as defined in eq. 5) of 5e-9 mbar with the pressure bump of nitrogen, the beam lifetime changed by as much as 30% (250 mA at 2 GeV).

Since the pressure is measured only at certain points of the ring with an accuracy that is increasing with pressure, expression (1) should be used with care bearing in mind that it is valid for homogeneous pressures around the ring. Thus for large deviations from homogeneity it may be preferable to use the dominant gas species with the highest local pressure for the estimations of elastic scattering lifetime. Additionally eq. (1) does not take into account the effect of local partial pressures of out-gassing species and subsequently local desorption coefficients.

During the gas injection experiments, bremsstrahlung gamma rays measurements have been performed for radioprotection purposes in a non restricted area outside the shielding wall.

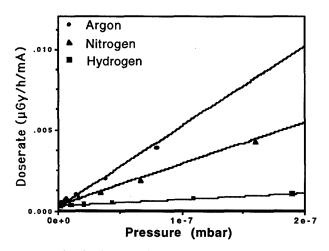


Fig. 4 - Gamma dose rate versus pressure

One of the environmental ionization chambers, used to monitor radiation levels around the beam-lines, allowed us to evaluate how different conditions of the vacuum in the chamber produced relevant changes in the bremsstrahlung radiation that is channeled into the beam-line during operation with the beam.

The gamma monitor is placed at about 3 m from the beam-line hutch in a position aligned with the straight section. It detects the secondaries generated by the bremsstrahlung gamma rays after interacting with the first optic component of the beam-line, such as the first mirror, and after the attenuation due to the lead shielding wall placed in the beam-line hutch.

The plots of gamma dose rates normalized per mA of stored current as a function of the local pressures in the chamber obtained with Ar, N_2 and H_2 injections, are shown in fig. 4. Fits indicate a linear dependence according to:

$$G = G_0 + cZP \tag{6}$$

with G_0 =3.e-4 μ Gy/h/mA and C~3.5e+3 μ Gy/h/mA/mbar as expected [5]. On the contrary, the gasses injected did not affect the bremsstrahlung gamma rays emission detected by a reference ionization chamber installed at the end of another straight section of the ring.

Data showed that any local increase of pressure in the straight section chamber, although not preventing beam injection and storage, can cause, from the radio-protection point of view, a significant increase of radiation levels outside the shielding around the corresponding beam-line exit

Studies of ion trapping during the Gas Injection Experiments (GIE) have been reported elsewhere [6]. Here it is enough to mention that observations of beam characteristics were carried out for various beam configurations, currents and energies. The increase in vertical beam size with beam current that occurs only with high local pressure and 100% filling and which is large at low energy, is clearly evidence of ion trapping.

4 CONCLUSIONS

The Gas Injection Experiments at ELETTRA are very useful not only because they help in understanding the validity of approximations used but also because they reveal valuable information on the behavior of vacuum chambers having a higher pressure profile. New straight section vacuum chambers made from extruded aluminum are to be installed and these studies will highly help us to better analyze any future complications.

- J. LeDuff, "Current and Density Limitations in Existing Electron Storage Rings", Nucl. Instrum. Methods A239,83 (1985)
- [2] C. Benvenuti, R. Calder, O. Grobner, "Vacuum for Part. Accel. and Storage Rings", CERN-LEP-VA/87-66
- [3] J. Miertusova, "New Asp. on the Vac. Syst. Design for the Future Synchr. Light Sources", Vacuum, 48, 7-9, p.751
- [4] F. Giacuzzo, J. Miertusova, "Total Pressure Measurements", Proc. PAC'95, Dallas, U.S.A., 1995, p.684
- [5] A. Rindi, "Gas bremsstrahlung from electron storage rings", Health Physics, Vol. 42, No. 2, 1982
- [6] E. Karantzoulis et. al., "Collective Effects at ELETTRA", Proc. EPAC 1998, Stockholm, Sweden, 1998, p. 960

TRACKING STUDIES OF TOP-UP SAFETY FOR THE ADVANCED PHOTON SOURCE*

M. Borland, L. Emery, ANL, Argonne, IL

Abstract

The Advanced Photon Source (APS) is a 7-GeV, third-generation synchrotron radiation source. To provide more stable beam for users, we are pursuing a new operating mode called "top-up" [1, 2]. In this mode, the beam current is not allowed to decay as it normally would, but instead is maintained at a high level through frequent injection. A safety question with top-up mode is, during injection with photon shutters open can injected beam ever exit a photon beamline? This might happen, for example, due to full or partial shorting of a dipole coil. Extensive, detailed tracking studies were performed to assess the possibility of such an accident given the planned safety measures. We discuss the safety philosophy, the scenarios simulated, and the advanced computational techniques employed. A companion paper [1] discusses analytical estimates of top-up safety.

1 SAFETY ISSUES FOR TOP-UP

The basic safety issue for top-up is whether it is possible, through an equipment malfunction or other circumstance, to extract injected beam down a photon beamline. If this occurred, a significant radiation level would result outside the accelerator enclosure. For example, if a dipole immediately downstream of an ID straight section shorts (has zero field), the electron beam entering the dipole would continue on the same path as the ID photon beam and exit the accelerator enclosure. In principle, this could continue for an arbitrarily long time. In practice, radiation monitors would probably prevent this, but we considered this alone inadequate.

Instead, we started from the realization that synchrotron light sources are safe with photon shutters open when there is no injected beam, because stored beam cannot be extracted down a photon beamline as it will be lost on a aperture first. Extending this, we postulated that it is impossible to extract injected beam while maintaining stored beam, even when the two beams travel on different trajectories. If this is true, then top-up safety can be assured by disabling injection if stored beam is lost while shutters are open. Analytical methods [1] bolster one's confidence in this postulate, but provide no proof. As a result, we undertook tracking studies to further strengthen our confidence in this assumption.

2 SIMULATION METHODOLOGY

A "top-up accident" is a situation where stored beam exists while injected beam is exiting the accelerator enclosure

*Work supported by U.S. Department of Energy, Office of Basic Energy Sciences, under Contract No. W-31-109-ENG-38.

via a photon beamline. This requires, at minimum, a fully or partially shorted dipole magnet that leads into a photon beamline (i.e., the dipole that shorts is the one that normally diverts the beam path from entering the photon beamline). At APS, 35 of 40 sectors each have the potential for two beamlines (see Figure 1), namely, an ID beamline on the upstream (AM) dipole and a bending magnet beamline on the downstream (BM) dipole.

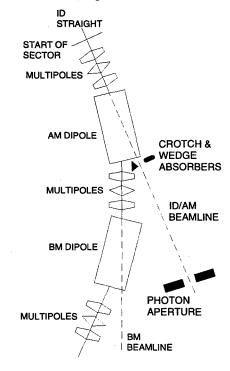


Figure 1: Schematic representation of an APS sector

For a fully shorted dipole, it is clear that injected beam can be extracted. For an unshorted dipole, it is clear that stored beam can survive. The possibility of an accident occurs somewhere between these two extremes, where one might have stored beam while extracting injected beam. (Note that the injected and stored beams need not enter the dipole at the same position or slope. If they did, it would be impossible to have an accident.) Hence, the simulations must be done with the degree of dipole shorting as a variable quantity, called the fractional strength error or FSE (equal to 0 for no short and -1 for a full short.) As illustrated in Figure 2, the simulations find the minimum FSE at which stored beam survives and the maximum FSE at which injected beam exits via the beamline. If the former is greater than the latter, we have a positive "FSE gap" and a safe situation.

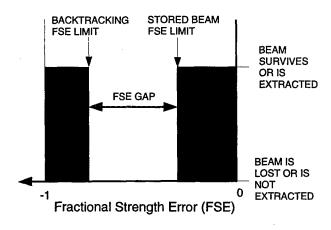


Figure 2: Illustration of the FSE "safety gap." In the middle region, stored beam is lost *and* injected beam does not exit the photon beamline.

In addition to dipole shorting, we simulate other faults that might conspire to produce an accident. For example, suppose that a magnet downstream of the shorted dipole also malfunctioned, producing a "conspiratorial" kick that compensated the missing field from the dipole. In such a scenario, the perturbation of the stored beam orbit could be greatly reduced, making the FSE gap smaller.

For each scenario we must simulate the stored beam and injected beam. For the stored beam we simply compute the closed orbit in the presence of a particular FSE and other errors; we then track a single particle on this closed orbit to see if it is lost on an aperture.

The acceptance of a photon beamline is easily computed from knowledge of the apertures and does not depend on magnet settings or other variables. Hence, for the injected beam, we chose to track backwards from the photon beamline using an acceptance-filling beam, ending at the upstream end of the ID straight. If any particles exit the sector, then we assume that they might also reach the injection point, i.e., the parameters of that simulation correspond to extraction of injected beam. If no backtracked particles exit the sector, then no injected particles could exit via the photon beamline under those conditions. Tracking only to the beginning of the sector greatly reduces the number of possible parameters that might influence the computations, with the downside that our results may be very conservative.

The apertures in the ring and photon beamline are clearly crucial to these simulations. In the simulations, we used all available apertures in the ring: the extrusion and (per sector) eight bellows, two "crotch absorbers," and three "end absorbers." Since the photon beamlines are drift spaces for the electron beam, we used only the two acceptance-defining apertures, namely, the crotch absorber and wedge absorber (which form a pair at the start of the beamline) plus the photon safety shutter. Not all sectors have identical aperture configurations, but all have the same elements.

Because the position of most of the apertures cannot be measured directly, we determined tolerances on their positions. In the simulations, these tolerances were included by increasing the apertures by the tolerance amount. For example, a ± 43 mm aperture with a ± 5 mm tolerance is simulated as a ± 48 mm aperture. This extremely conservative procedure was necessary because of the time required to do randomized simulations using tolerances.

3 ACCIDENT SCENARIOS

We chose a number of scenarios that are most likely to lead to an accident. To make our results somewhat lattice-independent, we used 22 lattices with integer-spaced horizontal tunes from 18.2 to 39.2, except where noted. Also, except where noted, simulations vary FSE so that the limiting values (indicated in Figure 2) are found. The scenarios are the following:

Type 1 A single dipole shorts, but no other faults occur.

Type 2 A single dipole shorts and there is a worst-case compensating dipole field in a quadrupole or sextupole downstream of the dipole in the same sector. The worst-case compensating field is the one that best corrects the orbit distortion, limited by the maximum field that can be produced by the magnet. This scenario simulates both large single-multipole misalignments and shorting of the multipole (in a conservative way, as the quadrupole or sextupole field is not affected). Since the the compensating field is downstream of the dipole, it affects stored beam but not backtracked beam, which is the worst possible scenario.

Type 3 A single dipole shorts and there is a combination of a gradient error and worst-case dipole field in a single quadrupole in the same sector. The gradient errors take 20 values that range between the limits that move the tune into the integer and half-integer resonances, subject to constraints on the polarity of the quadrupole. To reduce computation times, these simulations are performed only for $\nu_x = 35.2$ (the standard tune) and $\nu_x = 20.2$ (the worst case for Type 2). In addition, a fixed FSE is chosen for each of the stored-beam and backtracking runs. The result is evaluated and the FSE inputs are adjusted until approximate boundaries are found for each type of run. Once these are found for one aperture configuration, they are generally valid for similar configurations, which saves considerable computation at the expense of sometimes giving pessimistic estimates of the FSE gap.

Type 4 A single dipole shorts and a single quadrupole in the same sector has its polarity reversed. These runs are done only for backtracked beam, as we assume that the tune error is compensated by adjustment of other quadrupoles in the ring, so that the stored-beam simulations from Type 1 can be used. This scenario is one that might arise if during replacement a power supply converter is miswired and the beam is stored again after adjusting the tunes using the other quadrupoles.

Figure 3 shows some representative data from simulations for Type 1. When all scenarios have been performed for an aperture configuration, we analyze the data to obtain the minimum FSE gap. Given the many conservative assumptions and the extreme nature of the scenarios, a positive minimum FSE gap indicates a safe configuration.

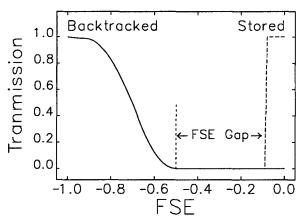


Figure 3: Typical Type-1 simulation results.

4 COMPUTATIONAL METHODS

Given the complexity of the top-up tracking, some might expect that we would have developed a new code for our problem. However, the program used was elegant [3], an existing code that does 6-dimensional tracking and other accelerator computations. The physics demands on the code were modest and could have been met by any number of codes. The only modification made to elegant was the addition of integration of field maps, necessary for backtracked beam simulations where the beam is very far off axis in sextupoles or quadrupoles. What was vital for our purposes was that elegant uses the Self-Describing Data Sets (SDDS) file format [4, 5]. Like all SDDS-compliant programs, elegant does essentially no postprocessing or data display itself. Rather, it relies on the powerful SDDS Toolkit, a group of about 70 generic data processing and display programs, that permits simplified development of postprocessing scripts for analysis of large amounts of data from many simulations.

For top-up safety tracking, about 500 runs are required for aperture configuration. These runs are grouped according to whether they simulate stored beam or backtracked beam, and according to the failure scenario. For each scenario type, a Tcl/Tk script is used to set up and submit the simulation runs. This script is itself usually invoked by another script that starts all the runs involved in a particular aperture configuration. These scripts greatly simplify the task of setting up and running a new round of simulations. A round of simulations for a sector takes about two days to run on 20 Sun Ultra 1 and Ultra 30 workstations managed by the Distributed Queueing System [6].

For each scenario, a specific script is used to postprocess the data and produce a simple results file (again, an SDDS file). These scripts also detect problems (e.g., missing data that might result from a workstation crashing), and to prevent using bad data, any simulations with problem data are deleted and must be run again. The user can easily do this by reinvoking the submission script. Like startup, postprocessing can be invoked with a single command. This command executes the scenario-specific scripts, then collates the scenario-specific results files into a single result file. In

addition, the script produces a single value—the minimum FSE gap—showing whether the configuration is unsafe.

Both the startup and postprocessing scripts use the SDDS Toolkit for data preparation and analysis. In addition to using SDDS files for all output, elegant uses SDDS files for configuration of tracking and for tracking input. Most of these files are prepared automatically by the scripts or by other elegant runs (a few represent external input, e.g., the apertures, and are prepared manually). For example, in some scenarios a closed-orbit simulation with conspiratorial orbit correction will be performed, and a series of values giving quadrupole and corrector strengths will be saved. These data are loaded sequentially by a backtracked beam simulation, in order to replicate exactly the conditions of the stored-beam simulation. Thus, there is no manual copying of data from one simulation to another, speeding the work and eliminating the possibility of transcription errors (an important consideration given the safety-related nature of the computations). Other examples of SDDS data used as simulation input are the coordinates of the acceptance-filling particles for backtracking and the multipole strengths for the 22 different lattices used in the simulations.

5 ACKNOWLEDGEMENTS

The authors wish to acknowledge the suggestions and advice of John Galayda (ANL), Jeff Corbett (SLAC), Al Garren (LBL), and James Safranek (SLAC).

- [1] L. Emery, M. Borland, "Analytical Studies of Top-Up Safety at the Advanced Photon Source," these proceedings.
- [2] L. Emery, M. Borland, "Top-Up Operation Experience at APS," these proceedings.
- [3] M. Borland, ANL, unpublished program.
- [4] M. Borland, "A Self-Describing File Protocol for Simulation Integration and Shared Postprocessors," Proc. 1995 PAC, May 1-5, 1995, Dallas, Texas, pp. 2184-2186 (1996).
- [5] M. Borland, "A Universal Postprocessing Toolkit for Accelerator Simulation and Data Analysis," Proc. 1998 ICAP Conference, Sept. 14-18, 1998, Monterey, California, to be published.
- [6] T. P. Green, "Research Toward a Heterogeneous Networked Computer Cluster: The Distributed Queuing System Version 3.0," SCRI Technical Publication, 1994.

BUNCH CLEANING STRATEGIES AND EXPERIMENTS AT THE ADVANCED PHOTON SOURCE*

N. S. Sereno, Argonne National Laboratory, Argonne, IL

Abstract

The Advanced Photon Source (APS) design incorporated a positron accumulator ring (PAR) as part of the injector chain. In order to increase reliability and accommodate other uses of the injector, APS will run with electrons, eliminating the need for the PAR, provided another method of eliminating rf bucket "pollution" in the APS is found. Satellite bunches captured from an up to 30-ns-long beam from the linac need to be removed in the injector synchrotron and storage ring. The bunch cleaning method considered here relies on driving a stripline kicker with an amplitude modulated (AM) carrier signal where the carrier is at a revolution harmonic sideband corresponding to the vertical tune. The envelope waveform is phased so that all bunches except a single target bunch (eventually to be injected into the storage ring) are resonated vertically into a scraper. The kicker is designed with a large enough shunt impedance to remove satellite bunches from the injection energy of 0.4 GeV up to 1 GeV. Satellite bunch removal in the storage ring relies on the single bunch current tune shift resulting from the machine impedance. Small bunches remaining after initial preparation in the synchrotron may be removed by driving the beam vertically into a scraper using a stripline kicker operating at a sideband corresponding to the vertical tune for small current bunches. In this paper both design specifications and bunch purity measurements are reported for both the injector synchrotron and storage ring.

1 INJECTOR SYNCHROTRON BUNCH CLEANING

The APS storage ring is designed to be filled one bunch per cycle at a 2-Hz rate. The principal bunch cleaning requirement is to prepare a single bunch by removing any beam that gets captured in all but a single bucket of the 432 possible injector synchrotron buckets. The bunch cleaning method presented here is based on an rf stripline kicker that is used to deflect the beam vertically into a scraper. Each kicker stripline is driven by a 250-watt broad-band (10 kHz-220 MHz) amplifier. The injector synchrotron ramps linearly from injection (350 MeV) to extraction (7 GeV) in 223 ms. Bunch cleaning will be done at relatively low energies starting at the synchrotron injection energy to

about 1 GeV so that the kicker amplifier power requirement is minimized.

Originally, injector synchrotron bunch cleaning was to be accomplished by driving the rf kicker with an amplitude modulated (AM) signal. The choice of AM is motivated by the fact that the kick must be zero at the bucket containing the bunch to be injected into the storage ring. The AM signal has the form,

$$V(t) = A(n\omega_o)\cos((m-\nu)\omega_o t)$$
 (1)

$$A(n\omega_o) = V_o \sin(\frac{n\omega_o t}{2}), \qquad (2)$$

where $A(n\omega_o)$ is the amplitude term, ω_o is the injector synchrotron revolution frequency, $\nu=0.8$ is the fractional vertical tune, and n, m are integers. The AM voltage waveform given by Eq. (1) has frequency components at the standard sum and difference frequencies

$$\omega_{\pm} = \{ (n \pm m) \mp \nu \} \omega_o, \tag{3}$$

which represent revolution harmonic sidebands at the tune frequency. Driving at a tune sideband enhances the effectiveness of the kicker because radiation damping is very small at the synchrotron injection energy and so large resonant centroid beam displacements are possible. Ultimately, the maximum amplitude is limited by the amplitude dependent tune shift due to sextupoles and Landau damping in the injector synchrotron. The parameter n is chosen so that the period of the amplitude term given by Eq. (2) is at minimum equal to the length of the linac pulse in injector synchrotron buckets (10 buckets for a 30-ns linac pulse). The value n=36 statisfies this requirement so that $A(n\omega_o)$ has a period of 12 buckets. The parameter m is chosen to minimize bandwidth, which requires that m=0.

The basic advantage of this system is that it minimizes the bandwidth required of all system components (hybrids, splitters, amplifier). The drawbacks, however, include the fact that any particles injected into buckets that happen to be at a zero crossing of the amplitude term will not be removed. A remedy to this problem would be to switch the value of n part way through the bunch cleaning cycle to the next lower half integer. Another drawback is that buckets near a zero crossing for $A(n\omega_o)$ receive only a fraction of the maximum kick. A way to increase the kick applied to buckets adjacent to a zero crossing would be to use a square wave for $A(n\omega_o)$ or increase the power output of the amplifier. On balance, these drawbacks complicate the implementation of a bunch cleaning system based on an AM

^{*} Work supported by the U.S. Department of Energy, Office of Basic Energy Sciences, Under Contract No. W-31-109-ENG-38.

[†] Email: sereno@aps.anl.gov

waveform and outweigh the single advantage of minimum bandwidth required of system components.

A simpler method was therefore chosen to perform synchrotron bunch cleaning at APS. The idea consists of driving the kicker at a vertical tune sideband so that the beam is removed at a vertical scraper. When the bucket containing the bunch to be injected into the storage ring passes the kicker, a fast gallium arsenide switch turns off the rf briefly so no kick is applied. This system is shown in Fig. 1. The principal component of this system is a fast switch with a risetime of 1.5 ns gated once every injector synchrotron turn. The speed of the switch is dictated by the requirement that the injection bucket receive no kick and buckets adjacent to it must receive a maximum kick from the kicker. This means that the switch must turn on and off in at least one rf period less the full width tenth maximum (FWTM) bunch length of 1 ns or 1.84 ns. In practice, the smallest bandwidth component will determine the system's overall speed.

The speed of the switch requires the 180° hybrid, highpower amplifiers and kicker to be broad-band devices. The broad-band hybrid is a relatively inexpensive off-the-shelf item and the stripline kicker is an inherently broad-band device to be described in the next section. The two high power amplifiers are, however, quite expensive due to both the bandwidth and high power requirement. The amplifier chosen was available in house and has a bandwidth of 220 MHz (250 watt) and therefore a rise time of 4.54 ns. This rise time is a bit long but should be adequate if the switch is commanded to start turning off the rf 1.5 rf periods (4.3 ns) before the target bunch passes the kicker. The switch must turn the rf back on as soon as the injection bunch passes. The slow amplifier rise time ultimately means that bunches adjacent to the target bunch will receive approximately 67% of the maximum available kick from the kicker. This should not be a practical problem as long as enough time is allowed for resonant displacement of the adjacent bunches to build up and saturate (in practice a few thousand turns).

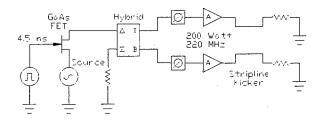


Figure 1: Time domain bunch cleaning schematic circuit diagram.

2 HIGH SHUNT IMPEDANCE STRIPLINE KICKER DESIGN

The bunch cleaning system described in the previous section relies on a high shunt impedance stripline kicker to

deflect the beam. This kicker is a modified version of the APS 352-MHz quarter-wavelength stripline kicker used for injector synchrotron tune measurements. The new kicker was modified by decreasing the stripline vertical separation by a factor of two, thereby increasing the kicker shunt impedance [1]. Figure 2 shows the kicker geometry. Each stripline is electrically connected and mechanically supported via a vacuum feedthrough at each end. The elliptical injector synchrotron vacuum chamber is mechanically matched to the smaller cross section kicker chamber by a transition piece.

MAFIA calculations [2] show that the shunt impedance of the new kicker is a factor of nine larger than that for the original tune measurement kicker. Measurements made for beam energies near injection using the tune measurement kicker show that for 180 watts total input power, the beam was deflected approximately 1 mm at a vertical scraper. The modified kicker should therefore be able to deflect the beam at least 5 mm at the scraper at injection using two 250-watt amplifiers. This amount of deflection should be more than adequate to keep the injection bunch well clear of the vertical scraper.

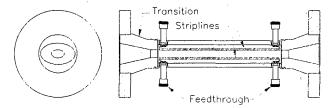


Figure 2: High shunt impedance kicker design.

3 STORAGE RING BUNCH CLEANING

Storage ring bunch cleaning is required in the event some charge remains in satellite buckets after cleaning in the injector synchrotron. The bunch cleaning system considered here relies on the fact that any satellite bunches injected will necessarily have much less current than the injected bunch. The small satellite bunches will therefore have a tune that is different from the large current bunches, due to the vertical transverse coupling impedance (mostly generated by the APS small-gap chambers [3, 4]). The satellite bunches can be removed by selectively driving the beam using a kicker at (or very near) the single particle tune frequency. The resonantly driven bunches can be removed by a suitably positioned vertical scraper.

This method was tested during storage ring machine studies time. The ring was filled with a standard user pattern consisting of six 1.67-mA bunches filled in buckets 0 through 5, followed by 25 2.00-mA bunches starting at bucket 72 and separated by 36 buckets (the storage ring consists of 1296 buckets) for a total current of 60 mA. Then 25 0.1-mA "contamination" bunches to be cleaned were filled three buckets downstream of each of the 25 2.00-mA bunches. The first six bunches are used to reliably trigger the BPM system so that orbit correction (both real time

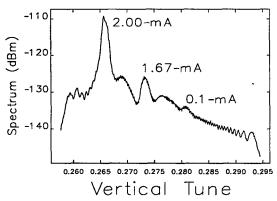


Figure 3: Storage ring tune spectrum for bunch cleaning 6+25 user pattern and 25 0.1-mA contamination bunches.

and slow) can be used to keep the beam fixed. Figure 3 shows the tune spectrum for this pattern. The large peak at $\nu_u = 0.266$ is due to the 2-mA bunches, the peak at $\nu_y = 0.274$ is due to the 1.67-mA bunches, and the peak at $\nu_y = 0.281$ is due to the 0.1-mA bunches. Figure 4 shows the APS bunch purity monitor triggered to view once per turn only the 25 2.00-mA bunches and 25 0.1-mA bunches. The purity monitor diagnostic counts photons incident on a photomultiplier and bins them in time. The figure shows the large current bunches as the central peak and the 0.1mA bunches both upstream and downstream of the large current bunches (downstream is toward zero bunch position in the figure) on a log scale. Since the 25 0.1-mA bunch pattern was filled only downstream of the large bunches, the diagnostic shows that during injection some of the 0.1mA bunches were unintentionally filled upstream of the large bunches.

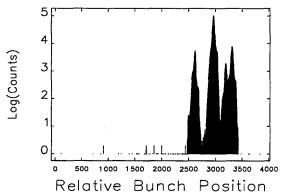


Figure 4: APS bunch purity monitor showing the 25 2.00-mA bunches and 25 0.1-mA bunches.

The bunch cleaning experiment used the tune measurement stripline kicker to drive the beam. The vector signal analyzer (VSA) was used as a signal source set to drive the tune of the 0.1-mA bunches. A vertical scraper was slowly moved toward the beam while orbit correction was running to keep the orbit fixed. Figure 5 shows the bunch purity monitor after the scraper had been moved to a position to intercept the resonantly driven 0.1-mA bunches. The figure shows that the charge remaining in the satellite bunches was five orders of magnitude below the 2.00-mA

bunch. The final beam current remaining was 52.5 mA, indicating that some of the beam in the desired user fill pattern was also removed. This is because the tune measurement striplines only produce approximately 20-30 micons centroid displacement when driven at full power. Any fast fluctuation in beam position that orbit correction cannot correct can therefore result in beam loss from the user pattern. The cleaning efficiency can be greatly improved by driving the small bunch beam centroids resonantly to larger amplitudes. This can be accomplished by using a higher shunt impedance kicker and/or more powerful amplifier.

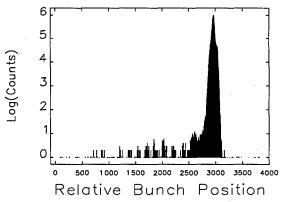


Figure 5: APS bunch purity monitor showing only the 25 2.00-mA bunches remaining after removal of the 25 0.1-mA bunches.

4 ACKNOWLEDGEMENTS

The author would like to thank M. Borland, L. Emery, G. Decker, and J. Galayda for providing valuable insight and discussion regarding bunch cleaning in rings. A. Lumpkin of ASD and E. Alp and T. Toellner of XFD jointly developed and commissioned the bunch purity monitoring diagnostic used in the storage ring bunch cleaning experiment. B. Lill and C. Gold of the APS Diagnostics Group provided engineering design and technical support for the injector synchrotron bunch cleaning system. E. Rotella of the APS Mechanical Group provided the the mechanical design for the high shunt impedance stripline kicker.

- [1] D. A. Goldberg and G. R. Lambertson, AIP Conference Proceedings, 249, 584 (1992).
- [2] S. H. Kim, private communication
- [3] N. S. Sereno et al., "A Potpourri of Impedance Measurements at the Advanced Photon Source Storage Ring," Proceedings of the 1997 Particle Accelerator Conference, Vancouver BC, 1700 (1997).
- [4] K. C. Harkay et al., "Impedance and the Single-Bunch Limit in the APS Storage Ring," these proceedings.

EFFECTS OF VERTICAL GIRDER REALIGNMENT IN THE ARGONNE APS STORAGE RING*

E. Lessner[†], E. Crosbie, S. Milton Argonne National Laboratory, Argonne, Illinois 60439 USA

Abstract

The effects of vertical girder misalignments on the vertical orbit of the Advanced Photon Source (APS) storage ring are studied. Partial sector-realignment is prioritized in terms of the closed-orbit distortions due to misalignments of the corresponding girders in the sectors. A virtual girder-displacement (VGD) method is developed that allows the effects of a girder realignment to be tested prior to physically moving the girder. The method can also be used to anticipate the corrector strengths needed to restore the beam orbit after a realignment. Simulation results are compared to experimental results and found to reproduce the latter quite closely. Predicted corrector strengths are also found to be close to the actual local corrector strengths after a proof-of-principle two-sector realignment was performed.

1 INTRODUCTION

The long-wavelength distortions induced by ground settlement are not, in general, too detrimental to beam stability, but can result in large beam-orbit corrector magnet currents. In the APS storage ring, magnets are supported by girders that can become misaligned due to ground settlement, particularly in the vertical direction. The displaced magnet centers cause orbit distortions that require correction. We examine the effects of vertical girder misalignment in the APS storage ring closed orbit. We study changes in the user orbit due to a partial girder realignment and the corrector strengths needed to reestablish that orbit to within the required tolerance. We also introduce an analytical method that provides a mean to perform machine tests to mimic the closed-orbit distortions that would be introduced by selected girder movements, prior to the physical realignment. Comparisons are made of machine tests vs. simulations and of corrector strengths predicted by simulations vs. the actual changes in correctors after a partial realignment of the ring.

2 EFFECTS ON THE CLOSED ORBIT

The storage ring magnets are mounted on six distinct girders per sector, in a total of 40 similar sectors. Figure 1 shows one sector of the nominal low- β_y lattice. Girders 1 and 5 support three quadrupoles, one sextupole, two beam position monitors (BPMs), and two combined-function vertical/horizontal correctors. Girders 2 and 4 support the bending magnets, two sextupoles, one vertical/horizontal

corrector, and two BPMs. Girder 3 holds two defocusing and two focusing quadrupoles, one sextupole, two correctors, and one BPM. The sixth girder is reserved for insertion devices. The floor settlement affects the vertical closed orbit primarily through the odd-numbered girders, due to the strong-focusing quadrupoles mounted on them.

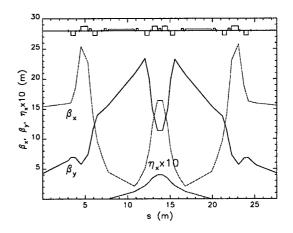


Figure 1: One sector of the APS lattice.

In 1997 the APS Survey Group performed a comprehensive vertical survey of the storage ring magnets. The data showed some displacements exceeding the \pm 0.15 mm vertical displacement tolerance limit with respect to the "smoothed" orbit [1]. We used the program elegant [2] to simulate the effects of the displacements on the closed orbit and to establish an order of priority for partial realignment, since a complete realignment of the ring is not feasible during a single shutdown. We identified the sector or group of sectors whose misalignments contributed most to the closed-orbit distortions. In particular, the displaced girders within and around Sector 16 were responsible for almost as much orbit distortions (about 1.6 mm rms uncorrected) as the distortions caused by the displacements over the entire ring (on the order of 1.7 mm rms uncorrected). Those were the first set of girders chosen to be vertically realigned, according to the established priority.

3 THE VGD METHOD

A partial or whole girder realignment will introduce perturbations in the established closed orbit ("golden orbit"). In particular, the resulting perturbations in the user orbit slope need to be corrected to within $\pm 10~\mu$ radians. The VGD method provides an analytical means to estimate those perturbations, quantify local corrector strengths needed to

^{*} Work supported by U. S. Department of Energy, Office of Basic Energy Sciences under Contract No. W-31-109-ENG-38.

[†]Email: esl@aps.anl.gov

reestablish the orbit, and an experimental means to test the realignment effects.

The method calculates the deflection (kick) at a corrector on a girder that is equivalent, in the rms sense, to the displacement of quadrupoles supported by the same girder. If we equate the rms of the distortions caused by a kick $\delta y'$ in a corrector V on a girder G, to the rms of the distortions caused by a displacement δy of the quadrupoles on the same girder, we obtain [3]:

$$(\delta y')_{V} = \frac{(\delta y)_{Q}}{(\langle \sqrt{\beta} \rangle)_{V}} (R_{1}^{2} + R_{2}^{2} + 2R_{1}R_{2}cos(\Delta\phi_{1} - \Delta\phi_{2}))^{1/2}, \quad (1)$$

where β denotes the vertical betatron function at the corrector and $R_i = (\sqrt{\beta_i} K_i l_i)$, with K_i, l_i and $\Delta \phi_i$, the strength, length and incremental phase advance of the i^{th} quadrupole, respectively. We assumed two quadrupoles on the girder, for illustration.

Table 1 lists the VGD equivalent kicks for the lattice model used in the simulations. Verification of the VGD

Table 1: VGD equivalent kicks

Girder	Corrector	Equivalent Kick
		$\delta y'/\delta y$ (mrad/mm)
1,5	A:V2, B:V2	0.1111
3	A:V4 and B:V4	0.0568

method is shown in Fig. 2 where we plot the differences between a real girder displacement near the 420-m mark and a VGD at the same location. For the latter, a 1-mm girder displacement is replaced by a 0.1-mrad kick. As shown in the figure, the residuals are less than 50 μ m, whereas either alone produces an rms orbit distortion of about eight times that or 0.40 mm.

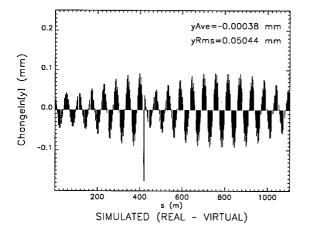


Figure 2: Residuals between real and virtual displacement.

4 CORRECTION OF REALIGNMENT EFFECTS

The VGD method also provides a local correction scheme. By adjusting the corrector strengths to *minus* the equivalent quadrupole displacements, we can artificially bring the girders to the correct elevation on the lattice.

Perturbations to the users' orbit, introduced by girder realignment, can be reduced by a factor of 10 by a local correction that uses the correctors defined by the VGD algorithm. The local correction may not be enough to bring the users' orbit to within the $\pm 10~\mu$ radians tolerance; however, this tolerance can be easily achieved by a further "global" correction, normally done using one corrector on each Girder 1 and one corrector on each Girder 5.

In Fig. 3 we compare the simulated changes in the users' orbit after a local correction, shown in the upper plot, to simulated changes after a local plus global correction, shown in the lower plot. The latter correction requires a maximum corrector strength of 0.3 mrad. Although there is little improvement in the residual closed-orbit distortions when the global correction follows a local correction, as expected, the overall corrector-strength rms can be 10% lower for the "local plus global" scheme, compared to the rms from a "global-only" scheme.

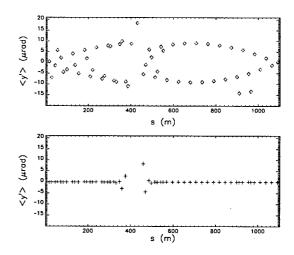


Figure 3: Users' orbit after a local correction (upper plot) and a local plus global correction (lower plot).

4.1 Experimental Tests

We conducted machine tests on the most misaligned girders in the ring, wherein the correctors in Table 1 were set to the values estimated by the VGD method. We tested virtually displacing individual girders and sets of girders, with and without orbit correction after the displacements. We found very good agreement between the experimental and simulated values of the uncorrected orbit at the BPMs for Girder 1 in Sector 16. For Girders 3 and 5, those values differed by less than 5% rms. This can be accounted for by

the measured differences between the simulated and actual machine β_y -values at the quadrupoles.

In the lower plot of Fig. 4 we show the experimental values of the orbit at the BPMs after a virtual displacement of all the quadrupole-supporting girders (1, 3, and 5) in Sector 16. The other plots in the figure show the corresponding simulation results, where "simulated real" indicates distortions obtained by displacing the quadrupoles, sextupoles, and BPMs on a girder by the survey-fitted values; and "simulated virtual" corresponds to distortions obtained by setting the correctors to their respective VGD values. As seen in the figure, the simulated virtual orbit reproduces the experimental virtual orbit to within 2% rms.

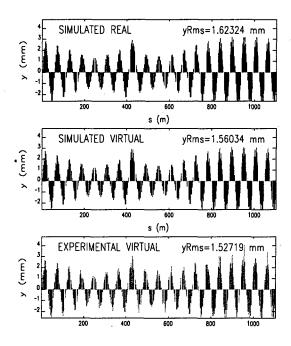


Figure 4: Closed orbit from experimental and simulated tests.

4.2 Measured Effects

In December of 1998, the girders on Sectors 16 and 17 were realigned vertically. The change in the machine vertical corrector strength for the correctors in the vicinity of the realigned sectors was about +0.034 mrad rms, compared to the values held just before the realignment. When all sectors were taken into account, the changes in the vertical corrector strengths were very small, about $+2 \mu radians$.

In Fig. 5 we compare the measured values of the correctors needed to reestablish the closed orbit to those predicted by the VGD method. Both the machine and simulation correction configuration included the local correctors, indicated in Table 1 and depicted in the figure by a continous line, and the nominal global correctors, depicted by a dashed line. The simulated values for the global correctors agree quite well with the machine values but less so for the local correctors. This is attributed to a different, al-

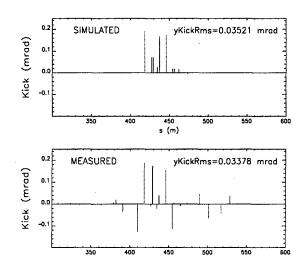


Figure 5: Corrector changes after a two-sector realignment.

beit equivalent, orbit-correction algorithm used during actual machine operation.

5 SUMMARY

We have simulated the effects of vertical girder realignment on the APS storage ring using both a method of "real" displacements and a method of "virtual" displacements. In the first method, the measured survey values of girder misalignments are distributed over all the relevant magnet elements on a girder and the effects on the orbit are obtained by simulation. In the second method, a girder displacement is shown to be equivalent, in the rms sense, to deflections produced by a corrector on the same girder whose strength value can be calculated analytically. This VGD method allows a machine study to be performed prior to an actual realignment. The virtual realignment, its effect on the orbit, and the corrector strength required to bring the orbit to the nominal values can then be gauged.

Machine tests prior to any physical realignment showed that the simulated results agreed quite well with the experimental values. Finally, the simulation-predicted corrector values required to restore the user orbit for a realignment of girders in Sectors 16 and 17 were close to the measured changes in vertical corrector after the physical realignment of those girders.

- H. Friedsam, M. Penicka, S. Zhao, "Beamline Smoothing of the Advanced Photon Source," Proc. 1995 PAC, pp. 2084-2087, (1996).
- [2] M. Borland, "User's Manual for elegant," version 12.4, ANL Note LS-231 (1995), also www.aps.anl.gov/asd/oag/oagSoftware.html.
- [3] E. Lessner, E. Crosbie, S. Milton, "Effects of Vertical Girder Realignment in the Storage Ring," APS-LS Note, to be published.

LIFETIME MODELLING AT APS AND ESRF

A. Ropert, ESRF, BP 220, F - 38043 Grenoble Cedex

Abstract

Achieving long lifetimes is a major concern for all third generation light sources, even for high energy rings like the APS (7 GeV) or the ESRF (6 GeV). Due to the small electron transverse dimensions and the trend towards small gap undulator vacuum vessels, Touschek scattering and gas scattering make signficant contributions to the lifetime reduction. Taking action to improve the lifetime therefore requires a reliable lifetime model. The strategy used on both machines to decouple the different contributions to the lifetime is presented and the experimental results analysed. Practical limitations on the lifetime modelling are discussed.

1 INTRODUCTION

APS and ESRF are two third generation light sources optimized for the production of hard X-rays. Among the processes that limit the lifetime, the gas scattering lifetime reduction due to small gap undulator chambers (leading to a beam stay-clear of 5 mm at APS, 8 mm at the ESRF) and the enhanced Touschek scattering induced by the increased density in the bunch volume (horizontal emittance in the few nanometer range, coupling in the 1 % range) are the more critical.

Table 1: APS and ESRF relevant parameters

		APS	ESRF
Energy	GeV	7	6
Particles		e+ (in 1998)	e ⁻
Average β _v	m	15.76	20.74
Transverse acceptance	m.rad	9.2510 ⁻⁷	3.2 10-6
Horizontal emittance	nm	8.6	3.8
Coupling	%	1.6	0.7
Standard filling pattern	1	6+25 * 3	662
Lifetime	h	30@100 mA	48@200mA
RF voltage	MV	9.5	11.67
Natural bunch length	mm	8.5	3.7
Bunch lengthening		1.6	1
Energy acceptance	%	1.7	2.5
Average pressure	nТ	0.5	1
Gas composition H	2 %	66	93
CH	I ₄	7	
H_2	0	2	
C	O	21	6.5
CC)2	4	0.5

As shown in Table 1, many parameters play a role in the modelling of the different contributions to the lifetime. Since the 2 rings are Touschek lifetime dominated, good lifetime modelling requires dedicated experimental conditions in order to decouple the different contributions and to minimize the uncertainties on measured parameters [1], [2].

2 ELASTIC GAS SCATTERING LIFETIME

2.1 Measuring technique

Measurements were focused on the vertical gas scattering contribution which is the dominant effect (for instance, the horizontal acceptance is 4 times larger than the vertical one at ESRF).

The procedure consists in imposing an additional aperture reduction by progressively closing one jaw (upper or lower) of a vertical scraper and recording the lifetime evolution versus the scraper aperture at different beam intensities.

In order to minimize the Touschek contribution, the machines were operated in the following conditions:

- i) filling pattern with a large number of bunches (83 * 10 for APS, 662 for ESRF) to get a small bunch current
- ii) large coupling obtained by bringing the tunes closer to the coupling resonance (APS) or by detuning a skew quadrupole corrector (ESRF)

Simulations and measurements are summarized in Fig. 1 and Fig. 2. In the APS case for instance, the interesting zone for the scraper stands between 0.65 mm (quantum limit) and 2 mm (above this aperture, the contribution of the other lifetimes starts to be too large).

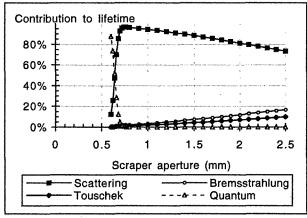


Figure 1: Evolution of the different lifetime contributions as a function of scraper aperture

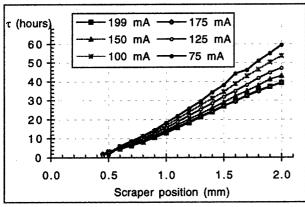


Figure 2: ESRF lifetime as a function of scraper position

2.2 Data analysis

The analysis of measurements is based on the expected dependence of the elastic gas scattering lifetime τ_G on the vertical acceptance A_v since:

$$\frac{1}{\tau_{G}} = C_{G} \frac{\beta_{A}}{A_{y}^{2}} \sum_{\text{atomsj}} \left[Z_{j}^{2} \sum_{\text{gasi}} \alpha_{ij} < \beta_{y} P_{i} > \right]$$

with C_G being a constant and β_A the β function at the location where the acceptance is limited. τ_G also depends on the gas composition which is defined by the residual pressure P_i , the atomic number Z_j and the number of atoms α_{ij} of the different species.

atoms α_{ij} of the different species.

Therefore $\frac{1}{\tau_{meas}}$ can be fitted to a linear law

 τ_{meas} b + aA_y⁻², where b accounts for scraper independent lifetime contributions. Using the same analysis for the different beam currents yields the gas scattering loss rate $\frac{1}{\tau_G} = \frac{\beta_{ID}}{\beta_{A_y}} \frac{a}{A_{ID}^2} = cI + d \ (\beta_{ID} \ and \ A_{ID} \ are the vertical <math>\beta$ and the aperture at ID location) and the pressure law $P = P_0 + \frac{\partial P}{\partial I} I \ (P_0 \ being the static pressure and <math>\frac{\partial P}{\partial I}$ the desorption coefficient). Table 2, Fig. 3 and Fig. 4 illustrate the results of this analysis.

Table 2: Results of the fitting procedure

	APS	ESRF
Loss rate (hours ⁻¹ .mA ⁻¹)	1.55 10 ⁻⁵	1.44 10 ⁻⁵
Desorption (Torr.mA ⁻¹)	2.94 10 ⁻¹²	1.96 10 ⁻¹¹

2.3 Modelling limitations and credibility

Any error in the position of the scraper with respect to the beam axis affects the analysis of raw data. In order to take into account alignment or displacement errors, an offset has to be introduced in the fit of the measured lifetimes. The error bars in Fig. 3 correspond to a $\pm 25~\mu m$ uncertainty on the scraper position.

In both machines, a significant discrepancy between measured and predicted pressures is observed. Several explanations can be advanced: non-ideal location and/or calibration of gauges, imprecision in the knowledge of the residual gas composition, long time constant for the pressure to get stabilized, importance of the weighting of the pressures by local β-functions. At ESRF, the moderate reproducibility of measurements linked to non-identical vacuum conditions (variation of the loss rate between 1.44 and 2.42 10⁻⁵ hours⁻¹.mA⁻¹) also illustrates the difficulties in obtaining good modelling.

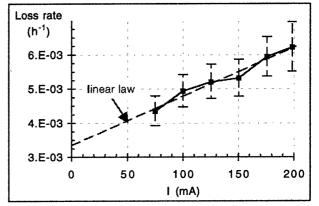


Figure 3: ESRF loss rate as a function of current

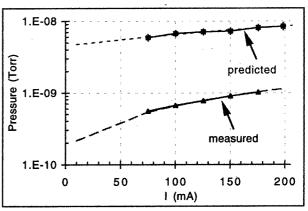


Figure 4: ESRF average pressure as a function of current

3 TOUSCHEK LIFETIME

The Touschek lifetime can be expressed as:

$$\frac{1}{\tau_{\rm T}} = \frac{Nr_0^2 c}{8\pi\sigma_{\rm x}\sigma_{\rm y}\sigma_{\rm L}\beta^3\gamma^2 \left(\frac{\Delta p}{p}\right)^3} f\left(\frac{\Delta p}{p},\sigma_{\rm x}\right)$$

where N is the number of particles per bunch, σ_x and σ_y the transverse dimensions, σ_L the bunch length and $(\Delta p/p)$ the energy acceptance which is determined by either the RF bucket or by transverse limitations (physical or dynamic aperture).

An almost pure Touschek lifetime is obtained when operating in single bunch mode at low coupling. Since the only unknown parameter is the energy acceptance, the strategy consists in recording the lifetime evolution as a function of the RF voltage and in deducing ($\Delta p/p$) from the fit of the experimental data.

The results of APS (5.4 mA, coupling \geq 1.6 %) and ESRF (3.5 mA, 0.77 % coupling) are shown in Fig. 5 and Fig. 6 and compared with simulations.

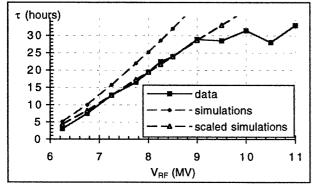


Figure 5: Lifetime evolution versus RF voltage at APS

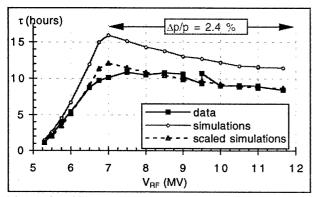


Figure 6: Lifetime evolution versus RF voltage at ESRF

In both machines, the asymptotic behaviour of the lifetime above a given RF voltage clearly shows that the limitation of the energy acceptance is dictated by transverse considerations and not by the available RF voltage.

The main sources of uncertainties come from the measured transverse emittances and bunch lengths since, for both machines, the bunch volume has to be scaled down (a factor 0.88 at APS and 0.76 at ESRF) in order to arrive at a good agreement between predicted and measured lifetimes.

4 BREMSSTRAHLUNG LIFETIME

The modelling of the Bremsstrahlung contribution is the most delicate since it is never the dominant contribution to the lifetime.

At ESRF, the method used was to record the evolution of the lifetime versus the RF voltage in conditions where the Touschek contribution is minimized (uniform filling, low current, large coupling). In addition to time consuming lifetime measurements, the already mentioned uncertainties on pressure, transverse beam sizes,.. make the comparison with simulations very difficult.

At APS, the lifetime evolution was recorded as a function of the current (Fig. 7) for different filling patterns (83 * 10, 83 * 2, 25 * 3 and 22 * 1 bunches).

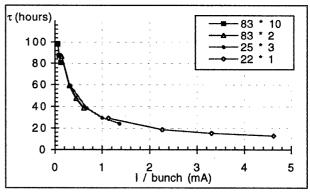


Figure 7: Lifetime dependence on bunch current at APS

Since the assumption of constant Bremsstrahlung and gas scattering contributions at a given current, whatever the filling pattern, looks reasonable, one can write:

$$\frac{1}{\tau_{\text{meas}}} = a + \frac{1}{\tau_{\text{T}}} = a + b \frac{I_{\text{bunch}}}{\sigma_{L}(I_{\text{bunch}})} = a + cI_{\text{bunch}}^{\frac{2}{3}}$$

using the dependence of $\frac{1}{\tau_T}$ on the bunch current and the

dependence of the bunch length on the bunch current which is given by:

$$\left[\frac{\sigma_{L}(I_{bunch})}{\sigma_{L}(I_{bunch} = 0)}\right]^{3} - \frac{\sigma_{L}(I_{bunch})}{\sigma_{L}(I_{bunch} = 0)} = kI_{bunch}$$

The fit of the measured lifetimes to the above analytical expression is excellent. The elastic and inelastic gas scattering loss rate can be estimated at: $\frac{1}{\tau_G} + \frac{1}{\tau_B} = 4.7510^{-5} \, \text{hours}^{-1} \, \text{.mA}^{-1} \, .$

5 CONCLUSIONS

The transverse-related limitation of the APS and ESRF energy acceptance was unambiguously established. The reasons for this are under investigation. The enlargement of the energy acceptance could significantly increase lifetime performance in the few bunch mode.

The strategy for modelling the gas scattering lifetime looks adequate but requires stable vacuum conditions to be fully exploited.

ACKNOWLEDGMENTS

I am very grateful to J. Galayda for giving me the opportunity of participating in the APS machine studies. I also want to thank the kind assistance of M. Borland, L. Emery and N. Sereno at APS, L. Farvacque at ESRF during the measurements.

- [1] A. Ropert, APS Light Source Note, Sept 1998
- [2] A. Ropert, ESRF Notes (74-96/MDT, 53-98/MDT, 08-99/MDT)

MASTERING BEAM LOSSES AND AGEING ISSUES AT THE ESRF

J.M.Filhol, L Hardy, U. Weinrich ESRF, Grenoble, France

Abstract

The ESRF accelerators have been in full routine operation for more than four years. The source delivers nearly 5600 hours of X-ray beam to 40 beam lines simultaneously, which in turn perform about 700 experiments (or 70.000 hours of experimental work) per year. To maintain free access in the experimental hall only public dose rates are allowed.

However, with the installation of small aperture vacuum vessels in straight sections a dramatic increase of bremsstrahlung outside the corresponding optic hutches was experienced. Hence, thorough studies to understand and master beam losses have been undertaken. This required the development of a beam loss detection system and the adoption of the strategy of using scrapers for beam collimating.

In addition, great care is taken to detect the first traces of ageing of equipment (for example due to irradiation) and therefore avoid, as far as possible, failures. It is indeed true to say that the more failures there are, the more the beam losses and the more the dose level!

BEAM LOSSES

1 BEAM LOSS MECHANISMS

The electron beam losses can be sorted into three major categories: beam losses during injection, electron losses during stable stored beam due to the finite lifetime and total beam losses following equipment failures or voluntary beam kills.

- Injection losses occur when the injected electrons do not fall within the longitudinal or transverse acceptance. At a typical injection efficiency of 80 % they are responsible for 20 % of the losses. Given the energy acceptance of the storage ring of more than 3 % most of the injection losses were measured to be due to transverse mismatching of the injected beam.
- Among the different contributions to the lifetime limitation only four effects appeared to be relevant: Elastic gas scattering, inelastic gas scattering, Touschek scattering and Compton scattering. In few bunch mode

delivery the Touschek lifetime dominates, by far, the losses whereas during the standard multibunch filling pattern all four contributions remain within the same range. The Compton scattering of photons on the electrons only takes place if the GRAAL experiment (which shoots with a laser on the beam) is in operation. The beam line is allowed to reduce the beam lifetime by no more than 20 %.

- Other major losses are experienced due to voluntary beam kill with a scraper jaw or due to equipment failure.

Only the lifetime losses and the equipment failures contribute to radiation problems around the optic hutches in user service mode whereas all losses are responsible for the chamber activation and radiation damage inside the tunnel.

2 BEAM LOSS POSITIONS

2.1 The beam loss detector system

To detect the losses a set of beam loss detectors were installed around the ring. The detection principle is based on the creation of light in a scintillator material when a high-energy particle crosses the detector volume. To suppress synchrotron radiation background the scintillator material is placed inside a protection of lead. Experience has shown that the detector readings are not very reliable due to too high synchrotron radiation background and damage caused during interventions. In addition, their positioning at the entrance of the ID vessels did not allow the comparison of the losses from different cells due to the different chamber and location configurations. An upgraded version with improved synchrotron radiation shielding was therefore installed and tested. The detectors are placed on the tunnel wall close to end of the straight section. First results show that the synchrotron radiation background is suppressed and that, in the case of loss changes, the signals of the detectors act correspondingly.

2.2 Tune shift with amplitude

Beam losses due to Touschek scattering were found to occur in the vertical plane. An explanation was found upon investigation of the tune shift with energy. Electrons with 3.5 % energy reduction find their vertical tune reduced from the nominal 11.39 to 11.00. Given that the integer resonance kills the beam, scattering effects with energy losses finally lead to a vertical oscillation.

This tune shift with amplitude effect was found to be the energy acceptance limiting factor. Consequently the majority of electron losses ended up in losses on Insertion Device chambers.

2.3 Scraping effect of a single chamber.

A vacuum chamber of the length 2 D and half aperture d has, for a minimum beta function β in the middle of the

chamber, a total acceptance of
$$A = \frac{\left(d^2 \cdot \beta\right)}{\left(\beta^2 + D^2\right)}$$
. If

the beta function is equal to half of the length of the vacuum vessel the total acceptance becomes maximum.

2.4 Interactions on chamber walls

Simulations were made to investigate the collision of the electrons on a chamber wall. One important result was that if the impact takes place with a rather small angle a large part of the electrons will be slightly scattered and will only loose a small fraction of their energy [1]. These electrons have the potential of being lost downstream. This effect was measured when closing a scraper jaw.

3 LOSS REDUCTION MEASURES

- -Low beta optics: One major change towards reduced losses was the switch to an optics with 2.5 m vertical beta function in the middle of the straight section. This is the optimum value in terms of vertical acceptance for the 5 m long vessels. This directly increased the vertical elastic gas scattering lifetime and the acceptance for vertical missteering during injection.
- The main filling pattern was changed from a 1/3 filling (350 bunches) to a 2/3 filling (700 bunch) thus doubling the Touschek lifetime.
- The septum sheet was placed further away from the beam (19.5 mm instead of 13.5 mm). This increased the transverse acceptance and therefore the Touschek and inelastic gas scattering lifetime.
- -For any operating mode, the refill consists of a toppingup and does not require to kill the stored beam.
- Limitation on injected beam: In order to comply with the maximum authorised dose rate in the experimental hall, and based on the radiation measured on the roof of the tunnel in case of localised loss, the amount of injected electrons into the storage ring was limited to $12\,\mu\text{C}$ per four hour period.

4 PROTECTION WITH SCRAPERS

Closing vertical jaws proved to be very efficient in removing the large majority of losses from the low aperture insertion device vessels. However, closing horizontal jaws also proved to help because this localises the losses due to the transverse acceptance limitation. A strategy was adapted which consists in closing all available scraper jaws to a position which hardly reduces the lifetime during stable stored beam. During injection the scraper jaws are closed even further to the limit of reducing the injection efficiency.

A new design for scrapers with appropriate shielding is being developed.

5 AGEING ISSUES & MAINTENANCE

5.1 Introduction

For a source which delivers 5600 hours per year of X-ray beam to 40 beamlines, the availability and the Main Time Between Failures (MTBF) must be as high as possible, which is a major challenge. We can assess that these goals are achieved at the ESRF since the availability in 1998 reached 95.3 % for a MTBF of 31 hours. In the remaining 4.7 %, only 3.7 % is due to faults and 1 % represents the dead time due to refills. Great care is therefore necessary to maintain this good performance at its present level, requiring significant preventive maintenance.

In addition, as explained above, a failure of equipment is synonymous to a beam kill and hence participates in the generation of radiation. This is also a good incentive to optimise the preventive maintenance strategy.

5.2 Preventive and curative maintenance

We can classify the failures into two types: those that last a long time (affecting the beam availability of the Machine) and those which are repetitive (with a greater effect on the MTBF). For this second class of failures, which create most of the doses due to 'beam kills', priority is given to our strategy of preventive actions.

- The first system concerned is the Radio frequency equipment (40 % of the total down time). As a preliminary step, a third RF unit (including a klystron and a pair of cavities) was added in the Storage Ring. In normal operation, two klystrons feed six cavities. This configuration, which is oversized with respect to our needs, enables the operation of each klystron below its maximum capacity and allows to distribute the power to six cavity couplers instead of four. Since then, the 'RF crowbars' which were the first cause of beam failures when operating close to the limits on both klystron and cavities, have completely disappeared. At the same time, more protective interlocks (RF arc detections) were integrated into the RF equipment, which on the one hand reduced the possibility of major failures, but on the other increased the frequency of beam trips. Fine tuning of the threshold of these interlocks had to be done to suppress wrong triggering. Finally the upgrading of the RF control

system, with fast data logging, proved to be very helpful in tracing the origin of the trips.

- Another source of frequent trips came from the vacuum controllers which were reading wrong values from vacuum gauges, triggering the closure of sector valves. Weaknesses in the electronic design were found which were enhanced by a non optimised shielding of the tunnel cables against the propagation of electromagnetic perturbations. Since then, all gauge controllers have been replaced and indeed, for one year now, the Machine has not been perturbed by problems of this type. Moreover, a systematic modification of the cables arrangement inside the tunnel which aims at reinforcing the shielding against EMC perturbations has begun.

5.3 Ageing issues

Most of the equipment is now eight years old and ageing effects have started to become apparent.

- -Several small vacuum leaks have started to appear since the end of 1997. The cause for these leaks was found to be a very slow corrosion process developing in the thickness of the stainless steel very likely caused by a welding agent which was badly removed at the time of manufacture of these vacuum vessels. Some of these leaks were temporarily fixed with "varnish" and a batch of spare vessels was ordered.
- A lot of blockage problems have been encountered with the various water cooling circuits and reduced flow rates have frequently been experienced. The latter have been recovered either by reversing the flow direction or by flushing the pipes with acid, which was particularly necessary on the small diameter pipes. We are currently carrying out an analysis of the small particles present in the water circuit which are responsible for the blockages.
- A complete review of the spare parts has been undertaken for all equipment and spares have been ordered for all critical items. Amongst others, this concerns electronic power components which appeared to have become obsolete and the procurement of which is time consuming.

5.4 Radiation damages

On a light source, radiation damages can be induced either by "conventional radiation", generated by the lost electrons (cascade) or by the intense X-rays which are emitted (or scattered) essentially on the beam axis plane. The crotch area (downstream the bending magnet) is the area were the highest X-ray dose is generated.

Since the first beam in 1992, about 4000 Amp.hours of electron beam current have been integrated and are producing synchrotron radiation (0.1 to 100 KeV), part of which hits equipment in the tunnels. During the first years of the Machine, some lead protection was progressively installed to shield some sensitive equipment located close

- to the medium plane (BPM/RF multiplexers, insertion devices optical encoders, ..). However, in 1998, the first disturbing effects associated with radiation damages really began to appear:
- Crazy readings of vacuum pressure levels: Several cables of Penning gauges were seriously toughened due to radiation and their insulation sheaths no longer performed their function. Since then, several of these cables have been found damaged and have been replaced. A systematic check is now done at every Machine shutdown. Furthermore, other cables driving low level signals such as magnet interlock have also been found damaged in areas close to the beam.
- On this occasion, we also found that most of the insulating sheaths of the sextupoles conductors had started to become brittle. Those which were more heavily damaged were immediately covered with a radiation-proof sheath. As a measure of preventive maintenance, all of the similar conductors have been re-insulated.
- Rather more serious problems occurred with the water flexible hoses. Guarantied to be "radiation resistant" most of them did not present any externally visible signs of ageing due to radiation. However, one after the other several of them tore (creating five water leaks in less than one year). Indeed, we discovered that the inner part of the hose had turned brown and had hardened. Once again, all the hoses that were most exposed were immediately replaced with another type of "radiation-proof" water pipe. This costly operation (~ 12\$/meter for the pipe) represented a workload of 1200 man-hours.

6 SUMMARY

The analysis of the loss mechanisms lead to the conclusion that the majority of losses take place on the small aperture insertion device chambers. Closing scraper jaws was found to be efficient in concentrating the losses on less critical points. Furthermore several improvements enabled to reduce the amount of losses. Following the success of the actions taken, half of the straight sections are now operated with 11-mm inner vertical aperture vessels without problems. In addition, several 8-mm inner vertical aperture vessels are now installed and in their test phase. In order to limit the number of beam kills due to failures, several preventive and curative actions took place. Following the first effects of irradiation on some material located in the tunnels in 1998, actions were quickly undertaken to resolve these problems. We expect to see the first beneficial effects in 1999.

[1] Behaviour of the beam in incident collisions with the scraper, T. Günzel, ESRF technical note 10-96 Theory, July 1996

STATUS REPORT OF THE ESRF

JM. Filhol, L. Hardy, U. Weinrich, ESRF, Grenoble, France

Abstract

The ESRF accelerators have been in full routine operation for more than four years. The source delivers 5600 hours of X-ray beam to nearly 40 beam lines simultaneously. Our first goal is to ensure good availability of the Machine as well as a satisfactory Mean Time Between Failures (MTBF). A third RF unit has been installed which, amongst other advantages, allows Landau damping from active modulation. A fast global feedback system to reduce the fast distortion of the closed orbit in the vertical plane has been put into operation and is giving results as expected. New filling patterns have been assessed and the Machine was successfully operated at 4 GeV (instead of the nominal energy of 6 GeV) in March 1999. Two years ago [1] several challenging short-term goals were defined. Most of them have been achieved or are actually in progress. The results are given below.

1 INTRODUCTION: THE ESRF TODAY

Three new associated members recently joined the ESRF (Portugal, Israel and Czech Republic) bringing to 15 the number of participating countries. The construction phase finished in December 1998 and the Operation phase then started. 37 beam lines (open to external Users) are now fully operational and three others are foreseen before year 2001. There are currently 54 insertion devices installed in the Storage Ring, which represent an integrated length of 85 metres. The number of shifts requested for experiments on the beamlines is approximately 2.5 times more than the ESRF can offer (5600 hours of beam time for Users in 1998). This justifies why the Machine Division's first goal is to ensure a high availability and Mean Time Between Failures whilst continuing challenging developments without disturbing the operation of the Machine.

2 MACHINE OPERATION

The number of hours in User Service Mode (USM) has gradually increased from 3000 hours in 1994 to 5600 hours in 1998. The major challenge over this four year period has been to increase the beam availability (percentage of scheduled time that beam is supplied for user operation) as well as the MTBF. We can consider that these goals have been achieved since the availability in 1998 reached 95.3 % (the highest score ever obtained at the ESRF) for a MTBF of 31 hours. Out of the remaining 4.7 %, only 3.7 % is due to faults and 1 %

represents dead time due to refills. Great care is taken to maintain this good performance, implying both preventive maintenance and upgrading of equipment [2].

3 RECENT DEVELOPMENTS IMPROVING THE MACHINE PERFORMANCES

Fast Global feedback

In November 1998 a fast global orbit correction system was put into operation. Its goal is to reduce, in the vertical plane, the fast distortions of the closed orbit due to mechanical vibrations of the girders supporting the quadrupole magnets of the Storage Ring. Indeed, the parasitic motion of the beam due to these vibrations must be kept at values as low as possible to avoid spoiling the good emittance figures so far achieved: ε_x = 4 nm rad and $\varepsilon_{r} = 30$ pm rad. The three main peaks of vibrations were observed at 7 Hz, 30 Hz and 60 Hz. This is why the bandwidth of this correction system has been set between 10⁻² and 100 Hz. This system uses 16 BPMs and 16 correctors to correct the orbit at a 4.4 kHz rate. This proved to work successfully (it is mostly efficient on the lowest frequency orbit distortions which are the most harmful for the users) and is now fully operational. The damping factor is up to 10 at 7 Hz and 2.5 when averaging all frequencies up to 100 Hz. The feedback brings the amplitude of the fast beam vertical position down to 1 µm rms all around the ring, as measured by independent fast beam position monitors, to be compared to the 10 µm vertical beam size (rms). [4]

• Fast Local feedback

At the request of a beam line, a local fast horizontal beam position feedback was installed on one straight section of the Machine. This system uses two BPMs to measure the horizontal electron beam position at both ends of the ID24 straight section and four fast steerer dipole magnets to produce a local correction bump (a closed bump which does not change the closed orbit on the rest of the machine). The amplitude of the vibration was reduced from 13 μ m (rms) to 1.1 μ m, to be compared to the 400 μ m horizontal beam size (rms).

• Installation of a third RF unit

In the second half of 1997, a new 1.3 MW transmitter, feeding a third pair of cavities, was put into operation on the ESRF storage ring. With this third transmitter the total accelerating voltage increased from 8 to 12 MV. In

addition, by modulating the RF voltage at the revolution frequency with this third unit it is possible to produce additional Landau damping of longitudinal multibunch oscillations. At the same time, this unit provides a redundancy to guarantee a smooth operation of the ESRF in case of a major intervention on one transmitter. A new associated control system was developed and commissioned in parallel.

Another great advantage of the redundancy is that one of the RF transmitters can be used to perform klystron testing on a dummy load (due to a system of wave-guide switches).

Installation of 8 mm (inner vertical height) vacuum vessels

Following the reduction of the vertical β function in all straight sections, new vacuum vessels (5 metres long, 8 mm high) have been developed enabling the gap of the corresponding insertion devices to be closed down to 11 mm. These stainless steel vacuum vessels are copperplated to minimize their contribution to the impedance of the Machine. Two of these vacuum vessels are now installed on the Storage Ring. First of all they are put in a dedicated straight section for several weeks to condition them after which time they are moved to the required straight section. Others will be installed in the forthcoming months.

• Longitudinal instabilities and fighting the HOMs.

Many efforts are being made to improve our understanding of HOMs and to avoid them developing in our cavities, mainly in multibunch mode at high intensity. One way of destroying the coherence of the participating particles is to spread out the synchrotron frequencies of the electrons of different bunches. This can be achieved by filling the ring in a non-uniform way (with fractional filling patterns). This is done to deliver high intensity in multibunch mode, where two thirds of the bunches are filled (2/3rd filling mode).

Another way is to produce Landau damping from active modulation. Owing to the new RF system, this is possible by driving one pair of RF cavities at $f_{RF} + f_0$, (one revolution frequency above the RF frequency). This method is now used to deliver the beam in multi-single bunch mode (16 or 32 bunches equally spaced).

New cooling devices were designed to regulate accurately the temperature of the RF cavities, thereby tuning away the HOMs. These devices are now in operation on the Machine and permit high intensity (200 mA) with uniform or symmetrical filling patterns.

4 BEAM MODES AND FILLING PATTERNS

The preferred mode for the Users is indisputably the 2/3 filling mode for which a high intensity of 200 mA with a good lifetime approaching 55 hours can be delivered. However, other time-structured modes such as the single bunch (16 mA with a lifetime of 5 hours) and the 16-

bunch mode (90 mA with a lifetime of 8 hours) remain of great interest for a few beamlines. The compromise between the two kinds of modes (high intensity or time-structured) is the hybrid mode (200 mA, 1/3 filling + 1 single bunch opposite the bunch train). Two years ago, the drawback of this mode was the long refill time (about 20 minutes) due to the necessity to kill the parasitic bunches around the single bunch (cleaning process). Since then, a new cleaning method (selective) has been developed and even allows a topping-up in this mode which takes about 10 minutes. The quality of these time-structured modes remains very high with an excellent purity (no parasitic bunches) routinely measured below 10^{-7} and sometimes even down to 10^{-10} .

At the request of one beamline, which requires time structure, a new fractional filling pattern was tried: the two times 1/3 filling, i.e. 2 bunch trains (350 bunches) separated by 150 unfilled bunches. This mode, which is close to a uniform full filling, required pushing the intensity thresholds due to HOMs (longitudinal coupled bunch instability). As a result of the new cooling systems installed on the RF cavities this was easily achieved: 200 mA were reached without any sign of instability with the same lifetime as in 2/3rd filling mode (55 hours at that time). In agreement with the Users, several shifts were successfully delivered recently in this mode.

Investigations are, however, also being made into the possibility of achieving both a real time-structured mode and a high intensity (for the flux) whilst keeping a high level of purity. This means remaining far from instabilities but maintaining enough current per bunch to be able to discriminate and kill the unwanted parasitic bunches. Up to now, the best compromise which matches all the constraints was 32 groups of 4 bunches with 1.25 mA in each bunch (total intensity of 160 mA). The instabilities were avoided by driving one pair of RF cavities in active modulation mode (frequency f_{RF} + f_0) and a perfect cleaning was obtained. This mode will be proposed to our Users in the coming months.



• Operating the ESRF at 4 GeV

By reducing the energy of the storage ring from the nominal 6 GeV to 4 GeV, record emittance values were achieved: $\epsilon_x = 1.7$ nm rad and $\epsilon_z = 12$ pm rad.

Even if the corresponding photon flux is significantly reduced at an X-ray energy above 10 KeV, the gain in brilliance and the corresponding increased coherence

properties of the X-ray beam could be interesting for some specific experiments. It is for this reason that two days of beam delivery at 4 GeV at the beginning of March were proposed. To achieve reasonable performances at 4 GeV, careful machine tuning had to be made, and in particular to raise the HOMs threshold. 100 mA were achieved (in 2/3rd filling mode) with a lifetime of 10 hours (essentially limited by Touschek effect). A lot of beam line teams took advantage of the beam to perform experiments up to 30 KeV, operating their insertion devices on very high-ranking harmonics (up to the 21st). Although it is not intended to change the nominal energy of the ESRF storage ring, again this demonstrated the high flexibility of our accelerators.

5 NEXT GOALS

RF fingers test bench

In multi-single bunch mode (16 bunch or 32 bunch mode), the maximum intensity of 90 mA is mainly limited by the overheating and the consequent outgassing of some of the RF liners of the vacuum chambers (due to damage). There is reason to believe that the design of the RF liners could be improved in order to push this limitation further. This is why in December 1998, one part of a straight section was equipped with an RF finger test bench. Two different RF fingers can be put on the bench at the same time and a thorough on-line check is possible by monitoring vacuum and RF parameters (temperature monitoring with infrared cameras, several thermocouples and RF pick-ups). The goal is to characterize experimentally the behaviour of our RF This will improve our understanding of the origin of the limitations of those damaged and enable us to define which need to be replaced and what improvements can be made. This test bench is very appealing since the RF fingers can be exchanged during a Machine Dedicated Day and therefore many tests can be done in a short period. Conclusive results are expected during 1999.

• RF waveguide extension

A project is in progress to extend the waveguide network so that one given RF klystron of the storage ring can replace its neighbouring RF unit or even feed the booster RF cavities. This will allow a high level of redundancy that will permit SR operation to be safeguarded even in case of a major failure on any single transmitter.

• Reduction of the coupling

Significant work has been carried out on a new method of correcting the coupling, based on the exploitation of the orbit cross-talk response matrix. According to simulations, it was found that by placing 16 skew correctors around the Machine at optimized positions, the actual coupling (1%) can be reduced to as low as 0.05%. Therefore, it was decided to install 16 additional skew correctors, symmetrically distributed. This gives a total

of 32 skew correctors now installed on the Machine. With this method, a vertical emittance of about 20 pm.rad was reached (corresponding to a coupling of 0.6 %) [3]. Another method was developed, in parallel, based on an empirical minimization of the coupling by reading the vertical emittance on two pinhole cameras. A vertical emittance of 13 pm rad was reached (corresponding to a coupling of 0.3 %).

Further studies will be performed to understand the limitations which presently prevent us from achieving a lower coupling.

New windows on Front ends

Some straight sections are equipped with three undulator segments (integrated length of 5 metres), and it is planned to close their gaps to the minimum (11mm) as soon as an 8-mm high vacuum chamber has been installed on their respective straight sections. This will result in a significant increase in the power density to be transmitted or stopped by the front-ends: 300 kW/mr², to be compared with the present 140 kW/mr². New X-ray absorbers and window configurations have been designed and will be tested during the year, at such a high power density.

6 SUMMARY AND CONCLUSIONS

Our main goal is to provide a reliable delivery of the X-ray beam. Year after year we can claim that this is the case. 1998 was the apogee since it ended with an availability of 95.3% for a MTBF of 31 hours. At the same time the challenge is to continue developments on the Machine without disturbing operation. The goals are to both improve the beam characteristics and to upgrade the equipment. Through several examples we have demonstrated that this is possible and that a balance can be found between operation and developments. We have also seen that the developments have had a direct repercussion on the beam quality. Consequently, we plan to continue the same policy in the forthcoming years.

- [1] L. Hardy, JM Filhol: 'Status report of the ESRF'. PAC 97
- [2] JM Filhol, L. Hardy, U Weinrich: 'Aging issues and mastering beam losses at the ESRF': PAC 99
- [3] R. Nagaoka: 'Correction of linear coupling on the basis of response matrix modeling & X-ray pinhole measurement. PAC 99
- [4] E. Plouviez & al: 'A fast global feedback system to correct the beam position deviation in the ESRF storage ring. EPAC 98

MODEL CALIBRATION OF BETATRON FUNCTIONS AND PHASE IN THE SPring-8 STORAGE RING

G. Liu

Shanghai Institute of Nuclear Research, Chinese Academy of Sciences P.O.Box 800-204, Shanghai 201800, China K. Kumagai, N. Kumagai, H. Ohkuma, K. Soutome*, M. Takao, H. Tanaka

SPring-8, Mikazuki, Sayo, Hyogo 679-5198, Japan

Abstract

We developed a model calibration method to measure the betatron function and phase of a large storage ring. The results of applying this method to the SPring-8 storage ring will be presented.

1 MODEL CALIBRATION METHOD

In third generation light sources, such as the SPring-8 storage ring, it is important to measure various errors which deteriorate the quality of a stored beam. For example, focusing errors coming from quadrupole field errors or from sextupole misalignments generate distortions of linear optics, coupling of horizontal and vertical betatron oscillations and spurious dispersion in the vertical direction.

A most conventional method of measuring the betatron function of a storage ring will be to vary the strength of a quadrupole magnet and detect the betatron tune shift. This method however requires a magnet power supply system that allows us to control the strength of each quadrupole magnet independently. Furthermore, the betatron function is obtained only at the position of quadrupole magnets.

Another method also used commonly is to measure the response matrix of a ring and use this data to fit the betatron function and phase. Here, the response matrix $R_{ij} \equiv R(s_i, s_j)$ is defined as the orbit change at the BPM position s_i for a unit kick given at the steering magnet position s_j . This method has a merit that BPM offsets are automatically canceled and the betatron function and phase are obtained consistently at the positions of BPMs and steering magnets. However, the accuracy of measurements could be dominated by calibration errors of BPMs and steering magnets.

We then developed a method by combining the response matrix and a model of the ring simplified suitably for the SPring-8 storage ring. The point of our approach (Model Calibration Method: MCM[1],[2],[3]) is that as fitting parameters of the ring we do not use the betatron function itself nor individual focusing errors generated by each quudrupole or sextupole magnet. Instead, we use effective focusing errors given by integrating individual errors over some magnets. In addition to such focusing errors, we introduce calibration factors of BPMs and steering magnets

defined by

$$g_i^{\text{BPM}} = \frac{\text{actual shift of beam position}}{\text{shift of BPM readout}}$$
 (1)

$$g_j^{\rm ST} = {{
m actual~kick~angle} \over {
m required~kick~angle}}$$
 (2)

and the energy shift δ_j generated by the horizontal unit kick by the j-th steering magnet located in a dispersive section. Note that this energy shift causes orbit shifts at BPM positions and the term $\eta_i \delta_j$ must be included in the model response matrix $R_{ij}^{(\text{model})}$, where η_i is the dispersion function measured at the i-th BPM. The best values for these fitting parameters are obtained by minimizing

$$\chi^2 \equiv \sum_{i,j} \frac{(R_{ij}^{\text{(model)}} - R_{ij}^{\text{(measured)}})^2}{\sigma_i^2}$$
 (3)

where σ_i is the rms noise of the *i*-th BPM. For calculating $R_{ij}^{(\mathrm{model})}$ as a function of the fitting parameters, we developed a simulation code based on the RACETRACK[4].

As seen from Eq. 3 the accuracy of fitting largely depends on the accuracy of BPMs. In the SPring-8 storage ring the value of σ_i has been measured at each BPM by using a stored beam and the results show that σ_i takes a value between $2\mu m$ and $5\mu m$, depending on the BPM position, in both horizontal and vertical directions.

2 MODEL

In the SPring-8 storage ring there are 288 BPMs, 285 horizontal and 283 vertical steering magnets, 480 quadrupole magnets and 336 sextupole magnets. Then, a direct application of MCM requires a huge memory size and a very fast CPU to computers. Furthermore, as will be shown later, an individual focusing error that each quadrupole or sextupole magnet generates can not be distinguished by the present resolution of BPMs.

To overcome these difficulties, we introduced a model of the ring in which a suitable number of integrated focusing errors are distributed. The total number of errors was chosen to be 240, which should be compared with the total number of quadrupole and sextupole magnets (816). This number of 240 was fixed with the help of computer simulations in the following way: First, we checked how fine we can distinguish the focusing errors by using the present

^{*}Corresponding author; Email: soutome@spring8.or.jp

BPM system. The results show that the expected resolution is $1.3 \times 10^{-3} m^{-1}$ when the response matrix data is taken by using a single kick of 0.05mrad. This resolution is too coarse to distinguish an expected individual error of about $2 \times 10^{-4} m^{-1}$ that each quadrupole or sextupole magnet will generate. This result indicates the necessity of introducing integrated focusing errors into our model.

We then searched an optimum number and distribution of integrated focusing errors, taking account of the betatron phase advance in both horizontal and vertical directions. Figure 1 shows how we can improve the accuracy of fitting of the betatron function and phase by increasing the number of distributed focusing errors in a unit cell. Note that even if we increase the number of errors per unit cell beyond 5, the accuracy of fitting is not improved any more. This level of accuracy is determined by resolutions of the present BPM system. We then fixed the number of errors per unit cell to be 5. We remark that the lattice structure of the SPring-8 storage ring is of the double-bend achromat type, and within a unit cell there are three girders separated by two bending magnets. The betatron phase advance within the first and third girder is small and a single error source was assigned to these. On the other hand, the betatron phase advance within the second girder is large and we assigned three error sources to this. In such a model, the accuracy of determining the betatron functions is expected to be better than 1% as seen from Figure 1.

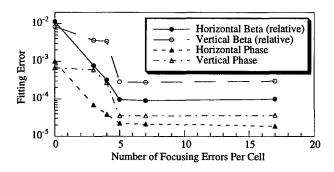


Figure 1: The accuracy of fitting as a function of the number of integrated focusing errors per unit cell.

We note that, in addition to the errors randomly distributed along the ring, there can be systematic errors arising from, e.g., incompleteness of the model. An estimation of such errors is generally difficult and the model finally obtained by MCM should be tested by some means.

We also remark that the coupling ratio of horizontal and vertical betatron oscillations has been deduced experimentally [5] and the results show that the ratio is much smaller than 1%. We then neglected the coupling.

3 RESULTS AND DISCUSSION

All elements of the response matrix were measured in 11 hours by giving a single kick of 0.05mrad to the stored beam. This kick angle was determined by requiring that a nonlinear behavior of the ring is sufficiently suppressed

and the difference of two orbits is measured with enough resolutions. Since the total amount of the data was huge, we divided it into four parts according to the position of excited steering magnets. A quarter of the data was then used for applying MCM and this procedure was repeated four times to cover the whole ring.

In Fig. 2 we show correlation between measured and model response matrix elements. The model response matrix was calculated in two ways - with (right) and without (left) application of MCM. We see that the model response matrix has been improved by applying MCM: the rms value of the difference between measured and model response matrix elements is reduced from $81\mu m$ to $3.3\mu m$ in the horizontal direction and from $85\mu m$ to $3.8\mu m$ in the vertical direction. This means that MCM almost converged to the level of the present resolution of BPMs.

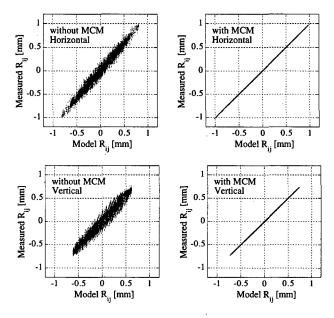


Figure 2: Correlation between measured and model response matrix elements.

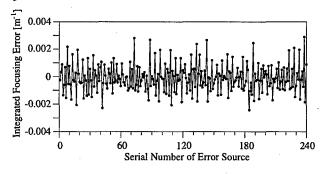


Figure 3: Focusing error distribution of the ring.

A distribution of effective focusing errors in the ring and calibration factors of BPMs and steering magnets were estimated, and the results are shown in Fig. 3, Fig. 4 and Fig. 5, respectively.

In Fig. 5, we see that some vertical steering magnets have a large deviation of the gain factor from unity. The reason

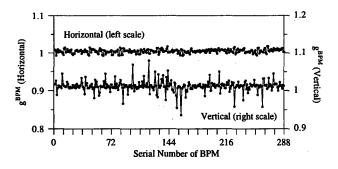


Figure 4: Gain factors of BPMs.

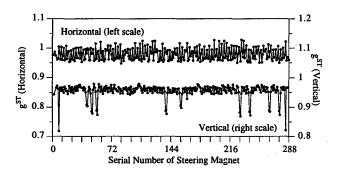


Figure 5: Gain factors of steering magnets.

for this was found to be the effect of a neighboring magnet settled close to these steering magnets: a fast kicker magnet or an auxiliary corrector magnet for an insertion device. This was checked experimentally by making a local bump orbit and observing its leakage with and without taking account of the gain factors. When we took account of the gain factors of the steering magnets, the leakage of a bump orbit was reduced as expected.

A part of the betatron function is shown in Fig. 6 by solid curves. For comparison, we also show model calculations without applying MCM by dashed curves. We see that distortions of the solid curves are very small. The horizontal and vertical betatron tunes of the ring corresponding to the solid curves are 51.235 and 16.308, respectively, which agree well with experimental values 51.234 and 16.307.

To check the betatron functions thus obtained, we measured their values at some quadrupole magnets by changing their strength independently and detecting the betatron tune shifts. In Fig. 7 measured values at 10 quadrupole magnets in one unit cell are plotted and compared with the MCM results. In addition to these local measurements, we also measured average values by changing the strength of 48 quadrupole magnets at the same rate, family by family. The results are shown in Fig. 8. The agreement between measured and MCM values is quite satisfactory.

Acknowledgment: The authors would like to thank Drs. S.Daté, K.Fukami, M.Masaki, T.Ohshima, S.Sasaki, M.Shoji, S.Takano and K.Tamura for useful discussions and cooperation in machine operations.

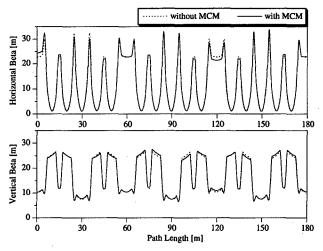


Figure 6: Betatron functions over 6 cells.

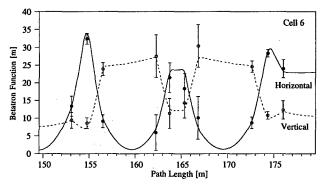


Figure 7: Betatron functions in one unit cell.

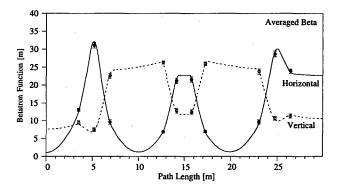


Figure 8: Averaged betatron functions.

- [1] G. Liu, et.al., SPring-8 Ann. Report 1997, p.174.
- [2] W.J. Corbett, M.J. Lee and V. Ziemann, SLAC-PUB-6111 (1993).
- [3] J. Safranek, Nucl.Instr.Meth. A388(1993)27.
- [4] A. Wrulich, DESY 84-026 (1984).
- [5] M. Takao, et.al., "Estimation of Betatron Coupling and Vertical Dispersion for SPring-8 Storage Ring", presented at this conference.

ORBIT STABILIZATION IN SPRING-8 STORAGE RING

N. Kumagai, H. Ohkuma, K. Soutome, M. Takao, <u>H. Tanaka</u>, JASRI / SPring-8 323-3, Mihara, Mikazuki-cho, Sayo-gun, Hyogo, 679-5198 JAPAN

Abstract

Stability of electron orbit is one of the most important properties to achieve brilliant photon beams for third generation synchrotron radiation sources. In the design of a SPring-8 storage ring, many ideas for orbit stabilization were thus considered. Consequently, without any correction, electron orbit stability of about 50 µm per day is obtained. Since a main part of the orbit movement is slowly varying components in time, we are developing both a periodic correction of electron beam energy and that of global orbit to realize the orbit stability of a few µm at source points along the ring. Up to now, we have achieved the stability at each insertion device within several microns per day in an amplitude of the main harmonic of the orbit movement and one correction scheme is now routinely used in user operation.

1 INTRODUCTION

For highly brilliant synchrotron radiation sources, stability of electron orbit is crucial to achieve brilliant photon beams averaged in certain measurement time. Toward the orbit stability of a few μm , perturbation sources for the orbit movement were suppressed as much as possible in the storage ring design. Items considered [1,2] are:

- Construction of a machine tunnel on a hard and stable rock bed.
- Adoption of double compartment structure to make the machine tunnel free from the changes of ambient temperature and sunshine.
- Stabilization of room temperature in a machine tunnel within 1 degree centigrade.
- Stabilization of cooling water within ± 1 degree centigrade.
- Insertion of thermal insulation between a magnet yoke and coils.
- Optimization of cooling water stream-pass to reduce the peak temperature of magnet coils.
- Reduction of heat loss of magnet power cables and of thermal invasion from both the power cables and cooling water pipes to magnets and magnet girders.
- Removal of vibration sources like a chiller from a machine tunnel and suppression of the magnitude of vibrations by using vibration proof foundation, etc.
- Suppression of the propagation of vibrations to magnet and magnet girders.
- Increment on mechanical hardness of magnet girders.
- Reduction of current ripple of magnet power supplies.

To the remaining orbit movement even after the above treatment, a suitable correction of closed orbit distortion (COD) is applied in accordance with a periodicity of the movement. At present, we have introduced one periodic COD correction scheme to suppress slowly varying components of the COD. We are also preparing to

Corresponding Author, Email: tanaka@spring8.or.jp

ntroduce periodic adjustment of an RF frequency to reducie the systematic orbit drift by stabilizing energy of the circulating electron beams. Here, we describe the orbit movement in the ring without any correction and then show our periodic correction scheme and obtained results.

2 ORBIT MOVEMENT IN SPRING-8 STORAGE RING

2.1 Slow Orbit Movement

Figure 1 (A) and (B) show respectively the slow changes of the horizontal and vertical orbit at one beam position monitor (BPM) located in the dispersion-free section of #41 cell. The sampling period of data is 30 seconds. In this example, the maximum horizontal and vertical changes per day are respectively 70 and 50 μ m. As seen in the figure, the changes don't have a clear periodicity of 24 hrs. And also, these are usually not described by a single error source except for a special case in a vertical plane. For several times, we have observed a large change in a vertical plane correlated with hard rainfall. In this case, the vertical orbit distortion is expressed by a single kick in #8 cell. This shows that the deformation of the ring due to rainfall is localized at #8 cell, but the mechanism has not been clearly understood yet.

Figure 2 shows a part of the data in Fig.1 (A) by magnifying the data about forty in a time scale. We can see clear periodic movement, of which period is $6 \sim 7$ min and amplitude is about 10 μ m. This is clearly correlated with the temperature change of the cooling water.

Figure 1 (C) shows that the horizontal orbit at one BPM located in the dispersive section of #22 cell. The maximum change per day is about 50 µm. This pseudoperiodic change can be clearly explained by earth tide [3]. Variation of the circumference due to earth tide causes the energy change of circulating beams and this systematic error shifts the orbit pseudo-periodically. We therefore expect that this drift can be cured by the proper control of an RF frequency to keep the energy constant.

2.2 Fast Orbit Movement

To check the magnitude of fast orbit movement, signal of the BPM located in #46 cell was measured with the sampling period of 2 msec. Since the noise level of this measurement is about $10~\mu m$, we couldn't see clear signal. From the measurement results we only estimate that the fast orbit movement is the noise level and less. We are now preparing to measure the fast movement more precisely.

3 PERIODIC COD CORRECTION SCHEME

3.1 Correction Scope

Measured data shows that the magnitude of the slow orbit movement is relatively larger than that of the fast one. We then tried to develop a scheme to correct the slow orbit movement with a period of a minute and longer.

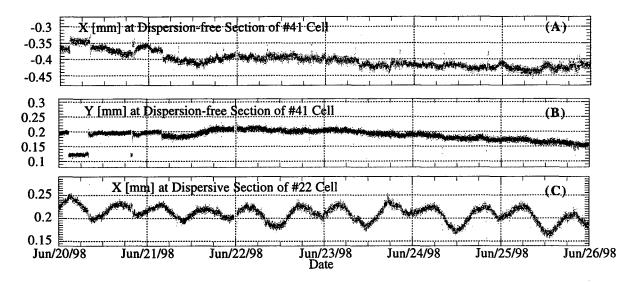


Figure 1: Slow orbit movement for 6 days in the SPring-8 storage ring without any correction. The graphs (A) and (C) show the horizontal orbit movement at one BPM located respectively in dispersion-free and dispersive sections. The (B) shows vertical orbit movement at one BPM located in the dispersion-free section.

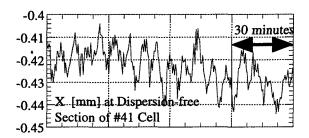


Figure 2: Magnified data of a part of Fig. 1 (A). Two hours data from Jun/25/98 12:00:00 ~ 14:00:00 are shown.

At this moment, we correct only harmonic components corresponding to a betatron tune and its satellite harmonics, which are main components of the global movement. Although the accuracy of our BPM system is $4 \sim 5 \, \mu \mathrm{m}$ in an r.m.s. value [4], the magnitude of random noise is reduced by the square root of the BPM total number through the data integration in harmonic expansion. In the SPring-8 storage ring, we have 288 BPMs and this noise reduction factor becomes about 17. This means that the BPM random noise is reduced down to ~0.3 $\, \mu \mathrm{m}$ for an estimation of the harmonic components.

3.2 Synthesis of Correction Target

Before starting the periodic correction, reference orbit should be set. The orbit is automatically measured with 288 BPMs along the ring and saved in an archive database. Periodically, the correction program subtracts the reference orbit from the latest one and calculates harmonic components of the difference between the two orbits.

For the correction of the global COD, three harmonics corresponding to the tune and tune ± 1 are used to synthesize target orbit. In harmonic analysis, we use a simple interpolation of the COD data. Although this treatment induces an error of the harmonic expansion especially at high frequencies, this error is corrected by an analytic correction formula at the synthesis of the target

orbit.

For the correction of the pseudo-periodic drift due to earth tide, the 0th harmonic component of the horizontal COD is only used.

3.3 Correction of Global COD

The period for the correction is a parameter and it is usually set to 1 min. Available steering dipoles in a horizontal and vertical planes are respectively 96 and 281. All horizontal steering dipoles are in the dispersion-free sections to avoid a cross talk between the corrections of the COD and beam energy. The number of steering dipole used in one correction step is also a parameter. Usually, 24 and 16 are set respectively for the horizontal and vertical corrections.

The best set of steering dipoles are chosen and the strength of each steering dipole is calculated by well known best corrector search algorithm [5]. A coefficient matrix describing the propagation of a steering kick is made of design parameters. Resolution of current setting is 0.15 mA, which is equivalent to \sim 0.03 and \sim 0.015 μ rad respectively in a horizontal and vertical planes [6].

3.4 Correction of Pseudo-periodic Orbit Drift due to Earth Tide

The RF frequency change Δf is related to the change of a 0th harmonic component of the horizontal orbit, a_0 by Eq. 1 obtained by fitting the measured data. The period for the correction is a parameter. In the case where the correction period is 5 min, we have 10 data of the a_0 every correction period. By using the least square method and Eq. 1, the RF frequency change is estimated to minimize the deviation from the reference. Resolution of frequency setting is 0.1 Hz.

$$a_0 \text{ [mm]} = -1.56 \times 10^{-3} \cdot \Delta f \text{ [Hz]}$$
 (1)

4 CORRECTION PEFORMANCE ACHIEVED

Figure 3 (A) and (B) show the amplitude changes of tune-

harmonics (51th for Hori. and 16th for Vert.) of the COD respectively without and with the correction of the global orbit distortion. The correction period was set to 1 min. 24 and 16 steering dipoles were used respectively for the horizontal and vertical corrections. The global COD correction controls amplitudes of the horizontal and vertical tune-harmonics, i.e., correction variables within several and a few mm, respectively. Since the tune-harmonic is a main term of the global orbit distortion in each plane, we predict that the global distortion is controlled at each insertion device within the same order as shown in Fig. 3 (B).

Figure 4 (A) and (B) show respectively the slow changes of the horizontal and vertical orbit at one BPM of #41 cell with the global COD correction. These data represents the local orbit movement under the correction is on. Thickness of each line in the figure is determined by the BPM reproducibility and the slow undulation seems to show the real orbit movement. The stability of about 10 µm per day was obtained by this correction, including the local orbit movement. Spurious horizontal and vertical dispersions here are respectively about 2 and 0.1 cm. Even in a horizontal plane, the deviations due to earth tide is only a few µm.

Figure 5 shows a result of the correction test for the pseudo-periodic orbit drift by periodically adjusting the RF frequency. The correction period was set to 5 min. The stability of several µm per 5 hrs was obtained for the 0th component of the horizontal orbit.

- [1] Conceptual Design Report, SPring-8 Project Part 1 Facility Design 1990 [Draft], JAERI-RIKEN SPring-8 Project Team (1991).
- [2] N. Kumagai, SPring-8 Information Vol.3 No. 5 (1998) 1 (in Japanese).
- [3] S. Date and N. Kumagai, Nucl. Instr. and Meth. A421 (1999) 417.
- [4] S. Sasaki, private communication.
- [5] B. Autin and Y. Marti, CERN ISR-MA/73-17 (1973).
 - K. Kumagai, private communication.

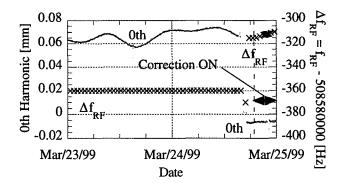


Figure 5: Correction of the 0th harmonic of horizontal COD by adjusting the RF frequency.

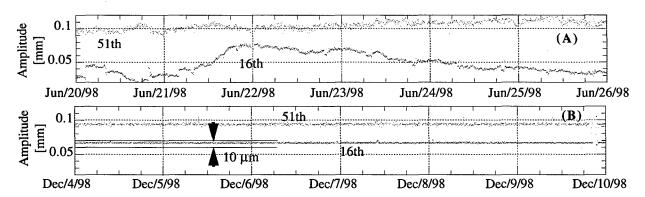


Figure 3: Slow amplitude changes of tune-harmonics (51th for Hori, and 16th for Vert.) of the COD for 6 days. The upper (A) and lower (B) graphs show respectively the changes without and with the periodic correction of the global orbit distortion.

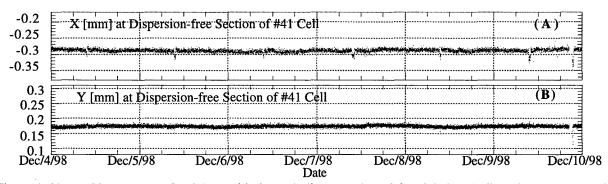


Figure 4: Slow orbit movement for 6 days with the periodic correction of the global orbit distortion. The correction period is 1 minute. The upper (A) and lower (B) graphs show respectively the horizontal and vertical orbit changes at one BPM located in the dispersion-free section of #41 cell.

CALIBRATION OF BEAM POSITION MONITORS USING A STORED BEAM IN THE SPring-8 STORAGE RING

K. Kumagai, N. Kumagai, H. Ohkuma, <u>K. Soutome</u>*, M. Takao, H. Tanaka SPring-8, Mikazuki, Sayo, Hyogo 679-5198, Japan

Abstract

A simple and practical method is proposed to estimate offsets of beam position monitors. It is reported that this method had been applied successfully to an 8GeV electron storage ring at SPring-8. Resulting offsets are compared with those measured by using a beam-based method.

1 INTRODUCTION

In particle accelerators, such as electron or positron storage rings, calibration of beam position monitors (BPMs) is an important subject for achieving a design performance of the beam quality. To eliminate systematic errors, or the offsets of BPMs, a beam-based method is generally useful[1], [2], [3]. This method, however, requires additional power supplies to quadrupole magnets and can not be applied to the whole ring immediately.

At the SPring-8 storage ring, a high quality of the beam is also required: high stability of an orbit, a small beam emittance, a small coupling ratio of horizontal and vertical betatron oscillations, etc. Since the total number of quadrupole magnets is 480 and only 40 of them can change their strength independently, all 288 BPMs in the ring can not be calibrated by the beam-based method.

We then estimated BPM offsets in a simple and practical manner by using closed orbit data[4]. In the following we explain how we carried out this and improved the quality of a stored beam.

2 METHOD

A part of BPM offsets can be estimated by summing Fourier components of COD whose harmonic number is much higher than betatron tunes. Such high harmonic components of the offsets should be eliminated in orbit corrections, since main magnets are usually aligned so that their magnetic centers are connected as smoothly as possible. At the SPring-8 storage ring, for example, the concept of "two-stage magnet alignment with common girders" was introduced[5] and main magnets were aligned carefully with a laser-alignment system with the accuracy of less than $20\mu m$ [6].

The procedure for obtaining the "offsets" is as follows:

- Store the beam and measure the closed orbit with BPMs. If necessary, make a rough orbit correction with a small number of steering magnets to prevent nonlinear behaviors of the BPM system. If possible, select an operation point with a small integer part of the betatron tunes so that low harmonic components coming from real orbit distortions and high harmonic components coming from BPM "offsets" are separated as clearly as possible.
- Make a Fourier decomposition of the orbit data as follows:

$$\frac{\text{COD}(s)}{\sqrt{\beta(s)}} = \sum_{n=0}^{\infty} (a_n \cos n\phi(s) + b_n \sin n\phi(s)) \quad (1)$$

$$\phi(s) \equiv \int_0^s \frac{ds'}{\nu \beta(s')} \tag{2}$$

where $\beta(s)$ is the betatron function at the position s and ν is the betatron tune.

- Reconstruct the orbit by collecting Fourier components whose harmonic number is smaller than some cutoff value. On determining the cutoff value we will discuss in the next section.
- Subtract the reconstructed orbit from a measured orbit to obtain the "offsets".

3 APPLICATION TO THE SPring-8 STORAGE RING

We note that the basic lattice structure of the SPring-8 storage ring is of the double-bend achromat (DBA) type with 48 unit cells. In each unit cell there are 6 BPMs (BPM1, BPM2, ..., BPM6) located in such a way that the phase difference of betatron oscillations between BPM1 and BPM2, BPM3 and BPM4, and BPM5 and BPM6 becomes small. Since each pair of these BPMs are welded on the same vacuum chamber and all nearby quadrupole and sextupole magnets are well aligned on the same girder, the difference of beam positions measured by each pair should be small. Then, we can expect that spurious spikes of the position data, or harmful BPM offsets, can be distinguished by the method described in the previous section.

Before applying this method we must determine the cutoff harmonic number so that the contribution from higher

^{*}Corresponding author; Email: soutome@spring8.or.jp

harmonic components of a real orbit distortion is much smaller than that of spurious BPM offsets. With the help of computer simulations we determined the cutoff harmonic number in the following way:

- Calculate a closed orbit by using alignment data and field strengths of main magnets measured beforehand.
 The result simulates an orbit without corrections.
- Make a Fourier decomposition of the calculated orbit and find a cutoff harmonic number above which the rms value of the sum of higher harmonic components becomes smaller than some tolerance. In the SPring-8 storage ring this toralence was set to be 50µm.

As can be seen from the above procedure, the cutoff value depends on the betatron tunes of the ring. Note also that in order to separate components coming from real orbit distortions and those from spurious BPM offsets as clearly as possible, it is better to lower the betatron tune. This can be seen from the following formula:

$$\frac{\mathrm{COD}(s)}{\sqrt{\beta(s)}} = \sum_{m=-\infty}^{\infty} \frac{\nu^2}{\nu^2 - m^2} f_m e^{im\phi(s)}$$
 (3)

where

$$f_m \equiv \frac{1}{2\pi\nu} \sum_{i} \sqrt{\beta(s_i)} \theta_i e^{-im\phi(s_i)} \tag{4}$$

and θ_i is the kick at the position s_i .

In the SPring-8 storage ring we examined five different optics with the following horizontal and vertical betatron tunes: $(\nu_H, \nu_V) = (51.23, 16.32), (42.20, 15.32), (42.24, 12.21), (21.35, 9.17)$ and (18.25, 13.69). The last three optics with low betatron tunes are not of the standard DBA type. These were designed especially for checking the optics dependence. In Fig. 1 we show the rms difference of full and reconstructed CODs as a function of the cutoff harmonic number for the optics with tunes (51.23, 16.32), (42.20, 15.32) and (21.35, 9.17). The cutoff values for these optics were determined from the saturation profile of this rms difference to be (150, 40), (150, 40) and (70, 40), respectively[7].

In Fig. 2 we show BPM "offsets" obtained experimentally by using the above three optics. We see that the optics dependence of the "offsets" is very weak, especially for the vertical direction. The rms value of the "offsets" for these optics differs only by $40\mu m$ in the horizontal direction and $10\mu m$ in the vertical direction. Then we can conclude that a dominant and harmful contribution to the "offsets" was obtained by the present method.

To go ahead with orbit corrections, we used the "offsets" for the optics with betatron tunes (21.35, 9.17) which are indicated by the solid curve in Fig. 2. The rms values of the "offsets" is $160\mu m$ in the horizontal direction and $210\mu m$ in the vertical direction.

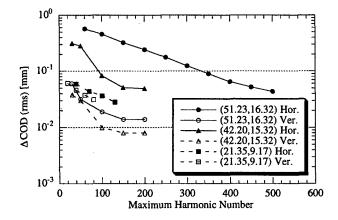


Figure 1: The rms difference of full and reconstructed CODs.

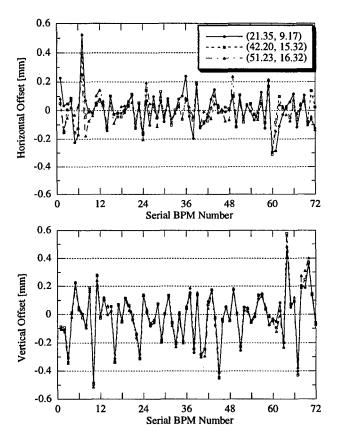


Figure 2: BPM "offsets" in a quarter of the ring obtained experimentally with three different optics in the horizontal (above) and vertical (below) directions.

4 COMPARISON TO BEAM-BASED METHOD

To check the reliability of the "offsets", we measured a beam position at some BPMs with respect to the center of a nearby quadrupole magnet by using a beam-based method. An example is shown in Fig. 3, where a magnetic center of a target quadrupole magnet is searched by changing its

strength and detecting the amplitude of an induced betatron oscillation. The technique used is essentially the same as those in [1], [2], [3], but our method is different in the point that (i) a single kick is used instead of a local bump to generate a parallel shift of an orbit at a target quadrupole magnet and (ii) a Fourier component corresponding to the betatron tune is plotted.

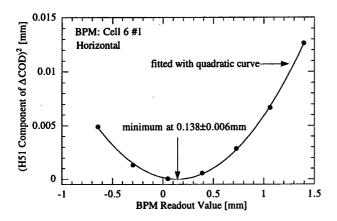


Figure 3: An example of beam-based measurement of a BPM offset.

With this method the offsets were measured at 24 BPMs. The results are shown in Fig. 4 by dashed curves. Also shown by solid curves are the corresponding "offsets" obtained from high harmonic Fourier components. The agreement between the solid and dashed curves is not perfect but satisfactory. We see that they have very similar tendencies. The rms value of the difference is about $150\mu m$ in both horizontal and vertical directions. This value is a measure of the amount of remaining low harmonic components of the BPM offsets.

5 CONCLUSION

After calibrating BPMs by using the "offsets" shown in Fig. 2, the quality of a stored beam has been improved. For example, we could further reduce COD by using steering magnets with weak strengths. The leakage of the dispersion function into straight sections also reduced from about 23mm to 12mm in rms values. We note here that the coupling ratio of the horizontal and vertical betatron oscillations has been deduced from Touschek lifetime and found to be very small [8]: much less than 1% without corrections by skew quadrupole magnets.

All of these facts indicate that the electron beam passes through the position close to magnet centers all along the ring and hence the BPM "offsets" shown in Fig. 2 worked well in orbit corrections.

Acknowledgment: The authors would like to thank Drs. S.Daté, K.Fukami, M.Masaki, T.Ohshima, S.Sasaki, M.Shoji, S.Takano and K.Tamura for useful discussions and cooperation in machine operations.

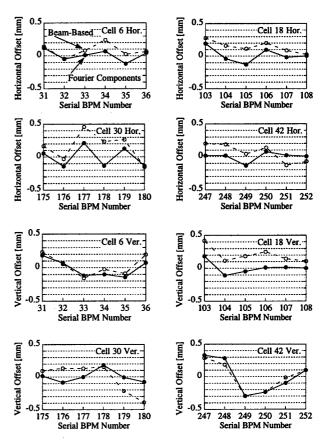


Figure 4: Comparison of BPM offsets obtained by two different methods.

- [1] See e.g., Proc. 4th Int. Workshop on Accelerator Alignment (KEK Proceedings 95-12), Tsukuba, 14-17 November 1995, chapter V.
- [2] P. Röjsel, Nucl. Instr. and Meth. A343(1994)374.
- [3] B. Dehning, G. -P. Ferri, P. Galbraith, G. Mugnai, M. Placidi, F. Sonnemann, F. Tecker and J. Wenninger, Proc. 6th European Particle Accelerator Conf., Stockholm, 22-26 June 1998, p.430.
- [4] H. Tanaka, K. Soutome, M. Takao, H. Ohkuma and N.Kumagai, SPring-8 Ann. Rep. 1997, p.188.
- [5] H. Tanaka, N. Kumagai and K. Tsumaki, Nucl. Instr. and Meth. A313(1992)529.
- [6] K. Tsumaki, N. Kumagai, S. Matsui, C. Zhang and J. Ohnishi Proc. 6th European Particle Accelerator Conf., Stockholm, 22-26 June 1998, p.1356.
- [7] For the optics (51.23, 16.32) the rms difference in the horizontal direction converges very slowly with the maximum harmonic number. We thus set the cutoff value to be 150 and used the resulting "offsets" only for comparison to other cases.
- [8] M. Takao, et.al., "Estimation of Betatron Coupling and Vertical Dispersion for SPring-8 Storage Ring", presented at this conference.

OPERATION AND PERFORMANCE OF THE SPring-8 STORAGE RING

S. Date, K. Kumagai, N. Kumagai, M. Masaki, T. Nakamura, <u>H. Ohkuma*</u>, T. Ohshima, K. Soutome, S. Takano, M. Takao, and H. Tanaka, JASRI/SPring-8, 323-2, Mihara, Mikazuki-cho, Sayo-gun, Hyogo 679-5198, Japan

K. Tamura, The Institute of Physical and Chemical Research (RIKEN), 2-1, Hirosawa, Wako, Saitama 351-0106, Japan

Abstract

Two-year operation experiences of the SPring-8 storage ring are presented. The commissioning of the storage ring was successfully completed, with the achievement of performance far beyond the target specifications. The beam lifetime is about 60 hours at 100mA in the multi bunch mode. The 7 nm·rad of the emittance measured for the horizontal plane is close to the theoretical value. From the beginning of the operation, vertical emittance is extremely small, about 10pm·rad and the coupling is about 0.2%. Furthermore, the procedures for decreasing the coupling have been tested. Purity in the few 10⁻⁶ range is routinely achieved in the single and several bunch operation of user service mode. We achieved a good orbit stability at source points, about 5 and 1 micron in an r.m.s. value respectively for horizontal and vertical planes. The beam performance of the SPring-8 storage ring is presented.

1 INTRODUCTION

Beam commissioning of the storage ring was started since March 13th and the first stage of it was successfully completed by accumulating the electron beams of about 20 mA one month later. This quick tuning was mainly due to the high completion of hardware. Especially, the precision of magnet alignment was so high that no steering magnet was used to store the first beam in the ring [1]. The major milestones up to now are listed Table 1.

Table 1: Progress of the SPring-8 Storage Ring

Date	Milestones
1997	
3/13	Start of SSBT tuning
3/13	Start of storage ring beam commissioning
3/14	Completion of first turn
3/25	Capture of electron beams in RF buckets
3/26	First observation of photon beams
	from a bending magnet
4/17	Stored current of 19.6 mA
	(lifetime ~3 hrs with ID gap fully opened)
5/14	Start of beamline commissioning (BL02B1 and
	BL47IN)
5/16	Operation with ID minimum gap of 8 mm

^{*}Corresponding Author; Email:ohkuma@spring8.or.jp

5/17-6/15	Period of beam self-clearing on vacuum components
	(lifetime 14~15 hrs at ~18 mA)
6/16-18	Periodical inspection of storage ring by the STA#1
7/3	License by the STA for storage ring operation
7/3	Start of test experiments at two beamlines
10/10	Start of user service mode
1998	
4/21	License by the STA for an increase
	of stored current up to 100 mA
5/13	Stored current up to 100 mA
9/16-18	Change of the operation point
	to reduce a vertical emittance

^{#1} the Science and Technology Agency

2 OPERATION

2.1 Injection efficiency

We tried to find the best parameter set of septum and bump magnet strengths to make injection efficiency as high as possible. The auxiliary DC bump was made in the injection part if necessary to reduce a coherent amplitude. At present, the efficiency of 80-90% has been achieved.

2.2 Operation time

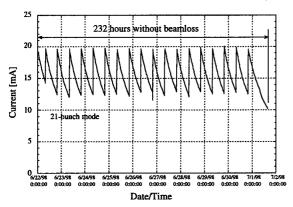
The storage ring is operated on three weeks basis (1 cycle), with 38×8 hour shifts for user service mode, another 6×8 hour shifts for machine studies, and about 48 hours for machine tuning and for beamline tuning.

In 1998, a total operation time of the storage ring is 4190 hours, and 2624 hours (62.6%) has been delivered to the users during the year 1998. The down time is 110 hours, 2.6% of the total operation time. The most significant incident in 1998 was an user time interruption of 15 hours when the breakdown of the power supply of the sextupole magnets happened. During the last stage of 1998, user time was often disturbed when an action of the interlock system of the magnet and photon-absorber occurred due to a drop of flow rate of the cooling water.

Typical operation is shown in Fig. 1, when the beam delivered 232 hours without a beam loss.

2.3 Filling modes

A 62.3% of the total user time were delivered in the multi-bunch mode as shown in Fig. 2. In the first half of



1998, a full filling mode was used for the user time operation. After the summer shutdown period of 1998, a 2/3-filling mode began to be used for the user time operation, where two third of the 2436 available RF buckets are filled continuously with electron. In the SPring-8 storage ring, the beam lifetime in the uniform filling mode is significantly longer than that in the partial filling mode. This origin may be that the electron beam size is growth by the instability due to an ion-trapping effect.

Figure 1: Beam delivery 232 hours without beamloss.

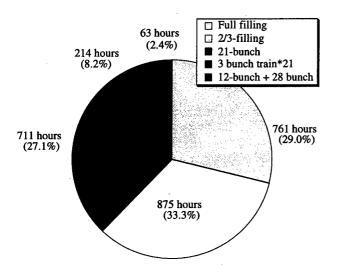


Figure 2: Filling modes for user time during 1998.

Nevertheless, the several bunch modes is increasing. For example, there were many time (724 hours) in 21-bunch mode (21 equally spaced bunches) between May and early in July 1998. Another several bunch modes are the 21-bunch train mode (21 equally spaced 3- or 7-bunches trains), 10-bunch + partially filled multi-bunch, and so on. Since we can select an arbitrary RF bucket among 2436 ones at each injection, the filling pattern in the storage ring can be controlled easily [2]. 1 or 0.5

mA/bunch are stored, and purities in the low 10⁻⁶ range are routinely achieved in the user time operation. The maximum current per bunch is about 12mA in machine studies.

3 PERFORMANCE OF THE STORAGE RING

The over-all performance are listed in Table 2.

Table 2: Performance of the SPring-8 Storage Ring

Designed	Achieved	
Unit cell type	Chasman-Green	<u>-</u> ·
Energy	8GeV	8GeV
Circumference	1435.948m	-
Number of cell		•
(normal / straight)	44 / 4	-
Current		
single bunch	5mA	12mA
multi bunch	100mA	100mA
Number of bucket	2436	-
Revolution time	4.79µs	-
Tunes (vx / vy)	51.22 / 16.16	51.16 / 16.31
Chromaticities -	115.86 / -40.03	3.21 / 3.93
	(natural)	(operation)
Energy Spread (ΔΕ/Ε)	0.0011	0.0012
Emittance	6.99 nm.rad	~7nm.rad
Coupling	10%	~0.1%
Lifetime		
100mA (full filling	g) 24hr	~60hr
1mA (single bunch	h) 6 hours	
Bunch length (FWHM)) 28.5ps ^{\$1}	~40ps\$2
Residual dispersion at	non-dispersive section	n
horizontal (rms)	0	1.4cm
vertical (rms)	0	0.4cm
COD		
horizontal (rms)	-	50μm ~ 0.1mm
vertical (rms)	-	50μm ~ 0.1mm

^{\$1} The design value is estimated at the Vrf=17MV.

3.1 Optics

The lattice structure of the SPring-8 storage ring is of double-bend achromat type, and there are 48 straight sections where the dispersion vanishes.

At the normal operation of the storage ring, the "hybrid" optics was used. In the "hybrid" optics, the horizontal betatron function β_X takes a large value (about 20m) and a small value (about 1m) alternately in the straight sections.

The storage ring is routinely operated near the

^{\$2} The achieved value is measured at Vrf=11.6MV.

coupling resonance (v_x =51.25, v_y =16.32) with a coupling ratio of about 0.4% before September 1998. After the summer shutdown period of 1998, the procedures for decreasing the coupling, i.e. tuning the mode tune separation to change the operation point, have been successfully performed. New operation point is (v_x =51.15, v_y =16.31). At this operation point, the coupling ratio is estimated to be around 0.06%. When compared with the 0.4%, this reduction of the coupling ration gives an equivalent gain of a factor of 0.4 in vertical beam size.

After the winter shutdown of 1999, in order to cure a short beam lifetime due to the Touschek effect in the several bunch mode, at the user time the storage ring have been operated with the enlarged coupling ratio of 0.2%, which resulted in ~1.5 times increase of the beam lifetime.

The "high-beta like" optics in which β_X and β_Y take a same value (β_X : 25m, and β_Y : 3.7m) in all the straight sections have been tested in machine studies. The "highbeta like" optics has a high symmetry and optimization for insertion device in all the straight section, compared with the "hybrid" optics. Betatoron tunes are ν_x =43.16 and ν_y =21.31. Two kinds of optics are shown in Fig. 3.

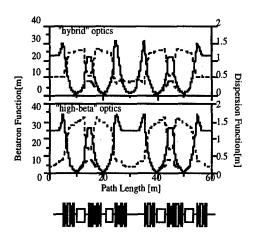


Figure 3: Optics of the SPring-8 storage ring.

3.2 Beam Reproducibility and Stability

The fill-to-fill and cycle-to-cycle reproducibility of the storage ring parameters are assured by strictly following a prescribed start-up sequence that includes conditioning of all magnets at start-up or after a failure that shuts down a power supply. The power supplies of magnets are continuously turned on between cycles, 4 or 5 days. The reproducibility is checked by measuring the betatron tunes, COD, and dispersion which are sensitive to both magnet setting. In order to stabilize the orbit of the storage ring, a periodic and global orbit correction is now routinely used in user time. Figure 4 shows the amplitude changes of betatron tune-harmonics (51th for horizontal

and 16th for vertical) of the COD with and without the correction of the global orbit distortion [3].

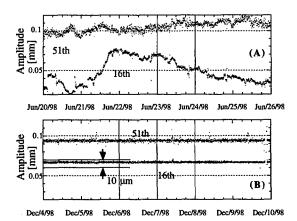


Figure 4: Amplitude changes of tune-harmonics (51th for horizontal and 16th for vertical) of the COD for 6 days. The upper (A) and lower (B) graphs show respectively the changes without and with the periodic correction of global orbit correction

3.3 VACUUM CONDITIONING AND BEAM LIFETIME [4]

The averaged pressure readings of the storage ring are $\leq 1 \times 10^{-8}$ Pa without electron beam, the order of 10^{-7} Pa with a beam current of 70 mA. Since then an integrated beam dose of 190Ah has been achieved up to now, and correspondingly, the dynamic pressure rise per stored beam current ($\Delta P/I$) decreased by two orders of magnitude. An integrated beam dose of 190Ah and a beam lifetime of 60 hours at 100 mA of the beam current were achieved in the multi-bunch mode after two years' operation. The lifetime in the several bunches mode is limited by Touschek effect. Touschek lifetime is about 6 hours at the single bunch operation (1mA/bunch) of the nominal machine parameter of the SPring-8 storage ring [5]. As the total lifetime (τ) in the 2/3-filling mode is 65 hours at the beam current of 70mA, gas scattering lifetime is estimated $\tau_e \approx 140$ hours.

- [1] H. Tanaka, N. Kumagai, and K. Tsumaki, Nucl. Instr. and Meth., A313 (1992) 529.
- [2] T. Ohshima, et al., Proc. of the 11th Symp. on Accelerator Sci. and Tech., Harima, Japan, 1997, 359.
- [3] H. Tanaka, et al., "Orbit Stabilization in SPring-8 Storage Ring", presented in this proceedings.
- [4] H. Ohkuma, et al., "Vacuum Performance and Beam Lifetime of the SPring-8 Storage Ring", presented in this proceedings.
- [5] M. Takao, et al., "Estimation of Betatoron Coupling and Vertical Dispersion for Spring-8 Storage Ring", presented in this proceedings.

ESTIMATION OF BETATRON COUPLING AND VERTICAL DISPERSION FOR SPRING-8 STORAGE RING

N. KUMAGAI, H. OHKUMA, K. SOUTOME, M. TAKAO*, H. TANAKA, SPring-8, Mikazuki, Sayo-gun, Hyogo 679-5198, JAPAN

Abstract

The results of investigations on the betatron coupling of the SPring-8 storage ring are described, which imply that the coupling of the normal operation is less than 0.1 %. The correction scheme of the vertical dispersion, which limits the vertical emittance as well as the betatron coupling, is also presented.

1 INTRODUCTION

The betatron coupling is one of the most important parameters of storage rings for high brilliant light source. By the precise alignment of the magnets [1] and the proper COD correction [2], the SPring-8 storage ring succeeded in achieving the very small linear betatron coupling without skew quadrupole corrector magnets. To prove this fact, we study the betatron coupling of the SPring-8 storage ring.

The measurement of the vertical emittance of the stored beam is the most preferable method to know the coupling. But, since the vertical emittance of the SPring-8 storage ring is too small to measure, at present we have not yet measured it. Hence, by measuring the dependencies of the various ring parameters on the betatron coupling, we prove the validity of our estimation of the betatron coupling.

2 COUPLING MEASUREMENTS

The operation point of the SPring-8 storage ring is in the neighborhood of (51.16, 16.32). The difference resonance of $\nu_x - \nu_y \approx 35$ mainly contributes to the betatron coupling. As changing the horizontal tune while keeping the vertical one constant, We investigate the response of the parameters of the SPring-8 storage ring.

2.1 Mode Tune Separation

By the single resonance approximation, the eigen (measured) tunes ν_I and ν_{II} are represented by unperturbed tunes ν_x and ν_y as [3]

$$\nu_{I,II} = \nu_{x,y} \mp \frac{\Delta}{2} \pm \frac{1}{2} \sqrt{\Delta^2 + C^2},$$
 (1)

where Δ is the distance from resonance and C is the driving term of resonance. Here the integral parts of the tunes are neglected. In Figure 1, we plot the tunes measured while changing operation point. The coupling ratio κ is calculated from Δ and C as

$$\kappa = \frac{C^2}{C^2 + 2\Delta^2} \,, \tag{2}$$

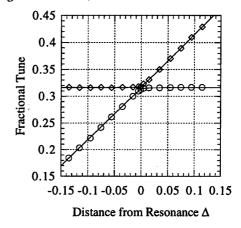


Figure 1: Measurements of mode frequency as a function of detuning.

which is shown in Figure 2. At the normal operation point, the coupling ratio κ is estimated to be around 0.06 %.

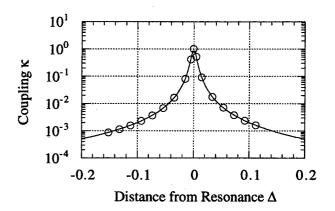


Figure 2: Linear coupling derived from mode tune.

2.2 Touscheck Lifetime

The Touscheck effect is crucial for electron storage rings with low emittance since the high beam density increases the probability for scattering between electrons. The Touscheck lifetime is proportional to the bunch volume and hence sensitive to the coupling ratio.

The dependence of the Touscheck lifetime on the coupling ratio is studied, which is shown in Figure 3. The solid line in Figure 3 represents the Touscheck lifetime calculated with the flat beam approximation [5]. The bunch lengths measured at that time did not change significantly in the present range of the coupling ratio, which almost

^{*}Email: takao@spring8.or.jp

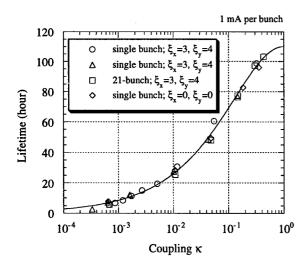


Figure 3: Lifetime as a function of betatron coupling κ .

equal to 45 ps at single bunch of 1 mA. The dependence of the Touscheck lifetime on the coupling ratio can be fitted to that of the bunch volume

$$au \propto \sigma_x \sigma_y \sigma_\ell \propto \frac{\sqrt{\kappa}}{1+\kappa} \,,$$
 (3)

where σ_x is the bunch width, σ_y is the bunch height, and σ_ℓ is the bunch length, respectively. The measurements were performed for single bunch with 1 mA and 21 bunches with 21 mA (1 mA per bunch) and chromaticity (ξ_x , ξ_y) = (3, 4), (0,0), which imply that the lifetime is scarcely depend on the chromaticity.

2.3 Coherent Oscillations

Although the Touscheck lifetime has the sensitivity to the coupling ratio, there is ambiguity in relating it to the coupling ratio. Hence we more directly study the coupling ratio by measuring the coherent oscillation after horizontal kick in terms of turn-by-turn beam position monitor. One then finds the beats in the envelopes of the coherent oscillations in the horizontal and vertical planes, which originate in the interchange of energy between the two oscillations. By firing a horizontal pulse magnet, we give about 50 μ rad kick to a single bunch. Measured oscillations with the estimated coupling ratio 0.06 %, 5 % and 35 % are shown in Figure 4, where the black and gray regions indicate the horizontal and vertical oscillations, respectively.

In terms of the ratio G of the minimum to the maximum of the horizontal envelope oscillation and the period T of the envelope beat oscillations, the distance from resonance Δ and the coupling driving term C are given by [3,4]

$$\Delta = \frac{G}{T}, \qquad C = \frac{\sqrt{1 - G^2}}{T}, \tag{4}$$

where T is scaled by the revolution period, i.e. equals to the turn number. The coupling ratios estimated from the data of turn-by-turn BPM are given in Figure 5. Note that we

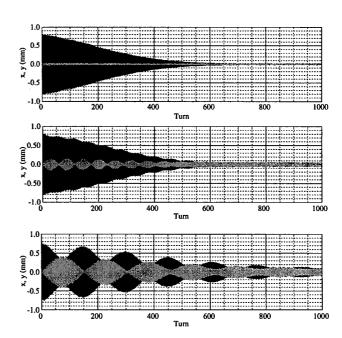


Figure 4: Coherent oscillation measured by turn-by-turn BPM.

can not measure the coupling ratio of the normal operation point by the coherent oscillations. The solid line in Figure 5 corresponds to the coupling ratio calculated from the mode tune separation. Figure 5 shows fairly good agree-

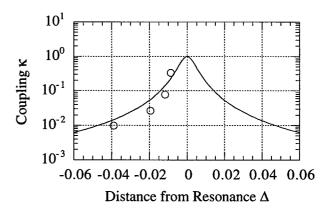


Figure 5: Horizontal Emittance as a function of betatron coupling κ .

ment between the couplings estimated from the coherent oscillation and derived by mode tune separation.

2.4 Horizontal Emittance

The horizontal emittance also directly represents the coupling ratio. By measuring the loss rate of a bunched beam when pushed to septum wall by injection pulse bump, we estimate the bunch width and then the horizontal emittance. Figure 6 shows the loss rate for the cases of the estimated coupling ratio 0.06 % and 43 %, where the open circles and the solid line denote the measured coupling and the fitted

result for the case of coupling 0.06 %, and the open triangles and the dashed line for 43 %. Figure 7 shows the de-

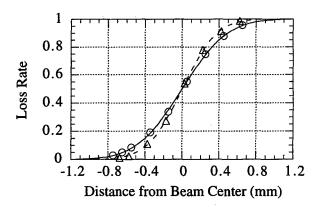


Figure 6: Loss rate of stored current as a function of beam position.

pendence of the horizontal emittance on the coupling ratio, which also implies that we fairly well estimate and control the coupling ratio.

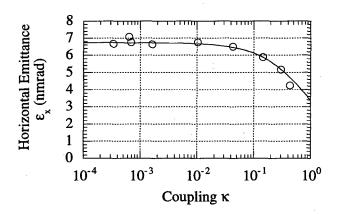


Figure 7: Horizontal Emittance ϵ_x as a function of betatron coupling κ . The solid line denotes the fitted result of $\epsilon_x = \epsilon_0/(1+\kappa)$, where $\epsilon_0 = 6.8 \pm 0.7$ nmrad is the natural emittance.

3 CORRECTION

The coupling ratio of the SPring-8 storage ring is so small that the faint skew quadrupole fields produced by the gap drives of some insertion devices immediately make the coupling a few times larger. The variation of the lifetime in the operation with several bunches, where the Touscheck effect dominates the beam lifetime, is shown in Figure 8. The sudden jumps of the lifetime correspond to the gap changes of some ID's which generate additional coupling driving term. These extra skew quadrupole fields can be simply corrected by one or two skew quadrupole magnets placed adjacent to the ID's.

At present the spurious vertical dispersion of the SPring-8 storage ring is order of one centimeter. The bunch height

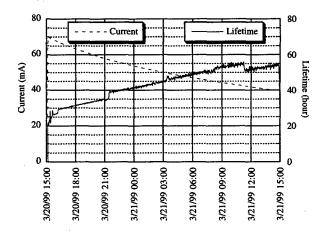


Figure 8: Current and lifetime during the user operation with several bunches.

spread due to the vertical dispersion is comparable to that due to the linear betatron coupling. It is intended to install 24 skew quadrupole magnets at the dispersive sections for correcting the vertical dispersion. The simulation result represented in Figure 9 shows that the skew quadrupole correctors reduce the vertical dispersion by half in r.m.s.. The correction of the vertical dispersion is limited by the measurement accuracy of BPM, which at present is order of a few μ m's. The correction scheme is imposed with the constraint of not exciting any other resonances so that it does not deteriorate the linear betatron coupling.

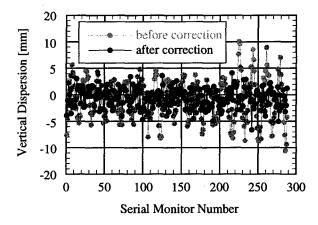


Figure 9: Vertical dispersion before and after correction.

- [1] H. Tanaka, et al., N.I.M. A313 (1992), 529.
- [2] H. Tanaka, et al., SPring-8 Ann. Rep. 1997, p.188; K. Soutome, et al., "Calibration of Beam Position Monitors Using a Stored Beam in the SPring-8 Storage Ring", in these proceedings.
- [3] G. Guignard, Phys. Rev. E51 (1995), 6104.
- [4] H. Tanaka and A. Ando, Part. Acc. 44 (1994), 17.
- [5] C. Bernardini, et al., Phys. Rev. Lett. 10 (1963), 407; J. Le Duff, CERN REP. CERN 89-01 (1989), 114.

VACUUM CONDITIONING AND BEAM LIFETIME OF THE SPRING-8 STORAGE RING

N. Kumagai, T. Noda, <u>H. Ohkuma</u>, M. Oishi, H. Saeki, K. Soutome, Y. Suzuki, M. Takao, H. Tanaka, Y. Taniuchi and K. Watanabe, JASRI/SPring-8, 323-2, Mihara, Mikazuki-cho, Sayo-gun, Hyogo 679-5198, Japan

Abstract

The installation of the vacuum system of the SPring-8 storage ring was completed during 1996. Most of the vacuum chambers are made of aluminum alloy. The main pumping system is a mixed one consisting of NEG strips, DIP, SIP, and LNP. In addition to the standard treatments for ultrahigh vacuum components, dust-controlled procedure was adopted in the manufacturing and the installation processes.

Beam commissioning of the SPring-8 storage ring started in March 1997. Since then an integrated beam dose of 190Ah has been achieved up to now, and correspondingly, the dynamic pressure rise per stored beam current (•P/I) decreased by two orders of magnitude. In the multi-bunch mode a lifetime of 65 hours at 70mA were achieved after two years' operation. Since the vertical emittance is extremely small, the beam lifetime is limited not only by dynamic pressure but also by Touschek effect even in the multi-bunch mode. The contributions of the gas scattering lifetime and Touschek lifetime are estimated in the case of the SPring-8 storage ring.

1 INTRODUCTION

In the synchrotron light source, due to the large desorption induced by the synchrotron radiation (SR), The dynamic pressure in the electron storage ring vacuum system is very high in the early stage of commissioning, in spite of the fact that a static ultrahigh vacuum environment has been achieved. The interactions between the electron beam and the gas molecules desorbed from the chamber surface result in beam loss and emittance growth. Many criteria must be considered when designing the vacuum system of an electron storage ring. The design, fabrication, and testing of the vacuum chambers have been described previously [1]-[3].

The operation of the vacuum system shows good features of quick beam self-cleaning. In this paper, the conditioning of the SPring-8 vacuum system and beam lifetime are described. The figure of merit for vacuum conditioning is the stored beam lifetime.

* Corresponding author; Email:ohkuma@spring8.or.jp

2 VACUUM SYSTEM OF THE SPring-8 STORAGE RING

The vacuum system of the SPring-8 storage ring is made of 44 normal cells and 4 long straight cells, isolated by all metal rf-shielded gate valves. Each normal cell is composed of three straight section chambers (SSC's) with an absorber, two bending magnet chambers (BMC's), two crotch chambers (CR's) equipped with an crotch-absorber, two rf-shielded gate valves, one dummy chamber (IDD), four bellows assembled chambers (BEC's). A dummy chamber will be replaced by the vacuum system of the insertion device one by one.

The vacuum chamber materials are mainly aluminum alloys to benefit from their low outgassing rate, high thermal conductivity, low radio activity, and so on. The SSC and the BMC are made of A6063-T5 aluminum alloy by extrusion with the cooling channels on the both sides. The SSC consists of a beam chamber and a slotisolated ante-chamber in which a pair of non-evaporable getter (NEG) strips, allowing for distributed pumping are installed. The BMC includes a rectangular pump channel in which a distributed ion pump (DIP) is installed, a beam chamber and a slot-isolated ante-chamber in which a NEG strip is contained. The beam chambers of the SSC and BMC are extruded with the same cross section in an ellipse 70 mm in width and 40 mm in height.

To achieve a beam lifetime of approximately 24 hours, the vacuum chamber with its pumping system should be designed so as to maintain the dynamic pressure of the order of 10⁷ Pa or less with a stored beam of 100mA. In our vacuum system, SR is almost intercepted by the crotch-absorbers and absorbers placed just downstream and upstream of bending magnets.

The main pumping system is based on NEG strips which are used in the SSC's and BMC's to evacuate the scattered molecules, and lumped NEG pump (LNP) for evacuating mainly SR-induced gases at the crotch and absorber location. In addition to the NEG strip, a DIP is installed in along side the beam chamber of the BMC. A sputter ion pump (SIP) which assists the LNP is also used. They offer the total pumping speed of about 10,000 l/s (=10m³/s) for one unit cell.

The photon absorbers are made from Glid-Cop because of high allowable thermal stress of 60 kg/mm², compared to 10 kg/mm² of OFHC. The absorbers have the structure in which particles such as reflected photons, photoelectron and SR-induced outgases are efficiently trapped. SR-induced outgases are evacuated locally by the high capacity pumping system before the outgases have a chance to bounce into the beam chamber. The part of the photon beam power from a bending magnet of 10.5 kW, about 6.6 kW (34 kW/cm²) is irradiated at the crotch-absorber and the remaining beam power deposited at the absorbers placed downstream of the crotch-absorber.

3 VACUUM CONDITIONING AND BEAM LIFETIME

All of the SSC's, BMC's and IDD's were 150 °C prebaked in advance of the chamber installation in the storage ring tunnel in order to remove chamber warps which were caused by the construction process and welding. The NEG pumps were activated at the last stage of pre-baking procedure. Residual pressure after the pre-baking was the order of 10⁸ Pa or less. All of the installation works were accomplished in a clean room or clean booth. After the installation of the vacuum system in the storage ring tunnel, the 140 °C baking of the vacuum system and the NEG activation were done. The installation of the vacuum system of the SPring-8 storage ring was completed in October 1996. Before the first beam injection on March 13, 1997, ultimate static vacuum pressure reached to about 9×10° Pa at the absorber section and 5×10° Pa at the SSC section. A thermal outgassing rate (q) of the extruded aluminum alloy chamber was measured for the R&D of the vacuum chamber of the SPring-8 storage ring [4]. As a result, q was 6.7×10^9 Pa·m³·m²·s⁻¹ after a baking at 140 °C for 40 hours. Because total inner surface area of the vacuum chamber per one unit cell is about 23m³, thermal outgassing amounts (Q) is $1.5 \times 10^{-7} \text{ Pa} \cdot \text{m}^3 \cdot \text{s}^{-1}$. As previously mentioned total pumping speed (S) of one unit cell is about 10.000 l/s (= 10m^3 /s). Therefore, 1.5×10^8 Pa of the pressure (=Q/S) is obtained. This value is good agreement with the ultimate static vacuum pressure after the installation and the baking.

The first stored beam was obtained in March 25,1997. With the beam stored, the pressure increased abruptly due to the photon induced gas loads. The amount of gas loads is proportional to the beam current and the molecular desorption yield so that at the early stage of commissioning, the gas loads mainly depend on the molecular desorption yield. The normalized pressure rise ($^{\bullet}P/I$) were measured as high as 3×10^{-2} Pa/A initially and reduced to 2×10^{-5} Pa/A before the summer shutdown period of 1997. After this period, the beam was stored as high as possible at overnight in order to clean up the photon irradiating surfaces by accumulating the total beam dose. As a result, the integrated beam dose reached to 11Ah and the beam

lifetime has increased from about 3 hours to 15 hours with a beam current of 20mA after the summer shutdown period of 1997.

In the summer shutdown period of 1997, all of the NEG strips and LNP were re-activated. The dynamic pressure was reduced by about one second at the SSC section, and then the beam lifetime increased. In the summer shutdown period of 1998, NEG activation was made again. A significant effect, however, could be observed in the dynamic pressure and in the beam lifetime.

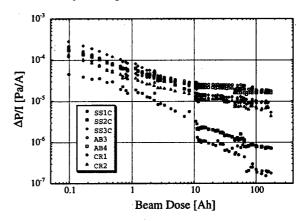


Figure 1: The normalized pressure rise $(\Delta P/I)$ as a function of the integrated beam dose.

The averaged pressure readings of the storage ring are $\leq 1 \times 10^{8}$ Pa without electron beam, 1×10^{7} Pa at the SSC and 9×10^{7} Pa at the crotch and absorber location with a beam current of 70 mA. After a continuous cleaning by the SR, the pressure rise due to the photon induced desorption (PID) effect was significantly reduced. Figure 1 shows the $\Delta P/I$ at the SSC, crotch and absorber section of No. 14 cell as a function of the integrated beam dose. The $\Delta P/I$ decreased by about two orders of magnitude after an accumulated beam dose of 190Ah. It shows the beam self-cleaning effect on the vacuum chamber. From this figure, in the early stage of commissioning $\Delta P/I$ decreases steadily with the slope of -0.57. For the CR2,

$$\Delta P/I = 3.7 \times 10^{-5} D^{-0.57},$$
 (1)

where D is the integrated beam dose. The photodesorption yields (η) at the crotch-absorber section, CR2, is estimated using the following formula [5]:

$$\eta = \Delta Q/\Delta N
= KS_{eff} (\Delta P / I)/(\Delta N / I) \text{ (molecules/photon)}, (2)$$

where $\Delta Q(\text{Pa m}^3 \cdot \text{s}^1) = S_{\text{eff}} \Delta P$ is the gas desorption rate, S_{eff} (Pa/s) $\approx 1 \text{m}^3$ is the effective pumping speed of the LNP at the crotch-absorber section, ΔP is the pressure rise due to PID, I(A) is the beam current, $\Delta N(\text{photons/s})\approx 8.05\times 10^{20}$ $EI(\Delta\theta/2^{\bullet})$ is the photon flux irradiates on the crotch-absorber, E=8GeV, $\Delta\theta(\text{rad})\approx 0.0325\text{rad}$ is the photon span

on the crotch-absorber, and $K\approx 2.26\times 10^{20}$ (molecules/Pa·m³) is the proportional constant. By using the data and formulas mentioned above, a photo-desorption yields at the crotch-absorber section is estimated,

$$\eta_{\text{CR2}} = 3.0 \times 10^4 D^{-0.57}$$
 (molecules/photon). (3)

At an accumulated beam dose of 10Ah, $\eta_{\text{CR2}}=8.1\times10^{-5}$ molecules/photon was achieved. A photo-desorption yields at the range of the integrated beam dose larger than 10Ah may be smaller than this value. A correct value can not be estimated, because some of the ionization gauges malfunctioned due to the effect of the photoelectron induced by SR, especially at the crotch-absorber and absorber section.

Figure 2 shows the product of the electron-beam current (I) and the beam lifetime (τ) versus the accumulated beam dose on the multi-bunch mode and several bunch mode operation. The one of the user operation mode of the SPring-8 storage ring is the multi-bunch mode where two third of the 2436 available RF buckets are filled continuously with electron. An integrated beam dose of 190Ah and a beam lifetime of 65 hours at 70 mA of the beam current were achieved in the multi-bunch mode after two years' operation. The lifetime in the several bunches mode is limited by Touschek effect.

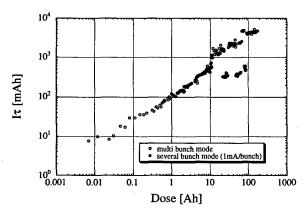


Figure 2: The product of the beam current (I) and the beam lifetime (τ) versus the accumulated beam.

In multi-bunch mode of 2/3-filling, the beam current of 70mA have been stored at user time, which means a population of 0.043mA/bunch. In the SPring-8 storage ring, the beam lifetime in the uniform filling mode is significantly longer than that in the partial-filling mode as shown in Fig. 3. In the electron storage ring, electron beam traps ions, which are produced by collisions of the electron beam with the residual gas molecules. Electrons and trapped ions, interact with each other and cause the instability. Ions are always trapped and electron beam size may be growth, so that the beam lifetime is longer in the uniform filling.

Another operation mode is several bunch mode. The

21-bunch mode (21 equally spaced bunches), the 21-bunch train mode (21 equally spaced 3- or 7-bunches trains), 10-bunch + partially filled multi-bunch, and so on are used at the user time. 1 or 0.5 mA/bunch routinely stored at the several bunch mode of the user time. The vacuum pressure in the several bunch mode is as same as in the multi-bunch mode (2/3-filling).

Touschek lifetime is about 6 hours at the single bunch operation (1mA/bunch) of the nominal machine parameter of the SPring-8 storage ring [6]. As the total lifetime (τ) in the 2/3-filling mode is 65 hours at the beam current of 70mA, gas scattering lifetime is estimated using a relationship: $1/\tau=1/\tau_t+1/\tau_g$, where τ_t and τ_g are Touschek and gas scattering lifetime, respectively. Since $\tau=65$ hours and $\tau_t=120$ hours (at a population of 0.43mA/bunch), $\tau_g=140$ hours.

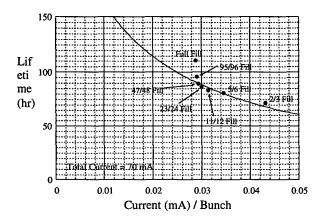


Figure 3: The beam lifetime versus the filling patterns of the multi-bunch mode.

4 CONCLUSION

The SPring-8 storage ring vacuum conditioning is progressing extremely well. A photo-desortion yields at the crotch-absorber section is 8.1×10^5 molecules/photon or less. About 65 hours beam lifetime was achieved at a beam current of 70mA in the multi-bunch mode. Touschek lifetime is about 6 hours at the single bunch operation, a population of 1mA/bunch. A gas scattering lifetime is about 145 hours at a beam current of 70mA with 2/3-filling mode operation.

- H. Ohkuma, et al., Proc. of the 9th Meeting on Ultra High Vacuum Techniques for Accelerators and Storage Rings. KEK, March 3-4, 1994, KEK Proceedings 94-3, 29.
- [2] K. Watanabe, et al., Proc. of the International Conference on Vacuum Science & Technology, India, 1995, 58.
- [3] H. Ohkuma, et al., Proc. of the 11th Symp. on Accelerator Sci. and Tech., Harima, Japan, 1997, 359.
- [4] S. Yokouchi, et al., RIKEN Accel. Prog. Rep. 23 (1989) 134.
- [5] G. Y. Hsiung, et al., J. Vac. Sci. Technol. A12 (1994)1639.
- [6] M. Takao, et al., "Estimation of Betatoron Coupling and Vertical Dispersion for Spring-8 Storage Ring", presented in this proceedings.

MULTIPOLE SPILLDOWN IN THE SPEAR 3 DIPOLE MAGNETS*

J. Corbett[†], D. Dell'Orco, Y. Nosochkov and J. Tanabe Stanford Linear Accelerator Center/SSRL, Stanford, CA 94309

Abstract

The main SPEAR 3 dipole magnets are 1.45 m long with a pole contour designed to horizontally deflect and vertically focus the electron beam. At the nominal beam energy (3 GeV), the field and gradient along the magnet centerline are 1.3 T and 3.3 T/m (k=-0.33 m⁻²), respectively. Due to the straight core construction, the beam passes through each dipole with up to 16.6 mm trajectory offset relative to the centerline. This paper describes a method used to characterize the spilldown effect from magnetic multipole fields as observed by the beam traversing the dipole magnets. Results of tracking studies utilizing the longitudinal variation of multipole fields are discussed.

1 SPEAR 3 DIPOLE MAGNETS

As illustrated in Fig. 1, the SPEAR 3 dipoles have pole faces contoured to produce a k-value of -0.33 m⁻² [1,2]. In order to simplify fabrication, a choice was made to construct the magnets with straight rather than curved cores. Figure 2 shows a plan view of the curved beam trajectory passing through the dipoles. To first approximation, the trajectory describes a hyperbolic cosine curve [3, 4] rather than a uniform radius curve. At the magnet entrance, center, and exit, the trajectory is offset from the nominal magnet centerline by 16.6 mm. The good field region (GFR) was specified by adding 32 mm to the trajectory offset for a total span of almost 98 mm. The wide GRF specification results in the wide magnet cross-section shown in Fig. 1.

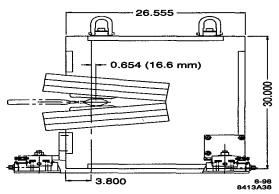


Figure 1: Cross section of a SPEAR 3 gradient dipole magnet.

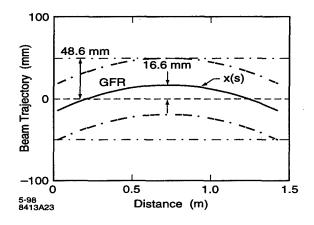


Figure 2: Beam trajectory through a SPEAR 3 dipole.

The error multipoles sampled by the off-axis beam are 'spilldown' terms from higher to lower multipoles. Simple examples of spilldown are the dipole kick received by a beam passing off-axis through a quadrupole, or the quadrupole and dipole field components seen by a beam passing off-axis through a sextupole. In a straight dipole magnet with multipole field content, the spilldown terms come from the lateral displacement of the beam along the curved trajectory.

In this paper, we present a matrix formalism to calculate the spilldown coefficients following the beam trajectory through the SPEAR 3 dipoles. The multipole content originates from systematic field errors caused by the finite extent of the poles. For tracking purposes the dipole magnets were sliced longitudinally, with each slice assigned appropriate multipole spilldown terms.

2 MULTIPOLE CALCULATIONS

The multipole content of the dipole magnets must be identified to evaluate lattice performance in tracking simulations. In practice, tracking codes typically specify multipole components with respect to the ideal beam trajectory. If the beam deviates from this trajectory (orbit errors, betatron oscillations) the multipole components 'kick' the beam resulting in tune shift, resonant excitation, etc. To be consistent, for a curved beam trajectory through a 'straight' dipole field the multipole spilldown fields should also be taken into account.

For SPEAR 3, we felt the +/-16.6 mm deviation of the *design* electron beam trajectory from the straight multipole axis in the dipole magnets was sufficiently large to warrant further investigation. The high order

^{*}work supported in part by Department of Energy Contract DE- AC03-76SF00515 and Office of Basic Energy Sciences, Division of Chemical Sciences.

^tE-mail: corbett@ssrl.slac.stanford.edu

multipoles could spilldown to components with potentially adverse effects on dynamic aperture.

To model this behavior, we 'sliced' the dipole magnets longitudinally and computed the net multipole terms in the center of each slice. The sliced magnets with associated multipole terms were then used for dynamic aperture simulations.

The multipole field components at any location displaced laterally by Δx from the magnet center can be expanded about the nominal center of the magnet as [5]:

$$\frac{B_n}{B} = \left(\frac{B_n}{B}\right)_{r_0} \left(\frac{z + \Delta x}{r_0}\right)^{n-1}$$

$$= \left(\frac{B_n}{B}\right)_{r_o} \left(\frac{1}{r_o}\right)^{n-1} \mathbf{X} \begin{pmatrix} z^{n-1} + (n-1)z^{n-2}\Delta x + \\ \binom{n-1}{k} z^{n-1-k} \Delta x^k + \bullet \bullet \bullet \Delta x^{n-1} \end{pmatrix}$$

where z = x - iy and $\binom{n-1}{k}$ is the binomial coefficient $\frac{(n-1)!}{k!(n-1-k)!}$.

Collecting terms with like powers of z from each straight multipole component, the net multipole spilldown coefficients are computed. The computation can be expressed as a matrix equation, $\mathbf{b}_{\text{spilldown}} = [\mathbf{T}]\mathbf{b}_{\text{center}}$ where the elements in the 'spilldown' column vector

$$\mathbf{b}_{\text{spilldown}}$$
 are $\left(\frac{B_n}{B}\right)_{r_0, \Delta x}$ and the elements in the center

column vector are $\left(\frac{B_n}{B}\right)_{r_0}$ for n\ge 2. Defining $\delta = \Delta x/r_0$, the

row/column elements T_{ij} in the transfer matrix [T] can be written as:

$$\begin{array}{ll} T_{ij} = k_{ij} \Delta x^{j \cdot i} \\ \text{where} & k_{1j} = j & \text{for } i, j \geq 1 \\ k_{i1} = 0 & \text{for } i > 1 \\ k_{ij} = k_{(i \cdot 1)(j \cdot 1)} + k_{i(j \cdot 1)} & \text{for } i > 1 \text{ and } j \geq 1. \end{array}$$

The structure of the transfer matrix is quite simple. For example a maximum multipole error index of n=6 (maximum i, j=5) has the transfer matrix:

Multipole	Nominal
n=3	+1.0x10 ⁻⁴
n=4	-1.0x10 ⁻⁴
n=5	-5.0x10 ⁻⁵
n=6	+1.0x10 ⁻⁴
n=7	-1.0x10 ⁻⁴
n=8	$+1.0 \times 10^{-4}$
n=9	$+1.0x10^{-4}$
n=10	-1.0x10 ⁻⁴

Table 1: Normal multipole content B_n/B in the SPEAR 3 dipoles evaluated at $r_o=30$ mm from the straight magnetic centerline.

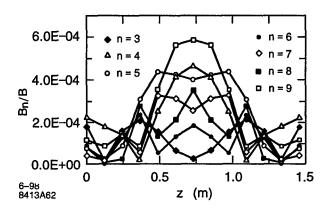


Figure 3: Normal multipole spilldown terms (B_n/B) at $r_0=30$ mm as a function of longitudinal position.

The binomial coefficients are evident in the columns of [T]. After computing the trajectory variation Δx through the magnet, the 'local' multipole spectrum $\mathbf{b}_{\text{spilldown}}$ is calculated by multiplying the nominal multipole spectrum along the straight magnetic axis $(\mathbf{b}_{\text{center}})$ by the transfer matrix [T].

For the SPEAR 3 magnets the systematic multipole errors normalized to the fundamental field were computed from ANSYS. The resulting values for B_n/B are listed in Table 1 [6]. Figure 3 shows the corresponding spilldown terms plotted as a function of longitudinal position. For comparison, SPEAR 3 tracking simulations are typically performed with $B_n/B = 5 \times 10^{-4}$ at $r_o=30$ mm for all systematic multipole fields throughout the full length of each dipole. The average values in Fig. 3 are considerably below 5×10^{-4} .

3 TRACKING STUDIES

The impact of spilldown on SPEAR 3 dynamic aperture evaluated with element-by-element tracking simulations. The spilldown effect was simulated in each of the twenty eight 1.45 m dipoles. Eight additional 3/4bend dipoles [2] have a smaller sagitta so spilldown effects were neglected. Each 1.45 m dipole magnet was sliced into 10 segments and assigned systematic multipole fields according to Table 1 and Figure 3. All magnets in the storage ring were seeded with rms main field errors, rms multipole errors, and alignment errors [7]. The lattice tracking code LEGO [8] then performed orbit correction, betatron tune fitting (Q_x=14.19, Q_y=5.23), chromaticity correction ($\xi_r = \xi_v = 0$) and coupling correction prior to tracking.

To test the sensitivity of dynamic aperture to multipole content in the dipoles, the set of straight-magnet multipoles in Table 1 was uniformly scaled to higher values, spilldown calculations performed and tracking simulations carried out. In this case, the simulations showed little or no reduction of dynamic aperture for a scaling factor up to 10 times the values listed in Table 1.

The insensitivity of dynamic aperture to multipole field amplitude in the dipole magnets is likely due the low value of the horizontal betatron function throughout much of the magnets and cancellations of multipole kicks as the electron beam trajectory traverses from inside to outside and back through the dipole magnets.

Although strong skew multipole terms are not anticipated from the dipole magnets (single piece lamination) skew effects were also studied by rolling the dipole magnet cores. Since the dipole magnets contain a quadrupole field, the nominal rms roll specification is 0.5 mrad. To increase the skew multipole terms, the rms roll was raised to as much as 5 mrad with the factor of 10 multipole scaling applied. Again, negligible effect was observed on the dynamic aperture. For these simulations, the vertical dipole kicks produced by rotating the vertical dipole field were partially canceled by applying a horizontal 'multipole' field $A_1 = \sin(\theta)/\rho$. The kick cancellation was necessary to produce stable (uncorrected) closed orbits in the vertical plane.

4 SUMMARY

This paper provides a simple yet elegant formalism to calculate the multipole spilldown terms for a curved beam trajectory through a straight dipole magnet. The method was applied to the SPEAR 3 dipoles to simulate the dynamical effects of lateral beam displacement. The local spilldown terms were found to exceed the 'straight' dipole values by as much as a factor of 5-10 at maximum beam displacement. The average values of B_n/B , however, are below the longitudinally constant field values B_n/B =

 $5x10^{-4}$ lr_o=30 mm used for most SPEAR 3 tracking studies [2.7].

Using a 'sliced' dipole model, multipole spilldown was found to have only a small effect on dynamic aperture even after the multipole strengths were scaled up by a factor of 10. Studies of skew multipole terms introduced by rolling the dipole magnet also showed little or no effect on dynamic aperture. Based on these studies, the straight magnet core design for the gradient dipoles appears to yield acceptable performance.

5 ACKNOWLEDGMENTS

The authors would like to thank Max Cornacchia and Klaus Halbach and Yunhai Cai for stimulating conversations and important theoretical contributions in the course of this study.

- [1] J. Tanabe, 'SPEAR 3 Gradient Magnets', SSRL Internal Memo, Sept. 19, 1997.
- [2] 'SPEAR 3 Conceptual Design Report', Stanford Synchrotron Radiation Laboratory, in press.
- [3] H. Wiedemann, <u>Particle Accelerator Physics</u>, Springer-Verlag, Berlin Heidelberg, 1993.
- [4] D. Dell'Orco, 'Beam Orbit through the SPEAR 3 Gradient Dipoles', SSRL Internal Memo, January 20, 1999.
- [5] J. Tanabe, 'SPEAR 3 Gradient Magnets Off-Axis Multipoles', SSRL Internal Memo, April 1, 1998.
- [6] J. Tanabe, 'SPEAR 3 Gradient Magnets Evaluation of Poisson Data', SSRL Internal Memo, March 28, 1998.
- [7] Y. Nosochkov, et al, 'Dynamic Aperture Studies for SPEAR 3', these proceedings.
- [8] Y. Cai, et al, 'LEGO: A Modular Accelerator Design Code', 1997 PAC, Vancouver, British Columbia, Canada, May 12-16, 1997.

EFFECT OF INSERTION DEVICES IN SPEAR-3*

J. Corbett[†] and Y. Nosochkov Stanford Linear Accelerator Center, Stanford University, Stanford, CA 94309

Abstract

The SPEAR 3 upgrade lattice will provide much reduced beam emittance to increase the brightness of synchrotron radiation beams from wigglers and undulators. Seven existing insertion devices will be used in the lattice. In this paper we review the wiggler parameters, outline the wiggler compensation scheme, and evaluate wiggler effect on the optics and dynamic aperture.

1 INTRODUCTION

Many of the drift sections in SPEAR 3 will contain wigglers or undulators. In the present machine, there are 7 insertion devices (ID). In this paper, we review the magnetic parameters for each of these ID's, estimate linear and higher order wiggler effects, evaluate radiation effects, and discuss correction of wiggler focusing using quadrupole trim windings. Tracking results show that dynamic aperture reduction due to wiggler effects is modest. All optics calculations were done with the MAD code [1], and the tracking simulations with the LEGO code [2].

2 WIGGLER PARAMETERS, EFFECTS AND MODELING

In SPEAR 3, the horizontally deflecting ID's reside in dispersion free straights where the unperturbed β functions are $\beta_x/\beta_y=10.1/4.8$ m. The magnetic field parameters for each ID are given in Table 1, where N is the number of periods, λ the period length, B_o the peak field. Future devices are likely to be ~ 10 -period wigglers similar to Beamlines 9 and 11. These devices will replace the wigglers on Beamlines 4 and 7 or illuminate new beam lines.

The main optical effects of the wigglers on the SPEAR 3 lattice are also summarized in Table 1. The parameter definitions and relevant formulas are listed below:

Bend radius	$\rho_o(m) = 3.3356 \frac{E(GeV)}{B_o(T)}$ $K = 93.44 B_o(T) \lambda(m)$
Wiggler parameter	$K = 93.44B_o(T)\lambda(m)$
Integrated focusing [3]	$\int k_y ds = rac{N\lambda}{2 ho_0^2}$
Linear tune shift	$\Delta Q_y = \frac{\beta_y}{4\pi} \int_{s}^{s} k_y ds$
Maximum β -beat	$\frac{\Delta \beta_y}{\beta_y} = \frac{\beta_y \int k_y ds}{2 \sin 2\pi Q_y}$
Amplitude dependent	$\Delta Q_y^{oct} = \epsilon_y \frac{\pi N \beta_y^2}{4\lambda \rho_o^2} \left[1 + \frac{2}{3} \left(\frac{N\lambda}{2\beta_y} \right)^2 \right]$
tune shift [4]	$+\frac{1}{5}(\frac{N\lambda}{2\beta_y})^4$

^{*}Work supported by the Department of Energy Contract DE-AC03-76SF00515.

Table 1: Wiggler parameters and main optics effects.

Beamline	4,7	5	6	9	10	11
N	4	10	27	8	15	13
λ (cm)	45	18	7	26	13	17.4
B_{o} (T)	1.8	0.9	1.3	1.93	1.45	1.98
ρ_o (m)	5.56	11.12	7.70	5.18	6.90	5.05
K	75.7	15.1	8.5	46.9	17.6	32.2
$\int k_y ds (m^{-1})$.029	.007	.016	.039	.021	.044
ΔQ_y	.011	.003	.006	.015	.008	.017
$\Delta \beta_y / \beta_y$ (%)	7.0	1.8	3.9	9.4	5.0	10.7
$\Delta Q_y^{oct}[10^{-4}]$	0.4	0.6	9.1	1.6	3.4	4.1

where Q_y =5.23 is the vertical betatron tune, ϵ_y the vertical emittance, and E=3 GeV the beam energy.

For a flat horizontal wiggler the field components can be expressed as [5]:

$$B_y = B_o \cosh(ky) \cos(kz), \tag{1}$$

$$B_z = -B_o \sinh(ky) \sin(kz), \tag{2}$$

where $k=2\pi/\lambda$, y and z are the vertical and longitudinal coordinates, and z=0 the center of a pole. The integral of the B_y field (Eqn. 1) with respect to the reference trajectory vanishes over each wiggler period. This leads to self compensation of the optics effects. For instance, the horizontal orbit and dispersion generated by B_y are fully localized within each period. The amplitude of the orbit and dispersion is proportional to $\lambda^2 B_o$, and the increase in beam path length is proportional to $\lambda^3 B_o^2 N$. Hence, the largest orbit oscillations are produced in the wigglers with the longest poles. The total increase of the path length for all 7 wigglers is 191 μ m.

Taking into account the horizontal orbit oscillations of the beam, the B_z field (Eqn. 2) can be decomposed into longitudinal and horizontal components on the beam orbit. Although the integral of the longitudinal component vanishes over each period, one can can find a non-zero integral of the field horizontal to the beam trajectory [3]:

$$\int_{0}^{N\lambda} B_{\bar{x}} dz = -\frac{N\lambda B_o^2}{2B\rho} (y + \frac{2}{3}k^2y^3 + \frac{2}{15}k^4y^5 + \ldots), (3)$$

where label \tilde{x} refers to the local horizontal axis with respect to the oscillating beam orbit.

The first term in Eqn. 3 ($\propto y$) is similar to the vertical gradient in quadrupoles and thus results in vertical focusing, namely the vertical tune shift ΔQ_y and vertical betatron beat $\Delta \beta_y/\beta_y$. The total linear tune shift is ΔQ_y =0.071 for all 7 wigglers. The pattern of the β -beat depends on the distribution of wigglers in the ring. The $\sim 90^{\circ}$ vertical phase advance per cell helps to minimize beta perturbations

[†] E-mail: corbett@slac.stanford.edu.

¹Beamline 5 can use five separate devices: (1) N=10, λ =0.18, (2) N=15, λ =0.12, (3) N=24, λ =0.07, (4) N=30, λ =0.06, and (5) elliptically polarized undulator (EPU). Here, we chose the N=10, λ =0.18 wiggler.

from a pair of wigglers if they are located on either side of the same cell. All 7 wigglers generate about $\pm 25\%$ vertical β -beat in the ring without correction.

The first non-linear wiggler effect comes from the second term in Eqn. 3 ($\propto y^3$). This octupole-like field generates quadratically increasing vertical tune shift with y-amplitude. For devices of similar length $(N\lambda)$ the effect is proportional to $1/\lambda^2$. In Table 1, this tune shift was evaluated for the maximum vertical emittance (ϵ_y =7.5 mm·mrad) defined by the smallest vacuum chambers at Beamlines 6 and 11 (y=6 mm, β_y =4.8 m). The maximum total tune shift for 7 wigglers is ΔQ_y^{oct} =0.002. This value is significantly smaller than the amplitude dependent tune shift caused by the sextupoles and was considered acceptable. Tracking simulations with wiggler effects confirm that the vertical dynamic aperture stays well outside the physical wiggler aperture.

For optics calculations, each wiggler pole was simulated by a shorter pole with constant vertical field and with gaps between the poles [3]. In this model, the pole field, $B_p = B_o \pi/4$, and pole length, $L_p = 4\lambda/\pi^2$, were set to produce the same bending and focusing effect as the actual wiggler field. Therefore, the model yields the correct linear tune shift, β -beat, and the net orbit and dispersion. For tracking studies, higher order multipole fields were added to simulate the effects of non-linear wiggler fields on dynamic aperture.

3 RADIATION EFFECTS

Synchrotron radiation and quantum excitation in wigglers increase the beam energy loss and change the equilibrium emittance and the beam energy spread. For a single ID, the relative increase in energy loss per turn is [6]:

$$\frac{U - U_o}{U_o} = \frac{N\lambda\rho_b}{4\pi\rho_o^2},\tag{4}$$

where ρ_b =7.86 m is the bend radius in the main dipoles, and U_o =913 keV/turn (without ID's). The energy loss with all 7 wigglers at full field increases by 23% to 1124 keV/turn. The total radiated wiggler power is 225 kW from a 200 mA beam.

The relative change in the beam energy spread due to each ID is given by [6]:

$$(\frac{\sigma_E}{\sigma_E^o})^2 = [1 + \frac{2N\lambda\rho_b^2}{3\pi^2\rho_o^2}]/[1 + \frac{N\lambda\rho_b}{4\pi\rho_o^2}].$$
 (5)

With 7 wigglers at full field, the net energy spread on the beam increases by only 1.6%, from σ_E^o/E =0.097% to

Table 2: Change in energy loss and energy spread due to wigglers.

Beamline	4,7	5	6	9	10	11
$\frac{U-U_o}{U_o}(\%)$	3.64	0.91	1.99	4.84	2.56	5.54
$\frac{\sigma_E - \sigma_E^o}{\sigma_E^o}(\%)$	0.35	-0.18	-0.13	0.66	-0.04	0.84



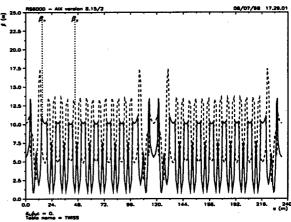


Figure 1: SPEAR 3 β functions with 7 wigglers (black boxes on the top) after correction.

0.0986%. The effects of individual ID's are listed in Table 2. Emittance calculations show that 7 wigglers reduce the horizontal emittance from 18.2 nm·rad to 15.3 nm·rad.

4 OPTICS COMPENSATION

The wiggler focusing from 7 wigglers at full field generates $\pm 25\%$ vertical β -beat and a linear vertical tune shift of 0.071. This distortion breaks the periodicity of the β -functions and phase advance between sextupoles, which could lead to stronger sextupole resonances and reduced dynamic aperture.

Several options are possible to correct the wiggler focusing. The preferred scheme is to locally compensate the distortion of β -functions and phase advance with four QF and four QD independent quadrupole trims located to either side of each ID. With this correction, the phase advance stays identical in all cells, the global tune adjustment is not necessary and the distortion of lattice functions at sextupoles is minimal. The required independent quadrupole trims are less than 10%. This correction scheme has been designed into the SPEAR 3 lattice and was used in tracking studies described in the following section. The SPEAR 3 β functions after correction of 7 wigglers are shown in Fig. 1.

5 EFFECT ON DYNAMIC APERTURE

Effects of IDs on dynamic aperture arise from reduced symmetry and lattice periodicity, distortion of β -functions and betatron phase, non-linear wiggler fields, wiggler field errors and misalignment. In tracking simulations, we studied the following effects of wigglers on dynamic aperture:

- Linear wiggler focusing,
- Effect of systematic multipole field errors in wigglers,
- Effect of intrinsic non-linear wiggler field.

Without correction of the wiggler focusing, the vertical dynamic aperture reduces by about 20% with all wigglers

Table 3: Multipole fit to the measured systematic multipole field error in the wiggler on Beamline 11 (G/cm^{n-2}) .

\overline{n}	1	2	3	4	5	6
$\overline{b_n}L$	20.3	-6.49	-15.5	-37.2	5.96	33.2
a_nL	19.4	17.9	-35.4	26.4	3.64	-65.0
\overline{n}	7	8	9	10	11	12
$\overline{b_n L}$	2.73	-7.40	-1.05	0.457	0.079	0.001
a_nL	13.9	33.3	2 55	5 57	0.227	0.297

active. With corrected wiggler focusing, linear wiggler effects alone do not reduce the aperture.

The study of wiggler multipole errors was based on measured systematic field errors in the wiggler on Beamline 11. A numerical multipole fit to the measured data was performed and the results for the integral of normal and skew systematic multipole field are shown in Table 3, where 'n' is the multipole order starting with dipole, $L = N\lambda$, and a_n, b_n are the skew and normal field coefficients defined as

$$B_y + iB_x = \sum_n (b_n + ia_n)(x + iy)^{n-1}.$$
 (6)

The effect of 7 wigglers on dynamic aperture is shown in Fig. 2, with the aperture calculated at the ID locations $(\beta_x/\beta_y) = 10.1/4.8$ m) for machine simulations with all errors in the ring magnets. Without multipole errors in the wigglers but with corrected wiggler focusing, the aperture is not affected. With the systematic multipole errors included in the 7 wigglers, the dynamic aperture reduction is about 10% (2 mm).

The wiggler-intrinsic high order terms (Eqn. 3) were not included in the previous simulation, but can further reduce the dynamic aperture. This field does not have the usual form of (x-y) multipole expansion normally used in lattice codes. To accurately study the effect of the octupole-like and higher order terms in Eqn. 3, one needs a symplectic model of this field. We used an approximation to evaluate the main effect of these terms. Since the non-linear $B_{\bar{x}}$ field generates kicks only in y-plane, the effect on dynamic aperture is expected to be mostly in the vertical plane, as it was observed in simulations for other machines [6].

One can notice that the $B_{\bar{x}}$ field can be reproduced at x=0 by the normal field of Eqn. 6 $(a_n=0)$. Using this approach, we used normal systematic multipoles in the form of $B_y+iB_x=\sum b_n(x+iy)^{n-1}$ to produce the non-linear terms of the wiggler field $B_{\bar{x}}$ on the vertical axis (Eqn. 3), and performed tracking to evaluate vertical aperture near x=0. Simulation of the octupole-like and dodecapole-like $(\propto y^5)$ fields with 7 wigglers showed only modest reduction of vertical dynamic aperture, from 11 mm to 8-9 mm. This aperture still remains well outside the 6 mm wiggler physical aperture.

6 SUMMARY

Tracking simulations with 7 wigglers in SPEAR 3 predict small impact on dynamic aperture when linear optics ef-

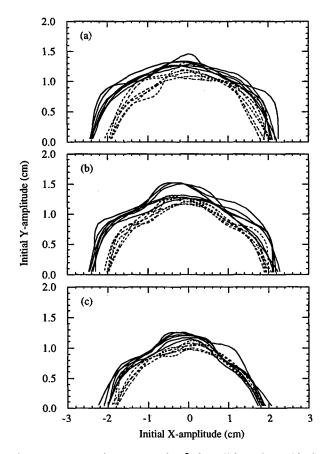


Figure 2: Dynamic aperture for δ =0 (solid) and 3% (dash) off-momentum oscillations and 6 seeds of random machine errors: (a) no wigglers, (b) 7 wigglers with corrected focusing but w/o errors, (c) 7 wigglers with corrected focusing and with systematic multipole errors.

fects are locally compensated with individually controlled quadrupole magnets. The 18 mm horizontal dynamic aperture is sufficient for 10 mm injection oscillations and long Touschek lifetime, and the vertical aperture remains well outside the 6 mm wiggler physical aperture. With all wigglers active, the increase in energy spread is negligible (<2%), and the beam horizontal emittance decreases to about 15.3 nm·rad at 3 GeV.

7 ACKNOWLEDGEMENTS

We would like to thank M. Cornacchia, H. Wiedemann and B. Hettel for useful discussions, suggestions and guidance.

- [1] H. Grote, F. C. Iselin, CERN/SL/90-13 (AP) Rev.4 (1994).
- [2] Y. Cai et al., SLAC-PUB-7642 (1997).
- [3] H. Wiedemann, "Particle Accelerator Physics II," Springer-Verlag, Berlin, Heidelberg (1995).
- [4] L. Smith, LBL-ESG Tech. Note-24 (1986).
- [5] K. Halbach, NIM, A187, p. 109 (1981).
- [6] A. Ropert, CERN 90-03, p. 142 (1990).

COLLECTIVE EFFECTS IN SPEAR 3

C. Limborg, J. Sebek SSRL/SLAC P.O Box 4349 MS69, Stanford, CA 94309-0219 USA

Abstract

SSRL is investigating an upgrade to run SPEAR with a small emittance (18 nm) and with a 200 – 500 mA current, significantly greater than the present 100 mA value of SPEAR 2. Using experimental measurements, numerical calculations of impedance, and results from tracking code simulations, an impedance model for SPEAR 3 is calculated. Beam quality and instability thresholds for these results are predicted. Based on these calculations, choices made for RF cavities, vacuum chamber material and cross-section, and BPM design are also discussed. The estimated beam lifetime for 500 mA is 22 hours.

1 INTRODUCTION

SSRL is investigating an upgrade project for its SPEAR electron storage ring that will increase current from the present 100 mA, initially to 200 mA, and ultimately to 500 mA [1]. The emittance of the machine, dedicated to synchrotron radiation production, will be reduced from 160 nm to 18 nm. This proposal calls for the reuse of existing beamlines, and facilities, but SPEAR 3 will have new lattice, magnets, vacuum chambers, power supplies, and RF system.

This paper presents the design considerations concerning impedance, instability thresholds, and lifetime. Specifications for the vacuum chamber material, cross-section, vacuum chamber profile, RF cavities, and feedback systems were based, in part, on this study.

2 IMPEDANCE BUDGET

2.1 RF Cavities

SPEAR 3 will need ~ 1.2 MW of RF power for 500 mA operation. The power capability of the existing RF system is limited by the 500 kW rating of the two cavities. The original scope of the project called for the reuse of these cavities in the initial stage of SPEAR 3, then upgrading the RF system for 500 mA. A study of the existing RF cavities was performed, showing that they could be tuned to operate stably at currents exceeding 200 mA with the SPEAR 3 parameters [2]. Cost considerations showed that it was more efficient to go immediately to the final RF system. Based on the excellent performance of the RF cavities at PEP II [3], SPEAR 3 has decided to opt for cavities of this style [4].

2.2 Coupled bunch instability thresholds

With the PEP II cavities, even the strongest HOM impedances will be far too small to cause longitudinal in-

Param.	SPEAR 2	SPEAR 3	SPEAR 3
ρ	12.8	8.4	8.4
U ₀ (keV)	560.0	855.6	855.6
h	280	280	372
V_{RF}	1.68	3.2	3.2
α	$1.5\cdot 10^{-2}$	$1.2 \cdot 10^{-3}$	$1.2 \cdot 10^{-3}$
δ	$7.4 \cdot 10^{-4}$	$9.7 \cdot 10^{-4}$	$9.7 \cdot 10^{-4}$
f_s (kHz)	23	9.6	11
σ_{τ} (ps)	75	18.8	16.3
$ au_x(\mathrm{ms})$	8.36	4.24	4.24
$ au_y(ext{ms})$	8.36	5.14	5.14
$ au_z(\mathrm{ms})$	4.18	2.87	2.87
$R_{\parallel}({ m k}\Omega)$	200	200	2.2
$R_{\perp}(\mathrm{k}\Omega\cdot\mathrm{m}^{-1})$	$2 \cdot 10^3$	$2 \cdot 10^3$	161
$I_{th,\parallel}(\mathrm{mA})$	10	72	3600
$I_{th,\perp x}({\sf mA})$	12	47	589
$I_{th,\perp y}({ m mA})$	137	100	1240

Table 1: SPEAR parameters (SPEAR 2, SPEAR 3 with existing RF system, SPEAR 3 with new RF system)

stabilities at 500 mA. One transverse mode might be dangerous, but moderate chromaticity will provide sufficient head-tail damping to oppose growth of this mode.

The operational experience at PEP II has shown all $R_{\parallel} \leq 2.2~\mathrm{k}\Omega$ and $R_{\perp} \leq 161~\mathrm{k}\Omega\cdot\mathrm{m}^{-1}$. The threshold currents presented in Table 1 were computed for the case of maximum impedance. As SPEAR 2 is presently stable at 100 mA in both planes, threshold currents presented are very conservative for those narrowband impedances. The broader width of HOM resonances for HOM damped RF cavities makes the calculated thresholds more probable for the PEP II style cavities. However, even if four such cavities were tuned on their strongest 2.2 k Ω longitudinal impedance, SPEAR 3 should be stable up to 900mA. The transverse coupled bunch instability thresholds were computed with $\beta_x/\beta_y=10.1~\mathrm{m}/4.8~\mathrm{m}$. No fast feedback systems should be necessary for stabilizing any coupled bunch instability.

2.3 Vacuum Chamber

Chamber dimensions The arc vacuum chambers will be replaced for SPEAR 3 [5]. These chambers will have an 84×34 mm² elliptical cross-section. An antechamber is joined to this chamber via a coupling slot 12 mm high. The dimensions of the antechamber are set by the size of the radiation fans and exit ports which vary greatly around the ring. A high coupling slot allows high pumping conductance, a decrease of power density deposited by the ra-

diation fan, and a large safe steering envelope. The actual slot height is a compromise between this large size and the small size needed to decouple the fields in the antechamber from the main beampipe. The cutoff frequencies of the dominant TM and TE modes have been calculated to be 4.7 GHz and 2.1 GHz, respectively [6]. A slot width needs to be many evanescent lengths of the dominant mode in order to insure this decoupling. For the 12 mm high slot of the chamber, the evanescent length of the TM mode is 3 mm. The minimum slot width of this chamber is 5 cm.

The image current on the elliptical chamber is not azimuthally symmetric; it is concentrated near the vertical axis (figure 1). From this distribution, the azimuthal posi-

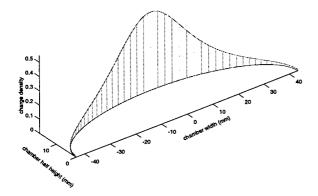


Figure 1: Image current density along the chamber wall.

tions of the beam position monitors were chosen to equalize the sensitivity to vertical and horizontal beam motion; the 15 mm diameter buttons will be placed 12 mm from the vertical axis. The effective radius of the chamber, used for resistive wall calculations, was computed to be 22 mm [7].

Chamber material The two materials under consideration for the chamber are copper and stainless steel. The main issues are the heat conduction and fabrication costs. The higher conductivity of the copper makes it a better choice for impedance minimization.

2.4 Broadband Impedance

The broadband impedance of small discontinuities around the ring was calculated using ABCI [8]. The results, shown in table 2, are consistent with those found for other rings. The total inductance in this table is 60 nH, corresponding to .5 Ω . Using a conservative value of 1Ω , a broadband impedance model was constructed with the characteristic parameters: $R_S=12~\mathrm{k}\Omega,\,Q=1,\,f_R=15~\mathrm{GHz}.$ The somewhat arbitrary choice of f_R was based on the fact that ABCI showed no strong peaks below 10 GHz, the cutoff frequency of the bunch. Using this impedance model, the tracking code gave a single bunch current threshold of 5 mA beyond which the energy spread starts widening. At 25 mA, the energy width of the bunch was 1.7 and its length was 2.2 times greater than the zero current values.

Element	k_L (V/pC)	No.	L_{Tot} (nH)
bellows shield	0.0107	80	5.8
RF seals	$4.4 \cdot 10^{-4}$	197	3.5
BPM	0.0027	90	3.3
transitions	0.02	10	10
trans. kicker	0.66	2	11
trans. pickup		2	26

Table 2: Broadband impedance

ξ_{norm}	$I_{th,Cu}$ mA	$I_{th,SS}$ mA.
0	190	103
0.1	506	274
0.2	822	446

Table 3: Resistive wall instability thresholds

2.5 Resistive Wall Impedance

The resistive wall impedance is strongest at low frequencies. The fractional parts of ν_x , ν_y were set below the halfinteger to maximize the system stability. Due to the shape of the chamber, this impedance is strongest in the vertical dimension. Since the small-gap insertion devices have small vertical heights, they contribute half of the total resistive wall impedance if the vacuum chamber is made from stainless steel. Using copper for the chamber reduces the total resistive wall impedance by a factor of two. The radiation damping force is not strong enough to compensate for the growth due to the strongest resistive wall growth term. Head-tail damping, calculated with the broadband model given above, adds to the total damping. Table 3 displays the resistive wall instability current thresholds for the two different chamber designs (copper with stainless steel insertion chambers and all stainless steel), at reasonable values of the normalized chromaticity. The $\langle \beta \rangle$ values used in these calculations are 8.5 m in the arc chambers and 4.5 m in the insertion devices.

2.6 Power Dissipation

The power dissipation due to resistive wall heating along the chamber scales as I_{Tot}^2/N_B where N_B is the number of bunches. An advantage of the new RF system is that at the higher harmonic number, N_B increases, so the power dissipation decreases. The chamber materials make a significant difference. The heating in the stainless steel chamber at 500 mA in 279 bunches is 7.5 W/m. For copper, this drops to 1.2 W/m. These values are both small compared to the heating in the insertion devices. The smallest gap undulator (half height 6 mm) heats up at a rate of 209 W/m. Higher order mode losses around the ring are negligible due to the low impedance design of the vacuum chambers.

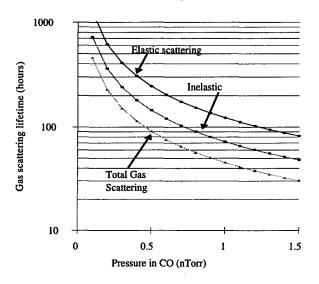


Figure 2: Total gas scattering lifetime as a function of vacuum chamber pressure in CO.

3 LIFETIME

3.1 Gas Scattering Lifetime

Electrons can be lost due to elastic (Coulomb) or inelastic (bremsstrahlung) collisions with the background gas molecules. The loss rate depends on the local and average β functions, the local gas pressure, and the ring acceptance. For SPEAR 3, the Coulomb and bremsstrahlung lifetimes are estimated to be 275 and 120 hours, respectively, at 200 mA. Taken in parallel, the total gas scattering lifetime is 83 hours at 200 mA, assuming a partial pressure in CO of 0.6 nTorr and an energy acceptance of 3%. This scales to 1.5 nTorr at 500 mA and a gas scattering lifetime of 30 hours.

3.2 Touschek Lifetime

At 3 GeV, SPEAR 3 is moderately sensitive to Touschek scattering. The energy acceptance, which sets the Touschek lifetime, is the minimum between the RF bucket size and the momentum dependent dynamic aperture. For a gap voltage of 3.2 MV, the bucket size is 3.1%. The lattice has been opimized to provide a momentum dependent dynamic aperture of 3% (particles 3% off-energy with amplitudes up to 20 mm in the 3 m straight sections will be kept in the ring). The energy acceptance will be RF bucket limited at 3.2 MV. For 200 mA beam current distributed in 279 bunches, and emittance coupling of 1%, the Touschek lifetime was computed to be 217 hours. For 500 mA the equivalent number is 87 hours.

3.3 Total electron beam lifetime

Lifetime calculations predict that the total lifetime is 60 hours at 200 mA. At 500 mA, the lifetime is 22 hours. After 24 hours, the initial 500 mA will decay to 200 mA.

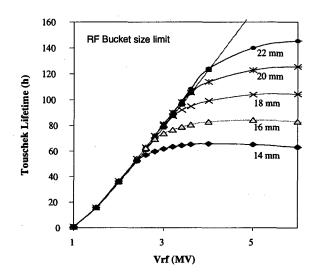


Figure 3: Touschek lifetime as a function of V_{RF} for different values of the mometum dependent dynamic aperture; ("22mm" = 22mm on energy and 19mm at 3%) 500 mA in 279 bunches, 1% vertical coupling;

4 CONCLUSION

The upgrade of the SPEAR storage ring to run with an 18 nm emittance and 500 mA current is presently under investigation. With a new RF system and new vacuum chamber, SPEAR 3 will be stable in both planes without the need for any fast feedback systems. A 22 hour lifetime is expected at 500mA.

Acknowledgements We would like to thank all the people from the SPEAR 3 team for valuable discussions.

- [1] R. Hettel *et al.*, "SPEAR 3 a low emittance source for SSRL," in *Proc. of PAC99*. in these proceedings.
- [2] J. Sebek and C. Limborg, "Characterization of RF cavity HOMs with beam," in *Proc. of 1997 ICFA Conference*, (Frascati), 1997.
- [3] R. A. Rimmer et al., "Updated impedance estimate of the PEP-II RF cavity," in Proc. of EPAC96, EPAC, (Sitges), pp. 2035–2037, CERN, 1996.
- [4] S. Park, "SPEAR 3 RF system," in *Proc. of PAC99*, PAC, (New York), IEEE-APS, March 1999. in these proceedings.
- [5] N. Kurita *et al.*, "Overview of SPEAR 3 vacuum system," in *Proc. of PAC99*. in these proceedings.
- [6] W. Bruns, GdfidL tutorial, usage, and syntax. Technische Universitat Berlin, Berlin, 1997.
- [7] L. Palumbo, V. G. Vaccaro, and M. Zobov, "Wake fields and impedance," in *Proc. of CAS 1993* (S. Turner, ed.), vol. 1 of *CAS*, (Geneva), pp. 331–389, CERN, September 1995.
- [8] Y. H. Chin, *User's guide for ABCI Version 8.8*. LBL, Berkeley, February 1994.

DYNAMIC APERTURE STUDIES FOR SPEAR 3*

J. Corbett, Y. Nosochkov[†], J. Safranek, SLAC, Stanford, CA 94309 A. Garren, UCLA, Los Angeles, CA 90095

Abstract

The SSRL is investigating an accelerator upgrade project to replace the present 130 nm·rad FODO lattice with an 18 nm·rad double bend achromat lattice: SPEAR 3. In this paper, we review the methods used to maximize the SPEAR 3 dynamic aperture including optimization of linear optics, betatron tune, chromaticity and coupling correction, and effects of machine errors and insertion devices.

1 INTRODUCTION

SPEAR 3 is a machine upgrade project under study at SSRL [1]. It aims at replacing the current 130 nm rad FODO lattice with an 18 nm rad double bend achromat (DBA) lattice. To reduce the cost of the project and to use the existing synchrotron light beam lines, the new design [2] closely follows the racetrack configuration of the SPEAR tunnel, with the magnet positions fit to the 18 magnet girders. The 3 GeV lattice has two-fold symmetry and periodicity with two identical arcs and two long straight sections.

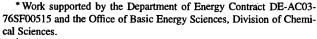
The lattice functions for one quarter of the ring are shown in Fig. 1. Similar to other light source rings, it has been found advantageous to use combined function bends to relax the optics and reduce sextupole strength.

Though the DBA design has an advantage of a high brightness beam, the strong focusing increases beam sensitivity to machine errors and generates larger chromaticity. The stronger sextupoles increase the amplitude dependent and non-linear chromatic aberrations and reduce the dynamic aperture. It is especially important to maximize the horizontal size of dynamic aperture to minimize the Touschek effect and allow large injection oscillations.

In the following sections we review the lattice optimization and tracking studies. The tracking simulation was done using LEGO [3]. The dynamic aperture was calculated at the symmetry point between arc cells where $\beta_x/\beta_y = 10.1/4.8 \text{ m}$.

2 ERROR FREE LATTICE

The DBA cell was made to fit the existing 11.7 m cell length with the magnet positions constrained by the existing photon beam lines and \sim 3 m space for the insertion devices (ID). This results in a compact DBA design with stronger focusing and increased sensitivity to machine errors. Vertical focusing added to the bends increased the separation of x and y focusing and reduced strength of the



[†]E-mail: yuri@slac.stanford.edu.

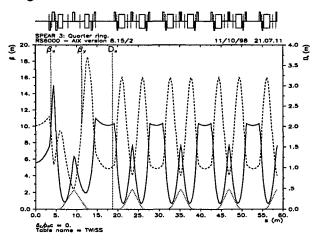


Figure 1: Optics of one quadrant of SPEAR 3.

quadrupoles and sextupoles. Further reduction of the sextupole strengths was achieved by moving the bends as far apart as possible.

The phase advance per arc cell was chosen to be near $\mu_x=0.75\times 2\pi$ and $\mu_y=0.25\times 2\pi$. This provides conditions for local cancellation of: 1) geometric aberrations from arc sextupoles located -I apart, and 2) first order chromatic beta waves from sextupoles and quadrupoles located $\pi/2$ apart, as well as systematic quadrupole errors. With this choice, the total tune would be near $\nu_x=14.5$ and $\nu_y=5.5$. To move the working tune away from the 1/2 resonance and to minimize resistive wall impedance effects, the tune was moved into the lower quarter on the tune plane ($\nu<1/2$).

The matching cell optics was optimized by performing a horizontal dynamic aperture scan across the matching cell phase advance. The dynamic aperture including $\delta = \frac{\Delta p}{p}$ up to $\pm 3\%$ was maximized at $\mu_{x,m} = 0.78 \times 2\pi$ and $\mu_{y,m} = 0.42 \times 2\pi$ per matching cell.

To minimize the effect of low order betatron resonances the working tune was chosen slightly below 1/4, away from the 3rd and 4th order resonance lines. The final choice ($\nu_x=14.19,\,\nu_y=5.23$) was based on favorable horizontal injection conditions and the results of dynamic aperture tune scan. With the chosen tune, the phase advance per arc cell is $\mu_x=0.7907\times 2\pi$ and $\mu_y=0.2536\times 2\pi$.

As mentioned previously, the chosen phase advance in the arc cells provides conditions for local compensation of chromatic and geometric aberrations. This scheme would work optimally for the number of arc cells of $4 \times integer$. With only 7 cells per arc, constrained by the SPEAR geometry, the correction is not complete.

The study showed that chromaticity correction with only 2 sextupole families did not provide adequate dynamic aperture for particles up to $\delta=\pm3\%$. Since the 2 families only compensate linear chromaticity, the off-momentum

Table 1: Systematic rms multipole field errors.

Magnet	r(mm)	n	$\Delta B_n/B$
Dipole	30	2	1×10^{-4}
		3-14	5×10^{-4}
Quadrupole	32	6,10,14	5×10^{-4}
Sextupole	32	4	-8.8×10^{-4}
		5	-6.6×10^{-4}
		9	-1.6×10^{-3}
		15	-4.5×10^{-4}

aperture is limited by the non-linear chromatic effects. A significant amount of non-linear chromaticity is generated in the matching cells which break periodicity of the 14 arc cells and contribute $\sim\!20\%$ to the total chromaticity. Two additional sextupole families (SFI, SDI) placed in the matching cells reduced the non-linear terms by a factor of 3 and significantly improved the off-momentum aperture.

The matching cell sextupoles also generate geometric aberrations and therefore have to be kept relatively weak in order to preserve the on-momentum aperture. The optimum strengths of the SFI, SDI were evaluated through a horizontal aperture scan versus SFI, SDI strengths.

To increase optical separation between the SF and SD sextupoles two other options were studied. In one option, the SD was combined with part of the adjacent bend. This increased β_y but reduced dispersion at the SD which led to smaller dynamic aperture. In the second study, the SF was combined with the center quadrupole QFC. This increased dispersion and β_x at the SF and reduced its strength, but dynamic aperture did not improve.

3 MACHINE ERRORS

In tracking simulations, we included random main field errors, random and systematic multipole errors, and random alignment errors. In addition, a skew octupole component was added to skew quadrupoles combined with sextupoles, and a feed-down multipole field was included due to a large trajectory in the bends [4].

The alignment rms errors for bends, quads and sextupoles used in the study were: $\Delta x, \Delta y = 200 \ \mu\text{m}$, roll = 500 μ rad. The rms main field errors due to differences in magnetic core length were assumed to be $(1-2)\cdot 10^{-3}$.

The multipole field errors were defined in terms of ratio of the multipole field ΔB_n (normal or skew) to the main magnet field B at radius r, where $n=1,2,\ldots$ is the multipole order starting with a bend. The normal systematic and random rms values $\Delta B_n/B$ used in the study are listed in Tables 1,2. Conservatively large values were specified for n=3,6,10,14 multipoles on the quads.

The skew quadrupoles physically combined with chromatic sextupoles provided an efficient coupling correction. In total, we used 24 skew quads arranged in 4 families. The induced vertical dispersion was small and far outweighed by the improved aperture. As a future option, the vertical dispersion can be corrected as well by using more independent skew quads. The combined skew quad and sextupole

Table 2: Random rms multipole field errors.

Magnet	r(mm)	n	$\Delta B_n/B$
Dipole	30	2	1×10^{-4}
Quadrupole	32	3,6,10,14	5×10^{-4}
		4,5,7-9,11-13	1×10^{-4}
Sextupole	32	5	$1.5 imes 10^{-3}$
		7	4.8×10^{-4}

gives rise to a skew octupole field that was systematically added in the simulations.

4 DYNAMIC APERTURE WITH ERRORS

For tracking simulations, LEGO first generates a set of magnet errors, then applies tune, orbit, chromaticity and coupling corrections, and finally tracks the particles. For tune correction, two families of doublet quads in the cells were used. Linear chromaticity typically was adjusted to zero with the SF, SD sextupoles. An RF voltage of 3.2 MV was used to generate synchrotron oscillations.

The resultant dynamic aperture without ID's for 6 random seeds of machine errors is shown in Fig. 2. The horizontal dynamic aperture is 18-20 mm for $\delta=\pm3\%$ momentum range. This provides sufficient aperture for a long Touschek lifetime and injection oscillations.

In real machines, the linear chromaticity $\xi = \Delta \nu / \delta$ is typically set slightly positive. Since non-zero chromaticity increases the momentum dependent tune spread, the offmomentum particles would cross more betatron resonances during synchrotron oscillations. Resonance effects can reduce the $\delta \neq 0$ aperture if ξ is large. The $\delta = 0$ aperture is affected only by the increased sextupole strength.

Fig. 3 shows dependence of horizontal dynamic aperture on ξ for various δ (the vertical dependence is similar). In this study, the chromaticity was set equal in both planes. Clearly, for the SPEAR 3 tune the particles lose stability near 1/2 resonance, when $\Delta\nu\approx$ -0.2. Though the dynamic aperture for the core beam (small δ) is not much affected, the Touschek lifetime can be reduced for $\xi>5$.

In the study, typical β distortions after correction were $\Delta \beta/\beta < \pm 10\%$. In a real machine larger modulations can

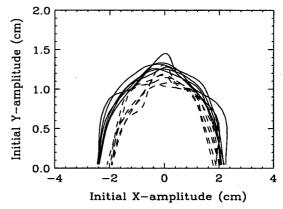


Figure 2: Dynamic aperture for 6 seeds of machine errors for $\delta = 0$ (solid) and 3% (dash).

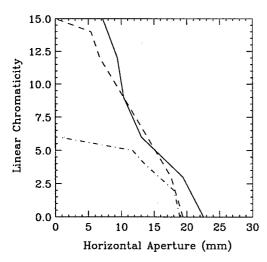


Figure 3: Horizontal dynamic aperture versus linear chromaticity for $\delta = 0$ (solid), 1% (dash) and 3% (dot-dash).

occur. To verify the effect of large β modulation the quad field errors in two matching quad families were increased to generate $\Delta\beta_x/\beta_x \approx \pm 30\%$ and $\Delta\beta_y/\beta_y \approx \pm 20\%$. The observed aperture reduction was about 15%. Though this aperture is still adequate to operate the machine, such large errors have to be resolved in practice.

The effect of large orbit distortions was studied by including an additional set of uncorrected rms alignment errors. For rms orbit distortions of Δx =3 mm, Δy =1.5 mm a maximum of 2 mm reduction of dynamic aperture was observed for the particles within $\delta < \pm 3\%$.

Similarly, large sextupole misalignments were studied while the orbit was well corrected. In simulation, 1 mm rms sextupole misalignments were included which are equivalent to about 10 times the focusing errors from ring quadrupoles. Of the 6 seeds studied, 5 cases showed >17 mm horizontal dynamic aperture for δ =0 particles. The vertical aperture was larger than the \pm 6 mm ID chamber size. At δ =3%, the horizontal aperture remained >13 mm.

The actual physical aperture can be a limiting factor for a beam lifetime. In the vertical plane, SPEAR has two ID's with $y=\pm 6$ mm vacuum chamber. In case of strong coupling, the large off-momentum horizontal motion can be transferred into vertical amplitude which could increase beam loss at the vertical physical aperture. To study this effect, we monitored the maximum vertical excursion at an ID location as a function of initial horizontal amplitude. Fig. 4 shows the peak y-orbit averaged over 6 random sets of machine errors with $\delta=0-3\%$ energy oscillations. At 10 mm injection oscillations, the induced vertical amplitude is below 2 mm and should not limit the beam lifetime.

In addition to chromatic effects, sextupoles generate geometric aberrations such as amplitude dependent tune shift and high order resonances. Clearly, the dynamic aperture would reach its maximum if the geometric aberrations were zero. One way to verify this limit is to track particles with fixed δ =0 and without sextupoles. The simulation showed that on-momentum aperture could be 40% larger without sextupole aberrations.

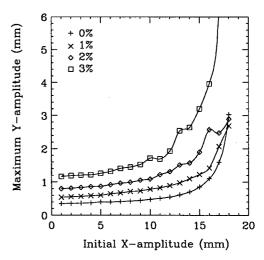


Figure 4: Peak vertical excursion vs initial horizontal amplitude for $\delta = 0, 1, 2, 3\%$.

The geometric effects can be reduced by using 'harmonic' sextupoles placed in non-dispersive regions. Based on analysis in [5] we tested a scheme of two harmonic sextupole families placed in the arc cells. The sextupole strengths were scanned to maximize dynamic aperture. The harmonic correction reduced the amplitude dependent tune shift by about 40% and the error free dynamic aperture improved by 10-15%. With machine errors, however, the improvement reduces to a minimum. Currently, the harmonic correction is not included in the design.

The fields in insertion devices further reduce the dynamic aperture. The detailed report of wiggler effects in SPEAR 3 is presented in [6]. In summary, the first order wiggler focusing will be locally compensated using cell quadrupoles on either side of a wiggler. Simulations showed that with corrected wigglers, included systematic multipole errors and intrinsic wiggler fields up to dodecapole, the dynamic aperture reduces to about 18 mm and 8-9 mm in x and y planes, respectively.

5 CONCLUSIONS

Tracking studies combined with optimization of SPEAR 3 lattice show sufficient dynamic aperture for 10 mm injection oscillations and >100 hrs of Touschek lifetime. The dynamic aperture results have also been confirmed by M. Borland with the tracking code ELEGANT.

- R. Hettel, S. Brennan, Synchrotron Radiation News, 11, No. 1 (1998).
- [2] SPEAR 3 Conceptual Design Report, in press.
- [3] Y. Cai, et al., SLAC-PUB-7642 (1997).
- [4] J. Corbett *et al.*, "Multipole Spilldown in the SPEAR 3 Dipole Magnets", these proceedings (1999).
- [5] E. A. Crosbie, Proceedings of the 1987 IEEE Part. Acc. Conf., Washington, DC, p. 443 (1987).
- [6] J. Corbett, Y. Nosochkov, "Effect of Insertion Devices in SPEAR-3", these proceedings (1999).

SSRL RF SYSTEM UPGRADE*

Sanghyun Park
Stanford Linear Accelerator Center, P.O. Box 4349, Stanford, California 94309, USA

Abstract

The Stanford Synchrotron Radiation Laboratory started its operation as a parasitic light source in 1973, becoming a fully dedicated user facility in 1992. A project was approved in 1998 to upgrade the storage ring to a third generation source. In order to sustain higher current in a tightly reconfigured magnetic lattice, it became necessary to upgrade the RF system from the present 5-cell cavity to four units of single-cell cavities to be powered by one high-power or two low-power klystrons. We present an overview of the upgrade project to be completed by the year 2002.

1 INTRODUCTION

The SPEAR (Stanford Positron Electron Asymmetric Ring) was originally built for high energy physics studies in early seventies, the two-mile linac being an injector. In 1990 a dedicated injector consisting of a RF electron gun, three sections of travelling wave linac, and a booster synchrotron was completed.

About two years later, SPEAR became fully dedicated synchrotron radiation (SR) facility. For a stored current of 100 mA at 3.0 GeV, one RF system was powered up to about 180 kW of RF power for 1.6 MV of gap voltage at the 26 M Ω (=V $_g^2/P_{rf}$) rated 5-cell cavity and 80 kW of beam power. There is also a twin system in a standby mode. The two systems are fully independent of, and equivalent to, each other.

The SSRL Booster synchrotron [1] accelerates a bunch of 10¹⁰ electrons from 100 MeV to 2.3 GeV at the rate of 10 bunches per second. The injection energy is presently limited by the White circuit. When the stored beam current reaches 100 mA, the beam energy is ramped to 3 GeV for user run. The injection energy will be raised to 3.0 GeV (at-energy). The RF system modification needed for this change turns out to be minor.

At the SPEAR, the major upgrade is in magnetic lattice from the FODO to a double bend achromatic (DBA) configuration in order to improve the beam emittance from 160 to 16 nm-rad. This entails bending radius reduction from 12.47 to 7.858 m, thus increasing

* This work was supported by the U.S. Department of Energy under contract number DE-AC03-76SF00515.

the SR power by 63%[2]. This additional loss must be compensated for by higher RF power. The contribution from the insertion devices remains the same since the beam energy stays unchanged at 3.0 GeV. This insertion device term increases slowly over time when new wigglers and undulators are added on. Therefore, the RF power capability must not be a limiting factor for some years to come in the overall light source operation.

2 RF SYSTEM DESIGN CRITERIA

The SPEAR has 11 beamlines including the latest one undergoing a commissioning process. In order to preserve the configurational integrity of those beamlines, or to minimize the changes in the source points, the storage ring circumference must be essentially fixed. This puts a constraint in RF frequency choice. One obvious option is to keep the present frequency of 358.54 MHz, but there is no existing single-cell cavity design at that frequency. Any cavity at wrong frequency must be scaled. In this case, it is beneficial to follow the ones with the minimal frequency deviation from the SPEAR so that the extent of modification is rather minor, and the risk of introducing some unexpected higher-order modes (HOM) is reduced. For this reason the APS-type cavities operating at 352 MHz were extensively studied for their possible adaptation to the upgraded SPEAR RF system.

At the APS cavity[3] HOM's are picked up by the E-and H-type coaxial probes, go through a high-pass filter to contain the fundamental mode (FM), and get dissipated at the matched loads. Those probe-filter-load assemblies are to be added on as the stored beam current is raised and the HOM power is thus increased. This scheme of the HOM damping is yet to be perfected for reliable operation and effective out-coupling of HOM's.

The second candidate considered was the KEK Photon Factory (PF) type cavities[4]. They have nose cones for higher shunt impedance, and larger size beam pipes for the HOM's to spill out, then damped by two silicon carbide loads. These loads are circular cylindrical pipes inside the beam pipe, at some distance upstream and downstream of the cavity so that the FM power level there is sufficiently low. This way, the shunt impedance of the FM is preserved. From the SPEAR point of view, however, the longitudinal length of the cavity is too long to fit into a long straight section of the ring. Another

point of concern was that the HOM damping at the beam pipe may have to be supplemented by the APS-type dampers as the stored beam current reaches the design maximum.

Finally a decision is about to be made to use the PEP-II single-cell cavities[5] without frequency scaling or other modification. The PEP-II cavity has three waveguide loads for HOM damping. The PEP-II low energy ring (LER) stores up to 2.25 A of positrons at 3.1 GeV, while SPEAR 3 will have 500 mA electron beam at 3.0 GeV. For SPEAR the cavity is over-built by a large margin, but it provides ample room for the future growth. The following sections will describe how these cavities will be installed and operated.

3 RF SYSTEM PARAMETERS

The table below shows the comparison between the present (SPEAR2) and upgraded (SPEAR3) RF systems and the beam parameters.

Table 1. Changes in beam and RF parameters

Parameter	Unit	SPEAR2	SPEAR3
Beam Energy	GeV	3.0	3.0
Beam Current	mA	100	500
Bend Radius	m	12.47	7.858
SR Power	kW	57.5	473
Power from ID*	kW	15.4	75.0
Energy loss/turn*	MeV	0.73	1.12
RF frequency	MHz	358.54	476.35
Harmonic number		280	372
RF voltage	MV	1.6	3.2
Cavity type		5-cell	single-cell
Number of cavities		1	4
Shunt impedance	$M\Omega$	26	31
Cavity wall loss	kW	100	330
Beam power	kW	73	570

^{*}With insertion devices as of 1999

Presently one 400kW-rated klystron powers the cavity at less than half the rated maximum. In SPEAR3 the RF power is close to 1 MW, which can be generated by two units of 500 kW klystrons or by one 1.2 MW klystron. For the low power klystrons existing power supplies can be used, whereas the high power tube needs 95 kV power supply for a 2 MW of DC power.

RF Power Balance

The PEP-II cavities were designed to dissipate up to 120 kW of wall power. At 7.8 M Ω the maximum gap voltage per cavity is 0.96 MV per cavity. The operational limit was set at 330 kW for 3.2 MV over the four cavities in order to prevent multipactoring at the cavity. As

shown in the Table 1 above, the total RF power needed is about 900 kW for 500 mA stored current.

The reflected power from the cavity can be minimized at the maximum current by optimizing the coupling factor. Doing so, however, will change the RF characteristics of the cavity assembly that includes waveguide network. Since the reflected power will be only less than 1%, the coupling factor of 3.6 will be left unchanged. Taking the losses at waveguide and reflected power into account, the system still has some operational margin left for RF phase and amplitude control even with a 1.0 MW power source.

Unlike colliders, all the light sources have insertion devices (ID's) that grow in number and intensity over the years. The SPEAR has 18 straight sections available for ID installation: 16 are short (4.5 m), 2 are long (6.5 m). Presently there are seven sections occupied by ID's of 2 meter length each. Their rms magnetic field strength is 1.5 T on average. Let the klystron output power be P_k in kW and αP_k be delivered to the cavities of total shunt impedance R_s in M Ω . For total RF voltage V_g in MV, the cavity wall loss in kW is $1000V_g^2/R_s$. When the remaining power drives a beam of E GeV through insertion devices of total length L meters with magnetic field of B Tesla, the maximum current at SPEAR3 is

$$I(A) = (\alpha P_k - 1000V_g^2/R_s)/(11.26E^4 + 0.633E^2B^2L)$$

For the beam energies of 3.0 to 3.6 GeV, and for the ID lengths of 12 to 36 meters, the maximum current possible is show on the Fig.1 below.

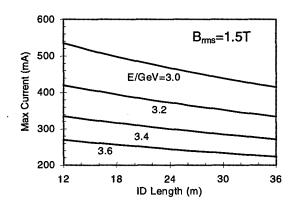


Fig 1 The maximum current possible in SPEAR 3 as a function of total insertion device length, with 4 cavities driven by 1.0 MW RF power for higher beam energies.

With 2 units of 500 kW klystrons, it is still possible to sustain 500 mA current, but the maximum power capability will be reached within a few years as new ID's are added to the existing ones. After this point is

reached, either the current is reduced, or the RF voltage must be lowered at the expense of the beam lifetime.

System Configuration

The high power systems of klystron, circulator, waveguide, magic-T's, and cavities are configured as shown in Fig. 2 below.

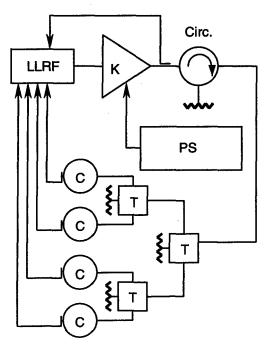


Fig. 2. Block diagram of the SPEAR3 RF system showing the low-level RF (LLRF), klystron (K), power supply (PS), circulator (Circ.), magic-T (T) with high-power matched loads, and cavities (C) with RF probes.

One loop across the klystron is to compensate for the RF phase ripple caused by the power supply. The probes at each cavity are for feedback control of RF phase across the cavity through the movable tuners. The intercavity power balance and phasing are realized by matching the waveguide network. They are not in the control loop. When the RF phase between the nearest cavities is $2(n\pm0.25)\pi$, any reflected power from the two cavities are dissipated at the magic-T load upstream of them. If the relative phase deviates from this value, some portion of the reflection reaches at the circulator load. The LLRF also contains master oscillator and control circuitry for gap voltage, RF phase angle as well as RF parameter displays and interlocks. The basic setup of the LLRF will be modeled after the PEP-II. The effect of a small difference in RF frequency is negligible both in LLRF and in high power systems.

Timing

Since the Booster frequency will remain unchanged at 358.54 MHz, the SPEAR and Booster must share a common base frequency of 476.3361/93=5.121894MHz

which is multiplied by 70 for 358.5325MHz of Booster frequency through phase-locked loops. This is to preserve the injection efficiency.

Cooling System

As the 5-cell cavities are replaced by single-cell ones and four water loads are added at the circulator and magic-T's, the cooling water demand is increased beyond the existing facility can supply. Four single-cell cavities will take 320 GPM of water with temperature regulation of better than ± 0.1 °C for the beam stability. The water loads are not precision tuned in frequency so that there is no need for temperature regulation, but the flow must be sufficient for high power. Some additive such as ethylene glycol is to be added to the circulating water for better absorption of the RF power. Klystron cooling requirement remains the same as in the SPEAR2 system. A stand-alone cooling tower will provide chilled water to cool the cavity water and load water through two separate heat exchangers. The supply temperature is to be regulated by using a 3-way valve where the return water from the cavities is mixed with chilled water from the heat exchanger. The mixing ratio is feedback controlled by a PID type controller.

4 PLAN FOR THE FUTURE

The RF system installation depends on available straight sections, which are influenced by existing and proposed beamline locations and magnetic lattice. From the RF point of view it is best to install all four cavities in one location side by side. The West pit, where the old MARK II detector was, is the prime candidate. Then comes a question of radiation shielding and size of the tunnel, and space available next to the cavity location for klystron and power supply, as well as the water system. All these issues will be addressed before the end of 1999. Then detailed engineering design will be made as to how all these high power systems will be installed and integrated.

Thus far there doesn't appear to be any problems of excessive difficulties associated with the proposed RF system. To insure the system reliability for the benefit of users, sufficient number of spares will be acquired for all the subsystems. By employing the system that is basically identical to the PEP-2, which is on the same site, it is possible to share the spare systems.

- [1] H. Wiedemann, et al., PAC91 Proc.
- [2] R. Hettel, et al., These proceedings
- [3] G. Decker, et al., PAC97 Proc.
- [4] M. Izawa, et al., PAC97 Proc.
- [5] R.A.Rimmer, et al., PAC95 Proc.

DEVELOPMENT OF A SOURCE OF FEMTOSECOND X-RAY PULSES BASED ON THE ELECTRON STORAGE RING*

A. Zholents[†], J. Byrd, S. Chattopadhyay, H. Chong, T.E. Glover, P. Heimann, R. Schoenlein, C. Shank, M. Zolotorev, LBNL, Berkeley, CA 94720

1 INTRODUCTION

The dynamic properties of materials are governed by atomic motion which occur on the fundamental time scale of a vibrational period ~ 100 fs. This is the time scale of interest for ultrafast chemical reactions, non-equilibrium phase transitions, vibrational energy transfer, surface desorption and reconstruction, and coherent phonon dynamics. To date, our understanding of these processes has been limited by lack of appropriate tools for probing atomic structure on an ultrafast time scale. The time resolution of high-brightness 3-rd generation synchrotron light sources is more than two orders of magnitude too slow for these studies. However, the desired x-ray pulses may be achieved by selecting radiation which originates from a thin ~ 100 fs temporal slice of an electron bunch.

2 LASER / E-BEAM INTERACTION

A \sim 100 fs temporal slice of an electron bunch can be created through the interaction of a femtosecond laser pulse co-propagating with an electron bunch in a wiggler magnet [1]. The high electric field present in the femtosecond laser pulse produces an energy modulation in the electrons as they traverse the wiggler (some electrons are accelerated and some are decelerated depending on the optical phase ϕ). The optimal interaction occurs when the laser wavelength λ_L satisfies the resonance condition $\lambda_L \simeq$ $\lambda_W(1+a_W^2/2)/2\gamma^2$ where γ is the Lorentz factor, a_W is the deflection parameter, and λ_W is the wiggler period. In addition, the far field laser radiation must overlap with the far field spontaneous radiation from the electron passing through the wiggler, and the laser spectral bandwidth (number of optical cycles per pulse, M_L) must match the spectrum of the fundamental wiggler radiation (determined by the number of wiggler periods M_W). Under these conditions, the energy absorbed by the electron from the laser field (or transferred to the laser field) is calculated by considering the energy of the superposition of the fields of laser radiation and the spontaneous electron wiggler radiation in the far field region [1]:

$$(\Delta E)^2 = 4\pi\alpha\hbar\omega_L \frac{a_W^2/2}{1 + a_W^2/2} \frac{M_W}{M_L} A_L \cos^2\phi,$$
 (1)

where \hbar is the Planck's constant, α is the fine structure constant, A_L is the laser pulse energy, $\omega_L = 2\pi c/\lambda_L$, and c is the speed of light. We estimate that a 35 fs laser

pulse with a photon energy $\hbar\omega_L$ =1.55 eV, and pulse energy $A_L=100\mu\mathrm{J}$ will produce an energy modulation $\Delta E\simeq 10$ MeV, using a wiggler with M_W =19, λ_W =16 cm, and $a_W\simeq 13$ at electron beam energy of 1.5 GeV.

Only electrons which temporally overlap with the laser pulse experience this modulation. The laser-induced energy modulation is several times larger than the rms beam energy spread in the typical 1.5 GeV electron storage ring. The accelerated and decelerated electrons are then spatially separated from the rest of the electron in the bend magnets of the storage ring by a transverse distance that is several times larger than the rms transverse size of the electron beam. Finally, by imaging the displaced beam slice to the experimental area, and by placing an aperture radially offset from the focus of the beam core, we will be able to separate out the radiation from the offset electrons. Figure 1 schematically shows all three phases of preparing the femtosecond x-ray pulses.

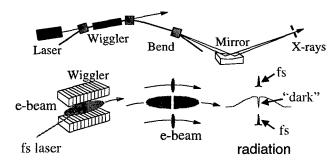


Figure 1: A schematic of generation of the femtosecond pulses of synchrotron radiation.

Since the spatially offset electrons result from interaction with the laser pulse, the duration of the synchrotron radiation produced by these electrons will be approximately the same as the duration of the laser pulse, and will be absolutely synchronized. Furthermore, the extraction of an ultrashort slice of electrons leaves behind an ultrashort hole or dark pulse in the core of the electron bunch. This time structure will be reflected in the generated x-rays by beam core electrons, and can also be used for time-resolved spectroscopy.

The average flux of the femtosecond radiation is defined by three factors: $\eta_1 = \tau_L/\tau_b$, $\eta_2 = f_L/f_b$, and $\eta_3 \simeq 0.2$, where τ_L and τ_b are the laser pulse and electron bunch durations, f_L and f_b are the laser and electron bunch repetition rates, and η_3 accounts for the fraction of electrons that are in the proper phase of the laser pulse to get the maximum energy exchange suitable for creating the large transverse separation. Taking τ_L =35 fs, f_L =10 kHz and using

^{*} Work supported by DoE under contract No DE-AC03-76SF00098.

[†] Email: AAZholents@lbl.gov

typical ALS electron beam parameters τ_b =30 ps, f_b =500 MHz, we estimate a femtosecond x-ray flux of $3x10^5$ photons/sec/0.1 % BW at 2 keV ($5x10^4$ photons/sec/0.1 % BW at 10 keV) from a bend-magnet beamline at the ALS with a 3 mrad \times 0.4 mrad collection optic.

Synchrotron radiation damping provides for recovery of the electron beam between interactions. Since the laser interacts sequentially with each bunch, the interaction time is given by n/f_L , where n is number of bunches in the storage ring. Furthermore, the bunch slice is only a small fraction of the total bunch. Thus, the storage ring damping time is more than sufficient to allow recovery of the electron beam between laser interactions (even for laser repetition rates as high as 100 kHz).

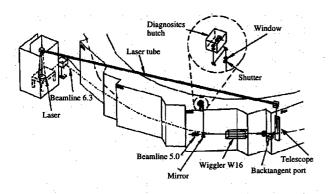


Figure 2: The layout of the experiment.

A proof of principle experiment for the technique described above has been conducted at the ALS storage ring at LBNL. A schematic of the experimental set up is shown in Figure 3. A femtosecond Ti:Sapphire laser synchronized to the storage ring is located near beamline 6.3.2, and the laser beam is projected across the storage ring roof blocks to sector 5, where it enters the main vacuum chamber through a back-tangent optical port. Amplified femtosecond laser pulses co-propagate with the electron beam through wiggler W16 in sector 5. A mirror following the wiggler reflects the laser light and the visible wiggler emission out of the vacuum chamber for diagnostic purposes. Images of the near field and far field wiggler radiation are observed on a CCD camera, and the near and far field modes of the laser propagating through the wiggler are matched using a remotely adjustable telescope at the back tangent port. The spectrum of the laser is also matched to the fundamental wiggler emission spectrum. The efficiency of the laser/e-beam interaction is tested by measuring the gain in the intensity experienced by the laser beam passing with the electron beam through the wiggler [2]. This gain is a direct indication of the magnitude of the energy exchange between the laser and the electrons. Femtosecond duration synchrotron pulses are directly measured by cross-correlating the visible light from bend-magnet beamline 6.3.2 with the synchronized laser pulses. Figure 3a shows a laser pulse and a synchrotron radiation pulse crosscorrelation measurement on a 100 ps time scale. The measured synchrotron pulse duration, σ =16 ps, corresponds to the overall electron bunch duration. Measurement with ~100 times higher time resolution (Figure 3b) shows the femtosecond "dark" pulse (σ =112 fs) which appears as a narrow $\sim 25\%$ deep hole in the main pulse, and originates from the central core of the sliced electron bunch. Both, the width and the height of the hole appear to be close to the expected values. The pulse duration is mainly defined by a spread of the pathlengths of the electron trajectories between the wiggler and the 6.3.2 bend-magnet. Figure 3c shows a measurement of the femtosecond pulse (σ =161 fs) originating from the spatial wings of the sliced electron bunch. Note that the femtosecond time structure is invariant over the entire spectral range of bend-magnet emission from the near infrared to the x-ray regime. An important point is that in the far infrared region ($\lambda = 100 - 300 \mu m$) the narrow hole in the electron bunch radiates coherently such that the intensity of the radiation is proportional to the square of the number of missing electrons in the hole. We estimate that this radiation carries ~1 nJ per pulse.

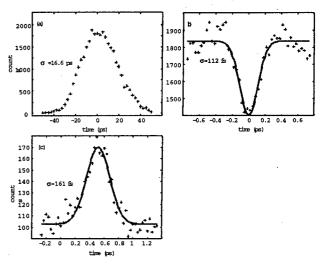


Figure 3: The measured synchrotron radiation pulses duration. See text for explanation.

3 RF ORBIT DEFLECTION

Another way to create femtosecond slices of electrons is to use the RF orbit deflection [3]. This technique implies that the femtosecond slices of the electron bunch are made by creating a correlation between the longitudinal coordinates of the electrons within the electron bunch and their vertical angles. This correlation can be initiated by the first dipole mode E_{110} of an RF cavity accelerating structure.

While passing the accelerating structure, electrons are deflected by the RF magnetic field an amount equal to:

$$y'(z) = \theta_0 \sin(kz), \quad \theta_0 = \frac{eU}{E_b},$$
 (2)

where z is the electron longitudinal coordinate relative to

the bunch center, E_b is the beam energy, e is the electron charge and eU is the energy gain in the accelerating structure calculated at the coordinates with the maximum electric field. It is assumed that the RF phase is chosen in a such way that $\psi=0$ when the bunch center is at the center of the cavity.

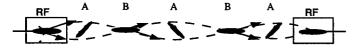


Figure 4: A schematic of the beam coupling produced by the RF cavities operated at E_{110} mode.

This deflection couples the longitudinal and transverse motion of the electrons. In order to confine this coupling in a section of a storage ring, a second accelerating structure is placed an integer number of betatron wavelengths downstream of the first accelerating structure.

Figure 4 schematically shows two accelerating structures, trajectories of the head and tail parts of the electron bunch and side views of the bunch profile in several locations as it propagates from left to right. There are two types of locations along the orbit, which are convenient source points of synchrotron radiation for our purpose. At the A locations, the coordinate displacements of the electrons have reached their maxima:

$$\delta y(z) = \theta_0 \sqrt{\beta_{rf}\beta} \sin(kz), \qquad (3)$$

where β_{rf} is the vertical beta function at the RF cavity and β is the vertical beta function in the A locations. Instead, at the B locations, the variation in angle of the electron trajectories has its maximum value:

$$\delta y'(z) = \theta_0 \sqrt{\frac{\beta_{rf}}{\beta}} \sin(kz),$$
 (4)

where β is taken now in the B locations.

For zero beam emittance we can say that the radiation of each femtosecond slice is separated from the radiation of the neighboring slices if the difference in angle or coordinate between the neighboring slices is larger than the opening angle of the radiation, $\sigma_{r\prime}$, in the case of the angular separation or the diffraction-limited size of the radiation, $\sigma_r = \lambda/4\pi\sigma_{r\prime}$, in the case of coordinate separation.

For a non-zero beam emittance we need to account for the broadening of the radiation field due to the coordinate and angular spread of electrons and consider $(\sigma_y^2 + \sigma_r^2)^{1/2}$ and $(\sigma_y^2 + \sigma_{ri}^2)^{1/2}$ instead of σ_r and σ_{ri} , where σ_y and σ_y , are the vertical electron beam size and divergence at the source position. This broadening is much less in the vertical direction because vertical beam emittance in the storage ring is much smaller than the horizontal emittance.

Defining the length of the femtosecond slice as σ_s and the bunch length as σ_z , we can write a magnitude $\delta y (\sigma_z)$ in the A locations and a magnitude $\delta y' (\sigma_z)$ in the B locations

needed for a spatial separation of the radiation of $M = \sigma_z/\sigma_s$ femtosecond slices:

$$\delta y(\sigma_z) \ge M(\sigma_y^2 + \sigma_r^2)^{1/2}$$

$$\delta y'(\sigma_z) \ge M(\sigma_{y'}^2 + \sigma_{r'}^2)^{1/2}.$$
(5)

One also needs to check that the vertical beam tilt is larger than the opening angle of the radiation, i.e. that $\arctan \left[\delta y\left(\sigma_z\right)/\sigma_s\right] > \left(\sigma_{y\prime}^2 + \sigma_{r\prime}^2\right)^{1/2}$. Usually this condition is easily satisfied.

Using Eqs.(3,4) in the left hand side of Eqs. (5), and assuming $k\sigma_z \leq 1$, we find the energy gain eU required for the creation of M femtosecond slices:

$$\frac{eU}{E_b} \geq \frac{M}{k\sigma_x} \sigma_{y'}^{rf} \sqrt{1 + \left(\frac{\sigma_r}{\sigma_y}\right)^2}
\frac{eU}{E_b} \geq \frac{M}{k\sigma_x} \sigma_{y'}^{rf} \sqrt{1 + \left(\frac{\sigma_{r'}}{\sigma_{y'}}\right)^2},$$
(6)

where $\sigma_{y'}^{rf} = \sqrt{\epsilon_y/\beta_{rf}}$ is the vertical angular beam size in the location of the RF cavity, and ϵ_y is the vertical beam emittance.

Compression of the radiation of all beam slices into a single x-ray pulse of the order of ~ 150 fs may be performed in the x-ray beamline. Asymmetrically-cut crystals may be used as optical elements for x-ray pulse compression [4]. Because of the different incident and diffractive angles, they produce a variable path length across the x-ray beam. Alternatively, one can use the angle-time or coordinate-time correlation of the radiation for simultaneous observation of different time delays on a position sensitive detector.

The disadvantage of the RF orbit deflection technique is a requirement of a ≤ 100 fs jitter in a synchronization of the laser to the electron beam in a storage ring. It is factor of four better than the best obtained results [5]. The advantage of this technique is that the femtosecond x-ray pulses are generated by every electron bunch and on every orbit turn and all electrons contribute to the radiation. Therefore, the resulting flux of the x-rays is many orders of magnitude higher than in the first technique ($\sim 10^{14}$ photons/sec/0.1% BW at 5 keV for undulator radiation). However, the real flux that currently can be utilize in practice in a pump-probe measurement is approximately three orders of magnitude less because of the repetition frequency and pulse energy limitations of present femtosecond lasers.

Acknowledgement. The authors wish to aknowledge the technical support of the LBNL laser safety oficer K. Barat and the staff of the ALS in setting-up this experiment.

- [1] A. Zholents and M. Zolotorev, PRL v.76, (1996)912.
- [2] M. Zolotorev, et. al. in Proc. of this Conf., reprot WEP102.
- [3] A. Zholents, et. al., LBNL-42045, to be published in NIM.
- [4] T. Matsushita and H. Hashizume, Handbook of Synchrotron Radiation v.1, ed. E.E. Koch, p.261, Amsterdam (1993).
- [5] G.M.H. Knippels, et.al., abstract at 20th FEL Conf., 1998.

SLOW ORBIT FEEDBACK AT THE ALS USING MATLAB

G. Portmann*, Lawrence Berkeley National Laboratory, Berkeley, CA 94720 USA

Abstract

The third generation Advanced Light Source (ALS) produces extremely bright and finely focused photon beams using undulators, wigglers, and bend magnets. In order to position the photon beams accurately, a slow global orbit feedback system has been developed. The dominant causes of orbit motion at the ALS are temperature variation and insertion device motion. This type of motion can be removed using slow global orbit feedback with a data rate of a few Hertz. The remaining orbit motion in the ALS is only 1-3 micron rms. Slow orbit feedback does not require high computational throughput. At the ALS, the global orbit feedback algorithm, based on the singular valued decomposition method, is coded in MATLAB* and runs on a control room workstation. Using the MATLAB® environment to develop, test, and run the storage ring control algorithms has proven to be a fast and efficient way to operate the ALS.

1 INTRODUCTION

Maintaining the proper electron beam orbit is an important operational issue for all light sources. The most commonly used figure-of-merit for orbit stability is that the beam should be stable to one-tenth of the beam size. That is, the optics for most light source experiments can tolerate a ten percent fluctuation in the beam before it adversely affects the experiment. Shown in Table 1, this implies a very tight tolerance for orbit motion at the ALS (table calculated assuming 1.8% coupling), [1].

Table 1: Beam stability requirements

Beam Location	Horizontal	Vertical
Straight Section	24.6 μm	2.0 µm
Bend Magnet #1	5.3 μm	4.4 μm
Bend Magnet #2	10.3 μm	1.2 μm

In reality, obtaining this tight a control over the obit over all frequency ranges is extremely difficult. Local and global orbit feedback algorithms can potentially regulate the beam position to accuracy of the position monitor (BPM) system, however, building a BPM system which is accurate to the micron level is quite difficult. Many third generation light sources have BPM

systems capable of sub-micron level accuracy over relatively short time intervals. At the ALS, the electron beam can be accurately measured to .6 μ m horizontally and .8 μ m vertically over a .1-300 Hertz frequency range. The problem for measuring beam motion at the ALS is over longer time intervals. The two major sources of error are current dependence of the BPM electronics and physical motion of the vacuum chamber. Harmonic correction algorithms can mitigate these problems, but it is very difficult to maintain micron level orbit stability over long time periods. Due to these problems, we have taken a very conservative approach to adding orbit feedback to the ALS storage ring.

In addition to the original 96 BPMs in the ALS storage ring, a pair of very accurate BPMs have been installed in each insertion device straight section (20 BPMs in total), [2]. By rigidly mounting these BPMs to each insertion device structure that is installed in a temperature controlled housing, the positional stable of the BPM is very good. The relative motion between the BPM and storage ring floor is a few microns per week, [3]. With the addition of these new monitors, global orbit feedback in the horizontal plane has been added to the standard operation of the ALS.

High-level magnet control and conditioning of the ALS storage ring is done using a commercial software package from the Mathworks Inc. call MATLAB*, [4]. MATLAB* is an excellent language for algorithmic prototyping. The global orbit feedback algorithm was designed and implemented in MATLAB*. Although MATLAB* is far from a real-time programming language it has proven to be an efficient and stable software product for running global orbit feedback.

2 ORBIT MOTION AT THE ALS

For a light source, electron beam stability is important over a huge frequency range—days to hundreds of megahertz. This paper focuses on slow orbit motion. Slow orbit motion will be subdivided into really slow motion, less than .1 Hertz (drift), and faster motion, .1-300 Hertz. Table 2 is a relatively conservative listing of the observed orbit stability at the ALS without feedback. (0-300 Hertz is the bandwidth of the BPM system.)

2.1 Slow Orbit Drift

The dominant source of orbit motion in the ALS is slow drift due to temperature variations. There are three basic causes of thermal variations: 1) change in ambient air temperature of the storage ring tunnel, 2) change in the low conducting water (LCW) temperature, and 3)

^{&#}x27;This work was supported by the Director, Office of Energy Research, Office of Basic Energy Sciences, Materials Sciences Division, of the U.S. Department of Energy under Contract No. DEAC03-76SF00098.

^{*}Email: gjportmann@lbl.gov

change in the photon beam power as the electron beam decays. The regulation specification is $\pm .2$ and $\pm .1$ degrees Celsius for the air and LCW temperature, respectively. However, temperature regulation to this level is difficult to achieve day-to-day.

Insertion device motion is the next largest source of slow orbit distortion. The ALS experimenters can freely adjust the insertion device gap at any time. Feed forward tables are empirically generated to compensated for this motion. The accuracy of a given table is 5-10 μ m rms.

Figures 1-2 show the electron beam orbit in the insertion device straight sections for a typical day before the orbit feedback system was operational. The horizontal orbit is more sensitive to temperature variation.

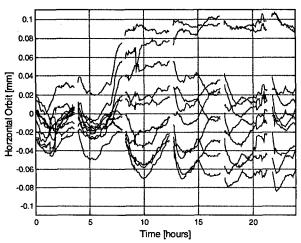


Figure 1: Horizontal orbit stability without feedback, August 15, 1998.

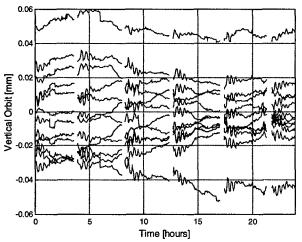


Figure 2: Vertical orbit stability without feedback, August 15, 1998.

2.2 "Fast" Orbit Motion

The dominant cause of "fast" orbit motion, .1-300 Hertz, at the ALS is vibrations. Power supply regulation is a common cause of orbit stability problems in this

frequency range, however, it thankfully has not been an issue at the ALS. Figure 3 shows the power spectrum for of the orbit motion in the horizontal plane from .3-50 Hertz. The rms motion from .1-300 Hertz is typically 3.0 μm horizontally and 1.2 μm vertically. These numbers have not changed very much over the last five years which implies that the ALS can inherently meet its stable goal, Table 1, in this frequency range without orbit feedback.

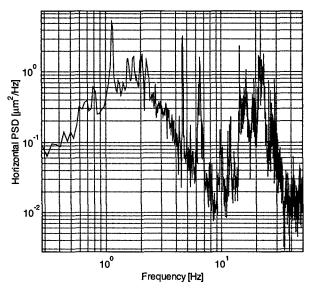


Figure 3: Power spectral density of the horizontal orbit.

Table 2: Beam stability w/o orbit feedback

Frequency	Magnitude	Dominant Cause
	Horizontally	1. Magnet hysteresis
Two weeks	±200 μm	2. Temperature
		fluctuations
(A typical	Vertically	3. Component heating
experimental	±100 μm	between 1.5 GeV and
run)		1.9 GeV
	Horizontally	
1 Day	±125 μm	Temperature
	Vertically	fluctuations
	±75 μm	
	Horizontally	1. Temperature
4 Hour Fill	±50 μm	fluctuations
	Vertically	2. Feed forward errors
	±20 μm	
Minutes	5 to 10 μm	Feed forward errors
.1 to 300 Hz	1 to 3 μm	Ground vibration

3 SLOW GLOBAL ORBIT FEEDBACK

A slow global orbit feedback system in the horizontal plane has been in operation at the ALS since September 1998. Before that time, orbit correction was only done at the beginning of an experiment run. Besides the feed forward correction to compensate for insertion device motion, the storage ring magnet control would be static for the length of the run—typically two weeks. As shown in Table 2, the ALS is surprisingly quite stable

without orbit correction. However, in order to meet the tolerances in Table 1 a slow global orbit feedback system needed to be developed.

3.1 The Global Feedback Algorithm

The following example is the entire horizontal global orbit correction routine for the ALS using a singular valued decomposition (SVD) method. The present algorithm uses 18 BPMs, 12 corrector magnets, and the first 10 singular values of the response matrix, Sx.

X = getx; [U, S, V] = svd(Sx); DeltaAmps = - X / U(:,1:10);stepsp('HCM', DeltaAmps);

Once the ALS database access functions getx (get the horizontal orbit) and stepsp (step the corrector magnet setpoint) have been written, this relatively involved global orbit correction method can be accomplished in four lines: 1) get the horizontal orbit, 2) compute the SVD of the response matrix, 3) find the corrector changes via Gaussian elimination, and 4) apply the correction.

3.2 Results

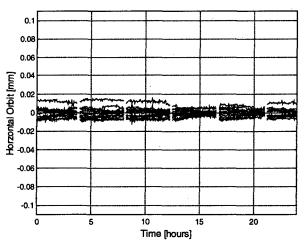


Figure 4: Horizontal orbit stability with feedback on, February 6, 1999.

One could correct the orbit in Figure 4 to the micron level, however the orbit correction algorithm is presently run over-constrained. This is a conservative measure done so that the feedback system does not track vacuum chamber motion so well. More corrector magnets will be used in the future since the measured motion of the vacuum chamber in the insertion device straight sections is small—a few microns, [3].

3.3 An Aside

The word "feedback" is used in a rather cavalier way in this paper. The transient response of the beam position

to a corrector magnet change is only a fraction of a second (the aluminium vacuum chamber is quite thin at the location of the straight section corrector magnets). If the data rate of the "feedback" loop is 10 seconds, then it is essentially an open loop system. In fact, only the open loop system dynamics are important. A more appropriate word for this type of orbit correction would be a retry system.

4 ACCELERATOR CONTROL USING MATLAB

MATLAB* is a high-level matrix manipulation language originally developed to be an efficient programming environment for using the LINPACK and EISPACK libraries in the heyday of FORTRAN. MATLAB* is convenient software package to control particle accelerators for a number of reasons.

- Matrix algebra is coded very similar to how it is written on paper.
- MATLAB[®] supports a huge number of subroutines.
- An active workspace eases debug and development of algorithms. This is particularly important during accelerator physics studies when machine time is very expensive.
- Excellent graphics.
- Ease of importing and exporting data.
- Basic graphical users interface capabilities.
- Interfaces to C and Fortran subroutines. Hence, connecting MATLAB* to the ALS database and EPICs was relatively easy.
- Platform independence.

MATLAB* is an interpreted language, hence the computational speed does not compare favourably to a compiled language. However, the fact that MATLAB*'s built-in functions are compiled greatly mitigates the speed disadvantage of using an interpreted language. When controlling magnet power supplies, the slow link in the system is the ramp rate of the supply, not MATLAB*.

5 ACKNOWLEDGMENTS

The authors would like to thank D. Robin, W. Decking, and A. Jackson for their support and encouragement during this study.

- [1] D. Robin, private communications.
- [2] J. Hinkson, private communications.
- [3] G. Krebs, "Measurement of Storage Ring Motion at the ALS," PAC 1997.
- [4] G. Portmann, "ALS Storage Ring Setup and Control Using Matlab®," LSAP Note #248, June 1998."

EXPERIMENTAL STUDIES OF THE NONLINEAR MOMENTUM COMPACTION FACTOR AT BESSY II *

J. Feikes, G. Wüstefeld[†], BESSY GmbH Rudower Chaussee 5, 12489 Berlin, Germany

Abstract

Experimental studies were performed, to measure the nonlinear behavior of the momentum compaction factor α at the BESSY II electron storage ring. Based on these results the momentum acceptance of the storage ring can be derived. Several sets of measurements at different values of the horizontal chromaticity in the range of $\Delta Q_x/(\Delta p/p_0) = \xi_x = -5.5 \ldots + 8.1$ were generated. Depending on tune and horizontal chromaticity particles in the range from $-4\% < \Delta p/p_0 < 8\%$ could be stored.

1 INTRODUCTION

BESSY II is a 1.7 GeV, low emittance, high brilliance synchrotron radiation light source recently started operation at Berlin-Adlershof [1]. The lattice of the storage ring is a 16-cell 'Double Bend Achromat' with alternating high and low β -values and zero dispersion in the straights. The ring circumference is 240 m. The transverse tunes are $Q_x = 17.8$ and $Q_y = 6.7$, the natural chromaticities are $\xi_{nat.,x} = -52.7$ and $\xi_{nat.,y} = -26.8$.

A source of major life time limitations of the stored electron beam are scattering processes, were electrons suffer a sudden energy change, well known as Touschek effect and bremsstrahlung process [2]. To avoid a loss of these scattered particles and to achieve a good beam lifetime, the transverse and longitudinal momentum acceptance of the machine is designed for $\Delta p/p_0 \pm 3\%$. One task of the presented measurements was the determination of the actual machine momentum acceptance.

2 THE MOMENTUM COMPACTION FACTOR α

2.1 Definition of α

The length of the particle orbit together with the magnetic field on this orbit defines the energy of the electrons. The rf-frequency and its harmonic number define the path length of the electrons in the ring. Because of the fast radiation damping, the particle energy will follow a change of the rf-frequency or the magnetic field within few milliseconds. In the experiments discussed here the rf-frequency at fixed magnetic field was detuned to change the electron energy.

To describe changes of the path length for electrons with small momentum deviations it is common, to apply a series expansion of the path length with respect to the momentum deviation [2]. The influence of betatron oscillations on the momentum compaction factor can be ignored here, because their amplitudes are less than 1 mm. It seems that there is not a unique definition of the type of series expansion in literature. For the following discussion two types of definitions for the momentum compaction factor α are required:

$$lpha_p = rac{dL}{dp}/rac{L}{p}$$
 , and $lpha = rac{\Delta L}{\Delta p}/rac{L_0}{p_0}$.

In case of the first definition $\alpha_p = \alpha_p(p)$ is based on small changes of the momentum around some specified momentum value p. It is given by the differential change of the path length L with respect to the momentum. This α_p depends on the local properties of the particle orbit, independent of the reference orbit length L_0 and reference momentum p_0 . In our experiments p could typically differ from the reference value p_0 by a few percent, whereas the 'differential' changes are about a factor ten smaller.

The second, similar definition is based on difference expressions, valid for larger momentum changes of the order of few percent with respect to the reference momentum p_0 . It is normalized with respect to the reference values of momentum p_0 and orbit length L_0 . Both definitions, α_p and α , are functions of the momentum p.

The definitions of α and α_p are not independent of each other, they are connected by a differential equation:

$$\alpha_p = \frac{1 + \Delta p/p_0}{1 + \alpha \Delta p/p_0} \frac{d(\alpha \Delta p/p_0)}{d(\Delta p/p_0)} \ .$$

In the case that p approaches p_0 both definitions yield the same limiting value α_0 :

$$\lim_{p\to p_0}\alpha=\lim_{p\to p_0}\alpha_p=\alpha_0.$$

Based on linear approximations, this value can be calculated:

$$\alpha_0 = rac{1}{L_0} \oint_{\mathrm{ring}} rac{D_x}{
ho} ds,$$

were D_x is the linear dispersion function and ρ the dipole bending radius. For the present storage ring optics we have $\alpha_0 = 7.3 \cdot 10^{-4}$.

^{*}Work supported by the Bundesministerium für Bildung, Wissenschaft, Forschung und Technologie and by the Land Berlin.

[†] Email: wuestefeld@bessy.de, feikes@bii.bessy.de

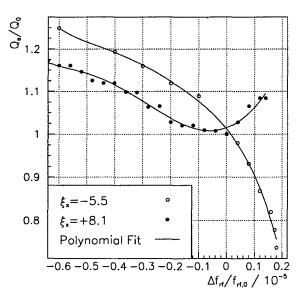


Figure 1: Measured normalized synchrotron tune Q_s as a function of the relative rf-frequency change $(\Delta f_{rf})/f_{rf,0}$ for two different values of the horizontal chromaticity ξ_x . The measured points are fitted by a polynomial (line).

2.2 Reconstruction of α from measurements

From the longitudinal beam dynamics the expression for the longitudinal tune Q_s of the synchrotron oscillation is given by [2]:

$$Q_{s,p}^2 = \frac{h\eta_p e V_{cav} \cos \psi_p}{2\pi\beta_p c p},$$

were h is the harmonic number, V_{cav} the effective peak Voltage of the rf-frequency, ψ is the phase angle of the synchronous particle and βc the velocity of the particle. The index p is used to point out that these values are related to the local properties of the orbit, defined for a given momentum p. Only the local orbit dynamics is involved, because the relative energy spread of the bunches is 'differentially' small, less than 10^{-3} .

The accurate estimate of the effective rf-Voltage seen by the beam is rather difficult. By relating the longitudinal tune to the tune at $p=p_0$ the expression can be simplified and becomes independent of the Voltage:

$$\frac{Q_{s,p}^2}{Q_{s,0}^2} = \frac{\eta_p \cos \psi_p}{\beta_p p} / \frac{\eta_0 \cos \psi_0}{\beta_0 p_0} \; . \label{eq:Qsp}$$

The phase angle ψ defined by the large amplitude of the rf-Voltage and a comparably small energy loss per turn is only some few degrees. The change of this angle with respect to the few percent changes of the momentum considered here is even smaller and will be neglected, we set $\cos \psi_0 = \cos \psi_p$. At typical BESSY II energies a small change of the particle momentum hardly changes the particle velocity. Therefore, the 'frequency slip factor' η_p can be well approximated by $-\alpha_p$ and $\beta_p = \beta_0$. Taking into account these approximations yields the simple result:

$$\frac{Q_{s,p}^2}{Q_{s,0}^2} = \frac{\alpha_p}{\alpha_0} \frac{p_0}{p} \ .$$

The left-hand-side expression involving the synchrotron tunes was measured by varying the rf-frequency, two typical examples of the measurements plotted as $Q_{s,p}/Q_{s,0}$ are shown in Fig.1. It was shown by simulations, that fluctuations of the measured points could be explained by misalignment errors.

Replacing α_p in the equation by its definition and rearranging:

$$lpha_0 rac{dp}{p_0} = rac{dL}{L} rac{Q_{s,0}^2}{Q_{s,0}^2} \,.$$

Integrating both sides yields:

$$\alpha_0 \frac{p - p_0}{p_0} = \int \frac{Q_{s,0}^2}{Q_{s,p}^2} \frac{dL}{L}.$$

The orbit changes can be expressed by appropriate rf-frequency changes $\frac{dL}{L}=-\frac{df_{rf}}{f_{rf}}$, which transforms the integrant into only rf-depended terms:

$$\alpha_0 \frac{\Delta p}{p_0} = -\int \frac{Q_{s,0}^2}{Q_{s,p}^2} \frac{df_{rf}}{f_{rf}} = -\int \frac{Q_{s,0}^2}{Q_{s,p}^2} \frac{dr}{(1+r)} .$$

For the last step f_{rf} was substituted by $(1+r)f_{rf,0}$. The whole integrant can be constructed from the measured data and fitted by a polynomial of the type $a_i(\Delta f_{rf}/f_{rf,0})^i$, similar as shown in Fig.1, were a fit to the original data was applied.

The polynomial can be integrated analytically

$$-\alpha_0 \frac{\Delta p}{p_0} = \frac{\Delta f_{rf}}{f_{rf,0}} + \frac{1}{2} a_2 \left(\frac{\Delta f_{rf}}{f_{rf,0}}\right)^2 + \frac{1}{3} a_3 \left(\frac{\Delta f_{rf}}{f_{rf,0}}\right)^3 + \dots$$

and the relative momentum deviation as a function of the relative rf-detuning is obtained.

The integration smoothes the measured data, at this point results of measured, fitted and simulated data are compared, see Fig.2. Results are shown for two examples with the most detuned chromaticities, at $\xi_x = +8.1$ and $\xi_x = -5.5$. Similar results from data for $\xi_x = +5.6$, +2.2, -1.6 and -5.2 are not presented here. The simulation was done with the beam optical code MAD [3] applying some minor adjustments, such as a 1 % change of α_0 and a small shift of the absolute momentum scale.

The polynomial fit has the advantage, that critical numerical expressions of small numerator and denominator, such as $(\Delta f_{rf}/f_{rf,0})/(\Delta p/p_0)$ can be calculated analytically. A second fit applied to the reverse function $r=r(\Delta p/p_0)$ yields the rf-detuning and the change of the orbit length as a function of the momentum deviation:

$$-\frac{\Delta f_{rf}}{f_{rf,0}} = \frac{\Delta L}{L_0} = \frac{\Delta p}{p_0} \left(\alpha_0 + \alpha_1 \left(\frac{\Delta p}{p_0} \right) + \alpha_2 \left(\frac{\Delta p}{p_0} \right)^2 + \ldots \right).$$

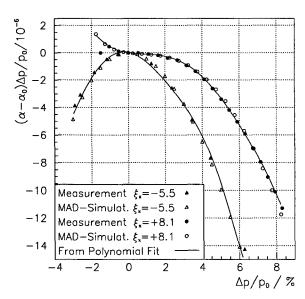


Figure 2: $(\alpha - \alpha_0)\Delta p/p_0$ as as a function of the momentum deviation $\Delta p/p_0$. Two typical results for $\xi_x = +8.1$ and $\xi_x = -5.5$ are shown for measured, fitted and simulated data. For the absolute scaling of the horizontal axis $\alpha_0 = 7.34 \cdot 10^{-4}$ was assumed.

Commonly, the coefficients of this last expansion (or a similar one) are abbreviated by α_i . The first term of this series is by definition $\alpha_0 \frac{\Delta p}{p_0}$. α_0 can not be extracted from these results, the value $\alpha_0 = 7.3 \cdot 10^{-4}$ was used. For α follows the series expansion:

$$\frac{\Delta L}{L_0} / \frac{\Delta p}{p_0} = \alpha = \alpha_0 + \alpha_1 \left(\frac{\Delta p}{p_0}\right) + \alpha_2 \left(\frac{\Delta p}{p_0}\right)^2 + \dots$$

Fig.3 shows α/α_0 as a function of the momentum deviation. For a given momentum value this ratio gives the required correction of the rf-frequency, which is of the order of $\pm 30\%$, due to the influence of higher order terms of the momentum compaction factor.

3 THE MEASUREMENTS

The transverse and longitudinal tunes were measured at beam currents of around 10 mA. The coherent beam signal in all 3 directions was measured using a strip line signal and analyzed with a 'Rohde & Schwarz FSEA' spectrum analyzer. The accuracy of the transverse and longitudinal tune measurements are determined by the line width of the beam tune signal, which was in the order of 0.5 %. The vertical chromaticity was not changed and kept at $\xi_y = 1.6$, only data for different horizontal ξ_x -values were recorded. The rf-frequency was detuned until beam loss. Beam loss by critical transverse resonances was avoided by readjusting the quadrupole settings if required; it was verified, that the longitudinal tune was not influenced by this. For fixed horizontal chromaticity but different values of vertical chromaticity it was confirmed, that the longitudinal tune is not dependent on the vertical chromaticity. Different cavity voltages showed also no influence on the normalized longitudinal tunes.

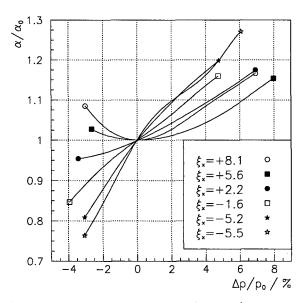


Figure 3: Momentum compaction factor α/α_0 as a function of the momentum deviation $\Delta p/p_0$. Start and end point of each line indicate the range, were stable beam storage is possible. The results of this figure are derived from the polynomial fit.

4 SUMMARY AND CONCLUSION

The momentum compaction factor can be measured to a very high accuracy by applying frequency based methods. If fitted by a polynomial, the results shown in Fig.2. would require a polynomial of 5th order. The value of α_0 was yet not measured, but taken from a simulation code. In case the momentum acceptance is calculated only with this linear term, the estimated rf-frequency change needs a further correction of the order of $\pm 30\%$, depending on the chromaticity. As expected, the momentum compaction factor is very sensitive to the horizontal chromaticity. The measured results could be excellent reproduced with the simulation code MAD. From these measurements the momentum limits for stable beam storage was found to be $-4\% < \Delta p/p_0 < +8\%$.

5 ACKNOWLEDGMENTS

It is a pleasure to thank Georg Hoffstätter from DESY and Nghiem Phi from Soleil for valuable discussion on this subject.

- R. Bakker et al., Status and Commissioning-Results of BESSY II, see these proceedings.
- [2] Helmut Wiedemann, 'Particle Accelerator Physics', part I and II, Springer-Verlag, Berlin, Germany 1993 and 1995.
- [3] H. Grote, F. Ch. Iselin, 'The MAD Program', User's Reference Manual, CERN/SL/90-13 (AP), Geneva, Switzerland, 1994.

ESTABLISHMENT OF A MODEL FOR INTERPRETATION AND CORRECTION TOOLS FOR BESSY II*

R. Bakker, D. Krämer, B. Kuske[†], P. Kuske, R. Müller, BESSY, Berlin, Germany

Abstract

From the very beginning of the commissioning of the Synchrotron Radiation facility BESSY II, work has been facilitated by online interpretation and correction procedures that utilise a commonly accessible online model of the storage ring optics. The software covers all linear properties like beta functions, orbit correction, tune variation etc. Initially the model has been set up from construction and alignment data and magnetic bench measurements. All relevant parameters are retrieved from a central reference database. During commissioning, the model has been adjusted in several steps, feeding back results from orbit response measurements. The achieved agreement is demonstrated.

1 INTRODUCTION

The BESSY II storage ring [1] has been commissioned during the last 9 months of 1998, and is in user-operation since the beginning of 1999. During 9 two-weeks machine development runs the reference optics has been established and the design parameters have been reached or surpassed [2].

The BESSY II control system [3] provides an online model of the storage ring optics, based on the GOEMON optics library [4]. Constant data, like the geometries and the conversion factors (current to magnetic field) which initially where extracted from magnetic bench measurements are taken from the ORACLE database. In combination with the actual currents read back from the power supplies, an online model is set up during the initialization phase of the orbit control software and the optic program and can be continuously updated. The calculated beta functions, tunes, chromaticities etc. can be displayed, and are used in correction algorithms, as e.g., the sensitivity matrices in the orbit correction. The correct translation from the power supply currents into the model was of essential importance for the progress during commissioning. Orbit response measurements (ORM) where used to get a better understanding of the storage ring hardware and improve the model.

2 MODEL EVOLUTION DURING COMMISSIONING

Already during the first run ORM were taken and revealed few hardware bugs, like a systematic polarity twist of all correction coils in the dipoles. Measurements taken during the second run, where the machine was run without sextupoles, led to a rise of 2-3% of the conversion factors

† Email: kuskeb@bii.bessy.de

for the two defocusing quadrupole families located next to the dipoles. The initial difference between calculated and measured vertical tune could thus be fixed. The discrepancy to the bench measurements might be attributed to effects of the dipole edge, or to shielding effects. The conversion factors of the other Q-families were confirmed on the 1 percent level. The resulting orbit correction reached rms values of ≈ 1 mm. During run 3, the sextupoles where switched on, and first measurements could be taken with a corrected orbit and better lifetimes. This led to a second adaption of the quadrupole conversion factors on the subpercent level. The resulting model was successfully used during the rest of the commissioning. The corrected orbit reached typical rms-values of 0.1 mm in both planes. The model has also been used to determine the locations of the BPMs with respect to the centers of the quadrupoles using beam based techniques [6]. The reference orbit going through the center of all 144 quadrupoles is accomplished to better than 0.15 mm in both planes. Beginning from run 7, the linear optics started to settle, and 9 ORMs where at the same quadrupole settings, although the sextupoles, and definitely the steering coils were tuned differently. Only these measurements are presented in order to avoid the effect of different magnet settings and to outline the limits of an online model.

3 ORBIT RESPONSE MEASUREMENTS

The description and the analysis of ORMs has been published e.g., in [5]. Due to the positive experience at BESSY I and elsewhere, the measurement has been included as an automatic procedure in the control system, as well as the extraction of the sensitivity matrices from the measured data, since the beginning of the commissioning. Usually, the 64 horizontal and vertical steering coils included in the sextupoles are varied by ± 0.07 A, while the weaker 16 horizontal coils in the dipoles are varied by ± 0.7 A. Ten orbits are recorded for each setting of all steerers, where one orbit already represents a 100 ms average. The position error is $< 1 \mu m$ at any of the 112 BPMs [6]. This corresponds to an average error of the matrix elements, which are determined by linear regression, of 0.022 mm/A in the horizontal and 0.017 mm/A in the vertical plane. The quality of the horizontal data has been reduced by oscillations at multiples of 50 Hz. However, the deviation between different measurements is large. It exceeds the accuracy of single measurements by more than an order of magnitude, even if the power supply settings of the ring only differ in the correction coil currents. These differences are attributed to differences in magnetic field history or drifts in temperature or current, or other parameters that have not been recorded.

^{*}Funded by the Bundesministerium für Bildung, Wissenschaft Forschung und Technologie and by the Land Berlin

They complicate the extraction of a generally valid model.

3.1 The Fitting Procedure

The K-values of the quadrupoles and the conversion factors of the corrector magnets were fitted to match the experimental conditions with the aid of the GOEMON tool. A singular value decomposition procedure has been used for the non-linear fit of the K-values while the conversion factors of the correction coils have been adjusted by a least square fit, iteratively. An 8-fold symmetric model has been utilised to determine the properties of the magnet families. Families equally powered and located in equivalent positions where fitted as one parameter, as the fit showed a tendency to differ between equivalent types of magnets without increasing the accuracy of the fit. The K-values of 7 types of quadrupoles and the conversion factors for 4 horizontal and 4 vertical types of corrector magnets were determined. Individual BPM sensitivities have not yet been included, as they could not be reliably extracted from the data. Malfunctioning BPMs where excluded from the data. Ambiguous BPMs could be determined during the fit, by comparing the measured and the calculated matrices Fig. 1. The rms deviation between the measured and the adjusted matrices was taken as indication of the quality of the approximation.

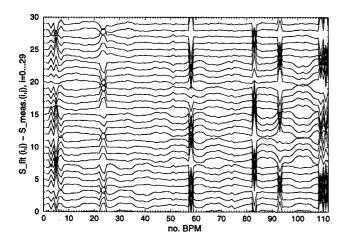


Figure 1: Malfunctioning BPMs show up as clear peaks in the difference between measured and fitted sensitivity matrices

3.2 Results

The resulting K-values and conversion factors of the 9 measurements taken for identical linear optics were compared and are displayed in figures 2 to 4. The quality of the fit varies between 0.220 and 0.500 mm/A. Fig. 2 shows the relative deviation of the resulting K-values to the averages for all families. The K-values converge with increasing quality of the fit. For good fits ($\sigma < 250$ mm/A) they agree to better than 0.2 percent. No correlation with the settings of the sextupoles during the measurements could be detected, neither in degree of approximation nor in the scattering of the resulting K-values.

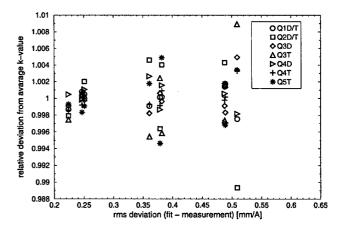


Figure 2: The resulting K-values from different runs agree to better than 0.2 percent for good fits

The resulting conversion factors for the steering coils are displayed in a similar way in Fig. 3. The deviation from the average value of all measurements is plotted over the quality of the fit. The spread is much wider than for the quadrupoles, and there is no correlation with the quality of the fit. Also in this case there was no correlation found between the settings of the sextupoles and the resulting conversion factors of the steerers included in the sextupole magnets.

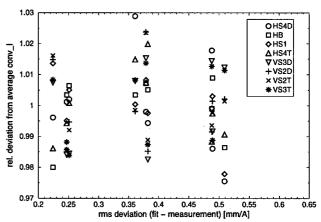


Figure 3: The conversion factors for the steering magnets show rms values of ≈ 1 percent, independent of the quality of the fit

Fig. 4 shows the resulting tunes for all fits, the black symbols refer to the three best fits. For measurements where the working points have been recorded, there is a 10^{-4} agreement between the calculated and the measured tunes. Thus, the wide spread of tunes of almost 0.1 in both planes for different measurements taken for identical quadrupole currents does represent a real difference in the conditions during the measurement. The sextupole settings seem to correlate to some degree with the resulting tunes. Two fits show a clearly lower vertical tune (circle). Only in those measurements the chromatic sextupoles where reduced in current. Switching off the harmonic sextupoles

(triangle) seems to cause a small rise in the both working points. But even measurements with identical sextupole settings (triangle) show a $\delta Q_x \approx 0.04$.

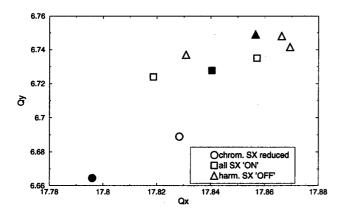


Figure 4: The tunes for all fits reveal a tune shift for cases where the chromatic sextupoles where reduced in current

3.3 Interpretation

The 8-fold symmetry of the ring can be used to average the effect of always eight equivalent steering elements, and create averaged, but symmetric sensitivity matrices. Comparing the averaged effects of the steerers with the original matrix, a rms deviation of 0.2 - 0.6 mm/A was found. This varying degree of symmetry in the machine, just like the wide spread in tune and the difficulty to determine the steerer conversion factors indicate different (unretrievable) machine conditions during the measurements. It is expected that these differences will diminish for a machine in full operation. So far, it does limit the achievable accuracy of the model. There is a clear correlation between the accuracy reached in the fit and the degree of divergence of single steerers from the average. This correlation indicates that even for reproducible machine conditions, the accuracy of the fit can be only improved by splitting up the magnet families and allowing individual conversion factors. According to the bench measurements the deviation of single quadrupoles from their families average is of the order of a few per mill. Out of the 3 best fits ($\sigma < 0.25$ mm/A), only one measurement utilises the regular settings of all sextupoles, and it was taken to set up the new model. Fig. 5 shows the very satisfactory agreement between the beta functions calculated from the new model and those determined by local variation of the quadrupole fields.

3.4 Latest Results

During the last machine shift, (March 1999), the oscillation of the horizontal beam position could be considerably reduced, and the quadrupoles have been slightely adjusted to achieve more symmetrical beta functions. Three ORM have been performed during 2 days and show a good reproducibility in tune of 10^{-4} . The fitted K-values agree to better than 0.1 percent, but there are reproducible differences to up to 0.5 percent to the K-values of the new model

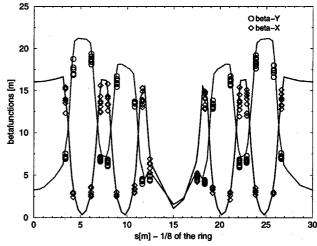


Figure 5: The measurement of local beta functions agrees well with the new model

extracted from the last measurements, which might be due to the optics changes.

4 CONCLUSION

The utilisation of an online model in combination with the very early realization of ORMs has proven very fruitful during the BESSY II commissioning. In two steps a quality was reached that satisfied commissioning needs. For a more detailed analysis, especially effects of single magnets, the optics has to be finally settled and the conditions during the ORMs have to be recorded more carefully in order to isolate the effects that lead to the bad consistency of the extracted sensitivity matrices. The model has to be extended from magnet families to individual magnets in order to improve the approximation to be comparable to the accuracy of the measurements. With increasing confidence in single measurements also the individual sensitivity of the BPMs has to be included in the model.

- [1] E. Jaeschke et al., "Lattice Design for the 1.7 GeV Light Source BESSY II", IEEE Part. Acc. Conf. Washington, (1993), p 1474.
- [2] R. Bakker et al., "Status and Commissioning Results of BESSY II", this conference.
- [3] R. Müller et al., "Rapidly Installable High Performance Control System Facilitates BESSY II Commissioning", EPAC Stockholm (1998), p 1676.
- [4] H. Nishimura, "Object-oriented software construction at ALS", Nuclear Instruments and Methods in Physics Research A 352 (1994) 379-382.
- [5] J. Safranek, "Experimental Determination of Storage Ring Optics using Orbit Response measurements", Nuclear Instruments and Methods in Physics Research A 388 (1997) 27-36.
- [6] P. Kuske et al., "Experience with the Beam Position Monitor System of the BESSY II storage Ring", this conference.

EXPERIENCES WITH COMMISSIONING SOFTWARE TOOLS AT BESSY II *

R. Bakker, T. Birke, B. Kuske, R. Lange, R. Müller, BESSY, Berlin, Germany

Abstract

Software requirements evolve rapidly during the short commissioning period of a third generation light source. Main focus moves from atomic device control to complex conditioning, experiment performance, measurement data taking, beam quality maintenance and performance monitoring tasks. From the very beginning the essential tools have to be set up properly and need to be sufficiently adaptive to easily absorb the actual findings of the running in procedures. In this paper the major software modules at BESSY II are depicted and their relevance for the progress of the commissioning is rated. Implemented functionalities and used methods are described in more detail for the basic working horses (like compound devices, handling of snapshot files, orbit control). Explanations are given why certain tools turned out to be less accepted or useful (yet).

1 APPLICATION DEVELOPMENT ENVIRONMENT

With respect to software requirements commissioning of a light source storage ring is a very demanding phase. Tools with a wide variety of functionalities have to be available (see fig. 1). Many new insights into the behaviour of the new machine are achieved in a very short time. Numerous requests for creation or modification of software support arise.

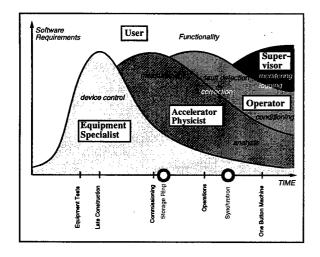


Figure 1: Typical Lifecycles of Operations Software

Based on the EPICS toolkit used at BESSY a large number of generic applications is available that noticably facil-

† Email: mueller@bii.bessy.de

itates the set up of a device control layer. In addition a few tools are suited to satisfy operator or supervisor requests. Standard measurement and analysis tasks are feasible with the aid of the SDDS toolkit[1] and shell programming.

For performance analysis and correction procedures involving accelerator physics describing accelerator behaviour a number of solutions and toolkits developed in other laboratories had been investigated. Amount of adaptation work, resulting flexibility and related arguments led to the decision to pick up ideas and create these programs within the software context available at BESSY. For that purpose three fundamental design decisions turned out to be very helpful: to use (1) the relational DB ORACLE as global reference repository, (2) the unique C++ toolkit goemon[2] for model descriptions, (3) a well separated interface to the graphical user interface[3]. That infrastructure allowed to build additional utility toolkits e.g. a magnet-power supply support library convenietly connecting physics and model description with device I/O and engineering units.

2 DEVICE CONTROL

2.1 Status Displays, Control Handles

Comprehensive synoptic views have been built with the EPICS display manager that allow for hierarchical structured navigation and provide a web of light weight and user friendly control panels. For specific tuning problems a knob manager connects the setpoints of interest to dial boxes. Strip chart recording software is available for simple stability analysis as well as for correlation tests and preliminary measurements. Supervisory tasks take care of sensitive devices, e.g. sending OFF to the microtron contrapole causes a software controlled graceful ramp down procedure. Thus for the control of single devices a intuitive, 'complete', and robust man-machine interface has been set up that is well accepted and adequately operatable from a single operator seat equipped with two monitors and five workspaces.

2.2 Pseudo Devices

Dependent on the operation mode quadrupole and sextupole power supplies are combined to families. Or the kicker amplitudes have to be tuned until a closed bump is formed. Then the closed bump amplitude has to be optimized for injection efficiency. To operate these groups of devices by pseudo set points has been made possible through sophisticated programming on the front end computer (IOC) level. Especially in the early phase of beam threading the rapid, easy and consistent switching between single device access and groupwise operation turned out to be extremely helpful.

^{*}Funded by the Bundesministerium für Bildung, Wissenschaft Forschung und Technologie and by the Land Berlin

For temporary, not yet settled or less elementary applications an easy configurable 'multi-knob' is available on the work station level. It is e.g. used for the energy scaling of transfer line and storage ring or the orthogonal adjustment of vertical or horizontal tune and chromaticity.

3 MACHINE CONDITIONING

3.1 Save / Restore

For literally every setpoint there is a global and persistent memory field available. This is very convenient for manual tuning procedures. With mouse clicks one can save the starting point or the local optimum and return to this point when the attempt to improve does not promise success.

For global storing and reloading of relevant machine settings a tcl/Tk program overcomes the typical problems connected with the classical approach to dump all data into one file. The script provides a very transparent framework for handling snapshot file catalogs, data aging and partial recall. By a flexible and hierarchical area selection mechanism arbitrary collection of devices can be quickly defined in both dimensions: equipment location and device type. The corresponding setpoints (and readbacks) can be stored in file sets, that are completely hidden from the users. Reference is done by arbitrary comments, date and time or serial number. Partial or subsequent re- or overloading is feasible by definition of sub-areas or by specification of filter functions.

For a specified device collection it is possible to compare (in any combination) setpoint and readback values of snapshot files and corresponding values actually in effect for the running machine. Differences exceeding a configurable percentage are highlighted. For administration purposes the user may remove files (into the attic) or add it to the list of favourite files. For offline analysis the export options 'print out', 'dump to file' or 'send email' are widely used. By its structure this facility is easy maintainable and adaptable. It is well accepted, robust and very reliable.

3.2 Cycling Procedures

Only specific devices (e.g. microtron linac) are conditioned by programs running on the IOC. For procedures involving groups of devices the adaptation of an appropriate tool [4] has been foreseen but had to be postponed. As an interim solution a tcl/Tk script has been set up for the cycling of the storage ring and transfer line magnets. Main functionality of the script is to call the database, group the power supplies, set up and run the sequence. This quick solution encountered problems trying to meet unclear given specifications and to absorb rapidly changing requirements. The initially insufficient operational safety has been quickly overcome, but for future operations it will be replaced and embedded into a more general sequencer facility.

3.3 Alarms

As soon as new devices have been stable and continously available they have been included into the alarm handler configurations. Major or minor error conditions for the areas microtron, transfer lines, booster, storage ring, RF system and magnet interlock are reported. In a structured and hierarchical way the operator is guided to the malfunctioning device and provided with the appropriate control panel needed to analyse and fix the problem. For fault detection it increasingly replaces the use of synoptic views. For further analysis received alarms are logged to files.

4 DATA AQUISITION AND EVALUATION

4.1 Measurements, Analysis

During commissioning systematic measurements are a difficult field of improvisation. Both machine, control system and software tools are not yet familiar. Mostly coarse manual scans dominate. Further evaluation of data is done with PC standard office tools or dedicated programs that are usable only by the author. Occasionally the correlation engine Xtract [5] has been used for scraper measurements, one and two-dimensional tune scans or stepping of the harmonic sextupoles to find the best dynamic aperture.

Only orbit correlations are taken systematically and a couple of standardized analysis programs are available. Routinely corrector response matrices are measured and postprocessed offline (e.g. [6]). In the beam based alignment set-up an additional power supply is switched to all quadrupoles and stepped automatically and the response matrices are used to determine the BPM offsets[7].

4.2 Data Logging

With respect to the importance of an archive containing all signals suited to identify unknown sources of performance degradation the present situation is a minimum effort solution. Beam current, lifetime, orbit, vacuum, power supply stability data are sampled and stored in binary format. Only for orbit data and correlated signals a display, retrieval and correlation browser exists that is configurable with a graphical user interface. Beam intensity and vacuum data are converted to standardized graphics accessible by WEB navigators. Shortcoming of the SDDS based data collectors are the fixed time intervals between data aquisition. Frequently notification on data change is appropriate. The continuously increasing demand on archived signals emphasizes the embryonic state of the present system as well as the need for a major development effort.

5 ACCELERATOR PHYSICS

5.1 Orbit

Data aquisition, display and control of the orbit in all segments of the accelerator complex, i.e. transfer lines, synchrotron (SY) and storage ring (SR) is handled by a generic, event driven program called *Orbit*. It features a 'All-in-One' graphical user interface consisting of a main program control panel, a context sensitive BPM data display and a context sensitive corrector control panel.

The main panel is for display of statistical summary, setup of the fundamental orbit control types, selection of basic measurement modes, configuration of data I/O, modification of BPM system operation parameters and display of program informations, warnings and error reports.

BPM data are displayed as high precision averaged closed orbit, specific turn number of single turn data (SR), orbit at a specific energy during the ramping cycle (SY) - both absolute and as difference to an arbitrary reference orbit. For each individual BPM stability of displacement, intensity, averaging quality is recorded and statistically analysed. Additionally turn-by-turn changes (SR) or energy dependencies (SY) at a selectable BPM can be displayed. BPM data may be logged to files together with arbitrary correlation channels.

One fundamental orbit control mode are closed bumps. Required bumps may be choosen from a list (e.g. center of insertion device, achromat) or freely configurable with arbitrary target position and corrector combination. According to requested amplitude and angle bumps are calculated with the embedded online-model according to the actual set points of the accelerator. The bump predictions are reliable on the percent level. A systematic bump scan during start up of the storage ring helped to pinpoint destructive aperture limitations within one meter[8].

Global orbit correction to an arbitrary reference orbit is the other control mode. Standard correction method is based on Singular Value Decomposition (SVD). For fault analysis the most effective corrector method is available too. Calculated model values or experimental results supply response matrices. On faulty BPM reading or corrector status change the elements are automatically removed from the correction scheme until they are available again. The operator may manually exclude or reenable BPMs or correctors with a mouse click. The reference orbit may be choosen from beam based alignment data (optimized) and the logging archive (comparison). It can be modified with mouse drags (bumps).

Two automatic correction schemes are presently under study: (1) a mixture of fixed frequency (e.g. 0.1 Hz) and a deviation threshold (e.g. two times the noise) (2) a PID type regulator. Both methods converge relatively fast and keep the RMS orbit deviations stable at the optimal value but the minimal invasive method with optimal reduction of residual noise is not yet identified.

The program is an accurate working horse. Its basic functionality has been set up and consolidated for the booster. As a consequence it worked reliable at start-up of the storage ring. Without modification the embedded online model allowed to correct the orbit at all presently established energies (0.9, 1.7 and 1.9 [GeV]) with comparable precision.

5.2 Optics

A generic online model program called Optics helps to understand certain tunings of any segment of the accelerator complex (transfer lines, SY, SR). Interface to the real accelerator is the capability to load and save snapshot files and to read and modify power supply setpoints. The program displays beta function, trajectory and dispersion. It calculates the spot size and position on an intercepting fluorescent screen. To allow studies of dependencies on parameter variation input controllers for power supply (family) setpoints, beamline matching conditions and extraction / injection bump parameters are available. The influence of fundamental model approximations can be compared: standard hard edge magnets, current dependant conversion factors or saturation induced variable magnetic length. For the rings fitting procedures for requested fractional tune or chromaticity are available. Tune adjusting quadrupoles can be restricted to selectable families.

The program is frequently very useful. Precision is approaching reality. Since there is no online data source for tune and chromaticity available yet and there has not been a commitment for a serious and systematic testing so far *Optics* has still the quality of a beta release.

6 EXPERIENCES, SUMMARY

The mature EPICS toolkit provided the framework for a powerful basic operational set. Within the BESSY software context generic applications have been built that evolved 'downsteam' with the installation process. For the commissioning an adequate set of easy to use and reliable operations program has been available. The software system is transparent and robust. It could mostly adopt requests for changes without noticible delays or inconsistencies. Frequently new functionalities have been anticipated and installed when the existing features began to be appreciated. A number of additional tools are ready to be set up for various tasks. They lie idle because utilization would require a certain user programming capability and effort.

- [1] M. Borland, L. Emery, N. Sereno, Proceedings of the 1995 ICALEPCS, Chicago, 1995, p.382
- [2] H. Nishimura, Nucl. Instr. Meth., A 352 (1994), p.379
- [3] R. Bakker et al., Proceedings of the 1998 EPAC, Stockholm, 1998, p.1676
- [4] T. Birke, R. Lange, R. Müller, Proceedings of the 1995 ICALEPCS, Chicago, 1995, p.648
- [5] Xtract has been developed at TJNAF. See: http://help.bessy.de/xtract/xtract/.html.
- [6] B. Kuske et al., 'Establishment of a Model for Interpretation and Correction Tools for BESSY II', this conf. (WEP48).
- [7] P. Kuske et al., 'Experience with the BPM System of the BESSY II Storage Ring', this conference (WEA84).
- [8] R. Bakker et al., 'Status and Commissioning Results of BESSY II', this conference (TUCL3).

EXTENDING THE RANGE OF A LOW ENERGY SR-SOURCE TO HARD X-RAYS *

M. Abo-Bakr, W. Anders, K. Bürkmann, V. Dürr, P. Kuske, R. Müller, K. Ott, M. Scheer, E. Weihreter[†], G. Wüstefeld, BESSY, Berlin, H. Winick, SSRL/SLAC, Stanford, H. Kaiser, J. Koupsidis, M. Marx, G.-A. Voss, DESY, Hamburg

Abstract

An outline design is presented for a SR-source providing high brilliance VUV/soft X-Rays and high flux hard X-rays based on existing hardware of the BESSY I storage ring, which will be shut down by the end of 1999. Essential features are a 6-cell double bend achromat lattice, with low beta in three of the 6 long straight sections to facilitate the use of superconducting multipole wigglers. Beam optical implications are discussed together with technical modifications of existing hardware and possible operation at 1.0 GeV. A design of a 7.5 T multipole wiggler is given.

1 INTRODUCTION

The second generation SR-source BESSY I in Berlin, which consists of an 800 MeV storage ring [1] with a full energy injector synchrotron [2], has been used over the last 18 years for a large scientific program in the VUV/soft Xray range. The recent start of user operation of the third generation ring BESSY II makes it necessary to close down BESSY I by the end of 1999. Based on the available hardware an outline design is presented for a SR-source providing high brilliance VUV/soft X-rays as well as high flux hard X-rays from insertion devices [3]. The increasing demand of hard X-rays for structural analysis, protein crystallography, environmental research and many other activities has motivated the present ring concept, which would allow to rejuvenate the old BESSY I ring making use of a large part of the subsystems and hardware components for a versatile SR-source covering the energy range from 10 eV to about 20 keV.

There are two essential modifications of the BESSY I ring which will allow to achieve this important spectral extension: the installation of superconducting 7.5 T multipole wigglers and an upgrade of the beam energy to 1.0 GeV.

High field multipole wigglers are best arranged at places of low beta function values in both planes. This will provide for higher flux density of the photon beams, while at the same time keeping the undesirable linear and nonlinear focusing effects of the wiggler small. Further increase in photon energy is achieved by modifying the bending magnets to permit 1.0 GeV operation.

Changing the original lattice of BESSY I with 4 straight

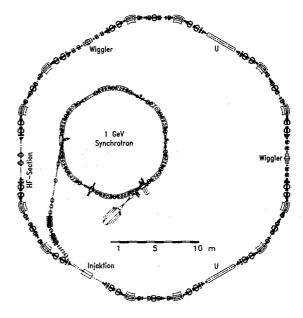


Figure 1: Accelerator and storage ring lay out.

sections of intermediate length (3.6 m) to one of 6 straight sections, each 6 m long, the facility can provide up to 20 dipole beamlines with a critical photon energy of $\epsilon_c=1.25$ keV, two straight sections for the installation of 7.5 T multipole wigglers ($\epsilon_c=5.0$ keV) with up to three beamlines per wiggler offering a flux in excess of $4\cdot10^{13}$ at 12 keV and two straight sections of undulators to provide high brilliance photon beams in the energy range from a few tens of eV to 2 keV. The resulting increase of storage ring circumference from 62.4 m to 100.8 m creates enough space at the inside of the ring to accommodate the injector synchrotron and the microtron preaccelerator. Figure 1 shows a foot print of the new storage ring lay-out.

2 THE OPTICAL LATTICE

The new optics is based on a 6 cell double bend achromat lattice with alternating high and low beta functions in the straights. For flexible matching of the straight sections a symmetric doublet structure is used in the high β straights, and a symmetric quadruplet structure in the low β sections, giving a total of 19 quadrupole families. The lattice functions of the unperturbed optics (no wigglers or undulators) are shown in Fig. 2 and the essential optical parameters are listed in Tab. 1. In the wiggler section a low vertical

^{*}Work supported by the Bundesministerium für Bildung, Wissenschaft, Forschung und Technologie and by the Land Berlin and the US Department of Energy.

[†] Email: weihreter@bessy.de

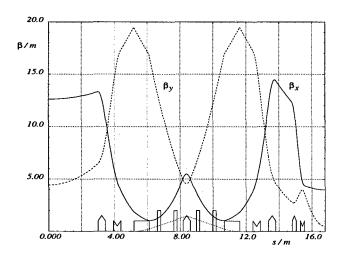


Figure 2: Optical functions of the unperturbed lattice for one sixth of the ring.

beta function is required to reduce the linear and nonlinear focusing effects of the wiggler. The simulation of the wiggler related effects are based on the assumption that there are only longitudinal and vertical field components, and no focusing or defocusing terms influencing the horizontal beam motion. The vertical beta function should not

Table 1: Storage ring parameters

electron energy	1.0 GeV
beam current	700 mA
circumference	100.8 m
periodicity	2.3
working point Q_x/Q_y	5.2/3.2
nat. chromaticity ξ_x/ξ_y	-8.1/-7.2
momentum compaction factor α	0.005
free space in high β straight	6 m
free space in low β straight	2.5 m
beta functions at the center of:	
high β -straight β_x/β_y	13 m / 4.5 m
low β straight β_x/β_y	4 m/0.5 m
max. beta function β_x/β_y	14.5 m/19.5 m
max. dispersion η	1.4 m

differ too much from the rms bending radius ($\rho=0.63$ m at 1.0 GeV) of the electrons in the wiggler field. Tracking calculations indicated that there is a broad optimum for the dynamic aperture around $\beta_y\approx 0.5$ m. To get a high photon flux density from the wiggler beamlines the horizontal beta function in the wiggler section should be also small. From beam optical considerations a horizontal tune of $Q_x=5.2$ was chosen which gives a good behaviour of the optics together with a horizontal beta function of $\beta_x\approx 4$ m. The dynamic aperture of the bare lattice (Fig. 3) shows very good results, harmonic sextupoles are not required. The calculation is based on 1000 stable particle turns with small field and alignment errors assumed for the magnets, leading to rms closed orbit errors of about

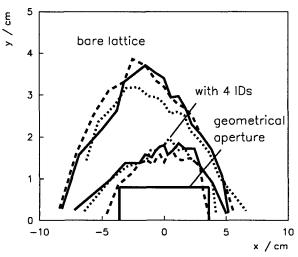


Figure 3: Dynamical and geometrical aperture in the middle of the high β straight section for $\Delta p/p = 0, \pm 2\%$.

1 mm. The lattice has a large chromatic acceptance which is required for a good Touschek lifetime. The nonlinear chromatic tuneshift is smaller than 0.06 in the range of $-1.5\% \leq \Delta p/p \leq +1.5\%$, if the chromaticity is adjusted to $\Delta Q/\Delta p/p_0=+1$ in both planes. The dynamic aperture including two superconducting wigglers and two U49 undulators is shown in Fig. 3. Here the wigglers have been modeled by a 2-D scalar potential function starting from the wiggler field $B_y(s)$. As expected, the dynamic aperture is significantly reduced due to the nonlinearities of the insertion devices. With ± 30 mm horizontally and ± 15 mm vertically the dynamic aperture, however, is still comfortably large to guarantee stable beam operation.

The two 7.5 T wigglers enhance the radiation damping strongly and consequently reduce the equilibrium emittance significantly, a welcome feature of this source concept. A comparison of the transverse emittances, energy spread, energy loss per turn and related damping times for the bare lattice and with one to two wigglers are summarized in Tab. 2.

Table 2: 7.5 T Wiggler dependent damping effects

bare lattice and N wigglers	N=0	N=1	N=2
nat. emittance ϵ_n in 10^{-9} radm	115	70	50
nat. energy width σ_e/E_0 in 10^{-4}	6.5	8.0	9.0
damping times $\tau_x = \tau_y/\tau_s$ in ms	14/7	8/4	6/3
energy loss per turn in keV	50	85	120

3 BEAM LIFETIME

To estimate the lifetime at 1.0 GeV for beam currents up to 700 mA gas scattering (elastic Coulomb and inelastic Bremsstrahlung scattering) and Touschek scattering has been considered. With a vertical acceptance of $A_y = 11.6$ mm mrad limited in the dipoles, a mean vertical beta function $<\beta_y>=12.4$ m, a base pressure of

 $p_0=1\cdot 10^{-9}$ mbar assuming a nitrogen (N₂)-equivalent gas distribution and a pressure rise of $1.4\cdot 10^{-10}$ mbar per 100 mA of stored current, a total gas scattering lifetime of 8.7 h can be expected. The Touschek effect depends sensitively on the bunch volume, on the number of electrons per bunch and on the energy acceptance. Taking turbulent bunch lengthening with a longitudinal broadband impedance |Z/n| of 3 Ω and an energy acceptance of $\Delta E/E=1.3\%$ into account for a bunch filling pattern where only 2/3 of the 168 rf-buckets are filled the Touschek lifetime is 8.4 h. As a result a total beam lifetime of about 4.2 h can be expected for a stored current of 700 mA.

4 THE 7.5 T MULTIPOLE WIGGLER

The wigglers are based on the following concept [4]: A one meter long iron yoke has 15 poles (including 2 half poles at the ends) with a period length of 14 cm and a magnetic gap of 20 mm. Each pole is excited by a racetrack shaped coil made from a suitable multifilament NbTi wire in a rectangular copper matrix. The coils have two separate windings to optimize the current with respect to the different critical field at the windings. Fig. 4 presents a vertical cut through the iron yoke showing the beam chamber with a 14 mm vertical aperture and the clamps for prestressing of the whole structure, and a horizontal cut showing the iron poles and the racetrack coils. The complete magnet assembly including the beam chamber is immersed in a liquid He bath.

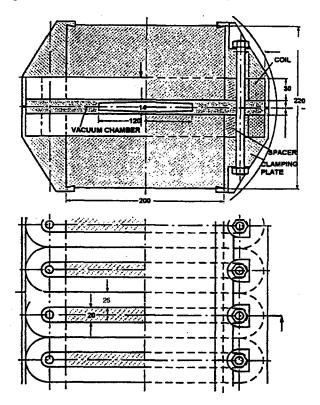


Figure 4: Vertical (top) and horizontal (bottom) cut through (a part of) the wiggler magnet.

5 HARDWARE MODIFICATIONS

Dipole magnets: To increase the energy from 800 MeV to 1.0 GeV, the dipole field must be increased from 1.5 T to 1.875 T. Reduction of the magnetic gap from 60 mm to 44 mm and narrowing the width of the pole from 190 mm to 90 mm allows to reach this relatively high field keeping the magnetic induction in the yoke at a tolerable level. Field calculations (2-D) indicate that after optimization of the pole profile the field homogeneity is better than $5 \cdot 10^{-4}$ within ± 15 mm horizontally. The dominant multipole is a sextupole which can be compensated in part by the chromatic sextupoles.

<u>Vacuum system:</u> A copper (CuSn2) vacuum chamber based on technology developed at DESY for HERA and DORIS is proposed which offers significant advantage in handling high radiation power densities. The dipole chamber can be fabricated by milling and vacuum brazing. Water cooling channels are brazed at the outside which can also be used for in-situ baking at temperatures up to 150° C by applying hot water at a pressure of 4.8 bar. A total of 48 ion getter pumps (70 l/s) supplemented by Ti sublimation pumps will be used to obtain a working pressure of $1 \cdot 10^{-9}$ mbar.

Injection system: The new topology with the synchrotron inside the storage ring favours horizontal injection, and with the straight section length of 6 m there is sufficient space available to place 4 kickers and a septum magnet in one high β straight. With a max. strength of 8 mrad a local injection bump can be produced with a horizontal amplitude of 20 mm. A new transfer line must be built for beam transport from the synchrotron to the injection septum.

RF-system: Thanks to the higher beam energy and the two wigglers the radiated power is significantly enhanced as compared to BESSY I. For a beam current of 700 mA the power radiated in the dipoles and in the wigglers is 34.8 kW and 48.8 kW respectively. A minimum cavity voltage of 300 kV must be provided for a 1.3% energy acceptance, giving a Touschek lifetime of 8 h. With a second DORIStype cavity and two 70 kW rf-transmitters these conditions can be satisfied.

Beside the above modifications it is clear that after nearly 20 years of continuous operation some critical components and subsystems have to be replaced or refurbished. This is particularly true for the control system, the orbit measurement system and some of the power supplies.

- [1] G.v. Egan-Krieger, D. Einfeld, W.-D. Klotz, H. Lehr, R. Maier, G. Mülhaupt, R. Richter, E. Weihreter, IEEE-Trans. N.S., NS-30, No 4, 3103(1983)
- [2] G.v. Egan-Krieger, D. Einfeld, H.-G. Hoberg, W.-D. Klotz, H. Lehr, R. Maier, M. Martin, G. Mülhaupt, R. Richter, L. Schulz, E. Weihreter, IEEE-Trans. N.S., NS-30, No 4, 3094(1983)
- [3] BESSY Ia, Conceptual design study, BESSY, 1999
- [4] G.-A. Voss, Internal Technical Note M99-01, DESY, 1999.

THE CONVERSION OF SURF II TO SURF III

M.L. Furst*, R.M. Graves, A. Hamilton, L.R. Hughey, R.P. Madden*, R.E. Vest, NIST, Gaithersburg, MD, W.S. Trzeciak, R.A. Bosch, Synchrotron Radiation Center, Stoughton, WI, L. Greenler, P. Robl, D. Wahl, Physical Sciences Laboratory, Stoughton, WI

Abstract

The Electron and Optical Physics Division of the Physics Laboratory has operated the Synchrotron Ultraviolet Radiation Facility (SURF) at the National Institute of Standards and Technology (NIST) for over 30 years. Initially operated in a parasitic mode at the NIST electron synchrotron, the facility was converted into the SURF II electron storage ring in 1974. Since then, SURF II has been the United States national standard of irradiance in the vacuum ultraviolet spectral region, but the radiometric accuracy of SURF II was limited by the uniformity of the magnetic field encountered by electrons as they traversed Variations of up to 0.5% limited the knowledge of the local bending radius at any tangent point and restricted the accuracy of the irradiance calculations. To improve the radiometric accuracy of SURF, an entirely new magnet structure was installed in the summer of 1998. The azimuthal uniformity of the SURF III magnetic field has been improved by a factor of 50 at 388 MeV and a factor of 25 at 260 MeV, allowing irradiance calculations to be made with much higher accuracy than SURF II could achieve. As an additional benefit, the use of improved magnet material, a smaller air gap between the poles, and new magnet windings has increased the magnetic field strength at the electron orbit, allowing SURF III to store electrons at energies as high as 400 MeV, compared to 300 MeV for SURF II. The higher electron energy will extend the usable range of radiation from SURF to shorter wavelengths, enabling experiments in the "water window" from 2.3 nm to 4.4 nm. We present here the major design goals and features of the SURF III magnet, the results of magnet field mapping and other measurements, and the facility performance to date.

1 BACKGROUND

The NIST Synchrotron Ultraviolet Radiation Facility (SURF) began as an electron synchrotron operating at 180 MeV in 1961. In 1962 the synchrotron was modified to study properties of the synchrotron radiation continuum and construction was begun on instrumentation for optical experiments using this radiation. The advantages of an electron storage ring design for spectroscopy and radiometry led to the conversion to the SURF II electron

Email: furst@nist.gov

storage ring in 1974 [1]. SURF II operated from 1974 to 1997 over an energy range from 140 MeV to 300 MeV with stored beam currents as high as 390 mA. Most of the magnet structure was not modified for the conversion to a storage ring. The upper and lower yokes, backlegs, and upper and lower poles remained the original laminated steel used for the synchrotron. A laminated design limited eddy current effects in the synchrotron electromagnet operating at 60 Hz. In order to achieve suitable operating characteristics of the magnetic field for a storage ring, five correction coils and new main coils were designed and manufactured by the University of Wisconsin for the SURF II configuration. Despite limitations in the laminar design, careful assembly of the electromagnet, alignment of the poles, and accurate measurement of the appropriate parameters resulted in SURF II becoming a primary standard source of irradiance in the UV and VUV. Ultimately the relative uncertainties in irradiance at 284 MeV (combined standard uncertainties with a coverage factor of two) ranged from ±9.0% at 4 nm to ±0.8% at 400 nm.

2 A NEW DESIGN

With an eye towards expanding the role of SURF in national radiometric standards, personnel at the University of Wisconsin-Madison (UW-Madison) Physical Sciences Laboratory (PSL) and Synchrotron Radiation Center (SRC) were approached to design a new electromagnet. Using POISSON and ANSYS programming codes, the UW-Madison designers, based on information gathered from modeling the old electromagnet, developed a new design using modern solid 1008 magnet steel. It was decided to use solid 1008 steel for the entire magnet structure to take advantage of its higher saturation level compared to the old steel and to increase the density of steel by filling in the gaps of the laminated structure. With these changes and a smaller pole gap, operation at an energy near 400 MeV would become a possibility. Because of concerns about eddy current creation in the poles during rapid ramping of the magnetic field from injection field to operating field, it was decided to make each pole in two C-shaped segments. The poles were then assembled onto a backing plate with a 76 µm thick mylar shim between the two segments. The general layout of the magnet steel is shown in Figure 1 which shows a N-S cross section through the magnet.

There are five blocks comprising each of the upper and lower yokes that are held together with four horizontal tie

^{*}R.P. Madden is retired from NIST

rods. These blocks, each weighing about 134 kN (15 ton), were aligned using leveling jacks to within 25 μm of each other.

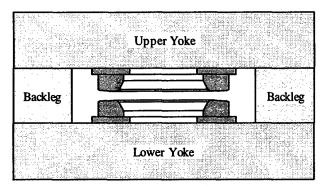


Figure 1: Cross-sectional view of SURF III magnet steel including upper and lower poles.

At the factory, the entire steel structure was assembled, precision holes were drilled between blocks, and then locating pins were inserted. The structure was then disassembled for shipping. The cylindrical hardened steel locating pins were manufactured to a tolerance of 2.5 µm and used to reassemble the structure with the proper alignment. Once the lower yoke was assembled on the leveling jacks, the assembly was lifted into place on a support structure so that its geometric center was the same as that of the lower magnetic pole of SURF II to within 0.25 mm. At the factory two blocks were welded together to form a backleg weighing about 128 kN (14.4 ton). The two backlegs were placed on top of the lower yoke again with the aid of locating pins. The lower pole was then placed on the lower yoke and centered. A dial indicator was attached to an arm bolted to an air bearing rotary table to measure the alignment of the poles. Each pole has precision horizontal and vertical fiducial surfaces machined near its perimeter. By mapping the dial indicator readings of these surfaces, the level and centering of the poles could be determined. centering and level maps for the lower pole are shown in Figure 2.

A set of 10 pie-shaped azimuthally equidistant spacers were attached to each pole backing plate to provide about 7.4 mm of gap between each backing plate and its yoke. In between each pair of spacers a pie-shaped shim carrier was inserted capable of carrying shims up to 0.5 mm thick. These shims were used to make small adjustments to the azimuthal uniformity of the magnetic field. Once the upper pole was mounted to the upper yoke we were able to measure the gap between the poles directly with an inside micrometer. After initial measurements revealed the poles were slightly nonparallel, the pole gap was adjusted by adding shims between the tops of the backlegs and the upper yoke. The resulting map of the pole gap measured between upper and lower horizontal fiducial surfaces is shown in Figure 3. After the poles were aligned, new main coils were mounted and centered on the

poles. A pair of upper and lower trim coils were included in the design to allow for adjustment of the radial field index, defined as:

$$n \equiv -\frac{r}{B} \frac{\partial B}{\partial r}$$

Where r is the radius and B is the magnetic flux density.

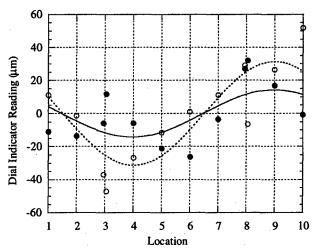


Figure 2: Centering (solid line with solid circles) and level (dashed line with open circles) of the lower pole. The points are deviations from the average of 10 measurements of the vertical (for centering) and horizontal (for level) fiducial surfaces at approximately 36° intervals, location 3 being due south. The lines show fits to the equation:

$$y = A\cos[36(x-\theta)]$$

Where A is the amplitude of the cosine wave and θ is the phase, their respective values being 14.2 μm and 9.0 for centering and 31.4 μm and 9.0 for level.

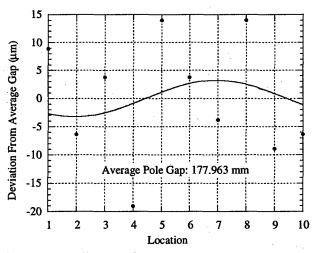


Figure 3: Parallelism of the upper and lower poles as measured by the distance between upper and lower horizontal fiducial surfaces. The coefficients of the cosine curve fit are $3.2 \, \mu m$ and 6.9. (See Fig. 2)

To operate in the storage ring mode, the index is required to be less than 0.75. The new magnet was designed to have an index of 0.6 to avoid resonant coupling of the horizontal and vertical betatron tunes at values of 0.56 and 0.64. Also an index near 0.6 provides a reasonable balance between radial and longitudinal damping of the electron beam. The trim coils were included to provide for small adjustments of the index during ramping to final energy and possibly at the highest energies where the index was expected to have a significant radial gradient. During operation of the storage ring for radiometric experiments the trim coils would be disconnected.

The new design also included some modifications to the storage ring vacuum chamber. Two new ports were added to accommodate new beamlines that pass through holes cut through the backleg steel. One magnetic field probe port was added, and two older ports were modified to accommodate magnetic field probes at approximately 120° intervals around the orbit.

3 MAGNETIC FIELD MEASUREMENTS

In order to measure the ability of the new electromagnet to provide a perfect circular orbit and the appropriate index profile, a large number of magnetic field maps were obtained. UW-Madison provided us with a computer-driven precision field mapping system capable of measuring field variations of about 0.003%. Magnetic field probes were constrained to move in measurable independent azimuthal and radial increments relative to the fiducial surfaces. Also, the probes were set to move in the midplane between the poles. The absolute accuracy of the knowledge of probe positions was approximately 0.2 mm.

Azimuthal field maps were obtained at the orbital radius over a range of main coil currents from 18.5 A to 900 A, corresponding to magnetic flux densities of 0.04 T to 1.66 T and equivalent to electron energies from 10 MeV to 417 MeV. After optimizing the configuration of the shims in the shim carriers and adding poleface shims at the joints between the pole segments, the azimuthal field maps showed variations no greater than ±0.03% from equivalent energies of 52 MeV to 417 MeV. Figure 4 shows the results of shim optimization with 700 A in the main coils. Figure 5 shows a comparison of the azimuthal field uniformity for SURF II at its nominal operating energy of 284 MeV with SURF III at its initial expected operating energy of 331 MeV. The average maximum deviation for SURF II was ±0.686% whereas for SURF III it is ±0.014%. We expect to realize a magnetic field uncertainty of ±0.05% at the 331 MeV initial operating energy. The contribution of this component to the total uncertainty in irradiance at a wavelength of 4 nm would be ±0.4% as compared to ±9.0% for the contribution from the ±0.6% uncertainty of SURF II.

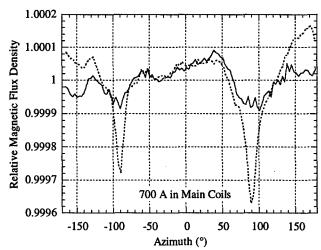


Figure 4: Results of shim optimization on magnetic field azimuthal uniformity at 700 A (equivalent to 352 MeV). The dotted line shows normalized field measurements with identical shims in the twenty shim carriers and no poleface shims. The solid line displays measurements after adjusting the shim configuration and installing poleface shims.

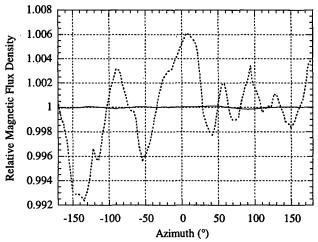


Figure 5: Comparison of azimuthal field maps of SURF II at 284 MeV operating energy (dotted line) and SURF III at initial 331 MeV operating energy (solid line).

We gratefully acknowledge the help of Dave Eisert and Don Holly from UW-Madison, Ping-Shine Shaw from NIST, and Rebecca Friedman from Union College.

4 REFERENCES

[1] E.M. Rowe, et al, "The Conversion of the NBS 180 MeV Synchrotron to a 240 MeV Electron Storage Ring for Synchrotron Radiation Research," Proceedings of the 9th International Conference on High Energy Accelerators, SLAC, Stanford, CA, May 1974.

BEAM STABILITY STUDIES AND IMPROVEMENTS AT ALADDIN

W. S. Trzeciak, M. A. Green, and the SRC Staff, Synchrotron Radiation Center, 3731 Schneider Dr., Stoughton, WI, 53589-3097, USA

Abstract

Recent improvements in beam position stability at Aladdin, the 1 GeV electron storage ring at the Synchrotron Radiation Center, are reported. Stabilizing the beam position monitors (BPM's), in conjunction with the use of a global feedback system, keeps the beam position within ±3 µm of its starting value during a user fill. Relocation of transformers and the dipole power supply choke have made substantial reductions in the 60 and 720 Hz motions of the electron beam, allowing a broader scope to the infrared experimental program. Work on stabilizing the synchrotron radiation source characteristics under various operating conditions is presented. Studies of weak resonances near the standard operating tune are leading to the use of closed loop tune control to maintain beam size stability. Lattice corrections employed during the scanning of undulators keep the source sizes fixed down to the 2% level. Future plans for improved optical beam position and size monitors, renovation of the BPM electronics, implementation of a hydrostatic leveling system, and temperature monitoring of the ring components is also presented.

1 INTRODUCTION

Aladdin is a 1 GeV electron storage ring dedicated to synchrotron radiation. The University of Wisconsin, Madison, operates it under contract to the National Science Foundation. It has been in operation since 1985, and, in many respects, it performs at the level of third generation synchrotron radiation sources.

The ring-operating schedule has been unchanged for several years now [1,2]. Regular operation is 20 hours per day, 5 days per week, with the additional possibility of 4 hours of user beam every weekday morning or full day operation on weekends.

While Aladdin is a 1 GeV storage ring, most of the operating time for user beams is at 800 MeV, starting out at about 250 mA and has a current-lifetime product of about 950 mA·h. Typical measured source sizes from the bending magnets are $\sigma_x = 450 \, \mu m$, and $\sigma_y = 85 \, \mu m$, whereas calculated source sizes in the middle of long straight sections (undulator source points) are $\sigma_x = 814 \, \mu m$, and $\sigma_y = 72 \, \mu m$.

2 POSITION STABILITY

2.1 General

Several improvements in the structure of the vacuum chamber have been made over the last few years. New stripline pairs, used as beam position monitors (BPM's), have been installed in the whole ring, except for one final long straight section. The new monitors are thicker and more robust; there is essentially no warpage during bakeout or when heated by synchrotron radiation. The monitors are mounted in chamber sections that pass through quadrupoles that are now uncoupled, via a bellows, from the downstream dipole vacuum chamber section. In the past, small changes in the dipole section position, e.g. to reset a photon-beamline port, would change the BPM position in the upstream quadrupole doublet. This no longer happens. Since the BPM's are now mechanically uncoupled from the dipole sections, they are now firmly clamped to the quadrupole bases, which are mounted, via short steel pedestals, to the bedrock under the floor.

Calibration of the BPM's is accomplished by the usual current-shunting technique. Most BPM's are located at quarupoles. While 1 or 2% of the current is alternately shunted and not shunted around a quadrupole, the beam is steered until the closed orbit is invariant. At that point the BPM reading is the calibration offset.

Some of the ring quadrupoles have back-leg windings that are used as dipole steering corrections. Since we've mechanically uncoupled the chamber from its adjacent quadrupole, we've measured a large difference in calibration (as much as $164 \, \mu m$) comparing with and without current in the "piggy backed" dipole steering. Non-linear effects of the uncorrected orbit traversing the BPM at a large angle may explain this.

Prior to the upgrade one of each stripline pair also doubled as an ion-clearing electrode. The new chamber sections have a separate ion clearing strip, simplifying the electrical hookup of the BPM's and eliminating a potential source of noise in the BPM electronics.

2.2 Long Term

Over the length of a user fill, 4 to 8 hours, the orbit is stable to within $\pm 3~\mu m$. In order to get this level of stability, the Global Feedback system is active for all user beams. This system simply reoptimizes the orbit to a

^{*} Work supported by the NSF grant DMR-95-31009. walter@src.wisc.edu

target orbit at a 2 Hz rate. Day to day orbit position repeatability is about $\pm 6\,\mu m$. Three photon monitors record the beam position: two photodiode arrays and a CCD camera.

Recognizing that the long-term beam position stability is affected by the positional stability of the ring components, (including the BPM's, both beam driven and optical) two measurement systems are being installed on the ring. We are placing 20 (soon to add 80 more) computer readable temperature sensors on various ring components: e.g. quadrupole stands and dipole stands. Changes in temperature that produce ring component position changes, especially in the vertical direction, will be monitored and correlated with beam position variation.

A hydrostatic leveling system (HLS) has been acquired. This is the same type of system used at ESRF. Once the system is tested and installed, the relative vertical position of ring components will be constantly monitored. The resolution of the system is at the $1\,\mu m$ level, with an accuracy $\leq 5\,\mu m$. It appears that some resolution is lost because of the need to move the sensing electronics away from the sensing head. This was necessary because the combined sensor and electronics is not meant to work in even modest external magnetic fields.

Another hydrostatic problem that we are just starting to investigate is the presence of ground water in the bedrock under the concrete floor that supports the ring. Shortly after a large water spill, several photon beamlines required realignment, indicating that the stored beam position had somehow been changed as a result of the water seepage under the floor.

As indicated above, Aladdin regularly runs at either 800 MeV or 1 GeV. The central orbit is in a different position at the two energies, causing some user beamlines to require either readjustment or, for some high resolution beamlines, simply to avoid using the 1 GeV beam altogether. Accompanying the change in position there is an excessively large increase in vertical beam size and a change in beam rotation of 6°. The size and rotation variations are consistent with changes in the ring coupling. Measurements have shown that the coupling varies almost linearly from 0.013 at 800 MeV to 0.029 at 1 GeV. Original dipole field data show the magnets "shorten" at fields corresponding to 1 GeV operation. This combined decrease in [B,ds and increase in coupling may be the cause of the different orbit, but there are still many unanswered questions. For example, why there are differences between BPM calibrations at the two energies, as much as 160 µm.

2.3 Short Term

In the realm of fast changes in beam position, frequencies faster than a few hertz, many problems have been identified and solved. The infrared beamlines are very sensitive to beam motion at the ac power line

frequency, 60 Hz, and its harmonics. The main ring dipole power supply has a 12-phase rectifier circuit, and horizontal beam motions at 720 Hz were quite large (See Figure 1). The cause was a large series inductor (choke) that was located close, about 40 cm, to the beam orbit. We relocated the choke and observed a large reduction in the 720 Hz horizontal beam motion (Figure 1).

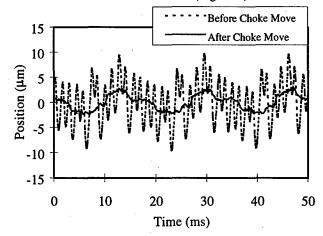


Figure 1: Reduction of 720 Hz Beam Motion

Figure 1 also shows residual 60 Hz beam motion. Several sources have been identified and either fixed or shortly will be fixed. The 60 Hz beam motion was reduced by a factor of 10 after four ac service transformers were relocated from adjacent to the beam orbit to about 3 m away [2]. Replacing the ac solenoids with a dc type removed the 60 Hz noise contribution of the ring sector valves. However, the actuators of the beamline front-end valves are also known to be a source of 60 Hz oscillations and will be replaced later this year. Also, the main rf system will be tested to verify that there is not some 60 Hz modulation that is affecting beam motion.

To reduce the 60 Hz beam motion even more, several improvements are scheduled. The main ring dipole magnet power supply will get a transistor passbank (there is none now) and each of the quadrupole and dipole power supplies will have new controllers, all with digital signal processors (DSP's).

3 SIZE STABILITY

3.1 General

Section 1 notes that a typical vertical beam size at a dipole source point is $85\,\mu m$. This size can vary depending on the level of coupling in the ring. Two operational regimes should be distinguished. The first is how the ring is set for users at the start of a user experimental run. At this time four skew quadrupoles around the ring can provide some control of beam size and rotation, and they are used to set beam size to a standard value. This can only set the beam size within

rather narrow limits, however, and more skew quadrupoles would be required to provide better-localized size control.

The main cause of variability in beam size during a user fill is the scanning of uncorrected undulators. The correction scheme used for each undulator is to shunt some current around the upstream and downstream vertically focusing quadrupoles. The amount of current shunted is a function of the peak undulator field. The main residual correction is almost entirely correction of the vertical tune. With this scheme the tune can be kept constant, but the smallest average vertical beam size variation observed during scanning is 2%. For many users, especially those employing experiments that rely on the difference between the above and below median plane polarization of the radiation, vertical beam size changes of 1% are too large. We are continuing to look at ways to further reduce these beam size changes. The most promising avenues are choosing a different operating point, keeping the global tune constant, dynamic control of skew quadrupoles, or, most likely, a combination of the above.

3.2'Long Term

Over the course of a user fill the beam size doesn't vary by more than $\pm 3\,\mu m$, with most of the variation occurring in the first 2 h, most likely from the well known effect of high current on beam size. From one fill to the next the starting beam size is dependent on the ring tunes and the initial state of the three undulators in regular use. The machine operators normalize the beam size at one optical monitor by varying skew quadrupole settings. This can and does lead to too much beam size variation at other sources around the ring. The normal operating point is relatively close to several weak resonances.

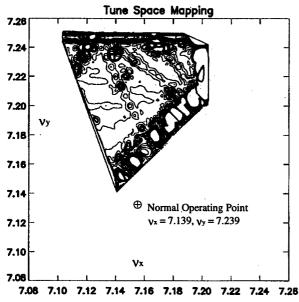


Figure 2: Tune Space near Operating Point

Figure 2 shows a beam size mapping of the tune space around Aladdin's operating point. At that point small changes in ring parameters, even scanning of well-compensated undulators, can cause small beam size changes. Under investigation is a permanent move to a different operating point. In the near future, usage of a software feedback loop to keep the tunes constant will become a normal mode of operation.

4 IMPROVEMENT PLANS

4.1 Diagnostic Stations

Besides the tune control, temperature monitors, and HLS mentioned above, four new diagnostic stations are in the design stage. These stations, one in each corner of the ring, will be dedicated to measurements of beam size, rotation, and position in both planes. Each station will have a CCD camera to look at the beam cross section and measure beam size. Also, each station will have a position sensitive device (PSD) to measure the position of the beam down to the 1 µm level. At least one of the stations will have additional linear photodiode arrays to look for high frequency beam motion. A prototype of the optical design has been tested, and the 45° mirrors that take the light into the stations have been procured. The stations should be operational by the end of the year.

4.2 BPM Electronics

Modern advancements in electronics have seen the increased use of digital signal processors (DSP's). To make use of this modern technology the electronics that measures beam position will be completely rebuilt to utilize DSP's. This will increase the resolution of the BPM system by a factor of 10.

- D. L. Huber, et al, 'SRC: Current activities and plans for the future', Nuclear Instruments and Methods in Physics Research A 347 (1994) 49-51.
- [2] W. S. Trzeciak and Staff, 'Aladdin, Present and Future', Proceedings of the 1997 Particle Accelerator Conference, Vancouver, B. C., Pg. 865.

INFRARED EDGE RADIATION BEAMLINE AT ALADDIN

T. E. May, <u>R. A. Bosch</u> and R. L. Julian, Synchrotron Radiation Center, University of Wisconsin-Madison, 3731 Schneider Dr., Stoughton, WI 53589

Abstract

An infrared beamline has been constructed at the 800 MeV electron storage ring, Aladdin. The beamline is located downstream of a short straight section, where it collects edge radiation produced by electrons exiting and entering the bending magnets at the ends of the straight section. Measurements at wavelengths of 1–5 μm suggest that the edge radiation is brighter than standard synchrotron radiation. When used for Fourier transform infrared (FTIR) microspectroscopy, the signal-to-noise ratio is 20 times that measured with a glower source. Several applications of the beamline are described.

1 INTRODUCTION

Long-wavelength radiation produced at the edge of a bending magnet was observed at the electron storage ring, Aladdin, in 1993 [1]. At the operating ring energy of 800 MeV, the visible light several meters downstream of a straight section forms an intense whitish spot on axis with angular extent of several mrad. The light distribution changes to that of ordinary synchrotron radiation as one moves horizontally off axis. Similar features are evident in photographs taken at the Daresbury Laboratory [2]. At a ring energy of 250 MeV, the visible spot on axis is less pronounced, while colored crescents (again with an angular extent of several mrad) are observed whose position and intensity depends upon the steering bumps introduced into the straight section. The bright spot on axis appears to be "edge radiation" produced at the edge of a bending magnet [3]. The crescents are apparently the result of small deflections in quadrupole magnets caused by steering windings and misalignments [4,5,6].

The measured spatial distribution of edge radiation at a wavelength λ of 1 μ m agrees with computations [7]. Using lenses to image the sources of 0.5 μ m radiation within a straight section, the most intense source was observed at the location of the downstream bending magnet edge [8]. Additional weaker sources were also observed, consistent with radiation produced in quadrupoles by small deflections (with deflection angle \leq 2/ γ , where γ is the relativistic mass factor [6]). From these images, the beam dimensions at the locations of the quadrupoles and edge were obtained, yielding very good agreement with theoretical values for horizontal beam sizes of ~400 μ m $\approx \lambda \gamma/2$. Reasonable agreement was also obtained for vertical beam sizes of ~80 μ m $\approx \lambda \gamma/10$ [8].

At the suggestion of O. V. Chubar, we investigated the possibility of using edge radiation for an infrared (IR) beamline at Aladdin. Computations indicated that an edge

radiation source might provide a greater brightness than ordinary synchrotron radiation, with a smaller opening angle [7]. In an experimental comparison of IR edge radiation and ordinary synchrotron radiation, described in Section 2, edge radiation allowed a greater flux to be imaged through pinholes smaller than 100 μ m with f/4 optics. This experiment suggests that the edge radiation is brighter, so it was decided to use an edge radiation source for the Aladdin IR beamline. To avoid conflict with insertion devices on the long straight sections, the IR beamline was constructed downstream of a short straight section, whose length is 3 m.

2 THE ALADDIN IR BEAMLINE

The IR beamline is located at Port 031, an on-axis port at the end of a short straight section. The entrance aperture is 30.5 mm horizontal x 22.3 mm vertical, located 1.4 m downstream of the entrance poleface of a 30° bending magnet. Imaging of visible radiation shows that the edge radiation source is located 10 cm upstream of the poleface. The measured bending magnet fringe field is approximately a linear ramp extending 10.8 cm from the poleface. Thus, the source is located at the entrance of the bending magnet fringe field, where the electron is deflected from its straight-line trajectory through an angle exceeding $1/\gamma$ in several cm. The entrance aperture is,

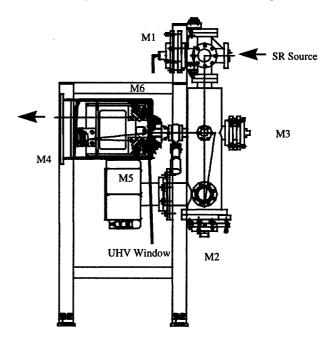


Figure 1. A diamond UHV window separates the two mirror boxes of the IR beamline.

therefore, located 1.5 m downstream of the source, subtending 20 mrad horizontal x 15 mrad vertical.

Figure 1 shows the mirror boxes of the IR beamline. Each mirror box can be adjusted vertically and horizontally as a single unit to align to the port. Three mirrors in ultra-high vacuum (UHV) bring the IR light to a focus near its passage through a UHV window. Further downstream, three mirrors in rough vacuum collimate the light and transfer it to an FTIR interferometer. All mirrors are gold-coated; two are f/6 sphericals. The UHV window is type IIa diamond, 10 mm in diameter, 0.25 mm thick, with a 1.87° wedge angle to prevent "channel" fringes. The beampipe is 2-inch stainless steel, terminated by a brass cell holding a 5-cm diameter KBr window.

Downstream of the KBr window, a Nicolet Instrument Magna 550II FTIR bench with external source port is centered between two microscopes. Kinematic mounts support the FTIR bench and microscopes. The path length of the beam is modulated by the interferometer on the bench; the beam may be directed either to the sample compartment or to the side-port microscopes. A Spectra-Tech IR-Plan microscope is mounted on the right side of the FTIR bench. It has a 15x, 0.58 numerical aperture (n.a.) Schwarzchild objective, 10x, 0.71 n.a. condenser, and an integral 0.25-mm mercury cadmium telluride detector. The left side has a NicPlan microscope with computer-controlled sample stage and both 15x and 32x objectives. Apertures at focal planes upstream and downstream of the sample allow the beam to be restricted at the sample plane, permitting the highest spatial resolution.

At the operating ring energy of 800 MeV, FTIR measurements were performed to compare the edge-radiation source with a standard synchrotron radiation ("bend") source located in the uniform-field region of a bending magnet. For this comparison, standard synchrotron radiation was extracted through an aperture of size 28 mm x 14 mm located 1.3 m downstream of the source, subtending 22 mrad horizontal x 11 mrad vertical. The edge radiation was extracted through an adjustable aperture 2.6 m downstream of the edge source, adjusted to

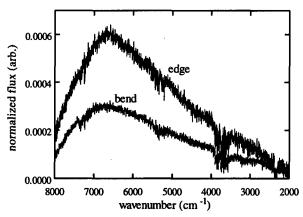


Figure 2. Flux focused through a 10 micron pinhole with f/4 optics, normalized to ring current.

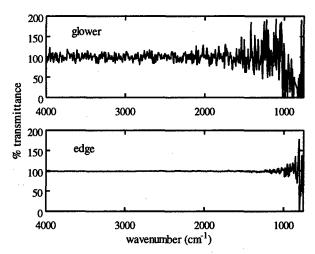


Figure 3. Transmittance data shows a 20-fold noise reduction with edge radiation compared to a glower.

also subtend 22 mrad x 11 mrad. The bend measurements were limited to wavelengths below 5 μ m because a sapphire window was used. The microscopes were unavailable at the time, so a brightness comparison was performed using pinholes of diameter 400, 100, 25 and 10 μ m. The spot, focused in the FTIR sample compartment by an f/4 mirror, was 110 μ m x 60 μ m. A 400- μ m pinhole blocked most of the room-temperature blackbody radiation that peaks at 1000 cm⁻¹.

The edge source produced less flux through the 400-µm pinhole, nearly-equal flux through the 100-µm pinhole, 70% more through 25-µm pinhole, and ~2 times as much flux through the 10-µm pinhole. Figure 2 shows current-normalized edge and bend flux through a 10-µm pinhole, collected for one minute at 4 cm⁻¹ resolution. Because more flux is focused through small pinholes with the edge source, the data suggest that the edge source is brighter. Thus, it was decided to use the edge-radiation source for the Aladdin IR beamline.

Figure 2 also shows that the relative noise levels are about the same with the edge and bend sources. Because FTIR spectroscopy is sensitive to noise at 60 Hz and its harmonics, the choke for the bending magnets' power supply and several transformers were moved away from the electron orbit; the choke circuitry was also modified. These actions reduced the electron beam motion, improving the signal-to-noise ratio of FTIR data by more than an order of magnitude over the levels of Fig. 2.

After reducing the 60-Hz noise, a noise comparison was performed between the edge radiation source and a glower. Figure 3 shows transmittance data through the NicPlan microscope, where a 10-µm pinhole was used at the sample stage while data was collected for one minute at 4 cm⁻¹ resolution. The rms noise level is 0.62 % transmittance (%T) over 100 cm⁻¹ for the edge compared to 12.5 %T for the glower, a 20-fold reduction.

3 APPLICATIONS

Conventional IR microspectroscopy requires sample areas of 20 μ m x 20 μ m or larger. The brightness of the Aladdin IR source permits a higher spatial resolution, as demonstrated by the following two examples.

To interpret the geological history of rocks, the fluid phase of the rocks may be analyzed. These fluids are commonly preserved as tiny 2–50 μ m fluid inclusions. The fluids can be a vapor, an aqueous or non-aqueous fluid, a silicate melt, or a combination. Inclusions exceeding 25 μ m in diameter are commonly studied using freeze/thaw techniques and visible microscopy; smaller inclusions must be studied spectroscopically.

Figure 4 shows infrared spectra of a 16-μm inclusion that has a 6-μm "bubble" inside it. The upper spectrum shows the overall "liquid" phase. The peak at 2350 cm⁻¹ is CO₂, the broad peak around 3400 cm⁻¹ is H₂O, and the small peaks below 3000 cm⁻¹ are hydrocarbons. By changing the focus on the sample, the "vapor" phase in the bubble can be distinguished, as shown in the lower spectrum. This spectrum shows primarily CO₂.

Hippocampus tissue of Alzheimer's disease patients is characterized by the buildup of plaques. Previous studies of these plaques have involved staining techniques that can contaminate and modify the protein structure. Other studies have extracted plaques for external investigation. Because protein structure is dependent on the material surrounding it, conclusions obtained from extracted plaques can be erroneous. With FTIR microspectroscopy, the tissues can be mapped to study plaques, neurofibrillary tangles and corpora amylacea in situ.

The upper trace in Figure 5 shows the spectrum of a corpus amylaceum smaller than 10 µm in Alzheimer's white matter tissue. This is compared to the spectrum of the surrounding white matter. Note that the carbohydrate area around 1100 cm⁻¹ is enhanced. The amide I profile

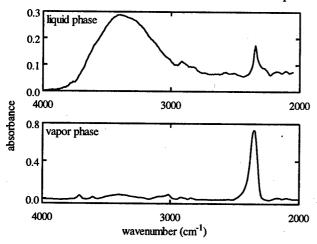


Figure 4. Measurement of a 16-μm fluid inclusion with a 6-μm vapor bubble. Measurement in transmission mode, 8 cm⁻¹ resolution, 128 scans. Data courtesy of P. Brown and T. Lee, Dept. of Geology, University of Wisconsin-Madison.

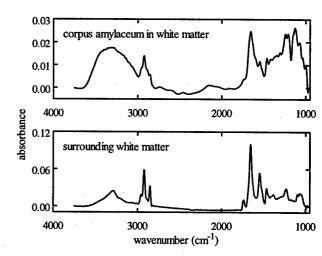


Figure 5. Measurement of Alzheimer's patient brain tissue showing the <10 μm corpus amylaceum and the white matter surrounding it, demonstrating different protein forms. Measurement in reflectance mode, 8 cm⁻¹ resolution, 256 scans. Data courtesy of K. Gough and P. Bromberg, Dept. of Chemistry, University of Manitoba.

around 1650 cm⁻¹ is quite different than for the white matter, indicating a change in the types of protein present. White matter is primarily ^a-helical while a slight shift in the carbonyl frequency and appearance of shoulders at 1630 cm⁻¹ and 1673 cm⁻¹ indicates the presence of ^β-sheet or aggregated ^β-strands in the corpus amylaceum.

4 ACKNOWLEDGMENTS

The authors appreciate valuable discussions with O. V. Chubar, M. A. Green, R. Reininger and W. S. Trzeciak. This work was supported by NSF grant DMR-95-31009.

- [1] M. A. Green, R. A. Bosch and W. S. Trzeciak, "Study of radiation along the extended axis of the long straight sections", in Synchrotron Radiation Center 1994 Yearbook (1994) p. 63.
- [2] Daresbury 1984/5 Annual Report, Daresbury Laboratory, Warrington, Cheshire, UK (1985) front cover.
- [3] O. V. Chubar and N. V. Smolyakov, J. Optics (Paris) 24, 117 (1993); Proc. 1993 IEEE PAC, 1626 (1993).
- [4] R. Coïsson, Phys. Rev. A 20, 524 (1979).
- [5] R. A. Bosch, M. A. Green and W. S. Trzeciak, "Incidental radiation along straight section axes in an electron storage ring", SRC Technical Note SRC-158, Synchrotron Radiation Center (1996).
- [6] R. A. Bosch, Nucl. Instr. And Meth. A 386, 525 (1997).
- [7] R. A. Bosch, T. E. May, R. Reininger and M. A. Green, Proc. SRI '95 (CD-ROM), Rev. Sci. Instrum. 67, 3346(K) (1996).
- [8] D. Mossessian, "Infrared radiation from the Aladdin U3 straight section", SRC Technical Note SRC-171, Synchrotron Radiation Center (1996).

COMPUTATION OF FLUX INTO THE ALADDIN INFRARED BEAMLINE

R. A. Bosch, Synchrotron Radiation Center,

University of Wisconsin-Madison, 3731 Schneider Dr., Stoughton, WI 53589

Abstract

The Aladdin infrared beamline extracts edge radiation downstream of a short straight section of the 800 MeV electron storage ring, Aladdin. For wavelengths of 1–1000 microns, the flux into the beamline is computed. The flux rolls off at wavelengths exceeding ~100 μm , where the central cone of near-field edge radiation is no longer contained within the entrance aperture.

1 INTRODUCTION

The radiation from electrons entering or exiting a bending magnet (edge radiation [1,2,3,4]) may be used as a bright infrared (IR) source. Recently, an infrared beamline using edge radiation has been constructed downstream of a short straight section of the 800 MeV electron storage ring, Aladdin [5].

The bending magnet fringe field is approximately a linear ramp over a distance of 10.8 cm, while the uniform field region bends the electron orbit with a 2.083 m radius of curvature. An electron entering the magnet is bent through an angle of $1/\gamma$ in a distance d of 1.7 cm, where γ is the relativistic mass factor. Intense edge radiation may thus be expected for wavelengths $\lambda >> d/\gamma^2 = 7$ nm [6].

The straight section length L is 3 m, while the entrance aperture is at a distance R of 1.5 m from the downstream end of the straight section with dimensions of 30.5 mm horizontal x 22.3 mm vertical; its full angular extent is 20 mrad x 15 mrad. Near-field broadening is expected to diminish the flux through an aperture for $\lambda > \theta_{1/2}RLJ(R+L)$, where $\theta_{1/2}$ is the half-angle subtended by the aperture [7,8]. The horizontal aperture is expected to cut off flux for $\lambda > (10 \text{ mrad})^2(1.5 \text{ m})(3 \text{ m})/(1.5 \text{ m} + 3 \text{ m}) = 100 \,\mu\text{m}$, while the vertical aperture may cut off flux for $\lambda > (7.5 \text{ mrad})^2(1.5 \text{ m})(3 \text{ m})/(1.5 \text{ m} + 3 \text{ m}) = 56 \,\mu\text{m}$. Intense flux may therefore be expected for $7 \text{ nm} << \lambda < 56-100 \,\mu\text{m}$.

2 FLUX COMPUTATION

The electric field from an electron, in SI units, obeys [9]

$$\vec{E}(\vec{X}, \omega) = \frac{e}{4\pi\varepsilon_{o}c} \int_{-\infty}^{\infty} \frac{\hat{n} \times [(\hat{n} - \vec{\beta}) \times \vec{\beta}]}{(1 - \hat{n} \cdot \vec{\beta})^{2} R(t)} e^{i\omega t_{o}(t)} dt + \frac{e}{4\pi\varepsilon_{o}\gamma^{2}} \int_{-\infty}^{\infty} \frac{\hat{n} - \vec{\beta}}{(1 - \hat{n} \cdot \vec{\beta})^{2} R(t)^{2}} e^{i\omega t_{o}(t)} dt.$$
(1)

The first term on the RHS is the "acceleration field" describing far-field radiation. The second term is the "velocity field" which contributes in the near field. Here,

 $\vec{X} = (X, Y, Z)$ is the observer location, ω is angular frequency, c is the speed of light, $\vec{\beta}(t)$ is the electron velocity divided by c, e is the electron charge, and ε_o is the permittivity of free space. R(t) is the distance from the electron to the observer and $\hat{n}(t)$ is the unit vector pointing from the electron to the observer. The observer time t_o is related to the time t of radiation emission by

$$\frac{dt_o}{dt} = 1 - \hat{n}(t) \cdot \vec{\beta}(t) \,. \tag{2}$$

Consider an electron which enters the fringe field of a bending magnet, located at the coordinate origin, at time t=0. Let $R=|\vec{X}|$ and $\hat{n}(0)=(x,y,z)$ describe the distance and direction to the observer from the magnet entrance. Modeling the fringe field as a linear ramp over a distance l to the value B_y in the central region of the magnet, the normalized acceleration, $\dot{\beta}/\dot{\beta}$, obeys

$$a(t) = \begin{cases} (\omega_c / \tau) t & 0 < t < \tau \\ \omega_c & t > \tau \end{cases}$$
 (3)

where $\omega_c = eB/m\gamma$ is negative for a bend in the +x-direction, and $\tau \equiv l/\beta c$ is the fringe-field traversal time.

Letting
$$A(t) \equiv \int_{0}^{t} a(t')dt'$$
, we have

$$\vec{\beta}(t) = \beta(-\sin A(t), 0, \cos A(t)), \tag{4}$$

$$\vec{\dot{\beta}}(t) = \beta a(t)(-\cos A(t), 0, -\sin A(t)), \tag{5}$$

and

$$A(t) = \begin{cases} (\omega_c t^2 / 2\tau) & 0 < t < \tau \\ \omega_c (t - \tau / 2) & t > \tau \end{cases}$$
 (6)

Approximating $\sin A(t) \approx A(t)$ to evaluate the electron position (X_s, Y_s, Z_s) versus time gives

$$X_{e}(t) = \begin{cases} -\frac{\beta c \omega_{c} t^{3}}{6\tau} & 0 < t < \tau \\ -\beta c \omega_{c} \left[\frac{\tau^{2}}{24} + \frac{(t - \tau/2)^{2}}{2} \right] & t > \tau \end{cases}$$
 (7)

and $Z_{\epsilon}(t) \approx \beta ct$.

From eq. (2) we have, for $t_a(0) \equiv 0$

$$t_{o}(t) = \int_{0}^{t} \left[1 - \hat{n}(0) \cdot \vec{\beta}(t') dt' \right] + \int_{0}^{t} \left[\hat{n}(0) - \hat{n}(t') \right] \cdot \vec{\beta}(0) dt' + \int_{0}^{t} \left[\hat{n}(0) - \hat{n}(t') \right] \cdot \left[\vec{\beta}(t') - \vec{\beta}(0) \right] dt'$$
(8)

(10)

The first term on the RHS of eq. (8) is the expression for $t_o(t)$ applicable when the time-variation of $\hat{n}(t)$ may be neglected, i.e. for a distant observer. Its value is [2]

$$t_{o}(t) = \begin{cases} t(1-z\beta) + \frac{x\beta\omega_{c}t^{3}}{6\tau} + \frac{z\beta\omega_{c}^{2}t^{5}}{40\tau^{2}} & 0 < t < \tau \\ t(1-z\beta) + x\beta\omega_{c} \left(\frac{\tau^{2}}{24} + \frac{(t-\tau/2)^{2}}{2}\right) & t > \tau \end{cases}$$
(9)

The second term on the RHS of eq. (8) is approximately $\Delta t_o(t) = \left(x^2 + y^2\right) \left(\frac{\beta^2 c t^2}{2R} + \frac{\beta^3 c^2 t^3}{3R^2}\right) + \frac{\beta^2 c \omega_c x}{R} \left(\frac{t^4}{24\tau} + \frac{\beta c t^5}{30R\tau}\right) 0 < t < \tau$ $= \left(x^2 + y^2\right) \left(\frac{\beta^2 c t^2}{2R} + \frac{\beta^3 c^2 t^3}{3R^2}\right) + \frac{\beta^2 c \omega_c x}{R} \left(\frac{t^3}{6} - \frac{t^2 \tau}{4} + \frac{t \tau^2}{6} - \frac{\tau^3}{24} + \frac{\beta c}{R} \left(\frac{t^4}{8} - \frac{t^3 \tau}{6} + \frac{t^2 \tau^2}{12} - \frac{\tau^4}{120}\right)\right) \quad t > \tau$

The dominant contribution to the third term is

$$\delta t_o(t) = \begin{cases} \frac{\beta^2 c \omega_c x}{R} \left(\frac{t^4}{8\tau} + \frac{\beta c t^5}{10R\tau} \right) & 0 < t < \tau \\ \frac{\beta^2 c \omega_c x}{R} \left(\frac{t^3}{3} - \frac{t^2 \tau}{4} + \frac{\tau^3}{24} + \frac{\beta c}{R} \left(\frac{t^4}{4} - \frac{t^3 \tau}{6} + \frac{\tau^4}{60} \right) \right) & t > \tau \end{cases}$$

$$\tag{11}$$

The radiation emitted when t>0 may be evaluated by substituting eqs. (3)–(11) into eq. (1) and numerically integrating over $0 < t < t_{max}$, where t_{max} is sufficiently large that radiation from later times is negligible. By including eqs. (10) and (11), the expression for $t_o(t)$ is sufficiently accurate that computations agree with the results of Chubar [8] for observer locations within the Aladdin IR beamline entrance aperture. However, inaccurate results are obtained for the ordinary synchrotron radiation observed at larger horizontal displacements. This is an apparent limitation of the approximate expression for $t_o(t)$.

Now consider radiation emitted before this electron enters the straight section at time $t=-L/\beta c$, where L is the straight section length. If we instead consider an electron entering the straight section at time t=0, where $t_o(0)\equiv 0$, eqs. (3)–(11) apply with the substitutions: $R\to R+L$, $\tau\to \tau$, $0< t<\tau\to -\tau< t<0$, $t>\tau\to t<\tau$; the unit vector pointing from the upstream straight-section end to the observer must be substituted for (x,y,z). Inserting these expressions into eq. (1), we integrate numerically over $-t_{max}< t<0$ to obtain $\vec{E}(\vec{X},\omega)$. To convert $\vec{E}(\vec{X},\omega)$ to the observer time coordinate where $t_o=0$ when downstream edge radiation arrives, we multiply by the phase $\exp\{-i\pi R_n(\lambda)[L/R+\phi(X,Y)^2L/(R+L)]\}$, where $R_n(\lambda)\equiv R/(\lambda\gamma^2)$ and $\phi(X,Y)\equiv \gamma(x^2+y^2)^{1/2}$.

Lastly, the velocity field from the straight section is [7]

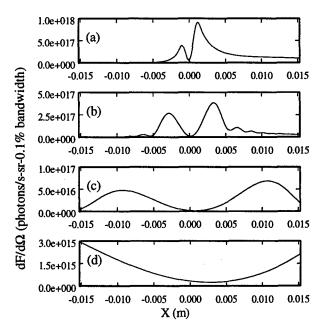


Figure 1. Flux density 1.5 m downstream of the entrance edge of an Aladdin bending magnet preceded by an infinitely-long straight section, for an electron current of 200 mA and energy of 800 MeV. Flux density is plotted versus horizontal position in the plane of the electron orbit, for electrons deflected in the positive x-direction. (a) $\lambda = 1 \, \mu m$. (b) $\lambda = 10 \, \mu m$. (c) $\lambda = 100 \, \mu m$. (d) $\lambda = 1000 \, \mu m$.

$$E(\vec{X}, \lambda) = \left(\frac{e\gamma}{\pi\varepsilon_{o}cR}\right) \left(\frac{e^{i\pi R_{n}(1-\phi^{2})}}{\phi}\right) \int_{\frac{R\phi}{R+I}}^{\phi} \frac{w}{(1+w^{2})^{2}} e^{i\pi R_{n}\phi(w-1/w)} dw$$
 (12)

The x- and y- components of eq. (12) are obtained by multiplying by $x/(x^2+y^2)^{1/2}$ and $y/(x^2+y^2)^{1/2}$.

Summing the electric fields from the edges and the straight section gives the electric field from an electron. For a bunch length exceeding the observed radiation wavelength, the flux density from a current, I, is [9]

$$\frac{dF}{d\Omega} = \alpha \frac{\Delta \omega}{\omega} \frac{I}{e} \left(\frac{2R\varepsilon_{o}c}{e} \right)^{2} \left| \vec{E}(\vec{X}, \omega(\lambda)) \right|^{2}. \tag{13}$$

where the solid angle $d\Omega$ is defined with respect to the downstream bending magnet entrance.

3 RESULTS

Figure 1 displays the computed flux density 1.5 m downstream of an Aladdin bending magnet preceded by an infinitely-long straight section. The flux density in the plane of the electron orbit is plotted versus horizontal position X for locations within the IR beamline entrance aperture. For the wavelengths shown, λ exceeds R/γ^2 , so that near-field effects must be considered [7].

At a wavelength of 1 μ m, λ is slightly larger than R/γ^2 ($\lambda = 1.75R/\gamma^2$), and the velocity field makes only a small contribution. The peaks of flux density are approximately

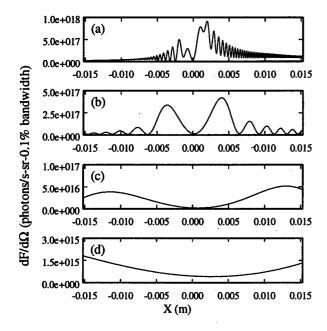


Figure 2. Flux density 1.5 m downstream of the entrance edge of an Aladdin bending magnet, for a current of 200 mA and straight section length of 3 m. Flux density is plotted versus horizontal position in the plane of the electron orbit, for electrons deflected in the positive x-direction. (a) $\lambda = 1 \, \mu m$. (b) $\lambda = 10 \, \mu m$. (c) $\lambda = 100 \, \mu m$. (d) $\lambda = 1000 \, \mu m$.

at the far-field angles of $\pm 1/\gamma = \pm 0.64$ mrad. For large positive values of X, the radiation is similar to ordinary synchrotron radiation. At wavelengths of 10–1000 μ m, λ greatly exceeds R/γ^2 , so that the peaks of the flux density occur at $X \approx \pm (\lambda R)^{1/2}$ [7]. For wavelengths of 1–100 μ m, the central cone of radiation lies within the horizontal aperture, while most of this cone lies outside the aperture for $\lambda = 1000 \ \mu$ m.

Figure 2 shows the computed flux density for the Aladdin short straight section length L of 3 m. At $\lambda = 1$ μ m, the straight section length exceeds the "radiation formation length" of $\lambda\gamma^2$. The interference between the two ends of the straight section results in fringe spacing small compared to the angular scale of the single-edge flux distribution. At the longer wavelengths of 10–1000 μ m, where λ greatly exceeds R/γ^2 and L/γ^2 , the peaks of the flux density occur at $X \approx \pm (\lambda R(R+L)/L)^{1/2}$ [8]. The peaks are ~20% further from the straight-section axis than with an infinite straight section length. Again, the central radiation cone is largely contained within the horizontal aperture for wavelengths of 1–100 μ m.

Figure 3 shows computed flux into the IR beamline for the Aladdin short straight section length of 3 m and also for an infinite straight section length. For $\lambda > 100 \, \mu m$, the flux is diminished because the central cone of near-field radiation is not contained within the entrance aperture, consistent with our estimate that the aperture will reduce flux for $\lambda > 56-100 \, \mu m$. We also show the flux into an

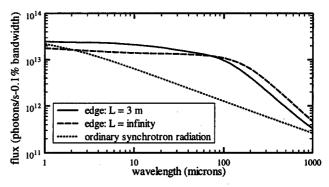


Figure 3. Computed flux into the Aladdin IR beamline for an electron current of 200 mA (solid line). The edge-radiation flux for an infinite straight section length and the ordinary synchrotron radiation flux into an identical aperture are also shown.

identical aperture located 1.5 m downstream of an ordinary synchrotron radiation source at Aladdin.

4 SUMMARY

The flux of edge radiation into the Aladdin IR beamline has been computed. The computations show a large flux at the wavelengths of 1–20 μ m typically used for Fourier transform infrared (FTIR) microscopy. At wavelengths exceeding ~100 μ m, the flux is diminished.

5 ACKNOWLEDGMENTS

The author appreciates discussions with O. V. Chubar, M. A. Green, R. L. Julian, T. E. May, R. Reininger and W. S. Trzeciak. This work was supported by NSF grant DMR-95-31009.

- [1] O. V. Chubar and N. V. Smolyakov, J. Optics (Paris) 24, 117 (1993); Proc. 1993 IEEE PAC, 1626 (1993).
- [2] R. A. Bosch, T. E. May, R. Reininger and M. A. Green, Proc. SRI '95 (CD ROM), Rev. Sci. Instrum. 67, 3346(K) (1996).
- [3] R. A. Bosch, Nucl. Instr. and Meth. A386, 525 (1997).
- [4] Y.-L. Mathis, P. Roy, B. Tremblay, A. Nucara, S. Lupi, P. Calvani and A. Gerschel, Phys. Rev. Lett. 80, 1220 (1998).
- [5] T. E. May, R. A. Bosch and R. L. Julian, "Infrared edge radiation beamline at Aladdin," these proceedings.
- [6] R. A. Bosch, Il Nuovo Cimento D20, 483 (1998).
- [7] R. A. Bosch and O. V. Chubar, Proc. SRI '97, Tenth US National Conference, AIP Conf. Proc. 417 (AIP, NY, 1997) p. 35.
- [8] O. V. Chubar, "Presentation of a computer code and results on a common problem," in Workshop on Infrared Synchrotron Radiation, 1st Meeting: The Source, organized by J.-L. Laclare, M.-P. Level and P. Roy (1997).
- [9] J. D. Jackson, Classical Electrodynamics, 2nd ed. (Wiley, NY, 1975) p. 670.

TEN YEARS OF COMPACT SYNCHROTRON LIGHT SOURCE AURORA

T. Hori

Laboratory for Quantum Equipment Technology, Sumitomo Heavy Industries, Ltd. 1-1 Yato-machi 2-chome, Tanashi, Tokyo 188-8585 Japan

Abstract

From mid 1980's, we have been developing compact SR rings named AURORA. The first one, AURORA-1 (A1), which employed a superconducting magnet to make the ring as compact as possible, has unique features came from its constitution, one circular 360° bending with no focus magnets. After observed first SR in 1989, we continued to improve the whole system, then transferred to Ritsumeikan Univ. in 1995. It has been in routine operation since then. In parallel with the A1's improvements, we started developing another concept in early 1990's. We adopted normal conducting magnets instead of superconducting's to the second, AURORA-2 (A2), keeping compactness by increasing the bending field, 2.7 Tesla, as high as somewhat comparable to the superconducting's. The most outstanding feature of A2 lies in the bending magnets, whereas the configuration of A2, racetrack, is very conventional. There are two versions in A2; one pursued compactness, the same purpose as A1, for X-ray lithography, and the other modified for scientific research taking advantage of its capability of accommodating insertion devices (ID's). In 1997, the latter was installed in Hiroshima Univ. as HiSOR in combination with two undulators. On the contrary, the former has been in commissioning at our Tanashi Works.

1 INTRODUCTION

A compact synchrotron light source has been being developed since mid 1980's from the viewpoint of optimization for industrial use, especially for X-ray lithography. AURORA was originally designed under the trends of those days in applying superconducting technology to such the small SR rings. A1, the world's smallest SR ring, is quite unique by its constitution of a single-body superconducting bending magnet, to which the function of weak-focusing is added to avoid additional focusing magnets. To make the system compact as a whole, a 150-MeV racetrack microtron was newly developed as a reliable and stable injector. The operation of the total system is quite simple, therefore to be suited for industrial application. Extremely small beam size in vertical, originated from very weak x-y coupling, is another attractive feature for scientific experiments.

It proved somehow inadequate to the industrial system, however, because of rather a long maintenance period and recovery time from failure. We thus concluded to adopt room-temperature magnets avoiding superconducting technology in the second version under the restriction of maintaining A1's compactness. It was achieved by an innovative idea of dipole magnets that brought us enough a high magnetic field for normal conducting magnets.

We have some flexibility in the design of new AURORA, depending on how to use straight sections of the racetrack ring. One which pursued compactness by the shortest straight section is called AURORA-2S (A2S), where S means Q-Singlet in the straight section. This quadrupole acts on horizontal focusing, whereas edge-focusing on vertical. The other having 3-m free space in the straight section is called AURORA-2D (A2D), where D means Q-Doublet. A2D has 4-sets of the doublet. Two types of ID, undulator and/or wiggler, are available for A2D. A2D in combination with two undulators was constructed in 1997 as HiSOR. Furthermore, the capability to install even a superconducting wiggler in such a compact ring as A2D using the low-energy-injection scheme was also proved by the other A2D.

2 THE FIRST AURORA (A1) [1-5]

A1 is the only circular ring in the world, which is the ultimate shape of compactness. The ring's outer diameter is ~3m, whereas the orbit diameter is 1m. The ring is unique because of its injection method using half-integer resonance. A1 is one of typical superconducting SR rings of those days, however, which was considered inevitable to produce a compact one. After the end of R&D, A1 was moved to Ritsumeikan University who established SR Center in 1996.



Fig. 1 Whole view of AURORA facility at SR Center in Ritsumeikan University.

Soft X-rays are intensively used for various analyses in material science. Micro-machining is one of unique applications, where LIGA and TIEGA (Teflon Included Etching Galvanicforming) are included. Some of 16 beam lines in total are able to use photons even at 3m distance from the source point, which is one of a merit of self-shielding. It means that the users can greatly benefit by a higher photon density than that of other rings. In addition, it was recently measured by

interferometer that the beam size σy is quite small, 17µm, in spite of a larger emittance than 10^6 m rad [6]. The beam is usually maintained 0.14mm of σy , however, to avoid too short Touschek lifetime. Thus, the ring is operated twice a day of injection, starting from 300mA stored current and terminated at about 150mA after 6 hours of accumulation.

3 THE SECOND AURORA (A2) [7, 8]

A2 is a compact ring of racetrack type using normal-conducting magnets, which takes over many advantages of A1, the 150-MeV injector microtron [9], cryopanels for high vacuum, self-shielding function, etc.

3.1 HiSOR — A2D with undulators [10, 11]

One A2D with two undulators was built at Hiroshima Synchrotron Radiation Center (HSRC) as HiSOR, which was established in 1997 by Hiroshima University. The most outstanding feature of HiSOR lies in these linear and helical undulators. These devices offer the users higher flux densities than 10^{15} photons/sec/mrad²/0.1%b.w. at 300 mA of the specified current, covering a spectral range from a few to hundreds eV.



Fig. 2 Overall view of HiSOR at HSRC in Hiroshima University.

In the early stage of A2D's commissioning, we recorded 318 mA of stored current at 700 MeV, starting acceleration from 384 mA of 150-MeV injected beam which resulted in 83% of acceleration efficiency. After the completion of vacuum system upgrading, the beam lifetime was improved to 10 hours at 100 mA, where the vacuum pressure was 1×10^9 Torr on the average. The operation cycle has reduced to twice a day from three times a day since then. The integrated current has passed beyond 100 A·Hr. At present, ten of sixteen beam lines, two of them are for undulators, has already been occupied.

3.2 A2D with 7 Tesla Wiggler [12-15]

The system check of A2D with a superconducting wiggler was performed in 1997 within a very limited period, ~3 weeks of net commissioning, prior to the reassembling to A2S. The test was carried out under the very poor vacuum condition, ~1x10⁻⁷ Torr while beam injection and acceleration, because of no baking and aging process for beam ducts and vacuum chambers. The result was, however, very satisfactory for us.

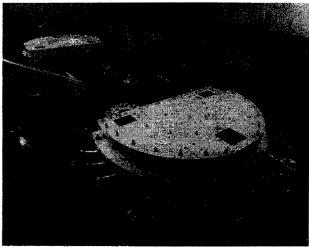


Fig. 3 Photo of A2D with 7 Tesla wiggler taken at our Tanashi Works.

We succeeded in proving the fact that even a compact ring with low-energy-injection scheme like A2D can accommodate a superconducting wiggler as an ID.

The test condition was as follows: The main pole of the wiggler is kept at 1.5 Tesla while injection, and ramped up to 7 Tesla taking 5.5 minutes of acceleration. The accumulated current was limited to 19 mA because of the poor vacuum in a short test period. We have acquired enough evidence, however, to confirm that the compact ring with 7 Tesla wiggler should work well notwithstanding a large amount of influence on the beam from the wiggler.

3.3 A2S [16, 17]

A2S is the world's smallest normal conducting SR ring. After the successful test of A2D, it was immediately disassembled and reassembled to A2S in late 1997.



Fig. 4 Photo of A2S before wrapped up in the shielding materials.

Successfully curing the coupled bunch instability using the new RF cavity by which harmful HOM's were greatly suppressed, we went beyond the specification within a month and recorded 719 mA of stored current so far. Commissioning of A2S has been continued to improve the lifetime, where 3 hours at 500 mA is observed after 120 A·Hr of the integrated current. We

found no difficulties in the acceleration when ramping more than 800 mA of injected beam up to 700 MeV in two minutes. The maximum injected beam already exceeded 1A. The reliability check had been done prior to covering the ring with radiation shielding materials as seen in Fig. 5, that is, more than ten days of 24-hours-aday operation terminated successfully.

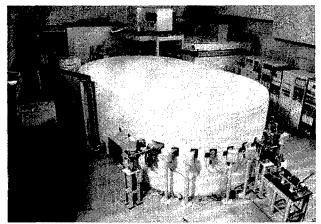


Fig. 5 Photo of A2S after coverd with the polyethylene neutron shielding.

4 CONCLUSION

More than a decade, we have been developing compact SR rings for industrial applications. Recently, the applications are extending from X-ray lithography to micromachining such as LIGA and TIEGA. A1 is convenient to obtain high dose rate with ease by placing a target close to the source.

We established a system of easy-handling by eliminating superconducting elements from A2. It was proved to accept either undulators or superconducting wigglers in A2D as ID's, thus even such a small SR ring as HiSOR is quite useful for scientific researches.

Another variation, A2S, has been proved to accumulate much more current than specified. The reliability was checked by a long-term continuous operation. Next step to be proved is its self-shielding capability. The ring is ready for exposure test of X-ray lithography, where a special beam line and a new SR stepper are in the final stage of preparation.

5 ACKNOWLEDGMENTS

The author is indebted to Y. Yamamoto of SR Center in Ritsumeikan Univ. for the information of superconducting AURORA, and to K. Goto of HSRC in Hiroshima Univ. for those of HiSOR.

- [1] N. Takahashi, "Compact Superconducting SR Ring for X-Ray Lithography", NIM B24/25 (1987) pp.425-428.
- [2] T. Takayama, "Resonance Injection Method for Compact Supercond. SR-Ring", NIM B24/25 (1987) pp.420-424.
- [3] H. Yamada, "Commissioning of aurora: The smallest synchrotron light source", J. Vac. Sci. Technol., Vol. B8, 1990, pp.1628-1632.

- [4] "SR Center Activity Report", 1996 version /1997 version, Ritsumeikan Univ.
- [5] H. Iwasaki, et al., "Compact Superconducting Ring at Ritsumeikan University", J. Synchrotron Rad. (1998) vol.5, pp.1162-1165.
- [6] T. Mitsuhashi, et al., "A Measurement of Beam Size of AURORA by the Use of SR-Interferometer at SR Center of Ritsumeikan University", 11th Symp. Accel. Sci. Tech., Japan (1997) pp.441-443.
- [7] T. Hori, et al., "AURORA-2: Compact Advanced SR Ring as an X-ray Source", 4th Int'l Conf. on SR Sources and 2nd Asian Forum on SR, Korea (1995) pp.148-158.
- [8] T. Hori, et al., "Development of New Compact SR Ring AURORA", APAC'98.
- [9] T.Hori, et al., "Improvement of 150 MeV Racetrack Microtron", PAC'91, pp.2877-2879.
- [10] K. Yoshida, et al., "Compact Synchrotron Light Source of the HSRC", J. Synchrotron, Rad. (1998) pp.1176-1179.
- [11] K. Yoshida, et al., "Commissioning of Compact Synchrotron Radiation Source at Hiroshima Univ.", APAC'98.
- [12] T. Takayama, et al., "Compact Synchrotron Radiation Source AURORA-2 with 2.7T Normal Conducting Bending Magnets", EPAC'96, pp.709-711.
- [13] H. Tsutsui, et al., "Aperture Calculation of AURORA-2D Compact Electron Storage Ring with a Superconducting Wiggler", PAC'97.
- [14] T. Hori, "Present Status of AURORA-2D", 11th Symp. Accel. Sci. Tech., Japan (1997) pp.534-536.
- [15] T. Hori, et al., "Operation Results of Compact SR Ring AURORA-2D with 7T Wiggler", EPAC'98, PP.581-583.
- [16] H. Miyade, et al., "Initial Commissioning of Dedicated SR Ring AURORA-2S for X-Ray Lithography", EPAC'98, pp.2413-2415.
- [17] H. Miyade, et al., "Beam Test of Compact SR Ring AURORA-2S for X-Ray Lithography", this conference.

	A2S	A2D+W	A1
Energy (GeV)	0.70	0.70	0.575
Stored current (A)	0.5 (1.0)	0.3	0.3
Circumference (m)	10.97	21.95	3.14
RF voltage (kV)	160	220	120
Harmonic number	7	14	2
RF frequency (MHz)	191.36	191.24	190.86
Energy loss (keV/turn)	24.42	29.07	19.34
Tune: horizontal	1.46	1.59	0.797
Vertical	0.73	2.10	0.604
Natural ε (π mm·rad)	0.528	0.935	1.68
Radiation damping:			
horizontal (msec)	2.13	5.60	1.3
vertical (msec)	2.10	3.53	0.43
longitudinal (msec)	1.04	1.49	0.16
Bunch length (mm)	26.5	36.2	52.0
Touschek life (hour)	20.	9.9	*(0.5)
Bending field: B (T)	2.7	2.7	3.8
n-value	0.0	0.0	0.365
QF (T/m)	12.5	10.9	
QD (T/m)		-12.3	

Table 1 Parameters of A2S, A2D+wiggler, and A1. *under the extremely small ex-ey coupling (~2x10⁴)

BEAM TEST OF COMPACT SR RING "AURORA-2S" FOR X-RAY LITHOGRAPHY

D. Amano, T. Hori, <u>H. Miyade</u>, H. Murata, T. Takayama Research & Development Center, Sumitomo Heavy Industries, Ltd. 2-1-1 Yato-cho, Tanashi-city, Tokyo 188-8585 Japan

Abstract

From January 1998, we started the beam test of "AURORA-2S" (A2S) with the same method as used for "AURORA-2D" (A2D) and were able to accumulate 0.7GeV-electron beam in a comparatively short period. In the mean time, though, we found some problems while injection which were serious not for A2D but for A2S. In September 1998, however, we have succeeded in managing such the problems and obtained the following results so far; more than 1A of injected current with maximum increasing rate of 640mA/min, and stored current exceeding the specification 500mA with typical acceleration efficiency over 80%. Since then the A2S has been operated without any serious troubles, in February 1999 the integrated current exceeded 110A.H and the beam lifetime reached 150min at 500mA. Moreover the acceleration efficiency increased to 97%.

1 INTRODUCTION

"AURORA-2" (A2) is a new type compact SR source. The outstanding feature lies in normal conducting bending magnets excited up to 2.7 Tesla, therefore operation and maintenance of the ring are simplified in the results compared with the superconducting's[1].

One of two types of A2 is "AURORA-2D" (A2D) for the scientific research. A2D has two long straight sections where insertion devices can be installed. A2D is at Hiroshima University, named HiSOR, with two undulators and has been routinely operated since 1997[2].

The other is "AURORA-2S" (A2S), which is optimised for the industrial use, mainly X-ray lithography. For A2S the straight sections are shortened and the whole size becomes as small as possible. A2S is designed as the size of the electron beam keeps uniformity in the bending magnet, therefore it can provide same light through each port. Furthermore lead and polyethylene surround the whole machine for radiation shielding so that the wall of the machine room can be thinned.

Parameters of A2S are summarised in Table 1 and the schematic view is shown in Fig. 1.

Table 1:Parameters of AURORA-2S				
Energy: Storage	0.7	GeV		
Injection	0.15	GeV		
Circumference	10.97	m		
Harmonic number	7			
RF frequency	191.2	MHz		
Energy Loss	24.42	keV/turn		
Tune: horizontal	1.46			
vertical	0.73			
Natural emittance	527.6	π nm.rad		
Radiation damping:				
horizontal	2.13	msec		
vertical	2.10	msec		
longitudinal	1.04	msec		
Touschek life time	6.6	hours		
		(at 1A)		

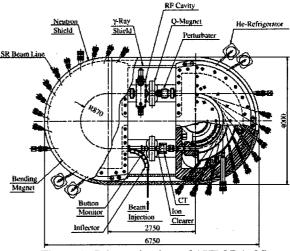


Figure 1: Schematic view of AURORA-2S

2 BEAM TEST OF A2S

2.1 Results and Problems of the First Beam Test

First we constructed A2D in our laboratory and made a performance test in 1997. After obtaining satisfactory results[3],[4] the A2D was reassembled to A2S.

The first beam test was started from January 1998 with the same method of beam injection, acceleration, and

^{*} Email: Hrk_Miyade@shi.co.jp

accumulation as used for A2D[3], and then we succeeded in accelerating the electron beam up to 0.7GeV in about a week. After then we optimised various parameters and finally obtained the following results[5].

Maximum injection current: 340 mA
Maximum stored current: 110 mA
Acceleration efficiency: 70 %

The exciting rate of the main magnetic field was 6A/s in constant and the time during excitation was about 2min.

After that, however, we found some problems while injection which were serious not for A2D but for A2S and we could not get better performance. The problems were as follows:

- The beam could not be injected at the designed operation point (vx=1.46, vy=0.73), but only at a different point (vx~1.3, vy~0.8).
- The instability might occur. Changing in position of the tuners in the cavity could diminish it a little. But it was powerless in the rapid varying situation such as in acceleration.
- Radiation from the light port was abnormally intense.
 It might be suggested that much of the electron beam were lost at the ion clearer in the bending magnet.

2.2 Counterplans to the Problems

After that we found an effect of the perturbater (PTB), which is a kicker magnet for injection, with a simulation; such that during the excitation of PTB the circumference became too short in the operation at the designed point, then the difference between the revolution time and the RF cycle grew more and more, at last it reached 150 degrees in RF phase.

To correct the difference we tried the method that the frequency modulation (FM) was piled up on the RF in a series of pulses simultaneously with the excitation of PTB. The shape of the pulse was same as the excitation pattern of PTB, that was a half-sine wave with 1µsec width. The width of FM was about 500kHz at the peak.

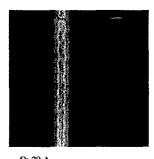
During the first beam test, in the cavity there were two tuners, a remote-controlled and a manual-controlled. After the test we made one more remote-controlled tuner, therefore we had been able to control two tuners remotely and one manually. Moreover we made the speed of motors of the tuners faster. With this we had been able to operate the machine in wider range and more quickly.

For the problem of the intense radiation we removed the ion clearer. In the vacuum chamber whose inner half height was 15mm, the ion clearer was installed with a distance of 4mm from the bottom of the chamber. Removing it, the aperture was extended from 26mm to 30mm.

As soon as we started the second beam test from September 1998, we found the effect of the

reconstruction; such that the beam could be injected near the designed operation point and the injection speed increased extremely. Then we succeeded in accumulation of the specification 500mA.

Fig. 2 shows the behaviour of the beam when the FM is on (left) or off (right). They were observed with the streak camera. In each figure the ordinate means the time with 120µsec full scale and the abscissa means the horizontal deviation of the beam with an arbitrary unit. The steep peak on the upper side represents the moment when the PTB was excited. In FM-OFF, a large oscillation, which may be a synchrotron oscillation, occurs according to the excitation of PTB. On the other hand in FM-ON the oscillation is inhibited.





Q: 29 A FM: ON Current: 270 mA PTB: 8.5 V RFLOW: 1000

Q: 29 A FM: OFF Current: 280 mA PTB: 8.5 V RFLOW: 1000

Figure 2: Effect of frequency modulation on RF

In the second beam test the following results were obtained;

Maximum injection current: 1020 mA
 Maximum stored current: >500 mA
 Maximum injection speed: 640 mA/min
 Acceleration efficiency: >80 %

2.3 Routine Operation

In November 1998 we installed a new cavity and a Landau cavity. They will be mentioned in the next section. In this subsection we will mention the third beam test.

The third beam test started from February 1999. The main purposes were ageing the vacuum chamber and lengthening the lifetime. To make an ageing efficiently the integrated current was needed as much as possible in a short period. So we needed to operate the machine without stopping in the test period and therefore some of members in our laboratory, they were not necessarily experts on the operation, were needed to operate it. From November 1998 to February 1999 we made an effort to simplify the operation for the amateur operators but not to increase the stored current nor to research the effect of the new and the Landau cavities.

The test had been done for two weeks (272 hours) with stored current of 500mA routinely. There were no devices damaged or troubled during the test, so we could make sure the high reliability of A2S. Finally the integrated current exceeded 110A.H (including 25A.H before the test) and the lifetime" reached 150min at 500mA and 240min at 300mA(see Fig.3). Moreover the injection efficiency increased to more than 97 %. However these were not satisfactory results, because the lifetime was shorter than we expected. This means the ageing was not enough. In fact the vacuum pressure in the main cavity was 1.0x10⁶Pa at 500mA and was an order of magnitude higher than our expectation. To reach the enough vacuum pressure and the satisfactorily long lifetime, we need more several hundreds A.H or the pumping system should be reinforced.

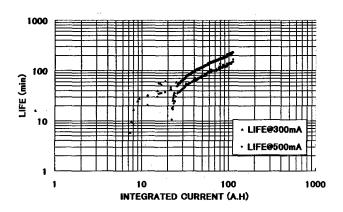


Figure 3: Integrated current and lifetime

3 NEXT STEP

With the above test the performance of A2S has reached almost full specification. But there still exist some problems. One of them is the existence of the instability. We can still observe the synchrotron oscillation occurs even in storing beam with the energy of 0.7GeV. Even under the instability we could accumulate the beam up to 500mA and the light from the ring had no problems for use, however it might disturb trying to accumulate the beam more than 500mA.

The instability is caused by a higher order mode electromagnetic field (HOM) in the cavity. So we designed and constructed a new cavity, which had less HOMs than the old cavity had (see Fig. 4). Moreover also a Landau cavity whose fundamental frequency is three times higher than the main cavity's was constructed. The new cavity and the Landau cavity have already been installed in the ring in November 1998.

#The lifetime ' τ ' is defined as follows;

$$\tau = -I/(dI/dt)$$

Our next step is to diminish the instability with the new cavity and the Landau cavity, and to achieve the upgraded goal, 1000mA of stored current at 0.7GeV.

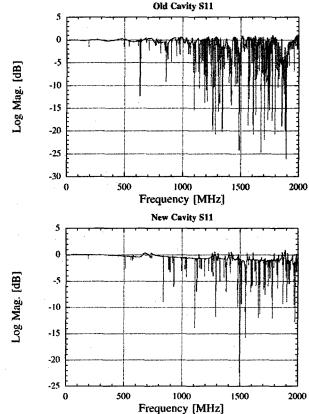


Figure 4: Characteristics in frequency with the old (upper) and the new (lower) cavities

- [1] T. Hori, et al., "AURORA-2: Compact Advanced SR Ring as an X-ray Source", 4th Int'l Conf. On SR sources & 2nd Asian Forum on SR, Kyongju, Korea (1995) pp.148-158
- [2] K. Yoshida, et al., "Commissioning of a Compact Synchrotron Radiation Source at Hiroshima University", APAC'98, KEK, Tsukuba, Japan, March 23-27 1998
- [3] T. Hori, "Present Status of AURORA-2D", 11th Symposium on Accel. Sci. and Tech., Harima, Japan (1997) pp.534-536
- [4] T. Hori, et al., "Operation Results of Compact SR ring AURORA-2D with 7Tsla Wiggler", EPAC'98, Stockholm, Sweden (1998) pp.581-583
- [5] H. Miyade, et al., "Initial Commissioning of Dedicated SR Ring "AURORA-2S" for X-ray Lithography", Epac'98, Stockholm, Sweden (1998) pp.2413-2415

MACHINE STUDY AND IMPROVEMENT OF THE HLS STORAGE RING

Y. Jin*, Z.Liu, W.Li, Y.Li, A.Zhou, W.Zhang, O.Jia, B. Sun, NSRL, USTC, Hefei, China

Abstract

The machine studies and improvements for the HLS storage ring are presented here. Since 1993 some beam instabilities such as head-tail instability and bunch lengthening as well as beam-cavity interaction have been observed and studied. The ion-trapping phenomenon is being studied. An RF knock out system for single bunch or for non-uniform filling to get high beam current has been installed into the ring and got some good results. A superconducting wiggler of 6 Tesla and an optical klystron (OK) used for FEL experiments as two insertion devices have been installed into the HLS. The wiggler has been commissioned and got more than 100 mA beam current. In order to make further improving performance of the machine, a Phase-II Project is going on.

1 INTRODUCTION

The HLS (Hefei Light Source) is a second generation synchrotron radiation source. It consists of an 800 MeV storage ring and a 200 MeV linac injector. It was constructed in 1989 and the first stored beam was got on April 26, 1989. The machine commissioning was completed in June 1991[1]. The main body of the HLS is a storage ring. The lattice of the storage ring is TBA structure[2]. It is a separated function strong focusing type. The circumference of the ring is 66.1308 meters. Its critical wavelength is 24 Å. The harmonic number is 45. There are four periods with four long straight sections of 3.36m each. A superconducting wiggler of 6 Tesla has been installed in the long straight section that the RF cavity had occupied. An optical klystron has also been installed in the another long straight section of the ring.

The lattice of the storage ring has two different operating configurations: (1) GPLS (General Purpose Light Source); (2) HBLS (High Brilliance Light Source). The configuration of GPLS is in routine operation now; the HBLS is a low emittance configuration (ϵ_x =13.5 nm), because of some difficulties for injection, is not in operation yet. But after the Phase-II project, the injection system will be rebuilt, the HBLS configuration will be put in operation.

2 MACHINE STUDIES

We have carried out some beam instabilities research in HLS storage ring. It includes head-tail instability, bunch

*Email: jin@ustc.edu.cn

lengthening and energy spread widening, beam-cavity interaction, etc. The ion trapping is being studied.

2.1 Head-tail Instability

The current threshold of the head-tail instability of the HLS storage ring that calculated by Sacherer formula is about 40 µA per bunch only, but actual current threshold of head-tail instability in HLS storage ring that measured is about 2.1 mA per bunch. The experimental value is about 50 times larger than the theory value. After researched, we found that the clearing electrodes existing in the vacuum chamber played the role of the Landau damping[3]. There are 17 clearing electrodes distributed along the vacuum chamber of the whole storage ring in order to eliminate the ion trapping. They are added DC voltage of 800-1000 volts. They will produce an electric field of dipole, quadrupole, sextupole, octupole, etc. The octupole component would produce a tune spread about 1×10^{-3} in the betatron oscillation of the particles in a bunch. The tune spread will stabilize the beam by Landau damping, and increase the current threshold of the head-tail instability.

2.2 Bunch Lengthening and Energy Spread Widening

The bunch lengthening and energy spread widening were observed in the HLS storage ring. The bunch length was measured by a digital oscilloscope of 20 GHz. The energy spread was measured by decreasing the longitudinal acceptance via lowering the RF voltage until the longitudinal quantum lifetime becomes dominant. Then we can get the energy spread from measured quantum lifetime and the height of the RF bucket. The experiment results show that as the current increase from several mA to 130 mA, the bunch length (σ_s) has a lengthening from 3.8 cm to 10.33 cm. The experiment results also show that the energy spread widening occurred at about 0.2 mA per bunch, which is the current threshold of the longitudinal instability. While the beam current reached 2 mA per bunch, the energy spread from 4.6×10^{-4} goes up to 5×10^{-4} [4].

2.3 Beam-Cavity Interaction

Research of the beam-cavity interaction in the HLS storage ring has gotten some progress. Two kinds of longitudinal oscillation of the beam were observed in HLS storage ring. The frequency of the first one is 875.11 MHz, and the second one is 1541 MHz. They are

excited by the two HOMs (High Order Modes) of the TM_{012} and TM_{032} of the RF cavity respectively [4]. The storage ring working at 800 MeV, we did not observe beam loss due to the above two longitudinal oscillations. But in the case of injection at 200 MeV, we found the longitudinal oscillation induced by TM_{012} mode is dependent on the tuner position. If the tuner position is at 25.4 mm, the longitudinal oscillation of frequency 875.11 MHz is so strong that the beam accumulating is very difficult, and energy ramping from 200 MeV to 800 MeV, the beam may be lost. In this case, we can keep the tuner position off 25.4 mm, and the injection has no problem.

2.4 Ion Trapping Phenomenon

The ion trapping is being studied. It causes tune shift of betatron oscillation and beam blow-up in transverse direction. The tune shift was measured for beam current of 100 mA as $\Delta v=0.0015$ for vertical direction and corresponding neutralization factor η_i is 0.6%. There are two types of ion clearing electrodes in the storage ring. One of them is DC clearing electrode used to overcome attraction of beam potential to ions, the other is RF clearing electrode used to shake ions away from beam orbit. The measurement shows that the minimum clearing voltage is about 350V and the corresponding electric field is 46 V/cm for DC clearing electrode (for beam current of 77 mA). For RF clearing electrode, the best shaking frequency lies in 1.4-1.6 MHz range for CO⁺ ions. In addition, we found that the partial-filling injection modes can also overcome ion trapping. This study is being continued.

3 MACHINE IMPROVEMENTS

3.1 Miscellaneous Improvements

We have made a beam profile monitor of the storage ring, in order to measure beam cross-section and beam emittance. The monitor is composed of an imaging optical system and CCD TV camera. The image of the profile is displayed in the central control room [5]. We remade the cooling water loop for the bending magnets so that the local over-heating phenomena have disappeared. We have made a RF knock out (RFKO) system for single bunch research. The Hefei machine is usually operating at the multiple bunches configuration. There are totally 45 bunches in the storage ring. In order to satisfy requirements of time-resolved spectroscopy experiments and machine studies, the storage ring must operate in different configurations of single bunch, 3 bunches, 5 bunches, etc. From 1994, the R &D of an RF knock out (RFKO) system began. A prototype of RFKO has been completed now. Preliminary test has been carried out. The current of single bunch reached 30 mA in the storage ring. Using the RFKO system can achieve

to fill a part of the buckets to avoid multi-bunch instability and increase beam current. The maximum current reached 350 mA.

The other up-grade and improvement plans will put in the phase-II project.

3.2 Superconducting Wiggler

In order to extend the spectrum range of HLS from VUV to hard X ray, a 6T superconducting wiggler of one period with three poles was designed in 1994-1995, constructed in 1996, completed in 1997. It includes a main body of superconducting wiggler magnet and cryostat system, power supplies system, control system, helium gas recovery system, special vacuum chamber, etc. All of them were completed at the end of 1997. In the beginning of 1998, the wiggler was installed into the HLS storage ring. In March of 1998, the wiggler was preliminary commissioned with beam, and got a beam of more than 100 mA at 800 MeV in the storage ring. The peak value of the magnetic field of the wiggler reached 6.04 Tesla. The magnetic field ramp of the wiggler from zero to 6 Tesla spent 6 minutes, the rise speed is 1 T/min, and did not occur quench phenomenon. From October to December 1998, the superconducting wiggler and the XAFS beam line as well as experimental station were commissioned in combination and tested for 45 days, with the wiggler of 6 Tesla in successful operation. The specification of the wiggler is listed in table 1.

Table 1 Specification of the superconducting wiggler

Specification	Designed	Measured
Peak field	6 Tesla	6.04 Tesla
Main current	460 A	462 A
Compensation current	<20 A	<5 A
Field wavelength	200 mm	188 mm
Beam tube size (H×V)	90×24 mm ²	90×24 mm ²
Ramping rate	1 T/min	1 T/min
Critical wavelength	4.85 Å	4.82 Å

The main body of the superconducting wiggler magnet with cryostat was manufactured by Kurchatov Institute in Russia. The coils of the wiggler were made of Nb-Ti. The liquid He consumption is 25-30 liters per day. The performance of the wiggler satisfies design requirement. The wiggler is located on a long straight section at the down stream of the RF cavity. It will induce tune (vx, vy) shift and closed orbit distortion as well as dynamic aperture reduction. The calculation results show that the β_{vmax} will rise from 13m to 32m and v_v will shift from 2.58 to 2.678, that is near the 1/3 resonant line. The particle tracking shows that the dynamic aperture has been changed so much that injecting and storing beam is impossible. Therefore the lattice parameters must be compensated [6]. During the preliminary commissioning, we adjust two sets of quadrupole to reduce the v_y from 2.68 to 2.61 to avoid the 1/3 resonant line.

3.3 FEL

A pure permanent magnets Optical Klystron (OK) has been designed and constructed for Storage Ring FEL. It will be used for the coherent harmonic generation (CHG) experiments firstly. The total length of the OK is 1.944 m. It consists of three sections, one dispersion section and two undulator sections. Each undulator section is consists of 12 periods with period length 72 mm. The two undulator sections are identical. The magnetic field is 0.3 Tesla with gap 40 mm. Between the two undulator sections is a dispersion section of 216 mm, one period. The magnetic field of the dispersion section is 0.6 Tesla with gap 40 mm. They are assembled in a frame. The gap of three sections can be adjusted independently from 36mm to 140 mm. The Optical Klystron has been installed into the storage ring and commissioned. The experiments of spontaneous radiation have been carried out. The measured modulation factor of the spontaneous radiation spectrum is increased from 0.236 initially to 0.76. The further more work will be continued.

4 PHASE-II PROJECT

The Hefei Light Source was built in 1989. A series of important experiments have been completed at five stations, but some defects of the machine have also been exposed. In addition, the five existing beamlines and five experiment stations are obviously insufficient for such a dedicated light source, so a phase-II project was proposed in 1994. The main contents of the project are rebuilding and improving some parts or equipment of the machine, and adding 8 beamlines and 8 experiment stations. This project was approved by the government in 1996. It has been put into practice from FY 1997 and finished by 2001. The total budget is about US\$14 million. The main contents of the phase-II project include:

4.1 Machine Improvement

- (1) RF system: Make a new RF cavity and a new RF power supply. The cooling loop of the new cavity will be more reasonable and the frequency tuning capability will be larger than the old one. The RF power of the new transmitter will be larger than the old one.
- (2) Injection equipment: Use thyratrons for pulse switch of the kicker power supply instead of the spark gap of the old one. Put four kickers in the same straight section for injection instead of the three kickers in the three straight sections of the former injection scheme.
- (3) Power supplies for magnets: There are 180 DC power supplies for the magnets of the storage, transport line and linac. 40-50 DC power supplies need to be replaced with new ones, because some of them are not stable, and some of them are at high fault rate.

- (4) Vacuum chamber of the storage ring: Nonevaporable Getters (NEG) will be put in the downstream of each bending vacuum chamber to reduce dynamic pressure gradient of the storage ring vacuum chamber. Use hydraulic pressured bellows instead of the welded bellows. Increase vacuum monitoring points.
- (5) Control system and beam diagnostic: The original control system has no shared database and has little communication between microcomputers. The goal of updating this system is set up a local network consisting of two working stations, some servers and PCs. Set up a database. Improve beam diagnostic system, and enhance its function of failure judgment.
- (6) Linac: Use a 3 GHz solid microwave source to drive high power klystron instead of the medium power klystron. Improve the I/Φ/A unit, and improve the energy monitor and feedback system, etc.
- (7) Undulator: Plan to set up a permanent magnet undulator as an insertion device. Its wavelength range will be from 100 Å to 2000 Å. The brilliance of the undulator radiation will be higher than the bending magnet radiation by two to three orders.

4.2 Construction of 8 New Beamlines and 8 New Experiment Stations

- (1) Surface Physics (with angle-resolved photoemission);
- (2) X-ray diffraction and scattering;
- (3) LIGA technique;
- (4) Atomic and molecular physics;
- (5) Photo-acoustic and Photo-thermal spectroscopy;
- (6) Infrared and far infrared spectroscopy;
- (7) Soft X-ray magnetic circular dichroism;
- (8) Spectral radiation standard and metrology.

- [1] Y. Jin, Status of the Hefei Synchrotron Radiation Source, Proceedings of The Third Joint Symposium on Synchrotron Radiation Sources (Nov. 1992, Korea).
- [2] Y.Jin, Z. Liu et al, The Magnet Lattice of the Storage Ring for HESYRL, Proceedings of the International Conference on Synchrotron Radiation Applications (1989, Hefei, China).
- [3] L. Chen, B. Sun, J. Wang, Y. Jin, Single Bunch Instabilities in HLS Ring, Proceedings of the Workshop on Beam Instabilities in Storage Rings (July 1994, Hefei, China).
- [4] J. Dai et al, Study of Multiple Bunch Instability Oscillations for Hefei Synchrotron Radiation Storage Ring, Journal of China University of Science and Technology, Vol.27, No.4 (1997).
- [5] Z. Fang, G. Wang et al, Monitoring the Beam Profile in HLS with Synchrotron Light, N.I.M in Physics Research A 370 (1996).
- [6] N. Liu, Y. Jin, Z. Liu, The Influence of Superconducting Wiggler on HLS Storage Ring Lattice Parameters and Its compensation, Proceedings of The Sixth China-Japan Joint Symposium on Accelerators for Nuclear Science and Their Applications (Oct.1996, Chengdu, China).

BEAM ORBIT STABILITY AT TAIWAN LIGHT SOURCE

K.T. Hsu, <u>C.C. Kuo</u>, C.H. Kuo, H.P. Chang, Ch. Wang, H.J. Tsai, J.R. Chen, K.K. Lin, and R.C. Sah

Synchrotron Radiation Research Center
No 1. R&D Rd VI, Hsinchu Science-Based Industrial Park, Hsinchu, Taiwan

Abstract

Beam orbit stability has been one of the major accelerator improvement programs at the SRRC since the storage ring started to be operational in 1993. In the past several years, several tasks have been carried out to tackle the orbit stability problems, e.g., the air and cooling water temperature regulation, the electrical and electronic noise reduction, the orbit feed-forward and feedback systems, etc. This paper presents the current status of the beam orbit stability at the SRRC storage ring TLS.

1 INTRODUCTION

The Taiwan Light Source (TLS) of the SRRC has been operated successfully for more than 5 years. In the meantime, a number of accelerator developments have been instrumented and commissioned in order to upgrade the performance of the light source operation so that it can provide a stable, high quality synchrotron radiation light source to the user. These include the installation of the insertion devices and orbit feedback systems, the increase of the beam energy to 1.5 GeV, suppression of the mechanical vibration sources and electrical noises, stabilization of the air conditioning and water cooling temperature, cure of the coupled-bunch instabilities. The orbit stability is of primary importance for the light source users. In this report, we describe the recent status of the beam orbit stability at TLS.

2 IMPROVEMENT OF THE WATER AND AIR TEMPERATURE CONTROL

An intensive study and upgrade activity of the TLS water temperature control units as well as air temperature handling units in the past two years results in a quite remarkable improvement for the daily usage of the systems.[1,2] The typical variation in the normal operation days could be kept within $\pm 1^{\circ}$ C for the air temperature in the storage ring tunnel. The outlet temperature for the cooling water temperature systems could also be held within $\pm 2^{\circ}$ C. However, it was found that after a long shut-down the air temperature in the tunnel would take several hours or even a few days to get in an equilibrium state. It was also observed that after such a long shut down, the ring circumference decreased 1

mm or so. To keep the orbit constant, we also performed the tuning of the radio frequency in the daily operation of the storage ring. The aluminum beam pipe of the storage ring is water cooled in the synchrotron radiation side. It was noticed that the temperature variation of the beam pipe demonstrated a strong correlation with the beam orbit changes. The inlet temperature changes as well as the operation beam current caused the temperature fluctuations of the beam pipe. Figure 1 shows the inlet and outlet temperature of the aluminum water system, and beam pipe temperature in a test run. Notice that the initial stored current after refill was 200 mA. The beam orbit changes from beam position monitors in a test run are given in Figure 2. To reduce the water-temperaturedependent orbit change, we optimized the water control settings and as a consequence beam orbit oscillation was suppressed.

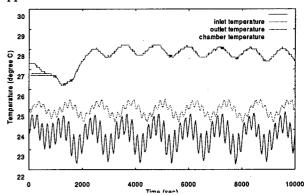


Figure 1: Water temperature (lower) and beam pipe temperature (top) in a test run.

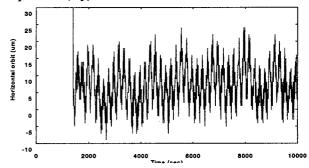


Figure 2(a): Horizontal orbit at one BPM with the condition given in Figure 1.

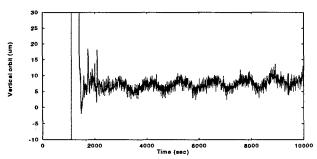
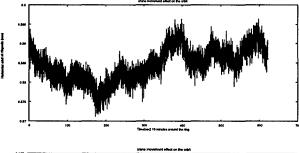


Figure 2(b): Vertical orbit at one BPM with the condition given in Figure 1.

3 MECHANICAL AND ELECTRICAL NOISE

Mechanical vibration such as air cooling fan at 18 Hz was observed couple years ago which induced beam oscillations in a few microns. This noise source has been eliminated and the fast beam orbit oscillation thus was within an acceptable level. Notice that during the users operation mode, the crane around the experimental hall is not allowed to move because its motion induces beam orbit change as shown in Figure 3(a) and 3(b). Although the fast feedback system can correct the beam orbit, the photon beam line components are still susceptible to this mechanical motion.

Electrical noise from the magnet power supply was well under control and it seemed to be not a major contribution to the orbit variation.



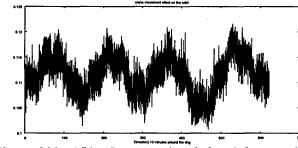
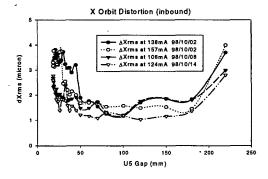


Figure 3(a), 3(b): Crane motion induced beam orbit change. The crane moves around the experimental hall for one turn.

4 INSERTION DEVICE EFFECTS

In the operation of the insertion devices, we need to change the magnetic gaps and the residual orbit thus is perturbed. To compensate such an orbit perturbation, the end-corrector strengths of the insertion devices are pre-set in the look-up tables. With such settings, the rms orbit perturbation could be reduced to a few microns as

illustrated in Figure 4(a) and 4(b). Since the current dependent BPM offset may contribute to the residual orbit readings. We have measured the current-dependent orbit readings using a scraper to reduce the beam current from 200 mA to 100 mA in 5 minutes and it showed that it could be varied by 10 μm or so. In the slow orbit feedback operation, these offsets were taken into account in the orbit data.



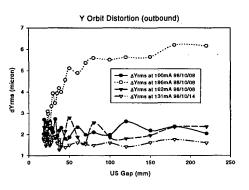


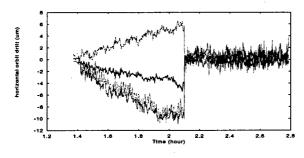
Figure 4(a), 4(b): Residual orbit of the ring as a function of the magnetic gap of one insertion device U5.

5 SLOW ORBIT CORRECTION

We have built a workstation-based slow orbit correction system. The bandwidth is about 0.1 Hz in both planes. We used almost all valid BPMs and correctors in the calculation of the correction matrix. Micado method was employed and only 5 most useful correctors were selected in the correction in both planes. Figure 5(a) and 5(b) depict the orbit with and without turning on the slow orbit correction system. Note that in this measurement, the fast orbit feedback system was off. It showed that the residual orbit drift could be down to less than 2 micron (the BPM readings were averaged 100 times).

6 FAST ORBIT CORRECTIONS

Digital global orbit feedback system has been implemented in the routine operation in the TLS. [3] The overall bandwidth of the system is about 10 Hz. Due to the lack of enough DSP processors, we can now only use a limited number of BPMs and correctors for both horizontal and vertical orbit planes. Presently, we



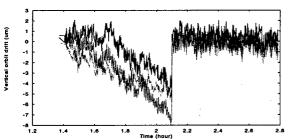


Figure 5(a), 5(b): Several BPM reading drifts with (right-hand side) and without (left-hand side) turning on slow orbit corrections.

emphasize the orbit correction in the vertical plane. However, in some demanding photon beam lines, we need to steer orbit locally in both planes.

We used SVD method to calculate the eigen-values of the corresponding corrector strengths. The achievable suppression level of the orbit fluctuation was $10\,\mu m$. As a matter of fact, the orbit noise spectrum revealed that it was buried in the BPM resolution region in a very short period, say 1 Hz. Therefore, at present, we optimized the system bandwidth in the low frequency region in favor of the suppression of the temperature-induced orbit drift. However, for the operation of insertion gap change as well as the EPBM photon beam line, which was constantly generating angular bump, we do need to tune the system to a wider bandwidth, say a few Hz.

7 OPERATION ACHIVEMENT AND FUTURE UPGRADE

In the daily operation in the user shifts, we turned on the fast orbit feedback system in the vertical plane and sometimes the horizontal fast feedback system as well. The system bandwidth was usually tuned to the low frequency part and the workstation-based slow orbit correction system did not help too much. In figure 6(a) and 6(b), we randomly choose the recent typical orbit data in the user shift. These BPMs are located at both upstream and downstream of the wiggler photon beam line. The BPM data are obtained from the ILC local signal processor and these are not averaged. As shown in figure 6(a), the horizontal orbit drift is about 10 micron in the first one hour after injection and then stay within 5 micron for the rest of the run in an 8-hour shift. In figure 6(b), the vertical orbit can be held within 10 micron in an 8-hour shift, and the orbit changes between refill are also within 10 micron.

In the future operation, we will strengthen the horizontal plane and we will also incorporate the photon BPM data as well as many local feedback systems in a package. The slow orbit correction could also be integrated. The mechanical rigidity will be examined. The full energy injection will be implemented soon. We will replace the exiting RF cavity with HOM-free ones to reduce coupled-bunch instability as well as orbit stability. The last, but not the least, the water cooling and air temperature control will be further improved.

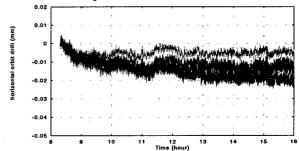


Figure 6(a): Typical horizontal orbit drift in one user shift for the BPM located at both upstream and downstream of a wiggler beam line.

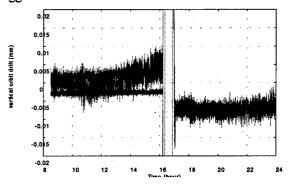


Figure 6(b): Typical vertical orbit drift from the BPM readings (without averaging) near a wiggler beamline. The orbit drift can be kept in 10 micron range and the refill causes a shift of orbit by 10 micron too.

8 ACKNOWLEDGEMENT

The authors would like to thank Z.D. Tsai for providing the water temperature data. We thank for the support from director, C.T. Chen. We also thank the whole Accelerator Division members for their help in one way or the other in this issue.

- J.R. Chen, et al., "The Correlation Between the Beam Orbit Stability and the Utilities at SRRC", 1998 EPAC Conf. Proc., p. 2309.
- [2] H.M. Cheng, et al., "Utility Optimization for the Beam Orbit Stability at SRRC", this proceedings.
- [3] C.H. Kuo, et al., "Digital Global Orbit Feedback System Developing in SRRC", PAC97 Conf. Proc., p.2374

PRELIMINARY TRANSVERSE AND LONGITUDINAL PHASE SPACE STUDY AT TLS

Jenny Chen, C. S. Chen, K. H. Hu, K. T. Hsu, C. C. Kuo, C. H. Kuo, K. K. Lin, T. S. Ueng

Synchrotron Radiation Research Center
No. 1 R&D Road VI, Hsinchu Science-Based Industrial Park, Hsinchu, Taiwan, R. O. C.

Abstract

Turn-by-turn beam position monitors and phase detector have been implemented recently for Taiwan Light Source (TLS). Transverse as well as longitudinal phase space has been explored using turn-by-turn beam position and phase measurement in single bunch mode. Single bunch longitudinal beam transfer function measurement is also performed with various excitation amplitudes. Preliminary results of these experiments are summary in this report.

1. INTRODUCTION

Phase space portrait is useful tools in nonlinear beam dynamic study [1][2][3][4]. A six-dimensional phase space monitors is implemented to study turn-by-turn beam dynamics in Taiwan Light Source (TLS). This tools is also useful as an on-line diagnostic tool for TLS. Longitudinal beam transfer function (BTF) measurement is a standard diagnostic method and extensive study recently [5][6]. Experimental setup is implemented to measure longitudinal beam transfer function in TLS. Preliminary transverse phase space and longitudinal BTF measurement are performed. Systematic study will follow soon. These tools will use to study various issues of non-linear dynamics at TLS in near future.

2. TOOL DESCRIPTION

A six-dimensional phase space monitor includes two sets of BPMs to measure horizontal position and angle, two BPMs to measure vertical position and angle. One BPM located at dispersion region is used to extract momentum error, a phase detector to observe the energy oscillation. Log-ratio processors are implement to measure turn-byturn beam position [7]. Beam phase is extracted by phase detector. The raw data is recorded by multi-channels 128 kW/256 kW transient digitizer located at VME crate. Functional block diagram is shown in Fig.1. The server software on VME crate is in charge of data acquisition. Client software running in control console is used to access raw data, to analysis and to display result. The data acquire is synchronize with revolution clock. Memory depth of transient digitizer limited record length.

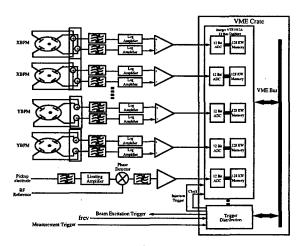


Figure 1. Block diagram of 6-dimensional phase space monitor.

Longitudinal BTF is measured by using phase detector and RF phase modulation. Dynamic signal analyzer (DSA) worked in swept-sine mode is used to acquire BTF directly. The DSA is connected to control system via GPIB to ethernet adapter. The data acquisition operates automatically. Experimental setup is shown in Fig. 2 for longitudinal BTF measurement.

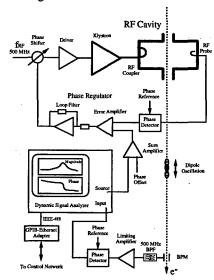


Figure 2. Experiment setup of longitudinal beam transfer function measurement.

3. TRANSVERSE PHASE SPACE EXPLORATION

Transverse turn-by-turn beam position was processed by newly installed log-ratio processors and digitized by digitizers. Only horizontal plane is presented in hear due to easily in beam excitation. One of an injection kicker is used to excite the stored beam. Preliminary study is done near 4Vx = 29, 5Vx = 36, 6Vx = 43. Fig. 3 shown the stored beam is kick about 1 mrad, and tune close to 4th order resonance. The damping is strong. When tune closed to 5th order resonance, turn-by-turn beam position is shown in Fig. 4. Phase space plot of near 5th resonance with slightly difference in tune shown in Fig. 5,6,7. Phase space portrait near 6th order resonance shown in Fig. 8.

Since the injection kicker pulse is a 1.5 µsec half-sine, it will affect up to four turns of the stored beam. Effective kick strength is difficult to estimate if kicker fire asynchronous with the bucket address of the stored bunch. Synchronous kicker trigger with revolution clock will be added in next study. The storage ring does not have vertical kicker. Vertical excitation can be done by resonance excitation at this moment. Applied vertical betatron frequency burst to beam excitation system can excite vertical betatron oscillation. However, the experiment is inconvenient slightly.

Experiments report in here is still in its infancy. There are some inconvenience was found during the experiment. Various on-line tools will be development to provide a convenient environment for study. The tools will provide beam position versus turn display, shown tune immediately, record related machine parameters with the measured data, ... etc.

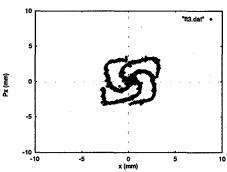


Figure 3: Horizontal phase space portrait near 4Vx = 29 resonance.

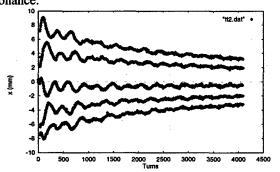


Figure 4: Horizontal beam position evolution near 5Vx = 36 resonance.

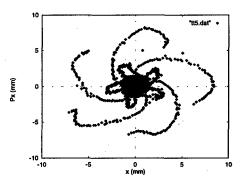


Figure 5: Horizontal phase space portrait near 5Vx = 36 resonance.

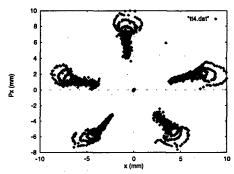


Figure 6: Horizontal phase space portrait near 5Vx = 36 resonance.

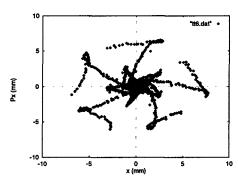


Figure 7: Horizontal phase space portrait near 5Vx = 36 resonance.

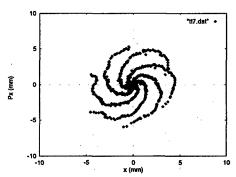


Figure 8: Horizontal phase space portrait near 6Vx = 43 resonance.

4. LONGITUDINAL PHASE SPACE OBSERVATION

With the longitudinal phase-space monitor, both the phase oscillation and momentum deviation can be simultaneously observed. The measurement was done under the single-bunch operation with RF phase modulation. Longitudinal phase space is performed by using the phase detector and a BPM located at dispersion region. Turn-by-turn momentum error is extracted by deduce from relationship $\Delta p/p = \Delta x/\eta$. Preliminary measured results are shown in Fig. 9. The data is slightly noisy. Performance of the monitor should improve further.

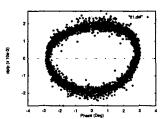


Figure 9: Longitudinal phase space portrait with RF phase modulation..

5. LONGITUDINAL BEAM TRANSFER FUNCTION MEASUREMENT

Preliminary longitudinal BTF is measured also. Fig. 10 is shown longitudinal BTF of a typical sweep in linear regime, resonance occurs at synchronous frequency and the phase shift 180 degrees at resonance.

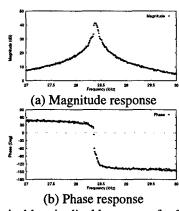


Figure 10: Typical longitudinal beam transfer function.

First experiment is performed on the topics of excitation amplitude dependent BTF. Longitudinal BTF have been studied intensively by J. Byrd [5][6] in ALS. However, further study is helpful to investigate the usage of longitudinal BTF. In this report we measure longitudinal BTF by vary excitation amplitude. BTF of upward and downward sweep is recorded. Preliminary experiment data is shown in Fig. 11. Hysteresis effect is prominence that is a typical behavior of nonlinear system. Notch occur at the low frequency side in the

magnitude response of BTF is due to out of phase in inner and outer beamlet oscillation [5], and phase detector cannot detect the signal.

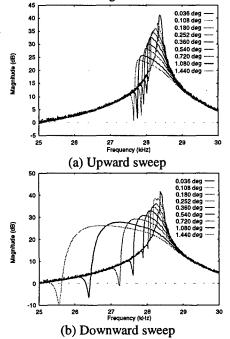


Figure 11: Longitudinal beam transfer function with various excitation level; (a) upward sweep, (b) downward sweep.

6. SUMMARY

A six-dimensional phase space monitor is implemented in SRRC recently. Preliminary nonlinear beam dynamic experiments is on going. We have been performed transverse phase space experiments near 4Vx = 29, 5Vx = 36, 6Vx = 43 resonance. Third order resonance experiment is in study. Simulation, analysis measured data and improves the performance of the monitor is current efforts. Further study for amplitude dependent tune shift and phase space trajectories near nonlinear resonance will perform in next step. Preliminary longitudinal BTF performed also. Analysis acquired BTF data and prepared next experiment is underway.

- [1] S. Y. Lee, "Beam Dynamics Experiments at the IUCF Cooler Ring", AIP Conf. Proc. Vol. 326, pp. 12-51, Dallas, TX, 1992-1993.
- [2] D. D. Caussyn, et al., "Experimental studies of nonlinear beam physics", Phys. Rev. A46, 7942 (1992).
- [3] G. Morpurgo, "The BOM 1000 Turn Display: A Tool to Visualize the Transverse Phase-Space Topology at LEP", Proceeding of EPAC'98, pp 1571-1573, Stockholm, June 22-28 1998.
- [4] V. Kiselev, E. Levichev, V. Sajaev, V. Smaluk, "Experimental Study of Nonlinear Beam Dynamics at VEPP-4M", Nucl. Instrum. and Meth. A 406 (1988) 356-370).
- [5] J. M. Byrd, et al., "Nonlinear Effects of Phase Modulation in an Electron Storage Ring", Phys. Rev. E57, 4706 (1998).
- [6] J. M. Byrd, "Longitudinal Beam Transfer Function Diagnostics in an Electron Storage Ring", Particle Accelerator, 1997, Vol. 57, pp. 159-173.
- [7] K. H. Hu, et al., "Turn-by-Turn BPM Electronics Based on 500 MHz Log-Ratio Amplifier", these proceedings.

STATUS OF THE TAIWAN LIGHT SOURCE

R.C. Sah', J.R. Chen, P.J. Chou, and K.K. Lin Synchrotron Radiation Research Center, Hsinchu, Taiwan

Abstract

The Taiwan Light Source (TLS) is a third-generation synchrotron light source located at the Synchrotron Radiation Research Center (SRRC) in Taiwan. The TLS is now operating routinely for user experiments, and the highest priorities are increasing user beam time, increasing machine reliability, and improving the stability of the stored electron beam. Many current machine upgrades are intended to improve beam stability: the longitudinal feedback system, orbit feedback systems, radiofrequency-system improvements (better higher-order-mode performance), and utilities upgrades. In addition, a major improvement program to increase the stored beam current is being planned.

1 INTRODUCTION

The Taiwan Light Source has served users for several years [1]. Recently, a great deal of the laboratory effort and budget has been devoted to improving the capability of the research center to support a wide spectrum of user groups. That is, the construction of insertion devices, photon beamlines, and experimental end stations has taken first priority.

As the construction of user facilities is starting to slow down a little, greater resources are starting to become available for accelerator-system repairs and upgrades. Therefore, changes in machine operations and machine upgrade programs are focused on the four following goals:

- To increase user beam time.
- To increase beam reliability,
- To improve the stability of the photon beams, and
- To increase the performance capabilities of the TLS.

2 USER BEAM TIME

The amount of beam time available for users has increased in recent years, because the number of days of machine operation has been steadily increased. Earlier, the Taiwan Light Source was operated for five days out of every week. In 1997, the operations were increased to six days per week, and now the machine is operated seven days per week. A three-day maintenance period requires a machine shutdown once per month, and long shutdowns are scheduled as needed.

Mondays are normally reserved for machine studies, and the change-overs between experiments are scheduled for the same time. In addition, many owl shifts are used for machine studies.

3 BEAM RELIABILITY

The overall reliability of the TLS has improved markedly over the past few years. During 1996 and 1997, the machine reliability was approximately 89%. Last year, however, the reliability increased to 96%. It is true that one year does not represent a great deal of statistics in terms of machine reliability; however, we believe that this improvement is indeed real.

First of all, problem areas, such as RF transmitters, have been upgraded both in terms of the equipment and in terms of the maintenance. Secondly, reorganizations of the maintenance staff have improved the maintenance of some systems, such as the injector. Lastly, some systems, which have started to suffer from ageing and performance degradation (such as the conventional utilities systems - cooling water, etc.) have undergone significant repairs.

4 BEAM STABILITY

Stable photon beams are a crucial requirement of most user groups, and considerable effort is being devoted to improving the beam stability. Up to now, much of the effort has focused on first improving the stability of the stored electron beam.

4.1 Sources of Noise and Instability

Sources of noise and beam instability were studied in the TLS, and the most serious problems have been resolved. Worn-out bearings for air-conditioning-system fans were found to be a source of vibration, and they have been replaced.

Also, the ongoing upgrade program for the conventional utilities (cooling water systems, air conditioning system, etc.) has improved the performance capabilities of these systems. The temperature regulation of these systems has been very significantly improved, and the system capacities have been increased to meet growing requirements.

4.2 Orbit Stability

A global feedback system has been developed to control overall motions of the electron-beam orbit, and a local

^{*} Email: sah@srrc.gov.tw

feedback system has been developed to control the orbit in local regions of the machine.

4.3 Other Feedback Systems

A transverse feedback system has been developed to suppress transverse instabilities, and a bunch-by-bunch longitudinal feedback system is being built to suppress longitudinal instabilities. In particular, the TLS is troubled sometimes by longitudinal coupled-bunch instabilities, which are very difficult to control. For the time being, the use of RF modulation, at about twice the synchrotron frequency, excites parametric resonances and helps to control these beam instabilities.

5 UPGRADE PROJECT

A new machine-upgrade program is being undertaken to increase the performance capabilities of the TLS.

5.1 Project Goals

The "500 mA Upgrade Project" is a major upgrade program with the following goals:

- To provide photon beams with significantly better stability, and
- To store up to 500 mA of electron beam, while maintaining the beam lifetime.

5.2 Approach

At this time, among the most troublesome causes of photon-beam instabilities in the TLS are the longitudinal coupled-bunch instabilities of the stored electron beam, as discussed above. These coupled-bunch instabilities are caused by the higher-order modes (HOMs) of the radiofrequency cavities, so we plan to replace the existing DORIS cavities with a new cavity, which has much weaker HOMs. Therefore, the major components of the 500 mA Upgrade Project are the following:

- A new RF cavity with reduced HOMs to provide improved beam stability and with the capability to store 2X higher beam current,
- Other RF system improvements to accommodate 2X higher stored beam current,
- Third-harmonic (Landau) cavities to lengthen bunch lengths by 2X, and
- Other machine improvements, such as to the vacuum system and to the utilities systems, to accommodate operation at higher beam current.

At this time, a number of advanced RF cavity designs already exist in various accelerator laboratories around the world. Most of these designs have been developed for high-energy-physics accelerator applications.

Only one or two new RF cavities need to be installed in the storage ring of the TLS, so our needs are relatively modest. We believe that the cost and technical risk of new cavity development are not warranted for so few cavities, so our approach will be to acquire existing technology from other laboratories

5.3 RF System Requirements

The upgraded RF system should meet the following requirements:

- Deliver 100 kW of RF power to the beam at 500 mA, which is enough power to accommodate the eventual addition of superconducting bend magnets or of superconducting wigglers,
- Provide additional RF power for cavity dissipation and operational safety margin, and
- Provide a gap voltage of 1.2 MV.

5.4 Cavity Selection

Advanced RF cavity designs have been studied at SRRC for well over a year, and we have recently selected the Cornell superconducting RF cavity [2].

We are planning a two-phased approach. Stable operation will be provided in Phase 1, using one new RF cavity powered by one of the existing 60 kW transmitters. Additional RF power will be installed to provide 500 mA operation in Phase 2.

A second RF cavity will be purchased and kept in readiness on a test stand. The ability to install a functional cavity on short notice will provide maximum machine reliability.

5.5 Project Status

The current goal is to sign a purchase contract for the new superconducting cavities by mid-1999, so that the first phase of this upgrade project can be completed by the year 2002. The staff at CESR (Cornell University) has generously agreed to help with the technology transfer.

- Y.C. Liu, et. al., "Operational Experience at SRRC", PAC'97, Vancouver, Canada, May 12-16, 1997, p.847.
- [2] S. Belomestnykh, et. al., "Development of Superconducting RF for CESR", PAC'97, Vancouver, Canada, May 12-16, 1997, p.3075.

Proceedings of the 1999 Particle Accelerator Conference, New York, 1999

THE OPERATIONAL STATUS OF PLS

J. Choi, J. Y. Huang, M. G. Kim, <u>T.-Y. Lee*</u>, E. S. Park, and S. S. Chang Pohang Accelerator Laboratory San 31, Hyoja-dong, Pohang, Kyungbuk, 790-784 KOREA

Abstract

The Pohang Light Source (PLS) has been operating successfully at 2.0 GeV. But now the energy can be raised up to 2.5 GeV by energy ramping in the storage ring. The operational status of PLS is presented including 2.5 GeV operation. Beam parameters such as emittance, lifetime etc. have been measured at a few energy levels. The measured results are presented and discussed with emphasis on their energy dependence.

1 OVERVIEW

PLS is a 2 GeV third generation light source in Korea. It has been operating successfully, after it started the user service on September 1995. The beam availability has been over 90 % except 1998, when the summer typhoon caused unexpected shutdown of a few days. The operation statistics of the last three years is shown in Table 1.

At the moment there are 8 beamlines are operational and 3 more beamlines will be available this year including the U7 beamline, the first insertion device beamline of PLS [1]. The operational beamlines are listed in Table 2.

The injected current ranged from 160 to 180 mA. The main reason of this current limitation is the longitudinal and transverse coupled bunch instabilities. At the moment, the only device we possess to overcome the instability is the RF cooling temperature system. Unfortunately the RF cooling temperature control is not enough to store more than 180 mA. Therefore we decided to use longitudinal and transverse feedback systems to suppress the coupled bunch instabilities.

This year, we have three plans of major upgrade. The first is the longitudinal and transverse feedback systems. The longitudinal feedback system was manufactured and is now under testing by SLAC. The transverse feedback system was manufactured in our Lab and now under fabrication. The two systems will be installed in April, and after full test will start operation in September. These two feedback systems are expected to increase the stored current more than 300 mA.

The second upgrade plan is the energy ramping up to

Table 1: Operation Statistics of PLS

			_hour
	1996	1997	1998
Scheduled	3,236	3,960	4272
Supplied	3,034	3,618	3,784
Percentage	93.8%	91.4%	88.6%

2.5 GeV in the storage ring. So far many x-ray users have not been satisfied with the hard x-ray flux of PLS as can be seen in Table 2. The critical photon energy of bending magnet beamlines is 2.8 keV for 2.0 GeV operation and 5.5 keV for 2.5 GeV operation. In general, it is said that photons of energy up to four times of the critical energy can be utilized. But high energy photon flux is not satisfactory. In the 2.5 GeV operation, the bending magnet photon flux of energy above 5 keV increases substantially compared with the 2.0 GeV operation. The photon flux of 10 keV is 3.8 times larger than that of the 2.0 GeV operation. Hence the 2.5 GeV operation is expected to satisfy many X-ray users. Both hardware and software were upgraded to perform the energy ramping up to 2.5 GeV. It takes about 5 minutes from 2.0 GeV to 2.5 GeV. The 2.5 GeV operation for users will start in April.

Table 2: Operational beamlines

Beamline	Energy range	
Photoemission	12 - 1230 eV	
X-ray scattering	4 - 12 keV	
White beam	4 - 12 keV	
Lithography	1 - 2 keV	
NIM	5 - 30 eV	
EXAFS	4 - 14 keV	
X-ray diffraction	4 - 12 keV	
SAXS	4 - 12 keV	

Finally we have a plan to upgrade the BPM electronics. The current BPM electronics system is what we developed and its measurement resolution is within 20 μ m. Even though this electronics system is still usable, we decided to upgrade it to the commercial one by Bergoz Co. [2]. This is for more reliable operation of insertion devices. The resolution of Bergoz BPM is expected to be within 10 μ m.

^{&#}x27;Work supported in part by the Korean Ministry of Science and Technology, and the POSCO company.

^{*}Email: tylee@postech.ac.kr

2 ENERGY RAMPING

2.1 Problems

Basically the ramping procedure is simply increasing currents of the magnet power supplies (MPS) step by step. But the real procedure is not easy by two requirements, fast ramping time and keeping the storage ring optics unchanged. Stability was the design key point of the PLS storage ring MPS. Therefore the storage ring MPS is relatively slow changing the currents compared with synchrotron booster MPS. More important is the control time. The computer control system of the PLS storage ring has three layers of hierarchy; operator interface computer (OIC), subsystem control computer (SCC), and machine interface unit (MIU). The SCC acts as a data gateway between the OIC and the MIU. The MIU layer is directly interfaced to individual machine devices for low-level data acquisition and control. Both the SCC and MIU layer is based on VMEbus standard with OS-9 real-time operating system. It takes considerable time, if the ramping procedure passes all the three layers.

The other problem comes from the fact that the relation of the MPS current to the corresponding magnet is not linear. In the normal operating region of 2.0 GeV, it is almost linear, but outside that region the discrepancy grows. Since the discrepancy is different for different magnets, even if all the MPS currents are increased by the same percentage, the real magnetic fields do not change correspondingly and thus the linear optics such as betatron tune is distorted. Even though the amount of distortion in each step is very small, if the ramping procedure keeps going this way, the betatron tune shifts keep growing and finally beam blows up.

2.2 Control System

To reduce the amount of time for the energy ramping significantly, the role of calculating and controlling the MPS current settings in each step was given to the MIU layer, not the OIC layer. The OIC just sends the start signal downwards. Since the various magnets have to change simultaneously in order not to kill the stored beam, the SCC layer generates synchronisation signals in each ramping step. The MIL-1553B field bus, which is already installed for low level data acquisition control, is used for the synchronisation network through which the SCC sends the synchronisation signals to the lower MIU layer. This way, the control time of the ramping was minimized.

Now the amount of ramping time is determined by the magnitude of each ramping step.

2.3 Linear Optics

We tried to keep the betatron tunes in each step. For the purpose, all MPS should not change by the exactly same

percentage, but each MPS current should be fine tuned with respect to the basic percentage that is the same for all MPS. The basic percentage was chosen to be 0.3%. By a number of machine studies, we obtained data of appropriate MPS current setting values to keep the betatron tunes in each step. Several machine studies proved that the scheme works. In order to be sure of safe and stable ramping, we chose the conservative value 0.3%. For this choice, the amount of time needed for ramping up to 2.5 GeV is about 5 minutes, which is endurable because the injection from the linac can be finished within a few minutes.

2.4 Current Storage

The amount of stored current depends on the RF cavity power. Since the dependence of radiated power on the beam energy is quartic, 150 mA of 2.5 GeV is equivalent to 366 mA of 2.0 GeV in the sense of RF power. We consider 150 – 200 mA proper region of 2.5 GeV operartion.

2.5 Emittance

The dependence of beam emittance on the beam energy is quadratic. The design emittance of 2.0 operation is 12 nmrad and the diagnostic beamline confirmed that we achieved the goal. Hence the design emittance of 2.5 GeV operation must be 18.9 nmrad. We achieved a value close to it.

2.6 Lifetime

The beam lifetime of PLS storage ring is mainly determined by the Touschek effect just like other third generation light sources. The Touschek lifetime is proportional to the 2.5 th power of the energy [4]. In reality, we raised the beam energy from 2.05 GeV to 2.50 GeV. Therefore we expect the beam lifetime to increase 1.65 times. The measured lifetime of 2.5 GeV operation is close to this expectation.

3 FUTURE UPGRADE PLANS

3.1 Beam Based Alignment

The PLS storage ring has the ground settlement problem. The ground is continuously lowered maximum 2 mm each year. Obviously this is a serious threat for the orbit stability. We survey the storage ring and realign the girders periodically (every two years). Also we survey the BPM positions periodically and use the data to recalibrate the BPM readings. However, we need more reliable methods of BPM calibration especially for the operation of insertion devices. Now we are preparing the beam based alignment that calibrates the BPM reading with respect to the quadupole center. The scheme was already prepared and tested successfully in one

superperiod. The remaining work is to extend the necessary hardware to the whole storage ring and construct control system.

3.2 Global Orbit Feedback

In conjunction with the beam based alignment, the global orbit feedback is also planed. The detailed scheme will be prepared soon.

3.3 Third Harmonic Cavity

The beam lifetime of 2.0 GeV operation is endurable at around 170 mA with 20 hours or so. But since the Touschek lifetime decreases with increasing current, the beam lifetime is expected to be very small (less than 10 hours) over 300 mA that will be achieved with the feedback systems soon. To keep the high brightness it is not permissible to increase the vertical size. Therefore the only way to increase the beam lifetime is to increase the bunch length using a third-harmonic RF cavity. A study is going on to apply the third-harmonic cavity to the PLS storage ring.

- [1] W. Namkung, "Present status of PLS", J. Synchrotron Rad., 5 p158 (1998).
- [2] http://www.bergoz.com/s_bpm.htm
- [3] J. C. Yoon et al., in this proceedings.
- [4] H. Wiedemann, Particle Accelerator Physics (Springer-Verlag, Berlin Heidelberg, 1993).

ORBIT CORRECTION IN THE LNLS UVX ELECTRON STORAGE RING

J.G.S. Franco, L. Jahnel, Liu Lin, C. Scorzato and P.F. Tavares*, LNLS, Campinas, Brazil

Abstract

The orbit measurement and correction system of the LNLS synchrotron light source is presented. Recent changes to the system including the addition of 12 vertical correctors and the use of 16 bit DACs to control the corrector magnet power supplies have improved the vertical orbit repeatability from fill to fill from $\pm 70~\mu m$ to $\pm 3~\mu m$. The improved resolution also allowed the implementation of automatic orbit corrections at 24 second intervals, thus reducing orbit variations along a user's shift from $\pm 70~\mu m$ to $\pm 5~\mu m$.

1 INTRODUCTION

The LNLS synchrotron light source, based on a 1.37 GeV electron storage ring, has been delivering beam for routine user operation since July 1997. It became clear from the early stages of beamline commissioning that orbit reproducibility from fill to fill as well as orbit stability over long periods (several hours) are critical performance figures of the light source from the user's point of view. Those user demands were the driving force behind a long term program aimed at identifying and correcting orbit variations, which included reviewing the vast number of topics related to the subject, applied to our specific case, such as: orbit stability requirements, techniques to identify undesirable sources of beam motion, capabilities of orbit monitoring equipment at LNLS (e.g. position measurement dependence on beam current), parameters for automatic orbit correction, relation between beam stability at the monitors and at the beamline source points, correlation of orbit drifts and oscillations with temperature variations etc. This program started even before the machine was officially delivered to users [1], with the identification of orbit drifts correlated to magnet temperature variations and the implementation of an orbit feedback system, which was able to keep orbit variations below ±70 µm along a user's shift (orbit stability) as well as from shift to shift (orbit reproducibility) with orbit corrections being performed once every hour.

All along 1997, further improvements were implemented in this system, including better knowledge of the ring optics and additional flexibility in the control software. Even though those improvements made the system more reliable and robust, they did not address its basic limitations, namely the correction and monitoring hardware. The beam position measuring system used RF switches to multiplex the monitor signals onto the BPM

electronics. This choice (dictated by cost considerations) along with the fairly low resolution ($\pm 8 \, \mu m$) of the 12 bit AD converters that read the BPM electronics output signal, made it necessary for the system to perform time consuming averages in order to obtain good resolution, which reduced its bandwidth. Also the RF switches were a constant source of connection problems and compromised reliability. Finally, the number of vertical correctors as well as the corrector strength adjustment resolution were found to be insufficient to guarantee orbit repeatability from fill to fill within the required tolerances.

In 1998, after theoretical work [2] demonstrated the need for additional vertical correctors, a hardware upgrade program was started that included the addition of 12 new vertical corrector magnets (actually, already existing coils in the quadrupole magnets were used), implementation of higher resolution in the steering magnets power supply controls, the implementation of a temperature stabilization system for the storage ring magnets (that is kept running even when the magnets themselves are turned off) and improvements to the orbit measuring system through the addition of new BPM electronics eliminating the need for RF multiplexing. In the following sections, we describe the present orbit measurement and correction system as well as the results obtained so far, concentrating on the improvements due to the upgrade started in June 1998.

2 NEW BPM ELECTRONICS AND CALIBRATION PROCEDURE

The storage ring has 23 beam position monitors (striplines) distributed along its six superperiods. Up until December 1998, the stripline signals were processed by 6 commercial electronic readout modules (manufactured by BERGOZ, France). Since there was only one read-out module per superperiod, each module must read four different BPMs. This was accomplished by multiplexing those signals via a computer controlled RF switchboard, which allowed the four monitors to be read in any order set by the high level control system. The total time for a complete scan of all four BPMS in a superperiod was dominated by the time needed by the RF switches to stabilize their output signal and it was 400 ms. Recently new BPM modules were installed providing one module per BPM and eliminating all RF switches. At the same time, sets of variable attenuators were added to the input of the BPM electronics so as to allow better equalization of beam signals (to compensate for different cable lengths

^{*}E-mail: pedro@lnls.br

and connector attenuations) and to bring the signal intensity down to the range where the electronics is mostly insensitive to beam current variations.

The geometrical BPM offset and gains were determined in a characterization bench where the beam was simulated with a stretched wire. An off-set and gain were also determined for the BPM electronics (in fact, this offset and gain include the effects not only of the electronics, but also of the cables and connectors). In the original installation (1996), the offset was determined with an equalized (better than 0.01 dB) four-way splitter fed by a 476 MHz signal and connected to the same cables, RF switches and connectors that take signals from the BPMs to their electronics (this measurement takes place in the machine hall). The measured dc voltages (horizontal and vertical) at the output of the BPM electronics gave directly the off-set. The gain was determined by adding attenuators to two of the output ports of the four-way splitter and again measuring the voltages delivered by the BPM electronics. When installing the new BPM electronics, a new calibration procedure was used that proved to be more precise and substantially reduced the spread in measured gains of the various electronic modules. In the new procedure, the offsets and gains are determined from a set of five measurements: first we measure the BPM output signal when the inputs to the BPM electronics come from the equalized splitter; next we add a single attenuator to each of 4 input channels of the BPM and again measure the BPM output signal. We model the experiment with the equations

$$X_{0} = K_{x} \frac{\alpha_{1} + \alpha_{2} - \alpha_{3} - \alpha_{4}}{\alpha_{1} + \alpha_{2} + \alpha_{3} + \alpha_{4}}$$

$$X_{1} = K_{x} \frac{\gamma \alpha_{1} + \alpha_{2} - \alpha_{3} - \alpha_{4}}{\gamma \alpha_{1} + \alpha_{2} + \alpha_{3} + \alpha_{4}} \quad X_{2} = K_{x} \frac{\alpha_{1} + \gamma \alpha_{2} - \alpha_{3} - \alpha_{4}}{\alpha_{1} + \gamma \alpha_{2} + \alpha_{3} + \alpha_{4}}$$

$$X_{3} = K_{x} \frac{\alpha_{1} + \alpha_{2} - \gamma \alpha_{3} - \alpha_{4}}{\alpha_{1} + \alpha_{2} + \gamma \alpha_{3} + \alpha_{4}} \quad X_{4} = K_{x} \frac{\alpha_{1} + \alpha_{2} - \alpha_{3} - \gamma \alpha_{4}}{\alpha_{1} + \alpha_{2} + \alpha_{3} + \gamma \alpha_{4}}$$

where X_0 is the voltage measured when no attenuator is added to the splitter, X_i is the voltage measured when we add an attenuation γ to the ith BPM input channel and K_r is the gain constant. The attenuation factors α_i , represent the effects of differences in cable lengths and connectors and the BPM offset can be calculated as a function of these factors. The same equations apply for the vertical voltage, with a different gain factor K_{v} but equal attenuation factors α . In this model, the horizontal and vertical offsets are not independent and by measuring X and Y voltages we actually get a cross-check of our results. Given this set of five measurements, the attenuation factors and gain constants can be determined by solving the set of five coupled equations, which can be reduced to solving a fourth-order polynomial root. Once the attenuation and gain constants of the setup are

determined, the offset and gain of the BPM electronics can be calculated by considering the expressions for the voltages induced in each stripline by a (slightly) offcentered beam.

If we take the horizontal plane, the voltage on the ith strip is (given that the BPM's are in a cylindrical chamber of radius b and are aligned at 45 degrees with respect to the plane of the orbit)

$$V_i = V_0 \left(1 + \frac{\sqrt{2}\Delta}{b\psi} \sin \psi \right)$$

where V_0 is proportional to beam intensity, Δ is the beam offset and $b\psi$ is the stripline width. Using those voltages we get for the BPM (horizontal) output voltage

$$X = K_x H + (1 - H^2) K_x \left(\frac{\sqrt{2} \sin \psi}{\psi} \right) \Delta,$$

where
$$H = \frac{\alpha_1 + \alpha_2 - \alpha_3 - \alpha_4}{\alpha_1 + \alpha_2 + \alpha_3 + \alpha_4}$$

and if we define the BPM gain (i.e., the gain determined solely by the BPM geometry) as

$$G_{GEO} = \frac{\sqrt{2}\sin\psi}{\psi} \frac{1}{b}$$

we get the BPM electronics gain and offset

$$G_E = (1 - H^2)K \quad O_{XE} = K_x H$$

Note the correction factor $(1-H^2)$ to the gain for a non-zero offset. As a result of this new calibration procedure, the spread of gains between different electronics was considerably reduced and measurements of the dispersion function, which previously presented unexpected asymmetries now fit better the theoretical expectations (Figure 1).

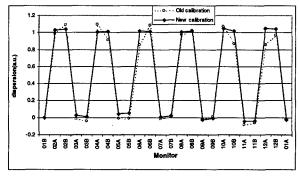


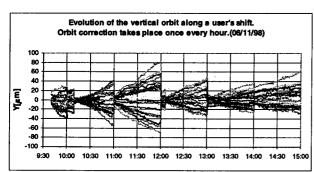
Fig. 1: Dispersion function measurement with the old (circles) and new (dots) BPM electronics calibration.

The BPM absolute accuracy is determined by the alignment procedure and is better than ± 0.1 mm. The BPM resolution is determined by the electronic noise and by the resolution of the AD converters used to read the BPM output voltages. At the moment the 12 bit converter resolution determines the resolution of $\pm 8 \, \mu m$. The

overall resolution can be improved to $\pm 2 \mu m$ by averaging over 5 seconds.

3 NEW VERTICAL ORBIT CORRECTORS AND CONTROLS

The orbit correctors are 10 cm long C-type (vertical) and H-type (horizontal) magnets. Originally there were 11 vertical and 18 horizontal correctors, capable of producing up to 70 gauss.m of integrated field, corresponding to 1.5 mrad deflection at 1.37 GeV. The corrector strengths could be adjusted in steps of 0.7 µrad. In June 1998, 12 new vertical correctors were added (by powering correcting coils inside quadrupoles) and in December 1998 new higher resolution A/D converter boards were installed to control the steering magnets power supplies reducing the smaller correction step to less than 0.05 µrad. Also the orbit correction software was changed to implement each correction as a sequence of small steps so as to minimize transient orbit perturbations. This improved the orbit repeatability from fill to fill from ±70 µm to ±3 µm and allowed us to implement a faster orbit feedback loop, with one correction every 24 seconds. Figure 2 shows the orbit stability along one user's shift before and after the upgrade of the orbit correction system. We see that the orbit stability has improved from $\pm 70 \, \mu m$ to $\pm 5 \, \mu m$.



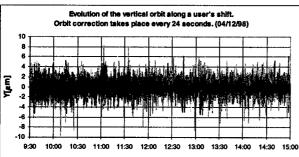


Fig. 2: Evolution of the vertical orbit along a user's shift before (a) and after (b) the orbit correction upgrade. All 23 monitors are plotted.

In figure 3 we show the results of an experiment performed to determine the vertical angular stability of the orbit with the new correction system. In this experiment, the X-ray beam intensity was measured

behind a thin slit with a scintillator (hard X-rays were select by means of 1.2 cm thick aluminum plates). The beam was then let to drift freely for about 20 minutes and the corresponding drift in X-ray intensity (normalized to beam current) was registered. At that point the correction system was turned on. The action of the correction system in correcting the slow orbit drift is clear.

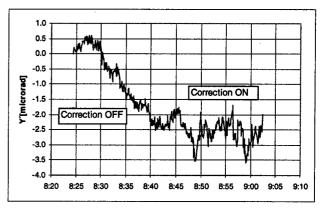


Fig. 3: Vertical angular stability with and without orbit correction. The angular variations are calculated from measured hard X ray intensity variations in a 10 meter long beam line with a thin slit.

CONCLUSIONS

The orbit measurement and correction system of the LNLS synchrotron light source has been upgraded with the addition of 12 new vertical correctors, new BPM electronics modules and changes to the orbit control software. All those changes have allowed the implementation of an automatic correction procedure that improved orbit repatability ($\pm 3~\mu m$) as well as orbit stability along a user's shift ($\pm 5~\mu m$). Future work will concentrate on improving BPM measurements (better ADC resolution) and studies of the origins of slow orbit drifts. In particular, changes to the air conditioning control system are foreseen that should bring the daily experimental hall temperature variation from $\pm 2~^{\circ}C$ down to less than $\pm 1~^{\circ}C$.

- [1] R.H.A. Farias, L.C. Jahnel, Liu Lin, D. Macedo, F.S. Rafael, A.R.D. Rodrigues and P.F. Tavares, Orbit Measurement and Correction in the LNLS UVX Storage Ring, PAC 1997, Vancouver Canada.
- [2] Liu Lin, Análise de um Novo Sistema de Correção de Órbita Vertical para o UVX, LNLS CT-08/98.

STATUS OF THE 2.5 GeV LIGHT SOURCE ANKA

R. Babayan, G. Buth, S. Doyle, D. Einfeld, A. Gies, J. Goettert, M. Hagelstein, A. Hagestedt, S. Hermle, F. Holstein, E. Huttel, M. Jäkel, H. Knoch, A. Krüssel, M. Lange, Y.-L. Mathis, W. Mexner, H. O. Moser, E. Pellegrin, E. Rathjen, U. Ristau, R. Rossmanith, H. Schieler, R. Simon, R. Steininger, S. Voigt, R. Walther; Forschungszentrum Karlsruhe (FZK), ANKA Project Group, Germany

F. Perez, M. Pont, Forschungszentrum Karlsruhe (FZK), ANKA Project Group (on leave of absence from LLS-IFAE, Barcelona, Spain)

M. Plesko, J. Stefan Institute, Ljubljana, Slovenia

Abstract

ANKA is a 2.5 GeV synchrotron light source under construction in Karlsruhe. ANKA will offer full service in Xray lithography, mainly for micro- and nanofabrication, and in analyzing, and investigating non-destructively various properties of samples. During the first operational period only the light from the bending magnets (1.5 T) will be used, later four long straight sections and one short straight section can be equipped with insertion devices. The light source is scheduled to get into operation in the year 2000. At present, the 53 MeV racetrack microtron as pre-injector is already commissioned. The 500 MeV booster synchrotron is being assembled, a 500 MeV electron beam is expected during the summer period. The girders, the cooling pipes as well as the cable trays are already installed. The assembly of the magnets, the r.f.and the vacuum-system will take place up to September 99 and we expect to get a 2.5 GeV accelerated beam at the end of 1999.

1 BUILDING

The building consists of three parts: a) the ANKA-hall, b) an annex and c) the cooling tower with the HVAT-system. The annex contains the control room, laboratories and the supplies for the electricity, water and heating/cooling. The floor within the hall is a single concrete slab with a thickness of 55 cm and without any insulation joint.

Within the ANKA-hall the following parts have already been installed: 53 MeV-microtron, the shielding around the microtron, the cable trays, the cooling pipes, the stands for the different racks as well as the girders for the magnets (see fig. 1). The commissioning of the microtron and the booster will be done from a temporary control room within the storage ring (see fig. 1). The cooling complex including the HVAT-system will be finished in May 99. The storage ring with a circumference of 110 m covers only 35 % of the hall. In the space left it is possible to build beamlines with a length of 27 m.

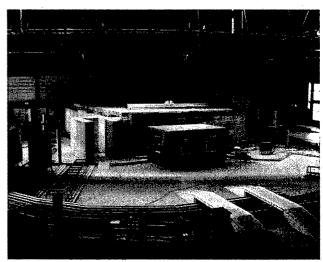


Figure 1: Status of the inside of the building as of March 99, showing the assembled girders, cooling pipes and cable trays. Furthermore the shielding around the microtron and the provisional control room for the commissioning of the injector can be observed.

2 INJECTOR

The 53 MeV racetrack-microtron has been installed and commissioned [1]. The accelerator of this machine is an sband linac with an energy of 5.3 MeV. The synchrotron light coming from the relativistic electrons accelerated within the turns 4 to 9 of the microtron bending magnets is shown in fig. 2 (this is the first synchrotron light produced at the light source ANKA). A 53 MeV beam with a pulse length of 1.2 µs and a maximum current of 16 mA has been reached. This pulse shape can be changed from 0.4 to 1.2 µs. The pulse shape of the beam at different energies is shown in fig. 3 for turns 3, 5, 7 and 9. This graph shows that there are no important beam losses during the acceleration from 26.5 MeV to 42.4 MeV. The next step in the commissioning phase of the microtron is to check the 250 MHz-chopper which should deliver a beam with a 500 MHz-structure according to the rfsystem of the booster synchrotron.



Figure 2: Synchrotron light coming from one of the main dipoles in the microtron. Shown is the light obtained from turn 4 to turn 9 (from right to left)

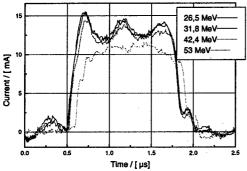


Figure 3: Pulse shape of the beam within the racetrack microtron at the turns 3, 5, 7 and 9.

The installation of the injection line and the 500 MeV booster is under way and the starting up of this complex will be in May 99. We expect to obtain a 500 MeV accelerated beam within summer 99. The assembly of the extraction line is foreseen for August 99. The company Danfysik in Denmark is building the whole injector as a turn key system.

3 MAGNETS

The series production of all quadrupoles (type Q320 and Q390) and the sextupoles (type SH and SV) is finished and all magnets have been delivered to ANKA[2]. 75 % of the bending magnets have been produced and the manufacturing of the rest will be finished in May 99. Parallel to the production of all magnets extensive mechanical and magnetic measurements have been performed in order to correlate the magnetic measurements to the geometry of the magnets. Figure 4 shows the specific magnetic field versus current for a typical bending magnet.

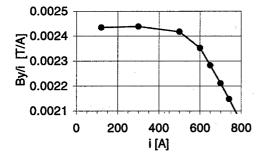


Figure 4: Specific magnetic field versus current for a bending magnet, nominal current is around 650 A

The magnetic measurements of all quadrupoles have been completed. Within the different families all quadrupoles reach the required specifications of $\Delta gL/gL \leq 4\cdot 10^3$. Figure 5 shows the specific integrated gradient versus current for a typical Q320 quadrupole. The measurements of the sextupoles and the bendings are under way. The installation of all magnets will be finished by the end of June 99.

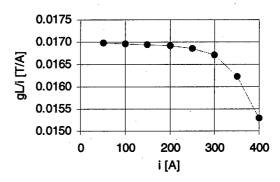


Figure 5: Specific integrated gradient versus current for a typical Q320 quadrupole, nominal current is around 350 A

4 VACUUM

The production of all elements of the vacuum system is under way. Half of the complicated dipole- and two third of the straight-section-chambers have been delivered and tested. Each element is after the production cleaned, baked and tested. The leakage rate is below 2.10-10 mbar·l/s and the thermal desorption rate below 2·10⁻¹² mbar·l/(s·cm²). In order to have an optimized clean system, the long straight sections will undergo a glow discharge cleaning process. This will be done at the Daresbury Laboratory. The installation of the vacuumsystem will start in June 99 and we expect closing the vacuum system in mid-October 99. The crotch absorbers have to absorb a power of up to 8.5 kW each. According to the operation scheme of ANKA (running only for 8 hours per day) the absorbers have to undergo a large number of cycles. For the optimization of this number of cycles a special design of the crotch absorbers has been performed [3].

5 RF-SYSTEM

The rf-system consists of 5 parts: a) cavity with the low level electronics, b) the waveguide system with the circulator, c) the klystron, d) the high voltage power supply and e) the controls. The waveguide system including the circulator has been tested and delivered [4]. The installation will take place during March and April 99. Two of the cavities including the low level electronic have been tested and will be delivered to ANKA in April 99. The factory acceptance test of the high voltage power supply (HV-PS) for the klystrons have been performed successfully. This device will be installed within April/May 99. The subsystems of the first klystron have

been assembled, the first klystron will be delivered by the end of April 99. We expect that the first rf-plant consisting of 2 cavities, the waveguide-system, the 250 kW klystron including the 400 kW HV-PS will be finished in June 99. The second plant should be ready in August 99. The rf-system has three levels of control: the machine control, the transmitter control and the fast interlock. For the transmitter control and for the fast interlock a new design has been made, which is described elsewhere [5].

6 POWER SUPPLIES

All power supplies are in the production phase. They will be delivered to ANKA in April/May 99. The acceptance test with the real load should be performed within July 99 after the installation of the magnets.

7 THE CONTROL SYSTEM FOR THE ACCELERATOR

The control system of the accelerator is based on client and server PC's running under WinNT and the LonWorks field bus with intelligent nodes and standard I/O modules to connect the individual devices directly to the server PC's. These server PC's communicate via CORBA with client PC's in the control room. All operator control is performed through Java applets/applications. The first real-world test of the system was performed on the 50 MeV microtron of ANKA during the period from October 98 to March 99, controlling it's vacuum system and power supplies [6]. At the moment, the present version of the control system is being optimized. In addition, the control of the RF system and the power supply ramping procedures will be tested to be able to control the booster synchrotron and the storage ring later this year.

8 TIMING SYSTEM

The timing system and instrumentation are at the moment under construction. The timing system will be based on commercially available delay generators. Two sets of delay generators are foreseen: one set is controlling the injection trigger chain into the synchrotron (triggering the gun, the microtron, klystron and the injection kickers), the second one is controlling the ejection from the synchrotron and is triggered by a revolution clock of the storage ring. With this system a gap in the filling can be produced in order to reduce ion effects on the stored beam. In the first stage the injection of single bunches and the storage of single bunches is not foreseen.

9 BEAMLINES

The optical components and experimental stations for eight beamlines are under construction. Three beamlines will be devoted to lithography. The beamlines for analytical services cover techniques from spectroscopy to diffraction and are taking advantage of the large spectral range from IR to hard X-rays emitted by the bending magnets. Two beamlines, a soft X-ray beamline for microscopy and spectroscopy and a beamline for protein crystallography, are planned and waiting for approval. In addition, one X-ray beamline is under construction which will be operated by the Max-Planck society.

Table 1: The beamlines and their main parameters

	Spectral range	Power or
		Photon flux
X-ray lithography I	1 – 4 keV	6 W
X-ray lithography II	3 – 8 keV	40 W
X-ray lithography III	4 – 30 keV	100 W
Soft-X	0.09 – 1.4 keV	>2 · 10 ¹⁰ ph./s
R-spectroscopy	$4 - 10^4 \text{ cm}^{-1}$	$>1 \cdot 10^{13}$ ph./s
Fluorescence analysis	1 - 30 keV	3 · 10 ¹³ ph./s
Protein crystallography	5 – 20 keV	1 · 10 ¹² ph./s
Diffraction	5 – 20 keV	2 · 10 ¹¹ ph./s
Absorption	2.4 – 30 keV	2 · 10 ¹¹ ph./s
Grazing incidence diffr.	6 – 20 keV	1 · 10 ¹¹ ph./s

10 SUMMARY

All subsystems for the erection of the storage ring ANKA are in the production state or have already been delivered. The microtron reached already the specifications and the commissioning of the booster will start in May 99. The magnet system including the power supplies will be finished in July 99. The rf-system should be running in August 99. The vacuum-system will be closed in October 99. The commissioning will start in November 99 and the first stored beam is expected at the end of 99. The installation of the beamlines will start in spring 2000. The first exposure for the LIGA-technique is foreseen for summer 2000.

REFERENCES

- [1] D. Einfeld et al., The injector for the synchrotron light source ANKA, these proceedings
- [2] D. Einfeld, A. Krüssel, M. Pont, Magnetic Measurements of the ANKA Storage Ring Magnets, these proceedings
- [3] S. Hermle, D. Einfeld, E. Huttel, G. Heidenreich, Layout of the Absorbers for the Synchrotron Light Source ANKA, these proceedings
- [4] D. Einfeld, F. Pérez, S. Voigt, A. Fabris, C. Passotti, M. Svandrlik, Status of the R.F.-System for the ANKA Storage Ring, these proceedings
- [5] D. Einfeld, F. Pérez, S. Voigt, M. Humpert, Interlock and Control for the rf-System of the ANKA Storage Ring, these proceedings

ACKNOWLEDGMENTS

The ANKA machine group wants to thank all the suppliers of ANKA components for their collaboration and continuous engagement to meet our tight time schedule.

STATUS OF THE INJECTOR SYSTEM FOR THE SYNCHROTRON LIGHT SOURCE ANKA

D. Einfeld, U.Ristau, R. Rossmanith
Forschungszentrum Karlsruhe, P.O. 3640, D-76021 Karlsruhe, Germany
N. Hertel, S. P. Møller, Institute of Storage Ring Facilities, Aarhus University,
DK-8000 Aarhus, Denmark

H.Bach, B.R. Nielsen, L. Praestegaard, Danfysik A/S, DK-Jyllinge, Denmark

Abstract

ANKA is a 2.5 GeV synchrotron light source under construction at the Forschungszentrum Karlsruhe. The facility consists of a 53 MeV microtron, an injection line, a 500 MeV booster synchrotron, and the ejection line. The whole injector is being built as a turn key system by the industry (Danfysik, Denmark). The interface between the injector and the storage ring is the entrance of the injection septum. The 53 MeV racetrack microtron is already commissioned. It delivers a beam of 53 MeV, 16 mA, 6 Hz and 1.2 μs. The installation of the injection line as well as the booster synchrotron is under way and the commissioning of the booster synchrotron will start in May 99. We expect to get an accelerated beam to 500 MeV before summer 1999.

1 INTRODUCTION

The ANKA injector is a 500 MeV booster synchrotron for the 2.5 GeV ANKA synchrotron which presently is under construction at Forschungszentrum Karlsruhe (FZK), Germany [1]. The injector complex (fig. 1) consists of a 53 MeV microtron pre-injector, a 500 MeV booster synchrotron, an injection line between the microtron and booster synchrotron, and a ejection line from the booster synchrotron to the ANKA storage ring. The microtron delivers an electron pulse with a duration of $0.5 - 1.2 \mu s$ and a current of more than 10 mA. The multi-turn injection process leads to a stored electron current of more than 15 mA in the booster synchrotron. The extracted electron pulse has a duration of ~ 56 ns, a current of more than 7.5 mA and an emittance of 0.15 mm mrad. The whole injection cycle is repeated with a rate of 1 Hz. The microtron has been commissioned at its final position in ANKA. The assembling of the booster will be done in April 99 and a 500 MeV accelerated beam is expected by summer 99. A detailed description of the optics of the booster synchrotron is presented elsewhere [2].

2 THE PRE-INJECTOR

The schematic layout of the microtron is shown in fig. 2, 3 and 4, while its main parameters are listed in table 1. The E-gun is a 70 keV spherical pierce type with a BaO cathode. The maximum gun current is around 500 mA, with a pulse length of 5 μs .

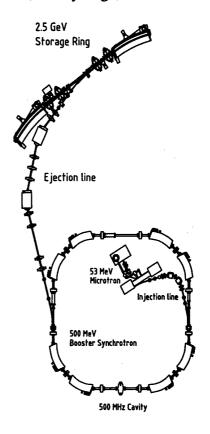


Figure 1: The injector complex of the ANKA project

Behind the E-gun the chopper is located, this will give the beam the 500 MHz structure according to the RF-system of the booster synchrotron.

Starting at the E-gun the electron beam is guided by a constant solenoid field and a horizontal focussing quadrupol singlet. Two achromatic 45° bending magnets deflect the beam to the linac axis. The linac is a side coupled 3 GHz standing wave Los Alamos Type with 7+2*1/2 Cells. The parameters of the linac are listed in table 1. After the first linac pass the beam is reversed and in the second linac pass accelerated in the other direction. After 10 passes through the linac the beam is extracted with a constant energy of 53 MeV with the help of a 15° bending magnet. Fig. 3 shows the top view of the microtron. In the tracks 1 – 9 horizontal and vertical steerers are located which allow to steer the beam through the machine.

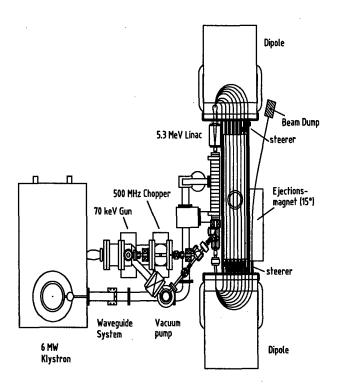


Figure 2: Outline of the ANKA microtron

Table 1: Main parameters of the racetrack microtron

Table 1. Main parameters of the facetrack inicrotron			
Injection energy	70 keV		
No. of Linac passes	10		
Energy gain per path	5.3 MeV		
Frequency	2.998 GHz		
Final electron energy	53 MeV		
Emittance (hor/ver)	• 0.2 mm mrad		
Energy spread	<0.3%		
Pulse current	10 mA		
Pulse length	0.4 – 1.4 μs		
Repetition rate	0-10 Hz		
Klystron	CPI/VKS-8262E		
Modulator	Line type pulser		
RF-power /peak	6 MW		
Q-value of linac	18000		
Length of linac	0.4 m		
Phase acceptance	13°		
Coupling	Side coupled		

The RF-power for running the linac is delivered by a 6 MW-klystron fed by a modulator consisting of a line type pulser. The energy for the modulator is stored in a pulse forming network which delivers a primary voltage to a 1:10 pulse transformer. The klystron energy is transported to the linac through a SF 6 filled wave guide system. Within the wave guide system is a -28 dB circulator which protects the klystron from being damaged by reflected RF-power of the linac. A bi-directional coupler is located at the input coupler of the linac. The reflected power signal and the RF-pulse are shown in fig. 5. The RF-pulse has a power of ~ 2.5 MW and a flat top of more than 1.5 μ s duration.

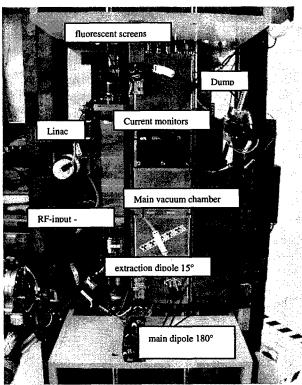


Figure 3: Top view to the ANKA microtron

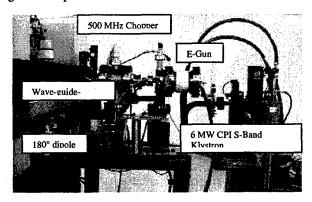


Figure 4: Microtron injection, klystron, linac wave guide, E-gun, 500 MHz chopper

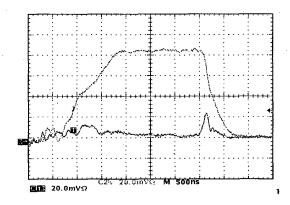


Figure 5: 3 GHz signal measured with a pickup at the end of the linac (green line). Reflected power signal measured in the wave guide (red line)

The diagnostic tools for measuring the properties of the beam within the microtron are summarized in table 2. There are overall 9 current transformers distributed in the racetracks. Three fluorescent screens are located at 10 MeV (track 2) and two additional ones at 15 MeV (track 3).

Table 2: The diagnostic tools of the Microtron

Diagnostic tool	Location	Number
Current transformer		9
Sync. light monitor	180-Bend	1
Fluorescent viewer	track 2, track 3	3
RF-Pick-up	Linac	2
Bi-directional coupler	Wave guide	2

Only the fourth track (20 MeV) has no diagnostic tools. From the fifth to the tenth track the beam can be observed either through the emitted synchrotron light or using the current monitors. The signals from the current monitor at the 5th, 6th, 8th and 10th track are presented in fig. 6. From this figure it follows that the beam losses between turns 5 to 8 are relatively small. A CCD camera is used to detect the synchrotron light which is observed in one of the main dipoles (see fig. 7).

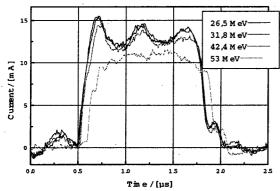


Figure 6: Pulse of the current monitor within the tracks 5, 6, 8 and 10

The extracted beam has a pulse width of up to $1.2 \mu s$ and an average amplitude of 11 mA. The vertical focusing of the microtron was modified during the commissioning by changing the gradient of one of the main dipoles.



Figure 7: The synchrotron light of the accelerated beam within the turns 4 to 10 (from right to left)

Figure 8 shows the size of the extracted beam measured at the beam dump. For this picture the dump was covered with a grid of a spacing of 1 mm. The spot size is about 3 x 3 mm which is close to the theoretical value of 2 x 2 mm. The specifications of the extracted beam are summarized in table 3.

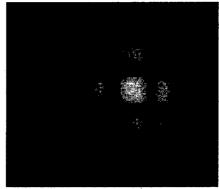


Figure 8: The 53 MeV extracted electron beam. The grid constant is 1 mm.

Table 3: Specifications of the extracted microtron beam

ne 5. opecifications of the extracted information board			
Item	Design	Guaran-	Commis-
		teed	sioning
Current/ mA	15	10	16
Pulse length /µs	1	1	1.6
Energy/ MeV	53	53	53
Repetition rate/ Hz	10	10	6
Frequenz modulation/MHz	500	500	500

3 BOOSTER SYNCHROTRON

The production of all items for the booster synchrotron and the transfer lines is finished. 8 subsystems, according to the number of bending magnets, will be assembled at the manufacturer and shipped to the site of ANKA. The installation of the subsystems at ANKA is foreseen for the end of April. The RF-System (cavitiy, low-levelelectronic, etc.) will be delivered by Sincrotrone Trieste. The acceptance test of the RF-system has been performed and the assembling at ANKA will take place also at the end of April. The control system for running the booster will be built by a collaboration of FZK and Jozef-Stefan-Institute in Ljubljana, Slovenia. A test of this system has already been made with the commissioning of the microtron. The part for controlling the booster will also be finished by May 99. The commissioning of the booster synchrotron will start in May 99 and an accelerated beam is expected for summer 99.

- [1] D. Einfeld et al., Status of the 2.5 GeV Light Source ANKA, these proceedings
- [2] H.Bach, D. Einfeld, L.Praestegaard, N. Hertel, U. Ristau, R. Rossmanith; The ANKA Injector EPAC 98, June 22-26, Stockholm, Sweden (1998)

BEAM LIFETIME STUDIES FOR THE SLS STORAGE RING

M. Böge, A. Streun, Paul Scherrer Institut, 5232 Villigen PSI, Switzerland

Abstract

SLS is a high brightness light source with 4.8 nm emittance at 2.4 GeV. Particle losses due to Touschek scattering will strongly affect the beam lifetime.

We present Touschek lifetime calculations based on a refined tracking procedure for determination of the lattice momentum acceptance. The dependency of lifetime on the gap height of insertion devices and on the RF cavity voltage is studied in detail for the reference optics of the SLS storage ring lattice.

Including gas scattering losses we expect 3.5 hrs of total lifetime for 1 nCb bunch charge and 0.1 % coupling. Installation of a 3^{rd} harmonic cavity for bunch lengthening would increase the total lifetime to 8 hrs and thus is recommended.

1 TOUSCHEK TRACKING

Touschek lifetime is approximately¹ given as function of momentum acceptance (MA) and bunch volume integrated over the lattice structure [6, 12].

While the RF MA is given by the cavity voltage and almost constant along the lattice, the lattice MA depends on where the scattering event occurred and varies along the lattice. In particular we have to distinguish between

- non-dispersive sections, where a scattered particle will
 just follow the dispersive orbit, and local MA is determined by the momentum range of closed orbit existence or physical aperture, and
- dispersive sections, where a scattered particle will start an oscillation around the dispersive orbit, and local MA may be determined by dynamic aperture or by mismatch of dynamic to physical aperture.

Usual calculations [13] assume a perfectly linear and chromaticity corrected lattice and obtain the local MA from

$$\delta_{acc}^{L}(s_o) = \min_{i=1...N} \left\{ \frac{a_{xi}}{\sqrt{H_o \beta_{xi} + \eta_i}} \right\}$$
(1)

with $\delta := \Delta p/p_o$, H_o the lattice invariant (dispersion's emittance) at scattering location and β_{xi} , η_i , a_{xi} horizontal beta function, dispersion and vacuum chamber half width at other lattice locations.

In modern light sources, designed for lowest emittance (at limited circumference), strong sextupoles for correction of large chromaticities generated by the required focusing, introduce significant nonlinearities into the lattice that have to be considered in MA calculations:

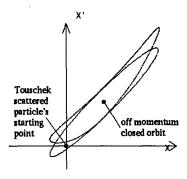


Figure 1: Nonlinear betatron motion: A Touschek scattered particle starting to oscillate around the off-momentum orbit would be accepted by the linear separatrix (ellipse) but not by the nonlinear separatrix.

- Momentum dependency of linear optics parameters: Calculations on light source lattices optimized for large MA [1] have to consider momentum deviations up to $\pm 10\%$. Within this wide range the $2\nu_x, 2\nu_y$ chromatic resonance drive terms from the sextupoles' Hamiltonian cause momentum dependent beta beats and second order chromaticities [2].
- Nonlinear variation of closed orbit with momentum, i.e. higher order dispersion as included earlier in calculations at SOLEIL [11].
- Nonlinear betatron motion: Momentum dependent dynamic apertures smaller than the physical apertures or distortions of the transverse eigenfigures and mismatch to the physical apertures as illustrated in Fig. 1 lead to a reduction of local MA.
- Synchrotron oscillation: Due to higher order chromaticity scattered particles walk over wide regions in the tune diagram crossing several betatron resonances. Hence we observe a significant reduction of MA when including synchrotron oscillations compared to fixed-δ calculations.
- Magnet alignment errors: Touschek lifetime depends on the emittance coupling factor $\kappa = \varepsilon_y/\varepsilon_x$. Including alignment errors generating nonzero κ in a flat lattice is required to predict numbers for average lifetime and its variation for different error distributions ("seeds").
- Mini gap insertions: The beam halo has larger coupling than the beam core, as observed for example at ESRF [10], since large amplitude particles from scattering suffer more from higher order coupling resonances. For the performance of light sources using undulators with full gap heights as small as 4 mm it is essential to know how this affects the lifetime.

¹The well-known integral formula assuming flat beams and nonrelativstic transverse motion agrees on a 10 % level with detailed Monte Carlo simulations [8].

In order to include all these effects from the Touschek lifetime point of view we take a brute force approach by starting particles from the beam core with some momentum deviation, i.e with the 6D initial vector $(x, p_x, y, p_y, \delta, \Delta s) = (0, 0, 0, 0, \pm \delta, 0)$ as it will be immediately after a Touschek scattering event [12]. Tracking and binary search for the maximum accepted δ gives the local MA. The resulting stepwise function of lattice MA $\delta^L_{acc}(s)$ then is entered into the Touschek integral. If misalignments are to be included the calculation is repeated for a number of random seeds. This procedure was implemented into the program TRACY [5].

2 MODEL PARAMETERS

The SLS lattice in "D2A optics" as current reference lattice has dispersion free straight sections with mini- β -optics, and a natural emittance of 4.8 nm at 2.4 GeV. The working point was set to 20.82/8.28 as a compromise between sextupole Hamiltonian suppression requirements [1] and vertical closed orbit distortion minimization. This is not the lattice mode with optimum dynamic aperture but still provides a TRELMA² of 5.1% (fixed- δ -calculation), which is larger than 3.9% provided by the 2.6 MV RF system [7].

At SLS magnets are rigidly mounted onto girders, the girders are connected into a "train link" by means of horizontal sensor and hydrostatic levelling systems [3]. The following table gives alignment (horizontal & vertical) and tilt errors considered as realistic (rms values, cut at 2σ):

	shift [µm]	tilt [µrad]
elements to girder	50	100
girder to girder	100	0
girder absolute	300	25

After setting the misalignments a SVD closed orbit correction was applied, preceded by a beam threader, if no initial orbit was found, and followed by an emittance coupling suppression by means of small skew quadrupoles [4]. The average coupling was 0.27% before and 0.10% after coupling suppression.

The narrow gap from insertion devices was included in tracking by reducing the vertical aperture on a length of 2 m in all six short straight sections ($\beta_u^* = 1.6 \text{ m}$).

Tracking was done for 1.5 synchrotron oscillation periods (100...300 turns). Binary search resolution for determination of local MA was 0.01%. All calculations assumed 1 nCb single bunch charge.

3 RESULTS

3.1 Touschek lifetime and RF voltage

Fig. 2 displays the Touschek lifetime, normalized to $\kappa = 0.1\%$, for the error free lattice in linear approximation

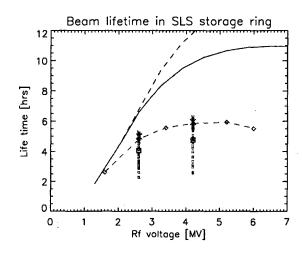


Figure 2: Touschek lifetime as a function of RF voltage for progressive model refinements:

linear lattice, no errors, fixed- δ (----) adding lattice nonlinearities (----) adding synchrotron oscillation (-- \diamond ---) adding alignment errors, $<\kappa>=0.27\%$, normalized to $\kappa=0.1\%$ (\square \square \square) adding coupling control, $<\kappa>=0.1\%$, (\times , \times ----)

according to eq.(1) and for the nonlinear optics in fixed- δ -calculation as well as with synchrotron oscillation. Mini gaps were not yet set.

Already for the ideal lattice we see a strong reduction of lifetime, i.e. lattice MA (dynamic aperture), when including nonlinearities and synchrotron oscillation. Thus increasing the RF voltage beyond the planned 2.6 MV would gain only little in lifetime.

After introducing misalignments and closed orbit correction we observe large spread of different seeds and further (κ -normalized!) lifetime decrease, however after applying coupling suppression the ideal lattice values are restored and the spread from different seeds is compressed as shown for two voltage values in Fig. 2.

3.2 Touschek lifetime and gap height

Fig. 3 displays the Touschek lifetime, again normalized to $\kappa = 0.1\%$, as a function of the mini gap full height. The ideal lattice assuming 100% halo coupling would have reduced lifetime for full gap heights ≤ 10 mm. Assuming 0.1% for both core and halo coupling the mini gaps show no effect. After introducing misalignment errors (fixed- δ -calculation) we see that the halo coupling is larger than the core coupling but not at 100%.

Including synchrotron oscillation seriously decreases lifetime for any gap height. However after coupling correction, the κ -normalized lifetime recovers and becomes almost independent of mini gap height.

Fig. 4 illustrates how lifetime limitations from the mini gap insertion are removed by coupling correction.

²The Touschek relevant effective lattice momentum acceptance is the MA value, where the RF alone (i.e. infinite lattice MA), set to the corresponding voltage, and the lattice alone (i.e. infinite RF MA) give equal Touschek lifetimes (normalized to bunchlength) [12]

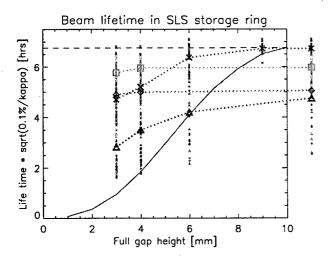


Figure 3: Touschek lifetime vs. insertion gap full height: Error free lattice for $\kappa_{halo}=100\%$ (——) and $\kappa_{halo}=\kappa_{core}=0.1\%$ (- - - -), (nonlinearities included, fixed- δ calculation, $V_{rf}=2.6$ MV) Lattice with alignment errors, fixed- δ calculation, $V_{rf}=2.6$ MV (· · · × · · ·) Tracking with synchrotron oscillations, $V_{rf}=4.2$ MV, $<\kappa>=0.27\%$, normalized to $\kappa=0.1\%$ (· · · Δ · · ·) Application of coupling suppression, $<\kappa>=0.1\%$, for $V_{rf}=4.2$ MV () and 2.6 MV (· · · α · · ·) Points outside plot window are for a full "gap" height of 32 mm, i.e. no insertions.

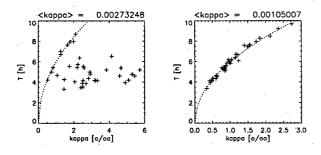


Figure 4: Touschek lifetime vs. emittance coupling factor κ without (left) and with (right) coupling correction for different seeds of alignment error settings. Points not lying on the dotted $T \propto \sqrt{\kappa}$ curve for the ideal lattice indicate beam losses at the insertion's 4 mm gap. Actually the average lifetime is higher with reduced coupling!

3.3 Gas scattering lifetime

Scattering of electrons on residual gas molecules also imposes serious lifetime restrictions: The cross section for electron losses after elastic scattering depends on the minimum transverse acceptance and on the vacuum conditions. With an insertion length of ≈ 2 m, $\beta_y = 2.2$ m at entrance and exit as provided by the "D2A" optics of the SLS lattice is almost at optimum. Assuming 1 nTorr of carbon monoxide for the residual gas, the gas scattering lifetime obtained

from the code ZAP [13] is 14 hrs for 4 mm insertion full gap height.

3.4 RF upgrade for lifetime improvement

Increasing the RF voltage in order to raise the RF MA or installation of a 3^{rd} harmonic cavity for bunch lengthening are two options for increasing the Touschek lifetime. Higher voltage gains little lifetime, at least for the lattice mode investigated here. The harmonic cavity however, fighting Touschek effect at its origin instead of curing the consequences, would lengthen the bunch and correspondingly the Touschek lifetime by a factor of 4 and thus is the method of choice [9]. The following table displays results of Touschek and total lifetime assuming 4 mm gap insertions without and with a 3^{rd} harmonic cavity³:

V_{rf}	Touschek	Gas	Total
[MV]	[hrs]	[hrs]	[hrs]
2.6 [+3 rd harm.cav.]	4.8 [19]	14	3.6 [8.1]
4.2 [+3 rd harm.cav.]	5.9 [24]	14	4.2 [8.8]

4 CONCLUSION

Mini gap insertion devices in the lattice partially reverse the usual dependency of Touschek lifetime on emittance coupling: suppression of the coupling factor to values as low as 10^{-3} gives optimum beam lifetime and removes sensitivity of the lifetime to particular alignment error settings while on the other hand providing high brightness. Larger emittance coupling does *not* increase the beam life time.

Increasing the RF voltage showed insignificant gain in lifetime, at least for the lattice mode studied here.

For SLS at standard operation conditions we expect a total lifetime of $3\frac{1}{2}$ hrs which may be increased to 8 hrs by means of a 3^{rd} harmonic cavity.

- [1] J. Bengtsson et al., NIM A 404 (1998) 237
- [2] J. Bengtsson, SLS-TME-TA-1997-0009, March 97
- [3] M. Böge et al., Proc. EPAC-98, p.644
- [4] M. Böge, M.Muñoz, A. Streun, these proceedings
- [5] M. Böge, SLS-TME-TA-1999-0002, April 99
- [6] H. Bruck, Accélérateurs circulaires de particules, Paris 1966
- [7] M. E. Busse-Grawitz et al., these proceedings
- [8] S. Khan, BESSY-TB 177/93
- [9] P. Marchand, these proceedings
- [10] G. Mülhaupt, priv. comm.
- [11] A. Nadji et al., Proc. PAC 97, p.1517
- [12] A. Streun, SLS-TME-TA-1997-0017, Nov. 97
- [13] M. Zisman et al., ZAP User's Manual, LBL-21270, Dec. 86

³All lifetime numbers are defined for decay of beam current to half its initial value

DIAMOND: A UK NATIONAL LIGHT SOURCE PROJECT

AA Chesworth, JA Clarke, GS Dobbing, DJ Holder, HL Owen, MW Poole, SL Smith, VP Suller, A Wolski, CLRC Daresbury Laboratory, Warrington WA4 4AD, UK

Abstract

Modifications to the original racetrack lattice concept as used in the feasibility study of the DIAMOND light source project are presented here. Double bend achromat structures with both 16 and 20 cells are described, with 4 fold superperiodicity. The production of higher brightness beams through lower emittance is achieved by optics solutions having finite dispersion in the long straights. The implications of insertion device minimum gaps and of the beam energy spread are discussed with reference to the specification of the radiation spectrum required by users.

1 PROJECT BACKGROUND

In 1998 the UK government announced that funding had been allocated for a new X-ray synchrotron source, to replace the existing SRS at the Daresbury Laboratory. These funds will be jointly provided by the Government and the Wellcome Trust, which has a remit to fund research in the life sciences. The announced funding covers the 3 year period from April 1999, but it is assumed that later allocations will cover the full 6 year project timescale.

A review of the synchrotron radiation needs of the UK user community has recommended construction of a medium energy ring that complements the ESRF facilities in Grenoble; however for applications below about 50-100 eV an alternative national low energy source has been envisaged [1]. The 3 GeV DIAMOND design has demonstrated the feasibility of an X-ray synchrotron source at a scale suitable for the needs of the UK user community. Designed originally as a 16 cell double bend achromat (DBA) racetrack [2], this has now been modified to a 4 fold superperiodicity to obtain improved flexibility and a better dynamic aperture [3].

Although a formal specification for DIAMOND is still in the process of being agreed, it is apparent that an important application of the facility will be in protein crystallography using samples of typical dimension 50µm and with very large cell dimensions. For this application high brightness photons at the selenium K-edge (12.7 keV) are essential, with energies up to about 20 keV also desirable, and several versions of the DIAMOND lattice have been studied to optimise performance against these criteria. High fluxes up to 50 keV will be provided by multipole wigglers (MPW), with energies beyond this available from high field insertions; DIAMOND is also

well optimised for high brightness output in the soft X-ray region down to 100 eV or below. The extent to which even lower output energy (5-50 eV) can meet a defined user case is still under investigation, but will not alter the overall DIAMOND optimisation.

Choosing between undulators or MPWs to deliver the required photon beams can have a significant influence on the facility specification, not least in the rf system demands. Additional factors are the ultimate minimum gap achievable with insertion devices and the electron beam energy. The study of these issues reported here indicates that a 3 GeV, 20 cell DBA lattice operated with finite dispersion in the long straights and with a circumference of about 400 m will produce the necessary high brightness beams up to 20 keV.

2 RACETRACK LATTICE

The original 16 cell racetrack lattice [2] consisted of 2 super-long cells together with 6 high and 8 low radial beta cells for injection, rf systems and more standard insertion devices. By independently powering the quadrupoles exact matching could be obtained between each type of cell. However the effect of the 2 super-long straights was to make the lattice fairly sensitive to errors and the 2-fold superperiodicity impacted strongly on the dynamic aperture achievable.

3 FOUR-FOLD LATTICE

With the continuing assessment of user requirements and after a review of the design of the racetrack machine it was decided that the basic DIAMOND design could be modified to obtain a number of improvements. Four-fold symmetry was selected with the prospect of better nonlinear lattice behaviour and the superstraights were shortened but able to accommodate all the accelerating cavities in one straight and injection components in another. Initial studies have been carried out on a DBA structure composed of 16 cells in four superperiods with straight section types in the following order: long – short(low βr) – short(high βr) – short(low βr).

It is important in determining the final performance of this type of lattice that the flexibility to vary the straight section beta functions is assessed; this however is dependent on fully optimising the nonlinear properties of the lattice in each configuration. At the moment both the achromat and the short straights are based on those of the previous racetrack machine. The long straights have the same quadrupole arrangement but are now matched into an 11.8 m straight instead of the shorter straight. Preliminary nonlinear studies of this type of lattice at a variety of tune points have been carried out, and the results indicate a significant improvement in the ease of obtaining reasonable dynamic properties compared with the more demanding two-fold symmetric racetrack machine.

4 20 CELL LATTICE

As a national facility designed to satisfy the UK's needs well into the next century, the DIAMOND design must have the potential to deliver the number of sources and the quality of beam expected by users throughout its lifetime. Therefore studies have been carried out to investigate the performance and feasibility of a facility based upon a larger circumference, lower emittance ring. By extending the 16 cell four-fold symmetric lattice to 20 cells, it has been possible to confirm a reduction of emittance by about a factor of two, together with a useful increase in straight sections available for IDs from 14 to 18.

The parameters for a potential 20 cell lattice are compared with those of the 16 cell lattice in Table 1. Although there is a significant increase in circumference over the original 16 cell lattices, this facility can fit comfortably on the Daresbury site. The table illustrates a four-fold symmetric solution but other options, such as a five-fold or even ten-fold symmetries, are still under consideration.

Table 1: Comparison of 16 and 20 cell lattices

Table 1. Comparison of 10 and 20 cen factices					
Lattice	16 cell	20 cell			
Energy [GeV]	3.0	3.0			
Circumference [m]	329.2	396.8			
Max length for IDs [m]	12 x 4.5	16 x 4.5			
_	4 x 8.0	4 x 8.0			
Injection energy [GeV]	3.0	3.0			
Beam current [mA]	300	300			
Emittance; h, v [nm rad]	12.9, 0.13	7.8, 0.08			
Source size (σ) [μ m ²]					
Long straight; h x v	497 x 31.5	249 x 15.3			
Short straight; h x v	374 x 10.2	279 x 11.2			

The theoretical minimum emittance in a DBA can be reduced by a factor of 3 by allowing finite dispersion outside the achromatic arc. Studies with various realistic lattices have confirmed that it is possible in practice to obtain significant reduction in emittance under such conditions. In the particular case of a 3 GeV, 20 cell lattice with 4-fold symmetry, the emittance can be reduced from 8 nm-rad to about 3-nm-rad, with consequent major benefits in the brightness. Table 2 shows the comparison between lattice parameters for zero and finite dispersion.

Table 2: Comparison of Zero/Finite Dispersion Settings

	16 cell		20 (cell
	n = 0	$n \neq 0$	n = 0	$n \neq 0$
Emittance \mathcal{E}_0 [nm rad]	12.9	4.95	7.8	2.67
Mom ^m compacn [10 ⁻⁴]	8.73	8.42	4.64	4.45
Betatron tune Q,	16.41	16.40	20.46	20.48
Betatron tune Q _v	9.85	9.88	11.93	11.29
Nat. chromat. ξ_x	-63.60	-46.63	-69.9	-69.4
Nat. chromat. ξ_y	-22.25	-22.63	-21.6	-27.6
Long straight η_x [m]	0	0.237	0	0.144
Short straight η_x [m]	0	0.185	0	0.155
Long straight β_x [m]	16.3	14.2	8.08	8.00
Long straight β_y [m]	6.55	9.00	3.05	2.10
Short straight β_x [m]	9.22	8.52	10.1	10.1
Short straight $oldsymbol{eta}_y$ [m]	0.690	0.753	1.63	1.20

Representative lattice functions for the finite dispersion solution of the 20 cell version are shown in Fig. 1.

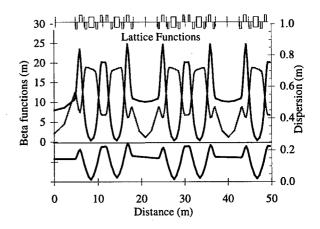


Figure 1: Finite dispersion lattice functions.

5 PHOTON OUTPUT

The photon output from DIAMOND will cover a large range, from infra-red to hard X-ray, although the source is optimised to provide undulator output from about 100 eV to at least 5 keV and multipole wiggler output to beyond 50 keV. The photon energy range between about 5 to 20 keV has recently taken on new importance with the greater emphasis on the user case for life sciences and, in particular, protein crystallography. This photon range is in the crossover region for use of multipole wigglers and undulators in a 3 GeV source. The assumptions applied in earlier parameter feasibility studies, such as the minimum insertion device gap and the highest undulator harmonics to use, have been studied more carefully and revised.

5.1 Insertion Device Gap

Early feasibility studies for DIAMOND assumed an initial insertion device gap of 20 mm with a gradual move towards smaller gaps (and therefore higher photon energy output from undulators) after the machine was commissioned and well understood. This approach is no longer possible as the source must now have undulator beamlines in the 5 to 20 keV region operating from day one. Calculations have confirmed that beam lifetimes longer than 10 hours should be available with 5m long vacuum vessels within an insertion device magnet gap of 15 mm or alternatively with shorter 2m long vessels within a reduced magnet gap of 10mm. The results of representative ideal gas scattering calculations are shown in Fig. 2 and illustrate that at small gaps the elastic (coulomb) component dominates the losses; good lifetime is however still obtained for beam-stay-clear apertures well under 10 mm, giving confidence in utilisation of small gap undulators. It is likely that in-vacuo solutions for DIAMOND insertion devices will also be explored.

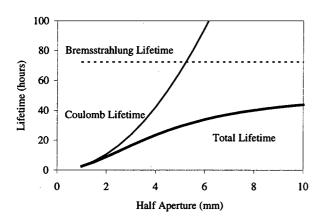


Figure 2: Gas scattering lifetime dependence on vertical aperture in a 5m long insertion device vessel.

5.2 Use of High Undulator Harmonics

Undulators have generally been designed to utilise the first, third and occasionally fifth harmonics. For hard Xray beam lines requiring high brightness in DIAMOND it will be important to exploit harmonic output beyond the fifth and this has been carefully assessed. It is well known that at high harmonics factors such as magnet quality, beam emittance and energy spread have greater influence on the quality of the photon output. When these factors are taken into account the on-axis beam brightness can reduce by one or two orders of magnitude in some circumstances. However, calculations with SRW [4] have shown that if all of the photons in the central cone can be accepted by the beamline, then the flux reduction is generally less than a factor of two from the ideal, even allowing for an energy spread well above the natural value. A summary of such a result is given in Fig. 3 and

an example 10 mm gap undulator tuning curve is shown in Fig. 4.

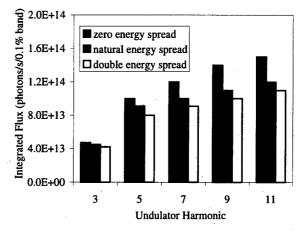
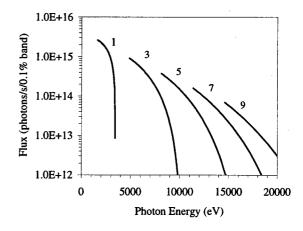


Figure 3: Undulator integrated flux at 10 mm gap.



Figure' 4: Example undulator tuning curve for a 25 mm period and 10 mm gap device.

DIAMOND can deliver high flux output from its undulators over a very wide energy range from below 100 eV up to 15 keV and beyond. It is evident that at the higher energy end such undulators can be used in preference to the MPWs for topics such as protein crystallography, at least between 5 and 15 keV. This has major implications for the source specification, reducing the overall radiation power loading and also ensuring that an electron energy increase above 3 GeV is unnecessary.

- VP Suller; "A Source Design Strategy Providing 5eV-100keV Photons", Jour Synch Radn, 1, pp5-11, (1994).
- [2] MW Poole & VP Suller, "Design Progress on DIAMOND", Proc European Particle Accelerator Conference, Sitges, 1996.
- [3] JA Clarke et al; "Update on the DIAMOND Light Source Project", Proc European Particle Accelerator Conference, Stockholm, 1998.
- [4] O Chubar & P Elleaume, "Accurate and Efficient Computation of Synchrotron Radiation in the Near Field Region", Proc European Particle Accelerator Conference, Stockholm, 1998.

THE LATTICE OF THE 1.0 GeV VSX STORAGE RING

H. Takaki, * K. Harada, T. Koseki, N. Nakamura, Y. Kamiya, ISSP, U. of Tokyo Y. Kobayashi, KEK-PF

Abstract

The University of Tokyo has been promoting a future project to construct a third-generation VUV and Soft X-ray light source (VSX). The VSX ring has an energy of 1.0 GeV, an emittance of about 0.7 nm•rad, a circumference of about 230 m and two 30 m long straight sections for insertion devices. The most significant characteristic of the VSX ring is that its emittance is below a diffraction limit for the photon energy of 100 eV. It can provide the VUV and Soft X-ray light with a maximum brilliance above 10^{20} [photons/sec/mm²/mrad²/0.1% b.w.] using a long undulator installed in 30 m long straight section.

1 INTRODUCTION

The University of Tokyo aims at constructing a thirdgeneration VUV and Soft X-ray light source (VSX) in the new Kashiwa Campus. In general, a "third-generation" light source is characterized by a low emittance and a long straight section for insertion devices.

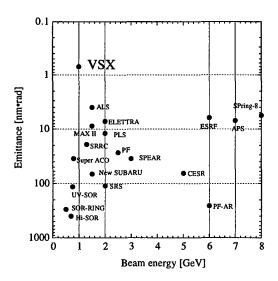


Figure 1: The emittance versus the beam energy for the typical synchrotron light sources in the world.

The beam emittance of the VSX ring is able to reach the diffraction limit, $\varepsilon \sim \lambda/4$ where λ is the wavelength of the emitted photon. For the typical photon energy of 100

eV ($\lambda \sim 12$ nm), the diffraction limit is about 1 nm•rad. The minimum value of the beam emittance is 0.73 nm•rad, which is extremely small compared with the existing synchrotron light sources around the world (see Fig. 1). For a maximum current of 200 mA, the emittance becomes slightly larger than 1 nm•rad due to the intrabeam scattering.

The VSX ring has two 30 m long straight sections for insertion devices. The 27 m long undulator will be installed in one of them, which is capable of providing a unprecedentedly brilliant synchrotron light in the VUV region.

In the following sections, the lattice configuration, the linear optics, the chromaticity correction and the dynamic aperture are reported.

2 LATTICE

The storage ring has a shape of racetrack with a circumference of 230.2 m (see Fig. 2). It is composed of 22 Normal Cells, four Matching Sections including four Half Cells and two 30 m long straight sections. The Half Cell is slightly different from a half of Normal Cell.

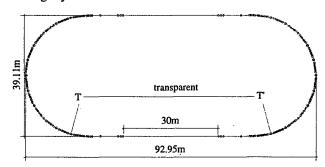


Figure 2: The VSX ring layout

2.1 Normal Cell

The lattice configuration of the *Normal Cell* is of Theoretical Minimum Emittance type [1], which has an emittance smaller than the DBA type by a factor of three. The theoretical minimum emittance is given by,

$$\varepsilon_{x0}^{\min} = \frac{1}{12\sqrt{15}J_x} C_q \gamma^2 \left(\frac{2\pi}{N}\right)^3,\tag{1}$$

where $C_q = (55/32\sqrt{3})(\text{hmc})$, J_X is the damping partition number and N is the number of bending magnets. As J_X is almost equal to 1 for the bending magnets of the separated function type, the theoretical minimum emittance is 0.56 nm-rad for N=24.

To realize this emittance in the VSX ring, the horizontal betatron function β_x and dispersion function η_x

^{*}Email: takaki@issp.u-tokyo.ac.jp

should be 0.075 m and 0.0063 m at the center of a bending magnet. Thus a very small beam size less than 10 μ m is attained at the magnet center, so that a high brilliant light can be supplied to bending beamlines.

2.2 Matching Section

A T-T' Section (see Fig.2 and 3) is composed of a long straight section and two Matching Sections. The Half Cell, the section between SD and BH, reduces the η_x of Normal Cells to be zero. For the T-T' Section to be "transparent" for the non-linear effects and behave as a Normal Cell, the phase advances should be,

$$\Delta \phi_{x} = 2\pi m + \phi_{x \text{ Normal Cell,}}$$
 (2)

 $\Delta \phi_{y} = 2\pi n + \phi_{y \text{ Normal Cell.}}$ (3)

For the VSX ring, m=1 and n=2 are chosen. Then the optics looks as if it were perfectly 24-fold symmetric for on-momentum particles.

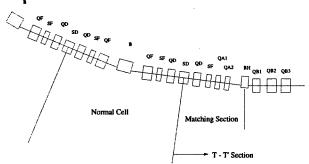


Figure 3: The Matching Section layout

3 OPERATION MODE

Since the Touschek effect is severe for Low Emittance Mode (LEM), a moderate operation of High Emittance Mode (HEM) is prepared for easy commissioning and stable operation.

3.1 Low Emittance Mode

The emittance of *Low Emittance Mode* is 0.73 nm•rad. The fundamental parameters of this mode are listed in Table 1. The Touschek lifetime is 5 hours due to the small beam size, while the Coulomb lifetime is about 10 hours at 10⁻¹⁰ Torr.

Table 1: Fundamental parameters of the VSX ring
(Low Emittance Mode)

(Low Emittance Mode)				
E [GeV	/] 1.0			
	Theoretical			
	Minimum			
•	Emittance			
Ns	~24			
C [m]	230.2			
	30 m x 2			
ε _{x0} [nm•	rad] 0.732			
σ _E /E	5.67×10^{-4}			
Factor a	4.49x10 ⁻⁴			
rizontal V _X	17.4			
	E [GeV Ns C [m] $\epsilon_{\chi 0}$ [nm• σ_{E} /F			

	Vertical	$v_{\mathbf{y}}$	7.71
Natural Chromaticity	Horizontal	ξ _x	-38.7
	Vertical	ξ _y	-39.3
Damping Time	Horizontal	τ_{X} [msec]	39.6
	Vertical	τ _y [msec]	39.8
	Longitudinal	$\tau_{\rm Z}$ [msec]	19.9
Revolution Frequence	y	f _{rev} [MHz]	1.302
RF Voltage		$V_{RF}[MV]$	0.5
RF Frequency		f _{RF} [MHz]	500.1
Synchrotron Tune		$\nu_{ m s}$	0.0037
Bunch Length	*	σ _z [mm]	2.52
RF-bucket Height		(AE/E) _{RF}	0.040

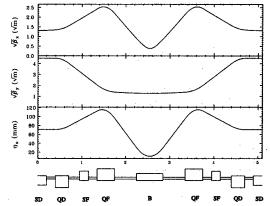


Figure 4: The optics of the Normal Cell (LEM)

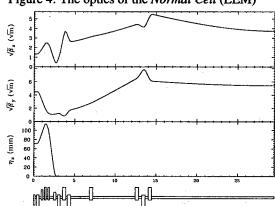


Figure 5: The optics of the Matching Section (LEM)

The optics of the *Normal Cell* and the *Matching Section* are shown in Fig. 4 and 5. The parameters of magnets are listed in Table 2.

The chromaticity is corrected by only 2 families of sextupoles (SF, SD) in the *Normal Cells*, but the so-called harmonic sextupole is not used. The horizontal and vertical dynamic apertures after chromaticity correction are shown in Fig. 8.

3.2 High Emittance Mode

The emittance of *High Emittance Mode* is 2.6 nm•rad. The fundamental parameters of this mode are listed in Table 3. Touschek lifetime becomes over 10 hours.

The optics of the *Normal Cell* and the *Matching Section* are shown in Fig. 6 and 7. The horizontal and vertical dynamic apertures after chromaticity correction are shown in Fig. 8.

Table 2: Parameters of Magnets

	I TOM	
	LEM	HEM
[T]	1.450 [T]	1.450 [T]
B'1/Βρ [1/m]	1.664	-0.622
B' 1/B ρ [1/m]	-0.715	0.630
(B" I/B ρ) [1/m²]	33.168	-7.590
(B" l/B ρ) [1/m²]	-26.747	4.015
	B' l/B ρ [1/m] B' l/B ρ [1/m] (B" l/B ρ) [1/m²]	B' l/B ρ [1/m] 1.664 B' l/B ρ [1/m] -0.715 (B" l/B ρ) [1/m²] 33.168

Table 3: Parameters for High Emittance Mode

Natural Emittance	ε _{x0} [nm•rad]	2.64
Momentum Compaction Factor	α	1.02×10^{-3}
Natural Chromaticity Horizontal	ξ _x	-34.6
Vertical	ξ _y	-18.7
RF Voltage	V _{RF} [MV]	0.7
Bunch Length	$\sigma_{\rm Z}$ [mm]	3.20
RF-bucket Height	(ΔE/E) _{RF}	0.032

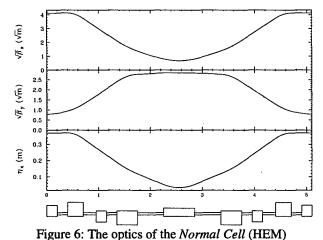
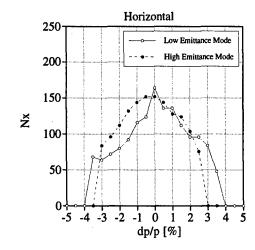
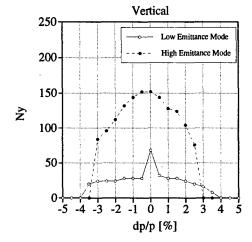


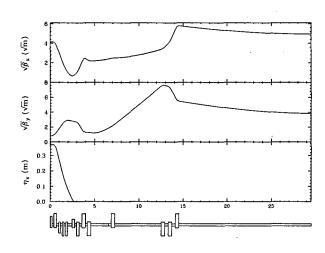
Figure 7: The optics of the *Matching Section* (HEM) Figure 8: The horizontal and vertical dynamic apertures normalized by $\sqrt{\beta \varepsilon_{x0}}$.

4 REFERENCES

[1] Y. Kamiya and M. Kihara, "On the design guideline for the low emittance synchrotron radiation source", KEK 83-16.







A FOUR CELL LATTICE FOR THE UCLA COMPACT LIGHT SOURCE SYNCHROTRON

A. A. Garren*, and M. A. Green**

- * UCLA Center for Advanced Accelerators, Los Angeles CA 90095
- ** Lawrence Berkeley National Laboratory, Berkeley CA 94720, USA

Abstract

The 1.5 GeV compact light source UCS proposed for UCLA must fit into a shielded vault that is 9.144 meters (30 feet) wide. In order for the machine fit into the into the allowable space, the ring circumference must be reduced 36 meters, the circumference of the six cell lattice. to something like 26 or 27 meters. The four cell lattice described in this report has a ring circumference of 27.0 meters. The four cell ring consists of twelve 6.5 T superconducting dipoles, twenty-four conventional quadrupoles, sixteen conventional sextupoles and four straight sections 1.02 meters long. The 1.5 GeV electron beam is bend in the dipoles to produce x rays with a critical energy of 9.8 keV. The superconducting dipoles have been modeled in three dimensions. modeling shows that magnetic induction falls off from its full design value to nearly zero in about 50 mm at the ends of the dipoles. The magnetic length of the dipole is Calulated to be 403 mm.

1 BACKGROUND

The six cell UCLA compact storage ring described in the 1997 Particle Accelerator Conference paper[1] appeared to be very good for producing intense high energy X rays. The six cell lattice had a low emittance and it tracked very well. The problem with six cell storage ring was the fact that it does not fit in an existing vault in the basement of a new building on the UCLA campus. The vault in the basement of building can not be enlarged to accommodate the six cell storage ring. As a result, the ring circumference must be reduced so that it can fit within a vault that is 9.142 meters (30 feet) wide. The length of the shielded vault is nearly 40 meters. This appears to be adequate for housing a ring injector and a number of experimental X ray beams. If the ring diameter can be reduced so the machine will fit in the vault, the new building at UCLA is adequate for the UCS ring.

Reducing the number of cells in the storage ring was the approach that was chosen to reduce the ring size. Three cell and four cell lattices were studied. Lattices with fewer numbers of cells have less space occupied by conventional quadrupoles and sextupoles. Ring circumference was also reduced by reducing the number of long straight sections. The object of the study was to reduce the number of the cells in the machine while trying to keep the beam emittance low.

2 THE REDUCED SIZED RING

The designs for the reduced diameter storage rings were driven by the desire to extract synchrotron X rays from all of the dipoles. Like the six cell machine described in Ref [1], there are twelve superconducting bending magnets where the high energy X rays are generated. Like the six cell machine, there was also a strong desire to reduce machine emittance so that the vacuum chamber throughout the ring can have the same cross-section. As a result, the quadrupoles and sextupoles would all have the same aperture. The number of types of quadrupoles could be reduced to two and there would be only one type of sextupole. The reduced emittance would lead to a smaller beam size in the dipoles and brighter x-ray beams.

The six cell ring had six identical 6 meter long cells. Each of the six cells contains two 30 degree superconducting dipoles. Each cell has a 1.34 meter long drift space (between two quadrupole doublets) and a section that contains all of the chromaticity sextupoles. The sextupoles surround QF3 focusing quadrupole, which forces the dispersion to be zero in the long straight section. The dipoles have parallel faces that provide vertical edge-focusing.

The four cell ring studied had four identical cells that were 6.75 meters long. Each cell contains three 30 degree superconducting dipoles, a 1.02 meter long drift space (between two quadrupole doublets) and two sections that contain all of the chromaticity sextupoles. A pair of sextupoles surround the two QF3 focusing quadrupoles, which forces the dispersion to be zero in the long straight section. Defocusing is provided by the dipole parallel faces that provide vertical edge-focusing. The four cell ring computer simulation converged immediately.

A three cell ring with 8 meter long cells was studied. Each cell contained one 1.02 meter long straight section, two 0.5 meter long straight sections, four 30 degree superconducting dipoles, seven conventional quadrupoles and four conventional sextupoles. This ring would fit in the UCLA vault in all orientations. Unfortunately, the ring design studied did not work when modeled on the computer.

Figure 1 compares the half of the six cell ring (which is 12.5 meters wide) with half of the four cell ring (which is 9.1 meters wide). The six cell ring clearly does not fit in a hall that is 30 feet wide, whereas the four cell ring fits, but the margin is slim. Table 1 presents the magnet parameters for the six cell and four cell rings. Table 2 compares the calculated lattice parameters for six cell and four cell compact storage rings.

^{*} This work was supported by the Regents of the University of California.

⁺ email: magreen@lbl.gov

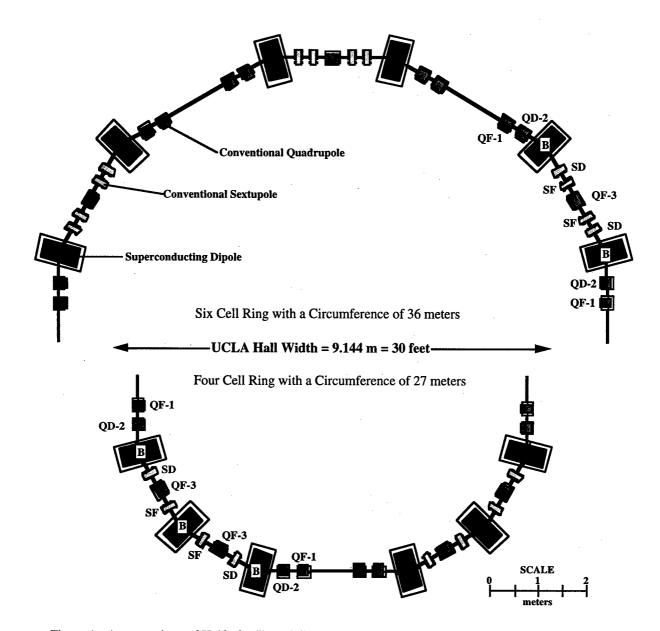


Figure 1: A comparison of Half of a Six 1.5 GeV Compact Storage Ring with Half of a Four Cell Ring

Table 1: Magnet Parameters for the Six Cell and Four Cell Rings

	Six	Cell Storage Rin	ng	Four	r Cell Storage R	ing
Magnet	Strength	Aperture Dia.	M Length	Strength	Aperture Dia	M Length
Type	(T, Tm^{-1}, Tm^{-2})	(mm)	(mm)	(T, Tm^{-1}, Tm^{-2})	(mm)	(mm)
Superconducting	g Dipole (T)	-				
В	6.468	40-180	405	6.468	40-180	405
Conventional Q	uadrupole (T m ⁻¹)					
QF-1	26.54	33.2	200	35.17	33.2	200
QD-2	-19.54	33.2	200	-36.00	33.2	200
QF-3	29.47	33.2	300	36.19	33.2	250
Conventional S	extupole (T m ⁻²)					
SF	1279.3	33.2	100	1788.0	33.2	120
SD	-1695.0	33.2	100	-1419.4	33.2	120

Table 2: Lattice Parameters for the Six Cell and a Four Cell 1.5 GeV Compact Rings

PARAMETER	6 Cell Ring	4 Cell Ring
Maximum Design Energy (GeV)	1.5	1.5
Injection Energy (GeV)	0.3	0.3
Max. Design Beam Current (mA)	200	200
Storage Ring Circumference (m)	36.0	27.0
Dipole Bend Radius (mm)	773.5	773.5
X-ray Critical Energy* (keV)	9.78	9.78
Number of X-ray Sources	12	12
Extracted X-ray Power* (kW)	123.2	123.2
X-ray Brightness** (MWm ⁻²)	3.42	3.94
Stored Electron Beam Energy* (J)	36.1	27.1
No. of Long Straight Sections	. 6	4
Long Straight Length (m)	1.34	1.02
Number of Cells	6	4
No. of S/C Dipoles per Cell	2	3
No. of Quadrupoles per Cell	5	6
No. of Sextupoles per Cell	4	4
Horz. Op. Emittance* (nm)	309	475
Vert. Op. Emittance* (nm)	34	53
Horizontal Tune	4.42	4.18
Vertical Tune	2.38	2.69
Horizontal Chromaticity	-5.24	-4.00
Vertical Chromaticity	-7.40	-14.82
Max. Horizontal Beta (m)	5.62	2.63
Max. Vertical Beta (m)	5.54	11.4
Max. Dispersion (m)	0.62	0.54
Energy Loss per Turn* (MeV)	0.617	0.617
RF Voltage (MV)	~1.2	~1.8
RF Frequency (MHz)	1299	1299
Energy Spread (parts in 1000)	1.52	1.52
Bunch Length* (mm)	8.1	7.2
Horz. Damping Time* (ms)	0.570	0.428
Vert. Damping Time* (ms)	0.584	0.438
Energy Damping Time* (ms)	0.295	0.222
Quantum Lifetime* (s)	$>1 \times 10^{10}$	1.5×10^9
Min. Physical Aperture* (sigma)	11.0	13.4

- * at the full design energy of the machine
- ** at full design energy and 5 meters from the dipole

3 DISCUSSION

In order for the four cell lattice to work as simulated, the superconducting ring dipoles must have the following characteristics: 1) The magnet gap is more than four times smaller than the pole width. In our case, the dipole gap is 40 mm while the pole width is 180 mm. 2) The magnetic field must be good to a few parts in ten thousand over 110 mm of the pole width. 3) The magnet must behave like an iron dominated magnet in that the magnetic length and the iron length must be nearly the same and the field must fall off rapidly at the ends of the magnet. In our case, the magnetic length is 405 mm; the iron physical length is 380 mm. (The coils at the end are about 32 mm longer than the iron.)

Three dimensional computer models of the dipole[2] show that the field can be made very uniform across the pole. The current in the coils can be adjusted so that the good field uniformity can be achieved from an induction of 0.432 T (corresponding to 100 MeV injection) to 6.918 T (corresponding to a maximum ring energy of 1.6 GeV. The magnetic field falls from 6.5 T to 0.02 T in less than 20 mm. The integrated field through the dipole is also very uniform. For a ring energy of 1.5 GeV the dipole induction at the center is less than 6.5 T.

In both the six cell ring and the four cell ring, the maximum pole induction for the quadrupoles was set to be about 0.6 T. The maximum pole induction for the sextupoles is about 0.5 T. As a result, the poles of the quadrupoles and the sextupoles can be shaped so that the magnets have a large good field region over the full range of machine energies.

The straight sections for both machines are short, but they are long enough for conventional 805 MHz RF cavities or 1300 MHz superconducting cavities. In both the six cell and the four cell machine, the RF cavities would occupy one straight section. In both machines, the injection elements would occupy two cells. The remaining cells could contain either superconducting or conventional insertion devices. The beam energy is low enough to allow the beam to be dumped into the vacuum chamber.

4 CONCLUSIONS

It appears that a four cell 1.5 GeV electron storage ring could be built to fit in the 9.142 m (30 feet) vault at UCLA. There is enough room in the four cell lattice for RF cavities, injection elements and perhaps an insertion device. The lattice has a long quantum life time, and the emittance is low enough to produce high intensity X ray beams for users. The X ray power and brightness is comparable to the six cell machine.

ACKNOWLEDGMENTS

The authors acknowledge discussions they have had with D. B. Cline and J. J. Kolonko of the UCLA Center for Advanced Accelerators. This work was performed with the support of the Regents of the University of California.

- [1] A. A. Garren and M. A. Green, "An Alternative Lattice Design for a Compact Light Source Ring," Proceedings of the 1997 Particle Accelerator Conference, p 520, IEEE Publications, New York (1997)
- [2] M. A. Green and C. E. Taylor, "Three Dimensional Field Calculations for a Short Superconducting Dipole for the UCLA Ultra Compact Synchrotron," to be published in the IEEE Transactions on Applied Superconductivity (1999)

LOW PERIODICITY LATTICE FOR THIRD GENERATION LIGHT SOURCES: AVOIDANCE OF DYNAMIC APERTURE REDUCTION BY SEXTUPOLE COMPENSATION

Yu. Senichev*, ISA, Aarhus University, Denmark

1 INTRODUCTION

The classic ring structure of a number of identical achromat cells arranged in a highly symmetric circular form has been used in the vast majority of synchrotron light sources. However, lattices with small electron emittances require smaller dispersion function and stronger sextupoles are needed in order to correct the chromaticity. In the same time, as is well known, the sextupoles dramatically decrease the dynamic aperture due to their nonlinear action. To avoid the influence of sextupoles on the dynamic aperture the multi-family sextupole schemes are used. But, unfortunately, all of them do not give complete compensation. In particular, for third generation synchrotron light sources the residual sextupole component becomes the stronger factor in comparison with errors and misalignments and this factor limits the dynamic aperture. Thus, the search of new solutions to decrease the influence of the sextupoles has remained to be actual. But let us ask ourselves, if we can not suppress effectively the influence of sextupoles, may be we should properly use the non-linearity of sextupole to stabilize motion? Such an instrument can be the non-linear tune shifts. Obviously, to realize this idea we should step aside from the classic ring structure, since it does not permit us to control the sign and the magnitude of tune shift independently on the tunes themselves. We propose a lattice consisting of many arcs containing combined function (or usual) magnets and focusing (and defocusing) quadrupoles separated by identical optical channels consisting of either one, two or more dispersionless straight sections[1]. A significant advantage of such a design is the ability to separate the functions of the arcs and the straight sections. The periodical part of the arcs is a pseudo-second order achromat joined with the straight sections through a dispersion suppressor and it differs from the second order achromat[2] by non-zero chromaticity. The lattice has one focusing and one defocusing family of sextupoles located on the periodical part of the arc. Varying the chromaticity of arcs by sextupoles and the chromaticity of straight sections by quadrupoles and keeping the total chromaticity equal zero, we can modify the tune shift at any working point.

2 SEXTUPOLE RESONANCES WITH NONLINEAR TUNE SHIFTS

In the proposed lattice the highest multipole is a sextupole. The resonance arises under the condition $q+k_x\nu_x+k_y\nu_y=$

 $\Delta \cdot \left(k_x^2 + k_y^2\right)^{1/2}$. Already in the first order of the resonance theory N=1 the sextupole excites four resonances $\{k_x,k_y\}=\{1,0;3,0;1,\pm 2\}$. The number of resonances and their order grow with the the order N as 2^{N+1} . In action-angle variables the averaging Hamiltonian of the motion can be written as:

$$H(I_{x}, I_{y}, \varphi_{x}, \varphi_{y}) = \frac{\left(k_{x}^{2} + k_{y}^{2}\right)^{1/2}}{k_{x}} \cdot \Delta \cdot I_{x} + \frac{\left(k_{x}^{2} + k_{y}^{2}\right)^{1/2}}{k_{y}} \cdot \Delta \cdot I_{y} + 2\left\langle h_{k_{x}, k_{y}, q} \right\rangle I_{x}^{k_{x}/2} I_{y}^{k_{y}/2} \cos\left(k_{x}\varphi_{x} + k_{y}\varphi_{y}\right) + \zeta_{x} I_{x}^{2} + \zeta_{xy} I_{x} I_{y} + \zeta_{y} I_{y}^{2}, \tag{1}$$

where the Fourier harmonic $h_{k_x,k_y,q}$ determines the effective strength of the resonance $k_x\nu_x + k_y\nu_y = q$ under the detuning Δ . It is proportional to the integral

$$\langle h_{k_x,k_y,q} \rangle \sim \int_{s_0}^{s} \beta_x^{k_x/2} \beta_y^{k_y/2} K_s(s) e^{i(k_x \mu_x + k_y \mu_y)} ds,$$
(2)

where $\mu_{x,y} = \int_{s_0}^s \frac{ds}{\beta_{x,y}}$ is the phase advance. Several formalisms of the perturbation theory up to the second order [3, 4] have been used to derive the expression of the tune shifts $\zeta_x, \zeta_{xy}, \zeta_y$ of the sextupoles. They all are the functions of the effective strength of the resonance and the detuning: $\zeta_{x,xy,y} = F\left(\frac{\left|h_{k_x,k_y,q}\right|^2}{\left|k_x\nu_x+k_y\nu_y-q\right|}\right)$. Thus, when we compensate the influence of the sextupoles, the strength of the resonance is suppressed proportionally to the first power of $h_{k_x,k_y,q}$, while the tune shifts are decreased as $\left|h_{k_x,k_y,q}\right|^2$.

2.1 Lattice classification

Let us consider the case of a third integer resonance in one plane. In the Hamiltonian system, where the friction force is absent, there are two types of fixed points. The fixed point $\overline{I_x}$, $\overline{\varphi_x}$ is the saddle, if the roots of the characteristic equation are real and it is the centre, when the roots are imaginary. The point itself is derived from the equations

$$\Delta + \frac{3}{2}h_{30q}\overline{I_x^{1/2}}\cos 3\overline{\varphi_x} + 2\zeta_x\overline{I_x} + \zeta_{x,y}I_y = 0 \quad (3)$$
$$\sin 3\overline{\varphi_x} = 0.$$

The last gives us plenty of combinations with the fixed points depending on the ratio between the parameters Δ ,

^{*} Email: senichev@dfi.aau.dk

 h_{30q} , ζ_x and $\zeta_{x,y}$. The influence of the non-linearity is specified by the discriminant D in the expression:

$$\overline{I_x^{1/2}} = -\frac{3h_{30q}\cos 3\overline{\varphi_x}}{8\zeta_x} \pm \frac{1}{4\zeta_x} \sqrt{\frac{9}{4}h_{30q} - 8\zeta_x (\Delta + \zeta_{x,y}I_y)}$$
(4)

Substituting $\overline{I_x}$, $\overline{\varphi_x}$ in the characteristic equation, we define what kind of fixed point it is.

From the lattice design point of view there are three interesting cases: $\zeta_x \ll h_{30q}$; $\zeta_x \sim h_{30q}$ and $\zeta_x \gg h_{30q}$.

The lattices with the small non-linearity $\zeta_x\ll h_{30q}$ are classified among the first or second generation synchrotron light sources. The system has one centre and three saddles. Since the non-linearity is negligibly small, the dynamic aperture is determined by the value of $\overline{I_x}\leq \left(\frac{2\Delta}{3h_{30q}}\right)^2$, when the motion is still stable. Under the resonance condition $\Delta=0$ the centre is degenerated into the saddle and the stable area shrinks into zero. In such a lattice the working point is kept as far from the resonance as possible. Usually these lattices have a small value of h_{30q} because the sextupoles are very weak and there is no problem with the dynamic aperture.

The lattices with $\zeta_x \sim h_{30q}$ have the moderate nonlinearity. In common case the system has four islands with four centres and three saddles. Such a lattice is used for the second and third synchrotron light sources, where the sextupoles have much stronger gradient in comparison with previous generation. To compensate sextupoles the multifamilies sextupoles schemes are used. Since the tune shifts are proportional to $\left|h_{k_x,k_y,q}\right|^2$ and the working points are chosen far away from integer tune, the non-linearity are decreased even faster than the third harmonic. Really the dynamic aperture is determined by how successful we have been in simultaneous adjustment of the appropriate value of ζ_x and h_{30q} .

The lattices with $\zeta_x\gg h_{30q}$ have to be classified as a special lattice, since it is a case, when the value of h_{30q} is effectively suppressed, but the non-linearity remain to be under control and strong. It is obvious from (4), if the sign of the detuning Δ coincides with the sign of the tune shift ζ_x , the discriminant is negative and the system has only one centre at $I_x=0$. Therefore this case corresponds to the maximum stable region and the lattice with these features is the most hopeful for the third and fourth generation source.

2.2 Nekhoroshev's criterium

So, in order to get the maximum stable region the sign of the non-linearity ζ_x has to be the same as the detuning Δ . However, we can see from (4), if ζ_{xy} has the opposite sign with the tune Δ , then under some amplitude of oscillation in the vertical plane I_y the total detuning $\Delta_{total} = \Delta + \zeta_{x,y}I_y$ can make the discriminant $D \geq 0$. It means that the two dimensional vector remains to be on the resonant surface. In other words the non-linear system is unable to leave the res-

onance at all and it behaves as quasi-isochronous system. The phenomena of quasi-isochronism for the nonlinear resonances was investigated by Nekhoroshev [5]. Let us apply Nekhoroshev' criterium to our two dimensional system. The non-resonant part of the Hamiltonian is $\delta H\left(I_x,I_y\right)=\zeta_xI_x^2+\zeta_xyI_xI_y+\zeta_yI_y^2$. The vector of frequencies passing through the point of the resonant surface $I^r=\left(I_x^r,I_y^r\right)$ is $\omega=\left(2\zeta_xI_x+\zeta_xyI_y;2\zeta_yI_y+\zeta_xyI_y\right)$. The quasi-isochronism condition by Nekhoroshev is fulfilled, when $k_x\left(2\zeta_xI_x^r+\zeta_xyI_y^r\right)+k_y\left(2\zeta_yI_y^r+\zeta_xyI_y^r\right)=0$ and $\zeta_xk_x^2+\zeta_xyk_xk_y+\zeta_yk_y^2=0$. The solution is $\frac{k_x}{k_y}=\frac{-\zeta_{xy}\pm\sqrt{\zeta_{xy}^2-4\zeta_x\zeta_y}}{2\zeta_x}$. If the non-linearity in both planes have the same sign and $4\zeta_x\zeta_y\geq\zeta_{xy}^2$ we get the absolutely convex (or concave) surface. They both have name of the steep surface. Thus, the maximum stable region is when all $\zeta_x,\zeta_y,\zeta_{xy}$ have the same sign.

3 THE LATTICES WITH $\zeta_X \gg H_{30O}$

What kind of lattice is needed in order to have a possibility to adjust the detuning Δ , the nonlinear tune shift $\zeta_x, \zeta_{xy}, \zeta_y$ and the effective sextupole harmonic $h_{k_x,k_y,q}$ separately. From our point of view the only appropriate lattice is the lattice with the separated functions of the arcs and the straight sections. Such a lattice has some number of superperiods consisting of the arc and the straight sections. Each arc includes eight periodical cells, containing combined function (or usual) bend magnets and focusing (and defocusing) quadrupoles. The tune of the arcs in the horizontal and the vertical planes is integer, $\nu_x = 3$, $\nu_y = 2$.

The sextupoles are placed on arcs periodically . To a first approximation in this condition $h_{k_x,k_y,q} \to 0$ (see eq.2), since each n-th sextupole is compensated by (n+4)-th in the horizontal and by (n+2)-th in the vertical planes correspondingly. However, since again the tune is integer, the nonlinear tune shift can be varied in a wide region, since $\left|h_{k_x,k_y,q}\right|^2 \to 0$ and $k_x\nu_x + k_y\nu_y - q \to 0$ simultaneously. The total chromaticity of whole ring is adjusted to zero, but the arc itself has a positive chromaticity, compensated by the negative chromaticity of the straight section. Changing the chromaticity of the arc, we can adjust the required sign and value of the non-linear tune shifts. The working point and the detuning Δ of whole ring is modified by the tune of the straight section, while the arc remain to be invariable.

Figure 1 shows the dynamic aperture tracking of ASTRID 2[1] versus the tune in the vicinity of the third integer resonance $\nu_x=9.33$, when the tune shift $\zeta_x=100$, the effective harmonic $h_{30q}=0.1$ and the detuning equals to -0.02; -0.01 and 0.01 correspondingly. During small change of the detuning the system runs through three stages, what is exactly in accordance with the Hamiltonian described above. In the early stage the system has four separated islands with four centres and three saddles. In the middle stage all four islands are surrounded by the stable trajectories. After change of the detuning sign the system has one fixed point. In case of a negative tune shift the

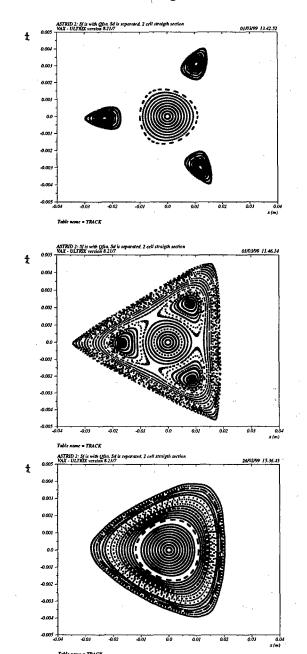


Figure 1: Dynamic aperture versus the detuning ($\Delta = -0.02; -0.01; 0.01$).

first and last stages are exchanged with each other. Moving away from the resonance $\nu_x=9.33$, the system appears in the vicinity of the next resonance $\nu_x=10.0$. Figure 2 (upper picture) shows the dynamic aperture in the middle of way between two resonances, when they compensate each other, and the triangular shape transforms into the oval. Approaching to the resonance $\nu_x=10.0$, the dynamic aperture becomes similar to the starting point (lower picture, fig.2). The behavior of the dynamic aperture has the periodic character. The working point is chosen slightly higher or lower than the resonance $\nu_x=9.33$ under positive or negative tune shift correspondingly.

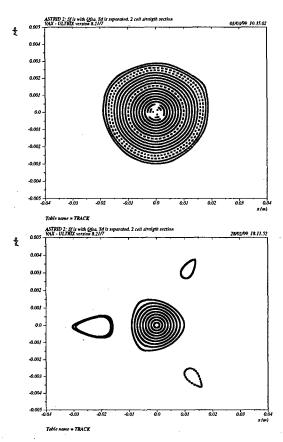


Figure 2: Dynamic aperture versus the tune ($\nu = 9.65$ and 9.98).

3.1 CONCLUSION

The emittance in this lattice is much smaller, than in a circular machine with the same number of magnets, and the dynamic aperture has a similar value with a lower sensitivity to third order resonances.

The author is very grateful to E.Uggerhoj, S.P.Moller for fruitful discussion and to N.Golubeva, S.Volin for cooperation in investigations of the proposed lattice[6].

- [1] Yu. Senichev, The proposed racetrack lattice for the synchrotron light source ASTRID II, EPAC-98, Stockholm.
- [2] K.L.Brown, Second-Order Magnetic Optical Achromat, IEEE Trans.Nucl.Sci., NS-26(3), p.3490, 1979.
- [3] G.Guignard, J.Hagel, Sextupolar correction and dynamic aperture: numerical and analytical tools, Particle Accelerator, 1986, vol.18, pp.129-165.
- [4] S. Volin, Coping with high order perturbation effects in the particle dynamics near 1/3-integer resonance, preprint INR-0863/94, 40 pages.
- [5] N.Nekhoroshev, Method of successive canonical replacement of variables, UMN 32/6 (1977).
- [6] Lattice Study of the ASTRID II Synchrotron Light Source, Internal report of INR, 1999.

LOW-FREQUENCY WIGGLER RADIATION

F. Méot, CEA, DSM/DAPNIA/SEA, 91191 Saclay, France*

Abstract

Classical formalism for synchrotron radiation interference between short sources is applied to analytical formulation of wiggler radiation in the low frequency domain.

1 INTRODUCTION

Considering the lasting interest in synchrotron radiation (SR) for beam diagnostics [1], due also to raising specific demand such as infrared SR [2], a detailed insight in the interference phenomenon between separate radiating sources and its understanding remains of concern. The case of wiggler SR has already been addressed in terms of interference [3] and more recently implications of the low frequency hypothesis have been discussed [4]. We re-visit the subject with recently developed material [5] and derive by this means a detailed analytical formulation of wiggler SR in the low frequency domain.

2 ANALYTICAL MATERIAL

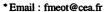
2.1 Low frequency model

In regular conditions of SR production the spectral angular energy density observed at large distance r (assumed constant) is given by $\frac{\partial^3 W}{\partial \omega \partial \phi \partial \psi} = 2\epsilon_0 c \mid {}^r \tilde{E}(\phi,\psi,\omega) \mid^2$ (the r-independent quantity ${}^r \tilde{E} = r \, \tilde{E}$ is introduced for simplicity) where $\tilde{E}(\phi,\psi,\omega)$ is the Fourier transform of the radiated electric field $\tilde{E}(\phi,\psi,t)$ (see Fig. 1) and ω is the observed frequency. In the low frequency domain one has

where indices σ and π designate polarisation components respectively parallel to the bend plane and normal to $\vec{E_\sigma}$; angles ϕ in the bend plane and ψ normal to it define the observation direction. Eqs. 1 holds over a few rms aperture (with $\gamma\phi_{rms}=\gamma\psi_{rms}=\sqrt{(1+K^2)}$) and up to a fraction of ω_{limit} as defined by

$$\omega_{limit} = \omega_c/(3K(1+K^2)) = \gamma^2 c/(L(1+K^2))$$
 (2)

in which $\omega_c = 3\gamma^3 c/2\rho$ is the critical frequency of the standard formalism, γ is the Lorentz relativistic factor, ρ is



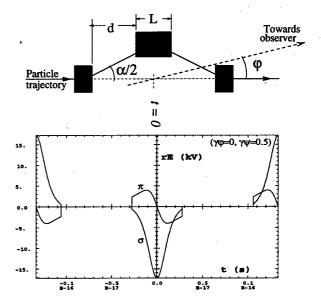


Figure 1: Up: A three-dipole wiggler. Definition of observation angle φ in the bend plane. Down: Typical shape of the electric field impulse ${}^{gr}E_{\sigma,\pi}(\varphi,\psi,t)$ at the observer.

the curvature radius, α is the particle total deviation, $L=\rho\alpha$ is the trajectory length in the magnetic field, and $K=\alpha\gamma/2$ is the deflection parameter.

2.2 Interference

As one knows the underlying physics in SR interference is in time coherence resulting from the geometrical arrangement of sources, which entails space and frequency modulation of the radiated signal. A series of N sources radiate electric field of the form

$${}^{N}E_{\sigma,\pi}(\phi,\psi,t) = \sum_{i=1}^{N} \delta(t+T_i) * E_{i\sigma,\pi}(\phi,\psi,t)$$
 (3)

where $E_{i\sigma,\pi}(\phi,\psi,t)$ describes the impulse from magnet i, T_i is the emission time of signal i, δ is the Dirac distribution and * denotes the convolution product. The Fourier transform gives the interferential amplitude density

$${}^{N}\tilde{E}_{\sigma,\pi}(\phi,\psi,\omega) = \sum_{i=1}^{N} e^{i\omega T_{i}} \tilde{E}_{i\sigma,\pi}(\phi,\psi,\omega) \tag{4}$$

whose modulus square provides the energy density

$$\frac{\partial^{3N}W_{\sigma,\pi}}{\partial\omega\partial\phi\partial\psi} = 2\epsilon_0 c \left(\left(\sum_{i=1}^{N} {}^{r}\tilde{E}_{i\sigma,\pi} \cos(\omega T_i) \right)^2 + \left(\sum_{i=1}^{N} {}^{r}\tilde{E}_{i\sigma,\pi} \sin(\omega T_i) \right)^2 \right)$$
(5)

Times T_i are obtained from the geometry of the magnet assembly by combining the duration $\Delta T = \frac{L}{2\gamma^2c}(1 + K^2/3 + \gamma^2(\phi^2 + \psi^2))$ of the impulse issued from a magnet, with the time of flight (in observer time) $\Delta T_d = \frac{d}{2\gamma^2c}(1 + \gamma^2(\phi^2 + \psi^2))$ between magnets distant d.

Note that Eqs. 4, 5 involve the exact Fourier transform of $\delta(t+T_i)$ hence possible low frequency approximation validity domain depends only on the characteristics (L and K) of SR sources, not on their distance d.

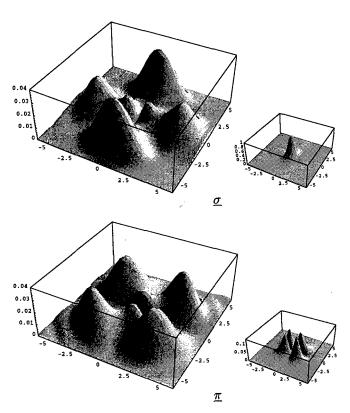


Figure 2: Low frequency energy density from a three-dipole wiggler (Eq. 6 for 2.5 GeV electron, at $\omega=1.9\,10^{15} {\rm rad/s}$ - $\lambda=10^{-6}{\rm m}$). The small boxes show the energy density from the central $(2/\gamma)$ dipole alone; comparison reveals a damping of about 0.04/1 due to the wiggler interference. (g.phi and g.psi stand for coordinates $\gamma\phi$ and $\gamma\psi$.)

3 SR FROM A 3-DIPOLE WIGGLER

For simplicity a single-bump wiggler based on $(1/\gamma)$ - and $(2/\gamma)$ -deviation magnets¹ is considered (Fig. 1). However what follows can be extended to arbitrary N, and as well to low frequency undulator radiation (N large and K < 1).

The low frequency limit simplifies into $\omega_{limit} \approx \omega_c/6 = \gamma^2 c/2 L$ (Eq. 2 with K=1) leading for instance to validity range $\omega < 4\,10^{16}$ rad/s ($\lambda > 40\,10^{-9}$ m) for a 2.5 GeV electron traversing a, e.g., 670 kG, $L=5\,10^{-2}$ m long dipole. Fig. 1 shows the typical shape of electric field impulse series so generated (Eq. 3 with N=3), the total

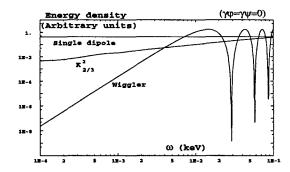


Figure 3: Forward spectrum of wiggler σ component (Eq. 6), and for comparison, spectra due to the central $(2/\gamma)$ -deviation dipole alone (K=1 in Eq. 1), and due to body SR from a strong dipole (regular $K_{2/3}^2(\omega)$ shape).

duration of which is $\Delta T \mid_{\frac{L}{2},\frac{K}{2},\phi=\varphi-\frac{K}{2\gamma}} + \Delta T_d \mid_{\phi=\varphi-\frac{K}{\gamma}} + \Delta T_d \mid_{\phi=\varphi-\frac{K}{\gamma}} + \Delta T \mid_{\frac{L}{2},\frac{K}{2},\phi=\varphi+\frac{K}{2\gamma}}$. Taking the origin at the centre of the central dipole, times in Eq. 3 write, $T_2=0$ and

$$-T_{1} = \Delta T \mid_{\frac{L}{2}, \frac{K}{2}, \phi = \varphi - \frac{K}{2\gamma}} + \Delta T_{d} \mid_{\phi = \varphi - \frac{K}{\gamma}} + \frac{1}{2} \Delta T \mid_{\phi = \varphi}$$
$$+T_{3} = \frac{1}{2} \Delta T \mid_{\phi = \varphi} + \Delta T_{d} \mid_{\phi = \varphi + \frac{K}{\gamma}} + \Delta T \mid_{\frac{L}{2}, \frac{K}{2}, \phi = \varphi + \frac{K}{2\gamma}}$$

Fig. 2 shows the resulting interferencial patterns which express as

$$\frac{\partial^{3}W_{\sigma,\pi}}{\partial\omega\partial\varphi\partial\psi} = 2\,\epsilon_0\,c$$

$$\left(\left({}^{r}\tilde{E}_{\sigma,\pi}|_{\frac{K}{2},\phi=\varphi-\frac{K}{2\gamma}}\cos(\omega T_1) + {}^{r}\tilde{E}_{\sigma,\pi}|_{-K,\phi=\varphi}\right.\right.$$

$$\left.\pm {}^{r}\tilde{E}_{\sigma,\pi}|_{\frac{K}{2},\phi=\varphi+\frac{K}{2\gamma}}\cos(\omega T_3)\right)^2 + \left(ST\right)^2\right) (6)$$

where (ST) designates the complementary sin term. Fig. 3 compares the radiation spectrum from the wiggler to that of a single K=1 dipole and to classical body SR from a $K\gg 1$ dipole.

- [1] A. Hofmann, Diagnostics with SR, Proc. Cern Acc. School "Synchrotron Radiation and Free-Electron Lasers", Grenoble (F), 22-28 April 1996.
- [2] Workshop on infrared SR, 1st meeting: the source, J.-L. Laclare, M.-P. Level and P. Roy organisers, Gif-sur-Yvette, France, 8-9 Dec. 1997.
- [3] K.-J. Kim, Characteristics of SR, AIP Conf. Proc. 184, US Part. Acc. School, Fermilab, 1987; R. P. Walker, Interference effects in undulator and wiggler radiation sources, Internal Report Sincrotrone Trieste, 1993.
- [4] R. A. Bosch, Long-wavelength radiation along the straight-section axis in anelectron storage ring, NIM A, vol. 386 (1997) 525-530.
- [5] F. Méot, A theory of low frequency far-field synchrotron radiation, report DSM/DAPNIA/SEA-98-05, CEA/Saclay (1998); F. Méot, N. Ponthieu, On low frequency far-field interference between short SR sources, report DSM/DAPNIA/SEA-98-53, CEA/Saclay (1998).

¹The latter has the merit of producing highest brightness low frequency SR.

Proceedings of the 1999 Particle Accelerator Conference, New York, 1999

SHORT PULSE SYNCHROTRON LIGHT FROM JEFFERSON LAB'S NUCLEAR PHYSICS ACCELERATOR *

G. A. Krafft,† TJNAF, Newport News, VA

Abstract

There has been recent interest in developing sources of Xrays, both coherent and incoherent, for advanced materials science and other scientific studies. In particular, there is interest in developing so-called fourth generation light sources, which are driven by electron linacs. One distinguishing feature of the fourth generation sources is the very short pulse length, usually under 1 psec rms, that is possible from a linac driven source. Because of recent successes in achieving very short bunches out of its injector, it is natural to investigate whether the Jefferson Lab nuclear physics accelerator might be used as a copious source of incoherent short-pulse synchrotron light. In this note we present the results of calculations of the expected synchrotron radiation spectrum from bend magnets at four locations in the CEBAF accelerator. The results show that substantial numbers of short pulse X-rays are produced.

1 INTRODUCTION

Thomson scatter events in the Jefferson Lab FEL will produce X-rays of energy up to about 15 keV, with photon brightnesses at the level of 10⁶ photons/mm²mrad²sec in a 1% bandwidth [1]. Because of our recent success in achieving very short bunches out of the Jefferson Lab main injector [2], it is natural to investigate whether the CEBAF accelerator might be used as a copious source of X-rays. In this note we present the results of calculations of the expected synchrotron radiation spectrum from bend magnets at four locations in the Jefferson Lab nuclear physics accelerator. The results show that substantial numbers of Xrays are produced. The fluxes are interesting enough that preliminary fourth generation X-ray experiments could be performed at Jefferson Lab, prior to installation in a beamline at the TESLA light source at DESY or the Linac Coherent Light Source (LCLS) proposed for Stanford. This is especially true given that all necessary X-ray producing equipment is already installed and "available". The precision timing in the accelerator allows one to time the Xrays at the 100 fsec level. It bears worth emphasizing that the repetition time in a typical experiment would be at the repetition rate of the accelerator, i. e., 500 MHz presently, and 31 MHz in about a year's time. This time structure is changed by a suitable change to the laser pulse structure on the source. In contrast, present day rings have pulse durations of order 30 psec, making them unsuitable as sources for studies involving ultrafast phenomena.

2 X-RAY BRIGHTNESS

The standard synchrotron radiation formulas were used to estimate the brightness (for $100 \mu A$ beam at 500 MHz) of the synchrotron radiation emerging from the nuclear physics machine at Jefferson Lab. Begin with Jackson's Eqn. 14.83 [3],

$$\frac{d^2I}{d\omega d\Omega} = \frac{e^2}{3\pi^2c} \left(\frac{\omega\rho}{c}\right)^2 \left(\frac{1}{\gamma^2} + \theta^2\right)^2$$

$$\times \left[K_{2/3}^2(\xi) + \frac{\theta^2}{(1/\gamma^2) + \theta^2} K_{1/3}^2(\xi) \right],$$
 (1)

for the emission spectrum (energy radiated per unit frequency interval per unit solid angle) of a single electron. Because the beam emittance is so small ($\epsilon^n_{rms} \approx 1.0$ mm mrad), a typical electron angle is of order 0.01 mrad or smaller at 4 GeV. As this angle is smaller than the $1/\gamma$ radiation emission angle, the brightness is not much changed due to the effects of finite electron beam emittance. Eq. 1 is used to estimate the photon brightness (at θ =0) as

$$B \approx \frac{\gamma^2}{2\pi\sigma_x\sigma_y} \frac{3\alpha}{\pi^2} \frac{\Delta\omega}{\omega} \xi^2 K_{2/3}^2(\xi) \frac{I}{e},\tag{2}$$

where α is the fine structure constant, $\xi = \lambda_{cr}/\lambda$, and $\Delta\omega/\omega$ is the bandwidth. Jackson's definition (Eqn. 14.85) of the critical wavelength $\lambda_{cr} \approx 2.09 \rho/\gamma^3$, is used in the tabulation. The average current I_{ave}/e is used to compute the average brightness, and the peak brightness is estimated using $I/e \approx q/\sqrt{2\pi}e\sigma_t$ where q is the charge per bunch and σ_t is the measured rms bunch duration of 85 fsec.

As results, the radiation spectrum into a 0.1% bandwidth is displayed for four possible magnets in the CEBAF accelerator. The first magnet is a first pass bend magnet at the end of linac 1 (445 MeV). The second magnet is a first pass bend magnet at the end of linac 2 (845 MeV). The third magnet is an arc nine bending magnet, before the final pass through the south linac (3645 MeV). The final magnet is a high energy bending magnet right before the Hall C entrance, where the beam energy is 4.045 GeV. Table 1 summarizes some of the properties of the synchrotron emission from these bend magnets. The beam sizes are assumed to be 100 μ m by 100 μ m at 4 GeV, scaled by $\gamma^{-1/2}$ for the lower energies, i. e., the beam optics β is assumed to be independent of energy. The brightness as a function of wavelength is shown in the Figures 1 and 2, which give the peak and average brightness of the synchrotron emission from each magnet.

Compared to, for example, an APS bend, the moin difference in the average brightness of magnet 4 are some

^{*}This work supported by U. S. DOE Contract No. DE-AC05-84ER40150, the Office of Naval Research, the Commonwealth of Virginia, and the Laser Processing Consortium.

[†] Email: krafft@jlab.org

Table 1: Electron beam and synchrotron radiation parameters for various magnets in the Jefferson Lab Nuclear Physics Accelerator

Magnet	E (MeV)	ρ (m)	λ_{cr} (Å)	E_{cr} (keV)
1	445	5	159	0.078
2	845	10	46.3	0.268
3	3645	30	1.73	7.16
4	4045	46	1.94	6.38

the reduced average current at the Jefferson Lab accelerator. On the other hand, the peak brightness from this magnet exceeds that of other bend magnet sources, because the pulse length is so short. Obviously, installing an undulator at Jefferson Lab could increase these brightnesses farther, as in the transition between 2nd generation and 3rd generation synchrotron sources. Such a brightness is already competitive with a proposed alternative storage-ring based source of short pulse radiation [4], as the average current producing the short-pulse radiation is comparable.

From the figure, it appears that either high energy magnet gives good X-ray brightness. The X-ray production rate is between 10^{11} and 10^{12} photons/sec mm² mrad² in a 0.1% bandwidth in the range of 1-10 angstroms. These X-rays will be distributed in a pulse that mirrors the e-beam pulse in time. Therefore, because it is possible to preserve the short bunch out of the injector, an X-ray pulse length of under 100 fsec should be possible.

3 LONGITUDINAL BEAM DYNAMICS

So far, it has been demonstrated experimentally only that short electron pulses emerge from the injector. No beam bunch length experiments have been performed at higher energies. On the other hand, there is high confidence, based on beam longitudinal dynamics measurements, that the short bunch length will be retained at high energies. Because the bunch is relativistic, and the accelerator recirculation arcs are designed to be isochronous, bunch lengthening can arise only from incorrect linac phasing coupled to residual uncorrected M_{56} in the arcs. Two pieces of experimental data indicate that this is not a problem. Typically, the bunch runs on crest in the accelerator within 0.5° of the phase of maximum energy gain. The cresting is continuously monitorred by observing synchrotron light at a high dispersion point of the arc, and by phase modulation measurements [5].

As part of the present arc setup procedure, the M_{56} is adjusted to under 10 cm, and the path lengths are adjusted so that the phase error in higher passes is a few tenths of a degree. The instrumental limit of the currently installed measuring devices is 1 mm for M_{56} and 50 μ m for the path length [6]. Even with worst-case assumptions about how potential errors add, a bunch length change under 10% during acceleration to high energy is indicated.

4 CONCLUSIONS

In this note it is shown that potentially interesting numbers of short-pulse X-rays are currently being produced at the CEBAF accelerator. It "only" remains to provide some access to these X-rays to allow experiments to proceed.

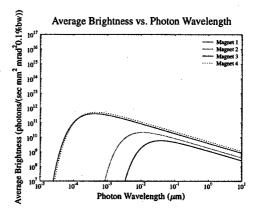


Figure 1: Average Brightness vs. Wavelength

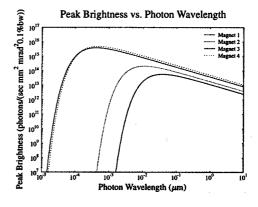


Figure 2: Peak Brightness vs. Wavelength

- [1] Krafft, G. A., "Use of Jefferson Lab's High Average Power FEL as a Thomson Backscatter X-ray Source", *Proc. of the* 1997 Part. Acc. Conf. (1997)
- [2] Wang, D. X., G. A. Krafft, and C. K. Sinclair, Phys. Rev. E, 57, 2283 (1998)
- [3] Jackson, J. D., Classical Electrodynamics
- [4] Zholents, A. A., and M. S. Zolotorev, Phys. Rev. Lett., 76, 912 (1996)
- [5] Tiefenback, M. G., "High-Precision Non-invasive Beam-RF Phase Monitoring at Jefferson Lab.", these procedings
- [6] Hardy, D. A., et. al., "Path Length Measurements in EPICS", Proc. of the 1997 Part. Acc. Conf. (1997)

PERFORMANCE OF THE ACCELERATOR DRIVER OF JEFFERSON LABORATORY'S FREE-ELECTRON LASER*

C. L. Bohn[#], S. Benson, G. Biallas, I. Campisi, D. Douglas, R. Evans, J. Fugitt, R. Hill, K. Jordan, G. Krafft, R. Li, L. Merminga, G. Neil, P. Piot, J. Preble, M. Shinn, T. Siggins, R. Walker, B. Yunn Thomas Jefferson National Accelerator Facility, Newport News, VA 23606

Abstract

The driver for Jefferson Lab's kW-level infrared freeelectron laser (FEL) is a superconducting, recirculating accelerator that recovers about 75% of the electron-beam power and converts it to radiofrequency power. In achieving first lasing, the accelerator operated "straight-ahead" to deliver 38 MeV, 1.1 mA cw current through the wiggler for lasing at wavelengths in the vicinity of 5µm. Just prior to first lasing, measured rms beam properties at the wiggler were 7.5±1.5 mm-mr normalized transverse emittance, 26±7 keV-deg longitudinal emittance, and 0.4±0.1 ps bunch length which yielded a peak current of 60±15 A. The waste beam was then sent directly to a dump, bypassing the recirculation loop. Stable operation at up to 311 W cw was achieved in this mode. Commissioning the recirculation loop then proceeded. As of this Conference, the machine has recirculated cw average current up to 4 mA, and has lased cw with energy recovery up to 710 W.

1 INTRODUCTION

The Thomas Jefferson National Accelerator Facility (Jefferson Lab) built and is commissioning a cw, kW-level,3-6 μm free-electron laser (hereafter called the IR Demo). The design of the machine is presented elsewhere [1]. It incorporates a superconducting accelerator comprising a 10 MeV injector and a 32 MeV linac to produce a nominally 42 MeV electron beam for kW-level cw lasing. The accelerator is designed to achieve the top-level electron-beam requirements listed in Table 1 of Ref. [1] while transforming 75% of the beam power back into rf power. Beam parameters originally thought to be required for first light differ from those needed for kW power, however, and they are listed in Table 1 below.

First lasing involved running the machine in the "straight-ahead" mode, in which the beam is deposited in a "42 MeV dump" [1,2]. Doing so enabled achieving the first-lasing milestone before construction of the recirculation loop had been fully completed. Subsequently the machine was run in the "recirculation" mode [1] with pulsed beam and with energy recovery from the pulses, first without lasing, then with lasing. In this mode, the beam lands in a "10 MeV dump" after decelerating through the cryomodule.

The eight klystrons powering the eight cryomodule

*Work supported by the U. S. Department of Energy under contract DE-AC05-84-ER40150, the Office of Naval Research, the Commonwealth of Virginia, and the Laser Processing Consortium.

cavities can each deliver up to 8 kW. In turn, the available power limits the cw average current to a maximum of 1.1 mA in the straight-ahead mode. However, once recirculation with energy recovery is established, the decelerated beam powers the accelerated beam, and the recirculation mode thereby provides for currents above 1.1 mA. The injector then sets the limit on average current, which by design is 5 mA. To date the IR Demo has recirculated up to 4 mA cw. It has lased cw at up to 311 W straight-ahead and 710 W with recirculation and energy recovery, in both cases at ~5 µm wavelength.

Table 1: Beam Requirements at Wiggler for First Lasing.

Parameter	Required	Measured
Kinetic Energy	38 MeV	38.0±0.2 MeV
Average current	1.1 mA	1.10±0.05 mA
Bunch charge	60 pC	60±2 pC
Bunch length (rms)	<1 ps	0.4±0.1 ps
Peak current	22 A	60±15 A
Trans. Emittance (rms)	<8.7 mm-mr	7.5±1.5 mm-mr
Long. Emittance (rms)	33 keV-deg	26±7 keV-deg
Pulse repetition rate	18.7 MHz	18.7 MHz

2 OVERVIEW OF COMMISSIONING

The performance of the accelerator driver is a key product of the commissioning process. The end result is a machine that stably recirculates several mA average current for many hours while lasing cw at several hundred watts. For example, during a recent "longevity" run, the machine lased nearly uninterrupted for six hours with 400 W cw output power and with 2.5 mA recirculated current. The run ended by choice, not by machine degradation. Recently it has been delivering as much as 12 hours of uninterrupted ~100 W light with ~1 mA cw current in support of the first user experiments. Presently its Achilles heel is poor (~30%) availability of the electron gun. Otherwise it is robust and its performance has generally been easy to restore by loading a "golden file" of saved settings. What follows is an overview of the commissioning process that led to the present capability.

2.1 Photocathode Gun

The gun was constructed and tested off-line. In the IR Demo, the space between the gun and the cryounit is too 'I to

^{*}Email: clbohn@jlab.org

accommodate beam diagnostics, so reasonable confidence in the gun's performance had to be established prior to its installation. During testing, the gun ultimately delivered bunch charges from 0-120 pC with phase-space parameters that were in reasonable agreement with PARMELA [3,4]. It also delivered up to 2 mA cw average current, but with an e-folding lifetime of only ~2 hours at this relatively high current. The short lifetime was believed to be due to the proximity of the cathode to the beam dump, which was located 2 m straight ahead from the cathode. Once favorable results were achieved off-line, the gun was installed in the FEL injection line.

To date the gun has been operated in the FEL to a maximum bunch charge of 60 pC in view of the first-light requirements in Table 1 as well as the desire to preserve cathode lifetime. The e-folding lifetime of the GaAs cathode has typically been ~10-20 hours at 60 pC, even at average currents in the 3-4 mA range [5]. The cathode wafer used in the most recent run delivered ~700 C total charge. Cathode lifetime is seen to depend sensitively on the quality of the ambient vacuum, which may influence beam operations via ionization of residual gas and back-bombardment of ions onto the cathode. Available data is too sparse to support a more quantitative statement. Of course, in the IR Demo, and unlike in the off-line tests, all beam dumps are located far from the cathode.

Based on findings of the Labes Polarized Source Group [6], we have tried anodizing the outer regions of the cathode wafer to suppress electron emission from these regions. Although the benefit has been hard to ascertain conclusively, subsequent operation leading to first light proceeded with easily achievable beam transmission to the straight-ahead dump at 1.1 mA cw, something that had been more difficult to achieve prior to anodization. While commissioning the recirculation loop, we have not been anodizing the cathode out of concern that the edge of the anodized region could be a site for field emission that may degrade gun availability. However, without anodization there has been evidence of beam scraping, and in the future we will likely revert to anodized cathodes to see whether scraping is reduced.

The principal reason gun availability remains low is lack of funding to implement planned improvements. We are building an apertured cesiator to reduce cesium deposition on the cathode electrode. We may soon replace the cathode electrode; ion implantation is under study as a possible means for suppressing field emission from the cathode electrode.

2.2 Electron-Beam Diagnostics

Diagnostics for the IR Demo include: arrays of beam-position monitors, optical-transition-radiation viewers, and beam-loss monitors; two interferometric bunch-length monitors, one (BL1) at the entrance to the linac cryomodule and the other (BL2) just after the wiggler; two multislit transverse-emittance monitors, one (MS1) after the injector cryounit and the other

(MS2) at the entrance to the linac cryomodule; and four rf cavities to monitor beam current and path length [7].

2.3 Straight-Ahead Mode

Commissioning the straight-ahead machine for first light proceeded well before construction of the recirculation loop was complete. Key diagnostics that ultimately led to the decision to install the wiggler and try for first light were BL2, a multimonitor emittance measurement using five viewers in the wiggler region, and an energy spread measurement using the dipole magnets and viewer in the second optical chicane. Cleanup of the electron beam proceeded systematically and led to gradual improvement in the six-dimensional properties of the beam. Measurements of the beam parameters at the wiggler were completed on 12 Jun 98. The results, listed in Table 1, motivated installation of the wiggler on 13 Jun 98. All agree with PARMELA to within 10% except the energy spread, for which the measured value was a factor of two higher, and correspondingly so was the longitudinal emittance.

The IR Demo achieved first light on 15 Jun 98, within six hours from turn-on of the electron beam after wiggler installation [2]. Two days later it lased stably at up to 155W cw with 1.1 mA current (60 pC bunches at 18.7MHz). First light involved a 2% outcoupling mirror that was subsequently replaced with a 10% outcoupling mirror. On 28 Jul 98 the power reached 311 W, again with 1.1 mA current. It is now easy to restore the straight-ahead machine from a file of saved settings and run it uninterrupted for hours at ~300 W.

Because beam quality at the wiggler is good, the injector has never been optimized. For example, it produces a total energy of 9.5±0.1 MeV as inferred from the injection-line dipole strengths, short of the design total energy of 10.5MeV. Measurements with MS1 gave a normalized rms transverse emittance of 5.5±0.6 mm-mr, about 30% higher than PARMELA [8]. The beam at MS2 is off-nominal enough that good measurements with MS2 or BL1 have yet to be possible, but the bunch compression inferred by measuring the M_5 transfer function (= $\partial \phi_{\rm in}/\partial \phi_{\rm out}$) using a pickup cavity is close to PARMELA.

2.4 Recirculation Loop

The first attempt to take beam around the recirculation loop occurred on 28 Jul 98. In the ten days of operation that followed, the recirculated cw current was pushed to 0.6 mA at 37.4 MHz with energy recovery, and the machine lased cw at low power while recirculating. Lessons learned from this experience motivated several modifications that expedited commissioning for high power. The most important of these were: adding a 74.8 MHz beam mode that would generate 4.4 mA beam with 60 pC bunches, putting a hole in the viewer foil at the cryomodule exit to pass the prelasing beam unperturbed and thereby permit a clean view of the 10 MeV energy-recovered beam, and adding a viewer after the

quadrupole telescope in the energy-recovery dump line to help set up the beam at that dump.

There have been ~60 days of operation between making the cited modifications and this Conference. That period brought pronounced improvement in performance, in part by implementing longitudinal matching and energy compression. The laser power eventually plateaued at ~550W and did not increase as the current was raised from ~3mA to 4 mA, the highest current achieved to date. The suspected cause was a thermal limit in the CaE mirrors comprising the optical cavity; they were specified to support first lasing at powers not exceeding ~200 W. Upon replacing the high reflector with a silicon mirror having better thermal properties, and despite the anticipated power limit of the remaining mirror, the IR Demo lased cw up to 710 W, at which the recirculated current was 3.6 mA. It is now straightforward to restore the recirculating machine from a file of saved settings and run it for prolonged periods at nearly 700 W.

3 ACCELERATOR EXPERIMENTS

Coherent synchrotron radiation (CSR) is almost surely present in the IR Demo's magnetic bends and may cause measurable growth in the transverse emittance [9]. With a 60 pC bunch charge, estimates indicate growths of about 10% in each optical chicane surrounding the wiggler, and about 50% in each recirculation bend. Concern about CSR-induced beam degradation was one motivator for placing the wiggler at the exit of the linac rather than following the first recirculation bend. However, the estimates carry considerable uncertainty, and the machine is an ideal platform for CSR experiments. Both self-consistent simulations and experiments in the form of parametric studies of emittance growth in the bunch decompressor following the wiggler and in the first recirculation arc have begun. Initial data suggest the presence of CSR-induced emittance growth, but conclusive, quantitative statements must await further measurements.

A series of beam breakup (BBU) experiments is being formulated. The motivation is to benchmark the code TDBBU that is used to predict thresholds for multipass BBU. Despite previous concerted effort [10], the code remains to be conclusively validated. The calculated BBU-threshold current in the IR Demo is 27 mA, well above the maximum achievable 5 mA. Planned experiments involve attempts to induce BBU in the recirculation mode by kicking the beam and/or powering deflecting modes with an amplifier. Beamtransfer functions would be measured while modulating the current moment \(\mathbb{L} \mathbb{X} \) at frequencies or subharmonics of higher-order modes in the cryomodule cavities. The single-pass beam-transfer functions would also be measured to obtain the transverse shunt impedances of the strongest deflecting modes, thereby providing the requisite input for code calculations.

4 SUMMARY

The IR Demo has performed admirably to date, reproducibly recirculating nearly 4 mA of cw beam and providing nearly 700 W of stable cw laser power. Efforts continue toward boosting the power to the full design value of 1 kW, as well as toward improving the availability of the electron gun. The accelerator is an ideal platform for experiments concerning beam-quality degradation from coherent synchrotron radiation and beam breakup. The project's success has led Jefferson Lab recently to propose upgrading the IR Demo to deliver ~10 kW infrared and ~1 kW ultraviolet cw lasing.

Rapid progress continues. During the week before this Conference, the accelerator recirculated 47 MeV beam at up to 3 mA current (all the cathode would produce) with energy recovery. The outcoupling mirror was replaced with a sapphire mirror of marginal quality, after which the IR Demo quickly lased cw at 3.2µm, thereby establishing its broadband capability. During PAC99 week, a new cathode wafer was being installed, and in parallel, plans are to install two high-quality, thermally robust sapphire mirrors to support high-power lasing at ~3 µm. These mirrors and the increased electron-beam power should be key to reaching the full 1 kW.

5 REFERENCES

[1] C. L. Bohn, "Recirculating Accelerator Driver for a High-Power FEL: A Design Overview", Proc. 1997 Part. Accel. Conf., IEEE Cat. No. 97CH36167, pp. 909-911 (1998).

[2] S. Benson, G. Biallas, C. L. Bohn, D. Douglas, H. F. Dylla, R. Evans, J. Fugitt, R. Hill, K. Jordan, G. Krafft, R. Legg, R. Li, L. Merminga, G. R. Neil, D. Oepts, P. Piot, J. Preble, M. Shinn, T. Siggins, R. Walker, and B. Yunn, "First Lasing of the Jefferson Lab IR Demo FEL", Proc. 1998 Free Electron Laser Conf., (in press).

[3] D. Engwall, C. Bohn, L. Cardman, B. Dunham, D. Kehne, R. Legg, H. Liu, G. Neil, M. Shinn, C. Sinclair, "A High-DC-Voltage GaAs Photoemission Gun: Transverse Emittance and Momentum Spread Measurements", Proc. 1997 Part. Accel. Conf., ibid., pp. 2693-2695 (1998).
[4] D. Kehne, D. Engwall, R. Legg, and M. Shinn, "Experimental Results from a DC Photocathode Electron Gun for an IR FEL", Proc. 1997 Free Electron Laser Conf., (Elsevier, Amsterdam, 1998), pp. II-75-76.

[5] As originally configured, the drive laser operated at 18.7 MHz and 37.4 MHz, yielding up to 1.1 mA and 2.2 mA, respectively, with 60 pC bunches. To obtain higher currents, a 74.8 MHz capability was added, which can yield up to 4.4 mA with 60 pC bunches, and the full 5 mA with 67 pC bunches. [6] C. Sinclair, private communication.

[7] G. A. Krafft, K. Jordan, D. Kehne, S. Benson, J. Denard, E. Feldl, P. Piot, J. Song, and R. Ursic, "Electron-Beam Diagnostics for Jefferson Lab's High Power Free Electron Laser", Proc. 1997 Part. Accel. Conf. ρp. cit., pp. 912-914 (1998).

[8] P. Piot, G. Biallas, C. L. Bohn, D. R. Douglas, D. Engwall, K. Jordan, D. Kehne, G. A. Krafft, R. Legg, L. Merminga, J. Preble, T. Siggins, B. C. Yunn, "Experimental Results for an Injector for an IR FEL", Proc. 1998 European Part. Accel. Conf., (Institute of Physics, London, 1998) pp. 1447-1449.
[9] R. Li, "The Impact of Coherent Synchrotron Radiation on the Beam Transport of Short Bunches", these Proceedings.

[10] N. R. Sereno, L. S. Cardman, "Studies of Multipass Beam Breakup and Energy Recovery Using the CEBAF Injector Linac", Proc. 1993 Part. Accel. Conf., IEEE Cat. No. 93CH3279-7, pp. 3246-3248 (1993).

PHYSICS OF JLAB FEL INJECTOR'

Byung C. Yunn, Thomas Jefferson National Accelerator Facility 12000 Jefferson Avenue, Newport News, VA 23606, USA.

Abstract

Jefferson Laboratory is currently commissioning a high-power kW-level cw IR FEL which recently demonstrated impressive high-power capability with the linac operating in a nonrecirculating mode[1]. The injector, which provides a 10 MeV electron beam with high bunch charge (60-135 pC) to the linac, consists of a 350 kV dc photocathode gun and two 5-cell superconducting rf cavities, along with a buncher cavity. Due to the nonrelativistic nature of the electron beam at 350 keV there is some interesting physics involved in the $\beta=1$ srf cavities during acceleration. This is discussed, as is the usual space-charge-originated emittance degradation at various injector components.

1 INTRODUCTION

Requirements at the wiggler for a high power kW-level cw IR-FEL at Jefferson Laboratory, which has been designed for a typical range of optical wavelengths between 3 μ m and 6 μ m, are quite stringent for a 42 MeV electron beam of 60 pC bunch charge. They are:

 $\varepsilon_{x,y} = 8.7 \pi \text{ mm-mrad}$ $\varepsilon_z = 33 \pi \text{ deg-keV}$ $\sigma_E/\sigma_z = 85 \text{ keV/0.5 deg}$

Space charge effects are significant throughout the injector beam line designed to deliver 10 MeV electron beam to the linac starting at photocathode. One must include them properly in a design study. For this purpose we have extensively used a version of PARMELA[2] which implemented a point by point space charge computational algorithm to simulate better 3-d beam.

2 NOMINAL INJECTOR PROPERTIES

A logical block sketch of JLAB FEL injector beam line is shown in Figure 1. Total beam line is 10.5 m long. Details can be found in several JLAB publications[3].

2.1 INJECTOR SETUP

Design study of JLAB FEL injector has been carried out with PARMELA supplemented by POISSON, MAFIA and DIMAD. Initial electron bunch produced at cathode by a laser spot of 6 mm in diameter is round with a uniformly distributed charge distribution transversely. Longitudinally, the bunch is 90 ps long with a Gaussian

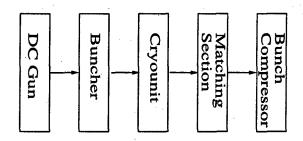


Figure 1: The beam line is also equipped with 3 viewers, 1 beam position monitor, 1 Happek device and 2 multislits.

distribution whose one σ value is taken to be 15 ps. A DC gun quickly accelerates electrons to 350 keV. After a 1497 MHz buncher at zero crossing electron beam gets a further acceleration to 10 MeV passing through 2 CEBAF 5-cell superconducting cavities. The 10 MeV beam is then transported to the entrance of a cryomodule via a matching section which consists of 4 quadrupoles and a bunch compressor. Alternatively, the beam can also be transported to a 10 MeV dump.

Optimized machine setups for various bunch charges ranging from 0 to 135 pC have been found. In this paper we list one for a 60 pC bunch charge in Table 1 as this is the most frequently used setup presently. For the sake of completeness, settings for the cryomodule cavities are included.

Table 1: 60 pC Machine Parameters

Element	Setting
1st Solenoid	260 G
Buncher	0.39 MV/m at zero crossing
2nd Solenoid	-205 G
Cryounit Cavities	
1 st Cavity	11 MV/m and on crest
2 nd Cavity	9 MV/m and -19.7 deg off
tere <u>e e e e e e e e e e e e e e e e e e</u>	crest
Cryomodule Cavities	
Gradient	8 MV/m for all
Phase	-7.5 deg off crest for all

2.2 BEAM PROPERTIES

Beam properties at various beam line locations in injector as expected from PARMELA simulations are summarised in Table 2.

^{*} This work was supported by the U.S. Department of Energy, under contract No. DE-AC05-84ER40150.

Table 2: Injector Performance

Location	ε _x /ε _y (π mm- mrad)	ε, (π deg- keV)	σ _e / σ _x (keV / deg)
Gun	1.3/1.2	2.2	0.7/8.7
Cryounit	3.9/3.8	7.1	15.5/0.9
Injector Exit	4.7/3.9	8.0	12.0/0.7

This optimized setup is fully capable of delivering an electron beam which meets all design beam specifications at the wiggler. PARMELA prediction of the beam quality at the wiggler is:

 $\varepsilon_x / \varepsilon_y = 5.3 / 5.1 \pi$ mm-mrad $\varepsilon_z = 10 \pi$ deg-keV $\sigma_E / \sigma_z = 50$ keV/0.2 deg

3 A DC PHOTOCATHODE GUN

In a DC gun there are no rf induced effects which degrade beam quality. However, one must quickly accelerate the beam to minimize space charge effects that become dominant in our bunch charge range between 60 to 135 pC. Presently, photocathode gun operates at 350 kV and the beam exits the gun after traveling a short distance of 14.4 cm. Longitudinal and transverse electric fields at 0.35 cm from the axis, which is just about at the beam edge, are shown in Figure 2.

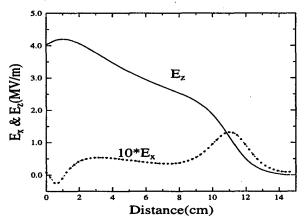


Figure 2: Electric fields at r = 0.35 cm. E_x has been multiplied by 10 to fit in the scale together with E_z

The fields are cylindrically symmetric. Longitudinal electric field within a volume occupied by the beam is independent of radial offset r to a good approximation, even though its dependence on z is quite complicated. Consequently transverse fields depend linearly on r and emittance degradation due to DC fields is minimal. Emittance degradation due to space charge is substantial as shown in Figure 3. Energy spread increases also exhibiting a typical S-shape. In order to minimize these degrading effects the gun voltage should be kept as high as possible. Original design calls for a 500 kV DC gun.

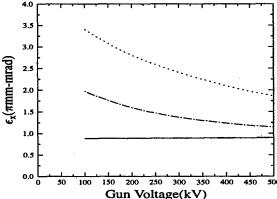


Figure 3: Emittance degradation due to space charge effects is shown as a function of a DC gun voltage. Dotted (dot-dashed) line is for a 135 pC (60 pC respectively) bunch charge. Solid line for the case without space charge.

4 ACCELERATION IN CRYOUNIT

A 350 keV electron beam enters a pair of CEBAF 5-cell superconducting cavities separated by 2.25 wavelengths an arrangement known as cryounit - for a further bunching and an acceleration. The first cavity which the beam encounters is powered at 11 MV/m gradient and the second one at 9 MV/m gradient as shown in Table 1. Electron beam becomes more or less relativistic at 10 MeV with β very close to 1 after the completion of acceleration through the cryounit. However, at an initial 350 keV energy, β for the beam entering the cryounit is only 0.8. As a result, electron acceleration in these cavities, which are designed for $\beta=1$ particles, turns out to exhibit a few interesting features. We find the following to be noteworthy:

1) Upper limit of an energy gain.

Presently, in the FEL injector the first superconducting cavity the beam sees is powered at 11 MV/m gradient. If we keep increasing the gradient of this cavity, the beam energy gain peaks at a gradient of about 40 MV/m.

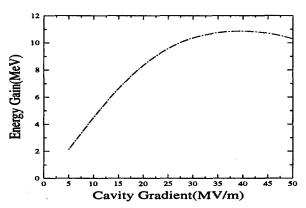


Figure 4: Maximum energy gain by a 350 keV electron beam traversing a 5-cell CEBAF cavity.

Of course, the cavity stops being efficient way before. Indeed, beyond about 20 MV/m gradient it is no more economical as Figure 4 shows.

In addition we also note a strong dependence of the cavity crest phase on the gradient. Particularly we point out a linear dependence starting at a gradient of about 11 MV/m up to a reasonably useable higher gradient.

2) Dependence of Crest Phase on Buncher Phase.

If buncher is not at zero crossing, electron beam gets accelerated or decelerated depending on phases, however small they may be. This in turn has a consequence in relative phasing between two cavities in the cryounit in addition to changing overall time of arrival at the unit. Fortunately, the effect appears to be small. For a 10 deg off zero crossing at the buncher relative crest phase change is about a half degree.

3) Time of Flight through CEBAF Cavity.

Time of flight for an electron to pass through a CEBAF 5-cell cavity depends strongly on initial rf phase of the cavity as a result of the electron not being relativistic at 350 keV at the cavity entrance. In Figure 5, difference of flight time (relative to the one for an electron gaining maximum energy) is shown as a function of rf phase when cavity gradient is 11 MV/m. Note that the flight time is a function of gradient, too.

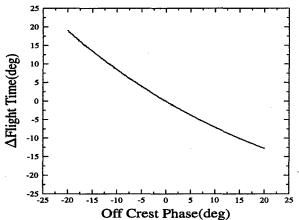


Figure 5: Time of flight difference as a function of cavity phase. The case of cavity gradient at 11 MV/m is shown here.

This 'M₅₅' property of the first cavity in the cryounit along with the fact that electron beam becomes fairly relativistic at the exit suggests a practical method of phasing cavities in the unit accurate to a few degrees. Namely, first find a crest phase of the 2nd cavity at an initial phase of the 1st cavity, and then locate maximum energy point by sliding phases of two cavities with a fixed relative phase (note that order of executing these steps can be reversed).

MATCHING AND BUNCH COMPRESSION

Matching section is a 235 cm long straight beam line consisting of four 15 cm quadrupoles separated by 60 cm from the center to the center. An electron bunch is compressed by passing through a bunch compressor consisting of three 20 degree bending magnets arranged in a right-left-right horizontal bend pattern. The dipoles are 175 cm apart from each other. The quads are set to degradation in the bunch minimize emittance compressor, and in the following linac. At same time transverse phase space at the linac exit must satisfy a few requirements to facilitate beam matching into the wiggler subsequently. Space charge effects are not substantial for a 60 pC bunch at 10 MeV in the matching section as evidenced by a following comparison between DIMAD and PARMELA computations. Emittance degradation is less than 5%.

Table 3: Twiss Parameters at the Matching Section Exit

	β./α.	β,/α,
Space Charge On	7.97 m/ 0.33	13.63 m/3.02
Space Charge Off	7.09 m/0.59	12.37 m/3.03
DIMAD	7.05 m/0.58	12.32 m/3.01

Bunch compressor is achromatic when space charge force is neglected, and has an M₅₆ of -19.25 cm that enables to rotate bunch longitudinally. M₅₆ behaves as a negative drift in the longitudinal phase space. Space charge effects observed in the compressor include 20% degradation of the horizontal emittance and 20% change in energy spread, up to 50% change in the bunch length, 20 to 70% change in \(\beta \) along with a drastic change in \(\alpha \)s. All these for a 60 pC bunch. Consequently, PARMELA has been an essential tool for a proper matching through the bunch compressor to generate a desired beam phase space before entering the cryomodule.

6 CONCLUSION

1 kW IR FEL is still in the middle of commissioning and we have been successful so far in achieving 700 watts of IR power with a little less than 4 mA electron beam recirculating and energy recovering. Even though injector setup is still in need of finalization, JLAB FEL injector is providing a quality beam which set many records in the operation of cw IR FEL.

- C. L. Bohn et al., "Performance of the Accelerator Drive of
- Jefferson Laboratory's Free-Electron Laser", these Proceedings.
 K. Crandall and L. Young, Los Alamos National Laboratory.
 The Laser Processing Consortium, "High-Power Ultraviolet and Infrared Free-Electron Laser For Industrial Processing", Reference Design Report, (1994).

FIRST RESULTS ON ENERGY RECOVERY IN THE JEFFERSON LAB IRFEL *

S. Benson, G. Biallas, C. L. Bohn, I. E. Campisi, D. Douglas, R. Evans, R. Hill, K. Jordan, G. A. Krafft, R. Li, <u>L. Merminga</u>*, G. R. Neil, P. Piot, J. Preble, M. Shinn, T. Siggins, R. Walker, B. C. Yunn

Thomas Jefferson National Accelerator Facility, Newport News, VA

Abstract

A recirculating, energy-recovering linac is used as driver accelerator for Jefferson Lab's high average power FEL. CW beam of 5 mA design current is transported from the superconducting RF (SRF) linac to the wiggler for lasing, and then recirculated back to the linac for deceleration and energy recovery. About 75% of the beam power is extracted before the beam is transported to the beam dump. Energy recovery reduces power consumption, RF equipment capital costs, and beam dump shielding requirements. It is arguably essential as FEL technology is scaled to higher average power levels.

To date, 4 mA of CW beam has been energy recovered successfully. There is no evidence of RF instabilities due to the energy aperture of the transport system, momentum compaction or the phase of the decelerating beam. HOM power from the beam has interfered with the operation of the IR interlock detectors, designed to protect the warm waveguide window from thermal runaway. Installation of copper screens appears to have solved the problem. More detailed studies of the HOM spectra and their correlation to the beam properties are planned.

1 INTRODUCTION

Jefferson Lab's IRFEL is presently being commissioned to produce CW, kW-level light at 3 to 6 µm wavelength. Output power of 710 W at 4.8 µm has been achieved to date [1], [2] with energy recovery. The IRFEL driver accelerator consists of a 10 MeV injector, which includes a 350 kV photocathode gun, followed by a copper buncher cavity and a CEBAF-type 1497 MHz superconducting RF (SRF) cryounit to generate an accelerating gradient of 10 MV/m. The linac uses a full CEBAF cryomodule to generate an average accelerating gradient of 8 MV/m, for a resulting beam energy of 42 MeV. The beam is transported from the linac to the wiggler where the lasing process takes place. A transport lattice recirculates the spent beam back to the linac for deceleration and energy recovery where about 75% of the beam power is converted into RF power. The 10 MeV beam is then transported to a dump.

In Section 2 we present our operational experience with energy recovery of 4 mA of CW beam in an SRF accelerator. In Section 3 we describe the problem we encountered with the IR detectors and link it to higher-order modes (HOM's) excited by the sub-micron long bunches.

2 OPERATIONAL EXPERIENCE WITH ENERGY RECOVERY

In the energy recovery mode of operation, the beam is accelerated by the SRF linac to a final energy of 38.5 MeV (as measured by the bending magnets), is then transported around the recirculation path, enters the same SRF linac approximately 180° out of the crest of the RF wave for energy recovery—thereby being decelerated to 10 MeV—and is finally transported to the dump. Therefore, at any time there are two beams in the linac cavities (one accelerating and one decelerating). Longitudinal dynamics imposes off-crest operation for the two beams. When the FEL is turned on, the accelerating beam is at a phase of 8° from the RF crest and the decelerating beam is at 180° from the accelerating beam. With 6 kW (unsaturated) klystron power, in the energy recovery mode, we have optimized the external Q's to 4×10^6 , which allows operation at 8 MV/m in the presence of microphonics of 370 Hz peak-to-peak for 5 mA of average current.

2.1 Power Requirements

To date we have accelerated and stably energy recovered up to 4 mA of continuous wave beam. demonstrated that energy recovery works equally reliably in the pulsed mode where 200 usec beam pulses enter the SRF cavities at several Hz rate (from 2 Hz to 60 Hz). Figure 1 demonstrates the difference between nonrecirculated operation and energy recovery, in pulsed mode. The signal plotted is GASK, the signal used to control the amplitude of the RF drive. When the 200 µsec beam pulse enters the cavity, there is a beam-induced gradient fluctuation due to transient beam loading. In response, the gradient modulator drive tries to compensate by demanding more klystron power, resulting in the waveforms depicted in Figure 1, with signal levels around 1.5 to 2 V. With energy recovery, however, the same GASK signals are very close to zero as the two signals

Supported by US DOE Contract No. DE-AC05-84ER40150.

^{*}Email: merminga@jlab.org

cancel each other thereby making the decelerating beam act as the power source.

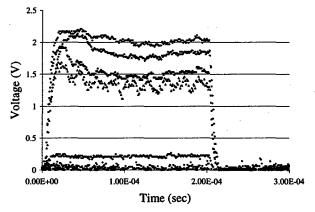


Figure 1: Gradient modulator drive signals in four different linac cavities, measured without energy recovery (signal level approx. 2 V), and with energy recovery (signal level approx. 0 V).

The power requirements for acceleration of 1 mA, 2.4 mA, 3 mA and 3.5 mA with energy recovery are shown in Table 1 and compared to those without beam. To enhance the contrast, power requirements for acceleration of 1.1 mA without energy recovery are also shown.

Table 1: Forward power to the cryomodule cavities under different beam conditions. The last four columns are for energy recovery.

Cav.	Beam off	1.1 mA	1 mA	2.4 mA	3 mA	3.5 mA
_1	2.47	5.11	2.17	2.23	2.37	2.20
2	2.02	5.05	1.95	1.95	1.84	1.90
3	1.14	3.46	1.18	1.33	1.27	1.32
4	2.11	4.63	2.29	2.33	2.57	2.36
5	1.53	3.99	1.68	1.83	1.71	1.83
6	1.91	4.81	2.01	2.00	2.27	2.06
7	1.87	4.37	2.15	1.94	2.07	1.87
8	1.73	4.23	1.84	1.79	1.73	1.63

2.2 RF Stability

Fluctuations of the cavity fields in the linac can cause beam loss on apertures, phase oscillations and optical cavity detuning [3]. All three effects change the beam-induced voltage in the cavities through the recirculating beam. Depending on the RF feedback characteristics, this can lead to instabilities both of the accelerating field and the laser output power. To date we have accelerated, energy-recovered and lased stably up to 3.6 mA of CW beam current with no evidence of any type of instability.

3 HIGHER-ORDER MODES AND IR DETECTORS

3.1 IR Interlock Detectors

Each cavity in the cryomodule is kept under vacuum by two waveguide windows, a ceramic one at 2 K and a polyethylene one at room temperature. The waveguide section between the windows is protected against arcing by an interlocked photomultiplier tube and against thermal runaway (mostly of the warm window) by a thermopile infrared detector. The IR detector is aimed at the cold waveguide's parts through a 16 mm diameter tube departing from the narrow sidewall of the high aspect ratio waveguide. During the first operation of the FEL with sizable CW beam (~1 mA), it was noticed that the signal from the IR detector (normally negative, since it detects a temperature lower than that of the detector's body) was increasing towards zero. This observation was ascribed to possible HOM emission, with consequent additional heating of the waveguide area, but no further action was taken. As the current was raised in recent weeks, the signal from the IR detectors in all cavities was observed to rise, until, at about 1.5 mA, it reached the set trip point of the IR interlocks, shutting off the beam and the RF power and virtually preventing operation of the machine. The observed anomalous response from the IR detector possesses the following characteristics: a) it appears only when the beam is on, and b) the response time with beam on/off is of the order of one second, a couple of orders of magnitude faster than the normal thermal response time of the waveguide subjected to a few kilowatts of incident power.

Based on these observations, it was thought that the IR detector was producing a spurious signal, not due to real temperature changes in the waveguide assembly. Bench tests of an IR detector assembly revealed that the detector is sensitive to direct exposure to RF, producing a positive signal with a response time of one second. Measurements performed around 20 GHz showed a sensitivity of the detector of about .4-.6 mV/mW. The 16 mm diameter tube in which the detector is assembled has a cut-off frequency of about 11 GHz in the TE, mode and about 14.4 GHz for the TM_{ot} mode. The installation of an RF screen with mmsized holes removes most of the signal associated with the beam's suspected HOM's, while still providing reasonable response from the fundamental RF power heating of the waveguide. The observation of the RF response of the IR detector provides us with a bolometric tool for the detection and analysis of the HOM's generated by the beam. An assembly of three detectors with different screens has been placed on one of the cavities' waveguides. The assembly is mounted at 90° from the direct line of sight of the interlocking IR detector on a 16 mm pipe "tee". The detectors in this assembly show no response under the zero power condition, since they are

not looking at the waveguide's cold surfaces, but at a room temperature part of the "tee". They also show no response to RF power on, indicating that the IR radiation is not coupled to it via the 90° "tee". When the beam is turned on, however, the IR detector responds with a positive signal with a one-second time constant (Figure 2). Only microwave energy between 11 GHz and a few tens of GHz can couple efficiently through the bend and propagate to the detector. This additional confirmation of the correlation of the IR response with RF, and not with heating, strongly supports the hypothesis that no additional heat is being generated which could endanger the safe operation of the superconducting cavities.

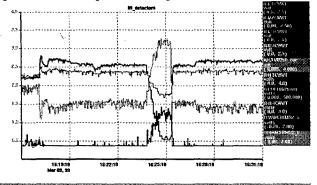


Figure 2. Traces of standard IR interlock detectors (changing from high to low, polarity reversed) and of 90° offset detectors (changing from low to high) as the beam is turned on.

The typical signal detected by the IR sensors indicated that the amount of HOM power reaching the detector is of the order of several milliwatts. At present, the coupling factor from total HOM power generated to that detected is unknown, although it should be very small, probably less than 10^2 .

3.2 Higher-Order Modes

Power emitted by the beam in the form of Higher-Order Modes has been estimated to be of the order of a few watts per cavity. A fraction of that power (at frequencies between 1.9 GHz and several GHz) should propagate into the HOM extraction waveguides and be absorbed by specially designed loads kept at the cryomodule thermal shield's temperature, 50 K. Other modes will propagate down the beam pipe and be absorbed anywhere in the cavities at 2 K or in the warm sections of the line. Thermal measurements of potential losses due to longitudinal modes have so far failed to detect additional heat loads due to HOM's, but the sensitivity of these measurements is of the order of a few watts per cavity. Additionally, modes' power will propagate into the fundamental power coupler and will be absorbed by waveguide filters in the guide's warm sections. Lightlycoupled electric field probes, coupling mostly to TE₂ modes in the high aspect ratio rectangular waveguide, have provided qualitative insight into the spectrum of the emitted RF (Figure 3).

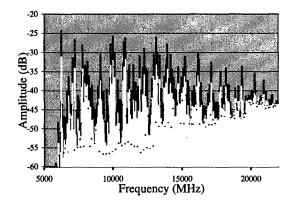


Figure 1. RF spectra sampled from the input waveguide of a cryomodule cavity. Black trace: 3.5 mA beam. White trace: 1.3 mA beam.

Preliminary results show a highly populated spectrum of lines spaced by 37.425 or 74.850 MHz (the bunch repetition frequency). The spectra start at about 6 GHz, the cut-off frequency of the TE_{01} mode in the guide. The spectra are detected up to 22 GHz, the upper frequency of the analyzer.

4 OUTLOOK AND CONCLUSIONS

We have successfully operated Jefferson Lab's IRFEL in energy recovery mode with up to 4 mA of CW recirculating current. No evidence of RF instabilities has been observed. The presence of HOM's from the short bunches in the SRF cavities has been confirmed by different methods. Detection of HOM power by the IR interlocks has interfered with operations, but the installation of copper screens appears to have solved the problem. The response of the detectors themselves to the HOM's is planned to be used to gain information about their dependence on beam properties such as bunch length, bunch repetition frequency and charge per bunch.

5 ACKNOWLEDGMENTS

We would like to thank W. Lacy, R. Nichols, R. Terrell and M. Wissmann for assistance during the measurements and J. Delayen and L. Doolittle for useful discussions.

- [1]S. V. Benson, "High Average Power Free-Electron Lasers", these proceedings.
- [2] C. Bohn, et al., "Performance of the Accelerator Driver of Jefferson Laboratory's Free-Electron Laser", these proceedings.
- [3] L. Merminga, et al. "Analysis of the FEL-RF Interaction in Recirculating, Energy-Recovering Linacs with an FEL", Proceedings of FEL Conference, Williamsburg, VA, August 1998.

QUASI-CONTINUOUS WAVE OPERATION OF MULTI-MEGAWATTS ELECTRON BEAM IN THE JAERI SUPERCONDUCTING RF LINAC FEL DRIVER

E.J.Minehara, M.Sawamura, R.Nagai, N.Kikuzawa, M.Sugimoto, T.Yamauchi and N.Nishimori JAERI, Tokai, Ibaraki, JAPAN

Abstract

Recently, the JAERI superconducting rf linac based FEL has successfully been lased to produce a 0.1kW FEL light and about 70kW electron beam output in quasi continuous wave operation. The 1kW class output as our present program goal will be achieved to modify the optical outcoupling method in the FEL optical resonator and to improve the electron beam optics and basic performances in the JAERI FEL driver. As our next program goal is a 100kW class FEL light and multi-MW class electron beam output in average, quasi continuous wave operation of multi-MW electron beam will be planned in the JAERI superconducting rf linac FEL driver facility within a few years. Conceptual and engineering design options needed for such a very high power operation will be discussed to modify and to upgrade the existing facility in the conference.

Email: eisuke@jfel.tokai.jaeri.go.jp

1 INTRODUCTION

As well known, a laser system consists of three major parts, i.e., a laser driver like a flash lamp, a gain medium like a glass or a crystal, and an optical resonator of paired or several mirrors. Since the invention of the laser in 1960's, efficiency and average power level of the conventional lasers have been seriously limited to very low by their huge heat losses in the laser drivers and gain media, and damages in the mirrors. Because a free electron laser(FEL) has an high energy electron beam in alternating magnetic field as the gain media, we could neglect the heat losses in the FEL gain media. Unfortunately, as long as conventional normal conducting accelerators were used to produce the high energetic electron beam as the FEL driver, we still have the large heat losses in the accelerator cavity wall of the FEL driver. Therefore, in order to make a highly-efficient, and high average power FEL, we resultantly have to minimize the heat losses in the driver to very low level in comparison with total rf power consumption. This is our motivation why we try to apply the superconducting rf linac to the JAERI FEL driver.

A developmental program[1,2] of the FEL system for a far-infrared region from the wavelength of 10µm to 100µm has been undertaken at Japan Atomic Energy Research Institute(JAERI), Tokai. The purpose of the present JAERI FEL program lies in constructing a very long pulse simulating the continuous wave(cw) and, or quasi- cw superconducting rf linac FEL driver of

100kW beam power, and demonstrating a high-average power FEL of 1kW in the far-infrared wavelength region.

Because the wall losses and required rf power become minimal in the superconducting accelerator cavity, we recently could realize the 100kW-class high-power rf linac driver in the quasi- cw, and hence the high-average power laser up to 0.1kW class. Each major part of the program including future plans has been reported in other papers [1,2] in detail. Here, we present an outlook of the program including the present status and future plans. Especially, the achievement of the present design goal of 1kW FEL output, and a quasi-cw electron beam of multi-MW class for realizing a 100kW FEL output will be discussed in briefly using an energy recovery scheme.

2 INJECTOR

An injector of the JAERI FEL consists of a thermionic cathode electron gun with a pulsing grid, a sub-harmonic buncher(SHB). The accelerating voltage in the single gap electron gun is typically around 235kV, and the gun is usable from 220 to 250kV recently. The cathode is mounted horizontally in a stainless-steel pressurized vessel with SF₆ gas to 2kg/cm² in order to prevent break down across a 45 cm-long insulating ceramic tube of the gun. The accelerating gap electrodes are fabricated in a re-entrant geometry to increase the accelerating gradient. As the old was located far from the pump, the new was made to locate just above the pump and to shorten the beam axis distance in September 1998. Resultantly, we could realize a arc or discharge related voltage degradation-free high voltage holding system. Conceptual design of the geometry and the optimization were made again by computer-modeling of electron beams using E-GUN[3], and beam parameter measurements, respectively.

The injector was first installed, and commissioned late August 1991, and had been operated routinely till the beginning of 1997. In 1997 and 1998, an intensive study of the pulser and electron gun performances and improvements had resulted in minimizing a pulse width and incresing the peak current and pulse charge. The improvements typically obtained are as follows: an electron beam ranging from 0.8 to 1.2A with 1ns bunch length was extracted from the gun at the accelerating voltage of 235kV. The beam was successfully compressed to 60 ps or less at around the time focus point by the bunching system[1]. Normalized emittances after the SHB were measured around 20 to 30 π mmmrad. Transmissions of the injector and the whole system were

measured to be around 100% by using the JAERI-made current core monitors, fast Faraday cups and others

Time jitters of the pulses were measured to be as small as several tens ps around the gun. No firing of the unwanted pulse during the quasi CW mode, and very small peak current deviation of being well lower than 1% in each pulse have been achieved.

3 SUPERCONDUCTING RF LINAC

The JAERI superconducting rf linac consists of two pre-accelerator modules of the single-cell cavity type and two main modules of the 5-cell cavity one. The resonant frequency of the cavities is 499.8MHz which is exactly the same with the buncher, and the sixth harmonic of the SHB one.

We decided to choose a superconducting 500MHz cavity design with similar geometry's being found in KEK, DESY, and other high energy physics labs, and the fabrication technology refined by Siemens Energieerzeugung KWU for the JAERI FEL superconducting rf linac accelerator late September,1990. Design values of the accelerating field strength and quality factor for the cavities are 5MV/m, and 2 x 10⁺⁹, respectively. In the beginning of 1993, we have successfully demonstrated a very good cryogenic performance of stand-by loss<4.5W at 4.2K, and accelerating fields' ones of 8.3MV/m and quality factor 2 x 10⁺⁹ in four JAERI superconducting accelerator modules, and installed them in the FEL accelerator vault.

As a main coupler was designed to have a variable coupling coefficient over 3 and half decades from the critical, we could inject not only low current but also high current electron beams into the accelerator cavity without losing rf power by mismatching in the coupler. In order to do some rf system diagnostics, we could easily and quickly perform low and high rf power tests anytime adjusting the coupler. Typical peak rf power for the coupler was measured up to the 50kW without any trouble in JAERI. The coefficient was designed to be adjusted by pushing and pulling a center conductor into the cavity over about 10cm.

Three sets of the higher mode couplers were made to suppress unwanted and harmful TE and TM modes having a higher resonance frequency. Two monitor couplers were used in monitoring and phase detecting in the feedback loop of a fast tuner. Slow and fast tuners were made to tune a resonance frequency of the cavity. The slow tuner consists of a stepping motor driver and an manually-controlled interface from the control system. The fast tuner consists of three sets of a piezo-electric actuator and a high voltage power supply, a feedback loop, an interface from the phase detector, and the control system in one module. During the beam acceleration, the system keeps the phase constant within 0.2 degree p-p, and keeps the amplitude constant within 0.05% p-p except for the first 10µs.

4 CRYOSTAT AND REFRIGERATORS

We have newly developed zero-boil-off (ZBO) multi-refrigerators system integrated into the superconducting accelerator module cryostat to realize a independent, and highly-efficient system without any liquid coolant. Instead of liquid He coolant, we need some amount of liquid He to stabilize the pressure and temperature inside the liquid He vessel and Nb cavity. Each accelerator module has own heat shield cooler and recondensor being equipped with two sets of refrigerator and compressor, independently. This modular structure of the cryostat makes it possible to remove any single module for repairing, and to add more modules without stopping and warming other module.

A 4K closed-cycle He gas refrigerator mounted just above a liquid-He supply tower of the module was adopted to cool down and to recondense cold vapor of liquid He around a heat exchanger in the liquid He container. Required electricity of a conventional liquefier is around 1kW for 1W cooling at 4.5K, and the required of the JAERI recondensor 1.8kW at 4.2K. In order to run the recondensor economically, we introduced a new heat buffering material of ErHoNi magnetic compound instead of Pb, and successfully reduced the required down to 0.9kW. A 40K/80K two-stage closed-cycle He gas refrigerator, which was mounted in a vacuum vessel of the module was adopted to cool down the 40K and 80K heat shields and other major components of the cryostat. These two kinds of the refrigerators are available commercially in Japan. The 4K refrigerator fixed in a heavy steel frame can be winched up and down to remove the heat exchanger out of the liquid He container, and to insert the exchanger into the container using two small inhouse cranes. Cooling capacity of the 4K refrigerator is about 11.5W at 4.2K and 60Hz. We could run the whole system continuously with no trouble and no additional supply of liquid He for one year in 1996. Recently, we have prepared to increase effective cooling power by increasing the number of recondensor twice or three times and increasing cooling capacity of the single recondensor up to 25W

The 40K and 80K heat shields are used to prevent heat invasion from outside into the liquid He container. In order to minimize heat loads to the container, the heat shields work as a thermal anchor, and make the heat flow return route having a temperature higher than 4.2K for all heat bridges from the outside. The 40K/80K refrigerator used here provides two cooling stages with a typical pair of temperature of 40K and 80K and heat load capacities of 40W and 120W, respectively. As heat loads of the two stages in typical condition were very small,2W and 50W respectively, operational temperatures of them were very low, 10K and 50K, respectively. We have had absolutely no trouble in the heat shield coolers for about 6 years continuous running.

These two refrigerators and whole ZBO system including the prepared multi-recondensor ones have been authorized to run with no operational crew as a open

dewar with the cooler by the Japanese central and local governmental offices under a full control of the Japanese pressure vessel codes.

5 RF POWER SUPPLIES

One of the largest merit of a superconducting accelerating cavity is very low power loss, which makes it possible to use all-solid-state rf power amplifiers for all of the cavities[1]. Because the required voltage of the all-solid-state amplifiers is lower than that of a klystron and a tetrode, a more stable, wider band width and faster-responsing rf power is expected to be realized. We chose two sets of all-solid-state 50kW rf power amplifiers for the main accelerators, two sets of 6kW for the preaccelerators, and 4kW for the SHB.

Performance of the rf power supplies has been successfully demonstrated to be better than 0.05% of amplitude and within 0.2 degree of phase stability at an rf power level of 35kW or more in lasing experiments. We have had no malfunctioning of the rf power supply since the installation, and we expect semi-infinite lifespan, no needs for aging, repairing and maintenance near future.

6 ELECTRON BEAM TRANSPORT SYSTEM

The energy of electron beams accelerated by the linac usually ranges from about 10 to 25 MeV. A conceptual design of the transport system was done by using the beam optics code TRACE-3D [4]. High current beams have to be fed to the undulator under isochronous or achromatic conditions for efficient lasing of FEL. Because of the large amount of charge density, space charge effects would become serious in a long transport line and a beam waist, especially from around the capture to just before the main accelerator module. Since the code could take into account partially space charge effects, the transport system has been investigated using the code.

A beam dump was capable of handling about $100 \mu A$ of true average current or more, and 2 kW of beam power. Cooling of the dump which was made from an Aluminum cylindrical block was provided by air flowing. About 40 cm-thick lead blocks surrounds the dump to reduce the radiation levels during routine operation to natural background levels outside the shielding walls made of 150 cm-thick concrete and soil.

7 PRESENT STATUS AND FUTURE PLANS

First saturated and stable FEL oscillation were observed to be around 25µm and 0.1kW at 16MeV electron energy in 26th February, 1998. An achievement of the present design goal of 1kW FEL output is partially discussed in each developmental items like the electron gun and others above. In addition to them, we planned

and prepared to improve the optical outcoupling in axially-symmetric manners.

As our next program goal is a 100kW class FEL light and multi-MW class electron beam output in average, quasi continuous wave operation of multi-MW electron beam is planned in the JAERI superconducting rf linac FEL driver facility. As an example, several tens mA and 50MeV linac driver in the energy recovery, and 100kW 1.5µm FEL device for heavy industries are under consideration in cooperation with Japanese private firms. Conceptual and engineering design options needed for such a very high power operation are now under preparation to modify and to upgrade the existing facility.

After the current developmental program will be successfully ended, we plan to build a large-scaled high average power FEL facility driven by a superconducting rf linac with a 200MeV recirculating configuration, or to build a UV and shorter wavelength FEL facility without a recirculating configuration. After or before the second step, an industrial superconducting rf linac based CW FEL machine(Industrial SCFEL) will be built to demonstrate 1.5µm 20kW high average FEL output power capabilities of the superconducting rf linac FEL driver. These three plans under consideration in JAERI are not approved yet by Japanese government.

8 SUMMARY

In conclusion, we have presented the status and purpose of the JAERI quasi-cw, high-average power FEL program concerning the superconducting rf linac driver, and other FEL opticals. We reported our successful demonstration on the performances of the JAERI superconducting rf linac driver and FEL device. We are now active in realizing a demonstration of the 1kW FEL output and next step of mutli-MW FEL driver using the energy recovery technology.

9 REFERENCES

[1]M.Sawamura, et.al., Nucl. Instrum. Method A318 (1992) 1 27.

[2]M.Ohkubo et.al., Nucl. Instrum. Methods A296 (1990)270.

[3]W.B.Herrmannsfeldt,SLACReport-226, November

[4]K.R.Crandall, et. al., LA-1054-MS, UC32 and UC28, 1987.

3D DESIGN OF THE FUSION-FEM DEPRESSED COLLECTOR USING THE GENERAL PARTICLE TRACER (GPT) CODE.

S.B. van der Geer, M.J. de Loos, Pulsar Physics W.H. Urbanus, A.G.A. Verhoeven, FOM-Rijnhuizen, Association EURATOM-FOM

Abstract

The "Rijnhuizen" Fusion Free-Electron Maser (FEM) is the pilot experiment for a high power, mm-wave source, tunable in the range 130-260 GHz. The FEM has generated 730 kW output power during 10 µs pulses.

To increase the overall efficiency to over 50 % and to reach a pulse length of at least 100 ms, an electron beam charge and energy recovery system is currently being designed and installed. This system consists of an electrostatic decelerator, which decels the beam from 2 MeV to an average of 200 keV, and a depressed collector. The EM-wave interaction inside the undulator can result in an energy spread of 300 keV behind the decelerator.

The multi-stage collector is designed so that electrons fall on the backside of one of three electrodes, thus ensuring that secondary particles will immediately be accelerated back towards the electrodes. However, scattered primary electrons can cause back streaming, hereby reducing the efficiency and possibly damaging the machine.

To reduce this back streaming to below a tolerable 0.1%, the General Particle Tracer (GPT) code is being used to calculate primary and scattered particle trajectories inside the collector. It will be shown that an off-axis bending scheme, using a rotating perpendicular magnetic field lowers the back streaming and hereby increases the pulse length of the machine. The bending scheme also improves the power dissipation in the collector.

1 INTRODUCTION

The Fusion-FEM is the prototype of a high power, electrostatic mm-wave source, tunable in the range 130-260 GHz [1]. The device is driven by a 2 MeV, 12 A dc electron beam and is designed to generate 1 MW microwave power, see Table A. Without decelerator and collector, the FEM has produced 730 kW during 10 μs pulses. In the future FEMs can be used as power sources

for electron cyclotron applications on magnetically confined plasmas in fusion research devices.

Because of its flexibility and capabilities, the General Particle Tracer (GPT) code has been used for the complete design of the FEM beam line [2]. The simulations include FEL interaction, space-charge effects, imported electrostatic and magnetostatic field data and misalignment.

To be able to meet the target efficiency of over 50 % and a pulse length of 100 ms, a beam and energy recovery system is crucial. The GPT code has been used to design this system and investigate the effects of an off-axis bending scheme. In this paper we will present simulation results for the FEM depressed collector.

Table A: Principal design parameters of the Fusion FEM

Table A. Timelpai design parameters of the Tusion TEM				
Parameter	Value			
Electron beam current	12 A			
Electron beam energy	1.35-2 MeV			
Pulse length	100 ms			
Microwave frequency	130-260 GHz			
Microwave net power	1 MW			
Target system efficiency	≥ 50%			
Target current losses	≤ 20 mA			
Linear gain per pass	7-10			
Gain at saturation	3.5			
Waveguide parameters	HE_{11} in $15 \times 20 \text{ mm}^2$			
Undulator period	40 mm			
First undulator section	20 periods with 0.20 T			
Second undulator section	14 periods with 0.16 T			

2 BEAM AND ENERGY RECOVERY

The beam and energy recovery system of the Fusion FEM consists of an electrostatic decelerator, a transport line and a depressed collector. GPT simulations have shown that the EM-wave interaction in the undulator results in a maximum energy spread of 300 keV behind the decelerator. For this energy distribution a depressed collector with three electrodes will suffice to obtain the required efficiency.

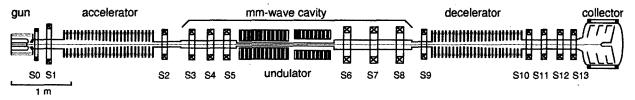


Figure 1: FEM beam line.

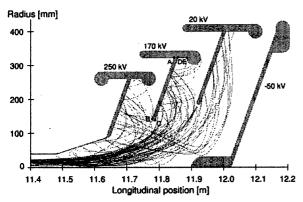


Figure 2: FEM depressed collector with sample trajectories. Both primary and scattered particles are shown.

As shown in Figure 2, in the depressed collector the electrons are collected on the backside of the electrodes. This assures secondary electrons to fall back on the electrodes. Scattered electrons, however, have an energy close to the initial energy and can cause back streaming via multiple scattering. As all beam loss and back streaming current has to be delivered by the 2 MV power supply, which can deliver only 20 mA, at least 99.8 % of the beam needs to be collected. Furthermore, back streaming could damage the machine.

To decrease back streaming, an off-axis deflection system is being installed. It consists of four solenoids generating a rotating perpendicular magnetic field. The coils are mounted directly on the surface of the collector housing to increase the effective area, resulting in a bent elliptical shape.

The deflection system causes an angle dependency for the current distribution on the collector electrodes, shown as an example in Figure 3. Only the top-bottom coils are powered, but the beam is pushed vertically due to the tail field of S13.

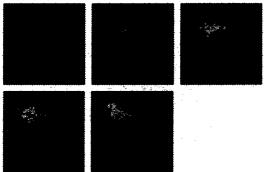


Figure 3: Simulation results for the current dissipation on the second collector plate. The plots represent 0, 0.5, 1.0, 1.5 and 2.0 mT in the deflection system.

3 GPT

The General Particle Tracer (GPT) [3,4] is a software package developed to aid in the design of accelerators and beam lines by using modern, particle tracking techniques. GPT is capable of tracking any number of particles

through complex electromagnetic fields taking all 3D effects and space-charge forces into account. A 5th order embedded Runge-Kutta integrator with adaptive stepsize control produces highly accurate and reliable results, while the simulation time is kept to a minimum.

The fields of physical structures are represented by so called elements. GPT comes with a large set of standard elements for basic structures such as solenoids, quadrupoles and accelerating structures. However, for specific cases custom elements can easily be added. Elements can be positioned anywhere and in any direction in 3D space. The effect of fringe fields can be taken into account. Measured or externally calculated fields can be used in the simulation.

4 SCATTERING IN GPT

Specifically for the FEM project, scattering of electron trajectories at 3D-boundaries was introduced in GPT. It makes use of a user-defined scattering model as function of material. A combination of 3D ray-tracing techniques and Monte-Carlo statistics is used to accurately model the scattered primary particles inside the collector.

4.1 Monte-Carlo approach

When a macro-particle trajectory intersects a surface during the simulation, the intersection point, energy and angle of incidence are calculated. Then, the incident particle is removed from the simulation and a new macro-particle is emitted. The deflection angle and reflection energy are chosen randomly, but following a prescribed function depending on the material of the boundary [5]. The overall scattering probability is accounted for by varying the number of electrons which the new scattered macro-particle represents.

4.2 Charge and energy dissipation

The total charge dissipated per incident macro-particle is given by:

$$Q_{in} - Q_{out} = q(N_{in} - N_{out})$$

where $N_{\rm in}$ and $N_{\rm out}$ represent the number of incoming and outgoing electrons which the macro-particles represent. If all incident electrons have the same energy, there is a close to linear correlation between dissipated charge and dissipated energy. However, GPT uses the general relativistic equation to be able to investigate non-linear effects:

$$E_{in} - E_{out} = N_{in} (\gamma_{in} - 1)mc^2 - N_{out} (\gamma_{out} - 1)mc^2$$

where γ is the Lorentz factor of the electrons.

4.3 Analysis

When a particle hits a surface, the dissipated charge and energy is recorded together with the intersection point. To ease the interpretation of the results, the 3D coordinates are "unrolled" along the collector plate. The first

coordinate is the distance along the collector plate boundary, starting from an arbitrary point. For the second FEM collector plate, this point is marked "A" in Figure 2. The second coordinate is the azimuthal angle. After this transformation, inverse mapping in ray-tracing terms, the results can be presented as 2D-density plots, a standard feature of GPTwin.

5 SIMULATION RESULTS

Using the scattering model of GPT, we have looked in detail at the effect of the deflection system on the current and power dissipation. Furthermore the amount of current flowing back from the collector towards the cathode was studied.

To illustrate the effect of the bending system, we show results for the second electrode of the collector. This plate receives the most current. Figure 4 shows typical GPT output for the power dissipation. The B, C, D and E markers correspond to the positions indicated in Figure 2. Without the bending system the electrons are distributed homogeneously over the plate, while with the deflection system a strong angle dependence can be seen.

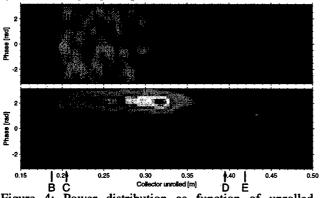


Figure 4: Power distribution as function of unrolled position and phase on second collector plate without (top) and with 1.5 mT bending field (bottom).

Because the FEM deflection system rotates, the angle dependence is smoothed. This results in averaging the current and power dissipation over the phase along the unrolled collector coordinate. Figure 5 shows the corresponding GPT output for the second collector plate. Without the bending system there is a nearly uniform distribution over the surface of the electrode. With the deflection system the beam is bent into the collector and the electrons hit the plate at a larger radius. This information is important for the design of the cooling system, which will be installed to further increase the pulse-length. Although the local intensity peak is very high with the bending system on, when the peak is smoothed over all angles the maximum value is not higher than with the uniform angle dependency.

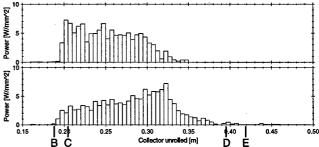


Figure 5: Power distribution as function of unrolled collector position without (top) and with 1.5 mT bending field (bottom).

The most important effect of the collector bending system is that it lowers the current flowing back from the collector towards the cathode. As shown in Figure 6, the deflection system decreases the return current from 100 mA to below a tolerable 10 mA. Therefore the deflection system is necessary to achieve the design efficiency.

The total power dissipation, summed over all collector plates, also decreases. Because the beam is actively bent into the collector, more particles hit the second plate that would otherwise have been collected on the first plate. This slightly decreases the total dissipated power at the cost of an asymmetric current load on the collector plates.

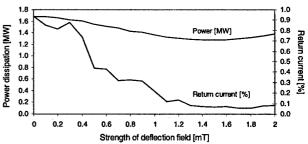


Figure 6: Total power dissipation and return current as function of bend strength.

6 CONCLUSION

The new scattering model in the GPT code has been used to investigate the effects of the off-axis deflection system for the FEM depressed collector. The return current is reduced to within the design specifications and the total dissipated power is reduced without affecting the maximum power dissipation on the collector plates.

- [1] W.H. Urbanus, et al, Nucl. Instr. and Meth. A375, (1996) pp. 401.
- [2] M.J. de Loos, S.B. van der Geer, Nucl. Instr. and Meth. in Phys. Res. B, Vol. 139, (1997) pp. 481.
- [3] S.B. van der Geer, M.J. de Loos, Proc. 1998 Particle Accel. Conf., Stockholm, Sweden (1998) pp. 1245.
- [4] GPT User Manual, Pulsar Physics, De Bongerd 23, 3762 XA Soest, The Netherlands, http://www.pulsar.nl/gpt.
- [5] J.L.H. Jonker, Philips Res. Rep. 12 (1957) pp.

BUNCH COMPRESSOR AND DE-COMPRESSOR IN THE FEL FOR SATELLITE POWER BEAMING*

W. Wan, FNAL, Batavia, IL and A. Zholents, LBNL, Berkeley, CA

Abstract

A FEL of average power 200 kW is being designed at the LBNL for satellite power beaming[1, 2]. It utilizes the radiation of ~100 MeV electrons with ~200 A peak current. In order to obtain the desired peak current, the 5mm long electron bunches delivered by a linear accelerator are compressed to 1mm. Furthermore, it is important for the FEL operations that the compressed bunches have a uniform longitudinal density distribution over the entire bunch length. After the FEL, the electron beam is returned to the linear accelerator for deceleration. Since the electron beam acquires approximately 6% energy spread during radiation in the FEL, bunch de-compressor is used between the FEL and the linac to expand the electron bunches back to its original length and to reduce the energy spread. In this paper we present design and analysis of the bunch compressor and the bunch de-compressor that perform needed functions.

1 INTRODUCTION

This work is part of a broader study aiming at the design of a FEL for satellite power beaming [1]. At present a FEL of average power 200 kW at the wavelength of 840 nm is being designed at the LBNL [2, 3]. The FEL utilizes a \sim 100 MeV electron beam with the average beam power of ~10 MW provided by a RF photoinjector and a linear accelerator. The design assumes a low beam peak current in the injector and the linear accelerator and a high beam peak current in the FEL. A compression of electron bunches is needed between the linear accelerator and the FEL. The goal of the compression is not only a short bunch in the FEL, but also a bunch that has a uniform longitudinal electron density profile over most of the bunch length. The former helps to improve the efficiency of the energy transfer from electrons to light; the latter helps to minimize the energy spread of electrons after the radiation. This is important because the FEL design assumes that the electrons are decelerated in the linear accelerator to below 12 MeV before they are sent to the dump, which is employed for energy recuperation in the linac and the elimination of induced radioactivity in the dump. Therefore, too large energy spread of the electrons will hamper the deceleration process.

In the process of the radiation in the FEL the electrons lose about 2% of their energy and acquire roughly an energy spread of 6%. Bunch de-compressor uses this energy spread to disperse the compressed electron bunch back to its original length. It also creates a correlation between energy of electrons and their position along the bunch, which

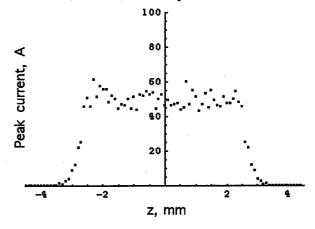


Figure 1: The longitudinal distribution of electron peak current at the end of the RF photoinjector. Point to point fluctuations on the plot are due to limited statistics in the simulation.

is used to reduce energy spread of electrons at the end of the deceleration.

2 BUNCH COMPRESSOR AND DE-COMPRESSOR

The design requirement for a bunch compressor is a reduction of the electron bunch length from approximately 5 mm at the end of the linear accelerator to 1 mm at the beginning of the FEL. This will raise the electron peak current in the FEL up to more than 200 A.

At this point we assume that an electron bunch leaving the RF photoinjector has a normalized longitudinal emittance of 6 cm and a uniform longitudinal distribution, as shown in Fig. 1 (This distribution is considered in a design of the RF photocathode gun). We begin bunch compression by creating energy shift of the electrons correlated with the electron position along the bunch. This is accomplished by accelerating the electron bunches in the linac at a -13° phase off the peak accelerating field. Ideally, we want to produce a linear dependence of the electron energy shifts on the longitudinal coordinates of the electrons relative to the bunch center. But, it is impossible because the acceleration takes place in a sinusoidal RF field and, together with the linear term, it inevitably produces nonlinear terms. However, one can use the actual dependency of the electron energy shift on the longitudinal coordinates and derive a required pathlength difference as a function of electron energy. Usually, the first three terms are sufficient for an accurate descrip-

^{*} Work supported by DOE under Contracts DE-AC03-76SF00098 and DE-FG03-95ER40926.

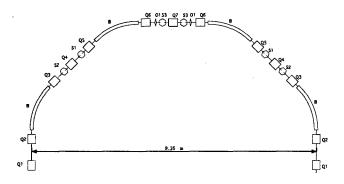


Figure 2: The layout of the bunch compressor

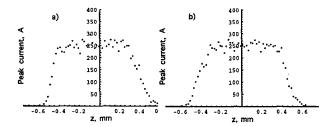


Figure 3: The longitudinal distribution of electron peak current after bunch compression: a) without errors, b) with errors. Point to point fluctuations on the plot are due to limited statistics in simulations.

tion. In our case they turn out to be:

$$\delta L = -0.514 \frac{\Delta E}{E} - 3.88 \left(\frac{\Delta E}{E}\right)^2 - 177 \left(\frac{\Delta E}{E}\right)^3 \tag{1}$$

where all coefficients on the right hand side of the equation have a dimension expressed in meters. Now, this function can be programmed into the performance of the bunch compressor to produce the uniform longitudinal distribution at the exit. This is to force all electrons to radiate in the identical conditions in the FEL and, therefore, to minimize the energy spread produced in the process of the radiation.

In this design we incorporated the bunch compressor into a magnetic arc performing a 180° beam turn from the end of the linear accelerator to the FEL. Its layout is shown in Fig. 2. The arc's lattice consists from two identical cells and resembles a second-order achromat. Each cell has 2 bending magnets, 8 quadrupoles and 4 sextupoles. The strengths of all quadrupoles and sextupoles are chosen to provide a smooth beam focusing in the arc and time-of-flight lattice terms defined by Eq. 1. Care was given to the choice of linear optics to minimize the strengths of the sextupoles. As a result, the magnetic field of the sextupoles at the pole tip is well below 1 kG (assuming 5 cm radius of the beam pipe).

To test the lattice we did particle ray tracing using COSY INFINITY [4]. We assumed 8 mm-mrad for normalized vertical and horizontal beam emittance. The result of simulation without lattice errors is shown in Figure 3. Here one can see the longitudinal distribution of the electron peak current after bunch compression. One can see that the final distribution has a flat top extended almost over the entire

	Static errors	
Setting errors	$\sigma(\frac{\Delta B}{B}) = 1 \times 10^{-3}$ a)	
Tilt errors (mrad)	$\sigma(ar{\Delta\psi})=0.2$	
Misalignment errors		
in x, (μm)	$\sigma(\Delta x) = 150$	
in y, (μm)	$\sigma(\Delta y) = 30$	
in z, (mm)	$\sigma(\Delta z) = 1$	
Multipole errors		
dipoles	$\sigma(\frac{b_3}{b_1}) = 1 \times 10^{-4} \text{ at } r = 3 \text{cm}^{-b}$	
quadrupoles	$\sigma(\frac{b_3}{b_2}) = 5 \times 10^{-4} \text{ at } r = 5 \text{cm}^{-b}$	

a) b₁, b₂ and b₃ are the dipole, quadrupole
 and sextupole components of the magnetic field

Table 1: Specification of the errors

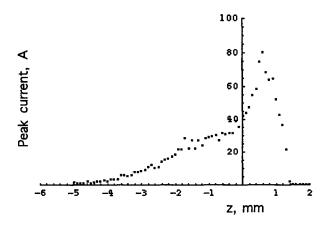
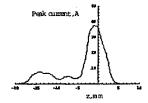


Figure 4: The longitudinal distribution of electron peak current after bunch compression with no errors and sextupoles and octupoles turned off.

bunch length even with all errors being included in simulation. Then we applied all kinds of lattice errors like misalignment errors, tilt errors, setting errors listed in Table 1 and use two families of quadrupoles to offset the linear perturbations to the lattice due to the setting errors. We assume that similar knobs will be used with an actual beam for an initial tuning of the lattice. Then we did particle ray tracing again. A typical result of a simulation for one seed of errors is shown in Fig. 3. Obviously, errors have little effect on the performance of the bunch compressor. To demonstrate the importance of the sextupole corrections we show the result of similar particle ray tracing for a case when all sextupoles are set to zero in Fig. 4. It is clear in this case that sextupoles play a crucial role in producing the desired beam profile. In fact, with sextupoles off, the term T₅₆₆, following the TRANSPORT notation, is about 135 m, responsible for 3.4 mm bunch lengthening of a beam with energy spread of $\pm 0.5\%$. Since the present solution with sextupoles turned on works well for our purpose, no extra effort was devoted to optimize the first-order layout to firther minimize the second-order aberrations.

b) the same for quadrupoles and sextupoles



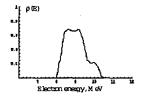


Figure 5: The longitudinal distribution of electron peak current and energy distribution of the spent beam at the end of the linac.

2.1 BUNCH DE-COMPRESSOR

The function of the bunch de-compressor is the reverse of the bunch compressor. It takes the compressed electron bunch with large energy spread acquired in the FEL and uses this energy spread to disperse electrons. For this purpose we use the second 180° arc to return electrons to the linear accelerator. Physically this arc is similar to the first arc, but quadrupoles and sextupoles are set to different strengths. The de-compressor creates the correlation desired between electron position in the bunch and its energy. This correlation is used in the linac for a partial compensation of the beam energy spread. This is accomplished by decelerating the electron bunches in the linac at a 13° phase off the peak accelerating field. A result of the decompression of the electron bunch and deceleration in the linac is shown in Fig. 5. Here we present a distribution of the electron peak current and a distribution of the electron energy in the bunch of spent electrons at the end of the linac.

One can see that at the end of the deceleration the total energy spread of the electrons is roughly 2.5 MeV, while at the beginning of the deceleration it is about 5 MeV as shown in Figure 5.

3 CONCLUSION

The study presented in this report shows that the carefully designed bunch compressor and de-compressor meet the requirement of the FEL for power beaming and thus enhance its efficiency.

- [1] H. E. Bennett, et. al., NIM A341, (1994)124-131.
- [2] K.-J. Kim, et. al., "FEL Options for Power Beaming", NIM A407, (1998)380.
- [3] A. Zholents, et al., "FEL Design for Power Beaming", to be published in SPIE Proc. 3614.
- [4] M. Berz, Technical Report MSUCL-977, Michigan State University, (1995).

CRITICAL SYSTEMS FOR HIGH PEAK POWER STORAGE RING FEL

I.V. Pinayev, G. Detweiler, M. Emamian, N. Hower, M. Johnson, V.N. Litvinenko, O. Oakley, S.H. Park, J. Patterson, G. Swift, Y. Wu, ELL, Durham, NC

Abstract

The Duke storage ring is a facility dedicated for the deep UV free electron laser (FEL) development [1]. It is especially designed for the high peak power applications, having a long optical cavity and large energy acceptance. In this paper we describe FEL gain modulator and optical cavity control system, which are essential for obtaining maximal peak power.

1 INTRODUCTION

Performance of the Duke storage ring and OK-4/Duke FEL [2] is shown in Table 1. The reflectivity of mirrors is very essential to the storage ring FELs, but even perfect mirrors do not ensure lasing if the entire optical system is poorly aligned or mechanically unstable.

Table 1: Duke Storage Ring and OK-4/Duke FEL Parameters

Operational Energy [GeV]		0.25-1.1
Circumference [m]	107.46	
Impedance of ring, \mathbb{Z}/n , $[\Omega]$	2.75	
Stored current [mA]		
multibunch	155	
single bunch	20	
Bunchlength [ps]		
natural	15	
with 5 mA in single bunch	n	60
Relative Energy spread, δE/E		
natural	0.9×10^{-4}	
at 5mA in single bunch	1.1x10 ⁻³	
Peak Current [A]		
with 5 mA/bunch	12	
with 20 mA/bunch	31	
Horizontal emittance [nm rad]		
5 mA/bunch @700 MeV	< 10	
3 mA/bunch @500 MeV		< 8
Demonstrated FEL tunability [nm]	217-600)

2 MIRROR FEEDBACK SYSTEM

To reduce power density and rate of degradation of a downstream mirror the Duke storage ring FEL has a very long optical cavity, which length is equal to the half of the ring circumference (53.7 m). To optimize the FEL gain the optical cavity has rather small Rayleigh range of 3.3 m. Due to significant mismatch between Rayleigh

range and the cavity length the OK-4/Duke FEL is especially susceptible to mirrors' vibrations and misalignments.

The 3 feet concrete slab with pillars going down to the bedrock provides stable and sturdy environment for the Duke storage ring and circulating electron beam. But the optical tables used for support of the mirror mounts are placed on the regular floor and, therefore, are prone to ambient vibrations. The tests showed that even changing of a static load on the optical table or to the floor nearby causes unacceptable changes of the mirror position. That is why an active feedback system for stabilizing mirrors, shown in the Fig. 1 was implemented.

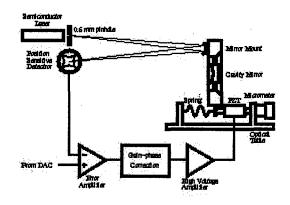


Figure 1: Active mirror feedback system

For this purpose two posts were installed inside the ring room, and reference semiconductor lasers and position sensitive detectors were mounted on the posts. The auxiliary concave mirror firmly attached to the optical cavity mirror mount reflects laser light. Tilt angle of the cavity mirror is measured by a position sensitive detector, which provides voltages proportional to the displacement of the light spot from the detector's center. The voltages from two digital-to-analog converters (DAC) set the desired tilt of the optical cavity mirror. The difference between the DAC voltage and detector voltage is used as an error signal in the feedback system. For the fast response the original stepper motors were replaced with the piezoelectric actuators, while coarse adjustment of the mirrors positions is performed with the help of manual micrometers.

From the optical mount inertia and piezoactuator stiffness the estimated cut-off frequency of feedback system can be up to 1 kHz. However, the mirror mount itself has a strong mechanical resonance at 100 Hz. A gain-phase correction filter was implemented for

providing stability of the closed loop system. After filter installation we were able to raise the cut-off frequency of the feedback system up to 50 Hz [3]. The vibrations with higher frequencies are suppressed with mechanical dampers incorporated to the optical table supports.

3 GAIN MODULATOR

The equilibrium between the energy spread growth, induced by the FEL power, quantum noise excitation and synchrotron damping set the limit on the average FEL power [4]. By modulating the optical cavity losses or the FEL gain, it is possible to compress the same level of average power into a number of giant pulses. This mode of operation is best suited for the high peak FEL power experiments.

The modulation of the optical cavity losses encounters a lot of technical difficulties: relatively low storage ring based FEL gain, high vacuum requirements. However, a modulation of the FEL gain by displacing the electron beam from the optical cavity axis can achieve the same results. Since the electron beam has negligible inertia, by using a set of fast steering magnets it is possible to switch on FEL instantaneously. More practical approach is to use a single corrector, providing adiabatic transition of the electron beam to the lasing orbit (adiabatic transition is required to avoid the excitation the electron beam oscillations). The Duke storage ring has tune frequencies of 700-900 kHz, and this requires a transition time of tens of microseconds.

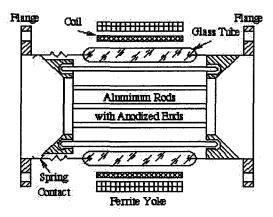


Figure 2: Gain modulator

The OK-4/Duke FEL gain modulator comprises a fast steering magnet with a ferrite yoke, control electronics, and a specially designed vacuum chamber (see Fig. 2). The vacuum chamber allows fast changes of the magnetic field and simultaneously provides smooth transition for the wake fields induced by the electron beam. Inside a glass tube, coated with a thin chromium layer, a cage of the aluminum rods is placed. The ends of the aluminum rods are anodized to provide capacitive coupling for the

currents induced by the electron beam and to prevent eddy currents caused by the changing magnetic field.

In Fig. 3 two oscilloscope traces show the gain modulator operation. The first trace is the voltage from a probe coil placed inside gain modulator, this voltage is proportional to the first derivative of the magnetic field. The second one is integral of the coil voltage and it shows the changes of the magnetic field inside of gain modulator. The time constant of the gain modulator was chosen equal to 10 microseconds, what is much greater then betathron oscillation period and much less then FEL optical power time constant.

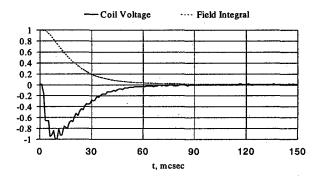


Figure 3: Signal from probe coil and field integral

Tests show that displacement of electron beam inside OK-4/Duke FEL is few millimeters in horizontal direction and less then 20 microns in vertical direction.

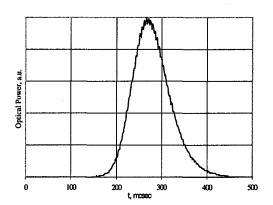


Figure 4: Giant pulse

The second trace is proportional to the optical power outcoupled from the OK-4/Duke FEL and measured with silicon photodiode.

4 CONCLUSION

Implementation of the optical cavity control system allowed to demonstrate stable lasing in the deep UV and visible range of the OK-4/Duke FEL. In future we want

to replace existing mirror mounts for a mirror "switchyard", what will permit fast interchange of mirror sets for various wavelength and increase of mirror feedback bandwidth.

The gain modulator proved its essential role for medical user applications such as laser refractive surgery and no future upgrades are expected. It will be also used for the studying of FEL dynamical behavior.

Authors thank all the Duke FEL Laboratory staff for the efforts, which made successful operation of OK-4/Duke FEL possible.

This work was supported by Office of Naval Research under the contract #N00014-94-C0818.

- [1] V.N. Litvinenko et al., "OK-4/Duke Storage Ring FEL Lasing in the Deep UV." To be published in the Proceedings of the 18th International FEL Conference, Williamsburg, USA.
- [2] Y. Wu et al., "The Performance of the Duke FEL Storage Ring." Nucl. Istr. and Meth., v. A375 (1996), pp. 74-77.
- [3] I.V. Pinayev et al., "System for the Control and Stabilizing of OK-4/Duke FEL Optical Cavity." AIP Proc. of 8th Beam Instrumentation Workshop, May 4-7, 1998, SLAC, Palo Alto, California, USA, pp. 545-551.
- [4] N.A. Vinokurov and A.N. Skrinsky, "Power Limit for an Optical Klystron Installed on Storage Ring", Preprint INP 77-59; A. Renieri, Nuovo Cimento 53B (1979), p. 160.

THE STATUS OF THE HIGH-GAIN HARMONIC GENERATION FREE-ELECTRON LASER EXPERIMENT AT THE ACCELERATOR TEST FACILITY

L.-H. Yu, M. Babzien, I. Ben-Zvi, A. Douryan, W. Graves, E. Johnson, S. Krinsky, R. Malone, I. Pogorelsky, J. Skaritka, G. Rakowsky, L. Solomon, X.J. Wang, M. Woodle, V. Yakimenko Brookhaven National Laboratory, Upton, New York 11973
 S.G. Biedron, J.N. Galayda, V. Sajaev, I. Vasserman

Advanced Photon Source, Argonne National Laboratory, Argonne, Illinois 60439

Abstract

The Accelerator Test Facility (ATF) at Brookhaven National Laboratory (BNL) is an accelerator and beam physics user facility capable of producing a high-brightness, 70-MeV electron beam. Currently, a high-gain harmonic generation (HGHG) free-electron laser (FEL) experiment is underway at the ATF. This is a collaborative effort between BNL and the Advanced Photon Source (APS). The experiment consists of two phases: 1) self-amplified spontaneous emission (SASE) and 2) HGHG. Here, a brief introduction to the HGHG theory, measurements in the SASE phase, the recent modifications in preparation for the HGHG phase, and future plans will be discussed.

1 INTRODUCTION

A free-electron laser (FEL) experiment is being commissioned at the Brookhaven National Laboratory (BNL) Accelerator Test Facility (ATF). There are two distinct project phases. In the first phase, the system will be operated in the self-amplified spontaneous emission (SASE) [1] mode. In the second phase, high-gain harmonic generation (HGHG) to full saturation at 5.3 μ m will be attempted [2]. Here, a brief description of the HGHG theory, the experimental design parameters and layout, and future plans will be discussed.

2 HGHG THEORY

In a SASE FEL, the spontaneous emission "noise" serves to ignite the FEL bunching process, resulting in a noisy output. In seeded FEL operation, the output quality is directly related to the quality of the seed. Also, the point of saturation along the undulator reveals the maximum available power and should occur in the shortest distance, for practical design purposes. From the linear theory, a high peak current, low emittance, and low energy-spread electron beam is required, as well as a properly shimmed undulator, to reduce magnetic error effects on the electron beam trajectory. To reach shorter wavelengths in these modes of operation, however,

Email: lhyu@bnl.gov

requires even higher currents, while maintaining this low energy spread and emittance at increasingly higher energies to produce a sufficiently short gain length and, in turn, saturation point.

Another possible mode of FEL operation capable of providing a very desirable output light beam is HGHG. Here, a coherent radiation source, at a subharmonic of the desired output radiation wavelength, enters a first undulator for energy modulation. Following this modulation, where the electron beam is forced to be resonant with the seed radiation, a dispersive section is traversed, where spatial bunching is induced with a strong higher harmonic content. The beam then enters a second undulator, the radiative section, tuned to resonance to the desired harmonic. (In this particular experiment, the second harmonic is of interest.) Coherent radiation and ultimately saturation at this higher harmonic is then achieved within a reasonable number of undulator periods and with an excellent beam quality, as compared to the SASE process. Recall that this better beam quality is defined by the coherent seed source. This method could quite possibly be extended to higher energies, where the radiator is tuned to a much higher harmonic, to achieve saturation in the UV, VUV, or x-ray regime. A schematic of the HGHG process is provided in Figure 1.

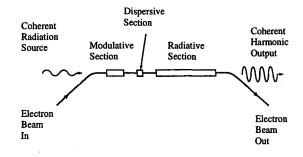


Figure 1: HGHG process

The existing ATF photocathode rf gun, linac, and coherent seed radiation source, a CO₂ laser, define the electron and seed beam parameter base found in Tables 1

and 2, respectively [3]. The value of the energy was specifically tailored to achieve the FEL resonance condition with an existing radiative section, supplied by the Advanced Photon Source (APS). The modulative section and dispersive sections for HGHG operation were designed, manufactured, and measured by BNL. These magnet parameters are found in Table 3.

Table 1: Designed electron beam parameters for HGHG

γ	82
Normalized Emittance	4π mm mrad
Peak Current	110 A
Micropulse Length	4 ps
Energy Spread	0.043%

Table 2: CO, seed laser beam parameters

Wavelength	10.6 μm
Input Seed Power	0.7 MW
Pulse Length	100 ns
Sliced Pulse Length	10-100 ps
Rayleigh Range	0.76 m

Table 3: Magnet parameters

Modulative Section	
Length	0.76 m
Undulator Period	7.2 cm
Number of Periods	9
Peak Magnetic Field	0.158 T
Dispersive Section	
Length	0.30 m
Magnetic Field	0.5 T
Induced Dispersion	1.5 (dψ/dγ)
Radiative Section	
Length	1.98 m
Undulator Period	3.3 cm
Number of Periods	60
Peak Magnetic Field	0.47 T
Betatron Wavelength	3.75 m

Experimental results for the SASE and HGHG modes of operation were predicted with the 1D analytical models and TDA3D simulations [4], in which a waterbag distribution was employed. In HGHG simulations, the electromagnetic field variation at the exit of the modulative section is mapped into an in-house code that tracks the particles through three horizontal corrector magnets (the dispersive section). This output is then mapped back into TDA3D with only one variation imposed in the code - that the integration over the phase bucket is opened to 2π instead of π , since the interest is shifted to the second harmonic. These modifications

must be implemented, since TDA3D is monochromatic and cannot simulate multiple harmonics simultaneously.

Based on these TDA3D simulations and power spectrum scaling [5], the expected SASE output power spectrum at 5.3 μ m is found to be 15 times larger than the spontaneous emission. The HGHG simulations predict a saturation power at 5.3 μ m of 37 MW after 1.8 m.

3 EXPERIMENTAL LAYOUT

The drive-laser system for the ATF photocathode gun is composed of a diode-pumped Nd:YAG oscillator coupled to a Nd:YAG amplifier. The amplifier is capable of delivering 40 µJ to the magnesium cathode. The 1.6-cell 2856-MHz photocathode rf gun and emittance compensation solenoid produce the high current, low emittance, and low energy spread beam necessary, with beam energies exceeding 5 MeV. The solenoid corrects the emittance before it is "frozen" in the linac. The ATF linac is composed of two 3-m accelerating structures, yielding up to 70-MeV electrons. After the linac exit, beam is transferred to an experimental area, where the modulative, dispersive, and radiative sections, as well as the optical diagnostics, exist.

4 SYSTEM COMMISSIONING

The optical diagnostics line is composed of exit windows, point-to-point optics, a scanning spectrometer, and a point detector. Also, five YAG crystal screens are mounted on actuators inside the radiative section to determine the electron trajectory in reference to a surveyed He-Ne alignment laser. A straight electron beam trajectory is important in both phases of operation, since simulations reveal a trajectory tolerance of < 100 μm . Full detail of the electron beam diagnostics and trajectory correction procedure are described separately in these proceedings [6].

Since the electron beam quality almost singly defines the resulting output spontaneous and SASE radiation, electron beam measurements are required relative to the radiation signal. The electron beam measurements can then be used along with the linear theory and simulation to compare the results against theory. Necessary electron beam measurements include the longitudinal current distribution, emittance, and energy spread.

The electron beam bunch length and corresponding charge distribution are measured by varying the rf phase of the second linac section to induce a linear dependence of the particle energy on longitudinal position. A collimating slit in a dispersive region behaves as an energy filter, passing a narrow slice in time [7], where a Faraday cup reveals the transmitted charge. In Figure 2, a measured longitudinal bunch shape with a charge of 1.1 nC is shown. The normalized emittance, as measured by a quadrupole magnet scan, was determined to be 5 mm-mrad.

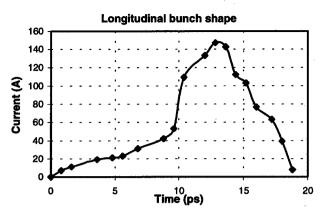


Figure 2: Longitudinal bunch shape for 1.1 nC

For the electron beam described above, a scan of output radiation intensity versus bunch charge was performed, by adjusting the width of the momentum slit to gradually reduce the charge. The result is presented in Figures 3 and 4, where the radiation signal and ratio SASE over spontaneous radiation are shown as functions of the bunch charge, respectively. The exponential rise above spontaneous points toward the existence of SASE output radiation. In Figure 4, the ratio of SASE radiation power over the spontaneous emission approaches 40.

The ratio of SASE radiation over spontaneous radiation can be calculated analytically and compared with experiment. The analytical estimate for start-up noise is based on a three-dimensional linear theory for an electron beam with step-function profile, zero energy spread, and zero angular spread. This idealized model for start-up noise can be used because the betatron motion is negligible during the start-up process. The output power of the SASE radiation is given by

$$\left(\frac{dP}{d\omega}\right)_{SASE} = \frac{1}{9}e^{\frac{L_{\omega}}{L_{G}}}C_{0}\left[\frac{2L_{G}}{L_{\omega}}\left(\frac{dP}{d\omega}\right)_{Spon}^{L_{\omega}}\right]$$

where L_{ω} and L_{c} are the wiggler and power gain lengths, respectively [1]. The calculation of the gain length and SASE ratio were performed for different sections of the electron beam based upon the measured bunch shape shown in Figure 2. This results is an estimated ratio of the SASE over the spontaneous radiation of 25. Considering the random SASE fluctuations that may have occurred and influenced each recorded radiation measurement during the charge scan, this estimate corresponds surprisingly well with the ratio in Figure 4, where the gain ratio approaches 40.

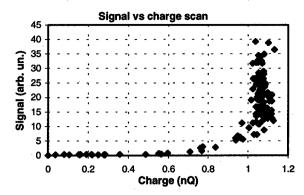


Figure 3: Signal versus charge

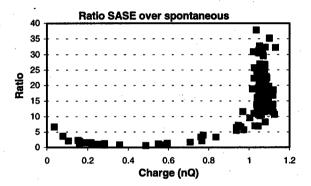


Figure 4: The ratio of SASE over spontaneous radiation versus charge

6 CONCLUSIONS AND FUTURE PLANS

The ATF at BNL is currently commissioning a twophase FEL project. The SASE phase is nearly complete and the HGHG phase is scheduled to begin over the next few months.

- [1] L.-H. Yu et al., Phys. Rev. Lett. 64, 3011 (1990).
- [2] L.-H. Yu, Phys. Rev A 44, 5178 (1991); I. Ben-Zvi et al., Nucl. Instrum. Meth. A318, 208 (1992).
- [3] M. Babzien, I. Ben-Zvi, P. Catravas, J-M. Fang, T.C. Marshall, X.J. Wang, J.S. Wurtele, V. Yakimenko, and L.-H. Yu, Phys. Rev. E 57, 6039 (1998).
- [4] T.M. Tran and J.S. Wurtele, Computer Physics Communications 54, 263-272 (1989); S. Reiche and B. Faatz, in NIM Proceedings of the 20th International FEL Conference (FEL98), Williamsburg, VA, USA, 1998.
- [5] L.-H. Yu, Phy. Rev. E 58, 4991 (1998).
- [6] V. Sajaev, L.-H. Yu, A. Doyuran, R. Malone, X. Wang, V. Yakimenko, "Diagnostics and Correction of the Electron and Beam Trajectory in the Cornell Wiggler at the Accelerator Test Facility," these proceedings.
- [7] X.J. Wang, X. Qui, I. Ben-Zvi, Phys. Rev. E 54, 3121, (1996).

DESIGN PARAMETERS OF THE HIGH GAIN HARMONIC GENERATION EXPERIMENT USING CORNELL UNDULATOR AT THE ATF

L.H. Yu NSLS, Brookhaven National Laboratory, Upton, NY 11973, USA

Abstract

We present the design parameters of a high gain harmonic generation (HGHG) FEL experiment to be carried out at the accelerator test facility (ATF) at BNL, in collaboration with APS. This experiment is a proof-of-principle experiment for the DUV-FEL at BNL. In the HGHG experiment we plan to double the frequency of a CO, seed laser by utilizing a 0.76 m long 9 period undulator (named the "Mini Undulator"), a 2 m long 60 period undulator the "Cornell Undulator A"), and a 0.3 m electromagnet chicane (the dispersive section). The first undulator will be used in conjunction with the CO, seed laser to generate a ponderomotive force that will bunch the electron beam. The bunching will then be enhanced by the dispersion section. The second undulator, the Cornell Undulator A. tuned to the second harmonic of the seed laser will serve as the radiator. In the beginning of the radiator the bunched beam will produce coherent emission (characterized by a quadratic growth of the radiated power), then the radiation will be amplified exponentially. We plan to study the evolution of the various radiation growth mechanisms as well as the coherence of the doubled, exponentially amplified radiation.

1 INTRODUCTION

The seeded single pass FEL has many advantages over other FEL concepts. The output bandwidth is controlled by the input seed, limited only by the pulse length, and a bandwidth of 10⁴ is possible. Similarly, frequency stability is also controlled by the seed; hence the electron beam energy stability influences only the output intensity fluctuations, relaxing the requirement on energy stability. Another obvious advantage is that the mirror loss and damage problems of FEL oscillators are eliminated. In addition, there is no need for a long train of micro-pulses. The electron beam can consist of single micro-pulses. High repetition rate can be provided by utilizing a superconducting linac. Thus, a seed beam makes it possible to achieve very good energy stability and high average power.

There are powerful, conventional high repetition-rate tunable lasers operating in the IR and visible frequency bands which may be harmonic-multiplied into the VUV and used as seed lasers for the FEL amplifier. The interest

in harmonic generation in FELs stems from the limitations of conventional laser harmonic generation techniques, such as low conversion efficiency, susceptibility to damage and limited tunability.

The generation of harmonics by bunching an electron beam in a undulator, using a seed laser, is well known and verified experimentally [1]. The use of prebunching in FELs was studied analytically [2] and in a 3-D numerical simulation [3]. The extension of this technique to the exponential growth regime including undulator tapering has been proposed and studied in detail as the basis for the DUVFEL at BNL [4-6]. An order of magnitude improvement in the performance of this system can be obtained by further modifications of the technique [7]. However, the complete process of generating the harmonics by prebunching in the fundamental and amplification in a undulator tuned to the harmonic has not been demonstrated experimentally as yet. The generation of harmonics and subsequent exponential growth poses many interesting questions. It is our intention to pursue these questions experimentally in the experiment at the ATF.

In the proposed HGHG experiment, we will demonstrate the bunching of a 42 MeV electron beam by a CO_2 laser of nearly 0.7 MW input power. We will study the coherent growth of the second harmonic at a wavelength of 5.3 μ m, the exponential growth regime, and saturation regime. We would like to verify our theoretical models and to answer important questions such as the effect of electron beam parameters on the coherence of the FEL, the effect of undulator and alignment errors, and the higher harmonic contents of the FEL output near saturation.

We have selected the parameters of the harmonic generation experiment to match the electron beam parameters which have already been demonstrated experimentally at the ATF[8]. These include: a normalized rms emittance of 4π mm mrad at a peak current of 110 Ampere, and the energy of 42 MeV; a CO₂ oscillator with a pulse length of nearly 100 ns and a power of 0.7 MW; a solid-state optical chopper on the CO₂ laser system which is synchronized to the electron beam. This chopper is capable of slicing a 10-100 ps long pulses. If necessary, these pulses can be amplified by a wide-band CO₂ amplifier. In the first stage, we shall use the 0.7 Mw 100ns output of the oscillator output because its repetition

rate, and because the chopper will lower the intensity. The amplifier repetition rate is lower than the oscillator, so only in the second stage when we need to increase the HGHG output power by increasing the CO₂ power we will use the chopper and the amplifier.

2 PARAMETERS OF THE HARMONIC GENERATION EXPERIMENT

The design and theory of the harmonic generation FEL has been described extensively in ref. [5]. Therefore we will confine this presentation to a brief description of the parameters of the experiment and the expected performance of the system.

Table 1 provides all the relevant parameters of the experiment: seed laser, electron beam, undulator, and expected FEL amplifier performance. The Rayleigh range, as well as the strength of the dispersive section have been optimized using a procedure, described in ref. [5].

Table 1 System parameters

Table 1 System parameters	<u> </u>	
Electron beam parameters:		
Energy γ	82	
Current I	110A	
Micropulse length	4 ps	
Emittance (normalized rms)	4x10 ⁻⁶ π mrad	
rms beam size σ_x (matched beam)	240 μm	
Local energy spread σ/γ	0.043 %	
Seed laser parameters:		
Wavelength	10.6 μm	
Input power P	0.7 MW	
Pulse length (initially)	100 ns	
Improved (sliced) pulse length	10-100 ps	
Rayleigh Range	0.76 m	
Modulator undulator:		
Length	0.76 m	
Period	8 cm	
Peak magnetic field	0.158 T	
Dispersive section:		
Length	30 cm	
Magnetic field	0.5T	
Dispersion $(d\psi/d\gamma)$	1.5	
Radiator undulator (Cornell Undulator A):		
Period	3.3cm	
Length	2 m	
Exponential section magnetic field	0.47 T	
Betatron wavelength	3.75 m	
FEL parameters:		
Wavelength	5.3µm	
Bessel factor JJ.	0.857	
Power e-folding length	0.263 m	
Pierce parameter ρ	0.0089	
Output power	37 MW	
Output energy for a 4 ps FWHM pulse	~ 0.2 mJ	

Following the optimization of the FEL parameters, the complete simulation of the HGHG FEL has been done using a modified version of the computer code TDA [10].

A schematic diagram of the harmonic generation experiment is shown in fig. 1.

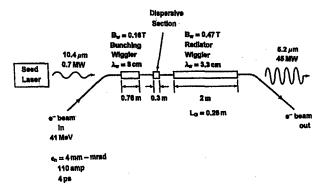
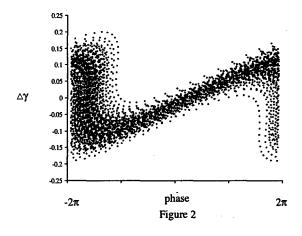


Figure 1: schematic diagram of the HGHG experiment

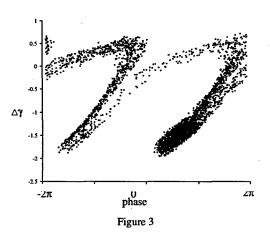
We will use a CO_2 seed laser at a wavelength of 10.6 μ m. The seed-laser pulse-length will be initially 100 ns at an input power of 0.7 MW. The electron-beam pulse-length at the ATF is assumed to be 4 ps FWHM.

Our system utilizes two undulator magnets separated by a dispersion section. The first undulator, the Mini-Undulator, is used to energy modulate the electron beam. The period of this undulator is 8 cm and the peak axial magnetic field is 0.158 T, making the 42 MeV electron beam resonant with the 10.6 μ m seed radiation. This is followed by the dispersion section with a magnetic field of 0.5 T, in which the energy modulation is converted into a spatial bunching with a strong second harmonic component at 5.3 μ m. At the end of the dispersion section, the energy phase distribution is given in figure 2, showing strong micro bunching.

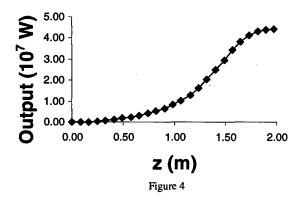


When the coherently bunched beam enters the 2 m long radiator undulator magnet (the Cornell Undulator A, resonant at $5.3 \mu m$), there is a rapid coherent generation of $5.3 \mu m$ radiation within the first two gain lengths, ie.,

about 0.5 meter. The radiation has a characteristic quadratic dependence on the distance traversed in the undulator. Then there is a transition to exponential growth which continues until about 1.8 m, where it reaches saturation, with output power of 37 Mw. At the end of the Cornell Undulator A, the energy phase distribution is plotted in figure 3, showing saturation, and the 5 μ m structure instead of the 10 μ m structure in the figure 2.



The three distinct FEL processes occurring in the second wiggier (the quadratic superradiant growth, the exponential growth, and saturation) are shown clearly when the radiation power is plotted against the undulator length in figure 4.



We have looked into the sensitivity of the FEL performance on electron beam parameters, such as the emittance and energy spread. Changing the emittance, from 4 to $6x10^6$ π mrad changes the power e-folding length of the second undulator from 0.26 to 0.29 m. Changing the current from 110 ampere to 90 ampere again increases the gain length to 0.29 m. Similarly, changing the FWHM energy spread from 0.1 to 0.2% changes the e-folding length from 0.26 m to 0.27 m.

To study the tolerance on the undulator errors, we simulated the system by seeding the calculation with different sets of random undulator peak to peak errors. For simplicity, we calculate for the case seeded with 5 micron CO₂ beam of peak power 10 kw. In figure 5, we plot the gain verses the rms displacement for each individual set of undulator errors. Each point in the plot represents one set of undulator error, and hence one particular trajectory. This plot shows that the output power is predominantly a function of the rms displacement. When the rms

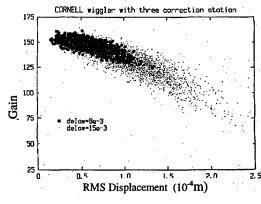


Figure 5

displacement is 100 micron, the gain drops from about 160 to about 120. Hence we choose 100 micron as our tolerance on trajectory displacement.

- [1] R. Prazeres, P. Guyot-Sionnest, J.M. Ortega, D. Jaroszynski, M. Billardon, M.E. Couprie, M. Velghe and Y. Petroff, Nucl. Instr. and Meth. A304 (1991) 72.
- [2] I. Boscolo and V. Stagno, Nucl. Instr. and Meth. 188 (1982) 483.
- [3] R. Bonifacio, L. de Salvo Souza, P. Pierini and E.T. Scharlemann, Nucl. Instr. and Meth. A296 (1990) 787.
- [4] I. Ben-Zvi, L.F. Di Mauro, S. Krinsky, M.G. White and L.H. Yu, Nucl. Instr. and Meth. A304 (1991) 181.
- [5] L.H. Yu, Phys. Rev. A44 (1991) 5178.
- [6] I. Ben-Zvi, L.F. Di Mauro, S. Krinsky, M.G. White, L.H. Yu, K. Batchelor, A. Friedman, A.S. Fisher, H. Halama, G. Ingold, E. D. Johnson, S. Kramer, J.T. Rogers, L. Solomon, J. Wachtel and X. Zhang, Nucl. Instr. and Meth. A318 (1992) 201.
- [7] I. Ben-Zvi, K.M. Yang and L.H. Yu, Nucl. Instr. and Meth. A318 (1992) 726.
- [8] I. Ben-Zvi, The BNL accelerator test facility and experimental program, Proc. 1991 Particle Accelerator Conf., San Francisco, CA.
- [9] L.H. Yu, S. Krinsky and R.L. Gluckstern, Phys. Rev. Lett. 64 (25) (1990) 3011.
- [10] T.M. Tran and J.S. Wurtele, LRP 354/88, Ecole Polytechnique Federale de Lausanne, Suisse (1988).
- [11] I. Ben-Zvi, R. Fernow, J. Gallardo, G. Ingold, W. Sampson and M. Woodle, Nucl. Instr. and Meth. A318 (1992) 781.
- [12] E.T. Scharlemann, J. Appl. Phys. 58 (1985) 2154.

MECHANICAL DESIGN OF THE VISA UNDULATOR

M. Libkind¹, L. Bertolini, P. Duffy, LLNL, Livermore, CA 94550 R. Carr, SLAC, Stanford, CA 94309 G. Rakowsky, J. Skaritka, BNL, Upton, NY 11973

Abstract

As part of the research and development effort for a 4th generation light source, we have designed a 4-meter long Free-Electron Laser (FEL) undulator. The undulator will be installed at the Accelerator Test Facility (ATF) at Brookhaven National Laboratory to conduct a Self-Amplified Spontaneous Emission (SASE) demonstration. The demonstration is called VISA, which stands for "Visible to Infrared SASE Amplifier." The undulator consists of 440 permanent dipole magnets per meter which are supported and aligned on a precision strongback. Focusing and defocusing permanent quadrupole magnets are also supported by the strongback. Each of the 4 one-meter sections of undulator are kinematically supported and housed within the vacuum vessel. The undulator and the vacuum vessel are supported independently to eliminate undulator misalignment during vacuum pump-down of the vessel. We describe the design requirements and features of the undulator, vacuum vessel and support system.

1 INTRODUCTION

SLAC, ANL, LANL, LLNL and UCLA are proposing to build a Free-Electron Laser (FEL) R&D facility operating in the self-amplified spontaneous emission (SASE) mode in the wavelength range 1.5-15 Å. This FEL, called "Linac Coherent Light Source" (LCLS) [1], utilizes the SLAC linac and produces sub-picosecond pulses of short wavelength x-rays with very high peak brightness and full transverse coherence. The Visible to Infrared SASE Amplifier to be installed at the Accelerator Test Facility (ATF) at BNL was designed to demonstrate SASE through saturation.

The critical component of the experiment is the 990-millimeter long undulator segment. VISA includes four of these segments, but the design, including vacuum vessel, was based on the need to extend the undulator to six meters for use at BNL in the Source Development Laboratory (SDL) upon the completion of the VISA experiment.

Significant challenges included a dipole gap tolerance of 10 microns with a profile of 25 microns per meter, absolute axial dipole positioning of 25 microns, vertical quadrupole positioning of 50 microns and a quadrupole gap tolerance of 50 microns.

2 UNDULATOR

Figure 1 shows the cross-section of the VISA undulator and Figure 2 shows the undulator with top strongback removed. The strongbacks and keepers were fabricated

using a combination of grinding and milling in order to obtain the required 25-micron profile.

Left and right keeper assemblies are precision mounted to the ground bottom strongback. The quadrupole holder assemblies (described below) are installed. The initial alignment of the holders is obtained using a temporary 1-meter long ground spacer bar. Threaded rods passing through the keepers hold the quadrupole holders in place and permit horizontal trajectory adjustment after assembly is complete.

The top 220 dipoles are then mounted using a precision installation mechanism and hold-down bars to obtain the required axial positioning.

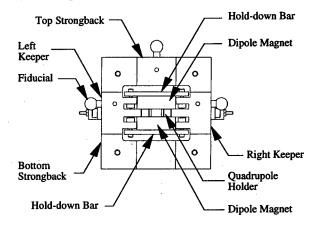


Figure 1. Cross-section of the VISA undulator

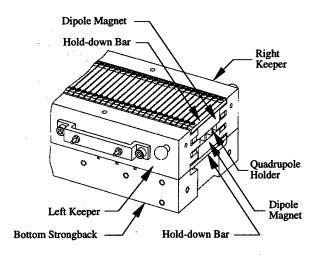


Figure 2. Undulator with top strongback removed

Next the top strongback is attached and the bottom strongback is removed. The remaining 220 dipole magnets are installed and the bottom strongback is re-attached.

¹ E-mail: libkind1@llnl.gov

After assembly a 1-mil nickel foil was installed to cover the dipole magnets in order to provide a better RF environment.

Built into the keepers are holes that permit insertion of diagnostic probes into the beam at the undulator segment quarter points.

Each left and right focusing or defocusing quadrupole section consists of three 30-millimeter long magnets that are mounted in a holder assembly (Figure 3). Physical constraints limit the thickness of the back of the holder and the thickness of the holder faceplate to 1.5 millimeters each. However, the clamping of the magnets between the holder and the faceplate creates a stiff laminated structure.

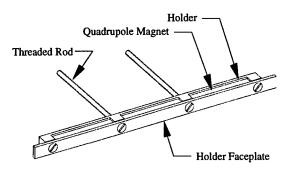


Figure 3. Quadrupole holder assembly

The straightness of the three quadrupole magnets in a section is obtained by assembling the holder against a precision ground plate with temporary shims to locate the magnets vertically. The height of the holder is controlled so that it is self-positioning between the top and bottom dipoles. The final design allows the maximum deviation of a quadrupole section from true vertical center to be 100 microns.

Fiducials are located at the ends of each undulator segment to facilitate alignment in ATF. The magnetic field is shimmed and the magnetic center of each undulator determined relative to the fiducials in the NSLS Magnetic Measurements Laboratory at BNL. To accomplish this, built into the each undulator is the ability to rotate it 90 degrees around the beam axis with negligible sag in the structure.

The ends of the undulator segments are designed to accept the attachment of termination magnets in a holder. These are used during magnetic shimming of each segment and on the upstream and downstream ends of the entire undulator during operation.

3 VACUUM VESSEL

The vacuum vessel for VISA must house the undulator, while remaining mechanically de-coupled from it, and support the diagnostic probes. It must also allow installation access and maintain vacuum integrity. Figure 4 is an isometric view of the vessel and support system.

The four-meter VISA vacuum vessel is constructed in two sections; one 1.5 meters and one 2.5 meters long. This permits installation in ATF and expansion of the vessel to six meters in SDL. The expansion is accomplished by installing a 2-meter vessel section between the 1.5 and 2.5-meter sections.

The cross-section of the vacuum vessel is limited to 203 x 203 millimeters by the dimensions of the external steering coils although access ports and diagnostics protrude beyond. Each coil has a removable top section that permits removal of the vessel covers. Ports on the top and one side of the vessel permit access to the fiducials on the undulator sections during alignment.

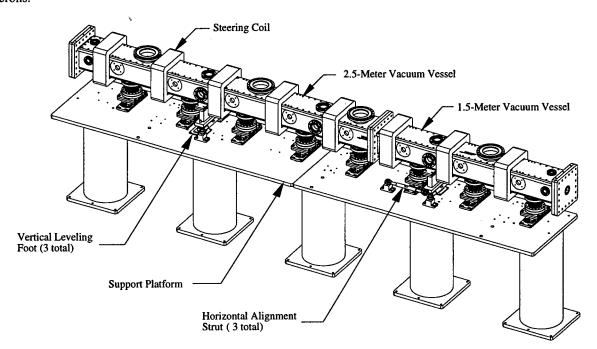


Figure 4. VISA vacuum vessel and support system

Finite element analysis was used to calculate the deformation of the vacuum vessel under gravity and vacuum loading. Vertical deformation of the vessel under these loads is within acceptable limits. Removable shoulder bolts through the vessel covers and top flanges restrain the vessel sidewalls from bending inward during pump-down. This is critical because the insertable diagnostic probes are attached to the vessel sidewalls. Shoulder bolts are used instead of specifying a required torque on the many cover bolts thereby reducing the vessel closing time.

Ports for the insertable diagnostic probes are located at the quarter points of the undulator segments. The probes are aligned to corresponding holes in the undulator keepers at atmospheric pressure. Oversize clearance holes in the mounting flanges provide the necessary vertical and horizontal adjustment range.

Fiducials are located at the ends of the vessel to facilitate alignment, which need only be on the order of one millimeter.

The vacuum vessel is supported on three leveling feet with reinforced Teflon pads. Two transverse and one axial struts control the horizontal positioning.

4 SUPPORT SYSTEM

The support platform consists of two aluminum plates and five cylindrical aluminum piers. The fundamental frequency of the support platform, vacuum vessel and undulators is 20 Hz. The plate also supports alignment hardware during installation.

Figure 5 shows the support system for the undulator segments. Each undulator is supported kinematically on three vertical adjuster screws at approximately the quarter points. A ball, free to rotate, forms the tip of each adjuster. The adjusters are connected to support pedestals that pass through the bottom of the vacuum vessel and

attach to slide mechanisms that permit the adjusters to be moved perpendicular to the beam axis. Vacuum integrity of the vessel is obtained using a welded bellows between the vessel and the blank flange located on each slide.

Axial positioning of one of the undulator segments is obtained by fixing one of its support balls in a cone; this forms the axial reference for the entire four meters. The remaining three undulator segments are fixed axially to the reference through a spring and adjuster mechanism. This design permits axial spacing of the undulator segments within less than the maximum thermal expansion.

5 SUMMARY

The design of the VISA undulator, vacuum vessel and support system has been described. The hardware is currently being assembled at BNL in the Accelerator Test Facility.

6 ACKNOWLEDGMENTS

The work of M. Libkind, L. Bertolini and P. Duffy was supported by the Office of Energy Research, Office of High Energy and Nuclear Physics Division, of the U.S. Department of Energy under contracts, DE-AC03-76SF00098 and W-7405-ENG-48-(LLNL). The work of R. Carr was supported by the U.S. Department of Energy, Office of Basic Energy Sciences under contract number DE-AC03-76SF00515. The work by G. Rakowsky and J. Skaritka was supported by U.S. Department of Energy under contract DE-AC02-98CH10886.

7 REFERENCES

[1] Linac Coherent Light Source (LCLS) Design Study Report, SLAC-R-521, UC-414, April 1998.

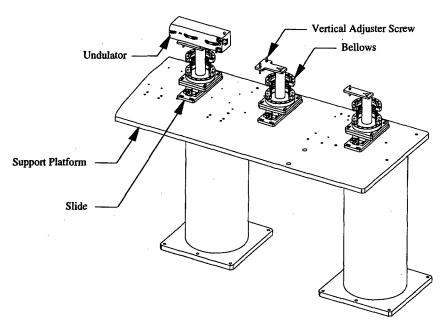


Figure 5. Support system for undulator segments

PHOTON BEAM DIAGNOSTICS FOR VISA FEL

A. Murokh*, C. Pellegrini, J. Rosenzweig, P. Frigola, P. Musumeci, A. Tremaine, UCLA M. Babzien, I. Ben-Zvi, A. Doyuran, E. Johnson, J. Skaritka, X. J. Wang, BNL K. A. Van Bibber, J. M. Hill, G. P. Le Sage, LLNL D. Nguyen, LANL M. Cornacchia, SLAC

Abstract

The VISA (Visible to Infrared SASE Amplifier) project is designed to be a SASE-FEL driven to saturation in the sub-micron wavelength region. Its goal is to test various aspects of the existing theory of Self-Amplified Spontaneous Emission, as well as numerical codes. Measurements include: angular and spectral distribution of the FEL light at the exit and inside of the undulator; electron beam micro-bunching using CTR; single-shot time resolved measurements of the pulse profile, using auto-correlation technique and FROG algorithm. The diagnostics are designed to provide maximum information on the physics of the SASE-FEL process, to ensure a close comparison of the experimental results with theory and simulations.

1 INTRODUCTION

The concept of self-amplified spontaneous emission [1] free electron lasers is of the great interest from both academic and practical point of view. The description of the process is a complicated relativistic theory on the merger of accelerator physics, radiation theory and plasma physics. The technological prospects are very promising, as it allows, among other things, the construction of the x-ray laser [2]. However, the experimental proof of SASE-FEL theory has taken place at much larger wavelengths (e.g. UCLA-LANL experiment in IR [3]). The objective for this device is to scale the experimental confirmation of theory and simulation into the visible and near IR region, as well as measure saturation and other different aspects of FEL performance.

The experiment will be held at the Accelerator Test Facility in Brookhaven National Laboratory [4]. It is a state of the art photoinjector accelerator, which can provide an electron beam of the desired quality (Table 1).

The undulator consists of four 1-meter long sections. It utilizes an array of focusing magnets, to provide a strong focusing in both planes, in order to minimize the bunch spot size. Optimization of the electron trajectories in the undulator is being done with the pulsed wire correction technique [5]. In addition, the external trim coils are built to minimize the trajectory walk-off during operation.

2 MEASUREMENTS

Achieving the maximum gain in the first harmonic, is a proof of principle experiment, to demonstrate the operation of SASE-FEL at shorter wavelengths.

Table 1: Relevant parameters for VISA FEL

Nominal Beam Energy	71MeV
Peak Current	200 Amp
Charge	1nC
Normalized Beam Emittance	2 π-mm-mrad
Undulator Parameter, K	1.26
Undulator Period	1.8 cm
Number of Periods, N _U	220
Electron Beam Beta-Function	30 cm
Radiation Wavelength, λ_r	800nm

The single particle spontaneous emission intensity within the coherent angle [6], for the VISA undulator is 1.5 photons per 100 electrons, which corresponds, in case of 200A beam, to the total radiated power of

$$P_{\rm SE} = .52 \frac{ek_r I_p}{\pi \varepsilon_0} \approx 4.7W \tag{1}$$

In order to saturate starting from noise, the FEL process has to proceed through at least 10 field gain lengths. The design parameters are chosen such that it is just enough to saturate over the length of 4 meters. For the 1nC beam the saturated power, according to simulations, is 60MW, which attributes to the total gain of G=1.3 10⁷.

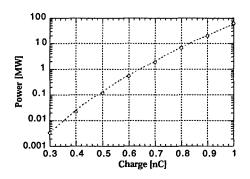


Figure 1: FEL radiation power dependence on charge

alex@stout.physics.ucla.edu

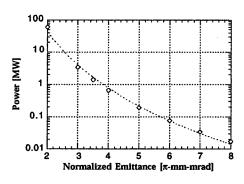


Figure 2: FEL power degradation due to the electron beam emittance increase

2.1 Power versus Charge

The measurement can be repeated for different charges, which should give a characteristic exponential curve on Fig. 1. However, the actual performance of the FEL will depend on the experimental conditions, such as quality of the beam, undulator performance, and proper matching and guiding of the beam through the undulator. Particularly important is the emittance of the beam. On Fig.2 there are simulations results for 1nC beam with the peak current of 200A, which demonstrate very requirements to meet the designed performance of the FEL. Increase in the average beam size by 20% would lower the radiation power by a factor of 4. To ensure proper control of the beam spot, the vacuum chamber is equipped with a YAG beam profile monitors every 50cm.

2.2 Spectral and Angular Fluence

After the exit of the undulator, the light will be transported into the measurements area, attenuated if necessary and then processed by the diagnostics. Relay imaging will be used to preserve profile and characteristics of a radiation pulse, during the transport.

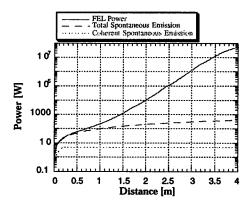


Figure 3: Simulations results for the radiation power along the length of the undulator

For the direct comparison of experimental results with the theory of SASE-FEL process, not only the radiation intensity, but also its spectral and angular distribution in the far field will be measured.

Expanding, and collimating the beam into the CCD array shall provide an accurate measurement of the total angular fluence; whereas the slit spectrometer will enable to obtain explicit results for $dl^2/dwd\Omega$.

2.3 Power Gain along the Undulator

VISA FEL design makes possible a set of rather novel measurements. First of all, it is a power gain along the undulator length. Fig. 3 shows the simulations of the power growth along the VISA undulator, performed with the GENESIS code. It indicates nearly linear behavior along at the beginning of the undulator (lethargy), where radiation is being dominated by the spontaneous emission (dashed line). The coherent fraction of SE (dotted line) starts the FEL process, and in a few gain lengths the exponential term prevails, providing for the overall high gain.

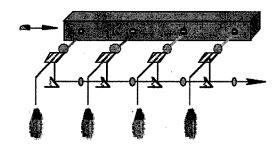


Figure 4: Optical diagnostics layout. Coated mirrors separate FEL radiation from the YAG light and send it into the relay imaging transport line.

In order to make that measurement possible, the undulator chamber was equipped with 8 diagnostics ports, 50cm apart. The probes are set up with both, YAG crystals for the electron beam diagnostics, and mirrors to get the FEL radiation out. Probe design utilizes periscope mirrors to compensate for mechanical hysteresis in the actuators. The optical transport system has been designed to provide for the optimal imaging of the FEL radiation into the diagnostics area. To satisfy the requirements of the experiment, the transport system should:

- provide for minimum losses, transporting the FEL radiation beam over 15-20 m;
- ensure the identical imaging properties for all ports;
- tolerate errors and imperfections in the optics.

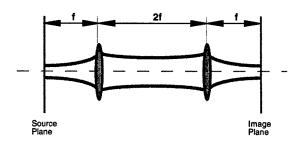


Figure 5: Single cell of the optical transport system

The design satisfying for these demands, is shown on Fig. 4. The light from the probe comes out through the vacuum window where it is being split by the mirror coated for 800nm. Most of the YAG light travels through the mirror into the camera, whereas FEL radiation gets into the transport line via the flipping mirror, which is automated to move in and out of the light path, so that it would not interfere with the light from a previous port.

In the transport line, the radiation light will go through the periodic lens array, converging to the identical image after each cell, shown on Fig. 5. It is straightforward, that this configuration translates the image into its identity, rotated 180°:

$$M = \begin{pmatrix} 1 & f \\ 0 & 1 \end{pmatrix} \begin{pmatrix} 1 & 2f \\ -\frac{1}{f} & -1 \end{pmatrix} \begin{pmatrix} 1 & f \\ -\frac{1}{f} & 0 \end{pmatrix} = \begin{pmatrix} -1 & 0 \\ 0 & -1 \end{pmatrix}$$
 (2)

Since the diagnostics ports are separated by 50 cm, we found the choice of 25-cm focal lengths to be the most adequate. One can see on Fig. 4, that with the proper positioning of lenses, the transport for each port will contain a series of 1 to 4 unit cells, before the common image plane. From there, the similar but more spread-out system will provide a long-range transport.

Such a transport system provides a unit magnification imaging from all the ports, with insignificant diffraction losses for the number of Hermit-Gaussian modes, including the fundamental. Another important advantage is, that it leaves no space for the systematic errors, so the

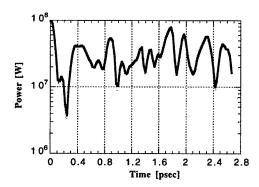


Figure 6: Spikes in the radiation temporal profile (Average period is 94µm)

tolerance is fairly high. The 5-cell array preserves all properties of the Gaussian beam within 95%, while the lens positioning accuracy is 0.5cm, focal length -0.5%, and angular mismatch at injection - 10mrad.

3 TIME DOMAIN DIAGNOSTICS

Spikes formation is another important property of SASE-FEL process. For VISA beam, the bunch length exceeds the cooperation length by two orders of magnitude, so the multiple spikes formation is anticipated [7] with the period of not bigger than 100µm. The time structure of the radiation pulse is shown on Fig. 6. Presence of spikes can be established indirectly, by measuring the radiation spectrum and power fluctuations [7] at the undulator exit, as it was done in previous experiment [3].

For the direct measurement of the radiation beam temporal profile the single shot autocorelator was developed at LLNL specifically for 800nm light. By utilizing a thinner crystal and narrowing the bandwidth it allows resolving a femtosecond structures in a pulse. With that tool the FEL radiation can be characterized completely, using the FROG algorithm.

4 CTR MICROBUNCHING MONITOR

Bunching of an electron beam (b_1) in the undulator can be measured directly by sending a bunched beam through a thin foil, and observing a backscattered coherent transition radiation [8]. The FEL radiation transport line and diagnostics can be used to propagate and characterize the CTR signal, respectively. Total intensity of the CTR at FEL wavelength is directly proportional to b_1^2 .

The results of a similar measurement in UCLA-LANL experiment [9] were in an excellent agreement with the FEL data. It was a little surprising, that the spectrum of the CTR signal was ~3% off, compare to the FEL radiation. One can speculate that the difference can be attributed to the sidebands in the SASE radiation, due to spikes. However, another experimental verification is necessary to fully understand the phenomenon.

- R. Bonifacio, C. Pellegrini, and L. Narducci, Opt. Commun. 50, 313 (1984)
- [2] "Linac Coherent Light Source (LCLS) Design Study Report", The LCLS Design Study Group, SLAC Report No. SLAC-R-521 (1998)
- [3] M. Hogan et al., "Measurements of Gain Larger than 10⁵ at 12 μm in a Self-Amplified Spontaneous-Emission Free-Electron Laser", Phys. Rev. Lett. 81, 4867 (1998)
- [4] D. Palmer et al., AIP Conference Proceedings 398, 695 (1997)
- [5] R.W. Warren, Nucl. Instrum. Methods Phys. Res., Sect. A, 272, 257 (1988)
- [6] J.B. Murphy, C. Pellegrini, "Introduction to the Physics of Free-Electron Laser", Laser Handbook, 6 (1990)
- [7] R. Bonifacio et al., Phys. Rev. Lett. 73, 70 (1994)
- [8] J.B. Rosenzweig, G. Travish, and A. Tremaine, Nucl. Instrum. Methods Phys. Res., Sect. A 365, 255 (1995)
- [9] A. Tremaine et al., Phys. Rev. Lett. 81, 5816 (1998)

The APS SASE FEL: STATUS AND COMMISSIONING RESULTS

S.V. Milton*, S.G. Biedron, P. Den Hartog, J.W. Lewellen, E. Moog, A. Nassiri, G. Travish Advanced Photon Source, Argonne National Laboratory, Argonne, Illinois 60439 USA

Abstract

A self-amplified spontaneous emission (SASE) freeelectron laser (FEL) is under construction at the Advanced Photon Source (APS). Three gun systems, an rf-test area, laser room, numerous diagnostics, a transfer line at the end of the linac, and a new building, which will serve as the experimental hall, have been added. The only remaining items to be installed are the undulators into the beamline. Here, the additions to the APS in support of this project as well as commissioning results and future plans will be discussed.

1 INTRODUCTION

The Advanced Photon Source (APS) at Argonne National Laboratory (ANL) has constructed an experiment designed to test, at a modest scale, the idea of a linac-driven free-electron laser (FEL) based on the single-pass self-amplified spontaneous emission (SASE) process [1]. The project resembles the current conception of a future fourth-generation synchrotron light source user facility [2]. Such a user facility would provide a light source with unprecedented brilliance and time-resolution capabilities far exceeding those currently available at third-generation light sources (including the APS.)

This paper will describe the APS SASE FEL. In particular, a brief overview of the project and its history will be given along with the project goals. The most recent commissioning results will then be discussed along with a brief summary of the immediate timeline.

2 PROJECT DESCRIPTION

The APS SASE FEL project will perform an end-to-end test of the SASE FEL process similar to that envisioned for a fourth-generation synchrotron light source facility. The initial goal will be to obtain saturation at visible wavelengths. The process will be thoroughly studied before raising the electron beam energy to push the FEL wavelength into UV. This process will be continued until the maximum energy of the APS linac is reached. Table 1 lists the experimental parameters for the three planned phases of the experiment.

*Work supported by U.S. Department of Energy, Office of Basic Energy Sciences, under Contract No. W-31-109-ENG-38.

Table 1: APS SASE FEL parameters with photocathode rf gun drive

Parameter	Phase I	Phase II	Phase III
Energy (MeV)	217	457	700
λ _R (nm)	530	120	51
L _{gain} (m)	0.4	0.72	1.2
L _{sat} (m)	8.7	15	24
P _{peak} (MW)	260	270	200
$B_{\text{peak}}^{\dagger} (\times 10^{28})$	5	20	37

†photons/sec/mm²/mrad²/0.1% bandwidth

3 COMPONENT DESCRIPTION

3.1 RF Gun Systems

There are three electron gun systems in the APS linac: two thermionic rf guns with alpha-magnet bunch compression and a photocathode rf gun.

Figure 1 shows the current configuration of the linac in the area of the two thermionic rf gun systems, either of which can serve as the primary injector for standard APS operation. Only the second, downstream thermionic rf gun is suitable as an FEL driver. The simulated expected performance of this downstream high-performance thermionic rf gun at the entry of the first accelerating structure is 150-A peak current, $5~\pi$ mm-mrad rms normalized emittance, and 10% energy spread (with energy filter installed) at 2.5 MeV.

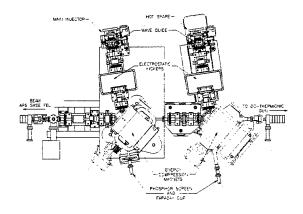


Figure 1: The two thermionic rf guns in the APS linac

In addition to the thermionic rf guns, an on-loan copy of the BNL/ATF-Gun-IV photocathode rf gun was installed

^{*}Email: milton@aps.anl.gov

at the head of the APS linac during the March 1999 maintenance period (Figure 2.) The photocathode rf gun system can produce a beam at 5 MeV with 300-A peak current, 3 π mm-mrad rms emittance, and 0.1% energy [3]. It will be used as the primary electron source for the APS SASE FEL.

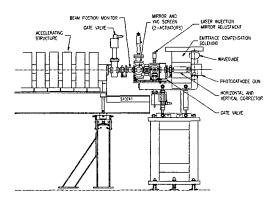


Figure 2: The photocathode rf gun in the APS linac

3.2 Laser System

The photocathode rf gun drive-laser system resides in a radiation shielded room immediately adjacent to the upstream end of the linac vault. The 119-MHz, Nd:Glass laser oscillator produces 260 fs FWHM pulses timing stabilized to better than 1 ps rms. A single pulse at 5 Hz is sent to the Nd:Glass regenerative amplifier. The amplified IR pulse is then up-converted to the UV. The maximum energy of the UV pulse is 400 μ J. Some bandwidth is lost in the amplification process, and so the minimum UV bunch length is ~1.5 ps FHWM.

3.3 Linac

The APS linac is composed of fourteen 3-m, 2856-MHz, SLAC-type, constant-gradient accelerating structures powered by six 35 MW klystrons, three of which are SLEDed. One klystron is used to power both a single accelerating structure and one of the two thermionic rf guns. Here, two high-power rf switches are used to select between either gun or an rf load. The sixth klystron is used is to drive the PC rf gun. The linac is capable of producing electron beam energies of up to 650 MeV.

In addition to the acceleration and requisite transverse focusing quadrupoles, the linac is equipped with many beam diagnostics. These include current monitors; beamposition monitors; Chromox, YAG, and optical transition radiation (OTR) screens; two spectrometer systems; bunch length measurement capability through a higher harmonic rf cavity or by use of a streak camera/OTR screen system; as well as all rf power and phase measurement diagnostics.

3.4 Transfer Lines

Originally, the beam from the linac was sent directly to the positron accumulator ring (PAR). For the FEL experiment, however, the beam follows a different path through a new beamline system. This additional beamline is directly in line with the linac and so avoids unnecessary bends, which could lead to emittance dilution. It is fully instrumented with appropriate diagnostics.

3.5 Undulator System

The undulators chosen for this FEL project are based on the standard undulator used in the APS. Table 2 lists the main undulator parameters.

Table 2: APS SASE FEL undulator parameters

Parameter	Value
Undulator Period [cm]	3.3
K	3.1
Peak On-Axis Field [T]	1.006
Undulator Length [m]	2.4
Cell Length [m]	2.7265
Peak Quadrupole Gradient [T/m]	16
Quadrupole Effective Length [mm]	56

A simple planar undulator system is used. For simplicity, the natural focusing of the undulator in the non-wiggle plane is used. Additional focusing in the orthogonal plane will be performed using quadrupoles placed in gaps between undulator sections. The required undulator system is made up of a series of undulator cells each 2.7265 m in length, of which 2.4 m is undulator. The remaining space is reserved for the combined function quadrupole/corrector magnets, diagnostics, and drift space.

The diagnostics in each undulator cell include a YAG fluorescent screen, wire position monitors, a mirror to pick off the generated light, and a very high resolution beam position monitor capable of single-pass submicron measurements [4].

3.6 Undulator Hall and End Station Building

The hall housing the FEL undulator system is 3.5 m in width and nearly 50 m in length. It is a separate radiation zone, and therefore access is permitted during standard APS operation. It is a concrete enclosure with earth berm used as integral shielding. The building was designed to house two beamlines both fed from the linac. This will allow testing of a beam-switchyard, multiplexed system as envisioned for fourth-generation light source facilities.

Attached to the end of the undulator hall is an endstation building. It is outside the radiation environment and may be occupied when beam is being delivered to the undulator hall. There are staggered penetrations for extraction of the undulator light. Additional optics in a transition area are used to send the light to the optical diagnostics benches in the end-station building. Also, this end-station building houses most of the technical services that power and control the equipment within the undulator hall.

4 COMMISSIONING RESULTS

4.1 Thermionic RF Gun

The high-performance thermionic rf gun is routinely used for APS operation, and so most tuning to date has been toward that goal [5,6]. Commissioning of diagnostics and diagnostic tools is still underway [7].

4.2 Laser System

The laser system is fully operational and all optical transfer lines into the radiation enclosures have been installed and aligned; however, fine-tuning of performance is ongoing. The laser system was used to generate photoelectrons from the photoelectron rf gun while the gun was located in the rf test area.

4.3 Photocathode RF Gun

Very preliminary testing of the PC rf gun was performed while it was located in the rf test area. This testing consisted of full rf conditioning and photoelectron production. It was then relocated to the head of the linac and is waiting dedicated commissioning time [8].

4.4 Beamlines and Diagnostics

Using the thermionic rf gun, the transfer line was commissioned to the beam dump at the end of the undulator hall in February 1999. Figure 3 shows a beam image on the YAG screen at this end dump. Calibration and testing of the diagnostics system are now underway [9]. When beamline commissioning is complete, the first two undulators will be moved in place and first SASE FEL experiments will begin.

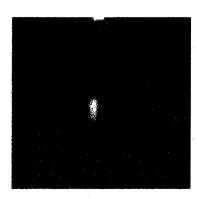


Figure 3: First beam at the end of the beamline.

5 IMMEDIATE TIMELINE

In April of 1999, the first two undulators will be installed. The photocathode rf gun will be ready to send beam to the undulator hall at this time.

A minimum of three undulator cells will be installed in the summer of 1999. Provided beam quality is sufficient, full saturation should be possible in the visible (Table 1). More undulators will be arriving at a rate of about one per month. Following success in the visible, the beam energy will be raised and additional undulators added. Full saturation in the UV will then be attempted. This process will be continued until the full energy of the APS linac is reached.

6 SUMMARY

The APS FEL system represents a prototypical fourthgeneration synchrotron light source and will be used to explore the many issues required to build a new synchrotron light source user facility in the future. Many components of the APS FEL are installed and commissioned. The first two undulators will be installed in April 1999 and FEL gain should be observed shortly afterwards. Additional undulators will be installed in the summer of 1999 and full saturation in the visible should be achieved.

ACKNOWLEDGMENTS

Many thanks to our friends at the Brookhaven National Laboratory Accelerator Test Facility, the Stanford Linear Accelerator Laboratory, the Argonne Wakefield Accelerator, Science Applications International Corporation, Femtochrome Research, and MAX-Lab in Lund, Sweden for their gracious support and assistance.

- S.V. Milton, et al., "The FEL Development at the Advanced Photon Source," Proceedings of Free Electron Laser Challenges II, SPIE San Jose, January 1999.
- [2] 10th ICFA Beam Dynamics Panel, Workshop on 4th Generation Light Sources, ESRF, Grenoble, January 1996.
- [3] M. Babzien, I. Ben-Zvi, P. Carravas, J.-M. Fang, T.C. Marshall, X.J. Wang, J.S. Wurtele, V. Yakimenko, and L.-H. Yu, Phys. Rev. E 57, 6039, 1998; F. Sakai, X.J. Wang et al., "Development of High Duty Factor Operation RF Photoinjector," BNL-65003, Proceedings of the 11th Symposium on Accelerator Science and Technology, Spring-8, Hyogo, Japan, October 21-23, pp. 473-475 (1997).
- [4] E. Gluskin et al., "The Magnetic and Diagnostic Systems for the Advanced Photon Source Self-Amplified Spontaneously Emitting FEL," Proc. of the 18th Int. Free-Electron Laser Conf., Williamsburg, Aug. 1998, to be published.
- [5] J. Lewellen, "Operation of the APS RF Gun," 1998 Linear Accelerator Conference, Chicago, Aug. 1998, to be published.
- [6] J. Lewellen, "A Hot Spare Injector for the APS Linac," these proceedings.
- [7] A. Lumpkin et al., "High Brightness Beam Diagnostics for the APS Linac," these proceedings.
- [8] S.G. Biedron et al., "The Operation of the BNL/ATF Gun-IV Photocathode RF Gun at the Advanced Photon Source," these proceedings.
- [9] A. Gorski and R. Lill, "Construction and Measurement Techniques for the APS LEUTL Project RF Beam Position Monitors," these proceedings.

THE APS SASE FEL: MODELING AND CODE COMPARISON

S.G. Biedron*, Y.-C. Chae, R.J. Dejus, B. Faatz*, H.P. Freund*, S. Milton, H.-D. Nuhn**, S. Reiche*
Advanced Photon Source, Argonne National Laboratory, Argonne, Illinois 60439 USA

*Deutsches Elektronen Synchrotron, Notkestrasse 85, 22603 Hamburg Germany

**Stanford Linear Accelerator Center, Stanford, California 94309 USA

Abstract

A self-amplified spontaneous emission (SASE) freeelectron laser (FEL) is under construction at the Advanced Photon Source (APS). Five FEL simulation codes were used in the design phase: GENESIS, GINGER, MEDUSA, RON, and TDA3D. Initial comparisons between each of these independent formulations show good agreement for the parameters of the APS SASE FEL.

1 INTRODUCTION

The Advanced Photon Source (APS) at Argonne National Laboratory (ANL) is currently commissioning a free-electron laser (FEL) based on the self-amplified spontaneous emission (SASE) process [1]. The design parameters were based on capabilities of the existing APS linear accelerator, the linear theory [2], and simulations. The codes used in the design include GENESIS [3], GINGER [4], MEDUSA [5], RON [6], and TDA3D [7,8]. Comparative simulations were performed using a specific set of input parameters for the APS SASE FEL.

2 CODE DESCRIPTIONS

2.1 GENESIS

GENESIS has its origin in TDA3D, a steady-state simulation code, which has been extended to perform multi-frequency simulations. The radiation field is discretized on a Cartesian grid and solved by the alternating direction implicit (ADI) integration scheme. The transverse motion of the electron beam, described by macroparticles, is calculated analytically, whereas the energy and phase are found by Runge-Kutta integration. In addition to the standard internal generation, an external seeding radiation field, undulator field, and longitudinal variation of the electron beam parameters can be supplied in input files.

2.2 GINGER

GINGER is a 3D multi-frequency particle tracking code with a 2D, axisymmetric representation of the radiation

field. The equations of motion are averaged over an undulator period. For non-waveguide simulations, GINGER uses a nonlinear, expanding radial grid, proportional to the square of the radius near the axis, and expands exponentially for large distances from the axis. The outer grid boundary, the number of radial grid zones, as well as the region over which the grid is linear are controlled by input parameters. GINGER is able to simulate a single segment of undulator as well as lumped, quadrupole focusing.

2.3 MEDUSA

MEDUSA is a 3D multi-frequency, simulation code where the electromagnetic field is represented as a superposition of Gauss-Hermite modes and where a source-dependent expansion is used to determine the evolution of the optical mode radius. The field equations are integrated simultaneously with the 3D Lorentz force equations. As such, MEDUSA differs from the other nonlinear simulation codes in that no undulator-period average is imposed on the electron dynamics. It is capable of treating quadrupole and corrector fields, magnet errors, and multiple segment undulators.

2.4 RON

RON is a linear, single-frequency code intended for design optimization of high-gain, short wavelength FELs, with features for multiple-segment undulators, field errors, and distributed focusing elements. The electron motion is along pre-calculated, period-averaged trajectories and the radiation field and the bunched beam current density are calculated at these trajectories from a set of linear integral equations. Explicit calculation of the radiation field (on an arbitrary grid) and the capability to use a measured magnetic field profile as input has been added recently. Although the linearity does not provide the saturated state, it does allow for fast run times.

2.5 TDA3D

TDA3D has been publicly available for over a decade. The latest official release is still a paraxial, single-frequency code. Extensions include non-axisymmetric radiation modes, wiggler errors, a strong quadrupole FODO lattice with arbitrary misalignments, as well as multi-segment undulators. In "expert" mode, arbitrary quadrupole focusing can be simulated.

^{&#}x27;Work supported by U.S. Department of Energy, Office of Basic Energy Sciences, under Contract No. W-31-109-ENG-38 and DE-AC03-76SF00515.

^{*}Email: biedron@aps.anl.gov

^{*}Permanent Address: Science Applications International Corporation

3 APS SASE FEL DESCRIPTION

The APS SASE FEL uses either a thermionic rf or photocathode rf gun, the 650-MeV 2856-MHz APS linac, two new transfer lines, and a new undulator hall and diagnostic end station. The project will evolve over three phases, to reach saturation in the visible, UV, and VUV wavelength regimes, respectively.

The design is based on known gun performance, constraints imposed by the APS linac, and the characteristics of currently available undulators. Tuning of the undulators has been optimized to meet the performance tolerances of the FEL.

For the simulation, a set of parameters for the first phase was used and a Gaussian electron beam distribution was assumed (Table 1). Test runs were made to determine the minimum number of particles needed in each code to achieve convergence. The optimum wavelength, corresponding to the minimum gain length, was then obtained for each code by scanning in wavelength about the resonant condition (516.75 nm). The optimal wavelengths for the five codes are given in Table 2; however, the fitted gain length is dependent on the fit region. This impacts the exact determination of the minimum and subsequently the peak power at saturation.

Table 1: Simulation and undulator cell parameters

Parameter	Value	
γ	430.529	
Normalized emittance	5 π mm mrad	
Peak current	150 A	
Undulator period	3.3 cm	
Undulator strength (K)	3.1	
Energy spread	0.1%	
Input start-up power	1.0 W	
Undulator Length	2.4 m	
Focusing/diagnostics Gap	36 cm	
Quadrupole strength	20 m ⁻²	
Quadrupole length	5 cm	

Table 2: Optimum wavelengths

	•
Code	Optimum λ (nm)
GENESIS	517.78
GINGER	516.80
MEDUSA	518.82
RON	518.8
TDA3D	517.78

4 RESULTS

In the first comparison, a single-segment parabolic pole face undulator was used. The actual design uses multiple 2.763-m undulator "cells," each of which is composed of a 2.4-m magnetic segment and a 0.363-m section for diagnostics, a combined quadrupole/corrector magnet, and drift space. The second comparison simulates this actual

case (less corrector fields) with flat pole face undulators and quadrupoles (Table 1). Note that GINGER was omitted from this second comparison because it does not easily treat the segmented undulator case. The output power versus distance along the undulator for the single segment case is shown in Figure 1. The curves for GINGER and MEDUSA are almost identical and differ primarily in that GINGER predicts a somewhat lower saturated power. The calculated radiated power for RON is scaled from the bunched beam current density that is valid for the behavior in the exponential growth regime only where the radiated power is self-similar to the beam current. Thus, only the gain length in RON should be compared with the other codes. The gain length is almost identical in GINGER, MEDUSA and RON. TDA3D and GENESIS yield nearly identical results, but the gain lengths are slightly longer than found by the other codes.

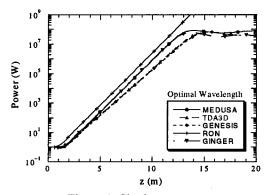


Figure 1: Single segment case

The output power versus distance for the multi-segment case is shown in Figure 2. Here, the shortest gain length is predicted by RON, the longest by MEDUSA, and GENESIS and TDA3D predict gain lengths in between these other results.

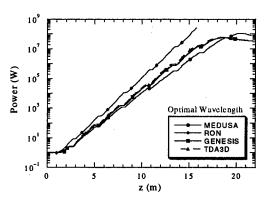


Figure 2: Multiple segment case

Table 3 summarizes the saturation point and power for the single- and multiple-segment cases as determined by the four nonlinear codes at the listed optimal wavelengths.

Table 3: Saturation point and power

Code	z(m)	Case 1 (MW)	Case 2 (MW)
GENESIS	15.5	69.4	58.0
GINGER	13.7	61.7	N/A
MEDUSA	14.0	87.4	109.4
TDA3D	15.4	68.9	61.3

Comparisons of the gain length predicted by the codes and by the linear theory for the single segment case were also performed. The energy spread was varied between 0.0-0.2%, the peak current between 50-300 A, and the normalized emittance between 1-10 π mm-mrad. Figures 3, 4, and 5 show the gain length versus these variations, respectively. It is evident from the figures that the codes are essentially in reasonable agreement over the entire range of parameters studied. In general, it appears that GENESIS and TDA3D predict slightly longer gain lengths than the linear theory, while GINGER, MEDUSA, and RON predict slightly shorter gain lengths. Note that the linear theory is used for comparison purposes only, and should not be assumed as "perfect" but considered as an additional model. While the maximum discrepancies are of the order of 20% at some of the extremes of these parameter ranges, the maximum discrepancies are typically less than 15% for the parameters of interest in the APS SASE FEL.

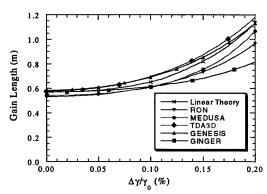


Figure 3: Gain length versus energy spread

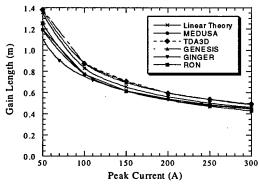


Figure 4: Gain length versus peak current

5 CONCLUSIONS

In summary, GENESIS, GINGER, MEDUSA, RON, and TDA3D all show reasonable agreement with each other and with the linear theory for the first-phase APS SASE FEL parameters, giving greater confidence to the required length of undulator needed to reach full saturation.

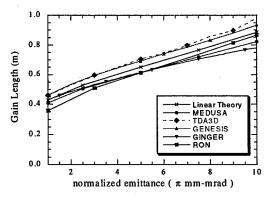


Figure 5: Gain length versus normalized emittance

- S.V. Milton et al., "The FEL Development at the Advanced Photon Source," Proceedings of Free Electron Laser Challenges II, SPIE, January 1999, to be published; S.V. Milton, et al., "The APS SASE FEL: Initial Commissioning Results," these proceedings.
- [2] L.-H. Yu et al., Phys. Rev. Lett. 64, 3011 (1990); M. Xie, in Proceedings of the IEEE 1995 Particle Accelerator Conference, p. 183, 1995.
- [3] S. Reiche, "GENESIS 1.3 A Fully 3D Time Dependent FEL Simulation Code," in NIM Proceedings of the 20th International FEL Conference (FEL98), Williamsburg, VA, USA, 1998.
- [4] W.M. Fawley, "An Informal Manual for GINGER and its postprocessor XPLOTGIN," LBID-2141, CBP Tech Note-104, UC-414, 1995.
- [5] H.P. Freund and T.M. Antonsen, Jr., Principles of Free-electron Lasers (Chapman & Hall, London, 1986), 2nd edition; H.P. Freund, Phys. Rev. E, 52, 5401 (1995).
- [6] R.J. Dejus et al., "An Integral Equation Based Computer Code for High Gain Free-Electron Lasers," in NIM Proceedings of the 20th International FEL Conference (FEL98), Williamsburg, VA, USA, 1998; R.J. Dejus et al., "Calculations of the Self-Amplified Spontaneous Emission Performance of a Free-Electron Laser," these proceedings.
- [7] T.M. Tran and J.S. Wurtele, "TDA A Three-Dimensional Axisymmetric Code for Free-Electron Laser (FEL) Simulation," in Computer Physics Communications 54, 263-272 (1989); S. Reiche and B. Faatz, "Upgrade of the Simulation Code TDA3D," in NIM Proceedings of the 20th International FEL Conference (FEL98), Williamsburg, VA, USA, 1998.
- [8] H.-D.Nuhn, "Overview of SASE Free-Electron Laser Simulation Codes," Proceedings of Free Electron Laser Challenges II, SPIE, January 1999, to be published.

MAGNETIC MEASUREMENTS AND TUNING OF UNDULATORS FOR THE APS FEL PROJECT

<u>I.B. Vasserman</u>, R.J. Dejus, P.K. Den Hartog, M. Erdmann, E. Gluskin, E. R. Moog, and E. M. Trakhtenberg, Advanced Photon Source, Argonne National Laboratory, Argonne IL 60439

Abstract

Two insertion device magnetic structures have been prepared for the Advanced Photon Source (APS) FEL project [1]. The magnetic structures are standard APS undulators, 2.4 m long with a 3.3-cm period. Measurements and tuning of the undulators have been completed at a magnetic gap of about 9.3 mm, where K is 3.1. Special measurement and tuning techniques were used to satisfy the tight trajectory straightness requirement that the second field integral be less than 3.3 kG-cm². The magnetic field strengths of the undulators must be well matched; this leads to the requirement that the magnetic gap must be controlled to better than 10 Proper phasing between the undulators is microns. ensured by adjusting the length of the drift space between the undulators. The drift space length that is needed is strongly affected by the end fields of the magnetic structures. The results of measurements of the magnetic field and calculations of the drift length are provided.

1. HORIZONTAL FIELD MEASUREMENTS

The tight requirements for vertical trajectory straightness of FEL insertion devices means that not only field integrals, but the magnetic field map as well, must be measured to high precision. The measurements of the horizontal field in the presence of a strong vertical field (up to 1 T) is difficult due to the planar Hall probe effect [2], but precise alignment of the probe can eliminate this effect for one particular pair of poles. The task becomes even more complicated for an undulator with a large number of poles that are not aligned with perfect accuracy. Due to specific tolerances of each particular magnetic structure, it is by no means clear that it is possible to align the probe to measure the horizontal field precisely enough along the entire device. To prepare for the FEL project at the APS a test was performed to check the reliability of horizontal field measurements [3]. types of probes were tested. These were a customdesigned two-axis Sentron analog Hall transducer [4] and a two-axis Bell probe. A stretched-wire rotating coil and an 81-mm-long moving coil were used to make the reference measurements. Insertion device Undulator A #3 was used for these measurements with a gap of 11 mm and a peak field of about 0.85 T. As the result of this test, a Sentron probe was chosen for horizontal field measurements. The main advantage of this probe is its small sensitivity to angular orientation. This feature makes it possible to obtain the proper field map of a device with many periods and imperfect alignment of the poles in the longitudinal

direction, Z. It is possible to use a moving coil to obtain the field map averaged over the length of the coil.

Although this approach is not sufficiently accurate to obtain the harmonic spectrum, it is good enough for the trajectory straightness determination. The disadvantage of the moving coil is a zero drift in the integrator that leads to the need for a large data set and extensive data reduction to obtain reliable results. Consequently, it is better to use the moving coil for reference measurements and to apply the Hall probe for tuning purposes. The tests show that the Sentron probe provides reliable results after proper alignment. The measurement results are shown in Fig. 1 for one of the devices used in the FEL beam line. It is worth noting that a very precise alignment in the vertical Y direction is required for this specific Hall probe and for the undulator itself.

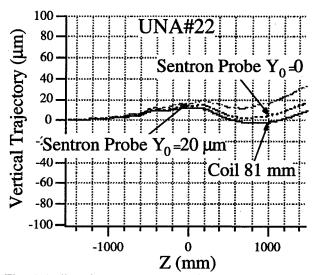
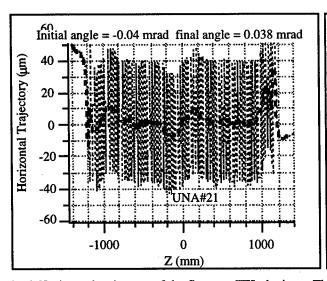


Fig. 1 Hall probe measurements with different Y offsets. A moving coil reference measurement is included for comparison. The particle energy is assumed to be 220 MeV.

2. RESULTS OF TUNING

The permanent support system for the FEL devices is an H-style fixed-gap structure, which allows only minor gap variations of 9.3 ± 0.2 mm. To facilitate shimming, the initial tuning for the FEL project was performed using a C-frame variable gap mechanism that allowed full side access for magnetic measurements. After performing the



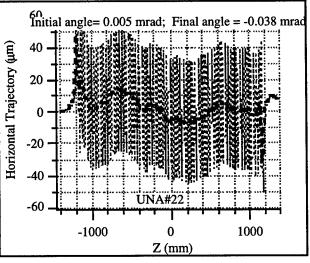


Fig. 2 Horizontal trajectory of the first two FEL devices. The dark line is the wiggle-averaged trajectory.

tuning on the C-frame and moving the devices to the fixed-gap support, changes in the field integrals and the sag profile were measured because of differences between the magnetic structure supporting points. Consequently, it was found necessary to perform a full set of measurements on the fixed-gap support in order to set the proper value of the wiggler strength parameter K, to tune the trajectories and to find the break length necessary for proper phasing of the devices. To accomplish this, a feature was designed to allow access to the gap of device for the magnetic sensors all along the device length, and a set of measurements was performed with the Hall probe and moving coils using this feature. Measurements of the gap at several locations along the device were performed with an accuracy better than 5 µm to provide a reference so the gap profile could be reproduced after moving the device to its location on the beam line. The break length required for proper phasing was calculated from measured data using the upgraded MA code [5]. The device was divided into 3 parts: a central part, and upstream and Polynomial fitting downstream terminations. performed to smooth the changes associated with local distortion of phases. The break length is strongly affected by the specific sag configuration of the device and varies by a few millimeters from device to device (see Table 1).

TABLE 1

	UNA #21	UNA #22
DS end (cm)	19.68	20.44
US end (cm)	20.02	20.12

It is possible to change the required break length to some extent by phase shimming. The results of final tuning are shown in Figs. 2 and 3 for horizontal and vertical trajectories, respectively. The requirement of 3.3 kG-cm² corresponds to 45 μm of trajectory displacement for a particle energy of 220 MeV. The maximum distortions for the first two devices are smaller than $\pm 15\,\mu m$.

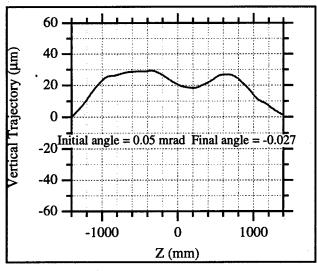
3. DISCUSSION

We would like to discuss some specific requirements associated with this project. Planar devices at small energy provide quite strong natural focusing in the vertical direction due to edge focusing from the magnets with parallel edges. The focusing of a device is given by [6]:

$$\frac{1}{f_v} = \frac{K^2}{2\gamma^2} k_p^2 L_w$$

where the relativistic γ is the ratio between the particle's total energy and its rest energy, $k_p = 2\pi/\lambda_W$, f_y is the focusing length of the device, L_W is the total length of the device, and λ_W is the period length of the wiggler or undulator.

This focusing makes the vertical alignment of the device critical: in our case the device must be aligned with an accuracy of 50 µm. It also means that measurement of the magnetic center of the device is necessary in order to find the difference between the magnetic and the geometric center, if any. Such measurements were performed using the well-known fact that the vertical magnetic field has its minimum at the median plane of the pair of poles that is the source of the magnetic field in hybrid structure devices. Scanning of the field in the vertical direction using the Hall probe allows one to obtain the location of the magnetic center with a precision better than $\pm 10 \, \mu m$. The set of measurements performed on the FEL devices showed that the magnetic and geometric centers coincide more closely than the position accuracy required [1]. While there are local distortions associated with shimming at a particular pole or with the strength of the adjacent permanent magnets (see Fig.4), the averaged behavior of the magnetic center follows the geometric center quite well. This means that for our particular case the geometry of the device can be used as the reference for alignment.



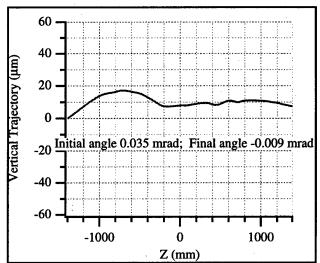


Fig. 3 Vertical trajectory of the first two FEL devices

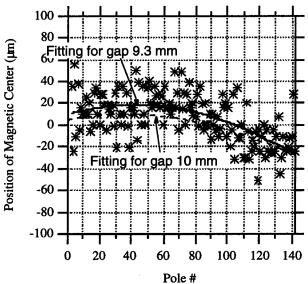


Fig. 4. Position of magnetic centers for UNA#21. The solid line shows the fit to the data; the corresponding fit for a gap of 10.0 mm is shown for reference. The overall 40 μm slope is due to the geometrical misalignment of the sensor and device.

4. ACKNOWLEDGEMENTS

This work is supported by the U.S. D.O.E., BES-Material Sciences, Under Contract # W-31-109-Eng-38.

We would like to thank Dr. J. Pflüger for his help in upgrading software for Hall probe and moving coil measurements.

5. REFERENCES

[1] E. Gluskin, et al., "The Magnetic and Diagnostic Systems for the Advanced Photon Source Self-Amplified Spontaneously Emitted FEL", to be published in the proceedings of the 20th International FEL98 Conference (Williamsburg, VA, Aug. 16-21,1998).

[2] M. W. Poole and R. P. Walker, IEEE Trans. Magn. MAG-17, 2129 (1981).

[3] I. Vasserman, "Test of Horizontal Field Measurements Using Two-Axis Hall Probes at the APS Magnetic Measurement Facility", Argonne National Lab. Report No. ANL/APS/TB-32 (Jan. 1998).

[4] B. Berkes, R.S. Popovic, R. Racz, and J. Hrejsa, "New type of a 3-axis Hall probe", presented at the 9th International Magnet Measurement Workshop IMMW-9 (June 19-22, 1995, CEA/Saclay, France)

[5] R. Dejus et al, Rev. Sci. Instrum. 66 (2), 1995, p. 1875.

[6] H. Wiedemann, <u>Particle Accelerator Physics II</u>, (Springer-Verlag, Berlin Heidelberg 1995).

CALCULATIONS OF THE SELF-AMPLIFIED SPONTANEOUS EMISSION PERFORMANCE OF A FREE-ELECTRON LASER*

R.J. Dejus#

Advanced Photon Source, Argonne National Laboratory, 9700 S. Cass, Argonne, IL 60439, USA O.A. Shevchenko and N.A. Vinokurov

Budker Institute of Nuclear Physics, 11 Ac. Lavrentyev Prosp., 630090, Novosibirsk, Russia

Abstract

The linear integral equation based computer code (RON: "Roger Oleg Nikolai"), which was recently developed at Argonne National Laboratory, was used to calculate the self-amplified spontaneous emission (SASE) performance of the free-electron laser (FEL) being built at Argonne. Signal growth calculations under different conditions are used for estimating tolerances of actual design parameters. The radiation characteristics are discussed, and calculations using an ideal undulator magnetic field and a real measured magnetic field will be compared and discussed.

1 INTRODUCTION

The code RON was derived from a system of linear integral equations for the particle distribution function in a high-gain FEL [1, 2] and was developed to aid in the actual design of the SASE FEL at Argonne. Specifically it can take into account nonideal magnetic systems such as segmented undulators with distributed focusing and real measured magnetic fields. A series of comparisons with other codes was conducted recently, and the results are presented elsewhere [3].

The system of linear equations describes the evolution of the Fourier harmonics of the electron beam current densities (a set of "thin" beams simulates the emittance of the real beam) versus the longitudinal coordinate z, which in the exponential growth regime scale self-similar to the radiated power. To simulate the SASE mode, i.e., the growth of initially uncorrelated density fluctuations, the initial currents for all but one beam were set to zero (similar to the calculation of the Green's function for density fluctuations). It corresponds to the situation when one particle (delta function of the electric current) is added to the beam with a timeindependent (constant) current; then the charge density perturbation in the beam caused by the radiation of the particle is calculated. The code also allows for the input of an external electromagnetic wave (the seed signal) in the form of a Gaussian beam.

2 CALCULATIONS

Initially we used RON to calculate signal growth of the beam current density under different conditions and to determine tolerances for the beam and the undulator segments. More recently we have added explicit calculation of the radiation field (on an arbitrary grid) and the capability to study the effect of real magnetic field errors on the performance. Further, since the code is fast, it has been feasible to run the code in an optimization algorithm to determine the optimal break length between undulator segments. In the following, we present some of our recent results.

2.1 Beam and mechanical tolerances

The code was initially used to investigate a variety of different mechanical designs including finding tolerances of important parameters for the design. First we showed that a high-gain FEL could be built without any significant loss in performance by using a distributed focusing approach with separated quadrupoles in break sections (between planar undulator sections) instead of a combined focusing undulator design. Second, alignment and beam tolerances were determined for the current FEL design with distributed focusing. We found that the undulators need to be aligned to better than 50 µm vertically, but both longitudinally and horizontally the tolerances are much more relaxed (1.0 mm). A summary of the results including beam tolerances is given in [4, 5]. We also made initial investigations of the sensitivity to magnetic field errors and found that a $\Delta K/K \sim 0.01/3.1 \sim$ 0.3% variation between undulator segments was well within an acceptable range. This value was later confirmed using a measured magnetic field as input - also see section 2.4 below.

2.2 Optimal break length between undulator segments

The calculation of the optimal length of the breaks between undulators has to take into account the real magnetic field at the ends of undulators. It has been possible to run the code in an optimization loop to

^{*}Work supported in part by the U.S. Department of Energy, BES, under contract No. W-31-109-ENG-38.

^{*} Email: dejus@aps.anl.gov

optimize the break length between undulator segments because of its speed (less than one min on a Pentium II 333 MHz PC per function evaluation). Optimization was carried out by varying two parameters: the detuning parameter (radiation frequency) and the break length. The value of the current density after five undulator sections was chosen as the figure of merit and the optimization was done using the Newton method. A typical optimization run took about one hour.

2.3 Radiation field

In the actual design, equipment is installed in each break section for beam and radiation diagnostics. It is extremely valuable to be able to calculate the radiation that can be measured experimentally, and we have therefore extended the code to calculate the radiation field on an arbitrary grid outside any undulator segment. We calculate the electrical field in the paraxial approximation that is given by the following expression

$$E(\vec{r}) = \frac{ik}{c} \int_{0}^{z} \sum_{n} \frac{j_{x}^{n} e^{ik(z-z')} e^{ik\frac{(x-x_{n})^{2} + (y-y_{n})^{2}}{z-z'}}}{z-z'} dz',$$

where c is the speed of light, $k = \omega/c$ is the wave number, j_x^n is the x-component of n-th beam current, and \vec{r} is the screen coordinate. The radiation pattern shown in Fig. 1 was obtained near the fundamental wavelength at 518 nm at 8.0 m from the end of the first undulator segment (when only one undulator segment is installed) using a beam energy of 220 MeV.

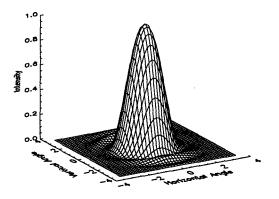


Figure 1: Angular distribution of the radiation field (square of the amplitude of the electric field). The angles are given in units of the inherent radiation opening angle $\sqrt{\lambda/2L}$, where λ is the wavelength and L is the length of one undulator segment.

2.4 Results using a measured magnetic field

Magnetic measurements of the undulators consist of large arrays of field values with typically up to one hundred points per undulator period. The period-averaged code RON needs a transformation of these arrays to smaller arrays with a fewer number of points, which to first order have the same influence on the particle motion. At each integration step in RON, the values of the undulator deflection parameter K and the vertical and the horizontal kick angles are read. (The integration step is typically one or several periods long.) A utility code was written that finds the arrays of undulator deflection parameters (K values) and horizontal kicks from a measured vertical magnetic field. (For the Argonne FEL, there is no horizontal focusing by the undulators.) The array of kicks was calculated to provide the same horizontal displacement at the end of each step as the averaged real field (see polygonal approximation in Fig. 2). The array of K values was derived from the slope of the phase versus distance. An "effective" magnetic length of the undulator was also determined by adjusting the length of the first and the last integration step.

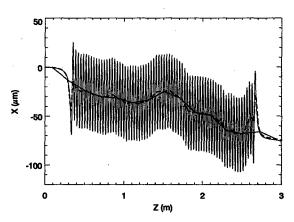


Figure 2: Approximation of the real electron trajectory with a polygonal curve. Real trajectory (thin solid curve), averaged trajectory (dashed curve), and polygonal approximation (thick solid curve) for one undulator segment calculated at 220 MeV.

The typical change in the K value from one step to another was about 0.3% as found from the utility code. For simulation purposes, we replicated the input values for five undulator segments because we had measured data for only one undulator. The calculated bunching of the beam current density is shown in Fig. 3.

Our results indicate that the magnetic field errors of real undulators for the Argonne FEL have little influence on the FEL performance. This is indeed a very important result, and it indicates that the undulators fabricated for this project are of high quality and in many cases may be treated as ideal. The measurement and tuning of the undulators are described elsewhere [6].

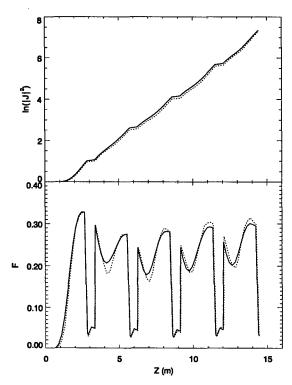


Figure 3: The calculated natural logarithm of the beam current density (top) and the dimensionless scaling factor (bottom) for the FEL using a replicated measured magnetic field from one undulator (dotted curve) versus an ideal field (solid curve).

3 SUMMARY

We have provided a few examples of the flexibility of the code RON, which has been valuable in the actual design of the undulator and break sections of the Argonne FEL. Further developments of the code include a more accurate simulation of undulator displacements and improvements to the initial transverse beam distribution functions (for simulation of the emittance), which is especially important for simulation of shorter wavelength FELs. The option to take into account horizontal field errors is also in progress.

- [1] R.J. Dejus, O.A. Shevchenko, and N.A. Vinokurov, "An integral equation based computer code for high-gain free-electron lasers", in NIM Proceedings of the 20 th International FEL Conference (FEL98), Williamsburg, VA, USA, 1998.
- [2] N.A. Vinokurov, "The Integral Equation for a High Gain FEL", Argonne National Laboratory Report, ANL/APS/TB-27, 1996.
- [3] S.G. Biedron, Y.C. Chae, R.J. Dejus, B. Faatz, H.P. Freund, S.V. Milton, H.-D. Nuhn, and S. Reiche, "The APS SASE FEL: Modeling and Code Comparison", this conference.
- [4] Argonne National Laboratory Report, "Experimental Facilities Division Progress Report 1997-1998", ANL/APS/TB-34, 1998, pp. 143-153.
- [5] R.J. Dejus and I.B. Vasserman, "Short Note on Undulator Alignments and Beam Tolerances for the APS FEL at 220 MeV", Argonne National Laboratory Internal Report, APS/IN/LEUTL/98-1, 1998.
- [6] I.B. Vasserman, R.J. Dejus, P.K. Den Hartog, M. Erdmann, E. Gluskin, E.R. Moog, and E.M. Trakhtenberg, "Magnetic Measurements and Tuning of Undulators for the APS FEL Project", this conference.

COHERENT SPONTANEOUS EMISSION IN HIGH GAIN FREE-ELECTRON LASERS*

Zhirong Huang and Kwang-Je Kim, APS/ANL, Argonne, IL 60439

Abstract

We investigate finite pulse effects in self-amplified spontaneous emission (SASE), especially the role of coherent spontaneous emission (CSE) in the start and the evolution of the free-electron laser (FEL) process. When the FEL interaction is negligible, we solve the one-dimensional Maxwell equation exactly and clarify the meaning of the slowly varying envelope approximation (SVEA). In the exponential gain regime, we solve the coupled Vlasov-Maxwell equations and extend the linear theory to a bunched beam with energy spread. A time-dependent, non-linear simulation algorithm is employed to study the CSE effect for a general beam distribution.

1 INTRODUCTION

Coherent spontaneous emission (CSE) has attracted much attention as the electron bunches become shorter and more intense in current experiments demonstrating the principle of self-amplified spontaneous emission (SASE). The onedimensional (1D) theory of SASE [1, 2] is based on the solution of the linearized Vlasov-Maxwell equations, for the cases of a coasting beam with energy spread [1] and a bunched monochromatic beam [2]. Attempts have been made to include the energy spread for a bunched beam, but only coherent bunching at the resonant wavelength was considered [3]. In Ref. [4], the evolution of the electric field is studied with the individual particle formulation for a bunched monochromatic beam, and the contribution of the incoherent and the coherent SASE are identified. In this paper, we extend the linear theory to a bunched beam with energy spread and calculate the effect of CSE for the high gain FEL. We also present a time-dependent, nonlinear simulation algorithm that takes CSE into account for an arbitrary beam distribution.

2 COHERENT SPONTANEOUS EMISSION

The 1D Maxwell equation for the transverse electric field of a plane wave propagating along the undulator axis z is

$$\left(\frac{\partial^2}{\partial z^2} - \frac{1}{c^2} \frac{\partial^2}{\partial t^2}\right) \vec{E}_{\perp}(z, t) = \mu_0 \frac{\partial}{\partial t} \vec{J}_{\perp}(z, t), \quad (1)$$

where μ_0 is the permeability of free space, and the charge density term is absent here due to transverse uniformity. Writing the transverse current as $\vec{J}_{\perp}(z,t) = \vec{e}J(z,t) + \text{c.c.}$,

with $\vec{e} = \hat{x}$ (a unit vector in the x direction) for a planar undulator and $\vec{e} = \hat{x} \pm i\hat{y}$ for a helical undulator, we have

$$J = -\frac{ec}{2\sigma} \frac{K}{\gamma_0} e^{-ik_u z} \sum_{j=1}^N \delta(z - z_j(t)) \Theta(t - t_j), \quad (2)$$

where σ is the beam cross section, K is the undulator strength parameter for the helical undulator and K[JJ] for the planar undulator after averaging over the undulator period k_u . We have also assumed that the j^{th} electron enters the undulator at $t=t_j(j=1,...,N)$ and z=0. Thus, the longitudinal position of the electron is $z_j(t)=\beta c(t-t_j)$, where βc is the average longitudinal velocity. $\Theta(t)$ is the step function, i.e., $\Theta(t)=1$ for t>0 and 0 otherwise.

In the absence of FEL interaction, the electric field in the form $\vec{E}_{\perp} = \vec{e}E(z,t) + \text{c.c}$ is found to be

$$E = \kappa_1 \sum_{j=1}^{N} \left\{ \frac{e^{ik_f[z - c(t - t_j)]}}{(1 - \beta)} \left[\beta c(t - t_j) < z < c(t - t_j) \right] + \frac{e^{-ik_b[z + c(t - t_j)]}}{(1 + \beta)} \left[(-c(t - t_j) < z < \beta c(t - t_j)) \right] \right\},$$
(3)

where $\kappa_1 = ecZ_0K/(4\sigma\gamma_0)$, $Z_0 = c\mu_0 \approx 377\Omega$, and the forward and the backward wavenumbers are

$$k_f = \frac{k_u \beta}{1 - \beta}, \quad k_b = \frac{k_u \beta}{1 + \beta}.$$
 (4)

Equation (3) describes a sum of N forward and backward wave packets, with the forward wave packets having much higher amplitude and shorter duration due to relativity.

For coherent spontaneous emission, we can define a relative position $\xi = z - \beta ct$ along the bunch and turn the sum into an integral by using the smooth approximation

$$\sum_{i=1}^{N} \rightarrow n_0 \int d(\xi') \chi(\xi'), \tag{5}$$

where n_0 is the maximum line density and $\chi(\xi)$ is the initial bunch density function $(0 \le \chi(\xi) \le 1)$. For a single-step pulse, $\chi(\xi) = \Theta(-\xi)$, the electric field in front of the pulse $(0 < \xi < (1 - \beta)z)$ is

$$E_c = \frac{\kappa_1 n_0}{i k_u} \left[1 - e^{i k_f (z - ct)} \right]. \tag{6}$$

Only the forward wave component is present as expected. The constant term terminates the field at the slippage distance $\xi_s = (1 - \beta)z$. The electric field inside the pulse is given by

$$E_c = \frac{\kappa_1 n_0}{i k_u} \left[1 - e^{-i k_b (z + ct)} \right]. \tag{7}$$

^{*}Work supported by U.S. Department of Energy, Office of Basic Energy Sciences, under Contract No. W-31-109-ENG-38

Thus, the coherent radiation comes from the sharp edge at $\xi=0$ for such a single-step pulse or from any density gradient for a general bunch distribution. A flat-top bunch can be constructed from two single-step pulses separated by the bunch length l_b , and the relative intensity of the incoherent versus the coherent spontaneous emissions can be obtained from Eqs. (3) and (6):

$$\frac{I_{incoh}}{I_{coh}} \sim \frac{Nk_f^2}{n_0^2} = \frac{(k_f l_b)^2}{N} = \frac{1}{N} \left(\frac{2\pi l_b}{\lambda_r}\right)^2,$$
 (8)

where $\lambda_r = (1-\beta)\lambda_u/\beta$ is the forward resonant wavelength. Equation (8) was derived in Ref. [5] by considering the initial coherent bunching factor. For $N \sim 10^{10}$ and $l_b \sim 2$ mm, $\lambda_r < 120$ nm makes the incoherent power larger, while $\lambda_r > 120$ nm favors the coherent power. Thus, the CSE effect should be negligible for the proposed x-ray FEL projects, but may play a significant role in current experiments in the IR and visible region. We note that the flat-top model requires the electron density to vanish within λ_r and tends to exaggerate the coherent effect.

3 LINEAR ANALYSIS

For FEL interaction, the backward wave is dropped and the slowly varying envelope approximation (SVEA) is invoked in the form

$$E(z,t) = \mathcal{E}(z,t)e^{ik_f(z-ct)},$$

$$J(z,t) = \mathcal{J}(z,t)e^{ik_f(z-ct)},$$
(9)

where \mathcal{E} and \mathcal{J} are assumed to vary slowly with z and t. The Maxwell equation becomes

$$\left(\frac{\partial}{\partial z} + \frac{1}{c}\frac{\partial}{\partial t}\right)\mathcal{E} = -\frac{Z_0}{2}\mathcal{J}.\tag{10}$$

It is convenient to define the electron coordinate as

$$\theta = k_f(z - ct) + k_u z = \frac{k_u}{(1 - \beta)}(z - \beta ct) \approx k_f \xi \quad (11)$$

and change the independent variables from (z, t) to (z, θ) . From Eq. (2), the transverse current is

$$\mathcal{J} = -\frac{ec}{2\sigma} \frac{K}{\gamma_0} k_f \sum_{i=1}^{N} \delta(\theta - \theta_i) e^{-i\theta}, \qquad (12)$$

where $\theta_j = -k_f c t_j$. Inserting this into Eq. (10), we reproduce the forward wave component of Eq. (3).

The phase space distribution of the electron beam is given by the Klimontovich distribution [1]

$$F(\theta, \eta, z) = \frac{k_f}{n_0} \sum_{i=1}^{N} \delta(\theta - \theta_j(z)) \delta(\eta - \eta_j(z)), \quad (13)$$

where $\eta = (\gamma - \gamma_0)/\gamma_0$ is the conjugate variable to θ . Equation (10) can now be written as

$$\left(\frac{\partial}{\partial z} + k_u \frac{\partial}{\partial \theta}\right) \mathcal{E} = \kappa_1 n_0 e^{-i\theta} \int d\eta F(\theta, \eta, z). \quad (14)$$

The Vlasov equation for the electron distribution is [1, 2]

$$\frac{\partial F}{\partial z} + 2k_u \eta \frac{\partial F}{\partial \theta} - \kappa_2 \mathcal{E} e^{i\theta} \frac{\partial F}{\partial \eta} = 0, \tag{15}$$

where $\kappa_2 = eK/(2\gamma_0^2 mc^2)$ is a constant.

In the exponential gain regime and without external field, we can regard the electric field in Eq. (15) as a small, first-order quantity. This includes the coherent and the incoherent spontaneous emissions as well as the stimulated emission. Hence the distribution function F consists of two terms: the zeroth-order term is the initial smooth distribution given by

$$F_0(\theta, \eta, z) = \chi(\theta - 2k_u \eta z)V(\eta), \tag{16}$$

where $V(\eta)$ is the initial energy spread of the beam normalized to $\int d\eta V(\eta) = 1$, and the first-order term ΔF contains both the initial fluctuation ΔF_0 and the bunching behavior through FEL interaction. Approximating F with F_0 in the third term of Eq. (15) yields

$$\Delta F = \Delta F_0 + \kappa_2 \int_0^z ds \mathcal{E}(\theta_0, s) e^{i\theta_0} \frac{\partial}{\partial \eta} F_0(\theta_0, \eta, s), \tag{17}$$

where $\theta_0 = \theta - 2k_u\eta z + 2k_u\eta s$. Since the FEL gain becomes negligible when the width of $V(\eta)$ is much larger than the FEL parameter ρ [1], where

$$\rho = \left(\frac{e^2 c Z_0 K^2 n_0}{32 \gamma_0^3 m c^2 k_u^2 \sigma}\right)^{1/3},\tag{18}$$

we have $2k_u\eta z \sim 2k_u\rho z \sim 2\pi$ in the exponential gain regime. We can therefore make the approximation $\theta_0 \approx \theta$ in the slowly varying \mathcal{E} and F_0 but keep the fast oscillatory phase $e^{i\theta_0}$. Inserting Eqs. (16) and (17) into Eq. (14) and applying the Laplace transformation, we obtain

$$\mathcal{E} = \frac{\kappa_1 k_f}{k_u} \sum_{j}^{\theta_j < \theta} e^{-i\theta_j} \int \frac{d\lambda}{2\pi i} e^{2i\lambda [k_u z - (\theta - \theta_j)]} \int d\eta \frac{V(\eta)}{\lambda - \eta} \times \exp\left(-2i\rho^3 \int d\eta \frac{dV/d\eta}{\lambda - \eta} \int_{\theta_j}^{\theta} \chi(\theta') d\theta'\right). \tag{19}$$

The λ -integration is along a straight path parallel to the real axis and below all singularities of the integrand. It is nonzero only when $\theta - \theta_j < k_u z$ or $\xi - \xi_j < \xi_s$ (the slippage length). Hence the total electric field at θ is the sum of fields that originated from the discrete radiators prior to θ but within the slippage length. The electron gain medium is treated as a continuous fluid à la Vlasov and is justified in Ref. [4]. For a monochromatic beam with $V(\eta) = \delta(\eta)$, Eq. (19) reproduces the result of Ref. [2]. Coherent SASE can be evaluated by turning the sum into an integral following Eq. (5) and calculating the contribution of the essential singularity at $\lambda = 0$ numerically [4].

Following Ref. [4], one can re-express Eq. (19) as:

$$\mathcal{E}(z,\theta) = \frac{\kappa_1 k_f}{2k_u} \sum_{j}^{\theta_j < \theta} e^{-i\theta_j} \int_{-\infty + i\epsilon}^{\infty + i\epsilon} \frac{d\nu}{2\pi i} e^{-i\nu(\theta - \theta_j)} \times \int \frac{d\lambda}{2\pi i} \frac{e^{2i\lambda k_u z}}{D(\lambda, \nu, \theta, \theta_j)} \int d\eta \frac{V(\eta)}{\lambda - \eta}, \quad (20)$$

where ϵ is an infinitesimal and positive number,

$$D(\lambda, \nu, \theta, \theta_j) = \lambda - \frac{\nu}{2} + \rho^3 w(\theta, \theta_j) \int d\eta \frac{dV/d\eta}{\lambda - \eta}, \quad (21)$$

and

$$w(\theta, \theta_j) = \frac{1}{(\theta - \theta_j)} \int_{\theta_j}^{\theta} \chi(\theta') d\theta' \le 1.$$
 (22)

For the coasting beam, $w(\theta,\theta')=1$ and $D(\lambda,\nu)=0$ is the dispersion relation including the energy spread [1]. Equation (21) provides a generalization to the bunched beam. When the bunch distribution does not change appreciably over the slippage length, $w(\theta,\theta_j)\approx \chi(\theta)$ from Eq. (22), and the FEL gain is affected only by the local electron current as expected.

4 SIMULATION ALGORITHM

In order to handle a general beam distribution and to study the nonlinear regime, we have developed a simulation code that is based on the individual particle formulation of FEL equations:

$$\frac{\partial \theta_j}{\partial \bar{z}} = \bar{\eta}_j,\tag{23}$$

$$\frac{\partial \bar{\eta}_j}{\partial \bar{z}} = -ae^{i\theta} + \text{c.c.}, \tag{24}$$

$$\left[\frac{\partial}{\partial \bar{z}} + \frac{1}{2\rho} \frac{\partial}{\partial \theta}\right] a = \chi(\theta) \left[e^{-i\theta} + \langle e^{-i\theta_j} \rangle\right], \qquad (25)$$

where $\bar{z}=2k_u\rho z$, $\bar{\eta}=\eta/\rho$, and $a=2\rho_\theta k_u \mathcal{E}/(\kappa_1 n_o)$ is the scaled electric field. Equation (25) follows directly from Eq. (14), where the contribution of the smooth (coherent) distribution and the fluctuating (incoherent) part are explicitly separated into two terms. The partial derivative with respect to θ in Eq. (25) describes the slippage between the electron and the radiation field.

A time-dependent simulation algorithm [6] can be constructed to take into account the slippage effect: one first divides the bunch into $N_b = l_b/\lambda_r$ buckets and loads each bucket with simulation particles that are uniform in θ and have the proper energy spread. Apply Eqs. (23), (24) and (25) without the slippage term in each bucket, and then slip the computed field one bucket forward after each undulator period. To start up the FEL process, one either gives a small initial bunching b_0 [6] or uses the shot noise simulation algorithm of Ref. [7]. However, such a discretization is not adequate for CSE simulation because the bunch distribution function $\chi(\theta)$ is only sampled with a sampling

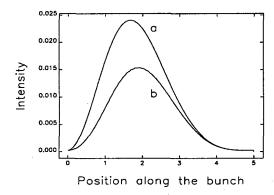


Figure 1: Coherent SASE intensity $|a_c|^2$ versus $2\rho\theta$ ($\rho = 1/(40\pi)$, $\bar{z} = 5$): (a) without initial energy spread, (b) with a flat-top energy spread of width ρ .

interval λ_r . Thus, the Fourier transform of $\chi(\theta)$ is defined only between the Nyquist critical frequency $f_c = c/(2\lambda_r)$ or $\omega_c = ck_f/2$, and the coherent bunching around the resonant frequency ck_f is left out.

We modify this time-dependent approach to include the CSE effect by decreasing the sampling interval to cover the resonant part of the bunch spectrum. For example, we can divide the bunch into $8N_b$ sections so that the critical frequency is $4ck_f$. The spectral power outside this frequency range should be sufficiently small to eliminate the effect of aliasing. The electric field is computed and averaged over the resonant wavelength, in consistent with the slowly varying envelope approximation. Compared with the multi-frequency approach to CSE simulation [8], the time-dependent approach is more straightforward and can include the shot noise in a natural way. Figure 1 shows an example of simulation where we have intentionally turned the noise off. The bunch is assumed to be longer than the slippage length. CSE from the trailing part of the bunch within the slippage length (i.e., $0 < 2\rho\theta < \bar{z}$) has been amplified and is shown in Fig. 1(a) for a case without initial energy spread and in Fig. 1(b) for the case with a flattop energy spread of width ρ . Figure 1(a) agrees very well with the calculation of Eq. (19). Such a simulation technique is also capable of studying the nonlinear behavior of the incoherent and the coherent SASE.

- [1] K.-J. Kim, Nucl. Instr. Meth. A 250, 396 (1986).
- [2] J.-M. Wang and L.-H. Yu, Nucl. Instr. Meth. A 250, 484 (1986).
- [3] K. -J. Kim and S. J. Hahn, Nucl. Instr. Meth. A 358, 93 (1995).
- [4] S. Krinsky, Phys. Rev. E 59, 1171 (1999).
- [5] R. Bonifacio, Opt. Comm. 138, 99 (1997).
- [6] R. Bonifacio et al., Phys. Rev. A 40, 4467 (1989).
- [7] C. Penman and B. W. J. McNeil, Opt. Comm. 90, 82 (1992).
- [8] N. Piovella, AIP Conference Proceedings 413, 205 (1997).

LOW SIGNAL FEL GAIN: MEASUREMENT, SIMULATION AND ANALYSIS*

R. Schoenlein[†], H. Chong, T.E. Glover, P. Heimann, A. Zholents, M. Zolotorev LBNL, Berkeley, CA 94720

Abstract

We describe an experimental set-up and measurement technique for measurement of the FEL gain at the Advanced Light Source. Measurement results are compared with computer simulations and analitical expression that includes effects of the laser beam difraction and finite electron beam size.

1 INTRODUCTION

This work is a part of a broader research effort to develop a source of femtosecond x-ray pulses based on an electron storage ring [1]. The technique that we are currently using at the ALS is based on energy modulation of the electrons as they traverse the wiggler with a co-propagating femtosecond laser pulse [2]. The optimal interaction of the electrons with the electric field in the laser pulse occurs when spontaneous electron radiation in the wiggler overlaps with the field of laser radiation in the transverse phase space, and when frequencies and spectral bandwidths of the electron emission and laser radiation are matched. The same conditions are required for achieving the maximum gain in the laser intensity, except the laser frequency is shifted to the point where the derivative of the spectral function of the electron spontaneous emission in the wiggler has a maximum (Madey's theorem [3]). Therefore, we determine the amplitude of the laser/e-beam energy modulation by measuring the gain in the laser intensity and use this as a diagnostic tool for a fine tuning of the experimental conditions.

2 MEASUREMENTS

Measurements of the gain of the laser pulse intensity for a laser pulse co-propagating with an electron bunch in the wiggler magnet have been performed at the Advanced Light Source. We use the electron beam at 1.5 GeV with horizontal and vertical beam emittances of $4x10^{-7}$ cm and $1x10^{-8}$ cm respectively and energy spread of $8x10^{-4}$. The wiggler magnet has a period λ_w =16 cm, 19 periods and its gap is adjusted to allow first harmonic electron emission at \sim 800 nm (wiggler deflection parameter $a_w \simeq 13$). A schematic of the experimental set up is shown in Figure 1.

The laser system consists of a Ti:Sapphire laser oscillator, stretcher, amplifier, and compressor. It produces ~ 0.5 mJ, ~ 70 fs laser pulses at 1 kHz repetition rate. The laser oscillator is synchronized to the storage ring RF mas-

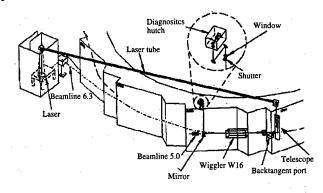


Figure 1: The layout of the experiment.

ter oscillator. The amplified Ti:Sapphire laser pulses enter the main vacuum chamber through a back-tangent window in the vacuum chamber of the wiggler insertion and co-propagate with the electron beam through wiggler. A mirror following the wiggler reflects the laser light and the electron wiggler emission out of the vacuum chamber for diagnostic purposes. Images of the near field and far field wiggler radiation are observed on a CCD camera, and the near and far field modes of the laser propagating through the wiggler are matched to the wiggler radiation using a remotely adjustable telescope at the back tangent port. A band-pass interference filter with ~40 nm bandwidth at 800 nm is inserted in front of the CCD in order to discriminate the higher-order harmonics. Spectra are measured using

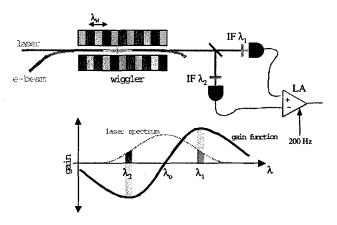


Figure 2: A schematic of the gain measurement (IF - interference filter, LA - lock-in amplifier).

a spectrometer. Temporal overlap between the laser pulse and a single electron bunch is accomplished by monitoring both pulses using a high-speed (~100 ps FWHM) photodi-

^{*} Work supported by DoE under contract No DE-AC03-76SF00098.

[†] Email: RWSchoenlein@lbl.gov

ode, and adjusting the path delay of the laser pulse.

Laser gain is measured with the following technique. Two interference filters with bandwidth ~ 10 nm are used to select two portions of the broadband laser spectrum which are near the maximum and minimum of the gain curve at ~ 815 nm and ~ 785 nm (see, Figure 2). This technique provides the additional advantage of differential detection, which effectively doubles the measured signal, and eliminates noise due to laser power fluctuations. The observed gain is modulated on and off by shifting the laser pulse timing by 14 ns (a round trip time in the laser oscillator) to be coincident and anti-coincident with the electron bunch at a modulation frequency of ~ 200 Hz. This allows for phase-

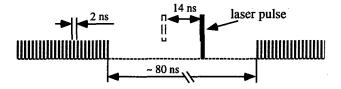


Figure 3: A schematic of the gain modulation.

locked detection of the laser gain. During multibunch operation the measurement is conducted with a single electron bunch positioned in the gap of the bunch train as shown in Figure 3. A result of the gain measurement is shown in Figure 4. During this measurement a short \sim 70 fs laser pulse is scanned in time through the electron bunch thus revealing the electron bunch longitudinal structure. We show in the next section that the gain is proportional to the electron peak current.

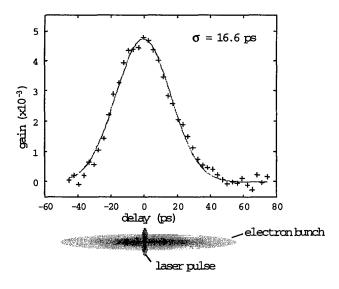


Figure 4: Gain measurement at different time delays of the femtosecond laser pulse.

3 ANALYSIS

An expression for the small signal gain of the laser spectral intensity in the FEL including effects of the laser beam diffraction and finite electron beam size has previously been found in [5]. Re-written for a planar wiggler and for arbitrary wiggler deflection parameter a_w it is:

$$g(\omega, \sigma_{\perp}, Z_R) = -4 \frac{a_w^2/2}{1 + a_w^2/2} (2\pi M)^2 \frac{I}{\gamma I_A} f(\nu, \xi, q),$$
 (1

where γ is the Lorentz factor, I is the electron peak current, $I_A \simeq 17$ kA is the Alfvén current, M is the number of wiggler periods, and the functional dependence of g on frequency ω , electron beam size in the wiggler σ_{\perp} , and Rayleigh length Z_R , is described by the gain function $f(\nu, \xi, q)$ with variables $q = L/Z_R$, where L is the wiggler length, $\xi = k\sigma_{\perp}^2/Z_R$, where k is the laser wave number, and $\nu = 2\pi M \frac{\omega - \omega_R}{\omega_e}$, where $\omega_e = \frac{2\pi c}{\lambda_w} \frac{2\gamma^2}{1+\alpha_w^2/2}$ is the frequency of the electron wiggler emission and c is the speed of light:

$$f(\nu, \xi, q) = Re \frac{d}{d\nu} \int_{0.5}^{0.5} d\tau \int_{0.5}^{\tau'} d\tau' \times$$

$$\frac{q \exp \{-i\nu (\tau - \tau')\}}{(1 + iq\tau') (1 - iq\tau) + \xi (2 + iq\tau' - iq\tau)},$$
(2)

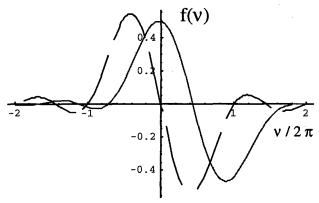


Figure 5: Gain function $f(\nu, \xi, q)$ calculated at ξ =0 and q = 4 (red curve). Dashed blue curve is the gain function in one dimensional approximation.

The function $f(\nu, \xi, q)$ calculated at q = 4 (shown to be an optimal choice for a maximum gain [5]) and $\xi = 0$ is plotted in Figure 5. For a comparison we also plot the gain function $d/d(\nu/2) [2\sin(\nu/2)/\nu]^2$ [3] that characterizes the small signal FEL gain for a 1D case (ignoring laser beam diffraction and finite electron beam size). The main difference of the gain function (2) from the 1D case consists of a spectral shift. It can be understood by recalling that formula (2) is written for the 3D case in which the laser beam is focused in the wiggler. The phase velocity of the laser field in the focus is greater than velocity of the light in vacuum (this effect is known as a Guoy phase shift). Therefore, in order to maintain optimal interaction with electrons over the entire wiggler length the laser frequency must be red shifted relative to the maximum frequency of the electron wiggler emission.

The same phenomena of the spectral shift can be equivalently explained by the angular-frequency correlation in the electron wiggler emission $\omega_e(\theta)=\omega_e(0)\left\{1+\frac{\gamma^2\theta^2}{(1+a_w^2/2)}\right\}^{-1}$, where θ is the observation angle. This correlation causes that the maximum spectral intensity of the electron wiggler emission integrated over the solid angle is the red shifted relative to $\omega_e(0)$. Therefore, for a better matching of the fields of the laser radiation and the electron wiggler emission in the far field region, the laser frequency must be red shifted by the same amount.

In the experiment we have L=3 m, $Z_R\simeq L/4$, and a beta function in the wiggler of $\beta\simeq 11$ m. With this beta function the angular divergence of the electron beam in the wiggler is negligible. Thus, Eq.(1) that accounts only for a finite beam size, correctly describes our experiment. Figure 6 shows the dependence of the gain on ξ . Calculation usings Eq.(1) is shown with red circles. For each ξ value the gain was taken at a position of the maximum of the gain function $f(\nu, \xi, q=4)$. The result of computer simulations using GINGER [4] is shown with blue rhombs. The nominal operation condition corresponds to $\xi=0.46$. A solid line in Figure 6 is a fit of the Eq.(1) using the following dependence of the gain on the electron beam size:

$$g(\omega, \sigma_{\perp}, Z_R) = g(\omega, \sigma_{\perp} = 0, Z_R) / (1 + \xi). \tag{3}$$

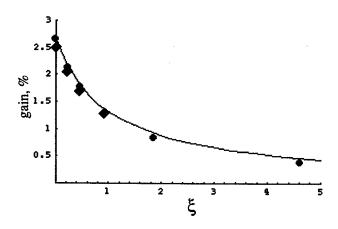


Figure 6: Gain versus ξ . Solid line is a fit following Eq.(3). Red circles are numerical calculations using Eq.(1). Blue rhombs are GINGER simulations. The rhomb and the circle overlap at $\xi = 0.92$.

At the time of writing we performed ~ 50 measurements of the FEL gain. Typically, measured gains are reproducible over period of ~ 8 hours, but vary somewhat on a day to day basis. Some days we measure $\sim 60\%$ of the predicted value and some days $\sim 40\%$. The discrepancy may be related to the imperfections in the mode structure of the laser light, which we do not test routinely. It seems less likely that the observed losses can be explained by seismic vibrations of the supporting structures for the optics or by air turbulence in the laser beam path.

4 CONCLUSION

Preliminary results of the FEL gain measurements at the ALS show that these measurements can be used for fine tuning of the efficiency of the laser/e-beam interaction in the wiggler. We found that the gain is a very sensitive indicator of any deviation from optimal interaction conditions. So far the measured gain disagrees with the predicted one in the analytical calculations giving $\sim 40-60\%$ of the expected value. The reasons for this discrepancy are being studied.

Acknowledgement. The authors wish to aknowledge the technical support of the LBNL laser safety oficer K. Barat and the staff of the ALS in setting-up this experiment.

- [1] A. Zholents, et. al. in Proc. of this Conf., report WEP44.
- [2] A. Zholents and M. Zolotorev, PRL v.76, (1996)912.
- [3] J.M.J. Madey, Nuovo Cimento 50B, (1979)64.
- [4] W. Fawley, GINGER documentation, unpublished.
- [5] A. Amir, Y. Greenzweig, NIM A250, (1986)404.

BEAM QUALITY MEASUREMENT OF 100-MeV TEST LINAC*

H. S. Kang*, J.-Y. Choi, S. H. Nam, and S. S. Chang Pohang Accelerator Laboratory, Pohang, Kyungbuk 790-784, Korea

Abstract

The 100-MeV Test Linac was constructed for the high brightness applications such as free electron lasers and coherent radiation generation experiments at PAL. The linac consists of a thermionic RF-gun, an alpha magnet, two accelerating structures, and a beam analysing magnet. The RF-gun is a one-cell cavity with a tungsten dispenser cathode of 3-mm diameter, and the longitudinal matching from the RF-gun to the first accelerating column is done by the alpha magnet. The RF frequency is 2856 MHz, and a SLAC 5045 klystron feeds RF power to two accelerating columns and the RFgun. In the initial beam test the achieved beam energy and current were 75 MeV and 50 mA, respectively. The longitudinal acceptance measurement with the alpha magnet is done to minimize energy spread, and the bunch length was measured with a streak camera by using OTR (Optical Transition Radiation). In this paper, the beam quality measurement results are described in detail together with the detailed description of the machine.

1 INTRODUCTION

An electron linac with a design beam energy of 100 MeV has been prepared for new R&D activities such as FEL (free electron laser) and SASE (self-amplified spontaneous emission) experiments at PAL (Pohang Accelerator Laboratory). New experiments like SASE require a high-brightness electron source; this implies a high peak current (10 A to 2000 A) and a low transverse emittance (2 to 80 mm-mrad) [1]. Emittance and peak current requirements for infrared-FEL is not stringent compared to SASE.

Thermionic RF-gun was chosen as an electron beam source for the Test Linac because it is quite compact and relatively inexpensive source for high brightness applications in spite of some disadvantages such as a large energy spread and a short cathode life time. For SASE experiment the RF-gun will be replaced with photocathode RF-gun in the near future. The linac incorporates an alpha magnet for longitudinal phase matching from the gun to the first accelerating column because thermionic RF-gun inherently generates an electron beam with a large momentum spread.

In the beam test of 1998 the achieved beam energy and current were 75 MeV and 50 mA, respectively. The beam loss was very large, about 50%, at the first accelerating column [2]. Focusing solenoid coils were installed at the first accelerating column to reduce beam loss. The longitudinal acceptance measurement with the alpha magnet was done to minimize energy spread and beam loss. Bunch length was measured with a streak camera by using OTR (Optical Transition Radiation). Dependence of bunch length on field gradient of the alpha magnet was measured.

2 MACHINE DESCRIPTION

The linac consists of a thermionic RF-gun, an alpha magnet, two quadrupole doublets, two SLAC-type accelerating columns (AC#1 and AC#2), a quadrupole triplet (QT), and a beam analysing magnet as shown in Figure 1. There are three beam current monitors (BCM) and three beam profile monitors (BPRM) for beam instrumentation. There is an experimental area at the end of linac for FEL and SASE experiments, which has a dimension of 5-m width and 7-m length. A 2-m long drift space is reserved between AC#1 and AC#2 to insert a magnetic bunching system and a bending magnet for FEL research.

The RF-gun is a one-cell cavity with a tungsten dispenser cathode of 3-mm diameter [3]. The RF frequency is 2856 MHz, and a SLAC 5045 klystron feeds RF power to two accelerating columns and the RF-gun. The maximum field gradient of the alpha magnet is 200 G/cm. Electron moves along a α-shaped trajectory in the alpha magnet, and the resultant bend angle is 278.6°. Two quadrupole doublets are used to focus the electron beam in the transport line from the gun to the first accelerating column. OTR bunch monitor chamber was installed at the linac end. The target is 2-mm thick plate of stainless steel, from which OTR emits when the accelerated electron beam strikes on it, and the surface was mirror-finished.

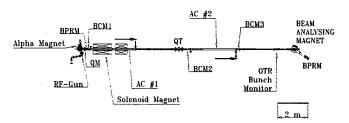


Figure 1: Layout of Test Linac.

^{*}Work supported by the Ministry of Science and Technology, Korea

^{*}Email: hskang@postech.ac.kr

3 BEAM QUALITY MEASUREMENTS

3.1 Beam Transmission and Energy Spread

The beam transmission rate was improved up to 72% by the solenoid field focusing. Table 1 shows the measured data as the alpha magnet current changes. BCM#1 measures beam current after the alpha magnet, and BCM#3 measures beam current at the end of linac. Transmission rate is determined by longitudinal and transversal matching. Though the injected beam to the first accelerating column is high at 7-A current setting, the beam loss is very large because the transversal beam quality is very poor. Optimum matching condition is obtained at the current setting of 11.5 A. The field gradient of alpha magnet at this current is 90.8 Gauss/cm.

The nominal RF power of the klystron is 30 MW at the experiment, and the RF power fed to one accelerating column and the RF-gun were 12 MW and 2.0 MW, respectively. The RF pulse width is 1.2 μ s and pulse repetition rate is 12 Hz.

The energy and energy spread were also measured as the alpha magnet current changed. Output beam energy increases as the field gradient of alpha magnet increases. Measured energy spread is $\pm 1\%$ at the beam loading of 100 mA. On the other hand the energy spread becomes biggest at the optimum matching condition. As shown in Fig. 2 low energy tail is a main cause to increase the energy spread at the current of 11.5 A.

Table 1: Transmission rate, energy and energy spread

Alpha Magnet Current [A]	BCM#1 [mA]	BCM#3 [mA]	Transm -ission [%]	Energy [MeV]	Energy Spread [± %]
7	209	97	46.4	57.3	0.67
11.5	94	68	72.3	59.5	1.16
12.5	57	34	59.6	62.3	0.94

The low energy tail originates from the difference of the cavity RF-filling time in the RF-gun and accelerating column. The cavity RF-filling times of the RF-gun and the accelerating column are 0.21 µs and 0.83 µs, respectively. However the effect of low energy tail becomes smaller at the current of 7 A and 12.5 A. A momentum filter with a fixed gap is on the maximum dispersion point of the trajectory in the alpha magnet. The energy of electron moving on the centre line of the trajectory is 0.9 MeV at the current setting of 11.5 A. At the current of 7 A, the median energy is 0.5 MeV, thus the momentum of the head of one macro pulse of electron beam, which is about 0.6 µs long, is too small to pass through the following accelerating column. It is possible to reduce energy spread by kicking out the head of one macro pulse of electron beam with a magnetic kicker.

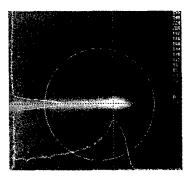
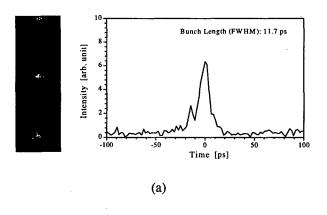


Figure 2: Horizontal and vertical beam profile of the profile monitor after beam analysing magnet at the alpha magnet current setting of 11.5 A. Horizontal profile represents a beam energy spread.

3.2 Bunch Length Measurement

The bunch lengths of the electron beams were measured using optical transition radiation with a streak camera of Hamamatsu Photonics Co. The bunch trains are shown in Fig. 3. The measured bunch length is 11.7 ps in FWHM before the RF phase adjustment. After the fine adjustment of RF phase to two accelerating columns, the bunch length reduces to 7.4 ps (FWHM).



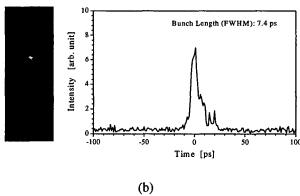


Figure 3: Streak camera images and its intensity profiles at the alpha magnet current setting of 11.5 A; (a) before and (b) after RF phase adjustment. Vertical lengths of camera images correspond to streak time spans of 1 ns for (a) and 500 ps for (b).

The variations of bunch lengths were measured as the alpha magnet current setting changed. It is observed that the bunch length decreases to 4.5 ps as the alpha magnet current is raised, as shown in Fig. 4. means that electron beam which exits from the RF-gun with higher momentum gets a better bunch compression in the alpha magnet transport line. Figure 5 describes a bunch length shortening during the beam transport in the alpha magnet. In this Figure the free space distance from the RF-gun to the first accelerating column is 95 cm and the energies of the head and tail particle of one micro bunch are assumed to be 1 MeV and 0.8 MeV, respectively. The resultant minimum time difference depends on the alpha magnet current setting. When the alpha magnet current is raised, the beam current at the linac end decreases down remarkably. In order to obtain a sufficient beam current the RF power to RF-gun should be raised.

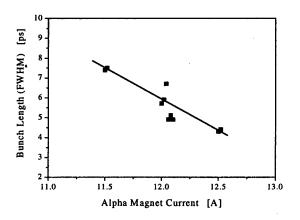


Figure 4: Dependence of bunch length on alpha magnet field gradient.

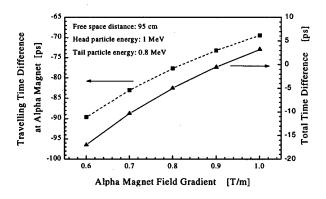


Figure 5: Travelling time difference of head and tail particle at the alpha magnet and total time difference including the travelling time in free space.

The bunches in a few us-long macro pulse of electron beam experience a different accelerating field due to transient beam loading, especially in the thermionic RFgun cavity. The length of each bunch in one macro pulse was measured by changing the trigger time to streak camera. The measurement result is shown in Fig. 6. The bunch length of the end part becomes slightly longer than the head of macro pulse. This increase might be partially caused by unevenness of RF power flattop during one macro pulse. The main cause is transient beam loading in the thermionic RF-gun cavity together with cavity temperature change due to cavity The effect of transient loading and wall dissipation. temperature effect are not fully understood yet and will be investigated in next experiments.

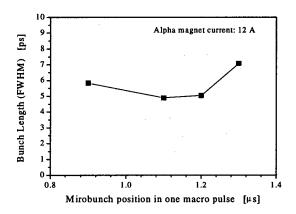


Figure 6: Dependence of bunch length on microbunch position in one macro pulse. Microbunch position represents trigger delay time to streak camera.

4 SUMMARY

The beam transmission rate was improved up to 72% due by the solenoid field focusing and good longitudinal phase matching compared to the previous experiments. Measured energy spread is ±1% at the beam loading of 100 mA, and the large energy spread at the optimum matching condition is due to cavity RF-filling time differences. The measured bunch length is about 7 ps in FWHM, and decreases to less than 4.5 ps as the alpha magnet current increases. But reduction in the beam current is a problem to solve. The length of each bunch depends on the position in one macro pulse which has a relation to transient beam loading in active RF cavity.

- Richard L. Sheffield, Proc. 1989 IEEE Particle Accelerator Conf. [1] p. 1098. H. S. Kang, et al., Proc. 1998 Asian Particle Accelerator Conf.
- H. S. Kang, et al., IEEE Trans. Nucl. Sci. 44, No. 4, 1639 (1997).

OUTPUT POWER CONTROL IN AN X-RAY FEL*

C. Pellegrini, X. Ding, J. Rosenzweig UCLA Physics Department, Los Angeles, CA

Abstract

Recent theoretical and experimental advances of the high gain Self-Amplified Spontaneous Emission free-electron laser (SASE-FEL), have demonstrated the feasibility of using this system as a 4th generation light source. This source will produce diffraction-limited radiation in the 0.1nm region of the spectrum, with peak power of tens of GW, subpicosecond pulse length, and very large brightness [1,2,3]. The peak power density in such a system is very large, and in some experiments it might damage the optical systems or the samples, or it might be simply larger than what is needed for the particular experiment being considered. Some options to reduce the power level, for example by using a gas absorption cell to reduce the X-ray intensity, have been studied [2]. In this paper we discuss another possibility to control the power output of an X-ray SASE-FEL by varying the charge from the electron source, and the longitudinal bunch compression during the acceleration in the linac.

1 INTRODUCTION

X-ray free-electron lasers (XFEL) based on the Self Amplified Spontaneous Emission (SASE) mode of operation can produce very large peak power and subpicosecond long pulse of coherent radiation in the 0.1 nm region of the spectrum [2,3].

In some experiments it may be useful to reduce the peak power to avoid damaging the sample under study, or some optical components. One method to do this is to use a gas cell to attenuate the X-ray pulse [2]. In this paper we discuss an alternative method based on changing the amount of charge in the electron pulse produced by the electron source. In the present design of XFELs the electron beam is produced in a photoinjector, and accelerated to 15 GeV in a linac. During the acceleration the electron bunch is also compressed to reach the peak current needed for FEL operation. The charge of the electron bunch can be changed by varying the laser intensity on the photocathode. The compression system is also flexible enough to provide a variable compression.

When varying the electron bunch charge, other beam parameters, like the emittance, pulse length and energy spread, also change. These changes have an effect on the XFEL gain length and output power. To estimate the overall effect we need to consider the FEL scaling laws and the photoinjector-linac scaling laws. The scaling

laws for these two cases will be discussed in the next section. We will then evaluate the XFEL performance using the LCLS as an example.

2 FEL SCALING

The gain length, saturation power, and saturation length of a SASE-FEL are defined by the FEL parameter ρ [4]

$$\rho = (\frac{K}{4\gamma} \frac{\Omega_p}{\omega_u})^{2/3},\tag{1}$$

where $K=eB_u\lambda_u/2\pi mc^2$ is the undulator parameter; B_u the undulator field and λ_u the undulator period; γ the beam energy in rest mass units;

$$\Omega_p = (4\pi r_e \ c^2 n_e / \gamma)^{1/2} \tag{2}$$

the beam plasma frequency; r_e and c the classical electron radius and the light velocity; n_e the electron density; $\omega_e = 2\pi c/\lambda_u$.

Since the FEL gain length and the saturation length are inversely proportional to ρ , and the output power is proportional to ρ , optimising the FEL is equivalent to maximise ρ . The gain length is given, in the simple 1D theory, neglecting diffraction and slippage by

$$L_G = \lambda_u / 2\sqrt{3}\pi\rho \tag{3}$$

Saturation occurs after about 10 gain lengths, and the radiation intensity at saturation is about ρ times the beam energy. Diffraction, energy spread and slippage, $S=\lambda N_n$, can increase the gain length over the 1D value if the conditions $\varepsilon < \lambda/4\pi$, $\sigma_E < \rho$, S < L, $Z_R > L_G$ are not satisfied, where ε is the beam emittance, N_u the number of undulator periods, and Z_R the radiation Rayleigh-range.

The FEL parameter depends on the beam density in the undulator, and is proportional to the beam plasma frequency to 2/3, or $(Q/\sigma^2\sigma_L)^{I/3}$, Q being the electron bunch charge, σ the radius, and σ_L the length. The beam density can be conveniently written as

$$n_e = \frac{N_e}{(2\pi)^{3/2} \varepsilon \beta \sigma_L},\tag{4}$$

^{*}Work supported in part by the US Department of Energy under grant DE-FG03-92ER40693

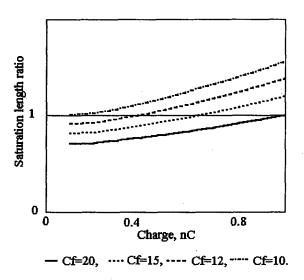


Fig. 1 Ratio of the saturation length to the reference case saturation length, as a function of electron bunch charge, and for different values of the compression coefficient. The reference case is defined as Q=1 nC and Cf=20. The curves show that it is possible to obtain the same saturation length when changing the charge from 0.1 to 1 nC, by changing the compression factor from 20 to 10.

where N_{ϵ} is the number of electrons in a bunch, ϵ the beam emittance, β the focusing function in the undulator. The beam density is determined by the electron source, and by the acceleration and compression processes. We assume the electron source to be a 1.6 cell photoinjector [5]. The scaling of the beam emittance, pulse length and energy spread with charge for this photoinjector has been studied and the results are presented in ref. [5]. We use the results of this paper, in particular the scaling of emittance and pulse length with charge,

$$\varepsilon = 1.45 \times 10^{-6} (0.38Q^{4/3} + 0.095Q^{8/3})^{1/2},$$
 (5)

$$\sigma_L = 0.63 \times 10^{-3} Q^{1/3} \quad . \tag{6}$$

where the charge is in nC, the emittance in mxrad, and the bunch length in m. The acceleration and compression process producing the beam used in the FEL is designed to preserve the transverse emittance, and reduce the pulse length by a compression factor C_r . As shown in [2] the emittance increase produced by wakefields is small, and we take it into account by using the additional factor 1.45 in (6).

During this acceleration and compression the wakefields in the linac and compressors increase the longitudinal emittance by a rather large factor. However the local energy spread, remains small. The term local refers in the FEL case to the energy spread within a slice of the beam corresponding to one co-operation length, defined as

 $L_c=L_g\mathcal{N}\lambda_s$, the slippage in one gain length [6]. The local energy spread is maximum at the largest charge, 0.02% at 1 nC, and in our analysis we assume it to remain constant at lower charges, a pessimistic assumption. We use this assumption to evaluate the XFEL gain length, saturation length and output power.

Table 1: LCLS Parameters. Energy spread, pulse length, emittance are rms values. Brightness is in number of photons per second, per (mm mrad)2, per 0.1% bandwidth. The energy spread is the local energy spread within a co-operation length. A correlated energy chirp of 0.1% is also present along the bunch.

Electro	on beam
Electron energy, GeV	14.3
Emittance, nm rad	0.05
Peak current, kA	3.4
Energy spread, %	0.02
Bunch length, fs	67
Und	ulator
Period, cm	3
Field, T	1.32
K	3.7
Gap, mm	6
Total length, m	100
Rad	iation
Wavelength, nm	0.15
FEL parameter, ρ	5x10⁴
Field gain length, m	11.7
Bunches/sec	120
Average brightness	4x10 ²²
Peak brightness	10 ³³
Peak power, GW	10°
Intensity fluctuations, %	8

Notice also that from (4), (5), (6) it follows that when the charge is in the range of 0.1 to 1 nC, the range that we consider in this paper, the beam density, and so the FEL parameter, is almost independent of charge.

3 XFEL PERFORMANCE

In this section we use the electron beam scaling with charge introduced before to evaluate the XFEL performance. We use a model based on the FEL code described in [7], which includes 3-dimensional effects. The basic set of parameters used is those of the LCLS project [2], given in Table 1. The FEL radiation characteristics given in this table are for the case of 1nC electron charge and compression of 20. In what follows we will use this as the reference case. We simulate a situation with an undulator of given, fixed length, and

change the electron bunch charge and compression factor to keep the saturation length constant and equal to the undulator length. The main results are shown in fig. 1 and 2.

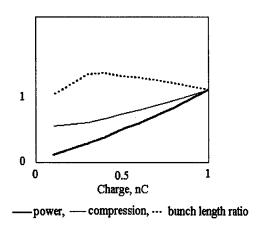


Fig.2 Ratio of peak power, bunch length, and compression factor, Cf, to that of the reference case, defined as Q=1 nC and Cf=20. The peak power changes almost linearly with charge, and is reduced by a factor of ten from 1 to 0.1 nC.

The results in figure 1 shows that it is possible, using the same LCLS undulator, to reach saturation at the undulator exit for a charge range between 1 to 0.1 nC, if one simultaneously reduces the compression factor by 2. The results in figure 2 show that in this situation the XFEL peak power is reduced by one order of magnitude, while the bunch length remain practically constant.

Figure 2 also shows that, when considering simultaneously the bunch length from the photoinjector and the compression, the final bunch length changes by no more than 25% when changing the charge. Hence the peak current for the XFEL scales almost linearly with charge, and is reduced to about 350 A at 0.1 nC.

2 CONCLUSIONS

We have shown that it is possible to change the output power of a XFEL, while keeping the same saturation length, by changing the electron bunch charge and the compression factor in the linac. This procedure can produce a large change in output power, as large as one order of magnitude in the LCLS case. This method is easy to implement and does not require additional hardware like the gas cell considered in ref. [2].

- [1] M. Hogan et al. Phys. Rev Lett. 81, 4867 (1998).
- [2] The LCLS Design Group, LCLS design Study Report, SLAC-R-521 (1998).
- [3] C. Pellegrini, "Is the X-ray free-electron laser the 4th generation light source?", Proc. 6th European Particle Accelerator Con., Stockolm (1998), p. 83.
- [4] R. Bonifacio, C. Pellegrini and L. Narducci, Opt. Comm. <u>50</u>, 373 (1984).
- [5] J.B. Rosenzweig and E. Colby, Proc. Of the Conf. On Advanced Acceleration Concepts, AIP vol.335, p. 724 (1995); J. Rosenzweig et al., "Comparison of split and integrated photoinjector performance", presented at this conference.
- [6] R. Bonifacio et al., Phys. Rev. Lett. 73, 70 (1994).
- [7] M. Xie, "Design Optimization for an X-ray FEL Driven by the SLAC Linac", IEEE Proc. 95CH3584 of the 1995 Particle Accelerator Conf., p. 183, (1996).

BUNCH COMPRESSOR II AT THE TESLA TEST FACILITY

M. Geitz, A. Kabel*, G. Schmidt, H. Weise Deutsches Elektronen-Synchrotron Notkestraße 85 D-22607 Hamburg, Germany, for the TESLA Collaboration

Abstract

In the TESLA Test Facility (TTF), short bunches with low emittance are needed for the operation of a free electron laser. Several stages of bunch compression by means of magnetic chicanes will be used to reach the required peak current. The second stage of the bunch compression system, bunch compressor II, has been taken into operation recently. We describe design and instrumentation of the bunch compressor II and communicate experiences made during commissioning.

1 INTRODUCTION

The TESLA Test Facility (TTF) aims to conduct a proof-of-principle experiment for a self-amplified spontaneous emission free electron laser. (SASE FEL). For FEL operation, high peak currents and low transversal emittances are crucial. To reach these quality conditions, the bunch has to be compressed longitudinally after it leaves the gun. In the case of the TTF FEL experiment, this is done in magnetic chicanes. Bunch Compressor II is the only chicane to be used for the proof-of-principle experiment, while a further stage of FEL operation, using smaller wavelengths, higher energy and a longer undulator, requires another stage of compression (Bunch Compressor III) The low-energy stage Bunch Compressor I will not be used for FEL operation.

2 BUNCH COMPRESSOR II

BC II is located between accelerating modules #1 and #2 of the TTF, operating at a design energy of 140MeV. It has been designed to compress a bunch of length 1mm down to $250\mu m$. [5, 8]

2.1 Geometry

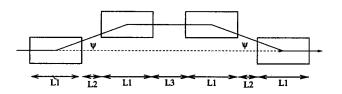


Figure 1: The geometry of a magnetic chicane

Bunch Compressor II comprises four rectangular dipole magnets with field signature +--+ arranged with their entry faces in parallel and perpendicular to the beam entering the first magnet. This arrangement is easily seen to be overall dispersion-free to all orders. For BCII, the dimensions are $L_1 = L_2 = 0.5$ m, $L_3 = 1.3$ m.

Optically, the chicane behaves like a drift space for the horizontal phase space plane (with an effective length exceeding the orbit length by $\Delta L = 4L_1 \left(\frac{1}{\cos\psi} - \frac{\psi}{\sin\psi}\right) + \frac{2L_2\sin^2\psi}{\cos^3\psi}$) and as a strongly focusing element for the vertical phase space.

The vacuum chamber and the magnets have been designed to allow for an deflection angle of $\psi=17^\circ\dots21^\circ$. From geometry, the path length is $S(\psi)=\frac{4L_1\psi}{\sin\psi}+\frac{2L_2}{\cos\psi}+L_3$. Thus, the linear matrix element $R_{56}=\frac{\partial S(\psi)}{\partial \delta}=\tan\psi\frac{\partial S}{\partial \psi}=4L_1\left(\frac{1}{\cos\psi}-\frac{\psi}{\sin\psi}\right)+2L_2\frac{\tan^2\psi}{\cos\psi}$ varies between $0.1594\mathrm{m}$ and $0.2546\mathrm{m}$.

From geometry, the offset in the symmetry point is

$$h = 2L_1 \frac{1 - \cos \psi}{\sin \psi} + L_2 \tan \psi, \tag{1}$$

from which one has the maximum linear horizontal dispersion

$$\eta_{x,center} = 2L_1 \frac{\psi(1 - \cos\psi)}{\tan\psi} + L_2(\tan\psi + \tan^3\psi)$$
 (2)

In the case of BC II, $h = 0.302 \text{m} \dots 0.377 \text{m}$ and $\eta_{x,center} = 0.310 \text{m} \dots 0.393 \text{m}$.

The energy acceptance is $\delta_{acc} \approx \frac{h_{max} - h_{min}}{\eta x, center}$, so one can expect transmission for beam energy variations of $\approx \pm 10\%$.

2.2 Compression

A bunch with a linear correlation element $d=\frac{\langle \delta x \rangle}{\sqrt{\langle x^2 \rangle}}$ will thus be shortened by $-dR_{56}$. A linear correlation between x and δ is achieved by shifting the acceleration module phase in front of the bunch compressor (normally accelerating from E_0 to E_0+E_1 , where $E_0\approx 15 {\rm MeV}$ and $E_1\approx 85 {\rm MeV}$ for the commissioning run) by $\Delta \phi$. Then, $d=-\frac{E_1\sin\Delta\phi}{E_0+E_1\cos\Delta\phi}$ and the linear part of the bunch length vanishes for

$$l_{\text{initial}} = dR_{56} \tag{3}$$

^{*} E-Mail: andreas.kabel@desy.de

. The quadratic term is $d_2=\frac{1}{1+\frac{E_0}{E_1}\cos\Delta\phi}$ and gives the minimum bunch length of $l_{\min}\approx d_2R_{56}l_{\mathrm{initial}}\frac{2\pi^2}{\lambda^2}$, where λ is the RF wavelength of $c/1.3\mathrm{Ghz}=0.231\mathrm{m}$.

Having the bunch travel through the chicane results in a phase slippage of $2\pi\frac{S(\phi)-4L_1-2L_2-L_3}{\lambda}$ compared to going straight to the bunch compressor section. This is close to π for the design value of R_{56} , which would result in a deceleration in the modules following the bunch compressor. A phase shifter—a length-adjustable waveguide—was installed to switch between straight and compression operation, allowing for on-crest acceleration from the 2nd module on in both operation modes.

2.3 Magnets

The dipole magnets of the chicane require high fields and high field quality over a wide horizontal range. We use H-type magnets custom-manufactured by danfysik with a pole gap of $d=25 \mathrm{mm}$. The pole width is $W=300 \mathrm{mm}$, but the admissable width for the vacuum chamber is limited by spacers to 216 mm. The offset of the horizontal positioning of the two inner dipoles was chosen as to fully exploit this range for variation of deflection angle. The maximum field strength is $0.375 \mathrm{T}$, allowing for a maximum deflection angle of 23.7° at $E=140 \mathrm{MeV}$.

The presence of quadrupole and higher moments in the field in the dispersive region will create additional transverse emittance. To avoid this, the field quality has to be quite high (specification values: sextupole: $< 0.0043 \mathrm{m}^{-2}$, decapole: $< 0.068 \mathrm{m}^{-4}$).

Electrically, the bending magnets are arranged as a series circuit, which guarantees equal field strengths, with individual trimcoils (giving up to 10% of main field value) in each magnet to correct leftover dispersion and horizontal steering errors.

The most crucial alignment issues are (1) equality of L_2 and its symmetric counterpart and (2) the tilt of the dipole magnets. Both errors would fail to close dispersion and would introduce angular kicks.

A total of four pairs (x and y plane) steerer magnets with a possible correction of ± 3 mrad have been inserted around the chicane and at the entrance and exit of the entrance and exit quadrupole triplet. They allow correction of all quad- and dipole-induced kicks within the tolerated misalignment.

3 INSTRUMENTATION

For commissioning bunch compressor II, it is important to get enough information to (1) steer the beam through the chicane, (2) reconstruct the bunch's phase space both longitudinally and transversally: the expected behavior for the longitudinal dynamics has to be checked, and it has to be ascertained that the emittance growth is within the expected limits.

The following instrumentation was installed in the bunch compressor II section or in connection with its installation:

- Toroids for transmission measurements
- An OTR foil in the dispersive region (middle of L_3), spanning the width of the vacuum chamber, thus allowing for energy spread measurement and steering the bunch through the chicane [2, 3]
- Viewscreen and OTR foil at the exit of the chicane.
 They can be used for threading the bunch through the chicane.
- Synchrotron radiation outlet windows have been inserted into the vacuum chambers, allowing synchrotron radiation to be viewed for each bend in the dispersive section. The OTR foil at the exit of the chicane can be used as an outlet mirror, allowing to look into the most downstream bend.
- Stripline [4] and cavity [9, 10] beam position monitors (BPMs) at the entrance and exit of the chicane, respectively. In conjuction with the "cold" cavity BPM in the preceding module, one has two pairs of BPMs allowing to observe positional and angular offset at the entrance and exit of the chicane. Thus, one can check the closure of the orbit bump generated by the chicane.
- Interferometric bunch-length measurement: following the accelerating module #2, OTR is generated in a foil and extracted using mirrors. A Martin-Puplett type interferometer is used to extract the autocorrelation function of the bunch's charge distribution. Pyroelectric detectors are used to measure the OTR's intensity.[1, 11]
- The chicane has a triplet of individually powered quadrupole magnets both upstream an downstream. In conjunction with OTR foils, they facilitate beam tomographic measurements, i.e. reconstruction of the transverse phase space.[6]

4 COMMISSIONING

We were able to steer a bunch of charge $10^{-9} As$ through the chicane. Excellent transmission could be reached; no current loss could be observed with the toroids. The transmission could be retained when varying the dipole current over a range of $\pm 6\%$, which is in agreement with the energy acceptance given above. Save the synchrotron radiation observation, all instrumentation of the bunch compressor section could be commissioned.

4.1 Compression

Bunch length measurements upstream of the bunch compressor using a streak camera showed an initial bunch length of 3mm...4mm¹, which is off the design value of BC II.

¹S. Schreiber, private communication

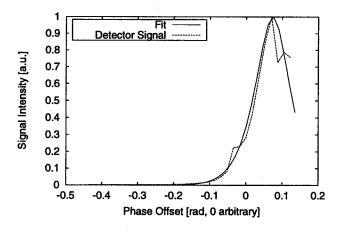


Figure 2: OTR Intensity measured with pyroelectric detectors and calculated intensity for purely gaussian bunches, see text

Thus, the minimum bunch length to be expected is around $700\mu m$ as opposed to the design value of $250\mu m$, which would be well above the minimum obtainable bunch length for $l_{initial} = 1 \text{mm}$.

4.2 Bunch Length Measurement

Since the pyroelectric detectors cut off frequencies < $150 {\rm GHz^2}$ (corresponding to bunch length components of > $2000 \mu {\rm m}$), their signal can be used to find the off-crest phase giving the minimum bunch length. We observed a maximum in signal at a phase of $\Delta \phi \approx 12.1^{\circ}$ for an $R_5 6 \approx 0.20 {\rm m}$, which gives, according to 3 an initial bunch length consistent with the streak camera measurements.

At this $\Delta\phi$ position, interferometric scans using the Martin Puplet interferometer was done. While the quality in terms of noise and resolution of the interferograms is good, the evaluation in terms of the bunch length still is inconclusive.

A more thorough evaluation of the amplitude measurements was done the following way: We assuming a coherent radiation intensity $I(\omega)$ as created by a Gaussian bunch with length σ_l equal to its rms length (note that the compression process creates deviations from gaussian shape near maximum compression) of the bunch. Assuming a sharp cutoff-wavelength of the detector, one has $\int I(\omega)d\omega \propto \frac{1}{\sigma_l}(1-\text{erf}(\sigma_l/\lambda_{cutoff}))$. This intensity can be fitted (with parameters λ_{cutoff}, R_{56} , and $\sigma_{l,initial}$) to the actual readout of the pyroelectric detectors. R_{56} is known to be $0.2m \pm 10\%$. One finds quite satisfactory agreement for $R_{56} = 0.215$ m, $\sigma_{l,initial} = 3.2$ mm and $f_{cutoff} = 150$ GHz. This strongly indicates the presence of compression, but the evaluation of interferometric measurements would be necessary for further clarification.

5 CONCLUSION

The Bunch Compressor II at the TESLA Test Facility has been taken into operation; preliminary measurements strongly indicate compression of bunches. The results are consistent with the predicted behavior. The usability of the instrumentation has been demonstrated. However, due to the off-design values of initial bunch length emittance the design value for the final bunch length could not be reached in this run. Further measurements and further evaluation of measurement data is needed.

- Ch. Berger, M. Geitz, B. Leissner, G. Schmidt, P. Schmueser,
 R. Siedling, M. Tonutti, "Bunch Length Measurements Using a Martin Puplett Interferometer", This Conference, WEA131
- [2] M. Castellano, V. A. Verzilov, Phys. Rev. ST Accel. Beams 1:62801 (1998)
- [3] M. Castellano, V. A. Verzilov, LNF-98-017-P, June 1998.
- [4] M. Castellano et al., "TESLA Test Facility Stripline Readout System", Conference Proceedings of the EPAC 96, Barcelona, June 1996
- [5] D. A. Edwards (Ed.), TESLA Test Facility LINAC Design Report, DESY Print March 1995, TESLA 95-01
- [6] M. Geitz, G. Schmidt, "Phase Space Tomography at the TESLA Test Facility", This Conference, WEA132
- [7] M. Geitz, K. Hanke, P. Schmuser, Y. Y. Divin, U. Poppe, V. V. Pavlovskii, V. V. Shirotov, O.Y. Volkov, M. Tonutti, "A Hilbert Transform Spectrometer Using a High-T(C) Josephson Junction for Bunch Length Measurements at the TTF Linac", DESY-TESLA-98-10, Apr 1998
- [8] T. Limberg, A. Molodozhentsev, V. Petrov, H. Weise, "The Bunch Compression System at the TESLA Test Facility FEL." DESY-TESLA-FEL-95-04A, 1995 and Nucl. Instrum. Methods A375 (1996) 322-324.
- [9] R. Lorenz et al., "Measurement of the Beam Position in the TESLA Test Facility", Conference Proceedings of the LINAC96, Genevea, August 1996
- [10] R. Lorenz et al., "First Operating Experiences of Beam Position Monitors in the TESLA Test Facility Linac", Conference Proceedings of the PAC 97, Vancouver, May 1997
- [11] J. Menzel, M. Tonutti, M. Geitz, P. Schmueser, Y. Y. Divin, U. Poppe, V. V. Pavlovskii, V. V. Shiritov, O. Y. Volkov "A Hilbert Transform Spectrometer Using a High T_C Josephson Junction for Bunch Length Measurements at the TESLA Test Facility Linac", This Conference, WEA133

²Boris Leissner, private communication

LASER FEL

M.Kumada and K.Nakajima¹

National Institute of Radiological Sciences, 4-9-1 Anagawa, Inage, Chiba, 263-8555, Japan KEK, High Energy Research Organization, 1-1 Oho, Tsukuba, Ibaraki, 305-0801, Japan

Abstract

A new Free Electron Laser(FEL) using high power laser system as a wiggler/undulator in a storage ring as a electron beam of transverse cooling with a combination of chicane for longitudinal compression is proposed. This new scheme will open an intense FEL hard X-ray laser with much compact system than those proposed in high energy linear accelerator at SLAC and DESY

1 INTRODUCTION

It is widely recognized that X-rays by synchrotron radiation(SR) light sources take advantage of X-ray imaging and medical diagnoses over conventional X ray tube by more than three order of magnitude[1]. The intravenous coronary angiography by SR is attractive as an advanced diagnosis. In particular, imaging the coronary arteries of humans following venous injection of contrast agent opened up new areas of coronary artery disease research to reduce a statistical risk of the diagnoses[2]. The preferred energy of the X-ray for the intravenous coronary angiography is around 33 keV. With a conventional wiggler, the preferred energy of the electron beam is about 2 GeV. A size of conventional storage ring of this energy range is too large and costly for actual medical application. To this end, compact electron storage rings dedicated and optimized to the coronary angiography have been proposed to fit into a clinical environment in a hospital[3,4]. A typical diameters of these compact machines are between 10 to 15 m.

A new approach has been pursued for further downsizing. It is a high power Terawatt Table Top laser which opens up this possibility. The idea of the mechanism, Thomson scattering or Compton scattering, has been proposed long ago[5]. After K. J.Kim proposed a generation of femtosecond X-rays by 90 degree Thomson scattering and the successful proof of principle experiment [6,7], a fever arose in an community of accelerator facilities which already have electron linac or storage ring. Further enthusiasm was added to the fever. Telnov pointed out that the process of laser electron is also a radiation damping process for the phase space of the electron beam and can be used to "cool" multi-GeV electrons[8]. Huang and Ruth[9] pointed out this cooling could be applied to

even lower energy range of a few MeV up to a few hundred MeV which energy lies in our interest for medical application for angiography[9]. In this paper, we first present the conceptional design of medical laser SR(Synchrotron Radiation) via a Thomson scattering where the whole size of the machine could be placed in only a room of a size of 5 m by 5 m with a necessary X-ray flux as much as larger machine for coronary angiography.

This laser SR then is served as a transverse cooler of an electron beam and the cooled beam is extracted and is undergone a longitudinal compression by a magnetic chicane[12] followed by a high power laser as an undulator for LASER FEL.

2 FLUX, ENERGY LOSS AND LASER RADIATIVE COOLING

A simple way to analyze the Thomson scattering(or Compton scattering) is to notice an analogy between the role of laser beam and a static magnetic wiggler(or undulater). The magnetic field B of the laser intensity dP/dA(power unit area) is simply[6]\

$$B = \frac{E}{c} = \sqrt{2Z_0 \frac{dP}{dA}} \tag{1}$$

where Z_0 =377 ohm is the free space impedance. In Terawatt laser application, where laser waist is squeezed to a size of its wavelength, the magnetic field strength is enormous compared to even a state of the art superconducting wiggler magnet; namely with 10 Terawatt laser, B=3266 Tesla. In addition, the electrical force adds to a Lorenz force and factor of 2 has to be multiplied to take into account its effect. The wave length of X-rays from an electron beam which interacts with laser field or wiggler are

$$\lambda_{x} = \frac{1 + 0.5a_{0}^{2}}{2\gamma^{2}} Y \lambda_{0x}$$
 (2)

where Y=2 for the laser undulator and Y=1 for a conventional wiggler and λ_0 the wave length of the laser, $a_0=0.85\times10-9$ I $1/2[W/cm^2]\lambda0$ [mm].

The spectral flux within the spectral of $\Delta f/f$ is

$$F[photons/s] = 8.4x^{16}I[A]P_0[GW] \frac{L}{Z_R} \frac{\Delta f}{f}$$
 (3)

where E is the electron beam energy, L is the laser electron interaction length, $Z_R = \pi r_0^2$ the Rayleigh length with the spot radius r_0 , P_0 the incident laser power. For 1GeV electron beam interacting with CO_2 laser, the energy loss is about 8 keV.

At the laser-electron interaction region, quantum excitation and radiative laser cooling balance and the electron beam is expected to be cooled by the laser. This balance leads to the minimum normalized emittances

$$\varepsilon_{x,y}^{n} = \frac{3}{10} \frac{\lambda_c}{\lambda_0} \beta_{x,y}^* \tag{4}$$

with λ_c =h/mc=2.43x10¹² m, with β * the betatron function at the interaction point. We have only two parameter to be manipulated by our hands toward smallest emittance as possible; smaller micro beta function at the interaction point and laser of longer wave length. CO_2 laser was chosen from this view point.

3 LASER COOLING AND STORAGE RING

To achieve a design flux of 10¹⁵ photons/s, the optical cavity of super high reflectivity mirrors referred to as a supercavity [11]with CO₂ CW laser stored in it was implemented in the 10 m circumference storage ring. The electron source is a RF Gun and the injector to the storage ring is a microtron. The system configuration is shown in Fig.1 below. The machine parameters are listed in Table 1. The beta function and dispersion are shown in Fig2.

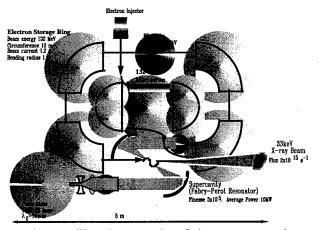


Figure 1. Fig.1 Laser cooler of electron storage ring schematic

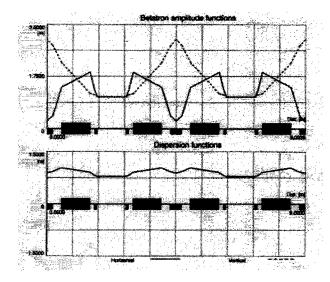


Figure 2: Beta function and dispersion of the laser cooler of electron storage ring.

4 CONDITIONS FOR LASER FEL

For a realization of FEL beam quality of the electron beam has to be very good. The necessary conditions for a single pass amplification are;

- (i) Beam Emittance, ε_n , smaller than or on the order of the wavelength λ ,
- (ii) Beam energy spread smaller than the FEL parameter ρ,
- (iii) Gain length shorter than the radiation Rayleigh range LR, (iv) Phase slip N_uλ_r, is much smaller that the bunch length σ..

Condition (i) can be satisfied by laser radiative cooling assuming that intra-beam scattering effect could be insignificant at this energy range.

Condition (ii) are done by cooler ring and magnetic chicane. It is argued that various effects such as non linearity in the compression and acceleration process,

space charge effects, transverse wake fields, coherent synchrotron radiation effects, longitudinal to transverse coupling, second order momentum compacti A supercavity can be made of high reflective mirrors with reflectivity of R=99.999. The finesse F of this optical resonator is,

$$F = \pi \sqrt{R}/(1-R) \tag{5}$$

The incident power builds up by factor/ π . To make spread over 20 mrad in beam size for large irradiation area for angiography, a single period of linear

Table 1: Parameters of the laser cooler storage ring of electron beam

SR X-ray parameters	
RF frequency	1500 MHz
photon energy	33keV
Peak RF voltage	126 kV
photon flux	10 ¹⁵ /s
energy aperture	1.1 %
natural spectral width	0.3 %
Quantum life time	1 hour
Electron beam parameters	
Beam radius at I.P.	100 µm
Beam energy	132 MeV
Laser parameters	
Beam current	1.2 A
Wavelength	10 µm
number of bunches	50
Peak power	1 GW
Circumference	10 m
Average power	10 MW
Bending radius	1 m
Spot radius at I.P.	100 µm
Energy loss per turn	30 eV
Damping time	155 ms
Equiv. energy spread	0.2 %
Equiv. norm. emittance	3.9x10 ⁻⁷ m.rad.
rms bunch length	4.9 mm

Table 2. Parameters of the laser cooler of electron beam

X-ray LASER FEL Angstrom region

Beta function at IP	1 cm
CO ₂ laser peak power	5 G Watt
В	365 Tesla
K	3.889
wavelength λ	5.8□□
$\lambda 4\pi$ 4.610	O-11
N	6.25x10°
bunch length before compression	5 mm
bunch length after compression	0.1 mm
$\mathbf{n}_{\mathbf{e}}$	$2X10^{25}$
plasma ang.freq.	1.5×10^{13}
laser ang. freq.	1.9x10 ¹⁴
FEL parameter p	0.003
momentum spread after compression	4x10 ⁻⁵
beam energy	132 MeV
absolute emittance	2.8x10 ⁻¹²
γ	264
Gain length L _G	1.1x10 ⁻⁴
Rayleigh length L _R	0.006

5 SUMMARY

A possibility of very compact X-ray laser induced FEL was presented. This scheme uses optical laser twice for single pass X-ray FEL in addition with a magnetic chicane. This scheme could be a compact and less expensive way to obtain hard X-ray laser

- [1] E,.Esary P. Sprangle and A.Ting, Nucl.Instr.Meth.A 331,545(1993)
- [2] W. Thomlinson et al., Rev.Sci.Instr.673,625(1992)
- [3] Wiedemen et al., Nuc.Instr.Meth. A 347,515(1994)
- [4] M. Torikoshi et al., Proc. of PAC97, (Vancouver), 820 (1997)
- [5] F.R. Arutyunian et al.: Phys. Lett. Vol.4, No.3, 176 (1963)
- [6] K -J .Kim, Nuc. Instr. Meth. A 341, 351(1994)
- [7] R.W. Schoenlein et al.; Science 274, 236(1996)
- [8] V.Telnov, Rev.Lett.74,2479(1995)
- [9] Z.Huang and R.D.Ruth, Phys. Rev. Lett.80, 976(1998)
- [10] K.Nakajima, et al.: EPAC98(Stockholm), 2371 (1998)
- [11] A.Moon and M.Fujita et al: JJAP, Vol.36, pp.L1446-L1448(1997)

THE PROPOSED ACCELERATOR FACILITY FOR LIGHT ION CANCER THERAPY IN HEIDELBERG

H. Eickhoff, D. Böhne, J. Debus, Th. Haberer, G. Kraft, M. Pavlovic GSI Darmstadt

1 INTRODUCTION

During the last four years GSI has developed a procedure for cancer treatment by means of the intensity controlled rasterscan-method. This method includes active variations of beam parameters during the treatment session and the integration of 'on-line' PET monitoring. Starting in 1997 several patients have been successfully treated within this GSI experimental cancer treatment program. The developments and experiences of this program accompanied by intensive discussions with the medical community led to a proposal for a hospital based light ion accelerator facility for the clinic in Heidelberg.

The main characteristics of this facility are the application of the rasterscan method with active intensity, energy-, and beamsize- variation in combination with the usage of isocentric light ion gantries. The accelerator is designed to accelerate both low LET ions (p, He) and high LET ions (C, O) to cover the specific medical requirements.

Major aspects of the design are influenced from the experiences of the GSI cancer treatment program; the requirements of this facility, however, exceed in many fields those of this GSI therapy program.

2 REQUIREMENTS

The basis of the accelerator concept has to satisfy the demands of the medical community for the treatment procedures. One of the key aspects of the proposed facility is the use of the intensity controlled rasterscan technique (Fig. 1), which is a novel treatment concept, developed at GSI and successfully applied within patient treatments of the GSI pilot project.

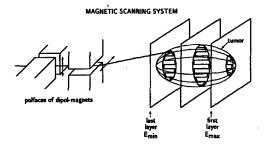


Fig. 1 Rasterscan-Method

The accelerated and slowly extracted beam enters 2 fast scanner magnets, that deflect the beam both in

horizontal and vertical direction to cover the lateral dimensions of the tumor. Ionization chambers in front of the patient measure the number of ions at a specific irradiation point and control the scanner excitation. Fast multiwire proportional counters detect the position and beam width at each scanning point. When a required dose limit has been reached the beam extraction is interrupted very fast (< 0.5 ms).

Whereas at presently existing therapy-dedicated protonand light-ion accelerators for cancer treatment the beamparameters are constant over the treatment interval, this method demands fast, active energy-variation to achieve different penetration depths and intensity-variation to minimize the treatment time [1].

The main requirements of the proposed facility were intensively discussed with radiotherapists and biophysicists and can be summarized as follows:

Table. 1: Therapy requirements

- intensity-controlled rasterscan method
- treatment both with low and high LET-ions
- relatively fast change of ion species
- wide range of particle intensities
- integration of isocentric gantries
- 3 treatment areas to treat a large number of patients
- ion-species : p, He, C, O
- ion-range (in water) : 20 300 mm
- ion-energy : 50 430 MeV/u
- extraction-time : 1 10 s
- beam-diameter : 4 10 mm (hor., vert.)
- intens. (ions/spill) : 1*10⁶ to 4*10¹⁰
 - (dependent. upon ion species)

3 LAYOUT OF THE ACCELERATOR FACILITY

Fig. 1 shows the cross section of ground floor of the building (about 70*60 m²), which gives an impression of the accelerator-sections, the position of the patients preparation areas, local control rooms and various laboratories. Additional space for housing the power supplies and further technical infrastructure is available at another floor of this building.

The following description mainly concentrates on a technical discussion of the various accelerator sections and their individual features.

a) Injector and low energy beamline

One significant medical requirement is the demand to change the ion species used for treatment (e.g. protons ond carbon ions) within less than 30 minutes; due to this specification the installation of two ECR sources is proposed, which permanently have to be in an operational state. The ECR source is chosen, as this type provides a very stable intensity over a long time without adjustment of the source parameters. The required particle currents between 80 μ A (for 160⁶⁺ and 1.2 mA (for p) are rather conservative; beam tests of this commercially available source indicate, that both the current and the requested beam emittance can easily be achieved.

Each source branch is equipped with a 90 degree analysing magnet for the definition of the requested ion charge state and the detection of contaminations, and a solenoid and quadrupole singlet for beam matching. The extraction voltage of the ECR-source is defined to 8 keV/u.

Both branches are combined by means of a switching magnet, which leads the beam to the low energy beam transport system (LEBT) up to the linac RFQ. The LEBT contains beside a matching quadrupole triplet, a macropulse chopper and a matching solenoid an rf-chopper-system to perform the requested intensity reduction up to 0.1% of the maximal ion intensity.

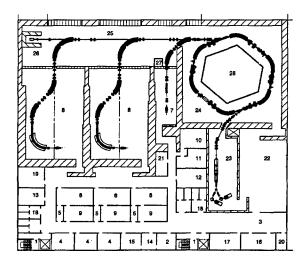


Fig. 2 Layout of the accelerator sections

b) Linac, Medium energy beam transport

A combination of RFQ and IH-linac structure with a total length of about 6 m is proposed to accelerate the ions up to 7 MeV/u. The RF-frequency of these structures is 216 MHz. The designed pulse length is 200 μ s, the repetition frequency 5 Hz. The normalized beam emittance is about 0.4 π mm mrad, the momentum spread 0.1%.

The medium energy beam transport consists of a stripping and a matching section to the synchrotron. In addition, for multiturn injection a chopper system is provided to match the pulse from the linac.

c) Synchrotron

For the synchrotron with a circumference of about 64 meters 6 bending magnets with a maximum flux density of 1.6 T and a doublet focusing structure are proposed. 6 long drift spaces are available for the installation of injection and extraction elements and the RF-cavity. After a 15 turn injection, corresponding to an injection time of 30 μ s, the acceleration takes place within 0.5 s. For slow extraction with variable extraction time between 1 and 10 s and multiple beam extraction at the same flat top the 'transverse knock out' method is proposed.

d) High energy beam transport

The high energy beam transport system leads the slowly extracted beam either to a beam dump or distributes it to three treatment places. Just after the synchrotron extraction section a fast deflecting magnet will prohibit the beam delivery in case of interlocks.

e) Treatment areas

In order to meet the demand for a patient flow of 1000 patients/year three treatment areas are foreseen. For the first area the beam will be delivered from a horizontal beam line, similar to that used at the GSI pilot project. The beam for the second and third treatment places will be delivered by a rotating beam transport system ('isocentric gantry'). All beam lines are equipped with horizontal and vertical scanning magnets and beam dignostic devices for the intensity controlled rasterscan. The integration of PET monitoring systems both in the horizontal and the gantry beam lines is proposed as well.

f) Gantry beam lines

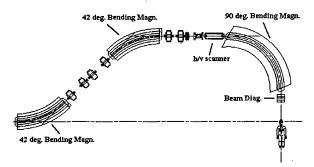


Fig. 3: Layout of the isocentric Gantry

A strong demand of the medical community is the installation of two gantry beamlines for irradiation angles between 0 and 360 degree. An isocentric gantry type with two 42 and one 90 degree bending magnets is proposed, in which the horizontal and vertical scanning magnets are located upstream before the last 90 degree deflection magnet in order to minimize the gantry-radius. The irraddiation field is 20 * 20 cm².

The total length of this gantry is about 20 m and the outer radius 6.3 m. In order to limit the concrete shielding

the counterweight of the mechanical rotator also serves as a radiation shielding.

A special ion optics is used which provides an achromatic beam transport to the treatment location independent from the gantry angle. In addition a constant beam diameter is achieved for different horizontal and vertical beam emittances.

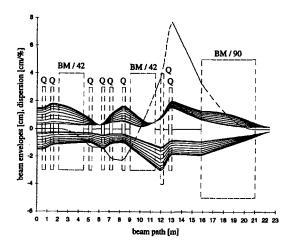


Fig. 4: Beam envelopes for gantry angles between 0 and 90 degree (ϵ_h / ϵ_h =0.5/5.0 π mm mrad)

(upper trace = hor., lower trace = vert. env. ---- = dispersion function)

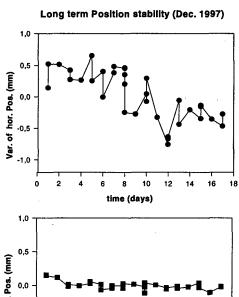
4 STATUS

To a certain extend the proposed projects benefits from the experiences that have been achieved within the GSI pilot therapy project.

- •The principles of the accelerator control based on the usage of approved settings, stored in nonvolatile memories will probably transferred. The demonstrated long term stability of the beam position (see Fig. 5) could be further improved with a moderate position feed back beam by means of the fast position monitors and the rasterscan-magnets.
- •The intensity controlled rastercan-technique has been approved within a large number of treatment fractions applied to patients. Despite the strong intensity modulation of the spill the requested dose uniformity could be reliably achieved.
- •The 'on-line' Positron-Emission Tomography (PET) has proved to be a valuable diagnostic tool for dose verification. The application of this method to the isocentric gantry is under investigation.
- •Most of the anticipated test procedures both at the accelerator and the treatment place have been evaluated.

At GSI for the proposed facility various ion optical design studies and first design studies of critical elements have been performed. These investigations concern all accelerator sections from the source to the treatment caves. Detailed calculations of the field homogenity for

the gantry 90 degree bending magnet have beeen done. Design criteria for this magnet were evaluated. In advance, dedicated studies of critical items (e.g. the gantry design) will be performed in collaboration between the GSI, the DKFZ, the Heidelberg Clinic and industries. Additional funding for the 'multifield irradiation technique' has been applied. [3] Within this application a test of the last gantry section with beam at GSI is proposed. First steps concerning the organization structures and the financing of this project have been undertaken.



0,5 - 0,0 - 0,5 - 1,0 0 2 4 6 8 10 12 14 16 18 time (days)

Fig. 5 Long-term position variations

It is planned to build the facility under the project leadership of the radiological clinic in Heidelberg with substantial support from industries. The know-how and the experiences of GSI shall be transferred to the industrial partners. The total project cost are assumed to be about 120 Mio DM. First patient treatments are scheduled around 2004/5 after an extensive commissioning phase of about 1 year.

- [1] J. Debus et al., 'Proposal for a dedicated ion beam facility for cancer therapy', 1998
- [2] H. Eickhoff et al, 'Accelerator Control For the GSI Cancer Therapy Project, EPAC 1998, 2348
- [3] J. Debus et al., HGF Strategy Fund Proposal Development of intensity controlled multifield-irradiation techniques for cancer therapy with ion beams', 1999

APPLICATIONS OF X-BAND TECHNOLOGY IN MEDICAL ACCELERATORS

S. M. HANNA⁺, Siemens Medical Systems-OCS, Concord, CA

Abstract

Most radiation therapy machines are based on microwave linear accelerators. The majority of medical accelerators use frequencies in the S-band range. Having a compact accelerator allows for a wide range of treatments. The size and weight of the accelerator is substantially reduced if a higher frequency is used. X-band frequencies are suitable for such applications. The X-band accelerator technology has been used in high-energy as well as industrial applications. In the radiation therapy field, it is already implemented in some machines. The Mobetron [1], an Intra-Operative Radiation Therapy (IORT) treatment system is one example. Another example is the Stereotactic Radiosurgery machine, the CyberKnife [2]. The compactness of these machines required the use of an X-band accelerator. The basis for choosing the X-band technology in some of the medical machines is analysed. A review of the exiting medical applications is included. We also discuss the availability of other X-band components in the machine, including high-power RF sources.

1 X-BAND ACCELERATOR TECHNOLOGY

X-band accelerator development has gained great momentum in the last ten years, motivated by the need for high-gradient accelerators for the future linear colliders in high-energy physics research [3]. Design of accelerator cells [4], manufacturing [5], and characterization technique [6] have been developed.

In the industrial [7] and medical [1,2] fields, there are obvious advantages for using frequencies higher than the S-band range that is prevalent in these applications. The dominant factor is the compactness of the accelerator with the attendant reduction in weight. Consequently, the linac motion can be precisely controlled. By implementing the X-band technology, one can use a shorter length for a given power to achieve a certain electron beam energy. The reasons for this are two-fold. First, the shunt impedance per unit length is higher than that of S-band. Second, the maximum permissible electric field strength is also higher. The frequency dependence of these accelerator parameters is listed in Table 1.

Table 1: Frequency Dependence of Accelerator
Parameters

Parameter	Frequency Dependence	
Shunt impedance per unit length (r)	f'^2	
Maximum permissible electric field strength	f'^2	
RF loss factor (Q)	$f^{\cdot I/2}$	
Power dissipation capability of accelerator structure	f^{-1}	

Certainly there are some trade-off factors to be considered with the use of X-band. These include the lower Q and lower power dissipation capability of the accelerator structure, as indicated in Table 1. These can be overcome by careful design of the cooling system. In addition, a better surface finish and tighter dimension tolerances are required.

2 MEDICAL APPLICATIONS

Currently, there are two different radiation therapy applications that use the X-band technology.

2.1 Inter-Operative Radiation Therapy

The Inter-Operative Radiation Therapy (IORT) technique basically refers to the delivery of radiation during an operation using an electron beam. This technique of radiation therapy has been proven to increase the survival rates in certain cancer cases. Conventional radiation therapy machines must be housed in special shielded rooms, requiring the patient to be moved from the operating room. A mobile radiation therapy machine, the Mobetron [1], engineered and developed by Intraop, has met the need for a self-shielded machine. Since the unit is mobile, it can be easily positioned in an operating room to treat cancerous growths with good precision during surgery, thus, increasing the effectiveness of radiation doses to tumors while reducing the dose to surrounding healthy tissue.

The design approach for the Mobetron exploits some of the unique advantages of using the X-band technology mentioned above. The Mobetron treatment head houses the X-band linac, the magnetron, the pulse transformer, RF loads, the circulator, and other RF circuitry.

^{*}Email: shanna@smsocs.com

The linac is composed of two colinear accelerator sections. The energy of the electron beam is changed by varying the power to the second section. This is done through a phasing technique using movable shorts driven by motors controlled by the energy control system. Thus, the Mobetron can deliver multiple electron energies, namely, 4 MeV, 6 MeV, 9 MeV, and 12 MeV at two dose rate settings (250 cGy/min and 1000 cGy/min). The electron beam exits the accelerator through a thin titanium vacuum window.

Siemens Medical Systems, Inc. – Oncology Care Systems (OCS), is manufacturing the Mobetron as well as marketing it in collaboration with Intraop Medical, Inc.

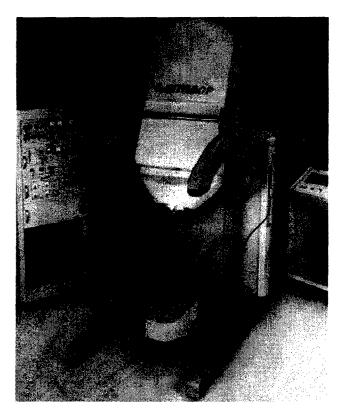


Figure 1: The Mobetron IORT system.

2.2 Stereotactic Radiosurgery

Another important application for the X-band technology is stereotactic radiosurgery. Accuray Oncology has developed the CyberKnife [2]. This machine uses an image-guided robotic system to precisely deliver an X-ray beam to focal lesions. It integrates treatment planning, imaging, and delivery components, all of which are controlled by a Workstation. The CyberKnife uses a compact X-band 6MeV Linac operating at 9.3GHz and weighing 285 lbs. The relatively lightweight Linac makes it possible for the robotic arm carrying it to be accurately positioned. Fig.2 shows the CyberKnife [8].



Figure 2: The CyberKnife stereotactic radiotherapy system.

3 HIGH POWER MICROWAVE SOURCES

The S-band has been the prevailing frequency range for linacs in medical and industrial applications. This is mainly attributed to the availability of high power microwave sources in this frequency range. Recently there have been efforts in the area of development for the X-band sources.

The RF high-power source for both the Mobetron and the CyberKnife linacs is the 1.5 MW pulsed magnetron (PM-1100X). The California Tube Laboratory, Inc, builds this tunable magnetron; it is shown in Fig. 3. Other efforts for developing X-band sources include the tunable 1.5MW X-band currently in development at EEV and the 4 MW klystron by Mitsubishi [9].

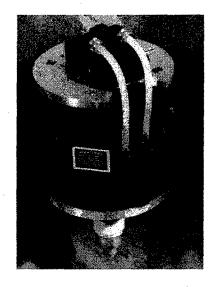


Figure 3: The CTL 1.5 MW X-band magnetron.

4 DISCUSSION

Recent X-band research and development for linear collider projects have been providing an impetus for the development of X-band accelerators and RF sources. Klystrons having output power of 50 MW and higher have been developed at SLAC. However, for the medical linacs, the need still exists for the development of X-band sources of a few MW of peak power.

- M. L. Meurk et al., "The Mobetron: A New Concept for Intraoperative Radiotherapy", 6th International IORT Symposium, San Francisco, CA (1996).
- [2] S. G. Chenery et al., "The CyberKnife: Beta System Description and Initial Clinical Results", Journal of Radiosurgery, Vol. 1, No.4, (1998).
- [3] J. W. Wang et al. "Accelerator Structures R&D for Linear Colliders", This Conference (1999).
- [4] J. Klingmann et al., "Fabrication of DDS-3, an 11.4 GHz Damped-Detuned Structure", This Conference (1999).
- [5] Z. Li, "RDDS Cell Design and Optimisation for the NLC Linac", This Conference (1999).
- [6] S.M. Hanna et al., "Development of Characterisation Techniques for X-Band Accelerator Structures", Proc. Of the 1997 IEEE PAC (1997).
- [7] R. G. Schonberg et al., "Portable X-Band Linear Accelerator System", IEEE Trans. On Nuc. Sc., Vol. NS-32, No. 5 (1985).
- [8] W. T. Main, Private Communication.
- [9] K. Hayashi et al., "X-band High Power Pulsed Klystron", Proc. Of the 1988 Linear Accelerator Conf., pp 562-564 (1988).

DESIGN OF A BEAM TRANSPORT SYSTEM FOR A PROTON RADIATION THERAPY FACILITY

W.P. Jones and G.P.A. Berg, Indiana University Cyclotron Facility, Bloomington, IN 47408

Abstract

A new beam transport system has been designed to bring the 210 MeV proton beam from the Indiana University Cyclotron to four proton therapy treatment rooms. The main trunk line will be achromatic and employ a fast beam splitting system to allow treatments simultaneously in different treatment areas. To enhance flexibility of operation, each treatment room will have its own energy degrader and energy selection system. There will be two treatment rooms with a fixed horizontal beam line. The first will be an upgrade to our current eye treatment facility and the second will be designed for head, neck, and brain treatments including stereotactic radiosurgery. In addition, there will be two rooms with iso-centric gantries for more complex multi-port treatments.

1 INTRODUCTION

The Indiana University Cyclotron Facility ("IUCF") is planning a conversion of the space formerly used for nuclear physics experiments into treatment rooms for proton radiation therapy treatments under the auspices of the Midwest Proton Radiation Institute ("MPRI"), an organization being developed by IUCF in conjunction with the Advanced Research Technology Institute ("ARTI") at Indiana University [1]. The 210 MeV cyclotron at IUCF will be used to provide protons to the treatment rooms. In addition there will be an experimental room for biological and radiation effects studies. This paper will describe the beam transport system being planned for this facility.

2 BEAM LINE OVERVIEW

The beam line has been designed to provide beams of easily adjusted energy and intensity to each of the treatment rooms in time slices on the order of hundreds of milliseconds. A portion of the full energy beam will be carried to a remote beam dump to aid in the control and stabilization of the cyclotron beam. The emittance of the full energy beam from the cyclotron is small ($< 3 \pi$ mm-mr). The energy degradation process significantly increases the beam emittance and the energy selection systems and gantries have been designed with an acceptance of 30 π mm-mr representing a compromise between intensity loss and magnet size and cost. The design has focussed on minimizing the number of new magnet designs and will use existing IUCF magnets wherever that is consistent with the clinical design requirements. The layout of the beam line is illustrated in Fig. 1.

2.1 Beam Achromat Section

Currently the cyclotron beam passes through a 45° dipole magnet and enters a beam corridor which leads to several experimental rooms. The current beam line has a large momentum dispersion to meet the nuclear physics experimental conditions. This initial section has been redesigned with the addition of a pair of opposed 30° dipoles. This section then can be tuned so that both spatial and angular momentum dispersions of the beam will be zero everywhere in the trunk line leading to the treatment rooms. This ion-optical condition reduces horizontal beam instabilities due to movements caused by momentum changes of the cyclotron beam.

2.2 Beam Trunk Line and Splitting Systems

Each treatment room will have its own local energy degrader system and as a consequence the trunk line will operate at a fixed energy and existing quadrupole magnets with solid iron returns can be used. The cyclotron beam with a maximum intensity of about 1.0 μ A will be transported the length of the trunk beam line into the main beam dump at the end of the system. Distribution of beam into the five rooms, R1-R5, will be done using a fast beam splitting system at the entrance to each room.

The splitter system to be used will be a modified (and simplified) version of those currently used in routine operations for the IUCF beam lines. Each splitting system will consist of a fast kicker dipole with a rise time of about 1 ms and a Lambertson septum magnet and will be installed in the drift space in the trunk line at the entrance to each area. When no beam is being requested from a treatment area the full beam will be transported down the trunk beam line into the main beam dump. When one treatment room requests beam, the appropriate kicker dipole will be activated for the duration of the request and beam will be kicked down into the Lambertson dipole gap and bent 12° horizontally into the energy selection system of the treatment room.

The present proposal is to have a 4 Hz cycle divided into four packets: treatment slot A (100 ms), treatment slot B (100 ms), radiation research (25 ms), and beam diagnostics (25 ms). Each time slot will be reserved for their dedicated purpose. The first treatment room to request beam will have the 100 ms of treatment slot A reserved for their sole use. If a reduced dose rate is required, the time slot can be reduced to a minimum of about 10 ms (set by the magnet rise and fall times). Further beam intensity reduction can be accomplished by the beam intensity modulation systems presently in use at the cyclotron. This consists of electrostatic quadrupoles in the low energy beam lines and allows modulation of the beam intensity on a time scale faster than

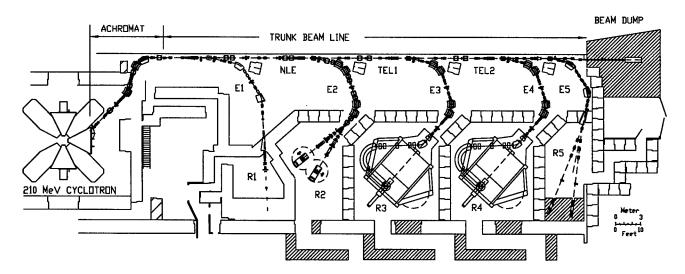


Figure 1: Layout of beam transport system and treatment rooms for the Midwest Proton Radiation Institute

the 1 ms of the splitter system. A second treatment room can independently request beam during time slot B of the 4 Hz cycle.

2.3 Non-Linear Expansion Section

For medical treatment the dose uniformity has to be constant to about \pm 2% over the treatment region. Cyclotron beams do not meet this requirement and beam spreading systems are necessary to prepare a usable beam distribution. The double scattering beam spreading system has the disadvantage of reducing the beam energy. Therefore the primary beam needs to have a significantly higher energy than that required at the treatment location.

Another technique for generating large area uniform beam distributions is using multipole magnets to alter the beam phase space as described by [2],[3], and [4]. Their designs provide for uniform beam distributions over areas of several hundred square centimeters using only static magnetic elements. This feature would provide significant advantages in terms of control, diagnostics, and operational flexibility in a radiation therapy setting. The section of beam line (NLE) between the first two splitters has been designed to allow for the possibility of incorporating such a system, by inserting multipole magnets at two locations: one where there is a horizontal waist and a large vertical beam width and a second where the horizontal and vertical conditions are interchanged. A preliminary design study of a non-linear expansion system has been done [5] to determine whether such a system is feasible using our energy selection systems and basic beam line design. At this point, it appears to be feasible to incorporate such a system in our design. The beam telescope systems after each splitter magnet do not change the modified phase space properties and allow a large area beam to be delivered to each treatment area if desired. What remains to be done is the determination of multipole requirements needed to match to both our energy selection system as it has evolved and the

isocentric gantries when their design is complete. Development efforts will also be required to guarantee meeting clinical dosage uniformity specifications.

2.4 Energy Selection System

Energy selection systems (E1-E5) will be installed after each kicker/Lambertson magnet combination at the entrance to each treatment room. The 210 MeV proton beam will pass through a degrader appropriate to the treatment energy and then enter the momentum analysis system. The fixed horizontal line and the two gantries (E2, E3, and E4) require fast and reproducible energy changes and so will be equipped with an achromatic energy selection system using laminated magnets. Since the modified eye line (E1) will operate at a fixed energy it will use existing solid iron magnets. Similarly, the research and radiation effects line (E5) will utilize existing magnets since it does not require rapid energy changes.

The energy selection systems (E2, E3, and E4) for the three new treatment rooms (R2, R3, and R4) will be identical. A variable thickness degrader will be followed by a magnet system consisting of four 30° dipole magnets and eight quadrupole magnets (QQDDQQQDDQQ). A horizontal slit system in the center of the system will provide momentum analysis of the beam. The resolving power of the system $p/\Delta p = R16/(2x_0*R11) = 420$ for a horizontal object size of $2x_0 = 3$ mm at the degrader, which provides a maximum energy spread of less than ± 0.5 MeV at 210 MeV. This resolving power is necessary to meet the medical distal fall-off requirement. The system will deliver an achromatic beam at the entrance to the gantries and the fixed beam line nozzles. The beam will be at a double waist (vertically and horizontally identical) at those locations.

2.5 Beam Telescopic Sections

The beam line sections (TEL1 and TEL2) connecting the splitter magnets leading to treatment rooms R2 and R3,

and connecting the magnets leading to rooms R3 and R4, have been designed to have unit transfer matrices so that the beam properties at the entrance to each of the energy selection systems will be identical and the three new energy selection systems will be identical.

3 TREATMENT ROOMS

The layout of the facility shows four treatment rooms R1 ... R4 and one experimental area R5 for biological and radiation effects studies. The first treatment area R1 closest to the cyclotron is a fixed horizontal beam designed for eye treatment. This area is already in operation and presently used for a study of age-related macular degeneration.

The second treatment room R2 accommodates two fixed beam lines which will be configured for head, neck and brain treatments. Also stereotactic radiosurgery will be possible in this room. For more complex treatments both treatment areas R3 and R4 will be equipped with isocentric gantries.

For optimal use of the beam of the cyclotron another room R5 at the end of the existing building will allow radiation effects in two fixed beam lines. Also biological studies will be possible in this room.

3.1 Beam Spreading Systems

In order to carry out large area irradiations, the beam line has been designed to be compatible with double scattering systems, magnetic wobbling systems, and eventually with a full three dimensional scanning system. The double scattering system is simplest and will be used wherever the limits imposed by additional energy and flux loss allow. Magnetic wobblers eliminate those problems but add some complexities in both dosage control and verification. However, those problems will require solution in order to develop a system capable of providing three dimensional intensity modulated treatments. It is also hoped that the static non-linear expansion system described earlier can be developed to provide irradiations with clinically acceptable uniformity.

3.2 Preliminary Gantry Design

We have concluded that a single plane gantry will better satisfy our requirements than either a corkscrew gantry [6] or a gantry of the type in use at PSI [7].

A single plane gantry consists of two dipole magnets which bend the beam first 45° away from the beam axis and 135° back to the isocenter, perpendicular to the original beam direction. Five entrance quadrupoles and five quadrupoles between the dipoles are needed to guide the beam of $30~\pi$ mm-mr emittance in both transverse directions through the narrow dipole gaps and to meet achromaticity and other beam requirements at the isocenter. Since the gantry will be used at arbitrary azimuthal angles it is important to provide an achromatic beam with identical emittances at the gantry entrance. The beam at the exit

of the energy selection systems meets those requirements and is further shaped by the entrance quadrupoles to meet the aperture restrictions of the gantries.

A single plane gantry is presently commercially available [8] and has been schematically shown in figure 1 with the addition of a fifth entrance quadrupole which improves the matching to our energy selection system.

4 MAGNET DESIGN

The new beam line requires the design of a new 30° dipole magnet. Two of these laminated magnets will be used in the beam achromat section preparing the beam for the trunk line and four of the dipoles will be used in each of the energy selection systems. No new quadrupole magnet designs will be required. Either existing beam line quadrupoles will be used (in the trunk line) or copies of one of the two types of quadrupoles used in IUCF's electron-cooled storage ring will be used. These laminated quadrupoles will be used in the energy selection systems and at a few locations in the trunk line where stronger fields or larger apertures (10 cm diameter) are required.

- [1] J. Cameron et al., to be published in the Proceedings of the 15th International Conference on the Application of Accelerators in Research and Industry.
- [2] E. Kashy and B. Sherrill, Nucl. Instr. and Meth. B26 (1987) 610.
- [3] B. Sherril et al., Nucl. Instr. and Meth. B40/41 (1989) 1004.
- [4] A. Jason, B. Blind, and K. Halbach, Proceedings of the 1997 Particle Accelerator Conference, p3782.
- [5] M. Schulze, private communication.
- [6] Koehler, A. M., Proc. 5th PTCOG Meeting, April 1987, Lawrence Berkeley Report LBL-22962 pp. 147-158.
- [7] Pedroni, E. and Enge, H., Med. Biol. Eng. Comp. 33 (1995) 271-277.
- [8] Y. Jongen et al., Nucl. Instr. and Meth. B79 (1993) 881.

CONTROL OF THE SLOW EXTRACTION PROCESS IN A DEDICATED PROTON SYNCHROTRON FOR HADRON THERAPY

A.Yu.Molodozhentsev[#], G.I.Sidorov, JINR, Russia

Abstract

The ring design of the synchrotron [1] for cancer treatment, based on the third-order resonant extraction, was been performed to meet the special medical requirements. The uniformity of the slow extracted beam from the proton synchrotron is the main requirement on the beam quality determined by the medical application. The smooth extraction during at least 400 msec should be realized for the 'raster' scanning of tumours. Control of the slow extraction over the whole spill time is discussed in this report. To keep all lattice functions of the ring constant during the extraction a slow moving of the accelerated particles into the resonance can be used. To reduce a degradation of the uniformity of the extracted beam by ripples from the power converters of the magnetic elements, the RF empty-bucket channeling method [2] should be utilized. This method allows reduce the ripple influence during slow extraction. Both methods are analyzed to control the slow extraction for the dedicated proton synchrotron. Main parameters of the betatron core for this machine are determined. To realize the 'empty-bucket' technique, the RF system of the synchrotron can be used with the maximum voltage at least 1.5 kV. Influence of the high-frequency ripple on the multiplying factor and the duty factor of the spill is studied.

1 INTRODUCTION

A conventional synchrotron seems to be the most acceptable accelerator for the 'active scanning' of tumours. The dedicated proton synchrotron should be designed to meet specific medical requirements on the beam quality, in particular, the spill homogeneity over full extraction period. The 'active scanning' technique needs in the slow extraction of the accelerated particles to perform on-line dosimetry at the patient and to switch the beam on and off according to the dose required. This directly determines the performance of the machine [1]. The customised lattice of the synchrotron has been developed to apply the Hardt condition. To perform the ultra-slow extraction, the moving the coasting beam into the resonance region is chosen. This method has the great advantage of leaving the optical parameters of the machine constant during the extraction. In particular, the beam is accelerated towards the stationary resonance by a betatron core [3], installed

in the dispersion-free drift space of the ring. The uniformity of the slow-extracted beam is degraded by ripples from the power supply of the magnetic elements of the synchrotron. Making the beam particle cross more quickly from the stable to the unstable region can reduce this effect. The RF-bucket channeling seems to be a good candidate for compensating low frequency ripples (<1MHz) in spills of the order of one second. The combination of these two accelerations ('smooth' and 'fast' accelerations) should guarantee the required beam quality for the medical application. Fig.1 illustrates this method of control of the slow extraction process.

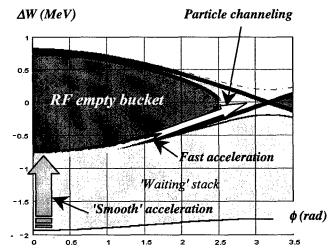


Figure 1: Illustration of the technique of moving the accelerated particles into the unstable region.

During the extraction (400 msec) the betatron core 'drives' the 'waiting stack' slowly into the resonance (changing $\Delta p/p_0$) to provide smooth acceleration of the particles with the momentum spread from the value of (-0.005) till (-0.001) [1]. The maximum deviation of the momentum from particle the resonance $(\Delta p/p_0 = -0.005)$ is chosen to avoid crossing of dangerous high-order resonance lines during the extraction. Changing the momentum, the particles will be pushed into the RF channel and will be accelerated rapidly. The particle velocity in this channel is increased, but the density is reduced. Then the particle flux is constant that determines the required quality of the extracted proton beam. To realize this scenario, it is necessary to determine the main parameters of the betatron core with the power supply and adapt the RF-system [4] for the 'empty' bucket

[#] Email: molod@se.jinr.ru

technique. Main parameters of the accelerated proton beam are collected in Table 1.

Table 1: Parameters of the dedicated proton machine.

Circumference	m	41
Accelerated particles		proton
Number of circulating particles		6.25×10 ¹⁰
Slow extraction scheme		Third-integer
L		resonance
Maximum kinetic extraction	MeV	220
energy, E_c		
β at E_c		0.586361
γ at E_c		1.23449
Momentum at E_c	MeV/c	679.123
Revolution period at E_c	μsec	0.2334
Beam intensity at E_c	mA	41.13
Magnetic rigidity at E_c	T⋅m	2.265
$(\Delta p/p)_{\text{full}}$ of the beam at E_c	%	0.4
Repetition rate	Hz	1
Typical cycle:		
Injection	Ms	50
Acceleration	}	200
Extraction flat top		500 (400)
Fall	<u> </u>	250

2 BETATRON CORE

To determine the main parameters of the betatron core and of the power supply, the required calculations have been made for the *Cockerill steel*. The required total magnetic flux variation needed to provide the momentum variation of 0.004 is equal to 0.371 Weber for the developed synchrotron. To get this flux, the magnetic field should be changed from B_{max} till $B_{min} = -B_{max}$. The maximum average magnetic field $< B >_{max}$ inside the betatron core should be equal to 1.2 Tesla to avoid the steel saturation. The core length should be 0.6 meter to be installed in the ring. The transverse dimensions of the betatron core are as follows: $r_{in}=0.120$ m, $r_{ext}=0.378$ m. Some special function of the current variation during the half of the whole cycle IN(t) has been defined (Fig.2) to meet the requirement $(d\Phi/dt = Constant)$.

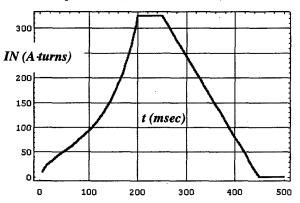


Figure 2: Current variation during a half of the time cycle.

The main characteristics of the betatron core and the power supply system are collected in Tables 2-3. It is necessary to underline that the extraction energy should be changed step by step from a maximum value till a minimum one to treat tumours.

Table 2: Main parameters of the betatron core

Required flux variation during extraction	Wb	0.371
Length	m	0.60
Maximum average magnetic field in yoke	T	1.2
Internal radius	m	0.12
External radius	m	0.378
Area of the section perpendicular to the magnetic field lines	m ²	0.155
Lamination thickness	mm	0.5
Steel density	kg/m³	7870
Steel mass	kg	1'890

Table 3: Main parameters of the power supply

Number of turns of the coil		10
Section of the wire	mm ²	10
Length of the wire	m	17.2
Copper resistivity at 60 °C	Ω·m	2.035×10 ⁻⁸
Maximum value of inductance	mΗ	100.93
Minimum value of inductance	mH _	4.15
Maximum current density	A/mm ²	3.25
Total coil resistance	mΩ	48.38
(copper + eddy current)		(35+13.38)
Total resistive power	W	14.4
Maximum absolute value of	V	32
voltage		

To evaluate the influence of the high-frequency ripple of the power supply, it is necessary to consider the voltage applied to the coil in the following $V_{coil} = V_0 + V \cdot cos(\omega t)$. The eddy currents in the betatron core prove a smoothing effect in the case of the highfrequency ripple. Increasing of the lamination thickness can reduce the current ripple. The present choice of laminations of 0.5 mm gives a time constant of about 8.3 msec. Then for the ripple voltage of the order of 3.5×10^{-5} (or 0.001 mV) at a frequency of 600 Hz the resulting current ripple is of the order of 3.3×10^{-6} A. This high-frequency current ripple is by 100 times smaller than the low-frequency component. Increasing the lamination thickness one can increase the eddy current time constant and the smoothing of the magnetic field ripples. But in this case the power dissipation will be bigger. The optimization of the power supply and the lamination thickness should be performed before the betatron core is developed for the dedicated proton synchrotron.

3 RF-CHANELLING

As was mentioned above, ripples from the power converters of the magnetic elements and the power supply of the betatron core degrade the uniformity of the slow-extracted beam from the synchrotron. The empty buckets cause obstacles for particle motion in the longitudinal phase-plane and create the channel for these particles. Using the betatron core the beam is pushed into this channel 'smoothly'. In this channel dN/dQ is reduced, and dQ/dt increased.

The parameters of the RF bucket are determined by the process of extraction. The RF frequency should be equal to the revolution frequency to keep the particle energy constant at the synchronous phase. The 'resonance' energy of the particles depends on their betatron amplitude: the higher betatron amplitude - the lower the 'resonance' energy. To get a high multiplying factor for all the extracted particles, the RF empty bucket should be located properly with the required bucket height.

To create the channel between the RF empty buckets, the reference phase should be a non-zero value, which can be obtained from the following condition. The energy change in the bucket should be compensated by the changes in the machine that are caused by the betatron smooth acceleration. From this relation of the main machine parameters it is possible to get a definition of the required phase of the RF system:

$$|\Gamma| = |\sin\phi_0| = \frac{\Pi_{ring}}{V_m} (B\rho) \frac{(\Delta p / p_0)}{T_{spill}} . \tag{1}$$

The RF empty bucket should be positioned so to get an improvement for all the betatron amplitude. The determined beam parameters require the 'waiting stack' to be located below the resonance energy. To study the ripple influence, the multiplying factor (K) and the duty factor (S) can be written in the following form:

$$K(\Delta E, \omega) = 1 + \frac{\cos[\phi_2(\Delta E)] - \cos[\phi_1(\Delta E)]}{[\phi_2(\Delta E) - \phi_1(\Delta E)] \cdot \left(\frac{\Pi_{ring}}{qV_m}\right) p_0 \cdot |\psi_0 + \omega \alpha_R \cos(\omega t)|}, \tag{2}$$

$$\Im(\Delta E, \omega) = \frac{1}{1 + \frac{1}{2K^2(\Delta E, \omega)} \left(\frac{\dot{p}_R}{\dot{p}_0}\right)^2} , \qquad (3)$$

where $v_0 = (\Delta p/p_0)/T_{spill}$, and $\alpha_R = PR\omega/p_0$

The function $K(\Delta E)$ for some values of the RF voltage (1000 V, 1600 V, 1800 V) is shown in Fig.3. The reference phase of the RF system for $V_m=1600$ V is equal to $\Gamma=5.813\times10^{-4}$ ($\phi_0=-0.033$ gedree).

The RF-empty bucket technique becomes less effective in the case of the high-frequency (ω >1000 Hz) ripple (Figure 3). Another specific feature of this method is that particles are extracted in a small interval of the RF

phase $(\Delta\phi)$. This results in modulation of the spill at the high harmonics of the RF system (few MHz). Nevertheless, for the medical machine the slow extraction process, the physical spot size and the integration time average this spill modulation in the on-line dosimetry system.

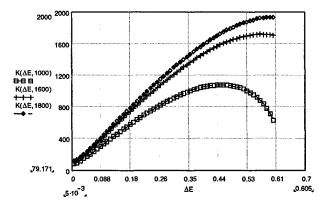


Figure 3: K-factor as a function of ΔE for different values of V_m (1000kV, 1600 kV, 1800 kV).

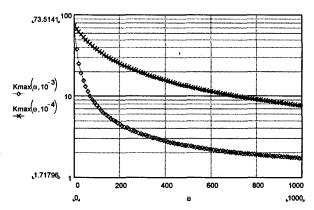


Figure 4: K-factor as a function of the ripple frequency for different values of α_R (10⁻³, 10⁻⁴).

4 CONCLUSION

Combination of the 'smooth' and 'fast' acceleration during the long extraction spill for the medical proton synchrotron has been studied. For the RF-channeling of the 'fast' acceleration of the extracted particles the RF system of the machine can be used.

We wish to thank Ph.Bryant, Ch.Steinbach and S.Rossi (PIMMS, CERN) for helpful discussions.

- [1] A.Molodozhentsev et al., "Design of dedicated proton synchrotron for the Prague Radiation Oncology Centre", in Proc. of the EPAC'98 Conference, Stockholm, Sweden.
- [2] R.Cappi, Ch.Steibach, CERN/PS/OP 81-10
- [3] L.Badano, S.Rossi, CERN-PS-97-019-DI, Geneva, 1997
- [4] A.Molodozhentsev, G.Sidorov et al., "RF system design of proton synchrotron for hadron therapy", JINR report, E9-98-259.

MUONS VERSUS HADRONS FOR RADIOTHERAPY *

N. V. Mokhov[†], and A. Van Ginneken, FNAL, Batavia, IL

Abstract

Intense low energy muon beams - as part of a muon collider complex - may become available for use in radiotherapy. It is of interest to compare their effectiveness in this application with that of hadron beams in a setting where processes common to these beams are treated exactly alike. Detailed simulations of physics processes for muon, proton, antiproton, neutron, kaon and pion beams stopping in various media have been performed using the MARS code with newly developed weighted algorithms. Special attention is paid to μ^- , π^- , and \bar{p} capture on light nuclei. Calculated distributions of energy deposition and dose equivalent due to processes involving primary beams and generated secondaries are presented for a human tissue-equivalent phantom (TEP). The important ratio of dose delivered to healthy tissue vs dose to tumor is examined within this model. The possibility of introducing heavier elements into the tumor to increase capture of stopped μ^- is briefly explored.

1 INTRODUCTION

Facilities needed for a muon collider[1] would provide an unprecedented variety of intense hadron and muon beams in an energy range well suited for radiotherapy. Hadron beams have been shown to offer certain advantages in cancer treatment compared to conventional photon radiotherapy[2]. To explore the potential of beams available at a muon collider, we have developed the coding necessary to simulate the detailed dose distributions associated with these beams. A large part of this effort concerns the processes occurring when particles are stopped. First results show that such beams can be used successfully in radiotherapy. Comparison of the effectiveness of various beams with each other and with simulations may offer valuable insight into this type of cancer treatment.

2 STOPPED HADRONS AND MUONS

A careful treatment of processes near and below the Coulomb barrier in hadron and muon transport has been implemented in MARS (stopping by ionization losses vs nuclear interaction vs decay).

2.1 Pions

A stopping π^+ decays into μ^+ of 4.1 MeV plus a neutrino while a π^- attaches to a nucleus (via a modified Fermi-

Teller law). While cascading down the atomic energy levels the pion is captured predominantly from a high orbit thus only a few low energy photons are emitted (which may be neglected here). The hadronic interaction of the stopped π^- is treated using the Cascade-Exciton Model [4] with a few modifications. When hydrogen is the target it is assumed there is a 60% probability for charge exchange $(\pi^- p \rightarrow \pi^0 n)$ whereupon the π^0 decays into two photons of 68.9 MeV each and the neutron acquires a small (0.4 MeV) kinetic energy. The remaining 40% of stopped π^- in hydrogen interact via radiative capture: $\pi^-p \rightarrow$ $n\gamma$. Here the photon acquires 129.4 MeV and the neutron 8.9 MeV kinetic energy. Other nuclides have a much smaller probability for radiative capture (1-2%) which is taken into account in competition with the non-radiative type as simulated by the CEM95 code. The photon energy is chosen from an empirical fit to experiment while the remainder is deposited as excitation energy.

2.2 Muons

A stopping μ^+ always decays into $e\nu\overline{\nu}$ while a μ^- attaches itself to a nucleus. When a μ^- stops in a compound or mixture one first decides to which nucleus the μ^- attaches (modified Fermi-Teller law). Following attachment the muon may still decay as decided by comparing capture and decay lifetimes of which the latter is favored for light nuclei (Z \leq 11). A captured μ^- then cascades down to the ground state of the muonic atom emitting photons along with some Auger electrons, all of which is simulated using approximate fits to the atomic energy levels. In hydrogen μ^- capture always produces a 5.1 MeV neutron via inverse β -decay. In complex nuclei the giant dipole resonance plays a role and results in an 'evaporation'-type neutron spectrum with one or more resonances superimposed. In addition smaller numbers of evaporation-type charged particles and photons may be emitted.

2.3 Antiprotons

Stopped \overline{p} attach to nuclei in the same way as π^- or μ^- . Annihilation at rest is assumed to produce only pions, neglecting some of the rarer modes involving strange particles. Charges of produced pions are slightly skewed towards π^- in view of the 'brought in' negative charge. Pion momenta are chosen from an inclusive distribution loosely based on experiment. The energy weighted distribution is normalized to twice the nucleon mass which predicts a multiplicity of 4.3—close to observation. In a complex nucleus the annihilation is treated as though it occurs on free nucleon except that each pion produced by the annihilation process

^{*} Work supported by the Universities Research Association, Inc., under contract DE-AC02-76CH00300 with the U. S. Department of Energy.

[†] Email: mokhov@fnal.gov

is given a 50% probability to interact within the nucleus. This shortcut attempts to include—at least qualitatively—participation by the constituent nucleons.

Total cross sections for $\overline{p}A$ in flight are estimated from geometrical considerations and from $\sigma_{\overline{p}p}$, $\sigma_{\overline{p}n}$, σ_{pp} , and σ_{pn} data. Annihilation in flight uses the same (Lorentz transformed) inclusive pion distribution as annihilation at rest. Above 0.1 GeV/c a small $\overline{p}p \to \overline{n}n$ component is included. Nuclear target effects are again approximated by allowing some re-interaction of emerging particles in the same nucleus. Quasi-elastic events of \overline{p} , \overline{n} with target nucleons rely on MARS algorithms for pA and nA but with the fastest emerging nucleon identified as its antiparticle.

3 DOSE DISTRIBUTIONS

A few selected results on dose delivered to the TEP are presented. For lack of space these are restricted to absorbed dose [5]. To facilitate inter-comparison, the beam energy for each type of particle is chosen to have a range of 15 cm in tissue: 147.2 MeV for protons, 68.3 MeV for pions and 61.8 MeV for muons. Each beam is uniformly distributed over $-0.5 \le x,y \le 0.5$ cm and is incident normally on a 30 cm slab TEP. A 70 MeV neutron beam is included for a comparison. Fig. 1 shows the absorbed energy as a function of depth for each beam. Isodose contours for absorbed dose produced by the p, π^- , and μ^- beams are presented in Fig. 2. In Fig. 3 the laterally integrated dose due to π^- and μ^- beams of the above energy is analyzed into its main contributing mechanisms. In both cases ionization losses are the main contribution up to and including the Bragg peak. For π^- there is comparable contribution near the peak from high-dE/dx charged particles associated with capture. Decay of the pions results in muons depositing 3.17 and 0.49 MeV for π^+ and π^- while neutrinos carry away 60.2 and 0.49 MeV, respectively. For μ^- the second largest dose contribution is due to electrons from μ decay and the showers induced by them.

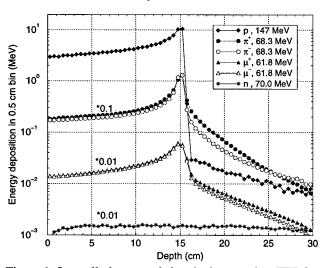


Figure 1: Laterally integrated absorbed energy in a TEP for proton, pion, muon and neutron 1×1 cm beams.

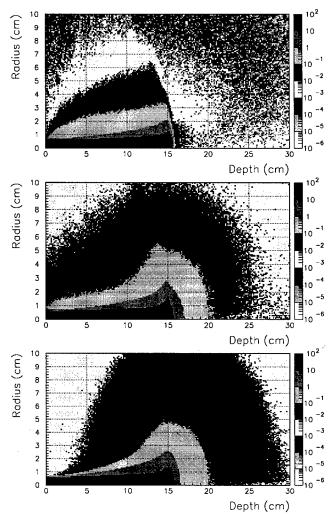


Figure 2: Absorbed isodose contours (nrad per incident particle) in a TEP for 147.2 MeV p (top), 68.3 MeV π^- (middle) and 61.8 MeV μ^- 1×1 cm beams.

As a rough measure of effectiveness of the various particle beams one may compare dose delivered at entrance with that at the peak. The entrance dose can be regarded as a general proxy for dose delivered to healthy tissue andin addition—is of particular interest in connection with the 'skin sparing effect' [2]. In this regard it makes sense to compare the ratio of peak absorbed dose, as a measure of radiotherapeutic effectiveness, to entrance dose equivalent as a measure of damage to healthy tissue (and in particular to the skin). This comparison is shown in Table 1 for doses averaged over Δr about the beam axis and over a depth of Δz near the peak for two cases: (1) $\Delta r = \Delta z = 0.5$ cm and (2) $\Delta r = \Delta z = 1.5$ cm. These can be thought to represent tumors with volume of 0.39 and 10.6 cm³, respectively. It is seen that by this measure π^- are most effective although, except for neutrons, the other beams come close—particularly for the larger region.

A stopping μ^- attaches more readily to a heavy nucleus than to a light one—such as found in tissue. To exploit this one might inject a heavy element or compound, in a slurry or solution, into the tumor region prior to irradiation. Such

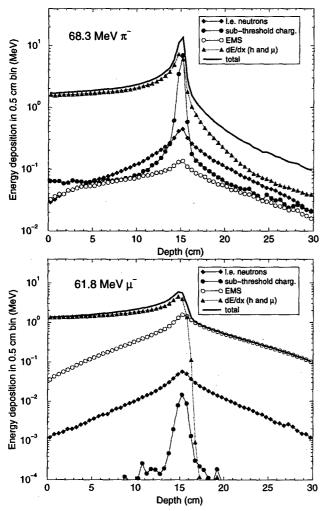


Figure 3: Laterally integrated absorbed energy and its components for 68.3 MeV π^- (top) and 61.8 MeV μ^- (bottom).

an agent must be chosen with some care not only with regard to its effectiveness in delivering a larger dose but also to its toxicity, residual radioactivity produced, capability for removal after irradiation, etc. To obtain a preliminary indication we tried a BaI_2 solution of a density 1.67 g/cm³, present in a 1.5 cm region around the dose peak. Fig. 4 shows that peak dose increases by about 30%. This strategy would have much less effect for π^- where capture is assured even for light nuclei.

Table 1: Peak absorbed dose to entrance dose equivalent

Case	p	π^+	π^-	μ^+	μ^-	n
1	1.31	1.00	1.42	0.73	0.71	0.08
2	2.03	2.55	2.97	2.52	2.49	0.12

4 CONCLUSIONS

The various beams available in connection with a muon collider might be of considerable interest to radiotherapy. En-

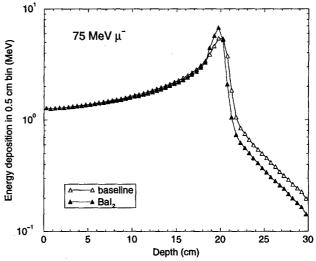


Figure 4: Laterally integrated absorbed dose for a 75 MeV μ^- 1×1 cm beam in a standard TEP and in one with BaI_2 solution at 18.5 \leq z \leq 20.5 cm and r \leq 1.5 cm.

ergy deposition distribution in a TEP induced by various beams show substantially different patterns which might be exploited by the therapist. Negative pion beams provide the best peak-to-entrance dose ratio but pure π^- beams are difficult to prepare. Cooled muon beams could rival proton beams with regard to purity and deliver a better peak-to-entrance ratio—particularly for larger tumors. Muon dose appears also to be more uniformly distributed compared with protons. An important aspect would be the ability to evaluate and intercompare the efficacy of the various beams in a common setting which might be provided by a muon collider complex.

- [1] C. M. Ankenbrandt et al., "Status of Muon Collider Research and Development and Future Plans", Fermilab-Pub-98/179 (1998).
- [2] P. L. Petti and A. J. Lennox, "Hadronic Radiotherapy", Annu. Rev. Nucl. Part. Sci., 44, 155-197 (1994). We wish to thank A. J. Lennox for useful discussion.
- [3] N. V. Mokhov, S. I. Striganov, A. Van Ginneken, S. G. Mashnik, A. J. Sierk, and J. Ranft, "MARS Code Developments", Fermilab-Conf-98/379 (1998); LANL Report LA-UR-98-5716 (1998); nucl-th/9812038 v2 16 Dec 1998; http://www-ap.fnal.gov/MARS/.
- [4] S. G. Mashnik, "User Manual for the Code JINR, Dubna, 1995; OECD Nuclear Energy Agency Data Bank, Paris, France, 1995; http://www.nea.fr/abs/html/iaea1247.html; RSIC-PSR-357, Oak Ridge, 1995.
- [5] Radiotherapists make use of an RBE-factor (relative biological effectiveness) in their evaluation of various beams but these factors are not readily applied to our calculations since they depend not only on particle type and energy but also on the time structure (fractionation) and absolute level of dose delivered. Overall, RBE-enhanced dose appears to resemble absorbed dose better than dose equivalent.

A COMPACT PROTON SYNCHROTRON WITH COMBINED-FUNCTION LATTICE DEDICATED FOR CANCER THERAPY*

A. MORITA[†], A. NODA, M. INOUE, T. SHIRAI, and Y.IWASHITA ICR, Kyoto University, K. HIRAMOTO, M. KATANE, M. TADOKORO, M. NISHI, and M. UMEZAWA HITACHI Co. Ltd.

Abstract

A compact proton synchrotron with combined function lattice has been designed as a dedicated machine for cancer therapy because of its merits of easy operation and low construction cost. The lattice has a six-fold symmetry and its radius of curvature and circumference are 1.9m and 23.9m, respectively. For the purpose of establishing a good reference design, we have constructed a model magnet based on the three-dimensional magnetic field calculation. Magnetic field measurement has been performed with use of three-dimensional Hall-probe. In the present paper, the results of these development is to be presented together with the outline of the reference design.

1 INTRODUCTION

Recently radiation cancer therapy has been paid attention because of its merit of preserving function and shape of human body and rather light load to the patient compared with the other therapy. Among radiation therapies, charged particle therapy has such a merit that it can localize the dose distribution to tumor largely reducing the damage to normal cells. In order to cure a lot of patients, it is required to construct at least one such facility in each prefecture, however, constructing and operating such charged particle therapy facility need many cost. From this point of view, We have been developing a compact proton synchrotron facility, which is easy for daily operation and required cost is rather limited[1]. As the machine for such proton accelerator, we have chosen a proton synchrotron with combined function lattice, because of its non-flexibility. This nonflexibility cause difficulty of tuning, however, such nonflexibility gives easy operation once a good design has been established. We develop the reference design of the combined function magnet with the help of three-dimensional magnetic field calculation code. In the present paper, we present our magnet system design and the measurement results of the model magnet.

2 DEVELOPMENT PROCESS OF REFERENCE MODEL

2.1 Primary Design

In our primary design, the synchrotron ring has a six-fold symmetry and the lattice is constructed by 60 degree bending sector magnet and 2 meters drift-space. On the central orbit in a bending magnet, the radius of curvature and the maximum field strength are 1.9m and 1.28T, respectively to accelerate a proton up to 250MeV. The focusing elements are implemented in bending magnets as FDF structure combined function[2]. For convenience of calculation, bending angles of F,D, and F sector are designed 15,30, and 15 degree, respectively. To set operating point $\nu \sim 1.75$, n-value of magnet sector is given 6.164 for D-sector and -5.855 for F-sector by matrix calculation. We consider that the magnet is made by laminated iron plates. Thus, both transition region between F and D sectors and end edge regions are designed as step function to approximate potential made by Rogowski curved pole at the medium plane of the magnet. The structure of the synchrotron ring is shown in Fig.1.

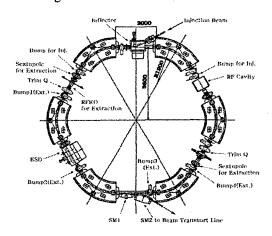


Figure 1: Structure of the synchrotron ring

2.2 Operating Point Evaluation

To verify the design, we evaluate the operating point. Both tune value and beta function are calculated using transfer matrix reconstruction method with particle tracking[3] on the magnetic field calculated by the three-dimensional magnetic field calculation code TOSCA. In the treatment of both fringing and transition of between F and D sectors

^{*}Work supported by Grant-in-Aid for Scientific Research from Ministry of Education, Science, Sports and Culture of Japan under the contact number 08559010

[†] morita@kyticr.kuicr.kyoto-u.ac.jp

and central-orbit deformation, this method based on particle tracking has advantage compared with ordinary method using the product of the transfer matrices defined by analytical results of uniform field.

2.3 Operating Point Tuning

The tune value evaluated from our primary design $(\nu_h, \nu_v) \sim (1.64, 1.86)$ is far from the design target. To move operating point to the design target, we modify the ratio of bending angles, which increases bending angle of F-sector in $\Delta\theta$ degree and decreases bending angle of Dsector in $2\Delta\theta$ degree. Of cause, for modifying tune value, n-value modification is essential, however, the pole shape has already been determined with the two-dimensional field calculation using POISSON. Changing the ratio of bending angles seems to correspond to local n-value modification at the boundary between F and D sectors. Thus, the theory of perturbation predicts that the ratio of horizontal and vertical tune value modulation is given by ratio of beta function at the boundary and the modulation magnitude of tune value is proportional to the modulation of bending angle $\Delta \theta$. Using $\Delta \theta$ tuning, we can control tune value on the linear line.

2.4 Model Magnet

Considering the operating point and resonance lines, we select $\Delta\theta$ parameter to 0.25 degrees and operating point (1.7, 1.75) as the final design to avoid resonance lines up to 6th order. To verify the reality of the three-dimensional calculation, we made a model magnet of the final design and made field measurement. Figure 2 shows the lower half



Figure 2: Lower half of the model magnet

of the completed model magnet. The poles of the magnet are made by the laminated iron plates whose thickness are 0.5mm.

3 MEASUREMENT OF MODEL MAGNET

Considering the symmetry of the lattice structure, we measured the half of the magnet by mapping on the cylindrical

coordinate using the three-dimensional Hall-probe ¹ fixed to the three-axis movable stage. The measurement has been performed by 5mm spacing in radial direction from 1.84m to 2m and 1 degree spacing in circumferential direction from the center of D sector to out side of magnet with 43 points. These measurement setup and the Hall-probe structure are shown in Fig.3 and 4, respectively. From the

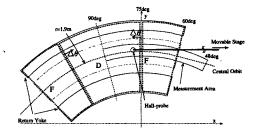


Figure 3: Geometry of the measurement

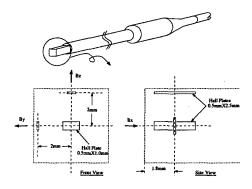


Figure 4: Structure of the Hall-probe

mirror symmetry between upper and lower poles, the magnetic field flux cross perpendicular to the medium plain. Thus the horizontal components of magnetic field should be equal to zero on the medium plane and anti-symmetric for the medium plane. But measured horizontal components shown in Fig.5 do not satisfy such symmetry and has obvious offset on the medium plane. These offset on the

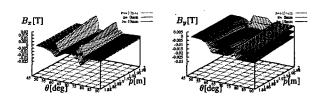


Figure 5: Raw horizontal components of the magnetic field

medium plane seems to be caused by vertical component B_z shown in Fig.6. Thus we consider that these asymmetries are caused by the rotation of the probe axes, because of both bending and rotating probe arm. To correct those asymmetry, we introduce two parameters of rotating angle

¹Lake Shore Model 460 & MMZ-2500-UH

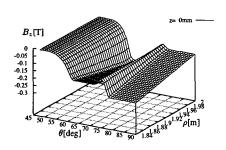


Figure 6: raw vertical component of the magnetic field

and determines these two parameters by fitting to minimize the ratio of square expectation value between horizontal components and vertical component. One of the corrected horizontal components are shown in Fig.7 and it is seem that symmetry is recovered.

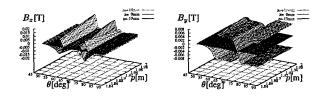


Figure 7: Corrected horizontal components of the magnetic field

4 RESULTS OF MEASUREMENT

To evaluate the magnetic field, we compared vertical components B_z and n-value on the central orbit. The global feature B_z and n-value calculated on the ideal central orbits shown in Fig.8 and 9 have good agreement between measurement and TOSCA calculated in edge shape at fringing and F-D transition, respectively. But the magnitude of n-value is slightly different in detail.

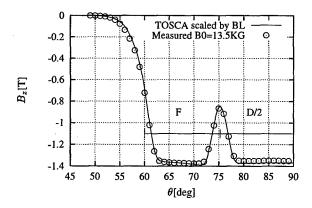


Figure 8: B_z on the central orbit

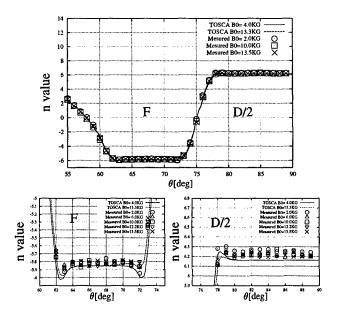


Figure 9: n-value on the central orbit

Following facts are considered as the problem in our n-value measurement process. In calculating n-value from measured field, we use linear fit to 25 data points in linear region to calculate field gradient. Stable flat top of n-value in the center of each sectors is predicted from TOSCA results, however, measured n-value contain some deviations. Our gauss meter give us 5-digit as measurement result and field difference between adjusted measurement grids is the order of 1 percent of the field strength. Then, the measurement precession is not enough to discuss n-value and tune value calculation on these field map.

To treat the magnitude of n-value more in detail, improvement of measurement precision by direct measurement of field gradient is now under investigation.

5 ACKNOWLEDGEMENT

The authors would like to present their sincere thanks to Drs. H. Ogawa, K. Noda and M. Kumada at NIRS for their support during three-dimensional field measurement.

- [1] A. Noda et al., "Dedicated accelerator project for proton therapy at Kyoto University", NIRS-M-103, HIMAC-008, Proc. of the NIRS International Seminar on the Application og Heavy Ion Accelerator to Radiation Therapy of Cancer in connection with the 21th PTCOG Meeting (1994) 292-294.
- [2] M. Tadokoro et al., "A combined Function Magnet for a Compact synchrotron", Proc. of the 1997 Particle Accelerator Conference, Vancouver, Canada (1997) 3294-3296.
- [3] A. Morita et al., "Tune Value Evaluation for Combind Dunction Lattice", Beam Science and Technology, Vol 3(1998) 23-26.

²1.9m curvature radius on the medium plane

MONTE CARLO SIMULATION AND EXPERIMENTAL EVALUATION OF PHOTONEUTRON SPECTRA PRODUCED IN MEDICAL LINEAR ACCELERATORS

C. Ongaro, DFS-UT**, J. Rodenas, A. Leon, DIQN-UPV°; J. Perez, HU-FE°°, A. Zanini, INFN-TO**; K. Burn, ENEA-ERGPSIEC[§]

Abstract

Linear accelerators for the cancer radiotherapy generally make use of high-energy photon beam. If the photon energy is greater than 6-7 MeV, neutrons are generated by photonuclear reaction in the accelerator head. The neutron spectrum and yield at the patient plane must be known in order to optimize the treatment and limit secondary malignancies. The spectrum of neutrons generated by (γ,n) reaction in the SL20I ELEKTA multileaf accelerator has been obtained at the patient plane with a Monte Carlo simulation. The calculated spectrum has been checked out against experimental measurements performed, in different positions at the patient plane, with a passive bubble spectrometer.

1 INTRODUCTION

The revaluation of the biological risk from neutron radiation has improved the importance of a reliable neutron dosimetry. There is an urgent request from medical physicist of an accurate estimation of the undesired neutron dose associated with the photon beams produced in the linear accelerator commonly used in the cancer therapy. The knowledge of the photon and neutron spectrum at the patient plane allows a more accurate evaluation of the total dose.

Measurements of such spectra are difficult, due to the high fluence rate of photon to respect to neutrons and the pulsed radiation field, which can produce saturation and noise problems in the electronic equipment. In this work the linear accelerator SL20I-ELEKTA [1], equipped with the multileaf collimation system (MLC) has been simulated with the new Monte Carlo code MCNP-GN, especially developed to treat the photoneutron production in medical linear accelerators. The neutron fluence, as a function of the neutron energy, has been calculated in different positions at the patient plane; the corresponding dose equivalent has been evaluated by using the ICRP74 [6] conversion factors.

The Monte Carlo results have been compared with the experimental spectra, measured with the passive bubble spectrometer BDS [4] at the Hospital of «La Fe» (Valencia, Spain) where a SL20I accelerator is installed. The BDS spectrometer system has been chosen because the passive characteristics and the photon insensitivity allow to overcome the experimental difficulties previously described. This Monte Carlo approach associated with the BDS spectrometer represents a new and complete tool to describe the neutron field.

2 SL20I ELEKTA MULTILEAF (MLC) ACCELERATOR

The fundamental requirement for a radiotherapy treatment

X+Y+L X+L X+Y+L X+Y+X+Y+L X+Y+L X+Y+L X+Y+L X+Y+L X+Y+L X+Y+X+Y+X+Y+L X+Y+X+Y+X+Y+X+

Figure 1: Irregular field profile with MLC.

is the delimitation of the irradiated region as close to the tumor volume as possible, minimizing the dose the surrounding healthy tissues. With this aim, the most modern machines are equipped with the multileaf system: a set of movable leaves is applied to define the field size and shape. The ELEKTA SL20I accelerator

uses a set of 80 lead+tungsten leaves, which define the treatment field in the Y direction; leaves are stepped to create an overlap and limit the leakage. Further collimation is provided by traditional X and Y shielding, to reduce the photon leakage between the leaves to acceptable levels (figure 1, table 1).

Table 1: SL20I characteristics.

Max photon energy	18 MeV	
Target	Tungsten	
Primary collimator Top	Tungsten	
Flattening filter	Iron	
Leaves	Tungsten+Lead	
Y back-up collimator	Tungsten	
X collimator	Tungsten+Lead	

^{*} Dip. Fisica Sperimentale, Università di Torino, Italy.

[°] Dep. Ingeniería Nuclear, Univ. Politécnica Valencia, Spain.

^{°°}Dep. Radioterapia, Hosp. La Fe, Valencia, Spain

^{**}Istituto Nazionale Fisica Nucleare, Sez. di Torino, Italy.

[§]ENEA, ERG, Bologna, Italy.

ongaro@to.infn.it

2 MONTE CARLO SIMULATION WITH MCNP-GN

The Monte Carlo code MCNP-GN has been especially developed to study the neutron leakage in medical LINACS used in the photon cancer radiotherapy. The physical routines of the Monte Carlo code GAMMAN [2] have been introduced in the Monte Carlo code MCNP4B [7]. The Monte Carlo code MCNP-GN evaluates the neutron production in high atomic number materials

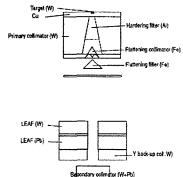


Figure 2: Geometrical model of SL20I MLC simulated with MCNP-GN.

through (γ,n) reaction in the energy region of the giant resonance (E<30 MeV). These characteristics, together with the capability to model complex geometries, make MCNP-GN especially useful for medical linear accelerator simulations. In fact, by use of an unique code, it is possible to obtain both the photon and the photoneutron spectra produced in the accelerator field. The realistic geometrical model of ELEKTA SL20I MLC (in the high power configuration) has been simulated to obtain a 10x10 cm² treatment field, irradiated with 1 Gy photon dose at the patient plane (figure 2).

3 THE BDS SPECTROMETER

The passive neutron spectrometer BDS [3] has been used to obtain neutron spectra in term of fluence as a function of neutron energy. The consists of a set of bubble dosemeters, characterized by 6 different energy thresholds of detection; the total energy range extends from 10 keV to 20 MeV. Each detector includes a polycarbonate vial filled with elastic tissue-equivalent polymer; superheated freon drops are dispersed inside the gel. The interaction between incident neutrons and polymer causes a proton emission; the consequent energy deposition generates the bubble forming, due to the metastable state of freon. The number of bubbles trapped in the polymer, proportional to the neutron fluence, is recorded. The neutron spectrum is then is obtained by processing the experimental data with the unfolding code BUNTO [4]. Due to the characteristics passivity and insensitivity to photons,

spectrometric system can be used in mixed neutron and photon fields, as the treatment room. Neutron spectral measurements can be therefore performed also in positions corresponding to the treatment area, unlike several other devices, commonly used for neutron dosimetry and radioprotection.

4 EXPERIMENTAL MEASUREMENTS WITH BDS SPECTROMETER

Spectral and integral measurements of neutron fluence and dose equivalent have been performed at various positions (figure 3) in the irradiation room of linear accelerator SL20I-ELEKTA, installed in the hospital «La Fe», Valencia (Spain). The measurements have been realized in the following conditions:

- 100 MU/Gy
- 10x10 cm² photon field at the isocenter
- 100 cm SSD (Source Surface Distance)

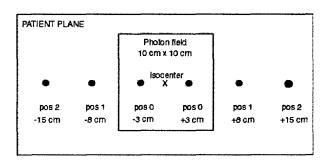


Figure 3: Measurement positions at the patient plane, SDD=100 cm.

5 COMPARISON BETWEEN SIMULATION AND MEASUREMENTS

In figures 4 and 5 the neutron experimental spectra evaluated at the patient plane, per 1 Gy photon absorbed dose (SSD=100 cm) are presented. The neutron spectra calculated by the Monte Carlo code MCNP-GN in the same positions are also shown. The comparison is very satisfactory; in fact the simulated spectra are uniquely normalized to the number of electrons giving 1 Gy photon dose at the isocenter. The spectral neutron dose equivalent (ICRP60 [5], [6]) (per 1 Gy photon dose at the patient plane) was also obtained from the experimental spectra at the different positions to respect to the beam axis. In figure 6 the neutron integral dose equivalent and the photon absorbed dose calculated with MCNP-GN at different positions are shown together.

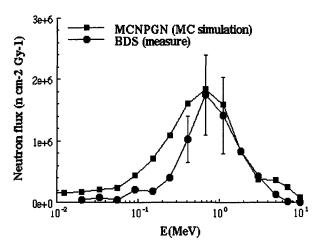


Figure 4: Comparison between experimental and simulated spectrum. Position pos1 – 8 cm from isocenter.

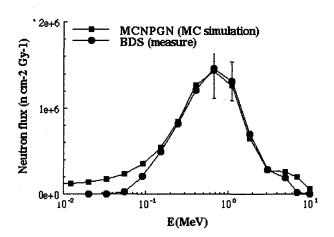


Figure 5: Comparison between experimental and simulated spectrum. Position pos2 – 15 cm from isocenter.

Table 2: Integral neutron fluence and neutron dose equivalent evaluated from spectral data at various positions.

		Integral neutron fluence per 1 Gy photon dose – cm ⁻² Gy ⁻¹		integral neutron dose equivalent per 1 Gy photon dose (ICRP 60) – mSv Gy ⁻¹	
		10 keV-20 MeV	300 keV-20 MeV	10 keV-20 MeV	300 keV-20 MeV
POSe	MCNP-GN (simulation)	1.87 x 10 ⁷	9.83 x 10°	4.99	4.37
< h	(BIJS e l d (experiment)	(2.06 ± 0.31) 10 ⁷	(9.62 ± 1.44) 10°	5.01 ± 0.75	4.60 ± 0.69
POS1	MCNP-GN (simulation)	9.86 x 10°	6.88 x 10*	3.53	3.04
	BDS (experiment)	(7.11± 1.64) 10 ⁴	(5.57 ± 1.28) 10°	2.66 ± 0.61	2.48 ± 0.57
POS2	MCNP-GN (simulation)	7.79 x 10°	5.39 x 10°	2.76	2.38
	BDS (experiment)	(7.60 ± 1.98) 10°	(5.18 ± 1.35) 10°	2.62 ± 0.68	2.28 ± 0.59

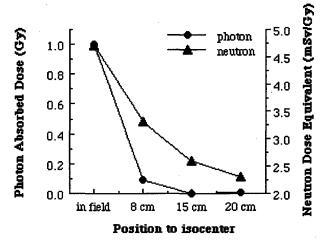


Figure 6: Integral photon absorbed dose and neutron dose equivalent calculated with MCNP-GN at the various positions with respect to the isocenter.

6 CONCLUSIONS

From these results it is pointed out that the neutron dose equivalent in a typical treatment is not negligible. In fact the neutron dose equivalent remains greater than 2 mSv/Gy also in far positions from the treatment field. Therefore, this new system, consisting of Monte Carlo simulation and spectral measurements, represents a reliable approach to evaluate the leakage neutron field and to optimize the treatment plan.

- [1] T.J. Jordan, P.C. Williams. The design and performance characteristics of a multileaf collimator. Phys. Med. Biol. 39 (1994) 231-251.
- [2] C. Ongaro, A. Zanini, U. Nastasi, Monte Carlo simulation of the photoneutron production in the high Z elements. Proc. of «Workshop on Monte Carlo method and models in energy and technology». Karlsruhe, may 1998.
- [3] BDS Bubble Detector neutron Spectrometer, BTI, HWY 17, Chalk River, Ontario, Canada.
- [4] C. Manfredotti, A. Zanini, C. Ongaro, L. Tommasino, Mean and high energy neutron spectrometry by passive detectors and unfolding techniques for routinely dosimetry. Proc. 5th Int. Conf. on Application of Nuclear Techniques Crete, June 9-15, 1996.
- [5] ICRP The 1990-1991 Recommendation of the International Commission on Radiological Protection, Pub. n.60, Oxford Pergamon (1991).
- [6] Advise on the implication of the conversion coefficients for external radiation published in ICRP Publication n. 74 and by ICRU Report n. 57, Rad. Prot. Dos., Vol 74, N.3 (1997).
- [7] G.F. Briesmeister, MCNP A general Monte Carlo code for neutron and photon transport, Version 4B, Los Alamos, New Mexico, (1997).

APPLICATION OF THE MONTE CARLO METHOD TO ACCELERATOR SHIELDING ANALYSIS. A NEW ESTIMATION OF THE TENTH-VALUE THICKNESS FOR X-RAYS IN MEDICAL LINEAR ACCELERATORS.

J. Ródenas⁴, A. León, G. Verdú,

Departamento de Ingeniería Nuclear, Universidad Politécnica de Valencia P. O. Box 22012, E-46071 Valencia (Spain)

C. Ongaro, Dipartimento di Fisica Sperimentale, Università di Torino, (Italy)

Abstract

In radiotherapy installations using accelerators it is very important to produce an accurate estimation of the shielding requirements to keep doses lower than limits. Shielding thickness is directly proportional to the tenth-value thickness, which can be obtained from curves recommended by the DIN-6847 standard and also estimated in terms of dose rates calculated for two different values of shielding thickness. In this work, the Monte Carlo method is applied to estimate the tenth-value thickness for X-rays in medical linear accelerators. Results are compared with older simulation data as well as with the values recommended by the DIN-6847 standard.

1 INTRODUCTION

Linear electron accelerators are widely used in radiotherapy installations. The importance of an accurate estimation of the doses that can be received by health workers, patients or public, as well as shielding requirements to reduce doses below established limits is obvious. On the other hand, lower dose limits were recommended in ICRP 60 [1]. According to those recommendations a Directive has been recently issued by the European Community to state a regulatory position to be followed by member states. Therefore, it may be necessary to re-evaluate safety parameters concerning medical installations using accelerators [2].

Two standards, NCRP-51 [3] and DIN-6847 [4], can be used to estimate shielding requirements in those installations. They were comparatively analysed in former works [2, 5]. The interest was focused on the estimation of the tenth-value thickness for X-rays produced in medical electron accelerators. MCNP code [6, 7] based on the Monte Carlo method was and has been again applied to perform this estimation.

2 SHIELDING ANALYSIS

In DIN-6847 standard [4], the shielding thickness is given by the following expression:

$$s_i = z_i \log_{10} \left(\frac{W_A U T K_i q_i}{H_w} \right)$$
 (1)

where, s_i is the shielding thickness for the ith radiation, referring to electrons, X-rays (primary, secondary, leakage) or neutrons (primary and scattered beam); z_i is the tenth-value thickness; W_A is the weekly workload at the reference distance of a_0 meters (Gy/week); U is the use factor; T is the occupancy factor; K_i is the reduction factor; q_i is the quality factor; and H_w is the weekly equivalent dose.

For primary X-ray beam, $q_i = 1$ and the reduction factor is given by:

$$K = \frac{a_0^2}{a_n^2}$$
 (2)

where, a_0 is the reference distance (1 m) and a_n is the distance (m) from the source to the point beyond the shielding where the dose is measured.

The tenth-value thickness, $z_i = z_r$, depending on the shielding material can be obtained from curves recommended by DIN-6847 that are reproduced in Figure 1. It can be noted that the same curve is used for aluminium and concrete, and also for iron and copper.

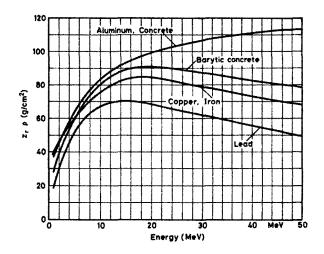


Fig. 1 Mass tenth-value thickness for X-rays.

The following expression for the equivalent dose rate H_w can be obtained from eq. (1) and (2):

^{*} E-mail: jrodenas@iqn.upv.es

$$H_{\rm w} = \frac{C}{a_{\rm n}^2} \left(\frac{1}{10}\right)^{\frac{\rm s}{\rm z}} \tag{3}$$

where C includes all terms depending on the installation and radiation involved. MCNP code was used with a lineal spectrum taken from Chilton [8], to calculate doses for shielding thickness from 0 up to 130 cm. The correlation coefficient between $\log(H_w \ a_n^2)$ and s was calculated to verify that they are linearly related [9, 10].

Therefore, the tenth-value thickness can be estimated in terms of the dose rates calculated for two different values of shielding thickness and related distances, as follows:

$$z = -\frac{s_2 - s_1}{\log_{10} \frac{H_{2w} a_2^2}{H_{1w} a_1^2}}$$
 (4)

3 RESULTS AND COMPARISON

MCNP code has been run to determine doses at distances considered, for various energy values from 0.5 up to 50 MeV and the materials of interest: aluminium, concrete, barytic concrete, iron, copper and lead.

The photon source was a point, isotropic, and monoenergetic, with all the particles being emitted inside a small solid angle to avoid the leakage radiation. Surface counters were placed in maximal dose zones. Cell importance was the only variance reduction technique applied, due to geometric features of the problem and the type of counters used.

Shielding thickness values have been taken in such a way that for each energy the doses obtained differ by at least an order of magnitude.

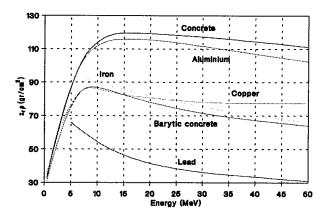


Fig. 2. Results from MCNP 3.2.

The first approach was done using the version 3.2 of MCNP [6]. Results were presented at PAC'93 [9] and MEDICAL PHYSICS 93 [10].

Results for direct radiation are shown in Figure 2. Comparing this figure with Figure 1, one can see that values obtained by MCNP match reasonably with those

from DIN-6847 except for lead. At the lowest energy (0.5 MeV) the Monte Carlo values are slightly lower than the DIN ones, whereas for higher values of energy they are higher: always for concrete, up to 40 MeV for aluminium, up to 10 MeV for barytic concrete, and up to 15 MeV for iron and copper. For the rest of energy values, the Monte Carlo obtained values are only slightly lower.

The highest discrepancies were shown for lead. The version 3.2 of MCNP code did not include the transport of photoelectrons, Compton electrons and electron-positron pairs. At higher energies these electrons collide with hard atomic nuclei producing electromagnetic radiation (Bremsstrahlung). These phenomena become more evident in lead. Therefore, results from MCNP 3.2 shall be discarded for lead.

DIN-6847 is less conservative for direct radiation than expected, as it was discussed by authors in an early paper [11] comparing tenth-value thickness from DIN-6847 with those from NCRP-49 [12] for concrete, up to 10 MeV.

On the other hand, the curves obtained for concrete and aluminium are very similar. Furthermore the calculated curves not only for iron and copper but also for barytic concrete are very similar too.

The results would have been in better agreement if we had considered a continuous spectrum rather than a monoenergetic source, but unfortunately these data were not available from the manufacturers.

MCNP determines errors for each calculated dose. With these data a statistical analysis has been performed to prove that results are significant, practically at 100% for relative error of 5%.

Calculations have been repeated with MCNP 4A [7] using the same methodology, materials, and model [13]. MCNP can provide dose conversion factors up to 15 MeV. For higher energies an extrapolation was necessary. However, in latter calculations dose conversion factors from Jaeger [14] have been used, improving results for higher energies, even for MCNP 3.2. Therefore, some calculations were also repeated using version 3.2, in those cases where dose conversion factors have been modified. Anyway it would be convenient to dispose of more appropriate dose conversion factors.

Results obtained from MCNP 4A calculations are represented in Figure 3. As electron transport has been incorporated to the code, all phenomena formerly omitted are now taken into account, so results are quite improved not only for lead but also for the rest of materials, especially at higher energies.

Comparing the three figures some comments can be done. For aluminium it can be noted that estimated values (MCNP 4A) are more conservative than DIN ones. Both curves have a similar shape. The 4A approach is better than that of 3.2. A similar statement can be made for concrete. For barytic concrete the behaviour is slightly differ-

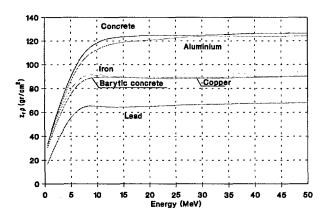


Figure 3: Results from MCNP 4A

ent in the 3 curves. Discrepancies between 4A and DIN are lower in general. For iron and copper the curves obtained from MCNP 3.2 agree better with DIN than those from MCNP 4A. Maybe it is due to the shielding thickness adopted for calculations. For lead, results have been fairly enhanced with respect to MCNP 3.2, which were not considered valid in former calculations. However they are not yet satisfactory, as its behaviour is similar to iron and copper for energies higher than 15 MeV, where the curves have opposite slope values. This difference can be due to dose conversion factors used.

4 CONCLUSIONS

Two versions of MCNP (3.2 and 4A) based on the Monte Carlo method have been used to estimate the tenth-value thickness for X-ray direct beams in medical electron accelerators. Results have been compared between the calculations and with values recommended by the DIN-6847 standard.

It has been verified for primary radiation that without significant errors the same curve may be used for different materials, in particular for concrete and aluminium and for barytic concrete, iron and copper, respectively, though "a priori" it did not appear very logical.

It is not easy to perform experimental dose measurements, in particular in a linear accelerator, so it turns out the importance of simulation methods. Anyway, the comparison between experimental measurements and simulation results is always welcome.

Since the primary beam spectrum in an accelerator is generally unknown, a monoenergetic source has been considered. Next developments will include the estimation of the tenth-value thickness using an actual X-ray spectrum for the accelerator. As well, calculations should be repeated using further versions of MCNP.

- ICRP Publication 60, "New Recommendations of the Commission", approved on 9 November 1990.
- [2] G. Verdú, J. Ródenas, J. M. Campayo, "Radiation Protection for Particle Accelerators", I International Conference on Implications of the new ICRP Recommendations, Salamanca (Spain), 26-29 November 1991.
- [3] NCRP Report 51, "Radiation Protection Design Guidelines for 0.1-100 MeV Particle Accelerator Facilities", National Council on Radiation Protection and Measurements, 1977.
- [4] DIN-6847, "Medizinische Elektronenbeschleuniger-Anlagen; Teil 2: Strahlenschutzregeln für die Errichtung", (Medical electron accelerators; Part 2: Radiation protection rules for installation), DIN Deutsches Institut für Normung e. V., 1977.
- [5] J. Ródenas, G. Verdú, "Análisis de la normativa aplicable al cálculo de blindajes en aceleradores lineales", PROTECCIÓN RADIOLÓGICA, Revista de la Sociedad Española, núm. 2, Mayo 1992.
- [6] W. L. Thompson, (Monte Carlo Group Leader), "MCNP A General Monte Carlo Code for Neutron and Photon Transport", Version 3, Los Alamos Monte Carlo Group, Los Alamos National Laboratory, Los Alamos, New Mexico, 1983.
- [7] J. F. Briesmeister (Editor), "MCNP A General Monte Carlo N-Particle Transport Code, Version 4A", LA-12625, Los Alamos National Laboratory, Los Alamos, New Mexico, November 1993.
- [8] A. B. Chilton, J. K. Shultis, R. E. Faw, "Principles of Radiation Shielding", Prentice Hall, 1984.
- [9] J. Ródenas, G. Verdú, "Application of the Monte Carlo Method to Estimate the Tenth-value Thickness for X-rays in Medical Electron Accelerators", PAC'93, IEEE, 1993 Particle Accelerator Conference, Washington, D. C., 17-20 May 1993.
- [10] J. Ródenas, G. Verdú, J. I. Villaescusa, J. M. Campayo, "Cálculo de dosis y estudio de blindajes en un acelerador lineal", MEDICAL PHYSICS 93, IX Congreso Nacional de Física Médica, Puerto de la Cruz, Tenerife, 22-24 Septiembre 1993.
- [11] J. Ródenas, G. Verdú, R. Máiquez, "Aplicación del método de Monte Carlo al cálculo de blindajes en un acelerador lineal", XVIII Reunión Anual de la Sociedad Nuclear Española, Jerez de la Frontera — Puerto de Santa María (Spain), 28-30 October 1992.
- [12] NCRP Report 49, "Structural Shielding Design and Evaluation for Medical Use of X-Rays and Gamma Rays of Energies up to 10 MeV", National Council on Radiation Protection and Measurements, 1976.
- [13] J. Ródenas, G. Verdú, A. Nieto, "La simulación del transporte de partículas mediante el método de Monte Carlo: el código MCNP 4A", XX Reunión Anual de la Sociedad Nuclear Española (SNE), Córdoba (Spain), October 1994.
- [14] R. G. Jaeger (Ed.), "Engineering Compendium on Radiation Shielding", Volume I: Shielding Fundamentals and Methods, Springer-Verlag, 1968.

CONVERSION OF THE 2.5MV SUPER HILAC INJECTOR POWER SUPPLY FROM 5mA TO 50mA FOR BORON NEUTRON CAPTURE THERAPY*1

L. Reginato, W. Chu, J. Galvin, J. Kwan, and B. Ludewigt Lawrence Berkeley National Laboratory Berkeley, California

Abstract

Renewed interest by several major university medical centers (UCSF-Standford, UC-Davis) in conducting Boron Neutron Capture Therapy (BNCT) led to the investigation of converting the decommissioned 5mA, 2.5MV Super HILAC injector to a 50mA, 2.5MV proton accelerator for the generation of neutrons. The original high impedance shunt-fed multiplier has been converted to a 55 stage air-coupled transformer with much lower impedance driven by a 200kW, 50kHz oscillator. The proton beam will be transported by electrostatic quadrupoles (ESQ) acceleration column housed axially within the power supply stages and biased by connecting sequentially to the desired voltage. The pressure vessel which houses the 2.5MV power supply and ESQ acceleration column has been moved near the patient treatment rooms in the Bevatron complex. As funds become available, we will finalize the design and assembly of all components required for the generation, transport and conversion of the proton beam to neutrons for patient treatment. Preliminary tests of the power supply and design of the ESO column will be presented.

1 INTRODUCTION

High voltage power sources have provided the injection particles to every major accelerator since the experiments of Cockcroft and Walton in 1932. The high voltage potential has been generated by a variety of techniques. The Cockcroft-Walton, as the DC high voltage generators became to be known, utilized a series of rectifiers and capacitors first suggested by Greinacher in 1920. This technique of series-fed or shunt-fed multipliers (dynamitron) is used to this day at low currents and moderately high voltages.

For stiffer power sources, the insulated-coretransformer consisting of multiple cascaded stages each with its rectifier and insulated from each other was also used. Initial high voltage tests for Boron Neutron Capture Therapy (BNCT) at Lawrence Berkeley National Laboratory were started by reactivating a shunt-fed multiplier constructed in 1970. Extensive tests on this device (Fig. 1) were performed at higher currents than originally designed for to establish its maximum capability. After a series of tests it was decided that in its present condition, this power supply could not deliver the 50mA desirable for BNCT. A design modification study was initiated to upgrade the Adam power supply from 5mA to 50mA at 2.5MV. After a

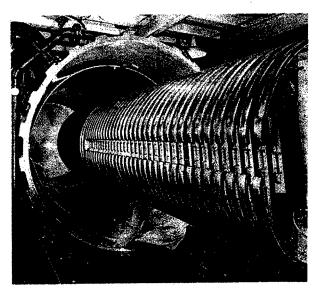


Figure 1: The Adam Injector power supply

brief invest-igation of the technology available for the production of high voltage and high current, it was decided to convert the capacitively coupled shunt-fed multiplier to the air-coupled transformer with multiple secondaries.

2 SYSTEM DESCRIPTION

The basic principle of operation of the air-coupled transformer has been well understood and analyzed but a simple description on how it is applied is included for continuity. Figure 2 is a simplified schematic of the proposed modifications to be made to the Adam power supply using the air-coupled transformer. It consists of a primary coil which is tapered in cross-section to allow for voltage holding. This primary coil generates a solenoidal field inside the coil with a return field

$$B_p = \int (\mu_0 / 2) (N_p i_p / z) \left[a^2 / (a^2 + x^2)^{3/2} \right] dx$$
 (1)

Work supported by the Director, Office of Energy Research, Office of Basic Energy Science, materials Science Division, of the U.S. Department of Energy under Contract No. DE-AC03-76F00098

between the pressure vessel and the coil itself. The flux density within the solenoidal coil can be obtained by summing the contributions of each turn of the coil. This results in a flux density.

Where: Np – number of primary turns, a-radius of the solenoid, z-length of the solenoid and dx is an element of length. At points within the solenoid not too close to either end, the flux density produced can be approximated by $B_p=\mu_0N_pi_p/z$.

Within the primary coil, 55 stages of multi-turn secondary coils are located. The flux generated by the primary (B_p) is coupled by magnetic induction to each secondary generating a voltage V_s=N_sA_sdB_p/dt where A_s is the cross-sectional area and N_s the number of secondary turns. Each secondary coil incorporates a rectifier and filter producing a self-contained power source. Each power source is series connected to the next producing a high voltage system. The coupled transformer system, like the shunt-fed multiplier, has an impedance which increases linearly with the number of stages and is a function of the coupling coefficient between the primary and secondary coil. The primary coil will be part of the main oscillator resonant circuit with an inductance $L_p \cong \mu_0 N_p^2 A_p/z$. This inductance will resonate with a capacitor $C_p=1/w^2L_p$. The secondary voltage induced will be $V_s=N_sA_swB_p$ and $B_p=\mu oN_pi_p/z$ where $i_p=V_p/wL_p$. By substitution $V_s=(N_s/N_p)(A_s/A_p)V_p$. The subscripts s and p refer to the secondary and primary respectively. Prior to modifying the Adam power supply, an eight stage coupled transformer bench top model was constructed and tested. A conducting cover was placed around it to simulate the pressure vessel. The test results were encouraging in that it confirmed our calculations and had an order of magnitude lower impedance than the shunt-fed device.

3 SYSTEM MODIFICATION

The coupling capacitors, the dees and the oscillator coil of the shunt-fed multiplier were removed. The dees were replaced by the primary. solenoidal coil with an increasing inside diameter toward the high voltage

dome (Fig. 3). The number of turns per unit of length or

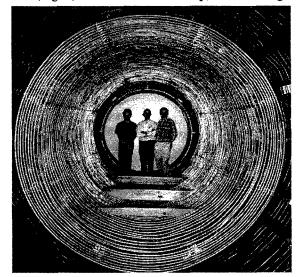


Figure 3: The air-coupled transformer primary

pitch

of the coil also increases linearly from the ground end to the high voltage dome in order to maintain a constant flux density or constant induced voltage into

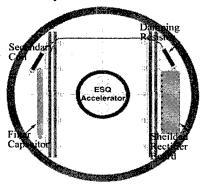


Figure 5: One of 55 series stages

the secondary coils. The number of turns was further increased at each end of the coil to correct for end effects of the dome and the ground. Figure 4 shows a plot of the induced voltage in the secondary coil along

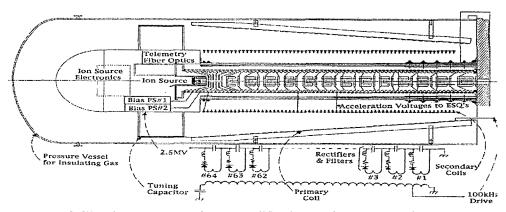


Figure 2: The air-coupled transformer modifications to the power supply

the length of the power supply where the acceleration column would be located. As can be seen, except for the ends, the induced voltage in each of the 55 secondary coils will be quite uniform. The secondary coils will begin about 12" from the end wall and will terminate about 18" from the dome to insure that the coupled voltage for the end stages is constant.

4 SYSTEM OPERATION

The master oscillator consisting of a 4 CW100,000 drives the primary coil with 50kHz at 50-75kV. The oscillator is powered by a 15kV, 12.5A regulated DC power supply and with a projected efficiency of 67% it will deliver 125kW to the beam or 2.5MV at 50mA. A closed loop feedback system will maintain the desired acceleration voltage on the electrostatic quadrupoles (ESQ) at any beam current.

The flux density generated by the primary coil couples to the 100 turn secondary inducing about 50 kV in each of the 55 stages which are series connected. The 50 kHz signal is rectified by the shielded diodes and filtered by a $10 k\Omega$ resistor and a 1nF capacitor. The diode shields and series resistor protect the diodes if an arcdown condition occurs.

The beam transport system will consist of electrostatic quadrupoles (ESQ) which have undergone considerable development in the LBNL neutral beam and heavy ion fusion programs. The protons are produced by a rf driven gas source which was also developed in the neutral beam program.

5 CONCLUSION

The air-coupled transformer with multiple secondaries provided the ideal upgrade to an existing power supply

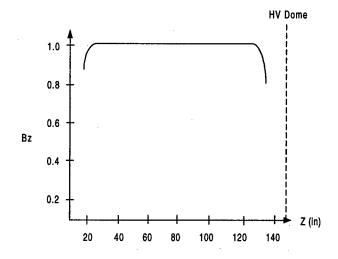


Figure 4: Flux density or coupled secondary voltage

from 5mA to 50mA for BNCT at a relatively low cost since many of the major existing components were reutilized. All the components for the power supply are on hand and as funds become available the complete system including ESQ's and beam transport will be designed and fabricated. The injector is located adjacent to the patient treatment rooms (Fig. 6) in Bldg. 51B.

6 REFERENCES

[1]B.A. Ludewigt, "An Epithermal Neutron Source for BNCT", Proc. Of Topical Meeting on Nuclear Appl., of Accel., Technology, Albuguerque, NM, (1997)

[2]J.W. Kwan, "Applications of Accelerators in Science and Industry", AIP Conference Proceedings, (1998)

[3]M.R. Clevland, IEEE, "Transactions on Nuclear Science", (1965), Vol. NS12

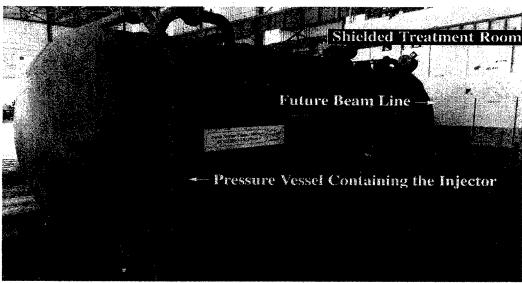


Figure 6: Injector adjacent to patient treatment rooms

NEUTRON TUBE DESIGN STUDY FOR BORON NEUTRON CAPTURE THERAPY APPLICATION*

J. M. Verbeke^{*a,b}, Y. Lee^a, K. N. Leung^a, J. Vujic^b, M. D. Williams^a,
L. K. Wu^a and N. Zahir^{a,b}

^a Lawrence Berkeley National Laboratory

^b Nuclear Engineering Department, University of California, Berkeley

Berkeley, CA 94720

USA

Abstract

Radio-frequency (RF) driven ion sources are being developed in Lawrence Berkeley National Laboratory (LBNL) for sealed-accelerator-tube neutron generator application. By using a 5-cm-diameter RF-driven multicusp source H yields over 95% have been achieved. These experimental findings will enable one to develop compact neutron generators based on the D-D or D-T fusion reactions. In this new neutron generator, the ion source, the accelerator and the target are all housed in a sealed metal container without external pumping. Recent moderator design simulation studies have shown that 14 MeV neutrons could be moderated to therapeutically useful energy ranges for boron neutron capture therapy (BNCT). The dose near the center of the brain with optimized moderators is about 65% higher than the dose obtained from a typical neutron spectrum produced by the Brookhaven Medical Research Reactor (BMRR), and is comparable to the dose obtained by other accelerator-based neutron sources. With a 120 keV and 1 A deuteron beam, a treatment time of ~35 minutes is estimated for BNCT.

1 INTRODUCTION

The RF-driven multicusp ion source developed at Lawrence Berkeley National Laboratory has found numerous applications ranging from neutral beam injection systems for fusion reactors to particle accelerators, proton therapy machines and ion implantation systems [1]. Such sources are simple to operate, have long lifetimes, high gas efficiencies and provide high density plasmas with high monatomic species yields. These characteristics make the RF-driven ion source a viable candidate for the next generation of compact, high-output, sealed-tube neutron generators, utilizing the fusion of deuterium and tritium, or deuterium and deuterium.

Recently, LBNL has developed a compact, sealedaccelerator-tube neutron generator capable of producing a neutron flux in the range of 10° to 10¹⁰ D-T neutrons per second [2-3]. The ion source, a miniaturized variation of earlier RF-driven multicusp ion sources, is designed to fit within a 5-cm-diameter borehole. Typical operating parameters include repetition rates up to 100 pps, with pulse widths between 10 and 80 µs (limited only by the available RF power supply) and source pressure as low as 5 mTorr. In this configuration, peak extractable hydrogen current densities exceeding 1 A/cm² with H⁺ ion yields over 94% have been achieved. From this output, a D-T neutron yield of 10° neutrons per second can be projected. Simple scaling of the ion source and extraction aperture size could bring the neutron output even higher.

These experimental findings together with recent ion source testing and moderator design [4] will enable one to develop compact 14 MeV neutron generators based on the D-T fusion reaction. In this new system, the ion source, the accelerator and the target are all housed in a sealed metal container without pumping. With a 120 keV and 1 A average D⁺ beam current, it is estimated that a treatment time of ~35 minutes is needed for boron neutron capture therapy (10¹⁴ neutrons/sec). This article describes the design and characteristics of the new neutron generator.

2 NEUTRON TUBE DESIGN

In order to achieve a neutron yield of 10¹⁴ neutrons/sec, a large multicusp source together with a multi-aperture extraction system to produce an ion beam current of 1 A, accelerated to 120 kV, and impinging on a well-cooled target is required.

The main components of the sealed D-T neutron tube are the ion source, the 120 kV accelerator column, the water-cooled target and the vacuum system. Figure 1 shows a schematic diagram of the sealed D-T neutron generator. It is a scale up version of the compact neutron tube that LBNL has developed. The characteristics of this neutron generator are as follows.

^{*} This work is supported by Sandia National Laboratory and the US Department of Energy under contract No. DE-AC03-76F00098.

^{*}Email: jmverbeke@lbl.gov

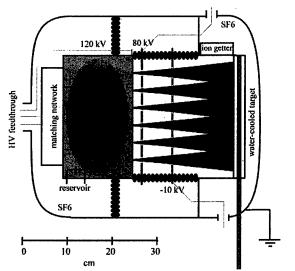


Figure 1: Schematic diagram of the sealed D-T neutron generator.

2.1 The ion source

The multicusp generator is a 30-cm-diameter cylindrical stainless-steel chamber surrounded with columns of samarium-cobalt magnets. The plasma is produced by RF induction discharge. In order to deliver RF power to the plasma, a coupler in the form of a multiturn induction coil is used. The RF power supply is a broad band power amplifier driven at 13.56 MHz by a signal generator.

To maximize the neutron output at the target, it is necessary to produce high D⁺ and T⁺ concentrations in the extracted beam. Experiments have been carried out with a 5-cm-diameter ion source to determine the fractions of hydrogen ion species. For a hydrogen pressure of 4 mTorr, the results are plotted in Fig. 2.

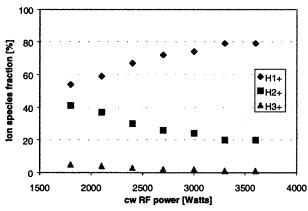


Figure 2: Hydrogen ion species fractions versus cw RF power for gas pressure of 4 mTorr, without magnetic filter.

The monatomic ion species H⁺ can be enhanced by installing a permanent magnetic filter in the source chamber [3]. Lower RF power is then needed to sustain

the plasma: 660 W instead of 1800 W without magnetic filter. For an input RF power of 1500 W, the minimum gas pressure to sustain the plasma also decreases, from 4 mTorr down to 2 mTorr.

Fig. 3 shows that the filter equipped source produces a higher H^{+} fraction than the source without magnetic filter.

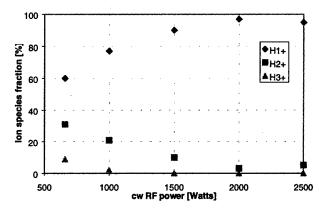


Figure 3: Hydrogen ion species fractions versus cw RF power for gas pressure of 4 mTorr, with magnetic filter.

In the best case, we obtained 97% of H⁺, to be compared with 79% without magnetic filter. Fig. 4 shows the hydrogen ion species for this particular case.

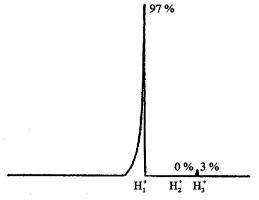


Figure 4: Hydrogen ion species for cw RF power=2 kW and gas pressure of 4 mTorr.

Apart from an area of about 5 cm from the chamber wall, the plasma density is very uniform in the central region of the 30-cm-diameter source. Thus, one can form multiple beamlets with good ion optics to enhance the extractable current.

Figure 5 shows the current density increasing linearly with the RF power. The magnetic filter strength was lower for these measurements due to prior overheating of the magnets. For an input RF power of 3 kW and assuming 50% transparency, we can estimate a total extraction area of ~60 cm² for a current density of 33 mA/cm².

We plan to operate the source in a pulsed mode with a 10% duty factor at a current density of 150 mA/cm². This will produce an average beam current of 1 A on the

target. The RF input power for the beam pulse is now higher, the operating pressure should decrease and the atomic species fraction should improve.

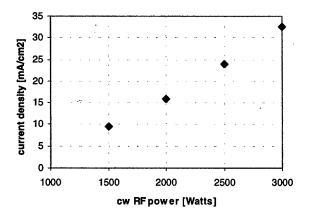


Figure 5: Current density versus cw RF power for gas pressure of 4 mTorr.

2.2 The 120 kV accelerator column

The beam extraction system which closes off the other end of the ion source chamber, contains three electrodes with multiple 5-mm-diameter apertures. The shape, the separation and the voltage distribution on these electrodes are designed by using the I-GUN computation code. The beamlets expand after they exit from the last electrode and therefore the power can be spread uniformly across the target. Source and electrode damages caused by high energy backstreaming electrons can be avoided by the presence of a suppressor electrode.

2.3 The water-cooled target

The target is a water-cooled copper plate covered by a layer of titanium which can absorb deuterium and tritium atoms efficiently. Since the concentrations of deuterium and tritium in titanium decrease with increasing temperature, it is important to keep the target as cold as possible. With a 400 cm² target area, the power density on the target due to the impinging D⁺ and T⁺ ions is ~300 W/cm² which can be easily handled by a modest water flow-rate. In order to maximize the lifetime of the target and to maintain a constant neutron output, a self-loading target will be used and the multicusp source will be operated with a 50% - 50% mixture of deuterium and tritium.

In normal operation, the entire tube will be at an ambient pressure of ~2 mTorr. Low gas pressure is essential for reducing both charge exchange and high-voltage break-down in the accelerator column. The deuterium and tritium gas pressures are controlled by a reservoir element consisting of a tungsten wire coated with zirconium. Release of deuterium and tritium gases is achieved by circulating a current in the tungsten wire. After operation, deuterium and tritium will return to the

reservoir element and target due to the decrease of their temperature. The absence of gaseous tritium in the tube between operations makes the sealed neutron tube safe. In order to control the helium pressure buildup in the tube, some getter pumps will be installed.

Since there is no weak component, the lifetime of the tube should be very long. Higher neutron output can be achieved either by increasing the extraction area or by operating the source with higher discharge power.

3 MODERATOR DESIGN

Epithermal neutrons of energy 10 keV are required for BNCT applications. Using a D-T neutron source of energy 14.1 MeV, one can generate the desired neutron energy spectrum by optimization of the moderator [4].

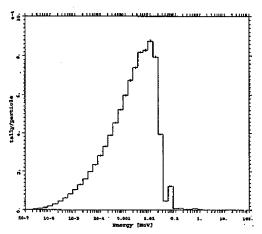


Figure 6: Neutron spectrum obtained after moderation of D-T neutrons.

The neutron spectrum obtained by simulation shown in Fig. 6 results in a dose to the center of the brain about 65% higher than the dose obtained from a typical neutron spectrum produced by the Brookhaven Medical Research Reactor (BMRR), and comparable to the dose obtained by other accelerator-based neutron sources. One can estimate a treatment time of ~35 minutes with a 10¹⁴ n/sec neutron output.

4 ACKNOWLEDGEMENTS

We would like to thank members of the Plasma and Ion Source Technology Group at LBNL for all the technical assistance. This work is supported by Sandia National Laboratory and the US Department of Energy under contract No. DE-AC03-76F00098.

5 REFERENCES

- [1] K. N. Leung, Rev. Sci. Instrum., <u>67</u>, 1302, (1996).
- [2] L. T. Perkins, P. R. Herz, K. N. Leung and D. Pickard, Rev. Sci. Instrum., <u>65</u>, 1186, (1996).
- [3] L. T. Perkins, et.al., Rev. Sci. Instrum., 67, 1057 (1996).
- [4] J. M. Verbeke, J. Vujic and K. N. Leung, Proc. of the 8th Int. Symp. on Neutron Capture Therapy for Cancer, La Jolla, CA, Sept. 1998.

ON-LINE EDUCATIONAL MEANS ON RADIOLOGICAL PROTECTION AND ACCELERATOR GENERAL SAFETY POLICY IN RADIOTHERAPY AND INDUSTRIAL STERILIZATION FACILITIES

B. Spyropoulos, Technological Educational Institution of Athens, Athens, Greece I. Marneris, BNL, Upton, NY

Abstract

On-line educational means were developed, which assist training in Radiation Protection and in Accelerator Technology Safety, in Radiotherapy Departments and Industrial Sterilization Facilities. Hypertext multimedia courseware are gaining importance in University and Professional Education, and may partially release the teaching staff, and offer them more time to concentrate on more substantive tasks, improving their interaction with the individual student. Radiation Protection in Radiotherapy and Industrial Sterilisation Facilities includes several aspects concerning their planning, the hazard-sources, the environmental protection and the general safety. This presentation attempts a methodological approach to the radiation protection policies for Low Energy (up to 50 MeV) and High Current (up to 1kA) Medical and Industrial Electron Accelerator.

1 INTRODUCTION

The purpose of this paper, is to describe on-line educational means, that were developed in order to assist training in Radiation Protection and in Accelerator Technology Safety, in Radiotherapy Departments and Industrial Sterilisation.

Radiation Protection in Radiotherapy and Industrial Sterilisation Facilities includes several aspects concerning their planning, the hazard-sources, the environmental protection and the general safety. This presentation attempts an on-line trainining oriented methodological approach [10][11][12], to the radiation protection policies for Low Energy (up to 50 MeV) and High Current (up to 1kA) Medical and Industrial Electron Accelerator.

2 THE STRUCTURE OF THE COURSE

The developed Hypertext courseware includes presently following topics:

2.1 Radiological Policy and Facility Planning

The Radiological Safety Aspects strongly influencing the site planning are initially dealt with. The accelerator room should usually be in the deepest basement, buried, taking into account the natural features of the ground and of the Hospital or Industrial facility lay-out. Patients or

bulky items should be brought into the vault through a radiation protection door [8], frequently moving on rails. Determination in final architectural lay-out of the location, is influenced by the shape and the dimensions of mazes, shafts and penetrations so that safety and functionality are optimised and by the definition of accessibility policy.

The electron and photon interactions with matter, leading also to a photo-neutron component [1][2][4] and the estimation of the associated radiation parameters which are necessary, in order to calculate the apropriate shielding of walls, roof and ceiling, that determines the civil engineering parameters, are also presented. In the present case, including low energy, skyshine contribution to public exposure is negligible.

Other necessary means are described such as radiation monitors, included in the electrical engineering planning in the irradiation areas, interlaced to the interlock system and the control console, as well as, the substantive considerations in the design of the ventilation, cooling and other auxiliary systems, concerning air, water, component, dust activation, and the formation of noxious gases through radiolytic reactions, during the facility operation.

2.2 Radiation Protection Instrumentation

During the facility operation, in several points around it, qualitative and quantitative measurements, should be performed, in order to assure the appropriate function of the entire installation.

Concerning real-time monitoring, the major controls and the corresponding equipment are illustrated, such as beam presence detected by fixed ionisation chambers or equivalent detectors, connected to the Operation Console, electron dose rate or the equivalent beam current measured by twin built-in ionisation chambers and Marcus chambers, X-Ray Dose Rate in Radiotherapy and Material Irradiation, measured by several types of external ionisation chambers, and neutron component monitoring outside the shielding, in control room, door etc. detected by BF3 or LiJ(Eu) detectors, associated with the Bonner Spectrometer.

Concerning professionally exposed personnel, who should be regularly monitored, through personal badge dose-meters, Thermoluminescence (TLD) albedo dosemeters and ionisation chamber based pocket and pencil dose-meters, and should be equipped with portable survey meters. The most important of these devices are also demonstrated.

Beyond personnel dosimetry, other systematic measurements of integral dose over some time period that might be necessary, as well as, activation measurements of parts of the equipment, the shielding and other materials and the associated equipment are examined.

Finally, Radiation Protection related Beam Diagnostics and the corresponding beam quality parameters, such as presence of the beam, beam current, alignment, and energy calibration are likewise mentioned.

2.3 Environmental Monitoring Program

The components of an environmental monitoring program, and more specifically, ambient (stray) radiation and background dose-rate measurements, aerosols and water radioactivity measurements, and noxious gases measurements [13] in the accelerator room that should be carried out frequently, are summarised in this section. The associated radiation protection and environmental monitoring laboratory is also described.

2.4 General Safety Requirements

The mechanical hazards presented, in the accelerator facilities under consideration, are related to the planning, the installation and the operation of the irradiation head, the gantry and the table in medical accelerators and the overhead cranes, conveyor belts, and load elevators, in industrial accelerators.

Further hazards are related to the design and the operation of the massive radiation protection doors, and to the cooling water, rain-water drainage or water processing units and pipelines, that in case of malfunction, might result in flood.

Electrical hazards included are concerning high voltage used in the klystron, the vacuum and beam-line monitoring instruments, the short-circuit hazards relative to the high current magnet power-supplies, as well as, the common electrical hazards, encountered in any industrial environment.

Disturbances caused by the high frequency on the accelerators monitoring equipment, such as ionisation chambers, if not properly RF-shielded, and general electromagnetic compatibility questions are also considered in this section.

Closely related to electrical hazards, is the threat of fire and the related fire-protection system of the facility including individual smoke detectors combined to with suitable extinguishers.

Finally, a general accident limitation operational policy, including all the remaining miscellaneous hazards, is also synopsized in this section.

2.5 Radiation Treatment Planning and Administration.

In this part, the Simulation and Localisation systems in Radiotherapy, and their functional relation to and mutual interaction with the Treatment Planning systems are presented. Some special techniques [3][5][6][7], beyond usual Tele- and Brachy-Therapy, such as Irregular and Large Field Irradiation, Stereotactic Irradiation, Radiosurgery, and Intra-Operative Radiation Treatment, combined to the appropriate equipment and the necessary radiation protection procedures, are also outlined.

Biological Treatment Planning in Radiotherapy, considering spatial and temporal dose distribution, forms another topic of interest. Systems that provide the means for the estimation of important biophysical parameters such as the Extrapolated Response Dose (ERD), the Tumor Response Probability (TCP), the Normal Tissue Complication Probability (NTCP) etc. are also examined. Most of them are based on probabilistic algorithms, including the concept of memory dose, and established on experimental data for normal tissue tolerance dose levels to therapeutic irradiation., obtained mainly through cell-series irradiation.

Programs for the patient Irradiation Management performed, including record keeping, fractionation, overlapping of past and present schemata etc. and enabling retrospective data analysis and prospective outcome judgement, are also referred to.

3 HEAVY CHARGED PARTICLES IN RADIATION THERAPY

Several attempts to improve the dose distribution and the biological efficiency in Radiotherapy, by using high-LET radiation are described in this future oriented part of the project.

Experiments carried out with pions have shown, that an increase of biological efficiency of only 20% occurred, in the stopping region of the pions, where the nuclear star reactions are taking place. There are problems to create high pion fluences, and, therefore, the overall treatment time is too long and beyond reason expensive for a routine therapy.

The application of fast neutrons in Radiotherapy, on the other hand, have caused severe late effects. Further, only a limited variety of radioresistant tumors can be treated successfully.

Heavy charged particles [9] are gaining importance in external radiotherapy of deep located tumors, because of the limited angular and lateral scattering and the growth of energy deposition with increasing penetration depth.

In this section of the on-line course, the physical and radiobiological advantages of particle beams due to the beam properties and the high LET effects are presented, as well as, the associated benefits, concerning the overall exposure of the patient.

The on-line control of the beam by PET techniques, the improved dose delivery by magnetic scanning and fast energy variation and the tumor conform treatment planning, when using heavy ion beam scanning, constitute further advantages, both, for the treatment of the patients and the radiological safety policy of the facility, that are also included in the presentation.

The performance of the existing accelerator facilities that develop medical activities and the future aspects of particle therapy are also outlined.

4 ON-LINE EDUCATIONAL MEANS AND TRAINING IN RADIATION PROTECTION

Hypertext and multimedia courseware are gaining importance in University and Continuous Education. Transforming conventional lectures or textbook material into an electronic format, offers limited benefits thus, the structure and the content of a course should be changed in order to take advantage of the technology. HTML-based teaching tools interact both with teachers and students and they may influence our understanding of the scientific subject matter under consideration.

Distance education using Web-based and other emerging technological alternatives promise to reach various groups, offering them continuous education services. These groups may comprise of those who are already engaged in professional work, in our case physicians, nurses, engineers, physicists etc. and of those isolated from such opportunities, due to other social conditions. These groups are not likely to receive the same educational experience as traditional, on-campus students. The concern that technology-based distance education is inferior, is probably not unwarranted. However, the new electronic media may offer a cost-effective way, to enhance formal or professional education alternatives.

A specialized course primarily consists of a mutually interacting group and "digital alternatives", such as email, electronic discussion groups, virtual classrooms etc., are very useful, not only for individuals, but even for Institutions, since they are not able nor willing to create an adequately high academic environment. Presently, it seems likely, that on-line courses, will not develop into a total substitute for in-person education, but rather an appropriate combination of traditional and on-line educational activities will follow.

Finally, on-line instructional material accessed by the students or trainees, may also partially release the teaching staff, and offer them more time to concentrate on more substantive tasks improving their interaction with the individual student or trainee.

The use of accelerator technology in Medicine and associated commercial activities is expected to grow rapidly in the dawn of the 21st Century.

Beyond Radiotherapy, Radiopharmaca production, medical applications of Synchrotron radiation and of free electron LASER are visible, at least in Research and Technological Development activities.

The needs for training in Radiation Protection and in Accelerator Technology Safety, in Medical and Industrial Facilities, will also increase accordingly, and the employment of carefully prepared and frequently updated related on-line educational means seems to be inevitable.

5 REFERENCES

[1]Fehrentz D., Spyropoulos B., Neutronen Dosimetrie an einem 42 MeV Betatron, Medizinische Physik 1981,s.693-696.

[2]Fehrentz D., Hassib G.M., Spyropoulos B., Neutronenverschmutzung in Roentgenstrahlenbuendel von Electronenbeschleunigern, Strahlentherapie 159, (1983), s. 703-712.

[3]Fehrentz D., Hensley F., Oetzel D., Spyropoulos B., Vodolan P., Verfeinerte Bestimmung der Dosisleistung bei Irregulaeren Photonenfelder, Strahlenentherapie, 12 (1992), 703-710.

[4]Hassib G.M., Spyropoulos B., Neutron leakage characteristics in high energy medical accelerators, Radiation Protection Dosimetry, Vol.3, No1/2, 1982,pp. 67-70.

[5]Frank C., Fritz P., Spyropoulos B., Trinh S., Flentje M.: Verstaerkung des Kontakteffektes nach LDR - Bestrahlung versus HDR - Bestrahlung in V 79 Sphaeroiden, Jahrestagung der Oesterreichischen Gesellschaft füer Radioonkologie, Feldkirch, 11 - 12.10.1991.

[6]Fritz P., Spyropoulos B., Frank C., Flentje M.: Strahlenbiologische Aspekte bei der gepulsten Brachytherapie, Deutsche Brachytherapie Konferenz, Koeln, Juni 1992.

[7]Fritz P., Weber K.J., Frank C., Spyropoulos B., Flentje M.: In vitro investigations concerning pulsed brachytherapy, "Brachytherapy 1992".

[8]Koutroumbas S., Spyropoulos B., Proimos B.: New shielding materials for the treatment suites of radiotherapy devices, Intern. Conf. Med. Phys. & Biol. Eng., Helsinki 1985.

[9]Kraft G., Radiobiological and physical basis for radiotherapy with protons and heavier ions, Strahlentherap. Onkol. 166, (1990), 10-13.

[10]Spyropoulos B., Radiological Safety aspects of the Design and the Operation of the 185 MeV Athens Race Track Microtron Facility, 1st Mediterranean Congress on Radiat. Protection, Athens, 5-7 April 1994.

[11]Spyropoulos B., Radiological Protection Policy Aspects concerning the preliminary design and operation modus of the Athens Racetrack Microtron Facility, Proceedings of the Particle Accelerator Conference, Dallas, Texas, May, 1-5th, 1995, TAA15.

[12]Spyropoulos B., Radiological Protection Policy Aspects concerning the Design and Operation Modus of Medium Energy (< 1 GeV) or High Current (> 25 MeV, » 1 kA) Electron Accelerators Facilities, Proceedings of the 7th Nuclear Medicine Conf., Athens, May 1996.

[13] Sullivan, A.H. A Guide to Radiation and Radioactivity Levels near High Energy Particle Accelerators, p. 71, Nuclear Technology Publishing, Ashford, Kent, 1992.

NON-DESTRUCTIVE RADIATION TESTING OF PHYSICAL AND MECHANICAL PROPERTIES OF SOLIDS*

V.Deruyga, A. Kalinichenko, Yu. Kresnin, <u>G.Popov*</u>, Kharkiv State University, Kharkiv, Ukraine

Abstract

The radiation-acoustic analyzer for real-time non-destructive investigation of phase state, mechanical and thermodynamic characteristics of solids was designed. Its action is based on original radiation-acoustic method, which includes probing of investigated materials by pulsed electron beam and registration of the excited acoustic waves. The results of radiation testing of some metallic alloys are discussed.

1 INTRODUCTION

The radiation-acoustic analyzer (RAA) has been developed for real-time simultaneous measurements of the Gruneisen parameter, sound velocity, elasticity modulus, the Poisson ratio, linear thermal expansion coefficient and specific heat of structural materials exposed to dynamic and static stresses, radiation and electromagnetic fields, temperature etc. It also may be used for investigation of kinetics of structure phase transition (SPT) of the first and second kind in metals, ceramics or polymers. Developed facility is especially useful for investigation of materials showing nonlinear behaviour in the vicinity of SPT where conventional static methods may not reveal some nonlinear effects.

2 RADIATION-ACOUSTIC METHOD OF MATERIAL INVESTIGATION

Radiation-acoustic method of measurement of characteristics of materials [1-7] includes the probing of investigated material by pulsed beam of ionizing particles (electrons, protons, gamma-quanta etc.) and registration of instantaneous acoustic stresses $\sigma(x - st)$ caused by fast heating of the material. Here x – distance between the center of the beam-target interaction spot and the acoustic detector, s – sound velocity, t – time. The magnitude of σ is determined by the density ε of energy, released by the beam in the target, the Gruneisen parameter Γ and the Poisson ratio μ of the target material:

$$\sigma(x-st)=\gamma \mathcal{E}(x-st)/2, \qquad (1)$$

where γ is the sound generation parameter, which is expressed through Γ and μ as [2, 3]:

$$\gamma_1 = (1 - 2 \mu) \Gamma$$

for one-dimensional (thin rod shaped) target,

$$\gamma_2 = \Gamma(1 - 2 \mu) / (1 - \mu)$$

for two-dimensional (thin plate shaped) target,

$$\gamma_3 = \Gamma$$

for three-dimensional target (in bulk of the material). The Gruneisen parameter is given by the formula

$$\Gamma = \alpha \mathbf{E}_{Y} / [3 \rho \mathbf{C} (1-2 \mu)],$$

where α is the coefficient of thermal expansion, $\mathbf{E}_{\mathbf{Y}}$ is the Young modulus, ρ is the target material density, \mathbf{C} is its specific heat.

By processing of the signal $\sigma(x - st)$ registered by acoustic detector connected to the target one can extract information about those characteristics of the target material which determine the stress magnitude. The time resolution of the method is determined by the particle pulse width, beam diameter, geometry and the bandwidth of the detector. For our equipment it is limited by 10 ns. Equation (1) is valid in the approximation of instant release of the energy in the target, i.e. $\tau << \tau_s = D/s$, where τ_s is the acoustic relaxation time, τ is the duration of the radiation pulse, and τ 0 is the beam diameter. It is also supposed that the condition

$$\gamma (T + \Delta T) - \gamma (T) << 1$$

is satisfies. It means that in the range of radiation overheating $\Delta T = \mathcal{E}/(\rho C)$ parameter γ , does not change significantly. T is the initial temperature of the material.

3 RADIATION-ACOUSTIC ANALYZER

The radiation-acoustic analyzer includes an electron accelerator, a testing bench on which the tested sample is exposed to programmed sequence of external actions and the radiation-acoustic system (See Fig.1).

The radiation-acoustic system includes a set of acoustic sensors and the sensors of temperature, static and dynamic

Work was supported by the STCU, Kyiv, Grant #155

Email: popov@pht.univer.kharkov.ua

stress, deformation, radiation flux, etc. The data acquisition and processing module of the system is controlled by IBM PC computer and consists of a strobig analog-digital convertor, a commutator of analog signals, a module of synchronization and automated remote control.

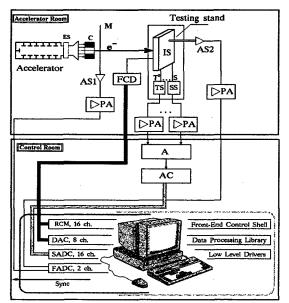


Figure 1. Scheme of the radiation-acoustic analyzer.
e - pulsed electron beam; ES - electromagnetic scanner; C -collimator; M - thermoacoustic monitor; AS1, AS2 - acoustic sensors; IS - investigated sample; TS - temperature sensor; SS - sensor of static and dynamic stresses; PA - preamplifier; FCD - set of final control devises; A - amplifiers; AC - commutator; SADC - high precision analog-digital converter; FADC - strobing analog-digital converter; Sync - clock pulse; DAC - digital-analog converter; RCM - remote control module.

Radiation probing of investigated samples is performed by single pulses of electron beam with energy 5-30 MeV and low-intensity $(10^7-10^{10}$ electrons in a pulse). The beam diameter is 1 - 4 cm, the pulse width 10^{-8} - 10^{-5} s. Radiation heating Δ T \leq 10^{-3} K of the sample material by such a pulse does not cause irreversible changes of investigated materials. To simplify the data analysis experimental samples are shaped as thin rods or plates. The sample thickness **d** must satisfy the conditions:

$$\mathbf{d}(\mathrm{d}\mathbf{E}_e/\mathrm{d}x) << \mathbf{E}_e, \qquad \mathbf{d} + s \, \tau_b << \mathbf{D} \quad (3) .$$

Here \mathbf{E}_e is the electron energy, $d\mathbf{E}_e/dx$ is the electron energy loss in the target material, $\boldsymbol{\tau}_b$ is the effective electron pulse width, \mathbf{D} - the beam diameter.

Acoustic pulses excited in the target IS and monitor M by the same electron pulse are recorded using radiationresistant broad-band (10MHz) piezoceramic sensors AS1 and AS2, and analog-digital converter SADC (See Fig.1). Amplitude, duration and shape of acoustic pulse and the delay between pulses from AS1 and AS2 are registered.

One- or two-dimensional thermoacoustic monitors M on the base of thin rods or plates allow as to determine the following characteristics of the beam: intensity, coordinates of the beam spot on the target and radial distribution of particles in the beam, instantaneous beam intensity, the energy of the beam pulse. The system also allows us to change programmatically the conditions of the experiment, for instance to change the temperature of the samples, static and dynamic stresses, radiation and electromagnetic field affecting the sample.

The software of the analyzer makes it possible to program the experimental routine, to control the experiment online, to read, process and display information. One can see on line the shape of acoustic signals, parameters of the acoustic pulse and the electron beam. Epures of temperature, stress and deformation can also be displayed on the monitor screen. The program calculates mechanical and thermodynamic characteristics of investigated materials, stores and reports the data.

4 APPLICATION OF RAA FOR INVESTIGATION OF STRUCTURE PHASE TRANSITIONS IN SOLIDS

The analyzer was used to study characteristics of materials with shape memory effect: CuAlNi, TiNi, TiNiFe, TiNiCu, TiNiHf (the phase transition martensite ↔ austenite); rare-earth metals: Gd, Dy (ferro ↔ paramagnetic transition); hot-pressed high-temperature superconducting ceramics (the phase transition to a superconducting state); polymers: polymetylmetacrylate, polythetraftorethylene, polyethylene etc. (glassy ↔ highly elastic state). Phase transitions were detected by the change of thermoelastic and thermodynamic parameters of the materials at the phase transition point. These studies were held in a wide range of temperature (80 - 500K) and in a wide range of tensile or bending stress (10 - 1000 MPA).

The hysteresis behaviour of the temperature dependencies of parameters γ (T), $E_{Y}(T)$, s(T), C(T) and α (T) was observed in the vicinity of the SPT for all investigated alloys with shape memory effect (CuAlNi, TiNi, TiNiFe, TiNiCu, TiNiHf). Such hysteresis is characteristic of martensite•austenite transitions. It is found that the shape of the hysteresis loop and its position on the temperature axis for parameters measured is depends on the concentration of the main components Ti, Ni and the admixtures Cu, Hf and Fe. It also depends on the stress caused by the sample deformation. For TiNi based alloys the elasticity modulus E_{Y} goes to a minimum in the region of SPT for both forward and backward transitions. It is connected with arising of "soft modes" in the vibration

spectrum of the metal and ultimate instability of the crystal lattice near SPT.

On Fig.2 temperature dependencies of elasticity modulus $E_Y(T)$ for TiNiFe alloy in a free state (solid lines) and in a stress-strained state (dashed lines) are shown. External stress ≈ 120 MPa was produced by a three-point bend at the temperature 280 K. The stress raises the temperature of the martensitic phase transition by the value of $\Delta T \leq 6K$ and reduces a degree of "softening" of crystal lattice $E_{m2} > E_{m1}$. By integrating of specific heat C(T) in the vicinity of the phase transitions the heat of direct (exothermic) austenite-martensite SPT $H_{A-M} = -18,3$ J/g and opposite (endothermic) martensite-austenite SPT $H_{M-A} = 16,9$ J/g were determined.

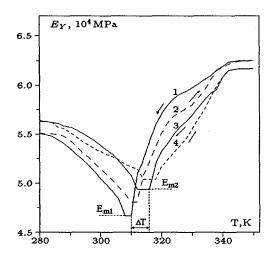


Figure 2. Temperature dependencies of the elasticity modulus $E_Y(T)$ for TiNiFe alloy.

Radiation-acoustic investigation of the alloys TiNi, TiNiCu, TiNiFe at their electrochemical saturation with hydrogen H_2 and deuterium D_2 were carried out. Saturation of the alloy with hydrogen or deuterium changes the amplitude σ of acoustic signal, and one can observe softening of the lattice and shifting of the hysteresis curves of γ (T) and E_{γ} (T) along the temperature axis by the value $\Delta T \leq 30$ K depending on concentration H_2 or D_2 concentration.

For hot pressed high-temperature superconducting ceramics the measurements of γ (T) in the temperature range of 85-300 K were carried out. It was found that the maximum of the generation parameter γ (T) is reached in the region of the superconducting phase transition (T_k = 92 K).

5 CONCLUSION

The major advantage of the radiation-acoustic method of the material properties investigation is its high productivity. Using this method one can obtain for an hour the amount of experimental data for obtaining of which by conventional methods one would have spend years. Therefore the method is extremely useful in technological the researches where the qualities of the end product depend on multiple parameters of the technological process. This method showed its power at the development of the technology of new polymer composite materials [8] where the amount of multiparameter experiments performed was so large, that it would have not be feasible without RAA.

6 REFERENCES

- [1] White R.M., J. Appl. Phys. 34, 3559 3563 (1963).
- [2] Zalubovskiy I.I., Kalinichenko A.I., Lazurik V.T. Introduction to radiation Acoustics (in Russian). Vishcha Shkola, Kharkov, 1986, p.86-111.
- [3] Kalinichenko A.I., Popov G.F. Akusticheskiy Zhurnal. 36, 950-952 (1990).
- [4] Popov G.F, Fizika Metallov i Metallovedenie. 75, 84-89 (1993).
- [5] Kresnin Yu.A., Popov G.F. Instruments and Experimental Techniques. 37, 592-595 (1994).
- [6] Kresnin Yu.A., Popov G.F. Bulletin of the American Physical Society. 40, 1100 (1995).
- [7]Popov G., Deryuga V., Kalinichenko A., Kresnin Yu. Proc. Intern. Conf. on Accelerator and Large Experimental Physics Control Systems. Chicago, USA, Oct.30, p.954-956, (1995).
- [8] G. Popov, I. Zalubovskiy, A. Avilov, V. Rudychev, Bulletin of the American Physical Society 42, N3. p.1375, (1997).

NON-WASTE AND RESOURCE-SAVING RADIATION PROCESS OF POLYMER MODIFIED WOOD PRODUCTION#

A.Avilov, V.Deruyga, <u>G.Popov</u>*, V.Rudychev, I.Zalyubovsky Kharkiv State University, Kharkiv, Ukraine

Abstract

Technology of modification wood with synthetic polymer is designed. It is useful for improvement of consumer value of low-grade soft wood such as poplar, aspen, alder or birch as well as for utilization of wood-making industry wastes such as cuttings, sawdust and chips. Composite materials are manufactured by impregnation of wood with synthetic monomers or oligomers and subsequent radiation polymerization. The materials excel all kinds of natural wood in their resistance to abrasion and corrosion. The development was carried out using a linear electron accelerator with electron energy 5 - 8 MeV and beam power 5 kW.

1 INTRODUCTION

The development of radiation technology of various polymer composite materials has been held at Kharkiv State University for the last few years [1-6]. Such base components as wood, fiber-board, paper; gypsum, tuff, calcite, sand and their mixtures, wastes of paper, textile and wood; crumbs and dust of marble, granite, gypsum, asbestos-cement, concrete, ceramic are used as the materials base. These capillary-porous materials are impregnated with liquid binder (synthetic monomer or oligomer). For polymerization of the binder in bulk of the materials we use microwave, electron or gamma radiation with energy less than 10 MeV.

It is found that by varying the conditions of polymerization one can significantly change the properties of the final material and obtain variety of products from the same row supplies. Low-value raw materials and waste products can be utilized with low energy consumption. When using molding, casting or extrusion for shaping goods one can have an extremely low waste of products. Polymer modified wood (PMW) having attractive look and exceptional durability is the first among developed materials to enjoy commercial success.

2 TECHNOLOGICAL PROCESS

The process of radiation-chemical modification of wood for production of chipboard, plywood veneer or another goods includes the following operations: drying of wooden supplies, bunching, degassing, impregnation with synthetic monomer or oligomer, hermetic encapsulation/shaping, radiation treatment, unloading of the end product, trimming/abrasion. The technological scheme of the radiation-chemical process of polymer-modified wood formation is shown in Fig.1.

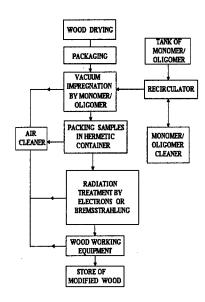


Fig.1. The technological scheme of polymer-modified wood formation under action of relativistic electrons or bremsstrahlung radiation.

The drying is carried out in microwave chambers or vacuum-thermal drying boxes. Dry wood or wooden articles are packed up in metal cassettes which measure $100x10x70 \text{ cm}^3$. Each cassette can hold up to 150 parquet strips or correspondent number of solid blocks of material (usually $100x10x7 \text{ cm}^3$). Our $1m^3$ vacuum chamber can hold up to 16 cassettes. Impregnation of wood with binder is carried out by "vacuum - atmospheric pressure – overpressure" method. After pumping the chamber it is filled with liquid binder from recirculating reservoir. Treatment time depends on necessary impregnation degree (40 -100 mass per cent).

After impregnation each cassette with wood is put to a light, transparent for radiation frame hermetically wrapped with 0.3-0.5 mm aluminum foil. These containers are placed consequently on a conveyor delivering them into the radiation field formed by scanning electron beam. Each container may pass the

Work was supported by the STCU, Kyiv, Grant #155

^{*} Email: popov@pht.univer.kharkov.ua

sides are irradiated.

3 EQUIPMENT

The facilities for PMW formation incorporate a microwave chamber for drying of wooden supplies, a vacuum system for evacuating of oxygen and residual moisture from base material, the system for impregnation of evacuated samples with liquid synthetic binder, facilities for purification of monomer/oligomer and air in work area, radiation-chemical installation for binder polymerization, woodworking equipment for machining of natural and modified wood and equipment for testing of physical and mechanical properties of PMW. The radiation-chemical installation includes a linear electron accelerator, the system for the electron beam scanning, a bremsstrahlung converter, the system for electron beam parameters control and radiation monitoring, and the technology control system. The linear electron accelerator "Electronica - U003" is used as a radiation source. It has the following characteristics: electron energy 4-8 MeV: electron beam current 0.5 mA; mean beam power 5 kW; pulse duration 1-4 µs; pulse frequency 1-250 Hz; frequency of electromagnetic scanner 1-8 Hz; the deviation angle of the scanner ±20°. The electron energy is converted to bremsstrahlung radiation with a tantalum converter placed in front of the container.

Beam parameter control system [7–9] is based on original rod/plate shaped thermoacoustic detectors. It allows measuring of the following instantaneous or integral parameters of electron/bremsstrahlung beam: intensity, diameter and position on the target, effective width, particle distribution in the beam cross section and on the surface of target, cumulative dose of radiation. It makes it easy to adjust radiation beam for particular technology needs.

4 EXPERIMENTAL RESULTS

The process of radiation-induced composite material formation for several combinations of base and binder was studied. Such kinds of wood as aspen, alder, poplar, birch, beech, oak, hornbeam and yew ware taken as the base. Vinylacetate, methylmethacrylat, butilmethacrylat, styrene, polyesther- and epoxy resins and their mixtures were used as the binder. Wide and flat samples (around 100x50 cm²) were treated by scanning electron or bremsstrahlung beams. Plane distribution of radiation flux on the surface of large samples was achieved by using a special form modulation current to feed the electromagnet of the scanning system. The samples, more than 100 cm, were treated by shifting step by step transversely to the electron beam. The radiation monitoring system allowed obtaining three-dimensional dose distribution experimental samples so as to make the radiationchemical experiments more precise.

factor for given chemical content of the material is the dose of electron/bremsstrahlung radiation. The type of radiation and the dose rate also have effect and should be considered when choosing the conditions of the radiation-induced polymerization of materials. Two-sided irradiation of thick PMW samples or sample stacks, which thickness is more than the electron range, was used. For thick high-density items it is useful to convert the electron beam to bremsstrahlung which has higher penetration ability and therefore produces more homogeneous absorbed dose.

The processes of polymerization and co-polymerization of monomer in capillary-porous or dispersed filler differs from one in pure monomer binder and has catalytic nature. That is why dispersion or specific surface of the base material have as much influence on polymerization degree as concentration of sensitizing impurities or temperature.

Methods of optimizing parameters of radiation treatment targeted to maximize productivity of the accelerator and obtain the most homogeneous dose distribution in the volume of processed materials were developed. On the basis of our experimental data as well as computer simulation of the radiation field in the target material a mathematical model of the polymerization process was built. The parameters of the model are electron energy, beam current, exposure time, temperature, geometric parameters of the scanning beam and the container, wood density, the chemical formula of the binder and impregnation degree. There are variants of the model considering two-sided irradiation of the container and conversion electron beam to bremsstrahlung. For the particular base-binder pair unknown parameters of radiation polymerization process are determined by a few technological experiments, and then one can calculate the optimal conditions of the process in terms of productivity and homogeneity of dose. In general the dose 5-50 Mrad necessary to achieve the desired degree of polymerization, and it takes 5-30 minutes of irradiation on such accelerator as we used. Overall productivity of our pilot model of installation is 20 000 - 40 000 m³ of parquet flooring per year.

Pilot series of goods and experimental examples of polymer-modified wood were manufactured. The following characteristics of new PMW were measured: mass density; hardness; bursting and bearing strength, toughness, compression and elasticity modules, abrasive wear, thermal expansion coefficient, moisture resistance; shape stability; waterproof, thermoinsulation and dielectric characteristics; fire resistance; biological and chemical resistance. It was shown that because of modification the wood the hardness increases 5-10 times, elasticity modulus increases 2–5 times, abrasion wear decreases 2–4 times, water absorption decreases 20-50

material to desired color, for example make the inexpensive wood looking like ebony or mahogany.

that all mechanical and operational properties of modified soft wood are better than properties of natural oak.

Some characteristics of modified with methylmethacrylat wood are compared with

Table 1. Comparative characteristics of natural and modified with methylmethacrylat wood

Characteristic	birch		aspen		oak
	original	modified	original	modified	original
Density, g/cub.sm	0.63	0.9 -1.2	0.47	0.9 -1.2	0.69
Hardness, MPa	40 - 48	120 - 180	25 - 30	110- 160	65 - 70
Cross-breaking strength,MPa	80 - 90	200 - 260	70 - 80	160- 200	90-110
Compressive strength, MPa	45 - 55	100 - 130	30 - 40	100- 120	45 - 58
Impact strength, KJ/sq.m	70 - 80	120 - 260	70 - 80	120- 220	65 - 80
Abrasion wear, mm	0.5 - 0.6	0.2	1.2	0.35	0.5
Water absorption for 24 hrs,%	70 - 80	3 - 6	70 - 95	3 - 6	25- 30

5 CONCLUSION

An ·advantage of the developed technology is the possibility to utilize wastes of woodworking industry such as wood, chipboard and veneer cuttings, sawdust and chips. Such soft low-grade wood as poplar, aspen, alder, and birch make high quality materials when modified with synthetic polymer. Polymer modified materials may be used for manufacturing such top-quality goods as furniture, window frames, doors, parquet, wall siding, gear drives, etc.

High hardness and shape stability, high thermoinsulation and waterproof characteristics, chemical and biological durability make the materials ideal for use in heavy conditions such as chemically aggressive environment or wet tropical climate, another prospective area of application is preservation and restoration of antiquities.

6 REFERENCES

[1] I. Zalubovskiy, A. Avilov, G. Popov, V. Rudychev, Proc. Int. Conf." Physics in Ukraine", Kiev, Ukraine, June, p.234-236, (1993).

[2] I. Zalubovskiy, A. Avilov, G. Popov, V. Rudychev, Bulletin of the American Physical Society 40, N3. p.1098, (1995).

[3] G. Popov, I. Zalubovskiy, A. Avilov, V. Rudychev, Bulletin of the American Physical Society 42, N3. p.1375, (1997).

[4]. G. F. Popov, V. A. Deryuga. ECAART 97, Eindhoven, the Netherlands, p.176, (1977).

[5]. G.Popov, A.Avilov, V.Rudychev, I.Zalyubovsky, "International Technology Transfer from the Newly Independent States of the Former Soviet Union", ITT-98, Des Moines, Iowa, USA, (1998).
[6]. I.Zalyubovsky, A.Avilov, G.Popov, V.Rudychev Proc.Int. Conf.

[6]. I.Zalyubovsky, A.Avilov, G.Popov, V.Rudychev Proc.Int. Conf. "Cyclotrons and Applications", 15-19 March 1997, Cairo, Egypt, p. 281-288, (1998).

[7].I.Zalyubovsky, A.Kalinichenco, Yu.Kresnin, G.Popov Proc.Int. Conf. "Cyclotrons and Applications", 15-19 March 1997, Cairo, Egypt,

p.434-443, (1998).

[8] A. Kalinichenko, G. Popov, Proc. Intern. IEEE Nuclear Scince Symposium. Anaheim, USA, Nov. 3-9, p. 83, (1996).

[9] G. Popov, V. Deryuga, A. Kalinichenko, Yu. Kresnin. Proc. Intern. Conf. on Accelerator and Large Experimental Physics Control Systems, Chicago, USA, Oct.30, p.954-956, (1995).

ULTRA-BRIGHT X-RAY GENERATION USING INVERSE COMPTON SCATTERING OF PICOSECOND CO₂ LASER PULSES

A. Tsunemi*, A. Endo, R&D Center, Sumitomo Heavy Industries, Ltd.
2-1-1 Yato-cho, Tanashi, Tokyo 188-8585, Japan;
I. Pogorelsky**, I. Ben-Zvi, K. Kusche, J. Skaritka, V. Yakimenko, Brookhaven National
Laboratory, 725C BNL, Upton, NY 11973, USA;
T. Hirose, Department of Physics, Tokyo Metropolitan Univ.,
1-1 Minami-Osawa, Hachioji, Tokyo 192-0397;
J. Urakawa, T. Omori, KEK, 1-1 Oho, Tsukuba, Ibaraki, Japan;
M. Washio, Waseda Univ., 1-6-1 Nishi-Waseda, Shinjuku, Tokyo, Japan;
Y. Liu, P. He, D. Cline, UCLA, 405 Hilgard Ave. Los Angeles, CA 90095, USA

Abstract

Laser-Compton scattering with picosecond CO_2 laser pulses is proposed for generation of high-brightness x-rays. The interaction chamber has been developed and the experiment is scheduled for the generation of the x-rays of 4.7 keV, 10^7 photons in 10-ps pulse width using 50-MeV, 0.5-nC relativistic electron bunches and 6 GW CO_2 laser.

1 INTRODUCTION

Laser Compton scattering can generate x-rays or γ-rays with high brightness and controlled polarization by applying high-peak-power laser pulses to relativistic electron bunches. We propose to use laser this method for generating circularly polarized y-rays which, by paircreation, produce circularly polarized positrons for JLC (Japan Linear Collider) project [1]. In this scheme, a picosecond CO₂ laser will be used as a photon source for Compton scattering. This choice is based on the wavelength proportional increase of laser photon flux per joule of the laser energy, the average power scalability, high wall-plug efficiency, and a capability to the highrepetition rate operation. In general, Compton scattering with CO2 laser has a promise to become a compact, highintensity, monochromatic, femtosecond x-ray source for a variety of applications beyond the polarized positron source [2].

We would like to acknowledge Igor Meshkovsky and Andrei Dyublov of Optoel Co. (St. Petersburg, Russia) who designed the Compton chamber and proposed and manufactured the target system with oxidized vanadium thin films.

Email:

* akr_tsunemi@shi.co.jp

2 EXPERIMENTAL SETUP

We have developed a laser-Compton scattering chamber for the proof-of-principle experiment, in which counterpropagating electron and CO2 laser pulses collide at the focal point. Fig. 1 shows the conceptual drawing of the Compton chamber to be installed in the linac beamline of the Accelerator Test Facility at Brookhaven National Laboratory. Picosecond CO2 laser beam is introduced through the side window and focused by an off-axis parabolic Cu mirror of the 50 mm diameter with the focal length of 15 cm. The Cu mirror has 5 mm diameter hole along the electron beam axis to let electrons pass through. An axicon telescope is placed on the CO₂ beam axis just before the Compton chamber. This telescope serves to modify the Gaussian spatial profile of the incident laser beam into the "donut"-shaped profile, as is shown in Fig. 2-(a). This allows the laser radiation to bypass the hole in the focusing parabolic mirror. Fig. 2-(b) represents a numerically calculated CO₂ beam profile at the focal point. The estimated beam waist size is about 100 µm (FWHM), that corresponds to the electron beam size at the colliding point. Diverging after the focal point the spent laser beam is recollimated by another parabolic Cu mirror and is extracted from the chamber through the output window.

The diagram of the experimental setup is shown in Fig. 3. Picosecond YAG laser pulses are split and delivered to the photo-cathode of the RF gun and for the CO₂ pulse slicing to the 180 ps FWHM by the optical semiconductor optical switching method. The sliced CO₂ pulses are amplified up to 6 GW by the high-pressure TE CO₂ regenerative laser amplifier [3].

Electron bunches with the charge of about 0.5 nC are generated by a photo-cathode RF gun. They are accelerated up to 50 MeV in the RF linac and focused by quadrupole magnets at the center of the chamber.

Since the same mode-locked YAG laser controls both processes of the CO₂ pulse slicing and photo-cathode illumination, the timing jitter between the CO₂ laser and

^{**} igor@bnl.gov

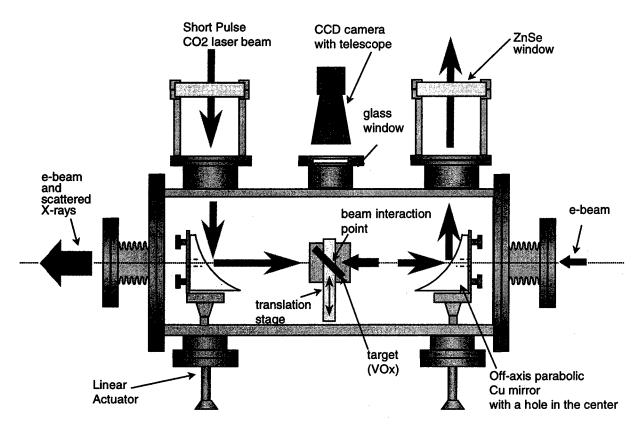


Fig. 1 Top view of the Compton chamber

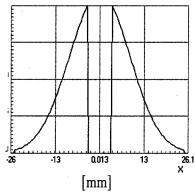


Fig. 2-(a) CO₂ beam profile at the entrance window

electron bunches is negligible to compare with the pulse duration.

For fine alignment of the laser and electron beams at the colliding point and the observation of their spatial profiles, we use a target composed of the vanadium oxide thin film coated on a mica substrate. This coating is sensitive to both electron and mid-infrared beams. In the preliminary test with a focused picosecond CO₂ laser pulse, beam profile image was clearly visible as about 100 μ m wide blackened spot. The image capture for the mid-infrared beam is physically based on the film reflectivity change in the visible region due to the phase transition in the oxidized vanadium crystal structure heated by the laser beam. Since the reflectivity shows hysteresis nature

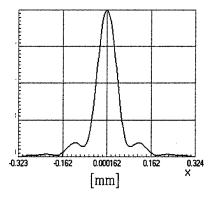
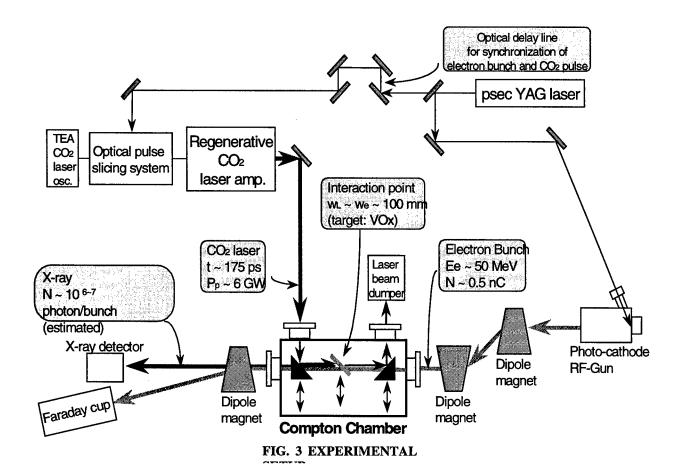


Fig. 2-(b) CO₂ beam profile at the focal point

in the response to the temperature, the laser spot image can be "grabbed" by maintaining the target temperature around 55°C.

Upon interaction of the 0.5 J laser pulse with the 0.5 nC electron bunch, we expect to observe up to 10^7 of the Compton scattered x-ray photons with the maximum energy of 4.7 keV and the angular divergence of 10 mrad. The x-ray pulse width will be 10 ps, which is approximately the same as the electron bunch length. The scattered x-rays will be detected by a silicon photodiode placed behind the Be window downstream of the dipole magnet that serves to separate electron and x-ray beams.



3 SUMMARY

The experiment to observe high-brightness x-ray generation using Compton scattering of the relativistic electron beam with the picosecond CO₂ laser is scheduled at the BNL Accelerator Test Facility.

The laser pulse to be applied to this experiment has about 6 GW peak power and the 180 ps pulse width, which is longer than the laser waist length at the

interaction region. In order to decrease the laser pulse length, multi-step pulse slicing system will be assembled and applied in the future experiments. In addition, 10-atm TE $\rm CO_2$ power amplifier is planned to be installed to increase the laser peak power up to the 1 TW level.

4 REFERENCES

- [1] T. Okugi et al., Jpn. J. Appl. Phys. 35 (1996) 3677
- [2] I. V. Pogorelsky, Nucl. Instr. & Meth. Res. A 411 (1998) 172
- [3] I. V. Pogorelsky et al., IEEE J. Quantum Electron., 31 (1995) 556

A COMPACT INDUSTRIAL HIGH-CURRENT CONTINUOUS WAVE ELECTRON LINAC

A.S. Alimov*, D.I. Ermakov*, B.S. Ishkhanov*, E.A. Knapp, A.F. Salakhutdinov*, V.I. Shvedunov*, and W.P. Trower, World Physics Technologies, Blacksburg VA

Abstract

We have designed a family of new Continuous Wave LINear ACcelerators for electron-based industrial, medical, and environmental irradiation applications. Our ten reliable, small, inexpensive high-power modular accelerators will produce beams with energies from 0.6 to 6.0 MeV in increments of 600 keV, each with a current selectable from 0 to 50 mA. We have constructed the critical gun-1st section model, which has undergone the first beam test. We have achieved beam parameters of 600 keV, 10 mA, and 6 kW and we have demonstrated all the innovations of our initial design [1].

1 INTRODUCTION

Particle accelerators with increasing beam power are being required for large-scale industrial production lines, as well as for the destruction of biological and chemical waste. Although direct current machines produce adequate beams of ~1 MeV, raising the beam energy significantly increases their size, weight, and cost. Thus, we are constructing a family of ten accelerators to produce electrons with energies from 0.6 to 6 MeV in increments of 600 keV with corresponding beam power from 30 to 300 kW. Only our 1st accelerating section is a non-standard section since it must accelerate 15 keV gun electrons to a relativistic energy of 600 keV. Subsequent identical sections will each increase the beam energy by 600 keV.

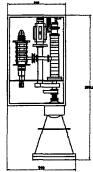


Figure 1: Gun-1st section LINAC schematic

Having completed the design of our accelerator family, we are commissioning a prototype gun-1st section model which uses a: (1) Low-energy 15 keV

thermionic electron gun joined directly to the first <u>A</u>ccelerating <u>S</u>tructure cell; (2) High capture efficiency for low-energy gun electrons AS; (3) Simple reliable <u>R</u>adio <u>F</u>requency power supply system; and (4) Common gun-klystron power supply. Our LINAC is shown in Fig. 1 and its principal parameters are listed in Table 1.

Table 1: Gun-1 st section parameters				
Output beam energy	y	0.6 MeV		
Beam current		0 to 50 mA		
Maximum beam po	wer	30 kW		
Length		1.2 m		
Weight		~70 kg		
Gun/klystron	high	15 kV		
voltage	_			
Plug power consumption		~75 kW		
Electric efficiency		~40%		

2 ELECTRON GUN

Since we have used a common power supply for the gun and the klystron, our electron gun beam energy is 15 keV. To make our accelerators compact, we eliminated the traditional bunching system, drift space, and focusing elements and mount the gun directly to the AS. The gun currents are selectable from 0 to 250 mA with 100 mA being the nominal operating current. The gun beam radii are less than 2.5 mm with crossovers at greater than 50 mm from the cathode so that the beam is convergent in the first AS cell.

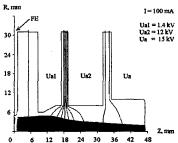


Figure 2: Gun schematic with beam trajectories [2]

We satisfied these requirements with a three-anode gun, shown in Fig. 2, that has a 8.6 mm diameter spherically concave cathode. The <u>Focusing Electrode</u> is at the cathode potential while the two intermediate anodes are held at Ua1 and Ua2 and the main anode,

^{*} Permanent address: Institute of Nuclear Physics, Moscow State University, Moscow, Russia.

[†] Email: wptinc@naxs.net

located at the gun exit, is held at Ua = 15 kV. The intermediate anode potentials are defined by $Ua1 = k \cdot 1.75 \text{ kV}$ and $Ua2 = k \cdot Ua$, where the coefficient, $0 \le k \le 1$, provides current regulation from zero (k = 0) to 250 mA (k = 1). Once manufactured, we tested our gun, as seen in Fig. 3, with currents up to 50 mA before installing it on the AS.



Figure 3: Gun at the test stand

3 BEAM DYNAMICS

The 1st AS has 14 cells with β from 0.237 to 0.888. Injecting a 15 keV direct current gun beam into the initial AS cells, which must then form bunches with energy up to ~75 keV, places large demands on the beam dynamics. We designed the subsequent β >0.5 cells by roughly scaling the cells with β =1. We calculated the beam dynamics [3] principally to optimize the longitudinal and transverse beam motion in the first AS cells and then to further optimize the entire AS beam dynamics using "real" electron gun beam parameters and space charge effects.

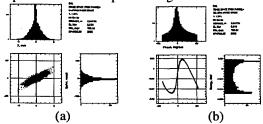


Figure 4: Second AS cell center phase space: (a) transverse and (b) longitudinal

We must provide high capture efficiency, I_{out}/I_{gun} , in the initial AS cell that is acting as a pre-buncher. To accomplish this we must provide the maximum bunching parameter (i.e., the maximum first current harmonic) at the second cell (the first accelerating cell) center. The transverse and longitudinal beam phase spaces at the 2^{nd} cell center, shown in Fig. 4, confirm the pre-buncher cell effectiveness by the tightness of the longitudinal phase space.

Table 2: Gun-1st section beam parameters

Igun	100 mA
I _{out}	51 mA
$\langle \mathrm{W}_{\mathrm{beam}} \rangle$	610 keV
ΔW_{beam}	± 20 keV
$\Delta \phi_{beam}$	~50 deg
Norm. $\langle \varepsilon_{x} \rangle$	27.5 mm \times mrad
Norm. (ε _y)	28.3 mm × mrad

The AS transverse and longitudinal output beam phase spaces are shown in Fig. 5 and the output beam parameters are given in Table 2.

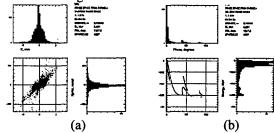


Figure 5: AS output phase space: (a) transverse and (b) longitudinal

4 ACCELERATING STRUCTURE

Initially we separately optimized the three low β cells and then the higher β cells. The pre-buncher cell has 1/9 the on-axis field amplitude of the first accelerating cell. We used the preliminary beam dynamics results to calculate the first two cells, shown in Fig. 6, whose gap lengths and distances were unchanged in the optimization.

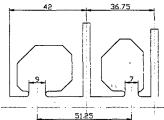


Figure 6: Pre-buncher and first accelerating cell geometry

We obtained the required on-axis AS field amplitude ratio with a 56° pre-buncher cell coupling slot and a 24° first accelerating cell coupling slot. After optimizing the coupling slot size and position and cell radii, we tuned the frequency and field ratio of the first two accelerating cells by scaling the pre-buncher, first coupling cell, and first accelerating cell dimensions. We then varied the second accelerating cell radius. Figure 7(a) shows the initial three AS cells in a mesh representation, while Fig. 7(b) shows the on-axis longitudinal electric field distribution.

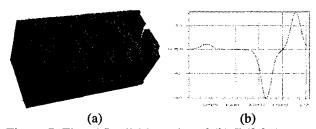


Figure 7: First AS cell (a) mesh and (b) $E_z(0,0,z)$

Next we optimized and tuned a $\beta = 1$ cell to obtain a 5% coupling and an 88 M Ω /m effective shunt impedance. RF losses to the structure wall were ~1.070

kW per cell for a 1 MeV/m accelerating gradient. We placed the coupling slots far off-axis to avoid overheating the cell noses and our large slots were beneficial when we pumped the structure. The accelerating cell coupling slot orientation was chosen to compensate for focusing in the adjacent accelerating and coupling cells. The coupling cells slot orientation was rotated by 90° relative to the accelerating cells. Finally, we manufactured, tuned, and brazed the AS and measured the on-axis E_z -field distribution, seen in Fig. 8, which agrees fairly well with our calculations.

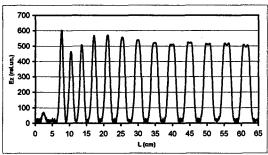


Figure 8: Measured on-axis longitudinal field

5 RADIO FREQUENCY SYSTEM

Our simple reliable RF system, seen in Fig. 9, uses self-excitation in a positive klystron-section feedback loop whose reliability we demonstrated experimentally with our previous prototype accelerator [1].

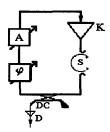


Figure 9: RF system schematic

We used a 50 kW CW klystron (K) to drive the AS. Some 15 kW of the klystron power is dissipated in the structure walls providing the accelerating field and, depending on beam current, up to 30 kW goes into the beam. When operating in the self-excited mode, the system oscillates at the structure resonant frequency, which the klystron frequency automatically follows. A RF probe provides the structure signal that passes through the electrically driven coaxial phase-shifter (φ) and p-i-n-attenuator (A), and then enters the klystron. The self-excitation phase conditions are chosen by the phase-shifter while the feedback p-i-n attenuator regulates the klystron output power and, consequently, the accelerating field amplitude. This amplitude is controlled by a diode (D) whose signal is used by the amplitude stabilization system that Thus our controls the p-i-n attenuator current.

accelerating field amplitude is stable to ~0.001, which is essential for our high beam loading.

We eliminated the traditional circulator by coupling the klystron directly to the AS and by operating in the self-excited mode. We tuned the system by determining the klystron body current dependence on the connecting wave-guide phase length. With the minimum body current, we found the length that minimizes the reflected RF power influence on the output klystron cavity. Thus, with no circulator, we reduced the accelerator size, weight, and cost. Our high power AS test set-up, seen in Fig. 10 with its circulator-less klystron system, operated stably for several hundred hours without component failures.

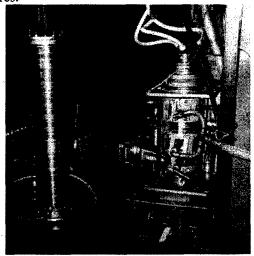


Figure 10: High-power AS tests

6 CONCLUSION

We have constructed the simplest of our new family of industrial CW LINACs, thereby validating our long held design ideas. In the first beam tests, our single section model has provided a 600 keV, 10 mA, 6 kW electron beam at a 20 mA gun current, thus demonstrating a design 50% capture efficiency and beam energy. The accelerator tests are now in progress. Increasing the beam current to 50 mA will require thorough electron gun training and modification of the Faraday Cup and vacuum system to improve the vacuum conditions in the accelerator.

7 REFERENCES

- [1] A.S. Alimov, A.S. Chepurnov, O.V. Chubarov, D.I. Ermakov, B.S. Ishkhanov, K.A. Gudkov, I.M. Piskarev, V.I. Shvedunov, and A.V. Shumakov, "Experimental Investigation of a CW Electron Linac with High Beam Current", Instrum. Exp. Tech. 37 (1994) 7; O.V. Chubarov, A.S. Alimov, and V.I. Shvedunov, "A Compact Industrial CW LINAC", IEEE Trans. Nucl. Sci. 44 (1997) 1037; and A.S. Alimov, O.V. Chubarov, and V.I. Shvedunov, "A High-Power LINAC Power Supply", IEEE Trans. Nucl. Sci. 44 (1997) 1033.
- [2] W.B. Herrmannsfeld, "EGUN an Electron Optics and Gun Design Program", SLAC-Report-331, 1988.
- [3] PARMELA code originally developed by K.R. Crandall.

CONCEPTUAL DESIGN OF 10 MeV, 100 kW CW ELECTRON ACCELERATOR FOR INDUSTRIAL APPLICATION

Hyeok-jung Kwon*, Yong-hwan Kim, Young-hwan Kim, Han-sung Kim, Sang-ho Kim Kang-ok Lee and Kie-hyung Chung

Dept. of Nuclear Engineering, Seoul National University, Seoul 151-742, Korea

Abstract

The application fields of intense gamma-ray or X-ray for industrial purpose are expanding. Electron beam accelerator which can generate X-ray whose dose rate is equivalent to the effect of several MCi gamma-ray source is a major candidate as a intense X-ray source. 10 MeV, 100 kW CW electron accelerator Fantron-I is conceptually designed for X-ray source to irradiate food, corn, forest products and so on. Electrons are accelerated seventeen times through two coaxial cavities with TM010 mode by means of bending magnet located outside the cavity. The resonant frequency of the cavity is about 160 MHz and the phase of one cavity is 180° shifted from that of the other. Higher order modes (HOM) which may cause beam instability are analyzed. The design parameters of beam lines and bending magnets are determined from the results of beam phase analysis, especially magnetic flux density and location of each bending magnet are carefully adjusted to synchronize the beam with the accelerating field. In this paper, characteristics and overall conceptual design of the Fantron-I are presented.

1 INTRODUCTION

There are efforts to reduce the chemical antiseptics which are harmful to both human beings and environments. One of the examples is the Montreal Protocol which decided to reduce the methyl bromide consumption, and there are strong needs of substitutions for chemical treatments. The gamma-ray or X-ray are considered to satisfy the above needs and electron beam accelerator is a major candidate as a intense X-ray source. 10 MeV, 100 kW CW electron accelerator Fantron-I is proposed and being conceptually designed. Fantron-I uses a TM010 mode in coaxial cavity as an accelerating mode and electrons are accelerated several times through the coaxial plane where the electric field has its maximum value. The operation principle is illustrated in Figure 1 which shows a two cavity accelerating mode. The designed resonance frequency is 160 MHz and tetrode is considered as a RF source. In fact, the concept of accelerating electrons several times using one or two cavities is not new one.[1] But Fantron-I has unique features such as using TM010 mode, having no

beam crossing point. Furthermore, it uses a radially focused uniform X-ray irradiator.[2]

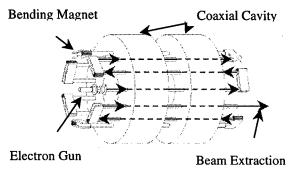


Figure 1. Operating principle of Fantron-I

2 CHARACTERISTICS OF FANTRON-I

2.1 Coaxial Cavity

In general, the shunt impedance in coaxial cavity TM010 mode decreases as outer conductor radius R2 or resonance frequency increase. If the R2 is fixed, the available minimum resonance frequency is determined from the realistically allowable size of inner conductor radius R1. As for a cavity length h, the shunt impedance increases at first and has its maximum value then decreases as h increase due to the combined effects of effective accelerating voltage and power dissipation. The general dependence of shunt impedance on cavity length is shown in Figure 2

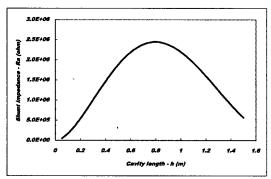


Figure 2. Shunt impedance vs. cavity length (f: 160 MHz, R1: 0.298 m, R2: 1.214 m)

^{*}Email: khj27@paragon.snu.ac.kr

2.2 Design Guideline

There are two conflicting aspects in cavity design. The required RF power is proportional to the square of the electric field intensity. As the electric field intensity decreases and the cavity crossing number increases, the required RF power can be lowered. This means that increasing the crossing number is advantageous in the respect of RF power efficiency. But as the crossing number increases, the gyroradius decreases at a fixed cavity size, which requires more magnetic flux density. Therefore the crossing number is restricted by the realistically available magnetomotive force in other words bending magnet power supply cost. After compromise between two conflicting aspects, about 200 kW RF power and 0.25 T magnetic flux density are selected as a guideline.

2.3 Acceleration Scheme

There can be several acceleration schemes. Using of one cavity needs many crossing numbers which require far above the value of the magnetic flux density given in section 2.2. Using two cavities can reduce the crossing number in the penalty of reduced effective accelerating voltage at the same input RF power. The crossing number can be further reduced as the cavity length increases above the values limited by the 0.5 λ synchronization condition. This scheme can be accomplished if the total length of cavity and bending section is equal to 1.5 λ and length of cavity and inter-cavity beam line is equal to 0.5 λ .

3 FANTRON-I PARAMETERS

3.1 Cavity

The $1.5~\lambda + 0.5~\lambda$ acceleration scheme is chosen because the crossing number can be further reduced in the penalty of accelerator size. The upper limit of the cavity length in this scheme is restricted by the available initial phase angle range of the electron beam because with large cavity length, the low energy electrons can not cross the cavity during the effective acceleration time interval and will be lost. The range of the available initial phase angle is chosen to be about 30° which results in 10 mA average current with 200 mA peak current.

3.2 Beam Line and Bending Magnet

The equation of motion of electrons in electromagnetic field is solved numerically using fourth order Runge-Kutta method to determine the cavity length, beam line length and magnetic flux density of the bending magnet. Once the cavity length is determined from the requirement of section 3.1, initial reference phase angle should be selected to determine the other parameters which are optimized to the electrons with the initial reference phase angle. Initial reference phase angle is

selected to be -10° because the deviations from reference gyroradius are less than 5 mm in all the available initial phase range. The results are shown Figure 3., 4. and 5.(f=159.31 MHz, R1=0.3 m, R2=1.22 m, h=0.7 m case) The electrons which have an initial phase angle range greater than 30° can reach the final beam energy above 10 MeV as can be seen in Figure 3, but in these range, electrons with phase angle of -5° - -35° are within the first gyroradius deviation limit. In Figure 4, the reference electron is injected into each cavity at a fixed phase angle taking into account the stability condition except first and second injection. The optimized beam line length and magnetic flux density of the bending magnet are shown in Figure 5. The inter-cavity beam line length and straight beam line section of the bending parts are 24 cm, 86 cm respectively. The maximum magnetic flux density is 0.269 T.

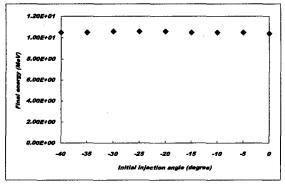


Figure 3. Initial injection angle vs final beam energy

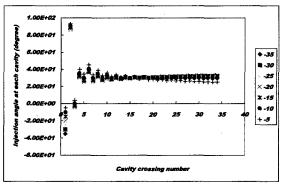


Figure 4. Entering phase angle at each cavity

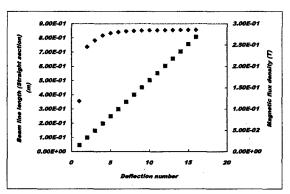


Figure 5. Magnetic flux density and beam line length

3.3 Fantron-I Parameters

The parameters are listed in Table 1.

Table 1. Fantron-I cavity parameters

Resonance frequency	159.31 MHz
Inner conductor radius R1	0.3 m
Outer conductor radius R2	1.22 m
Cavity length	0.7 m
Shunt impedance	$2.39 M\Omega$
Quality factor	51000
Number of Cavities	2
Acceleration scheme	$1.5 \lambda + 0.5 \lambda$
Total length including deflection region	3.6 m
Required RF power	220 kW
Maximum magnetic flux density	0.269 T
Number of bending magnets	16ea.

4 HIGHER ORDER MODES

4.1 Monopole Modes

In general cylindrical cavity, only longitudinal beam coupling impedance exists in monopole modes because the electric field intensity from all the monopole modes have its extremum at the beam crossing axis (usually center axis of the cavity). But the electric field of higher order mode has not extremum at the beam crossing axis in Fantron-I cavity, so transverse beam coupling impedance exists inevitably. The transverse coupling impedance can be derived from Panofsky-Wenzel theorem.[3] The longitudinal and transverse shunt impedances are shown in Figure 6.

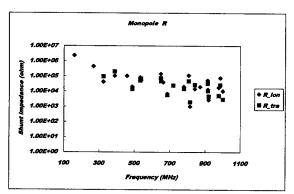


Figure 6. Longitudinal and transverse shunt impedances (monopole mode)

4.2 Dipole Modes

In Fantron-I cavity, the dipole mode can be generated if the center of the average beam crossing radius is shifted from the cavity center. Some assumptions are made to simplify the problem. In the simplified model, the beam is assumed to be shifted Δr in radial direction at two points which is separated 180° from each other. The

transverse shunt impedance is shown in Figure 7. In the Figure 7, TM120 or TM121 modes have a higher shunt impedance than TM110 mode because at the beam crossing radius, TM110 mode has nearly its electric field intensity extremum but TM120 or TM121 modes have nearly magnet field intensity maximum.

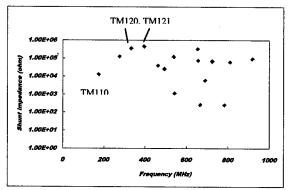


Figure 7. Transverse shunt impedance (dipole mode)

5 CONCLUSIONS AND FURTHER WORK

The design study on 10 MeV, 100 kW CW electron accelerator Fantron-I is presented. According to the characteristics of the Fantron-I, some compromises between required RF power and magnetic flux denstiy of the bending magnet should be done. Basic parameters were derived and cavity HOMs were calculated. In the future, focusing elements should be added. The beam instabiliy caused by HOMs should be analyzed and damper may be added if necessary.

6 REFERENCE

- [1]. J. Pottier, "A new type of RF electron accelerator: the rhodotron", Nucl. Instr. Meth. Phys. Res., Vol B40/41, pp943-945, 1989
- [2]. Young-hwan Kim, "Design of radially focused uniform X-ray source" in these proceeding
- [3]. S. Turner, Proc.of CAS RF Engineering for particle accelerators, 1992

DESIGN OF RADIALLY FOCUSED UNIFORM X-RAY SOURCE

Young-hwan Kim, Hyeok-jung Kwon, Yong-hwan Kim, Han-sung Kim, Sang-ho Kim, Kang-ok Lee and Kie-hyung Chung

Department of Nuclear Engineering, Seoul National University, Seoul, 151-742, Korea

Abstract

The 10 MeV, 100 kW CW electron accelerator (FANTRON I) is being developed in Department of Nuclear Engineering, Seoul National University (SNU) [1]. The X-ray generated by the accelerated electron beam will be used in sterilizing the agricultural, forest and aquatic products. For the effective irradiation and the safety of the irradiated products, the uniform irradiation is needed. The designed target is mainly featured by the radially focused uniform X-ray. The diameter of irradiation hole is 0.75 m. And the generated X-ray is emitted toward the center of the irradiation hole with uniform distribution along the circumference. To generate the radially focused uniform X-ray, the accelerated electron beam must be focused radially on the target that is the outer shell of the irradiation hole with high uniformity. Additionally the electron beam must be injected in the normal direction on the surface of target because the intensity of electron incident direction is dominant in the angular distribution of bremsstrahlung intensity of the electrons, which are accelerated up to 10 MeV. The basic principle of targetary is deflecting electron beam with proper magnetic field configuration. To find such configuration a series of numerical analyses are performed. This paper includes the requirements and design results of the radially focused uniform X-ray source.

1 INTRODUCTION

The uniform irradiation is needed to guarantee the safety of the irradiated products and the irradiation performance. Several methods are suggested to increase the radiation dose uniformity [2]. The radially focused uniform X-ray source is composed of scanning magnet, field shaping system and cylindrical irradiation hole. Fig. 1 shows the layout of target system. The 10 MeV electron beam scanned to proper angle is deflected along the optimized trajectories during passing the field shaping system and then collide against the target in the normal direction with azimuthally uniform distribution. The design process comprises three stages.

- Optimization of the electron trajectory
- Calculation of the magnetic field distribution
- Optimization of the magnet pole profile

The target system with 0.75 m-diameter irradiation hole

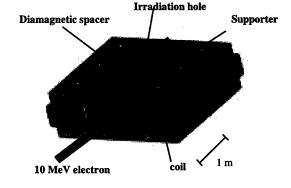


Figure 1. Layout of Target System

is designed to establish and verify the design procedure.

2 ELECTRON TRAJECTORY OPTIMIZATION

The deflected electron beam with proper angle after passing the scanning magnet should follow the trajectory along which they collide against the target in the normal direction. The Hermite curve, which is a kind of parametric cubic curve, is suggested as the electron trajectory. The Hermite curve is generated on the base of four control vectors composed of two location vectors and two tangent vectors [3]. The principle of curve generation is described in Eq. (1) and Fig. 2.

$$\vec{Q}(t) = (2t^3 - 3t^2 + 1)\vec{P}_1 + (3t^2 - 2t^3)\vec{P}_4 + (t^3 - 2t^2 + 1)\vec{R}_1 + (t^3 - t^2)\vec{R}_4 \qquad (0 \le t \le 1)$$
(1)

During the optimization, the magnetic field gradients corresponding to each trajectory are minimized and inflection point where the concavity of the curve changes is avoided. The optimized electron trajectories are shown in Fig. 3.

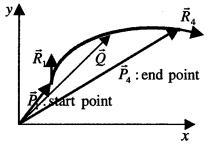


Figure 2. The Principle of Hermite Curve Generation

^{*} Email: hessee@paragon.snu.ac.kr

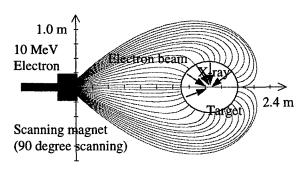


Figure 3. The Optimized Electron Beam Trajectories

3 MAGNETIC FIELD DISTRIBUTION

Magnetic field distribution is determined such that electron beam may be deflected along the optimized trajectory. The relativistic equation of motion is used in calculating the field distribution. Fig. 4 shows the magnetic field distribution.

4 MAGNET POLE PROFILE OPTIMIZATION

Magnet pole profile design is intrinsically the nonlinear reverse magnetostatic problem. The main approaches are classified into two cases, which are the numerical analyses of Poisson's equation with iteration processes and the analytic approaches. For linear problem, in the case that the magnetic field strength is so low that the saturation effects of iron core do not have any effect on field distribution, several kinds of analytic solutions are suggested [4].

Concerning the result of calculated magnetic field distribution, the maximum field strength is below about 0.05 Ts. So the analytic methods are adopted for magnet pole profile design. Three kinds of analytic methods are performed.

- Finite difference method
- Boundary integral method
- Downward continuation method

4.1 Finite Difference Method

Magnetostatic problem, in the case that the source free and isotropic region is considered, is solved using magnetic scalar potential in the similar way to electrostatic case. For the linear problem, the pole surface coincides with equipotential surface [4]. The Laplace equation and boundary condition are used in finding the equipotential surface.

$$\frac{\partial^2 \Phi}{\partial x^2} + \frac{\partial^2 \Phi}{\partial y^2} + \frac{\partial^2 \Phi}{\partial z^2} = 0$$
 (2)

$$\frac{\partial \Phi}{\partial z} = B_z(x, y)$$
 , on the midplane(z = 0) (3)

 Φ : magnetic scalar potential

The equipotential surface obtained from equation (2) and (3) with proper boundary conditions is shown in Fig. 5.

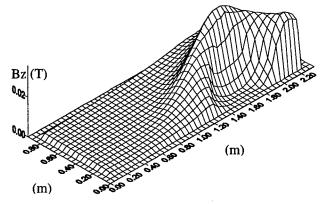


Figure 4. The Magnetic Field Distribution on the midplane of the Magnet

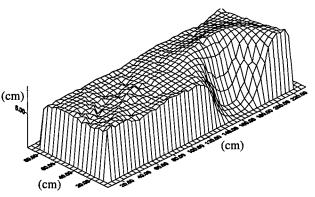


Figure 5. The Equipotential Surface Calculated using Finite Difference method

4.2 Boundary Integral Method

The boundary integral method is the approach that the set of points Q(l, m, z(l, m)) can be determined so that the performance criterion function F may be minimized [5]. The magnetic field distribution at points P(i, j, 0) is determined by the set of points Q(l, m, z(l,m)) as shown in Fig. 6. And the performance criterion function is:

$$F = \sum_{i} \sum_{j} \left[\frac{B(i, j, 0) - B_0(i, j, 0)}{B_0(i, j, 0)} \right]^2$$
 (4)

($B(i,j,\theta)$: calculated field, $B_o(i,j,\theta)$: reference field) The calculated pole profile is shown in Fig. 7.

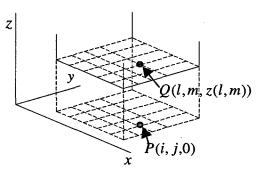


Figure 6. The Boundary Integral Method

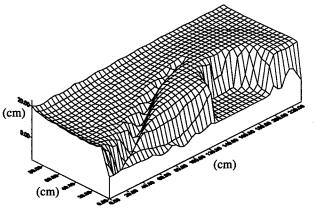


Figure 7. The Magnet Pole Profile Obtained using Boundary Integral Method

4.3 Downward Continuation Method

In geophysics, downward continuation method is usually used in estimating the shape of geomagnetic source from the measured magnetic field distribution [6]. This approach can be used to calculate the magnetic potential distribution toward the magnet pole from the midplane magnetic field distribution. The basic principles are Green's third identity (5) and Fourier transformation (6). Green's third identity:

$$U(P) = \frac{1}{4\pi} \int_{S} \left(\frac{1}{r} \frac{\partial U}{\partial n} - U \frac{\partial}{\partial n} \frac{1}{r} \right) dS$$
 (5)

U(P): harmonic function at point P

n: normal unit vector of the surface S

r: distance from point P to any point on S

Fourier transformation: (6)

$$U(x, y, z + \Delta z) =$$

$$F^{-1} \left[F[U(x, y, z)] / F \left[\frac{\Delta z}{2\pi} \frac{1}{(x^2 + y^2 + \Delta z^2)^{3/2}} \right] \right]$$

With equation (5) and (6) the potential U at elevated position is obtained from the midplane potential. The designed magnet pole profile is shown in Fig. 8.

There are some intrinsic drawbacks in using this approach [7], [8].

- The Fourier transformation is done in discrete
 manner
- The analyzed data are not continuous but discrete (sampled).
- The area over which the Fourier transformation is performed is finite.

5 CONCLUSIONS AND FUTURE WORKS

According to the design procedure, the trajectory of electron beam is optimized using Hermite curve. The

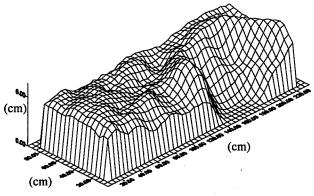


Figure 8. The Magnet Pole Profile Calculated using Downward Continuation Method

magnetic field distribution is determined such that it may deflect the electrons along the optimized trajectory. The magnet pole profile is designed using several analytic approaches. The difference in designed pole profiles between each method may be due to the difference equipotential levels and the intrinsic drawbacks of each method.

For the future works, the estimation of radiation dose uniformity and loss fraction of electron beam for the each pole profile using the 3d electron trajectory code are being done. The trim process, which is needed for practical three-dimensional manufacturing, will be done.

6 REFERENCES

- [1] Hyeok-jung Kwon, Yong-hwan Kim, Young-hwan Kim, Han-sung Kim, Sang-ho Kim, Kang-ok Lee and Kie-hyung Chung, Conceptual Design of 10MeV, 100kW CW Electron Accelerator for Industrial Application, submitted to PAC '99
- [2] A. S. Ivanov, et al., Electromagnetic electron irradiation field shaping system for industrial high voltage accelerators, Proceedings of the EPAC '94
- [3] James D. Foley, et al., Computer graphics: principles and practice, Addison-Wesley 1996
- [4] G. W. Foster, et al. Pole profile optimization of VLHC transmission line magnet, Proceedings of the EPAC '98
- [5] A. G. A. M. Armstrong, et al., Automated optimization of magnet design using the boundary integral method, IEEE Transactions on Magnetics, Vol. MAG-18, No. 2, March 1982
- [6] Richard J. Blakely, Potential Theory in Gravity and Magnetic Applications, Cambridge University Press, 1995
- [7] Y. Ricard, et al., A method to minimize edge effects in twodimensional discrete Fourier transformations, Geophysics, Vol. 53, No. 8, August 1988
- [8] L. Cordell, Reconciliation of the discrete and integral Fourier transforms, Geophysics, Vol. 47, No. 2, Feb. 1982

THE ELECTRON ACCELERATOR INSTALLATIONS WITH LOCAL SHIELDING FOR APPLIED PURPOSES*

G. Batskikh, G. Mamaey, A. Mischenko, V. Pirozhenko MRTI RAS, Moscow

Abstract

The use of the local shielding for electron accelerators considerably extends the capabilities of its application for various purposes, because they can operate in ordinary working rooms. So there is no need to construct special buildings with cumbersome shielding. Since the cost of local shielding depends on its sizes, the compact accelerators have developed in the MRTI.

Three accelerating installations are presented in the report: 8 MeV installation for custom inspection of large cargo containers, 5 MeV installation for sterilization of medical instruments, infectious waste, conservation food etc., and 200 keV installation for industrial techniques.

1 INTRODUCTION

The electron accelerators are widely used in industry and medicine. However, radiation danger appears in its operation. It requires application of biological radiation shielding. Two versions of radiation shielding are possible: local shielding, i.e. location of accelerators and basic technical equipment into the special container opaque to radiation arising in accelerator operation, or construction of a special room with shielded walls. The application of local shielding in many cases appears cheaper than construction of special rooms with thick concrete walls. Besides accelerating installation with local shielding appears compact and can be transportable. As a rule, the local shielding until recently was applied for accelerating installations for the energy up to 800 keV. In MRTI the installations with local shielding for the energy up to 8 MeV were created.

2 CUSTOM INSPECTION LINAC

The cost of biological shielding depends on the sizes of the accelerator, therefore compact linear electron accelerators (Fig. 1) were developed [1]. Its parameters are listed in Table 1.

The accelerating structure represents a set of coupled cavities (Fig. 2) $\pi/2$ standing wave excited.

Coupling cells located on axis between accelerating cells. The form of RF field in accelerating cavities provides not only acceleration, but also focussing of the beam. It allows to do without magnetic solenoids and to reduce the transverse sizes of the accelerator. Magnetrons

MI-456 with pulse power of 2,5 MW and mean power of 4 kW are used for an accelerating field excitation.

Table 1. Compact electron linac parameters.

1. Energy of accelerated particles, MeV	5	8	
2. Number of accelerating cells		17	
3. Accelerator length, cm	64	99	
4. Accelerator diameter, cm		13	
5. Operational frequency, MHz	27	97	
6. Pulse current, A	0,28 0,12		
7. RF pulse duration τ, μs		5,5 – 11	
8. Pulse duration of beam current, µs		5 – 10,5	
9. Repetition rate, Hz, at $\tau = 5.5 \mu s$ $\tau = 11 \mu s$		300 150	
10. Beam diameter, mm		2	
11. Mean power, kW		1,4	
12. Power consumption, kW		15	

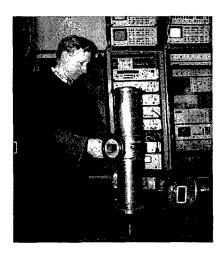


Figure 1: 8 MeV compact electron linac.

The accelerator with energy of 8 MeV is used in the installation for the X-ray control of auto vans, transport containers, lorries and etc. at customs inspection of cargoes (Fig. 3).

^{*}Works are supported in part by State Custom Committee of Russia, BioSteril Technology, Inc. and MRTI RAS.

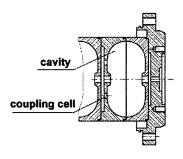


Figure 2: Accelerating structure

8 MeV accelerator provides depth of steel X-raying up to 340 mm, i.e. we can see the image of subjects behind a steel barrier 34 cm thick. Productivity of installation is up to 15 auto vans per hour. The application of accelerator with local shielding decreases many-fold a level of radiation in operating rooms. It allows to use for installation accommodation the modular facilitated building designs, that makes civil work cheaper and, basically, enables if necessary quickly reinstall it on a new place.

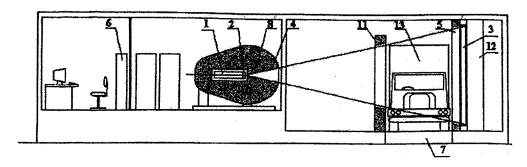


Figure 3: Installation for customs inspection of auto vans.

1 – accelerator; 2 – converter, 3 – local shielding; 4 – auto vane

3 ACCELERATOR FOR STERILIZATION

The accelerator with the energy of 5 MeV is applied in the installation for radiation sterilization of medical instruments and medical infection wastes in clinics and hospitals, sterilization of medical products at their production, sterilization of foods for essential increase of its storage time, and also suppression of microorganisms dangerous for human health. Installation view is shown in Fig. 4. The rotor transporter is applied in this case. There

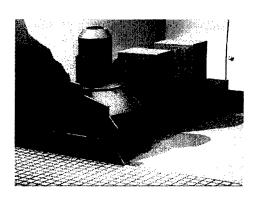


Figure 4: Installation for X-ray sterilization.

is a version with the linear transporter. Productivity of the installation is up to 200 kg of sterilized materials per hour. A design of shielding completely eliminates a capability of emergencies connected with radiation danger that allows to place the installation in any working

room. The installation is transportable, since its weight does not exceed 20 t.

4 INDUSTRIAL ACCELERATOR

Principe of local shielding was used for design of small-scale accelerator with the energy up to 180 keV [2].

Installation uses accelerated electron beam for material processing, for surface X-ray sterilization in clinics and for other purposes. The general external appearance of this installation is presented in Fig. 5.

Electron beam is generated by seal off electron gun. Gun is energized by high-voltage pulse transformer.

These units are combined in unified compact design. Radiation shielding makes it possible to use this installation in any room. Installation parameters are listed in Table 2.

Table 2. General parameters of installations.

Electron energy (regulated), keV	100 - 200
Repetition rate, Hz	200
Max. pulse power of extracted beam, kW	300
Irradiation area, mm	200×100
Max. pulse dose rate of electron beam, kGy/s	5·10 ⁴
Power consumed, kW	2
Overall dimensions (w/o computer), m	2×0.7×0.7

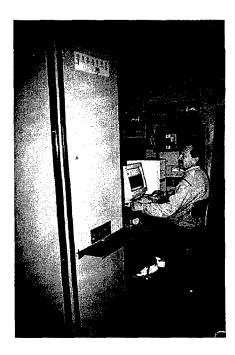


Figure 5: Installation for material processing by electron beam.

Shielding consists of two envelopes. The first (internal) shell of the shielding covers the electron gun and irradiation zone. The second (external) one covers the electron gun, irradiation zone and high-voltage transformer. All panels are 3 mm thick steel sheets to which 5 mm thick lead sheets are riveted, the rivets being made of tin, that is also material with good radiation attenuation.

REFERENCES

[1] A.A.Zavetsev, Yu.D.Petrov, MRTI RAS. "Standing Wave Linac Accelerating Structure for Technology Purposes", London, 1994, EPAC-94, p.2173.

[2] S.Krylov, T.Latypov, G.Mamaev, S.Mamaev, V.Pirozhenko, S.Poutchkov, I.Tenyakov, MRTI RAS, A.Korolev, K.Simonov, Istok. "Compact Pulse Electron Accelerator for Radiation Processing of Materials", this Conference.

COMPACT INSTALLATION FOR RADIATION PROCESSING OF MATERIALS BY ACCELERATED ELECTRONS*

S. Krylov, T. Latypov, G. Mamaev, S. Mamaev, E. Mirochnik, A. Pirozhenko, S. Poutchkov, I. Seleznev, I. Tenjakov, MRTI RAS, Moscow, Russia A. Korolev, K. Simonov, «Istok», Frjazino, Russia

Abstract

The installation has been designed for processing of articles and materials with the electron beam. The beam is generated by the sealed-off electron gun of unique design and is extracted to the irradiation area through thin Ti foil with 20×10 cm² area. The electron energy is up to 200 keV, pulse beam current - 7 A. The processing is performed in nitrogen. Maximum pulse dose rate is 5×10⁴ kGy/sec. The installation has compact highvoltage power supply, self-contained water cooling, and handy control with the beam parameters regulation within broad ranges. All the installation except the computer is packaged in one case with 2×0.7×0.7 m³ dimensions. The installation has its own radiation shielding and is safe to use: the radiation dose at any place outside the case is near the background radiation level.

1 INTRODUCTION

The installation has been designed for processing of the articles and materials with electron beams. The installations of this type can widely be used in research organisations for the investigation of the influence of the radiation on the materials, in clinics for surface radiating sterilisation, and also for other purposes.

Usually, the installations for radiation technology is based on electron accelerators, which work in a continuous current mode and are supplied with devices of linear scanning of the beam. We have the task to design the small, convenient accelerator working in pulse mode. The posed task has required application of the new approaches and original scientific and technical solutions. The electron beam is generated by the sealed off electron gun, which is supplied by the high-voltage pulse transformer, and they both presents joined compact device. The beam is distributed on all area of exposure and has a time structure of short intensive pulses. The installation has a reliable local radiating shielding, it is completely ecologically pure and can be maintained in any location. General parameters are shown in Table 1.

Table 1: General parameters of the installation

Electron energy (controlled)

Max. pulse power of extracted beam
Irradiation area

Max. dose rate of electron beam
Max. pulse dose rate of electron beam
Max. radiation dose outside the case
Max. power consumed
Overall dimensions (w/o computer)
Overall weight

100÷200 keV 300 kW 200×100 mm 10 kGy/sec 5×10⁴ kGy/sec 0.2 mGy/hour 2 kW 2×0.7×0.7 m 700 kg

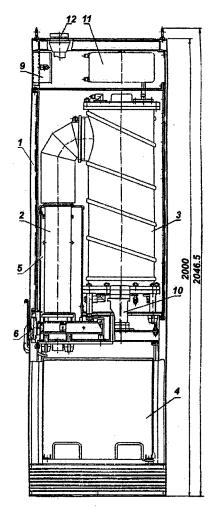


Figure 1: The design of installation.

^{*}Work supported in parts by the MRTI RAS, BioSterile Technology, Tukson Inc, Moscow

^{*}E-Mail: mamaev g@mail.sitek.ru

2 GENERAL DESCRIPTION

The design of the installation is shown in Fig. 1, and on the photos - in Fig. 2,3. The main items of the equipment, shown in Fig. 1, designated by numbers from 1 to 6. Item 1 - case for equipment siting.

2.1 Electron gun

Sealed off electronic gun with heated cathode (item 2, Fig. 1) realises generation and extraction of the wide electron beams to the atmosphere. The designed gun is compact and long-lived tube, does not require a system of a vacuum evacuation, has small time of preparation to maintenance, ensures interchangeability and good reproducing of the performances. This gun has a modular construction, which allows receiving a large area of exposure by arrangement of necessary number of guns located closely one to other.

2.2 High-voltage transformer

The developed construction of the step-up transformer (item 3, Fig. 1) and its connection with a gun allowed to reach the main purpose - creation of a small-sized construction with a good reliability of working on high voltages. Basic engineering solutions - modular construction of the transformer; high factor of transformation to reduce primary voltage; direct (without a cable) junction with a gun.

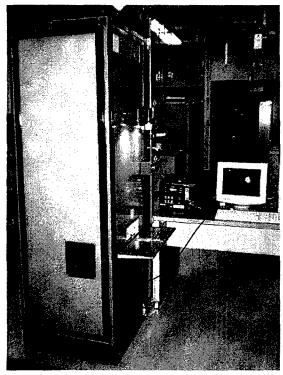


Figure 2: The installation for radiation processing.

The transformer contains 13 identical modules, which are connected in series. Each module contains ring

shaped ferromagnetic core, insulating rings mounted on the core; secondary winding wound on the insulating rings; insulating separators between the modules.

The ferromagnetic cores are wound from a thin tape (amorphous alloy). Insulation approximately of 2 microns thickness is applied between the layers of this tape. A thickness of the amorphous tape - 20 microns, induction of saturation - 1.4 T, B_r/B_s factor - 0.9.

Each module contains two identical secondary windings that are necessary for transmitting electron gun cathode filament current. The transformer has the following parameters:

Transformer voltage ratio	50
Maximum test output voltage	240 kV
Input voltage	2÷4 kV
Outside core diameter	200 mm
Maximum magnetic field	1.4 T
The tank length	840 mm
The tank diameter	300 mm

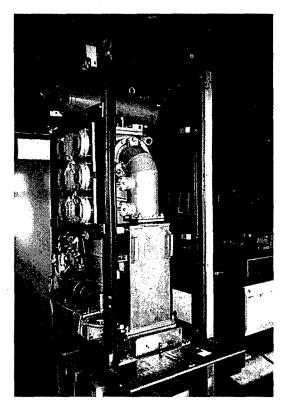


Figure 3: The installation without of a radiation shielding.

2.3 Pulse modulator

The modulator (item 4, Fig. 1) generates high-voltage impulses which supplies the input of the step-up transformer. The basic problems of the development of the modulator consist in achieving of the small dimensions, wide control bands of output voltage and pulse repetition rate, good reliability of work. The modulator contains the following main components:

high-voltage power unit, charging circuit, pulse formation circuit, thyratron switch, measuring voltage dividers.

The high-voltage power unit consists of 6-phase rectifier, filter, high-frequency generator (30 kHz), step-up transformer, and high-voltage rectifier. The unit contains its own control system for protection from overload and high-voltage breakdowns. Its has two feedback circuits, proportional load current and second – proportional output voltage. These feedback circuits allow having wide control of the power unit with properly limitation of the charge current. This technical solution excludes the limitation resistors, chokes etc.

The charging circuit is based on the high-voltage thyristor pole. The pulse forming circuit contains a set of capacitors and inductance.

The thyratron switch is assembled using TGP1-1000/25 thyratron that has the following basic parameters: maximum work current of 1000 A and maximum voltage 25 kV. Large reserve in the voltage provides the long operating life of the thyratron, which usually determines the trouble-free time of the modulator.

The modulator is built as a single device enclosed in a casing that serves as an electromagnetic shield designed to reduce the pulse interference directed from the powerful modulator circuits to other installation equipment. The modulator parameters:

Pulse voltage output (controlled

with accuracy better then 3%) 2 to 5 kV
Pulse duration 2 μ sec
Pulse repetition rate (controlled) 5 to 150 pps
Capacitance of pulse forming circuit Overall dimensions of the modulator 0.65×0.5×0.44 m

2.4 Radiation shielding

The basic requirement to a construction of a radiation shielding is the decreasing of the dose at any place near cabinet to a background level (0.1 mkG/h). The radiation shielding consists of two shells. The first (internal) shell covers the electron gun and irradiation zone. It consists of the set of lead sheets 5 mm thick with intricate shape. The second (external) shell covers the electron gun, the irradiation zone, and the high-voltage transformer. The shielding allows to decrease radiation in 10⁹ times.

The exposure of the samples is produced in the pressure tight camera (item 6, Fig. 1), filled with nitrogen, that eliminates the ozone formation and influence of air oxygen on radiation processing. The shell of the chamber consists of a carriage made of 2 mm thick stainless steel. Plates of 2 mm thick lead are fixed to the sides of the carriage. After installing of the carriage, plates were bent to the lead sheet of the base, providing a leek-free joint. Small concentration of oxygen in the chamber was achieved - no more than 20 promille.

2.5 Control system

The control of the installation is carried out by means of computer and is automated completely, therefore maintenance of installation can be carried out by not special personal. The computer realises sequential switching on of devices of installation, monitoring of parameters, inclusion of necessary regime and parameters of an exposure. The installation can be operated in three modes: single pulse, continuous, and serial (series of pulses with pauses). The electron energy, pulse repetition rate, duration of irradiation, and the pause intervals may be set within broad ranges. The radiating doze on a surface of an irradiated sample is calculated and shown on the display. The doze may be determined by operator, in this case the necessary time of an exposure is calculated and installed by the computer.

The reliability of safe work with installation is ensured also with system of interlocking, in which there are software and hardware interlocking. For example, the electron beam cannot be switched on, if the carriage removed or poorly entered, and the carriage cannot be removed, when the electron beam is generated.

3 CONCLUSION

Such installation is working in one of corporations of USA for more than year. The installation has shown reliable work full ecological safety.

APPLICATION OF LOW ENERGY ELECTRON BEAMS FOR TECHNOLOGY AND MEDICINE

¹B. Bogdanovitch, V. Senioukov, MEPhI, Moscow, Russia

A. Koroliov, K. Simonov, State Concern "Istok", Fryazino, Russia

Abstract

Though the low energy electrons (160-200 keV) do not penetrate deep into the material's surface the application of such beams can be effective enough in some technological processes, i.e. for processing the materials surface or for realizing processes in gases. For researching of low energy beams influence on the materials it was created a special experimental installation based on a powerful electron gun with wide rectangular output window. A number of different polymer materials were processed in this installation and it was obtained an increasing of durability, limit of elasticity, wearability and thermoresistivity in number of times. Its important to note that depth of materials properties changes is much higher then the electron penetration depth. Probably it is due to concurrent action of electron beam and intensive x-ray irradiation arising from the output window foil. Due to their properties such beams can be effectively used in agriculture and medicine also.

1 APPLICATION OF ELECTRON BEAMS

1.1 Interaction of Electrons with Substance

The accelerated electrons, getting in substance, electrostatically interact with electrons and nucleuses of atoms. The most part of the beam energy is spent for interaction with orbital electrons. The primary particle transfers them a part of their energy, owing to what they pass to orbits of greater radius (excitation) or come off atom (ionization). The average energy spent on formation of one pair of ions (an energy of ionization), practically does not depend on a primary electrons energy and makes for many substances ~ 30 eV. Potential of ionization of simple molecules is close to 10 eV. Other two thirds of a primary particle energy are spent for excitation and other processes. If the energy of primary electrons makes 100-200 keV, the complete loss of an energy occurs at the expense of repeated collisions.

The depth of electrons penetration in substance (for energies from 10 keV up to 1 MeV) can be defined with the help of expression:

$$\lambda_{\rm m} = 6.7 \cdot 10^{-11} \ W^{5/3}/\rho \ , \tag{1}$$

where l_m is a depth of electrons penetration in material [cm]; W - electrons energy [eV]; r - substance density [g/cm³].

The diagram of electrons with energy 160-200 keV penetration depth v.s. substance density is given on Fig.1. From this diagram it follows, that low energy electron beams can be most effectively used in gas environments, where their penetrating ability makes about 15-20 cm. Besides, the electron beams with small penetrating ability are necessary for processing surface layers of products in order to prevent the beam influence on internal areas that my be inadmissible.

1.2 Application of Electron Beams

At passage in substance the primary electrons cause breaks of molecular links. The formed charged and neutral splinters of molecules have high chemical activity and quickly react with each other and with other molecules, owing to what the molecular structure of a material changes and the substance with new properties is

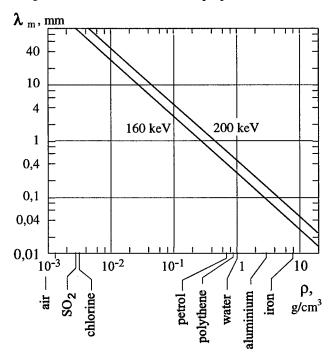


Figure 1: Penetration length λ_m for 160 and 200 keV electrons in substances with different density ρ .

¹ E-mail: bogdan@uni.mephi.ru

formed. The high chemical activity of reacting particles makes possible a realization of radiation-chemical reactions even at very low temperatures. Thus also disappears a necessity of the initiators and catalysts use, that allows to create a high cleanliness materials.

1.3 Radiating modification of polymers

Radiating polymerization processes are rather effective energetically and can be carried out at temperature, optimum for molecular circuits growth. The polymers properties modification by radiation is caused by processes of polymerization (seaming) and destruction of molecules. The radiation can stimulate both processes of molecule polymerization and one-dimensional polymer modifying in spatial one by intermolecular links creating. These links reduce displacement of molecules at mechanical influences, that results in increase of a limit of elasticity and reduction of plastic deformations. It decreases a material deterioration (in 2-4 times) and the range of working temperatures extends. The typical changes of the basic mechanical and operational characteristics of some plastics and rubbers used, in particular, for manufacturing of automobile linings, shock-absorbers etc. are given in Tables 1 and 2. The similar results can be got for processing other polymers.

The radiating processing of photo-polymers, used in polygraph, allows to increase their durability and thermoresistivity in a number of times. For some applications it makes it possible to use processed photo-polymer form instead metal ones.

Typical changes of material properties caused by destruction of molecules are the increase of substance solubility and reduction of its viscosity. The destruction process at irradiation in water solutions prevails for many polymers, that is due to participation in reactions the water radiolize products. Using of this process for industrial and household wastewater clearing is of practical interest. First of all it concerns to neutralization of synthetic superficial-active substances used for abstergents manufacturing. At water radiating processing its sterilization is taking place as well.

One of the most widespread technologies using combined radiating processes is radiating hardening of lacker and paint coverings. Unlike the traditional technology, radiating polymerization lasts less than 1 second and does not require additional polishing. Such coverings have high mechanical durability, chemical- and thermoresistivity. With the help of these processes thin layered plastics, foiled dielectrics, dielectric covering on various substrates, multilayer boards can be created also. Radiating hardening is used in a magnetic tape manufacturing, in a polygraph industry and some other processes. In hardening of a typographical paint on banknotes the positive results are received.

Table 1: Typical changes of materials parameters after radiation treating.

	Parameters changing (increasing)			
Material	Module of elasticity	Elastic limit	Wear- ability	Tempe- rature, °Ñ
Caprolon	1,0	3	1,6-1,7	_
Rubber	1,2-1,3	5-6		
Silicon rubber	-		_	- 60
Polyuretan			1,7-2	

Table 2: Operating temperature for different regimes

Polythene	Operating temperature for different time regimes, °Ñ		
seamed method	Long lasting	100 h/year	Shortly
chemically	90	130	250
radiationally	150	200	300

1.4 Radiating technological processes in gases, oil and petroleum processing

The processes of this type basically are used for clearing gases of the industrial enterprises of harmful impurity. The greatest danger represents sulfur dioxide SO_2 and nitrogen oxides NO_X . The radiating method with addition of ammonia allows to fix up to 80 % NO_X and up to 90 % SO_2 . The firm particles are formed which are grasped by electrostatic filter. Process of clearing from sulfurhydrogen H_2S can be carried out similarly.

The radiating influence on petroleum and oil allows to increase essentially a useful product output at cracking. Two kinds of cracking are applied now: thermal and catalyzed. These processes have the certain lacks both. Application of an electron beam as the chemical catalyst is effective enough, as it has volumetric action while the usual chemical catalyst - only superficial. Besides there is no necessity of catalyst regeneration.

1.5 Beams application for medicine and foodprocessing

The application of radiating technologies in medicine and food-processing industry is based on biological action of radiation. Depending on a doze of an irradiation the various results are possible: stimulation of development, genetic changes, sterilization, delay of growth, chemical decomposition. The sterilization of medical materials and tools is the first radiating process mastered in industrial scales. One of possible directions of foodstuff radiating sterilization is the products processing after their culinary treatment. After such processing the product can be stored at room temperature during several months without any preserves. In agriculture the radiating technologies are applied for a grain disinsection, growth stimulation before

crop, germination delay at storage etc. The irradiation doze of 50-150 Gr prevents potatoes from germination within 10-15 months at usual storage temperatures. For electrons this doze can be increased up to 300-500 Gr and storage time will be longer for 2-3 months. An onions can be exposed to the same processing. Advantages of radiating processing before chemical: absence of products impurity, smaller cost, line processing.

2 SPECIALISED ELECTRON GUN FOR RADIATING PROCESSES

2.1 The Electron Gun Construction

The electron gun of a modular type is a kind of a direct action particle accelerator (see Fig.2). Electron beam is extracting out through a thin foil and the irradiation of products is made over a large enough area without application of any additional devices.

The developed gun, unlike similar ones, is compact, durable, does not require vacuum pumps and provides good repeatability of characteristics. The large irradiation fields can be received by combining a number of guns. Several complex scientific and technological problems was solved for electron gun development. The main problems are: creation of a tight and reliable output window, development of electron-optical system with good beam distribution over an output window, creation of effective and reliable cathodes, and technology of gun assembling with a necessary vacuum maintenance.

The output window design is one of the basic problems in electron gun creation. A small density material should be used for foil and it must be as thin as possible. The best results (for mechanical, vacuum and thermal properties) were achieved using a titanium foil 30 μ m thick. With the help of diffuse welding the foil is welded on basic copper lattices, which besides carry out a cooler role. The welding is carried out in vacuum at high temperature with the help of special adaptations acting on basis of materials linear expansion factors difference. The optimum welding mode is determined experimentally.

The electron-optical system of beam formation provides a uniform distribution of current density over the output window and the cathode surface. Cathodes with flat emitting surface are used here.

A series of electron guns with various parameters was developed. The parameters of one of them with large average power of extracting beam are given in Table 3.

2.2 Use Efficiency of Low Energy Electron Beams

In all radiating processes mentioned above the application of electron gun is represented rather effective because it forms intensive flow of low energy electrons at rather low

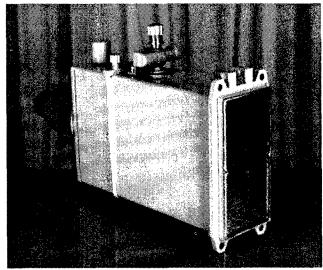


Figure 2: Appearance of the electron gun.

Table 3: Parameters of the Electron Gun with a High Average Power.

Average beam power	400 W
Output window cross section	200×100 mm ²
Electrons energy	200 keV (max.)
Cathode current	80 A
Output current	10 A
Surface absorbed doze rating	300 kGr/s (max.)
Pulse duration	5 μs
Pulse following frequency	50 Hz
Gun overall dimensions	400×230×114 mm ³
Gun mass	20 kg

costs of the gun and its exploitation. The gun provides rather high dozes of irradiation, that allows to create highefficiency installations. For example, for optimum modification of the characteristics polyvinilchloride (PVC) the dozes of an irradiation of the order 20-30 kGr are required. The area of a target window of a gun makes 0,02 $\rm m^2$. Then for 1 second can be processed 0,25 $\rm m^2$ of a surface of products from PVC or 900 $\rm m^2$ in one hour. For polythene with an optimum doze ~ 50 kGr the productivity of installation will make 400-450 $\rm m^2/hour$. Thus power requirements on 1 $\rm m^2$ the surfaces will not exceed about 0,004 kWh for PVC and - 0,008 kWh for polythene.

THE ELECTRON LINAC ON THE BASIS OF SYSTEM WITH NONSYNCHRONOUS WAVES FOR NUCLEAR GEOPHYSICS

B. Bogdanovitch¹, A. Nesterovitch, S. Stepanov, MEPhI, Moscow, Russia

Abstract

In nuclear geophysics the chinks carottage at the minerals search by means of radiation occurring in a ground with presence of bremsstrahlung produced by electron linac (Compton effect, $\gamma - \gamma'$ reaction) is widely known. An induction electron linacs of LIA-0,5/50 type developed in Institute of the Electrophysical Equipment (St.-Petersburg) have got the greatest advancement in Russia. Such devices have a diameter no more than 10 cm, length about 3 m, electron current up to 50 A, electron energy about 0,5 MeV and pulse duration of 50 ns. Linac, power supply system and control equipment are displaced in the same cylindrical module. The electric power is supplied through cable from a source placed on a ground surface. The signals from the control equipment are transmitted to the ground board [1]. A lack of such system is the rather small efficiency, that is characteristic for induction linacs, and limited service life in conditions of high temperatures (up to + 2000 C⁰), caused by degradation of ferrite cores of accelerating structure.

In the report given the results of preliminary research of the electron linac based on an auto resonant acceleration principle are described. Such linacs have certain restrictions on energy and acceleration rate, but are represented as most effective for the geophysics tasks decision by specific differences of single resonator accelerating system [2].

1 THE DEVICE DESIGN

The principle of the accelerator action consists in RF fields generation by cyclotron resonance maser type system. The scheme of the device is shown on Fig.1.

The device operates in the following way. The tubular shaped electron flow, emitted the cathode 1, gets into accelerating space between cathode and resonator 2 and begins to rotate as whole in the longitudinal magnetic field of solenoid 3. Thus significant part of longitudinal electron energy transforms into a rotary movement energy. The rotating electron flow gets into the resonator 2 and excites RF electromagnetic TE_{01n} mode in it.

The significant part of electrons gives back their energy to a RF field so electron beam radius of rotation decreases, as it is shown in [3]. These particles gets on a central part of a collimator 5. The accelerating resonator 6 is connected by coupling cells 4 to the generating resonator 2, therefore a RF field of a similar type also is exited in it. In collimator 5 area magnetic field comes to zero, so the electron trajectories become rectilinear, parallel to a longitudinal axis. Then the insignificant part of electron flow, not captured in a generation mode and having the greatest energy and rotation radiuses, gets into accelerating section 6.

If magnetic field induction increases upon length this part of electron beam is accelerated by means of nonsynchronous waves of TE01n mode up to energy about 0.8 MeV. Thus the electrons accelerated get onto a tungsten target 7 placed on lateral waveguide walls, producing a flow of bremsstrahlung (or y - radiation) in a transverse direction. The back scattered radiation from the ground is registered by the detector (not shown in a Fig. 1). The face wall 8 of the accelerating resonator is displacement is designed mobile, it's automatically by condition of a resonators 2 and 6 frequencies resonance. It is carried out by the reversal engine 9, controlled automatically by comparison of signals from two detectors (are not shown in a Fig. 1). If a frequency is deviated due to heating the automatic tuning of a magnetic field value by change of a solenoids current is carried out.

2 LINAC CALCULATED PARAMETERS

Generating and accelerating sections rectangular resonators with the cross sizes 44mm×72mm (operating frequency ~ 2800 MHz). The length of generating section is equal to 0.2 - 0.3 m, and accelerating section has length about 1 m. The injection current is equal to 40 A (after collimator - 0.5 A), injection voltage is equal to 50 kV, the pulse duration is equal to 2 µs, the repetition rate is about 50 Hz. The accelerating harmonic amplitude makes 50 kV/cm, pulsed accelerated current at an linac output - 0.1 A. The magnetic field is equal to 0,05 T in generating section. In accelerating section the magnetic field raises from 0.05 up to 0.12 T. Electrons get on the tungsten target, thus producing a bremsstrahlung flow with intensity up to 1.5 rad/hour. The cross dimensions of whole device does not exceed 0.14 m, length (with the power supply system and detector) is no more than 3 m.

¹ E-mail: bogdan@uni.mephi.ru

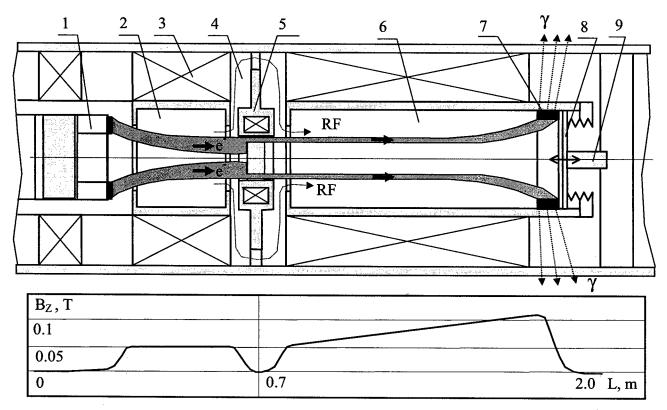


Figure 1: The scheme of device and magnetic field distribution (1 - electron source ring cathode;
2 - generating rectangular resonator; 3 - magnetic system coil; 4 - coupling cell (connects generating and accelerating resonator); 5 - collimator of a tubular beam; 6 - accelerating rectangular resonator;
7 - target; 8 - accelerating resonator mobile wall; 9 - reversal engine).

3 THE CONCLUSIONS

Precomputations and experiments, carried out in MEPhI and Tomsk Polytechnics Institute, have shown an opportunity of realisation of system proposed. It's electron efficiency can be higher the order in comparison with the induction accelerator, with raise of system durability and bremsstrahlung level increase a more than on the order at the same power consumption.

Nowadays in MEPhI a generating section model is successfully tested and the preliminary model tests of accelerating section were carried out. The model tests of the given acceleration method have confirmed an opportunity of acceleration in operating variant. The electron source current reached 20 A at voltage up to 100 kV. LaB₆ cathode ring has following diameters: external of 30 mm, internal of 10 mm. At a generating section input the rotating electron flow has a diameter about 20 mm. A pulse duration about (80-100) μsec , repetition rate is equal to 1 Hz. Numerical optimisation of a magnetic field distribution upon system length will be carried out nowadays.

4 REFERENCES

- [1] Yu.P. Vahrushin, A.I. Anatcky "Linear induction accelerators". Moscow, Atomizdat, 1978. (in Russian).
- [2] Y.V. Panitchkin, E.T. Protasevitch, Yu.G. Stein "Installation for an experimental research of the charged particles acceleration in smooth waveguides by fast electromagnetic waves at an increasing magnetic field ". Proceedings of Scientific Research Institute of nuclear physics, electronics and automatics at Tomsk Polytechnics Institute, Vol.3, "Charged particles accelerators". Moscow, Atomizdat, 1973, p.p.38-40. (in Russian).
- [3] Berezin V.M., Burjak V.S. et al. " *UHF electronic devices*". Moscow, Vysshaja Shkola, 1985 (in Russian).

MULTICUSP ION SOURCE FOR ION PROJECTION LITHOGRAPHY*

Y. Lee, a K.N. Leung, and M.D. Williams, Lawrence Berkeley National Laboratory, Berkeley, CA

W.H. Bruenger, Fraunhofer Institute for Silicon Technology, D-14199 Berlin, Germany

W. Fallmann, Technical University of Vienna, A-1040 Vienna, Austria

H. Löschner, and G. Stengl, IMS - Ion Microfabrication Systems GmbH, A-1020 Vienna, Austria

Abstract

The need to extend to smaller and smaller features (sub-100 nm) in integrated circuits has created the necessity to investigate new technologies beyond optical lithography. Ion Projection Lithography (IPL) is an advance lithographic concept that can provide the solution for the high volume fabrication of sub-100 nm integrated circuits. The IPL system requires low axial energy spread ions in order to minimise the chromatic aberration of the projected image on the wafer. Ion energy spread for the multicusp source has been reduced from 6 eV to below 2 eV by the use of a planar magnetic filter. And most recently, LBNL successfully reduced the energy spread to below 1 eV by employing a co-axial filter configuration. A similar source is being fabricated to be used for a novel IPL machine to be built by IMS in 1999 as part of the European MEDEA project headed by Siemens. This paper describes the multicusp ion source for lithography and shows some exposure results using this source.

1 INTRODUCTION

The enabling technology for integrated circuits is lithography: the repeated printing of fine line features in resist to define the various layers of circuit elements, precisely aligned from layer to layer. There are many lithographic techniques: optical, extreme UV (EUV), ion projection lithography (IPL), SCALPEL and 1:1 X-ray. Although optical lithography has been extended to far smaller dimensions than was predicted 15 years ago, there are definite physical barriers to extending it to the minimum dimensions of well below 100-nm.[1] Ion beam lithography could provide both small minimum dimensions and high throughput. Ions are well suited for lithography because they suffer little or no scattering in the resist unlike electrons.[2-7] IPL may turn out as the sub-100 nm lithography technique with lowest cost of ownership.

'This work is supported in part by the Defense Advanced Research Project Agency (DARPA), Intl. SEMATECH, Siemens Corporation and the U.S. Department of Energy under contract No. DE-AC03-76F00098 * Email: YYLee@lbl.gov

In IPL a uniform, collimated beam of light ions (H⁺, H₂⁺, H₃⁺, or He⁺) back illuminates a stencil mask. The image of this stencil mask is projected through a series of electrostatic lenses and demagnified onto the substrate (Fig. 1, [2]). IPL operates under vacuum and uses ions instead of photons to expose the mask features onto a resist coated wafer. IMS in Vienna, Austria has built two generations of ion projection lithography systems that have demonstrated many of the features needed for high throughput lithography.

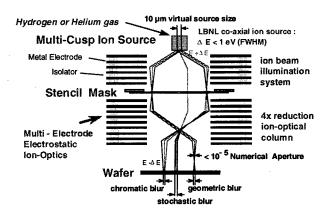


Figure 1: Schematic diagram of ion projection Lithography (IPL).

The ion source is an important component of IPL. Its performance determines many of the parameters of the beam downstream. The axial energy spread of the ion beam couples to chromatic aberrations in the ion optical column, and leads to blur in the printed pattern on the wafer. For a given design rule, the IPL system must achieve a compatible total error budget. For chromatic aberration to contribute a small fraction of this budget, the axial energy spread of the ion beam should be less than about 2 eV (full width at half maximum, FWHM). This paper will describe the source of choice for IPL.

2 MULTICUSP ION SOURCE

The multicusp source is capable of producing large volumes of uniform, quiescent and high-density plasmas with high gas and electrical efficiencies. Recently, it was found that the source can be used to produce low axial energy spread ions for lithography. Columns of

samarium-cobalt permanent magnets with alternating polarities surround the cylindrically shaped source. These magnets generate longitudinal line-cusp magnetic fields that can confine the primary ionizing electrons efficiently. One end of the chamber is terminated by an end flange, which is covered with rows of permanent magnets. The open end of the chamber is where the low axial energy ions are extracted. The schematic diagram of the source is shown in Fig. 2.

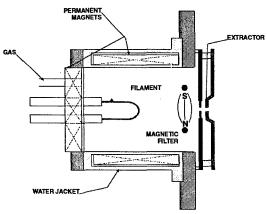


Figure 2: Schematic diagram of the multicusp ion source with the planar magnetic filter.

2.1 Without a magnetic filter

The axial plasma potential distribution inside the source has been studied in previous works by Ehlers, et.al.,[9] and its influence on the axial energy spread has been reported.[10] The plasma potential decreases monotonically towards the plasma electrode. Ions are formed with different energies if they are produced at different axial positions, thus the energy spread is large. The ion energy spread has been measured using a retarding field energy analyser (provided by IMS) and been reported to be approximately 6 eV for a 10-cm-diameter by 10-cm-long filament discharge source.

The importance of ions with low energy spread is clearly shown on the printed features. Although the multicusp ion source with this arrangement has not been tested in an actual IPL machine, exposure tests have been performed with the IPLM-02 research type ion projector at the Fraunhofer Institute for Silicon Technology using a duoplasmatron source. This source is known to have an energy spread of ≈ 12 eV. Figure 3 shows an exposure result in 390 nm thick DUV resist (Shipley UVIIHS): At 8.4 ion-optical reduction 74 keV hydrogen ions were used with an exposure time of 300 ms; exposure dose was 0.3 μ C/cm². The line spaces are 80 nm wide (> 4:1 aspect ratio).

2.2 With a planar magnetic filter

The multicusp ion source is provided with a removable magnetic filter system. The magnetic filter design is used to provide a limited region of transverse magnetic field, which prevents the energetic electrons in the discharge chamber from crossing over into the extraction region. The plasma potential distribution in this case is more uniform in the ion production region, resulting in a narrowed potential range where ions are actually formed. The axial energy spread has been reported to be approximately 2 eV for a 10-cm-diameter by 10-cm-long filament discharge source. The exposure result with this source presented a great improvement on the resolution [11]. Figure 4 shows 50-nm line spaces (> 6:1 aspect ratio) exposed with 75 keV helium ions in UVIIHS resist; exposure time 800 ms; exposure dose $0.3 \,\mu\text{C/cm}^2$.

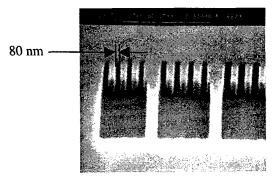


Figure 3: Exposure result using an ion source with a 12eV axial energy spread.

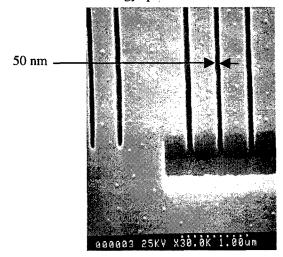


Figure 4: Exposure result using an ion source with a 2eV axial energy spread.

2.3 Co-Axial Source

The axial energy spread of the multicusp ion source can be further reduced by optimising the filter design. In this arrangement, both ends of the chamber are terminated by a flange, which is covered with rows of permanent magnets. One end of the chamber has an opening diameter of 5 cm where the extraction system will be placed. The filter has a co-axial cage configuration, 6-cm ID and 7.8-cm OD, and has 6 water-cooled rods of permanent magnets, shown in Fig. 5. Each rod is 0.8 cm in diameter. Plasma is generated between the source

chamber and the filter cage and diffuses into the center. This filter cage controls the plasma potential distribution more efficiently than the planar magnetic filter arrangement.

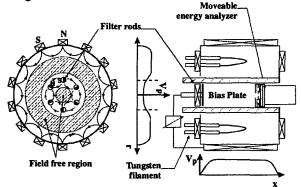


Figure 5: Schematic diagram of the co-axial ion source.

The plasma potential of the co-axial source has also been measured by using Langmuir probes placed in the central region as well as in the annular region of the source. In addition, a biasing plate can be installed in the central region for the purpose of modifying the radial plasma potential distribution, and therefore, the beam emittance.[12]

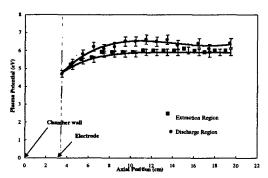


Figure 6: Axial plasma potential distribution for the coaxial source.

Axial plasma potential distribution has been measured in both the central and the outer annular regions. The plasma potential at the center is lower than that of the discharge region (by approximately 0.5 V) as it has been expected (Fig. 6). However, uniformity of the radial plasma potential distribution is not critical in reducing the axial energy spread. Nevertheless, the axial plasma potential distributions are quite uniform in both regions, as illustrated by the plots in Fig. 6. The axial energy spread for the co-axial source was found to be as low as 0.6 eV (FWHM). The resolution testing for this type of source is yet to be performed. This ion source is expected to yield sharp features.

Furthermore, in the co-axial source, the electron temperature (T_e) in the extraction region is lower than that in the discharge region. Electron temperature as low as 0.1 eV has been recorded at the extraction region, which is about an order of magnitude lower than that of

the discharge region. Such low electron temperature will enable the source usage in other lithographic technologies.

3 SUMMARY

A co-axial source is being designed and tested at the Lawrence Berkeley National Laboratory, and it will be used for the novel IPL machine to be built by IMS in 1999 as part of the European MEDEA project headed by Siemens Corporation [8]. Fig. 7 shows a drawing of the source to be used for the MEDEA project.

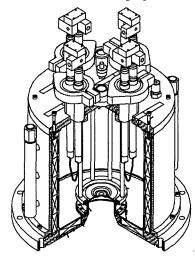


Figure 7: Schematic drawing of the co-axial ion source developed at LBNL for the MEDEA project.

4 REFERENCES

- J. Melngailis, A.A. Mondelli, I. L. Berry III, R. Mohondro, J. Vac. Sci. Technol. B 16(3), May/Jun 1998, 927.
- [2] R.L. Seliger and W.P. Fleming, J. Appl. Phys. 45, (1974) 1416.
- [3] L. Karapiperis and C. A. Lee, Appl. Phys. Lett. 35 (1979) 395.
- [4] M. Komuro, N. Atoda, and H. Kawakatsu, J. Electrochem. Soc. 126, (1979) 486
- [5] J. L. Bartelt, Solid State Technol. 29, (1986) 215.
- [6] J.N. Randall, D.C. Flanders, N.P. Economou, J.P. Donnelly, and E.I. Bromley, Appl. Phys. Lett. 45, (1983) 457.
- [7] H. Ryssel, K. Haberger, and H. Kranz, J. Vac. Sci. Technol. 9 (1981) 1358.
- [8] G. Gross, R. Kaesmaier, H. Löschner, and G. Stengl, J. Vac. Sci. Technol. 16 (1998) 3150.
- [9] K.W. Ehlers, K.N. Leung, P.A. Pincosy, M.C. Vella, Appl. Phys. Lett. 41 (1982) 517.
- [10]Y. Lee, L.T. Perkins, R.A. Gough, M. Hoffmann, W.B. Kunkel, K.N. Leung, M. Sarstedt, J. Vujic, M. Weber, and M.D. Williams, Nuc. Inst. and Meth. In Phys. Res. A 374 (1996) p. 1.
- [11] W.H. Brünger, H. Buschbeck, E. Cekan, S. Eder, T.H. Fedynyshyn, W.G. Hertlein, P. Hudek, I. Kostic, H. Löschner, I.W. Rangelow, and M. Torkler, J. Vac. Sci. Technol. B15, Nov/Dec 1997, pp. 2355; and Microelectr. Engng. 41/42, 1998,pp. 237-240
- [12]Y. Lee, K.N. Leung, J. Vujic, M.D. Williams, and N. Zahir, Nuc. Inst. and Meth. In Phys. Res. A. (accepted for publication)

RECENT DEVELOPMENTS OF THE EXCYT PROJECT

G. Ciavola, R. Alba, L. Barone Tonghi, L. Calabretta, L. Celona, G. Cuttone, G. Di Bartolo,
 P. Finocchiaro, S. Gammino, M. Menna, R. Papaleo, G. Raia, D. Rifuggiato, A. Rovelli,
 M. Silvestri, D. Vinciguerra, M. Winkler, H. Wollnik

INFN - Laboratori Nazionali del Sud, Via S. Sofia 44, 95123 Catania, Italy

Abstract

The EXCYT project at LNS, Catania, Italy aims to the production of radioactive ion beams to be accelerated by a tandem up to 8 MeV/amu. The primary beam coming from an ECR ion source goes into a K800 cyclotron and then to the target-ion source assembly. Here the species of interest are produced mainly by projectile fragmentation in a target thicker than the projectile range. The products diffuse through the heated target, are desorbed from its surface and go to the ion source via a transfer line. After ionization, the products are mass-separated and injected into the tandem to be post-accelerated and delivered to the users. It is worth noting that besides the post acceleration there is also an option to supply 300 keV beams for low energy experiments. In the following, the status of the project will be described into details.

1 ECR ION SOURCES AND SUPERCONDUCTING CYCLOTRON

In 1998 the superconducting ECR (electron cyclotron resonance) ion source SERSE has been installed. The source has already achieved the maximum primary beam intensities required by the EXCYT project (7 p μ A of totally stripped light ions) [1]. To ensure the continuous operation of the cyclotron, a second ECR ion source with room-temperature magnets has been recently added.

The K800 Superconducting Cyclotron (CS) is presently operated as a booster for the 15 MV tandem beam [2]. To allow its future use in a stand-alone mode and to obtain the beam intensities needed, axial injection has been chosen. The axial injection line from the two ECR ion sources to the CS is being completed; it will allow the rotation of the beam ellipse in the final matching point (MP). The remaining vertical section has been recently designed to achieve a small beam size at the entrance of the inflector [2]. For the new injection mode an inflector and a second harmonic central region (fig.1) will replace the present stripper system. To operate the cyclotron in a constant orbit mode the source, the dees and the inflector voltages will be varied according to the relation: $V/(\omega_0 B_0)$ = const., with a source limiting voltage of 30 kV [3]. The spiral inflector has a 6 mm gap and an applied electric field of 22 kV/cm: the latter value has been chosen to make the exit radius as large as possible (17.5)

mm for 30 kV injection voltage) for comfortably allocating the central region posts. The design of the central region is based upon the MSU K500 cyclotron [4], which has been refurbished to be coupled to the K1200 cyclotron. At MSU, the whole system is conceived to deliver intense primary beams for the production of radioactive ion beams by fragmentation. The puller, consisting of two posts at the RF voltage immediately accelerates the beam coming out of the inflector. The particular geometry of the RF and ground posts allows the particles to gain as much energy as possible. The beam is well confined inside the central region, while there is a radial dependence upon the phase at the end of the first turn. Here the last ground slit of the central region performs a rough phase selection, reducing the phase range down to approximately 35° (from 200° to 235°) which corresponds to the acceptance of the cyclotron.

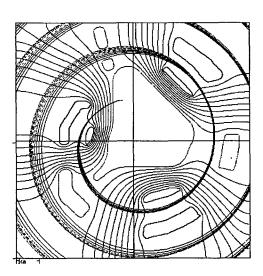


Figure 1: The 2nd harmonic central region of the LNS Superconducting Cyclotron. Central trajectories with starting times from 200° to 235° are plotted.

A slit system [2] has been designed to perform a fine phase selection out of the central region: it consists of three wedges that will discriminate among phases according to the simulations made in [5]. The matching between the line and the cyclotron in the new mode has been evaluated with good result [3] by considering separately: a) the beam ellipse transport from the MP to

the inflector exit and b) the evolution of the beam ellipse from the inflector exit towards the extraction. The central region parts and the inflector are planned to be installed in the cyclotron by November 1999.

2 HV-PLATFORMS

Two different 250 kV platforms will be built in separated rooms. The voltage has been chosen in order to enhance both the injection in the tandem and the performance of the mass separator. Most of the radioactivity is generated and confined within the first platform area housing the target-ion source assembly and the pre-separator; the whole area is contained in a shielded pit. The radioactivity level in the second platform area is much lower; this platform houses the charge exchange cell and the first stage of the isobaric mass separator. A high-voltage conduit carrying the beam line and the electrical cables through a 1-meter thick shield wall connects the two platforms. The conduit consists of two concentric pipes: a continuous electrically conductive inner pipe and a continuous epoxy outer pipe with flanges that extend into the 250 kV platforms by a few centimetres. The space between the two pipes is filled with 2 atm of SF. insulating gas. Moreover, within the span of the shield wall a stainless steel tube with field termination rings covers the epoxy tube. POISSON simulations showed that a) the electrical gradients are appropriate to prevent sparks; b) for a 250 kV platform voltage the maximum value of the electric field is located at both ends of the stainless steel tube and reaches up to 13 kV/cm.

3 TARGET-ION SOURCE ASSEMBLY

Several innovative high-power target geometries have been developed and are currently being constructed. The designs are based on the concept of redistributing the primary beam intensity over larger transverse and longitudinal target dimensions. At operating temperatures above ~2000 °C radiative cooling is the dominant heat process: transfer therefore geometrical configurations which allow maximum viewing of cool surfaces will radiate most efficiently. The surface is increased by tilting the target of an angle α (Fig.2) chosen to reach the desired level of temperature. By wiggling or defocusing the beam, its spot size on the target should be increased up to ~30 mm, thus effectively reducing the beam power density. The combined effect of increasing both the beam size and the target dimensions will increase the effective radiating surface area of the latter, thus resulting in a stable target operation with increased total beam intensities. Computer simulations by ANSYS finiteelement code, validated this concept which will be also used for the HRIBF at ORNL [6]. A special type of graphite with high open porosity has been chosen for the initial targets: this material should allow a good diffusion of the products.

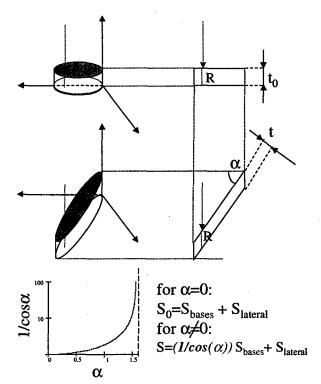


Figure 2: The scheme of the EXCYT tilted target of the Project. Assuming R as the range of each particle equal to t_0 , for any α value the particle will reach the bottom of the target. By increasing α , the target thickness increases as well as the surface area following the shown relation.

Three ISOLDE-type ion sources, namely positive surface ionisation, negative surface ionisation and hot plasma, are ready to be tested. A fourth negative ion source, developed for fluorine at the HRIBF will be built and tested for EXCYT. The microwave discharge ion source MIDAS has been completed in 1997. Gas efficiency tests showed fast ionization times (a few ms) and the almost complete independence on the ionic species. On the other hand, they also showed the inadequacy of using an antenna-based injection system. The source has been redesigned with a waveguide injection and a better extraction system. If the expected enhancement (up to 20%) will be achieved by the second prototype, a final version finely matching both with the target and with the front end will be designed. The ground electrode has been designed with an extraction optics able to interact with all of the above mentioned ion sources.

A massive experimental programme has been undertaken in order to estimate the formation of products inside the targets, their release by means of diffusion and desorption and finally the efficiencies of the ion sources. Cross sections for several nuclides produced by the reaction: ¹⁹F (50 MeV/amu) + ¹²C have been measured, with values: 91 mb for ⁷Be, 96 mb for ¹⁸F, 10 mb for ²²Na, 2.5 mb for ²⁴Na [7]. The figures for ¹⁸F and ⁷Be are very promising and can be increased with higher energy beams (e.g. 80 MeV/amu). Using ⁹Be as a projectile on graphite should

also increase the latter value. Experiments to determine the cross section for ${}^{9}\text{Be}$ (50 MeV/amu) + ${}^{12}\text{C} \rightarrow {}^{7}\text{Be}$ and the release of ${}^{7}\text{Be}$ from the target material are planned by the end of March 1999.

4 HIGH RESOLUTION MASS SEPARATOR

As described in [8], the secondary beams produced in the target-ion source system will go through a magnetic isobaric separator with a nominal resolution power $M/\Delta M = 20000$.

The EXCYT mass separator will consist of four sections: a pre-separator, two main separation stages at different potential and a transport section towards the tandem. The pre-separator with $M/\Delta M=170$ consists of an 18° bending magnet and a quadruplet of electrostatic quadrupoles placed in a 250 kV platform. Two triplets of electrostatic quadrupoles will guide and focus the beam to a charge-exchange cell.

The first separation stage with $M/\Delta M = 2000$ is placed on a second 250 kV platform and consists of two bending 77° and 90° magnets preceded and followed by a quadruplet of electrostatic quadrupoles. Finally, the second separation stage with $M/\Delta M = 20000$ consists of two large 90° bending magnets with surface coils assembled on their pole faces to compensate for misalignment effects. The different potential of the two main stages allows having zero energy dispersion. Consequently the system can be set as an energy achromatic separator to compensate the energy spread of the source.

The transport section consists of three 90° bending magnets preceded by a quadruplet of electrostatic quadrupoles. The magnets of the separator and of the primary beam line will be delivered in a few weeks; the electrostatic quadrupoles have been designed; one quadruplet has been manufactured and the other elements are under construction.

5 BEAM DIAGNOSTIC AND SAFETY

In order to perform the beam diagnostics, besides standard instrumentation we are going to employ tools specially suited for low intensity RIBs:

- A scintillating fibre-based beam profile monitor that
 can be assembled with either plastic or glass fibre
 according to the expected intensity range. This device
 has to be used with high energy beams (after the
 tandem acceleration) and is planned to be our
 standard tool for beam handling [9][10].
- A gas detector employing a glass microstrip readout electrode (MSGC), to be used with high energy beams in special cases when the minimum interceptivity is required [11].
- A CsI (Tl) based beam profiler for beams having both high energy and very low intensity. This device is

- also capable of self-calibration by single particle counting in its lower intensity range. As for the beam identification we are assembling two different complementary devices to be placed respectively before and after the tandem acceleration.
- A beam imaging and identification station based on the detection of the decay products from radioactive ions implanted on an inert tape. This device operating at 200 keV before the tandem acceleration is insensitive to the stable beams.
- A quantitative and qualitative beam analyser, to be used after the acceleration, based on a silicon telescope that detects the beam particles scattered from a thin gold target.

A robot will remove and store the activated target-ion source assembly. The same robot will then place a new assembly. In a similar way, activated parts from the CS (electrostatic deflectors, dees, etc.) will be changed by remote handling. As for the target-ion source assembly, the whole system will be ready by December 1999 while the rest is still under construction.

Gaseous and liquid waste from activated/contaminated areas will be treated before release in the environment. The design for both systems is ready and the relevant mechanical parts will be ordered in a few weeks.

5 REFERENCES

- [1] G. Ciavola et al., these proceedings and S. Gammino et al., Rev. Sci. Instrum. (in press)
- [2] D. Rifuggiato et al.; First years of operation of the LNS Superconducting Cyclotron, Proc. 15th Int. Conf. Cycl. Appl.; Caen, 1998 (in press)
- [3] D. Rifuggiato et al.; Axial Injection in the LNS Superconducting Cyclotron, Proc. 15th Int. Conf. Cycl. Appl.; Caen, 1998 (in press)
- [4] S. L. Snyder; Study and Redesign of the NSCL K500 Injection, Central Region and Phase selection Systems; Ph.D. Thesis, MSU, 1995
- [5] J. Bailey et al.; Proc. 13th Int. Conf. Cycl. Appl., Vancouver, (431) 1993
- [6] HRIBF News, Edition 7, nº 1, Winter Quarter 1999
- [7] M. Menna et al.; (in preparation)
- [8] G. Ciavola et al.; Design of the EXCYT Radioactive Ion Beam Separator; NIM B 126 (1997) 17
- [9]P. Finocchiaro et al.; A Scintillating Fibre-based Profiler for Lowintensity Ion Beams; NIM A 385 (1997) 31
- [10] P. Finocchiaro et al.; Low-intensity Ion Beam Profiling with Glass Scintillating Fibres; NIM A 419 (1998) 83
- [11] P. Finocchiaro et al.; Particle Detectors for Low Intensity Ion Beam Diagnostics; Proc. 15th Int. Conf. Appl. Acc. Res. Ind.; Denton, 1998 (in press)

START CONDITION AND NON-LINEAR SATURATION IN HIGH CURRENT FEL-OSCILLATOR

V.K.Grishin*, T.A.Novicova Institute of Nuclear Physics of Moscow Lomonosov State University

Abstract

Properties of high current free electron laser (FEL) with a collective regime of electromagnetic wave excitation are considered. Start value of electron current in a FEL-oscillator and non-linear saturation of field excitation are estimated. Possibility of such device creation on base MSU electron linear accelerator is discussed.

1 INTRODUCTION

In present, several high current FEL facilities are under construction and operation (see for example [1], in particular [2,3]). A high current FEL has coefficient of signal amplification, and this permits to extend the possibilities to create the coherent short-wave radiation sources. The high signal amplification is a result of a collective interaction of an electron beam with an electromagnetic wave. The latter can be realised if the density of electron is sufficiency high. With that an intense beam acquires the properties of optical waveguide, and the electromagnetic radiation is concentrated in the beam volume [4]. Therefore as it has been shown in previous paper [5], a high current regime can be realised in FEL having a moderate current but low emittances of particles that is peculiar for an electron accelerators of new generation.

In present paper the high current approach is being used to analyse the peculiarity of a scheme of FEL-Oscillator and to estimate its start and saturation conditions. It is of interest can we have here any application of this scheme on the MSU electron accelerator?

2 START CONDITION IN HIGH CURRENT FEL OSCILLATOR

Consider a traditional scheme of a charged beam generator. A system constructed along the axis z consists of undulator with a period λ_0 and length $L_{\rm und}$ which is located between two mirrors. The mirrors separated by distance L_m ($L_m > L_{und}$) are forming an open resonator. Along the axis z in a point placed before the undulator a continuous beam of monoenergetic electrons is being

*Email: grishin@depni.npi.msu.su

injected into the system (by means of supplementary magnet system). The electron energy is $E=mc^2\gamma_L$ where γ_L is Lorenz's factor, the initial electron velocity is $v_0=\beta_0c$. Passing trough the undulator the electrons acquire a transversal velocity $v_\perp=\beta_\perp c$ that permits them to interact with an optical (i.e. transversal) wave. After passage he undulator the electron beam is being deflected from the system (by means of second supplementary magnets).

Analyse start condition of high current FEL oscillator. Let an initial signal of frequency ω be brought in the system. The signal passing through the undulator can be amplified by an electron beam and then being partly irradiated and reflected from the mirrors returns to the initial point. Usually a start condition of FEL oscillator is estimated from one if the amplification of circling signal begins surpass its total absorption. But the high current FEL has its important peculiarities.

An electron beam in the undulator is an electromagnetic medium in which some transversal waves of different modes can propagate in both directions. An initial signal is distributed among the co-travelling with beam waves some of which can interact with the electrons. Its interaction becomes resonant if the double conditions are carried out:

$$\omega = kc$$
; $k = k_0 \beta_{0z} / (1 - \beta_{0z})$ (1)

where k is a wave vector, $k_0=2\pi\,/\,\lambda_0$, $\beta_{0Z}=(\beta_0^2-\beta_\perp^2)^{1/2}\,.$

Practically one can consider only the mostly amplified wave among the co-travelling ones after passing the undulator and only one back travelling wave because an electron beam do not disturb the electromagnetic oscillations in last case.

Hence the final balance of amplification and absorption in system gives the nest condition of reliable generation start (see [6] too):

$$R_1 R_2 \exp \left(i \int_{0}^{L_m} (k^+ - k^-) dz \right) = 1$$
 (2)

where $R_{1,2}$ are the coefficients of wave amplitudes reflection from the first and second mirrors respectively (value of R_2 includes the loss of signal due to its

irradiation), k^+ and k^- are the wave vectors of forward and back directions for given frequency and mode. Here we take into account that the waves coming in and out from an electron beam are almost not reflected.

Outside electron beam

$$k^{+} = k = \frac{\omega}{c}, \quad k^{-} = -\frac{\omega}{c}$$
 (3)

and inside one

$$k^{+} = k + \delta k^{+}; \quad \left| \delta k^{+} \right| << k$$
 (4)

Hence the equation (2) is reduced to

$$2kL_{m} + \delta k^{+}L_{und} = 2\pi M + i \ln |R_{1}R_{2}|$$
 (5)

where $M = S - arg(R_1R_2) / 2\pi$, S is an integer. Separating the real and imaginary parts of (4) one can write

$$2kL_{m}+Re(\delta k^{+})L_{und}=2\pi M$$

$$Im(\delta k^{+})L_{und}=-ln\left|R_{1}R_{2}\right|$$
(6)

This equation is written for a given value of frequency. And the first equation in (6) determines conditions when the wave excitation of given mode is possible in beam system. But already after the first wave circulation, the excitation of electromagnetic oscillations in mirror resonator goes to play the important role. Therefore it is necessary to add the condition of wave excitation in FEL resonator with the same value of frequency. Such condition produces a relation [7]

$$2kL_{m} = 2\pi (N + (n+q+1)/2 + \Delta)$$
 (7)

where N,n,q are the integers, Δ is a mode shift determined by resonator parameters.

The second equation in (6) determines the start condition for the electron beam current I_b . Really according with a solution of beam linear system the increment of wave excitation $\text{Im}(\delta k^+) = -A I_b^{\alpha}$ (see below). Due to this the second condition in (6) drives to the direct dependence of start value of I_b on $R_{1,2}$, A, and α ones:

$$I_{b_{st}} = \left(\frac{\ln|R_1 R_2|^{-1}}{AL_{und}}\right)^{1/\alpha}$$
 (8)

The magnitude of $\alpha \approx 1/3 - 2/5$ for a wide and compressed beam respectively [5]. For the latter case

$$A = k_0 \left(\frac{4}{k a_b I_A} \right)^{\alpha} \tag{9}$$

where $I_A = 17 \text{ kA}$, and $k = k_0 \gamma_0^2$.

The value of $R_2 = (1-\epsilon)^{1/2}$ where factor $\epsilon << 1$ including the fraction of electromagnetic flow irradiated through the second mirror. To determine the value of R_1 it is necessary

to take into analysis the fact of strong channelling of electromagnetic radiation in the beam volume. As a result the cross-section of electromagnetic flow becomes comparable with of beam one. The electromagnetic flow reflected from the second mirror returns to the first one and then to the undulator expanding due to a diffraction. As a result the fraction of electromagnetic flow returned in the beam volume is reduced to [8]

$$F = \left(\frac{a_b a_E k}{2L_d}\right)^2 \tag{10}$$

where $a_{b,E}$ are the radius of beam and electromagnetic flow canalised in it, $L_d=2L_m\text{-}L_{und}$. Finally

$$R_1 = F^{1/2} / N^+ \tag{11}$$

where N^+ is the number of forward travelling waves in beam system (usually $N^+ = 2-3$ [5,6]).

On the whole the collective regime indicates in FEL a relatively weak dependence of start current value on the resonator parameters.

Basing on the formulas obtained above one can get a simple estimate of increment value needed for lasing. It is not difficult to see that the spatial distribution of radiation field outside of electron beam is been described by function

$$E(r > a_b) \approx K_0(vr) \tag{12}$$

where K_0 is Bessel function of imaginary value, $v^2 = k^2 - (\omega/c)^2$. Therefore the radiation beam radius $a_E \approx 1/v$. Using a relation $Im(\delta k^+) \approx v^2/(2k)$ we see that $Im(\delta k^+) \approx 1/(2ka_E^{-2})$. In result the quantity

$$\zeta = \operatorname{Im}(\delta k^{+}) L_{\text{und}} \tag{13}$$

is determined by the equation

$$\zeta \approx \ln \zeta + \ln \sigma / 2 + \eta \tag{14}$$

where $\sigma = a_E/a_b$, a parameter $\eta \approx 1,5\text{--}3$. Thus the start value of $\zeta_{st} \geq 2\text{--}3$.

3 SOME COMMENTARIES. NON-LINEAR SATURATION

Notice some important effects of collective FEL. Resonance electron accelerators have a micropeaks longitudinal structure of beam with frequency of peaks repetition at several GHz. But its length exceeds the excited electromagnetic wave ones very considerable. Therefore all mentioned estimates retain correct. But the

main practical problem is an exact concordance the return of electromagnetic signal with the injection of next electron peaks. Besides the necessity of fine tuning of optical resonator it is important to take into account that, due to an intense beam acquires in undulator the properties of optical waveguide, the phase velocity v_{ph} of excited electromagnetic wave is been reduced, and

$$v_{\rm ph} = c \left(1 - \text{Re}\delta k^{+}/k \right) \tag{15}$$

It is of interest that this circumstance is very useful for to avoid a problem of lethargy or "anti-lethargy" [9].

Then discuss one important non-linear effect. How long is continuing the process of electromagnetic energy accumulation in FEL resonator? Taking into account the mechanism of electron-electromagnetic field interaction one can conclude that a process of electron energy transfer to a radiation goes to be saturated after electron trapping by the ponderomotive wave. In spite of resonant tuning, the velocity of ponderomotive wave becomes less (according with (15)) that the beam one. Longitudinal braking of particles is been caused by the interaction of particle with magnetic field H of exited electromagnetic wave and is been described by relation

$$mc^2 \gamma \gamma_z^2 \frac{d\beta_z}{dt} = -ev_\perp H$$
 (16)

Therefore trapping of electrons can realise if the mean electric field <E> reaches to the next saturation level (see (9)):

$$\langle E \rangle \approx \frac{AI_b^{\alpha}I_A\gamma^5\beta_z}{2ck_0L_{und}}$$
 (17)

Dependence of <E> value on FEL parameter is evidence.

4 FEL OSCILLATOR ON BASE OF MSU ELECTRON ACCELERATOR

In present time in Institute of Nuclear Physics of MSU there is a continuous wave electron accelerator with the particle energy of 1.2-2.4 MeV. The device is designed for different atomic and nuclear and applied researches. It produces a continuous electron beam with the average current magnitude up to 10-30 mA and small emittance.. The beam has a peak microstructure (frequency of repetition is 2.45 GHz) with peak current magnitude up to 0.4-1.5 A.

The values of $\gamma_0 = 3.4 - 5.6$ permit to use this accelerator for producing the electromagnetic radiation in millimeter and submillimeter ranges what opens a very important applications in biology and so on. Estimate the start current value.

Let the system and beam parameters be the next: $\lambda_0=2$ cm, $L_m=2L_{und}$, $a_b=0.1$ cm, $a_E=2-3$ a_b . Then for a real continuous beam the value of $I_{b\,st}\equiv 30$ mA is been reached with $L_{und}\equiv 200$ cm and 250 cm for the electron energies 1.2 and 2.4 MeV respectively. Thus this accelerator can be used as FEL oscillator.

5 REFERENCES

- [1] Proceedings of the 1995 Particle Accelerator Conference, IEEE-APS, Synchrotron Light Sources and FREE Electron Lasers, v.1, pp.155-311,
- [2] M.Hogan, C, Pellegrini, J. Rjsenzweig et al., ibid. p. 240.
- [3] D. Baunan<, D. Jianjiun, H. Shenzong et al., ibid, p.246.
- [4] J.M.J.Madey, J.App. Phys., v.42 (1971),1906.
- [5] V.K.Grishin, B.S.Ishkhanov. T.A.Novicova, V.I.Shvedunov, idid, p. 225.
- [6] E.M.Lifshits, L.P.Pitaevski, Physical Kinetics, § 65, Nauka Press, Moskva
- [7] O.Zvelto, Principles of Lasers, Plenum Press, New York.
- [8] L.D.Landau, E.M.Lifshits, Theory of Field, § 61, Nauka Press, Moskva.
- [9] T.C.Marshall, Free-Electron Lasers, New York, 1985.

COLLECTIVE EFFECTS IN POLARIZATION X-RAY BREMSSTRAHLUNG OF RELATIVISTIC ELECTRONS AND MICROSTRUCTURE ANALYSIS OF MEDIA*

S.V.Blazhevich, N.N.Nasonov, Belgorod State University, Belgorod, Russia A.S.Chepurnov, V.K.Grishin*, B.S.Ishkhanov, V.P.Petukhov, V.I.Shvedunov, Moscow Lomonosov State University, Moscow, Russia

Abstract

Peculiarities of collective effects in polarization X-ray bremsstrahlung (PB) which occur due to coherent interaction of fast charged particles with atomic electrons are discussed. Results of experimental study performed on base of 2.4 MeV electron CW linear accelerator of MSU are reported. The predicted strong difference between polarization bremsstrahlung properties for amorphous and polycrystalline targets in important for different applications region of X-ray radiation photon energies at 1-10 keV is observed for the first time manifesting clearly the polycrystalline structure of used aluminium target. The possibility of development of a method to test the structure of different substances with PB is indicated.

1. INTRODUCTION

The new emission mechanism known as the polarization bremsstrahlung (PB) is realised in the process of fast charged particle collision with an atom and interpreted due to scattering of the equilibrium electromagnetic field associated to this particle on atomic electrons [1]. Usually PB properties are investigated conformable to the process of fast particle interaction with a separate atom. Meanwhile theory predicts the strong dependence of PB characteristics in condensed medium upon the structure of this medium. The mentioned peculiarity is stipulated by the great enough value of PB effective impact parameter comparable with a size of atom. Due circumstance the collective response of medium atoms on the electromagnetic perturbation from the side of fast particle takes place for the case of condensed medium. In particular the strong difference between PB properties for the cases of amorphous and

polycrystalline structures of a medium was predicted in [2]. The aim of this work is to research experimentally the peculiarities of relativistic electrons PB in a polycrystalline aluminium foil.

2. EXPERIMENT

The experiment has been performed at Institute of of Moscow Lomonosov Nuclear Physics University linac (a 2.4 MeV continuos electron beam has been used). The block diagram of an experimental set-up is traditional. A beam of accelerated electrons with cross section 2 mm×2 mm is directed into aluminium foil with the thickness of 2 mkm placed in vacuum chamber. Electrons passing through the target are absorbed in a Faraday cup. Photons emitted in the process of relativistic electron beam interaction with the target in X-ray energy range are registered by a semiconductor Si(Li) cooling detector in a small solid angle (~1.5 msr) given by the photon channel located at an angle of 90° with respect to the incident electron beam (the plane of the target surface is located at an angle of 45° to beam axis). The distance between the target and the detector is about 0.5 m. The described geometry is most suitable for the achievement of contribution of normal bremsstrahlung comparable with the measured photon yield. The characteristic spectrum obtained in the experiment is presented in Fig. 1 simultaneously with the spectrum of external background measured on condition of the closed by lead plate photon channel. The dominant contribution to total number of registered photons is determined by Al K -x-ray peak located in the vicinity of 1.5 keV (in accordance with the theory PB intensity has on condition of the performed experiment a value less than 1% of Al-K x-ray intensity). Therefore the spectrum in the Al-K x-ray frequency range is not

^{*} Work is supported by Russian Foundation for Basic Researches under Grant #96-02- 17109.

[#] Email: grishin@depni.npi.msu.su

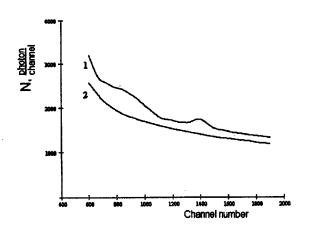


Figure 1. Experimental data: 1 is signal, 2 is background

shown in Fig. 1. The final observed spectrum is presented in Fig. 2 without the contribution of external

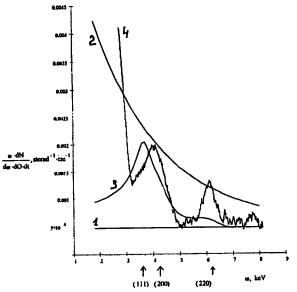


Figure 2. Spectral-angular distribution of PB intensity. Curve 1 is normal bremsstrahlung; curve 2 is PB in amorphous aluminium; curve 3 is PB in polycrystalline aluminium (theory); curve 4 presents the experimental data after external background subtraction.

background. The spectrum has been smoothed out in the limit of the detector energy resolution (~200 eV) in order to make use of the accumulated statistics in the right way.

3. DISCUSSION

There are some theoretical curves in Fig. 2. in addition to the experimental one. The curve 1 describes the spectrum of normal bremsstrahlung intensity of relativistic electrons moving in an aluminium. The curve 2 describes the spectrum of collimated PB intensity of relativistic electrons moving in amorphous aluminium. This curve is

calculated with taking into account the effect of isotropic spectral-angular distribution of relativistic particle PB [2] and the contribution of normal bremsstrahlung as well. The curve 3 describes the theoretical spectrum of PB intensity emitted by relativistic electrons moving through a polycrystalline target. This curve is calculated by the formula [2] with taking into account the contribution of normal bremsstrahlung and coherent part of the polarization bremsstrahlung by relativistic electrons interacting with accidentally oriented microcrystals constituting a polycrystal. The incoherent part of a fast particle PB in a polycrystal is suppressed strongly [2]. Therefore the PB yield in the case of amorphous target is greater than that in the case of polycrystalline one in the spectral region outside the vicinity of coherent peaks. Curve 4 presents the corresponding experimental data after external background subtraction. The nature of peaks mentioned above is analogous to that of Debye-Scherrer ones in the process of x-ray scattering in polycrystals [2]. The coherent PB peaks corresponding to Al crystallographic planes (111), (200), and (220) make the main contribution to PB yield on condition of performed experiment (the calculated spectral distributions of these peaks are shown especially in Fig. 3, each taken separately).

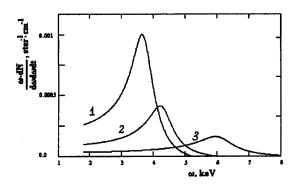


Figure 3. The peaks corresponding to the coherent scattering of particle's coulomb field on crystallographic planes of aluminium crystal. The curve 1 corresponds to (111), 2 to (200), and 3 to (220) planes.

One can see that the position of spectral peaks contained in measured spectrum corresponds to theoretical prediction. The value of the measured PB yield in the vicinity of (111) and (200) peaks is in agreement with the theory, but the essential discrepancy between theoretical prediction and observed contribution of the peak (220) takes place. The possible cause of this discrepancy connects with the coherent Bragg reflection of an incident electron electromagnetic field from the texture being available in the surface layer of the target. Thus, the spectral properties of PB of relativistic particles moving through a polycrystalline target differ strongly from that manifested in the case of relativistic particle interaction with an amorphous target in contrast to normal

bremsstrahlung [3]. Taking into account the difference between observed spectrum and that obtained earlier in experimental investigation of PB by relativistic electrons moving through a carbon like diamond film [4] one can affirm that PB mechanism is very sensitive to the target structure. This circumstance is of interest for the elaboration of the new method of solid structure diagnostic based on PB.

4. CONCLUSION

Two peculiarities of PB by relativistic electrons moving in a polycrystalline target are observed in this work for the first time: 1. The spectral-angular distribution of PB photons emitted in a polycrystal contains the sharp peaks appearing due to the ordered structure of microcrystals forming the polycrystalline medium. 2. The PB yield from a polycrystal outside the vicinity of coherent peaks is suppressed strongly in comparison with that generated by relativistic particles in amorphous medium

The authors are very thankful to Professor B.M. Bolotovsky for helpful discussion on the obtained results.

5. REFERENCES

- [1]. M.Ya. Amusia, V.M. Buimistrov, et al. Polarization bremsstrahlung of particles and atoms, Plenum Press, New York, 1992
- [2]. N.Nasonov, Nucl. Instr. Meth. B 145 (1998) 19.
- [3]. M.L.Ter-Mikaelian, High energy electromagnetic processes in condensed media, Wiley, New York, 1972.
- [4] S.Blazhevich, A.Chepurnov, V.Grishin et al. Phys. Lett.A 211 (1996) 309.

HIGH EFFICIENCY COMPACT SOURCE OF MONOCHROMATIC TUNABLE X-RAY RADIATION ON BASE OF ELECTRON ACCELERATOR WITH MODERATE PARTICLE ENERGY

V.K.Grishin⁺, S.P.Likhachev, Moscow Lomonosov State University, Moscow, Russia N.N.Nasonov, Belgorod State University, Belgorod, Russia

Abstract

Project of high efficiency compact monochromatic tunable X-ray radiation source is considered. Special magnet scheme for parametric x-ray radiation (PXR) generation arising in vicinity of Brag direction while an electron beam multiple hits a crystal target is proposed. Peculiarities of magnet system permitting stable electron circling are discussed. First results of computer simulation are reported.

1. INTRODUCTION

In present several kinds of relativistic electron coherent emission processes in condensed media are been studied as a candidate for quasimonochromatic highly directed X-ray source creation. One of the most effective possible x-ray sources may be basing on the parametric x-ray radiation (PXR) of relativistic electrons crossing a crystal [1-3]. The essential shortcoming of this emission mechanism connected with a small PXR intensity is stipulating the attempts to test the different schemes, which would permit to increase the photon yield.

How is it possible to raise PXR intensity of electrons? Evident step consists in increase of target thickness. But this way is not efficient. At first that produces increasing the angular dispersion of electrons. A permissible angular divergence of particles can not exceed here the magnitude of cone angle of radiation flow that is about $1/\gamma$ where γ is Lorenz factor of incident electrons. Besides the self-absorption of generated photons becomes very considerable in the substance of thick target.

Therefore this work is devoted to study of the possibility to create an effective x-ray source based on PXR by low relativistic electrons crossing repeatedly a thin crystalline target. The proposed arrangement permits generate the monochromatic, polarized, and tunable X-ray radiation, which can be very widely used in the different scientific and other applications.

2. PRACTICAL SCHEME. MAGNETIC SYSTEM

Thus, a special scheme of PXR generation in which

+ Email: grishin@depni.npi.msu.su

electrons are multiple crossing a crystalline target, is been considered. Low relativistic electrons are been used what allows obtain a compact size of layout.

The suggested experimental setup is presented in Fig.1.

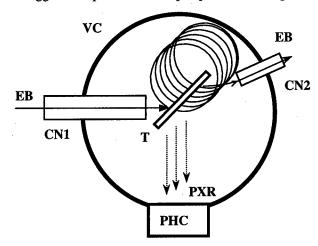


Figure 1.The scheme of experimental setup. VC is a vacuum chamber, T is a crystalline target, EB is an electron beam, PHC is photon channel for PXR, CH1 and CH2 are channels for injection and removal of electrons.

Here in a vacuum chamber VC, a crystalline target T is installed. The target is immersed in a magnetic field. The electron beam EB is injecting through a special channel CH1 in the work volume. Electrons circling in the magnet field are hitting the target several times. Then they are been removed through a channel CH2. PXR generated by electrons is been taken out through a photon channel PCH.

A gist of proposal is to force electrons to do stable multiple crossing of target after preceded ones. For this the special configuration of magnetic field is considered. Here a magnetic field must carry out two functions. The first one is ensuring a stable circulation of electrons with its properly focused fall on the target. The second one is a necessity to shift the rotating particles along the target. A suitable field configuration can be creating by means of magnetic poles of a simple form. These are two parallelepipeds placed over and below the target and stretched along it. The poles are slightly shifted across target plane. In this case the fields dispersed on poles

ridges are ensuring spatial focusing of circling particles. Due to a displacement of poles, mean magnitudes of fields are not equal left and right the target, and the latter provides a lateral drift of particles. By results of our previous works devoted researches of efficiency increase of usual bremsstrahlung source, the similar magnetic configurations provides reliable focusing of particle [4].

3. COMPUTER SIMULATION. EMISSION YIELD CALCULATION.

For testing the considered scheme we are applying a method of computer modeling. The whole procedure of modeling by a natural way breaks up to two parts. Change of energy of particles and their dispersion are defined basically by ionization losses of particles in substance of a target. Casual drawing of these events and accompanying radiation of bremsstrahlung quanta, and also dynamics of trajectories of particles in a magnetic field are been simulated on the basis of GEANT program library [5]. The process PXR is been simulated with the help of the additional software package, in which the casual drawing of the acts of radiation PXR photons is been described proceeding from the following physical representations.

PXR is a process of a fast particle coulomb field coherent scattering by a system of crystalline atomic planes. This emission has been studied well theoretically. Therefore we are calculating the spectrum of the photons emitted by an electron beam in a thin crystal using the well-known formula for PXR spectral-angular distribution (see for example [6]). In our calculations we are neglecting the dynamical diffraction effects as well as photoabsorption because of small enough emitting electron energy and crystal thickness, but taking into account the influence of emitting particle multiple scattering in a target and a finite angular size of a radiation collimator. The gaussian distribution function over beam electron scattering angles is been used. The final beam angular spread for the previous interaction of an electron beam with a target is been applied as an initial one for the subsequent interaction because the internal magnetic field in our scheme does not increase a beam angular spread. The orientation angle (see the emission geometry presented in Fig.1) is been selected to be equal to a half of inverse Lorentz factor that corresponds to the maximum PXR yield to small collimator. Notice, that the character PXR here poorly depends on energy of electrons, and is defined by length of radiation wave and Bragg angle. Therefore intensity of PXR of each particle grows proportionally to number of its target crossings within the limits of indicated angle.

Specify the basic physical parameters of modeling. The project is oriented on using of MSU 2.4 MeV electron CW linear accelerator which produces the continuous

beam current up to 1 mA and beam radius of \approx 1 mm (CW devices are the most suitable kinds of accelerators because they can produce a very high mean intensity of PXR). Hence Lorenz factor is \approx 6, and angle of radiation cone is about 10° .

In an initial configuration Bragg angle is chosen as 45°. A silicon crystal is chosen as a material of target. The crystalline target plane is made in such a manner that the reciprocal lattice vector <111> is lying along its surface. Basing on the facts mentioned above, the estimates indicate that the optimal value of silicon target thickness can be no more than 20-30 mkm.

The maximal magnitude of a mean current of electron beam can be estimated from following reasons. According to work [7], average maximal beam current is of order 0.5 A at beam radius of 1 mm. Therefore, taking into account displacement of particles along a target at their rotations, it is possible to admit that the planned for using accelerator can be under operation in limiting mode.

In Fig. 2 and 3 the first results of simulation of particle dynamics are presented.

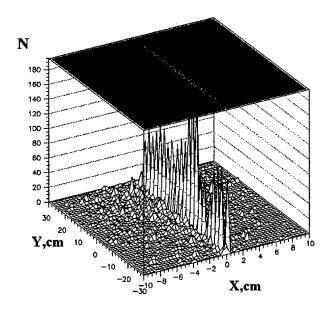


Figure 2. Spatial distribution of intersection points of circling electron trajectories with a target plane (demonstration test with the increased step of cross drift of electrons). X-axis is vertically directed, Y-axis is stretched along a target.

By this data, the particles can make some tens circulation's, and not less than one- two tens of revolutions are made within the limits of a demanded angle of radiation. With that the mean PXR intensity reaches up ten W/Sr.

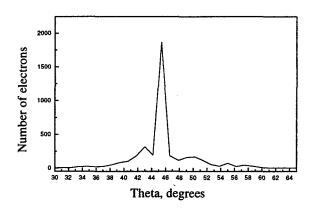


Figure 3. Angular (near to Bragg angle) distribution of electrons crossing a target plane.

4. CONCLUSION

Thus the developed analysis shows the possibility to create an effective compact x-ray source consisting of a linear electron accelerator with particle energy of the order of about units MeV, thin crystalline target providing the generation of quasimonochromatic highly directed tunable x-rays on the base of PXR mechanism and the magnetic system providing the multiple interaction of emitting particles with a target.

Moderate consumed power and compact sizes of similar devices (compare, for example, with [7]) open reliable prospects of their wide and various applications.

5. REFERENCES

- [1] M. Ter-Mikaelian. High energy electromagnetic processes in condensed media (Wiley-Interscience. New-York, 1972)
- [2] V.Baryshevsky, I.Feranchuk. Zh.Eksp.Teor.Fiz. 61 (1971) 944
- [3] G.Garibian, Y.Shi. Zh.Eksp.Teor.Fiz. 61 (1971) 930
- [4] V.Grishin, B.Ishkhanov, S.Likhachev et al., Proc. of Int. Conf. PAC97, APS-IEEE, 1997. P.3866.
- [5] R.Brun, F. Bruyant, M. Maine, GEANT3 (User's Guide), DATA HENDLING, CERN Geneva, Switzerland.
- [6] N.Nasonov, A.Safronov. Proc.Int.Symp. RREPS-93, Oct. 1993, Tomsk, Russia.
- [7] A.Andriyashkin, V. Kaplin, M.Pristrup et al., Appl. Phys. Lett., v. 72, N 11, p.1385 (1988).

THE SCROUNGE-ATRON: A PHASED APPROACH TO THE ADVANCED HYDROTEST FACILITY UTILIZING PROTON RADIOGRAPHY*

O. J. Alford, P. D. Barnes, Jr., A. K. Chargin, W. D. Dekin, E. P. Hartouni, J. N. Hockman[#], A. S. Ladran, M. A. Libkind, T. L. Moore, J. W. Pastrnak, R. E. Pico, R. J. Souza, J. M. Stoner, J. H. Wilson, Lawrence Livermore National Laboratory

G. Ruggiero, Brookhaven National Laboratory

S. Ohnuma, University of Houston

Abstract

The Department of Energy has initiated its Stockpile Stewardship and Management Program (SSMP) to provide a single, integrated technical program for maintaining the continued safety and reliability of the nation's nuclear weapons stockpile in the absence of nuclear testing. Consistent with the SSMP, the Advanced Hydrotest Facility (AHF) has been conceived to provide improved radiographic imaging with multiple axes and multiple time frames. The AHF would be used to better understand the evolution of nuclear weapon primary implosion shape under normal and accident There are three fundamental technologies scenarios. currently under consideration for use on the AHF. These include linear induction acceleration, inductive-adder pulsed-power technology (both technologies using high current electron beams to produce an intense X-ray beam) and high-energy proton accelerators to produce a proton beam. The Scrounge-atron (a proton synchrotron) was conceived to be a relatively low cost demonstration of the viability of the third technology using bursts of energetic protons, magnetic lenses, and particle detectors to produce the radiographic image. In order for the Scrounge-atron to provide information useful for the AHF technology decision, the accelerator would have to be built as quickly and as economically as possible. These conditions can be met by "scrounging" parts from decommissioned accelerators across the country, especially the Main Ring at Fermilab. The Scrounge-atron is designed to meet the baseline parameters for single axis proton radiography: a 20 GeV proton beam of ten pulses, 10¹¹ protons each, spaced 250 ns apart.

1 INTRODUCTION

The Comprehensive Test Ban Treaty does not allow nuclear weapons tests. In order to continue to certify the safety and reliability of the U.S. nuclear weapons stockpile in the absence of nuclear testing, the weapons complex will require a major new radiographic facility, the Advanced Hydrotest Facility (AHF) [1]. This facility

*Work performed under the auspices of the U.S. DOE by LLNL under Contract W-7405-ENG-48.

is to provide multiple radiographic pulses on multiple

One of the technologies under consideration is a high energy proton beam. Since there is minimal experience with protons as radiographic probes, it would be extremely valuable to perform a series of demonstration experiments to develop the tools, techniques, and understanding that will be required to determine if protons should be the technology of choice for the AHF. The purpose of this research is to determine if it is possible to build a proton synchrotron suitable for the experimental program as quickly and economically as possible. To accomplish this, the machine concept relies heavily on "scrounging" equipment from other decommissioned accelerators. As such, we refer to the accelerator as the "Scrounge-atron" [2].

2 DESIGN PARAMETERS

The design parameters for the Scrounge-atron are set by the experimental program requirements. These parameters are related to image spatial resolution, statistical variance of the image on a pixel-by-pixel basis, number of time frames and duration of frame, and repetition rate of the machine. The design requirements are shown in Table 1.

Table 1: Scrounge-atron Design Requirements

Parameter	Value	Unit
Final Energy	20	GeV
Repetition Period	1	min
Number of Proton Bunches	10	bunches
Bunch Separation	250	ns
Number of Protons / Bunch	1011	protons
Total Number of Protons/pulse	10^{12}	protons

The desired spatial resolution is less than 1 mm full-width at half-maximum (FWHM). This resolution, sufficient to identify image features of interest to the experimental program, is determined by Multiple Coulomb Scattering (MCS) in the beamline window located just downstream of the object. MCS in this window introduces image blur, whereas MCS in the upstream window and in the object do not contribute to this blur.

An assumption of the design is that the windows would mitigate shrapnel and blast shock wave but would not

[#]Email: hockman1@llnl.gov

need to guarantee confinement of the experiment. This allows aluminum windows to be used, or possibly a composite material like Spectra. Using these materials reduces the required beam momentum needed to achieve a specific image resolution. The beam momentum of the Scrounge-atron is chosen to be 20 GeV/c.

The intensity requirement for a single image is set by the area of the imaging array and the approximate attenuation of the beam pulse through the object and the other material in the beamline. Taking a 10 cm x 10 cm field-of-view and a detector at the image plane with 0.25 mm x 0.25 mm pixels results in 1.6 x 10⁵ imaging elements. To obtain a 1% intensity measurement for a pixel requires roughly 1 x 10⁴ protons per pixel or 2 x 10⁹ protons at the image plane. The proton beam intensity decreases exponentially in passing through material. For the purpose of estimating beam intensities we take the total attenuation of protons through the beamline windows and object to be of order 0.1-0.01. To obtain 2 x 10⁹ protons at the image plane would require between 10¹⁰ to 10¹¹ incident protons per beam pulse.

The number of beam pulses required for dynamic radiography can only be chosen based on experimental considerations. Currently no radiography facility provides more than 2 pulses on a microsecond time scale. We choose to provide 10 pulses, spaced 250 ns apart, with a 20 ns pulse width. These parameters are compatible with the AHF requirements. The simplest extraction scheme has the entire beam extracted in one turn, i.e., with 10 pulses equally spaced in time. The 10 pulses would then span roughly 2.5 microseconds. With more complex extraction schemes, a single pulse might be extracted at an arbitrary time allowing a variation in the pulse arrival time format spanning hundreds of microseconds. With 10 pulses, the total intensity required in the Scrounge-atron is roughly 10^{12} protons.

The maximum rate at which the beam should be delivered to the object is set by the detector data-download time which is compatible with 1 cycle per minute.

3 MACHINE DESCRIPTION

Figure 1 shows the Scrounge-atron layout. It consists of a 300 MeV injector linac, the linac-to-ring transfer line (LTRT), the 20 GeV synchrotron, the ring-to-radiography transport line (RTRT), and the radiography beamline. The main Scrounge-atron parameters given in Table 2 are roughly one-tenth the values of the Fermilab Main Ring. Therefore, we should expect that the Scrounge-atron will be scaled to roughly one-tenth of the Main Ring. synchrotron has a periodicity of two, with a reflection symmetry within the period. Each period contains a long arc, which together account for about 78% of the ring. The arcs are joined together by two insertions, on opposite sides of the ring. Injection equipment, extraction equipment, and the accelerating cavities are in one of the insertions in the transfer enclosure on the linac

side of the ring. All accelerator components can be transported into the tunnel enclosure through either the transfer enclosure or through alcoves at the other insertion and in the middle of the arcs. Eight major power supply utility substations are located around the accelerator; six serve the synchrotron proper, one serves the linac/klystron gallery and the other serves the radiography beamline.

The beam is transported to the firing site through the RTRT beamline. At the firing site the beam enters a radiography beamline, consisting of a diffuser, matching lens, intensity measurement station, first imaging lens, blast protection bullnoses around the object location, and two consecutive imaging lenses with collimators and measurement stations. At either end of the firing area, bullnoses protect the upstream and downstream beamline components and enclosures from shock and shrapnel.

The major civil construction consists of the linac enclosure, 100 m long; the ring enclosure, 1030 m long; the transfer line to the firing site, 180 m long; and the radiography beamline at the firing site, 150 m long.

Table 2. Lattice Parameters

Parameter	Value	Units
Lattice		
Periodicity	2	
# Straight Cells "CE"/ Period	6	
# Bend Cells "C"/ Period	20	
Cell Length	19.786	m
Ring Circumference	1028.851	m
B1 Type Dipoles		
Aperture (H x V)	12.70 x 3.81	cm ²
Length	6.071	m
Bending Angle	78.540	mrad
Bending Radius	77.313	m
Sagitta	59.606	mm
Ramp Rate	2.000	kG/s
Number of Dipoles	80	
Q4 Type Quadrupoles		
Aperture (H x V)	12.70 x 5.08	cm ²
Length	_1.321	m
Β" /Βρ	0.0779	m ⁻²
Ramp Rate	12.045	kG/m s
Number	104	
Drifts		
Short "O"	1.251	m
Long "D"	8.572	m
Accelerator Functions		
Phase Advance / Cell	61.2	0
$oldsymbol{eta_{max}}$	34.072	m
η_{max}	3.762	m
γ_T	7.387	
Tune		
Q_h - Horizontal Tune	8.84	
Q_{ν} - Vertical Tune	8.82	
ξ_h - Chromaticity	1.107	

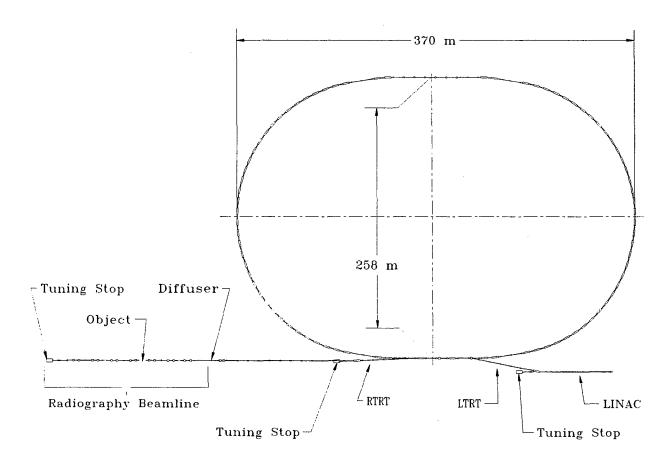


Figure 1. Scrounge-Atron Baseline Lattice

We can meet the schedule and cost goals by the following design procedure: (1) use existing parts where available and appropriate, (2) if parts are not available, use existing designs, and (3) only if these are not available, design and construct the required part. This procedure minimizes the total amount of design for the accelerator. This approach is possible because, for most of the accelerator systems, the characteristics required for radiography are far below the current state-of-the-art used in new accelerators.

Existing and available elements include, from FNAL, 120 B1 dipoles, 30 Q4 quadrupoles, corrector magnets, power supply components, ion pumps, heat exchangers, and Princeton-Pennsylvania Accelerator (PPA) ring rf cavities; from Lawrence Berkeley National Laboratory, a 5 MeV pre-injector. Designs available include, from Brookhaven National Laboratory, a Drift Tube Linac; from FNAL, a Cavity Coupled Linac.

4 CONCLUSIONS

The result of research on the Scrounge-atron concept as described above is that the machine is technically feasible and can be built within anticipated cost and schedule constraints. In order to accomplish this task, the machine relies heavily on the availability of components from the decommissioned Fermi National Accelerator Laboratory Main Ring. The Scrounge-atron will serve as a test bed and will provide important and timely information to the SSMP which cannot be obtained by any other means.

5 REFERENCES

- [1] Final Programmatic Environmental Impact Statement for Stockpile Stewardship and Management, DOE-EIS-0236, U.S. Department of Energy, September, 1996.
- [2] O. J. Alford, et. al., "The Scrounge-atron: A Proton Radiography Demonstration Accelerator," UCRL (Lawrence Livermore National Laboratory, in preparation).

PULSED NEUTRON SOURCE USING 100-MEV ELECTRON LINAC AT POHANG ACCELERATOR LABORATORY

G. N. Kim*, H. S. Kang, J. Y. Choi, M. H. Cho, I. S. Ko, and W. Namkung, POSTECH, Pohang 790-784, Korea J. H. Chang, KAERI, Taejon 305-600, Korea

Abstract

The Pohang Accelerator Laboratory uses a 100-MeV electron linac for the pulsed neutron source as one of the long-term nuclear R&D programs at the Korea Atomic Energy Research Institute. The linac has two operating modes; one for short pulse mode with the various repetitions between 2 ns and 100 ns and the other for long pulse mode with 1 µs. The major beam parameters are as follows; the nominal beam energy is 100 MeV, the maximum beam power is 10 kW, and the beam current is varied from 300 mA to 5A depends on the pulse repetition. We constructed and tested a test-linac based on the existing equipment such as a SLAC-5045 klystron, two constant gradient accelerating sections, and a thermionic RF-gun. We describe the characteristics of the test-linac and report the status of the pulsed neutron source facilities including a target system and time-offlight paths.

1 INTRODUCTION

The nuclear data project as one of the nation-wide nuclear R&D programs was launched by the KAERI in 1996 [1]. Its main goals are to establish a nuclear data system, to construct infrastructures for the nuclear data production and evaluation, and to develop a highly reliable nuclear data system. In order to build the infrastructures for the nuclear data production, KAERI is to build an intense pulsed neutron source by utilizing accelerator facilities, technologies, and manpower at the Pohang Accelerator The PAL proposed the Pohang Laboratory (PAL). Neutron Facility (PNF), which consists of a 100-MeV electron linac, a water-cooled Ta-target, and at least three different time-of-flight (TOF) paths [2]. We designed a 100-MeV electron linac [3] and constructed a test-linac based on experiences obtained from construction and operation of the 2-GeV linac at PAL.

In this paper, we describe the design of a 100-MeV electron linac and then present the status of neutron facility PFN compared with other pulsed neutron facilities in the world.

2 DESIGN OF 100-MEV E-LINAC

We assumed that the klystron is operated at 85% of its maximum capacity and 10% of the power is dissipated in the wave-guide system. The energy gains attainable with one SLAC-5045 klystron for various beam modes are listed in Table 1.

Table 1. Electron beam modes and parameters.

	Pulse	Beam	Beam	Beam Po	wer, kW
Mode	Width	Current	Energy	(RF pulse rep. Ra	
	[ns]	[A]	[MeV]	(180pps)	(300pps)
	2	5	97	0.17	0.3
Short	10	5	88	0.8	1.3
Pulse	100	1	79	1.4	2.4
Long Pulse	1000	0.3	77	4.1	6.9

^{*} The klystron is operated with the pulse repetition rate of 300 pps and with the RF pulse width of $2-\mu s$.

Assuming a negligible beam loading, we can obtain 100-MeV with one SLAC-5045 klystron in the 2-ns operation mode. Table 1 shows that we can obtain a maximum beam power of 6.9-kW by operating the klystron in the pulse repetition rate of 300 pps. In the case of the high-power operation the energy gain is reduced by a large amount due to the multi-bunch beam loading.

The 100-MeV electron linac consists of an e-gun, an S-band prebuncher and buncher, two accelerating sections, and various components, as shown in Figure 1. The electron beam is generated either by an RF-gun or by a triode thermionic gun for which a Cockcroft-Waltontype DC voltage generator supplies the accelerating voltage of 120 kV. Electron beams from the e-gun then enter to the bunching system, which consists of a prebuncher and a buncher. The prebuncher is a re-entrant type standing-wave cavity made of stainless steel with a resonant frequency of 2,856 MHz. The buncher is a traveling-wave structure with 14 cavities including the input and the output coupler cavities. The bunched beams are then accelerated to 100 MeV by passing them through two SLAC-type accelerating sections fed by one SLAC 5045 klystron.

Work supported in part by POSCO, MOST, and KAERI

[&]quot;Email: gnkim@postech.ac.kr

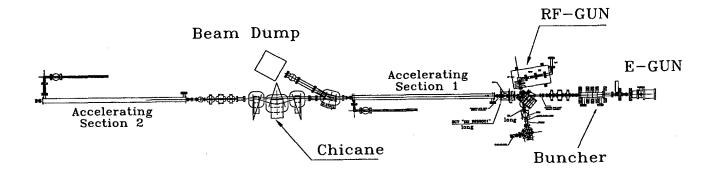


Figure 1. Configuration of 100-MeV electron linac

3 STATUS OF NEUTRON FACILITY

Pohang neutron facility (PNF) consists of a 100-MeV electron linac, a photoneutron target, and at least three different time-of-flight (TOF) paths.

3.1 Photoneutron Target

High-energy electrons injected in the target produce gamma rays via bremsstrahlung, these gamma rays then generate neutrons via photonuclear reactions. For a photoneutron target, it is necessary to use a heavy-mass material because the emission of gamma rays is almost proportional to the atomic number Z of the target material and to the energy of the incident electrons. We are considering tantalum rather than fissile materials because the technology for handling and characteristics of the targets are well known [4]. The neutron yield depends sensitively on the material and the geometry of the target. The design of the target system is done using the MC simulation codes, EGS4 and MCNP4. The target system, 4.9-cm in diameter and 7.4-cm in length, is composed of ten sheets of Ta plate, and there is 0.15cm water gap between them, in order to cool the target effectively [5]. The estimated flow rate of the cooling water is about 5 liters per minute in order to maintain below 45 °C. The housing of the target is made of titanium. The conversion ratio obtained from MCNP4 code from a 100-MeV electron to neutrons is 0.032. The neutron yield per kW beam power at the target is 2.0×10¹² n/sec, which is about 2.5% lower than the calculated value based on the Swanson's formula [6]. Based on this study, we have constructed a watercooled Ta-target system.

3.2 Time of Flight Path

The pulsed neutron facility based on the electron linac is a useful tool for high-resolution measurements of microscopic neutron cross sections with the TOF method. In the TOF method, the energy resolution of neutrons depends on the TOF path length. Since we

have to utilize the space and the infrastructures in the laboratory, TOF paths and experimental halls are placed in the same level as the main electron linac. Two or three different TOF paths range between 10-m and 100-m are arranged for experiments with various energy ranges.

3.3 TOF Test Facility

We have constructed a test-linac for the various R&D activities of the neutron facility by utilizing the existing components and infrastructures at PAL [7]. The test-linac consists of a thermionic RF-gun, an alpha magnet, four quadrupole magnets, two SLAC-type accelerating sections, a quadrupole triplet, and a beam-analyzing magnet. The test-linac is located in the tunnel beside the PLS 2-GeV linac.

After the RF-conditioning of the accelerating structures and the wave-guide network, we performed the beam acceleration test. The maximum RF power from a SLAC 5045 klystron was reached to 45 MW. The RF power fed to the RF-gun was 3 MW. The maximum energy is 75 MeV and the measured beam currents at the entrance of the first accelerating structure and at the end of linac are 100 mA and 40 mA, respectively. The length of electron beam pulse is $1.8~\mu s$ and the pulse repetition rate is 12~Hz. The measured energy spread is $\pm 1\%$ at minimum. The energy spread was reduced when optimizing the RF phase of the RF-gun and the magnetic field strength of the alpha magnet.

In order to get experiences for the TOF method, we constructed a TOF test facility using the test-linac. The electron beam is directed to a photoneutron target, which is located about 3 m below the ground level. The stainless tube of diameter 200 mm is used for TOF tubes. The detector station will be placed the second floor of the linac building, which will give the flight path lengths about 15 m. With this, the test of the Tatarget system and a data acquisition system will be performed.

4 COMPARISION OF NEUTRON FACILITIES

Neutron facilities based on the electron linac were used to support primarily the extensive nuclear energy programs during the last few decades. Thus, these facilities were mainly used to measure the high resolution microscopic neutron cross sections, such as neutron total cross sections, scattering cross sections, capture cross sections, fission cross sections, and others.

The design parameters for the PNF are compared with other pulsed neutron facilities in the world based on electron accelerators in Table 2. The table shows information on targets, beam energies, beam pulse currents, pulse length and pulse repetition rates, average beam power, average neutron yield, and lengths of flight paths. The average neutron yield is calculated by the Swanson's formula [6].

According to this table, the PNF is not a best facility in the world. However, this facility will be widely used for basic and applied problems of neutron interaction with matters and nuclei as well as for the nuclear data production in Korea.

5 REFERENCES

- [1] Ministry of Science and Technology of Korea (1999), "1997 Request for Project on Long-Term Nuclear R&D Program."
- [2] G. N. Kim, J. Y. Choi, M. H. Cho, I. S. Ko, W. Namkung and J. H. Chang, "Proposed neutron facility using 100-MeV electron linac at

- Pohang Accelerator Laboratory," Proc. Nuclear Data for Science and Technology, Trieste, May 19-24, 1997, p. 556, Italian Physical Society, Bologna, Italy (1997).
- [3] J. Y. Choi, H. S. Kang, G. N. Kim, M. H. Cho, I. S. Ko and W. Namkung, "Design of 100-MeV Electron Linac for Neutron Beam Facility at PAL," Proc. Of 1997 KAPRA Workshop (Seoul, Korea, Jun. 26-27, 1997), 88 (1997).
- [4] J. M. Salome and R. Cools, Nucl. Instr. Meth. 179, 13 (1981).
- [5] W. Y. Baek, G. N. Kim, M. H. Cho, I. S. Ko and W. Namkung, "Design of the Photoneutron Target for the Pulsed Neutron Source at PAL," Proc. Workshop on Nuclear Data Production and Evaluation (Pohang, Korea, Aug. 7-8, 1998).
- [6] W. P. Swanson, "Radiological Safety Aspects of the operation of Electron Linear Accelerators," IAEA Tech. Rep. 188 (1979).
- [7] H. S. Kang, J. Y. Choi, Y. J. Park, S. H. Kim, G. N. Kim, M. H. Cho, and I. S. Ko, "Beam Acceleration Result of Test Linac," Proc. 1st Asian Particle Accelerator Conf. (Tsukuba, Japan, Mar. 23-27, 1998) 743 (1998).
- [8] D. C. Larson, "The Oak Ridge Electron Linear Accelerator Pulsed Neutron Source," http://www.phy.ornl.gov/orela/orela.html, Oak Ridge National Lab., Tennessee (1996).
- [9] D. Tronc, J. M. Salome and K. H. Bockhoff, "A New Pulse Compression System for Intense Relativistic Electron Beams," Nucl. Instr. Meth., 228, 217 (1985).
- [10]R. C. Block, "The Gaerttner Linear Accelerator Laboratory at Rensselaer Polytech. Inst.," http://www.linac.rpi.edu/general.html, Rensselaer Polytechnic Institute, Troy, N.Y. (1996).
- [11]W. I. Furman, "New pulsed neutron source of the JINR-The IREN project," Proc. Nuclear Data for Science and Technology, Trieste, May 19-24, 1997, p. 421, Italian Physical Society, Bologna, Italy (1997).
- [12]K. Kobayashi et al., "KURRI-Linac as a Neutron Source for Irradiation," Annu. Rep. Res. Reactor Inst. Kyoto Univ., 22, 142 (1989).

Table 2. Comparison of neutron facilities

	GELINA	OREL	,A	Gaerttner- Linac	IREN	KURRI	Linac	PNF
Source/Location	Geel,	Knoxv	ille,	Troy,	Dubna,	Osaka,		Pohang,
	Belgium	USA		USA	USSR	Japan		Korea
Target	U		Та	Ta	U	Т	`a	Ta
Energy [MeV]	110	180	140	25 – 60	200	35	35	70 – 100
Pulse Current [A]	100	20	0.5	0.4 – 3	1.5	2.5-6	0.5	0.3-5
Pulse Width [ns]	<1	3	1,000	15 - 5,000	250	10-100	4,000	2-1,000
Pulse Repetition [Hz]	800	1,00 0	1,000	300 – 500	150	480	240	30-300
Beam Power [kW]	7.5	10.8	70	>10	10	10	16.8	0.2 ~ 7
Average Neutron Yield [10 ¹³ n/s]	3.4	2.2	14	4.0	2.1	2.0	3.4	~2.0
Flight Path [m]	8 - 400	9 -	- 200	10 – 250	10 - 1,000	10 -	- 50	10 – 100
Status	Operating	Ope	rating	Operating	Considering	Oper	ating	Planed
References	[8]		9]	[10]	[11]	[1	2]	

ISIR SUBPICOSECOND PULSE RADIOLYSIS SYSTEM

T.Kozawa*, A.Saeki, Y.Mizutani, M.Miki, T.Yamamoto, Y.Yoshida and S.Tagawa.
 The Institute of Scientific and Industrial Research, Osaka University,
 8-1 Mihogaoka, Ibaraki, Osaka 567, Japan
 S.Suemine

Unicom System, 6-24-28 Misaki, Suminoe-ku, Osaka 559, Japan

Abstract

The highest time resolution of the pulse radiolysis had remained about 30 ps since the late 1960's. To make clear the primary processes in the radiation chemistry and physics within 30 ps, we developed a stroboscopic pulse radiolysis system for the absorption spectroscopy with the time resolution of 2.0 ps (10-90% rise time). The time resolution of 2.0 ps was estimated from the time-dependent behavior of the hydrated electrons. The system consists of a subpicosecond electron linac as an irradiation source, a femtosecond laser as an analyzing light and a jitter compensation system.

1 INTRODUCTION

Pulse radiolysis is a very powerful method to detect and observe transient phenomena in radiation-induced reactions. The first experiment in the picosecond regime was carried out by the picosecond pulse radiolysis system of Toronto University with a time resolution of about 30 ps in the late 1960's [1]. Since then, several types of picosecond pulse radiolysis systems were developed [2-4] and many researches have been reported on ultrafast phenomena in radiation chemistry, physics, biology and applied fields such as material science.

Recently, a new picosecond pulse radiolysis system, in which a femtosecond laser was used as an analyzing light instead of the Cherenkov light, was proposed and developed at the Institute of Scientific and Industrial Research (ISIR), Osaka University [5], [6]. This system covered the wide wavelength from ultraviolet to infrared region by using second harmonic generation, third harmonic generation, optical parametric oscillation techniques and so on. The time resolution was several tens picoseconds. The primary processes in radiation chemistry of water, materials for microelectronics and so on have been investigated using this system.

Our pulse radiolysis system by using a femtosecond laser synchronized to the electron linac has a potential to detect ultrafast phenomena in the femtosecond region because the pulse width of analyzing light is less than 100 fs. We attempted to construct a higher resolution system for the investigation of the primary processes of the radiation chemistry and physics within 30 ps.

2 STROBOSCOPIC TECHNIQUE AND TIME RESOLUTION

To detect ultra fast phenomena in the time region of picosecond, a so-called stroboscopic technique is used [1-6]. The short-lived intermediates produced in a sample by very short radiation such as electron beams are detected by measuring the optical absorption of very short analyzing light such as Cherenkov radiation (femtosecond laser in our system). The time profile of the optical absorption can be obtained by changing the delay between the electron beam and the analyzing light.

The time resolution of the stroboscopic pulse radiolysis depend on the length of irradiation pulse, that of analyzing light and the jitter between them (Fig. 1). It does not depend on the time resolution of detection system such as a photodiode, an oscilloscope and so on.

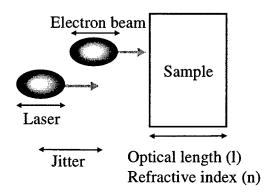


Fig. 1 Factors which limit the time resolution of the stroboscopic pulse radiolysis

^{*} Email: kozawa@sanken.osaka-u.ac.jp

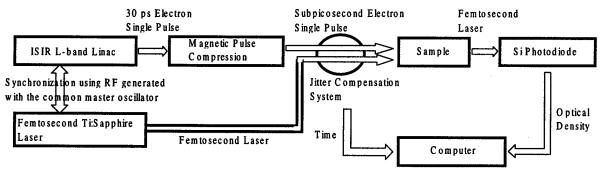


Fig.2 Subpicosecond pulse radiolysis method

For the development of subpicosecond pulse radiolysis system, a subpicosecond electron pulse, a subpicosecond analyzing light and precise synchronization are necessary.

Furthermore, the time resolution is limited by the difference between the velocity of the light and that of the electron pulse in a sample. The passing time of the electron pulse through a sample is given by $l/(\beta c)$, where l is an optical length of a sample, β the ratio of the velocity of electron to that of light in the vacuum and c the velocity of light in the vacuum. On the other hand, in the case of light, the passing time is given by ln/c, where n is a refractive index of a sample. Therefore, the time resolution is limited by the thickness of a sample. For example, the time resolution is limited to >1.8 ps (10-90% rise time) at n = 1.33 and l = 2 mm.

3 SUBPICOSECOND PULSE RADIOLYSIS SYSTEM

Figure 2 shows the subpicosecond pulse radiolysis system. The system consists of a subpicosecond electron linac as an irradiation source, a femtosecond laser as an analyzing light, and a jitter compensation system. A sample was irradiated by a subpicosecond electron single

pulse. The time-resolved optical absorption detected with was femtosecond laser which was synchronized to the electron pulse. The intensity of the laser pulse was measured by a Si photodiode. The timing between the electron pulse and the laser pulse was controlled by radio frequency (RF) system. The time profile of the optical absorption could be obtained changing the phase of the RF with an electrical phase shifter. All equipment described below was controlled by a personal computer. The acquisition time was 1 second per one shot.

The ISIR linac consists of an thermionic electron gun, two 108 MHz subharmonic bunchers (SHBs), a 216 MHz SHB, a 1300 MHz accelerating

tube and a focusing system [7]. The magnetic pulse compressor consists of two 45° sector magnets, four quadrupole magnets and a vertical beam slit as shown in Fig. 3. The longitudinal energy distribution of the electron pulse was modulated so that the energy of electrons in the early phase of the pulse was higher than that in the later phase of the pulse. The phase of accelerating electric field was 70°. The peak energy of accelerated pulse was 26.5 MeV. The energy spread after the modulation was 9.4 %. The pulse length was approximately 30 ps at the end of the accelerating tube. In the magnetic pulse compressor, high energy electrons in the early phase take a long path and low energy electrons in the later phase take a short path. By translating the energy dispersion into the difference of the trajectory length, the electron pulse is compressed at the end of the magnetic pulse compressor. This system can compress the 30 ps electron single pulse to subpicoseond [8].

A modelocked Ti:Sapphire laser (Tsunami, Spectra-Physics Lasers, Inc.) was synchronized to the ISIR L-band Linac using a commercially available phase lock loop. The frequency of the laser was 81 MHz. On the other hand, the ISIR L-band Linac was driven by 108 MHz RF. The frequency of 27 MHz, which is the greatest common divisor, was used as a common master

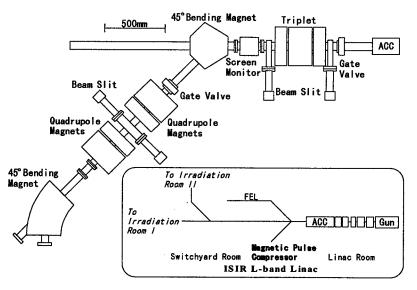


Fig. 3 Magnetic pulse compressor

oscillator. The jitter between the laser pulse and the electron pulse was several picoseconds from the measurement using a streak camera (C1370, Hamamatsu Photonics Co. Ltd.).

In order to avoid effects of the jitter between the electron pulse and the laser pulse on the time resolution, a jitter compensation system was designed as shown in Fig. 4. The time interval between the electron pulse (Cherenkov light) and the laser pulse was measured by the streak camera. The Cherenkov radiation was emitted by the electron pulse in air at the end of the beam line. The laser pulse was separated from the analyzing light by a half mirror. The precise time interval could be obtained by the analysis of the streak image.

4 PULSE RADIOLYSIS EXPERIMENT

Radiation induced reactions in the water was observed. Distilled water was used as a sample. The water was deaerated in a quartz cell with the optical length of 2.0 mm. It is known that a broad absorption due to hydrated electron with the maximum at the wavelength of 720 nm is observed in neat water at an irradiation of electron beam [9]. The formation process of hydrated electrons have been investigated by femtosecond laser flash photolysis. It has been reported that the hydrated electron is formed on a subpicosecond time scale [10-14]. Figure 5 shows the time-dependent behavior of the hydrated electron obtained in the pulse radiolysis at the wavelength of 780 nm. The 10-90% rise time was 2.0 ps. It is found that the time resolution of this system is less than 2.0 ps.

5 CONCLUSION

The direct observation of radiation-induced reactions with the time resolution of 2.0 ps (10-90% rise time) has been succeeded using the subpicosecond electron pulse, the femtosecond laser and the jitter compensation system.

6 REFERENCES

- [1] M. J. Bronskill, W. B. Taylor, R. K. Wolff and J. W. Hunt, Rev. Sci. Instrum. 41 (1970) 333.
- [2] C.D. Jonah, Rev. Sci. Instrum. 46 (1975) 62.
- [3] H. Kobayashi and Y. Tabata, Nucl. Instrum. Meth. B10/11 (1985) 1004.
- [4] Y. Yoshida, T. Ueda, T. Kobayashi and S. Tagawa, J. Photopolym. Sci. Technol. 4 (1991) 171.
- [5] Y. Yoshida and S. Tagawa, Proc. Int. Workshop Femtosecond Tech., Tsukuba (1995) p. 63.
- [6] S. Tagawa, Y. Yoshida, M. Miki, T. Yamamoto, K. Ushida and Y. Izumi, Proc. Int. Workshop Femtosecond Tech., Tsukuba (1996) p. 31.
- [7] S. Okuda, Y. Honda, N. Kimura, J. Ohkuma, T. Yamamoto, S. Suemine, T. Okada, S. Takeda, K. Tsumori and T. Hori, Nucl. Instrum. Meth. A358 (1995) 248.
- [8] T. Kozawa, Y. Mizutani, K. Yokoyama, S. Okuda, Y. Yoshida and S. Tagawa, Nucl. Instrum. Meth. A (1999) in press.
- [9] J. W. Boag and E. J. Hart, Nature, 197 (1963) 45.

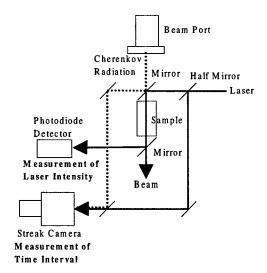


Fig. 4 Jitter compensation system for pulse radiolysis.

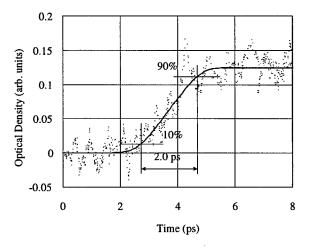


Fig. 5 Time-dependent behavior of hydrated electron obtained in the subpicosecond pulse radiolysis, monitored at the wavelength of 780 nm.

- [10] J. M. Wiesenfeld and E. P. Ippen, Chem. Phys. Lett. 73 (1980) 47.
- [11] A. Migus, Y. Gauduel, J. L. Martin and A. Antonetti, Phys. Rev. Lett. 58 (1987) 1559.
- [12] Y. Gauduel, S. Pommeret, A. Migus and A. Antonetti, J. Phys. Chem. 93 (1989) 3880.
- [13] F. H. long, H. Lu and K. B. Eisenthal, Phys. Rev. Lett. 64 (1990) 1469
- [14] J. L. McGowen, H. M. Ajo, J. Z. Zhang and B. J. Schwartz, Chem. Phys. Lett. 231 (1994) 504.

DEVELOPMENT OF A THIN FILM 9.17 MeV GAMMA RAY PRODUCTION TARGET FOR THE CONTRABAND DETECTION SYSTEM

S. T. Melnychuk, AES Inc., Medford, NY; R. Meilunas, Northrop Grumman Corp., Bethpage, NY.

Abstract

We will describe the development of a thin film ¹³C target for generating 9.17 MeV gamma rays via a (p, γ) reaction for use in a commercial Contraband Detection System (CDS) employing Nuclear Resonance Absorption. The target required for this system must consist of a thin ¹³C film backed by a high Z proton stopping layer. It must be able to withstand average proton beam powers of 17.5 kW, implanted ion doses greater than 10¹⁹/cm² and peak power densities approaching 50 kW/cm2 for extended periods of time. These requirements currently cannot be met by conventional target designs employing C/Au structures. After even short exposure times of several minutes to the proton beam the targets suffer from coating de-lamination and blistering. A new more durable target design has been developed which suffers no such degradation after many hours of beam exposure. The new design consists of a thin ¹³C film deposited onto a Ta layer which has been brazed onto a Cu cooling support.

1 INTRODUCTION

The design of the CDS accelerator has been described previously [1], and operating characteristics of the machine are given in [2,3]. For full power operation a 10 mA, 1.76 MeV circular spot beam is required with an rms radius of approximately 2.5 mm. For a Gaussian beam at 95% beam fraction this gives an average power density of 16 kW/cm² with peak densities at the center of the spot about 3 – 4 times greater.

In order to effectively cool the target a rotating water cooled disk design was chosen. The thermomechanical design is described in detail in [4]. The work described in this paper focussed on the thin film target design, testing and fabrications, and on the issues specific to radiation damage associated with high proton doses.

The generic structure of the gamma production target consists of a thin film of 13 C (1 - 2 μ m) deposited onto a high Z proton stopping material attached to a water cooled substrate. At 1.76 MeV the range of beam in most suitable stoppers is 12 -14 μ m with a straggle of about 2.5 μ m. In order not to generate any gamma rays that may interfere with the desired signal the proton beam is required to stop completely in the high Z layer.

Due to programmatic constraints target development and testing had to be initiated prior to the availability of the CW CDS accelerator. This was done using the AES 1.76 MeV pulsed linac capable of providing 20 mA at 700 µs and 10 Hz, and the Northrop Grumman VandeGraff accelerator.

Figure 1 shows the various configurations that were tested. Initially all target testing was done using 5 cm diameter coupons coated with ¹²C on various stopping layers and substrates.

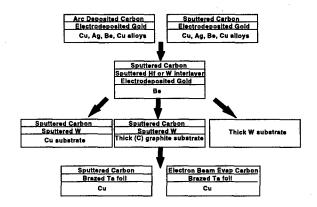


Figure 1. Target configurations we have tested.

The experimental program addressed the issues of: fabrication of ¹²C test coupons by techniques extendable to ultimate fabrication of a ¹³C CW target, measurements of target temperature rise during the beam pulse, effects of implanted hydrogen dose, measurements of gamma ray production.

2 EXPERIMENTAL RESULTS

Test coupons were mounted in a water cooled holder and exposed to the pulsed beam from the RF linac. The expected temperature rise of the target surface based on the solution of the 1d heat equation for a pulsed heat input is given by: $\Delta T = 2W\sqrt{(t' (\pi \rho ck))}$, where ρ is the density, c the specific heat, k the thermal conductivity, and W the power density.

Measurements of surface temperature rise during beam bombardment were performed using a specially designed radiometer with a 0.5 mm spatial resolution and a 1 µs time response. These measurements confirmed that the surface temperature rise was reasonably given by the expression above provided that the C thin film did not delaminate. If target blistering occurred then significantly higher temperatures were observed in localised areas where blisters were forming.

Typical measured temperature rises during the beam pulse were 300 K to 400 K depending on pulse length and power density used. Fig. 2 shows the results of scans along the major and minor axes of an elliptical beam on a sputtered ¹²C/Hf/Au/Be target. The solid curves show the calculated response.

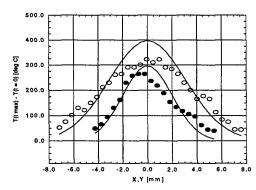
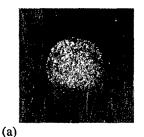


Fig. 2. Temperature profile of ¹²C/Hf/Au/Be. (O) Vertical. I: 10.4mA, Pulse: 440 μs, y(rms): 3.1 mm; (●) Horiz.. I: 7.4 mA, Pulse: 400 μs, x(rms): 1.9 mm.

Au electrodeposited on a variety of substrates showed deterioration of both the carbon and Au layers. The deterioration of the Au based targets was in the form of blister formation and delamination of both the C and Au layers from their underlying substrates. Fig. 3a shows arc deposited C on 10 µm of electrodeposited Au on Be after a 12 hour beam exposure at 10 mA, 500 µs pulse, and 10 Hz rep rate. Delamination of the C is evident. Fig. 3b shows the development of blisters on a C/Au/Cu target where the blister density increases at the beam edge with relatively little blistering at the beam center, and the blister size increases toward the beam center. development of this type of feature caused us to initially question the beam profile, however target temperature profiles as shown above, and independent beam profiles obtained with an emittance scanner confirmed that the beam was gaussian.



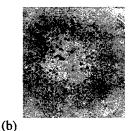


Fig. 3: (a) Sputtered 12 C on 10 μ m Au electrodeposited on Ni flashed Be. Avg. dose: 1.2e19ions/cm². (b) Arc deposited 12 C on 10 μ m Au electrodeposited on Cu.

This phenomenon of preferential blistering at the beam edge was observed on several of our samples, and similar effects have been observed in Cu implanted with 30 MeV α -particles in ref. [5 - p.291]. This has been explained as being due to the trapping of vacancies arriving from outside the implant range at the borders of the gas rich area.

To test if the observed blistering may not have been due to trapping of H at the Au/Be or Au/Cu interface

due to a film thickness comparable to the implant range, tests were conducted with 20 μ m and 40 μ m of Au electrodeposited on Be. These tests also showed blistering of the Au at average doses of 8E18 ions/cm², suggesting that this was a fundamental property of the Au/H system.

Based on the performance of the Au targets we began to investigate materials which were carbide formers in order to improve the adhesion of the C films to the high Z layer. Coupons were fabricated by magnetron sputtering 50 nm of W or Hf onto 20 µm of Au on Be followed by 1µm of sputtered C. Exposure of the C/Hf/Au/Be target to the beam at a dose of 9E18 ion/cm² showed only very minor blistering with no C delamination. Fig. 4a shows the C/Hf/Au/Be target after beam exposure. Some "wrinkling" of the surface is evident. Exposure of the W interlayer target to a comparable dose showed the development of small blisters at the beam edge similar to those observed in fig. 3b, however no C delamination was evident.



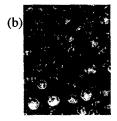


Fig. 4. Targets after beam exposure. (a) C/50 nm Hf/Au/Be. (b) Thick W plate.

The difference between the Hf/Au and W/Au systems is in the hydrogen solubility. Metals such as Mg, Al, Si, Cr, Mn, Fe, Co, Cu, Mo, Ag, W, Pt, and Au form simple solutions, do not form hydrides and are endothermic with respect to hydrogen solubility. When samples of these metals loaded with hydrogen at high temperature are quenched they tend to precipitate hydrogen in the form of bubbles.

Metals such as Ti, Zr, V, Nb, Ta, and Hf form more than one phase when the simple solution is saturated, can accommodate relatively high hydrogen concentrations, are strongly exothermic, and can accommodate approximately 1 H atom per metal atom [5].

Irradiation either of W plate or W sputtered films all showed significant deterioration after a dose of 5e18 ions/cm². Fig. 4b shows an irradiated W plate with the blister size varying from approximately $200 \mu m$ at the spot center to $< 50 \mu m$ at the beam edge, and an increase in blister density at the beam edge.

These results led to the abandonment of Au based targets in favor of 0.127 mm thick Ta foils vacuum brazed onto Cu. These foils showed no visible degradation after 12 hours of beam exposure and an average dose of 10^{19} ions/cm2 with a 3-5 times greater peak dose.

The brazed Ta on Cu structure has become our baseline for the first CDS targets.

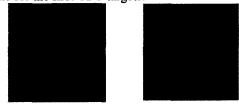


Fig. 5. (a) Sputtered C on brazed Ta foil. (b) ebeam evaporated C on brazed Ta foil. Dose: 1e19 ion/cm².

Two deposition techniques for ¹³C were used: magnetron sputtering; and electron beam evaporation. The advantage of sputtering is that we get good film adhesion, relatively low substrate temperatures are required (<300C), we have the ability to coat large areas by rotating the target, and the deposition rate is fairly uniform. The disadvantages are the relatively high cost of the ¹³C sputter target and poor sputter target utilization. This technique was used to coat the rotating high power target described in [4]. Electron beam evaporation has the advantage of maintaining a low substrate temperature, and the ability to coat large areas. The disadvantages of the process are a non-uniform deposition rate due to the sublimation of ¹³C from pressed powder pellets, poorer adhesion than from sputtering, and more labor required due to less process automation.

Brazed Ta on Cu targets were coated with ¹²C using both of these techniques. These targets shown in fig. 5, were tested for survivability at a dose of 10¹⁹ ions/cm2 with no degradation of the films.

Experiments were conducted on the VandeGraff accelerator to examine the gamma ray spectra of the sputtered and electron beam evaporated targets. Early targets produced in the sputter chamber showed evidence of fluorine contamination and characteristics fluorine lines were seen in the gamma spectra in the region of 5 to 7 MeV. This contamination was found to result from the use of fluoridated pump oil in the roughing pump.

After switching to a non-fluoridated oil and cleaning the chamber the fluorine spectral features disappeared from the sputtered targets. Fig. 6a shows spectra for an evaporated clean ¹³C target, and a contaminated ¹²C target. In the ¹³C target we can see the 9.17 MeV gamma ray grouping with the first and second escape peaks.

A target thickness measurement was performed using the VandeGraff on the ¹³C target by measuring the gamma ray yield as a function of proton beam energy. This showed an energy width of 4 keV implying at the target thickness was approx. $0.25 \mu m$. We have utilized this measurement to calibrate our electron beam evaporation rate and have since produced 1.0 µm, 1.5 µm and 2.0 µm thick evaporated targets. Fig. 6b shows the thin target response from the VandeGraff measurements and a target response obtained on the CW CDS accelerator showing that the target was thick enough to generate 9.17 MeV gammas across the entire CDS beam

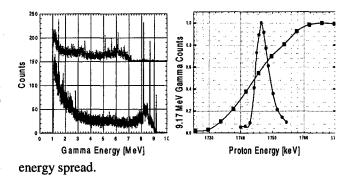


Fig. 6. (Left) Gamma spectrum showing F contaminated spectrum (upper) and clean spectrum (lower) with the 9.17 MeV grouping. (Right) 9.17 MeV gamma ray yield curve measured on CDS accelerator (11), and from the VandeGraff (●).

CONCLUSION

We have found a baseline target configuration utilizing either magnetron sputtered or evaporated ¹³C deposited on Ta foil brazed onto Cu. This configuration is able to withstand high hydrogen doses without deterioration of either the C or the Ta stopping layer because of a high hydrogen diffusivity and solubility in Ta, and the ability of Ta to form carbides and bind with the C thin film. This configuration has been operated under pulsed and CW beam conditions at average doses of 10¹⁹ ions/cm² with no deterioration. For a clean gamma spectrum fluorine containing pump oils must be avoided. Gamma yield measurements on the CDS accelerator show that the target was thick enough to use the full proton energy spread.

REFERENCES

- J.J. Sredniawski, et.al., Proc. of 18th Int. Lin. Accel. Conf., vol.
- 1, 26-30 Aug. 1996, p. 444. S. T. Melnychuk, et. al., Proc. of 18th Int. Lin. Accel. Conf., vol. 2, 26-30 Aug. 1996, p. 479.
- S. T. Melnychuk et. al., "Operating Characteristics of a High Current Electrostatic Accelerator for a Contraband Detection System", This Conference.
- J. Rathke, This Conference.
- B. Scherzer in "Sputtering by Particle Bombardment II" ed. By: R. Behrisch, Springer Verlag, NY, ISBN 3-540-12593-0 p. 271.

SUB-PICOSECOND PULSE RADIOLYSIS PROJECT AT NERL, UNIV. OF TOKYO

Y.Muroya*, N.Chitose, T.Watanabe, G.Wu, O.Urabe, J.Sugahara,
T.Ueda, K.Yoshii, M.Uesaka, Y.Katsumura
Nucl. Eng. Res. Lab., School of Eng., Univ. of Tokyo, 2-22 Shirakata-shirane, Tokai, Naka,
Ibaraki, Japan

Abstract

Pulse radiolysis is a method of time-resolved absorption of the chemical spieces. It is able to measure the reactions in the time range from sub-ns to ms. The highest time resolution has been achieved up to 100 ps. Many primary processes in the time scale of ps or even sub-ps are still remained to be investigated. A new sub-picosecond pulse radiolysis project at Nuclear Engineering Research Laboratory (NERL), University of Tokyo, is under construction. Generation of a sub-ps electron single pulse and a fs Ti:Sapphire laser pulse, and the synchronization of them within 1ps will be inevitable for this purpose.

1 INTRODUCTION

It is widely recognized that the pulse radiolysis technique is very useful and powerful to study chemical reactions in addition to laser photolysis. A large number of the rate constants of the reactions has been measured and much knowledge has been accumulated in liquids, especially in aqueous solutions. Therefore, the pulse radiolysis method has been applied to various subjects such as radical reactions in biology, medicine and atmospheric chemistry, and radiation effects in nuclear technology. At NERL, Univ. of Tokyo, intensive work using the pulse radiolysis method has been carried out not only in aqueous solutions but also in organic liquids and Accelymeric systems [1, 2].

There are two electron linear accelerators (see Fig. 1), both of which can provide single ps and sub-ps electron pulses. Much effort has been done to reach the higher time resolution. The time resolution of the pulse radiolysis method has attained to 100 ps. Many primary processes, which characterize radiation induced reactions, such as solvation of e_{aq} , anions and cations, geminate ion recombination and the formation of the excited states in organic liquids etc., are still remained to be investigated. These reactions take place in the time scale of ps, even sub-ps. Thus, in order to investigate the elementary processes of radiation induced phenomena, the development of the experimental system with much higher the time resolution has been expected.

In this paper, the present pulse radiolysis system and new system with time resolution of ps and sub-ps is presented which under construction at NERL. Details of the new system is presented taking into consideration several technical subjects which affect the time resolution.

2 PULSE RADIOLYSIS SYSTEM

2.1 Conventional system

The pulse radiolysis system consists of pulsed radiation and analyzing light sources together with synchronization system for them. In conventional systems, the 35 MeV linac is used as the pulse of electron source. The analyzing lights are cw and pulsed which are selected according to the time region of target reactions. The electron pulses and analyzing light are synchronized by the electrical devices including the delay units and phase shifters. Change of the analyzing light after passing the sample solution and a monochromator is detected by a photodetector and displayed on the oscilloscope combined with the computer for data acquisition and analysis. Absorption of the analyzing light obeys the Lambert-Beer law,

$$log_{10} (I_0 / I) = \varepsilon C l$$
 (1)

where I_0 , I, ε , l and C are the intensities of the analyzing light without and with absorption, a molar absorption coefficient, the length of the sample cell and the concentration of species of interest, respectively.

The time resolution of this system is determined by the speed of the detection system, the photodetector and the oscilloscope. This system can achieve to sub-ns only when the fast detector and oscilloscope are utilized. Therefore, a

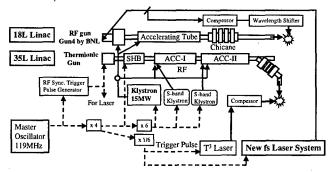


Fig. 1. Synchronization system

stroboscopic method, so called a pump & probe method, should be introduced to perform the experiments in a ps scale.

^{*}Email: muroya@tokai.t.u-tokyo.ac.jp

2.2 Present system

The stroboscopic method (see Fig. 2) was developed by Hunt in 1968 for the first time. In this method Cherenkov pulses associated with electron multi-pulses were used for the analyzing lights and the precise synchronization between Cherenkov and electron pulses is automatically fulfilled. Here, the electron and Cherenkov pulses can be assumed as pump and probe ones, respectively. The intensity of I_0 can be obtained by using a lead block in front of the sample to avoid irradiation and I is taken under irradiation after the optical delay line which can adjust the time delay [5, 6].

As mentioned before, single ps electron pulses are available and the single 65 fs (rms) light pulse is also fed by the Ti:Sapphire laser at NERL. In addition, the synchronization of the electron and laser pulses with the time jitter of less than 4 ps (rms) is attainable as shown in Fig. 3 [3]. As the preliminary step, the picosecond pulse radiolysis system was set up as shown in Fig. 1 before introducing the new one which is discussed later. The preliminary experiments were done to check the feasibility of the new system.

The fundamental light pulse of 790 nm from the Ti:Sapphire laser was splitted into two pulses used for a reference and an analyzing light detected by the two PIN photodiodes. The first measurement is to watch the temporal behavior of the hydrated electron at 790 nm. Another was a measurement of the spectrum of the hydrated electron using a optical multi-channel analyzer (OMA) based on after the generation and splitting of the white light produced by the focusing of the fundamental light in a water cell. Here, the two white light pulses were used as the reference and analyzing lights, which were fed into two optical fibers. The OMA consisting of the two photodiode arrays which are sensitive to the wavelength region of from 200 to 1000 nm is a kind of imaging spectrograph.

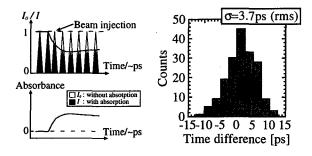


Fig.2. Stroboscopic method Fig.3. Synchronization of 35L linac & T³ laser

Obtained results are shown in Figs. 4 and 5. In spite of the not enough S/N ratio, the formation of the hydrated electron having the peak at 720 nm was confirmed. The experiences obtained at this system are useful to the new system. The delay was adjusted by the delay line of the cable. The timing between the laser and electron pulses

was adjusted by monitoring both the laser pulse and the Cherenkov radiation pulse associated with the electron pulse with the femtosecondstreak camera (FESCA200, Hamamatsu). The total time resolution is evaluated as around 10 ps (rms), which is determined by the widths of the electron (5ps(rms)) and laser pulses(65fs(rms)), the timing jitter of the electrical synchronization devices (about ps), the time delay between the electron and light pulses after passing through the 1.8 cm water cell.

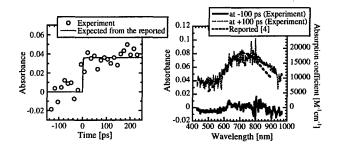


Fig. 4. Time profile of e_{aq} Fig. 5. Optical spectra of e_{aq}

3 NEW PULSE RADIOLYSIS SYSTEM

3.1 Synchronization system (see Fig. 1)

For further development to achieve higher time resolution, several technical subjects which govern the time resolution should be considered. These factors are classified into the two; the widths of the electron and analyzing pulses, and the timing jitter between them. As for the width of electron pulse, ps and sub-ps pulses are available by using the SHB buncher and the magnetic compressing system, respectively, at present. The analyzing light is fed from the newly installed fs Ti:Sapphire (44fs(rms), 0.3TW, 790nm) laser.

In the present system the synchronization devices provide the trigger pulses to the thermionic electron gun and the Ti:Sapphire fs laser so that its timing jitter hardly becomes down to 1 ps. Therefore, the new synchronization method is required. The fs laser light from the new Ti:Sapphire laser is splitted into two pulses, which are used for electron pulse generation at the laser photocathode rf-gun [7] and analyzing light. As the two laser lights are produced from the same source, the timing jitter should be rather small.

Next, the timing jitter from other sources is considered. The first is the jitter from the accelerating process in the linac, namely the fluctuation of the accelerating rf. In the present system, the two klystrons are used and the fluctuation from the two klystron attributes the timing jitter. In the new system, only one klystron with higher power (15MW) Is employed. This can reduce mutual rf fluctuation of the two klystrons. The stability of the modulator voltage of the klystron also contributes to the timing jitter. It can be said that the timing jitter of the new system would be ramarkably suppressed compared to that of the present system. Of course, precise inspection

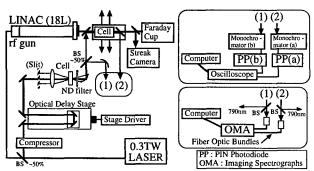
should be done after the construction.

3.2 Evaluation of the timing jitter

The timing jitter including the pump- and probe-sources was evaluated. Fluctuations of rf phase and power at the 15 MW klystron were measured to be 0.2 deg (p-p) and 0.02 dB (p-p), respectively. With these parameters, the timing jitter of the electron pulse in the acceleration process was simulated by PARMELA code to be 50fs (rms). Considering the timing jitter at Ti:Sapphire laser oscillator to be 100 fs (rms), the total timing jitter between the electron and laser pulses is expected to be less than 200 fs (rms) in the new experimental system.

3.3 Measurement system (Fig. 6)

Fig. 6. Measurement system of sub-ps pulse radiolysis



Total time resolution is determined by both the timing jitter of synchronization and the error in the measurement devices. Since the white light for probe is obtained by the non-linear conversion from the fundamental light (44fs(rms), 790nm), the jitter would be 100 fs (rms) at most. The accuracy of the delay line such as the reproducibility of the mechanical stage causes additional fluctuation. Furthermore, the time delay between the electron and laser pulses after passing through a sample cell because of the difference of their travelling speeds in the medium must be considered. It is clear from the equation (1) that the thinner sample cell introduces the smaller signal of absorbance. Therefore, it must be selected the optimal cell length.

4 CONCLUSION

A new sub-picosecond pulse radiolysis project at NERL, Univ. of Tokyo was introduced comparing with conventional and present system. By this system, direct measurement of the phenomena in the time range from sub-ps to ns, for example, electron solvation, geminate ion recombination in organic liquids and migration of electrons between organic and aqueous phase etc., is expected.

5 REFERENCE

- [1] Y.Katsumura, P.Y.Jiang, R.Nagaishi, T.Oishi, K.Ishigure and Y.Yoshida, J. Phys. Chem., 95 (1991) 4435.
- [2] S.Tagawa, N.Hayashi, Y.Yoshida, M.Washio and Y.Tabata, Radiat. Phys. Chem., 34 (1989) 503.
- [3] M.Uesaka, T.Watanabe et al., J. Nucl. Master., 248 (1997) 281.
- [4] F.-Y.Jou and G.R.Freeman, J. Phys. Chem., **81(9)** (1977) 909.
- [5] M.J.Bronskill, W.B.Taylor, R.K.Wolff, and J.W.Hunt, Rev. Sci. Instr., 41 (1970) 333.
- [6] C.D.Jonah, M.S.Matheson, J.R.Miller, and E.J.Hart, J. Phys. Chem., 80 (1976) 1267.
- [7] M.Uesaka, H.Harano, K.Kinoshita et al., Proc. Of EPAC98, 776.

FEMTOSECOND LINAC-LASER BASED TIME-RESOLVED X-RAY DIFFRACTOMETRY FOR VISUALIZATION OF ATOMIC MOTIONS

K. Kinoshita, H. Harano, S. Okita, T. Ueda, M. Uesaka, T. Watanabe and K. Yoshii

Nuclear Engineering Research Laboratory, University of Tokyo,

Tokai-mura, Naka-gun, Ibaraki-ken, Japan

Abstract

We carried out the time-resolved X-ray diffraction experiment where 100fs 3TW laser and 10ps X-rays are used as pump-and probe-pulses, respectively. We used the synchronized femtosecond electron linac and laser system. Using 10ps Cu Kα1,2 X-ray pulses via collision between 10ps electron beam and a Cu wire, we could obtain diffraction images from several monocrystal semiconductors(Si, GaAs, Ge), ion-crystals(NaCl, KCl) and alkalihalides (CaF2, BaF2). However, the change of the X-ray diffraction image could not be observed because of surface damage due to repeated laser irradiation. In order to get more X-ray photons and perform single-shot pump-and-probe analysis, we are going to proceed to laser plasma X-ray based analysis.

1 INTRODUCTION

Synchronized femtosecond electron and laser beams can be generated and measured at Nuclear Engineering Research Laboratory, University of Tokyo[1,2,3]. Those primary femtosecond beams are converted to far-infrared coherent radiation and X-ray pulses via transition radiation and collision with metal targets, respectively. Thus we can perform ultrashort quantum beam based pump-and-probe analysis to investigate ultrafast beaminteractions. Here atomic motions nonequilibrium thermal expansion, ablation, phase transition, soft-mode phonon are expected to be observed as snapshots of X-ray diffraction images. We proposed the new time-resolved X-ray diffractometry where ultrashort X-rays via electron-metal collision is used as a probe pulse[4]. X-ray diffraction images from several monocrystals using 10ps Cu Ka1,2 X-rays are presented and future subjects to be overcome are mentioned.

2 LINAC BASED EXPERIMENT

Experimental configuration is depicted in Fig.1. 35MeV, 10ps(FWHM), 1nC electron single bunch was irradiated with the $100\mu m^{4}$ Cu wire to generate Cu K α 1,2 X-rays(8.048, 8.028keV). Generation of 10ps Cu K α 1,2 X-

rays was confirmed by the numerical analysis using EGS4 code[4]. The 100fs 3TW Ti:Sapphire laser[5] was used as a pump pulse to induce nonequilibrium thermal expansion. Here the linac-laser synchronization system[1] was used to control the delay time of the probe-X-rays from the pump-laser.

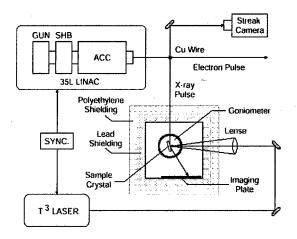
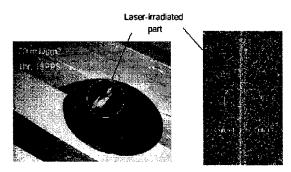


Figure 1: Configuration of the linac-based experiment.

We used monocrystal semiconductors of Si(111), GaAs (111), Ge (111), ion crystals of NaCl (200) KCl(200) and monocrystal alkalihalides CaF₂(220), BaF₂(111). X-ray diffraction image is drawn on an X-ray imaging plate set in the noise-radiation shielding box. Laser energy per shot is 68mJ. The number of photons of the X-ray per shot is estimated to be about 10⁶. Due to the limited solid angle at a specimen, only about 1/100 of them reach the specimen. Thus, we need 10⁴-10⁵ times repetition for the pump-and-probe shot. Cu Ka1.2 X-ray diffraction images from all specimens were successfully obtained. The pump-and-probe analysis was carried out for a GaAs specimen. However, its surface suffered laser-irradiation damage before the X-ray diffraction image for deformed lattice was obtained. Photograph of the damaged GaAs specimen and the Cu Ka1,2 X-ray diffraction images influenced by the damage are shown

in Fig.2. The damage may attribute physical ablation or photo-chemical reaction with air.

Let us clarify the characteristics of the electron linac based X-ray diffractometry. Based on the numerical analysis by EGS4, subpicosecond Cu Kα1,2 X-rays can be surely produced. However, due to lack of photon numbers, we need many times pump-and-probe shots to get the X-ray diffraction image. In this case, the phenomena to be observed have to be nondestructive. If the phenomena is destructive, we should choose the TW laser plasma based one.



GaAs wafer with damage due to laser irradiation

Figure 2: GaAs specimen with damage and Kα1,2 X-ray diffraction image.

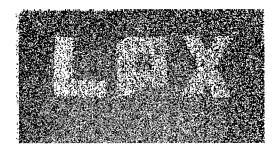
3 TW FS LASER BASED EXPERIMENT

When a TW fs laser is irradiated at a Cu plate, the ablation occurs and the plasma is generated. Then hot electrons over 10keV are also produced there. These electrons can induce Cu Kα1,2 X-rays. The main advantage of this process is a large number of X-rays photons as about 10¹¹ per shot, while the drawback is its long pulse width as a few ps[7]. In this case, it is expected that one laser-and-X-ray irradiation is enough to get a diffraction image. We carried out Cu Kα1,2 X-rays generation via this process using the 2TW 100fs laser light. The generation was confirmed by depicting the characters of "LPX" on the image plate as shown in Fig.3. We are going to use the laser induced plasma X-rays in the next step.

4 NUMERICAL ANALYSIS

We are developing a computer code to calculate the change of Cu Kα1,2 X-rays diffraction image due to atomic motions. We have already calculated the images of deformed lattices under several assumptions. Then, we are going to calculate the change of the image due to realistic nonequilibrium thermal expansion, phase-transition and soft-mode phonon. By using this code, we plan to perform an inverse analysis to evaluate deformed

lattice from measured X-ray diffraction images in the pump-and-probe analysis. The final goal is the animation of the atomic motions via computer graphics.



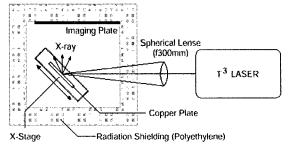


Figure 3: Configuration of the TW FS laser based experiment and result.

5 FEMTOSECOND ULTRAFAST QUANTUM PHENOMENA RESEARCH FACULTY

The titled facility is going to be installed in the laboratory. Here the upgraded femtosecond S-band twin linacs with 100fs stable Kerr-lens-model-locked Ti:Sapphire laser, 12TW50fs laser, X-ray diffraction analysis devices, the X-ray electron spectroscopy device and the Fourier transform infra-red spectroscopy device are introduced as shown in Fig.4.

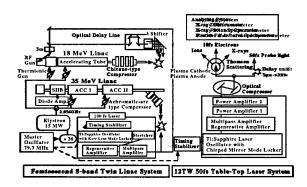


Fig.4 Femtosecond ultrafast quantum phenomena research facility.

Hundreds fs time-resolved pulseradiolysis for radiation chemistry is available using the first, while several basic researches of tens fs beam (electron, ion, X-rays) generation are performed via plasma cathode, plasma anode and relativistic nonlinear Thomson scattering using the second. After we have succeeded in the generation experimentally, we can proceed to a variety of tens fs time-resolved pump-and-probe analyses.

6 CONCLUSION

10ps Cu K α 1,2 X-rays was generated via 10ps elections-Cu wire collision using the electron linac. Cu K α 1,2 X-rays diffraction images were obtained for several monocrystals. Further, we produced picoseconds laser plasma Cu K α 1,2 X-rays via 2TW 100fs laser-Cu plate irradiation. In order to get X-ray diffraction images from deformed lattices in laser-induced nonequilibrium thermal expansion by single pump-and-probe shot, we plan to use the new 12TW 50fs laser in the next step.

7 REFERENCE

- [1] M. Uesaka et al., J. Nucl. Mater., 248, 380(1997).
- [2] M. Uesaka et al., Nucl. Instrum. Meth., A, 406, 371(1998).
- [3] T. Watanabe et al., Proc. of EPAC98, 1632(1998).
- [4] H. Harano et al., ibid, 2452(1998).
- [5] K. Nakajima et al., AIP Coference Proceedings 398, 83(1997).
- [6] C. Barty et al., http://www-wilson.ucsd.edu.
- [7] K. Kondo et al., Appl. Phys. Lett., 73(17), 1(1998).

THE SHIELDING DESIGN OF BESSY II*

K. Ott[†], BESSY, Rudower Chaussee 5, 12489 Berlin, Germany

Abstract

BESSY II consists of a 50 MeV microtron, a maximum energy synchrotron and the 1.9 GeV storage ring. The investigations of the radiation types occuring at those machines dependent of the electron energy, target and shielding materials, observating angles and geometric aspects are well established, often condensed in semi-empiric formulas and in good agreement with the results of the Monte Carlo programs EGS4 and FLUKA. But as important as the pure physical aspects of radiation are for a shielding design the operating times and modes and the consideration of possible crash scenarios. We present here a new approach of considering failure operating probabilities at electron storage rings based on years of radiation and operating observations of BESSY I. The shielding design of BESSY II was developed using a C++ class library which includes the most recent models for all radiation types and the new failure operating probability approach. Calculations and first measurement results of the commissioning are presented too.

1 LAW AND BUILDING UTILIZATION

For a shielding design of an electron storage ring facility are as relevant as the physical parameters the conditions given by law, operating times and planned utilization of machine and building. In Germany the annual personal doses of radiation workers (category B) and non-radiation workers are limited to 15 mSv/a and 5 mSv/a respectively.

If local doses can be higher than 15 mSv/a (2000 h stay) the respective area is a so called control area in which only radiation workers with personal dosimeters have access.

If at any failure operating (e.g. closed valve in the storage ring and full injection rate) the dose rate in an area could be higher than 3 mSv/h this area is a so called restricted area. Such an area has to be secured with a personal safety system, so that entering of it result in an immediate stop of radiation production.

The area accessible for the generality is named general area and has an annual dose limit of 0.3 mSv/a.

We decided, to hold this limit at the outer edge of the experimental hall, which would result in having no more than 2 mSv/a within the experimental hall.

The next design criterium was that the service area and the roof of both storage ring and synchrotron should be used for technical installations and so should be as accessible as the experimental hall with similar doses.

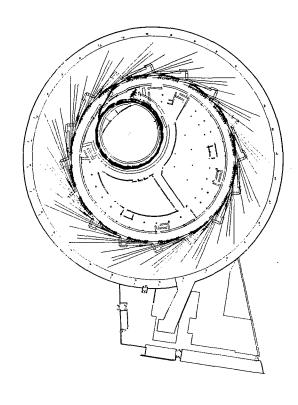


Figure 1: BESSY II overview

A further condition was that synchrotron and storage ring could be used independently to allow storage ring construction during synchrotron commissioning and later easy access for attendance work.

2 OPERATING OF BESSY II

For shielding design purposes, one has to distinguish between two cases of storage ring (synchrotron) operation:

- a) The machine is used just to inject and produce synchrotron radiation (user mode).
- b) The machine is used for machine tests, machine experiments and some phases of the commissioning (machine test mode).

The two modes differ considerable in electron losses and crash probabilities.

^{*} funded by the Bundesministerium für Bildung, Wissenschaft, Forschung und Technologie and by the Land Berlin

[†] Email: ott@bessy.de

Table 1: Operating times user mode

Operating of the storage ring / day	24	h
Operating of the storage ring / year	6000	h
Injections / day	5	
Injections / year	1200	
Operating of the synchrotron / injection	15	min
Operating of the synchrotron / year	300	h

Table 2: Operating times machine test mode

Weeks for machine tests / year	12	
Injections / day	10	
Injections / year	600	
Operating of the synchrotron / injection	15	min
Operating of the synchrotron / year	150	h

3 PHYSICAL ASPECTS

The main contribution of the radiation doses at electron storage rings causes from the electron losses during the short injection periods. When electrons hit under small angles the vacuum system bremsstrahlung is produced. This bremsstrahlung causes electron positron pair production and therefore an electron photon cascade with a maximum energy at about 1 MeV [3]. The bremsstrahlung also causes with (γ,n) processes giant resonance neutrons and fast neutrons with quasi deuteron fission [8]. The energy spectrum of the giant resonance neutrons is mainly determined by the material of the target (vacuum system) and the in case of steel it is similar to the Cf spectrum with a maximum at 1 MeV [7]. The production of myons in electro-magnetic cascades at electron accelerators is relevant for radiation safety from several GeV electron energy on. Because of an energy of 1.9 GeV at BESSY II the radiation caused by myons is two to three orders of magnitude smaller [2] than the doses caused by neutrons and gamma radiation outside the shielding walls, so it is neglectable for this case.

The activity of the primary cooling circuit water (without 15 O τ 2 min) at DESY synchrotron is about 0.37 Bq/l [6]. Radioactive substances are not given to the environment with water at BESSY II because of holding the cooling water of all machine components in closed cooling circuits.

The activation of accelerator components is at electron accelerators three orders of magnitude lower than at proton accelerators, because the activation is made here by secondary and ternary radiation. Another important point is, that at electron storage rings and synchrotrons the electron acceleration operates in pulsed mode therefore reducing the radiation power to a few watts. So altogether the activation of components of electron storage rings is typical 6 orders of magnitude lower than at proton or heavy ion accelerators.

Copper can cause some activation problems (20 μ Sv/h in 0.5 m distance) if exposed direct to the electron beam.

Synchrotron radiation is absorbed in the vacuum system at BESSY II with the exception of wave length shifter beamlines with critical energies about 10 keV.

Gasbremsstrahlung at BESSY II can be about 300 mSv/h for normal pressure [4] and requires 25 cm lead for absorption.

4 ELECTRON LOSSES

We will give here an overview over the electron losses at BESSY II. The electron losses are for the most part results of the machine components and there possibilities of operating and therefore close to an optimized state of the machine.

Microtron intern	70 %	15 MeV
Microtron extracted beam	crash	only
Transferline microtron-synchr.	5 %	50 MeV
Injection losses synchr. (a)	70 %	50 MeV
•	puls	$1 \mu s - > 300 ns$
	single	turn injection
Injection losses synchr. (b)	50 %	50 MeV
-	RF 3 GHz	- > 500 MHz

Injection losses synchrotron (relation 4:3:3) to

Injection septum	40 %
Extraction septum	30 %
10 Point sources (10 m)	30 %

Extraction losses synchrotron

(a)	16 %	1.9 GeV	kicker puls 50 ns/300ns
(b)	25 %	1.9 GeV	Septum channel

Without extraction recirculation to 10 - 20 MeV Losses to components (relation 4:3:3)

Injection losses storage ring
Transferline SY2ST 10% 1.9 GeV
Injection septum channel 30% 1.9 GeV
24 Point sources (10 m) 40% 1.9 GeV

Min. injection time: 32.9 sec for $9.98 \cdot 10^{11}$ e- (200mA)

5 FAILURE HANDLING

The above result of 30 second injection time to fill the storage ring has to be considered as an optimized state.

The worst cases are total electron losses at one place with full injection rate. The newer models are optimized for typical target geometries and observation angles at accelerators. So the dose rates can be predicted with good accuracy. But the approaches to estimate an annual dose from the possible failure operating scenarios differ widely.

One approach is the opinion, that those failure scenarios seldom occur and so there contribution to the annual dose is neglectable [5]. Another approach is that at every machine component, as specified in the last section, 5 % or

10 % of the annual operating time such a worst case scenario occurs [6]. For the storage ring BESSY II the first approach would result in a 0.5 m, for the second in a 1.5 m thick shielding wall. Both approaches are not easy to defend. The first because of obvious reasons, the second because of the fact, that the machine components have to be considered as a chain, so that the resulting annual crash times must be too pessimistic. Both approaches have the community, that they do not represent the daily operating of a storage ring adequately. An operator is expected to fill a storage ring (if no ramps are necessary) in a few minutes. So a crash scenario which lasts hours is unrealistic. The second point is, that storage rings are not optimized to decrease the injection time to the lowest possible level, they are optimized to fulfill the requirements of the users which are often in contradiction to a good machine performance. The third point is, that the injetion times are usually short, so also for synchrotron and microtron a more stable operating state is as least as important as a state with a higher performance but more unstable conditions.

So we start a new approach with the ansatz, that a typical injection time is longer than the optimal case. From the experiences at BESSY I we chose a lengthening factor of 3 for the user mode, and a factor of 30 for the machine test mode. The reason for the lengthening must be a failure function of one of the machine components as specified in the last section with equal probability. The failure function or crash probabilities follows results from the lengthening factors. So we differ between four modes. The user (1) and the machine test mode (3) and the user (2) and machine test mode (4) with failure functions. Te result for the annual operting times for the four modes for every machine component is then:

$$t_i^{(1)} = t_{max} \cdot \prod_{k=1}^i (1 - P_U) \tag{1}$$

$$t_i^{(2)} = t_{max} \cdot P_U \cdot \prod_{k=1}^{i-1} (1 - P_U)$$
 (2)

$$t_i^{(3)} = t_{max} \cdot \prod_{k=1}^i (1 - P_M)$$
 (3)

$$t_i^{(4)} = t_{max} \cdot P_M \cdot \prod_{k=1}^{i-1} (1 - P_M)$$
 (4)

 P_U is the failure function probability for the user mode, P_M for the machine test mode.

The t_{max} are:

t_{max} User mode	300	h/a
t_{max} User mode injection time	20	h/a
t_{max} Machine test mode	150	h/a
t_{max} Machine test mode injection time	100	h/a

6 RESULTS

The outer wall of the storage ring is dimensioned 1 m normal concrete and at the beamline angles 1 m heavy concrete with 5 cm lead stripe (beam height \pm 20 cm), at the injection 10 cm lead and 10 cm lead transversal of the injection septum. The outer wall of the synchrotron is dimensioned 1.1 m normal concrete.

The inner normal concret walls and the roofs of both storage ring and synchrotron are 0.7 m thick. The roofs are of heavy concrete above the area between extraction septum, transferline synchrotron storage ring and injection septum.

Table 3: Storage ring, point source transversal outside

$\gamma - \dot{H}_1$	2.27e - 01	Sv/h	$\gamma - \dot{H}_S$	1.21e - 07	Sv/h
$\dot{\gamma} = H_U$	1.28e - 06	Sv/a	$\gamma - H_M$	4.31e - 07	Sv/a
$\gamma = H^{fot}$	1.36e + 01	Sv/h	$\gamma = \dot{H}_{S}^{\hat{t}\hat{o}t}$	7.29e - 06	Sv/h
$\gamma - H_U^{\hat{t}ot}$	9.47e - 06	Sv/a	$\gamma = H_M^{tot}$	1.16e - 05	Sv/a
$giant_n - \dot{H}_1$	6.87e - 03	Sv/h	$giant_n - \dot{H}_S$	2.63e - 06	Sv/h
$giant_n - H_{II}$	2.77e - 05	Sv/a	$giant_n - H_M$	9.34e - 06	Sv/a
giantn - Htot	4.12e - 01	Sv/h	$giant_n = \dot{H}_S^{tot}$	1.58e - 04	Sv/h
$giant_n - H_{II}^{\frac{1}{t}ot}$	2.05e - 04	Sv/a	$giant_n - H_M^{tot}$	2.52e - 04	Sv/a
$fast_n - \dot{H}_1$	2.88e - 04	Sv/h	$fast_n - H_S$	6.53e - 06	Sv/h
$fast_n - H_N$	6.86e - 05	Sv/a	$fast_n - H_M$	2.31e - 05	Sv/a
$fast_n - H_1^{tot}$	1.73e - 02	Sv/h	$fast_n - H_S^{tot}$	3.92e - 04	Sv/b
$fast_n - H_{II}^{\frac{1}{t}ot}$	5.09e - 04	Sv/a	$fast_n - H_M^{tot}$	6.24e - 04	Sv/a

The complete calculated annual dose is 1.74 mSv/a, which is similar to the measured value for 1998 of 1.2 mSv/a. (3.8 mSv/a at injection). The measured γ doserates are close to the calculated values, the measured neutron doserates are typically a factor of two lower than the calculations.

7 REFERENCES

- K. Ott: Sicherheitsbericht für den Betrieb der Speicherringanlage BESSY II in Berlin - Adlershof, Tech. Rep. S4/97 BESSY (1997)
- [2] E. Bräuer, K. Tesch: Data on muon doses behind thick shielding at electron accelerators, DESY D3-62 (1987)
- [3] H. Dinter, J. Pang, K. Tesch: Calculations of doses due to electron-photon stray radiation from a high energy electron beam behind lateral shielding. Rad. Prot. Dos. 25,2 p107 (1988)
- [4] A. Esposito, M. Pellicioni: Gas bremsstrahlung production in the ADONE storage ring, LNF-86/23(NT) (1986)
- [5] S.-H. Jiang, J.-P. Wang: Detail conceptual shielding design of SRRC, SRRC-1-SA8 Rev819 (1988)
- [6] K. Tesch: Strahlenschutz für die 800 MeV Speicherringanlage BESSY, Tech. Rep. 2 BESSY (1978)
- [7] K. Tesch: Data for simple estimates for shielding against neutrons at electron accelerators. Part. Acc. 9, p201 (1979)
- [8] K. Tesch: Shielding against high energy neutrons from electron accelerators a review. Rad. Prot. Dos. 22,1 p27 (1988)

EVALUATION OF TARGET OPTIONS FOR ADVANCED RADIOGRAPHY FACILITIES

D. Sanders, S. Sampayan, R. Neurath, LLNL; M. Krogh, AlliedSignal, FM&T

Abstract

Initial results indicate that electron beams hitting targets used to generate x-rays during multipulse operation in advanced radiography facilities will generate plasma plumes which will disturb the electron beam during subsequent pulses. This, in turn, potentially can degrade the x-ray spot quality generated by the subsequent pulses. If this concern is substantiated, new facilities such as the Advanced Hydrotest Facility (AHF) will need a provision for mitigating this effect. One such provision involves moving the target with sufficient velocity that any plasmas formed are carried adequately far from the electron beam that they do not disturb it. We report the various approaches which have been considered and present data showing the maximum target rates which can be achieved with each approach.

1 DYNAMIC TARGET DEVELOPMENT

Development of a dynamic target delivery scheme required study of several relatively mature technologies. Those investigated as candidates include high velocity fly wheels, shape charge jets, and two types of high performance guns (burning propellant and compressed gas driven versions or as they are better know two-stage light gas guns). All of the systems investigated offer their own distinct advantages relative to the others; however, each also has its own particular weakness when compared to the design requirements for the intended application. DARHT (Dual Axis Radiography Hydrodynamic Test facility) and AHF (Advanced Hydrodynamic test Facility) require high dose X-ray pulses at very fast repetition rates. The energy deposited in target materials to create these high X-ray doses causes it to vaporize and ionize leaving a hole. Fresh material must be positioned in its place before the next X-ray pulse can be delivered from the system. The primary function of a dynamic target is to fulfill this material replacement need.

The problem statement used for determination of suitability for a given solution can be simply stated as followed:

- Deliver fresh material to the interaction area before the next pulse is required.
- Suppress or redirect the evolved plasma out of the electron beam path to avoid disturbance of beam focus.
- Use materials of the proper cross section (high Z) to maximize the radiation dose for a given energy input.
- Deliver the target material to the same location every time the system is operated.
- Deliver the same amount of material to the interaction region for every X-ray pulse.

All of the normal methods for accelerating materials to high velocities were considered. Explosively driven flyer plates (plates of material propelled in a direction normal to the plate surface) while providing adequate velocity, are not orientated properly with respected to the electron beam without extensive development of current technology. Electrically driven rail guns were also determined not provide the necessary velocity.

The flywheel offers a significant advantage over all of the other methods because it does not need to be synchronized with other hardware in the system or the object to be flash X-ray photographed. The velocities required to deliver fresh material to the interaction region may be greater than can be obtained with existing materials or composites. The best speeds are on the order of 3mm/µsec velocity at the tip of the rotor. With development, the technique might reach a value of 4 mm/µsec which could be adequate to replace material for subsequent pulses. Flywheels, by their nature, store large amounts of energy. Figure 1, shows that the flywheel stores the greatest amount of energy of the approaches considered.

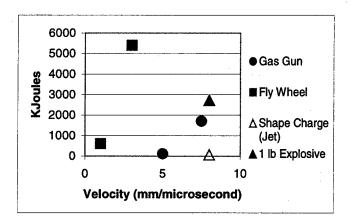


Figure 1: Comparison of energy for different dynamic target approaches.

Introduction of stress risers in the surface by punching holes in them with an electron beam introduces the potential for failure and instant release of this energy. If a flywheel concept is chosen, care will need to be taken to provide for adequate containment in case such failure occurs. The need to manage the destabilizing effects of the ion / plasma plume generated during beam interaction with the target will require an additional technique for plasma management since fly wheels do not provide the 8 mm/µsec velocity calculated to be required for such plasma management through target motion alone.

Shape charged jets offer the advantage of a very short cycle time for the total operation of injection of the target material. They also can reach the required velocities. The explosive is mounted relatively close to the electron interaction region and could be used to deliver material on demand under conditions where only a few microseconds pretrigger. This distinct advantage is mitigated by the fact that the jet of material expelled from the explosive is not of a constant cross section. Dimensions as small in thickness as 1millimeter (which is the thickness of tantalum currently required) are very difficult to obtain with this method. The density of the jet is normally on the order of 90% of solid density. Variability in the size of this material jet from shot to shot as well as along it's length in a particular stream of material makes delivery of a constant X-ray dose more difficult. This issue could be investigated through experiment along with contained management of debris generated by the Experiments are currently being designed to evaluate the precision with which a jet can be placed in both time and space, the uniformity of the jet that can be achieved, the management of the gases from the explosion, and the management of the shock wave from the explosion. At this time, this is one of the two approaches that can potentially deliver the necessary velocity.

The other approach which can deliver the 8mm/µsec thought to be necessary for plasma management is a light gas multiple stage gun. Figure 2 shows a series of experiments indicating that necessary velocities have been achieved by a number of organizations using a number of gun designs.

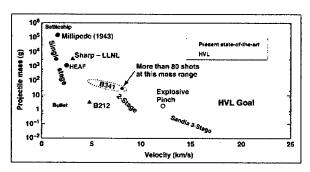


Figure 2: Experience of several organizations with high velocity guns. [1]

Research guns are currently under development (see HVL Goal in Figure 2) seek to double this velocity. An advantage of gas gun systems is their ability to deliver a predefined target geometry. Target projectile shape is defined before the gun is loaded and therefore can be well controlled. This ability allows the amount of material to be act'ed upon by the electron beam to be kept constant from pulse to pulse and hence a more constant X-ray dose from the system could be expected. The final selection criteria which makes the compressed gas version of the gun more attractive than the propellant style gun is the

issue of the uniformity of powder charges from lot to lot of powder produced by the manufacturer. Compressed gas versions of the gun minimize barrel fowling, cleaning issues, and lot variability is removed from the list of potential problems causing jitter in the operation of the gun system. Propellants are also very susceptible to temperature effects. Cold powder charges burn at different rates than those that are ignited when the powder is hot before ignition.

The compressed gas version of the two-stage gun is currently favored over an explosively driven version. Calculations have been performed with a basic two-stage system. The strategy chosen for this calculation was to select a standard baseline firing configuration and evaluate timing of critical events. Gas gun parameters that might affect launch times were compiled along with narrow ranges of these parameters within ranges where they can be controlled. Assuming the use of explosively driven valves, these calculations indicate that a total system jitter for a gun capable of delivering a projectile at a rate of 7.5mm/µsec will have an uncertainty in delivery of that projectile of 2-3 µsec. This uncertainty or "jitter" defines the length of target necessary to assure that target material is hit by the accelerator electron beam at the appropriate time.

Stability of the gun from a shot to shot perspective is greatly a function of the ability to measure accurately temperature, pressure, and wear in the gun barrels. Precise instrumentation for measurement of these parameters is readily available. Since the target projectile never leaves the barrel, it is fully constrained in all directions except down the axis of the gun bore, allowing accurate positioning of the target relative to the electron beam to be only a function of velocity. Utilization of a gas gun does force certain limitations on the overall systems capabilities. The total gun cycle time is on the order of 5 milliseconds and little adjustment can be made to modify the flight time or speed of the target projectile after the gun has begun to operate at the pre-selected parameters. Leakage of gas around the projectile is also of concern because it may affect the electron beam. Theoretical and experimental work is planned to alleviate the concern in these areas. Testing of this type could be done on existing guns and scaled to fit flash X-ray criteria. It should be noted that at the time of this publication target material experiments are still in progress to determine if the target material plasma and ion interactions with the beam are a real concern or of negligible effect to the overall system performance. The basic gun operating values satisfy the requirements for delivery of a dynamic target, but it remains to be demonstrated that targets with geometry leading to required x-ray generating properties can be moved by gas guns to the required velocity.

2 CONCLUSIONS

An evaluation has been started to determine the best method to deliver a fast moving target normal to the electron beam in proposed rapid multipulsed radiography facilities. Rail guns, flyer plates and fly wheels were

^[1]Raymond Finucane Lawrence Livermore Laboratory – private communication

considered and eliminated from further consideration they fail to deliver the necessary velocity of 8 mm/µsec, or in the case of the flyer plate, do not provide the target material properly orientated with respect to the electron beam. Both gas guns and explosively driven shaped charges have the potential for delivering the necessary velocity. Experiments are currently underway to address remaining concerns with each approach and to minimize the risk associated with fielding the one which is chosen for implementation.

The work was performed under the auspices of the U.S. Department of Energy by LLNL under contract W-7405-ENG-48.

RADIATION ENVIRONMENT RESULTING FROM MAIN INJECTOR BEAM EXTRACTION TO THE NUMI BEAM LINE *

A. I. Drozhdin, P. W. Lucas, N. V. Mokhov[†], C. D. Moore, S. I. Striganov, FNAL, Batavia, IL

Abstract

A 120 GeV Main Injector proton beam will be delivered to the NuMI beam line at Fermilab at the rate of 3.7×10^{20} per year. Realistic Monte Carlo simulations have been performed to examine the radiation environment in the beam extraction system and NuMI beam line elements. A complete 3-D model of the 160 meter extraction region has been implemented utilizing the computer code MARS. The model includes a description of the field of the electrostatic septa and POISSON calculated field maps of the Lambertson magnets and the other lattice components in the area. The beam element alignment and the source term have been simulated using the code STRUCT. Results on beam losses in the system, energy deposition in the core elements and residual dose rates on the components are presented.

1 INTRODUCTION

The projected intensity for the NuMI project of 4×10^{13} protons extracted at 120 GeV from the Main Injector every 1.867 s[1] can result in a severe radiation environment[2]. To explore this, full-scale Monte Carlo simulations with the STRUCT[3] and MARS[4] codes are performed for the beam loss and showers induced in the Main Injector and NuMI beamline elements.

2 SOURCE TERM AND BEAM LOSS

The Main Injector lattice with all the optics elements in the extraction system region, electrostatic deflector, three modules of the Lambertson magnet, and the NuMI beamline components have been implemented into the simulation codes. The Lambertson magnet modules are rotated with respect to the longitudinal axis by 0.22 rad, 0.098 rad and 0.037 rad, correspondingly, to bend the extracted beam out of the accelerator in both vertical and horizontal planes. All essential details of the accelerator and NuMI beamline elements are taken into account in the simulations. The beamline is aligned with respect to the extracted beam axis to prevent primary proton loss anywhere but at the electrostatic deflector wires. Extracted and circulating beam densities at the entrance to the electrostatic deflector ES are calculated as in[5] for the Main Injector circulating beam emittance of 30π mm·mrad and shown in Fig. 1.

The ES wire distribution and other septum details are assumed as in[6]. Two cases of septum wires are studied, 2 and 4 mil, or 0.0508 and 0.1016 mm, correspond-

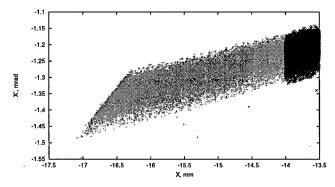


Figure 1: Circulating (black) and extracted (gray) beam horizontal phase space on the ES septum.

ingly. A 10⁵ proton sample in the extracted beam is taken in the calculations. About 2.5% of those hit the 2-mil electrostatic deflector wires, and twice that fraction the 4-mil wires. Some of these protons interact inelastically with the tungsten nuclei generating secondary particles responsible for radiation fields in the immediate vicinity of the ES. The others lose a small fraction of their energy, getting an angular kick due to multiple Coulomb and elastic scattering and electric field, resulting in long-range beam losses both in the machine and the NuMI beamline. Fig. 2 shows the calculated proton flux at the downstream end of the 2-mil

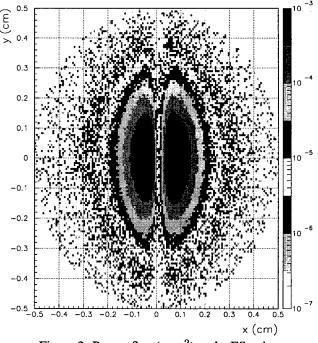


Figure 2: Proton flux (cm⁻²) at the ES exit.

^{*} Work supported by the Universities Research Association, Inc., under contract DE-AC02-76CH00300 with the U. S. Department of Energy.

[†] Email: mokhov@fnal.gov

wire septum. The β -function in the beamline after the ES and calculated heat load to the beam pipe due to high energy protons lost in the studied sections are shown in Fig. 3.

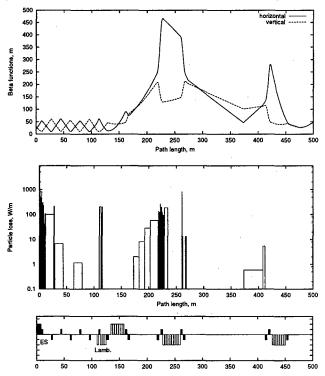


Figure 3: NuMI beamline β -function (top) and beam loss distribution in the accelerator and in the beamline (bottom).

A fine structure of the lost proton distribution along the first 160 m of the beampipe is given in Fig. 4 for 4-mil wires. One sees that most protons are lost on the septum and immediately downstream resulting in high radiation levels in the first 50 meter region. The second peak is at the Lambertson magnet as expected. In the 2-mil wire case, the particle loss on the pipe in the first 50 meter region is about three times lower, resulting in a more favorable radiation environment. The peak at the Lambertson is about the same. Fig. 5 shows calculated proton beam densities at the Lambertson magnets. The aperture of the quadrupole between the first and second Lambertson magnets is an ellipse of $R_x \times R_y = 61 \times 27 \text{ mm}^2$. To eliminate the extracted proton loss in the quadrupole, the beam orbit needs to be moved at extraction by δx =-4.5 mm and δy =-11.5 mm, using for example the Main Injector beam orbit correctors.

3 PROMPT AND RESIDUAL RADIATION

3.1 Septum Heating

Although a fraction of the beam hitting the 4-mil wires is twice that of the thinner wire case, the peak energy deposition density is about the same in both cases. It peaks at the beam center at about 10 cm from the upstream end and decays exponentially along the septum to negligible values at about 200 cm. Thermal analyses have been performed

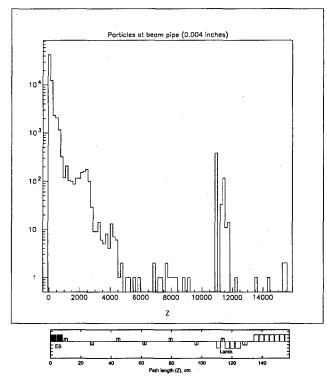


Figure 4: Proton distribution along the beampipe for the 4-mil wires of the electrostatic septum.

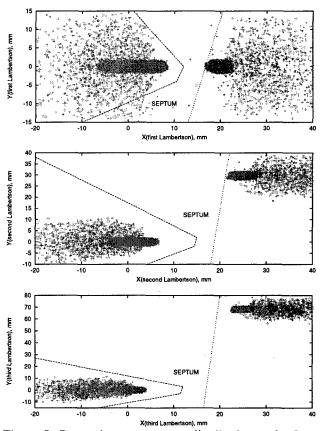


Figure 5: Proton beam transverse distribution at the first, second and third Lambertson magnets.

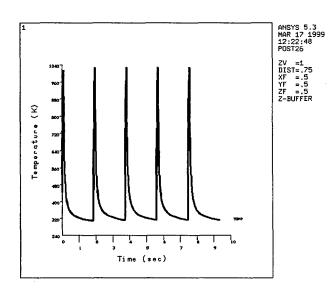


Figure 6: MARS-ANSYS calculated peak temperature in the 2-mil ES septum wires vs time for five sequential 120 GeV proton pulses of 4×10^{13} ppp separated by 1.867 s.

with ANSYS using the MARS calculated energy deposition density distribution in the wires made of 75% tungsten and 25% rhenium. It is assumed that the initial temperature is 300 K, and the wire ends are kept at the handler temperature of 300 K. The calculated peak temperature at the wire/beam center at the shower maximum ($z\sim10\,\mathrm{cm}$) for the 2-mil case is shown in Fig. 6 vs time for five sequential pulses separated by 1.867 s. The wires are cooled nicely between the pulses with no temperature build-up. The maximum temperature rise is 720 K, which corresponds to the maximum temperature of 747°C.

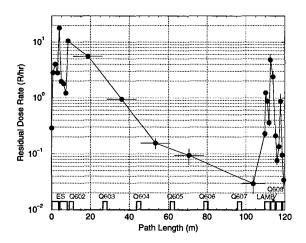


Figure 7: Residual dose rate on the outer surface of the Main Injector and NuMI beamline components due to 30 days of irradiation at the averaged over that period proton intensity of 1.6×10^{13} p/s and after 1 day cooling.

3.2 Equipment Activation

Equipment activation is rather high in the vicinity of the ES and in the Lambertson magnet region. The calculated residual dose rate on the outer surface of the components is presented in Fig. 7 for t_i =30 day irradiation and t_c =1 day cooling. The rates at the two hot locations are rather high. They go down approximately as 1/r with distance from the beamline, and can be re-scaled to other irradiation/cooling conditions via $\log(t_i/t_c)$.

4 CONCLUSION

The results of this study indicate that there will be manageable thermal effects from the desired intensity but the residual radiation levels in the extraction area will be very high. For the case given in Fig. 7 one observes that maintenance issues must be addressed for both the extracted beam line components and the near by components of the Main Injector itself. Longer irradiation times and a desire for access after shorter cooldown periods could lead to a several-fold increase in the dose rates shown in Fig. 7.

5 ACKNOWLEDGMENTS

We express our gratitude to J. Johnstone for information on resonant extraction and useful discussions, T. Kobilarcik for POISSON calculated magnetic field maps and I. Novitski for the help with ANSYS calculations.

- [1] "The Fermilab Main Injector Project, Technical Design Handbook", (1995).
- [2] C. M. Bhat and N. V. Mokhov, "Radiation Levels around the Fermilab Main Injector Extraction Septa", Proceedings of the 1997 IEEE Particle Accelerator Conference, Vancouver, May 1997.
- [3] I. Baishev, A. Drozhdin, and N. Mokhov, "STRUCT Program User's Reference Manual", SSCL-MAN-0034 (1994).
- [4] N. V. Mokhov, "The MARS Code System User Guide, Version 13(95)", Fermilab-FN-628 (1995); N. V. Mokhov et al., Fermilab-Conf-98/379 (1998); LANL Report LA-UR-98-5716 (1998); nucl-th/9812038 v2 16 Dec 1998; http://www-ap.fnal.gov/MARS/.
- [5] J. A. Johnstone, "A Simplified Analysis of Resonant Extraction at the Main Injector", Fermilab-MI-Note-91 (1993).
- [6] A. I. Drozhdin, M. Harrison, and N. V. Mokhov, "Study of Beam Losses During Fast Extraction of 800 GeV Protons from the Tevatron", Fermilab-FN-418 (1985).

ACCELERATION OF HIGH INTENSITY PROTON BEAMS

X. Altuna, G. Arduini, C. Arimatea, R. Bailey, R. Billen, T. Bohl, P. Collier, K. Cornelis, G. Crockford, B. Desforges, C. Despas, A. Faugier, A. Ferrari, R. Giachino, K. Hanke, M. Jonker, T. Linnecar, C. Niquille, L. Normann, G. Robin, G. Roy.

CERN Geneva, Switzerland

Abstract

In 1998 the CERN SPS accelerator finished a five years long program providing 450GeV proton beams for neutrino physics. These experiments required the highest possible beam intensity the SPS can deliver. During the last five years the maximum proton intensity in the SPS has steadily been increased to a maximum of 4.8 10¹³ protons per cycle. In order to achieve these intensities a careful monitoring and improvement of the vertical aperture was necessary. Improved feedback systems on the different RF cavities were needed in order to avoid instabilities. Also the quality (emittance and extraction spill) of the injector, the CERN PS, had be optimised.

1 GENERAL LAYOUT OF THE SPS CYCLE.

In Fig 1 a typical SPS cycle is shown as it was used for the last five years during the high proton intensity running:

Two 10µsec long batches are injected from the CPS in order to fill the whole ring. The injection energy is 14 GeV. The two injections come in with a 1.2sec time interval.

The beam is then ramped up to 450 GeV, crossing transition at 23.6 GeV. The maximum intensity accelerated up to now is 4.86 10¹³ protons/cycle.

At 445 GeV a first fast resonant extraction (FRE1) takes place. An intensity, up to 1.810¹³ protons, is extracted on the half integer, in straight section 6 (fig 2). The spill (fig 3), 6 msec long, is controlled by a quadrupole kicker. The pulse shape of this kicker is controlled by an IGBT (Insulated Gate Bipolar Transistor) in order to obtain an as flat as possible maximum [1]. This beam is sent to the neutrino experiment.

At 450 GeV, a shared slow resonant extraction (SSRE) on the third integer, takes part of the beam out in straight section 2 and 6. The phase advance between 6 and 2 is put exactly set to 9 betatron oscillations in the horizontal plane. The spill length is 2.3 sec and the extracted intensity can go up to $2 \cdot 10^{13}$ (fig 4).

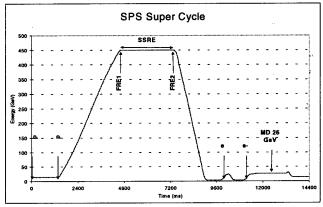


Fig 1: The SPS supercycle

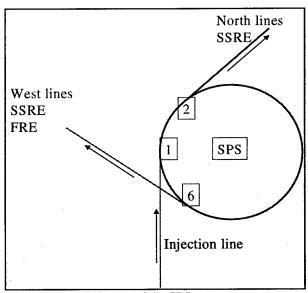


Fig 2: Schematic layout of the SPS.

The remaining beam is extracted for neutrino physics by a second fast resonant extraction (FRE2) on the half integer, in straight section 6. The spill is 6 msec long and the extracted intensity can go up to 1.8 10¹³ protons.

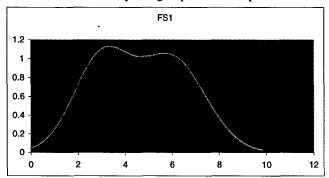


Fig 3: Typical spill of the fast resonant extraction.

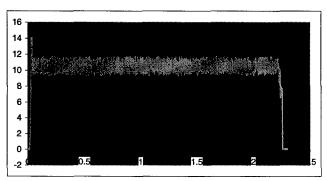


Fig 4: spill off the shared slow extraction (2.3 sec long).

After the proton physics cycle there are two LEP injection cycles (3.5 GeV - 22 GeV) for positrons and electrons.

At the end there is a 26 GeV injection plateau which is used for machine studies on the future LHC beam.

2 MAJOR STEPS TO INCREASE THE PROTON INTENSITY.

Since 1993 the intensity of the SPS proton beam has increased from 3.5 10¹³ protons /cycle to 4.86 10¹³ protons /cycle. This progress was achieved by the following measures:

- The proton intensity per CPS pulse was raised to 3 10¹³ protons per cycle
- The CPS improved the control of the extracted beam (5 turn extraction) in order to avoid peaks in the spill which give rise to very harmful peak power in the feedback for the superconducting cavities. These cavities are used for lepton acceleration and are actively damped during the proton cycle.
- A better "alignment" of the five extracted turns in the CPS could be obtained, so that they arrive with the

- same angle and position in the SPS, improving the overall emittance of the injected beam.
- The vertical aperture of the SPS was continuously monitored with bump scans and beam loss analysis. The bottle necks could be removed by re-aligning certain elements and exchanging magnets with distorted vacuum chambers inside. The aperture increased form 21mm to 37mm (at β=100m) over the last five years.
- Thanks to a yearly realignment program of the quadrupoles, the natural closed orbit distortion (without corrections) could be reduced to 2.3 mm rms in the horizontal plane and 1.2 mm rms in the vertical plane. Hence less corrector strength is needed and the closed orbit correction could be extended form 14 GeV to 50 GeV resulting in reduced losses at transition.
- The super conducting cavities that are used for lepton acceleration were more efficiently damped, using a feed forward loop and a one-turn feedback [2].
- The betatron- and dispersion mismatch at injection were carefully measured and could be reduced to less than 10% [3].
- Another problem with high intensities is the frequent sparking of the electrostatic septa. The ion traps inside the septa had to be trimmed carefully to empirical values in order to reduce the spark rate.

All these measures improved the overall transmission in the machine and a record intensity of 4.86 10¹³ could be reached. The loss pattern in the optimised machine is the following:

- 8% to 12% losses at CPS extraction.
- 0% to 2% losses at injection in SPS.
- 2% losses at start of acceleration (capture losses).
- 2% to 3% losses at transition.
- 1% to 2% losses at extraction
- 5% to 10% losses splitting and transfer to targets for the neutrino beam there is no splitting, and the transfer losses are negligible.

The gradual improvement over the last years can be seen form fig 5 where the total number of protons delivered to all targets is plotted. The total number of protons on the neutrino target is shown in fig 6.

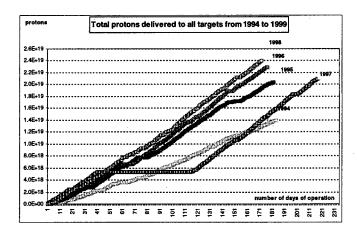


Fig 5: Total proton intensity on targets for the last five years. The long period without production in 1997 was due to a fire in BA3.

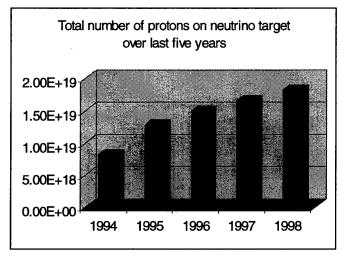


Fig 6: total intensity on the neutrino target over the last years.

- [1] E. Carlier, A. Heinemann, E. Vossenberg, Electronic regulation of the SPS extraction quadrupole current pulse shape for improved stability of the extracted beam, CERN-SL /note 96-78 (1996)
- [2] D. Boussard, G. Lambert, T. Linnecar, PAC –1993.
- [3] G. Arduini, M. Giovannozzi, K. Hanke, D. Manglunki, M. Martini, G. Metral, Measurement and Optimization of the PS-SPS Transfer Line Optics, these proceedings.

INITIAL ERROR ANALYSIS FOR THE LHC COLLIMATION INSERTIONS

D.I.Kaltchev, M.K.Craddock¹, R.V. Servranckx, TRIUMF, 4004 Wesbrook Mall, Vancouver, B.C., Canada V6T2A3 J.B.Jeanneret, CERN, CH-1211 Geneva 23, Switzerland

Abstract

The two cleaning insertions in the LHC, for betatron and momentum collimation, are optimized for an ideal lattice and collimator jaw setup. We have studied a collimation beam line with randomly generated jaw misalignments and quadrupole field and alignment errors, the resultant distortion of the reference orbit being corrected with the help of monitors placed near critical collimators. Different closed orbit errors and beam shapes are considered at the entrance. We report the level of errors for which no corrections are needed and the level for which corrections are not possible.

1 INTRODUCTION

The optics of the LHC betatron and momentum collimation insertions, and the locations and orientations of the collimator jaws, have been optimized so that the secondary halos, produced by scattering of circulating protons at the primary collimators, are restricted to the desired aperture [1]. The halo is defined as the beam of scattered particles within solid angle 2π – with initial non-normalized coordinates (x,y) (a point-like source on the primary collimator jaw surfaces) and initial angles (x',y') within $(-\frac{\pi}{2},\frac{\pi}{2})$.

We have studied how the collimation quality is affected by jaw and quadrupole alignment errors, quadrupole powering errors, and incoming beam positioning and mismatch. Since each warm quadrupole Q6L-Q6R consists of a group of 5-6 modules, both group and module misalignment has been considered. As a reference case without errors, we use the optimized layout for the betatron insertion IR7 (Fig. 1), with the primary collimator apertures set to 6σ , and 16 secondaries set to 7σ (injection optics). For this the halo particles escaping all secondary jaws are found to have a maximum combined transverse invariant $A = \sqrt{X^2 + X'^2 + Y^2 + Y'^2}$ of 8.4 in units of σ , while the maximum in-plane invariants are $A_x = 7.83$, $A_y = 8.16$.

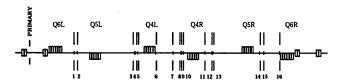


Figure 1: Betatron cleaning insertion layout.

2 ERROR ANALYSIS

The effects of quadrupole misalignments and powering errors were studied by using the code DIMAD [2] to trace the following beam parameters through IR7: reference orbit $x_{orb}, x'_{orb}, y_{orb}, y'_{orb}$, beta functions β_x, β_y and betatron phases μ_x , μ_y . Their values, computed at the secondary jaws, are passed to the code Distribution of Jaws (DJ) which finds the maximum invariants A, A_x and A_y of surviving halo particles. Orbit positioning errors and beam mismatch at the primary are taken into account by using nonzero initial values $x_{orb}^{(in)}, x_{orb}^{(in)}, y_{orb}^{(in)}, y_{orb}^{(in)}$ and initial beta functions $\beta_x^{(in)}, \beta_y^{(in)}$ different from the nominal ones.

In DJ, for a fixed set of halo sources, the jaw phases $\mu_x^{(k)}$, $\mu_y^{(k)}$ (k=1,...16) define A, A_x and A_y in the following way [1]: all jaws (pairs of parallel lines in normalized X-Y space) are transformed (rotated by angles $\mu_x^{(k)}$, $\mu_y^{(k)}$) to the entrance, and the "escape window" in initial-angle space is found—its vertices giving A, A_x and A_y . This procedure is equivalent [1] to linear tracking with the maximum escape angles being recorded, but is much faster.

To include the misalignment of a pair of jaws in this model, the corresponding pair of lines is displaced from the origin in normalized X-Y space by $\Delta x_{jaw_k}/\sqrt{\beta_{x,k}}$ and $\Delta y_{jaw_k}/\sqrt{\beta_{y,k}}$, in effect changing the escape window. Here $\Delta x_{jaw_k}, \Delta y_{jaw_k}$ are the horizontal and vertical displacements of the midpoint (centre) of the pair with respect to the reference orbit, which passes through the quadrupole centers. If the reference orbit at the k-th jaw is displaced by $x_{orb}^{(k)}$ with respect to the vacuum chamber axis, the jaw displacement in DJ is taken to be $\Delta x_{jaw_k} = -x_{orb}^{(k)}$ (and similarly for y).

Powering errors and incoming beam mismatch lead to different sets of jaw phases relative to the error-free case.

Orbit correction was performed by DIMAD, with 6 correctors and 6 double (horizontal and vertical) beam position monitors placed in the middle of each of the quadrupole groups (Fig 1), plus one additional vertical corrector at the beam line entrance. The orbit displacements at the monitors are minimized by the least square method.

Monitor alignment errors with respect to the vacuum chamber axis (rms lateral displacements $\sigma_{x^{mon}}, \sigma_{y^{mon}}$) are simulated by random misalignment of the jaws with respect to the reference orbit with the same rms values.

For all errors together, the tolerable increase in A is assumed to be $\approx \sigma$, i.e. the maximum acceptable value is 9.5.

Also at Dept. of Physics & Astronomy, UBC, Vancouver, Canada.

Table 2: Effects of random lateral misalignment of all quadrupoles, with and without orbit correction.

$\sigma_x = \sigma_y [\mu \text{m}] \qquad 100 \qquad 200 \qquad 400$					
As modules					
	$max_{10} \ \hat{x}_{orb}/\hat{y}_{orb} \ [ext{mm}]$	0.5 / 0.7	1.0 / 1.4	2.1 / 2.9	
No	$max_{10} \hat{x}_{orb}^{jaw}/\hat{y}_{orb}^{jaw}$ [mm]	0.5 / 0.6	1.0 / 1.3	1.9 / 2.5	
corr.	$max_{10} A/A_x/A_y$	8.7 / 8.1 / 8.3	9.1 / 8.7 / 8.5	10.2 / 9.8 / 8.9	
	$ave_{10} A/A_x/A_y$	8.5 / 7.8 / 8.1	8.7/8/8	9.1 / 8.3 / 8.0	
		As groups			
	$max_{10} \ \hat{x}_{orb}/\hat{y}_{orb} \ [ext{mm}]$	1.8 / 1.1	3.6 / 2.2	7.2 / 4.5	
No	$max_{10}~\hat{x}_{orb}^{jaw}$ / \hat{y}_{orb}^{jaw} [mm]	1.5 / 1	2.9 / 2.1	5.8 / 4.1	
corr.	$max_{10} A/A_x/A_y$	9.9 / 9.3 / 9.2	11.6 / 10.8 / 10.3	14.5 / 14 / 11.6	
	$ave_{10} A/A_x/A_y$	9.1 / 8.4 / 8.4	9.9 / 9.0 / 8.6	11.5 / 10.4 / 9.2	
	$max_{10} x_{orb}^{end}/x_{orb}^{'end}/y_{orb}^{end}/y_{orb}^{'end}$	0.8 / 10 / 0.6 / 14	1.5 / 20 / 1.2 / 28	3 / 41 / 2.4 / 56	
	[mm] / μ rad]				
	$ave_{10} \ x_{orb}^{end} / x_{orb}^{'end} / y_{orb}^{end} / y_{orb}^{'end}$	0/1/0.2/4	0.1/3/0.3/7	0.2 / -5 / 0.6 / -15	
	$max_{10} \ \hat{x}_{orb}, \hat{y}_{orb} \ [ext{mm}]$	0.2 / 0.2	0.3 / 0.3	0.7 / 0.7	
With	$max_{10}~\hat{x}_{orb}^{jaw}$, \hat{y}_{orb}^{jaw}	0.1 / 0.2	0.2 / 0.3	0.4 / 0.6	
orbit	$max_{10} A/A_x/A_y$	8.6 / 8.0 / 8.2	8.7 / 8.2 / 8.3	9.1 / 8.6 / 8.5	
corr	$ave_{10} A/A_x/A_y$	8.5 / 7.8 / 8.1	8.5 / 7.9 / 8.1	8.7 / 7.9 / 8.1	
	$max_{10} \ x_{orb}^{end} / x_{orb}^{'end} / y_{orb}^{end} / y_{orb}^{'end}$	0/1/0/2	0/3/0/4	0.1/6/0/8	
	[mm]/[μ rad]				
	max. corr. [μ rad]	6	12	24	
Jaws	_				
9,16	$max_{10} A/A_x/A_y$	8.5 / 8.0 / 8.2	8.6 / 8.1 / 8.3	8.9 / 8.4 / 8.4	

3 ERROR ANALYSIS RESULTS

Analysis of *individual jaw misalignment* for horizontal displacements (Fig. 2) shows that A is most sensitive to lateral shifts of jaws 8, 9 and 16. Similar behavior was observed in the vertical plane.

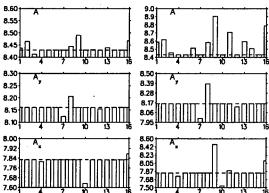


Figure 2. Effect of horizontal displacement of individual jaws: left: 0.1 mm; right: 0.5 mm.

Table 1 shows the effects of individual quadrupole group misalignment and group powering errors on A (nominal value 8.4). Left: horizontal/vertical displacement 100 and 200 μ m. Right: relative field error 5×10^{-3} . Transverse shifts of 0.1-0.2 mm lead to $0.5-1\sigma$ loss in collimation quality. Quadrupole powering errors up to the level 10^{-3} have little effect on A (see also **Table 3**).

Table 2 presents results from random transverse misalignment of quadrupoles. For each seed, Q6L-Q6R were

Table 1:

	Displacement hor. / vert. [μm]		Rel. field error $\Delta k_1 / k_1$
	100 200		5×10^{-3}
Q6L	8.8 / 8.7	8.6 / 9.4	8.5
Q5L	8.5 / 8.6	8.5 / 8.7	8.5
Q4L	8.7 / 8.6	8.5 / 9.1	8.5
Q4R	8.5 / 8.7	8.5 / 8.5	8.4
Q5R	8.5 / 8.3	8.3 / 8.6	8.4

randomly displaced with Gaussian distributions in both x and y planes, with equal rms values 0.1, 0.2 and 0.4 mm, truncated at 2σ . Here $\hat{x}_{orb} = max \, |x_{orb}|$ is the maximum absolute value of horizontal orbit excursion along the beam line and $\hat{x}_{orb}^{jaw} = max_k \, |x_{orb}^{(k)}|$ is the maximum excursion at a jaw (similarly for y). Also max_{10} and ave_{10} denote the maximum and the average values of 10 seeds, and superscript end is used for the residual orbit displacement and angle at the beam line exit. For example, for an rms displacement of 0.2 mm of all groups, the "worst" of the 10 seeds produces A=11.6 with residual horizontal orbit displacement at the exit $x_{orb}^{end} = 1.5$ mm, and $x_{orb}^{'end} = 0.02$ mrad. The 10-seed averaged values are A=9.9, $x_{orb}^{end} = 0.1$ mm and $x_{orb}^{'end} = 0.003$ mrad.

In so far as the alignment of individual modules within a group is expected to be better than alignment of the groups with respect to each other, an appropriate orbit correction is absolutely necessary, since group alignment errors of $100-200~\mu m$ will very likely be present. The same seed sequence was used both with and without correction. The last row

of Table 2 shows the effect of two monitors being relocated from the closest quadrupoles to the critical locations near jaws 9 and 16 identified in Fig. 2.

Table 3: Random powering errors in all quadrupoles.

$\Delta K_1 / K_1$	10^{-3}	5×10^{-3}	
$max_{10} A/A_x/A_y$	8.4 / 7.9 / 8.2	8.6 / 7.9 / 8.3	
$ave_{10} A/A_x/A_y$	8.4 / 7.8 / 8.15	8.5 / 7.8 / 8.2	

Table 4: Incoming beam steering.

Horizontal [mm,mrad]				
(x)	$(\stackrel{(in)}{orb},x'^{(in)}_{orb})]$	(1,0)	(0,0.02)	
	\hat{x}_{orb}	3.5	2.4	
No	\hat{x}_{orb}^{jaw}	3.2	1.9	
corr.	$A/A_x/A_y$	11.1/10.5/8.7	9.5/8.5/8.2	
	$x_{orb}^{end}/x_{orb}^{'end}$	1.5/7	0.5/ 16	
	\hat{x}_{orb}	1	1.2	
	\hat{x}_{orb}^{jaw}	0.6	0.9	
With	$A/A_x/A_y$	8.7/7.9/8.2	8.8/7.9/8.1	
corr.	$x_{orb}^{end}/x_{orb}^{'end}$	0/0	0/0	
	max. corr.	2.2	4.4	
		al [mm,mrad]		
$y_{orb}^{(in)}, y$	$y_{orb}^{\prime(in)}$ [mm,mrad]	(1,0)	(0, 0.02)	
	\hat{y}_{orb}	2.8	4.7	
No	\hat{y}_{orb}^{jaw}	2.4	3.4	
corr.	$A/A_x/A_y$	10.7/8.6/10.6	10.8/7.9/10.4	
	$y_{orb}^{end}/\hat{y}_{orb}^{'end}$	0.7/7	0.4/33	
	\hat{y}_{orb}	1	1.1	
	\hat{y}_{orb}^{jaw}	0.4	0.4	
With	$A/A_x/A_y$	8.5/7.8/8.2	8.6/7.8/8.2	
corr.	$y_{orb}^{end}/y_{orb}^{'end}$	0/0	0/0	
L	max. corr.	2.2	53	

Table 5:
$$\Delta \beta^{(in)}/\beta^{(in)} = 10 \%$$

	Hor.	Vert.
$A/A_x/A_y$	8.6/ 8/ 8.2	8.8/ 7.7/ 8.4

Tables 4 and 5 show the effect of a fixed incoming beam steering error in position (+1 mm) or angle (+0.02 mrad), either horizontal or vertical, and of 10% incoming beam mismatch.

Table 6 shows the effect of random misalignment of all jaws with rms values 0.2 and 0.4 mm. This is equivalent to introducing monitor misalignment (orbit measurement) errors of the same magnitude.

Table 7 was obtained with all errors together, at the acceptable level for each, as follows:

Fixed incoming beam steering error:

$$(x_{orb}^{(in)}, x_{orb}^{'(in)}, y_{orb}^{(in)}, y_{orb}^{'(in)}) = (0.5, 0, 0.5, 0) [mm/mrad];$$

Beam mismatch: $\Delta \beta_x^{(in)}/\beta_x^{(in)} = \Delta \beta_y^{(in)}/\beta_y^{(in)} = 0.1;$
Quadrupole misalignment: $\sigma_x = \sigma_y = 250 \ \mu m;$
Quadrupole powering errors: $\Delta k_1/k_1 = 1 \times 10^{-3};$
Monitor misalignment: $\sigma_{x^{mon}} = \sigma_{y^{mon}} = 250 \ \mu m;$

Orbit correction: as outlined above.

The largest A-values (A > 9.5) in Table 7 correspond to a few seeds (1-3 out of 40 for several different seed

Table 6: Monitor alignment $[\mu m]$

$\sigma_{x^{mon}} = \sigma_{y^{mon}}$	200	400	
$max_{10} A/A_x/A_y$	8.8 / 8.4 / 8.2	9.3 / 8.2 / 9.1	
$ave_{10} A/A_x/A_y$	8.7 / 7.8 / 8.1	9.0 / 7.8 / 8.3	

Table 7: All errors together.

All jaws $\sigma_{x^{mon}} = \sigma_{y^{mon}} = 0.25 \text{ mm}$			
$max_{40} \hat{x}_{orb} / \hat{y}_{orb}$ [mm]	1 / 0.9		
$max_{40} \hat{x}_{orb}^{jaw} / \hat{y}_{orb}^{jaw}$	0.4 / 0.4		
$max_{40} A/A_x/A_y$	10.1/9/9		
$ave_{40} A/A_x/A_y$	9.2 / 8.1 / 8.4		
max ₄₀ x _{orb} ^{end} /x _{orb} ^{'end} /y _{orb} ^{end} /y _{orb} ^{'end}	0.1/5/0/6		
[mm] / [µrad]			
max. corrector [μrad]	26		
$\sigma_{x^{mon}} = \sigma_{y^{mon}} = 0.1 \text{ mm at jaws } 8,9$			
$max_{40} A/A_x/A_y$	9.5 / 8.8 / 8.9		
$ave_{40} A/A_x/A_y$	9.2 / 8. / 8.4		

sequences), for which the random orbit and jaw displacements add up at some jaws. Most critical appear to be jaws 8 and 9 (spaced \sim 3 m apart) located in a region with a low horizontal beta function. Setting the monitor error at these jaws to $100~\mu m$ decreases the difference between maximum and average A-values from σ to $0.5~\sigma$. Table 8 demonstrates this for three beam steering errors.

Table 8.

steering error	rms monitor error 0.25 mm			or error=0.1 mm ws 8 and 9
Citor	$max_{40}A$	$ave_{40}A$	$\begin{array}{ c c c c c c c c c c c c c c c c c c c$	
0.5	10.1	9.2	9.5	9.2
0.3	10.1	9.2	9.4	9.1
0.1	9.9	9.1	9.4	9.1

4 CONCLUSIONS

We have found that the following combined misalignments and errors lead to less than 1σ increase in the maximum amplitude A of escaping particles:

- 1) fixed incoming beam steering errors below 0.5 mm in both transverse planes (with zero initial angles);
- 2) monitors and quadrupoles randomly displaced 250 μ m rms in each transverse direction with respect to the central axis of the primary jaws (with the exception of jaws 8 and 9, where the maximum monitor error used was 100 μ m);
- 3) incoming beam mismatch below 10%;
- 4) quadrupole powering errors below 10^{-3} .

Under these conditions the local correction has only a small effect on the rest of the ring – the exit orbit displacement is zero and the exit angle < 0.01 mrad.

- D. Kaltchev, M. K. Craddock, R.V. Servranckx and J.B. Jeanneret, *Proc. PAC97, Vancouver*, ed. M. Comyn et al. (IEEE, 1998) p. 153; CERN LHC Project Report 134 (1997).
- [2] R.V.Servranckx, *User's Guide to the Program Dimad*, TRIUMF Design Note, TRI-DN-93-K233, (1993).

OPTICS SOLUTIONS FOR THE COLLIMATION INSERTIONS OF LHC

D.I.Kaltchev, M.K.Craddock¹, TRIUMF, 4004 Wesbrook Mall, Vancouver, B.C., Canada V6T2A3 J.B.Jeanneret, A.Verdier, CERN, CH-1211 Geneva 23, Switzerland

Abstract

While the two collimation insertions in the LHC must have similar basic layouts and match to almost identical dispersion suppressors to respect the geometry of the existing tunnel, their different roles impose opposite requirements on the normalized dispersion within them. For betatron collimation it must be near zero, while for momentum collimation it must have a peak at the location of the primary collimator, immediately after the dispersion suppressor. The insertion lattice solution found for the latter case requires up to 30% asymmetry in the quadrupole gradients (in line with the current trend in LHC lattice development to break the exact antisymmetry within insertions). To achieve this using twin-aperture warm quadrupoles, the modules making up each quadrupole will be wired in such a way that the two beams still see the same sequence of focusing fields. We describe the optimum setup, flexibility and collimation quality for the two insertions.

1 INTRODUCTION

In the LHC, composed of superconducting magnets in which proton beams of both high energy and high current will be stored, the local power deposition associated with beam losses will be larger than the magnet quench level by several orders of magnitude [1],[2]. In addition the large size of the ring and the need for high magnetic field requires keeping the geometrical aperture (defined by the vacuum chamber) to a bare minimum. Not far outside the dynamic aperture the transverse motion of the particles becomes chaotic and can form a primary halo diffusing towards the geometrical aperture. The transverse extent of the halo is kept below the chaotic limit by absorbing these protons in primary collimators made of metallic blocks, called jaws below. At all energies proton absorption in the primary jaws is far from complete [2]. Protons which are not absorbed may be scattered elastically off the jaw, thus forming a secondary halo which can also induce quenches. Secondary jaws are therefore necessary to limit the extent of the secondary halo to a value smaller than the geometrical aperture. In the LHC, both betatron and momentum collimation are needed.

For colliding beams, beam-beam induced non-linearities, combined with residual magnetic imperfections of the quadrupoles in the experimental insertions, limit the dynamic aperture to $A_{dyn} \sim 6$ –10 in units of σ_{β} , the rms beam radius. The flux of protons diffusing outside this amplitude is estimated to be $\dot{n} \sim 3 \times 10^9 \ \mathrm{p \ s^{-1}}$ [1]. Most of these protons might touch the vacuum chamber at a single aperture limit, with the energy release spread longitudi-

nally by the hadronic shower process over $l_{shower} \approx 1$ m. In these conditions the local quench level is reached with $\dot{n}_q \sim 10^6$ p s⁻¹m⁻¹[2]. At ramping, rf-untrapped protons are not accelerated and migrate slowly towards the vacuum chamber. The flash of losses lasts $\Delta t \leq 1$ s, a time scale fixing the transient quench level at $\Delta n_q = 2.5 \ 10^{10}$ p m⁻¹. For a stored intensity $N_p = 3 \ 10^{14}$ protons with 5% off-bucket, the intensity of the flash is $\Delta n = 1.5 \ 10^{13}$ p [2].

A very efficient collimation system is therefore needed in both cases. It has been shown [2] that two-stage collimation is adequate and offers a good safety margin.

2 REQUIREMENTS FOR THE OPTICS

2.1 Betatron collimation

With an approximately circular normalized aperture, the primary halo must be intercepted by three primary jaws forming an octagonal primary aperture of inscribed radius n_1 . It is shown in [3] that the secondary halo can be cut close to the secondary collimator aperture $A_{sec} = n_2$ if, for each primary, four secondary jaws are installed at welldefined correlated betatronic phase advances μ_x and μ_y relative to the primary jaws. The long straight sections of LHC offer a phase advance $\Delta \mu_{x,y} \approx 2\pi$, which proved to be insufficient to satisfy the ideal phase conditions for the twelve secondary jaws. With the code DJ [4][5], various optics were studied, the present best result for a ratio $n_2/n_1 = 7/6$ being $A_{sec} = 1.2n_2 = 1.4n_1$. With a ring aperture $A_{ring} = 10$ (including tolerances, optical errors and momentum spread) and using the safe condition $A_{sec} < A_{ring}$, the allowed primary aperture is therefore $n_1 \leq A_{ring}/1.4 = 7.1$, a value which is adequate at both injection and collision beam energies.

2.2 Momentum collimation

In contrast to the betatron halo, which may drift away from the beam in all transverse directions, momentum losses in a ring with only horizontal dispersion are concentrated in the horizontal plane. Off-bucket protons lost at ramping keep their initial betatron amplitude [6] and are therefore confined in the range of betatron amplitudes $A_{x,y}\approx 2$. It is therefore sufficient to use a single horizontal primary collimator, with its four associated secondary collimators. Their phase advances relative to the primary jaw are given in Table 1 [3]. With the largest momentum offset passing the primary jaw $\delta_c=n_1/\chi_1$ (where the normalized dispersion $\chi_1=D_1/\sqrt{\epsilon\beta}$), the secondaries limit the horizontal betatron amplitude to $\approx \sqrt{n_2^2-n_1^2}$. In the arc of a ring, the aperture limit for a particle with momentum offset is located near horizontally focusing quadrupoles, where both

Also at Dept. of Physics & Astronomy, UBC, Vancouver, Canada.

 β_x and D_x are at their maximum. The largest horizontal excursions of the secondary halo must fit the arc aperture, i.e. $A_{x,\beta}+D\delta_p=N_{x,arc}$.

The smaller number of correlated phase advances for the secondary collimators makes solution easier than in the betatronic case, but a large normalized dispersion χ_1 (or $\eta_1 = D_1/\sqrt{\beta}$) is needed at the primary collimator. The value of η_1 depends mainly on the ring aperture $A_{ring}(\delta_p = 0)$ and on the maximum dispersion η_{arc} . We use [3]

$$\eta_1(n_1) = \frac{n_1 \eta_{arc}}{A_{ring}(\delta_p = 0) - (n_2^2 - n_1^2)^{1/2}}.$$
 (1)

In LHC, with $A_{ring}(\delta_p=0)=12$, $\eta_{arc}=0.2~{\rm m}^{1/2}$ (with optical errors) and $n_1=7$, $\eta_1=0.19~{\rm m}^{1/2}$ is needed [7]. The geometry of the dispersion suppressor connecting the arcs and the straight section is fixed by the existing tunnel and therefore offers little flexibility for altering the dispersion function in the insertion, which is suppressed for the nominal tune. The combination of dispersion and phase constraints therefore requires a lot of flexibility in the straight section itself where the quadrupoles can be located with more freedom.

Table 1: Secondary collimator locations μ_x and μ_y relative to the horizontal primary jaw of the momentum cleaning insertion and their X-Y azimuthal orientations α_{Jaw} . The angle ϕ is the scattering angle (projected on to the XY plane) for which the secondary does the most efficient cut; $\mu_0 = \arccos(n_1/n_2)$.

φ	μ_x	μ_y	α_{Jaw}
0	μ_o	-	0
π	$\pi - \mu_o$	-	0
$\pi/2$	π	$3\pi/2$	μ_o
$-\pi/2$	π	$3\pi/2$	-110

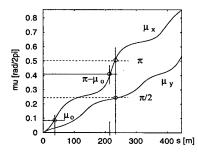
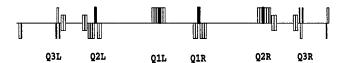


Figure 1: The phase advances along the momentum cleaning insertion relative to the location of the primary collimator. The three vertical marks indicate the optimum phase advances of Table 1.

3 COLLIMATION INSERTION LATTICES

So that the two beams in the LHC experience exactly the same sequence of focusing fields in a FODO lattice composed of twin-aperture quadrupoles, these are arranged left-right (L-R) antisymmetrically about the midpoint of each insertion. Thus the six straight-section quadrupoles QiL, QiR (i=1,2,3 - see Fig. 2 (top)) nominally have gradients $K_i^L = -K_i^R$ (these i values differ from the official LHC



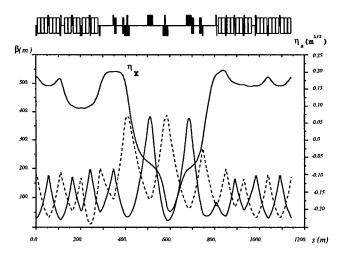


Figure 2: Momentum cleaning insertion lattice. Top: straight section layout. Bottom: beta functions and normalized dispersion.

ones). This condition was found too restrictive for both betatron and momentum collimation, and so new optics have been devised for the cleaning insertions whose basic feature is to give the quadrupoles an increased left-right symmetric component $(K_i^L + K_i^R)/2$. Other changes from the optics reported in [8] include replacement of the strongest warm quadrupoles Q3L and R by cold quadrupole groups, and repositioning of the separation magnets and the primary jaws to a new location between Q3L and Q2L. The latter allows neutral and low-momentum charged particles to be removed from the beam axis more efficiently.

3.1 Momentum collimation

The advantages of the new optics over an exactly antisymmetric setting are that they allow: (1) lower over-all focusing strengths, both for the straight section and dispersion suppressor quadrupoles, and (2) a higher normalized dispersion peak at the primary collimator, η_x =0.19-0.22 (Fig. 2, bottom), as momentum collimation requires. The suggested explanation for this is that with antisymmetry broken, the Twiss function values at the symmetry point can be set further away from the exact antisymmetry condition $\beta_{x,y}^{*L} = \beta_{y,x}^{*R}$, $\alpha_{x,y}^{*L} = -\alpha_{y,x}^{*R}$ (this condition was never forced as a constraint). With $K_i^L = -K_i^R$ (i=1,2,3), the best result for the normalized dispersion was $\eta_x = 0.16$ [8].

The four quadrupoles QiL and QiR (i=1,2) are in fact each composed of 6 warm quadrupole modules 3 m long, based on the "two channels in one bore" design concept [1]. Normally, these modules are wired so that the fields felt by the two beams are exactly reversed, one seeing an F quadrupole, and the other a D (as assumed for the antisymmetric lattice described above). Small deviations from equal powering of the two channels are possible, but are

Table 2: Quadrupole gradients (as % of maximum allowed) and normalized dispersion at the primary collimator for the momentum cleaning insertion matched to four arc cell tunes

$ u_x^{a.cell}$.2515	.2649	.28	.24
$ u_y^{a.cell}$.2401	.2377	.24	.20
K_1^A	81	84	84	83
K_1^S	54	49	50	57
K_2^A	-88	-86	-86	86
K_2^{S}	70	46	62	61
K_3^L	80	83	-74	-75
K_3^R	-74	-75	83	81
K_i^L	73	-17	55	39
for left	83	66	43	96
dispersion	45	38	71	25
suppressor	11	10	-5.5	21
and	-67	-81	-80	-1
2 arc trim	-25	-11	-29	8
quadrupoles	-14	-76	-63	-92
K_i^R	-75	-93	90	-95
for right	68	-74	-82	84
dispersion	-74	-67	-51	-62
suppressor	53	-47	12	-13
and	-7	20	3.5	20
2 arc trim	74	15	52	9
quadrupoles	4	-58	12	-23
η_x at prim. $[\mathrm{m}^{1/2}]$.2	.18	.194	.194
$d\eta_x/d\mu_x~[\mathrm{m}^{1/2}]$	012	042	039	010

limited to 10 - 15%, for reasons of field quality.

To achieve larger $|(K_i^L + K_i^R)/K_i^R|$ ($\sim 30\%$ is needed), while preserving identical straight-section optics for the two beams and also good field quality in the warm modules, a second kind of module is introduced, wired so that each beam sees the same field, both channels acting as F quadrupoles. These new "symmetric" modules (solid black in Fig. 2) are positioned near the middle of each quadrupole assembly, where they are most effective.

3.2 Matching and Flexibility

The cleaning insertions were matched to the arcs using MAD [9] with a total of 21 independent variables: 18 quadrupole strengths (2 K_i^S for the symmetric modules, 2 K_i^A for the antisymmetric ones, 2 for the cold Q3L and R, and 12 for the dispersion suppressor (DS) trims) plus the 3 positions of the straight-section quadrupoles. The most important constraint was the need for a maximum flattopped dispersion peak at the primary collimator. Table 2 shows the quadrupole strengths needed to match the momentum cleaning insertion to the arcs, while optimizing the normalized dispersion η_x and its derivative $d\eta_x/d\mu_x = (\alpha_x D_x + \beta_x D_x')/\sqrt{\beta_x}$. Four cases are shown, for different tunes of the arc cells: the first column is for the nominal tune, while the other three assure cancellation of various nonlinear resonance driving terms. The tune advances for



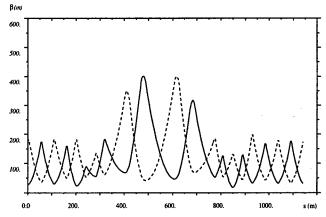


Figure 3: Betatron cleaning insertion lattice.

the nominal case are shown on Figure 1. For all four cases the quadrupole strengths are within limits, η_x is sufficiently high and $|d\eta_x/d\mu_x|$ is sufficiently small.

3.3 Betatron collimation

The betatron cleaning section (Figure 3) has in general preserved the optics described in [5]. As for momentum cleaning, symmetrically powered quadrupole modules help to increase flexibility and reduce quadrupole strengths.

4 CONCLUSIONS

By using the two-in-one warm quadrupoles of the collimation insertions in a flexible way, we have formulated a two-stage momentum cleaning insertion which satisfies the LHC machine requirements and which is also, to our knowledge, the first fully worked out design for any machine.

- [1] Large Hadron Collider, CERN/AC/95-05(LHC) (1995).
- [2] N. Catalan Lasheras, G. Ferioli, J.B. Jeanneret, R. Jung, D.I. Kaltchev and T. Trenkler, *Proc. Symp. Near Beam Physics*, *Fermilab*, 1997, edited by D. Carrigan and N. Mokhov, p. 117, and CERN LHC Project Report 156 (1998).
- [3] J.B. Jeanneret, Phys. Rev. ST Accel. Beams, 1, 081001 (1998).
- [4] D.I. Kaltchev, M.K. Craddock, R.V. Servranckx and J.B. Jeanneret, *Proc. EPAC96*, *Sitges*, 1996, ed. S. Myers et al., p. 1432 (IOP, 1996); CERN LHC Project Report 37 (1996).
- [5] D.I. Kaltchev, M.K. Craddock, R.V. Servranckx and J.B. Jeanneret, *Proc. PAC'97, Vancouver*, ed. M. Comyn et al., p. 153 (IEEE, 1998); CERN LHC Proj. Rept. 134 (1997).
- [6] N. Catalan Lasheras, CERN LHC Proj. Rept. 200 (1998).
- [7] J.B. Jeanneret, CERN LHC Project Note 115 (1997).
- [8] D.I. Kaltchev, M.K. Craddock, R.V. Servranckx and T. Risselada, Proc. EPAC98, Stockholm, p. 353 (IOP, 1998).
- [9] H. Grote and F.C. Iselin. MAD Program Version 8.16, User's Reference Manual, CERN/SL/90-13(AP) (1995).

CONSEQUENCES OF THE DIRECT SPACE CHARGE EFFECT FOR DYNAMIC APERTURE AND BEAM TAIL FORMATION IN THE LHC

F. Ruggiero, F. Zimmermann, CERN, Geneva, Switzerland

Abstract

The direct space charge detuning at the centre of a nominal LHC proton bunch is about 10^{-3} at injection energy. Owing to their slow synchrotron motion, particles with small betatron amplitudes sample a varying electric charge density within the bunch and thus experience a tune modulation at twice the 66 Hz synchrotron frequency. In conjunction with magnet nonlinearities, such tune modulation may give rise to particle diffusion to large betatron amplitudes and eventually to particle loss. Coherent quadrupole oscillations, caused, e.g., by injection mismatch, resonantly perturb the single-particle motion via the space-charge force, and can cause a rapid growth in the transverse amplitude. Using the results of numerical and analytical investigations, we show that these space-charge effects alone will not affect the LHC performance.

1 INTRODUCTION

With an injection energy of 450 GeV, space charge effects at the LHC would appear to be negligible. However, there are two mechanisms by which the direct space charge force could cause a modulation of the betatron tunes, and, thereby, degrade the dynamic aperture or generate large-amplitude beam tails: First, synchrotron oscillation in conjunction with the longitudinal bunch profile induces a tune modulation at twice the synchrotron frequency, with a modulation amplitude comparable to the space-charge tune shift. Second, if the beam is injected with a betatron mismatch, the oscillation of the beam size, prior to filamentation, will also result in a tune modulation, at twice the betatron frequency.

2 SPACE CHARGE FORCE

Considering an optical lattice with vertical normalized quadrupole gradient $K_y(s)$, the equation of vertical motion for a single particle can be written as $y'' = -K_y y + F_{sc,y}(x,y)$, where a prime denotes the derivative with respect to the longitudinal position s,x is the horizontal coordinate, and $F_{sc,y}$ the vertical space charge force. In linear approximation (for $y \ll \sigma_y, x \ll \sigma_x$, where σ_y and σ_x are the transverse rms beam sizes), this force is

$$F_{sc,y}(x,y) pprox rac{2F_{dist}r_p\lambda(z)}{\gamma^3\sigma_y(\sigma_x + \sigma_y)} y$$
 (1)

The function $\lambda(z) = N_b \exp(-z^2/(2\sigma_z^2))/(\sqrt{2\pi}\sigma_z)$ denotes the longitudinal distribution assumed to be Gaussian, N_b the bunch population, and γ the Lorentz factor. The factor F_{dist} depends on the transverse distribution: $F_{dist} = 1$ for a Gaussian, 1/2 for a KV (uniform) distribution [1], and

Table 1: LHC injection parameters [3].

parameter	symbol	value
circumference	C	26.7 km
beam energy	E_b	450 GeV
particles per bunch	N_b	10^{11}
normalized transv. emittance	ϵ_N	$3.75~\mu\mathrm{m}$
rms bunch length	σ_z	13 cm
average beta function	$oldsymbol{eta}$	90 m
rms energy spread	δ_{rms}	4.7×10^{-4}
synchrotron tune	Q_s	0.006

2/3 for a parabolic distribution [2]. The space-charge tune shift at the bunch center (z = 0) is

$$\Delta Q_y \approx \frac{Cr_p F_{dist} N_b}{4\pi \gamma^2 \epsilon_N \sqrt{2\pi} \sigma_z} \tag{2}$$

where β designates the average vertical beta function, and ϵ_N the transverse normalized emittance. Using LHC parameters (Table 1), we find $\Delta Q_y \approx 1.1 \times 10^{-3} \, F_{dist}$.

At larger amplitudes, the space-charge force is nonlinear. For a flat Gaussian distribution this force can be calculated in terms of the complex error function [4]. Expressions for the parabolic and for the uniform distribution can be found in Ref. [5]. Via $\lambda(z)$ the space charge force, Eq. (1), depends on the coordinate z. Therefore, a particle performing large synchrotron oscillations and small transverse oscillations will experience a modulation of its betatron tune of amplitude ΔQ_y , due to the harmonic variation in z. A tune modulation of comparable magnitude will also occur in the horizontal plane.

3 SYNCHROTRON OSCILLATIONS

The effect of the tune modulation due to space-charge force and synchrotron oscillations, was studied by particle tracking with MAD [6], for the same LHC model as described in [8]. In the simulation, we launched twin particles at different transverse initial amplitudes. From their separation as a function of time we computed the Lyapunov exponent, which is a measure of potential instability. The longitudinal amplitude was chosen as $1.6\sigma_{\delta}$ (equal to $\delta=7.5\times10^{-4}$, or three quarters of the rf bucket half size). The space charge force was modeled as a tune modulation of amplitude up to ΔQ_y at twice the synchrotron frequency, which was generated by harmonically varying the strength of the two main quadrupole families. In general, tune modulation is known to increase the chaotic (unstable) region of phase space [7]. However, comparing the Lyapunov exponents

obtained with and without the additional tune modulation reveals no significant effect for these parameters (see Fig. 1). The observed weak effect is consistent with the results of chromaticity scans [8], and may be attributed to the absence of simultaneous modulation at other frequencies.

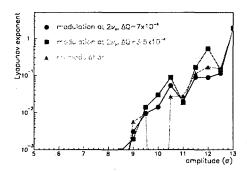


Figure 1: Lyapunov exponent computed by tracking over 5×10^4 turns as a function of the initial betatron amplitude, comparing cases with and without an additional tune modulation that represents the effect of space charge and synchrotron oscillations.

4 QUADRUPOLE OSCILLATIONS

The equation governing the evolution of the second moment $\sigma_y = \sqrt{\langle y^2 \rangle}$ (the angular brackets denote an average over the beam distribution) follows from the single-particle equation of motion [9]:

$$\sigma_y'' + K_y \sigma_y - \frac{\epsilon_{y,rms}^2}{\sigma_y^3} = \frac{2F_{dist}r_p \lambda(z)}{\gamma^3(\sigma_x + \sigma_y)}$$
(3)

The term on the right hand side is due to the space charge, and we have only taken into account the linear component of the space-charge force. Consider a beam injected with a vertical (betatron) mismatch of amplitude $\Delta\sigma_y(0)$ at s=0. The total beam size is the sum of the unperturbed (matched) value σ_{y0} and the perturbation: $\sigma_y = \sigma_{y0} + \Delta\sigma_y$. The equation of motion for the perturbed beam size is obtained by linear expansion around σ_{y0} :

$$\Delta \sigma_y'' + \left(K_y + 3 \frac{\epsilon_{y,rms}^2}{\sigma_{y0}^4} + \frac{2F_{dist}r_p\lambda(z)}{\gamma^3(\sigma_x + \sigma_{y0})^2} \right) \Delta \sigma_y = 0$$
(4)

For simplicity, we now assume a smooth focusing, replacing K_y by $1/\beta^2$. Also using the relation $\sigma_{y0}^2/\beta = \epsilon_{y,rms}$, which holds for a matched beam, and neglecting the spacecharge induced tune shift, we find the approximate solution $\Delta\sigma_y(s)\approx\Delta\sigma_y(0)\cos2s/\beta$. Next, we can insert the analytical solution for the oscillation of the beam rms size into the equation of motion for a single particle above, replace σ_y by $\sigma_{y0}+\Delta\sigma_y(s)$, and introduce the new 'time' unit $u=s/\beta$. We assume that the beam is perfectly matched in the other (horizontal) plane, that the variation $\Delta\sigma_y$ is small compared with the matched beam size, and, for simplicity

also that $\sigma_{y0} \approx \sigma_{x0}$ (which we call σ_0). Neglecting the shift in betatron tune, we finally obtain

$$\frac{d^2y}{du^2} = (-1 - D\cos 2u)y$$
 (5)

where

$$D \equiv \frac{3}{2} \frac{F_{dist} r_p \beta^2 \lambda(z)}{\gamma^3 \sigma_0^2} \frac{\Delta \sigma_y(0)}{\sigma_0}$$
 (6)

For LHC parameters and a Gaussian distribution: $D \approx$ $5 \times 10^{-5} \ \Delta \sigma_v(0) / \sigma_{v0}$. Equation (5) is Mathieu's equation. With Q denoting the total betatron tune, the tune modulation amplitude corresponding to D is $\Delta Q \approx \frac{1}{9}DQ \approx$ $0.0015 \, \Delta \sigma_{\nu}(0) / \sigma_{\nu 0}$. The solution of the Mathieu equation is of the Floquet type: $F_{\nu}(u) = e^{iu\nu}P(u)$, where P(u)is a periodic function of period π . For our parameters, ν has an imaginary component, and one solution is exponentially growing (the other shrinking). The exponent ν can be determined numerically (see [12]). With 20% accuracy we find that $e^{i\pi\nu} \approx 1 + D$ over a wide range of parameter values (e.g., for D between 10^{-5} and 10^{-1}). The growth per turn is $(1+D)^{2Q} \approx (1+2DQ)$, and the exponential growth time $\tau \approx C/(c[\ln(1+2DQ)]) \approx C/(2cDQ)$, with C the circumference, and c the speed of light. This relation is illustrated in Fig. 2, for the LHC parameters $2DQ \approx 0.006 \Delta \sigma_y(0)/\sigma_{y0}$ (using $Q \approx 63$). With an initial mismatch of 50%, the exponential growth time is of the order of 40 ms, while for 25% mismatch it is 60 ms.

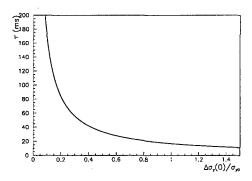


Figure 2: Exponential growth time as a function of the mismatch $\Delta \sigma_y(0)/\sigma_{y0}$. For the LHC 10 ms is about 100 turns.

Emittance growth and the generation of beam halo in proton linacs [10] and synchrotrons [11] has been studied by computing the trajectories of test particles inside and outside of a beam core whose dynamics is calculated independently. Following the same recipe, we numerically solved the single-particle equation of motion, using either the linear force of Eq. (1), or the full nonlinear force. The rms beam sizes σ_y , σ_x were modulated according to $\sigma_x \approx \sigma_y \approx \sigma_{y0} + \Delta \sigma_y(0) \cos 2s/\beta$. When the space charge kick for individual particles was calculated, we subtracted the linear force obtained for $\sigma_y = \sigma_{y0}$, since this would lead to the same tune shift for both the core and the individual test particles. Several hundred particles

were uniformly distributed up to $\pm 2\sigma$ with random betatron phase. With the linear force of Eq. (1) the simulation yields a mean-amplitude growth rate of about $\tau \approx 35$ ms for $\Delta \sigma_y(0)/\sigma_{y0}=50\%$, consistent with our analytical estimate. For the nonlinear force, the simulated growth rate is about 4 times slower (140 ms). The maximum amplitude over all test particles shows an oscillation whose phase is $\pi/2$ behind the core oscillation (each at twice the betatron frequency). Thus, the particle-core simulation is not self-consistent, since, in reality, the quadrupole oscillation would be affected by the growth of the individual particle amplitudes.

More realistic simulations can be performed with the program MAD, which was modified so that, at each lattice element, it applies a horizontal and vertical space-charge kick. The space-charge kick is calculated from the transverse rms spot size of a group of tracked macroparticles representing the beam. In Fig. 3 we depict typical results, that were obtained for a bunch population of $N_b=10^{12}$, 10 times the nominal, and a linear space-charge force. The MAD simulation shows growing or shrinking betatron amplitudes depending on the phase of the betatron oscillation with respect to the mismatch. The growth stops, once the quadrupole oscillation has vanished.

Without systematic octupole field components, the quadrupole oscillation is damped mainly by filamentation due to the space-charge tune spread. Only considering the variation of the space-charge tune shift with longitudinal position, the time constant for this filamentation is

$$\tau_{sc} \approx \frac{1}{2\pi\sqrt{2}\sqrt{\frac{1}{\sqrt{3}} - \frac{1}{2}}\Delta Q_y} \approx \frac{1}{2.5\Delta Q_y}$$
 (7)

In our example, it evaluates to 36 turns, in good agreement with the simulation. Interestingly, since both damping and growth rates are proportional to the charge per bunch, the final emittance growth resulting from the space-charge force is independent of the bunch charge. For smaller bunch charges other filamentation mechanisms, e.g., due to nonlinear magnetic fields, become effective, leading to an enhanced damping of the quadrupole oscillation (Fig. 4).

5 CONCLUSION

Tune modulation due to direct space-charge force along with synchrotron oscillations does not significantly increase the chaotic region in phase space. While a quadrupole-mode oscillation may cause fast amplitude growth rates, in practice this oscillation vanishes rapidly via filamentation due to space-charge induced tune spread and due to magnet nonlinearities. Thus, it is unlikely to result in serious emittance growth, for the LHC.

- [1] I.M. Kapchinskij and V.V. Vladimirskij, 2nd Int. Conf. on High Energy Accel. CERN, p. 274 (1959).
- [2] E. Karantzoulis, J. Maidment, DESY HERA 86-01 (1986).

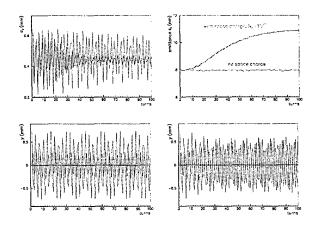


Figure 3: MAD tracking results using 1000 macroparticles, for an injection mismatch into the LHC of $\Delta\sigma/\sigma_{y0}\approx 0.5$ (or $\beta/\beta_0=2.6$). Top left: vertical beam size vs. time, with (solid) and without (dotted) space charge force; top right: emittance vs. time with (solid) and without (dotted) space charge; bottom left: vertical trajectories launched at 0.6σ of the injected beam with either initial offset (dotted) or initial slope (solid), without space charge; bottom right: same as the left figure but with space charge. The space-charge force was calculated in linear approximation, for $N_B=10^{12}$. Magnet octupole components were not included.

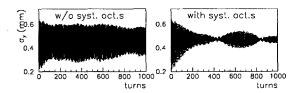


Figure 4: Vertical beam size vs. time, when the systematic octupole field components in the dipole magnets are corrected (left) or uncorrected (right).

- [3] LHC Conceptual Design Report, CERN/AC/95-05 (1995).
- [4] M. Bassetti and G.A. Erskine, CERN-ISR-TH/80-06 (1980).
- [5] M. Furman, Am. J. Phys. 62 (12), p. 1134 (1994).
- [6] H. Grote, C. Iselin, CERN-SL-90-13-AP-REV (1991).
- [7] M. Giovannozzi, et al., LHC Project Report 137 (1997).
- [8] Y. Papaphilippou, et al., this conference (1999).
- [9] A.W. Chao, "Physics of Collective Beam Instabilities in High Energy Accelerators", Wiley (1993).
- [10] J.S. O'Connell, et al., PAC93 Washington; R.A. Jameson, PAC93 Washington; J.-M. Lagniel, NIM A 345, p. 46 (1994);R. Gluckstern, et al., Phys. Rev. E 58, p. 4977 (1998).
- [11] S. Machida and M. Ikegami, KEK 98-189 (1998); K.Y. Ng and S.Y. Lee, FERMILAB-Conf-98/344 (1998).
- [12] M. Abramowitz and I. Stegun (eds.), Handbook of Mathematical Functions, Dover (1972).

ELECTRON CLOUD AND BEAM SCRUBBING IN THE LHC

O. Brüning, F. Caspers, I.R. Collins, O. Gröbner, B. Henrist, N. Hilleret*, J.-M. Laurent, M. Morvillo, M. Pivi, F. Ruggiero, X. Zhang, CERN, Geneva, Switzerland

Abstract

An adequate dose of photoelectrons, accelerated by low-intensity proton bunches and hitting the LHC beam screen wall, will substantially reduce secondary emission and avoid the fast build-up of an electron cloud for the nominal LHC beam. The conditioning period of the liner surface can be considerably shortened thanks to secondary electrons, provided heat load and beam stability can be kept under control; for example this may be possible using a special proton beam, including satellite bunches with an intensity of 15-20% of the nominal bunch intensity and a spacing of one or two RF wavelengths. Based on recent measurements of secondary electron emission, on multipacting tests and simulation results, we discuss possible 'beam scrubbing' scenarios in the LHC and present an update of electron cloud effects.

1 INTRODUCTION AND SUMMARY

An effective solution to reduce the heat load due to electron cloud build-up in the LHC dipoles is a beam screen with ribbed surface and reduced reflectivity [1], provided the maximum secondary electron yield $\delta_{\rm max}$ can be kept below a critical value that for nominal LHC parameters is about 1.3. For example a 10% reflectivity gives an acceptable heat load of about 200 mW/m for $\delta_{\rm max}=1.2$, assuming a photoelectron yield $\delta_{\gamma e}\simeq 0.2$ and a characteristic energy of 5 eV for the secondary electrons. However for a maximum secondary yield $\delta_{\rm max}=1.8$, i.e. above the critical value, the heat load remains around 5 W/m inspite of the lower reflectivity.

Secondary emission can be reduced by special coatings or by an adequate electron dose. As discussed in the following two sections, an electron dose of 1 mC/mm² is sufficient to lower the maximum secondary yield below the critical value of 1.3. Therefore 'beam scrubbing' scenarios are under study to condition the liner surface in the shortest possible time, while keeping the heat deposition within acceptable bounds. For example the nominal bunch intensity of 10^{11} protons can be reduced by a factor 4 or the nominal bunch spacing of 25 ns can be doubled; in both cases the heat load for $\delta_{\rm max}=1.8$ becomes about 400 mW/m at 7 TeV and can be further reduced by stopping the ramp at an intermediate energy. Another solution

to increase the critical yield during the conditioning period, possibly more effective in terms of beam stability control, is to have satellite bunches with an intensity of 15-20% of the nominal bunch intensity and a spacing of 5 ns (two RF wavelengths). Such satellites behave as clearing bunches and remove slow secondary electrons before the next nominal bunch arrives; for reduced reflectivity the corresponding critical yield can be increased to almost a value of two.

To get a rough estimate of the minimum time required for surface conditioning², let us assume a maximum heat load of 200 mW/m, compatible with cooling, and an average electron energy around 200 eV. This is consistent with simulation results discussed in Section 4 for a nominal LHC proton beam with satellite bunches. The corresponding linear flux of electrons bombarding the screen surface is $6 \times 10^{15} \, \mathrm{s^{-1}m^{-1}}$. Since a meter of LHC beam screen has a surface of $1.25 \times 10^5 \, \mathrm{mm^2}$, the electron dose accumulated per hour is $\frac{200 \, \mathrm{mW/m}}{200 \, \mathrm{eV}} \, \frac{\mathrm{m}}{1.25 \times 10^5 \, \mathrm{mm^2}} \, 1.6 \times 10^{-19} \, C \simeq 8 \times 10^{-9} \, \frac{C}{\mathrm{mm^2 s}}$ and the beam scrubbing time required to accumulate the required electron dose of 1 mC/mm² is about 35 hours.

2 MEASUREMENTS OF SECONDARY ELECTRON YIELD

The secondary electron yield $\delta_{\rm SEY}$ of metals is depending drastically on the composition and the roughness of the surface. It is therefore very important to measure the real $\delta_{\rm SEY}$ of technical materials used in accelerators such as the copper colaminated on stainless steel, the proposed material for the LHC beam screen. The $\delta_{\rm SEY}$ of a copper surface can be modified by surface treatments like titanium nitride deposition [3], air oxidation [4] or by in situ electron bombardment. This latter effect was first reported by M. Lavarec et al in Ref. [5]. Further investigation carried out at CERN have shown that this effect also exists for stainless steel, aluminium and copper. Figure 1 shows the variation of $\delta_{\rm SEY}$ as a function of the primary electron energy, for a sample of copper colaminated on stainless steel, before and after electron bombardment. This bombardment was made in an unbaked vacuum system at a pressure of 10^{-5} Pa, using 500 eV electrons and corresponded to an electron dose of 5×10^{-3} C/mm². The maximum yield δ_{max} decreased from 2.2 at an electron energy of 300 eV in the initial stage to 1.2 for an electron energy of 450 eV after this bombardment. The variation of δ_{SEY} during the bombardment under similar experimental conditions is shown in Fig. 2. The yield measured at the bombardment energy (respectively

^{*}Email: Noel.Hilleret@cern.ch

¹The corresponding low-frequency inductive impedance, estimated by M. D'Yachkov to a few m Ω , is very small compared to the LHC impedance budget of some 250 m Ω . The high frequency behaviour of the impedance and the parasitic losses for a periodic ribbed (or slotted) surface, especially in connection with a possible surface wave, are being investigated by A. Mostacci; according to preliminary estimates they should be negligible.

²This estimate, independent of reflectivity and photoelectron yield, has been suggested by C. Benvenuti.

500 eV and 100 eV) is plotted as a function of the dose received by the sample. Below a dose of 10^{-6} C/mm², $\delta_{\rm SEY}$ does not change significantly and correponds to the 'true yield' of the surface. For higher doses it decreases towards a stable value reached for a dose greater than 10^{-3} C/mm². The effect is similar for both primary energies of 100 eV and 500 eV. Although not fully understood, this effect can explain, at least partly, the efficiency of the well known procedure of 'RF conditioning' in RF devices. Other experiments have shown that the alteration of the yield is localised to the electron impact region and is permanent under vacuum. Part of the $\delta_{\rm SEY}$ reduction remains after an air exposure and the colour of the copper surface is slightly changed at the location of the beam impact. More investigations are underway to elucidate the origin of this very useful effect.

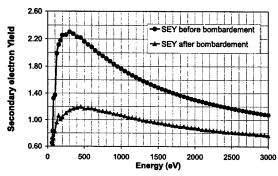


Figure 1: Variation of $\delta_{\rm SEY}$ as a function of the primary electron energy, for a sample of copper colaminated on stainless steel, before and after bombardment with 500 eV electrons, corresponding to a dose of 5×10^{-3} C/mm².

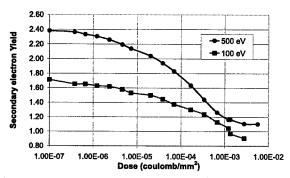


Figure 2: Secondary electron yield measured at the bombardment energy (respectively 500 eV and 100 eV) as a function of the dose received by the sample.

3 MULTIPACTING TESTS

We have investigated beam-induced multipacting by means of a travelling-wave coaxial multi-wire chamber, the electric field produced by a bunched proton beam being simulated by short square RF pulses applied to six equispaced wires parallel to the axis of a 1.4 m long stainless steel vacuum chamber with 100 mm diameter. The output from the

amplifier, driven by a pulse generator, is DC free and a bias voltage has to be applied to the wires to shift the pulses by the desired voltage; the power coming out from the chamber is then absorbed by a line load. Electrons close to the chamber wall are accelerated towards the center of the chamber by the pulsed electric field. They may reach the opposite side of the chamber and produce secondary electrons if their energy is sufficient. Resonance conditions are met if the next pulse is present at that time, and as a result, the electron multiplication grows up exponentially. Multipacting build-up is recorded by a positively biased electron pick-up, consisting of a round button probe with 1 cm diameter. Evidence of multipacting instability in the chamber is given by a fast pressure increase, while a negative current is recorded at the pick-up. In addition a complete suppression of the electron multiplication may be obtained by applying a solenoidal magnetic field with an intensity of only a few gauss. For a fixed pulse amplitude of 140 V and a period of 20 ns, multipacting is observed in a window of pulse widths between 7 and 16 ns. A similar behaviour is measured for the same pulse amplitude and a fixed width of 10 ns, in a window of pulse periods between 17 and 22 ns.

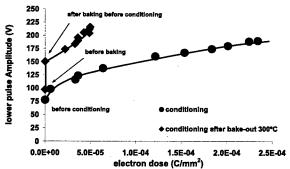


Figure 3: Minimum pulse amplitude required for multipacting as a function of the integrated electron dose: before bake-out (lower curve) or after bake-out at 300°.

Consistently with the results discussed in the previous section, a multipacting intensity decreasing exponentially with time has been monitored by measuring the minimum pulse amplitude needed to trigger the electron multiplication (see Fig. 3). Surface conditioning due to electron bombardment results in a reduction of the secondary emission yield, and the pulse amplitude has to be increased to supply the electrons with sufficient energy to have an average $\delta_{\rm SEY} > 1$ at the wall. After baking the cavity, the minimum pulse amplitude required for multipacting is increased by 50%. In addition, the same cleaning effect is achieved with one order of magnitude less electron dose. The latter is estimated by integrating the current measured by the electron pick-up during multipacting and normalising the accumulated electric charge by the pick-up surface.

An energy spectrum analyzer has been used to measure the energy distribution of the electrons hitting the wall of the chamber during multipacting. Such distribution is peaked around a single energy value and has a typical width of 10 eV. Figure 4 shows the linear dependence of the en-

ergy peak from 40 to 85 eV on the pulse amplitude from 80 to 200 V, then for higher electric fields the electrons are slightly decelerated before they reach the opposite side of the chamber, due to the electric field configuration.

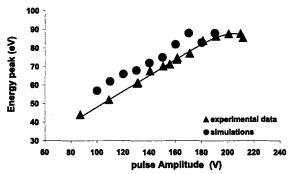


Figure 4: Peak of the energy distribution for the electrons hitting the wall during multipacting as a function of the pulse amplitude: experimental data (triangles) are in relatively good agreement with simulation results (circles).

4 SIMULATION RESULTS

The simulation results shown in Fig. 5 refer to the LHC dipole beam screen and have been performed assuming a photoelectron yield $\delta_{\gamma e} \simeq 0.2$ and a surface reflectivity of $10\%^3$. The maximum secondary electron yield corresponds to a primary electron energy of 300 eV and secondary electrons have a Gaussian energy distribution with 5 eV r.m.s. value and cut-off at 5 sigma. There are 50 slices per bunch and again 50 slices for each inter-bunch gap.

With nominal LHC bunch intensity and spacing, but with satellite bunches at a distance of 2 RF buckets, the heat load for $\delta_{\rm max}=1.8$ is 180 mW/m and the estimated scrubbing time is 43 hours. As shown in Fig. 6 there is a window around 15-20% for the relative intensity of satellite bunches, where the heat load is significantly reduced; the corresponding critical value of $\delta_{\rm max}$ is large (above 1.8). This effect is less pronounced for satellites at a distance of only one RF wavelength. For lower intensities of the satellite bunches, the effect of space charge repulsion is reduced and the heat load increases. For a reduced reflectivity of 2% and a photoelectron yield of 0.1, the heat load becomes only 15 mW/m and the corresponding scrubbing time increases to about 45 days. This is the same time estimated by taking into account only photoelectrons.

- [1] V. Baglin *et. al.*, "Beam-induced electron cloud in the LHC and possible remedies", CERN LHC Project Report 187 (1998) and Proc. EPAC'98, Stockholm (1998).
- [2] M. Furman and G.R. Lambertson, 'The Electron-Cloud Instability in the Arcs of the PEP-II Positron Ring', LBNL-41123/CBP Note-246/PEP-II AP Note AP 97.27 (1998),

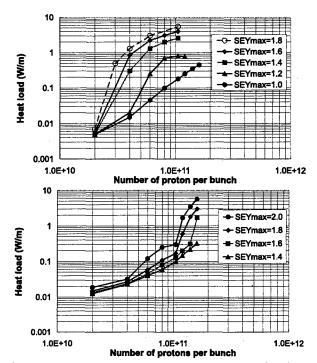


Figure 5: Heat load versus bunch population for different values of $\delta_{\rm max}$ and 10% reflectivity: without (top) and with (bottom) satellite bunches having 20% of the nominal bunch intensity and a spacing of 5 ns.

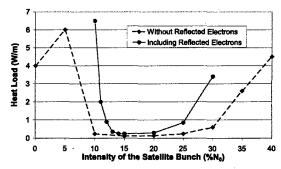


Figure 6: Heat load vs relative intensity of satellite bunches, following nominal LHC bunches at 2 RF wavelengths, with (solid line) or without (dashed line) elastic electron reflection as described in Ref. [2], with $\delta_{\rm max}=1.6$ and 10% reflectivity.

- Proc. MBI'97, KEK, Tsukuba (1997). See in particular Eqs. (4.10) and (4.11).
- [3] E.L. Garwin, F.K. King, R.E. Kirby, "Surface properties of metal-nitride and metal-carbide films deposited on Nb for radio-frequency superconductivity", J. Appl. Phys. **61**, 1145-1153, (1987).
- [4] C. Scheuerlein, I. Bojko, J.L. Dorier, N. Hilleret, "Der Einfluss von Luft auf die Sekundäreelektronenrate von Kupfer" to be published in DPG-Frühjahrstagung des AK Festkörperphysik Münster, 22–26 March 1999.
- [5] M. Lavarec, G. Boquet and A. Septier, "The lowering of the secondary electron emission coefficient of real surfaces due to the primary electron bombardment", Proc. 8th Int. Symposium on Discharges and Electrical Insulation in Vacuum, Albuquerque (1978).

 $^{^3}$ This means that 10% of the photoelectrons are uniformly distributed around the beam screen, while the remaining 90% have a Gaussian angular distribution with an r.m.s. angle of 22.5° from the horizontal plane.

50 TEV HIGH-FIELD VLHC WITH A LOW FIELD INJECTOR*

G. Dugan, Cornell University, Ithaca, NY 14853 M. J. Syphers, Fermilab, PO Box 500, Batavia, IL 60510

Abstract

The 50 TeV very large hadron colliders studied at the 1996 Snowmass workshop were taken to have an injection energy of 3 TeV. As the injection energy increases, the cost and complexity of the final injector increases, while that of the collider decreases. In this paper, we would like to consider the extreme case of a full energy injector. Presumably, this produces the maximum benefit, in terms of technical simplification and cost reduction, for the collider, at the cost of having to build a rather large injector. We consider the specific case of a 50 TeV high-field radiation-damped collider (12.5 T magnets), whose injector is a 50 TeV low-field (2 T magnets) machine. We discuss the general advantages and disadvantages of this approach.

1 INTRODUCTION

The 50 TeV very large hadron colliders studied at the 1996 Snowmass workshop were taken to have an injection energy of 3 TeV. With this injection energy, the 50 TeV ring must have a dynamic range of about 16; this is a reasonable, conservative choice. Existing hadron colliders have dynamic ranges varying from 7 (Tevatron) through 20 (HERA); LHC is planning to have about 16 also. The implicit assumption is that, to minimize the total costs, one should have as low an injection energy as possible. This strategy certainly minimizes the cost of the injector, but the cost of the collider may be higher, since it must operate over an extended dynamic range. It is not obvious that minimizing the cost of the injector serves to minimize the cost of the total project.

If one begins to consider a higher energy injector, it is natural to consider an injector which shares the same tunnel as the collider. This approach was considered in some early SSC studies[1]. Let us consider a 50 TeV high-field collider, with dipoles operating at 12.5 T. The injector will have an energy equal to 50 TeV times the ratio of its dipole field to that of the collider. For example, an injector made using SSC dipoles (6 T field) would provide about 25 TeV injection energy; an injector made using 2 T superferric magnets would provide 8 TeV injection energy. The collider dynamic range requirement is reduced to 2 or 6, respectively, in these cases. Some of the generic benefits of this approach are considered in [1].

In this paper, we would like to consider the extreme case of a full energy injector. Presumably, this produces the maximum benefit, in terms of technical simplification and cost reduction, for the collider, at the cost of having to build a rather large injector. We shall consider the specific case of a 50 TeV high-field radiation-damped collider (12.5 T magnets), whose injector is a 50 TeV low-field (2 T magnets) machine. (See Fig 1.)

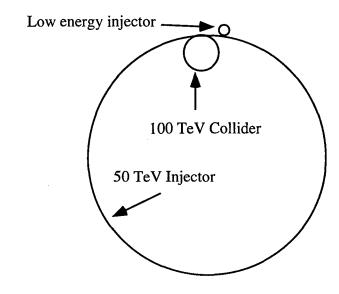


Figure 1: Layout of full-energy injector and collider.

2 ADVANTAGES AND DISADVANTAGES

There are several significant advantages to the collider with this approach. First of all, the magnet aperture can be made significantly smaller. The beam size at injection is quite small (see below), and if the closed orbit errors can be kept under control, the coil diameter may be able to be reduced to as small as 12-15 mm. The reduction in the beam emittance due to radiation damping, together with the fact that the machine's dynamic aperture will be determined in collision by the interaction region optics, should greatly ease the field error tolerance for the arc dipoles. The high field magnets will be able to be realized with lower currents, and the forces correspondingly will be reduced. Moreover, since the collider has a fixed field, persistent current problems will be absent: this may be particularly important for magnets that use high temperature superconductor. The magnets need only be optimized for one operating point, which could substantially ease their design.

Since acceleration is not necessary, the rf system is only needed to supply the energy lost through synchrotron radiation, and to provide the voltage needed for the required bunch length. This could result in a simpler rf system. Beam stability issues will be eased, despite the small aperture, since the beam is always at full energy. The beam

^{*} Work supported by the National Science Foundation and the U.S. Department of Energy.

abort system will be simpler, as it will operate at a fixed energy.

The collider will also be able to be filled very rapidly. In fact, the collider can be "topped off" periodically, which means the luminosity need never go to zero (except when the beam is lost), which will result in higher integrated luminosity.

The obvious disadvantage is the need to build a very large 50 TeV injector (together with its very large tunnel), and full energy transfer lines and injection systems. However, the 2 T magnets can be very simple: only one beam tube is required, so a simple C-magnet design may be the best approach, perhaps driven by a transmission line as in the Foster design[2]. The field quality requirements should not be very severe, as the beam emittance is not crucial, due to the radiation damping in the collider. The aperture could be small, since some multibunch stability issues are mitigated due to the low current needed for the final machine: only a fraction of the circumference needs to be filled. Single-bunch stability issues will remain important, although they may be minimized if a bunch coalescing scheme is adopted. The vacuum requirements should not be severe, since the beam does not stay in the ring for a very long time. The low-field machine would also be available for a 50 TeV fixed-target program between collider fills.

3 COLLIDER MAGNET APERTURE

The required aperture in a collider is typically determined by the beam size and the closed orbit deviations; in addition, an allowance is usually also made for injection errors. The maximum rms beam size at injection is given by

$$\sigma_x^2 = \frac{\epsilon \beta_{max}}{\gamma} + (\hat{\eta} \ \sigma_{\delta})^2. \tag{1}$$

Here ϵ is the normalized rms emittance, $\gamma = E_{inj}/mc^2$, and σ_{δ} is the rms relative momentum spread. For 90° cells of length 2L, we have $\beta_{max} = 3.41 L$ and $\hat{\eta} = 2.71 L^2/R$, where L is the half cell length and R is the ring radius. Using the beam parameters $\epsilon = 1$ mm-mrad and $\sigma_{\delta} = 50 \times 10^{-6}$, and with R = 16.7 km, L = 150 m, we have $\sigma_x = 208 \ \mu m$. The closed orbit deviation due to N random angular deviations of rms amplitude σ_{θ} is given by

$$\sigma_{co} = \frac{\sqrt{N\beta_{max}\bar{\beta}}}{2\sqrt{2}|\sin\pi\nu|} \ \sigma_{\theta} \tag{2}$$

in which $\bar{\beta}$ is the average amplitude function at the locations of the errors, and ν is the betatron tune. Angular deviations may arise from quadrupole alignment errors (taken to have an rms value of 200 μ m), the roll angle of the dipoles (rms value 250 μ rad), and the relative dipole field errors in the dipoles (rms value 3×10^{-4}). The total rms closed orbit deviation (quadrature sum of the contributions from these three sources) is about 10 mm without correction. Assuming the orbit is corrected perfectly at the

beam position monitors (located at focusing quadrupoles), the rms residual orbit error (including defocusing quad locations) would be about 60 μ m. We assume this is within the monitor resolution. The required beam pipe aperture would thus be dictated by the position monitor alignment with respect to the quadrupole centers, which is taken to be about 200 μ m. Adding this to the beam size contribution gives about 400 μ m; allowing a factor of five to encompass the entire distribution results in a required radial aperture of 2 mm.

Allowing an additional 1 mm radial aperture for injection errors and other miscellaneous effects brings the total radial aperture to 3 mm. The beam-stay-clear diameter is thus 6 mm. This could be accommodated in a 15 mm diameter magnet coil bore; the good field region is required to be 40% of the coil diameter, and a radial space of 4.5 mm is available for the implementation of the required beam screen/cryosorber system to pump the gases desorbed by synchrotron radiation.

The meaning of "good field region" in this case requires considerable study. The presence of synchrotron radiation damping means that emittance growth mechanisms with a time scale greater than the damping time (about 3×10^7 turns) will not be important. This may allow a more tolerant requirement on the field errors. The motion within the "good field region" may not need to be completely linear. The SSC CDR tracking studies found a dynamic aperture of 12 mm with a 40 mm coil diameter[3]. If the aperture scales with the square of the coil diameter, a 20 mm coil diameter would be required to obtain a 3 mm dynamic aperture. Study will be required to determine whether the field errors associated with a 15 mm coil diameter would be tolerable in the presence of synchrotron radiation damping.

There is considerable current interest in common-coil, block designs for high field magnets. Such designs should be able to more easily accommodate smaller apertures than cos-theta designs. In addition, the simplicity of the block magnet design should minimize the random errors, which must be extremely well controlled for small aperture magnets.

4 INJECTION

The simplest injection scheme loads the full-energy injection with a bunch train of the same length as the collider. This bunch train is then accelerated to full energy and transferred in a single turn into the collider. For the counter propagating beam, the polarity of the injector is reversed, the beam is accelerated, and transferred using a separate injection line into the collider.

For a low-field injector with a warm beam tube, it is important to limit the injected beam current because of potential stability issues related to the large resistive-wall impedance. Since only a fraction of the circumference is filled, multibunch stability problems are somewhat alleviated. Single bunch stability, which depends on the magnitude of the peak current, can also be enhanced by coa-

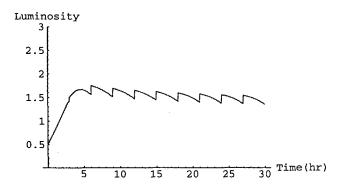


Figure 2: Topping off.

lescing. The injected beam can be distributed into a large number of bunches, with reduced intensity in each bunch, and accelerated to full energy in this form using a high frequency rf system. At full energy, before beam transfer, the bunches can be coalesced into a smaller number of bunches with the correct time structure, and then transferred to the collider. This limits the peak current per bunch at injection and raises the stability thresholds.

Although a conventional full-aperture kicker can be used in the collider, there may be a significant advantage in the use of a partial-aperture shuttered kicker at a point of high dispersion. In this scheme, additional beam may be injected while circulating beam is already in the machine; this is similar to the "topping-off" procedure used in electron colliders. In principle, a significant gain in integrated luminosity may be realized, since the beam need never be dumped, and the topping off can be used to replace the beam lost through interactions at the IP.

One possible arrangement to achieve this is the following. The beam is injected with a small relative energy offset $\delta = \Delta E/E$; the kicker is located at a point of dispersion, η . The distance between the on-energy beam and the injected beam is $\eta\delta$; this distance is made sufficiently large that a shutter can be inserted between the injected beam and the circulating beam. When the kicker fires to put the injected beam onto the closed orbit, the shutter is closed, and the circulating beam does not see the kicker field. The shutter is then opened. Due to the synchrotron radiation, the beam damps and eventually $\delta = 0$. During the damping time, because of the synchrotron oscillations, the injected beam will (longitudinally) miss the circulating beam at the IP, and so some reduction in luminosity will result. However, after a couple of damping times, the injected beam will merge with the circulating beam, resulting in full luminosity. This process can then be repeated. By adjusting the amount of beam injected each time, the luminosity may be maintained at a relatively constant level until a failure causes the loss of the stored beam. (See Fig. 2.)

5 CONCLUSION

In this paper we have considered some of the features of a high-field very large ($E_{cm} = 100 \text{ TeV}$) hadron collider with a low-field full-energy injector. Probably the principal advantage of such an approach is that the collider's high field magnets can be designed and operated at a fixed field, and may have a small aperture. Such magnets, which would be free from persistent current effects, could be smaller and less expensive than in the conventional approach, in which dynamic ranges greater than 10 to 1, and apertures sufficient to handle the low-energy injected beam, are required. Additional advantages include simplifications in auxiliary systems (abort, rf, focusing insertions) due to the fixed energy of the ring. The injection process can take place during collider operation, utilizing radiation damping to bring the beam onto the reference orbit. This could allow the machine to be "topped off," as is done with existing electronpositron colliders; an increase in the integrated luminosity could result.

The disadvantage to this approach is the need to build the low-field injector, and its very large tunnel. The key question regarding the economic viability of this scheme is whether the simplifications afforded in the collider result in sufficient savings to more than offset the cost of the large injector. A detailed trade study would be needed to answer this question.

- [1] C. Ankenbrandt, "A Multi-TeV Superferric Booster in the Main SSC Tunnel," p. 319, in "Proceedings of the 1984 Summer Study on the Design and Utilization of the Superconducting Super Collider" (Snowmass, CO 1984).
- [2] "Superferric magnets and prototype work at Fermilab," G. W. Foster, Mini-Symposium, APS Annual Meeting, Indianapolis, May 3, 1996; "Low-cost Hadron Colliders at Fermilab," G.W. Foster, Ernest Malamud Fermilab TM-1976, June 21, 1996.
- [3] "Superconducting Super Collider Conceptual Design,"J. D. Jackson, Ed., SSC-SR-2020, March 1986.

AN ep COLLIDER WITH $E_{cm} = 1 \text{ TeV}$ IN A VLHC BOOSTER TUNNEL

M. Derrick, H. Friedsam, A. Gorski, S. Hanuska, J. Jagger, D. Krakauer,
J. Norem, E. Rotela, S. Sharma, L. Teng, K. Thompson, ANL;
T. Sen, FNAL; E. Chojnacki, Cornell; D. P. Barber, DESY

Abstract

The low field option for the VLHC includes a 3 TeV proton booster with a circumference of 34 km. We are studying the option of an electron ring to fit in this tunnel which can produce ep collisions with a luminosity of 1 fb⁻¹/yr with a center of mass energy of 1 TeV. The machine would utilize superconducting rf and small low field magnets for the ~80 GeV electron beam. We describe the vacuum chamber / magnet system, rf power supply requirements, vacuum chamber cooling, interaction regions and installation of the facility in the tunnel, as well as provide preliminary estimates of beam stability and lifetimes.

1 INTRODUCTION

The present studies for the Very Large Hadron Collider (VLHC) [1] consider both high (10-14 T) and low field (2 T) options for reaching 100 TeV in the center of mass. The low field option includes a 34 km circumference tunnel for a 3 TeV booster. We are considering an 80 GeV electron ring in this tunnel to produce an ep collider which could extend the operating range for ep collisions to $\sqrt{s} = 1$ TeV. If this machine utilized existing detectors and some of the 352 Mhz superconducting cavities available after LEP was decommissioned, the cost could be considerably reduced. This machine could produce physics during the construction of the large VLHC collider ring.

We have assumed that the minimum requirements of such a machine would have: 1) sufficient luminosity to produce 1 fb⁻¹/y, 2) the ability to collide e⁺ and e⁻, 3) useful polarization, 4) adequate beam lifetime, 5) detector access to the maximum range of momentum transfer Q^2 , and, 6) $\sqrt{s} \sim 1$ TeV. In addition, the priorities of this machine seem to imply operation with or before, rather than after, the LHC.

We have looked at issues which would affect the cost and performance of the machine with the aim of determining its feasibility.

2 BASIC PARAMETERS

The parameters of the machine determined by fixing synchrotron radiation loss, and the β^* 's for the proton beam at the interaction point and limiting the beam beam tune shifts, ξ , for the proton and electron beams, are given

* e-mail: norem@hep.anl.gov

in the following table. We have assumed that the proton ring would be the low field VLHC injector described in [2], the injector chain would be located at Fermilab, and that the synchrotron radiation power is 50 MW.

PARAMETERS

Circumference	33962.13	m
ep Luminosity	$2.6 \cdot 10^{32}$	cm ⁻² s ⁻¹
Center of Mass energy	1	TeV
Electron energy, E _e	~80	GeV
Proton energy, E _p	3	TeV
Synchrotron radiation Power	50	MW
Electron ring dipole field	0.009 - 0.06	T
RF frequency in electron ring	352	MHz
Bunch Spacing	100	ns
Number of bunches	1140	
Arc Cell length	100	m
Bend Radius	4451	m
$oldsymbol{eta_{ ext{max}}}/oldsymbol{eta_{ ext{min}}}$ in cell	171/29	m
$\beta^*_{p,x}/\beta^*_{p,y}, \beta^*_{e,x}/\beta^*_{e,y}$ 2	/0.5, 0.115/0.115	m
	1, 0.0014/0.0068	
Equilibrium emittance	28	nm-rad
Electron Beam current	55.3	mA
Proton beam current	200	mA
protons/electronsperbunch 1	$.25 \cdot 10^{11} / 3.43 \cdot 10^{10}$	
Energy loss per turn	0.814	GeV
electron rf Voltage	1.09	GV
electron energy spread, σ_E/E	$1.03 \cdot 10^{-3}$	
Proton emittance, $\varepsilon_{RMS,N}$	3.6·10 ⁻⁶	mm-mr
Expected luminosity lifetime	~20	hr
Sokolov-Ternov polarization	time 0.9	hr

A detector similar to the HERA/ZEUS or H1 would have adequate range for the majority of experiments planned on this machine, with smaller detectors for low Q^2 events.

The electron ring would be located in the tunnel above the proton ring, and would be installed at the same time.

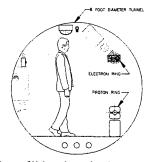


Figure 1, The collider rings in the tunnel.

2.1 Lattice Design

Our primary design criteria are a low beam energy spread, a low emittance beam to get a small spot size at the IP and a large bending radius to reduce the synchrotron radiation power. The electron ring contains two 180 degree arcs connected by 1.8 km straight sections. contain half cells with 46 m long dipoles, 1.5 m quads and 2.5 m straights. A phase advance of 90° is chosen in the horizontal plane to get an equilibrium emittance of 28 nm-rad. The phase advance in the vertical plane will be chosen to minimize the chromaticity burden and ensure sufficient dynamic aperture. We have assumed an emittance coupling ratio of 25 % to equalize the beam sizes of the protons and electrons at the IP. The Sokolov-Ternov polarization time for electrons is sufficiently short to produce polarization, but the large tune spread and density of depolarization resonances may require snakes to make the spin tune independent of energy.

A preliminary design of the triplets used to focus the electrons to the required spot sizes at the IP suggests that superconducting quadrupoles will be required for the interaction region. The smallest β^* achievable is determined by the available gradients, the distance to the first quadrupole and the maximum value of β in these quadrupoles. In order to ensure a good quantum lifetime, the magnet aperture must be greater than 10σ . With the value of β^* shown in Table I, the first quadrupole may have to be placed as close as 1m and no further than 3m from the IP. The focusing of the protons will start after the two beams are sufficiently separated so that the electrons will not be subject to the fields of the proton magnets. The design could be similar to that of the interaction region in HERA.

2.2 Lifetime

The electron beam lifetime has been calculated with the inclusion of the following effects: i) residual gas scattering with an initial pressure of 10^{-9} Torr together with synchrotron radiation induced desorption assuming a desorption coefficient of $2x10^{-9}$, ii) e-p bremsstrahlung at the single IP, iii) quantum lifetime assuming a physical acceptance of 10σ in the transverse planes and an RF acceptance of $10\sigma_E$, iv) Touschek scattering. These four effects lead to an electron lifetime of 26 hours. Other effects not included such as ion trapping, effects of orbit distortion, larger emittances and energy spread on the quantum lifetime, scattering off thermal photons etc. will reduce the lifetime somewhat from this value.

3 MAGNET / VACUUM CHAMBER

3.1 Vacuum Chamber

The vacuum chamber aperture is determined by requiring 10σ plus 0.2 cm for closed orbit distortion in both

horizontal and vertical planes. We have used an antechamber to increase the pumping conductance along the length of the chamber. The vacuum chamber is made of 6063-T5 aluminum extrusions with the profile shown in Fig. 2 There are 2 channels included to heat the chamber during bake-out with pressurized, hot water. The length of the chamber sections between bellows is limited by the thermal expansion and other effects to about 9 m. With a chamber section anchored at the center of a dipole section, both ends of the chamber expand about 2 cm during bake-out. The ends of the chamber sections are connected to 20-cm diameter, stainless steel vacuum flanges with bimetallic transition pieces. The transition pieces on the down stream ends also contain simple water cooled absorbers in the aluminum parts to intercept the synchrotron radiation that would strike the walls and bellows that are located in the sections just beyond the dipole sections.

The vacuum pumps for the ring are 30 l/s ion pumps located at the ends of each dipole section. The conductance of the chamber is sufficient to give pressures <10⁻⁹ torr at the centers of the chamber sections including the effects of both thermal and photo desorption. Provisions are included in the chamber profile to permit the use of NEG strips. This may allow the use of smaller and fewer numbers of ion pumps.

3.2 Dipoles

The electron ring must operate in close proximity to the proton ring, which produces peak fringe fields that are large compared to the field strength in the dipole at injection (90 G). The electron ring, therefore, is located inside at least a single layer, magnetic shield as shown in Fig. 2. The shield also provides the support structure for the ring. The choice of thickness and the number of layers in the shield depend on the separation between the two rings. A single layer of 6-mm thick low carbon steel has been calculated to reduce the fringe field strength to less than about 1 G near the center of the electron dipole when located at a distance of about 2 m from the center of the proton dipole. The core of the electron dipole is stacked from 1.5-mm thick low carbon steel laminations. Each dipole has a water cooled, copper coil consisting of one turn per pole.

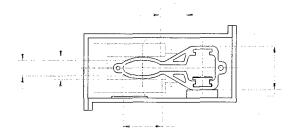


Figure 2. The magnet, vacuum chamber and support.

Each of the 608 lattice dipoles is made up of 5 sections. The sections have effective lengths of 8.96 m with 30-cm spacings. Each dipole section has a 3.5-cm gap height and produces central fields ranging between 0.009 T and 0.0616 T. The conductor size is 1.55 cm by 1.0 cm with a 0.66-cm diameter hole. The peak current through the dipole is 876 A resulting in peak power losses of 4.3 kW per section for a total of 6.6 MW for all the dipoles. Using a single cooling circuit in a section, a water flow of 0.1 l/s is required. This gives a temperature rise of 10°C in the water and a total flow of 160 l/s for the dipoles in the ring.

3.3 Quadrupoles

Each of the 608 lattice quadrupoles has an integrated strength of 7.545 T, a bore radius of 2.5 cm, and cores stacked from 1.5-mm thick low carbon steel laminations.

3.4 Vacuum Chamber Cooling

Most of the radiated synchrotron power is absorbed on the outside radius wall (right inside face in Fig. 2) of the chamber with an imbedded water channel used for cooling. The average power distribution of 1.64 kW/m through the 180° arcs gives 14.7 kW over the length of a chamber section. A water flow of 0.18 l/s gives a 20°C water temperature rise across a cooling channel and a total flow of 552 l/s(8750 gal/min). The heated water would be collected in pipes which would be located underneath the floor and these pipes would discharge into the two injector tunnels and then into the cooling ponds.

4 RF SYSTEM

Superconducting rf is required to obtain high luminosities at high energies, since the losses in normal rf cavities would require reduction in the electron beam current. The available luminosity at high energies is shown in Fig. 3.

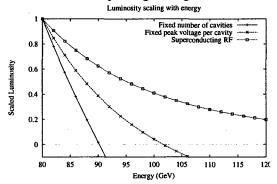


Figure 3, Luminosity for different rf options.

We require 1.1 GV of rf to maintain the electron beam and we assume this would be at 352 MHz. The cavities would be located in the long straight section opposite the detector. Minimizing the cost of SRF cavities is obtained

by optimizing the RF power per coupler, or the number of cells per cavity. We are looking at: 1) geometry changes to spoil multipactor resonances, 2) high temperature in situ bakable vacuum seals on RF components for high temperature bakes, and, 3) in situ RF processing utilizing a variable standing-wave apparatus to scan peak electric field over the coupler region. These improvements should allow delivery of beam power per coupler to levels limited by RF sources and vacuum windows, about 1 MW at 352 MHz.

The use of the LEP rf would require rebunching the protons at injection into the 3 TeV ring. We assume the electrons occupy one bucket in 35 at the LEP frequency (1140 bunches), and proton rf operates at 1/7 of the lepton rf, i.e. ~50.3 MHz. Proton rebunching should be done adiabatically, initially at 10 MHz. Rebunching and acceleration would be done at 50.3 MHz, after further bunching this frequency.

5 INJECTOR CHAIN

In addition to the present Fermilab injector, a new e⁺ / e⁻ linac would be required, which would include an accumulator ring for positrons. The present Booster and Main Injector could be used up to energies of 4.5 and 10.5 GeV, respectively, with existing rf. The Booster would require a lattice correction package to adapt the combined function lattice to electrons. Present positron sources produce ~9·10¹⁰ e⁺/sec, and the collider requires 3.26·10¹³ e⁺, so e⁺ production would take 6 min. An electron injector could look like Figure 4.

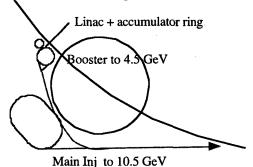


Figure 4. An electron injector chain.

6 CONCLUSIONS

We have done a preliminary study of an ep collider that could be installed in the low field booster of the VLHC. This machine could be operational before the LEP/LHC and would have a higher luminosity than HERA/TESLA.

- [1] Recent information is updated at http://vlhc.org
- [2] S. Mishra, VLHC Information Packet, FNAL (98)

ACCELERATOR TECHNOLOGY FOR THE VLHC*

J. Marriner and V. Shiltsev[†] Fermi National Accelerator Laboratory, P.O. Box 500, Batavia, IL 60510

Abstract

Accelerator Technologies useful or necessary for the construction of the VLHC (Very Large Hadron Collider are discussed. The VLHC workshop on this subject (held in February 1999 at Jefferson Lab) is summarized.

1 OVERVIEW

This paper is based on the results of a workshop held February 16-19, 1999 at Thomas Jefferson National Accelerator Facility [1]. This paper represents our summary of work done by many people. We have made an effort to refer to the original work whenever a written reference exists.

2 VLHC COSTS

The cost of the VLHC is not known. One goal of the VLHC R&D is to identify potential cost reduction strategies. For purposes of comparison a cost estimate for the SSC is shown in Figures 1 and Figure 2.

SSC Collider Costs

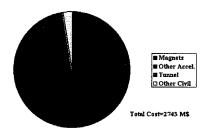


Figure 1: The total cost of the SSC collider includes all components of the large ring, but does not include the other accelerators, the detectors, or the infrastructure.

SSC Collider Costs Accelerator Components

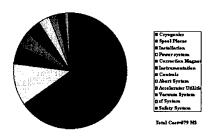


Figure 2: A breakdown of the costs of the "Other Accelerator" components shown on Figure 1.

3 CRYOGENICS

The cryogenic issues for every accelerator are:

- operating temperature
- temperature gradients
- temperature stability

From both a capital and operating cost standpoint, as well as availability, it is desirable to switch to sensible heat from latent heat systems: e.g., Nb₃Sn magnets operating between 4.5 and 5.5 °K versus 4.5 and 5.0 °K. For NbTi magnets the short sample curves are such a strong function of temperature that elevated temperatures are not an option. In fact, lower temperatures are often used. For Nb₃Sn, with its much higher critical temperature, the integrated design optimization may be different. There may also be major differences between the high and low field optimizations. These optimizations are trade off between:

- Magnet short sample limit
- Cryogenic complexity and availability
- Cooling passages and cryostat sizes

One of the most important parameters that drives both the cost and availability is string length and/or recooler spacing. It must also be noted that the costs of the HERA and LHC distribution systems are very similar to the total refrigerator cost.

3.1 Reliability and Maintenance

System optimizations require trade-off's between efficiency and availability: the most efficient systems usually do not provide adequate availability. Scaling LHC is not an option; a simple magnet cryogenic system is required for VLHC. The Snowmass 138 km LHC scale up would have had 8000 tunnel cryogenics valves (1 valve per dipole average). These valves would more than saturate the entire cryogenic un-availability budget.

One of the continuing issues is vendor qualification: will there be any cryogenic system vendors in 15 years? In the US, the industrial cryogenic expertise has decayed over the past 20 years, due to retirements and corporate decisions that large refrigeration systems are unprofitable.

3.2 Suggested R&D on Cryogenics

Some R&D should probably be carried out for the VLHC:

 Flow instabilities. The most important for the VLHC are "Density Wave Instabilities". Numerical simulations and experiments are needed.

^{*} Work supported by the U.S. Department of Energy under contract DE-AC02-76CH030000.
† marriner@fnal.gov or shiltsve@fnal.gov.

- Cycle and efficiencies for sensible heat vs. latent heat systems. Sensible heat systems typically provide system simplifications with some loss of efficiency. The relative advantages should be studied further.
- Magnetic bearing turbines. Highly reliable turbines
 that are easy to operate should be developed. Today,
 cryogenic turbines use either gas or oil as a bearing
 and also as a brake. In the future, turbines could be
 built with magnetic bearings and use regeneration as
 the brake.

4 BEAM SCREENS

The LHC beam screen system has received an enormous amount of attention and serves as an example for VLHC. The LHC primary cryogenic screen loads are Synchrotron radiation and photoelectrons, but resistive losses and nuclear scattering are not negligible. Even if the cryogenic impacts are neglected, a shield is required to prevent continual liberation of molecules adsorbed by the 1.9 °K beam tube. The regeneration interval required is much longer than a year.

Both 4.5 and 20 °K high field magnets will require a beam screen due to beam lifetimes; CERN data implies warm-ups every 50 hrs without a beam screen. LHC requires solutions for both their 4.5 & 300 °K magnets and has a major R&D effort in progress. Two options are outlined below and illustrated in Fig. 3.

- 1. Physical absorption
 - a) shield is required
 - b) absorber (e.g. metal sponge) is required
 - c) tri-monthly regeneration at 20 °K
- 2. Chemical adsorption
 - a) independent bore tube is required
 - b) annual regeneration at 600 °K
 - c) magnets are kept at their operating temperature
 - d) finite life

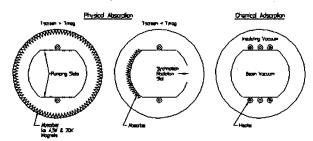


Figure 3: Concepts for a VLHC beam screen.

5 INSTRUMENTATION

There do not appear to be any VLHC devices or technologies that are especially challenging. The long distances and limited access to the tunnel require an unprecedented reliability for the VLHC instrumentation. The following design principles are suggested for the design of VLHC instrumentation.

- Placement of electronics near detectors
- Minimization of cable plant

- Use of standardized (commercial) electronics
- Placement of electronics to minimize radiation damage and monitoring the accumulated does (nonhardened electronics can typically tolerate a dose of 10 kRad)
- Achievement of reliability by redundancy
- Extensive use of self-diagnostics
- Use of modularity
- Integration of different systems, but allowing simultaneous of a variety of simultaneous maintenance activities

6 RF PARAMETERS

We have considered two options in Table 1: 478 MHz to increase the longitudinal spread in the vertices at the interaction point or 1274 MHz to give a higher momentum spread and synchrotron frequency. We assume that superconducting cavities will be used although room temperature copper cavities could be used.

Table 1: Two options for VLHC rf parameters.

f	478	1274	MHz
$\mathbf{f}_{\mathbf{r}}$			
Operating temperature	4.2	2.0	°K
$\mathbf{E}_{\mathtt{acc}}$	6	12	MV/m
Shunt R/Q	1000	1000	Ohm/m
Coupler	coax	waveguide	
Cells/cavity	4	7	
Volts/cavity	7.5	9.9	MV
Beam current	127	127	mA
$\cos(\theta_s)$	0.5	0.5	
Max. beam power	480	630	kW
Bucket length	21	7.8	cm
Voltage Cost	.06	.015	\$/V
Cavities for 200 MV*	27	20	

*We chose a total voltage of 200 MV for the low-field case and 40MV for the high-field case so that each case has the same acceleration time of about 15 min from 3 to 50 TeV.

7 INSTABILITIES

Instabilities that may occur in the VLHC were considered at the workshop [2]. Although the low field VLHC is more susceptible to some important instabilities, none of them can be considered as a "show-stopper." Even at the current status of accelerator physics and technology there appear to be adequate tools to damp or eliminate the potential instabilities.

7.1 Transverse mode coupling instability

The frequencies of coherent bunch motion (mode 0) and head-tail motion (mode 1) are shifted by the transverse impedance towards each other resulting in the transverse mode coupling instability. Several methods of eliminating this instability have been proposed and are summarized in Table 2. Not all of the methods can be applied simultaneously, and some of them are unproven. However, it seems likely that an effective solution can be found.

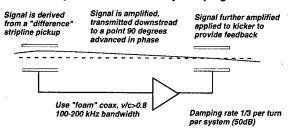
Table 2: Methods for damping TCMI.

Method	Threshold Increase
Coalescing at 50 TeV	29
"beam shaving"	23
thin Cu, Ag coating	~1.3
Asymmetric beam pipe	1.53
RF quadrupole	24
AC chromaticity	~10
Feedback system	25(more?)

7.2 Transverse Coupled Bunch Instability

The Coupled-bunch instability is most severe at 3 TeV and is proportional to the total beam current. It is driven by the low-frequency transverse impedance resulting from the finite conductivity of the beam pipe walls. The instability growth time in the low-field VLHC varies from 4 to 0.4 turns (depending on lattice parameters), and is about 180 turns in the high-field case. The instability can be damped with use of a distributed feedback systems [3] as shown in Figure 4.

VLHC coupled-bunch instability damping scheme



The fact that the signal is applied to succeding bunches does not matter much at these low frequencies

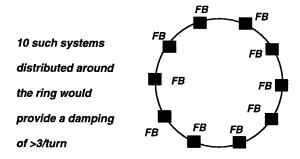


Figure 4: Proposed distributed coupled bunch instability damper system. The instability is less severe in the high field VLHC because of the smaller circumference and also because of the (assumed) higher conductivity of the cryogenically cooled beam pipe.

7.3 R&D Opportunities

There are several R&D opportunities discussed at the workshop:

 Study the TMCI experimentally, particularly in proton machines. It may be possible to excite the TMCI by a controlled increase of the Tevatron impedance with an electron beam set-up [4].

- Measure and optimize detuning wakes.
- Test a prototype rf quadrupole.
- Evaluation of different kinds of feedback systems for the TMCI.
- Simulate the distributed feedback system.
- Gain limitations in feedback systems.

A more detailed explanation of these proposals can be found in Ref. 1.

8 GROUND MOTION

Turn-to-turn dipole magnetic field fluctuations and vibration of quadrupole magnets can cause emittance growth if the resulting coherent motion is not corrected over its decoherence time (~1000 turns) [5]. Measured ground vibrations in deep Illinois dolomite tunnels are smaller than the tolerances for both LF and HF options [6]. Cultural noise level in the Tevatron tunnel is several times above the VLHC tolerances but small enough to be suppressed by the coupled bunch mode damper system discussed below. The frequency spectrum of the fluctuations in the magnetic field has not been determined, and experimental measurements are needed to determine the expected magnitude of the emittance growth.

9 FEEDBACK SYSTEMS

Table 3 lists the several feedback systems that may be necessary to avoid emittance dilution in the VLHC.

Table 3: VLHC Feedback Systems.

	System	Comments
1	Damp resistive wall	high gain
	coupled bunch modes	100-200 kHz bandwidth
	and injection errors	
2	Damp high frequency	one turn delay
	coupled bunch modes	26 MHz bandwidth
3	Damp azimuthal mode 1	moderate gain
	(bunch-by-bunch)	3 GHz carrier frequency
	•	26 MHz bandwidth
4*	Suppress emittance	moderate gain
	growth	5 kHz bandwidth
_ 5	Longitudinal feedback	

^{*}System 1 is more than adequate to perform the function of System 4.

10 REFERENCES

[1] The conference proceedings are available via the world-wide-web at $http://vlhc.org/AT_proc.html$.

[2] V. Shiltsev, V. Danilov, and J. Marriner, "Beam effects in the VLHC", these Proceedings.

[3] J. Marriner, "A Damper to Suppress Low Frequency Transverse Instabilities in the VLHC," in Very Large Hadron Collider Information Packet, ed. C.S. Mishra (January 1998).

[4] V. Shiltsev, V. Danilov, D. Finley, and A. Sery, "Electron Compression of Beam-Beam Tune Spread in the Tevatron", FERMILAB-Pub-98/260 (1998).

[5] V. Shiltsev, FNAL-TM-1987 (1996).

[6] B. Baklakov, et al., Phys. Rev. ST - Accel. Beams, 1, 031001 (1998). See also B. Baklakov, et al., these Proceedings.

ACCELERATOR PHYSICS ISSUES FOR THE VERY LARGE HADRON COLLIDER

C. S. Mishra⁺, M. Syphers, Fermilab^{*}, Batavia, IL 60510 A. Jackson, LBL[#], Berkeley, CA 94720

Abstract

The goal of the Very Large Hadron Collider (VLHC) is to extend the energy frontier beyond LHC. The proposed design center of mass energy for the VLHC pp collider is 100 TeV, with a luminosity of 1x10³⁴ cm⁻²sec⁻¹ and an integrated luminosity of about 100 fb⁻¹ per year. In this paper we present a summary of work conducted during a workshop and issues we feel are most important. Accelerator Physics issues and design aspects specific to both the high field and low field magnet technologies were studied, including general accelerator parameters, beam stability issues, magnet field quality and the R&D needed to relax the accelerator component tolerances. This paper summarizes the accelerator physics R&D the VLHC Accelerator Physics Working Group members are undertaking.

1 INTRODUCTION

Hadron Colliders are the "Discovery Machines" for high-energy physics. The high-energy physics (HEP) and accelerator physics communities are working together to extend the energy frontier beyond LHC. A very large hadron collider is a machine we know can be built today. The main issue is cost. Considerable R&D are needed in Accelerator Technology and in improving our understanding of Accelerator Physics to reduce the overall cost of the accelerator construction and operation.

The VLHC magnet R&D groups are investigating two different magnet technologies: high field (10-12 Tesla) [1-5] and low field (2 Tesla) [6]. The magnetic field quality at injection, eddy and persistent currents and hysteric effects limit the ratio of energy at collision increase to injection for a synchrotron. We have assumed this factor to be 20 for accelerator design.

The U.S. site for the VLHC is assumed to be Fermilab. We are planning to use the Fermilab injection chain of the Linac (400 MeV), Booster (8.9 GeV) and the newly commissioned Main Injector (150 GeV). These three are rapid cycling accelerators. The Main Injector can cycle to 150 GeV in about 2.4 sec. The Main Injector will be used as an injector in the VLHC. The VLHC will have two new accelerators, a 3 TeV High Energy Booster (HEB) and a 50 TeV, pp collider. Counter rotating protons will

be injected into the HEB by extracting protons from the Main Injector at MI40 and MI61.

There are several ways to categorize the accelerator physics issues for the VLHC. In this paper we choose to categorize them as single particle, multi-particle and energy deposition issues. Considerable experience has been gained in the past two decades of hadron collider operations and recent design efforts of the SSC and LHC. At present the VLHC efforts are predominantly on magnet technology and the R&D effort is a collaboration of national laboratories and industries. The accelerator physics R&D efforts are to support these technologies R&D effort for a final usable product.

2 SINGLE PARTICLE ISSUES

The single particle issues are concentrated on the basic accelerator design, i.e. lattice design, magnet quality, aperture requirements, correction system and schemes. The issues range from the basic cell length to the effect and benefit of synchrotron radiation.

The most fundamental question that needs to be addressed is the magnet field quality and aperture of the magnet at injection. For all magnet designs both the cost and the field quality are reduced as aperture decreases. With magnet cost expected to be an even more dominant component of VLHC costs than in any previous machines, accelerator physics will play a crucial role in the economic feasibility of the machine.

The mechanical construction of the high field magnet determines the field quality at full excitation. The field quality of Nb-Ti magnets has improved significantly in the last few years due to improvements in manufacturing, changes in design and reduction in measurement errors. The magnet production techniques have improved so that the random errors can be controlled to the point where systematic effects dominate. However at injection energy the field defects of high field magnets will be dominated by persistent current magnetization defects which depend on both excitation history and time.

For the low field option the field quality challenges occur at top energy as the iron enters saturation. At the 1-kG injection field the iron is above the point where

⁺ Email:mishra@fnal.gov

^{*}Operated by the URA, under contract with the U.S. DOE.

^{*} Work Supported by U.S. DOE

remnant fields dominate. The field quality of the low field option needs detailed studies. At present we have no data on the field quality of the low field magnet. Dynamic aperture calculations will be performed when field measurement data become available.

The cell length of the lattice has two competing effects. If random errors dominate, shorter cell lengths would be preferred while the opposite is true if systematic errors were dominant [7]. The cell length also has implications on the acceptable size of the magnetic higher order systematic multipoles. A calculation performed [8] with a study lattice (Figure 1) show that smaller cell length is preferred to relax the systematic multipole requirements. We need to perform calculations to find an optimal balance between the cell length, allowed systematic and random multipoles for a realistic aperture R&D magnet.

The high field option design has an advantage at collision energy due to synchrotron radiation damping. The damping time is smaller than the storage time. Figure 2. shows that the emittance of the bunch decreases as a function of store time due to synchrotron radiation [9]. The luminosity of the collider is enhanced for relatively modest bunch intensity. This effect only helps the magnet design and quality at high energy. The aperture and magnetic field errors at injection energy for both the high field and low field option need to be investigated by simulations. The beneficial effects of damping due to synchrotron radiation in the high field option should not be relied on to relax the requirements on the error fields at injection.

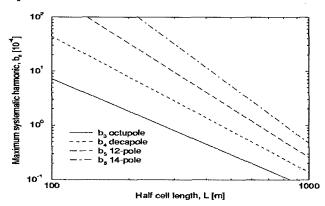


Figure 1. Maximum allowable systematic harmonics vs. half cell length, when $\Delta Q_x = 0.1$, $\phi_c = 90$ degrees, $\epsilon_x = 1$ μm , at an energy of 1 TeV, with a reference radius of 16 mm

An error budget for the dipole, quadrupole, sextupole, octupole and misalignments of the magnetic elements needs to be developed. The distribution of the dipole correctors has implication on the allowed size of the closed orbit error and hence on the beam pipe aperture. It is an important issue to determine how the minimal distance between dipole correctors scales with the parameters of the ring such as the energy, circumference, cell length, phase advance and aperture size. Based on the LHC simulation experience the higher order nonlinear correctors can be placed at well-chosen locations in the arcs. Simulations performed show that for this method to

be effective, an experimental measurement of the one turn map is required.

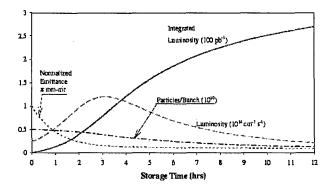


Figure 2. Beam parameters during a store for high-field VLHC.

The effects of ground motion on lattice design and machine performance need to be studied. Ground motion studies are being carried out at different laboratories and in the strata under Fermilab [10].

3 MULTI PARTICLE ISSUES

The effects of multi-particle dynamics will be an area of considerable R&D for both magnet technologies. Because of the large circumference of these machines, transverse instabilities tend to dominate. Since the Snowmass 96 workshop this has been a topic of interest because considerable attention needs to be paid to reduce or eliminate the effects of these instabilities in an accelerator design. None of these instabilities are considered as a "show-stoppers", but the low field magnet design has lower thresholds. There appears to be enough current state of the art technique to damp or eliminate all of these instabilities. Detailed description of R&D to study these instabilities and proposed ideas to reduce their effect can be found in ref [11].

The Transverse mode coupling instability (TMCI) also known as "strong head-tail" are due to the shift of the coherent bunch motion m = 0 and head-tail motion m = 1by the broadband transverse impedance. This instability has been observed at many electron storage rings (which normally operates with bunch length in mm range) but has not been observed in proton colliders (with bunch length in tens of cm). The calculated safety factor (SF) for TMCI is 1.1 and 28 for the low field (LF) and high field options This is an improvement over the respectively [11]. previously calculated value by a factor of two [12]. This is due to several parameter optimized for the low field design. There are several innovative ideas to increase the threshold of TMCI beside the obvious but costly ones like decreasing the circumference, increasing the beam pipe aperture or increasing the injection energy. One scheme of filling the Low Field (LF) machine from the Main Injector is to fill every 9th bucket. At injection one can reduce the intensity per bunch by nine times and fill every bucket. This could help increase the SF to about 9. Then one will have to coalesce bunches at high energy before collision. The TMCI SF also can be increased by about factor of 4 by using RF quadrupoles, which introduces

correlated tune, spread from the head to the tail of the bunch. Using an AC sextupole scheme to increase the lattice chromaticity can increase the SF by about 10. The effect of RF quadrupoles and AC sextupoles on the dynamic aperture needs to be studied, because they could potentially excite resonance. A relatively small amount of gain in threshold is possible by coating the beam tube and by using an asymmetric beam tube. The TMCI threshold can be further increased by a factor of 5 or more by implementing a feed back system. It seems likely that TMCI will impose luminosity ceiling above 10³⁵ even for the low field machine.

The coupled-bunch instability at injection has a growth time of 1.5 turns and 180 turns for the LF and HF designs respectively. Since the growth time of this instability is on the order of a single turn a distributed damping system has been proposed [11].

Other instabilities, which are being studied, are 1) electron cloud instability at 50 TeV, 2) coherent synchrotron tune shift at 50 TeV and 3) longitudinal microwave instabilities at 50 TeV. These instability studies need to develop along with the design of the machine lattice and need to be folded together in an overall design of the VLHC.

We need to understand these instabilities by careful experiments. Possible experiments are being examined for the Tevatron to excite TMCI in a proton machine and at VEPP-4M to study the effect of RF quadrupoles on TMCI.

4 ENERGY DEPOSITION ISSUES

In the design of any accelerator the operational and environmental radiation limits must be considered to determine the required accelerator tunnel depth, tunnel wall thickness and other protective measures like beam collimation, beam abort and beam dump design. The R&D and design efforts are progressing on radiation protection systems for two types of beam loss in the collider, operational and accidental [13]. In all colliders beam-gas interaction, intra-beam scattering, interactions at the IP, noise and other imperfections produce a beam halo. This beam halo interacts with the limiting aperture and produces radiation for the accelerator and background for detector elements. A collimation system is required to reduce the effect of operational beam loss. R&D on the collimation system design needs to progress in parallel with the lattice design. The stored beam energy in the accelerator is very large and beam size is very small at these energies. An accidental loss of a small fraction of beam during a short time will melt a hole through the magnet and can cause damage to the accelerator components. The beam abort system and beam dump needs to be developed and integrated into the machine lattice.

5 SUMMARY

The VLHC accelerator physics R&D program is being developed in collaboration with four laboratories, FNAL, LBNL, BNL and several universities in the U.S. Several

calculations and design simulations are already underway. This paper summarizes some of the issues we have start working on. This list is by no means complete. We are working together with the Magnet Technology and Accelerator Technology working groups towards the goal of a less expensive and cost-efficient hadron collider.

Almost all single particle issues and energy deposition issues are important to both the low and high field magnet designs. Since the magnet technologies are still being developed it might be premature to find an optimal solution for the VLHC design. But on the other hand we need to develop our understanding of hadron collider accelerator physics by modeling. We need to propose carefully planed experiments at existing hardon colliders to validate these theories.

The authors will like to thank everyone who contributed to the VLHC Accelerator Physics Workshop, which was held at Lake Geneva, WI, Feb 22-25, 1999, under the VLHC Steering Committee (http://vlhc.org).

- [1] T. Arcan et al., "Conceptual Design of the Fermilab Nb₃Sn High Field Dipole Model", Proceedings of PAC99.
- [2] K. Chow et al., "Fabrication and Test Results of a Prototype, Nb₃Sn Superconducting Racetrack Dipole Magnet", Proceedings of PAC99.
- [3] R. Gupta, "Field Quality in a Common Coil Design Magnet System", Proceedings of PAC99.
- [4] S. Caspi et al., "Mechanical Design of a High Field Common Coil Magnet", Proceedings of PAC99
- [5] A.K. Ghosh et al., "A Common Coil Magnet for Testing High Field Superconductors", Proceedings of PAC99.
- [6] G. W. Foster et al., "Measurements of a Crenellated Iron Pole Tip For The VLHC Transmission Line Magnet", Proceedings of PAC99.
- [7] R. Talman, VLHC Accelerator Physics Workshop, Lake Geneva, WI, Feb 1999.
- [8] S. Peggs, VLHC Accelerator Physics Workshop, Lake Geneva, WI, Feb 1999.
- [9] G. Dugan et al., "Really Large Hadron Collider Working Group Summary", Proceeding of DPF/DPB Snowmass 96 summer study.
- [10] V. Shiltsev, "Ground Motion Measurements for Fermilab Future Collider Project", Proceedings of PAC99.
- [11] V. Shiltsev et al., "Beam Instabilities in Very Large Hadron Collider", Proceeding of PAC99.
- [12] J. Rogers, Collective effect and Impedance in the RLHC", Proceeding of DPF/DPB Snowmass 96 summer study.
- [13] A.I. Drozhdin et al., "Energy Deposition Issues in the Very Large Hadron Collider", http://vlhc.org/lakeg/Drozhdin.pdf

DESIGN PARAMETERS FOR THE VERY LARGE HADRON COLLIDER

C. S. Mishra⁺ and P.J. Limon, Fermilab^{*}, Batavia, IL 60510

Abstract

The goal of the Very Large Hadron Collider (VLHC) is to extend the energy frontier beyond LHC. The proposed design center-of-mass energy for the VLHC pp collider is 100 TeV, with a luminosity of 1e34 cm⁻² sec⁻¹. At present accelerator designs and calculations are being carried out for two different magnet technologies, one using superferric magnets at 2 Tesla (T), the other using high-field design with B > 10 T. This paper will summarize the accelerator parameters for these two designs. We discuss the design parameters that have the largest effects on the performance of the accelerator and therefore need careful optimization.

1. INTRODUCTION

Hardon Colliders are the "discovery machines" for highenergy physics (HEP). The HEP and accelerator physics communities are working together to extend the energy frontier beyond LHC, and to understand the physics opportunities and the technical issues presented by the colliders.

A VLHC Steering Committee [1] was formed in response to the HEPAP subpanel Report [2] recommendation. The Steering Committee has representations from Fermilab, BNL, LBNL and Cornell University's Laboratory of Nuclear Studies and coordinates R&D efforts in the United States.

The main technical issue is cost reduction. Considerable R&D is needed in accelerator technology, superconducting magnets, accelerator physics, and to reduce the overall cost of the accelerator construction and operation.

Initially, the U.S. site for the VLHC is assumed to be Fermilab. Hence, the injection chain comprise a 400 MeV Linac, an 8.9 GeV Booster, and the newly commissioned 150 GeV Main Injector. The VLHC will have two new accelerators, a High Energy Booster (HEP) of 3 to 5 TeV and a 50 TeV per beam, pp collider.

Since the Indiana workshop in 1994 [3], work has been proceeding on the design parameters for the VLHC. During the Snowmass 96 meeting, the first set of comprehensive and self-consistent parameters was published [4]. Since that time we have modified several aspects of accelerator, resulting in a new set of parameters presented here.

2. ACCELERATOR ENERGY

The injection energy into the HEB is fixed near 150 GeV, because we want to use the Main Injector as an injector. Several discussions have taken place to use the Tevatron and inject at 1 TeV. However, the Tevatron requires 30 MW for its cryogenic plant. This high load for an injector that will be used for only a few moments each day seem excessive. Over the long run, the operating cost of the Tevatron is too high.

The VLHC magnet R&D groups are investigating two different magnet technologies: high field (HF) (10-14 Tesla) [5-9] and low field (LF) (2 Tesla) [10]. The magnetic field quality at injection, eddy currents, persistent current and hysteric effects limit the ratio of energy at collision to injection for a synchrotron (SF). The Main Injector has a scale factor of 16.8, Tevatron 6, HERA 23, and LHC is designed to achieve 15.5. We have assumed this scale factor to be 20 for our primary accelerator design. This assumption needs study from the magnet, beam dynamics, and cost optimization points of view. For an HEB that is entirely on the Fermilab site. high-field magnets operating at 4K could result in energy as high as 3-5 TeV. Operating injector at 1.8k is judged unreasonable due to cyclic energy loss. Obviously, a slightly larger machine could result in a lower vlhc SF at an expense of higher HEB SF. This problem could be eased by rebuilding a conventional accelerator, an MEB, in the existing Main Ring tunnel to increase the beam energy from 150 GeV to 300 GeV. Such a machine could

^{*}Email:mishra@fnal.gov

^{*}Operated by the URA, under contract with the U.S. DOE.

be quite inexpensive. For the low-field magnet, the HEB is limited by circumference of tunnel one is willing to build. A 3 TeV low field HEB requires about 35 km.

3. LUMINOSITY

The Fermilab accelerators have a minimum bunch spacing is 18.9 ns. The expense of reducing the spacing and the detector triggering requirements encourages us to leave this the same. The design goal for the VLHC luminosity is $1x10^{34}$ cm⁻² sec⁻¹. This has been chosen due to of detector limitation, but could easily be a factor of 10 higher. At 1e34 luminosity a detector in VLHC will have less than 30 interactions per crossing. Table 1 gives the luminosity goals for the two VLHC options. It is important to note that the luminosity is not limited by proton economics, also there are several parameters that can be adjusted to achieve the same luminosity, for example smaller emittance and smaller bunch current. Smaller emittance in the HF option is due to the emittance damping caused by synchrotron radiation at colliding energy.

·	50 TeV Collider p p option (Low Field)	50 TeV Collider p p option (High Field)
Proton Per Bunch	1.7E+10	1.2E+10
Number of Bunches	100000	16000
Revolution Frequency	0.5	3.2
(kHz)		
Beta Star at IP(m)	0.1	0.1
Proton Emittance(95%)	15	8*
Form Factor	0.48	0.48
Typical Luminosity (cm ⁻² sec ⁻¹)	1.1E+34	1.1E+34
Integrated Luminosity (fb ⁻¹ /year)	112	112
Interactions Per Crossing	28	28
Bunch Spacing (ns)	19	19
Inelastic Cross Section (mb)	127	127

Table 1. The Luminosity goals of the VLHC at 100 TeV center of mass. *HF option includes the effect of synchrotron radiation damping.

4. MACHINE CIRCUMFERENCE & BEAM PIPE RADIUS

The circumference of the low field (2 Tesla) machine is 520 km, whereas for high field (12 Tesla) machine it is 95 km. The radius of the beam pipe for these machines is important because of beam instabilities. Smaller radius is desirable for cost reduction; magnet field errors, beam dynamics requirements, and alignment errors might lead

to a larger radius. The proposed beam-pipe radius for the LF magnet is 9 mm. The beam-pipe radius for HF magnet designs varies from 12 to 20 mm. The beam pipe aperture is reduced from the physical magnet aperture by the thickness of the synchrotron radiation beam screen for the HF design.

The instability threshold for the transverse mode coupling instabilities (TMCI) is an issue for the LF design. This instability threshold is proportional to the cube of the beam pipe radius. It is expensive to increase the beam pipe radius and we are investigating several solutions to this instability.

The effect of ground motion, alignment, alignment drifts and vibration needs to be understood. Because of the large size of the ring in either design this could have implications on the correction system, when beam-pipe radius is small.

5. LATTICE PARAMETERS

Table 2 summarizes the lattice parameters for the two designs. The LF option uses combined function magnets. These magnets will have quadrupole and sextupole components. The phase advance per cell is chosen to be 60 degree. This reduces the requirement of large quadrupole strength and higher order correction schemes are easier to implement. These parameters are totally free and can be optimized, as the magnet data becomes available.

Parameters	Units	Low-Field	High-Field
½ Cell	M	122	260
Length			
Phase	Degree	60	60
Advance			
per cell			
Average	M	130	600
Beta			
Max	M	5	23
Dispersion			

Table 2. VLHC lattice parameters.

6. RF PARAMETERS

The frequency of the HEB and Collider must be a multiple of 53 MHz, which will make synchronization and injection easier. The VLHC will most likely use superconducting RF for acceleration although there is no serious problem using the normal conducting RF. Some of the RF parameters of general interest for superconducting RF system being discussed for the VLHC are summarized in Table 3 [11]. A total voltage of 200 MV for the Low field option and 40 MV for the high field option have

been chosen to keep the acceleration time to less than 15 minutes.

Parameters	Units	Value
$f_{ m RF}$	MHz	478
Operating temp	K	4.2
E_{acc}	MV/m	6
Volts/Cavity	MV	7.5
Length of Bucket	Cm	21
No of cavities for 200 MV LF injection		27
No. of cavity for 40 MV HF injection		5

Table 3. VLHC Superconducting RF parameters.

Finally the longitudinal parameters of the VLHC are summarized in Table 4. Most of these parameters can be optimized as design progress. The longitudinal emittance and bunch length effects the stabilities of the machine.

Parameter	Units	LF	HF
Long. Emitt	eV.sec	2	0.3
Long Damping time	Hrs	40	1.3
RF freq	MHz	478	478
RF harmonic number	- U. 1	8.28x10 ⁵	1.2x10 ⁵
Bucket Area	eV-sec	18	4
Synch tune (coll/inj)		0.2/5	1/14
Bunch Length (coll/inj)	Cm	7.6(5.5)	5.6(7.2)

Table 4. Longitudinal parameters for the VLHC.

7. SUMMARY

This paper gives a snapshot of some of the parameters being used in the accelerator design of the low field and high field VLHC. Collaborative efforts between magnet builders, accelerator technology developers and accelerator physicists throughout the process of accelerator design will be used to refine these parameters.

- [1] The VLHC Steering Committee website http://vlhc.org.
- [2] HEPAP Subpanel on "Planning for the Future of U.S. High Energy Physics, February 1998. (Gilman Panel).
- [3] Proceedings of the Workshop on Future Hadron Collider Facilities in the US, Bloomington 19994, Fermilab TM-1907.

- [4] G. Dugan, P. J. Limon and M. Syphers, "Really Larger Hadron Collider Working Group Summary", Proceeding of DPF/DPB Snowmass 96 summer study.
- [5] T. ARCAN et al., "Conceptual Design of the Fermilab Nb3Sn High Field Dipole Model", Proceedings of PAC99.
- [6] K. Chow et al., "Fabrication and Test Results of a Prototype, Nb3Sn Superconducting Racetrack Dipole Magnet", Proceedings of PAC99.
- [7] R. Gupta, "Field Quality in a Common Coil Design Magnet System", Proceedings of PAC99.
- [8] S. Caspi et al., "Mechanical Design of a High Field Common Coil Magnet", Proceedings of PAC99
- [9] A.K. Ghosh et al., "A Common Coil Magnet for Testing High Field Superconductors", Proceedings of PAC99.
- [10] G. W. Foster et al., "Measurements of a Crenellated Iron Pole Tip For The VLHC Transmission Line Magnet", Proceedings of PAC99.
- [11] L. Doolittle, "RF Choice for the VLHC", VLHC Accelerator Physics workshop, TJNAF, Feb 8-11, 1999.

SIMULATION OF THE RECYCLER RING DYNAMIC APERTURE

C. S. Mishra⁺ and D. Johnson Fermi National Accelerator Laboratory^{*} Batavia, IL 60510

Abstract

The Fermilab Recycler Ring is being built at Fermilab to support the Run-II and beyond physics goals of Fermilab. The role of the Recycler Ring is to provide more antiprotons for the Tevatron, which proportionally increases the luminosity. This paper will describe the Recycler Ring Lattice design and simulations of the dynamic aperture using data from the some of the magnets installed in the ring.

1. INTRODUCTION

The Main Injector, a rapid cycle 150 GeV proton synchrotron, will supply a larger flux of protons for antiproton production; more intense proton bunches for use in the collider, and higher efficiency acceleration for both proton and antiprotons. The role of the Recycler Ring [1] is to provide more antiprotons for the Tevatron, which proportionally increases the luminosity. Recycler accomplishes this by acting as a high reliability post-Accumulator and receptacle for recycled antiprotons from previous Collider stores. Prior to the development of the Recycler ring, the peak luminosity goal of the Fermi III upgrade program was $8x10^{31}$ cm⁻²sec⁻¹. With the construction of the Recycler ring, a typical peak luminosity of 2x10³²cm⁻²sec⁻¹ is expected The Recycler is also the foundation of future accelerator upgrades that can increase the Tevatron Luminosity up to $1x10^{33}$ cm⁻²sec⁻¹.

The Recycler is a fixed 8 GeV kinetic energy storage ring made up of permanent magnets. This Recycler ring lattice mimics closely the Main Injector lattice. The ring was designed using MAD [2] such that it replicated the Main Injector cell length and hence followed the footprint of the Main Injector. This paper describes the lattice design of the Recycler ring. Simulation results of the Recycler performance using data from initial gradient magnets are presented in this paper. The Recycler Lattice includes the magnetic field errors, both systematic and random, and misalignment errors. Studies of dynamic aperture and momentum aperture are presented in this paper. Results

shows that the simulated dynamic aperture using realistic magnet and alignment information meets the design specification of 40π mm-mr. The production magnets are of better quality as compared to the design specification [3]. A thin element tracking program TEAPOT [4] has been used for these simulations.

2. LATTICE DESIGN

The lattice is a strong focusing FODO lattice made up of either two gradient magnets or two quadrupoles. The Recycler ring is composed of fifty-four arc FODO cells (17.288 meter cell length) with eight zero dispersion straight sections distributed around the ring following the symmetry of the new Main Injector. The lattice has been design to have a base tune of $Q_x = 24.425$ and $Q_y = 24.415$ with a maximum horizontal dispersion of 2 m and a corrected chromaticity of -2 units in each plane. The phase advance per cell is $\phi_x = 85.4$ deg and $\phi_y = 79.2$ deg. The phase advance across high beta insert at MI-30 makes the integer part of the x and y tunes same.

The Recycler lattice is virtually indistinguishable from the Main Injector lattice with two exceptions. The one exception is at MI-60, the phase trombone sections and the other is at MI-30, the high beta insert for electron cooling. The phase trombone at MI-60 is used to adjust the tune variation caused by magnet imperfections.

The Ring is composed of two types of permanent magnet combined function magnets (CFM), 216 long "arc" magnets which have dipole, quadrupole and sextupole components, and 128 short "dispersion suppressor" magnets which only have dipole and quadrupole components, and 74 permanent magnet quadrupoles. The Recycler ring is designed to match the momentum of the new permanent magnet 8 GeV injection line.

In an earlier paper [3] we had outlined the magnetic field specifications for the Recycler Magnet. To date all the magnets have been build and installed in the ring. The simulations presented in this paper were performed at the

^{*} Email:mishra@fnal.gov

^{*}Operated by University Research Association under contract with the U.S. Department of Energy.

time when first 24 CFM's were build and its higher multipoles trimmed to the specification. Table 1. Shows the multipoles used in the simulations. All of these multipoles are better than specification. Final magnet data not used in this simulation is slightly better than these values. We have used a mean of 0.1 units and sigma of 0.25 units for pole 6 to 9. The quadrupole multipole data

	Normal	Normal	Skew	Skew
Pole	Mean	Sigma	Mean	Sigma
0	0.56	3.78	_	-
1	0.20	0.65	0.06	1.56
2	-0.27	0.31	-0.15	0.42
3	0.0	0.28	0.06	0.37
4	-0.07	0.19	0.13	0.25
5	-0.01	0.22	0.01	0.17

Table 1. Combined Function Magnet data used in the Simulation.

was not available at the time of these simulations. We continued to use the multipoles of 0.5 units mean and 1.5 Units sigma. The calculations also includes a misalignment errors $\sigma_x = \sigma_y = 0.25$ m and $\sigma_{roll} = 0.5$ mrad for all magnetic elements and BPMs.

3 DYNAMIC APERTURE

In this paper we describe the variation of magnet properties from ideal and their effect on dynamic aperture of the Recycler. Finally a simulation where all the effects are considered together is discussed. The measured longitudinal profile of the magnetic fields b0, b1 and b2 was found to have a shape different than parabolic, as assumed in earlier calculations. In these calculations we use an average of 20 CFMs longitudinal profile data to simulate the longitudinal b0, b1 and b2 variations. Dividing the CFM into 16 magnets simulates magnet profile. Each individual piece has its own deviations from the nominal. Figure 1., shows the longitudinal profiles used in simulations at various times. The three-bump profile (2) is from the magnet data. We have found that the longitudinal profile variations do not have much effect on the dynamic aperture.

Launching an array of particles at different amplitudes tests performance in the presence of a mixture of alignment and magnetic field error. Particles are tracked with betatron oscillation amplitudes relative to a corrected orbit. Following the introduction of errors the tune is adjusted to the nominal tune for zero momentum offset using the phase trombone. The particles are launched with equal horizontal and vertical emittance. Particles are

tracked with a constant momentum offset. Unless otherwise specified the momentum offset for these simulations are 0.3%. Net chromaticities in both planes are set to -2. Simulations are performed for five seed firle5 to 1e6 turns corresponding to a maximum of 10-sec store time.

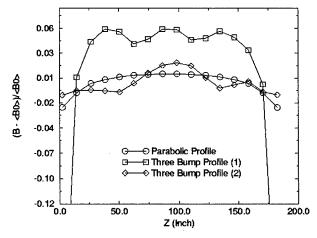


Figure 1. Longitudinal profiles of the CFMs.

As described earlier the "acr" CFM has sextupole component build into its body field. The Recycler Lattice has two families of distributed sextupoles correctors with enough strength to adjust the chromaticity by 10 units. There are 8 and 16 sextupoles in the H and V planes respectively, distributed around the ring. These correctors will compensate any change in chromaticity values due to any systematic sextupole offset from the design. During the construction of the arc CFM it was found that the body sextupole and other multipoles were different than the design specifications. The CFM body multipole components were trimmed by placing a specially designed multipole trim for that particular magnet at one end of the These trims also contained a component for systematic sextupole offset. We have simulated the effect of these end sextupole trims on the dynamic aperture of the Recycler. Any change in chromaticity due to this oneended correction was adjusted by using the distributed

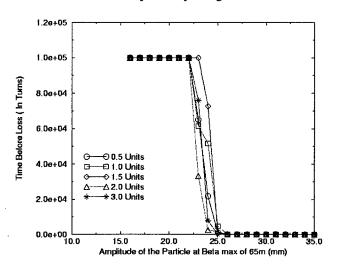


Figure 2. Dynamic Aperture for different size of end trims sextupole.

correction sextupoles. Figure 2. shows that for a 1 second simulation of the Recycler the dynamic aperture is independent of the size of the end trim sextupole.

A survival plot of the five seeds displaying how many turns a particle survived as a function of the initial launch amplitude is shown in Figure 3. This calculation included the longitudinal profile, the feed-down of higher multipoles due to curvature, measured magnetic multipoles, end shim sextupoles of 3 units. The dynamic aperture of the machine is defined as the smallest amplitude particle that did not survive the full 1e6 turns. From figure 3 we see that the dynamic aperture of the Recycler is predicted to be 24.2 + 1.5 mm corresponding to a normalized emittance of $78.9 + 1.0 \pi$ mm-mr.

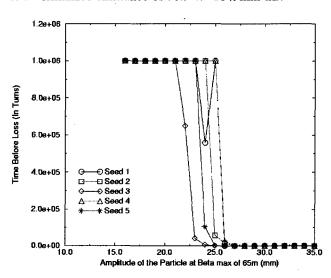


Figure 3: Dynamic Aperture of the Recycler. The number of turns survived is shown as a function of launch amplitude for five different collections of systematic and random alignment and magnetic field errors and a momentum offset of 0.3%.

The dynamic aperture as a function of momentum offset for the largest amplitude particles that survived 1e5 turns

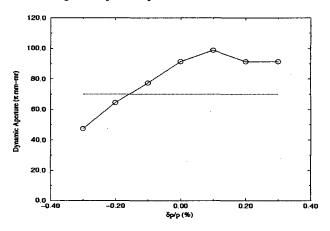


Figure 4: Dynamic Aperture as a function of momentum offset over the full range of the antiproton stack.

is shown in Figure 4. This plot indicates an aperture in excess of $60~\pi$ mm-mr is maintained over the full momentum spread expected in the antiproton stack. Loss in aperture for negative $\delta p/p$ indicates that the particles are moving towards a resonance. In principle this can be improved by small adjustment in the operating tune.

4 SUMMARY

The design criteria of the Recycler was that the dynamic aperture calculated based on 10 seconds simulation of the Recycler should be as large as the physical aperture. Also there should be no trend of particle loss. All the Recycler magnets have build, sorted and installed in the ring. The magnet data in most cases are better than specified. The commissioning of the Recycler ring is going to start during April 1999.

- [1] "The Fermilab Main Injector Technical Design Handbook", August 1994
- [2] "The Fermilab Recycler Ring Technical Design Report", Fermilab TM-1991, November 1996.
- [3] MAD, An Acceleration Design Code, CERN, Geneva.
- [4] D. E. Johnson et al.," Design and Simulation of the Antiproton Recycler Lattice", Proceeding of PAC97.
- [5] L. Schachinger and R. Talman, Particle Accelerators 22, 1987.
- [6] Al Garren and Dave Robin, "A Phase Trombone for the Recycler", internal MI note MI-0181, July 1995.

COMMISSIONING RUN OF THE LONG-BASELINE NEUTRINO OSCILLATION EXPERIMENT AT THE 12-GEV KEK-PS

<u>Hikaru Sato</u> and the Task Force Team High Energy Accelerator Research Organization (KEK), Tsukuba, 305-0801, Japan

Abstract

A prompt report for the commissioning run of the longbaseline neutrino oscillation experiments will be presented. Improvement of the KEK-PS main ring has been performed for recent years in order to prepare the long-baseline neutrino oscillation experiment. Intensity upgrade studies and the hard ware improvements result in a factor of 50% increase in the beam intensity to 5-6 \times 10¹² ppp up to now. It depends on the reduction of the micro-instability at the crossing of the transition energy and the fine tuning of the closed orbit distortion and so on. The neutrino oscillation experiment requests the fast extraction. It needs to construct the fast kicker magnet system, consists of the 12.5 ohm kicker magnets and Blumlein power supplies, and to re-construct the septum magnets and some other equipment. These works have been under going during a long shut down, which was scheduled for the preparation and construction of the neutrino oscillation experiments facility until January, 1999. The switching of the fast extraction and the slow extraction will be possible without the evacuation of the equipment in order to serve the beam for the multi-users as effective as possible. The prompt results of the commissioning run, which will start at the end of 1999, and the performance improvements of the KEK-PS main ring will be presented.

1 INTRODUCTION

The KEK-PS complex comprises two 750 keV Cockcroft-Walton pre-injectors, 40 MeV injector linac, 500 MeV booster synchrotron and 12 GeV main ring as shown in Figure 1. It has been operated successfully to serve a proton beam for more than past two decades [1]. Beams have been serving by the half integer slow extraction to East and North counter halls. Beam bunches accelerated in the booster except to the main ring are utilized as NML (Neutron and Meson Laboratory). To meet the need of new physics research, there are several objectives for the PS upgrade. Especially, an intensity upgrade is coming to the urgent problem for the long-baseline neutrino oscillation experiment [2]. This means the fast extracted highintensity beam creates the high current neutrino beam, which will be injected to Super-Kamiokande, about 250 km west of KEK. The main ring upgrade projects, intensity upgrade study, construction of the fast

extraction system have been performed [3, 4, 5, 6]. The neutrino beam line and the production target were constructed for same days by the beam channel group in the Institute of Particle and Nuclear Studies [7].

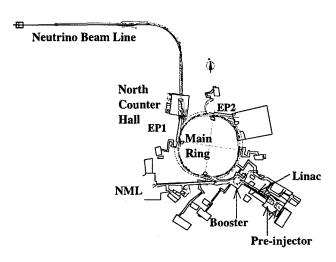


Figure 1: Layout of the 12-GeV KEK-PS.

2 INTENSITY UPGRADE STUDIES

Every effort to realize the upgrade of KEK-PS have been devoted. Booster synchrotron accelerates more than 2 x 10¹² ppp for NML, however, the main ring cannot accept the beam of this intensity. Machine studies for the intensity upgrade have continued to make clear the cause and cure of the difficulty. First of all, several tools for the machine study were developed and/or upgraded, such as an injection error monitor, a fast beam loss-monitor, a tune measurement system with an RF kicker, a fast wire scanner and NMR field monitor for the main ring bending magnet.

The concentrated studies in the spring of 1995 was focused on the beam injection to the main ring [3]. It seemed that the forth-order resonance was one candidate and in order to reduce the quadruple imperfection, several correction quadruples were necessary. However there were no installation space in the ring to install them, then the vertical tune was changed from 7.22 to 5.22 to cure the effect of the fourth-order resonance. In order to increase the vertical aperture, the re-alignment of the main ring magnet in the vertical plane was done during summer shut down, 1996. The injection efficiency has increased up to 95-

97%. During the magnet realignment was done, the fast floor movement, which seemed to depend on the weather condition, was observed. In order to confirm this phenomena, the measurement of the relative quadrupole magnet level and the floor tilt in the ring were going on [8]. Further, Porous Ceramics Osmometers were set in the soil bank to measure the moisture in the soil under collaboration with Radiation Science Center of KEK and the Geological Survey of Japan.

The loss observed around 80 ms after the beginning of acceleration results from the horizontal head-tail instability. The instability occurs due to a large change in the chromaticity produced by the sextupole field induced in the beam-pipe of the dipole magnets [4]. In order to suppress this phenomena octu-pole magnets were installed in the main ring and the studies to confirm the suppression of instability and to measure the dynamic aperture are now processing.

Since KEK-PS's impedance budget has been not concerned, a lot of high impedance materials were periodically located along the ring. The one-third of resonant impedance devices, vacuum ducts between the bending magnet and the quadrupole magnet and the beam position monitor, were replaced by low impedance ones in 1996 [5] to care the beam loss at the crossing of the transition. To cross the transition energy in stable condition, γ -jump magnet power supplies were upgraded to make the voltage twice.

The issues of the intensity upgrade are as follows,

- · realignment of the quadrupole magnets in the main ring,
- · replacement of bend-quad beam pipe,
- · upgrade of beam position monitors,
- · installation of beam instrumentation,
- upgrade of the power supply for the γ -jump magnets,
- · installation of octu-pole magnets.

3 FAST EXTRACTION SYSTEM

ast extraction of full circulating beam is requested for the neutrino oscillation experiment. The EP1 extraction system was modified so that both of slow and fast extraction are possible. According to the careful orbit analysis for the feasibility using existing slow extraction devices, such as bump and septum magnets system, the changeable system of the extraction kicker and electro-static septum in the same vacuum chamber was decided and the former design, distributed small kickers around in the ring [6], was rejected.

In order to double of the kicker magnetic field and save the transmission time, the Blumlein system was decided to construct [9]. The field strength is requested higher than 0.11T and this should be realized within the space of 3m in one long straight section.

The issues of the modification are as follows,

- · ESS-kicker chamber construction,
- · kicker magnets construction,
- · ESS replacement,
- · septum A, B magnets improvements,
- · septum C magnet power supply construction,
- · septum E magnet replacement,
- · beam ducts replacement,
- · control system upgrade.

4 NEUTRINO PRODUCTION SYSTEM

A neutrino beam line extended from EP1-A primary beam line of the north counter hall towards the direction of the Super-Kamiokande as shown in Figure 3. This comprises the straight section, the arc section, the target station, the decay volume and the μ-monitor pit [7]. A fast-extracted proton beam will be transported about 400 m and focused onto a production target.

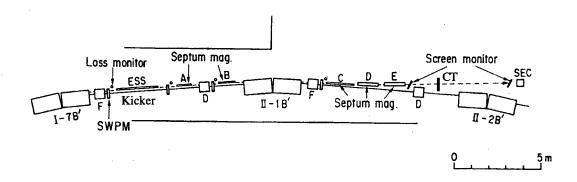


Figure 2: Layout of the EP1 extraction system. ESS and kicker magnets are installed in the same vacuum chamber. Fast extracted beam bunches are measured by CT at the exit of septum magnet E.

Two magnetic homs in the target station will focus produced pions to the forward direction, and enhanced by a factor of 14. The neutrino flux will be produced by decay-in-flight of pions in the 200 m decay volume. A primary proton beam will be stopped in the beam dump. A high-energy part of muons will be monitored at the µ-monitor pit. A positioning of the Super-Kamiokande from the KEK site was made by the global positioning system (GPS). It is found that the EP 1-A beam line must turn 88°44'25" to the left (west), and bent 10°4'30" downward with respect to the horizontal plane just before the production target [10].

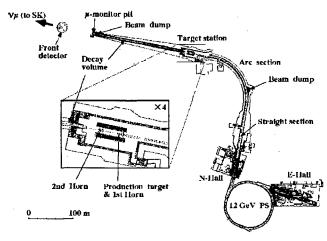


Figure 3: Layout of the nuetrino beam line and the production target system.

5 COMMISSIONING RUN

A fast extracted beam was confirmed on the production target at 16:00 on February 3. Commissioning run was performed as follows.

Main ring beam tuning started on January 27 by the slow extraction mode and the neutrino beam line tuning started on January 31 using slow-extracted beam. On the morning of February 3, the extraction system was changed from the slow extraction mode to the fast extraction mode after tuning the neutrino beam line except the horn system. System change was done in only three hours. Main ring beam tuning started again at 13:04. The kicker magnets were excited and the fast extracted beam was observed on the monitor screen at the exit of the septum magnet E. After short beam-off for the check of some instrumentation, the fast extraction tuning started again and the beam was confirmed on the production target at 16:00. Figure 4 shows the circulating beam bunches, kicker magnet wave form and the extracted beam bunches observed by the current transformer situated at the exit of the septum magnet E. Fast extraction started again on March 3 after the completion of the horn system. The first neutrino event will be expected.

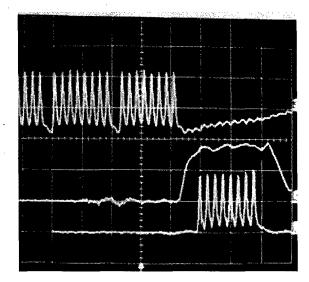


Figure 4: Beam bunches and the kicker wave form.

Upper sweep: Beam current circulating in the ring. One bunch was taken out for the kicker rise.

Middle sweep: Wave form of the kicker magnet. Lower sweep: Extracted beam bunches observed by the CT at the exit of septum magnet E.

6 ACKNOWLEDGMENTS

The authors would like to express their sincere thanks to M. Kihara, director general of accelerator laboratory and I. Yamane, director of PS division, for their encouragement. They are much indebted to many colleagues of PS and beam channel staff for their discussions and collaborations.

- K. Nakai and T. Ohshima, Summary of Experimental Programs at the KEK-PS in KEK-PS 1980's, 1990 and KEK-PS 1990-1994, 1994.
- K. Nishikawa et al., KEK Preprint 93-55/INS Report 297-93-9
 M. Sakuda, KEK Preprint 97-254, Feb., 1998 (Submitted to APCTP-WS)
- [3] Report on the 1995 Spring Machine Study at KEK 12 GeV Proton Synchrotron, KEK Internal 95-12 (in Japanese)
- [4] T. Toyama et al., Proc. of the 1997 Part. Accel. Conf., p.1599
- [5] K. Takayama et al., Proc. of the 1997 Part. Accel. Conf., p.1548
- [6] H. Sato et al., Proc. of the 1997 Part. Accel. Conf., p.1009
- [7] M. Ieiri et al., Proc. of the 1st Asian Part. Accel. Conf., Tsukuba, Japan, 1998, p.579
- [8] H. Sato et al., Proc. of the 1st Asian Part. Accel. Conf., Tsukuba, Japan, 1998, p.263
- [9] T. Kawakubo et al., Proceedings of the 5th European Particle Accelerator Conference, p.2441
- [10] H. Noumi et al., Nucl. Instrum. & Methods A 398 (1997) 39

COMMISSIONING OF THE NEW MULTIPOLE WIGGLERS IN THE SRS

J. A. Clarke and <u>G. S. Dobbing</u> CLRC Daresbury Laboratory, Daresbury, Warrington. WA4 4AD, UK

Abstract

Two new high field 2 T permanent magnet multipole wigglers have been installed into the SRS. This paper describes the effect of the new insertion devices on the SRS lattice. Closed orbit distortion, betatron tune change and emittance blow up have all been measured and the results are compared with lattice model predictions which are based on actual measured magnetic field values.

1 INTRODUCTION

The 1998 SRS Upgrade has been completed and two new multipole wigglers (MPWs) have been installed as planned [1]. These new additions complement the two superconducting wigglers and undulator that have been in the SRS for some time. One of the wigglers will provide light for two experimental stations, both dedicated to protein crystallography [2]. The other will have one station for studying the interaction of photons with molecules, nanoclusters and surfaces although provision has been made for adding a second station at a later date. The new multipole wigglers are identical permanent magnet insertion devices optimised for output around 10 keV. A design comprising nine 2 T poles and two 1.7 T end poles was chosen for the wigglers, yielding a 25 fold increase in photon flux per horizontal angle at 10 keV compared to an SRS dipole.

As the SRS is a second generation light source, installing the new insertion devices necessitated the relocation of several machine components, notably all four RF cavities were moved to alternative straight sections [3]. This upgrade also provided one further free straight, possibly to be occupied in the future by a helical undulator to give light with variable polarisation. Installation of the wigglers and manoeuvring of machine components was completed in a shutdown at the end of 1998. One of the narrow gap vessels for use with the new wigglers had already been installed in January 1998 so experience could be gained with a much-reduced vertical aperture.

2 MODELLING THE MULTIPOLE WIGGLERS

Before the multipole wigglers were installed much commissioning work had already been carried out. Numerous protective devices had been proved to work (e.g. magnet array tilt, temperature and beam position

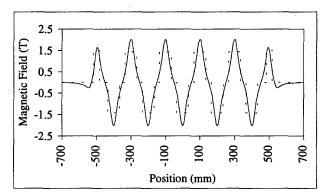


Figure 1: Measured magnetic field along the magnetic axis of an MPW at operational gap (solid line). The field assumed in the hard-edged lattice model is also shown (broken line).

interlocks) and the magnetic fields produced by the wigglers had been measured extensively [4]. These measurements were used to build a lattice model of the MPWs.

To predict the effect of the MPWs on the SRS electron beam a hard-edged model was used. The number of poles and the total length of a real MPW were conserved. Two types of pole were used; the MPW model was composed of two end poles and nine central poles, with zero-field drift spaces in between. Actual measurements of the magnetic field through an MPW are plotted in fig. 1 [4]. The magnetic field for the hard edged model is also plotted. Pole length and magnetic field in the model were varied to match integrals of powers of the on axis magnetic field. Measurements were taken from one of the MPWs, the other was found to be extremely similar. Net angle of bend produced by a magnetic field depends on the integral of the magnetic field along the electron path. Integrating the second power of the field gives the predominant focussing effect whilst change in emittance is affected primarily by the integral of the modulus of the third power of magnetic field on the electron path. The hard-edged model cannot match integrals of all three powers of magnetic field simultaneously so a model that gave the correct integrals of first and second powers was used to predict betatron tune shift. Similarly a model that matched measured integrals of the first and third power of field was used to predict emittance blow-up. It is interesting to note that this technique leads to a model in which the end poles have a higher field strength than the centre poles. This is the same approach that was used to predict the tune shift and emittance increase, accurate to

^{*} E-mail g.s.dobbing@dl.ac.uk

first order, due to the SRS superconducting wigglers that were installed in 1982 and 1993 [5,6].

The emittance increase and tune shift due to one of the MPWs predicted using the Daresbury lattice code "ORBIT" are shown in table 1. Values without the MPW are shown for comparison.

Table 1: Predicted emittance and tune shifts in the SRS for multibunch operations. It is estimated that an MPW at operational gap will cause an emittance increase of 4%.

	Without MPW	MPW at operational gap
Radial Emittance (nm rad)	104	108
Vertical Tune	3.350	3.366
Vertical Tune Shift	0	0.016
Horizontal Tune	6.198	6.198

3 MEASURED STORAGE RING BEHAVIOUR

3.1 Orbit Shifts

The first MPW was commissioned with beam in February 1999. As the magnet gap was closed the betatron tunes and closed orbit were recorded. Plots of the uncorrected RMS horizontal and vertical orbit as a function of magnet gap are shown in fig. 2. Fig. 3 shows the change in the integrated magnetic field through the MPW, measured before the MPW was installed and resulting change in the orbit at a typical horizontal beam position monitor as the MPW gap is closed. Excellent correlation is evident between the integrated field through the MPW and the resulting orbit distortion.

3.2 Tune Shift and Beam Size.

The SRS tune measuring system measures the coherent response of the beam to an electrostatic deflection. This signal is seen at a frequency corresponding to the fractional part of the betatron tune. Horizontal and vertical tunes were measured as the MPW magnet gap was closed. Horizontal tune was unchanged to within 0.002; a plot of vertical tune shift against magnet gap is shown in fig. 4. A strong correlation between the MPW peak field and the vertical tune shift is evident, as expected.

The discrepancy between the tune shift measured at the MPW minimum operating magnet gap of 20.5 mm and that calculated using the hard edged model is 16%. When used for calculations preceding the installation of the superconducting wigglers in 1982 and 1993 the discrepancies were zero (to within the accuracy of the measurement) and 6% too high respectively [7,8]. These results, taken with those presented in this paper suggest that the hard edged model becomes less accurate for high or complicated fields, as may be expected for a simple model. However, the discrepancies are not so large as to

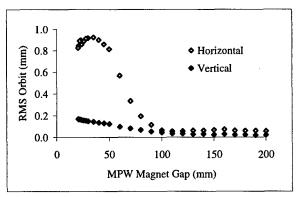


Figure 2: Horizontal and vertical RMS orbits at different MPW magnet gaps.

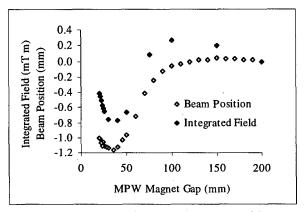


Figure 3: Changes to horizontal beam position at a typical BPM and integrated magnetic field as the MPW magnet gap is closed from 200 mm.

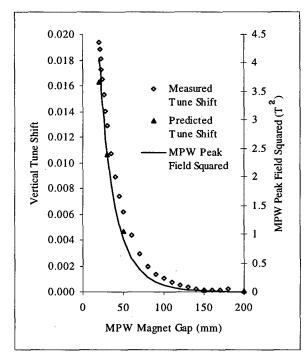


Figure 4: Measured and predicted vertical tuneshifts at different MPW magnet gaps. The MPW peak field is also shown.

make the approach used here invalid. In general calculations are only required to give an approximate estimate of effects on the electron beam, in order to specify the accelerator components required for correction. Therefore the hard edged model is still useful to accelerator physicists as a comparatively quick and accurate way of anticipating the effects that a proposed insertion device will have on an accelerators characteristics.

During commissioning the beam sizes at the SR diagnostic port were not seen to change (to within the 5% repeatability of the measurement). This is consistent with the very small predicted increase in the emittance, shown in table 1. No change in horizontal-vertical coupling was observed.

The MPW was not observed to have any effect on the electron beam lifetime.

3.3 Correcting the Effects of the MPWs on the Storage Ring

A similar correction scheme is used for the new MPWs as was successfully implemented for the superconducting wigglers at Daresbury [6]. Trim coils fitted around the magnet arrays correct the integrated field of the MPW to minimise the RMS horizontal orbit. An active shunt is fitted to the local vertically focussing quadrupole to correct for the vertical focussing of the MPW. During the commissioning of an MPW the currents required through the trim and shunt to correct both the orbit and tunes for several MPW magnet gaps were recorded. These values were then fed into the control system so that software may be used to automatically carry out orbit and tune correction as the magnet gap is changed during operations. Initial trials of these systems were very successful.

4 SUMMARY

As well as preparing one MPW for use, its radiation port has also been commissioned, although the beamline and experimental stations are not due for completion until May of this year. Radiation was successfully extracted from the port on 8th March 1999, at the first attempt, making it likely that the two new protein crystallography stations will be ready for users by September and November respectively [9]. The second MPW beamline will not be permitted to take beam until it is complete, for radiation safety reasons. This will happen during the second half of 1999.

- [1] Clarke, J. A., M. W. Poole, "Upgrading The Daresbury SRS With Additional Insertion Devices and its Implications For the Storage Ring Layout", Proc. 5th Euro. Part. Accel. Conf., Sitges, p 623, 1996.
- [2] Duke, E. M. H., R.C. Kehoe, P.J. Rizkallah, J.A. Clarke, C. Nave, J. Synchrotron Rad., 5, pp 497-499, 1998.
- [3] Dykes, D.M., "RF System Changes Associated With the SRS Upgrade", Proc. 5th Euro. Accel. Conf., Sitges, p1946, 1996.
- [4] Clarke, J.A., N. Bliss, D.J. Bradshaw, N.W. Harris, C.L. Hodgkinson, R. Marl, I.D. Mullacrane, M.W. Poole, M.J. Pugh, R.J. Reid, "Final Measurements of the SRS Multipole Wigglers", these proceedings
- [5] Marks, N., G.N. Greaves, M.W. Poole, V.P. Suller, R.P. Walker, "Initial Operation of a 5T Superconducting Wiggler Magnet in the SRS", Nucl. Instr. And Meth. Phys. Res. 208 (1983), p 97.
- [6] Poole, M.W, J.A. Clarke, P.D. Quinn, S.L. Smith, V.P. Suller, L.A. Welbourne, "Commissioning a Second Superconducting Wiggler in the Daresbury SRS", Proc. 1993 IEEE Part. Accel. Conf. Washington, 1993.
- [7] Suller, V.P., N. Marks, M.W. Poole, R.P.Walker, "SRS Behaviour With a Superconducting 5T Wiggler Insertion", Proc. 1983 IEEE Part. Accel. Conf., Santa Fe, 1983.
- [8] Clarke, J.A., D.M. Dykes, S.F. Hill, E.A. Hughes, P.A. McIntosh, M.W. Poole, P.D. Quinn, S.L. Smith, V.P. Suller, L.A. Welbourne, "Update on Commissioning and Operations With the Second Superconducting Wiggler at Daresbury, Proc 4th Euro. Part. Accel. Conf., London, p648, 1994.
- [9] http://www.dl.ac.uk/SRS/PX/events.html

FINAL MEASUREMENTS OF THE SRS MULTIPOLE WIGGLERS

J.A. Clarke, N. Bliss, D.J. Bradshaw, N.W. Harris, C.L. Hodgkinson, R. Marl, I.D. Mullacrane, M.W. Poole, M.J. Pugh and R.J. Reid, CLRC Daresbury Laboratory, Warrington, UK WA4 4AD.

Abstract

Two new high field 2 T multipole wigglers have been built for the SRS. Detailed mechanical and magnetic tests have been made and these are compared with the expected theoretical performance. These insertion devices have now been installed into the SRS and are operating successfully.

1 INTRODUCTION

Two new high field (2 T) hybrid Multipole Wigglers have been designed and constructed for the SRS Upgrade Project [1]. The two insertion devices are identical and have been specified to provide maximum flux at a photon energy of 10 keV. The chosen design will provide a source with about 25 times more photons per horizontal angle at this photon energy than a standard SRS dipole source. One of the beamlines will have 2 experimental stations, both dedicated to protein crystallography. The other beamline will initially have one station, for studying the interaction of photons with molecules, nanoclusters and surfaces, although provision has been made for a 2nd station to be added at a later date.

All aspects of the Multipole Wigglers were fully specified and designed by Daresbury Laboratory but the manufacture and assembly was carried out under a commercial contract by Sincrotrone Trieste SCpA. The contract was placed during the Summer of 1997 and both the insertion devices were delivered to Daresbury Laboratory 11 months later. The final magnet design is described in [2].

2 MECHANICAL MEASUREMENTS

A detailed series of mechanical measurements were carried out on both MPWs (referred to as MPW 1 and MPW 2) after they were delivered to Daresbury Laboratory. The gap between the steel pole pieces was set to the nominal minimum value of 19.2 mm and ceramic slip gauges with increments of 1 μ m were used to measure the gap under each of the 11 poles in two horizontal positions. As expected the gap was slightly larger on the inside of the magnet compared to the outside. This is simply due to the C shape design of the magnet support structure. The maximum gap difference along the whole of the magnet was 40 μ m for MPW 1 and 102 μ m for MPW 2. This compares remarkably well with the predicted 80 μ m from FEA calculations [3].

Measurements were also made of the repeatability of the carriages between the maximum gap of 200 mm and 19.2 mm. The pitch and roll were measured with a Kern Nivel 20 electronic level with a resolution of 1 μrad. The gap was opened and closed 5 times and the maximum angle variation observed at either gap for MPW 1 was 6 μrad of pitch and 11 μrad of roll and for MPW 2, 11 μrad of pitch and 8 μrad of roll. In each case the repeatability is excellent for a mechanical system where the force between the two arrays is increasing by about 5 tonnes as the gap closes.

3 MAGNETIC MEASUREMENT LABORATORY

A new Magnet Measurement Laboratory has been built at Daresbury Laboratory for measuring insertion devices. Two measurement facilities were designed, a Hall Probe Bench and a Flipping Coil Bench. The laboratory is temperature controlled to $\pm 1^{\circ}$ C to improve the repeatability of the measurements.

3.1 Hall Probe Bench

Table 1. Hall Probe Bench specifications.

Hall Probe	MPT-141-3m
Teslameter	DTM-141-DG
Longitudinal Range	1400 mm
Horizontal Range	200 mm
Vertical Range	100 mm
Longitudinal Resolution	1 μm
Horizontal Resolution	0.5 μm
Vertical Resolution	0.5 μm
	-
Nominal Longitudinal Velocity	1 mm/s
Maximum Calibrated Field	2.2 T
Hall Probe Precision	± 0.01 %
Hall Probe Resolution	0.5 G
Temperature Stability	± 10 ppm/°C
Sensitive Area	1.0 x 0.5 mm
	L

The Hall Probe Bench is designed to measure the magnetic field at discrete points in the insertion device. The Hall Probe can be scanned in all three linear axes with a resolution of $1 \mu m$ in the longitudinal direction and

0.5 µm in the horizontal and vertical directions. The Hall Probe and Teslameter used were supplied by Group 3 [4]. The specification of the Hall Probe System is summarised in Table 1. The system is fully automated and is controlled by a local PC running LabVIEW [5]. The PC uses RS232 to interface with the motors and encoders and GPIB to interface with the Hall Probe. The Hall Probe is normally oriented to measure vertical magnetic fields though it can measure in other orientations as required. At present the system moves the probe to the desired location and then takes a reading once it has stopped moving. The possibility of an 'on-the-fly' measurement has not yet been investigated. The time taken for a 1.4 m scan with a reading every 2 mm is approximately 30 minutes (less than 3 s per point).

3.2 Flipping Coil Bench

The Hall Probe system is designed to measure the field at discrete points, so it is ideal for mapping out the magnetic field along the axis, for example. However, since each field reading has an error associated with it (albeit small) the total error in any integral measurement can be significant. In order to measure the field integrals more accurately a flipping coil scheme was also designed. This will measure the integrals in a single measurement (in a few seconds) and the error in the measurement should be smaller than in a numerically calculated integral taken from the Hall Probe scan. A 20 turn coil, made by soldering individual 50 µm strands of Litz wire together to form a complete circuit, is mounted between two rotating heads. The coil mounting heads are approximately 2.5 m apart on a linear guide rail system. They can be moved manually in a longitudinal direction so that the correct tension can be set in the wire; a tensiometer is provided for this purpose. The heads can be moved remotely in the horizontal and vertical directions with a resolution of 0.5 μm. The heads can also rotate 360° about the longitudinal axis with a resolution of better than 0.001°. The full specification for the flipping coil system is given in Table 2. The system is fully automated and is controlled by a local PC running LabVIEW. The PC uses RS232 to interface with the motors and encoders and GPIB to interface with the HP Multimeter that is used as the Voltage Integrator.

The flipping coil system was only completed as the MPWs arrived for testing, therefore the commissioning time available was very short. The system gave reasonable results but the repeatability was never better than a few %. It became apparent that the repeatability was limited because of a noisy voltage signal from the coil. The noise appeared to be due to the coil vibrating as it was rotated. Vibration measurements have recently started to try to determine exactly which component of the system is responsible for the vibration so that remedial action can be taken. The integrated field measurements

presented in this paper were all calculated from the Hall Probe results.

Table 2. Specifications for the Flipping Coil Bench

Nominal Coil Length	2.5 m
Maximum Coil Length	3.0 m
Nominal Coil Width	10 mm
Nominal Rotation Velocity	20 °/s
Horizontal Range	200 mm
Vertical Range	100 mm
Rotation Resolution Horizontal Resolution Vertical Resolution	< 0.001° 0.5 μm 0.5 μm
Voltage Integrator	HP 3458A DMM

4 MAGNET MEASUREMENT RESULTS

The peak field measured under the central pole as a function of gap is given in figure 1. The maximum field variation between the 9 full strength poles at the minimum gap of 19.2 mm is less than 0.5 % for both magnets.

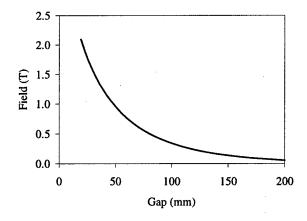


Figure 1. Measured peak field on axis against gap.

The vertical magnetic field as a function of longitudinal position at 19.2 mm gap is shown in figure 2. The full strength poles reach a field of 2.09 T and the two end poles are 1.71 T. The agreement with the three-dimensional model generated with Opera 3D [6] is very good with the largest difference between the two sets of data at the poles being 0.9%. The measured and modelled data for the central portion of one of the MPWs is shown in figure 3.

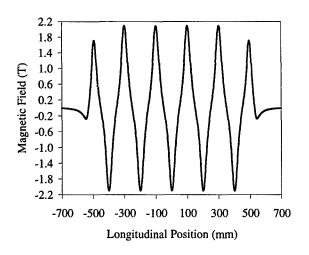


Figure 2. Measured field on axis against longitudinal position at 19.2mm gap.

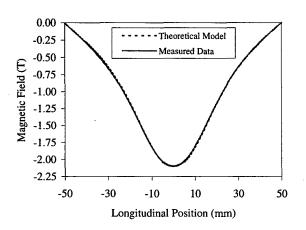


Figure 3. Comparison of the measured field values with the theoretical model over the central pole at 19.2mm gap.

The measured field integrated longitudinally at different horizontal offsets is given in figure 4 for both MPWs. A 6th order polynomial has been fitted to the data points to estimate the integrated sextupole. For MPW 1 the integrated sextupole at minimum gap is 1.37 T/m and for MPW 2 it is 2.60 T/m. The difference between the two magnets is due to the greater angle error between the two magnet arrays in the radial direction in MPW 2 compared with MPW 1 as discussed in Section 2.

The variation of the integrated vertical field on axis as a function of gap is plotted in figure 5. The maximum integral of 2.0 mT-m is easily compensated with the simple trim coil fitted to the MPWs. The maximum current required in the trim coils to maintain a no steering condition from the MPW is about 0.5 A, giving a current density within the air-cooled copper conductor of about 0.2 A/mm².

Both MPWs are now installed in the SRS and commissioning with beam has commenced [7]. Since the MPWs exceed the specified requirement of the beamlines

to operate at 2.0 T the operating gap will be 20.5 mm instead of the minimum of 19.2 mm.

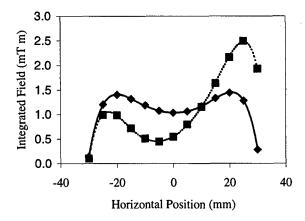


Figure 4. Integrated vertical field against horizontal position with a 6^{th} order polynomial fit. The solid line is for MPW 1 and the dashed line is MPW 2.

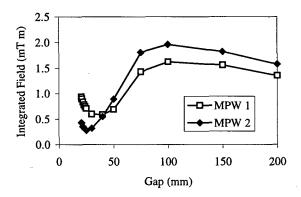


Figure 5. Integrated vertical field on axis as a function of gap.

- J.A. Clarke and M.W. Poole, "Upgrading the Daresbury SRS with Additional Insertion Devices and its Implications for the Storage Ring Layout", Proc. 5th Euro. Part. Accel. Conf., Sitges, June 1996, p623.
- [2] J.A. Clarke et al, "Progress with the SRS Upgrade Project", Proc. 6th Euro. Part. Accel. Conf., Stockholm, June 1998, p571.
- [3] J.A. Clarke et al, "Design of a 2 T Multipole Wiggler Insertion Device for the SRS", J. Synchrotron Rad. (1998). 5, p434.
- [4] Group 3 Technology Ltd, Rosebank, Auckland, New Zealand.
- [5] National Instruments, Austin, Texas, USA.
- [6] Vector Fields, Kidlington, Oxford, UK.
- [7] J.A. Clarke and G.S. Dobbing, "Commissioning of the New Multipole Wigglers in the SRS", these proceedings.

DESIGN, TESTING, AND COMMISSIONING OF AN ELECTROMAGNETIC UNDULATOR FOR SRC*

M.A. Green[#], W.R. Winter, M. Thikim, C.A. Baumann⁺, M.V. Fisher, G.C. Rogers, D.E. Eisert, W.S. Trzeciak, R.A. Bosch Synchrotron Radiation Center, 3731 Schneider Dr., Stoughton, WI 53589-3097

Abstract

In collaboration with one of its user groups, the SRC has installed a new planar electromagnetic undulator (EMU) on the Aladdin storage ring. Field quality, and resulting radiation-performance of the device, are sufficiently close to the ideal that no shimming was required. With slight exception, only minor, anticipated adaptation onto the Aladdin ring was needed to meet strict operational requirements. Major details of the design, fabrication, ex-citu and in situ testing, and commissioning are presented.

1 DESIGN

The EMU described here serves as a source for a high-resolution normal-incidence monochromator (NIM) beamline that covers the range from 6-40 eV [1]. The device was designed by SRC and constructed jointly with the Physical Sciences Laboratory (UW-Madison). The electromagnetic type was chosen for a number of reasons: favorable experience with a similar device for Iowa State University [2]; excellent field-quality control made possible with a copperiron geometry; and conventional construction that both uses inexpensive materials and enables in-house fabrication, leading to substantial cost savings.

1.1 Mechanical Design

The EMU operates in an environment for which the air temperature is 72 °F and the cooling water temperature is 95 °F. The elevated cooling temperature is used for all ring magnets and is related to the capacity of external cooling towers.

The pole material is 1006 hot-rolled, low-carbon steel. Each poleface surface is passivated against corrosion with an acrylic spray coating. The poles are affixed to 3"-thick intermediate, aluminum backing plates which in turn are bolted to upper and lower aluminum spars. Each spar assembly is supported at points which minimize spar deflection under combined gravitational and magnetic loading. Poles were dimensionally sorted, using an optical comparator, to achieve the greatest period uniformity. Stick micrometer measurements were made on the pole assemblies to verify positional accuracy. There is an observed increase in field, corresponding to a decrease in gap, over the center section of the device by 0.4% at zero field and 0.5% at full

excitation.

The coordinate system is right-handed with: x = trans- verse radially outward in the horizontal plane, y = vertically "up", and z = longitudinal in the direction of the beam. The EMU is mounted on the ring from the outside such that the +x-direction is toward the C-frame. Because of Aladdin's low injection energy of 108 MeV, the entire EMU is radially retractable on a motor-driven under-carriage as an additional safeguard against interference with injection.

Nominal mechanical and magnetic parameters are shown in Table 1.

Table 1: Mechanical & Magnetic Parameters

Parameter	Value
Magnet Gap, g	24 mm
Pitch, λ _u	10.9 cm
Pole Width	10.0 cm
End Termination Pattern (w/o signs)	1/4, 3/4, 1, 1 1, 1, 3/4, 1/4
Total Number of Poles	64
Overall Length	3.5 m
Peak Field	4.0 kG
Peak K-value	4.1

1.2 Electrical Design

Nominal electrical parameters are shown in Table 2.

Table 2: Electrical Parameters

Parameter	Value
Total Inductance	0.011 Henry
Current at Peak Field	257 A
Voltage at Peak Field	108 V
Total Ohmic Power at Peak Field	27.8 kW
Power Supply Regulation	≤ 0.4 mA
Peak Current Density in Copper	5070 A/in ²

The power supply used for operation is DCCT-regulated and capable of 300-A by 120-V output. Reflecting the onset of saturation, the required peak current at peak field is

^{*} Work Supported by NSF Grant DMR-95-31009

[#] E-mail: mike@src.wisc.edu

⁺ Physical Sciences Laboratory, 3725 Schneider Dr., Stoughton, WI

3.5% more than expected from lower-excitation linear extrapolation.

The upper and lower pole assemblies are not magnetically "strapped" together [3]. In this geometry any environmental B_y field is enhanced by roughly a factor of 2.5 resulting in an average B_y field of about 1 G from Earth's field. This field component is corrected by full-length coils around the upper and lower pole assemblies. Trim coils were provided on the first and last two poles (top and bottom), although their use has not been found necessary. Although also found unnecessary, passive current shunting of individual pole pairs (top & bottom) was considered for phase shimming.

2 FIELD MEASUREMENTS

2.1 Description

Environmental The EMU was tested in an environmentally controlled room, for which the temperature could be stabilized at the ring operating temperature of 72 °F. Similarly, a closed-loop, thermally-regulated source of cooling water at 95 °F was also provided. Under these conditions stabilized temperatures over the upper and lower aluminum spars varied by ± 0.2 °F and ± 0.7 °F, respectively.

Control & Data Acquisition The mapping system is composed of a Pentium-based PC with a stepping motor controller board, a GPIB board and a 16-bit ADC/DAC board. Two stepping motors are used by the system. One motor drives a Group 3 Hall probe longitudinally (z) through the undulator gap and the second motor positions the probe transversely (x). An on-axis laser interferometer is used to measure the probe's relative longitudinal position in the undulator. A digital micrometer is used at one end of the undulator to set/reset the initial absolute position. During mapping the laser interferometer issues TTL pulses every $25\,\mu m$ which trigger the ADC board to read the analog output from the Hall probe.

The mapping system collects 180000 data points on both forward (-z) and return (+z) passes. At the end of the forward pass the Hall probe enters, and briefly stops within, a magnetic shield where the software records 24000 background data points at about 8000/sec. A complete round trip of a forward pass, a background measurement, and the return pass takes about one minute. At this probe speed the peak data rate is also about 8000/sec. The software can make a series of round trip passes at preprogramed radial (x) displacements without user intervention.

Apparatus The analog output from the G3 Hall probe was precalibrate at the factory. The probe is supported on a carriage that has a manual y-motion stage and the computer-controlled x-motion stage. The carriage moves at a rate of about 200 mm/sec along a 4.5-m rail that extends about 0.5 m past each end of the EMU. Limit switches for the

longitudinal carriage drive are provided in the event of computer-drive error. The rail is supported off the lower spar keeping the probe at the same relative vertical position with respect to the median plane for a fixed-gap device. A retroreflector travels with the carriage along the z-axis such that laser interferometer measurements are not affected by offset errors. Refractive index air-path corrections were made for the interferometer measurements. Because of the elevated operating temperature, it was necessary to create turbulence in the air along the longitudinal axis for proper operation of the interferometer.

The probe is mounted in a holder which allows arbitrary 90° rotations about the z-axis allowing B_y , B_x , and flipped $-B_y$, $-B_x$ measurements. Measurements taken in the field-shielded region (between the forward and reverse passes) allowed determination of the Hall probe offset, the residual background, and any magnetization of the shield, which values were subsequently factored into the data analysis. No significant dependence of these parameters was found either on x-position or on device excitation.

It must be noted that the maximum excitation for testing was 240 A whereas that for operation is 257 A. The difference arises because the new power supply for operation had not been delivered in time for testing.

2.2 Results

<u>Hysteresis</u> As standard procedure, the device was always operated on a standard uni-polar hysteresis curve, attained by cycling from minimum to maximum to minimum excitation 5 times. The maximum difference between the lower and upper branches was about 15 G in field, or about 0.8% in relative photon energy.

<u>Multipoles</u> Simple summation of the 180000-point $B_y(x)$ or $B_x(x)$ data files result in the longitudinal integrals $IB_y(x) \equiv \int B_y(x,z) dz$ and $IB_x(x) \equiv \int B_x(x,z) dz$, respectively, all additionally as functions of the excitation. It is felt that rms errors in the IB's do not exceed about 1 G·cm. From the IB's, the respective normal and skew multipole moments are derived by fitting. Over all excitations, the required and

Table 3: Multipole Magnitudes, Over All Excitations

Multipole		Req'd	Meas.	Units
Dipole	Normal Skew	100·10 ⁻⁶ 100·10 ⁻⁶	See Text 170·10 ⁻⁶	T∙m
Quadrupole	Normal Skew	6.7·10 ⁻³ 1·10 ⁻³	0.9·10 ⁻³ 0.6·10 ⁻³	Т
Sextupole	Normal Skew	1.25 1.25	0.03 0.03	T/m
Octupole	Normal Skew	40 40	5 4	T/m²

measured multipoles are as shown in Table 3. Since a long-coil is present to correct IB_{y} , the normal-dipole component is variable; a single, fixed setting for this coil was found which satisfied the requirement. The skew-dipole (vertical steering error) is out of the original spec but is not so easily corrected. However, this component has been relaxed since the ring orbit control is quite able to cope with this steering error.

<u>% Ideal</u> The on-axis $B_y(0,0,z)$ and $B_x(0,0,z)$ fields are used to predict and assess the quality of the undulator radiation that would be emitted, using the UR code [4]. There are two systematic field errors which are known to affect the harmonic radiation in the present case. The first can be from the concentration of Earth's field, if the long B_y coil isn't used, and the second stems from the mid-section field enhancement. With fixed, long-coil correction active, degradation of the 3rd harmonic over its useful range is computed to be less than 10%, the majority of which is not due to the mid-section systematic error.

Internal Orbit Walk Vertical and horizontal orbit integrations interior to the undulator affect both the quality of the radiation (see above) and the effective source point of radiation for the beamline. Over all excitations, the variation of effective source point is $\leq 30~\mu m$ after gross steering correction.

<u>Phase Errors</u> A common measure of the field quality that affects the quality of radiation is rms phase error [5]. At selected values over the range of excitations, this value ranges from 1.0° at low excitation to 4.6° at high excitation.

3 CONTROL

Quad Shunting The undulator is situated in a long straight section between two FODOF triplets. A natural consequence of undulator operation is vertical edge focusing. SRC policy is presently to limit any dynamic, undulator-induced relative vertical beam size variations around the ring to $\leq 1\%$. If the additional vertical focusing were left uncorrected, the resulting relative vertical beam size changes would be excessive, thus necessitating correction. An approximate, yet satisfactory, means of correction is to shunt current in adjacent, upstream and downstream, quadrupoles. The degree of shunting required is nearly proportional to K^2 and is easily programmed into the control system.

BPM Offsets Aladdin has horizontal and vertical feedback control of the closed orbit. In the straight section containing the undulator there are basically four beam-position-monitor (BPM) and steering-magnet combinations in both vertical and horizontal planes with inner and outer pairs straddling the undulator. The inner-pair BPM-steerer combinations can have preset orbit offsets for position and angle steering of the undulator radiation source for alignment into

the attendant beamline. This done, the outer pairs maintain an unperturbed closed orbit everywhere else around the ring.

Hysteresis Operationally, a possible 0.8 % energy uncertainty from hysteresis was considered unacceptable. Therefore, a Hall probe was permanently installed on a pole-face and calibrated against the on-axis field. Precision of calibration is not very important (its within a few tenths of an eV) but the repeatability that this solution makes possible is. Software feedback control of the undulator's excitation is entered by the beamline user in eV and relies upon the Hall probe for its operation.

4 INITIAL EXPERIENCE

The EMU is now installed on the Aladdin ring where it is also paired-up with the new power supply. SRC maintains the option of installing magnetic shielding between any insertion device and neighboring quadrupoles. So far this hasn't been necessary, the present case in particular. Preliminary ambient-field mapping in the straight section where the device is installed was conducted, resulting in the correction of a very minor problem with an ion pump.

The radial retraction of the undulator for low-energy injection also is found empirically unnecessary. In fact, actually discovered by accident, injection is observed to proceed with little difficulty (with only steering correction) at 70 A of excitation.

Without quad-shunt correction, the observed relative vertical beam size changes at optical monitors around the ring are $\leq 8\%$. However, with quad-shunt correction the observed vertical beam size variations at the optical monitors are $\leq 1\%$ over the full operating range of excitations. Operationally, any beam positional variations around the ring, in the presence of global feedback orbit control, are entirely satisfactory. Further, no adverse coupling or lifetime effects have been observed.

Lastly, the attendant high-resolution NIM beamline is just now being commissioned. Consequently, comparative measurements and experience from the beamline are not yet available. It is anticipated that these will be reported in the near future.

- [1] R. Reininger, et al., Rev. Sci. Instrum. 66, 2194 (1995).
- [2] F.C. Younger, W.J. Pearce, B. Ng, Nucl. Instr. and Meth. in Phys. Res. A 347, 98 (1994).
- [3] Decided after private correspondence with Ross Schlueter (LBL).
- [4] R.J. Dejus and A. Luccio, Nucl. Instr. and Meth. in Phys. Res. A 347 (1994) 61.
- [5] R.J. Dejus, I. Vasserman, E.R. Moog, E. Gluskin, Rev. Sci. Instrum. 66, 1875 (1995).

RECENT DEVELOPMENTS OF INSERTION DEVICES AT THE ESRF

J. Chavanne, P. Elleaume, P. Van Vaerenbergh ESRF, B.P.220, F-38043 GRENOBLE Cedex France

Abstract

57 Insertion Devices (IDs) segments are now in operation in the ESRF Storage Ring serving 29 beamlines. A review of the present situation is made together with a detailed description of the recently built in-vacuum undulator. The mechanical and magnetic designs together with the pumping and conditioning with beam are described. No lifetime reduction is observed for any magnetic gap larger than 6 mm. A summary is made of the most important properties of several new innovative IDs including the 3 T permanent magnet wiggler, the quasi-periodic undulator and the fast switching helical undulator.

1 INTRODUCTION

The European Synchrotron Radiation Facility (ESRF) is a third generation synchrotron light source optimized to produce high brilliance X-rays in the 1-100 keV range by means of Insertion Devices. The IDs consist of 1.6 m long segments. A complete 5 m long straight section accommodates three segments. At present, 57 segments are in operation representing a cumulative length of 90 m and serving 29 ID beamlines. The IDs are built according to the specific requirements of each beamline user. As a result, more than 30 different magnetic designs have been implemented. Almost all IDs are made of permanent magnets with magnet blocks in the open air on both sides of a fixed aperture vacuum chamber. More than 80% of IDs are low field undulators which provide a record brilliance of up to 1.5x10²⁰ Phot/s/0.1%/mm²/mrad². Due to a mechanical and magnetic shimming process, the rms phase errors of the large majority of conventional undulators are in the 1-2 degree range at any useful gap, allowing safe operation on high harmonic numbers. The high energy range above 40 keV is covered by wigglers with a moderate brilliance. In an attempt to shift the undulator spectrum to higher energies, an in-vacuum undulator has been built and is now in operation. It is described in detail in Section 2. Other new special IDs are briefly discussed in Section 3, such as the 3 Tesla permanent magnet wiggler, the quasi-periodic undulator and the fast switching helical undulator.

2 IN-VACUUM UNDULATOR

An in-vacuum undulator, designed and built at the ESRF, was installed in the storage ring during the 1999 January shutdown. The commissioning took only a few days and less than a week after it had received the first beam, it was in use on the Material Science beamline, ID11.

2.1 Mechanical design of the carriage

The carriage and its vacuum system is shown in Fig.1.

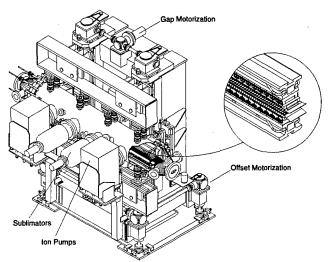


Figure 1: In-vacuum undulator carriage and vacuum system

This presents two remotely-controlled motorizations. The main one is dedicated to the magnetic gap tuning ranging from 0 to 30 mm at a maximum speed of 1 mm/s and a resolution of 0.6 µm. The other (the offset) vertically translates the full magnet assembly for a precise centering of the electron beam in the middle of the gap of the undulator in order to maximize the beam lifetime at small gaps. The offset, rarely used, enables an immediate re-alignment following any possible ground settlement. Stepper motors and absolute encoders are used to drive and monitor each motion. To minimize the size of the vacuum tank, a rigid girder is placed in the open air on the outside of the vacuum. This minimizes the deformation under the magnetic load. A smaller cross-section girder is located in the vacuum. Both girders are linked to each other by eight connecting rods equipped with UHV bellows.

2.2 Magnets

The magnet structure is a hybrid structure with 69 periods of 23 mm. It is expected that in extreme situations the gap will be the limiting aperture. This may result in a possible scraping of the electron beam by the magnetic assemblies. To minimize any risk of demagnetization from exposure to the electron beam [1] a grade of Sm₂Co₁₇ (INCOR26, produced by UGIMAG) was used for the magnet instead of the NdFeB material used in conventional undulators. The magnetic properties of

Sm₂Co₁₇ are more resistant to high temperature and to irradiation by electrons. The penalty is a 15 % reduction in magnetization. The magnet blocks are protected by a Nickel galvanic coating (10 µm thick) which simplifies the cleaning of the magnet surfaces. Following the delivery of the magnet blocks and soft iron poles (ARMCO steel), a special cleaning sequence [2] was applied: degreasing with Perchloroethylene vapour (at 120 °C), followed by an ultrasonic cleaning in an alkaline bath (at 60 °C), and finally rinsing with deionised water in an ultrasonic bath (at 60 °C). As a result of this cleaning, a small magnetization loss of 0.25 % was measured. Following the assembly of magnet and poles, and after magnetic correction, a Cu-Ni sheet (i.e. a 50 µm thick ribbon of Ni, plated with a deposit of 10 µm of Cu) was placed on the surface of the blocks and poles. Copper is used as a means of conducting the return current flowing at the surface of the blocks thereby minimizing the heat deposition. Nickel is magnetic and maintains the sheet in close contact with the pole faces without any corrugation (permanent or heatload induced). The small thickness of Nickel produces a negligible reduction of the undulator field. At both upstream and downstream extremities of the magnet structures flexible transitions are installed. These provide a smooth transition between the vertical aperture of the adjacent chambers and the vertical gap in the thereby undulator minimizing any impedance discontinuity of the vacuum chamber. In addition, some RF masks are placed laterally all along the 1.6 m long undulator on both sides of the magnet structure to minimize the penetration of high order RF modes into the rest of the vacuum tank. These masks are equipped with holes to provide sufficient pumping conductance.

2.3 Vacuum System

The vacuum tank is equipped with two 230 l/s and one 400 l/sec ion pumps as well as two Titanium sublimators each 1000 l/sec. Before inserting the magnetic assemblies, the vacuum tank and pumps were baked at 200 °C for 20 days. A number of bake-outs were later performed with the magnet assemblies in place at a maximum temperature of 120 °C for several days. Fig. 2 shows the pressure recorded in three places inside the vacuum system, normalized to the circulating ring current (mbar/mA), as a function of the time integrated ring current (A.h). Such plots are routinely performed at the ESRF following any replacement of a vacuum chamber. As a result of extensive cleaning, baking and pumping, a rapid conditioning of the undulator chamber was possible, thereby making it immediately available to the users without Bremsstrahlung down to a magnetic gap of 8 mm.

On both magnet jaws, some coaxial thermocouples were fitted on the flexible upstream and downstream transition sections as well as on the poles. As expected, the highest temperature of 120 °C was observed at the

junction between the flexible transition and the magnet assembly. However, over the first two months of operation the thermocouples, placed on the poles at 1/3 and 2/3 length of the undulators, never exceeded 40 °C.

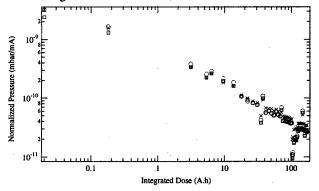


Figure 2: Vacuum conditioning curves

2.4 Effect on the electron beam

Due to a lack of time, it was not possible to correct and shim the magnet structure in the same way as other conventional undulators. As a consequence, a residual field integral of 150 Gcm was observed and later corrected with coils. No lifetime reduction was detected beyond 43 hours (8 hours) when the magnetic gap was reduced to 6 mm (5 mm) in the 200 mA 2/3 filling mode (80 mA 16 bunch mode). Due to a heatload limitation in the front-end part of the beamline, the minimum gap for user operation at 200 mA has been left for the moment at 8 mm, however, it is likely that it will be reduced to 6 mm in the near future. These lifetime observations are not surprising since the lifetime is defined by two scrapers permanently closed at 5 mm during the user mode of operation.

2.5 X-Ray Spectrum

Fig. 3 presents the undulator spectral flux computed with SRW [3] for a gap of 8 mm and 6 mm. Some overlap of the harmonics is observed due to the small horizontal beta function of the ring lattice at the source (0.5 m) which results in a large angular spread of the electron beam. An angular spectral flux six times higher and narrower harmonics are expected if this undulator is placed on an even straight section where the horizontal beta function is large (36 m).

Again, due to a lack of time, an unusually large phase error was left, resulting in a reduction of the angular flux per unit surface on the peak of the harmonics. Compared to an ideal undulator, the angular flux on harmonics 1,3,5 and 7 is expected to be 0.97, 0.74, 0.6 and 0.5 (respectively).

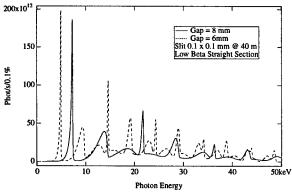


Figure 3: Spectrum through a 0.1×0.1 mm aperture located at 40 m from the source computed for an 8 and 6 mm gap

3 SPECIAL IDS

3.1 Three Tesla Wiggler

A 3 Tesla asymmetric wiggler, made of two periods of 378 mm, has been built [4]. It is essentially a hybrid design with poles made of VACOFLUX 50 and magnets made of VACODYM 383HR. The magnetic design was made in 3D using the RADIA code [5]. The measured peak field reaches 3.13 T for a gap of 11 mm (see Fig. 4) and 3.57 T for a gap of 6 mm. The advantage of such IDs is their low cost compared to a superconducting magnet.

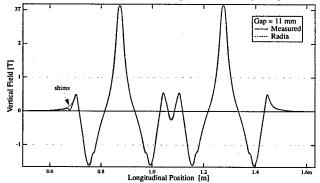


Figure 4: Field Plot of the 3 Tesla wiggler measured at a gap of 11 mm.

3.2 Quasi -Periodic Undulator

A novel and simple design of a quasi-periodic undulator has been tested [6]. It is derived from a conventional pure permanent magnet undulator design by shifting a few magnet blocks vertically. Its main advantage is its simplicity and high spectral flux per unit length. A rejection ratio greater than 8 (11) has been observed on harmonics 3 and 5. With the experience gained from this prototype, a 54 mm period quasi-periodic undulator was designed, and is now undergoing final tests. The fundamental harmonic of this device covers the 1-6 keV energy range with a large suppression of harmonics 3 to 9.

3.3 Fast Switching Helical Undulator

A new fast switching linear/helical undulator has been built and measured [7]. The vertical field of this ID is produced by a coil and a laminated iron structure while the horizontal field is produced by an array of permanent magnets located between the poles. The spatial period is 80 mm and its length is 1600 mm with a peak field around 0.2 Tesla. A fast flipping of the circular polarization from left to right is induced by reversing the current from + 250 A to - 250 A within a time span which can be as short as 6 ms. Initial tests have shown that a dichroism signal as low as 10^{-4} can be detected within a few minutes of integration time [8]. This device opens many new scientific opportunities.

4 ACKNOWLEDGMENTS

The authors would like to thank the Vacuum Group and the Drafting Office for their help in building the invacuum undulator and to all the members of the Insertion Device Group for their daily support. We would like also to thank the Spring8 team for a number of valuable discussions concerning all aspects of the engineering of in-vacuum undulators.

5 REFERENCES

[1] P. Colomp, T. Oddolaye, P. Elleaume, "Demagnetization of Permanent Magnets to 180 MeV Electron Beam", ESRF Internal Note, ESRF/MACH-ID/93-09 and J. Chavanne, P. Elleaume, P. Van Vaerenbergh, "Ageing of Permanent Magnet Devices at the ESRF", to be published at RADECS 99

[2] P. Van Vaerenbergh, Internal ESRF Note, PVV/memo/98-44

[3] O. Chubar, P. Elleaume, "Accurate And Efficient Computation Of Synchrotron Radiation In The Near Field Region", proc. of the EPAC98 Conference 1177-1179 (1998). SRW is freely available from

" http://www.esrf.fr/machine/support/ids/Public/Codes/software.html"

- [4] J Chavanne, P Van Vaerenbergh and P Elleaume, "A 3 Tesla Asymmetric Permanent Magnet Wiggler", NIM A 421 (1999) 352-360 [5] P. Elleaume, O. Chubar, J. Chavanne, "Computing 3D Magnetic Field from Insertion Devices", Proc. of PAC97 Conference, p.3509-3511 (1997). Available from: "http://www.esrf.fr/machine/support/ids/Public/Codes/software.html"
- [6] J. Chavanne, P. Elleaume, P. Van Vaerenbergh, "Development Of Quasiperiodic Undulators at the ESRF", Proc. of the EPAC98 Conference 2213-2215 (1998).
- [7] J. Chavanne, P. Elleaume, P. Van Vaerenbergh, "A Novel Fast Switching Linear/Helical Undulator", Proc. of the EPAC98 Conference p.317-319 (1998).
- [8] A.Rogalev et al., To be submitted to SPIE.

END FIELD STRUCTURES FOR LINEAR/HELICAL INSERTION DEVICES.

J. Chavanne, P. Elleaume, P. Van Vaerenbergh ESRF, B.P. 220, F-38043 GRENOBLE Cedex France

Abstract

The field integral tolerances required on third generation synchrotron sources are of the order of 10-20 Gcm in the whole gap range of an insertion device. This can be achieved without electromagnet correction by a proper magnetic design of the field termination. The paper describes several such end field terminations to be used for planar undulators. A new termination valid for an APPLE II undulator is presented which produces a field integral variation smaller than 20 Gcm for any useful setting of the magnetic gap and phase. It compares quite favorably with other known type of terminations.

1 INTRODUCTION

An ideal insertion device must not perturb the closed orbit and the dynamics of the electron beam in a storage ring for any value of the magnetic gap. The field integral is defined as a function of the transverse coordinates x and z as:

$$I(x,z) = \int_{-\infty}^{\infty} B(x,z,s) ds = \begin{pmatrix} I_x \\ I_z \end{pmatrix}$$
 (1)

The derivative of the field integrals vs. x and z must also be equal to zero. The second field integral defined as:

$$J(x,z) = \int_{-\infty}^{\infty} \left(\int_{-\infty}^{s} B(x,z,s') ds' \right) ds = \begin{pmatrix} J_{x} \\ J_{z} \end{pmatrix}$$
 (2)

must also be equal to zero. Two kind of magnetic errors are in general responsible for non zero field integral in real devices. The first one that we also call "random errors" come from the non-uniformity of the magnetization in the blocks and from positioning errors of the blocks. Because they are largely unpredictable, this type of errors cannot be taken into account at the design stage. They can be reduced with adequate choice of manufacturing process of the permanent magnets such as die pressing method and/or by characterizing magnetically each block and then by sorting and pairing the blocks in order to cancel the field errors introduced by each blocks. In addition, some field integral shimming [1] can be used to reduce the final errors. The second type of error that we call "systematic errors" originates from the extremities of the magnetic structure where the field periodicity is broken. Experience shows that it is difficult to efficiently correct the systematic errors using shimming and most people use correction coils (active correction). Nevertheless, systematic errors can be fully predicted and to some extent corrected using a 3D magnetostatics computer code (passive correction). In the particular case of pure permanent magnet undulators, the non unit permeability of permanent magnet materials (NdFeB, SmCo) can be responsible for a non-zero field integral generated at each extremity of the undulator. The next sections present several designs of passively corrected terminations to be used with either planar undulator or APPLE-II linear/helical undulators.

2 PLANAR FIELD UNDULATORS

Figure 1 presents a 3D view of a conventional termination (type A) of a pure permanent magnet undulator. The structure is terminated with a vertically magnetized half magnet.

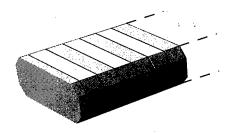


Figure 1: 3D view of a conventional termination (type A) of a pure permanent magnet undulator (lower part only).

The termination of type A shown in Figure 1 produces a significant variation of the field integral as a function of the magnetic gap (see Figure 4). This can be explained numerically by taking into account of the non unit permeability and the anisotropy of the magnetic material. From the experience made with blocks from magnet suppliers, we have found that NdFeB magnetically described with the remanent field given by the supplier and a linear (transverse) permeability of 1.06 (1.17). Two special end field structures have been designed at the ESRF using the code RADIA [2]. The first one called "B" is shown on Figure 2. It is derived from type A by adding at the end an horizontally magnetized block which longitudinal dimension (along the electron beam) is approximately equal to 3/20 of the undulator period λ_0 . As shown in Figure 4, type B termination reduces the field integral variations with gap by a factor 4 to 5. Nevertheless, contrary to type A, it does not allow the proper phasing between segmented undulators.

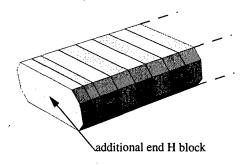


Figure 2:3D view of a termination of type B.

To satisfy both requirements of negligible field integral variation with gap and phasing between segments, we have designed and implemented the type C termination shown on Figure 3.

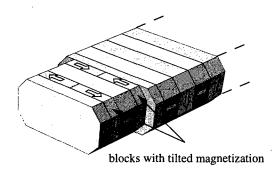


Figure 3: 3D view of C type termination

This termination includes a number of magnet blocks with smaller horizontal sizes, some of which have an inclined magnetization with respect to the vertical axis. This termination also presents the advantage that an air gap of 6 mm (for a 42 mm period) is left between two undulator segments while preserving the correct phasing for any useful gap value. All pure permanent magnet undulators of the ESRF include terminations of type B or C depending on the phasing requirements. From the reasons explained above, Type C structure is the preferred one. It has been implemented to undulator periods ranging from 20 to 42 mm.

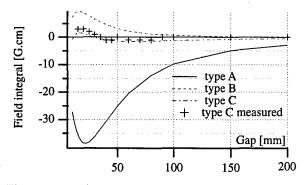


Figure 4: Vertical field integral/extremity computed for terminations of type A, B or C. The undulator period is 40 mm and the magnet are made of NdFeB. The crosses are the field integrals measured on an existing termination.

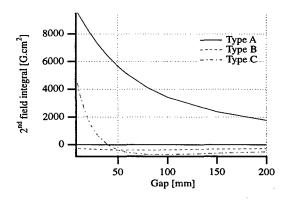


Figure 5: Second vertical field integral/extremity computed for the terminations of type A,B and C . The undulator period is 40 mm and the magnet are made of NdFeB .

3 APPLE II END FIELD STRUCTURES

Helical undulators based on the APPLE II structure [3] have been built or are under construction in a number of facilities [4],[5],[6],[7] and at the ESRF. These devices are pure permanent magnet structures. The magnet assembly is split into four magnet arrays. Two magnet arrays, one of the upper magnet arrays and one of the lower magnet arrays are simultaneously displaced longitudinally. The associated motion is called the phasing and it results in a change of the circular polarization from left to right hand side. Most APPLE II undulators built in the world are made with NdFeB blocks and terminated as in Figure 1. The non-unit permeability of NdFeB is responsible for some residual field integrals which depends on both the gap and the phase (see [8]).

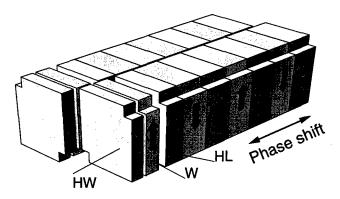


Figure 7: New end field structure for APPLE II type helical undulators.

Recently, a modified termination structure has been designed at ELETTRA for the construction of a number of APPLE II devices [6]. This type of termination has been optimized to produce displacement free trajectory and a reduced fringe field but the residual field integral is large and the operation of such a device at the ESRF would require the used of an active correction. Figure 7 presents a

novel type of end structure which greatly reduces the field integral variations induced by both the gap and the phase. It essentially consists in three magnet blocks placed at the end with some air gaps. For a 70 mm period and NdFeB material, the normal block dimensions are 35 x 35 x 17.5 mm (horizontal x vertical x longitudinal). The magnets of type HL, W and HW (See Figure 7) have the same cross-section but a different longitudinal dimension equal to 11.7, 8.7 and 7.3 (respectively). The air gap is 5 mm (2 mm) between the HL and W (W and HW) magnet blocks. The two air gaps have been optimized to reduce the vertical field integral dependence vs. phase shift. Figure 8 presents the predicted field integral vs. phase of the three type of extremities discussed above. They are all computed for a 70 mm period at the minimum magnetic gap of 16 mm assuming a symmetric (anti-symmetric) configuration of the vertical (horizontal) field components.

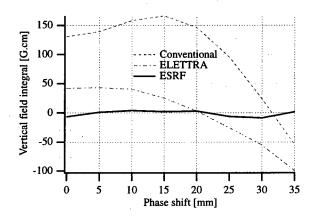


Figure 8. Vertical field integral vs. phase shift for an APPLE II undulator equipped with different field terminations. The period is 70 mm, the gap is 16 mm. The magnet blocks are made of NdFeB and the vertical field presents a symmetric configuration between each extremity.

A complete study of the field integral vs. gap and phase induced by the new termination is presented in Figure 9 and shows a maximal variation of ± 7 Gcm allowing the removal of the end correction coils.

4 CONCLUSION

By making use of a 3D magnetostatics code, it is possible to design passively corrected terminations for the planar and APPLE II linear/helical undulator. Full designs have been given for a particular period. If one needs to design an undulator with an other period, one can scale the longitudinal and transverse dimensions to the period and obtain a reasonable correction but a short re-optimization is likely to further improve the correction. The RADIA code has been found to be quite efficient for this task. A single structure is solved and the field integrals are computed within 30 seconds, allowing a systematic and

automatic investigation of a large number of magnet configurations. The ESRF ID group is presently starting the construction of several helical undulators of the APPLE II type with periods of 38 and 88 mm. In both cases a termination similar as that of Figure 7 has been optimized which produces a maximum field integral variations with phase and gap smaller than ±10 Gcm. Note that RADIA can also be used to design the termination of hybrid undulators and wigglers with reduced field integral variations with gap. Example of such hybrid terminations can be found in [9].

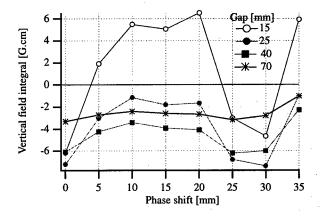


Figure 9: Vertical field integral vs. phase and gap computed for the new termination shown in Figure 7.

- J. Chavanne, P. Elleaume, Undulator and Wiggler Shimming, Synchrotron Radiation News, Vol. 8, No. 1, 1995, p 18-22
- [2] O. Chubar, P. Elleaume, J. Chavanne, "A 3D Magnetostatics Computer Code for Insertion devices", SRI97 Conference August 1997, J. Synchrotron Rad. (1998). 5, 481-484. The Radia code is freely available from "http://www.esrf.fr/machine/support/ids/ Public/Codes/software.html"
- [3] S.Sasaki et al., Nucl. Instr. Meth. In Phys. Res. A 331 (1993) 763-767.
- [4] J. Bahrdt et al., BESSY. A Double Undulator for the Production of Circularly Polarized Light at BESSY II, EPAC' 96, Barcelone, p. 2538
- [5] S. Marks et al., The advanced light source elliptically polarizing undulator. PAC'97, Vancouver, p. 3221
- [6] B. Diviacco et al., Construction of elliptical undulators for ELETTRA, EPAC'98, Stockolm, p.2216
- [7] Ch. Chang et al., Conceptual design for SRRC elliptically Polarizing Undulator EPU5.6. EPAC' 96, Barcelone, p. 2567
- [8] T.Bizen et al., Fabrication and magnetic field measurements of an apple-2 variable polarizing undulator, EPAC'98, Stockholm, p. 2243
- [9] J. Chavanne, P. Elleaume, P. Van Vaerenbergh, Segmented High Quality Undulators, Particle Accelerator Conference PAC95, Dallas May 1-5 1995. Proceedings p 1319-1321, IEEE Publication, New Jersey

THE 90-mm PERIOD UNDULATOR FOR SRRC

D.C. Quimby, S.C. Gottschalk, D.R. Jander, T.E. DeHart, K.E. Robinson, * A.S. Valla, * and J.F. Zumdieck STI Optronics, Inc., Bellevue, WA 98004 USA

Abstract

The U9/SRRC undulator has recently been completed by STI Optronics, Inc. (STI) for use at the Synchrotron Radiation Research Center (SRRC) in Hsinchu, Taiwan, R.O.C. This 4.5-m long, 90-mm period wedged-pole hybrid undulator builds on several aspects of previous STI designs [1] while including a number of significant enhancements. The magnetics are based on the wedged-pole geometry [2] with additional side magnets. At the 19-mm minimum gap the peak field is in excess of 1.28 T with less than 3 degrees of optical phase error. The magnetic structures are mounted on stainless-steel strongbacks and are connected to the gap separation structure in a method to specifically reduce optical phase errors. The magnetic structure is positioned by four closed-loop servomotors within cast aluminum C-frames. The entire structure is mounted onto a retraction system to easily move away from the vacuum chamber for servicing. The device is controlled by a real-time VME-based control system capable of autonomous local and remote operation.

1 DEVICE DESCRIPTION

Parameters of the U9/SRRC undulator system are summarized in Table 1. An overview of the undulator is shown in Figure 1. The gap separation structure consists of the C-frame necessary to support the magnetic structure and the drive train for adjusting the gap between the upper and lower jaws of the magnet structure. The range of motion of the drive train allows for a minimum gap of 19 mm and a maximum service gap exceeding 220 mm.

Table 1: U9/SRRC Undulator Parameters

Length	4.5 m
Period	90 mm
Minimum Gap	19 mm
Peak Field (max)	1.28 T
Spectral Tuning Range	K = 1.0 to 10.30
Number of poles	100
1 st and 3 rd Harmonic Spectral Intensity	>95% of ideal * throughout tuning range
Gap Encoder Resolution	1 <i>μ</i> m
Gap Setting Repeatability	$ \Delta g < 5 \mu m$ unidirect $ \Delta g < 10 \mu m$ bi-direct
Maximum Service Gap	>220 mm
Weight	9,050 kg
Mount/Retractor Positioning Repeatability	≤30 µm, 3-axes

[#] Ideal spectrum based on 94 full field strength poles

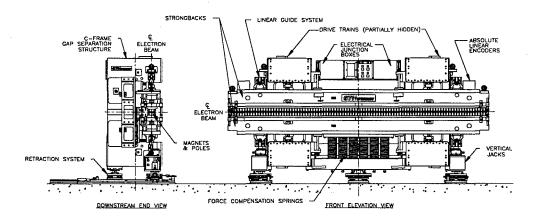


Figure 1. U9/SRRC Undulator.

^{*} Presently with Lawrence Berkeley National Laboratory

^{*} Presently with AVALLA Design, Inc.

Four servomotors drive precision acme lead-screws via precision enveloping-worm gear drives. The lowlead-error acme screws assure that the system is nonbackdriving so no motion occurs when power is cut to the motors. Coil springs acting on the lower strongback assure that the drive trains are loaded unidirectionally over the entire range of operation. Travel time from minimum to maximum gap is less than 4 minutes and the gap setting repeatability is within ±0.01 mm bidirectionally. The drives also meet a unique highacceleration requirement for a 0.1 mm gap move within 0.5 sec. Each drive is independently calibrated in order to achieve the specified position at its respective end of each jaw. Thus the four motors allow adjustment and control of the gap, gap centerline shift, and gap taper. Incremental linear encoders and absolute rotary encoders gauge the position of each drive. The gap at each end of the device is measured directly using absolute linear encoders. Encoder readings are compared continuously to monitor for inadvertent jaw taper during motion. While jaw taper is not an intended operating condition for this device, the strongback mounts and guides allow compliance for misalignments of ±6 mm and ±3 degrees, thus avoiding binding and damage in the unlikely event of excessive jaw taper.

The C-shaped support structure allows the undulator to be retracted from the vacuum chamber with minimal effort and without breaking vacuum. The undulator structure is supported at three points in a kinematic manner. Approximately equal loading occurs at each support point. Three-axis adjustments are provided for aligning the device to the beam line. This support system includes earthquake restraint and a motorized retraction system [3] for moving the undulator away from the beam line. SRRC requested a support system allowing the undulator to be retracted, dismounted from the floor supports, removed for service using an overhead crane, reinstalled on the floor supports, and moved back into position on the beam line without realignment. Measurements show that the positioning of the kinematic mount and retraction system is sufficiently repeatable that the device maintains alignment to within 30 µm in all axes following such an operation.

A key specification for this device is that the on-axis spectral intensity in the first and third harmonics is to be within 90% of the ideal peak value at all gaps over the K=1 to 10.3 tuning range. To achieve this the budgeted variance in the deflection of the strongbacks is limited to 50 μ m peak-to-peak (total gap) while the magnetic attractive force between the jaws varies from zero and 12.5 metric tons. This low value of strongback deflection is accomplished within the limited available envelope size using stainless-steel material together with hangers that distribute the support of each strongback to four points rather than two.

The U9/SRRC magnetic structure is a high-precision wedged-pole hybrid permanent-magnet array made up NdFeB magnets and vanadium permendur poles. Side magnets are provided to increase peak field without degrading pole saturation or transverse roll-off. The ends are terminated with partial strength and partial volume magnets to achieve near-zero displacement conditions [4] for the entrance and exit electron trajectory throughout the gap tuning range. The measured electron trajectory at two gaps is shown in Figure 2. Also shown are corresponding optical spectra as calculated using the MA code [5]. The undulator field distribution was specifically tuned to meet third harmonic spectral requirements. Over much of the tuning range the optical phase errors are less than 2 degrees, so that the peak on-axis spectral intensity exceeds 90% of ideal to high harmonics. At minimum gap the optical phase error remains less than 3 degrees in spite of the effects of gap-dependent strongback deflection.

Table 2 lists the range of measured first and second magnetic field integrals and other integrated higherorder moments at all gaps. The device was passively pre-tuned at the STI site to specifically account for the ambient field at the SRRC straight section and the gapdependent penetration of that ambient field to the beam line. Fully passive tuning is used for the horizontal field, B_x, while compensation of the vertical field, B_y, is supplemented with active fixed-gap saddle-coil end correctors. Rather than using passive tuning for the B_v first integral, the tuning strategy requested by SRRC was to passively minimize the shift of the optical axis of the undulator radiation throughout the spectral tuning range. The end correctors are used to select the angle of the optical axis and to minimize the change of the first integral relative to the ambient value. This places the peak of the spectral intensity on axis and makes the undulator as transparent as possible with regard to the storage-ring beam dynamics.

Table 2: Measured Beam Dynamic Quantities

Quantity	Specification	Measurement
First Integral:^		
B _x , passive	≤50 G-cm	-5 to 13 G-cm
B _y , active correction	≤50 G-cm	-5 to 3 G-cm
Second Integral:	_	_
B _v , passive	≤50,000 G-cm ²	≤30,000 G-cm ²
B _y , active correction	≤50,000 G-cm ²	≤15,000 G-cm ²
Integr. Normal Moments:		
Quadrupole	≤50 G	≤24 G
Sextupole	≤200 G/cm	≤7 G/cm
Octupole	≤300 G/cm ²	≤38 G/cm ²
Integrated Skew Moments:		
Quadrupole	≤50 G	≤37 G
Sextupole	≤100 G/cm	≤11 G/cm
Octupole	≤300 G/cm ²	≤19 G/cm ²

[^] Excludes ambient field at SRRC site

The VME-based control system is interfaced directly with the SRRC central control system and services the functions of gap motion, corrector current tracking, and interlock monitoring. Fiber-optic data links are used where possible for noise immunity of critical encoder circuits. The interlocks are designed for multiple levels of defense to prevent possible damage to the vacuum chamber or undulator. The levels of protection include

(1) gap command limits, (2) software limits, (3) hardware end-of-travel limit switches, (4) end-of-travel hardstops, and (5) end-of-jaw emergency-stop switches. The latter disable all motion independent of the control system if the jaws come too close to the vacuum chamber or to each other.

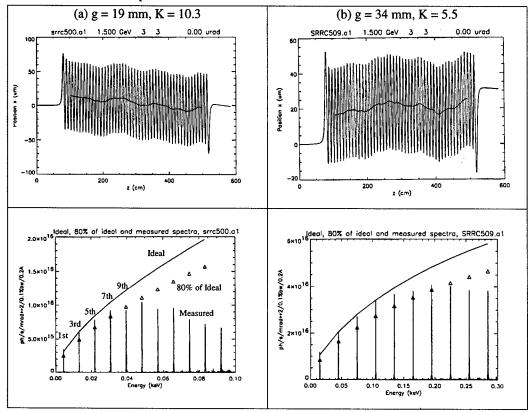


Figure 2. Measured electron trajectories and calculated spectral intensity at gaps = 19 mm and 34 mm.

2 SUMMARY

The U9/SRRC undulator project has satisfied a number of challenging requirements for positioning repeatability and spectral quality in a long, heavy device with large magnetic attractive forces. The high-precision undulator retraction system, harmonic spectral tuning, and pre-tuning of trajectory for ambient field effects prior to delivery represent significant accomplishments for commercially available undulators.

3 ACKNOWLEDGEMENTS

The authors would like to acknowledge the contributions of the employees of STI to the construction and measurements of the U9/SRRC

device. The advise of T.-C. Fan, C.-H. Chang, C.-S. Hwang and J. Chen of SRRC are sincerely appreciated.

- K.E. Robinson, M.P. Challenger, S.C. Gottschalk, and D.C. Quimby, "Advances in Undulator Technology at STI Optronics," Rev. Sci. Instr. 67 (1996), Paper C06 (CD-ROM issue).
- [2] D.C. Quimby and A.L. Pindroh, "High Field Strength Wedged-Pole Hybrid Undulator," Rev. Sci. Instr. 58, 339 (1987).
- [3] T.E. DeHart, J.F. Zumdieck, A.S. Valla, K.E. Robinson, "The SRRC-U9 Undulator Retraction System," presented at this conference.
- [4] S.C. Gottschalk, D.C. Quimby, and K.E. Robinson, "The Magnetic Design and Performance of the SRRC-U9 Undulator," in this proceedings.
- [5] R. Dejus, I. Vasserman, E.R. Moog, and E. Gluskin, "Phase Errors and Predicted Spectral Performance of a Prototype Undulator," Rev. Sci. Instrum. 66, 1875 (1995).

CONSTRUCTION AND PERFORMANCE OF THE ELLIPTICAL POLARIZATION UNDULATOR EPU5.6 IN SRRC

C.H. Chang, H.H. Chen, T.C. Fan, Jenny Chen, <u>C.S. Hwang</u>, M.H. Huang, K.T. Hsu, F.Y. Lin, C.D. Li, H.C. Liu, Ch. Wang, SRRC, Hsinchu, TAIWAN

Abstract

A 132 pole elliptically polarizing undulator (EPU5.6) with magnetic period of 5.6 cm for production of brilliant and soft x-rays has been constructed and performed the field measurement at Synchrotron Radiation Research Center (SRRC). The "Apple-II" type device was selected for this EPU5.6 structure. The key factors in the construction and assembly process stage will be described. In addition, the shimming algorithm for the magnetic field adjustment, the performance of the mechanical structure, magnetic field distribution without the field shimming will be presented in this paper. Meanwhile, the control performance also will be discussed.

1 INTRODUCTION

A 3.9-m long elliptical polarized undulator EPU5.6 has been constructed and field shimming was done for creating a high quality and high photon flux at SRRC. Two diagonal magnet arrays were fixed and the other diagonal arrays were free to be moved to create the right/left circular polarization. Therefore, this EPU5.6 [1] was only used for producing the linear polarized on vertical/horizontal and the right/left elliptical, circular polarization light. However, if the two fixed arrays are free, it can also create the linear polarization from 0° to 180° [2]. When it is operated under the 1.5 GeV SRRC storage ring, it will radiate 80-1500 KeV circularly and elliptically polarization light for the X-ray Magnetic Circular Dichroism (XMCD) experiments or other photon absorption experiment to analyze the magnetic material. In light of above circumstances, the magnet sorting and shimming technique must be developed to maintain the same quality of field and spectrum in different phasing modes for various polarization lights. Consequently, the magnetic field strength of B, and B, can be obtained by the 3-D Hall probe measurement system [3] to correct the trajectory and optical phase as well as the roll-off of each pole. Meanwhile, the integral field strength of \(\int B_d \) and B ds can be obtained by the long-loop-coil measurement system with the dynamic measurement method [4] to modify and maintain the harmonic field components within the specification.

*Email: cshwang@srrc.gov.tw

2 MECHANICAL ASSEMBLY AND ACCURACY TESTING

It is a 3.9-m long undulator and it is very difficult to get a high mechanical accuracy. Therefore it is very important to shim field for the field quality control. In addition, the magnet assembly is a key factor to maintain a good field quality. For maintaining a high quality mechanical system, two arrays of the diagonal pair were fixed and the other two arrays can be moved to change the phase.

2.1 Magnet block assembly

The magnet block should be very careful to be assembled on the keeper to avoid the mechanical error. Each magnet blocks of the magnetized direction in vertical/horizontal were glued on the individual holder by the epoxy. Meanwhile, the magnet block was fixed on the holder by the clamp [1]. Finally, the holder was fixed on the base plate by the stainless steel screw. This assembly process will be easy to create the mechanical errors that are the magnet tilt, horizontal or vertical position variation. These errors are mainly due to the strong clamping force, which is very difficult to be controlled. For solving this problem, an assembly fixture for gluing and clamping the block on the keeper is necessary for each block assembly. Each keeper can be adjusted in horizontal/vertical position on the base plate to tune the magnetic field.

2.2 Support system and backing beam assembly

The backing beam is made of stainless steel and the sliding beam is made of aluminum. Hence, when assemble the sliding beam on the backing beam that was fixed on the C-frame, the different thermal expansion coefficient on the bimetal material will induce a large mechanical distortion, especial on the long undulator which is larger than 2 m long. Therefore, we will be careful to control the tunnel temperature within 0.5°C.

2.3 Sliding beam of the driving structure

This part is also a crucial issue for the field quality control when change the phase. If the sliding beam structure on the backing beam is not sufficient rigid, especially the cross roller bearing between the upper or lower two arrays, to overcome the repulse or attractive force between the four arrays on the different phase. The harmonic integral field components and peak field will be

changed significantly in different phase position. Meanwhile, the sliding beams are guided by linear bearings that travel on the guide rails. These assemblies of these guided beams between the sliding beam and backing beam will be very careful to be adjusted to maintain the (1) good straightness, (2) parallel between each guide rail, and (3) the phasing direction should be parallel to the backing beam surface plane.

2.4 Mechanical performance

Using the laser interferometer and dial gauge in different phase position and gap to measure the mechanical performance. The 1 mm gap variation (The gap variation due to force difference on different phase position) between the two arrays on the lower/upper beam can be maintained within ±20 µm. The reproducibility of the phasing and gap moving can be controlled within ±1 µm by the feedback control system. When the magnet gap was operated in both direction, open and close loop, the backlash is about 10 µm. Temperature difference induce the mechanical distortion error (like as the sag distortion) of the backing beam will be 0.03 mm/°C-m, it is a significant amount to induce the field error for a long undulator. The tilt error on the vertical direction that is due to the unparalleled between the magnetic field axis and the phasing axis is about 50 µm.

3 FIELD SHIMMING ALGORITHM

When the 1-m prototype EPU5.6 was completed, we have revised a little about the shimming algorithm. We apply the shimming code to correct the four arrays individually. And then combine the magnetic field distribution of each magnet arrays on the lower or upper beam by means of the field measurement data of each array to simulate the optical phase and trajectory on different phase. The simulation method is to combine the two or three, even four array magnetic field strength (Because the magnetic field of the pure magnet structure is suited to use the superposition theorem). For the simulation purpose, the field measured interval distance should be smaller than 1 mm and the position precision should be within few micrometers. When using this shimming code to correct the field strength deviation, the difference of average peak field and half period integral strength between the four arrays should be kept within 0.5% which is corresponding to the common on-axis field. These simulation results will give us which pole belongs to whish's array should be shimmed. Finally, the combination of the four magnet arrays to simulate the phase error and the trajectory distribution to fine-tune the field error. When fine-tune is completely, the four arrays were assembled on the sliding beam to measure the magnetic field distribution. Based on the field-measured results and the shimming algorithm to correct the uncorrected trajectory and phase error, which are induced from the mechanical and simulation error of the entire magnet. Finally, the end pole was used to tune the fringe field effect. The trim magnets, which are located at the both end sides, were used to adjust the integral multipole field of By and Bx. Four air coils located at both ends to correct the horizontal/vertical axis trajectory (in the up/down stream) and offset which are on the different polarization mode.

4 MAGNETIC FIELD MEASUREMENT AND PERFORMANCE

The features of the peak magnetic field distribution of B_y and B_x are measured at the circular polarization condition and revealed in Fig. 1, which was measured before the magnetic field shimming.

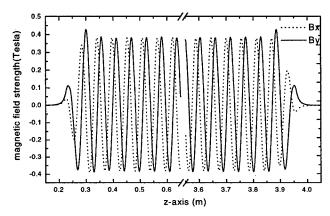


Figure 1: The magnetic field distribution of B_y and B_x along the longitudinal axis. Here exist a phase difference $\pi/2$ between B_y and B_y .

The scale of the roll-off range of the $\Delta B_y(x,y)/B_y(0,0)$ and $\Delta B_x(x,y)/B_x(0,0)$ at the circular polarization condition are measured and shown in Fig. 2 and 3. These figures reveal that the roll-off range seems very short at the circular polarization condition, especially in the vertical axis. If the field strength deviation was kept within $\pm 0.5\%$, the roll-off range in the vertical axis is about ± 1.2 mm of the vertical

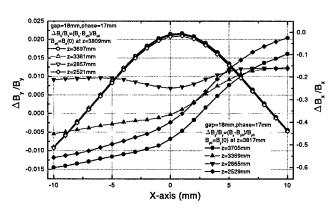


Figure 2: The roll-off range of the magnetic field distribution of B_y and B_x without shimming along the transverse x-axis.

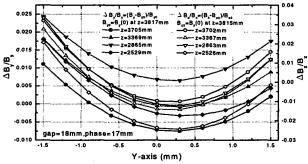


Figure 3: The roll-off range of the magnetic field distribution of B_y and B_x without shimming along the vertical y-axis.

field B_y and ± 0.8 mm of the horizontal field B_x (See in Fig. 3). If the field strength deviation was kept within $\pm 0.25\%$, the roll-off range in the horizontal axis is about ± 10 mm of the vertical field B_y and ± 1 mm of the horizontal field B_x (See in Fig. 2). This roll-off range is much smaller than the convention undulator. Such a short roll-off range is the crucial issue of the "Apple II" structure, especially the roll-off range of horizontal field B_x . Due to the problem, the real magnet center should be aligned accurately to be in the electron closed orbital plane of the storage ring. Otherwise, the photon flux will decrease much more. Fig. 2 also shows that the roll-off region is big difference on each pole. Therefore, it is a big trick task to correct the roll-off of each pole on the entire magnet to be within 0.5%, especially in the horizontal axis.

The integral field deviation on different phase and gap are also measured and revealed in Fig. 4 and 5. Measurement results show that the on-axis integral field strength was changed on different phase, but the variation of integral strength B_y and B_x can be maintained within 70 Gcm (see in Fig.5). Meanwhile, integral field variation and the profile of B_x in the central region (within ± 10 mm) on transverse axis also maintain within 100 Gcm in different gap (see in Fig.4). But the vertical integral field was changes much more than the horizontal field (see in Fig.4). This big variation can be controlled within 100 Gcm by the end pole and trim magnets adjustment.

5 CONCLUSION

Until now, the field features without any field shimming of this undulator seems not too bad. However, we have found several problems, (1) Mechanical stability is very difficult to be controlled in such a long backing beam, especial in a bimetal combination of the backing beam and sliding beam (This factor will produce the 0.3 mm mechanical distortion of each backing beam), (2) The horizontal phase moving plane is not parallel to the magnetic field axis (about 40 μ m), (3) the peak field and integral strength variation of each pole and half period have a big difference between the different phase (The rms field strength deviation will increase from 0.3% to

0.8%). These problems should be solved in the near future.

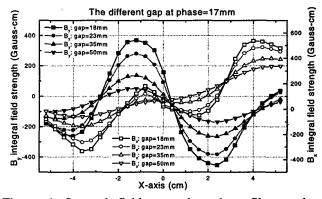


Figure 4: Integral field strength and profile on the transverse axis in different gap without shimming. Phase was fixed at the circular polarization condition.

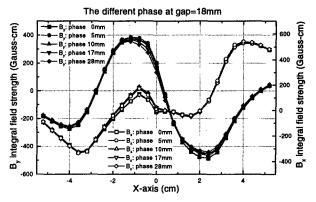


Figure 5: Integral field strength and profile on the transverse axis in different phasing position without shimming. Gap was fixed at the minimum gap of 18 mm.

6 ACKNOWLEDGMENTS

The authors would like to thank the National Science Council of Taiwan under the contract No. NSC88-2112-M-213-008. Director C.T. Chen (SRRC) and Dr. J.R. Chen (SRRC) are appreciated for supporting this project.

- [1] C.H. Chang, et al, "Optimization design for SRRC elliptically polarizing undulator", present in MT-15 (1997).
- [2] C.S. Hwang, Shuting Yeh, "Various polarization features of a variably polarized undulator with different phasing modes", Nucl. Instr. and Meth. A420 (1999)29-38.
- [3] C.S. Hwang, et al., "Advanced Field-Measurement Method with Three Orthogonal Hall Probes for an Elliptically-Polarizing Undulator", J. Synchrotron Rad. (1998). 5, 471-474.
- [4] C.S. Hwang, et al., "The long loop coil measurement system for the insertion device", Asia Particle Accelerator Conference (APAC'98), Japan, 1998.

ZERO-DISPLACEMENT END TERMINATION OF UNDULATORS AND WIGGLERS

S.C. Gottschalk, D.C. Quimby, K.E Robinson* STI Optronics, Inc., Bellevue, WA 98004 USA*Presently with Lawrence Berkeley National Laboratory.

Abstract

One of the more challenging aspects of hybrid permanent magnet undulator design is end-field termination. Klaus Halbach provided indication of correct excitation patterns for tapered wigglers', but implementation on hybrid undulators has proven more difficult. Initial results on APS undulators achieved complete passive gap dependence of both total residual angle and trajectory through the device, but with an entrance displacement.² We have further refined the end field termination system by employing both partial volume and partial strength magnets. This achieves an entrance field configuration that maximizes the number of full strength poles without entrance or exit displacement, independent of the magnetic gap. This is all achieved with passive compensation techniques. End pole tuning is then used to correct small (0.2%) deviations in the measured versus calculated end field steering. We present the design approach and results of five devices that have used this configuration.

1 INTRODUCTION

There have been a number of end field termination methods proposed. STI has used partial strength end magnets since 1986,³ as well as partial strength and reduced height poles for the ID's delivered to APS. Halbach⁴ proposed variable excitation ends for tapered wigglers, ALS extended this to include rotatable end magnets⁵ and ESRF⁶ has used adjustable positioning of the initial poles as well. One challenge has been to come up with a design which maximizes the number of spectrally useful poles without also displacing the trajectory off axis.

We first demonstrated zero displacements ends on the fixed gap TJNAF 2.2cm period IR FEL undulator in 1997. Two dimensional analyses indicated that zero displacement designs would be gap independent. This was confirmed experimentally on 55mm and 33mm period APS Undulator A ID's. We made several improvements to the design for the U9 device.

Heating magnets to reduce their field strength hampered our initial attempts to model end fields. We found that some magnets would cause a 300 G-cm steering change when the dipole strength of the first magnet was reduced from 90% to 80%, but other magnets would cause no steering change at all. The reason is that reducing the dipole strength by heating always makes the magnetization nonuniform. The open demagnetization of a magnet has larger demagnetizing fields at the center of the magnet than the edges. When the

magnet is heated to reduce it's dipole moment, the center portion suffers a larger irreversible magnetization loss than the edges. We tried heating magnets in a closed circuit configuration because then the entire magnet is at the same operating point. This failed because such high temperatures were needed that the plating came off the magnets before we were even able to reduce their strength 10%. We have found that the best method is to simply reduce the magnet volume.

There was a trade-off made between maintaining a large number of spectrally useful poles at all gaps and trajectory displacement. Our early APS end field designs maximized the number of useful poles at minimum gap, but at the expense of a large trajectory displacement. At the request of APS we changed the design to favor low displacement, but three poles were made partial strength. It was not possible to achieve both a large number of useful poles and small trajectory displacements if only the strength of the 1st magnet and height of the 1st two poles were varied. Another adjustment was needed: varying more magnet strengths was found to be sufficient.

2 DESIGN METHOD

There were two explicit goals in the end field design: 1) zero trajectory displacement and 2) maximize the number of spectrally useful poles over the spectral tuner's range. We achieved both goals by adjusting the volume of the 1st magnet and the strength of the 2nd and 3rd magnets.

Earlier end field analyses² showed that 2D FEA could be used for trajectory displacement calculations even in the presence of 3D effects such as non-zero entrance angles. The design approach we followed was to use 2D FEA for initial determinations of the magnet strengths. Refinements like changing the volume of the magnet were then added as needed. Finally we confirmed the design with a 10 pole 3D FEA.

The following description is for an example designused for the U9/SRRC undulator. We show in Figure 1 a correlation of trajectory displacement at K=10 and K=1 for a set of 7 different combinations of end magnet volumes and strengths. There is a clear linear correlation between small and large gap trajectory displacements. A zero displacement end will not change by more than 500 G-cm² over a very wide gap tuning range. This is not true for non-displacing ends: for example a 20,000 G-cm² end at K=10 will become an 18,100 G-cm² end at K=1. Clearly it will be sufficient to design the end at only one gap.

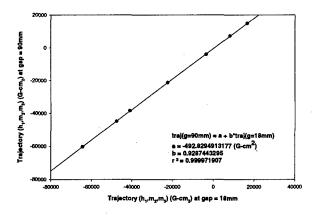


Figure 1. Linear regression of trajectory displacement at g = 18 mm against g = 90 mm.

Both the trajectory displacements as well as the peak field values are linear in the volume of the 1st magnet and the strengths of the 2nd magnet. We chose to keep the clamped surface of the 1st magnet at the same location as all the other magnets but to vary its vertical height. After the 5th pole, the remaining poles were insensitive to details of the ends. It was found that there were an infinite number of zero displacement ends. The only condition was that the height of the 1st magnet varies linearly with the strength difference between the 3rd and 2rd magnets, see Figure 2. Imposing a requirement on the 3rd peak gave a unique solution. The optimization result is shown in Figure 3. The combination in which the 3rd magnet is 95% of full strength can achieve zero displacement, but the 3rd and 4th peaks are imbalanced. Making the 3rd magnet full strength gave peak values of 100%, 99.91% and 99.86% for poles 3, 4 and 5 respectively. The dipole strength dispersion needed to achieve this was 9.5%. We decided to reduce the strength of the 2nd magnet to 90.5% by heating since such a small strength reduction should not produce any large magnet inhomogeneities.

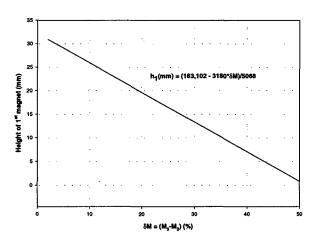


Figure 2. Zero trajectory displacement; entrance conditions on h and δm , gap = 18 mm, K = 10.

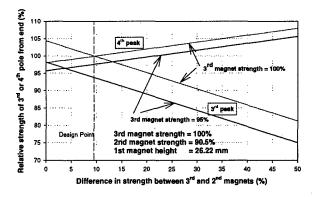


Figure 3. Relative peak field srengths of 3rd and 4th poles from end zero trajectory displacement, gap=18 mm, K=10.

3 RESULTS

The calculated end field and trajectory using 2D FEA is shown in Figure 4. The final part of the analysis was to include side magnets. A side magnet that is attached to a pole will steer the e-beam very strongly, especially on the ends. The 3D FEA prediction was that a side magnet at the 2nd pole would cause xxx G-cm of steering, but reducing the side magnet strength to 50% would eliminate the steering. We placed side magnets on one side of the upper and lower poles to give a 50% steering effect without causing any changes in normal or skew multipoles. Experimental confirmation of the end design for K=10 and K=1 are shown in Figure 5.

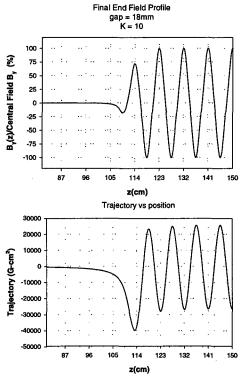


Figure 4. Field profiles and trajectory for final end field configuration.

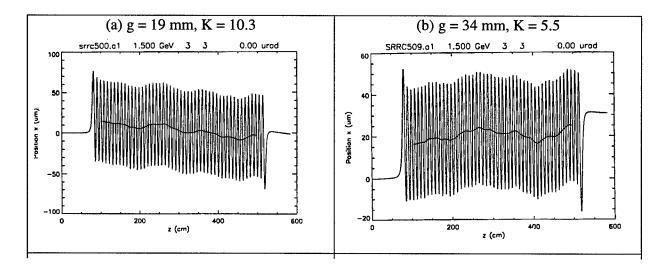


Figure 5. Measured electron trajectories and calculated spectral intensity at gaps = 19 mm and 34 mm.

4 CONCLUSION

We have demonstrated that gap independent zero displacement end fields can be achieved by varying the strength of the initial magnets. The design was chosen to produce a large number of spectrally useful poles. At minimum gap (K=10) only two poles at each end were not spectrally useful while at a large gap (K=1) only three poles were not useful. We are investigating the feasibility of further improvements if the shapes and/or locations of the last few poles are varied as well. The design goal would be to maintain resonance over as many poles as possible.

5 ACKNOWLEDGEMENTS

The authors would like to acknowledge the contributions of the employees of STI to the construction and measurements of the U9/SRRC device. The advise of T.-C. Fan, C.-H. Chang, C.-S. Hwang and J. Chen of SRRC are sincerely appreciated.

- K. Halbach, private communication. Comprehensive summary given by R. Schleuter, 2nd ICFA School of Synchrotron Light Sources, October, 1993.
- [2] S.C. Gottschalk, K.E. Robinson, I. Vasserman, R. Dejus, and E.R. Moog, "End Field Design and Tuning Methods for Insertion Devices," Rev. Sci. Instr. 67 (1996), Paper C)9 (CD-ROM issue).
- [3] K.E. Robinson, D.C. Quimby, and J.M. Slater, IEEE J. Quantum Electronics, QE-23 (1987) 1497.
- [4] "W16.0 Undulator Conceptual Design Report", Lawrence Berkeley Laboratory Publication 5256 (November, 1989).
- [5] U5.0 Undulator Conceptual Design Report, Lawrence Berkeley Laboratory Publication 5256 (November, 1989).
- [6] J. Chavanne, P. Elleaume,, and P. Van Vaerenergh, "Status of the ESRF Insertion Devices," Reev. Sci. Insr. 67 (1996), Paper C04 (CD-ROM issue).
- [7] S.V. Benson, "High Average Power Free Electron Lasers," presented at this conference.
- [8] D.C. Quimby, S.C. Gottschalk, D.R. Jander, T.E. DeHart, K.E. Robinson, A.S. Valla, and J.F. Zumdieck, "The 90-mm Period Undulator for SRRC, presented at this conference.

THE MAGNETIC DESIGN AND PERFORMANCE OF THE SRRC-U9 UNDULATOR

S.C. Gottschalk, D.C. Quimby, K.E Robinson* STI Optronics, Inc., Bellevue, WA 98004 USA

*Presently with Lawrence Berkeley National Laboratory.

Abstract

The magnetic design of the recently completed SRRC-U9 undulator system employs several enhancements to improve its performance. Side magnets to increase onaxis field augment the wedged-pole magnet geometry. Partial volume and partial strength end magnets and tuning bars achieve a zero-displacement, rapid turn-on, end-field configuration.² Gap dependent normal and skew component ambient (earth) field compensation has been included in the design. The design includes bot active and passive end correction. Optical phase and trajectory shimming techniques have been employed to optimize performance. For k=10 the performance is greater than 80% of ideal through the seventh harmonic. At a K=6.4 the calculated spectral performance is greater than 80% through the thirteenth harmonic. A complete battery of magnetic measurements has fully established the field, spectral and beam dynamic characteristics of the undulator.

1 INTRODUCTION

This paper describes the magnetic design of the U9 undulator.³ It is a wedged pole hybrid planar insertion device built for the Synchrotron Radiation Research Company located in Hsinchu, Taiwan, R.O.C. A detailed discussion of the magnetic design method that we use has been described elsewhere.⁴ This device had three new features: 1) side magnets which were added to increase the peak field, 2) non-displacing entrance and exit built by using partial strength and reduced volume end magnets and 3) pre-tuning to remove ambient field differences between the STI Optronics site in Seattle, Washington, and SRRC.

2 CENTRAL FIELD

Wedged poles hybrids were used to generate the high fields required by SRRC with 20% less magnet volume than a straight pole. In addition, wedged magnets were small enough to permit single piece fabrication, unlike straight sided magnets. An isometric view of a quarter period cell is shown in Figure 1. The wedge angle, chamfers and magnet recess were chosen to remove saturated parts of the pole, reduce demagnetizing fields, allow sufficient space for tuning shims and control higher field harmonics. The design approach was conservative: low remanence magnets were used for peak field

estimates but high remanence was used for pole saturation, transverse rolloff and parts tolerancing. This had two ramifications: 1) side magnets are needed for field strength margin, and 2) pole transverse width was increased to 8.0cm to keep the transverse rolloff small (0.035% at ± 10 mm was calculated), in the event that stronger magnets were delivered by the vendor.

Adding side magnets reduced transverse flux leakage to 0.5% without degrading the transverse rolloff, changing field harmonics or reducing the pole permeability. For ease of fabrication we selected a side magnet that increased the field strength 5.2%. Larger side magnets could have increased the field by 8%. While the side magnets did have clamps, the lack of a transverse overhang caused them to be so strongly attracted to the poles that special tooling was needed to remove them during end field adjustment. Our simulated annealing magnet sorting algorithm was modified to include steering and multipole moments that can be created by side magnets. Only a small, easily removed quadrupole was observed on the untuned device. When side magnets are properly sorted, they do not appear to degrade field errors.

Table 1: Comparison of magnet predictions with measured performance.

Quantity	Specification	MAGNET FEA	Experiment
Peak field, g=18mm	1.245 T	1.365 T	1.365 T
Transverse rolloff at 10mm	<0.1%	0.035%	0.037%
3rd Harmonic content	<10%	5.8%	5.8%

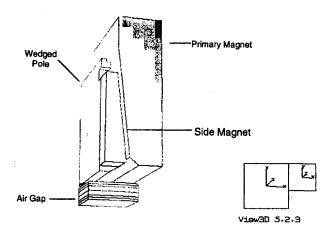


Figure 1: Isometric view of quarter period cell.

3 AMBIENT FIELD

Hybrid ID's can modify any ambient fields that are present causing gap dependent changes in beam dynamics which could require retuning the device at the new location. The following hypothetical example illustrates the point. Site A has a 0.2 Gauss ambient while site B has a 0.6 Gauss ambient. The ID 450cm long and has no 1st or 2nd integral. Normal field enhancement is about 1.8 at minimum gap. For site A the ambient field inside the ID is increased to 1.8*0.2 = 0.36 Gauss and the 1st integral changes by (0.36-0.2)*450=72 G-cm while the 2^{nd} has changed by 16,200 G-cm². The same ideal ID is moved to site B. Now the 1st integral changes by 216 G-cm as the gap is varied and the 2nd integral will appear to change by 48,600 G-cm². We analyzed these effects in advance and pre-tuned the device for the ambient field at SRRC. When we arrived at SRRC we found that the normal and skew integrals agreed to within 10 G-cm.

It is intuitively clear that at a small gap the ferromagnetic poles will shunt any skew ambient fields away from the e-beam and leave no on-axis skew field. Skew shunting will decrease as the gap is opened until it becomes absent for an infinite magnetic gap. Skew shunting is shown in Figure 2 where almost complete skew shunting can be seen at small gaps.

In the normal field direction, the field lines that would have gone through the magnets are shunted into the high permeability poles which leads to an overall normal field enhancement at small gaps. The field profiles for several gaps are shown in Figure 3. Skew and normal field effects after wiggle period averaging are summarized in Figure 4.

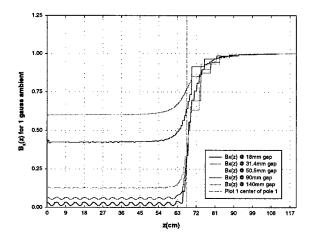


Figure 2. Skew field shunting at ends vs gap; gaps = 18 mm to 140 mm

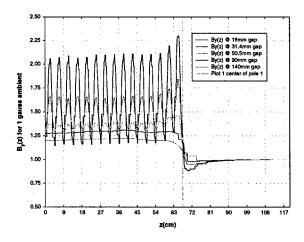


Figure 3. Normal field enhancement at ends vs gap; gaps = 18 mm to 140 mm

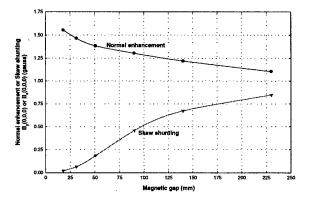


Figure 4. Gap dependence of centerline shunting effects, normal and skew fields.

4 AIR GAP END CORRECTORS

The U9 device is equipped with normal field, fixed gap, air core end correctors shown in Figure 5. If SRRC needs to actively point the photon beam, use of the control software can energize the correctors in a gap dependent manner. The coils have 49 turns and a rectangular shape with the steering legs are placed at ±30 degrees from vertical to eliminate sextupole moments. There is some loss in efficiency due to fringe fields being shunted into the first pole. The correctors did not introduce any significant multipole moments at their maximum currents of 10 amps. There are no skew field end correctors.

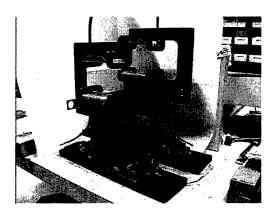


Figure 5. Air gap end corrector photo.

5 STRONGBACK SHAPING TO REDUCE GAP DEPENDENT PHASE ERRORS

For the U9 device there is a 12.5 metric ton variation in the attractive force between minimum and maximum gaps. Strongback deflections under magnetic loads will cause local gap variations which leads to a reduced spectral brightness. Spectral analyses for a collection of 25 previously built ID's having periods from 1.8cm to 8.5cm and K=11.9 to 0.5 were used to test the Walker phase error model. The model did an excellent job of predicting the *average* harmonic intensity loss caused by phase errors. This allowed us to predict phase errors based on local gap variations due to strongback deflections vs gap.

The ideal situation is to eliminate any deflection by using large, heavy strongbacks. For U9 there were overall height and weight restrictions. We used stainless steel strongbacks rather than aluminum and devised a new 4 point beam hanger system to reduce the deflection to 25 microns. This produced the gap dependent phase error variation of 2 degrees which would produce a 1.0% loss in 3rd harmonic intensity.

Experimental phase error plots showed that strongback deflection under load was responsible for almost all of the non-ideal spectral performance. The remaining spectral error sources were several micron gap dependent tapers (<0.5 degrees) and field errors.

6. CONCLUSION

The SRRC/U9 met all magnetic requirements. It used side magnets to increase the on-axis field without any performance degradation. Ambient field correction succeeded in predicting changes to 1st and 2nd integrals and internal trajectories due to gap dependent difference in the ambient fields at STI and SRRC. The Walker phase error model⁶ was verified on an ensemble of 25 APS ID's having $\lambda_w = 18$ mm through 85 mm and was used to specify strongback deflection.

7. ACKNOWLEDGEMENTS

The authors would like to acknowledge the contributions of the employees of STI to the construction and measurements of the U9/SRRC device. The advise of T.-C. Fan, C.-H. Chang, C.-S. Hwang and J. Chen of SRRC are sincerely appreciated.

- D.C. Quimby and A.L. Pindroh, "High Field Strength Wedged-Pole Hybrid Undulator," Rev. Sci. Instr. 58, pp. 339-345 (1987).
- [2] S.C. Gottschalk, D.C. Quimby, K.E. Robinson, "Zero-Displacement End Termination of Undulators and Wigglers," proceedings of this conference.
- [3] D.C. Quimby, S.C. Gottschalk, D.R. Jander, T.E. DeHart, K.E. Robinson, A.S. Valla, and J.F. Zumdieck, "The 90-mm Period Undulator for SRRC," proceedings of this conference.
- [4] S.C. Gottschalk, D.C. Quimby, K.E. Robinson, E.R. Moog, and R.J. Aparao, "Central Field Design Methods for Hybrid Insertion Devices," Rev. Sci. Instr. 67 (1996), Paper CO7 (CD-ROM issue).
- [5] S.C. Gottschalk, K.E. Robinson, D.C. Quimby, K.W. Kangas, I. Vasserman, R. Dejus, and E. Moog, "Multipole and Phase Tuning Methods for Insertion Devices."
- [6] B. Diviacco and R.P. Walker, "Recent Advances in Undulator Performance Optimization," Sincrotrone Trieste ST/M-95/3, Submitted to Nucl. Instrum. Meth., July 1995. See also B. Diviacco, et al., in the Proceedings of the 1993 IEEE Particle Accelerator Conf., Washington, D.C., 17-20 May 1993, IEEE Catalog No. 93CH3279-7, 1590 (1993).

DEVELOPMENT OF ELLIPTICAL UNDULATORS FOR ELETTRA

<u>B.Diviacco</u>*, R. Bracco, D. Millo, R.P. Walker, M. Zalateu, D. Zangrando Sincrotrone Trieste, Italy

Abstract

ELETTRA is presently operating six insertion devices, including an electromagnetic elliptical wiggler. Stimulated by the increasing interest in variable polarization sources, a series of new elliptical undulators has been designed to provide linear, circular and elliptical polarization in a wide spectral range. One of them will feature a quasi-periodic field in order to reduce contamination from high order harmonics. A chicane arrangement is foreseen in one straight section of the ring so that two experimental stations can be operated simultaneously. Two identical undulator segments, together with a phase modulation electromagnet, will be used in an optical klystron configuration for the storage ring FEL project. We present the construction, testing and magnetic measurement results of the first undulator of this kind (EU6.0). Progress with the other devices is also described.

1 INTRODUCTION

Six variable polarization undulators are presently under construction, whose main parameters are listed in Table 1 below. For the 60 mm period device (EU6.0) the actually measured field strengths are shown, which agree well with the initial design values [1].

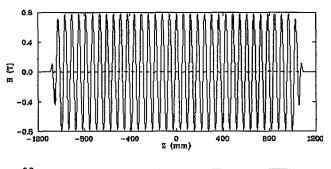
Table 1: Field strength and K values of the new undulators

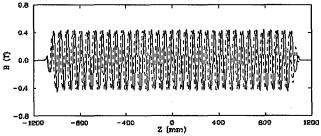
perio d (mm)	Np	Horizontal Polarization		1 1		Vertical Polarization	
		В0	K	В0	K	В0	K
48	44	0.57	2.58	0.29	1.30	0.33	1.51
60	36	0.78	4.41	0.42	2.39	0.51	2.87
77	28	0.91	6.56	0.53	3.85	0.65	4.69
100	20	1.01	9.45	0.63	5.85	0.78	7.27
125	17	0.78	9.06	0.47	5.48	0.60	7.04

All the undulators are of the APPLE type [2], consisting of four arrays of permanent magnets, two of which can be longitudinally shifted in order to change the polarization state.

2 EU6.0 UNDULATOR

The undulator was originally assembled on a modified support structure equipped with two translation units for the polarization control. Initial measurements showed significant deflection of the supporting arrays, due to the large forces acting between the adjacent row of magnets. For this reason the I-beams were locally stiffened to reduce their deformation under magnetic load. The undulator was finally re-assembled in January this year. The measured magnetic field in the horizontal, circular and vertical polarization modes is shown in Figure 1.





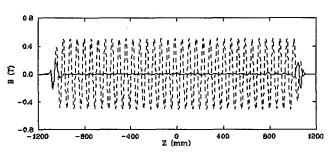


Figure 1: Measured field distribution at 19 mm gap in the horizontal (upper), circular (middle) and vertical (lower) polarization modes. Solid line = By, dotted line = Bx.

The peak field variation with gap and phase was found to be in good agreement with model calculations (see Figure 2) taking into account the actual shape of the blocks and the effect of non unit permeability of the magnetic material.

^{*} Email: diviacco@elettra.trieste.it

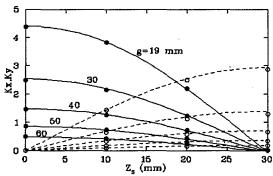


Figure 2: Measured (dots) and computed (lines) deflection parameters as a function of gap (g) and phase (Z_s) . Solid lines = K_y , dotted lines = K_x .

The transverse field distribution, as predicted by model calculations, showed a significant reduction of Bx off-axis (Figure 3). The poor homogeneity of the field introduces new problems, compared to the conventional vertical field undulators, with implications for the magnetic measurements (alignment of the measuring probes) and for the proper installation of the magnet in the storage ring (alignment with the electron beam).

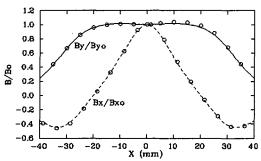


Figure 3: Measured (dots) and computed (lines) transverse field profiles.

The measured first field integrals showed a significant variation of Iy with the phase (see Figure 4), larger than for the 7-period prototype assembled last year [1]. The reason for this discrepancy is not presently understood; however, a set of correction coils placed at both ends of the device will provide compensation of the field integrals at any gap and phase.

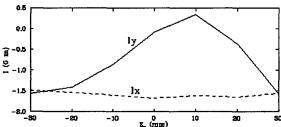


Figure 4: Measured variation of field integrals with phase at 19 mm gap, without any correction.

Multipole errors were dominated by a phase-independent integrated quadrupole of about 300 G. Attempts to use the conventional shimming method [3] to reduce it failed because of the strong dependence of the shimming effect on the phasing of the arrays. An alternative method was therefore developed, based on selective vertical displacements of a few magnetic blocks. The effect on the field integral is in this case phase-independent and could be used to effectively remove the quadrupole error. Figure 5 shows the vertical field integral distribution before and after the correction. A total of 4 blocks were moved by between 0.2 and 0.3 mm, with a corresponding reduction in useful magnetic gap of only 0.6 mm.

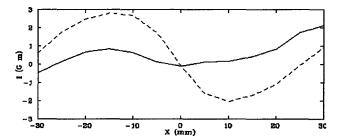


Figure 5: Measured vertical field integral distribution before (dotted line) and after correction (solid) (gap=19 mm, Δ =0).

Simultaneous reduction of the first and second horizontal field integrals was also achieved by this procedure, as can be seen in Figure 6, which shows the electron trajectory before and after the block displacement was applied.

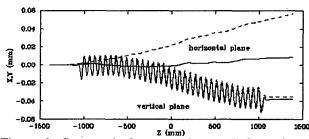


Figure 6: Computed electron trajectory before (dotted line) and after correction (solid) (gap = 19 mm, Z_s = 0, E=2 GeV).

The residual multipole errors, obtained by a polynomial fit of the transverse distribution of Ix and Iy over a range of ±20 mm, are shown in Table 2. The skew quadrupole component is difficult to correct with the methods described above, however its magnitude is within the maximum tolerable value specified for the ELETTRA insertion devices. Note how the errors decrease rapidly with the gap, possibly an indication of inhomogeneity of magnetization which becomes less important when the distance from the blocks is increased.

Table 2: Measured normal (N) and skew (S) integrated quadrupole and sextupole errors after correction

gap	Z_{s}	Qs	S _s	Q_{N}	S _N
(mm)	(mm)	(G)	(G/cm)	(G)	(G/cm)
19	-20	-129	-9	13	206
19	-10	-105	-40	-34	150
19	0	-61	-67	-15	90
19	10	-50	-71	43	57
19	20	-104	-47	76	139
30	0	-51	-14	-7	26
50	0	-33	13	1	-1

The uncorrected rms optical phase error is shown in Table 3. Spectral performance deteriorates rapidly as we move away from the horizontal polarization mode, with a 5th harmonic reduced to 45% of the ideal intensity in the worst case.

Table 3: Rms phase error in different polarization modes at 19 mm gap, before and after phase error correction

Confection	T"	,	T
\mathbf{Z}_{s}	polarization	σ _Φ (°)	σ _Φ (°)
Z _s (mm)	mode	before	after
		shimming	shimming
-20	circular	6.0	4.9
-10	elliptical	4.6	4.2
0	horizontal	4.5	2.3
10	elliptical	7.2	2.6
20	circular	10.0	4.8

The conventional phase shimming technique was not applicable in this case. The usual distinction between V and H shims [4] is complicated by the fact that in both types a field integral is generated which changes with the phasing between the arrays. Therefore a new method was developed, in which the basic shimming unit consists of 4 shims placed on two consecutive horizontally magnetized blocks (see Figure 7). In this way the net effect on the field integral is cancelled within the unit, and the remaining effect is a step change of the optical phase function.



Figure 7: Shimming unit used for phase error reduction

A further complication is that, due to the varying field distribution across the shims, they move on the surface of the magnets as the phasing reaches one half-period (vertical polarization mode). For this reason the shims will be permanently glued in their final position by means of a thin layer of epoxy resin.

As usual, a simulated annealing algorithm is used to find the optimal position and thickness of the shims. The resulting rms phase error, after applying 9 shimming units of thickness between 0.2 and 0.4 mm, is shown in the last column of Table 3. Improvement is significant, bringing 5th harmonic intensity to not less than 85% of the ideal value. As expected, no change is introduced on the first field integral distributions.

3 FUTURE DEVELOPMENTS

Based on the positive results obtained in the correction of the quadrupole error of the EU6.0 undulator, a new block holder (See Figure 8) has been designed for the next devices, which will allow both horizontal and vertical displacement of the blocks from their nominal position, with increased potential for multipole error control.

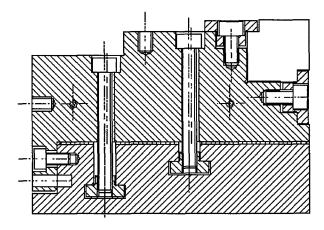


Figure 8: Block holder for the EU12.5 undulator.

At present the magnetic blocks for the EU12.5 and EU10.0 undulators are in the final manufacturing stage; the support structures are also under construction and assembly of the next magnet is due to start in a few months.

- B.Diviacco et al., proc. European Particle Accelerator Conference, Stockholm, 22-26 June 1998
- [2] S. Sasaki, Nucl. Instr. and Meth. in Phys. Res. A 347 (1994) 83-86
- [3] J.Chavanne et al., ESRF Internal Report SR/ID-89-27 (1989)
- [4] B.Diviacco, R.P.Walker, Nucl. Instr. Meth. in Phys. Res. A 368 (1996) 522-532

NEW CONTROL SYSTEM OF THE INSERTION DEVICES AT THE KEK PHOTON FACTORY STORAGE RING

T. Shioya and K. Tsuchiya*
KEK PF, Oho 1-1, Tsukuba, Ibaraki 305, Japan

Abstract

The control system of the insertion devices (IDs) at the Photon Factory storage ring (PF ring) has been renewed in accordance with the high-brilliance project of the PF ring. It consists of a workstation and VME systems, which are linked to dedicated user PCs in the SR experimental hall. Each user of the IDs can change the magnetic gap independently by accessing this workstation during their SR experiment. The closed-orbit affected by changing the gap is corrected using correction magnets system located at both ends of each ID. The vertical fluctuation of the gradients of the photon beam axis is suppressed to less than 2μrad.

1 INTRODUCTION

In the Photon Factory storage ring (PF ring; 2.5 GeV), five permanent-magnet insertion devices (IDs) are in operation, namely Undulator U#02; multi-pole wiggler MPW#13,16; revolver Rev#19; and elliptical multi-pole wiggler EMPW#28. Table.1 lists their main parameters. Each ID had been controlled by an individual personal computer (ID-PC) to change the magnetic gap and to correct the closed-orbit distortion (COD). The ID-PCs had been placed beside a ring control room. Users of IDs had called up a ring operator to change the gap for choosing the photon energy during their SR experiments.

Table 1: Main parameters of the IDs

Name	operation mode	λu (cm)	N	Kmax
U#02	-	6	60	2.3
MPW#13		18	13	25
MPW#16		12	26	16.8
Rev#19	A	5	46	1.3
	В	7.2	32	2.7
	С	10	23	5
	D	16.4	14	9.5
EMPW	elliptical	16	21	Kx :0.3
#28	MPW			Ky:15
	helical U			(Kx=Ky)
	linear U			

[&]quot; Email: tsuchiya@mail.kek.jp

This control system of the IDs has been renewed in accordance with reconstruction for the brillianceupgrading project of the PF ring [1]. This new control system has one workstation for the IDs (ID-WS) and five VME systems. Each of the VME systems performs the same role as that of the ID-PC. It controls both the gapcontroller of the ID and the steering magnets system for the COD correction, using the GPIB interface. The ID-WS controls these VME systems and communicates with them through the local-area network (LAN). Figure 1 shows a schematic view of the new control system of the IDs. A terminal for the man-machine interface (MMI) placed in the ring control room displays all status of the IDs at every moment. From this MMI terminal, the ring operator can control all IDs and steering magnets directly sending requests to the ID-WS.

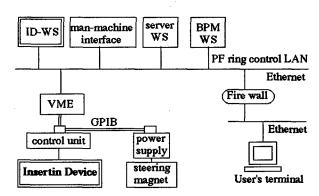


Figure 1: Schematic view of the new control system of the insertion devices.

Each beam line of the IDs has a dedicated PC terminal, which has permission to access the ID-WS. Users can send requests to the ID-WS for changing the gap through network communication. When the ID-WS has received a service request, it judges the condition for changing the gap by checking the operation status of the PF ring. In the case of the enabled condition, the VME system executes the command from the ID-WS. After changing the gap, the result is reported to the user's PC and the MMI. Also, information concerning the present gaps of every ID is open to the public on a Web page [2]. The logging data for gap changes are saved in a database of the PF ring.

This new control system of the IDs had been developed in the MPW#13 as the first case. Operation of the new control system in the MPW#13 was started in February, 1998. The control systems for the U#02 and EMPW#28 were unified to the new control system in October, 1998. The remaining systems, for the MPW#16 and Rev#19, will be unified in March, 1999. The system for Rev#19 is being developed by the Institute of Materials Structure, University of Tokyo.

2 THE COD CORRECTION FOR THE IDS

2.1 System

For the users of IDs, it is important to vary the photon energy freely by changing the gap during their SR experiments. This is the meaning of independent tuning of the IDs. However, a closed-orbit is sometime affected by changing the gap, which causes a fluctuation of the photon-beam axis at all beam-lines. To suppress this fluctuation by changing the gap, a COD correction has been made simultaneously by the steering magnets system located at both ends of each ID. Each of the VME systems has a corrective current data table for the steering magnets over the entire operating range of the gap. These current data tables for the steering magnets of all IDs have been taken for independent tuning before the user operation. The VME reads the present gap and sets a suitable current repetitively for changing the gap. The typical speed of changing the gap of ID is 20 mm/min, and the correction frequency is 7Hz in the case of MPW#13.

The steering magnet can generate an integral magnetic field up to 2000 Gauss-cm either in the horizontal or vertical direction, coupled with a 12-bits DC power supply (HP6633A). A permalloy has been adopted as the core material of the magnet in order to reduce the remnant magnetic field as much as possible and to obtain reliable reproducibility.

2.2 Acquisition of corrective data

The PF ring has several operation modes besides the nominal 2.5 GeV operation, such as 3 GeV operation. When the orbit of the electron beam is changed according to the operation mode, all correction data tables of the IDs are refreshed before user SR experiments in order to satisfy the condition for independent tuning of the IDs. The new data-acquisition program in the ID-WS searches these corrective current data so as to fit the closed-orbit to the standard one by the least mean-squares method over the operating range of the gap step by step. To obtain information about the beam position, a program to collect corrective data can use the new beam-position monitor (BPM) system of the PF ring [3] or the photon-BPM (PBPM) in the beam line [4].

The system of the BPMs was also renovated accompanying reconstruction of the PF ring. The number of new BPMs is 65 and the frequency of the COD measurement is 50Hz. The relative accuracy of the

measured beam position is less than 5µm. The averaged data of the BPMs during one second have been sent to the data-storage area, the so-called Data channel (DCh), in the shared memory of the server workstation [5]. The ID-WS can read the BPMs data accessing to the DCh, and calculates the optimum corrective current both the horizontal or vertical direction. To search for vertical corrective current data, four PBPMs at the beam lines (BL04, 06, 12, 21) are available.

2.3 Results of a COD correction

The corrective current data for the present closed orbit with an emittance of 36 nm-rad was adjusted using the new BPM system for both the vertical and horizontal directions. During the measurements, development of the new control system for the IDs was underway. Thus, for acquiring corrective data, the program of the old control system for the IDs was used, which was modified so as to use the new BPM data in the DCh. The program iterated the correction of the beam position at the selected three BPMs until the differences from the standard position had been reduced to less than 10µm. Figure 2 shows typical results of the COD correction during the change in the gap. The examples are for the case of U#02 and MPW#13.

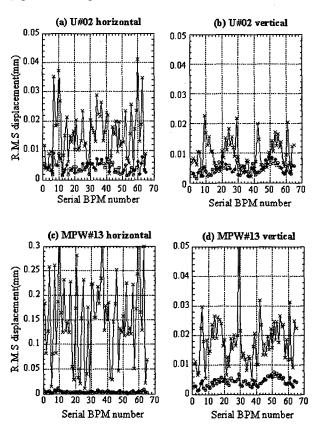


Figure 2: The results of the COD correction for the IDs. (circles: correction ON, crosses: correction OFF)

The horizontal and vertical r.m.s. displacements at the BPMs are plotted during a change from the minimum gap to the maximum gap. The displacements after a correction have been reduced to less than 10 µm all around the ring in the both directions. The results are the same in the cases of the other IDs. Because the time needed to measure one of these data is about 10 minutes, which is limited by the speed of changing the gap, these data of the displacements involve both the drift of the electron beam and the fluctuation due to the errors of the Figure 3 shows a comparison between the measured displacements with a correction and the background drift in the vertical direction. The COD corrections for the gap-changing work to suppress the fluctuation of the closed-orbit within the twice comparisons with that of the orbit in the steady state.

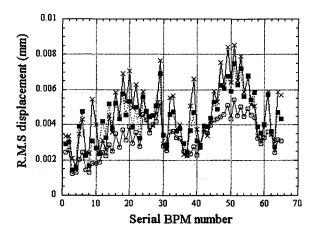


Figure 3: The comparisons of the vertical fluctuations (r.m.s) of the orbit. (circles: the background drift, crosses: the case of U#02, squares: the case of MPW#13)

The reliability of the corrective data was checked using four PBPMs located in the beam lines: BL04, 06, 12 and 21, respectively. The fluctuation data in the vertical SR beam positions of the PBPMs was recorded using chart recorders. Most of the fluctuations remained within the range of 20µm from the standard position, which corresponds to an axial gradient of 2µrad. A change in the gap beyond this range is allowed only just after the injection, so as to change the operation mode of the Rev#19 or the EMPW#28. The conformation of the corrective data using PBPMs is always performed after a long shutdown of the PF ring.

In practical operation of the PF ring for user experiments, the fast (10Hz) global feedback system works in order to stabilize the fluctuation of the vertical orbit [6]. Thus, the vertical orbit fluctuation during a change in the gap should be more reduced by using the feedback system simultaneously during the period of user experiments.

2.4 Improvement

The average time to take one corrective data set was about 2 hours. It was reduced to half compared with the case of using the old BPM system. However, the total time required to take data for all IDs was still several days. A curtailment of the time for data-acquisition is one of the important subjects for the new control system. A test of the new program in the ID-WS to collect corrective data was performed well and efficiently at MPW#13 using the new BPM system for both the vertical and horizontal directions. The new corrective data-acquisition system will be commissioned in April, 1999.

On the other hand, 12 new PBMPs were installed in the PF ring by the SR monitor group. Commissioning of the new PBPM systems is underway. The ID-WS communicates to the workstation for the new PBPM systems in order to obtain more information about the vertical SR positions. To utilize the additional new PBPMs systems, we will improve taking corrective data and checking it more carefully.

3 SUMMARY

The new control system for the IDs at the PF ring has been developed and operation of the system has started. The fluctuation of the electron beam-position due to changing the gap is suppressed to less than 10µm for independent tuning of the IDs.

- [1] M. Katoh, Y. Hori, Y. Kobayashi, S. Sakanaka, M. Izawa, K. Haga, T. Honda, T. Mitsuhashi, T. Obina, C. O. Pak, K. Ohmi, K. Tsuchiya,
- N. Kanaya, A. Ueda, M. Tadano, Y. Takiyama, S. Asaoka, T. Nogami,
- T. Shioya, A. Mishina, Y. Sato, S. Tokumoto, T. Takahashi, T. Kasuga, H. Maezawa, M. Kobayashi, and H. Kobayakawa, J. Synchrotron Rad.
- (1998), 5, 366
- [2] http://pfrpc1.kek.jp/nogami/DchJava/MPW.html
- [3] K. Haga, J. Synchrotron Rad. (1998). 5, 624
- [4] T. Mitsuhashi, K. Haga, and T. Katsura, IEEE PAC, Washington (1987), 576
- [5] C. O. Pak, Photon Factory Activity Report No.4 A-11
- [6] T. Obina, K. Haga, T. Honda, M. Tadano, T. Kasuga, M. Katoh, Y. Kobayashi, M. Satoh, and N. Nakamura, EPAC'98", Stockholm, (1998), 1726

COMMISSIONING OF OPHÉLIE: THE NEW ELECTROMAGNETIC CROSSED OVERLAPPED UNDULATOR AT SUPER-ACO*

M. Corlier[#], J.-C. Besson, P. Brunelle, J. Claverie, J.-M. Godefroy, C. Herbeaux, D. Lefebvre,
O. Marcouillé, J.-L. Marlats, F. Marteau, J. Michaut, P. Peaupardin, A. Petit, M. Sommer,
J. Vétéran and L. Nahon°, LURE, Univ. Paris Sud, Bât. 209 D, BP 34, 91898 Orsay Cedex, France

Abstract

OPHéLIE, the first electromagnetic Onuki-type undulator has been installed on the 0.8 GeV storage ring Super-ACO in February 1998. It consists in two identical 9-period crossed overlapped undulators whose magnetic fields (up to 0.12 T) are produced by conventional electromagnets. This insertion device is able to produce any kind of polarization in the VUV range with a potential polarization switching rate Measurements of focusing and closed orbit distortion a very good agreement with magnetic measurements. A compensation scheme has been developped in order to make the operation of the insertion device as user-friendly as possible. First results obtained on photon beam are very promising. Photon energy

calibration, flux optimization and polarization measurements are in progress.

1. INTRODUCTION

OPHéLIE (Onduleur Plan/Hélicoïdal du LURE à Induction Electromagnétique) [1] is the first Onuki-type undulator to be installed on a storage ring operating as a user facility (Fig. 1). This implies some severe constraints on the design and operation of such an insertion device in terms of non perturbation of other users. This is especially true if one considers the rather fast possible polarization switching at a speed of 1 Hz owing to its unique fully electromagnetic nature. We will present here the results of the magnetic measurements and the effects on the positron beam.

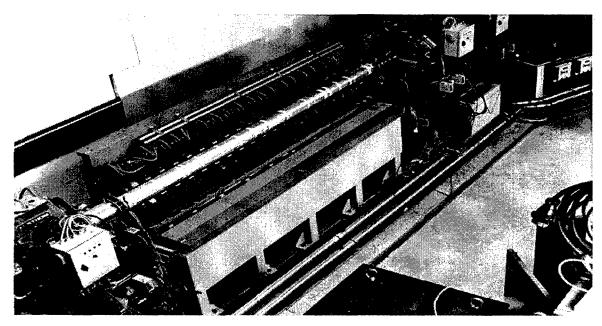


Fig. 1. View of one part of OPHéLIE in Super-ACO.

2. MAGNETIC DESIGN AND CONSTRUCTION

The device consists in two fixed-gap crossed overlapped undulators: a H-und. (resp. V-und.), which produces a horizontal field (resp. vertical field).

The V-und. can be translated along the longitudinal direction z. A $\phi=90^\circ$ phase corresponds to a 62.5 mm translation of V-und. Each undulator is made of 9 periods with $\lambda_o=250$ mm and 2 main poles per period. The electromagnetic technology was chosen for its versatility of polarization switching (with a bipolar power supply). The maximum field induction is produced both in the horizontal (0.12 T) and vertical (±0.12 T) planes at $|{\rm Imax}|=210$ A. Entrance and exit correctors have been designed [2] to center the positron trajectory in OPHéLIE.

^{*} Work supported by CNRS, CEA, MENESR.

^{*}Email: corlier@lure.u-psud.fr.

[°] also CEA/DRECAM/SPAM, Bât. 522, CE Saclay, F91191 Gif/Yvette.

This antisymmetric correction is realised with the help of two sets of correcting coils (i1 and i2 currents) located on the two first (resp. the two last) poles of the device (Fig. 2). These end poles were designed as small as possible in order to maximize the number of periods. Furthermore, each main pole is equipped with an additional compensation coil (ic current) (Fig. 2) able to compensate for a peak field spread up to 5 % [3]. Finally, these coils have been used to compensate for the residual field integral introduced by dephasing.

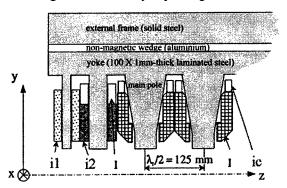


Fig. 2. End view of the V-und. upper part.

3. MAGNETIC MEASUREMENTS

Magnetic measurements were performed by Sigmaphi and LURE, using a Hall probe (Fig. 3 and Table) and a Pulsed Wire Technique (PWT) installed by LURE [4].

Due to the low saturation of the main poles, the peak field has a perfect linear dependance with the main current I. When the V-und. dephasing varies, the interaction with horizontal poles results in mutual flux capture. This leads to both an increase of the peak field value and in the appearance of a residual field integral.

In order to avoid any photon beam displacement during the vertical field switching, the positron beam has to be centered inside the insertion. The small size of end poles induces saturation and implies a complete calibration of i_1 and i_2 over the whole main current range of both undulators. The PWT [5] was used for this purpose because it provides a fast measurement of the 2nd field integral and allows to adjust quickly the correction currents (Fig. 4).

Central positions and angles of the trajectories (Fig. 4) remain within the tolerances: $\pm 40 \, \mu m$ and $\pm 40 \, \mu rad$. In order to compensate for the saturation effect in poles 2

and 21, a simple variation law was chosen for i2 (Fig. 5). The double "S" curve (V-und.) shows how the hysteresis effect changes i1 adjustments. A similar behaviour was found for the H-und.: a "U" curve in the 0-200 A range.

Finally, all the above characteristics: low peak field dispersion, low saturation in main poles and identity of the undulators were confirmed by the tests on photon beam. An example is shown in figure 6. The spectral flux is centered at $7 \, \text{eV}$ for several combinations of main currents (K = cste).

4. EFFECTS ON POSITRON BEAM

-Closed orbit correction for $\phi=0:i1$ and the compensation current on end pole #20 (i20) were optimized in order to limit the closed orbit excursion to less than 0.1 mm in both planes everywhere in the machine. The agreement with magnetic measurements is better than 6% for the two undulators (Fig. 5). Presently, average curves allow faster operation with good orbit correction.

- Closed orbit correction for $\phi \neq 0$: As predicted by magnetic measurements, the dephasing between the two undulators modifies the field integrals. The defects, located at one end of each undulator, depend on both the main current and the phase and have opposite signs for opposite phases. Compensation coils (poles 3-4-18-19) have been used to compensate for these defects. An empirical law was found in order to limit closed orbit excursions to less than 0.5 mm [4]. The dynamic feedback system on beam position [6] will then completely cancel the residual distortion.

- Additional focusing: Each of the two undulators introduces additional focusing in its magnetic field plane and a parasitic focusing in the perpendicular plane depending on the transverse field homogeneity [4]. The experimental tune variation with main current for the V-und. (measured after closed orbit correction) is given on figure 7. The agreement with magnetic measurements, in terms of peak field value and transverse homogeneity, is very good for both undulators. The working point of Super-ACO is located near coupling resonance, in order to maximize vertical beam size and Touschek lifetime. Then, rather small tune shifts must be compensated to avoid beam size variations. A fast feedback on tunes [7] will be used during OPHéLIE's operation.

	B _o	σB _o / B _o	$\Delta B/B_o = f(x)$	$B_o = f(I)$	$\Delta B/B_o = f(\phi)$
H-und.	0.12 T	0.4 %	6 % @ 10 mm	5.84 10 ⁻⁴ T/A	0.08 %/ deg.
and V-und.	@ 210 A			r = 0.999	

5. CONCLUSION

OPHéLIE, the first entirely versatile crossed undulator in the VUV was successfully installed on Super-ACO.

The behaviour of the device with the positron beam is very close to the one predicted by magnetic measurements. Two feedback systems on the machine will complete the compensation scheme of the undulator and allow an independent control of the device by the

users. The magnetic measurements have demonstrated the very good quality and identity of the H and V undulators. Photon beam characterization including polarization measurements is in progress as well as the commissioning in the AC switching mode.

6. ACKNOWLEDGEMENTS

Thanks are due to the whole LURE technical staff and especially A. Nadji for fruitful discussions.

- [1] L. Nahon et al., NIM A 396 (1997) 237-250.
- [2] M. Corlier et al., MT15 (1997), Vol. 1, 84-87.
- [3] T. Schmidt et al., NIM A341 (1994) ABS 9-ABS 10.
- [4] LURE Internal Report, SU5/98-20.
- [5] R.W. Warren, NIM A 272 (1988) 257-263.
- [6] L. Cassinari et al., this conference.
- [7] P. Brunelle et al., this conference.

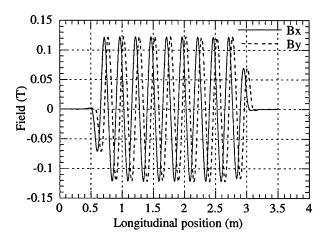


Fig. 3. Measured fields for 200 A at $\phi = 90^{\circ}$ (Hall probe).

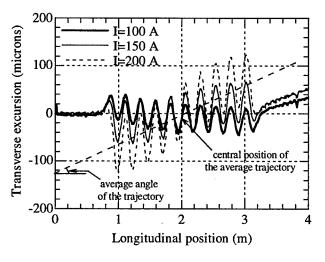


Fig. 4. V-und. optimized beam trajectories (PWT) for $\phi = 0$.

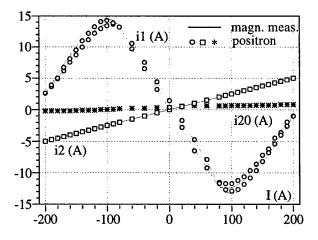


Fig. 5. V-und. variation of correction currents ($\phi = 0$).

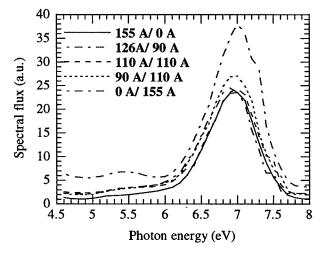


Fig. 6. Observed spectral flux for different currents (ϕ =0). The amplitudes of spectra differ from each other because the vertical polarization reflectivity of mirrors differs from the horizontal one.

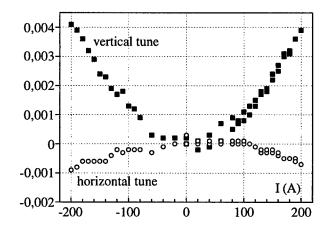


Fig. 7. Tune variation with main current (V-und.).

ANALYSIS FOR MAGNETIC AND RADIATION SPECTRAL PROPERTIES OF UNDULATORS AT HISOR

A. Hiraya, N. V. Smolyakov*, H. Yoshida, HSRC & Hiroshima University
 T. Muneyoshi, G. Rybalchenko, K. Shirasawa, Hiroshima University
 D. Amano, T. Takayama, Sumitomo Heavy Industries, Ltd.

Abstract

A compact, racetrack type storage ring HiSOR has been constructed at Hiroshima Synchrotron Radiation Center. A linear undulator and a new type of helical/linear undulator were installed at the two straight sections of HiSOR. Their magnetic fields were measured for different configurations and gaps. The analysis of experimentally measured magnetic field data and radiation spectra are made for HiSOR undulators and presented in this report.

1 INTRODUCTION

Hisor racetrack type storage ring [1] is planned for SR research on science and technology using VUV to X-ray up to 5 keV. It has two straight sections with the length 8240 mm. The stored electron beam energy is 700 MeV, the current is 300 mA bending magnetic field is 2.7 T, synchrotron radiation critical energy is 880 eV. Electron beam has the following parameters at the center of straight sections: horizontal size is 1.51 mm, vertical size is 0.126 mm, horizontal divergence is 0.412 mrad, vertical divergence is 0.063 mrad at 0.02 emittance coupling. Two undulators are already installed at Hisor storage ring [2].

This paper studies the influence of magnetic field errors on the performance of helical/linear undulator. Various studies of such kind effect have been carried out in a number of paper [3-11]. In the first papers [3-6] the quality of the wiggler field was characterised by its RMS peak magnetic field error. However, as it has been shown in [7], this deviation is not strongly correlated with the observed reduction in radiation peak intensity; instead, the radiation intensity is well correlated with the RMS phase error [7-9]. But the most straightforward way to estimate theoretically the performance of undulator is to calculate its radiation characteristics with the use of experimentally measured magnetic field. Such approach was used in a number of papers [6, 10, 11], and have been successfully applied in this study. The new effective, universal and fast computer code was created to calculate the variety of undulator radiation characteristics. Suffice it to say that it needs only 130 seconds to calculate radiation distribution in real geometry (90*90=8100 points on the screen, measured magnetic field with its length = 2.5 meters, real electron beam emittance) at PC Pentium II, 333 MHz.

*Email: nick@sci.hiroshima-u.ac.jp

2 PARAMETERS OF UNDULATORS

The linear undulator has a standard pure-permanent magnet design with eight magnetic blocks per period (including upper and lower jaws) and will generate the radiation with 25-300 eV photon energy. The helical/ linear undulator consists of upper and lower jaws same as standard planar undulator while each jaw consists of one fixed magnet array at the center and two magnet arrays at both sides. By longitudinal shift of side magnet arrays, the amplitudes of vertical and horizontal magnetic fields can be varied. In this way the proper polarization of radiation, generated by this undulator, can be selected as linear, elliptical, right- or left-circular. It gives almost perfect circular polarized light in 4 - 40 eV region in the helical configuration, as well as linear polarized light in 3 - 300 eV in the linear configuration. The main parameters of the undulators (with computed magnetic field amplitudes) are shown in Tables 1 and 2.

Table 1: Parameters of linear undulator

Period length	57 mm		
Number of periods	41		
Total length	2354.2 mm		
Gap distance	30 - 200 mm		
Permanent magnet	NdFeB		
Maximum magnetic field	0.41 T		
Deflection parameter	2.2		

Table 2: Parameters of helical/linear undulator

Period length	100 mm
Number of periods	18
Total length	1828.6 mm
Gap distance	30 - 200 mm
Permanent magnet	NdFeB
Max. magnetic field (helical mode)	0.347 T
Deflection parameter (helical mode)	4.6
Max. magnetic field (linear mode)	0.597 T
Deflection parameter (linear mode)	5.6

Calculated photon flux densities at helical and linear modes of the helical/linear undulator, those of the linear undulator (with sinusoidal magnetic fields) and the bending magnet at HiSOR are shown in Fig. 1.

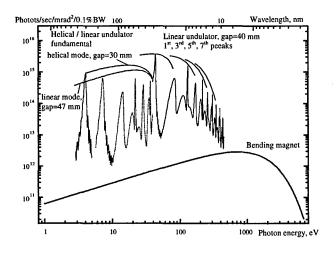
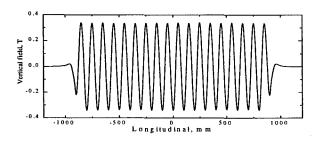


Fig.1. Calculated flux density distributions of two undulators and bending magnet at HiSOR.

3 PERFORMANCE OF HELICAL/ LINEAR UNDULATOR

3.1 Helical mode

The measured horizontal and vertical components of the undulator's magnetic field are shown in Fig. 2.



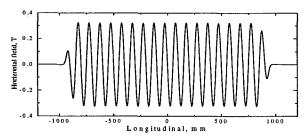


Fig. 2. Measured magnetic fields of helical/linear undulator at helical mode, gap=30 mm.

The analysis show that the horizontal B_x and vertical B_y fields can be fitted by the formula:

$$B_{x,y} = C_{x,y} + A_{x,y} \sin(2\pi z / \lambda_w + \varphi_{x,y})$$

where
$$C_x = -2.5$$
 Gs, $A_x = 3228$ Gs, $\varphi_x = 0$, $C_y = -7.1$ Gs, $A_y = 3397$ Gs, $\varphi_y = 1.6$, $\lambda_w = 100$ mm.

The computed horizontal and vertical trajectories of the electron in the measured field with steering magnets orbit adjustment are shown in Fig. 3. The twisted shape of these curves clearly exhibits the role of the constant term $C_{x,y}$.

Fig. 4 shows the calculated on-axis spectrum in the vicinity of the fundamental harmonic (4.385 eV) for the case of measured magnetic field and for ideal (pure sinusoidal) helical field for the zero emittance electron beam. Fig. 5 shows the horizontal distribution of the fundamental for measured and sinusoidal magnetic fields.

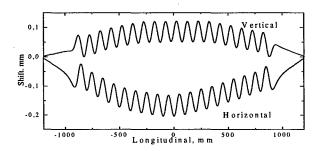


Fig. 3. Horizontal and vertical trajectories of the electron.

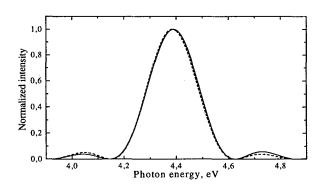


Fig.4. Computed on-axis brightness of the fundamental for the measured magnetic field (solid line) and for sinusoidal field (dashed line)

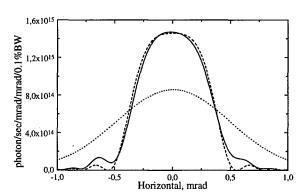


Fig. 5. Computed horizontal distribution of fundamental: measured field and zero emittance beam (solid curve),

measured field and real emittance beam (dotted curve), sinusoidal field and zero emittance beam (dashed curve).

Presented above results clearly demonstrate that the effect of magnetic field errors on the fundamental (which only will be used at helical mode) is negligible.

3.2 Linear mode

In the ideal case the magnetic field of any linear undulator has only one component (usually, vertical). But because of the complex arrangement of helical/linear undulator, its magnetic field contains both leading vertical magnetic field and slight horizontal field also, see Fig. 6. This horizontal component will shift the electron beam in vertical direction, see Fig 7. Electron beam has at the exit of undulator: horizontal deflection = 0.43 mrad, vertical deflection = -0.72 mrad.

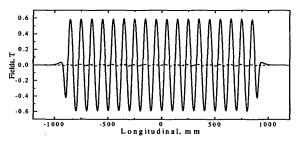


Fig. 6. Measured magnetic fields of helical/linear undulator at linear mode, gap=30 mm: vertical field (solid curve) and horizontal field (dashed curve).

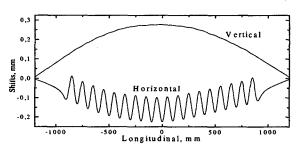


Fig. 7. Horizontal and vertical trajectories of the electron.

Again, let us consider the electromagnetic radiation properties that is our principal interest. Fig. 8 shows the on-axis spectrum (1st, 3rd, 5th, 7th and 9th harmonics) in the case of ideal magnetic field: sinusoidal vertical field and zero horizontal one. It is naturally that only the odd harmonics are generated by this magnetic field. The harmonic intensities increase with their number increase, because the deflection parameter is sufficiently large (5.6). Fig 9 shows the the on-axis spectrum in the case of measured magnetic field. From this figure we notice that the even harmonics are generated along the axis in the real case. The effect of higher harmonics degradation is clearly visible. But the shape and amplitude of the first harmonic are almost the some for both cases.

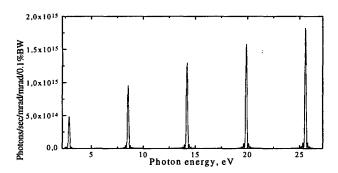


Fig. 8. On-axis spectrum in ideal planar magnetic field.

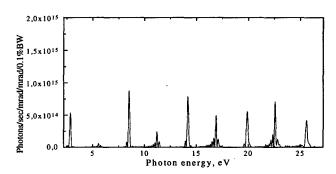


Fig. 9. On-axis spectrum in measured magnetic field.

- [1] M. Taniguchi and J. Ghijsen, J. Synchr. Rad., 5(3) (1998), p. 1176.
- [2] A. Hiraya, K. Yoshida, S. Yagi, M. Taniguchi, S. Kimura, H. Hama, T. Takayama and D. Amano, J. Synchr. Rad., 5(3) (1998), p. 454.
- [3] B. Kincaid, Nucl. Instr. and Meth., A246 (1986), p. 109.
- [4] E.E. Alp and P.J. Viccaro, Nucl. Instr. and Meth., A266 (1988), p. 116.
- [5] B. Kincaid, Nucl. Instr. and Meth., A291 (1990), p. 363.
- [6] R. Carr, Rev. Sci. Instrum. 63(7) (1992), p. 3564.
- [7] B.L. Bobbs, G. Rakowsky, P. Kennedy, R.A. Cover and D. Slater, Nucl. Instr. and Meth., A296 (1990), p. 574.
- [8] R.P. Walker, Nucl. Instr. and Meth., A335 (1993), p. 328.
- [9] Y. M. Nikitina, J. Pfluger, Nucl. Instr. and Meth., A359 (1995), p. 89.
- [10] S. Sasaki, N. Matsuki, T. Takada, Rev. Sci. Instrum. 63(1) (1992), p. 409.
- [11] R. Dejus, I. Vasserman, E.R. Moog and E. Gluskin, Rev. Sci. Instrum. 66(2) (1995), p. 1875.

THE PROPERTY OF UNIVERSALITY FOR PURE PERMANENT MAGNET WIGGLERS

M. N. Smolyakov*, Physical Department, Moscow State University, Moscow, Russia

Abstract

This paper deals with electromagnetic radiation generated by relativistic particles in arbitrary planar magnetic field (in a wiggler or undulator for example). Magnetic system producing this field is assumed to be planar and to consist of permanent magnets. It is shown that there is a special rotations for vectors of magnetization in such magnetic system: while magnetic field is varying but the spectrum of spontaneous radiation generated by relativistic particles remains the same. This property of radiation can be used in design of the new undulators and wigglers.

1 INTRODUCTION

Nowadays, permanent magnets are widely used in wiggler and undulator designs. Only permanent magnets are used in pure permanent magnet (PPM) wigglers [1]. Sometimes unusual undulator designs are used, especially for the microundulators [2-5]. To enhance the FEL gain, the non-standard scheme was chosen also for the PPM wiggler [6,7], i.e. with the magnetization vectors parallel and anti-parallel to the wiggler axis. That is why it is very important to investigate the general properties of the planar PPM undulators/wigglers and the electromagnetic radiation generated by relativistic electron beam in such systems. In particular the Rotation Theorem is well known [8]: if at each point of a PPM system all easy axis are rotated simultaneously by the angle θ , while the geometry remains the same, then all magnetic fields rotate by the opposite angle $-\theta$ without the change in amplitude.

This paper also deals with another general property of any planar PPM wiggler/undulator. It is shown that if all easy axis of the upper part of PPM undulator are rotated by the angle θ , and at the same time all easy axis of the bottom part of PPM undulator are rotated by the opposite angle $-\theta$ the shape of magnetic field clearly varies, but the module of it's Fourier transform remains constant.

2 FOURIER TRANSFORM INVARIANCE PROPERTY FOR MAGNETIC FIELD

Let us consider a PPM system that is infinitely wide and homogeneous along the X-axis (horizontal axis) with

magnetization $\vec{M}(y,z)$, see Fig.1. Magnetic field produced by such a system is given by [9]:

$$\vec{H}(\vec{r}) = \int_{V} d^{3}\vec{r}' \frac{3\vec{R}(\vec{M}(\vec{r}') \cdot \vec{R}) - \vec{M}(\vec{r}')R^{2}}{R^{5}}, \quad (1)$$

where $\vec{R} = \vec{r} - \vec{r}'$, $R = |\vec{R}|$.

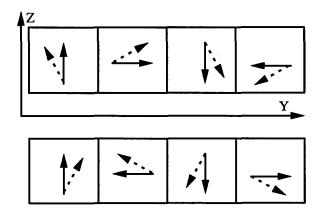


Figure 1: Rotation of easy axis in planar PPM wiggler: solid arrows show the initial magnetization, dashed arrows show the magnetization after rotation. Standard period of PPM wiggler is used as an example.

Let us consider the vertical magnetic field Fourier transform in the wiggler median plane (z = 0):

$$\widetilde{H}_{z}(p) = \int_{-\infty}^{\infty} e^{ipy} H_{z}(y, z=0) dy.$$
 (2)

Substituting (1) into (2) and making some analytical calculations yields the relationship [10]:

$$\widetilde{H}_{z}(p) = 2\pi \int A \exp(-ipy' - |pz'|) dy' dz', \qquad (3)$$

$$A = |p| M_z(y',z') - ipM_y(y',z') sign(z').$$
 (4)

Let us rotate the easy axis at each point of upper part of the PPM system (z' > 0) by the angle θ :

$$M_y'(y,z) = M_y(y,z)\cos(\theta) - M_z(y,z)\sin(\theta),$$

$$M'_z(y,z) = M_z(y,z)\cos(\theta) + M_v(y,z)\sin(\theta).$$

As a result we will find that at (z' > 0) and p > 0 the function A will obtain the additional phase factor:

$$A' = A \exp(-i\theta) \tag{5}$$

The rotation of the easy axis at each point of down part of the PPM system (z' < 0) by the angle $-\theta$ is given by:

^{*}Email: nick@smolyakov.msk.ru

$$\begin{split} M_y'(y,z) &= M_y(y,z)\cos(\theta) + M_z(y,z)\sin(\theta) \,, \\ M_z'(y,z) &= M_z(y,z)\cos(\theta) - M_y(y,z)\sin(\theta) \,. \end{split}$$

It is easy to see that the integral (3) over the bottom part of PPM system (z' < 0) will get the same phase factor as (5). As a result we have at p > 0:

$$\widetilde{H}'_{z}(p) = \widetilde{H}_{z}(p) \exp(-i\theta)$$
. (6)

Using the similar calculations, we have at p < 0:

$$\widetilde{H}'_{z}(p) = \widetilde{H}_{z}(p) \exp(i\theta).$$
 (7)

Magnetic field is a real function. It is evident from (6) and (7), that the complex conjugation of its Fourier transform is equivalent to replacing p by -p.

Eqs. (6) and (7) shows that if all the easy axis at each point of the upper part of PPM system are rotated by the angle θ and at the same time all the easy axis at each point of the bottom part of PPM system are rotated by the opposite angle $-\theta$, the module of Fourier transform of the magnetic field does not change (Fig. 1). But the phase factors in Fourier transform at p>0 and p<0 are different. It means that the shape of the magnetic field will be changed.

A brief analysis was made in [6] for the different magnetic fields produced by two different PPM undulators. Actually the second undulator in [6] could be derived from the first one by rotation of easy axis by the angle $-\pi/2$ at upper part of this undulator and by the angle $\pi/2$ at its bottom part. Results obtained in [6] are in excellent agreement with results obtained above in this chapter.

3 INVARIANCE OF ELECTROMAGNETIC RADIATION

Let us consider the spontaneous electromagnetic radiation, generated by relativistic particle in planar magnetic fields. At first, let us consider the case of relatively weak magnetic field. It means that the angle by which the particle is deflected by the magnetic field is small in comparison with the quantity $1/\gamma$, where γ is a reduced energy of relativistic particle. As this takes place, electromagnetic radiation is dipole-type. It means for undulators that the undulator deflection parameter is much smaller than unit. Electromagnetic radiation from the microundulators (undulators with period less than several millimeters) almost dipole-type. characteristics of dipole radiation are determined by the module squared of the Fourier transform of the magnetic field vertical component [11]. Let us transform the magnetic system as it was described above in section 2. Let us rotate the easy axis at each point of the upper part of PPM system by the angle θ and at each point of the bottom part of PPM system by the opposite angle $-\theta$ (Fig. 1). Using results obtained in section 2 and the property of dipole radiation noted above, we can conclude, that spectral characteristics of electromagnetic radiation of relativistic particle remain invariant under these transformations of PPM magnetic system.

Let us consider the planar PPM undulator with period l and infinite length. Integral of the magnetic field over the undulator period is equal to zero. Radiation wavelength λ , generated by the harmonic with number n at the angle θ to the undulator axis, is equal to:

$$\lambda = \frac{l}{2n\gamma^2} (1 + \gamma^2 \theta^2 + 0.5K^2). \tag{8}$$

Deflection parameter K for the nonsinusoidal magnetic field is equal to:

$$K^{2} = \frac{2}{l} \gamma^{2} \int_{0}^{l} \beta_{x}^{2}(y) dy, \qquad (9)$$

where $\beta_x(y)$ is a horizontal reduced speed of the particle. It is clear from the equations of motion that:

$$\beta_{x}(y) = \frac{e}{mc^{2}\gamma} \int_{0}^{y} H_{z}(y')dy' + \beta_{x}(0).$$
 (10)

The particle initial conditions were chosen in such a way that trajectory of the particle is a periodic function. The Fourier coefficients for the $\beta_{\mathbf{r}}(y)$ function are:

$$\beta_{xk} = \frac{1}{l} \int_{0}^{l} \exp(i\frac{2\pi}{l}ky)\beta_{x}(y)dy.$$
 (11)

Since the transverse drift of the particle along one undulator period is equal to zero, the Fourier coefficient at k=0 equal to zero, i.e. $\beta_{x0}=0$. Using Parseval theorem, we obtain:

$$\frac{1}{l} \int_{0}^{l} \beta_{x}^{2}(y) dy = \sum_{k=-\infty}^{\infty} |\beta_{xk}|^{2}.$$
 (12)

It is easy to show from (10) and (11) that at $k \neq 0$ Fourier coefficients for the reduced speed and Fourier coefficients for the undulator magnetic field are proportional to each other:

$$\beta_{xk} = \frac{i}{2\pi} \frac{el}{kmc^2 \gamma} H_{zk} \,, \tag{13}$$

where e is a particle charge, m is its mass, c is the speed of light.

$$H_{zk} = \frac{1}{l} \int_{0}^{l} \exp(i\frac{2\pi}{l}ky) H_{z}(y) dy.$$
 (14)

It is easy to obtain the formulae for the undulator magnetic field Fourier coefficients (14), which are similar to Eqs. (3), (4). Using (9) - (14), we can prove the following statement.

We transform now the planar PPM undulator by the method described in section 2. Let us rotate the easy axis at each point of the upper part of PPM undulator by the angle θ and at each point of the bottom part of PPM undulator by the opposite angle $-\theta$ (Fig. 1). As this takes place the Fourier coefficients (14) for undulator magnetic field and the Fourier coefficients (11) for the reduced speed will get the phase factor. It is evident from (9) and (12) that the undulator deflection parameter is invariant under this magnetic system transformation. It means that the position of undulator radiation harmonic does not shift also. But at the same time the intensity of undulator radiation at some harmonic might change, because of undulator magnetic field shape changes. This problem calls for further investigations.

- [1] K. Halbach, Nucl. Instr. and Meth. 187 (1981) 109.
- [2] G. Ramian, L. Elias and I. Kimel, Nucl. Instr. and Meth. A250 (1986) 125.
- [3] R. Tatchin and P. Csonka, J. Phys. D: Appl. Phys. 20 (1987) 394.
- [4] R. Tatchin, P. Csonka and A. Toor, Rev. Sci. Instrum. 60, No.7 (1989) 1796.
- [5] I. Kimel and L. Elias, Nucl. Instr. and Meth. A296 (1990) 611.
- [6] P.G. O'Shea, S.C. Bender, D.A. Byrd, J.W. Early, D.W. Feldman, C.M. Fortgang, J.C. Goldstein, B.E. Newnam, R.L. Sheffield, R.W. Warren, T.J. Zaugg, Nucl. Instr. and Meth. A341 (1994) 7.
- [7] R.W. Warren and C.M. Fortgang, Nucl. Instr. and Meth. A341 (1994) 444.
- [8] K. Halbach, Nucl. Instr. and Meth. 169 (1980) 1.
- [9] L.D. Landau and E.M. Lifshitz, The Classical Theory of Fields (Pergamon, Oxford, 1971).
- [10] N.V. Smolyakov, Nucl. Instr. and Meth. A308 (1991) 80.
- [11] R. Coisson, Phys. Rev. A20, No. 2 (1979) 524.

A SIMPLE DERIVATION OF THE LONG WAVELENGTH EDGE RADIATION FROM A BENDING MAGNET

M. Castellano*
INFN - Laboratori Nazionali di Frascati - CP 13 - 00044 Frascati - ITALY

Abstract

A simple derivation of the "edge radiation" emitted by an electron beam going through a bending magnet in the directions of its entrance and exit from the magnet itself is presented. This radiation is characterized by wavelengths much longer than the synchrotron radiation critical wavelength in the same magnet.

The far field radiation emitted by an electron following a curved trajectory inside a finite bending magnet can be approximated with any required accuracy by that produced by an electron following a segmented trajectory made of straight lines with sudden change of the velocity direction. The radiation field amplitude produced by a velocity direction change is that of a "prompt" bremsstrahlung in which the velocity module remains constant. The total amplitude is the sum of all the bremsstrahlung amplitudes with their relative phase difference.

For long wavelengths and around the direction of entrance or exit from the magnet, only few terms are required to give a good description of the radiation as compared with exact calculations

1 INTRODUCTION

The so-called "edge radiation" is emitted by an electron beam going through a bending magnet in the directions of its entrance and exit from the magnet itself. It is characterized by wavelengths much longer than the synchrotron radiation critical wavelength in the same magnet. It is considered for possible scientific applications because may be brighter than the analogous radiation emitted along the central trajectory inside the bending magnets.

It has been often assumed that this radiation could depend from the behavior of the magnet fringing field. I will demonstrate that it is only the standard synchrotron radiation from a finite length magnet.

R.A. Bosch has given a simple interpretation [1] that has some validity in the very long wavelength limit and can be considered a "zero order" approximation.

I will give a more general derivation, valid for all wavelengths and emission angles, which coincides with standard synchrotron radiation at short wavelengths.

The starting point is the observation that the far field radiation emitted by an electron following a curved trajectory inside a finite bending magnet can be approximated with any required accuracy by that produced by an electron following a segmented trajectory made of straight lines with sudden change of the velocity direction.

#michele.castellano@lnf.infn.it

The radiation field amplitude produced by a velocity direction change is that of a "prompt" bremsstrahlung in which the velocity module remains constant. The total amplitude is the sum of all the bremsstrahlung amplitudes with their relative phase difference.

For long wavelengths and around the direction of entrance or exit from the magnet, only few terms are required to give a good description of the radiation as compared with exact calculations [2]. The Bosch approximation consists in considering only the first term.

2 THEORETICAL CONSIDERATIONS

The starting point is the expression of the radiation intensity emitted by a charged particle in an arbitrary accelerated motion [3]

$$\frac{\mathrm{d}I^{2}}{\mathrm{d}\omega\mathrm{d}\Omega} = \frac{\mathrm{e}^{2}}{4\pi^{2}\mathrm{c}} \left| \int_{-\infty}^{\infty} \frac{\underline{\mathbf{n}} \times \left[\left(\underline{\mathbf{n}} - \underline{\beta} \right) \times \underline{\beta} \right]}{\left(1 - \underline{\beta} \cdot \underline{\mathbf{n}} \right)^{2}} \mathrm{e}^{\mathrm{i}\omega \left(1 - \underline{\underline{\mathbf{n}}} \cdot \underline{\underline{\mathbf{r}}(t)} \right)} \mathrm{d}t \right|^{2}$$

in which \underline{n} is the observation direction and $\underline{\beta}$ the particle velocity.

For a particle travelling only once trough a finite length bending magnet, the integral will be performed between the time of its entrance t_0 and the time of its exit t_1 .

We can always subdivide the integral as a sum of integrals on smaller time intervals

$$\frac{dI^{2}}{d\omega d\Omega} = \frac{e^{2}}{4\pi^{2}c} \left| \sum_{1}^{f} \int_{t_{i-1}}^{t_{i}} \frac{\underline{n} \times \left[\left(\underline{n} - \underline{\beta} \right) \times \dot{\underline{\beta}} \right]}{\left(1 - \underline{\beta} \cdot \underline{n} \right)^{2}} e^{i\omega \left(1 - \underline{n} \cdot \frac{\underline{r}(t)}{c} \right)} dt \right|^{2}$$

For sufficient short time intervals and long wavelength, we can assume that the phase factor is constant for each integral, so that we can perform an analytical evaluation

$$\frac{\mathrm{d}I^{2}}{\mathrm{d}\omega\mathrm{d}\Omega} = \frac{\mathrm{e}^{2}}{4\pi^{2}\mathrm{c}} \left[\sum_{1}^{f} \mathrm{e}^{\mathrm{i}\phi_{k}} \left[\frac{\underline{\mathbf{n}} \times \underline{\boldsymbol{\beta}}}{\left(1 - \underline{\mathbf{n}} \cdot \underline{\boldsymbol{\beta}}\right)^{2}} \right]_{k-1}^{k} \right]^{2}$$
(1)

This corresponds to approximate the curved path of the particle with a segmented trajectory, in which the particle velocity, constant in module, changes suddenly its direction.

The radiation amplitude for each change of direction can be written as that of a particle in uniform motion suddenly stopped, plus that of a particle starting with constant velocity in the new direction. The two amplitudes have opposite sign due to the different accelerations.

This approach of "prompt bremsstrahlung" has proven its efficacy in many radiation processes, from standard transition radiation to undulator transition radiation [4].

For our purpose, we can rearrange the terms of the sum in (1)

$$\frac{dI^{2}}{d\omega d\Omega} = \frac{e^{2}}{4\pi^{2}c} \left| e^{i(\phi_{f} - \phi_{o})} \left(\frac{\underline{n} \times \underline{\beta}_{o}}{\left(1 - \underline{n} \cdot \underline{\beta}_{o}\right)^{2}} - \frac{\underline{n} \times \underline{\beta}_{f}}{\left(1 - \underline{n} \cdot \underline{\beta}_{f}\right)^{2}} \right) + \sum_{l} \left(\frac{\underline{n} \times \underline{\beta}_{k-l}}{\left(1 - \underline{n} \cdot \underline{\beta}_{k-l}\right)^{2}} - \frac{\underline{n} \times \underline{\beta}_{k}}{\left(1 - \underline{n} \cdot \underline{\beta}_{k}\right)^{2}} e^{i(\phi_{k} - \phi_{k-l})} \right) \right| (2)$$

The first two terms in (2) represent, respectively, the radiation field amplitude produced by a particle that, moving at constant velocity, stops suddenly at the entrance of the bending magnet, and that of a particle at rest that starts moving in uniform motion at the exit of the magnet. Each of these amplitudes, that are often found in radiation phenomena, as Optical Transition Radiation, produce a radiation angular distribution with a maximum intensity at an angle equal to $1/\gamma$ with respect to the particle velocity, γ being the particle relativistic factor.

If the bending angle caused by the magnet is much larger than $1/\gamma$, the two amplitudes do not interfere, independently of the wavelength, and we have two separate sources each with the properties of a prompt bremsstrahlung. This is the approximation introduced in [1]. In this case the radiation is distributed symmetrically around the direction of entrance and exit of the beam from the magnet, and has a flat spectrum. Exact numerical calculations [2] show that this approximation has some validity only for very long wavelengths, and is not able to give the radiation intensity at larger angles, where the other terms in (2) are much more important.

These terms also are not new in the radiation panorama. Each element of the sum represents the field amplitude produced by a particle starting, from rest, at constant velocity in a given direction and then stopping after a finite path length. In the segmented trajectory model, this represent the radiation amplitude produced by the particle in a single rectilinear segment. This amplitude has been studied in transition radiation emission as the interference between two radiating foils, and, equivalently, but less known, as an under threshold Cherenkov radiation.

To better understand the effects of these terms on the total amplitude, we will analyze the behavior of one of

them in the horizontal plane, where its contribution is more sensible.

We have two equal amplitude of opposite sign separated by a phase difference that can be written as

$$\phi = \frac{2\pi d}{\lambda} (1 - \beta \cos \theta)$$

in which d is the distance traveled by the particle and θ is the observation angle with respect to the particle velocity.

The intensity distribution produced by a single segment of the trajectory is given by

$$\frac{dI^2}{d\omega d\Omega} = \frac{e^2}{c} \left(\frac{d}{\lambda}\right)^2 \sin^2\theta \left(\frac{\sin\frac{\phi}{2}}{\frac{\phi}{2}}\right)^2$$

It is clear that the smaller is the ratio d/λ , the lesser is the intensity, but spanning a larger angle range. This must be kept in mind when deciding how segmenting the trajectory and how many terms of the sum in (2) should be considered.

3 NUMERICAL SIMULATIONS

To demonstrate the effectiveness of this approach, I have calculated the radiation angular distribution in the horizontal plane for a real case, i.e. the Super-ACO storage ring, for which exact calculations and measurements exist [2].

The machine parameters relevant for this calculation are summarized in Table 1.

Table 1 - Relevant parameters of Super-ACO

Energy	800	MeV
Bending angle	π/4	rad
Curvature radius	1.7	m

The large bending angle prevents any interference between amplitudes at the entrance and exit of the magnet, for all reasonable wavelength value, so that the first two amplitudes in (2) can be considered separately.

In the following I will show some example of the radiation angular distribution along the exit direction from the magnet. In this case the first term in (2) can be neglected. In Fig. 1 the effect of a single bremsstrahlung amplitude (second term in (2)) is shown. This corresponds to the "zero length" model presented in [1]. Intensity and angular distribution of the radiation do not depend from wavelength. It must be noted that for practical reasons the intensity is given in arbitrary units, but the scale is the same for all the pictures, which can be directly compared.

Positive angles are towards the inner part of the curved trajectory.

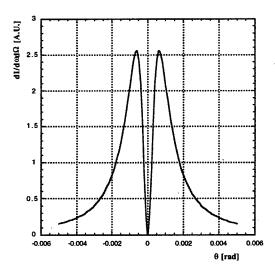


Fig 1 – Edge radiation angular distribution produced by a single bremsstrahlung amplitude

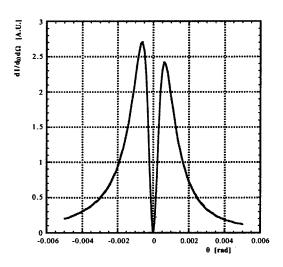


Fig 2 – Angular distribution of edge radiation at 500 μm

In Fig. 2 it is represented the same distribution for a radiation wavelength of 500 μm obtained from (2) approximating the curved trajectory as 15 linear segments, but considering only the contribution of the last three.

The asymmetry between the two lobes is now evident, and can be compared with that calculated in [2].

Even if based on a small number of terms, this result is accurate, compared to exact evaluations, to better than 1% on the peaks and to better than 5% on the tails.

Increasing the number of segments and the number of terms considered in (2), the intensity distribution at shorter wavelength can be computed with the same accuracy. As it is shown if Fig. 3, the asymmetry of the lobes increases and the distribution approaches the flat behavior of the "standard" synchrotron radiation.

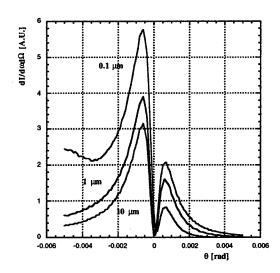


Fig 3 - Edge radiation angular distribution at shorter wavelength

4 CONCLUSIONS

The approximation of the trajectory inside a bending magnet as a sum of straight segments allows an intuitive and simple evaluation of the radiation emitted along the directions of entrance and exit from the magnet. In the case of long wavelengths an accurate result can be obtained by a simple expression. The use of prompt bremsstrahlung amplitudes allows also to consider the interference with other possible source of radiation along the straight section, due to insertion devices or even the mirror used to extract the edge radiation, in a simple way.

- [1] R.A. Bosch, Il Nuovo Cimento 20D, 483, (1998)
- [2] P. Roy et al., Il Nuovo Cimento 20D, 415, (1998)
- [3] J.D. Jackson, Classical Electrodynamics, J. Wiley & sons
- [4] M. Castellano, Nucl. Instr. and Meth. in Phys. Res. A391, 375 (1997)

MEASUREMENT AND OPTIMIZATION OF THE VISA UNDULATOR*

G. Rakowsky⁺, J. Aspenleiter, L Solomon, BNL, Upton, NY 11973 R. Carr, R. Ruland, SLAC, Stanford, CA 94309 S. Lidia, LBL, Berkeley, CA 94720

Abstract

The Visible-Infrared SASE Amplifier (VISA) undulator is an in-vacuum, 4-meter long, 1.8 cm period, purepermanent magnet device, with a novel, strong focusing, permanent magnet FODO array included within the fixed, 6 mm undulator gap. The undulator magnet is constructed of 99-cm long segments, joined into a continuous To attain maximum SASE gain requires structure. establishing overlap of electron and photon beams to within 50 microns rms. This imposes challenging tolerances on mechanical fabrication and magnetic field quality, and necessitates use of laser straightness interferometry for calibration and alignment of the magnetic axes of the undulator segments. This paper describes the computerized magnet sorting, pulsed-wire magnetic measurements, trajectory shimming magnetic axis calibration performed to meet this goal.

1 INTRODUCTION

The Visible-Infrared SASE Amplifier (VISA) [1] is a multi-institutional, collaborative experiment whose objective is to demonstrate and analyze Self-Amplified Spontaneous Emission (SASE) from noise to saturation in the 800-600 nm range. The experiment is being installed at Brookhaven's Accelerator Test Facility (ATF) linac, operating at 70-85 MeV.

Simulations of the VISA FEL [2] have shown that gain is degraded when trajectory wander exceeds 50 μm rms. This means that initial trajectory straightness, determination of magnetic centerline, fiducialization and alignment must each be accomplished to within 25 μm rms, equivalent to the peak wiggle amplitude at 72 MeV. These represent challenging requirements for magnetic and mechanical design, magnetic measurement and metrology. These challenges are addressed in this paper and in companion papers by Libkind [3] and Ruland [4].

2 UNDULATOR DESIGN

The VISA undulator has been described in detail previously. [1] It was designed to provide sufficient gain to reach saturation in less than 4 meters, the length available in the ATF beamline. Its compact, modular design is based on a planar, pure-NdFeB, Halbach structure with parameters shown in Table 1.

Table 1: Undulator parameters

Period	18 mm
Gap	6 mm (fixed)
Block dimensions	30 x 10 x 4.45 mm
Remanence B _r	1.25 T
Intrinsic coercivity H _{ci}	>20 kOe
Peak field B	0.75 T
Number of periods	220 (4 x 55/section)

The device is built in four 99-cm long sections, joined into a seamless, 220-period undulator. (Additional sections can be added in the future). Non-steering, displacement-free terminations at each end complete the dipole array.

2.1 Distributed Strong Focusing

To attain the needed gain length of <0.4 m, distributed strong focusing was added to the Halbach array. The compact quadrupole array is formed by pairs of vertically polarized NdFeB bars, placed lengthwise in the undulator gap, as shown schematically in Figure 1. The proportions were chosen to produce equal vertical and horizontal gradients in the vicinity of the axis. Magnets are mounted in 10-cm long modules, forming a FODO array with 24.75 cm period, for a total of 16 periods in 4 meters.

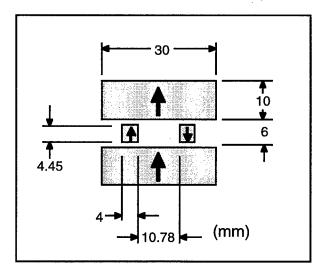


Figure 1. Schematic end view of VISA undulator, showing quadrupole magnets within the undulator gap.

This geometry creates a beam channel only 6 mm high and about 8 mm wide between quadrupole holders. An internal vacuum chamber would have reduced the vertical

^{*}Work supported in part by U.S. Department of Energy under Contract No. DE-AC02-98CH10886.

⁺E-mail address: <u>rakowsk1@bnl.gov</u>.

aperture even more, leaving too little room for BPM's, diagnostics, or even an alignment laser beam. For this reason the entire undulator was put inside a vacuum vessel. The magnet surfaces facing the beam are lined with $25~\mu m$ thick nickel foil, for image current continuity.

3 MAGNET SORTING

The VISA lattice is comprised of some 1772 magnet blocks forming 220 undulator periods, and 192 blocks forming 16 FODO cells. We specified magnetization tolerances of 1.5% in magnitude and 1.5 degrees in angle. Left uncorrected, these block errors produce random errors in the field, resulting in excessive beam trajectory walkoff and degradation of FEL interaction. To minimize this adverse accumulation of field errors, the magnetic moments of each magnet block were first measured by the manufacturer. We then used a Monte Carlo algorithm called "threshold acceptance" (similar to simulated annealing) to sort the blocks.[5] A localized 'cost', or 'free energy' function in terms of the moment errors is calculated at each block location along the beamline, then summed to obtain a measure of the level of field error. Starting with a random selection of magnets from the database, the algorithm swaps magnets and recalculates the cost function millions of times, until the total level of field error is reduced to a minimum. In our case, sorting reduced the rms field error by a factor of 14. The resulting reduction in trajectory walk-off is illustrated in Figure 2.

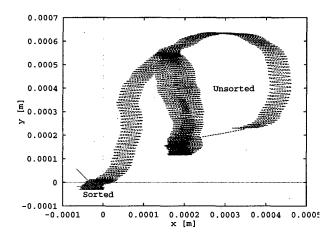


Figure 2: Comparison of undulator trajectory in VISA after sorting vs. a random magnet selection. The view is y vs. x, with the beam axis perpendicular to the page.

For the quadrupole lattice, variations of quadrupole gradient due to errors in the block magnetization only affect betatron motion. However, the quadrupole magnets also contribute dipole errors which cause trajectory errors as well. These errors stem either from magnetization errors or from positioning errors of the quadrupole magnets. Sorting of the quadrupole blocks produced only a very small theoretical improvement in trajectory error. On the other hand, dipole errors due to random quadrupole

positioning errors were found to be the dominant cause of trajectory deviation in VISA and became the focus of our measurement and field correction efforts.

4 PULSED WIRE MEASUREMENT

The enclosed beam channel severely limits access by conventional magnetic measurement devices, such as Hall probes. Since we cannot measure field or field errors directly, we rely on magnet block measurement and sorting to assure undulator field quality. To measure and correct trajectory errors, we chose the pulsed wire as the primary measurement tool.[6] Driven by a current step, it provides an instant image of the trajectory, permits rapid, iterative trajectory correction, and is an excellent null-finding device for locating the quadrupole axis. However, the observed wiggle amplitude in the wire is much smaller, and the betatron wavelength is much longer than that of a 72 MeV electron.

The pulsed wire can also be driven by a current impulse to give an image of angular deviation. However, in this application, the trajectory is the more useful diagnostic.

The pulsed wire technique requires care in setup and interpretation. First, we set up the pulsed wire bench on a massive granite table for stability. Two VISA undulator sections at a time are supported in the center of the table on posts with kinematic supports and X and Y adjusters, identical to those used in the final assembly [1]. Smaller granite blocks sit atop the ends of the table, supporting the 4-m long wire, the oil bath vibration damper and the wire position detector. The setup is shown in Figure 3.

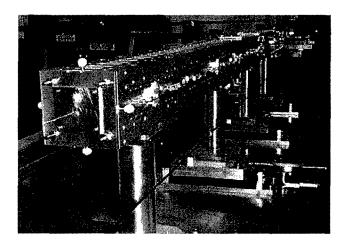


Figure 3: Two VISA sections on the pulsed wire bench.

Despite the stable support structure, the wire tends to vibrate at its resonant frequency (31 Hz), driven by the electro-magnetic pulses, air currents and environmental sources. To damp the vibrations, one end of the wire is immersed in an oil bath. The 31 Hz is suppressed by filtering and by the oscilloscope's averaging feature.

Wire sag affects the measurement of the y-component of the trajectory. For this reason the undulator sections were designed to be mounted normal or inverted for x-trajectory measurement, or rotated 90° to measure the y-trajectory in the horizontal plane, independent of wire sag.

Earth's field also contributes a significant error to the trajectory signal. To provide a field-free environment, we added rectangular Helmholtz coils spanning the full length of the bench. The currents needed to cancel Earth's field were determined empirically by observing the trajectory signal without the undulator present.

Thanks to the high gradients and careful setup, we are able to locate the quadrupole centerline in pairs of VISA sections to about $5 \, \mu m$ rms.

5 TRAJECTORY CORRECTION

Quadrupole misalignment turns out to be the dominant contributor to trajectory error. Despite precisely machined mounting surfaces and the use of a ground spacer bar during installation, random position errors of up to 50 μ m remained. In a 33 T/m gradient, this translates to large steering errors of up to 150 G-cm per quadrupole module. For this reason the quadrupole holders were mounted on threaded studs accessible from the outside, permitting local x-position adjustment of the quadrupole axis. No vertical adjustments were provided, although they would have been desirable. (Cam-type adjusters for vertical positioning are being designed into two additional VISA sections for future expansion.) Instead, y-trajectory corrections were accomplished by strategically clamping discrete NdFeB magnets symmetrically to the sides of the structure.

The undulator sections were also provided with access ports in the upper and lower strongbacks to permit insertion of trim magnet assemblies close to the undulator arrays. The $3 \times 3 \times 2$ mm trim magnets, mounted in sets of four in adjustable holders, are able to provide local steering corrections of up to 30 G-cm in x or y.

The magnet sections were first trimmed one at a time. Then they were set up two at a time, to check the trajectory across the joints. Using a combination of quadrupole repositioning, external magnets and the trim magnets, we were able to reduce x and y trajectory errors from several wiggle amplitudes down to a peak-to-peak

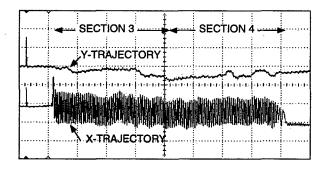


Figure 4: Y (upper trace) and X (lower trace) trajectory in Sections #3 and #4 after final trimming. Both have same arbitrary vertical scale. Horizontal scale is ~25 cm/div.

error of less than one wiggle amplitude over 2 meters (or <10 µm rms). As an example, Figure 4 shows x and y trajectories in Sections #3 and #4, after final trimming.

6 FIDUCIALIZATION

To measure position and alignment to better than 25 μm in a structure several meters long exceeds the capability of conventional optical survey techniques. We therefore chose laser straightness interferometry, described in detail by Ruland.[4] The interferometer is set up on the bench parallel to the pulsed wire. When the magnetic axis has been aligned to the wire, the straightness interferometer measures the offset of each fiducial from the wire center (i.e., form the magnetic axis). These measurements are done first with the VISA sections in normal orientation, then rotated 90 degrees. This calibrates the magnetic axis relative to the fiducials in both planes. In tests we have demonstrated fiducialization accuracy to <10 μm.

During installation of the undulator in the vacuum vessel at the ATF, two straightness interferometers, one in the x-z plane, the other in the y-z plane, will be used to align the undulator sections to the beamline reference laser by reproducing the x and y offsets measured on the bench. The expected accuracy of this operation should also be in the 10 µm range.

7 CONCLUSIONS

We have constructed four 1-m long, strong-focusing undulator sections, located their magnetic axes and trimmed the peak-to-peak trajectory deviations to less than one wiggle amplitude, using the pulsed wire technique. We can locate the magnetic axis of each section, measure fiducial offsets and, it is hoped, align the VISA sections to achieve a final trajectory error well below the required $50 \ \mu m \ rms$.

8 ACKNOWLEDGEMENTS

The authors thank Michael Lehecka (NSLS) for assistance in magnetic measurements, Pedro Frigola (UCLA) for constructing the Earth's field coils, Pietro Musumeci (UCLA) for GENESIS simulations, and all the VISA team members for stimulating discussions and support.

- [1] R. Carr et al., Proc. 1989 Free Electron Laser Conf.
- [2] P. Emma & H-D. Nuhn, Proc. 1989 Free Electron Laser Conf.
- [3] M. Libkind et al., these Proceedings.
- [4] R. Ruland et al., these Proceedings.
- [5] S.Lidia and R.Carr, Rev. Sci. Inst. 66 (1995) p.1865.
- [6] R. Warren & C. Fortgang, Nucl. Inst. & Methods A341 (1994) p.444.

COMPONENT OBJECT MODELING FOR BEAM PHYSICS PROBLEMS

S.N.Andrianov*, SPbSU, S.Petersburg, Russia

Abstract

In recent years sufficient success was achieved in the modeling and optimization of beamlines on the base of highorder maps. In this paper a new approach based on symbolic representation of high-order aberrations in matrix forms is described. We discuss all the pros and cons of such approach.

1 INTRODUCTION

In recent years many accelerator design and simulation codes was developed. The most of them are based on numerical simulation all steps of modeling process. Among them we should mention the works by J.Jrwin, Y.T.Yan and their colleagues (for example, [1]), the work by E.Forest, K.Hirata [2] and the work of Leo Michelotti [3], M.Berz [4]. Besides these there are several works devoted to the programming design using modern achievements in software (see, for example, [5]-[6]). Unfortunately, the problems of formalizing of the tasks of beam physics in many respects remain unsolved. Their solution would ensure a capability to store knowledge obtained as results of computing experiments, to fill up the knowledge base with new knowledge without destruction of its structure, to use the similar objects for the solution of the different problems arising in beam physics. On the one hand, the development of the software allows to introduce into modeling practice symbolic calculations (methods and codes of computer algebra), modern ideas of object-problem modeling. On the other hand we witness an enormous growth of capabilities of modern computer technology, for example, parallel computers, which can calculate both in symbolic, and in numerical modes. There are rather many authors who use computer algebra in their investigations. But usually they use computer algebra codes as a powerful calculator. It is necessary to mention the works of B.Autin and his colleagues who try to use computer algebra methods and codes maximal widely [8]. In this paper we suggest a new approach which is based on symbolic representation of necessary information on the one hand and object-oriented design approach on the other hand. These two sides of modeling process allows to create flexible and powerful codes for particle beam study including high order aberrations and space-charge forces. For this purpose we use Component Object Modeling Technique (COM-technique) which permits to ensure for wide classes of beam physics problems

* Serge.Andrianov@pobox.spbu.ru

necessary flexibility and efficiency of calculations, and simultaneously to store knowledge during usage of the offered COM-technique.

2 BASIC CONCEPTS AND IDEAS OF THE COM – TECHNIQUE

The object-oriented design based on the usage of object-oriented models for design the program systems and their components. Speaking about object-oriented design, we mean:

- Object-oriented methodologies (technology) of designing program systems.
- The tools maintaining these technologies.

The object-oriented design can begin at the very first phase of biotic cycle; it is irrelevant what the programming language will be used for implementation of the developed program system: this language can and to not be object-oriented. During the development cycle the objects are some formal designs (for example, quadrupole as physical object) bound with their future implementation on one of the programming languages. The objectoriented software engineering is related to application of object-oriented methodologies (technologies). Usually these object-oriented methodologies are supported by tool software, but even without it they are useful, because they allow to understand different aspects and properties of the developed program system which essentially facilitates implementation, testing, tracking, and designing of the new versions and more essential modification.

2.1 Database of Physical Control Elements

So, before the development of the software we should create the structured system of elementary objects, which will allow us to create computer model for the fulfillment of this or that task. Outgoing from the designer's purposes of beamline systems, it is necessary to create database of physical control elements. The point is that for the different problems even the concept such a simple object as a drift will essentially differs. As a basic element for any control element we shall consider so-called ideal object: a ideal drift, ideal quadrupole and so on. The subsequent complication of control elements is implemented on the unified information frame by addition of new properties. Here we deal with inheritance paradigm which is already known

from the theory of object—oriented design. If necessary each object of this constructed database is accompanied by the help information ensuring its interactive usage. At this phase the designer deals with the only physical information permitting him purposive to manipulation of control elements from the database and to create the personal project. If it is necessary to have on a designer's desktop the structural map of a constructed system. Such map can be built on a computer display or in an iconic kind, or in a selected scale which geometrical parameters of the objects.

2.2 Formalization of the Structure Objects Database

At the second phase of designing the designer addresses to the database of the second level, which contains the information on parameters of units ensuring their operation. Here, first of all, it is necessary to attribute the information on fields generated by these objects. In this approach we use the well known philosophy of a perturbation theory which allows to structure the field information. The fringe fields can be included using virtual (as fringe fields do not exist without element by itself) object. For this purpose we use a database of model functions for fringe fields. The selection such as distributions is determined by a principle of the adequate description of experimental data and efficiency of the mathematical description. As base the piecewise constant approximating of distribution of fields is considered. The selection of a necessary object can be carried out from the database of physical objects. It is necessary to consider a problem of space-charge forces specifically. In this case we use the database of model distributions [5].

2.3 Motion Equations and Matrix Formalism

The knowledge of field decomposition in used objects allows us to define the approximation order for the motion equation which can be written in the following form [6]:

$$\frac{dX}{ds} = \sum_{k=0}^{\infty} \mathbf{P}^{1k}(s) X^{[k]},\tag{1}$$

where $\mathbf{P}^{1k}(s)$ are matrices depending on field and its derivatives values calculated on an electrical axis of a control object. Using of the information of the database of the second level (field of objects) we constraint the database of the third level — database of matrices, which appropriate to used objects. According to the matrix formalism concept the basic objects are the matrices $\mathbf{P}^{11}(s)$, that are transfer matrices for ideal objects with independence from the fields. The matrices \mathbf{P}^{1k} ($k \geq 2$) can be calculated for rather wide class of functional dependence from . Thus, objects of the third level database are the matrices \mathbf{P}^{1k} , calculated in symbolic forms using computer algebra codes (for example, MAPLEV) up to some approximation order N. Similarly we can construct the other matrices which are necessary for our modeling process [7].

2.4 The Solutions of Motion Equation

Following the matrix formalism concept solution of motion equation (1) is searched as

$$X(s) = \sum_{k=0}^{\infty} \mathbf{M}^{1k}(s|s_0) X^{[k]},$$
 (2)

$$X_0 = X(s_0), \ \mathbf{M}^{1k} = \mathbf{M}^{11} \cdot \mathbf{Q}^{1k}, k \ge 1.$$

According to our approach we build the fourth level database. It is necessary to note, that this database, as well as previous, consists of two parts: first contains block matrices \mathbf{M}^{11} — linear transfer matrices for control elements, the second contains block matrices \mathbf{Q}^{1k} , describing aberrations generated in the corresponding control element. Similarly we compute block matrices \mathbf{M}^{11} , \mathbf{Q}^{1k} , describing the contribution of space—charge forces. These matrices depend on model distribution functions of the space—charge in a phase (or configuration) space.

2.5 Selection of Local Coordinate Systems

For each control element there is some coordinate system, where the motion equation has a simplest form. Such coordinate system is selected as base one, and in this coordinate system we evaluate both matrix \mathbf{P}^{1k} , and matrix \mathbf{M}^{11} , \mathbf{Q}^{1k} . The transition from local coordinate systems to a global system (used for description of the total beamline system) is realized using transformation matrices of coordinate systems \mathbf{T} . Such set of matrices makes content of one of auxiliary databases. In particular, the transfer matrix for a solenoid has an extremely simple form in a rotated coordinate system, therefore such matrix \mathbf{P}^{1k} and corresponding matrices \mathbf{M}^{1k} enter in the appropriate database. For implementation of direct calculations we use a homothetic transformation for return to the global coordinate system.

3 SYMBOLIC OPERATIONS

For realization of a simulation procedure we should construct as from LEGO blocks a beamline system either in the language of motion equation (using matrix \mathbf{P}^{1k}), or in the language of evolution matrices M^{1k} , describing time evolution of particle beam. If the necessary matrix object is missing in the appropriate database, we should use one of computing modules to calculate a required matrix in the symbolic form and then to update the database. Let's remark, that for this purpose we use the program package (in codes MAPLE V and REDUCE) ensuring the necessary operations with non-commutative objects (for example, for the CBH-formula) and with matrices (using of the extended matrix operations such as Kronecker sums and products). The existing symmetries allow to use a block structure of matrices and for the reduction of matrix dimensions M^{1k} , that essentially reduces computing costs (especially for the high orders of approximation N). Let's remark also, that for the research of a long-time evolution of beams there is a necessity to construct evolution matrices

on large intervals. In this case representation by matrices allows us to decrease temporary costs of calculations essentially. This has allowed to study explicitly enough the processes in extract resonance system [8] and problem of influence of space—charge forces (for example, the problem of a halo formation [9–10]).

4 COMPUTER EXPERIMENT

In this paper for realization of the approach described above we use the system of RAD - DELPHI, permitting, on the one hand, to build simply a user interface, and on the other hand, to use the dynamic modeling paradigm [11–12] for computing experiments using prepared databases. Moreover, latest versions of DELPHI allow to implement the client–server technology and thus distributed calculations concepts. The second moment, which it is necessary to point, is related to a capability of wide application of paralleling procedures for calculations. The point is that the matrix formalism admits parallel processing realization naturally as the beam simulation problems can be resolved by manipulation with matrix objects. Thus the parallel calculations can, basically, be performed both in numerical, and in symbolic modes.

5 REFERENCES

- Y.Cai, M.Donald, J.Jrwin, Y.T.Yan LEGO: A Modular Accelerator Design Code, Proc. of the 1997 Part. Acc. Conf.
 — PAC'97, Vancouver, Canada, (1998), pp.2583–2585.
- [2] E.Forest, K.Hirata A Contemporary Guide to Beam Dynamics, Nat. Lab. for High Energy Physics, KEK Report 92-12(1992).
- [3] L.Michelotti "MXYZPPLK: a Version of Differential Algebra, Fermi Nat. Lab. Report FN-535 (1990).
- [4] M.Berz Differential Algebraic Description of Beam Dynamics to Very High Orders, Part. Acc., 24, 1989, pp.???.
- [5] S.Shasharina, J.R.Cary, D.L.Bruhwiler Status of MAPA (Modular Accelerator Physics Analysis) and TECH-X Object-Oriented Accelerator Library, Proc. of the 6th European Acc. Conf., Stockholm, Sweden, 1998, pp.1174-1176.
- [6] N.Malytski, R.Talman Unified Accelerator Libraries, Proc. of the 1996 Comp. Acc. Phys. Conf. CAP'96, Sept. 24–27, Williamsburg, Virginia, USA, eds. J.J.Bisognano, A.A.Mondelli, AIP Conf. Proc. 391, NY, 1997, pp.361–372.
- [7] S.Andrianov Dynamic Modeling Paradigm and Computer Algebra, Proc. of the 9th Intern. Conf. "Computational Modelling and Computing in Physics", September 16–21, 1996, D5, 11–97–112, pp.60–65, Dubna, 1997.
- [8] B.Autin (ed.), C.Carli, T.D'Amico, O.Grobner, M.Martini, E.Wildner BeamOptics: A Program for Analytical Beam Optics, preprint CERN 98-06, 1998, 129 p.
- [9] S.Andrianov, High-Order Optics with Space Charge: Analytical Approach, Proc. of the Sixth European Part. Acc. Conf. EPAC-98, Stockholm, 22–26 June 1998, Inst. of Phys. Publ., Bristol, UK, pp.1091–1093.
- [10] S.Andrianov, N.Edamenko Halo Formation and Control, presented on this Conference.
- [11] S.Andrianov *Dynamic Modeling in Beam Dynamics*, Proc. of the Second Int.Workshop on Beam Dynamics & Optimization BDO'95, July 4-8, 1995, St.Petersburg, Russia, St.Petersburg, 1996, pp.25–32.

[12] S.Andrianov, A.Dvoeglazov Beam-Lines Design Codes: Dynamical Modeling Approach, Proc. of the Sixth European Part. Acc. Conf. — EPAC-98, Stockholm, 22-26 June 1998, Inst. of Phys. Publ., Bristol, UK, pp.1150-1152.

BEAM_LINER -- AN OBJECT ORIENTED BEAM LINE MODELING C++ CODE

I.P. Yudin**, A.V. Trofimov, JINR, Dubna 141980, Moscow region, RUSSIA

Abstract

An integrated expert system has been developed to solve the charge particle beam optics problems [1,2]. The optics elements are a drift space, a bending magnet, a quadrupole, a sextupole, an octupole, a solenoid, an accelerating tube and some elements introduced by the users. BEAM_LINER is coded by the C++ language and the UNIX operation system with a graphical user-oriented interface on the PC Pentium II.

1. Introduction.

The user-oriented interface is created allowing to solve the beam matching problem, to compute of betatron functions, of phase advances and to investigate other problems. The beam motion is described on of the envelopes (of β-functions) and the frequencies of betatron oscilations (what is by the ideology of the methods of the snooping abroad of phase multitude). The motion of the single particles of the beam (trajectories) is described on the simple language of the transfer matrixes. But it is possible by the numerical integration, also.

2. The description of member functions and the class structure.

BEAM_LINER is written by means of object-oriented design [3] in X Window system without the using of ready libraries of control elements (such as Motif, Athena and etc.). That is why we created some minimal set of classes which are necessary for the building of user-oriented interface (some buttons, the edit boxes, the message boxes, etc). Moreover, we created the base class (Xelement) for the representation of elements, of which the system of beam optics itself is to be constructed. Below we will describe four from the set of elements: those are a drift of space, a quadrupole, a solenoid, and dipole. For them we created four different classes successors of Xelement. Fact is that all classes of control elements are successors of one abstract base class and inherit its member functions - that allows to curtail greatly the measures of the main loop which receives and handles the events. The using of virtual functions lets us not to rewrite the same fragments of code for the elements of different types.

In header-files obj1.h, obj2.h are described:

- 1) Abstract class Xobject
- 2) Class Xbut, successor of Xobject
- 3) Class Xbut1, successor of Xbut
- 4) Class Xfield, successor of Xobject
- 5) Abstract class Xelement.
- 6) Class Xdrift, successor of Xelement.
- 7) Class Xquadro, successor of Xelement.
- 8) Class Xdipol, successor of Xelement.
- 9) Class Xsolen, successor of Xelement.

2a. Classes of control elements:

class Xobiect

{ public: Display *dis;

Drawable win; /*main window's descriptor*/ GC *prGC;/*points at the structure of graphic context*/

unsigned int x; unsigned int y; unsigned int dx;

unsigned int dy; unsigned short deep; unsigned short cr; unsigned short col; char title [20]; char text [20]; int f; unsigned short tp; virtual void show (); virtual void hide (); virtual void set_p(); virtual void click1 (); virtual void click2 (); virtual void key_pressed (char, int); Xobject (Display, Drawable, GC, unsigned int, unsigned int, unsigned

int, unsigned int);};

class XBut: public Xobject

{public: unsigned short deep; unsigned short cr; void hide (); virtual void click1 (); void click2 (); void key_pressed (char, int); void show (); void show_pr();

XBut (Display, Drawable, GC, unsigned int, unsigned int, unsigned short, unsigned short, unsigned short, char, unsigned short, unsigned short);};

class XBut1: public Xbut

{public: void click1 (); XBut1 (Display, Drawable, GC, unsigned int, unsigned int, unsigned short, unsigned short, unsigned short, char, unsigned short, unsigned short);};

class Xfield: public Xobject

{public: unsigned short p; void get_symbol (char, int); void set_p (); void show (); void click1 (); void click2 (); void hide (); void key pressed (char, int); Xfield (unsigned int, unsigned int, unsigned short, unsigned short, char, Display, Drawable, GC, unsigned short);};

^{*} Work supported in part by Russian Federal Program 'Integration', contract No. K0085.

⁺ E-mail: yudin@cv.jinr.ru

Here dis points on the main display, win is the descriptor of window which owns an object, prGC points at the structure of the graphic context of window, x, y, dx, dy are coordinates of upper left corner and the measures of an object, accordingly. All these parameters are handed over when the constructor is being called. Fields deep and cr matter only for Xbut and Xbut1 classes, they define the geometry of buttons (for example, deep defines the thickness of buttons), as well as field f is, which indicates if the button is pressed or not. Col value defines the color of an object, line title contains inscription on button, or over the edit box in case of Xfield, and text line is appointed to store a text, inputed by user. At the window's creation it is being defined by masks, that only Expose, MotionNotify, KeyPress, and ButtonPress events will be handled in main loop. Event Expose, forcing window to redraw itself, comes, for example, with hitting one of buttons or with the text appearance or changing in an edit box; certainly, all control elements will be re-drawn in updated state. When one of three last events is being intercepted, program looks through the array which contains pointers at all existing control objects (the pointers are of Xobject * type). Using of virtual functions lets us to use this single scheme of objects' reaction on incoming events, though different classes may react differently.

Virtual functions click1 (), click2 (), key_pressed (char, int), inherited by all classes – successors of Xobject - define, how an object should respond on clicking with the left or right mouse key, or on events from keyboard, accordingly. Show() and hide() functions are responsible for showing/hiding some object when window is being updated. Class Xfield ignores Buttonpress events, the text box becomes active in the very moment the mouse's cursor comes in its borders. Besides, class Xfield has special member function get_symbol (...) for the input and processing of information, coming to edit box. Only this class really treats this event (classes Xbut and Xbut1 just ignore its).

2b. Classes Xelement, Xdrift, Xquadro, Xdipol, Xsolen:

class Xelement

{public: Display *dis; Drawable win; Drawable win2; GC *prGC; unsigned short obj_type; unsigned int num; double lenght; unsigned int col; char name [20]; void show (unsigned int); void OpenWin2 (unsigned int, unsigned int); void respond (unsigned int, unsigned int); Xelement (double, unsigned int, Display, Drawable, GC, unsigned short); virtual double get_e1 (); virtual double get_e2 (); virtual void set_e1 (double); virtual void set_e2 (double); virtual double get_B (); virtual void set_B (double);};

class Xdrift: public Xelement

{public: Xdrift (double, double, unsigned int, Display, Drawable, GC, unsigned short); void set_e1 (double); void set_e2 (double); void set_B (double); double

get_e1 (); double get_e2 ();
double get_B ();};

class Xquadro: public Xelement
{public: Xdrift (double, double, unsigned int, Display,
Drawable, GC, unsigned short);
void set_e1 (double); void set_e2 (double); void
set_B (double); double get_e1 (); double get_e2 ();
double get_B (); private: double B;};

class Xdipol: public Xelement
{public: Xdrift (double, double, unsigned int, Display,
 Drawable, GC, unsignedshort);
 void get_e1 (double); void set_e2 (double); void
 set_B (double); double get_e1 (); double get_e2 ();
 double get_B (); private: double B; double e1; double
 e2;};

Class Xelement and it's successors demand particular description. dis, win and prGC values have the same specification, as in class Xobject. Descriptor win2 is appointed to access to control panel, which opens with the hitting of the right key of mouse. Panel is necessary to set values of the parameters of elements. After all values had been set, function respond (...) is called, which in its turn calls function OpenWin2 (...), assigning recommendations to the windows manager and creating window for panel, and then launches the main loop to intercept and handle the events. Window contains several edit boxes and a button, which has to be hit to stop the loop, and then the characteristic values of elements admit meanings stated in corresponding edit boxes.

All constructors and the member functions of classes are described in header files obj2.h, obj3.h, and obj_draw.cpp

3. The interface description.

The whole code of program is split into separately compilable modules. Module main.cpp contains function main, which fills objects array, creates the main program's window and launches the main loop. Main loop acts in the following way: in the moment when next event has been received, an array of objects is being looked through. If the mouse's cursor were located in the frontiers of an object (lets call such an object "active"), then it's corresponding response-function and then function ResponseTable, residing in file response.cpp, are being called. After they finished, the window is to be updated. If the right key of mouse (rEvent. type==ButtonPress, rEvent. xbutton. button==Button2) were pressed while cursor were located over the special position, averted for an element then, in case, if this position were not empty, a respond(...) element's member function is being called. If it was left key (rEvent. type==ButtonPress, rEvent. xbutton. button==Button1), while cursor where over one of the positions, then an element defined by significance obj_flag (this significance changes by hitting one of the buttons - Drift, Quadro, Solenoid, Dipol) is being placed in the position. All values, characterizing element, are assigned to equal zero by the default and may be changed later in the function respond(...), or an element maybe destroyed. By the hitting of button SAVE created configuration will be stored in file with the name, given in edit box filename. Previously saved configuration maybe downloaded later again by the hitting of LOAD button (all functions corresponding are described load_save.cpp). File is just a sequence of records, which contain the type of element and it's values. While loading, they are being read one after one, and elements are being placed in corresponding positions. Finally, Quit button brings to exit from program without saving of current configuration.

Buttons Drift, Quadro, Solenoid and Dipol serve to select the elements, button NEW destroyes the configuration and cancels all settings. Algorithm, calculating the trajectory itself, starts working with the hitting of Go button.

rec_col.cpp module also contains receive_colors(...) function, which defines colors. One of the first actions, performed by function main after standard procedures - the setting connection with graphic server, the definition of the number of main screen, and so on - is receive_colors()'s call; as a result, global variables which contain color values are defined. Uconv.cpp contains several accessorial functions, usefull for the conversion of type char in double, and etc.

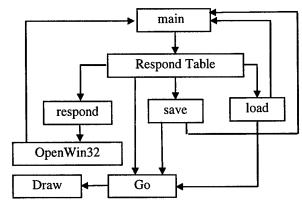


Fig.1. The base modules of the program.

Drawing itself is performed by function Draw which uses, in its turn, special graphic library PlPlot [4].

All global variable, constants and the prototypes of functions are described in header files init.h, init2.h.

More discriptions are avaible in [5].

4. References

- [1] Andreev V. V., Yudin I. P. Third-Order Optics of the Real Solenoid Lens. In Proc. International Conference on HEACC'92. Humburg, Germany, July 15-18, 1992.
- [2] Brown K.L., et al. TRANSPORT. A Computer Program for Designed Charged Particle Beam Transport System. SLAC-91, Rev. 2 UC-28 (1/A). May 1991.
- [3] Grady Booch. Object Oriented Design. With Application. The

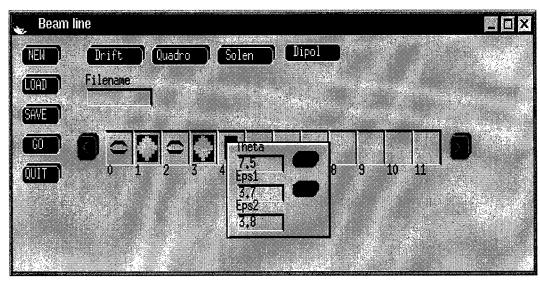


Fig.2. Example of control menu.

Behjamin/Cummings Publishing Company, Inc. [4] PlPlot User Guide.

New York, 1991.

ftp dino.ph.utexas.com

[5] I.P.Yudin, A.V. Trofimov BEAM_LINER User Guide, JINR, Dubna, March 3, 1999.

TOCA: A HIGHLY USER FRIENDLY APPLICATION PROGRAM FOR THE TUNE, ORBIT, DISPERSION AND CHROMATICITY CORRECTION

F. Iazzourene, Sincrotrone Trieste, Trieste, Italy

Abstract

In order to ease and speed up the intervention of the operators on the machine optics parameters, e.g. the orbit correction, a highly user friendly application program has been developped and fully used from the start of last year (1998). The program allows the acquisition and correction of the closed orbit, the dispersion, the tune and the chromaticity in the storage ring, and the acquisition and correction of the trajectory along the transfer line and the first turn in the storage ring, with a minimum intervention of the operator. The correction strengths are calculated using calculated theoretical optics or measured response matrix. The methods of correction implemented are the SVD method and for the orbit and the trajectory also the MICADO method.

1 INTRODUCTION

Going towards an increased automation of machine parameter characterization, a highly user friendly multitask application program, TOCAⁱ (Tune, Orbit, Chromaticity Application program), has been developped[1]. The program is written in C and the graphical user interface is based on the X11 Motif toolkit. Its main panel is shown in the figure 1. The first vertical window is dedicated to the trajectory along the transfer line and the first turn in the storage ring, and to the orbit and dispersion in the storage ring. The second and the third ones are dedicated to the tune and the chromaticity respectively. Each window has at the bottom three buttons: MEASURE ONLY, MEASURE-CORRECT-MEASURE and UNDO CORRECTION. The first window has also MEASURE and PLOT to get a plot of the selected trajectory or the orbit and/or dispersion. Figure 2 shows the plot of the orbit measured during a shift. The user gets the mean, rms, the min, max and the peak to peak value on the plot. Using the arrows of the keypad, the user can get on the plot the name of the monitor and the position of the beam at the monitor, or the dispersion for a plot of the dispersion. The scales are done by the program. The program performs the requested tasks without any intervention of the user. Furthermore, the button UNDO CORRECTION becomes sensitive only after the user has done a correction. The button, MEASURE-CORRECT-MEASURE for the trajectory, orbit and dispersion becomes sensitive only after the user has selected the plane on which he wished to correct, etc... The one go multitask style of the program is not however a complete black box for the user. In the window at the bottom of the main panel, the program writes in step by step every

action undertaken and refers in any useful information for the user, for example the results of the correction, the error messages, etc.... The text can be printed by simply clicking in the "print" of the text menu.

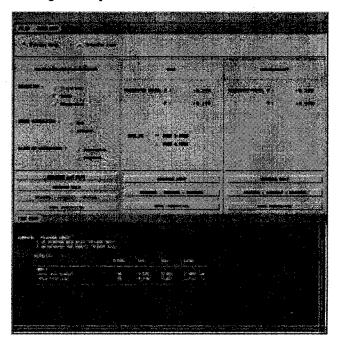


Figure 1: Main panel of the application program TOCA.

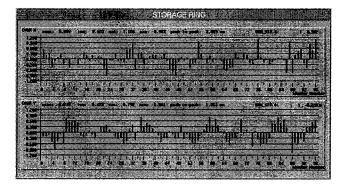


Figure 2: Measured closed orbit during a shift.

To speed up and ease the intervention of the user, all the selections which are more frequent are preselected when the application is started. For example, the chosen system is the storage ring, the families of quadrupole power supplies for the tune correction are PSQ2 and PSQ3, instead of PSQ2 and PSQ1, as the quadrupoles Q3 are better decoupled from the quadrupoles Q2 than the quadrupoles Q1; the requested values for the tune and the chromaticity are preset to the most requested values; the method of correction for the orbit correction is SVD,

ⁱ The new name for the program Orbit-OpticsOptimization.

etc.... The data needed by the program is predefined, so that the user can start any task directly. Some of the data are anyway available to the user via two temporary files created each time the user starts the application, so that he can change them as wished. There are two input files, one for the storage ring, the other for the transfer line. A special effort is done to control the data changed by the user to avoid dangerous mishandlings. A temporary output file contains a summary of all the measured parameters: orbit, dispersion, tune, chromaticity and trajectory together with the beam energy and the time of acquisition.

2 CORRECTION METHODS

It is well known that the SVD method allows a good rms orbit correction with minimum corrector strengths as compared to the other methods of correction. The chosen method is thus SVD for the orbit and/or dispersion correction in the storage ring, and also for the correction of the beam trajectory along the transfer line. The method is also used for the tune and chromaticity correction for sake of generality. For the orbit and the trajectory, the MICADO method is also available, but we mostly use it to find eventual defective correctors rather than for a correction of the beam orbit or trajectory. By default the method of correction is SVD. The user can choose MICADO method by changing a number 0 to 1,2,3, etc..., for a MICADO method with 1,2,3, etc... correctors in the transfer line input file for the beam trajectory correction, or the storage ring input file for the correction of the beam orbit in the storage ring. The spurious dispersion can be corrected with the SVD method. As a correction of the dispersion alone worsens usually the closed orbit, the user is forced to simultaneously correct both the orbit and dispersion, so to select both orbit and dispersion. The orbit correction is weighted via the ratio of the first eigen values found for the orbit and the dispersion separately and a factor preset to 1. To correct the dispersion alone, the user can set this factor to 0. As the program is forseen to be used by non physicists, the program sets limits not only on the maximum corrector strengths but also on the additional correctors kicks. The program makes also a severe control on the changed data and sets them to safe values if the user enters values above the maximum allowable. Furthermore, if the number of eigen values chosen by the user lead to kicks or/and additional kicks above the maximum values, the program does not scale the kicks, instead, it decreases the number of eigen values and searches for new correctors strengths up to where the results are within the limits.

3 RESPONSE MATRIX

The response matrix can be constructed from the calculated optics, using the well known theoretical response matrices, or measured on the machine. By default, the program creates the response matrix from the calculated optics. To use the measured response matrix, the user

simply opens the window found in the menu "auxiliary" and measures the response matrix by clicking in a button "MEASURE RESPONSE MATRIX", if not done yet, then select "Measured response matrix". For the tune, there is also what is called in the program "calculated sensitivity matrix" which constructs the response matrix via changes of the quadrupoles strengths, in theory and not on the ring, and the computation of the changed tunes. It is a calculated response matrix using the change of the tune rather than the specific optics at the quadrupoles. The results of the correction give usually better results than those using the calculated \(\beta \) at the quadrupoles. For the tune and chromaticity, the efficiency of the measured response matrix as compared to the theoretical one, depends largely on the tune system measurement accuracy and resolution and also on the stability of the beam. For the tune, there is also the compromise between a large enough change of the tune to be able to see the difference together with the care of not crossing some resonance. In this respect, values have been preset which allow a safe tune change during the response matrix measurement, which take into account that the horizontal tune is 0.299. At Elettra, the use of the response matrix can be helpful when the beam energy is larger than 2 GeV where the quadrupoles and particularly the bending magnets are highly in saturation and the optics are much less known. The response matrix can be measured for the orbit and the dispersion. The efficiency of the measured response matrix depends of course on the BPMs accuracy and resolution, but also on the stability of the beam. The user can hide from the program any monitor or corrector simply by writing in the input file the name of the monitor or the corrector power supply followed by 0. They can be seen again by the program simply by changing the 0 to 1 or by commenting or deleting the line. This can be done for both the measurement of the orbit and/or dispersion, and for the measurement of the response matrix. The program takes care that the monitors and correctors ignored or found bad during the measurement of the response matrix are also ignored when it calculates the new correctors strengths even if the user might have set the flags differently during the correction or/and the measurement of the orbit or the dispersion. For the transfer line, the input file is created with known defective or taken away monitors with flag 0.

4 OTHER TOOLS

4.1 Correctors scaling

The correctors can be scaled. The window is under "auxiliary" menu.

4.2 Correction with respect to a reference orbit

The correction of the orbit can be performed with respect to a reference orbit. The user opens the window under "auxiliary" menu. He can acquire the reference orbit, plots it, acquire it again, and go back to the previous acquired one. To do the correction with respect to that reference orbit, he just selects "yes" in the window.

4.3 Tune server

For the tune measurement, the program accesses the tune server and locks it so that no other user can access it. The program then searches the peaks, reads the tunes, and so on. The tune server is released when the user exits from the application program. To free the server while the application program is running, the user simply clicks in "yes" on the "release tune server" widget which is under the menu "auxiliary".

4.3 Tune diagram

The user can view the theoretical tune, the measured tune and a selected working point on a tune diagram by simply clicking in "tune diagram" under the menu "auxiliary". This tool has been provided to get a quick comparison between the theoretical tune and the measured one, to check new tune position, and so on (figure 3).

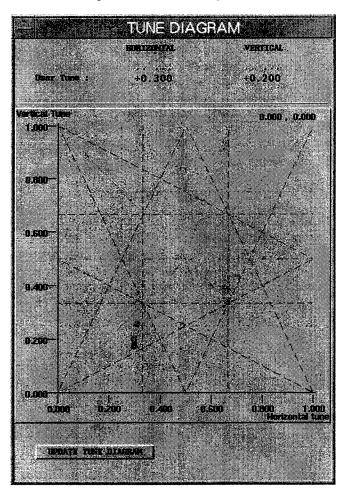


Figure 3: Tune diagram taken during a shift with theoretical tune (blue), measured tune (orange), user tune (green).

5 ACKNOWLEDGEMENTS

The author would like to thank the colleagues F. Radovcic and C. Scafuri for their help in the Motif toolkit use.

6 REFERENCE

[1] F. Iazzourene, TOCA user's guide, Sincrotrone Trieste (1999).

A Free Interactive Matching Program*

J.-F. Ostiguy[†], Fermi National Laboratory, Batavia, IL

Abstract

For physicists and engineers involved in the design and analysis of beamlines (transfer lines or insertions) the lattice function matching problem is central and can be timeconsuming because it involves constrained nonlinear optimization. For such problems convergence can be difficult to obtain in general without expert human intervention. Over the years, powerful codes have been developed to assist beamline designers. The canonical example is MAD (Methodical Accelerator Design) developed at CERN by Christophe Iselin[3]. MAD, through a specialized command language, allows one to solve a wide variety of problems, including matching problems. Although in principle, the MAD command interpreter can be run interactively, in practice the solution of a matching problem involves a sequence of independent trial runs. Unfortunately, but perhaps not surprisingly, there still exists relatively few tools exploiting the resources offered by modern environments to assist lattice designer with this routine and repetitive task. In this paper, we describe a fully interactive lattice matching program, written in C++ and assembled using freely available software components. An important feature of the code is that the evolution of the lattice functions during the nonlinear iterative process can be graphically monitored in real time; the user can dynamically interrupt the iterations at will to introduce new variables, freeze existing ones into their current state and/or modify constraints. The program runs under both UNIX and Windows NT.

1 INTRODUCTION

Until just a few years ago, research software was difficult to localize and the distribution mechanisms were inefficient, making it difficult to build upon work done by others. The internet has dramatically altered this state of affairs. Before attacking a problem, it is now the norm to acquire and study existing source code. In this paper, I describe the BeamLine Interactive Matching Program (BLIMP), an interactive lattice design application assembled with various freely available software components. The objective is not to compete with commercial products, but rather to provide an application that can be modified and adapted to meet specialized needs. There are few available non-commercial interactive applications to perform beamline design. A well-known example is TRACE3D, which, despite being written in Fortran more than twenty years ago and adapted for interactive usage around 1988 is still widely used.

The design goals for BLIMP were the following: (1) given a nominal description of a beamline, allow a user to specify all aspects of a matching problem interactively (2)

provide graphical feedback and allow the user to dynamically interrupt a nonlinear iteration to change the state of variables and constraints. As it stands now, BLIMP is still work in progress; nevertheless, basic features have been implemented and are fully functional.

2 THE MATCHING PROBLEM

The matching problem is a common lattice design problem. It can be simply stated as follows: given a beamline and a set of lattice functions specified at one extremity, determine the strength and/or longitudinal position of beamline elements necessary for the lattice functions to assume certain specified values at one or more distinct locations. The problem arises typically in the following situations: (a) a beamline is needed to transfer beam from one circular machine to another (b) a beamline with special optical properties is to be inserted into the regular lattice of a circular machine without perturbing the region lying outside of it.

In most situations of practical importance, horizontal and vertical motion are decoupled and a beamline is to first order, completely characterized by a set of ten quantities: $\beta_{x,y}$, $\alpha_{x,y}$, $\mu_{x,y}$, $\eta_{x,y}$ and $\eta'_{x,y}$, where β and α are the familiar Courant-Snyder functions, μ is the phase advance and η and η' are respectively the dispersion and its derivative with respect to the longitudinal coordinate. The effect of a mismatch in η' is often ignored; it is also common not to constrain the phase advance.

3 CODE STRUCTURE

BLIMP is written in ANSI standard C++ and makes use of the Standard Template Library. Variables are defined independently of basic beamline elements and can in principle involve arbitrary linear combinations of element strengths, making possible the definition of families of elements sharing a common power source. The user can dynamically define both local and global constraints. Typically, local constraints involve equalities while global constraints involve inequalities (e.g. β function smaller than a prescribed maximum). Figures 1 and 2 are screen shots of the user interface. BLIMP has been put together by using freely available software components which are now briefly described.

3.1 MXYZTPLK/BEAMLINE LIBRARIES

The MXYZTPLK and Beamline Libraries, authored by Leo Michelotti [1, 2], have been under development in the Beam Physics department since 1989. MXYZTPLK is a stand-alone library of C++ classes for performing automatic differentiation and differential algebra. In an nutshell, automatic differentiation is the systematic application of Liebnitz's chain rule to evaluate derivatives of ar-

^{*} Work supported by the US Department of Energy.

[†] Email: ostiguy@fnal.gov

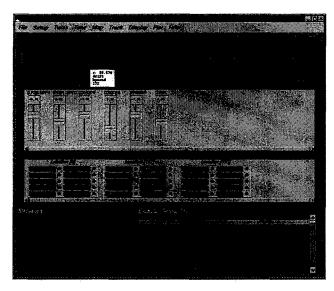


Figure 1: BLIMP user interface. The top window is a display of the beamline. The user can grab an element and move it interactively. In the second window, a sliding cursor is displayed for each variable that has been defined. Each variable can have constrained limits. The third window shows local constraints. Each of these constraints is editable. The bottom right window is a text browser that contains a description of the beamline elements. The user uses this window to select elements (variables) or locations (constraints).

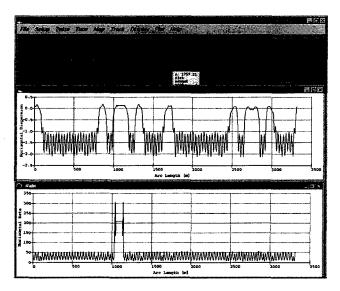


Figure 2: BLIMP displaying lattice functions. The plots are dynamically connected to the variable sliding cursors; changes are reflected in real time in the plot window(s).

bitrary order to machine precision. The Beamline class library built on top of MXYZTPLK, is a rich set of classes supporting lattice related calculations. Beamlines are represented by doubly linked lists whose nodes can either point to other beamlines or to basic elements such as dipoles, quadrupoles, RF cavities etc. Beamlines can be edited, concatenated, cloned, flattened (i.e. no hierarchi-

cal structure) etc. Most quantities of interest to accelerator physicists can be computed, including lattice functions, dispersion and chromaticity. Both field and alignment errors can be included if necessary. Maps of arbitrary order can in principle be computed to machine precision in either 4-dimensional (i.e. transverse) phase space or full 6-dimensional phase space. The desire to compute high order maps actually provided much of the motivation for developing the automatic differentiation library. BLIMP uses functionality from the Beamline class library to compute lattice functions, track individual particles or distributions and compute maps.

3.2 NONLINEAR OPTIMIZER

Numerical nonlinear optimization is a vast and highly specialized field. Nevertheless, problems can generally classified according to (1) whether or not the objective function can be expressed as a continuous, differentiable function of the independent variables and (2) the nature of the external constraints that need to be enforced, if any. For matching problems, the objective function are usually differentiable functions of the elements strengths and positions. In that case, variants of the gradient and Newton methods are most efficient. The Newton method has the advantage of quadratic convergence if the extremum is sufficiently close; the rate of convergence for gradient methods tends to be less favorable. However, because it is typically more expensive to compute and invert a Hessian matrix than to compute a gradient vector, a common strategy is to start with a gradient iteration and switch to a Newton iteration only within close proximity of the extremum. Constraints are most easily handled by adding penalty terms to the objective function. These penalty terms must obviously be differentiable; quadratic terms are useful for equality constraints while exponential terms can be used for inequality constraints. When inequality constraints apply to independent variables, a useful technique is to use an inverse trigonometric transformation and to consider the transformed variables as free.

At the moment, BLIMP uses the facilities of the MI-NUIT library from CERN [4], a good general purpose optimization library. It supports the optimization strategies described above and is freely available for research institutions. Unfortunately MINUIT suffers from various limitations associated with its Fortran heritage. Among the most problematic issues are the following: all I/O involves the Fortran I/O subsystem which cannot be mixed with the C/C++ I/O in a portable way; the objective function must be passed to the library as a static function and there is therefore no straightforward way of using functors objects. The BLIMP optimization code is encapsulated into an Optimizer class; this should allow an alternative to MI-NUIT to be substituted with minimal side effects.

3.3 GRAPHICAL USER INTERFACE

The choice of a user interface toolkit has been driven by two requirements: (1) object orientation and (2) need for portability between various flavors of UNIX and Windows NT. The Fast Light Toolkit (FLTK) [5] satisfies both requirements and is available under the terms of the GNU Public Library License. FLTK also provide support for OpenGL (or MESA, a free compatible alternative).BLIMP takes advantage of the facilities offered by OpenGL to efficiently display the beamline at different scales.

3.4 PLOTTING

BLIMP uses the SciPlot scientific plot widget[6]. SciPlot was written for the Xt toolkit and therefore uses an event model that is incompatible with FLTK. This difficulty was circumvented by running plot widgets in separate threads. At the moment, this is the only part of BLIMP that does not compile under Windows NT without modifications. One interesting aspect of the plotting functionality in BLIMP is that all user interface control elements are dynamically connected to the various plots, allowing a user to dynamically observe the sensitivity of a solution to small parameter variations, or to explore the parameter space before attempting a non-linear optimization.

4 APPLICATIONS

We now describe two applications that motivated the development of BLIMP.

4.1 PHASE TROMBONE

The Fermilab Recycler ring is a new machine for antiprotons accumulation and recycling scheduled to be commissioned in the spring of 1999. The Recycler has the distinction of being the first machine to make large scale utilization of permanent magnet technology. The machine operates at fixed energy of 8 GeV with a lattice based on fixed field combined function magnets. The tune of the machine is adjusted by varying nine electromagnetic quadrupoles grouped in five symmetric families within a region where $\eta_{x,y} = \eta'_{x,y} = 0$. Four hard constraints must be met i.e. at the symmetry point $\alpha_{x,y} = 0$ and the two phase advances set to the desired values; an additional softer requirement is to prevent the beta functions from exceeding a maximum value. Since this region is part of a matched insertion, the lattice functions outside the insertion remain unperturbed when the tune is adjusted. The maximum tuning range is approximately $\pm 1/2$. Since the settings of the quadrupole families is different for each tune, it is anticipated that BLIMP will be useful to both to adjust and diagnose the phase trombone.

4.2 LOW BETA INSERTION

In a low-beta insertion, the objective is to use a pair of quadrupole doublets or triplets to focus counter-circulating beams into a very small size interaction region. In general, the insertion has to match the lattice functions of the ring at both extremities; the phase advance is unconstrained. At the interaction point, $\beta_{x,y}$ must assume specified values and the beam envelope must go through a minimum i.e. $\alpha'_{x,y}=0$. It is also often required for the dispersion to be as small as possible and one usually demands $\eta_{x,y}=0$. Constraining η' may also be desirable. The result is 24 local constraints. In practice, low insertions are symmetric and one can concentrate one one-half of the insertion, reducing the number of constraints to 16, possibly 14 if η' is ignored. Global constraints are usually introduced to limit the amplitude of the beta functions inside the high gradient quadrupoles.

Low beta insertions are notoriously nonlinear. Without experience, it is difficult for a novice to find a satisfactory solution and interactivity is certainly no substitute for experience. However, the ability to quickly experiment with different strategies and stop the iterations dynamically is proving to be a significant advantage.

5 CONCLUSION

BLIMP is still work in progress, although it is certainly already useful as it stands. In the immediate future, the program will acquire the ability to read and write in a "standard" beamline specification format. Even though the format used at this moment is application specific it is a very simple matter to describe a simple beamline with a few dozen elements. A beamline editor allowing the user to specify or modify beamlines interactively would also be an interesting improvement. All source code should eventually become freely available to the accelerator community, at least for non-commercial use. Please contact the author for further informations.

- L. Michelotti, "MXYZPLTK Version 3.1 User's Guide: A C++ Library for Differential Algebra", Fermilab Publication FN 535-REV, October 1995
- [2] L. Michelotti, "MXYZPLTK and Beamline: C++ Objects for Beam Physics", Advanced Beam Dynamics Workshop on Effects of Errors in Accelerators, their Diagnosis and Correction, AIP Conf. Proceedings No 225, 1992
- [3] C. Iselin and H, Grote, "The MAD Program (Methodical Accelerator Design), User's Reference Manual, CERN/SL/90-13(AP), Geneva, Switzerland
- [4] F. James, "MINUIT Minimization Package Reference Manual Version 94.1", CERN Program Library D506, Computing and Networks Division CERN Geneva, Switzerland
- [5] Information about FLTK is available at the following URL: www.fltk.org
- [6] Information about the SciPlot widget is available at the following URL: www.ae.utexas.edu/~rwmcm/SciPlot.html
- [7] Fermilab Recycler Ring Technical Design Report Revision 1.2, November 1996

UAL-BASED SIMULATION ENVIRONMENT FOR SPALLATION NEUTRON SOURCE RING*

N. Malitsky[†], J. Smith, J.Wei, BNL, Upton, NY R. Talman, Cornell University, Ithaca, NY

Abstract

This paper outlines the major activities and applications of the Unified Accelerator Library environment for the Spallation Neutron Source (SNS) Ring.

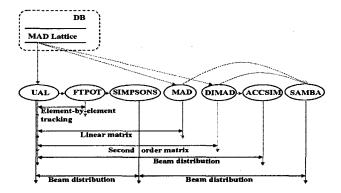
1 BACKGROUND

The Unified Accelerator Libraries[1] are designed as a customizable and extendible environment for developing diverse accelerator applications. Its main architectural principle is a separation of physical entities and mathematical abstractions from algorithms. accelerator algorithms are implemented as classes that share data via Common Accelerator Objects (Element, Bunch, Twiss, etc.). This highly flexible structure has facilitated selecting and implementing more appropriate software design patterns and accelerator approaches, supporting project-specific requirements, and connecting the UAL applications with heterogeneous data sources. At this time, the UAL joins several object-oriented accelerator programs: PAC (Platform for Accelerator Codes), TEAPOT (Thin Element Program for Optics and Tracking), ZLIB (a numerical library for differential algebra), and ALE (Accelerator Libraries' Extensions). The Application Programming Interface (API), written in Perl, provides a universal homogeneous shell for integrating and managing all these components and project extensions. The UAL environment has been successfully applied to several accelerator projects: LHC, RHIC, and CESR. This paper outlines the major activities and applications for the new project, Spallation Neutron Source (SNS) Ring.

2 SIMULATION ACTIVITIES

The SNS ring dynamics presents a complex combination of several physical effects and dynamical processes[2]. Some of them, such as field errors and misalignments, are supported in general-purpose accelerator codes. Other effects, such as space charge and collimator surface grazing, are actual only for high intensity hadron rings and distributed into a set of independent specialized programs (Table 1). The mismatch among diverse data formats, units, and notations complicates the usage of these programs and increases the risk of errors and misinterpretations. Besides, the accurate simulation of the very low beam loss (10) requires the simultaneous

consideration of several different effects in a single scenario. The UAL open environment addresses all these tasks. It supports the incremental development of independent components and their configurable packaging into the accelerator applications. For the SNS project, the UAL is being extended with the following features: injection painting, collimator, and space charge. To facilitate the implementation and employment of new modules we have developed a benchmark infrastructure that provides the consistent interfaces among alternative accelerator approaches:



2.1 Injection Painting

During the multi-turn injection into the SNS ring, protons are painting over a large phase space volume in order to reduce the space charge tune shifts and to minimise the number of traversals through the stripping foil. The ACCSIM code offers the most consistent approach for optimization and simulation of these dynamical processes. However, the control of the different scenarios is hidden behind of the ACCSIM input language impeding the inclusion of new physical effects (field errors, misalignments, etc.). In UAL, all these dynamical processes are programmed directly with the Perl API that provides an unlimited access to the UAL core packages, project-specific extensions, and a wide variety of general-purpose supporting tools and applications (Graphics, GUI, etc.).

2.2 Field Errors, Misalignments, Correction

In the UAL, all accelerator elements are located in the central repository, the Standard Machine Format (SMF). The SMF supports both the hierarchy of beam lines and

Work performed under the auspices of the US DOE

[†] Email: malitsky@bnl.gov

generic elements as well as parameters associated with individual elements of the as-installed machine. Magnetic errors and misalignments are implemented as fine-grained sets of element attributes and can be assigned to an arbitrary design element. The SMF structure is neutral to accelerator approaches, and the accelerator physicist can employ either the UAL core modules or local extensions (e.g. IR filter for RHIC and LHC [9]). For the simulation of nonlinear magnetic fields and misalignments, we are using the TEAPOT library that provides a rich set of simulation tools (conventional element-by-element tracker and DA integrator) and correction algorithms (tuning, closed orbit correction, chromaticity fitting, and global decoupling).

2.3 Collimator

The collimator is designed to prevent spreading up beam halo into the SNS ring tunnel and localized it at a level from 10 to 10 in one controlled place. Its relative sizes and forms depend on many factors, such as an injection painting scheme, lattice parameters, and others. Then the simulation model has to be adaptable to an arbitrary combination of lattice and collimator variants. It can be achieved by implementing the collimator system as an insertion device and splitting the one-turn tracking procedure into three steps: propagating particles (e.g. using TEAPOT module) from the injection point to the collimator system, applying the collimator algorithms, and completing the turn by following particles back to the injection point. In the UAL environment, this scenario is controlled directly from the Perl script, and it is open for arbitrary representations of the collimator module. For example, this module can be implemented as a local adapter to the independent FORTRAN program (e.g. LAHET) or the HEP C++ shared libraries (e.g. GEANT 4). This solution looks very interesting from the perspective of integrating the accelerator and high energy physics software. However, its complete implementation assumes the significant overhead for this particular task. Then we are considering the ACCSIM approach that provides an optimal set of algorithms for particle-target interactions (Landau and Bethe-Bloch energy loss distributions, Moliere multiple scattering, and nuclear interactions).

2.3 Space Charge

The space charge effect has a large impact on the beam dynamics and halo growth in the SNS ring and has to be included in the common model for evaluating the beam distribution and uncontrolled beam loss in the ring tunnel. The implementation of the 3D space charge effects is a difficult task because it involves the trade-off between the performance and accuracy of available algorithms. Then there is a need in a configurable module that enables the exchange of several alternative approaches. The UAL framework will address this task by providing the uniform

mechanism for assembly and reuse of independently developed algorithms [11].

2.5 Fringe Field Models

Since the aperture of the ring magnets is comparable to the magnetic length, fringe field impact must be considered. Taylor maps extracted from fringe field models (e.g. MaryLie[10]) will be incorporated into element-by-element tracking. This approach has been employed in previous UAL applications for simulating RHIC helical dipoles and CESR wigglers.

2.6 End-to-End Simulation

The SMF structure allows one to consider several different lattices in the same process. This feature is very important for optimization of IR sections, injection and extraction systems. In the SNS project, we plan to concatenate various sections of machine lattices (e.g. HEBT line + ring + RTBT line) for the end-to-end simulation of particles with various charge states (H⁺, H⁰, H).

3 UAL FRAMEWORK

The UAL framework is a necessary and logical step in the UAL evolution. It intends to offer a single object-oriented integration environment for compatible and independent implementation of diverse accelerator applications. This will enable accelerator scientists and software developers with different kinds and levels of skill to participate in the common development process and will promote selection, sharing, and standardization of the most effective accelerator approaches and solutions. The UAL framework is being developed using the component-oriented technology and provides the following systems [11]:

- uniform mechanism for assembly and reuse of independently developed accelerator algorithms;
- uniform infrastructure for optimization and correction approaches

The off-line SNS Ring Simulation Facility is considered the first application of this infrastructure.

4 INTEGRATION WITH ACCELERATOR CONTROL

The value of theoretical algorithms depends to a large extent on the possibility to employ them in a real experiment. In the past, simulation programs and control system applications were developed and deployed as two independent products. We intend to merge these efforts in the single direction based on the online Accelerator Simulation Facility (Fig.1). The concept of online modelling is becoming very popular in the accelerator community because it provides them with new interesting possibilities:

- development and validation of control system applications before the commissioning stage based only on the "virtual" accelerator,
- online analysis and comparison of runtime accelerator parameters with theoretical models during commissioning and operation.

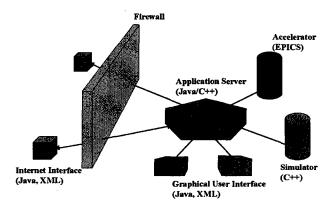


Figure 1: The UAL-based SNS Simulation Facility.

The SNS online facility will have a multi-level architecture. At this time, EPICS has implemented the lowest layer, a homogeneous interface to physical devices. However, EPICS exchange data types are too generic for object-oriented higher level applications, such as simulation and correction modules, and require an additional layer to map device parameters into accelerator

domain constructions. Until recently, there has not been a portable solution for this problem. At this time, several industrial technologies address this task by providing new communication concepts, such as the Java Serializable object and the CORBA Object-by-Value semantics, that allow developers to apply seamlessly the same object-oriented models and patterns to local simulation programs and distributed control systems. We plan to evaluate these and other industrial technologies from the perspective of their integration with the UAL and EPICS environments.

We thank D. Abell, J. Beebe-Wang, M. Blaskiewicz, F. Jones, J. Galambos, H. Ludewig, A. Luccio, and S. Machida for many useful discussions.

- [1] N.Malitsky and R.Talman, AIP 391, 1996.
- [2] J.Wei et al, these proceedings.
- [3] L.Schachinger and R.Talman, Particle Accelerators, 22, 35(1987).
- [4] H.Grote and F.C.Iselin, CERN/SL/90-13.
- [5] R.V.Servranckx, et al., SLAC Report 285 UC-28, 1985.
- [6] F.W.Jones, TRIUMF Design Note TRI-DN-90-17, 1990.
- [7] J.Galambos, et al. AIP 448, 1998.
- [8] S.Machida, Nucl. Instrum. Methods, A309, 43(1991).
- [9] J.Wei, at al, these proceedings.
- [10] A.Dragt et al., MaryLie 3.0, 1999.
- [11] N.Malitsky and R.Talman. ICAP98, 1998.

Table 1: Accelerator programs used in the SNS project.

	UAL [1]	FTPOT [3]	MAD8 [4]	DIMAD [5]	ACCSIM [6]	SAMBA [7]	SIMPSONS [8]
Interface	PERL API	FTPOT	MAD	DIMAD	ACCSIM	SuperCode	SIMPSONS
MAD elements	Yes	Yes	Yes	Yes	Yes (via nodes)	Yes (via nodes)	Yes
Errors	Yes	Yes	Yes	Yes	No	TBC	Yes
Dynamic Processes	Yes (via PERL)	No	No	No	Injection	Yes (via SuperCode)	Bp and RF
Tracking	Thin lenses	Thin lenses	Lie algebra	Simplectic TRANSPORT	Linear matrices + node -lenses	Linear matrices + node-lenses	Thin lenses
Mapping	Any order	Second order	Third order	Second order	Linear order	Linear order	No
Space Charge	TBC	No	No		3D	3D	2D and 3D
Analysis (Twiss,)	Yes	Yes	Yes	Yes	No	TBC	No
Lattice Optimization	TBC	No	Yes	Yes	No	TBC	No
Correction(Orbit,)	Yes	Yes	Yes	Yes	No	TBC	No
Concatenation of several lattices	Yes	No	No	No	No	No	No
Support of third party extensions	Yes	No	No	No	No	Yes	No
Painting	Yes	No	No	No	Yes	Yes	No
Injection Foil	Yes	No	No	No	Yes	Yes	No
Collimator	April 99	No	No	No	Yes	No	No

THE APPLICATION OF THE SXF LATTICE DESCRIPTION AND THE UAL SOFTWARE ENVIRONMENT TO THE ANALYSIS OF THE LHC*

W. Fischer, F. Pilat[†], V. Ptitsin, BNL, Upton, New York

Abstract

A software environment for accelerator modeling has been developed which includes the UAL (Unified Accelerator Library), a collection of accelerator physics libraries with a Perl interface for scripting, and the SXF (Standard eXchange Format), a format for accelerator description which extends the MAD sequence by including deviations from design values. SXF interfaces have been written for several programs, including MAD9 and MAD8 via the doom database, Cosy, TevLat and UAL itself, which includes Teapot++. After an overview of the software we describe the application of the tools to the analysis of the LHC lattice stability, in the presence of alignment and coupling errors, and to the correction of the first turn and closed orbit in the machine.

1 INTRODUCTION

The modeling of large accelerators such as the LHC requires a sophisticated, flexible and powerful modeling software environment. On the one hand, complex problems have to be studied requiring non-standard modeling techniques, such as tracking two beams, assigning measured values to individual magnets, dealing with complex alignment tolerances for triplet assemblies, etc. On the other hand, large accelerators are nowadays international collaborative efforts among laboratories and the necessity arises to exchange lattice and measurement information between groups in a transparent, model independent way. To fulfill the first set of requirements we built up our model in the framework of the UAL software, and to fulfill the need of information exchange we use a flat machine representation, the Standard eXchange Format (SXF) to describe the accelerator.

Section 2 will explain in more detail the software building blocks, UAL and SXF. Section 3 will discuss the unique challenges of modeling the LHC, in particular the study of alignment tolerances in the interaction region dipole and triplet assemblies. In Section 4 as an example of application, we will discuss a way to close the first turn and to correct the orbit in the LHC in the presence of realistic alignment errors.

2 THE MODELING SOFTWARE ENVIRONMENT: UAL AND SXF

The Unified Accelerator Library (UAL) [1] is an object oriented and modular software environment for accelerator physics which comprises an accelerator object model

for the description of the machine (SMF, for Standard Machine Format), a collection of *physics libraries*, and a *Perl shell* that provides a homogeneous interface for integrating and managing these components. Currently available physics libraries include TEAPOT++, a collection of C++ physics modules conceptually derived from TEAPOT [2], and ZLIB [3], a differential algebra package for map generation and manipulation.

UAL has already been used to build up a realistic model of the Relativistic Heavy Ion Collider (RHIC) where measured field and alignment data are automatically read from a relational database and applied to individual elements in the machine [4] [5]. It has been used to model CESR and is being used, as we will describe in the following, for the LHC. Access to the UAL suite is provided via a Perl-based *shell* environment. Each UAL project (RHIC, CESR, LHC, etc.) has developed a set of Perl modules which provide a user friendly means of calling the ensemble of UAL programs, e.g., correction procedures, particle tracking via TEAPOT++ or differential algebra and mapping techniques.

The SXF (Standard eXchange Format) is an ASCII accelerator description that carries lattice information and also individual quantities specific to an element such as measured field and alignment data. SXF has been developed as an answer to the need for easy exchange of lattice information among laboratories. SXF parsers to several existing codes, such as UAL, MAD, Cosy and TevLat, have been written and used.

An SXF lattice description is an ASCII listing that contains one named, flat, ordered list of elements, delimited as {...}, with one entry for each element. The list conceptually resembles a MAD "sequence" describing the entire machine. The difference is that an SXF sequence can carry additional information such as field harmonics, alignment errors, aperture limitations, etc. that are specific to the individual element. The syntax is supposed to be adapted for ease of reading by human beings and for ease of parsing by LEX and YACC. Here is an example of a simple SXF sequence of 2 elements, a dipole and a marker:

^{*} Work performed under the auspices of the US Department of Energy

[†] Email: pilat@bnl.gov

```
exit.dev={kl=[0.001..] kls=[0.001..]}
align.dev={al=[0.005 0.005 0 0 0.001] }
aperture={ap=[1 0.03 0.02 0.001 0.001]}
};
m1 marker { };
endsequence at=200.0
}
```

SXF supports MAD attributes; attributes are grouped in logical "buckets" such as body, which contains the element general attributes, align, which describe intentional misalignments, etc. The buckets that end with ".dev" contain deviations from the design values, such as field (body.dev) and alignment (align.dev) errors. Quantities that are logically related, such as field multipoles, misalignments, apertures are grouped in vectors, such as kl, al, ap. The vector kl for instance contains normal field harmonics up to order 20; only orders up the last non-vanishing order need to be explicitly written. A more detailed description of the grammatical and lattice description rules of the SXF, as well as more examples of SXF sequences can be found in [6].

3 THE ALIGNMENT MODEL FOR THE LHC INTERACTION REGIONS

Since SXF is a *flat* ordered list of elements it does not support the simultaneous misalignment of adjacent elements. The introduction of an element *hierarchy* is needed to align several elements by the same amount. This is of interest for two reasons. First, magnets are often modeled by more than one element and all these elements should be misaligned by the same amount. For example, a magnet model may consist of a body and two end kicks; the body itself may be modeled by several kicks. Second, sometimes there are several magnets assembled in one cryostat. It is then desirable to displace the whole cryostat while allowing for the individual magnets within to be independently misaligned relative to the cryostat.

The proper description of alignment errors is of great importance to the US-LHC collaboration since the US will deliver assembled cryostats of interaction region magnets to CERN. In the design phase an estimate of tolerable alignment errors is needed. Once magnets are assembled in a cryostat, the best position of the cryostat must be found in order to minimize the harmful effects of field and alignment errors.

We developed a SXF-like description that allows the simultaneous misalignment of adjacent magnets and a filter program that can merge this information into a canonical SXF file. Here is an example of how several entities can be misaligned with respect to a common cryostat, which also has a global misalignment relative to the reference axis.

```
// a misaligned element that contains
// misaligned elements
q2con = {
```

```
align = { al = [ 0.002 -0.001 0.003 }
                   0.005 -0.005 0.007]}
components = {
  a1t2.r1 = {
   align.dev = { al = [.0 -0.002]
                     0. 0. -0. 0.007}
  q1t3.r1 = {
   align.dev = { al = [ 0.001 0. 0. 0. ]}
                    -0.006 0.]}
   components = {
     x1.r1 = {
      align.dev = {al=[ 0. 0.2 ]}}
     x2.r1 = {
      align.dev = {al=[ .2 0. 0. ]}
                          0. 0. 0.1]}}
} } } }
```

we used this technique to assign alignment errors to the LHC interaction region assemblies and study the impact of such errors on the first turn and closed orbit correction. The analysis and preliminary results are summarized in the following section.

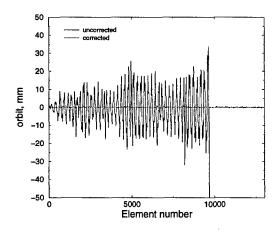
4 FIRST TURN AND CLOSED ORBIT CORRECTION

In the presence of misalignment the particle orbit is no longer ideal. The orbit excursions, even with moderate amount of misalignment, in a large machine like the LHC may become so big that a particle reaches the aperture limits defined and gets lost. As in the case of a real accelerator ring, in order to keep the beam closed orbit inside the physical aperture, a first turn beam steering method must be applied.

Two first turn beam steering techniques were implemented in TEAPOT++. One is the method recently developed by H. Grote for MAD [7]. This method performs the correction using two beam steering correctors and two beam position monitors in the region where the orbit excursions become too large. With the spacing between the two BPMs about $\pi/2$ in betatron phase it provides in fact correction of both the orbit position and the orbit angle.

The other method implemented in TEAPOT++ is the so called sliding-bumps method. The closed bumps are set with of three neighboring dipole correctors. The whole ring interval is divided in a series of consecutive bumps that are overlapping since every corrector can be used in the construction of three different bumps. Each bump by definition only affect the orbit inside itself.

One correction step consists of consecutive one-by-one bump corrections along the ring until a lattice point is reached, where a particle loss or a big particle trajectory deviation is detected. The limit value of the trajectory deviation that defines the start of the correction procedure is determined as a parameter to the first turn steering command. Because the trajectory downstream of the corrected interval should also be affected by the correction, the last



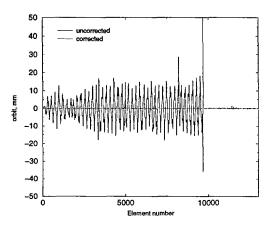


Figure 1: First turn correction in horizontal and vertical planes

bump of the corrected interval is made "open", meaning that the strength of one or two of the last bump correctors is set to zero. After one correction step is done, the particle is tracked again through the lattice (or, operationally, the beam is injected again) until the next limit trajectory deviation is encountered (or, with beam, the next beam loss point) and the correction is repeated. Using the slidingbumps technique not only steers the particle through the first turn of the accelerator but also provides a corrected orbit at all BPM positions along the ring. However, this method is more time consuming than the one previously described. The sliding-bumps method is used in within TEAPOT++ also as a closed orbit correction algorithm. The only differences are that the input data are closed orbit instead of particle trajectory data and that there is no need to "open" any bumps.

Simulation studies confirmed that the correction methods implemented work well for the LHC lattice in the presence of alignment errors, both for first turn steering and closed orbit.

Figure 1 and 2 show the horizontal and vertical particle

trajectory during the first turn for the LHC, before and after correction. The method used here is the sliding-bumps.

Figure 2 show the horizontal closed orbit before and after correction.

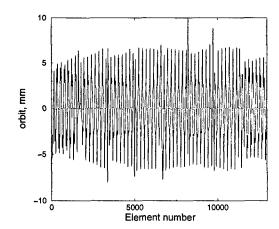


Figure 2: Closed orbit correction in the horizontal planes

5 CONCLUSIONS

A software environment has been developed for LHC simulations whose flexibility and modularity ease the task of adding new modeling features. A standard interface, the SXF, extends the functionality of the MAD sequence and can interface several existing accelerator codes. We used this environment to study the effect of misalignment of the IR assemblies on beam dynamics, noticeably on the first turn trajectory and the closed orbit. The model and correction methods proved to work for the LHC lattice and we plan to use them for systematic studies in the near future. We plan on adding the capability of modeling roll alignment errors in the IR assemblies and study the resulting coupling effects in the next few months.

- [1] N. Malitsky and R. Talman, AIP 391 (1996).
- [2] L. Schachinger and R. Talman, Particle Accelerators, 22, 35 (1987).
- [3] Y. Yan, SSCL-300 (1990).
- [4] F. Pilat, C. Trahern, J. Wei, T. Satogata, S. Tepikian, "Modeling RHIC using the Standard Machine Format Accelerator Description", PAC97 (1997).
- [5] F.Pilat, M.Hemmer, V.Ptitsin, S.Tepikian, and D.Trbojevic, "Processing and analysis of the measured alignment errors for RHIC", PAC99 (1999)
- [6] H. Grote, J. Holt, N. Malitsky, F. Pilat, R. Talman, C. Trahern, "SXF: definition, syntax, examples", RHIC/AP/155 (1998).
- [7] H. Grote, "Beam Threading in the LHC", EPAC98 (1998)

LATTICE FUNCTION MEASUREMENT OF FNAL MAIN INJECTOR AT 8-GEV[†]

S. Assadi, C.S. Mishra, F. Tecker, M.J. Yang[‡], Fermilab

Abstract

The commissioning of Fermilab Main Injector had been very successful and the project is at its final phase. Even with the machine working as well as it did plenty of improvements are still to be made. Measuring and to understanding the machine lattice function should eventually lead to the improvement of the machine. In this write-up the preliminary measurement and analysis of the lattice function is reported.

1. INTRODUCTION

The Main Injector is a newly commissioned machine. Although effort was made to ensure that it performs as designed the possibility of magnetic field error is always there. It is important to know the actual lattice function in order to improve the machine performance. It is needed to properly match the 8-GeV transfer line to the ring, to assess possible aperture restriction, and to design extraction transfer line optics. Comparing the measurement to the design will help locating the origin of errors.

The effort to measure the lattice function of Main Injector is still at its early stage. A measurement at 8-GeV injection energy is an important first step. This write-up reports the preliminary analysis result from data taken during the commissioning run in the February of 1999 and is presented as a progress report. More measurement undoubtedly will be made in the very near future to validate the result.

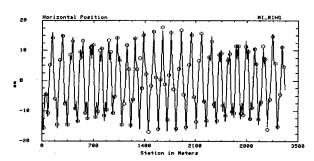


Figure 1. The horizontal difference orbit caused by 1-bump kick at the corrector H104, which was set 2.5 amp lower.

2. DATA

There are a total of 208 BPMs around the Main Injector ring, 104 horizontal plane BPMs at focusing locations and 104 vertical plane BPMs at de-focusing locations. The reading from all were collected during study at any one data sample. Along with that are the currents for bend bus, quad bus, and trim correctors. The RF frequency and

intensity reading are also included. This was accomplished using the on-line analysis program [1] and analyzed.

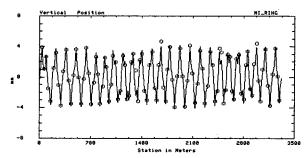


Figure 2. The vertical closed orbit due to 1-bump kick from corrector V105 that was set to 1.5 amps above nominal.

To do the lattice function measurement two dipole correctors from each plane were chosen. The design phase advance between the two correctors is close to 90 degree in either plane. Shown in Figure 1 is an example of horizontal plane orbit data taken with H104 corrector. In Figure 2 is an example in the vertical plane using corrector V105. With each corrector a series of BPM orbit data were collected, with corrector current changed in steps of 0.5 Amps. This corresponds to about 120 µrad in horizontal kick for H104 and H106 correctors at 8-GeV energy. The vertical correctors are weaker and the kick was only about 50 µrad for V105 and V107. Figure 3 shows a plot of BPM position reading at MI 122 location as a function of the kick angle from H104. Figure 4 shows the vertical position at VP407 as a function of kick angle from V105. The slope of linear least square fit to the data points will be used for subsequent analysis.

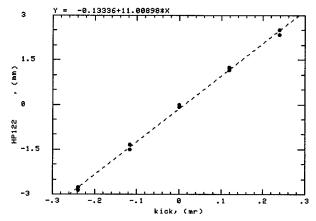


Figure 3. The orbit data taken at BPM HP122. Horizontal corrector H104 current was changed in step of 0.5 amps. The result of least square fit to the data points is shown at the top and plotted in dashed line.

[†] Work supported by the US Department of Energy under contract DE-AC02-76CH00300.

[‡] E-mail: YANG@FNAL.GOV

In order to measure the dispersion function the Main Injector RF frequency was changed at 250-Hz steps, about 0.053% in •p/p. Both horizontal and vertical data were taken for analysis. Figure 5 is an example of data taken for dispersion function measurement at HP208 location.

3. ANALYSIS

The lattice function analysis is based on the equation:

$$x_{i}^{(t)} = \frac{\sqrt{\beta_{i}\beta^{(t)}} \cdot \Delta\theta^{(t)} \cos\left[2\pi \left(\psi_{i} - \psi^{(t)}\right] - Q/2\right)}{2 \cdot \sin(\pi Q)}$$
(1)

The index k denotes the corrector element used and i the BPM index. The symbol Q is the machine tune and Ψ the phase advance in units of 2π . This equation can be rewritten as:

$$y_i^{(b)} = \frac{\sqrt{\beta \beta^{(b)} \cdot \cos\left[2\pi\left(\psi_i - \alpha^{(b)}\right)\right]}}{2 \cdot \sin(\pi Q)}$$
 (2)

Where $y_i^{(k)} = x_i^{(k)}/\Delta\theta^{(k)}$ is the slope in the example shown in Figure 3 or Figure 4.

And $\alpha^{(k)} = \psi^{(k)} \pm Q/2$, the adjusted corrector phase. The negative sign is needed when $\psi_i < \psi^{(k)}$.

With two sets of corrector data the equations for the phase advance can be written:

$$\cos(2\pi\psi_{,}) = \frac{+2\sin(\pi\mathcal{Q}) \cdot \left[\sqrt{\beta^{(2)} y_{,}^{(1)} \sin(2\pi\alpha^{(2)})} - \sqrt{\beta^{(1)} y_{,}^{(2)} \sin(2\pi\alpha^{(1)})} \right]}{\sqrt{\beta_{,}\beta^{(1)}\beta^{(2)} \sin(\alpha^{(1)} - \alpha^{(2)})}}$$
(3a)

$$\sin(2\pi\psi_{i}) = \frac{-2\sin(\pi Q) \cdot \left[\sqrt{\beta^{(1)}} y_{i}^{(1)} \cos(2\pi\alpha^{(2)}) - \sqrt{\beta^{(1)}} y_{i}^{(2)} \cos(2\pi\alpha^{(1)}) \right]}{\sqrt{\beta_{i}\beta^{(1)}\beta^{(2)}} \sin(\alpha^{(1)} - \alpha^{(2)})}$$
(3b)

Using these two equations the phase advance ψ at the *i*-th BPM location can be calculated. With phase advance from either data or from model the beta function can be calculated using Equation (2).

The analysis of the dispersion function requires the knowledge of the momentum error. This is calculated from the RF frequency recorded during the data taking using the equation:

$$\frac{\Delta p}{p} = -\eta \frac{\Delta f}{f},$$

Where the phase slip factor η defined in $\frac{1}{n} = \frac{1}{\gamma^2} - \frac{1}{\gamma^2}$

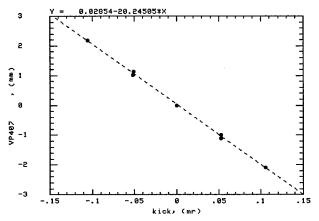


Figure 4. Vertical plane position data at VP407 as a function of kick angle from vertical corrector V105, at every 0.5 amps.

4. RESULTS

The analysis of the phase advances, beta function, and the dispersion function will be reported here. The statistical error analysis was performed and displayed with the plotted data points. The work is just starting to sort out systematic errors that could affect the analysis, i.e. beta, phase, machine tune, the corrector kick strength, the phase slip factor.

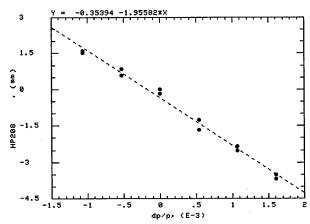


Figure 5. Horizontal beam position at location 208 as a function of the momentum error.

4.1 Phase advances

Figure 6 shows the deviation of the measured phase advances from that of model calculation, for both plane. The phase advance analysis is in principle immune to the BPM calibration error. The RMS deviation as shown in the plot amounts to about 4 degrees of error.

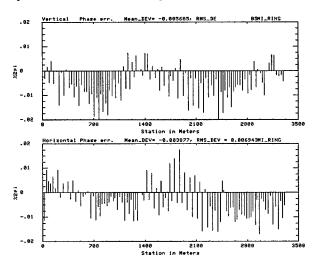


Figure 6. This is a plot of differences between the measured phase advances and phase advances calculated from model. The quantity displayed is in unit of 2•. The lower plot is for the horizontal plane and upper plot for vertical plane.

4.2 Beta function

The beta function, on the other hand, is dependent on the calibration of the BPM signal, along with all other assumptions that go into the analysis. Figure 7 shows the measured beta function along with the model calculation. The fractional deviation from the model is plotted in Figure 8. In both plot the horizontal plane is shown at the bottom and vertical at the top.

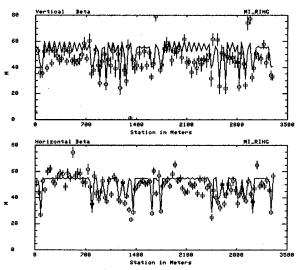


Figure 7. The measured Main Injector beta functions are shown here in green circles. The calculated beta functions, at the corresponding BPM locations, are shown in solid line.

4.3 Dispersion function

Dispersion-free regions are part of Main Injector design and are important to the function of the machine. This is confirmed readily from the data in part because it requires only null result, i.e. no position movement as function of energy error.

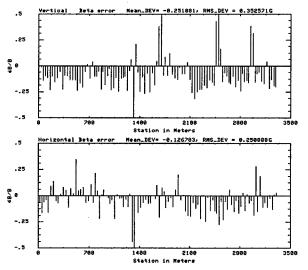


Figure 8. The horizontal plane beta function errors are shown in the lower plot and the vertical plane errors in the upper plot. The vertical axis is the fractional deviation of the measured beta function with respect to the calculated values.

The measured dispersion functions in both horizontal and vertical plane are shown in Figure 9. No vertical dispersion function is apparent, as expected. There are, however, plenty of locations where the dispersion function deviates from the design value by as much as 0.4 meters.

The negative dispersion function seen on the plot is because Main Injector was designed to runs counter clockwise with proton. For a right-handed coordinate system positive horizontal direction is toward inside of machine. Beam particles with larger momentum will move toward outside, i.e. the negative direction.

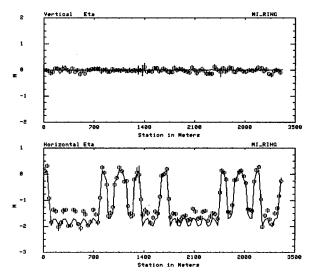


Figure 9. The measured dispersion functions are plotted in green circles and the calculated dispersion functions at the corresponding BPM locations are shown in solid line.

5. CONCLUSION

The analysis result shown here is considered very preliminary. More measurement in the future will no doubt shed more light on the consistency of measurement.

During commissioning the BPMs have worked well. The measurement of lattice function, however, might require a level of precision that is yet to be understood. Cross-plane signal coupling is a known issue for the Main Injector BPMs. Resolution and calibration measurement using beam data is still to be done.

The measured phase advances around the Main Injector ring were not far from the design values. The measured beta function in the vertical plane appears to deviate more significantly. The fact that data appears to follow the variation of the design suggests some credibility. The measured dispersion function is another indication of imperfection in the existing lattice and that can not be explained as from BPM error.

6. REFERENCES

 M.J. Yang, "Beam Analysis program for Main-Injector Commissioning." this proceeding.

THE RHIC/AGS ONLINE MODEL ENVIRONMENTS: EXPERIENCES AND DESIGN FOR AGS MODELING*

K. Brown[†], J.Niederer, T. Satogata, A. Alai Tafti, N.Tsoupas, J. van Zeijts, BNL, Upton, NY

Abstract

The RHIC/AGS online modeling environment, a general client-server modeling package that supports cdev and straightforward integration of diverse computational modeling engines (CMEs), is being adapted to model the AGS and Booster at BNL. This implementation uses a version of MAD modified at BNL that allows traditional lattice structure analysis, single pass beam line analysis, multi-particle tracking, interactive graphics, and the use of field maps. The on-line model system is still under development, a real working prototype exists and is being tested. This paper will describe the system and experience with its design and use for AGS and AGS Booster online modeling.

1 BNL MAD

One of the paths of model development at BNL has emphasized graphics based enhancements to the usual collection of traditional calculations. This emphasis has also provoked efforts to speed up these calculations, and to introduce various tools that make it easy to add features and new sets of calculations. These graphics based programs are similarly attractive as on line tools which can aid in operating the various accelerators and transfer lines in the AGS RHIC complex. Techniques are centered around a library of prepared commands stored in the BNL MAD data base, which are called by menu from the console. Graphics services are contained within the program and coupled directly to the orbit and tracking calculations. Parameters can be changed by means of menus and sliders, and steps repeated as the effects of parameters are observed and evaluated.

1.1 Calibration of the Model

Ideally, live data is drawn from the various components of the accelerator, and used to describe the corresponding elements of the model. Orbits are computed, and compared with measured orbits. If sufficient care has been taken both to verify the data and to build the model, perhaps the orbit of the model agrees with the measurements. In our experience, there have often been glaring discrepancies between the two, compromising any reliance on the use of models. The kinds of problems are all too familiar. A few unreliable measurements, misaligned apparatus, inaccurate elements

in the models all take their toll. While all of these irritants can be improved upon over time, they are rather unhealthy obstacles to satisfactory on line models.

We can make use of a series of virtual correctors in our models to bring model computed orbits into agreement with measured values. In this technique various harmonics are placed on the virtual correctors, and fitted so the resulting computed orbit best matches the measured orbit. The scheme is rather insensitive to missing monitors or correctors, works particularly well for our smaller machines, and produces decent matches to the measured orbits without marked distortions. Accompanying graphics shows the build up of the fitted harmonics, and whether the results can be trusted. The fitted virtual corrector patterns follow the details of the actual orbits considerably better than a simple harmonic fit to the measurements. In effect, the model is now realistically matched to the actual machine, and further work with it is likely to be more credible.

Figure 1 illustrates this kind of fit to a ragged Booster orbit. This fit is drawn beyond the actual orbit to show its continuity.

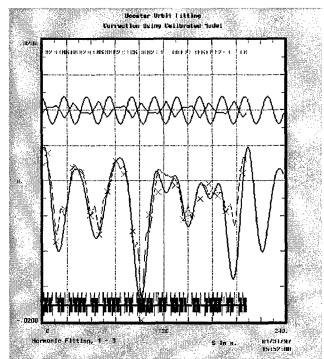


Figure 1: Booster Orbit Flattening Calibration

^{*} Work supported by the U.S. Department of Energy.

[†] Email: kbrown@bnl.gov

1.2 Dynamic Orbit Correction

We have developed models of automatic orbit correction systems with displays that help to evaluate stability. Components include neuron like objects that collect signals, apply filters, and pass the signals on to overall controllers and then correctors. The components are coupled non linearly, like actual neurons, which is easily shown to increase the stability of these schemes. A Micado based controller is particularly effective at localizing responses to orbit distortions. Graphics aids help to demonstrate convergence, effect of gain, and onset of instabilities. Various time delays can be introduced, and their effects on responses observed. In Figure 2, we show the response of a 24 corrector system to an artificial orbit spike in an AGS model, over six cycles of read, filter, analyze, and set correctors. Here the gain of .4 is a little too large, so there is a noticeable overshoot.

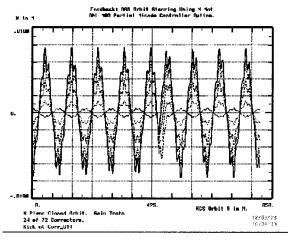


Figure 2: AGS Orbit Flattening

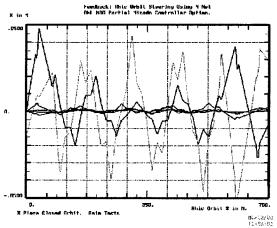


Figure 3: RHIC Micado based Orbit correction

A similar configuration can be used to observe convergence with the controller algorithm. In Figure 3, we show the response of a Micado based correction scheme to an exaggerated static error distribution used for spin preservation studies on RHIC. Both X and Y planes are shown for three cycles of a Micado iteration with all the signal filters turned off. The insertion region correctors are not included.

1.3 Stability Studies

The graphics offer a particularly dramatic way to evaluate the stability of a particular lattice configuration. A calculation of orbits is easily iterated for a few values of some parameter, such as the strength of a line quadrupole, and the lattice functions observed. The range of iterated values typically covers plausible error margins. If the envelopes of these iterated functions are narrow, the design is most likely very stable. Similarly, the behavior of the lattice functions can also be observed for varying momentum offsets and the various other optical input parameters. Competing designs, and set up parameters can be easily compared. In Figure 4, the stability of a suggested transfer line design is probed by varying all quads in the line by a few amperes. In Figure 5, the stability of an early LHC insertion design with respect to quad strengths at injection is displayed. Both designs appear to be unusually stable with respect to drifts in quad values. Both are similarly insensitive to a range of particle momenta.

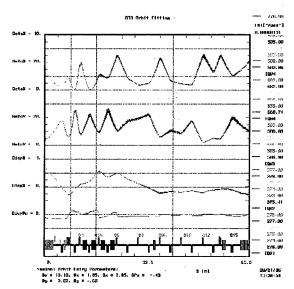


Figure 4: AGS Booster to AGS transfer line

While lattice designs usually involve complicated multiparameter fitting via conventional matching calculations, once in place their operation is greatly aided by graphics displays that show relative sensitivities of orbit functions and dispersion to various parameters. Knob twiddling is seldom the best way to optimize among twenty or so variables involved in steering beams.

A related issue in accelerator designs is the sensitivity to various misalignment and mispowering errors. There is often some doubt about bias introduced by the use of random distributions, which tends to be explored by iterating with numerous other distributions. Again, our orbit function graphics can be used to show the spread of effects due to a variety of random number seeds used to generate error distributions.

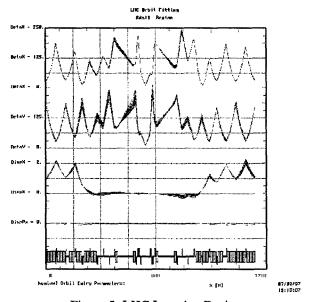


Figure 5: LHC Insertion Design

1.4 Particle Tracking

A graphics based procedure has been developed for tracking charged particles in the presence of magnetic fields changing in time relative to the usual reference conditions, as in acceleration and ejection scenarios. For tracking models to be realistic, accurate aperture data and time profiles of the changing fields must be included in the description of individual lattice elements. Groups of particles can be selectively captured in septum elements, and then further tracked down branch lines radiating from the septum. Various initial track patterns can be generated by selecting from a stored library of commands, and single or multiple track groups can be followed. This tool is particularly helpful for operating auxiliary beam lines.

A rather simple example is shown in Figure 6 in which an AGS Booster beam is coasting inwards as the main field increases.

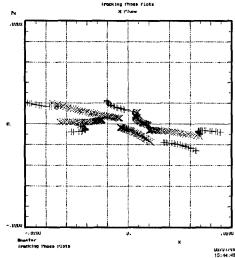


Figure 6: AGS Booster, Tracking with Time Varying Fields

2 THE ON-LINE MODEL SERVER

The model server is described in detail in [Satogata [1]]. It is built using the cdev generic server and is designed to allow integration of diverse computational model engines. Integration of BNL MAD is more involved (as would be any monolithic application that interfaces solely with file I/O), since it is built with no support for general Unix interprocess communication.

2.1 Server Interface

To connect BNL MAD to the model server a set of "wrapper" functions are built which are encapsulated into the model server. The wrapper functions for BNL MAD connect to the executable using named pipes and can be put into a separate server, to allow the model server to communicate over a network. The main part of this work builds a middle-ware which allows the model server to communicate to any model engine, locally or over a network. The reason for taking this approach is that other model engines are in use at BNL (transport, turtle, marylie, etc.), and we will want to be able to interface these model engines to the system. Much of this work is still under development. To first order the server is only interested in obtaining numerical results for other controls applications to make use of (using BNL MAD as just a sophisticated calculator). But we also intend to have clients that make use of the BNL MAD graphics utilities and the full power of BNL MAD, and so the interface is designed to be encapsulated directly into client applications also.

2.2 Supported Platforms

Presently BNL MAD with all its functionality is only supported on Silicon Graphics workstations. This is because the graphics utilities make use of the pre-OpenGL tools IrixGL. The computational engine of BNL MAD has been ported over to the Sun OS platforms, and the graphics is currently being ported over to OpenGL.

3 CONCLUSIONS

BNL MAD is a versatile and powerful set of tools which is well established in the BNL community and beyond. These tools are capable of solving complicated design problems as well as being used to test against experimental results. With the added capabilities of its graphics interfaces, problems can be studied and solved very quickly. The design process is greatly enhanced as a result. It is natural to want to incorporate these sophisticated applications into the actual accelerator controls, or at least, put it into the hands of the accelerator operators to be used as a tuning guide. We believe this is feasible and have taken the first steps in implementing it.

4 REFERENCES

[1] T.Satogata et al, "The RHIC/AGS Online Model Environments: Design and Overview", These proceedings.

ADIABATIC EXCITATION OF LONGITUDINAL BUNCH SHAPE OSCILLATIONS*

M. Bai, <u>K. Brown</u>[†], W. Fischer, T. Roser, K. Smith, N. Tsoupas, J. van Zeijts BNL, Upton, New York 11973, USA

Abstract

By modulating the rf voltage at near twice the synchrotron frequency we are able to modulate the longitudinal bunch shape. We show experimentally that this can be done while preserving the longitudinal emittance when the rf voltage modulation is turned on adiabatically. Experimental measurements will be presented along with theoretical predictions.

1 INTRODUCTION

We have studied adiabatic excitation of bunch shape oscillations both theoretically and in experiments performed at Brookhaven's Alternating Gradient Synchrotron (AGS). rf voltage was adiabatically modulated in order to excite parametric resonances. Similar studies are described in [1, 2, 3]. In our studies we focused on the adiabatic creation of a parametric resonance, such that the emittance of the bunch was preserved. In this way we were able to achieve very tight bunches at high proton beam intensities.

This technique was exploited during our fast proton extraction run for the g-2 experiment [4], which needed short muon beam pulses produced by short proton bunches, to most effectively exploit the pulse width of the injection kicker into their storage ring. Beam is extracted in single multiple bunch pulses at a rate of 30 Hz. To synchronize the extraction kicker pulses with the minimum bunch width we modulated the AGS rf gap voltage at 180 Hz, and adjusted the average rf gap voltage such that the synchrotron frequency of the central particle was just under 90 Hz. This allowed the bunch shape to modulate at almost 50% of the normal bunch width. This is more than twice the range achievable by just raising the gap voltage of the AGS rf cavities.

In our experiments we slowly ramped the drive amplitude of the rf voltage. We ramped the drive frequency while ramping the drive amplitude. While ramping the voltage amplitude and while holding it in steady state with fixed frequency at the peak amplitude, the average rf voltage amplitude is kept constant over a full modulation cycle, so that the average synchrotron tune is unchanged. If the drive frequency is just above twice the synchrotron frequency then, as we will show, there is no blow-up of the longitudinal emittance. In experiments we studied the effects of drive frequencies from well above twice the synchrotron

frequency, as well as frequencies well below twice the synchrotron frequency.

We compare tomographic reconstructions of the bunch to our models. The reconstructions required great care, since the rf amplitude varied over a large range. Despite this fact we were able to accomplish very good reconstructions.

2 LONGITUDINAL MOTION WITH MODULATED FOCUSING STRENGTH

The synchrotron motion can be described using the conjugate phase space coordinates $(\phi, \delta = \frac{h\eta}{\nu_s} \frac{\Delta p}{p})$ where ϕ is the particle phase relative to the synchronous particle, h the harmonic number, η the phase slip factor, $\nu_s = \sqrt{\frac{h|\eta|eV}{2\pi\beta^2E}}$ the synchrotron tune at zero amplitude without modulation and p the particle momentum. The discrete synchrotron equations for a stationary bucket above transition can then be written as [5,3]

$$\phi_{n+1} = \phi_n + 2\pi\nu_s \delta_{n+1}$$

$$\delta_{n+1} = \delta_n + 2\pi\nu_s [1 + \epsilon \sin(\nu_m \theta_{n+1} + \chi)] \sin \phi_n$$
(1)

where ϵ is the percentage of rf voltage modulation, ν_m is the modulation tune, χ the initial modulation phase and the orbital angle θ a time-like variable. Eqs. (1) corresponds to the Hamiltonian

$$H = \frac{\nu_s}{2} \delta^2 + \nu_s [1 + \epsilon \sin(\nu_m \theta + \chi)] [1 - \cos \phi]. \tag{2}$$

For particles within a bucket the canonical transformation $\phi = \sqrt{2J}\cos\psi$, $\delta = -\sqrt{2J}\sin\psi$ to action-angle variables can be used, which allows to go into a rotating coordinate frame later. The Hamiltonian can now approximated by [3]

$$H = \nu_s J - \frac{\nu_s}{16} J^2 + \nu_s \epsilon \sin(\nu_m \theta) [1 - J_0(\sqrt{2J})]$$

$$+ \sum_{k=1}^{\infty} (\Delta H_{2k}^{(+)} + \Delta H_{2k}^{(-)}) \quad \text{with} \quad (3)$$

$$\Delta H_{2k}^{(\pm)} = \nu_s \epsilon (-1)^{k+1} J_{2k}(\sqrt{2J}) \sin(\nu_m \theta \pm 2k\psi).$$

The J_n are Bessel functions of the order n and we have set $\chi=0$ for convenience. If the modulation tune is only slightly different from twice the synchrotron tune the term $\Delta H_2^{(-)}$ in Eq. (3) is only slowly changing with time while all other terms $\Delta H_{2k}^{(\pm)}$ are rapidly oscillating and

2725

^{*} Work supported by the U.S. Department of Energy.

[†] Email: kbrown@bnl.gov

are therefore neglected. We now go into a coordinate system that rotates around the origin with half the modulation tune by using the canonical transformation $J=\tilde{J},$ $\tilde{\psi}=\psi-\frac{\nu_m}{2}\theta-\frac{3\pi}{4}.$ The new Hamiltonian has terms oscillating at $\nu_m,2\nu_m,...$ which average to zero over time and the time averaged Hamiltonian in this coordinate system is [3]

$$\langle \tilde{H} \rangle = (\nu_s - \frac{\nu_m}{2})\tilde{J} - \frac{\nu_s}{16}\tilde{J}^2 + \frac{\nu_s}{4}\epsilon\tilde{J}\cos 2\tilde{\psi} \tag{4}$$

The investigation of fixed points of the Hamiltonian (4) leads to the following result:

- (a) If $\nu_s(2+\frac{\epsilon}{2}) < \nu_m \implies$ The origin J=0 is the only fixed point, a stable one.
- (b) If $\nu_s(2-\frac{\epsilon}{2})<\nu_m<\nu_s(2+\frac{\epsilon}{2}) \Rightarrow$ There is one unstable fixed point at the origin and two stable fixed points at $J=8(1-\frac{\nu_m}{2\nu_s})+2\epsilon$ and $\tilde{\psi}=0,\pi$.
- (c) If $\nu_m < \nu_s(2-\frac{\epsilon}{2}) \Rightarrow$ There is a stable fixed point at the origin, two more stable fixed points at $J=8(1-\frac{\nu_m}{2\nu_s})+2\epsilon$ and $\tilde{\psi}=0,\pi$ and two unstable fixed points at $J=8(1-\frac{\nu_m}{2\nu_s})-2\epsilon$ and $\tilde{\psi}=\frac{\pi}{2},\frac{3\pi}{4}$.

We work in the regime (b) where particles are pushed away from the origin and held in two islands. This situation is depicted in Fig. 1 and known as a parametric resonance [6].

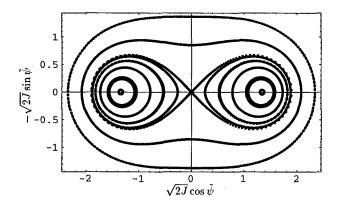


Figure 1: Particle trajectories in a surface of section of the Hamiltonian (4) for case (b).

To reach the state depicted in Fig. 1 the modulation depth ϵ is increased adiabatically, typically over 25 synchrotron periods.

3 EXPERIMENTAL RESULTS

The experiments of adiabatically modulating the rf cavity were conducted with the AGS high intensity proton beam at 24 GeV.

To achieve the adiabatic excitation of the parametric resonance, the amplitude of the rf voltage modulation was slowly ramped up in about 10 synchrotron oscillations, kept fixed for about 30 synchrotron oscillations and then slowly

ramped down to zero. Fig. 2 shows typical scope signals of this process: the modulated rf voltage, the beam peak detector signal and the beam current signal.

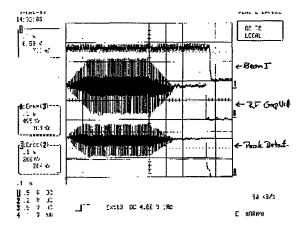


Figure 2: Typical scope signals with the modulated rf voltage signal, the beam peak detector signal and the beam current signal. The time scale on the horizontal axis is 0.1 sec/div.

The rf voltage was driven by an amplitude modulated sinusoidal signal generated by a waveform generator (WaveTek 296). The average of the rf voltage was kept unperturbed. The beam peak detector measures the peak of the beam pulse obtained from a wall current monitor. Assuming the beam current is constant, the narrower the bunch length, the higher the beam peak detector signal.

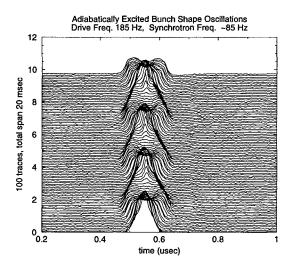


Figure 3: Driven bunch shape oscillations seen with the wall current monitor.

The average synchrotron frequency in Fig. 2 is 85 Hz, and the rf voltage drive amplitude $\epsilon=0.8$. The rf voltage signal and the beam peak detector signal shows that the bunch shape oscillations nicely follow the rf voltage modulation. The staronger the rf voltage is driven, the stronger the bunch shape oscillates. As the rf voltage modulation is

ramped down to zero, the bunch shape oscillation is also diminished. This indicates that the parametric resonance was excited adiabatically.

The corresponding beam longitudinal profile evolution is shown in Fig. 3 in the mountain range fashion. It clearly shows the bunch shape oscillation when the rf voltage was driven at 185 Hz, twice the synchrotron oscillation frequency.

Since $\nu_s = 0.23$, $\nu_m = 0.5$ and $\epsilon = 0.8$ satisfy

$$\nu_s(2 - \frac{\epsilon}{2} = 0.368 < \nu_m < \nu_s(2 + \frac{\epsilon}{2}) = 0.552,$$
 (5)

two stable fixed points (SFTs) were developed. The beam was stretched into the two islands around these two SFTs and shaped like a "dumb-bell", as shown in the Tomographic reconstruction of the bunch Fig. 4.

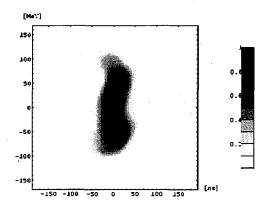


Figure 4: Phase space reconstruction of the bunch.

The bunch length was also measured with different modulation frequencies while the rf voltage drive amplitude was kept fixed. Fig. 5 shows that the minimum bunch length becomes shorter when the rf voltage is driven closer the resonance frequency

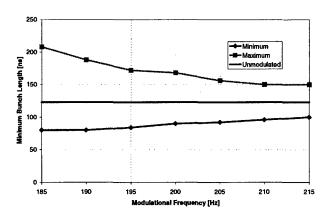


Figure 5: Measured bunch length versus modulation frequency.

4 CONCLUSIONS

By modulating the rf voltage at twice the synchrotron frequency, a parametric resonance can be excited. The longitudinal beam emittance can be preserved if the excitation is adiabatic. This technique can allow us to obtain very short bunches and was successfully applied in the AGS fast extraction of high intensity proton beam for the g-2 experiment, which requires proton beam with short bunch length.

5 ACKNOWLEDGMENTS

The authors wish to acknowledge and thank Steve Hancock and Mats Lindroos, CERN, for there valuable assistance in Tomographic reconstructions. The reconstruction program used, TOMO, needed modifications in order to compensate for the changing rf voltage. They made the necessary modifications and provided very valuable advice and stimulating discussions.

- [1] H. Huang et al, Phys. Rev. E 48 4678, 1993.
- [2] D. Li et al, "Experimental measurement of resonance islands induced by rf voltage modulation", Physical Review E Rapid Communications, Vol. 48, No. 3 1638-1641 (1993).
- [3] D. Li et al, "Effects of rf voltage modulation on particle motion", Nucl. Instr. and Meth. in Phys. A 364 205-223 (1995).
- [4] R.M.Carey et al, "New Measurement of the Anomalous Magnetic Moment of the Positive Muon", Physical Review Letters, Vol.82, Issue 8, pp. 1632-1635, Feb. 22, 1999
- [5] D.A. Edwards and M.J. Syphers, "An introduction to the physics of high energy accelerators", John Wiley, New York (1993).
- [6] L.D. Landau and E.M. Lifschitz, "Mechanics", 3rd ed., Pergamon, New York (1976).

THE RHIC/AGS ONLINE MODEL ENVIRONMENT: DESIGN AND OVERVIEW *

T. Satogata[†], K. Brown, F. Pilat, A. Alai Tafti, S. Tepikian, J. van Zeijts BNL, Upton, NY, USA 11973

Abstract

An integrated online modeling environment is currently under development for use by AGS and RHIC physicists and commissioners. This environment combines the modeling efforts of both groups in a CDEV[1] client-server design, providing access to expected machine optics and physics parameters based on live and design machine settings. An abstract modeling interface has been designed as a set of adapters[2] around core computational modeling engines such as MAD and UAL/Teapot⁺⁺[3]. This approach allows us to leverage existing survey, lattice, and magnet infrastructure, as well as easily incorporate new model engine developments. This paper describes the architecture of the RHIC/AGS modeling environment, including the application interface through CDEV and general tools for graphical interaction with the model using Tcl/Tk. Separate papers at this conference address the specifics of implementation and modeling experience for AGS and RHIC.

1 MOTIVATION AND SCOPE

Over the past five years, an infrastructure has been developed in the RHIC project that integrates delivered magnet measurements, offline long-term particle tracking, and survey of installed RHIC components. Both design and `as built' optics models of RHIC are routinely produced. Accelerator applications being developed for commissioning require a consistent optics model framework that builds upon this effort, maintaining consistency from design through construction and installation to commissioning. However, the tracking and optics programs used for design and magnet production feedback could not be easily adapted for use by RHIC controls applications.

We have developed an online modeling environment used by various RHIC correction applications (e.g. orbit, tune, chromaticity, coupling) to access design, as-built, and live optics data generated by optics model engines. By using a client-server model and an abstracted modeling interface layer, this becomes a generic modeling environment that can also be used for AGS and AGS/Booster application modeling and calculation. Multiple model engines with different interfaces and implementations are supported by a common CDEV interface for application use.

The online model design discussed here is not intended to supply a full control-system simulation of an operational accelerator control system (cf. Fermilab's Open Access Server). At this time there are no plans to implement such a simulation service for RHIC.

- 1. Read/write flat machine lattice descriptions
- 2. Read/set individual magnet parameters:
 - Strength (including combined function magnets)
 - Offset from design (2D)
 - Multipole corrections and errors
 - Survey and layout
- 3. Read/Set boundary conditions
 - Single-particle initial coords, energy, species
 - Bunch initial conditions (groups of particles)
 - · Beamline initial lattice functions
- 4. Calculate optics to reasonable order:
 - Tunes (Q_x, Q_y, Q_S)
 - Transition energy, γ_T
 - Lattice functions $(\beta, \alpha, \text{ phases}, \eta, ...)$
 - 6D orbit, football transfer matrices
 - First-turn and closed orbits
- ... Future development, specialty CMEs
 - Perform constrained model-based corrections
 - Produce Taylor Expansions, maps, DA forms
 - Perform single-particle and bunch tracking

Table 1: A summary of CME computational capabilities in the RHIC/AGS Online Model Environment.

2 COMPUTATIONAL MODEL ENGINES

A computational modeling engine (CME) is an accelerator simulation that provides an interactive interface (usually an interpreted script) to a small set of modeling capabilities. These CMEs are the core of any accelerator modeling, online or offline — they are the algorithmic guts and interfaces that transform lattice and beam definitions into beam physics output. UAL/Teapot⁺⁺is the CME currently in use for RHIC design and commissioning. Other commonly-used CMEs include Teapot, TRANS-PORT, SYNCH, COSY, and MAD, and several locally-modified versions of MAD are also used and maintained by AGS beam physicists [4].

Online modeling requires interactive, real-time CMEs. Most popular CMEs are used by accelerator designers and modelers in a batch job mode, driven by command scripts written in highly idiomatic command languages, and parsed and interpreted line by line. Though the script interface can also be used interactively, optics output is usually only output to files, an inefficient path for application interaction with a CME. The online modeling architecture described here abstracts the common features of many CMEs into a simple network command interface that can

^{*} Work supported under the auspices of the U.S. Department of Energy

[†] Email: satogata@bnl.gov

be used by accelerator applications on distributed controls consoles.

CMEs load accelerator lattice definitions using another idiomatic language, though there is much more commonality here as many accelerator codes use the the MAD input language, Standard Machine Format (SMF). However, SMF is cumbersome or deficient in some areas required to model a fully hierarchical design model of an accelerator, modified by `as-built' constraints. Recent collaborative efforts between several labs have made progress towards developing SXF, a Standard Exchange Format, to supersede SMF for collaborative LHC design work [5]. The RHIC/AGS modeling environment provides an abstract interface to lattice and strength table read/write, allowing adaptors to be easily written that integrate local lattice databases and definitions with various CMEs in the online model.

Functional requirements for CMEs are derived from application and commissioning priorities, as well as commonality of existing CME functionalities. Experience has shown that the most common requests to an online CME during commissioning are those shown in Table 1. In particular, one must be able to change magnet strengths and offsets, and calculate full 6D linear optics parameters for use in control application analysis and correction. Many CMEs are capable of these calculations with very similar interfaces, though they vary wildly in their implementations and compromises between speed and completeness.

3 SERVER ARCHITECTURE

The client-server architecture for RHIC/AGS online modeling is shown in Figure 1. Client applications interact with the model via CDEV calls, as described in Section 4. Each model server for a supported CME is compiled from several C⁺⁺classes. The CDEV modeling interface is provided by a CDEV Model Server class that is derived from the CDEV Generic Server[6]; derived servers may extend the interface to provide extended access to underlying CME capabilities and data structures.

3.1 Generic model data classes

The model server uses a small set of generic model data classes to provide the data interface between optics and magnet settings in the CME and the model server class. This supports the CME capabilities in Table 1, and includes arrays of lattice functions at user-specified monitor elements, as well as matrices for higher-order optics. All model data follows Teapot unit and coordinate conventions, for initial implementation convenience. However, the current strongly-typed model data class is not dynamically extensible to accommodate different CME data structures, and this data class will be reimplemented as a generic cdevData container extension in the near future.

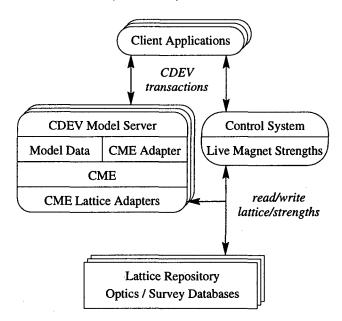


Figure 1: The RHIC/AGS online model architecture. Each running model server is a separate unix process, binding the server interface to an instance of a CME.

3.2 CME Adapters

Each CME must have an adapter class that translates generic method calls from the server to CME-specific function calls or implementations. Writing such an adapter is the major effort required to integrate a new CME into this environment. All CME adapters are derived from a parent interface class; this general interface is then used by the model server when making requests, and the model data classes are used to retrieve optics and lattice output.

CME translation and interface becomes complicated when the CME only has a parsed scripting interface that is not easily bindable (e.g. AGS/MAD, or MAD with no source libraries). In these cases the CME adapter must fork a separate process instance of the CME and interact with it via file descriptors, generating command text and parsing output files as requests are made. Other CMEs (such as UAL/Teapot⁺⁺) that have direct C⁺⁺object interfaces may be used directly in the CME via shared libraries that are loaded at run-time.

3.3 Lattice adapters

Lattice adapters provide translations from one lattice representation to another within a given environment, such as a control system or accelerator design project. They separately implement read/write of accelerator lattices and survey (slowly-changing or static layout), and magnet strength (dynamic control) information. In particular, they can also implement methods to load live accelerator magnet settings from the control system into the model, allowing interactive online comparisons between live and expected machine optics.

- 1. Names and Strengths:
 - SiteWideNames
 - ModelStrength: in physics units
- 2. Model Output:
 - LatticeFunctions
 - Orbit
 - muX, muY: tunes for circular lattices
 - chromX, chromY: chromaticities
 - gammatransition
- 3. Response Matrices:
 - SteeringMatrix: for beamline steering
 - ClosedOrbitMatrix: for closed orbit correction
 - OscillationMatrix: for coherent oscillation correction
 - MatchingMatrix: for betatron matching
 - TuneMatrix: for tune correction
 - GammaTransitionMatrix: for γ_t correction

Table 2: Model keywords for requests to the CME server

4 CDEV CLIENT INTERFACE

The client side of the CME server consists of several CDEV 'device' classes, and specific attributes for each class. The attributes for a model device are summarized in Table 2. The message interface allows access to the model by using 'get' and 'set' verbs, or notification on-change by using the 'monitorOn' verb, where callbacks will be triggered when the underlying data changes. This notification allows multiple clients to stay synchronized when magnet parameters or injection parameters are changed within the model.

For retrieving response matrices we have followed the naming conventions used in the 'BeamOptics' code [7]; in Table 2 we list the requests for several types of these matrices. Each request takes appropriate lists of magnet names and position pickups, which are then sent as tagged entries in cdevData interface to the model. Optionally, the outgoing context data specifies an interest in a subset of the default return data; for instance, this allows a lattice function call to only return β_x and α_x instead of the full set.

5 APPLICATION EXAMPLES

Currently several applications at RHIC use the interface described here to access the UAL/Teapot⁺⁺CME. They include the RHIC orbit correction application, the RHIC injection application[8], the ATR emittance measurement application, the RHIC Ramp Editor[9], and several Tcl/Tk scripts that are used for lattice function visualization, and what-if scenarios. As an example we show in fig. 2 the interface to the RHIC injection application, displaying a CME-derived orbit.

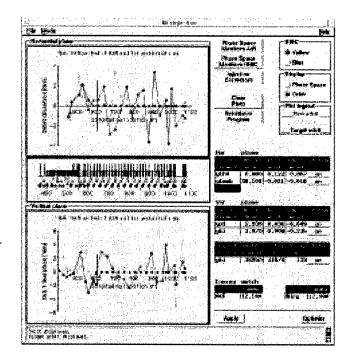


Figure 2: The RHIC injection application.

6 ACKNOWLEDGEMENTS

Our thanks to Nikolay Malitsky and Dick Talman for their development of the UAL/Teapot⁺⁺modeling environment that inspired this work. Future developments of this environment may extend to restructuring the client-server model around CORBA, providing a more flexible and dynamic binding between modeling components and adapters.

- J. Chen, et al., "CDEV: An Object-Oriented Class Library for Developing Device Control Applications", Proceedings of ICALEPCS 1995.
- [2] E. Gamma, et al., *Design Patterns*. (Addison-Wesley, Reading, Massachusetts, 1995)
- [3] N. Malitsky and R. Talman, "The UAL Infrastructure for Accelerator Optimization and Correction", these proceedings.
- [4] K. Brown, et al., "The RHIC/AGS Online Model Environments: Experiences and Design for AGS Modeling", these proceedings.
- [5] F. Pilat, et al., "The application of the SXF lattice description and the UAL software environment to the analysis of the LHC", these proceedings.
- [6] W. Akers, "An Object-Oriented Framework for Client/Server Applications", Proceedings of ICALEPCS 1997.
- [7] B. Autin, "BeamOptics: A Program For Analytical Beam Optics", CERN publication 98-06.
- [8] W. Fischer, J.W. Glenn, W.W. Mackay, V. Ptitsin, T.G. Robinson, N. Tsoupas, "The RHIC Injection System", these proceedings.
- [9] J. Kewisch, J. van Zeijts, S. Peggs, T. Satogata, "Ramp Management in RHIC", these proceedings.

LATTICE ANALYSIS OF THE KEKB COLLIDING RINGS

K. Akai, N. Akasaka, A. Enomoto, J. Flanagan, H. Fukuma, Y. Funakoshi, K. Furukawa,

- S. Hiramatsu, K. Hosoyama, N. Huang*, T. Ieiri, N. Iida, T. Kamitani, S. Kato, M. Kikuchi,
- E. Kikutani, H. Koiso, M. Masuzawa, S. Michizono, T. Mimashi, T. Nakamura, Y. Ogawa,
- K. Ohmi, Y. Ohnishi, S. Ohsawa, N. Ohuchi, K. Oide, D. Pestrikov[†], K. Satoh, M. Suetake,
- Y. Suetsugu, T. Suwada, M. Tawada, M. Tejima, M. Tobiyama, N. Yamamoto, M. Yoshida, S. Yoshimoto, KEK, Tsukuba, Ibaraki, 305-0801, Janan

Abstract

A low beta lattice with $\beta_x^*/\beta_y^*=100/1$ cm has been realized in the KEKB colliding rings. The basic optical parameters have been measured and compared with the model.

1 MODELING

KEKB[1]is an 8 GeV electron + 3.5 GeV positron doublering collider (HER and LER) with a single interaction point (IP) for the Belle detector. The beta function at IP is designed to be 1 cm in the vertical plane ($\beta_y^* = 1$ cm) and a horizontal beam crossing angle of 22 mrad is adopted for collisions at a bunch spacing of 59 cm. Following counter solenoids which locally compensate the detector solenoid field, eight special quadrupole magnets, listed Table 1, are installed around IP. QCSR and QCSL are superconducting magnets which are common in both rings. The other normal magnets have special shapes with field free space for the counter-rotating beams. The modeling of those special magnets is one of the most important issues in the lattice design. The results of magnetic field measurements have been taken into account in the model as much as possible. Design and simulation works have been done by the code SAD[2] developed at KEK.

Magnet(Type)	r_b	B'	x_m/y_m	Beam
	(mm)	(T/m)	(mm)	
QC2LE (N)	60	3.2	68/13	$e^-\downarrow$
QC2LP (N)	45	6.1	57/10	$e^+\uparrow$
QC1LE (N)	38	-14.2	22/21	$e^-\downarrow$
QCSL (S)		-21	13/20	$e^-\downarrow e^+\uparrow$
IP				
QCSR (S)		-21	14/24	$e^-\downarrow e^+\uparrow$
QC1RE (N)	70	-13.2	29/27	$e^-\downarrow$
QC2RP (N)	42	2.9	69/12	$e^+\uparrow$
QC2RE (N)	60	10.8	69/16	$e^-\downarrow$

Table 1: Special quadrupole magnets near IP. r_b is the bore radius, B' the field gradient, x_m and y_m the maximum amplitudes of the injected beams in the horizontal and vertical planes.

1.1 QCS and solenoid

The field distribution along the longitudinal direction in the solenoid area is given by 4 cm-thick slices with a constant field. Both QCSs are included in this area, and are also divided into slices with normal and skew multipoles up to the 32-th pole. The magnitude of multipole components were estimated from the results of field measurements[3]. Since the outgoing beams pass the QCSs at off-axis, it is necessary to express the transverse distribution with sufficient accuracy at $\sim 60~\mathrm{mm}$ away from the center. To optimize the x-y coupling, the QCSR and QCSL are set to be rotated by 35.6 and -10.8 mrad, respectively.

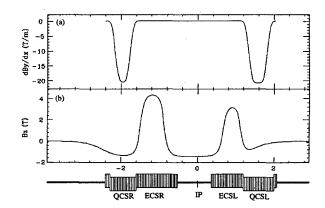


Figure 1: Model of QCS and compensation solenoid system.

1.2 QC1RE and Others

QC1RE is a half quadrupole for HER. The beam passes through 45 mm off-axis of the virtual center of QC1RE in the horizontal plane. The integrated dipole field obtained from the field measurement along the beam trajectory is consistent with 3-dimensional calculation and amounts to an additional kick of 1.1 mrad, which is incorporated as thin dipole magnets attached at both edges of QC1RE. The dynamic aperture with measured values of the higher multipoles was checked for some of the normal quadrupoles, which was found to be marginal compared with the requirements.

^{*} visiting from IHEP, China

[†] visiting from BINP, Russia

1.3 Lattice for BEAST

The commissioning has commenced with $\beta_x^*/\beta_y^*=100/2$ cm, and the reduction of β_y^* to =1 cm has been succeeded in both rings[4]. The chromaticity correction has fully utilized 52-family noninterleaved sextupole pairs and vertical 2-family pairs for the local correction only in LER. The commissioning lattice has slightly modified for the BEAST detector, removing the detector solenoid. Because QCSs are already rotated, the x-y coupling should be corrected even without the detector solenoid. The rotations of normal IR quadrupoles have also been changed and the compensation solenoids have been excited to 10% of the nominal values to minimize strengths of skew quadrupoles. In order to adjust orbits and dispersions, local orbit bumps have been applied in the interaction region (IR) as shown in Fig. 2.

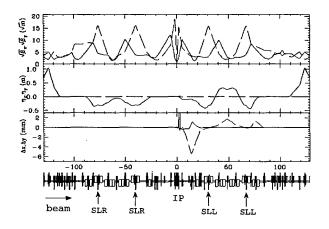


Figure 2: LER optical functions in IR. SLL and SLR are sextupoles for the local chromaticity correction.

2 MEASUREMENT OF BASIC PARAMETERS

2.1 Closed Orbit

The global closed orbit has been successfully corrected with conventional methods (SVD and MICADO) better than 0.6 mm rms. The local bumps has also been used for fine tuning and for diagnostics of machine errors.

2.2 Transverse tune

Even a few steps of improvements of the model lattice as listed Tables 2 and 3, the measured tunes still have some difference from the model in both rings. It is necessary to precise calibration between various magnets (superconducting, normal, IR quadrupoles with special shapes) to identify error sources.

2.3 Dispersion

The measured values of horizontal dispersions agree with the model within 16% in LER and 6% in HER. Sometimes a large vertical dispersion has been observed, which depends on the vertical orbit. The vertical dispersion has been decreased to a reasonable level by adequate tuning of the vertical orbit, in particular, at sextupoles.

Source	Δu_x	Δu_y
(a) Flat rectangular dipole	0	0
(b) Edge angle	0	0.40
(c) Slope of B_y , $B_y = B_y(s)$	0	-0.037
(d) Integrated quadrupole	0.057	-0.056
(e)Integrated sextupole,		
$\int B_y''(s)x(s)ds$	0.114	-0.112

Table 2: Model of LER dipole magnet. The quadrupole and sextupole components are estimated from the results of field measurements[5]. ModelB and A are with and without Source(e).

	LER	HER
	$\Delta u_x, \Delta u_y$	$\Delta u_x, \Delta u_y$
$\beta_y^*=2$ cm		
Adjust energy, QCS	-0.01, -0.30	0.12, -0.08
LER dipole modelA		
with fudge factors (*)	+0.04, -0.10	
LER dipole modelB		
(no fudge factors)	-0.14, -0.20	
Adjust QCS		
$\beta_y^*=1$ cm	-0.13, -0.19	0.12, -0.09
Adjust tunes, orbits,		
chromaticity, etc.	-0.07, -0.22	+0.07, -0.06

Table 3: History of tune deviations from the model lattice. (*)Fudge factors of -0.4% and -0.8% were applied for tow families of quadrupole magnets in unit cells, QD3P(40) and QD5P(48), respectively.

2.4 Chromaticity

The examples of the chromaticity measurement are shown Fig.4. The differences from the model are not so big, but amount to 5 in the vertical direction in the β_y^* =1cm case. It is necessary to adjust tunes of the model lattice to the measured ones in finding solution of strengths of sextupoles.

2.5 β Function

Big mismatch of LER optics in the vertical direction was observed both in the response of single kick orbits [6] and in measurements with trim coils of normal quadrupoles as shown in Fig.6. The matching was greatly recovered by adjusting field strengths of QCSs by +0.8%, which was determined by analyzing the leakage orbit of the local bump at QCSs. After recent refinements of the QCS model by subtracting effects of the return yoke of the Belle detector,

QCSs still look stronger by 0.37% than other quadrupole magnets in LER. In HER, β_y at QCSs and QC1s are consistent with the model in 10%. Further measurements and analysis are now being in progress.

The authors thank K. Egawa, S.-I. Kurokawa, K. Nakayama, K. Tsuchiya for helpful discussions and comments.

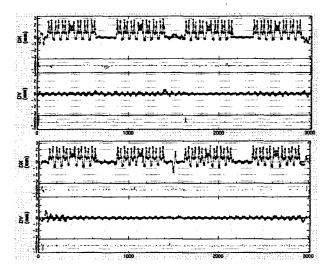


Figure 3: Measured and calculated dispersions (above:LER, below:HER).

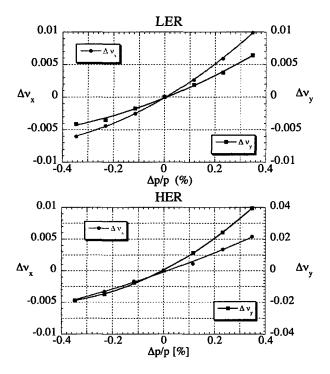


Figure 4: Measured chromaticities (above:LER, below:HER) in the case of $\beta_x^*/\beta_y^*=100/1$ cm.

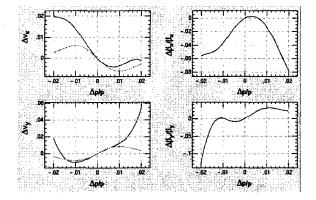


Figure 5: Calculated chromaticities of LER in the case of $\beta_x^*/\beta_y^*=100/1$ cm.

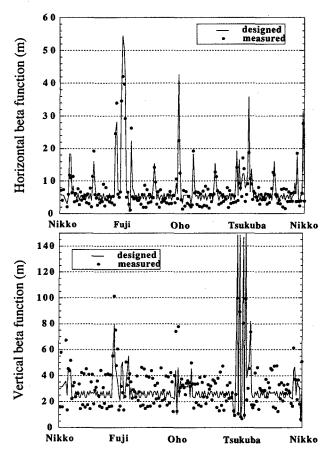


Figure 6: Measurement of β -function with trim coils of quadrupole magnets in the case of $\beta_x^*/\beta_y^*=100/2$ cm. The field strength of each quadrupole was changed typically 1.5% by the trim coil.

- [2] http://www-acc-theory.kek.jp/SAD/sad.html
- [3] N. Ohuchi et al., Proc. of EPAC98 (1998).
- [4] K. Oide et al

3 REFERENCES

[1] KEKB B-Factory Design Report, KEK-Report 95-7, (1995).

BEAM DYNAMICS SIMULATIONS FOR LINACS DRIVING SHORT-WAVELENGTH FELS

M. Ferrario, F. Tazzioli, LNF-INFN, Frascati L. Serafini, Univ. of Milan and INFN-Milan

Abstract

The fast code HOMDYN has been recently developed, in the framework of the TTF (TESLA Test Facility) collaboration, in order to study the beam dynamics of linacs delivering high brightness beams as those needed for short wavelength FEL experiments. These linacs are typically driven by radio-frequency photo-injectors, where correlated time dependent space charge effects are of great relevance: these effects cannot be studied by standard beam optics codes (TRACE3D, etc.) and they have been modeled so far by means of multi-particle (PIC or quasistatic) codes requiring heavy cpu time and memory allocations. HOMDYN is able to describe the beam generation at the photo-cathode and the emittance compensation process in the injector even running on a laptop with very modest running times (less than a minute). In this paper we show how this capability of the code is exploited so to model a whole linac up to the point where the space charge dominated regime is of relevance (200 MeV).

1 GENERAL CRITERIA FOR OPTIMIZATION OF A PHOTO-INJECTOR

The art of designing optimized RF Photo-Injectors capable to deliver high brightness electron beams has moved in the last decade from a cut and try procedure, guided by rule of the thumb guesses and going through time consuming simulations, up to a fast parameter space scanning guided by the analytical results of the theoretical model for laminar beams [1], achieved by means of a fast running code based on a multi-beam multi-envelope description of the beam dynamics. By this technique it is possible to study the time dependent space charge problem inherent in the beam dynamics of such devices, so to reach the optimum operating point which corresponds to maximum beam brightness.

The code HOMDYN [2] is actually tailored to describe, within a multi-envelope multi-beam frame, the space charge dominated dynamics of laminar beams in presence of correlated, or time dependent space charge forces: because it's not a multi-particle code, but a multi-envelope one, the code behaves like any beam transport code like TRACE-3D or TRANSPORT, giving rise to very fast modeling capability for photo-injectors.

It has been by now understood that the optimization of a photo-injector corresponds to accelerating and propagating the beam through the device as close as possible to two beam equilibrium, a laminar Brillouin flow (in drifts) and the so-called invariant envelope (in accelerating sections) which is a generalization of Brillouin flow for an accelerated beam. In this case the beam undergoes cold plasma oscillations, i.e. the space charge collective force is largely dominant over the emittance pressure, where the betatron motion (trajectory cross-over) is almost absent (laminar flow) and the frequency of the plasma oscillations due to mismatches between the space charge force and the external focusing gradient is to first order independent on the current. It is such a frequency independence that brings emittance reversible normalized oscillations: accelerating the beam through the invariant envelope just makes these oscillations damped like the square root of the beam energy, bringing the normalized emittance at the injector exit down to a steady state minimum when the oscillations are properly tuned.

The laminar behavior of an electron beam is characterized by the laminarity parameter

$$\rho \equiv \left\{ \frac{\left[Ig(\zeta)/2I_0 \right]}{\varepsilon_{n,th} \gamma \sqrt{3\gamma'^2/4 + \Omega_L^2}} \right\}^2$$

which is defined in terms of the beam average energy γ , the peak current I ($I_0=17\,$ kA), the accelerating gradient $\gamma'=eE_{acc}/mc^2$, the Larmor frequency of the solenoid focusing field $\Omega=\frac{eB_{SOL}}{2m}$ and the rms normalized thermal emittance $\varepsilon_{n,th}$. The beam is said to be laminar whenever

ho >> 1, which occurs from the photo-cathode surface up to energies even in excess of 100 MeV for beams carrying about 100 A of peak current.

The time dependence of the space charge field effects is expressed through the geometrical factor $g(\zeta)$, which is a function of the longitudinal position in the electron bunch (the so-called slice position), defined as $\zeta \equiv z - \beta ct + z_0$.

Whenever the geometrical factor $g(\zeta)$ has a significant variation along the bunch, we obtain a beam perveance term in the rms envelope equation, which is slice-dependent, therefore we are in presence of time (or slice) dependent effects. In the case of a cylindrical bunch we have for instance

$$g \cong 1 - \frac{2A^2}{\gamma^2} \left[1 + 12 \left(\frac{\zeta}{L} \right)^2 + 80 \left(\frac{\zeta}{L} \right)^4 \right] ,$$

showing that when the bunch aspect ratio $A \equiv R/L$ is not much smaller than 1 the dependence on the slice coordinate can be quite relevant.

It has been shown that the rms projected normalized emittance $\varepsilon_n \equiv p \sqrt{\langle x^2 \rangle \langle x'^2 \rangle - \langle xx' \rangle^2}$ oscillates with a frequency $\sqrt{2K_r}$ at an amplitude $\Delta \varepsilon_n \propto \sqrt{\frac{I\langle g \rangle}{\gamma}} \sqrt{\langle g^2 \rangle / \langle g \rangle^2 - 1}$ whenever a bunched beam (i.e. $g(\zeta) \neq 1$) is rms matched into a focusing channel of gradient K_r , i.e. on a Brillouin flow equilibrium $\sigma_B(\zeta) = \sqrt{\frac{Ig(\zeta)}{2I_0\gamma^3 K_r}}$ (where σ is the rms

beam spot size, eventually slice dependent). Accelerating on the invariant envelope $\sigma_{inv}(\zeta) = \frac{2}{\gamma'} \sqrt{\frac{Ig(\zeta)}{3I_c\gamma}}$,

which is a particular exact solution of the rms envelope equation in the laminar flow regime, brings the emittance to damped oscillations. The basic point in the design of a photoinjector is therefore to match properly the beam at injection into any accelerating section, according to these criteria:

 $\hat{\sigma}' = 0$, implying a laminar waist at injection

$$\gamma' = \frac{2}{\sigma_w} \sqrt{\frac{I\langle g \rangle}{3I_0 \gamma}}$$
, i.e. an rms match on the inv. env.

These also requires that focusing elements in drifts be spaced close to one quarter of plasma oscillation wavelength, given by $\lambda_p = \frac{4\pi\gamma}{\gamma'}\sqrt{\frac{2}{3}}$.

2 APPLICATION TO THE TTF-FEL LINAC

In this section we study how to implement these matching criteria into the actual design of the TTF linac. up to the end of the second cryomodule, corresponding to a beam energy of 200 MeV. A previous analysis [3] was devoted to a general lay-out for the linac with complete degree of freedom in the spacing of focusing elements and accelerating sections (i.e. the cryostats containing 8 SC accelerating cavities, each with 9 cells working at 1.3 GHz). In the following we will compare those results to the best one can do with the actual lay-out neglecting compressor magnets, not yet implemented in to the code. The 1 nC beam is generated in one and half cells RF-gun operating at 1.3 GHz with 40 MV/m peak field on the cathode, by a 8 ps (sigma) long laser pulse with 1.5 mm radius. The gun is embedded in a 0.11 T split solenoid

field. In the drifting tube downstream the gun the rms emittance reach a first minimum (0.9 mm mrad) corresponding to the minimum ($\sigma'=0$) envelope ($\sigma_r=1.18$ mm) at z=1.2 m from the cathode, where the booster is placed,(Fig. 1).

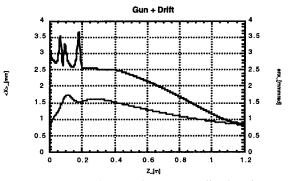


Figure 1: Beam envelope and rms normalized emittance in the gun and drift up to the booster entrance.

To match the booster cavity (9 cells 1.3 GHz superconducting cavity) to the beam we use the previous criteria to compute the accelerating field needed. It results to be 10 MV/m with I=40 A and γ = 10.

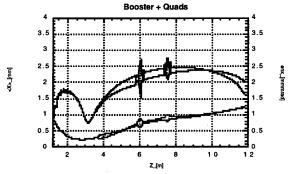


Figure 2: Beam envelope and rms normalized emittance in the booster and drift up to the cryomodule 1 entrance.

Downstream the booster the rms emittance reach a second minimum (0.8 mm mrad) in the drift and at the booster exit (z=2.4 m) the beam envelope ($\sigma_r = 0.35$ mm) is still parallel to the z-axis with $\gamma = 35$. In the ideal case, as discussed in [3], the envelope should be allowed to perform small oscillations around the equilibrium value reached in the booster and smoothly transported to match the condition $\sigma'=0$ at the entrance of the first cryo-module. The situation is here complicated by the technical constrains of the drift section, foreseen to house focusing elements (one quadrupole doublet and two triplets), diagnostic stations and a chicane compressor. In addition by using quadrupoles as focusing elements the envelope and the emittance oscillations are split in the x and y planes, resulting in a difficult task to match both planes to the cryo-module.

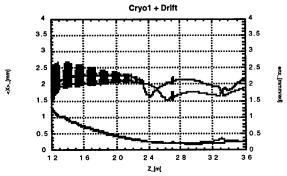


Figure 3: Beam envelope and rms normalized emittance in cryomodule 1 and drift up to the cryomodule 2 entrance.

The best solution we found results to be the less perturbing to the cylindrical symmetry of the beam (Fig. 2). We allowed indeed the envelope to diverge up to $\sigma_r = 1.75$ mm with low quadruoles gradients so that to keep the emittance oscillation in phase in both planes up to the entrance of the first cryomodule (z=11.7 m). The beam is there boosted with 11 MV/m accelerating field, a low gradient is chosen to avoid over focussing in the accelerating section. Emittance oscillations are damped during acceleration around 2 mm mrad (Fig. 3).

With the same care the beam is transported to the second cryomodule through a quadrupole focusing channel and boosted up to 200 MeV in the second cryomodule (Fig. 4).

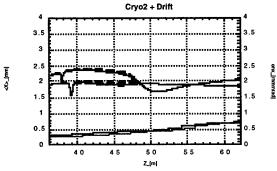


Figure 4: Beam envelope and rms normalized emittance in cryomodule 2 and drift.

4 CONCLUSIONS

By joining the analytical predictions and optimizing criteria produced by the theory of intense relativistic laminar beams with the powerful capability of the new code HOMDYN to model a full photoinjector up to full scale energy (200 MeV) in very short cpu times (minutes on a laptop), the optimization of a new design or the search for the optimum operating point of a present layout can be accomplished quickly and easily. We believe that the general design of future injectors will benefit from such a new user-friend procedure.

- [1] L. Serafini, J. B. Rosenzweig, "Envelope analysis of intense relativistic quasilaminar beams in rf photoinjectors: a theory of emittance compensation", Phys. Rev. E, 55, (1997)
- [2] M. Ferrario, A. Mosnier, L. Serafini, F. Tazzioli, J. M. Tessier, "Multi-bunch energy spread induced by beam loading in a standing wave structure", Part. Acc., 52 (1996)
- [3] M. Ferrario, L. Serafini, "Multi-bunch dynamics in rf photoinjectors through an envelope equation approach', Proc. of VI EPAC, Stockholm (1998).

MODELING RELATIVISTIC ELECTRON BEAMS WITH FINITE-ELEMENT RAY-TRACING CODES*

S. Humphries, Jr. **, Field Precision, Albuquerque, NM J. Petillo, SAIC, Burlington, MA

Abstract

Ray-tracing codes determine self-consistent electric fields in high-current electron devices by an iterative procedure of orbit tracking and space-charge deposition with field recalculation. Methods to find beam-generated magnetic fields for relativistic beams are less standardized. Existing approaches (like ray counting or the relativistic transverse force approximation) have limited accuracy and do not include effects of current flow in source and collector electrodes. We describe a new method for two-dimensional finite-element codes where the beam current is deposited on the faces of the conformal elements of the electrostatic mesh. The resulting balanced calculations of electric and magnetic forces are resistant to numerical filamentation instabilities. With simple rules it is possible to assign boundary currents even in complex structures.

1 CURRENT ASSIGNMENT TO ELEMENT FACES

Figure 1 shows the conformal mesh used in the ETrak code to represent a high-current electron gun. The solution volume is divided into a number of small volumes (or *elements*) with triangular cross-section. In low-energy devices, the beam behavior is dominated by electric fields. In this case, the following procedure is used to find particle orbits consistent with applied and space-charge electric fields [1].

- Start with a vacuum solution for electrostatic potential at vertices.
- Initiate several model electrons near an emission surface, each carrying a portion of the beam current I_i. The model particles can be specified or determined by the code from a local application of the Child law.
- Integrate the orbit of each particle using a time step Δt, depositing charge I Δt in each element that the particle crosses.

- Recalculate the fields including the electron space charge.
- Repeat the orbit and field calculations until the solution converges.

Some ray-tracing codes use finite-difference methods on a regular mesh [2,3,4] and others employ finite-element methods [5,6]. The advantage of the finite-element approach with conformal mesh is apparent is Fig. 1. Accurate field calculations are possible on curved surfaces and every part of the solution volume has a unique material identity. In ETrak elements are divided into regions that share common characteristics. For example the tan elements in Fig. 1 are part of the cathode electrode, grey elements comprise the anode, and white elements represent vacuum. For particle tracking element properties are divided into three types: vacuum, material and secondary material. Electrons propagate through vacuum materials and stop when they enter a material element. Secondary elements are discussed in Ref. [7].

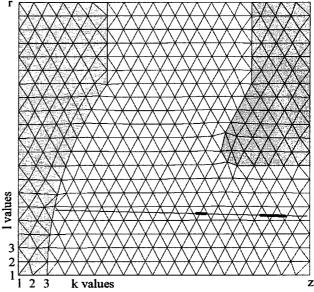


Figure 1: Schematic view of a conformal mesh for a ray-tracing solution. The colored elements represent material regions. The red line is a model electron trajectory. The marked segments represent the particle orbit vector over a single time step for short and long values of Δt .

Work supported by Los Alamos National Laboratory and the USDOE under Contract DE-FG04-97AL77993 and Subcontract 4400000474 from Science Applications International Corporation under Contract N00014-97-C-2076 from the Naval Research Laboratory.

Permanent address, Dept. of Electrical and Computer Engineering, University of New Mexico, Albuquerque, NM 87131

^{*}Email: humphries@fieldp.com

Next consider assignment of electron current on the conformal mesh to calculate beam-generated magnetic fields. To satisfy current conservation, the current must be associated with element faces rather than volumes. Electrostatic field interpolations during tracking already provide information on the elements occupied by electrons at times t and t+Δt. Figure 1 shows two incremental orbit vectors for short and long values of Δt . In the first case, the electron crosses to an adjacent element. Here the current +I, is assigned to the common face if the particle moves in the positive z-direction, while the value -I, is assigned if the particle moves backward. When ETrak detects that an electron has crossed several elements in a step, the code makes a local search of faces near the average position and assigns ± 1 , to any that intersect the increment particle vector. Face current is always assigned before terminating an electron orbit that enters a material element. This convention ensures correct current assignment to collector surfaces. After tracking all model electrons the process yields a complete set of face currents that satisfy the condition that the divergence of j is zero.

2 ENCLOSED CURRENT AND TOROIDAL MAGNETIC FIELD

After all orbits are tracked, the face current information is used to find values of enclosed current and B_a, both vertex quantities. The enclosed current is the total beam current that passes between the point and the axis. It is relatively easy to find enclosed current in the structured mesh of ETrak. Following Fig. 1, vertices are labeled in the horizontal direction (z) with the index k and in the vertical direction (r) with index l. The procedure for standard vacuum points is first to set the enclosed current equal to zero along the row l=1. Next the code works outward toward increasing l, processing all vertices in a logical row. ETrak uses a mesh where all standard vertices are surrounded by six elements and connected to six vertices along six faces. Figure 2 shows the face and vertex numbering conventions around Vertex 0. Faces 4 and 5 connect to vertices with smaller values of l, 3 and 6 to vertices on the same tow, and 1 and 2 to higher l.

At each point, the code checks connections to points 4 and 5 on row l-1. These points should already have values of enclosed current, I_4 and I_5 . The enclosed current at the point is given by

$$\Delta z_4 = z_0 - z_4, \Delta z_5 = z_5 - z_0,$$

$$\bar{I} = \frac{I_4 \Delta z_5 + I_5 \Delta z_4}{\Delta z_4 + \Delta z_5},$$

$$\Delta \bar{I} = \frac{\Delta I_4 \Delta z_5 + \Delta I_5 \Delta z_4}{\Delta z_4 + \Delta z_5},$$

$$I_0 = \bar{I} + \Delta \bar{I}.$$

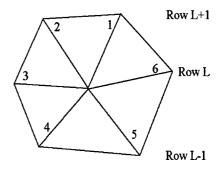


Figure: Relative face and vertex numbers at Point 0.

The equation involves vertex coordinates z_4 , z_5 and z_0 and connecting face currents ΔI_4 and ΔI_5 . Weighting in the formula gives preference to current on vertical faces.

Field averaging between iteration cycles is essential for the stability of the ray-tracing technique. Consider, for example, space-charge assignment for Child law emission. On one cycle, a strong electric field near the cathode would lead to large particle currents. The high space charge would suppress the local field on the next cycle. The solution is to average the newly-calculated space-charge with values from previous cycles. In ETrak the same averaging algorithm is used for beam-generated magnetic field to preserve the balance of forces.

$$B_{\theta}(new) = \varsigma \frac{\mu_{\theta} I_{enc}}{2\pi r} + (1 - \varsigma) B_{\theta}(old).$$

In the equation, the quantity ζ is a number less than unity.

3. BOUNDARY CONDITIONS

For valid interpolations of B_θ over the solution volume, material vertices adjacent to vacuum must have correct values of enclosed current. There are two classes of boundary vertices:

- Emission points. These should include the current of the emitted beam even though the electrons do not cross the associated faces.
- Collector vertices. Particles pass through some of the connected faces when stopping in a material.
 The enclosed current must reflect the incident beam current over all enclosed faces.

Regarding the emission surface, the challenge is to define a method that works for all cathode shapes and arbitrary distributions of electrons. In ETrak an emission surface is a special set of vertices marked as a line region during mesh generation. The program analyzes the mesh, making a list of all faces on the emission surface and confirming that they are adjacent to vacuum. The set of nearby initial electrons is either specified by the user or generated by the code using a space-charge algorithm. In either case the code processes the list of electrons,

associating each particle with the closest emission face. The present particle currents are assigned to the faces at the beginning of each iteration cycle. To account for concave spherical cathodes and other reentrant structures, the assigned current is always positive, regardless of the emission direction.

The next task is to assign face currents to general material boundaries. For the enclosed current calculation all material regions are treated as perfect conductors. The following procedure is used to process boundary vertices.

- Make a list of all vertices adjacent to material regions and connected to at least one vacuum element.
- Track electron orbits and assign face currents.
- Carry out the enclosed current calculation described in the previous section. Handle boundary points the same as standard points if they have one or more downward connections.
- If a boundary point has no downward connection to a processed vertex, use the following rule. Check Points 3 and 6. If one of the points has been processed, the enclosed current at Point 0 equals the enclosed current of the neighbor plus the face current of Side 6 or 3.
- If there are no sideways connections, check upward connections to Vertices 1 and 2. In this case, the enclosed current equals the enclosed current of the upper point *minus* the face current of Side 1 or 2.

In most situations, the rule propagates the enclosed current over the boundary correctly, even for highly reentrant collector structures.

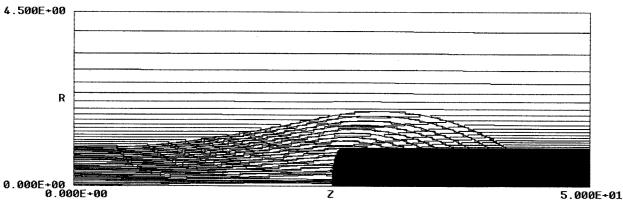
4 BENCHMARK CALCULATIONS

ETrak was applied to a variety of high-voltage gun designs previous treated with Trak 4.0[8]. The code showed good agreement and smooth beam distributions without use of the relativistic force approximation. The solution of Figure 3 demonstrates the accuracy of the technique. The test addresses free expansion of a uniform current-density, 1 MeV, 617.4 A electron beam with an initial radius of 1.0 cm. The plot shows computed orbits of 20 model electrons and contours of

constant B_a. Here the transverse forces are created solely by the beam. The electric and magnetic forces balance to within $1/\gamma^2 = 0.114$. In the absence of the downstream collector the code predicts an envelope expansion over the 50 cm solution length within 0.3 per cent of the analytic prediction [9]. Figure 3 shows a solution with the addition of a grounded collector with spherical tip (note that there is a 5X vertical exaggeration in the plot). The entrance surface is defined as an emission plane and is treated as a Neumann boundary for the electric field calculation. The parallel magnetic field contours show the effectiveness of the emission surface current assignment. The beam follows the free expansion curve until it reaches the vicinity of the collector. The rod partially cancels the beam electric field allowing the magnetic forces to predominate. In this way, the smalldiameter rod collects the full beam current. Note that this effect depends critically on the correct spatial variation of enclosed current over the outer surface of the collector. The parallel magnetic contours outside the beam confirm that the method conserves current.

- [1] See, for instance, S. Humphries, Field Solutions on Computers (CRC Press, Boca Raton, 1997), Sect. 10.7.
- [2] W.B. Herrmannsfeldt (Stanford Linear Accelerator Center, SLAC-331,1988), unpublished.
- [3] A.C. Paul (Lawrence Berkeley Laboratory,LBL-13241,1982), unpublished.
- [4] J.E. Boers (Sandia National Laboratories, SAND 79-1027,1980), unpublished.
- [5] R. True, IEEE Trans. Nucl. Sci. NS-32, 2611 (1985).
- [6] S. Humphries, J. Comp. Phys. 125, 488 (1996).
- [7] S. Humphries, N. Dionne and J. Petillo, Secondary-electron emission models for charged-particle simulations on a conformal triangular mesh, submitted to Phys Rev Special Topics Accelerators and Beams.
- [8] S. Humphries, in R. Ryne (ed) Computational Accelerator Physics (APS, New York, 1994), 597.
- [9] See, for instance, S. Humphries, Charged Particle Beams (Wiley, New York, 1990), Sect. 5.4.

Figure 3: Relativistic beam impinging on a grounded collector. Dimensions in cm.



TRACKING OF ELECTRON BEAMS WITH NUMERICALLY DETERMINED SPACE CHARGE FORCES*

J. Staats*, T. Weiland, Theorie Elektromagnetischer Felder, TU Darmstadt; S. Kostial, A. Richter, Institut für Kernphysik, TU Darmstadt

Abstract

A tracking algorithm for the description of electron beams using grid-based space charge fields is compared to a method based on point-to-point calculations. The charged particles' equations of motion are solved with a fifth-order embedded Runge-Kutta method using the concept of macroparticles. The space charge forces are determined in the bunch's restframe with a multigrid-method [1].

1 INTRODUCTION

In cases of space charge fields being approximately piecewise constant, the space charge fields can be determined in the beam's rest frame. Using a grid-based method for calculating the electrostatic potential φ' within the beam has advantages with respect to particle statistics. The electric field of a relativistic electron with velocity ν in the laboratory system is focused in transverse direction. The space angle enclosing a certain share of the electron's electric flux (field cone) thus has a decreasing transverse opening angle if the particle's energy increases. The transversal dominated space charge fields of a 10 MeV electron beam demonstrate the asymmetry due to relativistics (see Fig. 1).

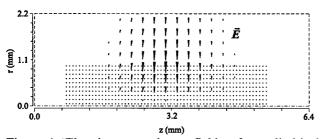


Figure 1: Electric space charge fields of a cylindrical Gaussian electron beam, 10 MeV, calculated with MAFIA TS2 code.

Calculating space charge forces by summation over all point-to-point interactions one has to use enough particles in order to keep the statistical fluctuation of the number of adjacent particles lying within a particle's field cone small. That is to say, the granularity of the charge density represented by the macroparticles has to be, depending on

A grid-based algorithm for field calculation determines the space charge fields from a charge density free from granularity, typically modeled linearly between the grid points. The number of particles N required for approximating the charge density appropriately is therefore independent of energy. In addition, assuming the minimum number of particles per grid-cell being fixed, the computation time for determining the fields in a grid-based algorithm is linear in N when using a multigrid-method. The number of operations in point-to-point calculations however is of $O(N^2)$.

2 GRID BASED METHOD

An objectoriented 3D tracking program Q has been developed [2] realizing a grid-based tracking algorithm.

The finite difference Poisson solver developed for the tracking code Q uses a geometrical Full-Multigrid-method [3]. This algorithm's linear dependency of the number of operations on the number of gridpoints is shown in Fig. 2. After the conversion of the charge-density onto a coarsest grid, Poisson's Equation is solved directly. The solution is succesively interpolated onto the next, by a factor of two finer grid, on which high frequency errors are smoothed by several relaxation steps using a classical iteration scheme. Low frequency errors are smoothed by multigrid-cycles of V type. The electric field at the distinct particle positions is determined by linear interpolation and transformed into the lab frame (see Fig. 3).

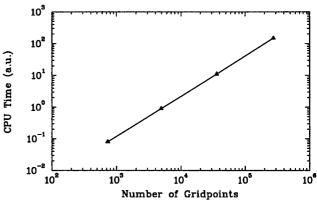


Figure 2: CPU-time for solving Poisson's Equation with a Full-MG solver showing a linear growth.

energy, sufficiently fine-grained in order to model the physical interaction properly.

^{*} Work supported by DFG under contract No. Ri 242/12-1 and through the Graduiertenkolleg "Physik und Technik von Beschleunigern"

^{*} Email: staats@temf.tu-darmstadt.de

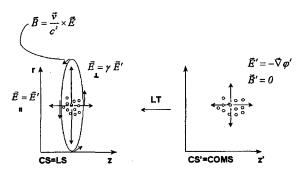


Figure 3: Lorentz-transformation of the electric field.

3 POINT-TO-POINT METHOD

The simulations with a code using a point-to-point method to calculate the space charge fields were performed with the **General Particle Tracer** (**GPT**) [4], a well established 3D tracking code. As tracking code Q it uses a fifth-order embedded Runge-Kutta method with adaptive stepsize control to integrate the particles' equations of motion.

The space charge induced fields at the position of particle i are the summation of the fields generated by the particles $j \neq i$. In the rest frame of macroparticle j this particle generates an electric field

$$\vec{E}'_{j\to i} = \frac{q\vec{r}'_{ji}}{4\pi\varepsilon_0 |\vec{r}'_{ii}|^3}$$

which acts on particle i, \vec{r}'_{ji} is the distance measured in the rest frame. Transforming back to the lab frame yields the electromagnetic fields. To avoid unrealisticly strong defocussing effects if two macroparticles are moving close together, the macroparticles act as clouds with radius R instead of pointlike charges. Overlapping of two homogeneous particle clouds results in a reduced electric field:

$$\vec{E}'_{j \to i} = \frac{q\vec{r}'_{ji}}{4\pi\varepsilon_0 R^3} \text{ if } |r| < R$$

The results of the simulation strongly depend on the number of macroparticles N per bunch. By increasing N the effect of granularity, which induces an overestimation of the space charge effects, is reduced.

For a given number of macroparticles the radius of the particle clouds takes an effect on the results. An oversized radius reduces the space charge fields. By reducing the radius the behaviour of the bunch like the emittance and the transverse standard deviation converges.

4 COMPARISON CALCULATIONS

In the model problem a uniformly charged cylindrical beam with a total charge of 1 nC, a transverse standard deviation of $\sigma_x = 0.5 \, \text{mm}$ and zero emittance drifts at an energy of 10 MeV over a length of 1.5 m. These beam parameters are comparable to those being discussed to

arise in the capture cavity of the Tesla Test Facility, there with a normalized emittance of 1 mm mrad.

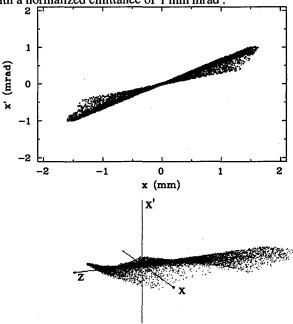


Figure 4: Phase space distribution after 1.0 m drift calculated with **Q**. The deviation from a line shape is due to nonlinear transverse effects at the head and the tail of the bunch, as can be seen in the 3D plot with z (direction of drift) as the second abscissa.

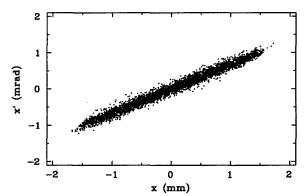


Figure 5: Phase space distribution after 1.0 m drift calculated with GPT.

There is a good agreement in the results of the spacial standard deviation between the two models (see Fig. 6). In the point-to-point method the description of the emittance as the most significant statistical quantity is rather strong dependent on the number of macroparticles. The low dependency of the emittance determined with the gridbased method is due to the fact, that the charge density used for calculating the electric field is free from granularity.

This independency of the determined space charge forces on statistics gives rise to the description of nonlinear effects away from the beam's longitudinal center and a conservation of phase space volume at-fixed z (see Fig. 4).

The deviation in the phase space plot calculated with GPT (see Fig. 5) is significant. In the center of a symmetric relativistic beam the determined phase space volume is not conserved due to a high statistical relative error in the relativistic electromagnetic fields determined from point-to-point calculations.

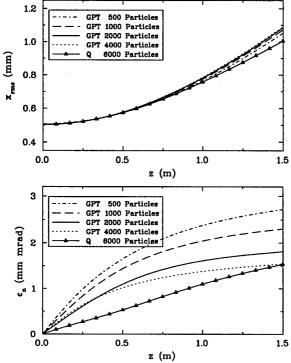


Figure 6: x_{ms} and transverse emittance along driftspace.

4.1 Particle-in-Cell Method and analytical linear Model

In a Particle-in-Cell scheme (eg. the $2\frac{1}{2}$ -dimensional MAFIA TS2 code [5]) the coupled problem of Maxwell's Equations and the equations of motion are solved consistently. As can be seen from calculations with a Gaussian beam ($\sigma_z = 0.8 \text{ mm}$), presented in Fig. 7, the methods lead to comparable results on the first 0.5 m. The deviation arising in the TS2 result is understandable due

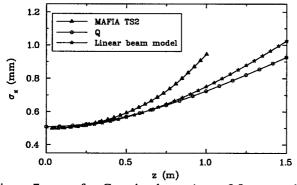


Figure 7: σ_x of a Gaussian beam ($\sigma_z = 0.8 \, \text{mm}$ at 10 MeV) along driftspace.

to numerical noise in the field calculation, which would be compensatable by an increase in the number of particles only.

The high number of time steps, which are necessary to dissolve the beam's charge-density spacially (Courant Levy Condition), is countered by the fact, that the problem of field calculation is restricted to a matrix-vector multiplication [5]. The main computation time in an electrostatic code on the other hand is needed for solving Poisson's Equation. It's stability in time depends mainly on the trajectories' integration algorithm. Computation time thus depends on the interval, within which the assumption of a piecewise constant space charge field holds and can remain practible for long distance calculations in such cases.

Alternatively to particle methods the calculation with an analytical model for a self-consistent description of a beam in an accelerator [6], which takes into account linear forces and is suited for rapid estimations of the significant beam parameters, leads to a comparable result.

5 CONCLUSIONS

We find agreement between calculations with the tracking algorithm using grid-based space charge fields **Q**, the point-to-point method **GPT** and **TS2** concerning the spatial distribution. The description in phase space however leads to different results. One explanation favoured by the authors is, that in a point-to-point method the granularity of the charge density modeled by the macroparticles limits the achievable accuracy of the space charge forces determined in a relativistic beam. This leads to a lower estimation of nonlinear effects away from the transversal center of a space charge dominated electron beam and to a stronger statistical error in regions of linear space charge forces. The statistical limits of a Particle-in-Cell code such as MAFIA TS2 due to numerical noise in the field calculation were shown.

- [1]J. Staats, "Simulation of Low Energy Electron Beams", Poster in the course of CERN-Accelerator School September'97 in Gjøvik, Norway.
- [2] J. Staats, T. Weiland, "Tracking Program Q for the Simulation of Low Energy Electron Beams in a Linear Accelerator", Grako News 1/98, Graduiertenkolleg Physik und Technik von Beschleunigern, (1998)
- [3]William H. Press, Brian P. Flannery, Saul A. Teukolsky and William T. Vetterling, "Numerical Recipes, The Art of Scientific Computing", Cambridge University Press, 2nd edition, (1992)
- [4] GPT User Manual, Pulsar Physics, Flamingostraat 24, 3582 SX Utrecht. The Netherlands.
- [5]P. Schütt, this conference
- [6] A. Novokhatski, T. Weiland, "The Model of Ensembles for the Beam Dynamics Simulation", this conference

THE MODEL OF ENSEMBLES FOR THE BEAM DYNAMICS SIMULATION *

A. Novokhatski[†], and T. Weiland, TEMF, TU Darmstadt

Abstract

It is proposed to use the "Ensembles" of particles for modeling the beams in accelerators. Each ensemble describes the longitudinal and transverse dynamics of the nonmonochromatic bunch in the six dimensional phase space, taking into account all coupling effects, coming from the relativistic relation between variation of the velocity projection and energy spread. Ensemble parameters include average values of coordinate and momentum, bunch dimensions, noncorrelated momentum spread and all second order correlation parameters. Self- consistent equations for the Ensemble are derived from the Vlasov equation. The presentation by vector and matrix gives the possibility to define an implicit algorithm for computer simulations. Examples of application of this model for the calculation of the beam dynamics in the accelerators are presented.

1 INTRODUCTION

In the beam dynamics calculations the beam is usually described by a set of "macro" particles. "Macro" particle is an ensemble of particles for the bunch field calculation. However for the trajectory calculation, a "macro" particle becomes a single particle. The motion of the particles inside "macro" particle is not considered. Therefore, the simulation of the beams with small emittance needs a relatively large number of 'macro" particles.

There is another possibility to describe the beam by the phase distribution function $f(\overrightarrow{r}, \overrightarrow{p})$ of particle density in the phase space of coordinates and momenta. Phase distribution function f satisfies the Vlasov equation

$$\frac{d}{dt}f = \frac{\partial f}{\partial t} + \overrightarrow{grad_r}(f) \bullet \overrightarrow{\overrightarrow{p}}c + \overrightarrow{grad_p}(f) \bullet \overrightarrow{\overrightarrow{F}}c = 0$$

where normalized momentum (\overrightarrow{p}) and energy (γ) are used

$$\overrightarrow{p} = \frac{\overrightarrow{P}}{mc}$$
 $\gamma = \frac{E}{mc^2} = \sqrt{1 + \overrightarrow{p} \cdot \overrightarrow{p}}$

and \overrightarrow{F} is the force, acting on the particles $\frac{d}{dt}\overrightarrow{p} = \frac{\overrightarrow{F}}{mc}$. The direct numerical solution of the Vlasov equation in a 6 dimensional space needs a great amount of the computer memory. If we take only 50 mesh points for each direction, then the total number of mesh points will be $50^6 = 1.56 \ 10^{10}$, that is equal to the real number of particles in the bunch.

2 SELF-CONSISTENT BEAM MODEL

However, the Vlasov equation can be numerically solved "much easily" for the linear forces. In this case the distribution function is described by a small number of parameters, only by the first and second order moments. Let us define such a bunch as an "Ensemble". If we have the full description of the dynamics of an Ensemble, then by a set of Ensembles we can describe the dynamics of any beam and all kinds of forces. Nevertheless, even one Ensemble can give a lot of information about beam dynamics in accelerator. Opposite to the usual model [1], [2], [3] for the second order moments, the model of Ensembles [4] includes longitudinal motion of the particles, and all corresponding correlations with transverse motion.

2.1 Presentation by Vectors and Matrices

The average coordinate and momentum of the Ensemble are described by vectors $\bar{\mathbf{X}}$ and $\bar{\mathbf{P}}$. The second order moments

$$M_{\xi
u} = \langle \xi
u
angle = \int f(t, \overrightarrow{r}, \overrightarrow{p}) (\xi - \langle \xi
angle) (
u - \langle
u
angle) d \overrightarrow{r} d \overrightarrow{p}$$

are grouped in matrices $\{S\},\{L\}$ and $\{T\}$

$$S_{ik} = M_{x_i x_k}$$
 $L_{ik} = M_{x_i p_k}$ $T_{ik} = M_{p_i p_k}$ $i, k = x, y, z$

The determinant of the matrix $\{M\}$

$$V^2 = det\{\mathbf{M}\} = det \left(egin{array}{cc} \mathbf{S} & \mathbf{L} \\ \mathbf{L^t} & \mathbf{T} \end{array}
ight)$$

is the square of the 6 dimensional normalized emittance of the Ensemble. In the case of the uncoupling motions the full emittance is the multiplication of emittance projections

$$\epsilon_{\nu} = \sqrt{{\sigma_{\nu}}^2 {\sigma_{p_{\nu}}}^2 - \langle \nu p_{\nu} \rangle^2} = \sqrt{M_{\nu\nu} M_{p_{\nu}p_{\nu}} - M_{\nu p_{\nu}}^2}$$

However, if the correlated moments appear, then the emittance projections are changed in order to keep the full emittance constant. For example, the full emittance is the difference of the positive values

$$V^2 = \epsilon_y^2 (\epsilon_x^2 \epsilon_z^2 - M_{xp_z}^2 \sigma_{p_x}^2 \sigma_x^2)$$

when the moment M_{xp} , is excited.

2.2 Time Equations

Time equations for the Ensemble parameters can be derived from the Vlasov equation under two assumptions:

1) If the applied forces satisfy the condition

$$\langle \mu ullet \overrightarrow{grad_p} \overrightarrow{\overrightarrow{F}} \rangle = 0$$

^{*} Work supported in part by DESY, Hamburg.

[†] Email: novot@temf.tu-darmstadt.de

for any Ensemble parameter μ , then the full emittance is invariant.

2) The energy deviation in the beam is not very large and the energy can be presented in the following expanded way

$$\frac{1}{\gamma} = \frac{1}{\gamma_m} - \frac{1}{\gamma_m^3} \sum_n [\langle p_n \rangle (p_n - \langle p_n \rangle) + \frac{1}{2} ((p_n - \langle p_n \rangle)^2 - M_{p_n p_n})]$$

where γ_m is the average beam energy

$$\gamma_m = \sqrt{1+\sum_n[\langle p_n\rangle^2+M_{p_np_n}]}$$
 In this presentation the average velocity \overrightarrow{v} contains addi-

tionally the momentum correlations

$$v_n = \langle \frac{p_n}{\gamma} \rangle = \frac{\langle p_n \rangle}{\gamma_m} - \frac{1}{\gamma_m^3} \sum_k \langle p_k \rangle M_{p_n p_k}$$

mula for average value

$$\frac{\partial}{c\partial t}\langle\mu\rangle = \langle \overrightarrow{grad_r}\mu \bullet \overrightarrow{\overrightarrow{p}}\rangle + \langle \overrightarrow{grad_p}\mu \bullet \overrightarrow{\overrightarrow{F}}\rangle$$

With this formula we present the time equations for moments in vector and matrix form: $\frac{\partial}{\partial t} \bar{\mathbf{p}} = \mathbf{F}$

$$\begin{split} \frac{\partial}{\partial t} \mathbf{\bar{P}} &= \mathbf{F} \\ \frac{\partial}{\partial t} \mathbf{\bar{X}} &= \frac{1}{\gamma_{\mathbf{m}}} \{ \mathbf{E} - \frac{1}{\gamma_{\mathbf{m}}^2} \mathbf{T} \} \otimes \mathbf{\bar{P}} \\ \frac{\partial}{\partial t} \{ \mathbf{S} \} &= \{ \mathbf{V} \} \otimes \{ \mathbf{L} + \mathbf{L^t} \} \\ \frac{\partial}{\partial t} \{ \mathbf{L} \} &= \{ \mathbf{V} \otimes \mathbf{T} + \mathbf{F_x} \otimes \mathbf{S} + \mathbf{F_p} \otimes \mathbf{L} \} \end{split}$$

$$\frac{\partial}{c\partial t} \{ \mathbf{T} \} = \{ \mathbf{F_x} \otimes \mathbf{L} + \mathbf{F_p} \otimes \mathbf{T} \} + \{ \mathbf{F_x} \otimes \mathbf{L} + \mathbf{F_p} \otimes \mathbf{T} \}^{\mathbf{t}}$$

Matrix {V} is the symmetric matrix of combinations of velocity pairs $(v_i \text{ and } v_k)$

$$V_{ik} = \frac{1}{\gamma_m} (\delta_{ik} - v_i v_k)$$
 $v_k = \frac{\tilde{p_k}}{\gamma_m}$

 $\delta_{ik} = 1$, if i = k and $\delta_{ik} = 0$, if $i \neq k$

Vector \mathbf{F} is the normalized average force $\mathbf{F} = \frac{1}{mc^2} \mathbf{F}(\mathbf{\bar{X}}, \mathbf{\bar{P}})$

$$\mathbf{F} = \frac{1}{mc^2} \mathbf{F}(\mathbf{\bar{X}}, \mathbf{\bar{P}})$$

Matrices $\{F_x\}$ and $\{F_p\}$ are coordinate and momentum derivatives of the force

$$F_x^{ik} = \frac{1}{mc^2} \frac{\partial}{\partial x_k} F^i \mid_{\bar{X}, \bar{P}} \quad F_p^{ik} = \frac{1}{mc^2} \frac{\partial}{\partial p_k} F^i \mid_{\bar{X}, \bar{P}}$$

PROPERTIES OF THE ENSEMBLE

3.1 Fundamental Conservation Laws

We can check the model for realization of the dynamic laws for average values. It is easy to show, that from the presented above equations one obtains:

$$\frac{\partial}{c\partial t} \langle \gamma \rangle^2 = \frac{\partial}{c\partial t} \gamma_m^2 = 2 \langle \overrightarrow{p} \bullet \overrightarrow{F} \rangle$$

$$\frac{\partial}{c\partial t} \overrightarrow{\mathcal{M}} = \frac{\partial}{c\partial t} \langle \overrightarrow{r} \times \overrightarrow{p} \rangle = \langle \overrightarrow{r} \times \overrightarrow{F} \rangle$$

So, the model fulfills the fundamental conservation laws for average momentum, energy and angular momentum.

3.2 **Emittance Equation**

We can also estimate the modification of the full emittance for the case, when the first assumption is not fulfilled. When we have only longitudinal force and transverse average momenta are zero, the model gives the following equation for longitudinal emittance

$$\frac{\partial}{c\partial t}\epsilon_z^2 = 2M_{zz}\langle (p_z - \langle p_z \rangle) \frac{F_z}{mc^2} \rangle - 2M_{zp_z}\langle (z - \langle x \rangle) \frac{F_z}{mc^2} \rangle$$

When the force is $F_z = \alpha mc^2 p_z$ (proportional to the momentum) the equation takes the form

$$\frac{\partial}{\partial t}\epsilon_z^2 - 2\alpha\epsilon_z^2 = 0$$

From this equation we get the exponential growth or damping of the emittance in time. The module of $1/\alpha$ determines the effective time and the sign of α gives the type of the force: generator ($\alpha > 0$) or friction ($\alpha < 0$). We note, that at the same time the transverse emittances are invariant

$$\frac{\partial}{c\partial t}\epsilon_x^2 = 0 \qquad \frac{\partial}{c\partial t}\epsilon_y^2 = 0$$

3.3 Bunch Compression in Free Space

Here we check the modification of the relativistic bunch in free space, when it has negative initial correlated momentum spread $M_{xp_x}^0$, or $M_{yp_y}^0$, or $M_{zp_z}^0$ If $\langle p_z \rangle \gg \langle p_x \rangle$, then

$$M_{xx} = M_{xx}^0 + 2\frac{c\Delta t}{\gamma_m}M_{xp_x}^0 + (\frac{c\Delta t}{\gamma_m})^2 M_{p_x p_x}^0$$

$$M_{zz} = M_{zz}^0 + 2\frac{c\Delta t}{\gamma_m^3} M_{zp_z}^0 + (\frac{c\Delta t}{\gamma_m^3})^2 M_{p_zp_z}^0$$

The minimum size of the bunch is determined by the emittance and uncorrelated momentum spread

$$min(\sigma_x^2) = M_{xx}^0 - \frac{(M_{xp_x}^0)^2}{M_{p_xp_x}^0} = \frac{\epsilon_x^2}{M_{p_xp_x}^0} = \frac{\epsilon_x^2}{\sigma_{p_x}^2}$$

APPLICATION OF THE MODEL

The derived equations for the Ensemble parameters are nonlinear. So the numerical calculations need implicit algorithm. Nevertheless there are some analytical solutions for simple cases. We present examples of analytical and numerical solutions.

4.1 The Ensemble in an Accelerating Structure

Let the center of the bunch move with the speed equal to the phase velocity of the accelerating wave, having the phase displacement φ_0 . Accelerating force is approximated by the linear part $\frac{F_z}{mc^2}=e+\delta E(z-\bar{z})$

$$e = \frac{e}{mc^2} E_{acc} \cos \varphi_0 \quad \delta E = \frac{e}{mc^2} E_{acc} \frac{2\pi}{\lambda} \sin \varphi_0$$

The model gives the following equations for M_{zz} and M_{zp} .

$$\frac{\partial}{c\partial t}M_{zz} = \frac{2}{\gamma_m^3}M_{zp_z}$$

$$\frac{\partial}{c\partial t}(\gamma_m^3\frac{\partial}{c\partial t}M_{zp_z}) + 4\delta E M_{zp_z} = \delta E M_{zz}\frac{\partial\gamma_m^3}{c\partial t}$$

From these equations we can estimate the frequency of the phase oscillations ϖ , when $\sin \varphi_0 > 0$

$$\varpi/c = \sqrt{\frac{\delta E}{\gamma^3}} = \sqrt{\frac{2\pi}{\lambda}} \frac{eE_{acc}}{\gamma^3 mc^2} \sin \varphi_0$$

We've got exactly the M.Kapchinskiy formula [1].

4.2 Space Charge Effect

We use the estimation for the space charge force, derived out for the relativistic bunch of ellipse form, in the approx-

imation of the homogenous charge density [4]
$$\frac{\overrightarrow{F}}{mc^2} = \frac{r_0 N}{\gamma^2} \frac{\overrightarrow{R}}{V_g} = \alpha \overrightarrow{R} \qquad V_g = (\sqrt{5})^3 \sqrt{\det\{\mathbf{S}\}}$$

The force is linear with the distance R and inversely proportional to the effective geometrical volume V_q . N is the number of particles in the bunch, r_0 is the radius of the electron $r_0 = e^2/mc^2$.

Our model gives the following equations for the transverse beam size $\sigma_x = \sqrt{M_{xx}}$ and correlated momentum spread $\sigma_{p_x} = \sqrt{M_{p_x x}}$

$$\begin{split} \frac{\partial}{c\partial t}M_{xx} &= \frac{2}{\gamma_m}M_{xp_x} \\ \frac{\partial^2}{c^2\partial t^2}M_{xp_x} &- \frac{4\varpi}{\gamma_m}M_{xp_x} = 0 \end{split}$$

The effective distance L_{eff}^{\perp} , where the transverse beam size increases more than twice is

ases more than twice is
$$L_{eff}^{\perp}=\sqrt{rac{\gamma_m}{lpha}}=\sqrt{rac{\gamma_m^35\sqrt{5}\sigma_x\sigma_y\sigma_z}{r_0N}}$$

One can find that this estimation is in very good agreement with the classical consideration [1], [3]. The effective parameter for the longitudinal size is γ_m times larger.

4.3 The Ensemble in the Magnetic Field

A relativistic bunch with initial energy spread $\delta \gamma$ is injected into the magnetic field. Particles with different energy have different radiuses of rotation and therefore different time for one turn $T=\langle T \rangle \frac{\gamma}{\langle \gamma \rangle}.$ $\langle T \rangle$ and $\langle \gamma \rangle$ are respectively the average period and energy. The bunch size σ is $\sigma=\langle R \rangle \sin(2\pi \frac{t}{\langle T \rangle} \frac{\delta \gamma}{\langle \gamma \rangle})$

$$\sigma = \langle R \rangle \sin(2\pi \frac{t}{\langle T \rangle} \frac{\delta \gamma}{\langle \gamma \rangle})$$

After the time $T = \frac{\langle T \rangle}{4} \frac{\langle \gamma \rangle}{\delta \gamma}$ the bunch takes the circumference of the circle of the radius $\langle R \rangle$ Now we use numerical calculations to study this phenomena in the frame of our model. We have made calculations for the bunch with initial energy spread of ± 1 %. Computer results are shown on Fig.1. After 25 turns, the center of the bunch comes to the center of rotation and the beam size reaches the value of the rotation radius, the average momentum and its projections become zero, but the energy spread reaches maximum value. This position is repeated with the period of 50 turns.

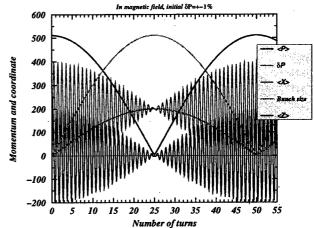


Figure 1: Average momentum, momentum spread, average X-coordinate, bunch size and average Z-coordinate.

4.4 Chicane Bunch Compression

Chicane bunch compressor consists of four rectangular dipole magnets, where the bunch is deflected in transverse direction and then is forwarded back. When the bunch gets the transverse displacement X, it also gets correlated moments M_{xp_x} , M_{zp_x} and $M_{p_xp_z}$, M_{xz} , that change the emittance projection

$$\Delta\epsilon_x^2 = \frac{X^2}{\gamma_m^2} M_{p_x p_x}^0 M_{p_x p_x}^0$$

In a symmetrical chicane the emittance projection comes back to the initial value. The space charge effect destroys the symmetry of the compression dynamics and increases the emittance projection. Results of computer simulations are presented on Fig.2.

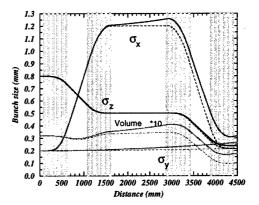


Figure 2: Bunch compression. The dashed lines show results without consideration of the space charge effect.

- [1] I.M.Kapchinskiy, Theory of Resonance Linear Accelerators, (Harwood Academic Publishers, Chur, 1985)
- [2] A.Chao, Physics of Collective Beam Instabilities in High Energy Accelerators, (J.Wiley & Sons, New York, 1993)
- [3] M.Reiser, Theory and Design of Charged Particle Beams, (J.Wiley & Sons, New York, 1994)
- [4] A.N.Novokhatski and T.Weiland,"Self-consistent Model for the Beams in Accelerators", Proc. of ICAP, Monterey, 1998.

3-D CALCULATIONS FOR A 4 kA, 3.5 MV, 2.5 MICROSECOND INJECTOR*

T. P. Hughes[†], R. E. Clark, Mission Research Corp, Albuquerque, NM S. S. Yu, Lawrence Berkeley National Laboratory, Berkeley, CA

Abstract

The DARHT-2 machine under construction at Los Alamos National Laboratory requires a long-pulse (2.5 μ sec) 2– 4 kA, 3.5 MV, low-emittance electron beam source. The injector is being designed at LBNL and consists of a largearea thermionic cathode mounted atop a vertical column. The 90° bend between the horizontally emitted beam and the column produces dipole and higher-pole fields which must be corrected. In addition, the fast rise of the current flowing into the vacuum tank excites RF modes which cause transverse oscillations of the beam centroid. We have modeled these effects with the 3-D electromagnetic code LSP. The code has models for pulsed power transmissionlines attached to boundaries, space-charge-limited emission and transport of charged particles, externally applied magnetic fields, and frequency-dependent absorption of RF. We calculate the transverse displacement of the beam as a function of time during the current pulse, and the positioning and thickness of ferrite absorber needed to damp the RF modes. The numerical results are compared to analytic calculations.

1 INTRODUCTION

The DARHT radiographic facility at LANL requires two linear induction accelerators at right angles to each other. The second accelerator is currently being designed and will provide a long-pulse (2 µsec flat-top) high current (2-4 kA) beam. This paper describes calculations carried out for the beam injector, shown in Fig. 1. The thermionic emitter is mounted on top of a vertical high-voltage conductor and insulator column inside a large vacuum vessel. This arrangement simplifies the problem of supporting the weight of the long insulator column. The diode is driven directly by a Marx bank which sits underneath the vacuum vessel. In order to produce a linear potential drop across the insulator column, resistors are wound helically around the insulator column, connecting the cathode dome on top to ground at the bottom. The beam is extracted at right angles to the high-voltage feed, and this results in both quasi-static and RF transverse forces on the beam. To calculate these effects, we have used the parallelized 3-D electromagnetic particle-in-cell code LSP[1].

2 QUASI-STATIC PERTURBATIONS

The largest perturbation to the beam is due to the transverse magnetic field produced in the AK gap by the current flowing in the vertical high-voltage conductor and the return

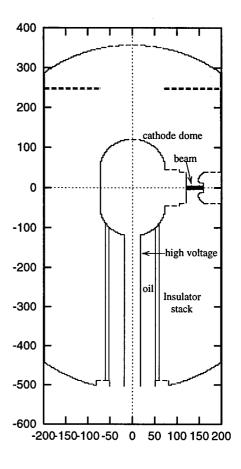


Figure 1: Injector geometry used in 3D simulations. Dimensions in cm.

currents flowing in the outer wall. The force is analogous to the hoop-stress in an electron-beam ring, and deflects the beam upward in Fig. 1. If we neglect wall currents, the Biot-Savart law applied to the net current I_{net} (high-voltage conductor current less the resistor current) gives

$$B_{\perp} \approx \frac{\mu_0 I_{net}}{4\pi R_{AK}} \tag{1}$$

in the AK gap, where R_{AK} is the radius of the AK gap. For $I_{net}=4\,\mathrm{kA}$, $R_{AK}=1.35\,\mathrm{m}$, this gives about 3 gauss. The resulting deflection of the beam is given roughly by $\frac{1}{2}(eB_{\perp}/\gamma m_e c)d^2$, (where d is the AK gap length and γ is the average relativistic factor in the gap) which is of order a few mm at the anode. In order to include the effect of wall-currents, and obtain time-dependent effects, we carried out a calculation through the approximately 500 ns rise-time of the voltage pulse using LSP. In this calculation, the Marx

^{*} Work supported by Los Alamos National Laboratory.

[†]Email: tph@mrcabq.com

bank is approximated using a simple $745\,\Omega$ transmission-line (matched to the nominal $875\,\Omega$ diode impedance in parallel with a $5\,k\Omega$ resistor) connected to the coaxial conductors at the bottom of Fig. 1. The numerical grid dimension is about 3 cm and the timestep is the Courant-condition value. The $5\,k\Omega$ resistor is represented by a cylindrical shell of finite conductivity. The current and voltage at the inlet (the bottom of Fig. 1) and the beam current and AK voltage are shown in Fig. 2. The difference between the steady-

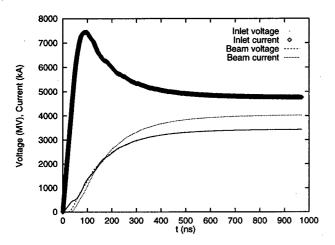


Figure 2: Inlet and AK current and voltage vs. time

state inlet current and the beam current flows in the $5 \, k\Omega$ resistor on the inside of the insulator stack. The effect of the asymmetry of the wall return currents on the azimuthal magnetic field is shown in Fig. 3, where we see that there

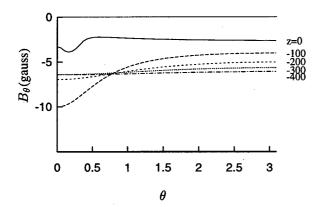


Figure 3: Azimuthal variation of B_{θ} at different z positions, at a radius of 134 cm. AK gap is at $\theta = 0$.

is a strong azimuthal asymmetry at the elevation of the AK gap.

The transverse magnetic field in the AK gap and the beam deflection 30 cm from the cathode (the AK gap is about 30 cm) are plotted in Fig. 4. In this simulation, no external focusing fields are applied. In practice, the anode contains solenoidal magnets to capture the high-current beam. To compensate for the transverse magnetic field in the AK gap, static dipole coils wound on the solenoidal

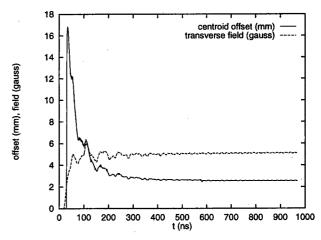


Figure 4: Transverse magnet field 14 cm from the cathode and beam deflection 30 cm from the cathode.

magnets will be used to steer the beam back on axis. If the deflecting field were proportional to the beam current, as would be the case if the system had a matched impedance from the Marx to the AK gap, then the correction fields would need to vary with the beam current to keep the beamhead on axis. However because of the large capacitance of the vacuum vessel (about 320 pF), the risetime of the current flowing into the vacuum vessel is much shorter than the risetime of the beam current (see Fig. 2). It turns out that the deflecting field in the AK gap is almost constant during the rise of the beam current, as shown in Fig. 4. As a result, static correction fields provides much better steering for the beam-head than one might expect.

On the cylindrical stalk to which the emitter is attached, the difference between the current flowing in the top and bottom halves is about 740 A for a 4 kA beam current. This asymmetry is consistent with a simplified calculation of the dipole current on the surface of a conducting cylinder immersed in a transverse magnetic field. The dipole current is given by $I_d=(1/\mu_0)\int_0^{\pi}B_{\theta}dl=4B_0a/\mu_0$ where B_0 is the transverse magnetic field as $r \to \infty$, and a is the radius of the stalk. Inserting the values for the stalk in Fig. 1, i.e., $a = 0.4 \,\mathrm{m}$, $B_0 \approx 3 \times 10^{-4} \,\mathrm{T}$ (3 gauss), we get $I_d \approx 380 \,\mathrm{A}$. This is in reasonable agreement with the simulation value $(740/2 = 370 \,\mathrm{A})$. On the emitting disk of the cathode, the current density is determined by the normal electric field stress, which is symmetric about the center of the cathode to a high degree. Thus the asymmetric currents flowing in the cathode stalk rearrange themselves on the emitting face to produce an (almost) symmetric beam. There may be some higher-pole magnetic fields associated with this process, but we have not yet attempted to extract them from the simulation.

3 RF PERTURBATIONS

The LSP calculations reveal that, in addition to a quasistatic deflection, the beam centroid undergoes smallamplitude transverse oscillations. The beam displacement 40 cm from the cathode surface is shown on a magnified scale in Fig. 5. The frequency spectrum shows peaks at 38,

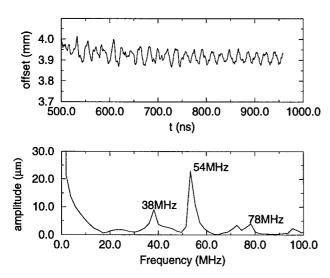


Figure 5: Beam transverse displacement vs. time plotted on a magnified scale, and its Fourier transform.

54 and 78 MHz. By externally driving the injector cavity at each of these frequencies to establish the mode-patterns, we find that they are predominantly TE_{11} -like modes. The dispersion-relation for TE_{11} modes in a cylindrical cavity of length L, radius b with a center conductor of radius a is

$$J_1'(a\gamma)Y_1'(b\gamma) - Y_1'(a\gamma)J_1'(b\gamma) = 0 (2)$$

where $\gamma = \sqrt{\omega^2/c^2 - k_z^2}$ and $k_z = (2n-1)\pi/L$, $n=1,2,\ldots$, is the axial wavenumber. For $a=0.5\,\mathrm{m}$ (the radius of the $5\,\mathrm{k}\Omega$ resistor), $b=2\,\mathrm{m}$, $L=8\,\mathrm{m}$, the lowest frequency is about 44 MHz. In the actual geometry, this is lowered to 38 MHz (see Fig. 5), probably by the AK gap structure. The frequencies in Fig. 5 are in rough agreement with eigenmode calculations using the MAFIA code and a LANL finite-element code[2].

Since the amplitude of the transverse oscillations is about the same magnitude as the design specification for beam alignment (100 μ m), schemes for damping the RF modes have being modeled numerically. In one scheme, we placed a ring of ferrite material 50 cm high and 3 cm thick around the inside wall of the vacuum vessel near the bottom, where the magnetic field of the TE₁₁ modes have a maximum. The effect was modeled using the dispersivematerial model in LSP, with the real and imaginary permeability values for "ETA-II ferrite" in the region of 50 MHz ($\mu_r \approx 50$, $\mu_i \approx 100$) as given in Ref. [3]. The numerical results show a strong damping of the RF-driven centroid oscillations to below 20 μ m, as shown in Fig. 6. In the simulation, the thickness of the ferrite ring cannot be made smaller than the radial cell-size (3 cm). Thinner ferrite may have a larger damping effect, however. From the expression for the reflection coefficient of a normally-

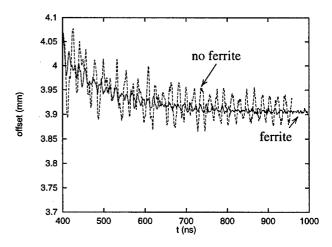


Figure 6: Comparison of beam centroid motion with and without ferrite-ring damper.

incident wave[3], we find that the optimal thickness for frequencies in the range 40–70 MHz is on the order of 1 cm. The enhanced absorption is due to reflection of the incident wave from the conducting surface behind the ferrite. We have verified this result in coaxial geometry using LSP.

4 CONCLUSIONS

The asymmetric design of the DARHT-2 injector produces both quasi-static and RF transverse displacements of the beam centroid. We have modeled these effects with the 3-D electromagnetic particle-in-cell code LSP. For a 4 kA beam current, the quasi-static transverse magnetic field is on the order of 3 gauss and produces a beam deflection of several millimeters at the anode. The effect will be corrected using static magnetic dipoles. The RF oscillations are produced by TE_{11} -like modes of the injector vessel excited by the current rise. Using ferrite damping, the oscillation amplitude can be reduced to $< 20 \,\mu\text{m}$. The DARHT-2 injector will initially be operated at 2 kA, which further reduces the amplitudes by about a factor of 2.

5 ACKNOWLEDGMENTS

We thank Bill Fawley, Enrique Henestroza, Eric Nelson and Dan Prono for useful discussions.

- [1] LSP is a product of Mission Research Corp. Albuquerque,
- [2] Enrique Henestroza (LBNL), Eric Nelson (LANL), private communications.
- [3] J. F. DeFord and G. Kamin, *Proc. 1990 Linear Accelerator Conference*, Albuquerque, NM, p. 384.

SIMULATION FOR AN RF GUN TEST APPARATUS IN THE SPring-8 LINAC

H. Abe, T. Asaka, H. Hanaki, <u>A. Mizuno</u>*, S. Suzuki, T. Taniuchi, K. Yanagida, SPring-8, Hyogo, 679-5198, JAPAN

Abstract

A photo cathode rf gun has been studied in the SPring-8 Linac to obtain lower emittance beams. In order to compare an observed beam emittance or beam size by simulation, we are also developing a beam tracking code for this test apparatus. In this paper, we describe the outlines of our code, and some calculation results for our test apparatus.

1 INTRODUCTION

In the SPring-8 Linac, we are developing a photo cathode rf gun for a conventional injector for the linac, and also for future applications such as a single pass FEL based on the SASE. We simultaneously require lower emittance of around several π mm·mrad and a higher peak charge of around several nano Coulomb per bunch, especially for the SASE. In order to achieve these conditions, we must develop some calculation codes that can predict beam characteristics as accurately as possible. However, the readymade tracking codes are not considered sufficient, because a lot of assumptions are included. Thus, we have developed our own simulation code that is suitable for our rf gun apparatus and includes as few assumptions as possible.

2 TEST APPARATUS

The outline of our apparatus and an rf cavity [1] are shown in Fig.1. The s-band rf cavity is a single-cell cavity since the field distributions in the cavity are simpler than that for a multi cell-cavity, and this makes a comparison with simulations easier. The bottom side of the cavity, which is made of copper, is used as a cathode. The rf from the right hand side port travels to the opposite port and is fed to a dummy load.

There are two sets of x-y slits for emittance measurement and a bending magnet for energy analyses.

3 OUTLINE OF OUR CODE

Our code is a three-dimensional particle tracking code that includes the production of electrons and space charge effects. As a result of recent increases in CPU speed, we try to calculate all space charge effects of each electron in the tracking code, but we assume that the charge and mass of each particle are larger than those of real electrons. The electron is accelerated in the cavity, but a calculation procedure for the space charge that includes acceleration becomes to be complicated so much. Thus, if we assume uni-

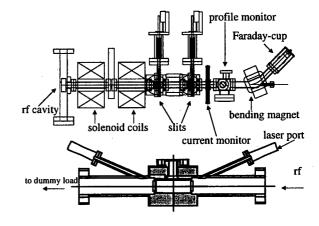


Figure 1: Rf gun test apparatus and cross section of rf cavity with two windows for laser injection.

form motion for electron, the electric and magnetic fields at point A caused by electron B are expressed as follows;

$$\mathbf{E}_{A} = \frac{1}{4\pi\epsilon_{0}\gamma^{2}} \frac{-e\mathbf{r}}{\left[|\mathbf{r}|^{2} - \frac{|\mathbf{v}_{B}\times\mathbf{r}|^{2}}{c^{2}}\right]^{3/2}} \qquad \mathbf{B}_{A} = \frac{1}{c^{2}}\mathbf{v}_{B}\times\mathbf{E}_{A}$$
(1)

where \mathbf{r} is a vector from B to A, \mathbf{v}_B is a velocity of electron B, and γ is a relative factor of electron B. These fields act on electron A as follows:

$$\mathbf{F}_A = -e\left(\mathbf{E}_A + \mathbf{v}_A \times \mathbf{B}_A\right) \tag{2}$$

The equation of motion for each electron is derived to the following equation and becomes adaptable for the Runge-Kutta method.

$$-e\left(\mathbf{v}\times\mathbf{B}+\mathbf{E}\right) = m_0 \frac{d\left(\gamma\mathbf{v}\right)}{dt}$$

$$\downarrow \qquad \qquad \downarrow \qquad \qquad (3)$$

$$\frac{d\mathbf{v}}{dt} = -\frac{e}{\gamma m_0} \left(\mathbf{v}\times\mathbf{B}+\mathbf{E}-\frac{\left(\mathbf{v}\cdot\mathbf{E}\right)}{c^2}\mathbf{v}\right)$$

We consider two types of extra electromagnetic sources in our code. One is an rf cavity for a part of the electron production, and the other is a set of two coils for focusing the electron beam. The fields in the cavity are calculated in the MAFIA code and are included in our code. The fields of the solenoid coils are calculated in our code. We treat the extra fields in the same way for the fields due to space charge as shown above in Eq.3.

We also consider the image charge effect caused from the copper cathode in our code.

^{*} Email: mizuno@spring8.or.jp

4 COMPARISON WITH OTHER CODES

It is important to confirm the accuracy of our code by comparing it with other conventional codes. Fig.2 shows some comparisons with MAFIA's calculations, which include the electron production and tracking in the cavity. Table 1 lists parameters in their calculations.

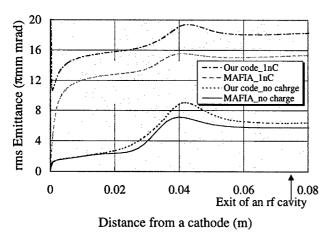


Figure 2: Comparison between our code and MAFIA ver4.0. An exit flange of rf cavity corresponds to 0.074 m in horizontal axis.

An initial rf phase ϕ in Table 1 is defined by

$$E_{cavity} = E_{max} \cos(\omega t - \phi) \tag{4}$$

To reduce memory size, MAFIA calculates in a two-dimensional space, so the definitions of some parameters are quite different from our three-dimensional code. However, in this case, input parameters are selected in the same way if possible. The transverse distributions of initial beam radius are set as gaussian in the cylindrical coordinate, and the field distribution in the cavity is calculated with the assumption that the cavity is perfectly cylindrical. An emittance in Fig.2 is the normalized rms emittance, which is defined by $\epsilon_x = \langle \gamma \rangle \langle \beta \rangle \sqrt{\langle x^2 \rangle \langle x'^2 \rangle - \langle x \cdot x' \rangle^2}$ for our code, and $\epsilon_r = \frac{1}{2} \langle \gamma \rangle \langle \beta \rangle \sqrt{\langle r^2 \rangle \langle r'^2 \rangle - \langle r \cdot r' \rangle^2}$ for MAFIA.

Table 1: Calculation Parameters used in Fig.2

Charge per bunch	1.0[nC] or none
Initial beam transverse profile	Gaussian
Initial beam radius on cathode	$1.5[\text{mm}](1\sigma)$
Longitudinal bunch profile	uniform
Bunch length	10[ps]
Initial emittance	$0[\pi \text{mm} \cdot \text{mrad}]$
Maximum field in cavity	150[MV/m]
Initial rf phase	45[degree]
MAFIA's mesh size	0.1[mm]

Our code and MAFIA show good agreement when the space charge effects are ignored. However, our code shows

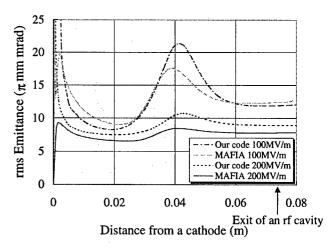


Figure 3: Comparison between our code and MAFIA. Charge is 1 nC per bunch. Initial beam spot size is 0.25 mm (1σ), which is almost comparable to MAFIA's mesh size. Maximum field in cavity varied as shown in the figure. Other parameters are the same as Table 1.

about 20 % larger emittance than MAFIA in the calculation including charges of 1 nC per bunch.

In the case of Fig.2, an initial beam radius is 1.5 mm, because MAFIA's mesh size of 0.1 mm is selected. However, in the actual experiment, the laser beam spot size is expected to be more smaller. Fig.3 shows calculation results for small size of 0.25 mm (1σ), which corresponds to an actual spot size of the laser beam.

In Fig.2, magnitudes do not agree, but the distributions of the rms emittance show good agreement. However in Fig.3, even distributions do not agree when the fields in the cavity are low. This shows the limits of MAFIA's ability. In MAFIA, to set up more smaller mesh size or even three-dimensional calculations are available, but more memories are needed. Moreover, if the fields in the cavity is low, the dependence on the space charge effects become large. Thus high calculation accuracy is required in these cases.

Our code also shows agreement with PERMELA, but it is useful when non-cylindrical fields or beams must be considered, or high accuracy is required.

5 CALCULATIONS FOR THE TEST APPARATUS

The calculation of the emittance varieties for the actual test apparatus were carried out using our code. In this section, we do not use the assumption of symmetrical cavity. The transverse distribution of the initial beam is set to be gaussian distribution in the rectangular coordinate. Fig.4 shows the results that depend on the cavity field.

The emittance becomes lower as the field in the cavity increases. In a region over 200 MV/m, it becomes almost constant. However, it is very difficult to increase the field of the cavity because of discharges or dark currents in actual experiment.

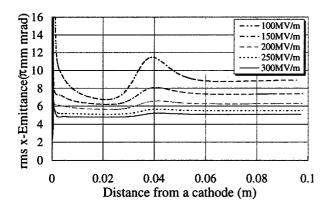


Figure 4: Emittance varieties depend on maximum cavity field changed from 100 MV/m to 300 MV/m. Charge is 1 nC per bunch. Initial beam radius is 0.25 mm (1σ). Other parameters are the same as Table 1.

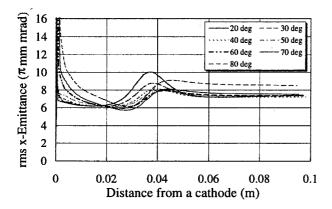


Figure 5: Emittance varieties depend on initial rf phase. Charge is 1 nC per bunch. Initial beam radius is 0.25 mm (1σ). Maximum field in cavity is 150 MV/m. Other parameters are the same as Table 1.

Figure 5 shows an initial phase dependence. As shown in Eq.4, if the initial phase is equal to zero, the field of the cavity becomes maximum when the laser is injected to the cathode surface. Therefore, the fields become lower as the initial phase increases. In a region from 20 degrees to 60 degrees, the emittances at the exit of the cavity are almost constant. This is because there is not so much difference in electron speed just after the cathode in this region, but in a region from 60 degrees to 80 degrees, the emittance becomes larger as the phase increases. This is because an electron speed just after the cathode becomes slower. In addition, a beam energy increases as the initial phase increases, and energy becomes almost constant of 3.5 MeV with the cathode field of 150 MV/m in a region of over 60 degrees. Thus, the optimum initial phase is considered to be around 60 degrees.

Figure 6 shows the calculated emittances and beam sizes from the cathode to the Faraday-cup, which is located 1.5 m downstream of the cathode. This simulation includes the fields of the two solenoid coils. The first coil is positioned 0.174 m from the cathode, and the second coil is located

at 0.374 m. The x and y beam sizes are slightly different because of the asymmetry of the cavity.

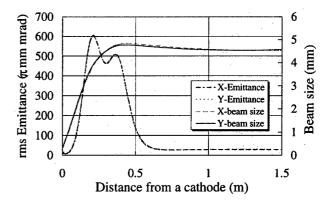


Figure 6: Calculated emittances and beam sizes from cathode to Faraday-cup. Parameters: 1nC charge, 0.25 mm (1σ) initial beam radius, 150 MV/m field in the cavity, 60 degrees initial rf phase,400 number of particles. Field of first and second solenoid coil corresponds to 1500 and 800 Gausses, respectively.

The x-emittance and y-emittance change dramatically in the solenoid coils, because the x and y component of magnetic fields are coupled in solenoids, that is, the x component of the fields is the function of both x and y, and even z. Therefore, the emittance must not be constant. The emittance becomes smaller after the solenoid coils by choosing the optimum solenoid fields. In the experiment, we can measure the emittance only downstream of the solenoids, so when we estimate the emittance of the cavity, this calculation is very important.

The beam size fits our apparatus flange size of ICF70 in this condition. The calculated emittances are higher than expected. But main purpose of our test apparatus is to make comparisons in simulations.

6 SUMMARY

The particle tracking code including space charge effects for the rf gun test apparatus has been developed. Calculated emittances show good agreement with MAFIA and PERMELA. However, our code is suitable for precious or asymmetric calculations. In the near future, we are going to remove an assumption of uniform motion for electron in our code. Now, the experiment has just started. In actual measurements, new problems will be occurred, for instance, the transverse or longitudinal photon distributions of a laser pulse have a great influence on the emittance in our calculation. We are expected to observe these effects in practice.

7 REFERENCES

[1] T.Taniuchi et al., "Initial Results of RF Gun Experiment", this conf., New York, (1999).

GREEN'S FUNCTION DESCRIPTION OF SPACE-CHARGE IN INTENSE CHARGED-PARTICLE BEAMS*

Mark Hess, Renato Pakter, and Chiping Chen
MIT Plasma Science and Fusion Center, Cambridge, MA 02139

Abstract

We present two- and three-dimensional models of space charge in intense charged-particle beams using Green's functions. In particular, we compute the electrostatic Green's function for a periodic collinear distribution of point charges located inside of a perfectly conducting drift tube. As applications of the Green's function description, we analyze the matching and transport of an initially axisymmetric beam into a quadrupole channel and the interaction of a particle with its induced surface charge.

1 INTRODUCTION

Our electrostatic models of periodic space charge in an infinite conducting cylinder use both 2-D and 3-D Green's functions. The Green's function provides the complete electrostatic potential inside of the interaction region due to both point charges and induced surface charges. From this potential, the electric fields at any point inside of the cylinder can be deduced, and space charge dynamics may be simulated.

Our paper is organized as follows. In Sec. 2, both 2-D and 3-D Green's functions are obtained analytically and computed. In Sec. 3, use is made of the 2-D Green's function to simulate matching of an axisymmetric intense beam into a quadrupole focusing channel, and of the 3-D Green's function to simulate single particle dynamics.

2 GREEN'S FUNCTION DESCRIPTION

The 3-D Green's function satisfies Laplace's equation with periodic point charge sources [1],

$$\nabla^2 G_{3D} = -\frac{4\pi}{r} \delta(r - r') \delta(\theta - \theta') \delta_L(z - z'), \qquad (1)$$

where

$$\delta_L(z-z') = \sum_{n=-\infty}^{\infty} \delta(z-z'-nL), \qquad (2)$$

L is the spacing of the point sources, the primed coordinates denote the locations of the unit point charges. The Dirichlet boundary condition and the periodic boundary conditions for translational and rotational symmetries require that

$$G_{3D}(r,\theta,z+L;x') = G_{3D}(r,\theta,z,x'),$$

$$G_{3D}(r,\theta+2\pi,z;x') = G_{3D}(r,\theta,z,x'),$$

$$G_{3D}(a,\theta,z,x') = 0,$$
(3)

Work supported by DOE and AFOSR.

where a is the radius of the cylinder. The solution of (1) can be constructed by expanding in terms of the eigenfunctions of Laplace's equation in cylindrical coordinates. We obtain the following solution,

$$G_{3D}(x;x') = \frac{2}{L} \sum_{n=-\infty}^{\infty} \sum_{l=-\infty}^{\infty} e^{in(\varepsilon - \varepsilon')} e^{il(\theta - \theta')} \frac{I_{I}(n\delta_{<})}{I_{I}(n\alpha)}$$

$$\times [I_{I}(n\alpha)K_{I}(n\delta_{>}) - I_{I}(n\delta_{>})K_{I}(n\alpha)],$$
(4)

where

$$\delta = \frac{2\pi r}{L}, \ \delta' = \frac{2\pi r'}{L}, \varepsilon = \frac{2\pi z}{L}, \ \varepsilon' = \frac{2\pi z'}{L}, \alpha = \frac{2\pi a}{L}, \quad (5)$$

and the symbol > (<) denote the greater (lesser) of δ and δ' . Separation of the n=0 terms from the n>0 terms yields the following form for G_{nn} .

$$G_{3D} = \frac{1}{L}G_{2D} + \frac{4}{L}\sum_{n=1}^{\infty} \cos[n(\varepsilon - \varepsilon')] \frac{I_0(n\delta_{<})}{I_0(n\alpha)} \times \{I_0(n\alpha)K_0(n\delta_{>}) - I_0(n\delta_{>})K_0(n\alpha)\} + \frac{8}{L}\sum_{n=1}^{\infty}\sum_{l=1}^{\infty} \cos[n(\varepsilon - \varepsilon')]\cos[l(\theta - \theta')] \frac{I_1(n\delta_{<})}{I_1(n\alpha)} \times \{I_1(n\alpha)K_1(n\delta_{>}) - I_1(n\delta_{>})K_1(n\alpha)\}$$
(6)

where G_{2D} is the 2D Green's function defined by,

$$G_{2D} = \ln \left[\frac{\alpha^2 + (\delta_{>}\delta_{<}/\alpha)^2 - 2\delta_{>}\delta_{<}\cos(\theta - \theta')}{\delta_{>}^2 + \delta_{<}^2 - 2\delta_{>}\delta_{<}\cos(\theta - \theta')} \right]. \tag{7}$$

When we take the limit as $L \rightarrow 0$ in (6), we recover the 2-D Green's function

$$G_{2D} = \lim_{L \to 0} LG_{3D} \tag{8}$$

This is because the second and third terms of (6) vanish as $L \rightarrow 0$.

We tested the Green's function's convergence properties for a triply extreme case of (6) with $\delta' \to 0$, $\alpha \to \infty$, and $\delta \to 0$. This corresponds to choosing a line charge in free space and examining the electric field between any two points. We found exact numerical agreement between the known result and the one computed from G_{3D} , when we included the first 15,000 terms in the summation.

3 APPLICATIONS

3.1 Two-Dimensional Case

In many beam systems, an axisymmetric particle beam is generated at the electrode and is injected into a structure that is not axisymmetric. Typically, the rms envelope equation is used to determine the matching conditions for the system. However, the rms matching gives no information about the detailed phase-space evolution. Here, we make use of two-dimensional Green's function based self-consistent simulations to perform a detailed phase-space analysis for the matching and transport of a high-intensity axisymmetric particle beam in a quadrupole channel. In particular, we analyze the effects of a nonlinear transverse macroscopic velocity profile in the initial particles distribution. The nonlinearity in the velocity profile models, for instance, the effects of the concave shape of the electrode.

We consider a continuous, intense beam propagating with average axial velocity $\beta_b ce_1$ through a quadrupole channel with magnetic field given by

$$\frac{q\mathbf{B}(s)}{\gamma_b \beta_b mc^2} = \kappa_q(s)(y\mathbf{e_x} + x\mathbf{e_y}). \tag{9}$$

Here, q and m are the particles charge and mass, respectively, $\gamma_b = \left(1 - \beta_b^2\right)^{-1/2}$ is the relativistic mass factor, s is the axial coordinate, and $\kappa_q(s)$ is the quadrupole coupling coefficient. We assume for $\kappa_q(s)$ the profile shown in Fig. 1, corresponding to a tapered channel where the first lattice period has quadrupoles with increasing magnetic fields that match, in an rms sense, the beam into the periodic channel formed by the remainder lattice. The lattice period is S.

The rms matching is obtained by analyzing the solutions of the rms envelope equations [2]

$$\frac{d^2a}{ds^2} + \kappa_q(s)a - \frac{K}{2(a+b)} - \frac{\varepsilon^2}{16a^3} = 0, \qquad (10)$$

$$\frac{d^2b}{ds^2} - \kappa_q(s)b - \frac{K}{2(a+b)} - \frac{\varepsilon^2}{16b^3} = 0, \qquad (11)$$

where, $a = \langle x^2 \rangle^{1/2}$ and $b = \langle y^2 \rangle^{1/2}$ are the rms envelopes, $K = 2q^2 N_b / \gamma_b^3 \beta_b^2 mc^2$ is the perveance of the beam, ε is four times the unnormarlized rms emittance (which is assumed to be the same for x and y), N_b is the number of particles per unit axial length of beam, and $\langle \rangle$ denotes average over particles. In particular, for a given beam intensity and periodic channel parameter C_s (see Fig. 1), we make use of Eqs. (10) and (11) to determine the injection parameters for the axisymmetric beam, namely a, b and their derivatives at s = 0, as well as the magnetic field strengths of the quadrupoles in the first lattice period, denoted by C_s and C_s in Fig. 1. We focus here on highintensity beams, which are highly space-charge dominated, such that the emittance terms in the envelope

equations are negligible in comparison to the perveance

terms. To illustrate the matching process, the curves in Fig. 2 show the solution for a(s) and b(s) for a periodic

channel with vacuum phase advance $\sigma_0 = 70.8^{\circ}$ ($S^2C_1 = 70.8^{\circ}$)

10.0, $\eta = 0.3$) and beam perveance $SK/\varepsilon = 16.0$

(corresponding to a space-charge-depressed phase advance of $\sigma = 5.4^{\circ}$).

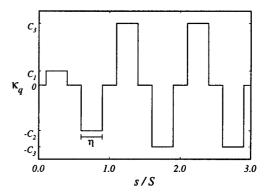


Fig. 1 Quadrupole coupling coefficient. Here, S is the lattice period and η is the filling factor.

To analyze the effects of the nonlinear tranverse macroscopic velocity profile in the phase-space evolution of the beam we make use of self-consistent particle simulation. We consider an initially axisymmetric cold beam with particles homogeneously distributed up to a radius of $r_b = 2a(0) = 2b(0)$ and with transverse velocity given by

$$\mathbf{r'} = \frac{a'}{a} \mathbf{r} \left[1 + \nu \left(1 - \frac{\mathbf{r}^2}{2a^2} \right) \right],\tag{12}$$

where $\mathbf{r} = x\mathbf{e}_x + y\mathbf{e}_y$ is the transverse displacement, the prime denotes derivative with respect to s, and v is the parameter that measures the nonlinearity in the velocity profile (for v = 0 the velocity profile is linear). It can be shown that the nonlinearity induced by the concave shape of the electrode leads to v > 0.

First, we analyze the behavior of the rms envelopes. The symbols in Fig. 2 correspond to the rms envelopes obtained from the particle simulation for an initial velocity nonlinearity of $\nu=0.25$. The channel and beam parameters are the same as those used in the rms envelope equations represented in the figure by the curves. The evident agreement reveals that even in the presence of nonlinearities in the velocity profile, the beam matches well (in an rms sense) to the quadrupole channel.

Second, we analyze what happens to the particle distribution as the nonlinearity in the velocity profile is introduced. The results are summarized in Fig. 3, where we compare particle distributions for the cases with and without initial velocity nonlinearities at three axial positions: s/S = 0.0, 1.0 and 2.5. Note that at these axial positions the beam is such that a(s) = b(s). In Fig. 3, the plots shown on the left correspond to v = 0 and those on the right correspond to v = 0.25. While for v = 0 the beam propagates coherently, for v = 0.25 the initially rounded beam develops edges after the first lattice period, becoming partially hollow subsequently (at s/S = 0.0).

2.5). The hollow profile of the beam at s/S = 2.5 is confirmed by analyzing the density function (not presented here), which shows that the density at the edge is twice the density at the center of the beam.

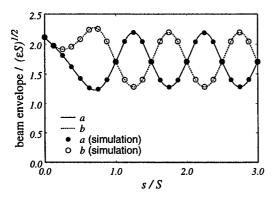


Fig. 2 RMS envelopes obtained from the rms envelope equations and self-consistent simulation.

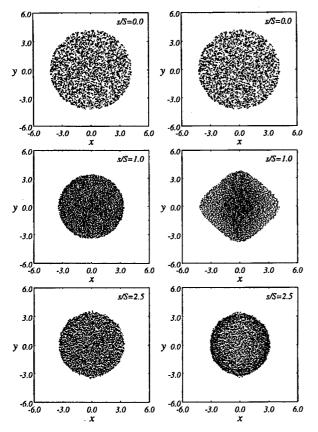


Fig. 3 Particles distribution for v = 0 (left) and v = 0.25 (right). The coordinates x and y are normalized to $\sqrt{\varepsilon S}$.

To summarize briefly, we have analyzed the matching and transport of an initially axisymmetric high-intensity beam in a tapered quadrupole channel. The rms envelope equations have been used to determine the matching conditions. Using a two-dimensional Green's function based self-consistent simulation code, we have investigated the effects of an initial nonlinear transverse

macroscopic velocity profile on the beam dynamics. It has been found that the rms radii evolution agrees with the rms envelope equation analysis, and that the presence of nonlinearities in the velocity leads to changes in the detailed particles distribution and the onset of beam hollowing.

3.2 Three-Dimensional Case

As a necessary component of a one-particle simulation, we compute the electrostatic self-field (field of a particle due to its induced surface charge. This radial electric field is given by the following expression:

$$E_{self} = \frac{4\pi}{L^2} \left(\frac{\delta}{\alpha^2 - \delta^2} \right) + \frac{8\pi}{L^2} \sum_{n=1}^{\infty} \frac{nI_0(n\delta)I_1(n\delta)K_0(n\alpha)}{I_0(n\alpha)} + \frac{16\pi}{L^2} \sum_{n=1}^{\infty} \sum_{l=1}^{\infty} \frac{nI_l(n\delta)I_l'(n\delta)K_l(n\alpha)}{I_l(n\alpha)}.$$
(13)

Utilizing the electrostatic self-field force, we are able to simulate one string of particles interacting with its induced charge. We apply a constant magnetic field parallel to the axis of the pipe. The Lorentz forces are only in the transverse direction, so longitudinal motion can be ignored. As an example, a radially confined orbit is shown in Fig. 4 for $\alpha=2\delta(initial)=0.2$.

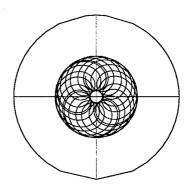


Fig. 4 Trajectory of a trapped particle in the conducting pipe with initial conditions $P_r = \theta = 0$, $P_\theta = 0.001$ (normalized to $8\pi^2 c/qL^2B$), and $\xi = 32\pi^2 mc^2/L^3B^2 = 0.001$.

4 SUMMARY

Both two- and three-dimensional models of space charge in intense charged-particle beams have been presented using Green's functions, and applied, respectively, in the analyses of the matching and transport of an initially axisymmetric beam into a quadrupole channel and of the interaction of a particle with its induced surface charge.

- [1] J. D. Jackson, *Classical Electrodynamics* (John Wiley, New York, 1975).
- [2] F. J. Sacherer, IEEE Trans. Nucl. Sci. NS-18, 1105 (1971).

THE EFFECT OF TRAPPED BACKSTREAMING IONS ON BEAM FOCUS AND EMITTANCE IN RADIOGRAPHIC ACCELERATORS

T. Houck, J. McCarrick, LLNL, Livermore, CA

Abstract

The use of electron beam accelerators in advanced X-ray radiography requires that the beam be focused to a very small spot size on a metallic bremsstrahlung converter target. The energy deposition of the beam into a small volume of target material rapidly converts the target into a high-density plasma. The space-charge density of the focused beam sets up a strong electric field at the surface of the grounded target, which then accelerates ions of target plasma and lighter contaminants into the beam. These "backstreaming ions" form a long channel which partially neutralize the space charge of the beam, disrupting the beam focus and degrading the radiographic performance. One solution to this problem is to confine the backstreaming ions in a short channel with a selfbiased inductive trap. Such a trap has been proposed for testing on the ETA-II accelerator. We will present numerical simulations which show the effect of the high trapped-ion charge density on the beam spot size and emittance.

1 INTRODUCTION

Accelerator systems for X-ray radiography transport a high-current relativistic electron beam to a final-focus system, where the beam is concentrated to a small (~ 1 mm) spot size on a metallic converter target. X-rays are produced via bremsstrahlung in the converter material. The high energy deposition of the beam into the target rapidly heats it, creating a plasma of target material and any light contaminants. Since the metallic target and subsequent plasma form an equipotential surface, and since the target system is usually grounded, the high space-charge density of the electron beam generates a large axial electric field in front of the target. This electric field extracts ions from the target plasma and quickly accelerates them upstream into the beam, in a process referred to as "ion backstreaming." The ion space charge neutralizes the beam space charge, so that the beam's own magnetic field overfocuses the beam and degrades the X-ray production. This process is shown schematically in the upper portion of Figure 1. Simple analytic models of this process [1] show that a very small supply of ions, parts per billion relative to the solid density of the target, is enough to generate space-charge limited (SCL) ion flow into the beam, on a fairly fast time scale (10-20ns) relative to a typical beam pulse (50-60ns) if light ions are present.

The best tactic for avoiding backstreaming ions would be to suppress completely the formation of plasma at the target, but no plausible scheme for accomplishing this has been found. Another technique is to dynamically adjust the

beam and its focusing system to compensate for the presence of the ions [1]. However, the most straightforward technique is to inductively [2] or resistively [3] bias the target to counteract the axial electric field produced by the electron beam.

In the inductive case, a modified accelerating cell is placed in front of the converter target and operated in reverse of its normal polarity, creating a potential well in front of the target which traps ions before they can form a channel of sufficient length (the *disruption length*) to defocus the beam. This is shown in the lower portion of Figure 1. Note that during the flattop of the voltage pulse on the induction cell, a static field model can be used and the concept of a potential is applicable.

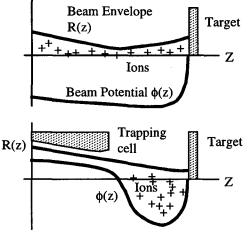


Figure 1. Untrapped (upper) and trapped (lower) backstreaming ion configurations.

Such a cell has been designed and will be tested as part of the ongoing experimental campaign on the ETA-II accelerator (see, for example, [4]) to evaluate this technology for use in the DARHT-II project. Previous modeling [2] of this cell shows that it can confine backstreaming ions, but these simulations did not include the self-consistent behavior of the electron beam as modified by the trapped ions. Since the results showed that the trapped ion density is much higher than the SCL value normally used to estimate the disruption length, it is not clear that trapping the ions actually preserves the beam spot size; it is also possible that such a dense ion channel produces emittance growth, which degrades X-ray production. Therefore, we have performed fully self-

consistent numerical modeling of this inductive ion trap using DARHT-II beam parameters.

2 NUMERICAL RESULTS

Two types of simulations have been performed of the inductive ion trap. Time-dependent particle-in-cell (PIC) modeling has been done, and when it was observed that the system settles into a steady-flow configuration, a Vlasov electron model was employed for more accurate calculation of the beam envelope and emittance.

The geometry and typical beam and ion configuration, as used in the PIC runs, are shown in Figure 2. The simulation runs for 20ns; hydrogen ions are emitted in SCL flow beginning at 1ns, after the beam has ramped up to a steady current of 2kA and an energy of 20MeV. The beam hard-edge radius at the target, prior to ion emission, is slightly over 0.5mm. The voltage across the gap of the induction cell is 400kV.

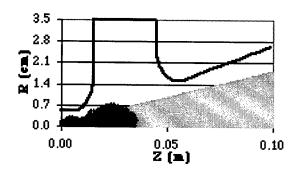


Figure 2. Computational geometry, showing beam, ions, aperture plate, and induction cell electrode.

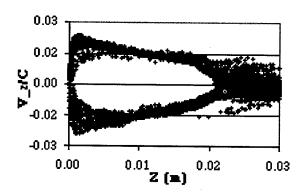


Figure 3. Steady circulation in ion Z-Vz phase space.

Figure 3 shows the z-v_z phase space of the ions at 20ns. The ions have reached a steady circulation in the trapping field, suppressing further emission from the target plasma. (Note that over the duration of a beam pulse, the target plasma does not expand significantly from the original surface.) Figure 4 shows the ratio of ion charge density to beam charge density on the axis; they are of the same order, as opposed to the ~10% value reached

in unconfined SCL flow. The ion channel length is quite short, however, at about 3.4cm. Figure 5 shows the beam spot size and emittance at the target as a function of time. Here we see that the beam spot size is controlled, but at the expense of substantial emittance growth.

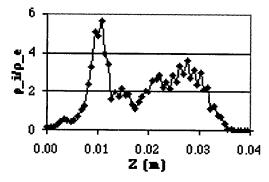


Figure 4. On-axis ratio of ion charge to beam charge.

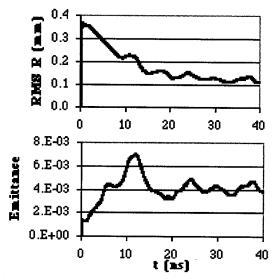


Figure 5. Beam envelope and emittance, at the target plane, as a function of time.

Because of concerns that the PIC code generates significant numerical emittance growth, the steady-state ion density was fed into a Vlasov electron model to confirm the degradation of the beam emittance. The beam envelope and emittance as a function of axial distance from the target are shown in Figure 6. It is important to note that the target plane is at z=0.3cm in this model. These results show less emittance growth than in the PIC runs but nevertheless a substantial rise over the initial value of 1200π -mm-mrad (normalized).

Parametric studies have been performed to examine the variation of spot size control and emittance growth with cell voltage and gap size. However, due to strong engineering constraints on combinations of voltage and gap size that will avoid breakdown in the presence of an expanding plasma, and the limit on channel length to prevent spot size variation, no significant departure from the behavior shown here could be attained.

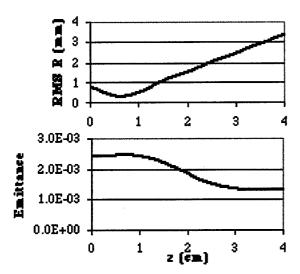


Figure 6. Steady state spatial profile of beam envelope and emittance from Vlasov model. Note the target plane is at z=0.3 cm in these results.

CONCLUSIONS 3

A fully self-consistent model of an electron beam and backstreaming ions in an inductive trap has been studied, to see the effect of the high trapped ion charge density on the beam. The beam spot size is controlled successfully as the ions are confined to a short channel, and reach a steady-state configuration. However, there is considerable emittance growth in the beam due to nonlinear focusing. Parametric studies performed within the engineering constraints of an induction cell have not yielded an alternate design.

ACKNOWLEDGEMENTS

We would like to thank Peter Rambo for insightful discussions and code benchmarking. This work performed under the auspices of the U.S. Department of Energy by LLNL under contract W-7405-ENG-48.

- Y-J. Chen, et. al., "Controlling Backstreaming Ions from X-ray Converter Targets with Time Varying Final Focusing Solenoidal Lens and Beam Energy Variation." Proceedings, 19th International Linear Accelerator Conference, Chicago, IL, 1998
 J. McCarrick, et. al., "Trapping Backstreaming Ions from an X-ray Converter Using an Inductive Cell." Proceedings, 19th International Linear Accelerator Conference, Chicago, IL, 1998
 T. Kwan, et. al., "Design Simulation for Spot Size Stabilization in ITS/DARHT." Proceedings, 19th International Linear Accelerator Conference, Chicago, IL, 1998
 G. A. Westenskow, et. al., "Experimental Investigation of Beam Optics Issues at the Bremsstrahlung Converters for Radiographic Applications." Proceedings, 19th International Linear Accelerator Conference, Chicago, IL, 1998

Progress towards simulating heavy ion beams for Inertial Fusion Energy based on 1) A Darwin model field solver, and 2) A semi-Lagrangian Vlasov solver *

E. Sonnendrücker, LBNL, Berkeley, CA & CNRS, Nancy, France †, A. Friedman and D.P. Grote, LLNL, Livermore, CA

Abstract

We introduce in this paper two numerical methods, a Darwin model field solver and a semi-Lagrangian Vlasov solver, which may be appealing for beam simulations and discuss their properties.

1 THE DARWIN MODEL FIELD SOLVER

1.1 Introduction

The Darwin Particle-In-Cell formulation was introduced by Nielson and Lewis in 1976 [1]. This model, as described in detail in the next section, eliminates only the propagating light waves from the system, while retaining other slower time scale electromagnetic effects arising from the particle current sources. It has proved to be a mixed blessing over the years. Many authors have used the technique to great advantage, but have noted the difficulties sometimes encountered in its implementation [1], [2]. These problems arise from modifications of the originally hyperbolic system of equations which make the resulting system elliptic. Thus boundary conditions must be carefully formulated in order to ensure the problem is well-posed. Some of the most violent numerical instabilities experienced in plasma computations are associated with naive implementations of the Darwin method. However, certain beam simulations, which involve much less dense plasma might be spared these instabilities, and this could make the Darwin model very appealing in such cases.

1.2 The Darwin model

The Darwin approximation of Maxwell's equations is introduced to remove what is often the stiffest time scale in electromagnetic simulations, namely the propagation time of light waves from zone to zone. This model eliminates electromagnetic waves, but keeps other important parts of the physics, in particular the low frequency phenomena.

The electric field \mathbf{E} is decomposed into two parts, a longitudinal part \mathbf{E}_L which is curl free and a transverse part \mathbf{E}_T which is divergence free:

$$\mathbf{E} = \mathbf{E}_L + \mathbf{E}_T$$

where $\nabla \times \mathbf{E}_L = 0$ and $\nabla \cdot \mathbf{E}_T = 0$. Furthermore, as $\nabla \times \mathbf{E}_L = 0$ we can write $\mathbf{E}_L = -\nabla \phi$. Darwin's approximation consists in dropping the transverse part of the displacement current from Ampere's law:

$$\nabla \times \mathbf{B} = \mu_0 \mathbf{J} + \frac{1}{c^2} \frac{\partial \mathbf{E}_L}{\partial t},$$

and keeping the other three Maxwell's equations unchanged.

1.3 Asymptotic derivation from Maxwell's equations

Let us assume that the time derivatives are small in Maxwell's equation. To emphasize this we write the dimensionless Maxwell's equation introducing the small parameter ε :

$$-\varepsilon \frac{\partial \mathbf{E}}{\partial t} + \nabla \times \mathbf{B} = \mathbf{J},$$

$$\varepsilon \frac{\partial \mathbf{B}}{\partial t} + \nabla \times \mathbf{E} = 0,$$

$$\nabla \cdot \mathbf{E} = \rho,$$

$$\nabla \cdot \mathbf{B} = 0.$$

We express the fields E and B such that

$$\mathbf{E} = \mathbf{E}^0 + \varepsilon \mathbf{E}^1 + \varepsilon^2 \mathbf{E}^2 + \dots$$
$$\mathbf{B} = \mathbf{B}^0 + \varepsilon \mathbf{B}^1 + \varepsilon^2 \mathbf{B}^2 + \dots$$

Plugging them into Maxwell's equations, we get by gathering the terms in the same power in ε : The first order terms:

$$\nabla \times \mathbf{B}^0 = \mathbf{J}^0, \qquad \nabla \cdot \mathbf{B}^0 = 0,$$
$$\nabla \times \mathbf{E}^0 = 0, \qquad \nabla \cdot \mathbf{E}^0 = \rho^0.$$

The second order terms:

$$\nabla \times \mathbf{B}^{1} = \mathbf{J}^{1} + \frac{\partial \mathbf{E}^{0}}{\partial t}, \qquad \nabla \cdot \mathbf{B}^{1} = 0$$
$$\nabla \times \mathbf{E}^{1} = -\frac{\partial \mathbf{B}^{0}}{\partial t}, \qquad \nabla \cdot \mathbf{E}^{1} = \rho^{1}.$$

Notice that $\nabla \times \mathbf{E}^0 = 0$ such that $\frac{\partial \mathbf{E}^0}{\partial t}$ which appears in the second order terms only involves only the longitudinal displacement current. Therefore the following system yields the same terms in the expansions:

^{*} This work was supported by the Director, Office of Energy Research [Office of Fusion Energy Science], U.S. Department of Energy under contracts No. DE-AC03-76SF00098 and W-7405-ENG-48.

[†] Email: ESonnendrucker@lbl.gov

- An equation for the scalar potential ϕ where $\mathbf{E}_L = -\nabla \phi$

$$-\nabla^2\phi=\rho,$$

- A system for the magnetic field B

$$\nabla \times \nabla \times \mathbf{B} = \nabla \times J,$$
$$\nabla \cdot \mathbf{B} = 0.$$

 A second order approximate model (E¹ and B¹ are also identical to those in Maxwell's equations), is obtained if we include the transverse electric field

$$abla imes
abla imes
abla imes \mathbf{E}_T = -\frac{\partial
abla imes \mathbf{B}}{\partial t},$$
 $abla \cdot \mathbf{E}_T = 0.$

This derivation has been performed in more detail and in a mathematically rigorous manner in [3].

Instead of Maxwell's equations, which are hyperbolic, we now have three elliptic equations. Thus the Courant condition on stability no longer constrains the timestep.

1.4 The time differencing instability

In Nielson and Lewis [1] and Sonnendrücker, Ambrosiano and Brandon [4], it is shown that there is a stability condition for the numerical time differencing of the source term for \mathbf{E}_T . This reads

$$\frac{{\omega_p}^2}{c^2k^2} \le 1.$$

The smallest k seen by a mesh is π/L , where L is the length of the computational domain. Practically speaking, this means that if $c/\omega_p \geq L/\pi$ the simulation should be stable. Therefore the straightforward time-differencing can be used only for problems of length at most of the order of the collisionless skindepth. This condition is not fulfilled in most plasma problems where the Darwin model might be interesting (see [4] for a discussion). There is a remedy to this instability, but it involves gathering more moments from the particles and solving the following problem in dimensionless units

$$\begin{split} \rho \mathbf{E}_T + \nabla \times \nabla \times \mathbf{E}_T &= -\int_{\Omega} v(v.\nabla_x f) \, dv + \rho \mathbf{E}_L \\ + \mathbf{J} \times \mathbf{B}, \\ \nabla \cdot \mathbf{E}_T &= 0 \end{split}$$

which is numerically costly as the right-hand-side of the first equation is not divergence free.

However certain beam simulations which involve much lower ω_p should be in the stable regime and hence make the Darwin model numerically a lot less costly. We are studying the possibilities.

SOLVER

2.1 Introduction

Up to now space charge dominated beam simulations have been performed most of the time using Particle-In-Cell (PIC) methods such as those in WARP [5], which afford satisfying results with relatively few particles. However, it may be useful to have an alternative numerical approach in order to be able to separate more easily numerical and physical features in the simulation results. Therefore, we have adapted the semi-Lagrangian Vlasov method [6] to 2D slice beam simulations.

2.2 The semi-Lagrangian scheme for 2D advection

The semi-Lagrangian method consists of looking for the value of the solution f at a set of mesh points by walking down the characteristics backward in time. The characteristics are the solutions of the differential system

$$\frac{dX}{dt} = \mathbf{v_{D}}_x(x, y, t), \quad \frac{dY}{dt} = \mathbf{v_{D}}_y(x, y, t).$$

They are such that $\frac{d}{dt}f(X(t),Y(t),t)=0$, i.e. f is constant along the characteristics.

The function f being known at the mesh points at the previous time steps, this property can be used to compute its new value. More precisely for a mesh point (x_i, y_j) , we have

$$f(x_i, y_j, t_n + \Delta t) = f(X(t_n - \Delta t; x_i, y_j, t_n + \Delta t),$$

$$Y(t_n - \Delta t; x_i, y_j, t_n + \Delta t), t_n - \Delta t),$$

where we denote by (X(t; x, y, s), Y(t; x, y, s)) the value at time t of the solution whose value is (x, y) at time s.

Hence the algorithm can be decomposed in two steps: 1) Look for the starting point of the characteristic for each mesh point. 2) Compute f at the starting points of the characteristics. This interpolation is realised using a tensor product of cubic B-splines.

2.3 The electrostatic case

In the case where the Vlasov equation is coupled to a Poisson equation and submitted to a given external electric field, it can be split into two 2D advections, with a uniform advection field.

$$rac{\partial f}{\partial t} + \mathbf{v} \cdot
abla_x f = 0$$
 and $rac{\partial f}{\partial t} + \mathbf{E}(x,t) \cdot
abla_v f = 0.$

The "feet" of the characteristics are known explicitly. The displacement from the mesh points is the same everywhere, namely $v\Delta t$ (or $E\Delta t$). The only numerical work in this case is to interpolate the distribution function at the previous time step using cubic splines.

In the case of hard-edged quadrupoles a residence correction needs to be applied to get the correct force. This enters or leaves a quadrupole during a time step the applied field needs to be multiplied by the fraction of the time spent in the quadrupole. More precisely, if \mathbf{E}_{app} is the quadrupole field and Δt_1 is the time span spent in the quadrupole, then the applied field for this time step needs to be

$$\frac{\Delta t_1}{\Delta t} \mathbf{E}_{app}.$$

2.4 Parallelization methodology

Solving a four dimensional Vlasov equation is obviously very costly in time and memory. Therefore it requires massively parallel computing facilities.

The most computationally intensive parts of the algorithm are the tridiagonal solves linked to the spline interpolation. These cannot be parallelized individually with good scalability. For this reason we chose 1D band decompositions of the domain. We use a decomposition in bands parallel to the x-axis for the x-advection and a decomposition in bands parallel to v_x -axis for the x-advection.

2.5 Performance

We tabulate below the performance obtained on the NERSC T3E computer "mcurie" with $64^4 = 1.68 \times 10^7$ grid points, 1 lattice period, and 30 time steps.

PEs	time (s)	speed up	time/step/grid point (ns)
4	326.36	1	648.22
8	167.26	1.95	332.31
16	88.28	3.70	175.39
32	49.32	6.62	97.99

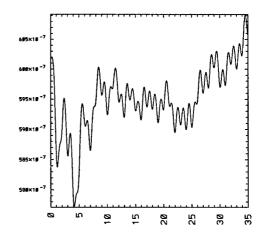
2.6 Propagation of a matched beam in a FODO channel

We compare the emittance evolution over 35 lattice periods of a matched beam. Figure 1 gives the WARP result and Figure 2 gives the SLV result for a 128⁴ grid.

The results look quite comparable over this lapse of time. However, numerical dissipation is a serious problem in the semi-Lagrangian algorithm. In order for it to be kept small over a longer period of time the beam needs to be covered by a sufficient number of grid points. This implies the use of a very fine grid due to the beam oscillations in a FODO channel if a regular grid is to be used. More advanced methods, including adaptive grids, may prove useful in this regard.

3 REFERENCES

- C.W. Nielson, H.R. Lewis, Methods in Computational Physics 16, 367 (1976).
- [2] D.W. Hewett and C.W. Nielson, J. Comput. Phys. 29, 219 (1978).
- [3] P.A. Raviart, E. Sonnendrucker, Numer. Math. 73, 329 (1996).



plot hepsk habbass 25 m. plot hepsk habbass 25 m. plot m. plot

Figure 1: rms emittance from WARP calculation

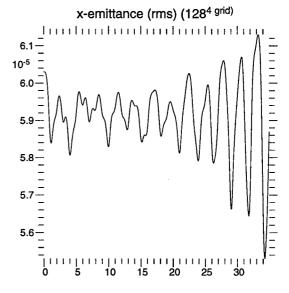


Figure 2: rms emittance from SLV calculation

- [4] E. Sonnendrucker, J.J. Ambrosiano, S.T. Brandon, J. Comput. Phys. 121, 281 (1995).
- [5] D.P. Grote et al., this conference.
- [6] E. Sonnendrucker, J. Roche, P. Bertrand, A. Ghizzo, J. Comput. Phys. 149, 201 (1999).

RELEASE OF MARYLIE 3.0*

Alex J. Dragt[†]

Physics Department, University of Maryland, College Park, MD 20742

1 INTRODUCTION

The latest version of MARYLIE 3.0 is being released along with a 750 page User's Manual [1]. MARYLIE 3.0 is a 3rd-order charged-particle beam transport code that exploits the power of Lie-algebraic map methods to treat the full 6-dimensional phase including all possible linear and nonlinear transverse and longitudinal couplings. A serial version is available for ordinary computers, and a parallel version is available for the 512 processor CRAY. A Multi-Platform Graphic User Interface version, designed to facilitate all operations and comparisons between various codes, is also being released [2].

The current version of MARYLIE models approximately 30 different kinds of beamline elements. In addition there are about 40 simple commands and another 40 advanced commands. Many of these commands work with and exploit the maps associated with the various beamline elements. There are also commands for input and output, the production of various kinds of plots, and the production of geometrical information including floor-plan layout drawings. Finally, there are approximately 20 procedures and fitting and optimization commands to facilitate system design. All together, the MARYLIE 3.0 main program and approximately 500 subroutines comprise approximately 37,000 lines of FORTRAN 77 code.

MARYLIE can be used to generate particle distributions, including linearly and nonlinearly matched distributions. These distributions can then be tracked using element-by-element maps, lumped maps, or full-turn maps. Maps can also be applied to functions and moments.

In addition to fast tracking studies, MARYLIE can be used to design and analyze lattices for both single-pass systems and circulating storage rings. Analysis commands include the calculation of all aberrations through third order; tunes and anharmonicities and first and second-order chromaticities; first, second, and third-order phase-slip factors; first, second, and third-order dispersions and all other linear lattice functions and their energy dependence through second order; nonlinear lattice functions; nonlinear phase-space distortion; transfer map normal forms; nonlinear resonance driving terms; nonlinear invariants; and moment data including eigenemittances and all moments through 4th order.

The User's Manual contains numerous examples ranging from the simple to the complex including sextupole corrected electron microscopes having sub-Angstrom resolution, 3rd-order achromats, the SLAC Final Focus Test

*Work supported in part by U.S. Department of Energy grant

DEFG02-96ER40946.

Beam facility, and the Fermilab Tevatron. Figures from some of these examples are displayed below.

2 EXAMPLES

Figure 1 shows a MARYLIE generated ray plot for a simple quadrupole spot-forming system. The quadrupoles occupy the shaded areas.

Figure 2 shows a sextupole corrected electron microscope, and figure 3 shows the focal spot pattern for this system.

Figures 4 and 5 show the predicted final beam spot for the SLAC Final Focus Test Beam facility. Three different energies are displayed.

Figures 6, 7, and 8 show Tevatron tracking data when strong distortion sextupoles are powered.

Figures 9 and 10 show MARYLIE generated graphic data for the Los Alamos Proton Storage Ring.

- [1] A.J. Dragt, D.R. Douglas, F. Neri, C.T. Mottershead, E. Forest, L.M. Healy, R.D. Ryne, P. Schutt, J. van Zeijts, MARYLIE 3.0 User's Manual, University of Maryland Physics Department Report (1999).
- [2] G.H. Gillespie et al., Using MARYLIE with the Particle Beam Optics Laboratory, these proceedings, 3 pages (1999).

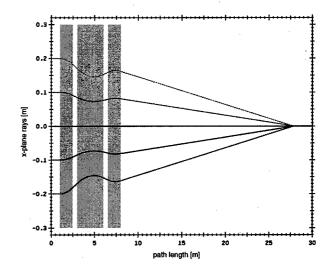


Figure 1: Horizontal plane ray plot for a simple quadrupole spot-forming system.

[†] dragt@physics.umd.edu

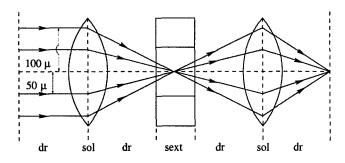


Figure 2: A simple electron microscope spot-forming system consisting of two solenoids and suitably chosen drifts.

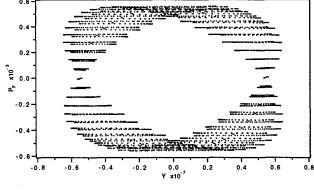


Figure 5: Vertical projection of phase-space final conditions for SLAC Final Focus Test Beam facility.

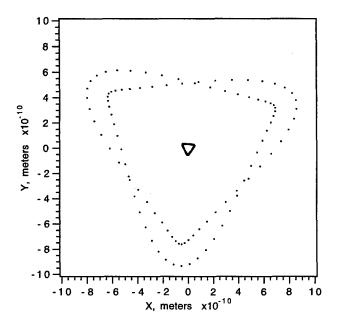


Figure 3: Focal spot pattern for sextupole corrected electron microscope.

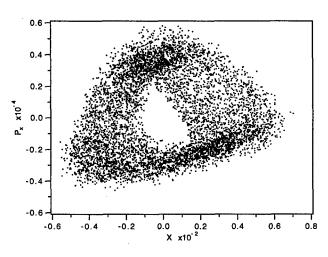


Figure 6: Horizontal projection of lump-by-lump phasespace tracking data for Tevatron with strong distortion sextupoles.

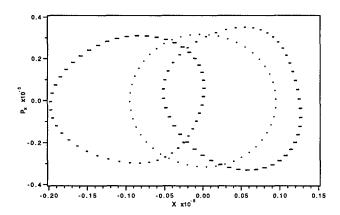


Figure 4: Horizontal projection of phase-space final conditions for SLAC Final Focus Test Beam facility.

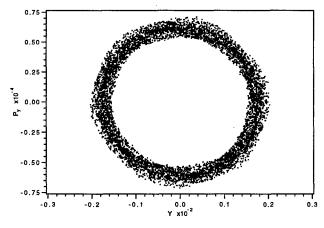


Figure 7: Vertical projection of lump-by-lump phasespace tracking data for Tevatron with strong distortion sextupoles.

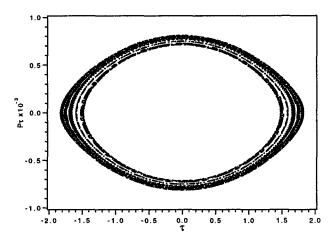


Figure 8: Temporal projection of lump-by-lump phasespace tracking data for Tevatron with strong distortion sextupoles.

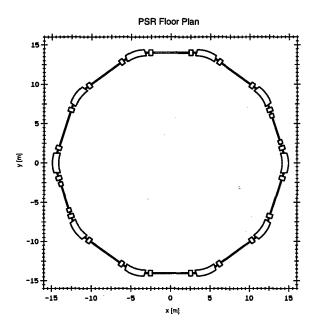


Figure 9: Floor-plan layout drawing for the Los Alamos Proton Storage Ring.

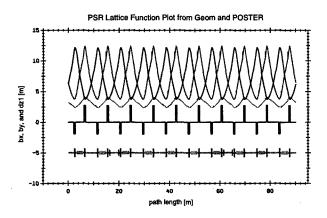


Figure 10: Lattice function plots for the Los Alamos Proton Storage Ring.

EIGENMODES OF SUPERCONDUCTING CAVITIES CALCULATED ON AN APE-100 SUPERCOMPUTER (SIMD)

F. Neugebauer*, DESY Zeuthen, U. van Rienen[†], University Rostock

Abstract

The construction of modern accelerators is usually supported by the numerical determination of eigenmodes in the accelerating cavities. Often the rotational symmetry of the cavity is used to simplify the numerical simulation. However, in cases where the cavity lacks rotational symmetry resp. where attached components like couplers have to be taken into account, a fully three dimensional treatment of the maxwell equations is necessary. This requires more computer power than is available on a normal high end workstation. Therefore, in the present approach a parallel SIMD super computer (APE-100) is used to compute the eigenmodes of accelerating cavities. As an example parts of the superconducting TESLA structure are investigated. The geometry input is parsed by MAFIA which transfers the resulting system matrix, incorporating geometry and material information, to the APE-100. The result of the diagonalization procedure is then read back to the MAFIA host where further data analysis and visualization can be done.

1 INTRODUCTION

The construction of modern accelerators is usually supported by the numerical determination of eigenmodes in the accelerating cavities. Often the rotational symmetry of the cavity is used to simplify the numerical simulation. However, in cases where the cavity plus attached rf-components lacks rotational symmetry a fully three dimensional treatment of Maxwell's equations is necessary which requires more computer power than is available on a normal high end workstation. In addition the three dimensional approach allows for the simulation of fabrication errors and surface roughness which are usually not considered to have rotational symmetry.

In the framework of the Finite Integration Technique (FIT) developed by Weiland and coworkers [1] Maxwell's equations in integral representation are transformed to a set of matrix equations. Using rectangular grids the discretization volume is partitioned in two sets of cells which can be considered dual. In the case of determining the eigenmodes of a cavity the grid voltages along neighboring gridpoints are the degrees of freedom of the resulting eigenvalue problem. The system matrix connects grid voltages of a single cell only to grid voltages of adjacent cells. This "next neighbor connection"—property makes the eigenvalue problem especially well suited to be solved on an APE-100 su-

percomputer for this type of computer is capable of a very fast data exchange between neighboring nodes.

APE-100 supercomputers are mainly used in QCD theory where a profound experience in solving eigenvalue problems [2] does exist. However, the parallel structure of the computer requires the use of special programming tools and a language (TAO) dedicated to the computer topology which is inefficient in programming advanced file IO, string evaluation and in managing pointers.

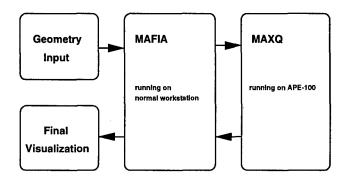


Figure 1: Schematic view of the MAXQ software interface

The parsing of the geometry input, which is mainly a linear task, is left to MAFIA which is running on a usual workstation. The resulting system matrix incorporating geometry and material information is transfered to the APE-100 by means of the MAFIA toolkit (MTK). Then, on the APE-100 supercomputer the numerical expensive task of finding the lowest eigenvalues and corresponding eigenvectors of a large sparse matrix is performed. The result of the diagonalization procedure is then read back to the MAFIA host where further data analysis and visualization can be done.

The approach has been tested first for simple geometries such as sphere and brick in a box which allows for comparison with analytically known results. Next, parts of the TESLA superstructure were studied for a timing comparison between APE-100 and a HP 735.

2 FINITE INTEGRATION TECHNIQUE AND THE APE-100 TOPOLOGY

The Finite Integration Technique is based on a discretization of Maxwell's equations using a set of two rectangular grids which can be considered dual to each other [1]. The integral representation of Maxwell's equations is transferred to a discrete version by specifying the integration paths as to be along the edges of the discretization cell. For the case of area integrals the 6 bordering rectangles of the

^{*}Email: fneug@ifh.de

[†]Email: van.rienen@e-technik1.uni-rostock.de

cell are chosen as the integration area. The degrees of freedom in the discretized version of Maxwell's equations are not the fields themselves, but the grid voltage along neighboring grid points or the flux over a cell surface for example. Therefore the discretized Maxwell's equations remain mathematically equivalent to the continuous case. There is no discretization error and the discretized Maxwell's equations exactly obey the conservation law for charge and current density.

Starting point for the calculation of eigenmodes in superconducting cavities is the matrix equation

$$\left\{ D^{-1/2} \tilde{C} \tilde{D} C D^{-1/2} - D^{1/2} \tilde{S}^T \tilde{S} D^{1/2} \right\} \vec{u} = \omega^2 \vec{u} \,, \quad (1)$$

where the matrices D,C and S contain material and mesh information and represent the $curlcurl-graddiv=-\nabla^2$ operator. \vec{u} denotes the vector of all grid voltages and ω is the frequency of the wanted eigenmode. In the case of homogeneous material distribution Eq.1 is known as Helmholtz's equation.

An important feature of the matrix equations is its locality. Actually this is due to the fact that the chosen integration space is restricted to the neighboring cells of the selected degree of freedom. As a consequence the resulting system matrix of which the eigensystem has to be determined is sparse with a priori known pattern of entries. A detailed treatment of the theory yields that 13 elements of the system matrix are non zero for each degree of freedom. These elements connect to degrees of freedom belonging to neighboring cells.

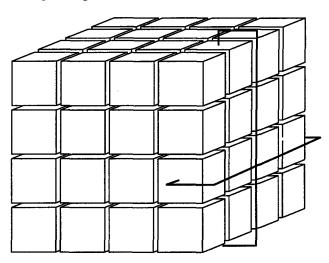


Figure 2: Topology scheme of the APE-100: Each node can access the memory of its six neighbors without latency. The whole cube is subjected to periodic boundary conditions along x-,y- and z-direction resulting in a hyper torus. On each node resides the same amount of grid points and the associated parts of the system matrix (see Eq.1) and the vector of the grid voltages u.

The cells of the discretization volume are distributed to the nodes so that each processor is responsible for its own segment of real space. Then the matrix-vector multiplication is mainly a local operation on each node. Only in cases where the cell lies on the segment boundary data exchange with neighboring nodes will occur. The APE-100 is perfectly suited to such a situation because the SIMD character of the supercomputer accounts for a very fast data transfer with neighboring nodes without latency.

3 RESULTS

The efficiency of the proposed procedure definitely depends on the chosen eigenvalue algorithm. At the moment only a simple variant of a polynomial iteration algorithm is installed. It searches for the lowest eigenvalue in the subspace orthogonal to all eigenvectors already found. No convergence checking has been installed, the interation is simply performed 5000 times. In examples this number has been found sufficiently high to give precise results.

The application of more sophisticated algorithms is in progress. An accelerated conjugate—gradient algorithm for the computation of the lowest eigenvalues is known from Lattice—QCD and tested on the APE—100[2]. Another candidate is the Jacobi—Davidson algorithm.

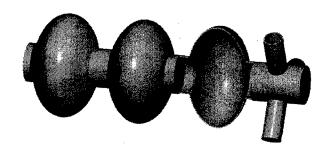


Figure 3: Scetch of the part of the TESLA structure under consideration: Three half cells and a HOM-coupler.

As realistic example a part of the TESLA superstructure consisting of 3 half cells and the beam pipe was discretized on a mesh of 400000 grid points. The first 10 eigenvalues were searched for on a HP 735 in a regular MAFIA session and on the QH4 (512 nodes) running MAXQ. Even with the simple eigenvalue algorithm the APE-100 computed the eigenvalues within only 15 minutes whereas the HP 735 needed about three hours for the same task. The speed-up will be surely increased by the use of better eigenvalue algorithms.

Another important influence on the efficiency comes from the code performance of the matrix by vector multiplication which is the heart of every iterative eigenvalue algorithm for sparse matrices. Measurements show a range from 10 to 20 % of the peak performance depending on the number of grid points per node. Usually, as the number of grid points increases the performance ratio rises. This gives a total computer power of about 2.5 to 5 GFlops on

the QH4.

The total number of grid points which can be used in the discretization is restricted due to memory limitations. Furthermore the used eigensolver needs additional memory for every eigenvector to be found. The memory needed per gridpoint is 52 octets for the system matrix and 12 octets for every eigenvector. This leads to

$$M_{total} = 12 * N * (n+5)$$
 octets (2)

for an expression for the total memory used. N is the number of gridpoints and n denotes the number of eigenvectors to be found.

On the QH2 (8x8x4) with 16 MB per node (2) results in:

Number of eigenvectors	Available gridpoints	
1	60.000.000	
2	51.000.000	
5	36.000.000	
10	24.000.000	
100	3.400.000	

Investigations considering the role of the single precision floating point arithmetic of the APE-100 are still necessary. The scalar products are reported to be sensitive to the single precision / double precision problematics. Therefore the scalar products are coded using a software emulation of double precision arithmetics. The same procedure has already been applied in the original MAFIA package to save memory and keep rounding errors at a minimum.

4 CONCLUSIONS

The calculation of eigenmodes on a three-dimensional basis is crucial for the simulation of accelerating cavities. Only a fully three-dimensional treatment of Maxwell's equations can account for effects connected to fabrication errors and surface roughness and most important to effects which arise from devices such as input couplers or HOMcouplers. These coupling devices inevitably break the rotational symmetry of the cavity and cannot be neglected for the determination of eigenmodes of the cavity. However, the lack of computional power on high end workstations normally avoids the inclusion of the three-dimensional effects described above. Therefore in the present paper an approach to a supercomputer solution of the eigenmode problem of superconducting cavities has been made. The reached speed-up by using the APE-100 is at the moment at a factor of about 12, but it is promising that the implementation of better eigenvalue algorithms will increase the efficiency by another factor in the range between 3 to 10.

Not only the computation time for moderate problems is dramatically decreased, moreover the recent approach now opens the possibility to model large scale problems of several 10^6 grid points.

5 ACKNOWLEDGEMENTS

The authors wish to thank Prof. Th. Weiland and his coworkers, especially M. Timm for many helpful discussions on MAFIA and MTK and H-W. Glock and D. Hecht for providing MAFIA command files containing the TESLA geometry. Thanks also to H. Simma for helping implementing the eigensystem solver and for many hints concerning the APE-100. The support given by DESY in providing computing time for the MAXQ project (Maxwell's Equations on Quadrics) is gratefully acknowledged.

- [1] Th. Weiland, 'On the Numerical Solution of Maxwell's Equations and Applications in Accelerator Physics', Part. Acc., 15, 245–291 (1984)
- [2] Th. Kalkreuther, and H. Simma, 'An accelerated conjugate gradient algorithm to compute low-lying eigenvalues a study for the Dirac operator in SU(2) lattice QCD', DESY 95-137, HUB-IEP-95/10 (1995)

IMPROVEMENTS IN GDFIDL

W. Bruns*, Technische Universität Berlin, EN-2, Berlin, Germany

Abstract

The finite difference code GdfidL computes 3D electromagnetic fields. It has been rewritten to implement better material dicretization with generalized diagonal fillings, modern absorbing boundary conditions in time domain and periodic boundary conditions in x-y- and z-direction when computing eigenvalues. The generalized diagonal material fillings reduce the frequency error caused by the boundary approximation by a factor of 10. The modern absorbing boundary conditions work for arbitrarily large port dimensions without the need to consider any portmodes.

1 GENERALIZED DIAGONAL FILLINGS

Material-fillings are parameters of the differential equations or, when perfect electric or magnetic materials are present, they are boundary conditions for the differential equations. The approximation of the material fillings often deteriorates the quality of the solution more than the approximation of the differential equation itself. The simplest material approximation is the assumption of a homogeneous filling inside every single cell. This is the "staircase" approximation. The approximation with triangular prismatic cells allows that there are two different materials in each cell. This approximation is in wide use and gives good results for geometries that are essentially cylindric. For boundaries with general curvature, the approximation with prismatic cells gives results only slightly better than a staircase approximation.

Fortunately, the filling with prismatic cells can be generalized. Since the finite difference coefficients for a field component depend only on the material in the immediate vicinity of the edge where the component is defined on, one can work easily with a mesh-filling that is constructed by a boolean combination of prismatic fillings. Figure 1 shows some of the possible discretized material distributions. A similiar mesh filling is mentioned in [1]. Figure 2 shows an example of the quality of the material approximation.

In order to show the effect of the generalized filling, figure 3 shows the computed resonance frequency of the fundamental mode in a sphere as a function of the mesh-spacing. For comparison, the results for prismatic filling and the optimal quadratic behaviour is plotted also. The error with the improved filling is about as low as the optimal quadratic behaviour. If the boundary conditions, ie. the materials would have been discretized perfectly, the result would not be much better.

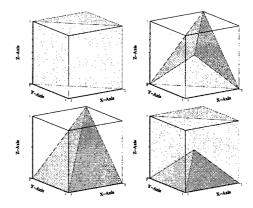


Figure 1: Some examples of the possible inhomogeneous fillings of a cell. Upper left: a prism. Lower left: Intersection of two prisms. Upper right: Intersection of three prisms. Lower right: Union of "upper left" and "lower left". The prism in the upper left can be oriented in 2×3 different kinds in a cell, the other three material fillings are possible in $4 \times 3 \times 2$ different orientations.

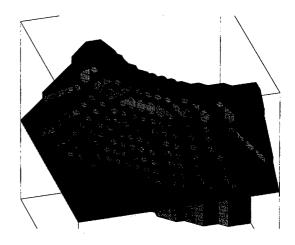


Figure 2: Detail of the "nose" of a reentrant cavity, discretized with the generalized diagonal fillings.

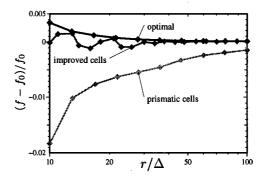


Figure 3: Error in the computed frequency of the lowest mode in a sphere as a function of gridplanes / radius.

^{*} bruns@tetibm2.ee.TU-Berlin.DE

2 PERIODIC BOUNDARY CONDITIONS

GdfidL's resonant solver allows periodic boundary conditions in all three cartesian directions simultaneously.

To demonstrate the capability, the periodic boundary conditions are applied to compute the dispersion relation in a crystal made of an rectangular array of conducting spheres connected by round rods. Figure 4 shows an elemental cell of this array. Figure 5 shows the computed frequencies as a function of the wave-vector \vec{k} .

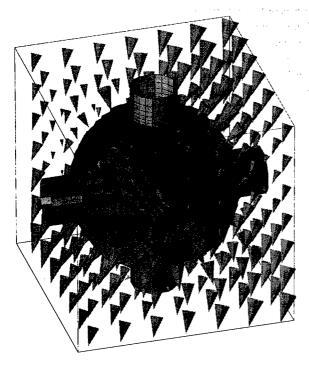


Figure 4: The elemental cell of a 3D array of perfect conducting spheres, connected by round conducting rods. The lattice constant a is the same in all three directions, the radius of the spheres is 0.375 a, the radius of the rods is a/10. The spheres are located at (x, y, z) = (la, ma, na), $(l, m, n \in \cdots -2, -1, 0, 1, 2, 3 \cdots)$. The shown field is the real part of the fundamental mode with $\vec{k} = (1, 1, 1) \frac{\pi}{4a}$.

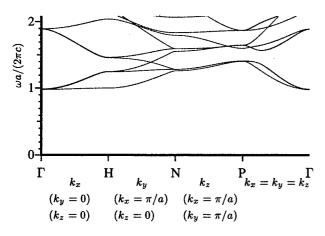


Figure 5: The band structure for the first few modes in the 3D array.

3 PML'S AS ABSORBING BOUNDARY CONDITIONS

GdfidL's time domain solver uses Berenger's "Perfectly Matched Layer" (PML) [2] to implement its aborbing boundary conditions (ABC's). The previous GdfidL [3] used an expansion in orthogonal port modes to implement its ABC's.

Compared with the expansion in orthogonal functions, PML's have two major advantages: 1.) Even for extremely large waveguides, one has negligible reflection for all fields without having to compute with a large number of portmodes. 2.) It is possible to have excellent broadband absorbing boundary conditions also for waveguides that are inhomogeneously filled with dielectrics.

Figure 6 shows such a geometry with large absorbing planes, inhomogeneously filled with dielectrics.

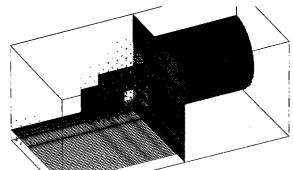


Figure 6: A coax to microstrip transition. The microstripline as a waveguide with an inhomogeneous dielectric is matched with an inhomogeneous PML.

4 CONCLUSION

An improved mesh filling has been implemented that reduces the frequency error by a factor of ten as compared to a prismatic filling.

Periodic boundary conditions are available for all three cartesian directions simultaneously.

PML's as absorbing boundary conditions allow inhomogeneously filled ports in broadband s-parameter computations.

- [1] W. Müller, J. Krueger, A. Jacobus, R. Winz, T. Weiland, H. Euler, U. Hamm, W. R. Novender, "Numerical Solution of 2- or 3-Dimensional Nonlinear Field Problems by Means of the Computer Program PROFI", Archiv für Elektrotechnik 65 (1982) pp. 299-307
- [2] J. P. Berenger, "A Perfectly Matched Layer for the Absorption of Electromagnetic Waves", J. Comput. Physics, vol. 114, pp. 185-200, Oct. 1994.
- [3] W. Bruns, "GdfidL: A Finite Difference Program with Reduced Memory and CPU Usage", Proceedings of the PAC-97, Vancouver, vol. 2, pp. 2651-2653, http://www.triumf.ca/pac97/papers/pdf/9P118.PDF

BEAM DYNAMIC ASPECTS OF THE TESLA POWER COUPLER

M. Zhang and Ch. Tang*
CST GmbH, Lauteschlägerstraße 38, 64289 Darmstadt, Germany

Abstract

We studied the beam dynamic behavior of the RF power coupler of the TESLA superconducting cavities. It is found that the transverse RF kick is not negligible. A transverse beam wandering of 1 to 2 mm was predicted and subsequently observed on the TESLA Test Facility. Two proposals are presented to reduce the kicks.

1 INTRODUCTION

TESLA is a superconducting RF based large linear collider project [1]. Its 9 cell superconducting cavity operating at L-band is fed by a coaxial coupler [2]. Due to its non-symmetrical layout, a transverse kick caused by electromagnetic fields is clearly inevitable. In order to address this issue, we conducted an intensive and systematic investigation into the complete dynamic process involving power feeding, bunch injection, kick accumulation, and emittance growth by means of both numerical and analytical methods.

The analytical and numerical results show a good agreement with each other, which are confirmed by the experiment. The transverse RF kick of the coupler is more than 120 times as strong as that of transverse wake fields of a TESLA 9 cell cavity by a 1 mm (σ_z) 1 nC bunch at 1 mm off-axis. The time variation of the kicks is directly responsible for the emittance growth, which is as high as 27%. The transverse offset at the exit of the first TESLA accelerating module in the TESLA Test Facility (TTF) is found to be $1 \sim 2$ mm at $E_0 = 15$ MeV and $E_{acc} = 15$ MV/m.

With a view to reducing the transverse kicks, two proposals are presented. One is by adopting alternating coupler arrangement; The other by symmetrical coupler. Both RF kicks and emittance dilution can be reduced dramatically.

2 SIMULATION APPROACH

The simulation is carried with MAFIA [3] in two steps: T3 for field and TS3 for beam simulations.

2.1 Field Simulation

The geometry is shown in Fig. 1. RF power is fed at the outer terminal at $x = x_{max}$. The two lowest cavity modes are E01-0 and E01- π .

2.1.1 Field Ratio

Table 1 lists \hat{E}_x , $c\hat{B}_y$, and \hat{E}_z at different Q_l values at 1 W input power. With this table, we derive the following

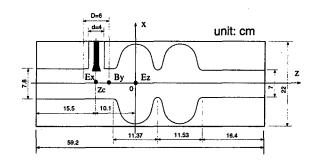


Figure 1: Geometry for time-domain simulations. At the three marked points, E_x , B_y , and E_z are monitored.

Table 1: Amplitudes of E_x , cB_y , and E_z

Q_l	\hat{E}_x (V/m)	$c\hat{B}_y$ (V/m)	\hat{E}_z (V/m)
1000	110	13.5	400
2000	110	15.0	800
4000	110	16.5	1600
6100	110	24.0	2700

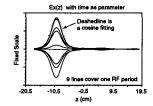
relations:

$$\alpha_E \equiv \frac{\hat{E}_x}{\hat{E}_z} \approx \frac{10^3}{4Q_l^{\alpha}}, \ _B \equiv \frac{c\hat{B}_y}{\hat{E}_x} \approx 0.075(2 + \frac{Q_l}{10^{-4}}).$$
 (1)

With the above, we can obtain coupler fields at any Q_l by extrapolation, thanks to the linear scaling law.

2.1.2 Spatial and Temporal Dependence

The spatial field distributions along the beam axis are shown in Fig. 2. As an approximation, we use following functions for the spatial dependence of E_x and B_y near the coupler,



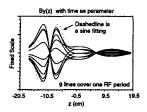


Figure 2: Spatial dependence of E_x and B_y

$$E_x(z) = \begin{cases} \hat{E}_x \cos \frac{\pi}{D} (z - z_c) & |z - z_c| \le \frac{D}{2} \\ 0 & \text{otherwise,} \end{cases}$$
 (2)

$$B_y(z) = \begin{cases} \hat{B}_y \sin \frac{\pi}{D} (z - z_c) & |z - z_c| \le D \\ 0 & \text{otherwise.} \end{cases}$$
 (3)

^{*} Accelerator Laboratory, Department of Engineering Physics, Tsinghua University, Beijing, China, 100084

Figure 3 shows E_x and B_y phase distributions along axis at different Q_l 's. For low Qs, $\phi_{E,l}=-\frac{\pi}{2}$ and $\phi_{B,l}=\pi$;

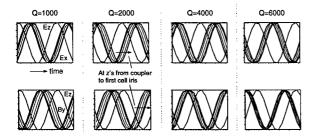


Figure 3: Temporal dependence of E_x (top) and B_y (bottom) with respect to E_z . Each plot has 8 curves which are monitored at 8 points along axis from z=-9.5 to -2.5 cm.

While for high Qs, $\phi_{E,h} = -\pi$ and $\phi_{B,h} = \frac{\pi}{2}$.

A complete set of expressions for E_x and B_y near the coupler can be written as follows:

$$E_x(z,t) = \hat{E}_x \cos \frac{\pi}{D} (z - z_c) \cos(\omega t + \phi_0 + \phi_E)$$

$$|z - z_c| \le \frac{D}{2},$$
(4)

$$B_y(z,t) = \hat{B}_y \sin \frac{\pi}{D} (z - z_c) \cos(\omega t + \phi_0 + \phi_B)$$

$$|z - z_c| \le D,$$
(5)

where ϕ_0 is injection phase. \hat{E}_x and \hat{B}_y are given by Eq. 1.

2.2 Kick Simulation

A full 3D geometry is used for kick simulations. Q_l is 6000. RF power of 1 MW is fed at t=0. A 1 nC 5MeV bunch of length 20 ps is injected at t=200 ns from either side of the cavity with $\phi_0=-45.6^o$ off-crest. The results are presented in Fig. 4. The beam divergences for both directions are

$$x'_{+z,num} = 2.9 \times 10^{-4}$$
 and $x'_{-z,num} = 5.8 \times 10^{-4}$. (6)

3 ANALYTICAL FORMULATION

With the above derived equations, we obtain

$$P_{x} = \frac{q\alpha_{E}\hat{E}_{z}d}{|c|} \frac{\frac{3}{\pi}}{1 - (\frac{3d}{\lambda})^{2}}$$

$$\left[\cos(\pi \frac{3d}{2\lambda})\cos(2\pi \frac{z_{c}}{\lambda} + \phi_{0} + \phi_{E}) + s\alpha_{B}\sin(\pi \frac{3d}{\lambda})\sin(2\pi \frac{z_{c}}{\lambda} + \phi_{0} + \phi_{B})\right]. (7)$$

For -z beam direction, change λ to $-\lambda$, s from 1 to -1, and ϕ_0 to $\phi_0 + \pi$.

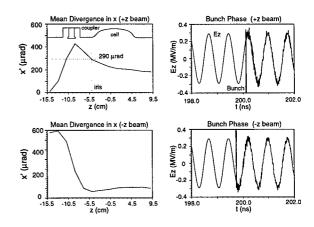


Figure 4: Kick simulation results. Top row: +z beam direction; Bottom: -z beam.

By inserting the parameters used in Section 2.2 into Eq. 7, $\hat{E}_x = 1.12 \times 10^5$, $\alpha_B = \frac{c\hat{B}_y}{\hat{E}_x} = 0.112$, we get

$$x_{+z,ana}^{'} = 2.6 \times 10^{-4}$$
 and $x_{-z,ana}^{'} = 6.1 \times 10^{-4}$. (8)

Comparing with the numerical results (Eq. 6), we find they agree within 10%. This nice agreement provides a solid basis for an extrapolation to high Q cases.

The RF kick for an actual TESLA cavity is estimated as follows. Given $Q_l=5\times 10^6, \hat{E}_z=30$ MV/m, $\phi_0=-15^o, d=4$ cm, $\lambda=23$ cm, $z_c=-10.1$ cm, we get (Beam goes in -z)

$$P_x = 2.9 \times \cos(2\pi \frac{z_c}{\lambda} + \phi_0)$$
 (keV/c) (9)
= $2.9 \times \cos(2\pi \frac{-10.1}{-23} + \pi + \phi_0) = 2.3$ (keV/c).

This value is more than 120 times stronger than transverse kick factor k_t^{9cell} , which is 18 V/nC/mm for a 1mm (σ_z) 1 nC bunch [4]. Another equivalence can be made to the wake field kick (k_t^{cplr}) of the coupler itself. Simulation shows $k_t^{cplr} = \frac{k_t^{9cell}}{5.3}$ for a 1 mm σ_z bunch, i.e. $k_t^{cplr} = 3.4$ V/nC (on-axis). To reach the 2.3 keV/c RF kick, the bunch charge should be as high as 676 nC!

Relative emittance growth can be estimated with

$$\frac{d\epsilon_{n,x}}{\epsilon_{n,x}} = (1 + \alpha^2) \left(\frac{d\sigma_x}{\sigma_x} + \frac{d\sigma_{P_x}}{\sigma_{P_x}} - \frac{d\sigma_{xP_x}}{\sigma_{xP_x}} \right) + \frac{d\sigma_{xP_x}}{\sigma_{xP_x}}.$$
(10)

Assume that the coupler kick is instantaneous, then $d\sigma_x = 0$. If the bunch comes into the coupler fields with $\alpha = 0$, Eq.10 can be simplified to

$$\frac{d\epsilon_{n,x}}{\epsilon_{n,x}} = \frac{d\sigma_{P_x}}{\sigma_{P_x}}, \text{ with } d\sigma_{P_x} = \frac{dP_x}{d\phi_0}\sigma_z,$$
 (11)

where σ_z is rms bunch length. With Eq. 9, we get $\frac{dP_x}{d\phi_0}=1.74$ (keV/c). At the entrance of the first cryomodule, $\sigma_z=1$ mm, so $d\sigma_{P_x}=47$ eV/c, i.e. $d\sigma_{(\gamma\beta_x)}=9.2\times 10^{-5}$. Assume $\epsilon_{n,x}=0.6\pi$ mm-mrad and $\sigma_x=0.2$ mm (TTF

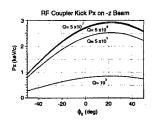


Figure 5: $P_x(\phi_0, Q_l)$. At certain Q_l , P_x may vanish.

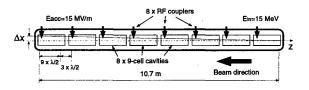
FEL 0.5 nC optimized case [5]), it yields $\sigma_{(\gamma\beta_x)}=3\times 10^{-3}$. And finally, we have

$$\frac{d\epsilon_{n,x}}{\epsilon_{n,x}} = \frac{d\sigma_{P_x}}{\sigma_{P_x}} = \frac{d\sigma_{(\gamma\beta_x)}}{\sigma_{(\gamma\beta_x)}} = \frac{9.2 \times 10^{-5}}{3 \times 10^{-3}} \approx 3\%. \quad (12)$$

For the cryomodule of eight couplers, there will be as high as 27% emittance growth. For FEL operation, this number is obviously not small. P_x shows a strong dependence on ϕ_0 and Q_l (Fig. 5).

4 ESTIMATION OF RF DISPLACEMENT IN THE FIRST TTF CRYOMODULE

The TESLA accelerating module (cryomodule, Fig. 6) is composed of eight cavities, each of which has an RF power coupler. The couplers are mounted at the downstream end of the cavities. We traced a single particle through the



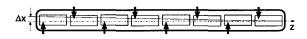


Figure 6: Top: Original TESLA cryomodule; Bottom: Alternating RF coupler placement – A proposal that reduces beam displacement by a factor of 5.3.

structure with lumped transverse kicks from the couplers. The accumulated offset Δx is $1 \sim 2$ mm. It has a strong dependence on ϕ_0 and Q_l . Since the absolute value of RF kicks is independent of initial beam energy, it is therefore more harmful at low beam energies. The displacement was confirmed by measurement [6].

5 SYMMETRICAL RF POWER COUPLER AND SUPER²STRUCTURE

The RF kick comes from non-symmetrical stationary field pattern near coupler. A natural solution is to use a symmetrical coupler. With particle simulations, emittance growth can be reduced by 17%. We propose to use such symmetrical coupler to feed two superstructures [7] in the middle,

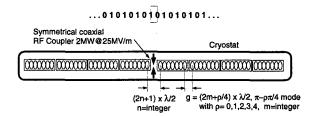


Figure 7: Super² structure proposal for TESLA. The symmetrical coupler ought to provide a 2 MW RF power, 1 MW for 4 cavities at 10 mA beam current [8]. Mode "a-b" is defined as (cell-to-cell)-(cavity-to-cavity) phase advance.

so called super² structure (Fig. 7). Effective accelerating length of a super² structure is 13% higher than that of the original structure. Given n=1, ρ =0, and m=1, the net geometrical length of a super² structure is 8x8=64 cells; Accelerating length is 8x7=56 cells. For the original structure, they are 8x12-3=93 cells and 8x9=72 cells, respectively. The gain ratio is then

$$\frac{\text{super}^2 \text{structure}}{\text{original TESLA}} = \frac{\frac{56}{64}}{\frac{72}{93}} = 1.13. \tag{13}$$

6 CONCLUSIONS

We made a systematic investigation of transverse kicks on beams by the TESLA RF power coupler. The analytical and numerical results agree quite well with each other. The theoretical prediction was confirmed by the experiment. The accumulated beam displacement in the TTF cryomodule is $1 \sim 2$ mm. Emittance growth is found to be as high as 27%. The proposed super² structure can not only exploit the effective accelerating length of TESLA, but also dramatically reduce the RF kicks.

- [1] R. Brinkmann, G. Materlik, J. Rossbach, A. Wagner (eds.), Conceptual Design of a 500 GeV e+e- Linear Collider with Integrated X-ray Laser Facility, DESY 1997-048 and ECFA 1997-182
- [2] D. Proch, P. Schmüser (eds.), TESLA Input Coupler Workshop, DESY Print, TESLA Report 96-09, August 1996
- [3] MAFIA version 4.013, CST GmbH, Lauteschlägerstraße 38, D-64289 Darmstadt, Germany, http://www.cst.de
- [4] A. Mosnier, Longitudinal and Transverse Wakes for the TESLA Cavity, DESY Print, TESLA Report 93-11, May 1993
- [5] M. Zhang, T. Limberg, PARMELA and COMFORT optimization results
- [6] S. Fartoukh and et al, RF Kick Measurement on TTF and Comparison with the TESLA Specifications, CEA/DAPNIA/SEA-98-42
- [7] J. Sekutowicz, M. Ferrario, Ch. Tang, Superconducting Superstructure for TESLA Collider, DESY Print, TESLA Report 98-08, April 1998
- [8] D. Proch, TESLA collaboration meeting, March 1998

EXPERIMENTAL AND ANALYTIC STUDIES OF AN RF LOAD RESISTOR*

D. L. Borovina*, J. M. Gahl, S. Humphries, Jr., UNM, Albuquerque, NM
 D. Rees, LANL, Los Alamos, NM, L. Toole, WSRC, Aiken, SC

Abstract

The pulsed output of an 850-MHz klystron was directed into a load assembly containing a water-cooled, 50-ohm resistor. The load was systematically subjected to high peak-power pulses from the klystron. Several thin-film resistors were tested and exhibited various damage patterns for different combinations of peak microwave power (33 kW – 500 kW) and heat input. In order to better understand the phenomena observed, the electromagnetic field distribution inside the resistor housing was studied with WaveSim, a two-dimensional, finite-element scattering code. The conformal mesh of the program allowed accurate representations of the complex assembly geometry.

1 INTRODUCTION

The Low Energy Demonstration Accelerator (LEDA), currently in the construction stage at the Los Alamos National Laboratory (LANL), will provide design confirmation and operational experience toward accelerator production of nuclear isotopes for defense and medical applications. Throughout the LEDA beam acceleration process, RF fields are established in the accelerating cavities using a large number of klystrons as compact, high-power-microwave sources. For this reason, a large number of microwave power-dissipating loads is also required.

LEDA utilizes 200-kW water loads containing thin-film resistors manufactured by Altronics Research, Inc. (ARI) through a proprietary process. Due to the initial rate of failure for these resistors, a study was initiated to test 25-kW water loads of identical design at various power ratings and levels of dissipation, to be supplied by ARI. An extensive information database has been created as the basis for future design improvements. These tests were performed at the University of New Mexico (UNM) using an 850-MHz klystron test stand.

2 EXPERIMENTAL LAYOUT

The UNM klystron uses a modulated anode to generate pulsed microwave bursts up to 2-ms long at a frequency of 850-MHz. The klystron amplifier produces a gain of 55.4 dB and a peak output power of 1.26 MW[1].

The amplified signal is extracted and fed to a test stand or an antenna using a waveguide equipped with an RF isolator to prevent reflected signals from damaging the klystron tube. For these experiments, the test stand consisted of a thin-film resistor and its housing (see Fig. 1), and was connected to the waveguide as a matching load.

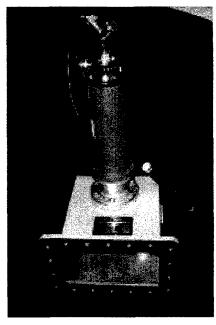


Figure 1: Photograph of the type 9725 resistive-load assembly for 850-MHz.

2.1 Resistor Design

The type 9725 resistor utilizes the same substrate and resistive film as the LEDA (type 57200) resistors, at approximately 1/10th physical scale. The cylindrical resistor substrate is composed of ground 96% aluminum oxide (cermet) and overcoated with bismuth rutinate, a metallic oxide. There is a single resistive layer (0.001 in thick) deposited on the cermet which is mechanically and chemically bonded through the fabrication process. The oxide is overcoated with glass and processed in air at 850°C. The glass coating was added to protect the film against water erosion.

Although the resistive film is deposited only on the outside surface, the tubular substrate is hollow in order to allow coolant (distilled water) to flow through the inside of the element as well as the outside.

Work supported by the U. S. Department of Energy under Contract No. DE-FG04-97AL77993.

^{*}Email: dlborovina@aol.com

Loading on the 57200 resistor (2.0x34 in) is about 99 W/in² based on a film surface of 202 in². In order to obtain a comparable film loading, the 9725 resistor (1.1x10 in), which has a total film surface area of 80 in², was initially powered at 30-33 kW. There is a physical difference in the resistor enclosures, which may not allow exact scaling for best possible data. This issue was addressed with the electromagnetic field distribution modeling performed using WaveSim.

2.2 Failure mechanisms

Two distinct mechanisms appear to be involved in observed film failures: thermal stress and dielectric breakdown.

Thermal stress usually occurs due to insufficient coolant flow, air bubble formation caused by pressure drop through the resistor housing, as well as small transients in the flow rate, such as those caused by water supply pressure variations. Heat damage to the resistor is usually caused by either localized boiling of the water coolant, or by differential expansion among several layers of dissimilar materials, both of which can result in the localized shattering of the resistive film.

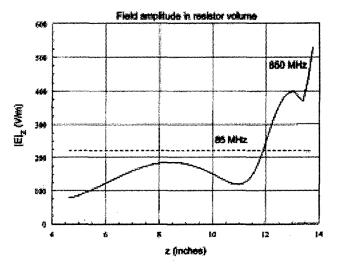
Dielectric breakdown occurs when the resistor is subjected to a high peak-power microwave pulse, which generates increased power dissipation throughout the resistive film, overloading the resistor. Localized areas are then formed where permanent physical damage has occurred and the resistive properties have changed. This kind of localized damage will continue until enough areas are affected, ultimately resulting in complete failure of the resistor as a load.

3 FIELD DISTRIBUTION ANALYSIS

In order to predict and explain any damage pattern observed during these experiments, the electromagnetic field distribution inside the resistor housing was modeled for both the 9725 and the 57200 elements. The simulation program used was WaveSim[2], a two-dimensional, finite element scattering code with applications in radar, communications and microwave devices. The fine conformal mesh used in the layout of the program allowed an accurate representation of the various layers and the complex assembly geometry involved.

The modeling showed a significant variation of the field magnitude along the length of the resistor, which indicates non-uniform power dissipation (see figure 2). When using water coolant, there is a strong concentration of the field near the downstream end connector. The power dissipation there is over 25 times that at the upstream end of the resistor. This result was consistent with early experimental results, in which the film was damaged circumferentially adjacent to the downstream connector.

Clearly, different input microwave frequencies create uneven power dissipation levels along the axis of the resistor element. At the resistor's test frequency (850 MHz), enhanced fields up to 5.7 kV/m were predicted compared to the approximately uniform field of



2.25 kV/m at a lower frequency (85 Mhz). Failures due to severe dielectric stress in this region were observed experimentally as noted in Section 4.

Figure 2: Field amplitude plotted from input end (left) to water downstream end (right) assuming 25W input power.

4 OUTLINE OF TESTS

UNM's klystron was used to first determine the limits of dielectric film strength. Resistor elements manufactured without protective glass coatings were chosen for this test, in order to allow sectional film resistance to be measured. This feature allowed significant thickness variations in the film to be observed both axially and rotationally (probably due to the manufacturing process). These initial tests bounded the film's rating for low power, low duty-cycle operation. No degradation was noted for 30,000 shots of 2 ms/1Hz pulses at 33 kW. Although the sample size was not statistically valid, this test suggested robust film performance is likely at the rated load. Similar tests were applied at peak powers up to 150 kW, eventually causing failure. A characteristic failure pattern was observed near the downstream connector, corroborated by WavSim modeling. ARI modified the contact ring design in response to this failure.

At the end of the first test phase, it was observed that coolant was causing film erosion and unwanted film aging during the experiment. Therefore, all subsequent tests were performed using ARI's coated stock elements. Test goals were also modified to allow data to be taken over a wider range of both temperature and input RF power. In order to standardize the effect of film aging, a fixed pulse sequence was chosen.

LEDA's requirements for resistive loads target 75% availability or 6,570 hrs per year, but at intermittent loading. A valid test for a resistor rated at 50,000 hrs MTBF (Mean-Time Between Failure) requires a simulation of 50/6.57 = 7.5 years of life in order to insure that at least one life-cycle's operation has been tested. Further, each resistor will be required to withstand 20 reflected power events per day in the first year, tapering to 5 per day in three years, then continuing at that rate until failure. Based on these assumptions, a final series of tests were performed to identify the failure curve for this scenario. They are described in Section 5.

5 EXPERIMENTAL RESULTS

5.1 Test Setup

The microwave output of the klystron was fed into the resistor load in pulses about 1-ms long at a repetition rate of 3 Hz. In this way, approximately 13K shots for each data point were obtained in roughly one hour. The input pulse, as well as the reflected pulse, was closely monitored to observe the functioning of the resistor. Since the dissipated thermal energy was low, an independent means of controlling film surface temperature was required. Heat input was varied by use of a thin, 2.5 kW electrical water heater that was inserted into the inlet cooling channel. Due to its geometry, some uneven flow distribution along the inside resistor surface occurred which cannot be easily quantified. The amount of heat rise needed for each test was controlled by varying the flow of the cooling water. A resistor was declared 'failed' as soon as a significant increase in the reflected microwave power became measurable, indicating a change in the load impedance.

5.2 Failure Curve

Three different resistors were used, each at a different amount of heat rise, ΔT , roughly 15 °C, 7 °C, and 3 °C. Each resistor was initially subjected to a relatively low power level, after which peak power was increased in increments of 33 kW. Tests were continued until failure of each resistor occurred.

The results of this extensive series of tests are shown in the graph of Figure 3. All data below 15 °C were obtained through direct measurement, while the remainder was estimated from vendor specifications. Reliable operation is implied in the region to the left of the failure curve. Published ratings are 25 kW continuous dissipation at 20 °C rise.

It should be noted that the failure region cannot be precisely defined with this method since such effects are gradual, i.e., conditioning is a significant factor. If a longer pulse width (50-100 ms) had been chosen, the region would likely be more constrained. Conversely, if a shorter pulse series (less than 13,000) had been applied at

each test point, the region may have been less constrained. The ultimate value of performing such tests lies in their general ability to highlight areas of needed design improvement.

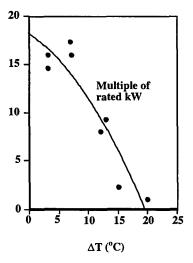


Figure 3: Failure curve for the 9725 resistor (Multiple of Rated Power vs. Heat Rise, ΔT).

6 CONCLUSIONS

A variety of conclusions were drawn from the results of this study, namely:

- 1. The electromagnetic field distribution inside the resistor housing was modeled accurately using the simulation code WaveSim, resulting in a design change.
- 2. The combined effect of heat and dielectric stress are causal factors in film breakdown, as summarised above.
- 3. Manufacturing variability adds an unquantified dimension to the problem of applying film resistors at RF power densities near their ultimate ratings. In this operating regime, further work is needed to insure component reliability.
- 4. Additional test data for RF film resistors are needed in applications such as LEDA. Specific issues include: scaling to larger elements, continuous versus pulse power ratings, and the impact of water flow instability.

7 ACKNOWLEDGEMENTS

We acknowledge and thank Lee Terry of UNM for the help in experimental preparations, as well as Gary Youell of WSRC for his participation and helpful insight.

8 REFERENCES

[1] D. L. Borovina, J. M. Gahl, D. Rees, "Spectral Analysis of Breakdown at or Near RF Windows", presented at the Particle Accelerator Conference PAC'99, New York, April 1999.

[2] WaveSim, authored by Dr. Stan Humphries, Jr. of UNM-EECE, Albuquerque. N.M. Contact: humphrie@warlock.eece.unm.edu

CLANS2-A Code for Calculation of Multipole Modes in Axisymmetric Cavities with Absorber Ferrites*

D.G. Myakishev, Budker INP, Novosibirsk, Russia 630090 V.P. Yakovlev, Omega-P, Inc, 345 Whitney Avenue, New Haven, CT 06511

Abstract

The code CLANS2 is an improved version of SuperLANS code [1] for calculation of axisymmetric cavities. This code permits the evaluation of multipole modes in cavities with partially loss dielectric and ferrite fillings. The code solves a complex eigenmode problem. A self-consistent problem is solved for frequency-dependent dielectric permittivity and magnetic permeability.

1 INTRODUCTION

The cavities with high loss ferrite filling are used in many Ferrite insertions are used, for example, in superconducting accelerating cavities for HOM damping [2] and in high power RF amplifiers for self-excitation damping (see, for example, [3]). Most RF cavities have rotational symmetry, with a small amount of weak distortion produced by coupling elements. So 2D codes continue to play an important role in practical calculations. A calculation of the monopole modes in the presence of high loss materials can be produced using codes, such as CFISH [4] and CLANS [5]. In the present paper we describe a new code, CLANS2, for multipole mode calculations in axisymmetric systems. multipole mode calculation is necessary, for example, for analysis and optimisation of transverse impedance of accelerating cavities with ferrite HOM dampers in cyclic accelerators [2]. It may also be useful for design and optimisation of RF sources, where operating modes have azimuthal variations, i.e., gyrotrons, gyroklystron, etc.

2 SOLUTION METHOD

CLANS2 is based on the same method as SLANS2 [5]. Unlike the scalar problem for monopole modes, the problem of multipole mode calculation is a vector problem. For example, the magnetic field is described by wave equation:

$$rot \frac{1}{\varepsilon} rot \vec{H} - \omega^2 \varepsilon_0 \mu_0 \mu \cdot \vec{H} = 0, \qquad (1)$$

where ε and μ are complex permittivity and permeability. Eliminating azimuthal field component, we obtain a system of the two equations for H_z and H_r , which has no spurious solutions [6,7]. The boundary conditions for

magnetic field on a metallic surface have the following form [8]:

$$\frac{\partial H_{\rm r}}{\partial n} + K \cdot H_{\rm r} = 0, \quad H_{\rm n} = 0 \tag{2},$$

where K - is the curvature of surface in (r, z) plane. Solving the eigenvector problem for radial and axial components of magnetic field, we can reconstruct the azimuthal component of magnetic field and all components of electric field using Maxwell equations. Notice that it is also possible to solve the eigenmode problem for the same components of electric field. In this case the field equations have the same form, except that the boundary conditions on a metallic surface are [8]:

$$\frac{\partial E_n}{\partial n} + (K + \frac{n_r}{r})E_n = 0, \quad E_r = 0$$
 (2'),

where n_r is radial component of unit vector normal to surface in (r, z) plane. The two-component field equation is solved using the finite element method. We use a scalar eight-node rectangular isoparametric elements. These curvilinear elements provide a second-order approximation, and permit the describing of the geometry with high accuracy. The algebraic system of equations for the mesh node field values is obtained using Galerkin's method. The matrix system in our case is complex and asymmetric. To satisfy the boundary condition on a metallic surface we use the method described in [8]. We rewrite the equations for the mesh nodes on metallic surfaces for the normal and tangential field components: H_n , H_τ or E_n , E_τ and combine these equations to satisfy (2 or 2'). On ferrite or dielectric surfaces the problem of satisfying the boundary conditions is more complicated. In (r, z) plane only the tangential field components H_{τ} and E_{τ} are continuous. So we rewrite the equations for B_{n} , H_{τ} or D_n , E_τ (instead of H_n , H_τ or E_n , E_τ) for the mesh nodes on ferrite or dielectric boundary to satisfy the boundary conditions [5]. This method allows the use of a regular finite element mesh. To find several modes simultaneously in an arbitrary spectrum domain, we use subspace iteration method with frequency shift for an asymmetric algebraic problem [9]. If the permittivity and permeability of the lossy filling depend on frequency, the self-consistent problem is solved. The iterations are produced in the following way. The solution for fixed permittivity and permeability is used as an initial

^{*} Work was supported in part by the grant JJ7100 from the International Science Foundation

approximation. Then for this frequency the new values of permeability and permittivity are chosen. Using these values of permittivity and permeability, we find the new frequency by the method of inverse iteration with frequency shift, which provides the effective separation of required mode, and so on utill convergence. We use the frequency of the previous iteration as a new frequency shift. As a rule, several iterations are enough to obtain the self-consistent solution. Iterations are produced automatically if a file with permittivity and permeability frequency dependencies is prepared.

3 TESTS AND EXAMPLES OF **CALCULATIONS**

A spherical cavity with concentric spherical dielectric or ferrite insertion with high losses ($tg\delta = 1$) was used as a test. For a mesh containing only 100 elements the difference between analytical calculations and CLANS2 results is less than 0.3% for the frequencies of the first 10 dipole modes. The code CLANS2 is currently used for multipole spectrum simulations in CESR superconducting cavity having ferrite HOM dampers [10]. The finite element mesh, which is used for dipole mode calculations, is shown in the Fig.1. The lines, where $r \cdot E_{\omega} = const$, are shown for two modes in the Figs. 2-4. Second mode is a "ghost" mode, which is located near the ferrite insertion and has very low quality factor. The field map $r \cdot E_{\omega} =$ const for multipole modes is not, of course, a physical vector field, as for monopole modes, but it is helpful for mode identification. The code calculates the transverse impedance for modes, which is used for calculation of the beam instability growth rates. Another example of the multipole calculation is a variant of the room-temperature "single mode" cavity, proposed by V.M. Petrov [11]. A coaxial line with absorber is used to damp HOMs, both longitudinal and transverse. The position and size of the coaxial line is chosen in such a way that the fundamental mode does not propagate into the coaxial line. perfectly matched load is simulated by the lossy ferrite filling of the end part of the coaxial line (see Fig. 6 and 7). The filling parameters are chosen in such a way as to eliminate reflection. The cavity spectrum and transverse impedance for multipole modes was calculated by CLANS2. The field map of the lowest dipole mode, which is damped by the coaxil load, is shown on Fig.6 and Fig.7.

4 CONCLUSIONS

A code has been developed that permits the deermination of multipole modes in cavities with partially loss dielectric and ferrite fillings. It may be used to solve the following problems:

calculation of multipole modes in RF cavities with ferrite HOM dampers,

- simulation of the cavities of RF sources having lossy
- simulation of the RF cavities with a matched external

The code is written for Windows and UNIX platforms.

5 ACKNOWLEDGMENTS

The authors would like to thank Dr. B. Hafizi for careful reading of the manuscript.

- [1] D.G. Myakishev, V.P. Yakovlev, "An Interactive Code SuperLANS for Evaluation of RF-cavities and Acceleration Structures", in IEEE Particle Accelerator Conf. Rec., 1991, vol.-5, pp.3002-3004.
- [2] S. Belomestnykh et al. Superconducting RF System for the CESR Luminosity Upgrade: Design, Status, And Plans. in Proc. of EPAC96 Conf., pp 2001-2003
- [3] H.W. Matthews, W. Lawson, J.P. Calame, M.K.E. Flaherty B. Hogan, J. Cheng, and P.E. Latham, "Experimental Studies of Stability and Amplification in a Two-Cavity Second Harmonic Gyroklystron", *IEEE Trans. in Plasma Sci.*, v. 22, N5, pp. 825-833 (1994)

 [4] M.S. de Jong et al., *J. Microw. Power Electromagn. Energy*, 27:136-142 (1992)

 [5] D.G. Myakishev, V.P. Yakovlev, "The New Possibilities of Syncol ANS. Code. For Furbration of Assistance of Assistance of Syncol ANS. Code. For Furbration of Assistance of A
- SuperLANS Code for Evaluation of Axisymmetric Cavities", in *Proc. of PAC95*, pp 2348-2350
 [6] M.M. Karliner, B.M. Fomel, V.P. Yakovlev, "LANS2 A
- Code for Calculation of Oscillation with Azimuthal Field Variations in Axisymmetric Cavities." Preprint Budker INP 83-114 (in Russian).
- [7] T. Weiland, "Transverse Beam Cavity Interaction, Part 2. Long Range Forces (On The Computation of Resonant Modes in Cylindrically Symmetric Cavities)," Preprint DESY 83-005,1983.
- Yu. Portugalov, "Method of Eigenmode Calculation in Cavities of Arbitrary Shape", Preprint IHEP 83-2, Serpukhov (in Russian).
- [9] A.I. Fedoseev, "Subspace Iteration Method for Asymmetric General Eigenvalue Problems", Preprint IHEP 85-25, Serpukhov (in Russian).
- [10] S. Belomestnykh, private communication.[11] V.M. Petrov, V.N. Volkov, E. Kenjebulatov, private communication.

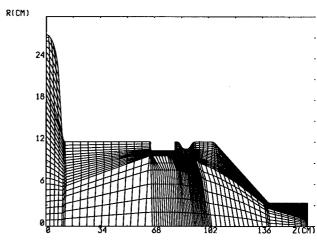


Figure 1: Finite element mesh for CESR superconducting cavity.

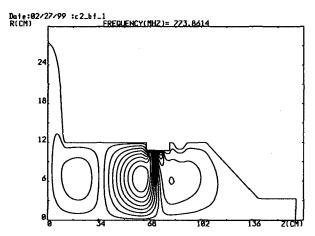


Figure 2: Field pattern of real part of a dipole mode of CESR superconducting cavity.

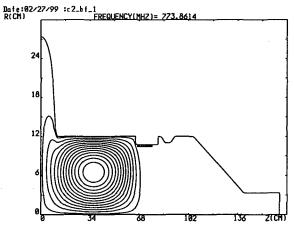


Figure 3: Field pattern of imaginary part of a dipole mode of CESR superconducting cavity

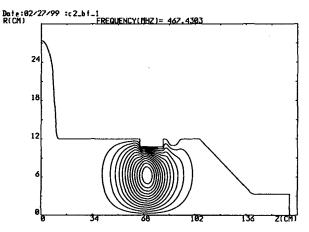


Figure 4: Field pattern of real part of a dipole "ghost" mode of CESR superconducting cavity.

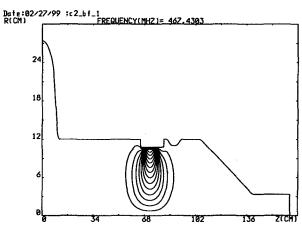


Figure 5: Field pattern of imaginary part of a dipole "ghost" mode of CESR superconducting cavity.

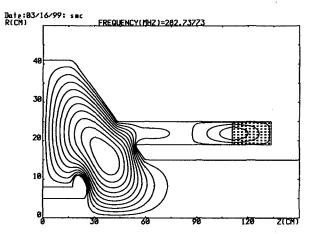


Figure 6: Field pattern of real part of a dipole mode of room-temperature "single mode" cavity.

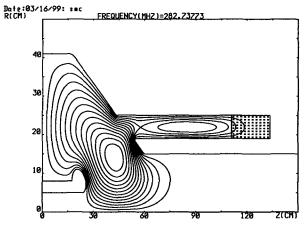


Figure 7: Field pattern of real part of a dipole mode of room-temperature "single mode" cavity.

COMPARISONS OF PARTICLE TRACKING AND CHARGE DEPOSITION SCHEMES FOR A FINITE ELEMENT GUN CODE*

E.M. Nelson[†], LANL, Los Alamos, NM; K. R. Eppley, J. J. Petillo, SAIC, Boston, MA S. J. Humphries, Jr., Field Precision, Albuquerque, NM

Abstract

A new finite element gun code is under development. In an effort to improve the gun code model, a concept[1] has been proposed recently that treats fields in a typical way, but includes a unique, formal approach to both particle tracking and source allocation. Being a new approach, there are concerns about the speed, accuracy, and appropriateness of this proposal for the electrostatic, steady-state particle-in-cell (PIC) gun model. In order to resolve some of these issues, a variety of particle tracking and charge deposition schemes are being evaluated with respect to accuracy, speed, robustness, and effect on the model. This includes various methods for computing the electric field at the particle locations. For this study, we are using the SAIC 3D gun code AVGUN as a testbed to incorporate and evaluate these methods. Results of a theoretical analysis of the methods will be presented, and a comparison will be made with the empirical results.

1 INTRODUCTION

Some concepts for a new finite element (FE) gun code were proposed recently[1]. This new FE gun code will model complicated 3D problems. The proposed concepts focused on dealing effectively with issues a gun code will encounter on an unstructured grid.

For example, rays are traced through the unstructured grid element by element using local coordinates in each element. Such a particle-tracking scheme has numerous qualities which we will not enumerate here. Concerning the finite element field calculation, the potential is a linear combination of basis functions $N_i(\mathbf{x})$,

$$\phi(\mathbf{x}) = \sum_{i=1}^{n} \alpha_i N_i(\mathbf{x}). \tag{1}$$

The electric field is the derivative of this potential with no additional smoothing,

$$\mathbf{E}(\mathbf{x}) = -\nabla \phi(\mathbf{x}) = -\sum_{i=1}^{n} \alpha_i \nabla N_i(\mathbf{x}). \tag{2}$$

The charge deposition scheme follows from the formal application of the finite element formulation: the linear

charge density multiplied by the basis functions are integrated along the ray trajectories,

$$b_i = \int_{\Omega} \rho N_i \, d\Omega = \sum_{j=1}^{n_r} \int_{R_j} \frac{I_j}{v_j(s)} N_i(\mathbf{x}_j(s)) \, ds. \tag{3}$$

There are numerous questions concerning the speed, accuracy and utility of the proposed concepts. In this paper we compare and contrast three charge deposition schemes and three electric field interpolation schemes in the context of a simple 1D problem which can be solved analytically. The basis functions N_i for ϕ are linear. The charge deposition schemes studied are constant (where the charge in an element is shared equally among the element's nodes), nearest grid point (NGP) and linear (i.e., Eq. 3). The field interpolation schemes are constant (i.e., Eq. 2) and two forms of linear interpolation discussed below.

2 THE TEST CASE

We studied a simple 1D diode problem which can be solved analytically. The parameters of the problem are listed in Table 1. A finite particle energy at the cathode was chosen so that the singularity at a space charge limited (SCL) cathode is avoided. Similarly, the current transported across the diode was fixed. Differences in SCL emission algorithms in various codes do not affect this study. The limiting case of perfect integration of the equations of motion in the presence of the discretized fields was pursued, so issues arising from finite integration steps are mitigated. The voltages were chosen so that the problem is essentially non-relativistic. The meshes are uniform.

Table 1: 1D Diode Test Case Parameters

anode-cathode gap, d	0.05 m
anode-cathode voltage, $\phi_d - \phi_0$	4.5 kV
electron energy at cathode, ϕ_0	10eV
current density, J	-250 A/cm ²
cathode electric field, $E(0)$	-34.9187 kV/m
anode electric field, $E(d)$	-115.782 kV/m
transit time, $ au$	2.86391 ns

For this 1D problem there are only two measures of the quality of the beam calculation: transit time and particle energy. The computational schemes presented in this paper

^{*} Work supported by DOE, contract W-7405-ENG-36, and ONR, NRL contract N 00014-97-C-2076.

[†]Email: enelson@lanl.gov

all conserve energy precisely at the anode. That is, the particle energy will be exactly the anode voltage, regardless of the discretization of the anode-cathode gap. The transit time is not exact in any of the schemes studied here, so transit time error will be our main measure of the quality of the beam calculation. The analytic results in Table 1 were computed with a non-relativistic model.

The quality of the field calculation can be measured by the error of the computed potential at the nodes. Alternatively, the transit time error can be considered an integral measure of the error in the field calculation. The transit time is

$$\tau = \int_0^d \frac{dx}{v(x)} = \int_0^d \sqrt{\frac{-m}{2q\phi_e(x)}} \, dx,\tag{4}$$

where $-q\phi_e(x)$ is the kinetic energy of the particle. The potential ϕ_e derives from the integration of the electric field.

$$\phi_e(x) = \phi_0 - \int_0^x E(x') \, dx'. \tag{5}$$

In the analytic case there is no distinction between ϕ_e and ϕ (we take the arbitrary constant difference to be zero), but in the discretized problem the field interpolation algorithm may introduce a distinction. The transit time error is

$$\tau_{h} - \tau = \int_{0}^{d} \sqrt{\frac{-m}{2q\phi_{e}(x)}} - \sqrt{\frac{-m}{2q\phi(x)}} dx$$
 (6)
$$\cong \int_{0}^{d} \sqrt{\frac{-m}{8q\phi^{3}(x)}} (\phi_{e}(x) - \phi(x)) dx.$$
 (7)

3 TESTS WITH AVGUN

AVGUN is a 3D gun code which employs a Cartesian mesh. For this study, the code was modified to allow both linear and constant charge deposition schemes, and both linear and constant field interpolation schemes. In AVGUN, the linear field interpolation is performed on a dual grid, as is typical for finite difference (FD) codes. The electric field on the half dual cells at the ends of the grid is constant. An FE field solution option was added to AVGUN's existing FD field solver.

The details of the matrix equation representing Poisson's equation in 3D are different between the FD and FE algorithms, but for a 1D problem the matrices are equivalent. The 1D test problem was modeled with AVGUN using both algorithms, and the FE case agrees with the FD case.

The quality of the AVGUN calculations was measured by the error in the electric field at the cathode. This electric field was computed by linearly extrapolating the electric fields in the first two cells (E(h/2)) and E(3h/2) to the cathode. The integration step size $h_{\rm ray}$ was varied, and the results were linearly extrapolated to infinitesimal step size. The dependence of the relative error on integration step size was approximately $(600\%)h_{\rm ray}/d$. The results are shown in Fig. 1. From this test, it appears that the constant charge deposition scheme performs better than the linear charge

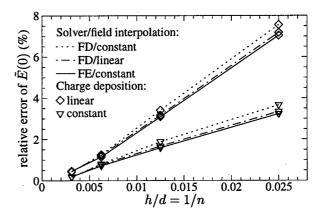


Figure 1: Relative error of the electric field $\tilde{E}(0)$ at the cathode, computed by linear extrapolation of the electric field in the first two cells, versus cell size h.

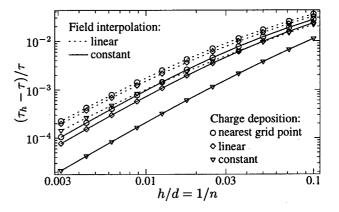


Figure 2: Relative error of the transit time τ_h versus cell size h, using various field interpolation and charge deposition schemes.

deposition scheme. Furthermore, the choice of field interpolation scheme shows no significant effect.

Transit time in the AVGUN simulations was also scrutinized, but the results were difficult to interpret due to additional random errors, perhaps residual errors left by the iterative solvers, which were about the same size as the transit time errors of interest.

4 TESTS WITH A 1D CODE

Further tests were performed with small 1D codes that integrated the equations of motion cell by cell, either analytically or with a high order adaptive integrator. Furthermore, the matrix equations were solved directly instead of iteratively, and the relaxation procedure was performed to the limit dictated by numerical precision. The results are shown in Figs. 2-4. Linear field interpolation in this case means an average electric field is computed at each node, and then these average electric fields are interpolated linearly within each cell. There is no dual grid.

The transit time errors shown in Fig. 2 would indicate once again that the constant charge deposition scheme was superior. These two results were surprising to the authors,

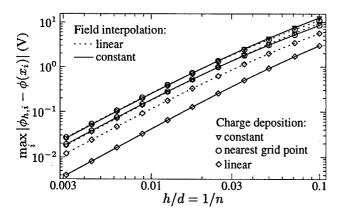


Figure 3: Maximum error of the nodal potentials $\phi_{h,i}$ versus cell size h.

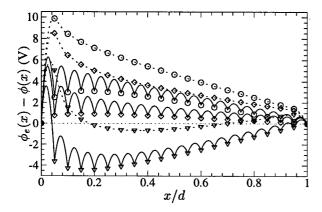


Figure 4: Potential error $\phi_e(x) - \phi(x)$ for h/d = 1/20 and various field interpolation and charge deposition schemes. Symbols identify the potential error at nodes. See Fig. 3 for legend.

so further explanation was pursued. In contrast, looking at the error in the potential at the nodes, shown in Fig. 3, one would conclude that the linear charge deposition, constant field interpolation scheme is superior.

Detailed examination of the potential reveals the source of this apparent discrepancy. While the potential at the nodes is very good in the linear charge deposition, constant field interpolation scheme, the error in the potential is dominated by the limited ability of the linear basis functions to interpolate the exact potential. The large bumps in Fig. 4 illustrate this. Error analysis of the finite element method[2, 3] also suggests this—the electric field error is minimized directly. Minimization of the potential error is secondary. Referring to Eq. 7, one can see that the transit time error arises mainly from the first few "interpolation error" bumps, where the particles are slowest and the relative velocity error is largest.

The dependence of the transit time error on the charge deposition schemes can now be understood. The constant scheme deposits more charge in the gap (in the sense that the components b_i of the source vector are larger), so the potential is depressed, and the transit time error due to interpolation error is partially cancelled. The NGP scheme

deposits less charge in the gap, so the potential is increased, adding to the interpolation error and thus the transit time error.

This situation does not depend on the particular parameters of the 1D test problem. Choosing a case with a smoother charge distribution (e.g., by injecting the beam at a higher energy) reduces the magnitude of the error, but the constant charge deposition scheme will still give a better transit time than the linear charge deposition scheme.

Fig. 4 suggests that an electric field calculation scheme which better interpolates the potential at the nodes would significantly reduce the transit time error. The linear field interpolation schemes studied here are defective in the sense that ϕ_e from Eq. 5 does not agree with the potential $\phi_{h,i}$ at the nodes. The potentials ϕ_e for these cases are systematically higher than the corresponding constant field interpolation cases, as shown in Fig. 4. This difference is mainly due to the field interpolation—the change in the nodal potentials is relatively modest in comparison. This difference in ϕ_e increases the transit time error.

Some existing FE gun codes (e.g., DEMEOS[4] and TRAK[5]) fit the potential at nearby nodes to a quadratic function, and then base the electric field on derivatives of this fit potential. A similar scheme which ensures agreement of the fit potential at the cell's nodes could make the linear charge deposition scheme unambiguously superior. Likewise, a higher order (e.g., quadratic) basis for the potential would significantly reduce the interpolation error and at the same time significantly reduce the error at the nodes.

5 CONCLUSION

A study of three charge deposition schemes and three field interpolation schemes in the context of a simple 1D problem indicates that the constant charge deposition, constant field interpolation scheme provides for the best simulation of the beam. However, the results also suggest that the path to further improvement of a linear basis FE gun code involves linear charge deposition combined with a better field interpolation scheme.

- Eric M. Nelson and John J. Petillo, "Conceptual Description of a Novel Finite Element Gun Code," ICAP'98.
- [2] Claes Johnson, "Numerical Solution of Partial Differential Equations by the Finite Element Method," Cambridge Univ. Press, 1987.
- [3] Strang and Fix, "An Analysis of the Finite Element Method," Prentice-Hall, 1973.
- [4] R. True, "A General Purpose Relativistic Beam Dynamics Code," CAP'93.
- [5] S. Humphries Jr., "Finite-element Methods for Electron Gun Design," ICOPS'96.

CALCULATION OF LONGITUDINAL FIELDS OF HIGH-CURRENT BEAMS WITHIN CONDUCTING CHAMBERS

L.G. Vorobiev and R.C. York NSCL, Michigan State University, East Lansing, MI 48824

Abstract

A technique for computing the longitudinal electric fields of a bunched beam propagating inside a conducting pipe is presented. A beam bunch is represented as a series of discs or slices, and the total electrical field is found by superposition of the fields of individual slices. The results of this technique agree well with other independent algorithms. The primary motivation for developing this technique is to provide efficient space charge calculations for beam dynamics simulation. However, the formalism may be employed in other applications to find electric fields for various beam density distributions in the presence of conducting boundaries.

1 INTRODUCTION

Simulations that include the effects of space charge provide a crucial basis for the design of high-current accelerator systems. In some cases, particularly for unbunched beams, two-dimensional (2-D) beam simulation particle-in-cell (PIC) codes are sufficient. However, for the case of bunched beams, the longitudinal effects can become important, and 3-D or nearly 3-D simulations are required.

The general 3-D PIC methods provide completely selfconsistent models, but frequently require very long computational times. As a result, the exploration of possible design space can, as a practical matter, be limited. An alternative approach is the modification of a 2-D PIC formulation to include important aspects of the longitudinal dynamics that will provide a nearly complete physics model and a computational speed that dramatically exceeds the general 3-D approach. A simple linear model of the longitudinal electrical field, corresponding to parabolic line charge density, is valid for ellipsoid-like beams in free space. However, in the presence of a conducting beam chamber with dimensions comparable to the transverse beam size, the longitudinal electric field becomes non-linear due to image charges. The non-linearity is especially apparent for the case of long or longitudinally asymmetric bunches. This paper describes a fast and accurate computational approach for the calculation of the longitudinal electrical field of beams with a relatively arbitrary charge density distribution within a conducting boundary. We believe the proposed method provides a unique strategy for the inclusion of longitudinal dynamics in simulation codes.

2 THE PROBLEM TO BE SOLVED

A common analytical approach to calculate the space charge electric fields of a beam propagating inside a conducting chamber is to find the solution of the Poisson equation. For rectangular or free space regions, the space charge potential may be found via the convolution integral in a rather simple and fast way [1]. However, with the inclusion of a conducting cylindrical surface, the Green's function, satisfying the zero boundary conditions, is expanded via modified Bessel functions. Simple analytical evaluation in this case is possible only after simplifying assumptions [2]. Even for such a simple situation as an ellipsoidal bunch in a cylindrical pipe, numerical methods are required to find the fields. Poisson Solvers using Cartesian or cylindrical grids [3] employing the FFT technique are now in common use in PIC codes. The approach described below is related to a Green's function formalism based on the charge density method [4] appropriate for PIC simulation.

Charge Density Method

For free space, the potential u, produced by the charge density ρ within the volume V is equal to

$$u(\mathbf{r}_0) = \int_{V} \frac{\rho(\mathbf{r}')}{\mathbf{R}} dV(\mathbf{r}')$$

where $1/\mathbf{R} = 1/|\mathbf{r}_0 - \mathbf{r}'| = 1/\sqrt{(x_0 - x')^2 + (y_0 - y')^2 + (z_0 - z')^2}$ is the Green's function. When V represents a symmetrical bunch, the potential may be rewritten as:

$$u(x_0, y_0, z_0) = (1)$$

$$= \int_{-Z_b}^{+Z_b} \int_{0}^{2\pi} \int_{0}^{R(z, \varphi)} \frac{\rho(r, \varphi, z) \ rdr \ d\varphi \ dz}{\sqrt{(r\cos \varphi - x_0)^2 + (r\sin \varphi - y_0)^2 + (z - z_0)^2}}$$

where for the particular case of an ellipsoid-like bunch $R(z,\varphi) = R_b \sqrt{1 - (z/Z_b)^2}$ (with R_b and Z_b the bunch radius and half-length correspondingly). If the charge density is given, then equation (1) determines the corresponding potential u. Conversely, if the potential u is known, then the corresponding ρ may be found from an integral equation (1). The formalism known as the moment method described below is from [5]. A similar technique called the charge density method [6] is commonly used in electron and ion optics.

3 SLICE FORMALISM

The original charge density method is too slow to be used repeatedly during step-by-step PIC simulation. We have developed a modification of the charge density method, which assumes a discrete representation of the bunch via charged discs or slices (see Figure 1). The total beam field is determined by superposition of individual fields.

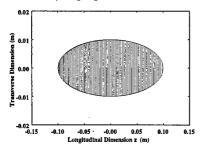


Figure 1. A uniformly populated ellipsoidal beam bunch modeled as 100 discrete slices. The bunch radius is R_b =0.01 m and the half bunch length is Z_b =0.1 m.

For a single slice of radius R^{slice} and charge density $\sigma^{slice}(r)$ the potential in the free space can be expressed:

$$u_{free}^{slice}(x_{_{0}}, y_{_{0}}, z_{_{0}}) = \int_{0}^{2\pi} \int_{0}^{R^{slice}} \frac{\sigma^{slice}(r) r dr d\varphi}{\sqrt{(r\cos\varphi - x_{_{0}})^{2} + (r\sin\varphi - y_{_{0}})^{2} + z_{_{0}}^{2}}}$$
(2)

(The integration over z is not required for the infinitesimally thin slice). If the point (x_0, y_0, z_0) is on the cylindrical surface, then $x_0^2 + y_0^2 = R_{cyl}^2$ and $u(x_0, y_0, z_0)$ defines the potential due to a single slice on the cylindrical surface at longitudinal position z_0 . The same potential evaluated at the position of that boundary $(r = R_{cyl})$ with opposite sign, is used to find the unknown surface image charge density σ^{image} on the cylinder from a single slice:

$$-u(x_{o}, y_{o}, z_{o}) =$$

$$\int_{0}^{2\pi} \int_{-z_{L}}^{+Z_{L}} \frac{R_{cyl}\sigma^{image}(r) dz d\varphi}{\sqrt{(R_{cyl}\cos\varphi - x_{o})^{2} + (R_{cyl}\sin\varphi - y_{o})^{2} + (z - z_{o})^{2}}}$$
(3)

with $z_o \in [-Z_L, +Z_L]$ ($Z_L = 4Z_b$ was found empirically). Reapplication of (3) for $x_o^2 + y_o^2 = r^2$ ($0 \le r \le R_{cyl}$) and for the determined σ^{image} provides $u_{image}^{slice}(r,z)$. The total potential: $u_{ioual}^{slice}(r,z) = u_{free}^{slice}(r,z) + u_{image}^{slice}(r,z)$ will then automatically satisfy the zero boundary conditions. The longitudinal on-axis potentials (r=0) for the middle slice are given in Figure 2.

When this procedure is applied in a PIC code, it is proposed that the potentials and electrical field values be calculated once for different slices and stored. During the simulation, these values with interpolation would be used to provide an accurate model of the longitudinal dynamics without the penalty of long computational time [4].

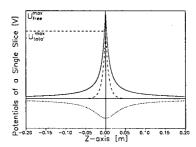


Figure 2. The free space (solid curve), image charge (dotted) and total (dashed) potential for a single slice.

4 APPLICATIONS OF THE SLICE TECHNIQUE

In the numerical examples below, we consider a specific case of an elliptical bunch inside a conducting cylindrical pipe of radius 0.02 m as shown in Figure 1. The half bunch length, is $Z_b = 10$ cm, the maximum transverse radius is $R_b = 1$ cm, and the total charge is $Q_{total} = 10^{-11}$ C. The transverse dimensions of the beam were assumed circular with a uniform radial charge distribution. The longitudinal dimension was assumed parabolic thus resulting in a parabolic line charge density $\lambda(z)$. In this example, the bunch was modeled as 100 individual slices.

For the full bunch in the absence of the conducting chamber, superposition of potentials for all slices results in parabolic potential and linear field. With the inclusion of a conducting cylinder, the total field (by superposition) is given in Figure 3. Note that, for this case, the $E_z(z)$ within the bunch is strongly non-linear. The potential and fields, calculated for Z_b / R_b =10, 5, 1 are in very good agreement [4] with reference [7] page 407.

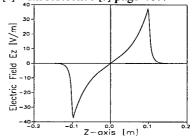


Figure 3. The longitudinal electric field $E_z(z)$ [V/m] along the beam axis, for the case of a bunch with m and the half bunch length is $Z_h / R_h = 10$.

More complicated situations, such as when the bunch has a non-symmetrical form in the longitudinal direction, can also be accommodated by the algorithm. Shown in Figure 4, is a possible asymmetrical bunch within a 4 cm diameter conducting pipe again modeled as 100 individual slices with the calculated $E_z(z)$ given in Figure 5. Though the geometrical shape of the bunch of Figure 4 is not dramatically different from that of Figure 1, the electric potential and field have significantly different profiles. The $E_z(z)$ is more non-linear, than that of Figure 3,

changing sign four times. In this case, the g-factor method [7] would lead to the wrong result.

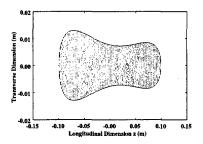


Figure 4. Asymmetrical bunch.

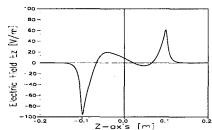


Figure 5. Longitudinal field $E_z(z)$ [V/m] found by slice superposition for the asymmetrical bunch of Figure 4.

Off-axis Electrical Field

So far we have computed only on-axis field $E_z(z)$ - at zero radial position. Shown in Figure 6 are the potentials and fields for different radial positions. From Figure 6 (all dimensions are the same as those of Figure 1), the approximation of simply using the on-axis value for $E_z(z)$ will cause significant errors only near the bunch ends. However, the maximum $Z_{max}(r)$ values for the example shown are $Z_{max}\{r=(0, 0.4, 0.8)\times R_b\}=0.1, 0.09, 0.06$ m. (The symbols are plotted at Z_{max} values in Figure 6) I.E., there are few or no particles in the area of significant deviation from E_z on-axis value.

Note that the off-axis potential u(r,z) as a function of r may be used to determine the transverse field E_r for all (r,z) that additionally could be employed, under some circumstances, to produce a very fast algorithm.

5 DISCUSSION AND CONCLUSIONS

For the examples given, a cylindrical vacuum pipe was assumed. However, the procedure can be used to accommodate more general chamber boundaries and beam shapes and this generalization is planned. To reduce simulation time, a range of slice geometries (in the simplest case – a range of discs of different radii) will be calculated and tabulated.

The required number of these "template" slices is an order of magnitude less than the number of slices representing the bunch. In the examples presented, 15 different slice configurations were used requiring a computational time of about 5 min (on a multi-user 433 MHz DEC Alpha). The example bunch configurations were modeled as 100 distinct slices with the potential for each slice derived from appropriate interpolation of the tabulated data and scaling for charge density. The construction of the total bunch potential required only about 0.2 s. Since the presimulation calculations (about 5 min) need only be done once while the accelerator simulations require many computations of the total bunch potential (about 0.2 s) as the particles are tracked through the system, the decrease in overall computational time will be enormous.

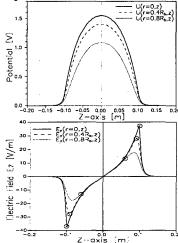


Figure 6. The dependence of u(r,z)[V] and the field $E_z(r,z)[V/m]$ as a function of z for $r = (0, 0.4 \text{ and } 0.8) \times R_b[m]$.

We are aware that the proposed sub-3-D PIC code will not be completely self-consistent since the planned presimulation calculational procedure will be unable to reflect all possible evolutions of the particle density. However, preliminary studies of the radial dependence of $E_{\rm c}$ field for different distributions suggests that the effect of variations in the transverse charge distribution is minor, and therefore, the analysis will be nearly self-consistent. Comparisons with the general 3-D codes are planned.

The authors are grateful to F.Marti for useful discussions.

- [1] J.D.Jackson "Classical Electrodynamics", Wiley, New York (1975), pp.116-118.
- [2] E.Henestroza, HIFAR Note 379, LBNL, Berkeley (1989).
- [3] L.G.Vorobiev, Preprint ITEP-193, Moscow (1984).
- [4] L.G.Vorobiev and R.C.York, MSUCL-1117, MSU/NSCL, East Lansing, October (1998).
- [5] R.E.Harrington, "Field Computation by Moment Methods", Macmillan, New York (1968).
- [6] M.Szilagyi, "Electron and Ion Optics", Plenum, New York (1988).
- [7] M.Reiser, "Theory and Design of Charge Particle
- Beams", John Wiley & Sons, New York (1994).

CALCULATION OF FINITE-LENGTH, HOLLOW-BEAM EQUILIBRIA

Jinhyung Lee* and John R. Cary[†] CIPS[‡] and Department of Physics, University of Colorado, Boulder, CO

Abstract

Finite-length equilibria occur in a number of intense-beam and plasma applications. Penning traps permit the study of intra-beam collective effects, as the additional freedom gained from having an internal conductor permits greater control over the plasma profile, so that monotonic, but not constant, plasma profiles can be obtained. On the basis that the thermal velocity of background neutrals and the drift velocity of the electrons are much lower than the thermal velocity of the electrons, and the rotation frequency is small compared to the gyrofrequency, the equilibrium equation can be reduced to a self-consistent Poisson equation where the source depends on the potential. We solve for these equilibria using a Gauss-Seidel relaxation method. Our results show the shape of the equilibria for various electrode configurations.

1 INTRODUCTION

Penning traps with nonneutral plasma under the influence of a magnetic field have been studied for a variety of experiments including plasma physics[1],[2], and Coulomb crystals[3]. Recently, these traps have been used for experimental tests of the CPT theorem, which predicts that various quantities such as masses, gyromagnetic ratios, and charge-to-mass ratios are equal for particles and antiparticles. The comparison of charge-to-mass ratios for the antiproton and proton in the trap is much more accurate than earlier comparisons made with other techniques[4].

In principle, plasma can be confined perfectly in an ideal trap with cylindrical symmetry. O'Neil and coworkers[5],[6],[7] derived and solved the equilibrium equations for a nonneutral plasma without a center conductor. They assume that the plasma is in thermodynamic equilibrium. A particular thermal equilibrium can be obtained from specific values of total number, total angular momentum, and total energy. Similarly, a nonneutral plasma beam in a solenoid at magnetic field has identical dynamics.

However, in practice, the particles cannot be confined indefinitely. Collisions with background neutrals and anomalous transport[8](which is independent of pressure) cause the plasma in the trap to expand radially[9]. Since the geometry and dynamics are similar to those of a Penning trap, these kinds of effects can be determined in the nonneutral beam. Thus penning traps permit study of intra-beam collective effects.

The equilibria of nonneutral plasma can be described by the self-consistent Poisson equation. Without a center conductor, the plasma evolves toward thermal equilibria in which the physical parameter, such as maximum number density, angular velocity, and temperature, are determined by the total number, the total angular momentum, and the total energy. However, for the trap with a center conductor, the bias potential is an additional parameter. This provides a mechanism to control the plasma. To study these systems, we have developed a method to find the solution numerically.

In this paper, we investigate the equilibria in two different cases. In the following section, we briefly explain how to get the thermal equilibria in both isothermal and adiabatic cases and show the results in one dimensional adiabatic process in which the entropy is constant, when the plasma is cylindrically symmetric, and it is long compared with the radius of the outer shell. In the next section, we develop a method to calculate two dimensional equilibria.

2 THERMAL EQUILIBRIUM

A modified Penning trap with a center conductor that is electrically biased allows control of equilibrium by changing the central potential. As shown in Fig. 1, an outer conducting cylinder is divided axially into three sections with a center conductor. Compared to the central section, the two remaining end sections are at more negative potential to confine negative charged particles axially. A uniform axial magnetic field with the electric field between two shells provides radial confinement.

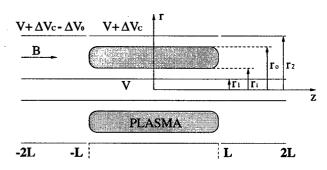


Figure 1: The side view of Modified Penning Trap. Here, B = 350G.

In order to understand the equilibrium state in the trap, we need to take an appropriate Hamiltonian. The plasma approximation (weak correlation) determines the equilibrium. The plasma approximation, that the plasma can be treated as a continuous fluid, requires that the number of particles in a Debye sphere be large, $(\bar{n}\lambda_D^3) \gg 1$). In this case the total Hamiltonian is the sum of the Hamiltonians for each particles, with the potential given by Poisson equa-

^{*}Email: jinhyung@ucsu.colorado.edu

[†] Email: cary@colorado.edu

[‡] Center for Integrated Plasma studies

tion where the charge density is the fluid density.

With such an approximation, the one particle Hamiltonian is

$$H = \frac{1}{2m}(p_r^2 + p_z^2) + \frac{1}{2mr^2}[p_\theta + \frac{e}{c}A_\theta(\vec{r})r]^2 - e\phi(\vec{r})$$
 (1)

where $A_{\theta}(\vec{r}) = \frac{Br}{2}$.

In a thermodynamic description[7] with conservation of total number, total angular momentum, and total energy, the distribution(a canonical ensemble) has the form

$$\rho(\vec{r}, \vec{p}) = Z^{-1} \exp\left[-\frac{H - \omega p_{\theta}}{T}\right]$$
 (2)

where Z can be determined from the total number. Integrating both sides over \vec{p} gives the number density

$$n(\vec{r}) = \bar{n} \exp \left[\frac{1}{T} \left\{ e\phi(\vec{r}) - \frac{m}{2} \omega(\Omega - \omega) r^2 \right\} \right]$$
 (3)

where ω is the constant angular velocity in the trap and \bar{n} is maximum number density.

Therefore, the self-consistent Poisson equation

$$\nabla^2 \phi(\vec{r}) = 4\pi e n(\vec{r}) \tag{4}$$

which gives equilibrium states, will be reduced to a dimensionless equation

$$\frac{1}{\rho}\frac{\partial}{\partial\rho}\rho\frac{\partial\psi}{\partial\rho} + \frac{1}{\rho^2}\frac{\partial^2\psi}{\partial\theta^2} + \frac{\partial^2\psi}{\partial\zeta^2} = e^{\psi} - (1+\gamma) \tag{5}$$

in terms of new dimensionless variables

$$\gamma \equiv \frac{m\omega(\Omega - \omega)}{2\pi\bar{n}e^2} - 1, \quad \psi \equiv \frac{e}{T}\phi - \frac{1 + \gamma}{4}\rho^2,$$

$$\lambda_D^2 \equiv \frac{T}{4\pi\bar{n}e^2}, \quad \rho \equiv \frac{r}{\lambda_D}, \quad \zeta \equiv \frac{z}{\lambda_D}.$$
(6)

Now we will briefly discuss adiabatic variation of equilibria. As we mentioned, each isothermal equilibrium in one dimension can be found by solving the self-consistent Poisson equation with conservation of total number, angular momentum, and total energy when the longitudinal length of plasma is sufficiently long compared to the radius of the outer shell on which the potential is constant. However, for the trap with a center conductor, a small and slow change of bias potential permits some electrical work between two shells, which means that total energy in the system is no longer a conserved quantity. But a slow change of the potential guarantees no entropy change in this system. Therefore, we can get the equilibria by changing the bias potential slowly.

From the definition of entropy, we can easily redefine the entropy as

$$S = -2\pi \int_{r_1}^{r_2} dr \ r \, n(r) \ln[n(r) \, T^{-3/2}] \tag{7}$$

where r_1 and r_2 is the radii of inner and outer shell[5]. With conservation of total number, angular momentum, and entropy, a particular bias gives other physical quantities, such as maximum number density, angular velocity, charges on the shells, and temperature.

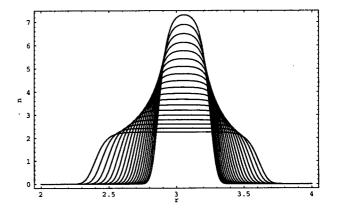


Figure 2: The density profiles $10^{-6}n(r)$'s vs r(cm) in adiabatic process. Here, $r_1=0.32, r_2=5.10, N=5\times 10^7 cm^{-1}, \frac{P_0}{m\Omega}=-2.35\times 10^8 cm$, and $S=-1.07\times 10^8 cm^{-1}$.

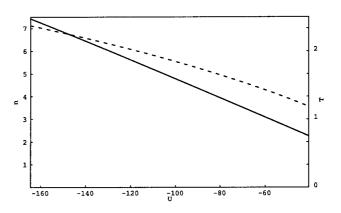


Figure 3: The maximum number density $10^{-6}n$ (Solid line) and The temperature $10^{-2}T(K)$ (Dashed line) vs potential difference U(eV).

From Fig. 2 and Fig. 3, we can see how the profile can be changed as the potential between two shells is changed. The figures show that smaller potential difference gives wider annular profile. They also show that the temperature decreases as the difference goes down, which means that the trap can be used to cool an electron plasma.

3 FINITE-LENGTH EQUILIBRIUM

For the case of a finite length column, the number density and the potential are independent of θ and those are determined by three parameters, γ , ΔV_C , and ΔV_0 (see Fig. 1

In this case, the dimensionless Poisson equation can be

reduced to

$$\frac{1}{\rho} \frac{\partial}{\partial \rho} \rho \frac{\partial \psi}{\partial \rho} + \frac{\partial^2 \psi}{\partial \zeta^2} = e^{\psi} - (1 + \gamma) \tag{8}$$

where the potential dependency of source term in the righthand side makes it more difficult to solve the equation.

We solve this equation numerically by using a nonlinear variant of the Gauss-Seidel iteration procedure for elliptical equations. The value, $\psi_{i,j}$, at a grid point depends on the values of the nearest grid points, $\psi_{i+1,j}$, $\psi_{i-1,j}$, $\psi_{i,j+1}$, $\psi_{i,j-1}$, and $\psi_{i,j}$ itself because the source term depends on ψ . Therefore, the relation can be of a form

$$\psi_{i,j} = f(\psi_{i,j}, \psi_{i+1,j}, \psi_{i-1,j}, \psi_{i,j+1}, \psi_{i,j-1}). \tag{9}$$

Finally the equation can be reduced to

$$\psi_{i,j}^{(n+1)} = \frac{1}{2(1 + \frac{\Delta\rho^2}{\Delta\zeta^2})} \left[-\Delta\rho^2 (e^{\psi_{i,j}^{(n)}} - 1 - \gamma) + (1 + \frac{\Delta\rho}{2\rho_i}) \psi_{i+1,j}^{(n)} + (1 - \frac{\Delta\rho}{2\rho_i}) \psi_{i-1,j}^{(n)} + \frac{\Delta\rho^2}{\Delta\zeta^2} (\psi_{i,j+1}^{(n)} + \psi_{i,j-1}^{(n)}) \right].$$
(10)

With the convergence condition, $|\psi_{i,j}^{(n+1)}-\psi_{i,j}^{(n)}|<\delta$ for sufficiently small δ ($=10^{-4}$), the equilibrium is obtained.

Since the length is sufficiently large compared to radius of outer shell, we may suppose that the cross section (z = constant) near the center should coincide with the one dimensional solution that is independent of θ and z, and that the profile varies little with z in the central region far from the end sections of outer shell. Our numerical solution does bear this out. Fig. 4 shows the two dimensional density distribution.

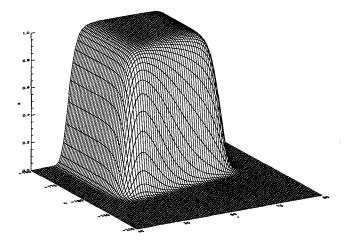


Figure 4: The 2D density profile $n(r,z)/\bar{n}$ near the z=-L in isothermal process. Here, $L=200\lambda_D,\ r_1=40\lambda_D,\ r_2=80\lambda_D,\ \gamma=1.0\times 10^{-5},\ V=3.70\,V,\ \Delta V_C=12.30\,V,\ \Delta V_0=12.30\,V,\ T=118.33\,K,$ and $\lambda_D=5.0\times 10^{-2}\,cm.$

4 CONCLUSION

Modified Penning traps allows us to confine and cool electron plasma both radially and axially with two potential differences. By changing the radial potential difference slowly, all physical parameters including temperature can be controlled. In the adiabatic process, the plasma is wider and colder as the potential difference is smaller.

- [1] J. S. deGrassie and J. H. Malmberg, Phys. Fluids 23, 63(1980).
- [2] G. Rosenthal, G. Dimonte, and A. Y. Wong, Phys. Fluids 30, 3257(1987).
- [3] W. M. Itano, et al., Science 279, 686(1998).
- [4] G. Gabrielse, et al., Phys. Rev. Lett. 74, 3544(1995).
- [5] T. M. O'Neil and C. F. Driscoll, Phys. Fluids 21, 266(1979).
- [6] S. A. Prasad and T. M. O'Neil, Phys. Fluids21, 920(1978).
- [7] T. M. O'Neil and Daniel H. E. Dubin, Phys. Plasma 5, 2163(1998).
- [8] D. L. Eggleston, Phys. Plasma 4, 1196(1997).
- [9] C. F. Driscoll, K. S. Fine, and J. H. Malmberg, Phys. Fluids 29, 2015(1986).

WAKE FIELD CALCULATION FOR THE TTF-FEL BUNCH COMPRESSOR SECTION

K. Rothemund, U. van Rienen
Institut für Allgemeine Elektrotechnik, Universität Rostock
Albert Einstein-Straße 2, D-18051 Rostock, Germany

Abstract

The TTF Free Electron Laser needs very short bunches to produce self-amplified spontaneous emission (SASE). This short bunch length is produced in a magnetic bunch compressor where the trajectories of particles with different energy have different path length in a way that the bunch is longitudinally compressed. As a parasitic effect the wake fields produced by the passing bunch will have the possibility to interact with the bunch itself and cause emittance growth. The high frequency behaviour of the beam pipe in the bunch compressor has to be analysed in order to identify trapped higher order modes (HOM) and to estimate beam distortion. Because of the complexity of the bunch compressor section direct eigenmode calculation is not possible due to lack of available computer power. A technique is presented which allows to compute eigenmodes of rf-structures by using scattering-parameters of subsections of the bunch compressor. This is done numerically based on the computer code MAFIA to model the different sections of the beam pipe.

1 INTRODUCTION

Numerical eigenmode calculations for complex components, such as the TTF bunch compressor, are limited by the available computer power, especially the available storage. In this paper a hybrid technique is presented to calculate eigenmodes and wakefields of geometrically complex structures via domain decomposition and mode matching.

The bunch compressor splits up into several subsections which are less complex and may be simulated individually with much smaller numerical effort of each single run. Since only the complete closed structure results in the eigenvalue problem determining eigenmodes and -frequencies, a splitting has to be done in terms of waves propagating between the sections described here using scattering-(S-)parameters.

2 BASIC IDEA

A rf-component can be represented by scattering- or Sparameters which describe signal reflection and transmission between each of the ports. It can be summerized in the scattering-matrix S:

$$\vec{b} = \begin{pmatrix} S_{11} & \cdots & S_{1n} \\ \vdots & & \vdots \\ S_{n1} & \cdots & S_{nn} \end{pmatrix} \vec{a}$$
 (1)

with $\vec{a} = (a_1, \dots, a_n)^T$ representing all input- and $\vec{b} = (b_1, \dots, b_n)^T$ the output signals. S_{ij} describes the transmission of the signal from port i to j; it is a complex function of frequency: $S_{ij} = |S_{ij}(\omega)| \exp\{j\varphi_{ij}(\omega)\}$

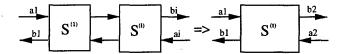


Figure 1: Describing a chain of rf-components with S-parameters.

The S-parameter formalism allows to connect several structures by combining their S-parameters (see [1]):

$$S^{(t)} = S^{(1)} \odot S^{(2)} \odot S^{(3)} \dots$$
 (2)

To solve for a resonator the open ports of the structure have to be closed which yields an eigenvalue problem. This is done by setting $a_1 = r_1b_1$ and $a_2 = r_2b_2$ and leads to

$$\begin{pmatrix} b_1 \\ b_2 \end{pmatrix} = \begin{pmatrix} S_{11}^{(t)} & S_{12}^{(t)} \\ S_{21}^{(t)} & S_{22}^{(t)} \end{pmatrix} \begin{pmatrix} r_1 & 0 \\ 0 & r_2 \end{pmatrix} \begin{pmatrix} b_1 \\ b_2 \end{pmatrix}$$
(3)

For example setting $r_1=r_2=-1$ will create a loss free electric short cut at both ports. In general r_1 and r_2 also depend on ω .

The eigenfrequencies are given by the solutions of

$$\det(\mathbf{SR} - \mathbf{E}) = 0 \tag{4}$$

with $R=\begin{pmatrix} r_1 & 0 \\ 0 & r_2 \end{pmatrix}$ and ${\bf E}$ the unity matrix. This is equivalent to

$$S_{11}^{(t)}r_1S_{22}^{(t)}r_2 - S_{11}^{(t)}r_1 - S_{22}^{(t)}r_2 + 1 - S_{21}^{(t)}r_1S_{12}^{(t)}r_2 = 0$$
(5)

3 SIMPLE TEST EXAMPLE

To verify the formulation given above a handy test geometry was modelled (see Fig. 2). Its eigenmodes could be

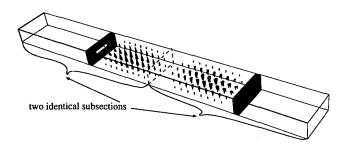


Figure 2: Test geometry with the \vec{E} -field of the third mode found by MAFIA, the boundaries are closed electrically.

calculated directly with the MAFIA [2] E-module. Both ports are closed electrically $(r_1 = r_2 = -1)$. The test geometry consists of two identical subsections of waveguide, each with an asymmetrically placed iris.

Assuming a reciprocal $(S_{mn} = S_{nm})$ and loss-free $(S^*S = E)$ structure in the simple case of a single propagating mode equation (5) leads to the following equation for the eigenfrequencies ω_0 :

$$\sin(\varphi_{11}^{(t)}(\omega_0) - \varphi_{12}^{(t)}(\omega_0)) = |S_{11}^{(t)}(\omega_0)| \sin(\varphi_{12}^{(t)}(\omega_0))$$
 (6)

The S-parameters of one subsection were calculated with MAFIA in time domain for frequencies of 1.2...1.6 GHz.

Fig.3 shows the plot of the left and right hand side of (6) in this interval. The eigenfrequencies are given by the intersections of both plots. As shown in table 1 the direct eigenmode calculation and the calculation via S-parameters correspond very good.

The presented procedure allows to divide a complex structure into smaller subsections for which S-parameters can be calculated with a reasonable amount of computer power. Combining the single results yields the S-parameter matrix of the total structure and their eigenfrequencies.

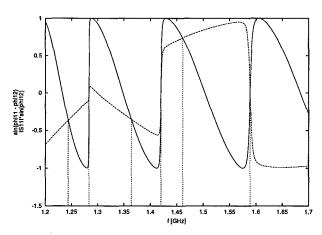


Figure 3: Plot of $\sin(\varphi_{11}^{(t)} - \varphi_{12}^{(t)}) = |S_{11}^{(t)}| \sin(\varphi_{12}^{(t)})$ versus the frequency (f = 1.2...1.6 GHz).

S-parameters	MAFIA E-mod.	rel. error in %
1.243639 GHz	1.243016 GHz	0.50
1.283487 GHz	1.283967 GHz	-0.04
1.363857 GHz	1.363793 GHz	0.005
1.419875 GHz	1.420691 GHz	-0.06
1.461280 GHz	1.459711 GHz	0.11
1.588825 GHz	1.589970 GHz	-0.07

Table 1: Comparison of the eigenfrequencies found by the S-parameter method and by MAFIA E-module.

4 THE TTF-FEL BUNCH COMPRESSOR

Figure 4 shows the bunch compressor section with the two junctions and the middle chamber. The straight part of the beam pipe is not modelled because its cut-off frequency f_{co} is 3.0 GHz. So there are no propagating modes in the frequency range of 1.6...2.2 GHz. The middle chamber itself can be subdivided again: two steps, two bellows and a flange used for a vacuum pump and a beam position monitor.



Figure 4: The TTF-FEL bunch compressor section.

4.1 Exploiting the Symmetry

The overall length of the bunch compressor is about 4.5 meters, whereas some of the subsections contain structures with a dimension in the order of 5 mm (bellows). This may illustrate the difficulty of proper discretisation of the complete structure.

The subsections can be chosen in such a way that they show symmetries (except the step). This allows to calculate the full S-parameter matrix in a single run.

4.2 Terminating the Structure

The beam pipes at the outermost parts of the junctions are rectangular waveguides with a cut-off frequency of 3.0 GHz. The cut-off frequency of the inner part of the junction section is 1.66 GHz, cut-off frequency of the second propagating mode in the middle section is 2.32 GHz. Therefore a frequency range of $1.7\dots 2.2$ GHz was chosen for this calculation. Within this frequency range multimodal wave propagation can be excluded and the junctions "naturally" terminate the structure. Thus they are described by a single quantity, a frequency dependent reflection coefficient $r(\omega)$.

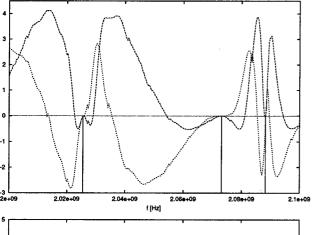
With $r_1 = r_2 = r$ the equation for the eigenfrequencies then turns into

$$(S_{11}^{(t)}(\omega_0)S_{22}^{(t)}(\omega_0) - S_{12}^{(t)}(\omega_0)S_{21}^{(t)}(\omega_0))r^2(\omega_0) - (S_{11}^{(t)}(\omega_0) + S_{22}^{(t)}(\omega_0))r(\omega_0) + 1 = 0$$
(7)

4.3 Results

All S-parameters were calculated using MAFIA's time domain solver T3. Due to different mesh and time steps the data set of each S-parameter calculation has different frequency steps. This requires interpolation when concatenating the subsections. (cf. eq. (2)):

The eigenfrequencies found by examinating the resulting data set (linear interpolation) are 1.79449, 1.81490, 1.82200, 1.84152, 1.86134, 1.88619, 1.90186, 1.91547, 1.95155, 1.95658, 2.02550, 2.07312, 2.08820, 2.10578, 2.11272, 2.13198 and 2.16954 GHz. Fig.5 displays a plot of the real and imaginary part of the left hand side of (7) in the frequency range of 2.0...2.1 GHz (upper plot) with eigenfrequencies at 2.02550, 2.07312 and 2.08820 GHz. The lower plot (frequency: 2.0...2.1 GHz) shows eigenfrequencies at 2.10578, 2.11272, 2.13198 and 2.16954 GHz.



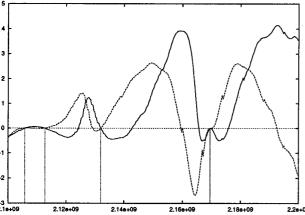


Figure 5: Real and imaginary part of the left hand side of (7) vs. frequency.

5 CONCLUSION

The S-parameter formalism offers a possibility to calculate eigenfrequencies of a structure that is too complex for direct simulation. A validation for this procedure was given in the case of a simple test geometry. Even though the overall effort of this method is higher than that of the direct calculation this procedure enables the computation of eigenfrequencies of complex structures in cases where this would exceed the limits given by computer storage usually available.

As described above, for the time being, the frequencies calculated for the bunch compressor section can not be compared with direct eigenmode calculation but have to be measured for validation.

6 PROSPECT

To calculate the wakefields using the mode matching method furthermore the electromagnetic fields corresponding to the eigenfrequencies have to be known. They can be determined by exciting monochromatic waves with the eigenfrequencies at each port of each section and calculating the fields in the steady state. Superposition of the steady state fields yields the eigenmode fields of the total structure in each component.

7 ACKNOWLEDGEMENT

The author would like to thank H.-W. Glock for many fruitful discussions.

8 SUPPORT

This work was supported by DESY, Hamburg.

- U. van Rienen, Higher Order Mode Analysis of Tapered Disc-Loaded Waveguides using the Mode Matching Technique, Particle Accelerators, 1993
- [2] MAFIA V4.0, CST GmbH, Lautenschlägerstr. 38, D-64289 Darmstadt

"DIPOLE MAGNETS" - A COMPUTER-BASED TUTORIAL*

R. R. Silbar, A. A. Browman, W. C. Mead, R. A. Williams WhistleSoft, Inc., 168 Dos Brazos, Los Alamos, NM 87544

Abstract

Dipole Magnets is one of a set of self-paced interactive training tutorials on particle accelerators that target a broad audience. It covers the bending and focusing properties of dipole magnets. The tutorial contains five sections, four of which are accessible to undergraduate science majors and accelerator technicians.

1 INTRODUCTION

Four years ago WhistleSoft, Inc., began developing a set of computer-based multimedia tutorials on particle accelerators and charged-particle beams. We originally designed the Accelerators and Beams tutorials for the academic market. Our publisher, Physics Academic Software, is in fact marketing four earlier pieces to that audience.

However, we have always had in mind that we might eventually customize these tutorials for particular purposes by National Laboratories running accelerators and by companies producing accelerators for commercial uses. Thus we have taken pains to keep as much material as possible at a level that it is comprehensible to lower undergraduates and accelerator technicians. In fact, most of our work up to the development of *Dipoles* can be understood by end-users who have taken an algebra-based introductory physics course.

Dipole Magnets, like its brothers, integrates interactive On-Screen Laboratories[™], hypertext, progressive disclosure (so the student chooses the pace of presentation), line drawings, and photographs. Of particular importance, we feel, is the use of two- and three-dimensional animations to illustrate the sometimes geometrically complex concepts involved in electromagnetism. We also strongly feel that these multimedia techniques enhance the student's rate of learning and length of retention of the material studied.

Our tutorials are available for both Windows and Macintosh platforms in essentially equivalent versions.

2 TUTORIAL CONTENTS

The *Dipoles* module consists of 43 Content pages, 29 Question and Answer pages, and includes Laboratories. The tutorial is presented in five sections:

- Uniform Bending Magnets, including discussion of bending angle, magnetic rigidity, radial focusing, and radial betatron oscillation.
- Non-Uniform Magnets, including definition of field index and vertical focusing.
- Fringe Field Effects, including a demonstration of edge focusing or defocusing.
- The Kerst-Serber Equation, in which the restoring force equation ("tune") is derived. This section is more difficult than the others in that some knowledge of calculus and Maxwell's Equations is assumed.
- The Double-Focusing Spectrometer, which is essentially an example bringing together all of the above material. Students who have worked through the Kerst-Serber section, will understand why field index $n = \frac{1}{2}$ is optimal for such a device and why the total bend angle is $\pi \sqrt{2}$ radians. Figure 1 shows the concluding page of this section.

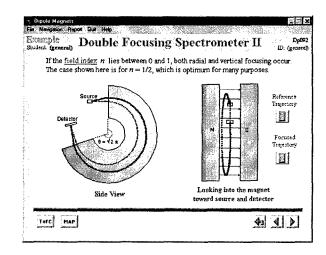


Figure 1: Double focusing spectrometer page.

^{* &#}x27;Work supported by the U.S. Department of Energy under a Phase II SBIR grant. Email: silbar@whistlesoft.com; Web pages: http://www.whistlesoft.com/~silbar

3 EXAMPLE OF RADIAL FOCUSING

The first section, on uniform bending magnets, also goes into a number of related topics that are simple enough, but not necessarily obvious to the neophyte. Figure 2 shows the page that discusses how such uniform magnets can provide focusing in the radial direction.

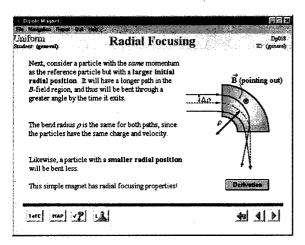


Figure 2: Radial focusing page.

This page is opened in progressive disclosure, one paragraph at a time, with the student in control of when to proceed to the next paragraph. (On subsequent returns to this page, such as through a hyperlink, the page opens without waiting for the student's prompt, but with short pauses between the various sections.) The red particle paths are animated, and the "Derivation" button leads to a page showing how the geometry leads to a focusing effect.

Among the buttons at the bottom of the page, the third from the left (with the question mark) leads to a set of multiple choice questions that the student can use to test his or her comprehension of the concept being discussed. The number of correct answers to these questions, as well as a record of how much of the tutorial the student has seen, is available from the "Report" pulldown menu item at the top of the page.

Another button, fourth from the left, leads to a Laboratory, in which the student can vary the displacement, $\Delta \rho$, from the principal axis. In this case, that also shows very graphically the aberrations that arise when this displacement becomes too large. Other buttons here take the student back to the Table of Contents, to a hyperlinked Concept Map, to the last page visited, and to the previous and next pages in this framework for the uniform magnet section.

4 EXAMPLE: BETATRON OSCILLATION

Section 2, on non-uniform magnets, discusses the vertical focusing effect that occurs when the magnet's field index $n > \frac{1}{2}$. This leads to a betatron oscillation (similar

to that which the student may already have seen in Section 1, but in the radial plane). This page is reproduced in Fig. 3.

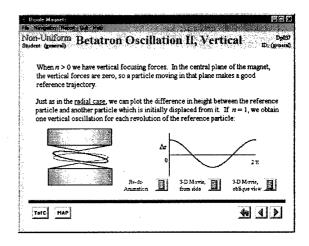


Figure 3: Vertical betatron oscillation page.

This page also opens with progressive disclosure, and when the figures appear, the program traces out the red particle orbit at the same time that it plots the deviation from the principal axis on the right. There is a hyperlink (the blue, underlined "radial case") back to the page in Section 1 discussing radial betatron oscillation. The animation can be replayed, as desired. The other two "movie" buttons show the animation much more realistically in three dimensions, both from the side and from a more oblique point of view.

5 AN INTERMEDIATE-LEVEL PAGE

The previous three figures have blue background borders, indicating they are at an introductory level. In Section 3 there are a few pages at an intermediate level, such as that shown in Fig. 4:

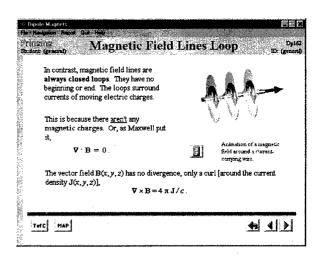


Figure 4: Intermediate-level page from Section 3.

The beige borders indicate this change of level. We called this page "Intermediate" because of the differential form of Maxwell's equations.

Figure 4 also shows the end-frame of the 3D animation showing the build-up of magnetic field about a current carrying wire as the current turns on.

6 POP-UP WINDOWS

The blue underlined word "aren't" that you see in Fig 4 looks like a hyperlink to a new page, but in this case it really brings up a temporary pop-up window (mentioning the lack of magnetic monopoles in the universe as we now know it). Figure 5 shows a similar pop-up window that occurs in Section 5, on the double focusing spectrometer.

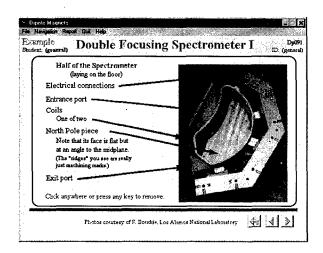


Figure 5: Pop-up window from Section 5.

The photograph shown here (with its callouts) is of the LAMPF Clamshell Spectrometer, which was used for low-energy pion-nucleus scattering experiments in the last decade of LAMPF's existence as a meson factory.

7 SUMMARY, FUTURE DIRECTIONS

This brief overview of the *Dipole Magnets* tutorial should convince you that it can provide good self-paced training on this subject. It should be particularly useful both to new students, undergraduate and graduate, and to accelerator technicians and operators.

Dipoles will be available from Physics Academic Software later this year.

WhistleSoft expects to complete this project with two other tutorials. The one closest to completion is entitled *Quadrupoles*, and it will consist of six sections:

- Overview, indicating why quads are used in charged-particle beam transport.
- Quadrupole Singlets, with a discussion of thicklens quads as well as thin-lens quads.
- Matrix Transport, quads and drifts.
- Systems of Quads, doublets and triplets.
- Special Topics: fringe field effects, higher-order multipoles, and harmonic analyzers.
- Arrays and Stability of Beams, using a FODO cell and array as an example.

The first two sections are at an introductory level, the next three are intermediate, and that last is advanced. *Quads* should be submitted to our publisher for review sometime early this summer.

The other tutorial in development, but still in rough form, is *Properties of Charged-Particle Beams*. This piece will cover topics such as the definition of beam size, phase space, beam envelopes, and space charge effects. We hope to have *Beams* ready for review by this fall.

8 ACKNOWLEDGEMENTS

Other persons who have been involved in this project in various ways are Charles Brownrigg, Richard K. Cooper, Matthew Goldman, Kristen T. Kern, Cathy Malloy, and. J. Patrick McGee. We have had the benefit of many useful suggestions from a large number of user testers and reviewers of our prototype tutorials. We also thank Prof. John S. Risley, editor of Physics Academic Software, for his advice and criticism.

VECTOR POTENTIAL AND STORED ENERGY OF A QUADRUPOLE MAGNET ARRAY

S. Caspi, LBNL, Berkeley, CA

Abstract

The vector potential, magnetic field and stored energy of a quadrupole magnet array are derived. Each magnet within the array is a current sheet with a current density proportional to the azimuthal angle 2θ and the longitudinal periodicity $\frac{(2m-1)\pi}{L}$. Individual quadrupoles within the array are oriented in a way that maximizes the field gradient. The array does not have to be of equal spacing and can be of a finite size, however when the array is equally spaced and is of infinite size the solution can be simplified. We note that whereas, in a single quadrupole magnet with a current density proportional to $\cos 2\theta$ the gradient is pure, such purity is not preserved in a quadrupole array.

1 INTRODUCTION

It has been proposed that commercial electricity can be generated economically from ion beam-driven fusion of deuterium and tritium in tiny target pellets [1]. A leading driver candidate is a high energy, high current heavy ion accelerator. To achieve high currents it is generally desirable to accelerate multiple beams in parallel through a low impedance accelerating structure; a long pulse induction linac can be designed to do this. Efficient transport of beam current in the multibeam accelerator would be accomplished with multiple channel superconducting quadrupole magnets operating in a DC mode with warm bore[2].

The vector potential and the magnetic field have been derived for an array of quadrupole magnets with a thin $\cos(2\theta)$ current sheet at a radius r=R. [3][4]. The field strength within each coil varies purely as a Fourier sinusoidal series of the longitudinal coordinate z in proportion to $\omega_{\rm m}z$, where $\omega_m=\frac{(2m-1)\pi}{L}$, L denotes the half-period, and m is an integer associated with the longitudal harmonic. The analysis is based on the expansion of the vector potential in the region external to the windings of a single quad, and the use of the "Addition Theorem" to revise the expansion to one around any arbitrary point in space.

Email: s_caspi@lbl.gov

This work was supported by the Director, Office of Energy Research, Office of High Energy and Nuclear Physics, High Energy Physics Division, U. S. Department of Energy, under Contract No. DE-AC03-76SF00098.

The quad current density J (A/m) (a form that satisfies the conservation condition $\nabla \cdot \vec{J_s} = \frac{\partial J_s}{\partial z} + \frac{1}{R} \frac{\partial J_{\theta}}{\partial \theta} = 0$), is:

$$\begin{split} \vec{J}(\theta,z)|_{r=R} &= \sum_{m=1} J_{0z,m} \left[\left(\frac{\omega_m R}{2} \right) \sin 2\theta \sin \omega_m z \hat{\mathbf{e}}_{\theta} + \right] \\ &\cos 2\theta \cos \omega_m z \hat{\mathbf{e}}_z \\ J_{0z,m} &= -\frac{1}{\mu_0} \frac{8RG_{2,m}}{(\omega_m R)^3 K_2'(\omega_m R)} \\ \omega_m &= \frac{(2m-1)\pi}{L} \end{split}$$

G_{2,m} is gradient at z=0 and L denotes the half period.

Quadrupoles are combined into an array with a center to center spacing of 2S and alternating current direction that maximizes the gradient (Fig. 1 and 2).

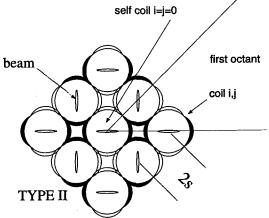


Figure 1: Cross section showing current density arrangement

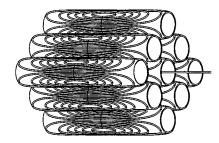


Figure 2: View of a 3x3 quadrupole array. The windings (of constant current) correspond to three terms m=1,2,3 which provide axial free space between arrays.

Based on such a current distribution the resulting vectorpotential \vec{A} and magnetic field \vec{B} within the bore R of each quad, are:

$$\vec{A}_r = \begin{cases} \sum_{m=1}^{\sum} \sum_{k=1}^{\frac{\mu_0 J_{0z,m} R(4k-3)!}{2\left(\frac{\omega_m R}{2}\right)^{2(2k-1)}} \cos 2(2k-1)\theta \\ \times \sin\left(\omega_m z\right) \begin{bmatrix} C_{k,m}^+ I_{2(2k-1)}'(\omega_m r) + \\ 2(2k-1)C_{k,m}^- \frac{I_{2(2k-1)}(\omega_m r)}{\omega_m r} \end{bmatrix} \\ \vec{A}_\theta = - \begin{cases} \sum_{m=1}^{\sum} \sum_{k=1}^{\frac{\mu_0 J_{0z,m} R(4k-3)!}{2\left(\frac{\omega_m R}{2}\right)^{2(2k-1)}} \sin 2(2k-1)\theta \\ \times \sin\left(\omega_m z\right) \begin{bmatrix} C_{k,m}^- I_{2(2k-1)}'(\omega_m r) + \\ 2(2k-1)C_{k,m}^+ \frac{I_{2(2k-1)}(\omega_m r)}{\omega_m r} \end{bmatrix} \\ \vec{A}_z = \begin{cases} \sum_{m=1}^{\infty} \sum_{k=1}^{\frac{\mu_0 J_{0z,m} R(4k-3)!}{2\left(\frac{\omega_m R}{2}\right)^{2(2k-1)}} \times \\ C_{k,m}^+ I_{2(2k-1)}(\omega_m r) \cos 2(2k-1)\theta \cos \omega_m z \end{cases} \end{cases}$$

$$C_{k,m}^{+} = \sum_{i=1}^{\infty} \sum_{j=1}^{\infty} \frac{\begin{bmatrix} K_{4(k-1)}(\omega_m S_{i,j}) \cos 4(k-1)\theta_{0i,j} + \\ K_{4k}(\omega_m S_{i,j}) \cos 4k\theta_{0i,j} \end{bmatrix}}{\times \frac{16I_2(\omega_m R)}{(4k-3)!} \left(\frac{\omega_m R}{2}\right)^{4k-2}} \times \frac{\begin{bmatrix} K_{4(k-1)}(\omega_m S_{i,j}) \cos 4(k-1)\theta_{0i,j} - \\ K_{4k}(\omega_m S_{i,j}) \cos 4k\theta_{0i,j} \end{bmatrix}}{\times \frac{16I_2'(\omega_m R)}{(4k-3)!} \left(\frac{\omega_m R}{2}\right)^{4k-1}}$$

Where I_n and K_n are the "modified" Bessel functions of the first and second kind of order n, and the prime denotes differentiation with respect to the argument. The summation i,j is carried over the quads in the first octant of the array.

The magnetic field components are,

$$B_{r} = \sum_{m=1}^{\infty} \mu_{0} J_{0z,m} \sum_{k=1}^{\infty} \left(\frac{2}{\omega_{m}R}\right)^{4k-3} (4k-3)!$$

$$\times C_{k,m}^{-} I_{2(2k-1)}^{\prime}(\omega_{m}r) \sin 2(2k-1)\theta \cos \omega_{m}z$$

$$\sum_{m=1}^{\infty} \mu_{0} J_{0z,m} \sum_{k=1}^{\infty} \left(\frac{2}{\omega_{m}R}\right)^{4k-3} 2(2k-1)(4k-3)!$$

$$\times C_{k,m}^{-} \frac{I_{2(2k-1)}(\omega_{m}r)}{\omega_{m}r} \cos 2(2k-1)\theta \cos \omega_{m}z$$

$$B_{z} = -\sum_{m=1}^{\infty} \mu_{0} J_{0z,m} \sum_{k=1}^{\infty} \left(\frac{2}{\omega_{m}R}\right)^{4k-3} (4k-3)!$$

$$\times C_{k,m}^{-} I_{2(2k-1)}(\omega_{m}r) \sin 2(2k-1)\theta \sin \omega_{m}z$$

The format used here for \vec{A} and \vec{B} was specifically chosen to avoid a singularity that may rise when L is large (e.g. when the 3d problem reduces to 2d).

2 ANALYSIS

Consider a quadrupole with its center at $(S_{i,j}\cos\theta_0, S_{i,j}\sin\theta_0, z)$ as shown in Fig. 3. The expansion of the vector potential in the region outside the current sheet $(\rho > R)$ and around that center is,

$$\vec{A}_{\rho} = \sum_{m=1}^{\frac{\mu_0 J_{0z,m} R}{4}} (\omega_m R) \cos 2\beta \sin \omega_m z$$

$$\vec{A}_{\beta} = \sum_{m=1}^{\frac{\mu_0 J_{0z,m} R}{4}} (\omega_m R) K_3(\omega_m \rho) - I_1(\omega_m R) K_1(\omega_m \rho)]$$

$$\vec{A}_{\beta} = \sum_{m=1}^{\frac{\mu_0 J_{0z,m} R}{4}} (\omega_m R) \sin 2\beta \sin \omega_m z$$

$$\vec{A}_{\beta} = \sum_{m=1}^{\frac{\mu_0 J_{0z,m} R}{4}} [I_3(\omega_m R) K_3(\omega_m \rho) + I_1(\omega_m R) K_1(\omega_m \rho)]$$

$$\vec{A}_{z} = \sum_{m=1}^{\frac{\mu_0 J_{0z,m} R}{4}} I_2(\omega_m R) K_2(\omega_m \rho) \cos 2\beta \cos \omega_m z$$

The relations between the components of the vector (A_r, A_θ, A_z) around (r, θ, z) and the above components (A_ρ, A_β, A_z) are,

$$A_r = A_\rho \cos(\theta - \beta) + A_\beta \sin(\theta - \beta)$$

$$A_\theta = -A_\rho \sin(\theta - \beta) + A_\beta \cos(\theta - \beta)$$

$$A_\tau = A_\tau$$

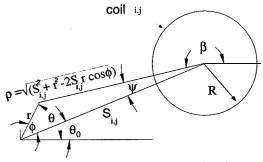


Figure 3: The geometry associated with the Addition Theorem[5].

If we wish to consider an ininite size array where the eight fold symmetry exists for each and every quad located at , $S\mathrm{e}^{\mathrm{i}\theta_0}$, we shall add the contributions of quads with their centers at $S\mathrm{e}^{-\mathrm{i}(\pm\theta_0)}$, $S\mathrm{e}^{-\mathrm{i}(\pm\frac{\pi}{2}\pm\theta_0)}$, $S\mathrm{e}^{-\mathrm{i}(-\pi\pm\theta_0)}$ and consider farther summations to be within the first octant only (quads on the symmetry line will require a weight factor of 1/2).

Once the vector potential has been derived, the field components within the bore R can then be calculated from,

$$\vec{B} = \nabla \times \vec{A}$$

Finally the arithmatic is check assuring the divergence of the vector potential and field are zero

$$\nabla \vec{A} = 0$$
 , $\nabla \vec{B} = 0$

3 STORED ENERGY

The stored energy can be calculated by integrating the product of current density and vector potential $\vec{J} \cdot \vec{A}|_{r=R} = J_{\theta} A_{\theta} + J_z A_z$:

$$E = rac{1}{2} \int \int \int ec{J_a} \cdot ec{A} dv = rac{1}{2} \int \int \int \int ec{J} \cdot ec{A} R d heta dz$$

(the current density is per unit length and the unit of energy is J).

Applying the orthogonality relations, the stored energy in a single quad is,

$$E_{total} = -\frac{\pi R^2 L \mu_0}{8} \sum_{m=1}^{J_{0z,m}^2 K_2' (\omega_m R) I_2' (\omega_m R) \times \frac{4C_{1,m}^-}{(\omega_m R)^3 K_2' (\omega_m R)}$$

where the second term in the square bracket corresponds to the contributions that arises from all neighboring coils in the array.

4 SIMULATION OF CURRENT DENSITY AND FLOW LINES

To generate flow lines we make use of a technique first demonstrated by J. Laslett and W. Fawley of this laboratory. The character of the flow lines (Figure 4) for a quadrupole magnet n=2 with a current density $\vec{J} = \sum_{m=1}^{\infty} J_{0z,m} \left[\left(\frac{\omega_m R}{2} \right) \sin 2\theta \sin \omega_m z \hat{\mathbf{e}}_{\theta} + \cos 2\theta \cos \omega_m z \hat{\mathbf{e}}_{z} \right]$ will follow by integrating the differential equation, $\frac{Rd\theta}{dz} = \frac{J_{\theta}}{J_{\theta}}$, so that

$$\sin 2\theta = \frac{\sum\limits_{m=1}^{m-1} J_{0z,m}}{\sum\limits_{m=1}^{m-1} J_{0z,m} \cos \omega_m z} \sin 2\theta_0$$

where θ_0 denotes the value of θ at z=0.

In a special case, we may choose special values for $J_{02,m}$ such that,

$$J_{02,m} = J_{02} \frac{1}{2^{2(M-1)}} \frac{(2M-1)!}{(M+m-1)!(M-m)!}$$

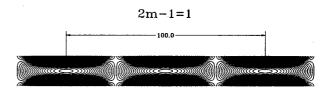
where M corresponds to the number of m terms and J_{02} is a constant.

With that, the flow lines reduce to the simple expression,

$$\sin 2\theta = \frac{1}{\cos^{2M-1}\left(\frac{\pi z}{L}\right)}\sin 2\theta_0$$

and the current density components are,

$$\vec{J} = J_{02} \left\{ \begin{cases} 0\hat{\mathbf{e}}_r \\ \frac{\pi R}{2L} (2M - 1) \cos^{2(M-1)} \frac{\pi z}{L} \sin \frac{\pi z}{L} \sin 2\theta \hat{\mathbf{e}}_{\theta} \\ \cos^{2M-1} \frac{\pi z}{L} \cos 2\theta \hat{\mathbf{e}}_z \end{cases} \right\}$$



2m-1=1 and 2m-1=3



2m-1=1 and 2m-1=3 and 2m-1=5





Figure 4: View of flow lines over a half period quad (M=1,2,3). These special cases reveal the reduction in crowding between magnets at the expense of an increased non-linear field.

5 CONCLUSION

The 3D expressions for the vector potential, field and energy have been derived. We note that neighboring coils within the array give rise to harmonic terms (m) which do not exist in a single quad with $\cos(2\theta)$ current density. We also point out that the coefficients associated with $C_{k,m}^+$ in the vector potential drop out in the expressions for the field and energy.

- [1] Entire issue, "Fusion technology", Vol 13, No. 2, 1998.
- [2] K. Chow A. Faltens S. Gourlay R. Hinkins R. Gupta E. Lee A. McInturff R. Scanlan C. Taylor S. Caspi, R. Bangerter and D. Wolgast, "A superconducting quadrupole magnet array for a heavy ion fusion driver", to be published in IEEE Trans. on Applied Superconductivity, October 1998.
- [3] S. Caspi, "The 3d vector potential, magnetic field and stored energy in a thin cos(2theta) coil array", Lawrence Berkeley Laboratory, LBNL-40564, SC-MAG-598, July 1997.
- [4] S. Caspi, "Multipoles in cos(2theta) coil arrays type ii", Lawrence Berkeley Laboratory, SC-MAG-596, June 1997.
- [5] G.N. Eatson, "Theory of bessel functions", Cambridge University Press, page 361.

Accurate Calculation of Magnetic Fields in the End Regions of Superconducting Accelerator Magnets Using the BEM-FEM Coupling Method

S. Kurz*, S. Russenschuck
*ITE, University of Stuttgart, Germany
CERN, Geneva, Switzerland

Abstract

In this paper a new technique for the accurate calculation of magnetic fields in the end regions of superconducting accelerator magnets is presented. This method couples Boundary Elements (BEM) which discretize the surface of the iron yoke and Finite Elements (FEM) for the modelling of the nonlinear interior of the yoke. The BEM-FEM method is therefore specially suited for the calculation of 3dimensional effects in the magnets, as the coils and the air regions do not have to be represented in the finite-element mesh and discretization errors only influence the calculation of the magnetization (reduced field) of the yoke. The method has been recently implemented into the CERN-ROXIE program package for the design and optimization of the LHC magnets. The field shape and multipole errors in the two-in-one LHC dipoles with its coil ends sticking out of the common iron yoke is presented.

1 INTRODUCTION

The design and optimization of the LHC magnets is dominated by the requirement of an extremely uniform field which is mainly defined by the layout of the superconducting coils. Even very small geometrical effects such as the insufficient keystoning of the cable, the insulation, grading of the current density in the cable due to different cable compaction and coil deformations due to collaring, cool down and electromagnetic forces have to be considered for the field calculation. In particular for the 3D case, commercial software has proven to be hardly appropriate for the field optimization of the LHC magnets. Therefore the ROXIE program package was developed at CERN for the design and optimization of the LHC superconducting magnets. Using the BEM-FEM coupling method [1] yields the reduced field in the aperture due to the magnetization of the iron yoke and avoids the representation of the coil in the FE-meshes.

2 THE BEM-FEM COUPLING METHOD

The total magnetic induction \vec{B} in a certain point $\vec{\xi}$ in the aperture of the magnet can be decomposed into a contribution $\vec{B}_{\rm S}$ due to the superconducting coil and a contribution $\vec{B}_{\rm R}$ due to the magnetic yoke. If the fields are expressed in terms of the magnetic vector potential $\vec{B} = {\rm curl}\,\vec{A}$, then the decomposition into source and reduced contributions gives

$$\vec{A} = \vec{A}_{\rm S} + \vec{A}_{\rm R}.\tag{1}$$

This approach has the following intrinsic advantages: (1) The coil field can be taken into account in terms of its source vector potential \vec{A}_{S} , which can be obtained easily from the filamentary currents I_S by means of Biot-Savart type integrals without meshing of the coil. (2) The BEM-FEM coupling method allows for the direct computation of the reduced vector potential \vec{A}_{R} rather than the total vector potential \vec{A} . Then numerical errors do not influence the dominating contribution $\vec{A}_{\rm S}$ due to the superconducting coil. (3) The surrounding air region needs not to be meshed at all. This simplifies the preprocessing and avoids artificial boundary conditions at some "far" boundaries. Moreover, the geometry of the permeable parts can be modified without taking care of the mesh in the surrounding air region. This strongly supports the feature based, parametric geometry modelling which is required for mathematical optimization.

When the BEM-FEM coupling method is applied, only the magnetic sub-domain Ω_i which coincides with the magnetic yoke has to be discretized by finite elements. Iron saturation effects can then be dealt with within the finite element framework. The nonmagnetic sub-domain Ω_a which represents the surrounding air region and the excitation coil is treated by the boundary element method. Only the common boundary Γ needs to be discretized by boundary elements. The source vector potential \vec{A}_S can be obtained from the filamentary current I_S by means of the Biot-Savart type integral

$$\vec{A}_{\rm S} = \mu_0 I_{\rm S} \oint u^* \, \mathrm{d}\vec{l}. \tag{2}$$

In (2), the Green's function u^* is the fundamental solution of the Laplace equation, which is in 2D

$$u^* = -\frac{1}{2\pi} \ln |\vec{x} - \vec{\xi}| \tag{3}$$

and in 3D

$$u^* = \frac{1}{4\pi |\vec{x} - \vec{\xi}|}. (4)$$

 $\vec{\xi}$ is the evaluation point of $\vec{A}_{\rm S}$ and \vec{x} is the integration point on \mathcal{C} .

2.1 The FEM part

Inside the magnetic domain Ω_i a gauged vector-potential formulation is applied. With Maxwell's equations

 $\operatorname{curl} \vec{H} = \vec{J}$ and $\operatorname{div} \vec{B} = 0$ for magnetostatic problems, the constitutive equation

$$\vec{B} = \mu(\vec{H}) \cdot \vec{H} = \mu_0(\vec{H} + \vec{M}) \tag{5}$$

and the vector-potential formulation $\vec{B} = \operatorname{curl} \vec{A}$ we get

$$\frac{1}{\mu_0} \operatorname{curlcurl} \vec{A} = \vec{J} + \operatorname{curl} \vec{M}. \tag{6}$$

Introducing the penalty term $-\operatorname{grad} \frac{1}{\mu_0}\operatorname{div} \vec{A}$ the weak formulation reads

$$\frac{1}{\mu_0} \int_{\Omega_i} (\operatorname{curl} \vec{w} \cdot \operatorname{curl} \vec{A} + \operatorname{div} \vec{w} \operatorname{div} \vec{A}) \, d\Omega_i
- \oint_{\Gamma_{ai}} \vec{w} \cdot \left(\frac{1}{\mu_0} \operatorname{curl} \vec{A} \times \vec{n} - \frac{1}{\mu_0} (\operatorname{div} \vec{A}) \vec{n} \right) \, d\Gamma_{ai}
- \int_{\Omega_i} \vec{M} \cdot \operatorname{curl} \vec{w} \, d\Omega_i = \int_{\Omega_i} \vec{w} \cdot \vec{J} \, d\Omega_i$$
(7)

which can be transformed to

$$\frac{1}{\mu_0} \int_{\Omega_i} \operatorname{grad}(\vec{A} \cdot \vec{e}_a) \cdot \operatorname{grad}w_a \, d\Omega_i$$

$$-\frac{1}{\mu_0} \oint_{\Gamma_{ai}} \left(\frac{\partial \vec{A}}{\partial n_i} - (\mu_0 \vec{M} \times \vec{n}_i) \right) \cdot \vec{w}_a \, d\Gamma_{ai} =$$

$$\int_{\Omega_i} \vec{M} \cdot \operatorname{curl}\vec{w}_a \, d\Omega_i + \int_{\Omega_i} \vec{w}_a \cdot \vec{J} \, d\Omega_i \qquad (8)$$

a = 1, 2, 3 and

$$\vec{w}_1 = \begin{pmatrix} w_1 \\ 0 \\ 0 \end{pmatrix}, \ \vec{w}_2 = \begin{pmatrix} 0 \\ w_2 \\ 0 \end{pmatrix}, \ \vec{w}_3 = \begin{pmatrix} 0 \\ 0 \\ w_3 \end{pmatrix}. \tag{9}$$

The continuity condition of \vec{H}_{t} on the boundary between iron and air leads to

$$\frac{\partial \vec{A}^{\text{FEM}}}{\partial n_{i}} - (\mu_{0}\vec{M} \times \vec{n}_{i}) + \frac{\partial \vec{A}^{\text{BEM}}}{\partial n_{a}} = 0.$$
 (10)

 \vec{n}_i is the normal vector on Γ_{ai} pointing out of the FEM domain Ω_i and \vec{n}_a is the normal vector on Γ_{ai} pointing out of the BEM domain Ω_a . The boundary integral term on the boundary between iron and air Γ_{ai} in (7) serves as the coupling term between the BEM and the FEM domain. Let us now assume, that the normal derivative on Γ_{ai}

$$\vec{Q}_{\Gamma_{ai}} = -\frac{\partial \vec{A}_{\Gamma_{ai}}^{\text{BEM}}}{\partial n_{a}} \tag{11}$$

is given a priori. If the domain Ω_i is discretized into finite elements (C^0 -continuous, isoparametric 20-noded hexahedron elements are used), and the Galerkin method is applied to the weak formulation, then a non linear system of equations is obtained

$$\begin{pmatrix} \begin{bmatrix} K_{\Omega_{\mathbf{i}}\Omega_{\mathbf{i}}} \end{bmatrix} & \begin{bmatrix} K_{\Omega_{\mathbf{i}}\Gamma_{\mathbf{a}\mathbf{i}}} \end{bmatrix} & 0 \\ \begin{bmatrix} K_{\Gamma_{\mathbf{a}\mathbf{i}}\Omega_{\mathbf{i}}} \end{bmatrix} & \begin{bmatrix} K_{\Gamma_{\mathbf{a}\mathbf{i}}\Gamma_{\mathbf{a}\mathbf{i}}} \end{bmatrix} & T \end{pmatrix} \begin{pmatrix} \begin{Bmatrix} \vec{A}_{\Omega_{\mathbf{i}}} \end{Bmatrix} \\ \begin{Bmatrix} \vec{A}_{\Gamma_{\mathbf{a}\mathbf{i}}} \end{Bmatrix} \end{pmatrix} = \begin{pmatrix} 0 \\ 0 \end{pmatrix}$$

with all nodal values of \vec{A}_{Ω_i} , $\vec{A}_{\Gamma_{ai}}$ and $\vec{Q}_{\Gamma_{ai}}$ grouped in arrays. The subscripts Γ_{ai} and Ω_i refer to nodes on the boundary and in the interior of the domain, respectively. The domain and boundary integrals in the weak formulation yield the stiffness matrices [K] and the boundary matrix [T]. The stiffness matrices depend on the local permeability distribution in the nonlinear material. All the matrices in (12) are sparse.

2.2 The BEM part

By definition the BEM domain Ω_a does not contain any iron and therefore $\vec{M}=0$ and $\mu=\mu_0$. One more integration by parts of the weak integral form (8) and choosing the Cartesian components of the vector weighting function as the fundamental solution of the Laplace equation yields

$$\frac{\Theta}{4\pi} \vec{A} + \oint_{\Gamma_{ai}} \vec{Q}_{\Gamma_{ai}} u^* d\Gamma_{ai} + \oint_{\Gamma_{ai}} \vec{A}_{\Gamma_{ai}} q^* d\Gamma_{ai}$$

$$= \int_{\Omega_a} \mu_0 \vec{J} u^* d\Omega_a \qquad (13)$$

with the abbreviation $q^* = \frac{\partial u^*}{\partial n_a}$. The right hand side of Eq. (13) is a Biot-Savart type integral for the source vector potential \vec{A}_s . The vector potential \vec{A} at any arbitrary point $\vec{r}_0 \in \Omega_a$ can be computed from (13) once the vector potential $\vec{A}_{\Gamma_{ai}}$ and its normal derivative $\vec{Q}_{\Gamma_{ai}}$ on the boundary Γ_{ai} are known. Θ is the solid angle enclosed by the domain Ω_a in the vicinity of \vec{r}_0 . For the discretization of the boundary Γ_{ai} into individual boundary elements $\Gamma_{ai,j}$, C^0 -continuous, isoparametric 8-noded quadrilateral boundary elements are used. The functions $\vec{A}_{\Gamma_{ai}}$ and $\vec{Q}_{\Gamma_{ai}}$ are expanded with respect to the element shape functions and (13) can be rewritten in terms of the nodal data of the discrete model.

$$\frac{\Theta}{4\pi}\vec{A} = \vec{A}_{s} - \left\{\vec{Q}_{\Gamma_{ai}}\right\} \cdot \left\{g\right\} - \left\{\vec{A}_{\Gamma_{ai}}\right\} \cdot \left\{h\right\}. \tag{14}$$

In (14), g results from the boundary integral with the kernel u^* and h results from the boundary integral with the kernel q^* . The discrete analogue of the Fredholm integral equation can be obtained from (14) by successively putting the evaluation point $\vec{r_0}$ at the location of each nodal point $\vec{r_j}$. This procedure is called point-wise collocation and yields a linear system of equations,

$$[G]\{\vec{Q}_{\Gamma_{ai}}\} + [H]\{\vec{A}_{\Gamma_{ai}}\} = \{\vec{A}_{s}\}. \tag{15}$$

In (15), $\{\vec{A}_s\}$ contains the values of the source vector potential at the nodal points \vec{r}_j , $j=1,2,\ldots$ The matrices [G] and [H] are unsymmetric and fully populated.

2.3 The BEM-FEM Coupling

An overall numerical description of the field problem can be obtained by complementing the FEM description (12) by the BEM description (15) resulting in

$$\begin{pmatrix}
[K_{\Omega_{i}\Omega_{i}}] & [K_{\Omega_{i}\Gamma_{ai}}] & 0 \\
[K_{\Gamma_{ai}\Omega_{i}}] & [K_{\Gamma_{ai}\Gamma_{ai}}] & [T] \\
0 & [H] & [G]
\end{pmatrix}
\begin{pmatrix}
\{\vec{A}_{\Omega_{i}}\} \\
\{\vec{A}_{\Gamma_{ai}}\} \\
\{\vec{Q}_{\Gamma_{ai}}\}
\end{pmatrix} = \begin{pmatrix}
0 \\
0 \\
\{\vec{A}_{s}\}
\end{pmatrix}.$$
(16)

Equation (15) gives exactly the missing relationship between the Dirichlet data $\{\vec{A}_{\Gamma_{\rm ai}}\}$ and the Neumann data $\{\vec{Q}_{\Gamma_{\rm ai}}\}$ on the boundary $\Gamma_{\rm ai}$. It can be shown [2] that this procedure yields the correct physical interface conditions, the continuity of $\vec{n} \cdot \vec{B}$ and $\vec{n} \times \vec{H}$ across $\Gamma_{\rm ai}$.

3 RESULTS

The Large Hadron Collider (LHC) to be built at CERN requires high-field superconducting magnets to guide the counter-rotating beams in the LEP tunnel with a circumference of about 27 km. The design and optimization of these magnets is dominated by the requirement of an extremely uniform field, which is mainly defined by the layout of the superconducting coils. In order to study, with a fast turnaround rate, the influence of individual coil parameters, the pre-stress in the coil, the collar material and the voke structures, a short-model dipole program was established at CERN. 20 single-aperture models and 3 double-aperture models have been built and tested since mid 1995 in addition to 5 long-model prototypes built in European industry. Unlike in the main dipole prototypes with a magnetic length of 14.2 m, the field quality in the center of the short dipole models (with a coil length of 1.05 m and the length of the magnetic yoke of only 402 mm) is affected by the coil ends. In order to study systematic effects in the field quality due to manufacturing tolerances, and coil deformations due to assembly and cool-down of the magnet it is necessary to calculate, with a high precision, the 3D integrated multipole field errors. This is important as the measurement coil used at present has a length of about 200 mm (half the length of the magnetic yoke). Fig. 1 shows the geometric model of the coiltest facility (CTF). Fig. 2 shows the relative multipole components b_3 , b_5 and b_7 (related to the main field B_1 of 8.2452 T calculated at 11530 A for the two dimensional model, at 17 mm ref. radius, in units of 10^{-4}) as a function of the z-position. z = 0 is the center of the magnet. The iron voke ends at z = 201 mm.

At about nominal current, the b_3 component in the center of the short model dipole does not reach the 2D cross-section value of 4.2 units due to globally different saturation effects. At 4000 A the b_3 shows a local enhancement of only about 0.3 units near the aperture and reaches its cross-section value of 2.9 units about 100 mm inwards the yoke. The b_5 and in particular b_7 and higher order multipoles are little influenced by three-dimensional effects.

4 CONCLUSION

The BEM-FEM method is specially suited for the calculation of 3D effects in superconducting magnets, as the coils

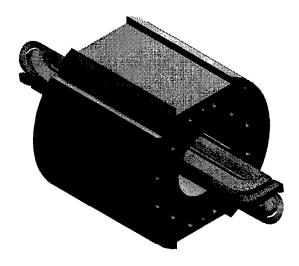


Figure 1: ROXIE model of the CTF

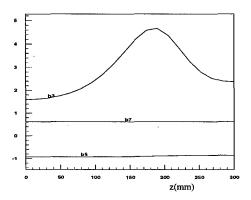


Figure 2: Relative multipole components (at r= 17 mm, in units of 10^{-4}) as a function of the axial position

and the air regions do not have to be represented in the finite-element mesh and discretization errors only influence the calculation of the yoke magnetization. The method has been applied to the calculation of multipole errors in the short dipole models for the LHC. Results show that the models are representative for the long dipole prototypes only at low and medium excitation. At nominal excitation, the sextupole measured in the center of the magnet is more than one unit lower than in the center of the long magnets.

- [1] J. Fetzer, S. Abele, and G. Lehner. Die Kopplung der Randelementmethode und der Methode der finiten Elemente zur Lösung dreidimensionaler elektromagnetischer Feldprobleme auf unendlichem Grundgebiet. *Archiv für Elektrotechnik*, 76(5):361–368, 1993.
- [2] S. Kurz, J. Fetzer, and W. Rucker. Coupled BEM-FEM methods for 3D field calculations with iron saturation. Proceedings of the First International ROXIE users meeting and workshop, 1998.

THE COMPUTER CODE FOR INVESTIGATION OF THE MULTIPACTOR DISCHARGE IN RF CAVITIES

L.V. Kravchuk, G.V. Romanov, S.G. Tarasov, V.V. Paramonov, Institute for Nuclear Research RAS,117312, Moscow, Russia

Abstract

The special code has been developed for numerical simulation of the multipactor discharge during long-time INR activity in the development and construction of accelerating structures. The code simulates the secondary emission electron trajectories at different levels of rf field using real electromagnetic field distribution (calculated with modern 2D or 3D software) in the cavity that has a complicated boundary shape. Special implementations have been developed for phase stability investigations. The velocity spread of secondary electrons also may be considered. The results of the simulations were compared with experimental data, showing good coincidence.

In this report, the methods of simulations, particularities and realization of the code are described. The examples of applications for discharge simulations in accelerating cavities also are presented.

1 INTRODUCTION

The Multipactor Discharge (MD) is a wellknown phenomenon in the development and construction of accelerating cavities. The discharge takes place at a low level of the electric field and usually MD can be seen during rf conditioning of accelerating cavities. However, in some regions of the cavity MD may take place at the operating level of the electric field at accelerating gaps, deteriorating parameters of the cavity. Many papers are dedicated to the MD study. In some papers and books, [1, 2] general properties of discharge are considered. These general conclusions allow providing some estimations and preliminary predictions for simple cavities. But MD is very complicated phenomena depending on real distribution of electromagnetic field (which can not be described analytically for complicated shapes of modern accelerating cavities), the level of fields, the surface conditions and so on. A direct numerical simulation is mostly the only way to investigate the MD possibility in the given accelerating cavity and to develop such cavity modifications that allow avoiding this possibility.

2 PROBLEM DESCRIPTION

During previous activity and at present stage attention has been paid to the MD study in accelerating cavities that have the symmetry of rotation. In the cylindric coordinates system we directly solve the equation of motion for nonrelativistic electron in single-particle approximation.

To simulate electron motion, the real distribution of the electromagnetic field should be calculated by specialized codes and stored in the file. The code uses calculated values of electric field components Ez, Er and magnetic field H_{-} in the meshpoints. If fields values between meshpoints are needed, the fast method of interpolation with spline-technique is used. To integrate the equation of motion, the conservative scheme of discretization is used and forth order Adams-method is applied.

3 CODE ABILITIES

First, the cavity boundaries should be specified to simulate the electron's motion in the cavity. The cavity boundaries may be formed partly of straight lines and partly of circular ones.

The introduced language for the boundary description is the same as well known SUPERFISH code. Such standardization simplifies essentially the user's work. The distribution of the electromagnetic field also may be taken from SUPERFISH, and the specially developed editor allows using for this purpose practically any known codes. This editor is rather simple.

The code simulates the electron emission from the specified part of the cavity boundary and simulates the electron motion to impact with another part of the boundary. The calculation of the phase of the electron flight precedes to the sorting of trajectories, which allows to specify resonant ones. The conditions of resonant discharge require that the flight phase of electrons in the discharge must be equal to $2\pi n$ (n- integer) with respect to the rf field period 2π .

The order of the discharge and the number of collisions should be specified. It allows considering resonant trajectories of different configurations (for example, single-point discharge).

Wide possibilities of the code allow to investigate both the electron motion from specified point, under the given field level and the defined emission phase, and allow considering for one electron to run from the part of the boundary within the ranges of rf field levels and emission phases.

Considering relations between the phases of the electron emission and impact, a conclusion may be done concerning to the phase stability for resonant trajectories [5]. The special algorithm has been developed for this purpose. A lot of attention was paid to develop a user-friendly interface of the code. The user can see at the screen both trajectories directly and a lot of another useful information concerning to zones of stable discharge.

The typical example of the multipactor computing for the omega-shaped accelerating cell is shown on Fig. 1

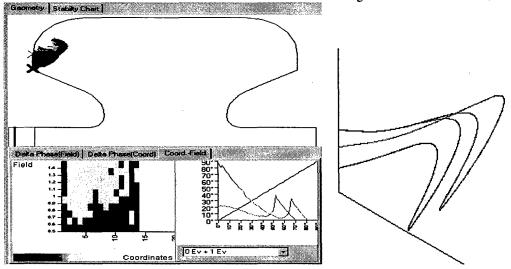


Fig. 1. Multipactor computing for the omega-shaped accelerating cell.

The present version of the code is developed under MS Windows-95 (NT) platform and may be run at any PC computer using this software. The control is totally mouse-driven.

4 EXAMPLES OF APPLICATION

The code was used for many applications in the development and construction of accelerating cavities at the INR. Historically first applications were for the MD

study in the Disk and Washer accelerating structure during the construction of the high-energy part of the Moscow Meson Factory linac. Results of investigations were used for rf conditioning of DAW accelerating cavities.

The results of the MD investigations for PETRA cavities one can find in [3] For coupling cells of the Onaxis Coupled Structure (narrow cylindrical cavity, Fig.2) our investigations show the discharge excitation practically for all conditions of OCS applications [4].

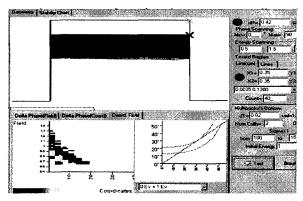


Fig. 2. Multipactor computing for coupling cells of the On-axis Coupled Structure.

More complicated case takes place for coupling cells of the Side Coupled Structure (Fig.3). Usually this cell is formed having a central part like a capacitor. There are conditions for MD excitation in the central part of this

capacitor. These conditions are simple enough if one considers electrons with zero emission energy and are more complicated if the real spread of emission energies is under consideration.

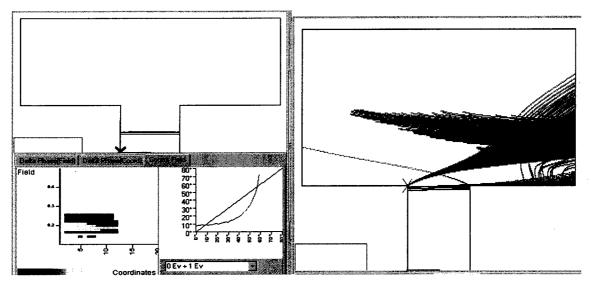


Fig. 3. Multipactor computing for coupling cells of the Side Coupled Structure.

Near outer radius of the capacitor, the non uniform electric field pumps out electrons (Fig.3), destroying conditions of the MD space stability [4].

5 SUMMARY

The described above code has been developed to investigate the multipactor phenomena taking into account real distributions of electromagnetic fields, real shapes of the cavity boundaries, different particularities of the discharge. Collected together in one powerful user-friendly code these possibilities allow to provide the investigation in conditions that are very close to the real ones, provide practical recommendations for the cavity shape modification, cavity conditioning and so on. The

abilities of the code (and results obtained) exhibit it as an effective tool for investigations and an effective part of the design-kit for a cavity designer.

- Slivkov I.N. Processes at high voltage in vacuum. Energoatomizdat, Moscow, 1986, (in Russian) and related references.
- [2] D.Proch, D.Einfeld, R.Onken, Measurement of multi pacting currents... Proc. 1995 PAC Conf., p.1776-1778, 1995.
- [3] I.Gonin, L.Kravchuk, G.Romanov et al. A study of multipactor phenomena in the 53 MHz PETRA II cavity at DESY. Proc. of the 1994 EPAC, v.3, 2197, 1994.
- [4] V. Paramonov, S. Tarasov, The possibility of multipactor discharge in coupling cells of coupled-cells accelerating structures. Proc. of the 1998 Linac Conference, Chicago, 1998 (to be published)
- [5] V.A.Puntus, G.V.Romanov, Multipacting in the Phase Beam Monitor at MMF. Proc. of the 1998 EPAC, 1583, 1998

VIT 030 - THE SPECIAL CODE FOR COMPUTER SIMULATION OF THE RF PROCESS IN VEPP-5 PREINJECTOR.

V.V.Podlevskih Budker INP, 630090 Novosibirsk, Russia

Abstract

This paper presents the analycis of algoritm and description of the special code for computer simulation of the RF process in linear accelerator.

This program may be used for preliminary analysis of the RF process, RF system setup and monitoring.

1 INTRODUCTION

RF system of VEPP-5 preinjector consists of the separate RF module. The main elements of each module are:

- a) klystron amplifier;
- b) SLED type power multiplying system consisting of two high Q cavities and 3dB directional coupler;
- c) accelerating section connected with waveguide and RF load by a coupler;
- d) RF load:
- f) waveguide section including straight waveguide parts, E and H turns, directional coupler etc.

The objectives of RF process simulation are:

- a) representation of each RF system element by a limited set of parameters mostly characterizing the operation of the device;
- b) creation of a model of interaction between separate elements of the RF system.

RF process under investigation (that can be measured) are electromagnetic wave amplitudes in the defined cross-sections of the waveguide section (including the disk loaded accelerating structure).

2 BASIC EQUATION

Scheme of the RF modules of VEPP-5 preinjector RF system module is shown in Fig.1.

A spectral representation of RF process is their most suitable form for the points, marked in Fig1. Time depend and spectral representation are connected by the following equations:

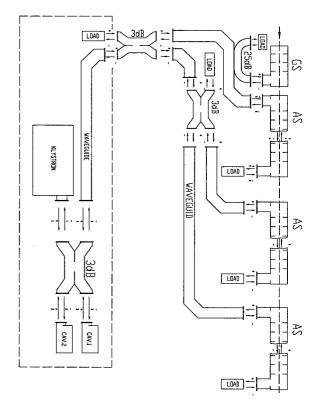


Figure 1: Scheme of the RF module of VEPP-5 preinjector.

$$V(f) = \frac{1}{\sqrt{2\pi}} \int_{-\infty}^{\infty} U(t)e^{-i2\pi ft} dt$$
 (1)

$$U(t) = \frac{1}{\sqrt{2\pi}} \int_{-\infty}^{\infty} U(f)e^{i2\pi f t} dt$$
 (2)

In terms of Fig.1 designations connection between the signal ganged by 3dB directional coupler has the following form:

$$\begin{pmatrix} V_{1}^{-} \\ V_{2}^{-} \\ V_{3}^{-} \\ V_{4}^{-} \end{pmatrix} = \frac{1}{\sqrt{2}} \begin{pmatrix} 0 & 1 & -i & 0 \\ 1 & 0 & 0 & -i \\ -i & 0 & 0 & 1 \\ 0 & -i & 1 & 0 \end{pmatrix} \begin{pmatrix} V_{1}^{+} \\ V_{2}^{+} \\ V_{3}^{+} \\ V_{4}^{+} \end{pmatrix}$$
(3)

$$\begin{pmatrix} V_{1}^{+} \\ V_{2}^{+} \\ V_{3}^{+} \\ V_{4}^{+} \end{pmatrix} = \frac{1}{\sqrt{2}} \begin{pmatrix} k_{1} & 0 & 0 & 0 \\ 0 & k_{2} & 0 & 0 \\ 0 & 0 & k_{3} & 0 \\ 0 & 0 & 0 & k_{4} \end{pmatrix} \begin{pmatrix} V_{1}^{+} \\ V_{2}^{+} \\ V_{3}^{+} \\ V_{4}^{+} \end{pmatrix} + \begin{pmatrix} V_{0} \\ 0 \\ 0 \\ 0 \end{pmatrix}$$
(4)

Where V_0 is an amplitude of the wave at the klystron amplifier output when operating to the matched load.

All the variables and constants in equations (3,4) are functions of a frequency (i.e. $V_i^{\pm} \equiv V_i^{\pm}(f)$ and $k_i^{\pm} \equiv k_i^{\pm}(f)$). A compact matrix form of the equations 3 and 4 is: $V^- = SV^+$ and $V^- = K_sV^- + V_0$ with joint solution: $V^- = (S^{-1} - K_s)^{-1}V_0$ and $V^+ = S^{-1}V^-$.

The following equations connect wave amplitudes at the input and output of the accelerating structure:

The following equation describes connection between signals at the input and output of the waveguide section which connects the power multiplying system with the accelerating section:

$$\begin{pmatrix} V_4^+ \\ V_5^+ \end{pmatrix} = \begin{pmatrix} k_{44} & k_{45} \\ k_{54} & k_{55} \end{pmatrix} \begin{pmatrix} V_4^- \\ V_5^- \end{pmatrix}$$
 (5)

or in matrix form: $V^+ = K_L V^-$, where K_L is S matrix of the waveguide.

The following equations connect wave amplitudes at the input and output of the accelerating structure:

$$\begin{pmatrix} V_5^- \\ V_6^- \end{pmatrix} = \begin{pmatrix} k_{55} & k_{56} \\ k_{65} & k_{66} \end{pmatrix} \begin{pmatrix} V_5^+ \\ V_6^+ \end{pmatrix}$$
 (6)

or in matrix form: $V^- = K_{as}V^+$, the matrix K_{as} describes in following section.

It may be shown that Eqs.(4,5,6) can be united in one (that is the reason for there common indexation), salving which sumultaniosly with Eqs.(3) determines uniquely all components of vectors:

$$V^- = (V_1^-, V_2^-, V_3^-, V_4^-, V_5^-, V_6^-)$$
 $V^+ = (V_1^+, V_2^+, V_3^+, V_4^+, V_5^+, V_6^+)$

at given input pulse V_0 (f) and matrix coefficient $K_I(f)$ and $K_{as}(f)$.

3 SIMULATION OF RF ELEMENTS

3.1 Klystron amplifier.

Klystron amplifier is an RF power source for each module in preinjector. If an output signal of the klystron amplifier $U_1^+(t)$ does not change occasionally from pulse to pulse, it may be represented as a sum:

$$U_1^+ = U_0(t) + \int_0^t K^{kl}(t, t') U_1^-(t') dt'$$
 (7)

where $U_0(t)$ is an output signal of the klystron amplifier operating to the matched load. The addend determines the klystron output signal depending on possible reflections from the RF module waveguide section. If $K^{kl}(t,t') \equiv K^{kl}(t-t')$, equation (7) becomes:

$$U_1^+(t) = U_0(t) + \int_0^t K^{kl}(t - t')U_1^-(t')dt'$$
 (8)

or in spectral representation:

$$V_1^+(f) = V_0(f) + K^{kl}(f)V_1^-(f) \tag{9}$$

According to designations introduced in section 1 coefficient k_1 in (2) is equal to coefficient K^{kl} in (9)

3.2 Power multiplying system cavities.

Power multiplying system contains (see Fig.1) two hight-Q cavities coupled by a slot with the input waveguide. The general view of each cavity as well as circuit representation are shown in Fig.2.



Figure 2: RF cavity coupled with input waveguide and its circuit representation.

Coupling between the input and output cavity signals is:

$$V_{out}(f) = K^{sl}(f)V_{in}(f) \tag{10}$$

where $K^{sl}(f)$ is frequency dependence of the cavity reflection coefficient:

$$K^{sl}(f) = \frac{r - 1 - i\xi}{r + 1 + i\xi} \tag{11}$$

r is the coupling coefficient between the cavity and input waveguide;

$$\xi = Q_0 \frac{(f - f_0)}{f_0}$$
 is the generalized cavity frequency detuning;

 f_0,Q_0 are the cavity resonant frequency and Q factor.

According to designations introduced in section 1, coefficient k_{22} and k_{33} in Eqs.(1,2) are equal to the reflection coefficient determined by (11) with substituting in it parameters of each cavity.

3.3 Accelerating structure.

The accelerating structure is designed as a round diskloaded waveguide and is connected with RF power source and RF load through the input and output couplers. Equivalent circuit of the accelerating structure is shown in Fig.3.

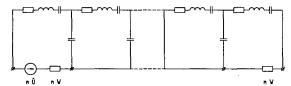


Figure 3: Circuit representation of the accelerating structure.

In this case we can write:

$$a_1 = 1 - \frac{f^2}{f_1^2} + i\frac{f}{f_1}\frac{1 + \beta_1}{Q_1}, \ a_N = 1 - \frac{f^2}{f_N^2} + i\frac{f}{f_N}\frac{1 + \beta_N}{Q_N}$$

and
$$a_n = 1 - \frac{f^2}{f_n^2} + i \frac{f}{f_n} \frac{1}{Q_n}$$
, where:

 f_n , Q_n are the resonant frequency and Q-factor of the n-th cell:

 β_1 , β_N are the coupling coefficient between 1-th and

N-th cavities with input and output waveguide.

 k_n is the coupling coefficient n-tn and (n+1)-th cell.

The reflection coefficient of the accelerating structure and the transmittient coefficient for n-th cell may be found directly from the matrix coefficient of the system (12):

$$k_{55} = -1 - 2i \frac{f_1}{f} \frac{\beta_1}{Q_1} \frac{\Delta_1}{\Delta}$$
 (13)

$$k_{5n} = \frac{\Delta_1}{\Lambda} \tag{14}$$

where Δ is the determinant of the system (12), Δ_n is the determinant of the system (12) without n-th column and n-th line.

4 CONCLUSION

The mathematical algorithm described above was completely realized in the original VIT 030 code. It allows us to solve the linear accelerator RF module design problems as well as questions arising during RF module tests and conditioning fast and with good quality.

The code which will allow us to take into account

discharges in the system and to perform the expeditious diagnostics of the RF module is under development now on the base of VIT 030 code.

- [1] Simon Ramo, John R., "Field and waves in communication electronics", Second Edition, John Willey & Sons, 1984.
- [2] R.E. Collin, "Foundations for microwave engineering", Mc Graw-Hill, 1955.

EXTERNAL DATA INTERFACE TOOLS FOR THE PARTICLE BEAM OPTICS LABORATORY

George H. Gillespie, Barrey W. Hill, Hendy Martono and John M. Moore G. H. Gillespie Associates, Inc., P.O. Box 2961, Del Mar, CA 92014, U.S.A.

Abstract

An external data interface tool has been developed for the Particle Beam Optics Laboratory (PBO LabTM). The PBO Lab application provides an environment for the graphical set up of beam line models and execution of multiple optics programs that are implemented as Application Modules in a single user-friendly graphic interface shell. The external data interface (EDI) tools that have been implemented in PBO Lab version 2.0 support the import and export of beam line model parameters, as well as exporting diagnostic data generated from the different PBO Lab Application Modules. A variety of data exchange capabilities are provided through the EDI tools, including a basic implementation using ASCII text files in several different formats. However, one new EDI tool is described here that supports dynamic data exchange with MATLABTM. In addition to the exchange of beam line model parameters and computational diagnostics, this tool also implements an integrated simulation loop. allows the user to modify beam line model parameters and specify the execution of PBO Lab Application Modules in a loop that is externally controlled from MATLAB using C or Fortran MEX files, or MATLAB M files.

1 INTRODUCTION

The Particle Beam Optics Laboratory [1] is a multiplatform software package that combines the capabilities of several different particle optics programs under a single graphic user interface (GUI) shell. The focus of the PBO Lab package is on improving the ease-of-use and accessibility for legacy optics codes trusted in the accelerator community, as well as supporting recently developed object oriented codes, all within a consistent user interface shell. A multi-platform open architecture framework called the Shell for Particle Accelerator Related Codes (S.P.A.R.C.-MP) [2] has been developed for the implementation of optics codes as Application Modules in the PBO Lab environment. The framework implements a sophisticated beam line object model [3] and an extensive library of GUI components that support a variety of optics codes and add-on tools. This provides an environment for the graphical set up of beam line models and the execution of multiple optics programs from a single user-friendly interface, without requiring any knowledge of the various formats and specific syntax of the input required by the different optics programs. PBO Lab is capable of generating all the necessary input for each Application Module supported by the framework.

The S.P.A.R.C.-MP framework also provides external data interface tools that extend the users ability to configure PBO Lab for specific tasks in a variety of ways. One such tool is described here, for integrating PBO Lab with the MATLABTM environment. MATLAB by The MathWorks, Inc. [4], provides users with a mathematical workspace environment, development tools for creating user interface windows and plotting data, as well as supporting both compiled and interpreted programming languages. The PBO Lab version 2.0 GUI enables pointand-click selection of import/export variables and application-specific diagnostic output data to be used with the EDI tools. The PBO Lab EDI tool for MATLAB allows the user to exchange their selected beam line model parameters and diagnostics with the environment. This data is made accessible directly in the MATLAB workspace. The MATLAB EDI tool supports compiled execution of С functions Fortran subroutines, in addition to routines written in MATLAB's interpreted programming language. A basic simulation loop is provided for the automation of user defined operations.

2 PARTICLE BEAM OPTICS LABORATORY

The Particle Beam Optics Laboratory provides a unique graphic user interface shell (described in References [5,6,7]) for multiple particle accelerator related codes. Selected windows from a new version of the PBO Lab currently under development are shown in Figure 1. The PBO Lab environment presents a consistent and intuitive graphic user interface for related functionality in different optics codes. For example, a wide variety of fitting capabilities are supported by the different Application Modules in PBO Lab and the native specification of fitting variables and constraints for each of these codes is considerably different. The consistent treatment in PBO Lab, of similar capabilities in different optics programs, greatly reduces complexity for the user. The S.P.A.R.C.-MP framework provides PBO Lab with a variety of data visualization tools that are used to generate ellipse plots, scatter plots, line plots and bar graphs from the diagnostic data generated by the different Application Modules. The framework architecture also supports plugin tools such as an interactive particle trajectory module, a hypertext help system, interactive tutorials, and external data interface tools.

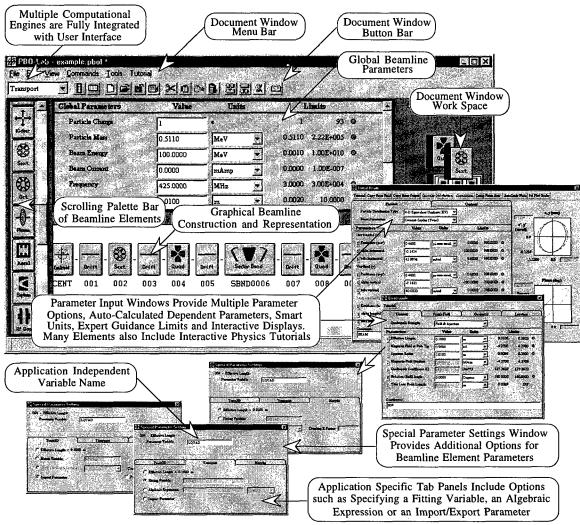


Figure 1. Screen Shots from the new Particle Beam Optics Laboratory on WindowsTM.

3 PBO LAB EXTERNAL DATA INTERFACE TOOLS

The PBO Lab external data interface tools are implemented in the S.P.A.R.C. MP framework as independent modules that import and/or export specific data formats through a generic EDI tools interface. The EDI tools can be described as a system of modules (Data Repositories) that fill an intermediate data structure (Data Interchange) which represents the generic interface for the development of plug-in tools for specific import/export targets. The Data Interchange is application independent and supports import/export targets that range from simple ASCII files in a variety of specific formats, to more dynamic data interfaces with external environments, such as the MATLAB EDI tool described here. Although not currently under development, an application-programming interface for the end user to create EDI plug-ins could be supported with the S.P.A.R.C. MP framework.

A new external data interface tool has been developed for PBO Lab that supports dynamic data exchange with

the MATLAB environment. MATLAB is an interactive computing environment numerical for computation, visualization and simulation [4]. The PBO Lab EDI tool for MATLAB supports the exchange of beam model parameters (Control Parameters) Application output (Computational Diagnostics) with the MATLAB environment. The EDI tool also implements an integrated simulation loop with MATLAB that allows the user to modify PBO Lab model parameters, control the execution of Application Modules and access diagnostic data in the MATLAB environment. The simulation loop can be controlled from MATLAB using C or Fortran MEX files, or MATLAB M files [8,9].

The user directly controls the basic import/export tool for MATLAB, i.e. the user executes the import and export commands from PBO Lab to exchange selected Control Parameters and Computational Diagnostics with MATLAB. If MATLAB is not running then it will be launched and the data will be placed in the MATLAB workspace. MATLAB can then be used for a variety of tasks such as post-processing diagnostic data for custom graphics or additional analysis with MATLAB toolboxes and/or user defined operations. Model Control Parameters

are modifiable directly from MATLAB and are extracted from the MATLAB workspace at the users' request in PBO Lab.

The PBO Lab EDI Tool also implements an automated dynamic data interface with MATLAB, passing Model Control Parameters, Simulation Control Parameters and Computational Diagnostics in a simulation loop that is illustrated in Figure 2. The simulation loop automates the external control of PBO Lab Application Modules by using compiled MEX files or MATLAB interpreted M files to perform a user-defined function. Figure 2 illustrates the Simulation Loop execution and data flow.

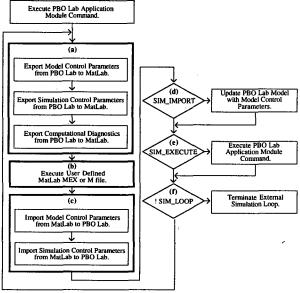


Figure 2. Simulation Loop Flow Chart.

Control Parameters passed to MATLAB (Figure 2(a)) are modifiable in the MEX or M files executed in the simulation loop (b). Simulation Control Parameters passed to MATLAB (a) and returned to PBO Lab (c) are used to control: (d) updating the PBO Lab beam line model with modified Control Parameters, (e) executing an Application command, and (f) terminating the simulation loop. After execution of MEX or M files (b), PBO Lab will import the Model Control and Simulation Control Parameters from MATLAB (c). Model Control Parameters are held in the Data Interchange while the Simulation Control Parameters are used by PBO Lab to execute (d), (e) and (f) of the Simulation Loop. The SIM_IMPORT parameter indicates whether the PBO Lab beam line model will be updated with the imported Model Control Parameters. The SIM_EXECUTE parameter is used to execute an Application command, and SIM_LOOP is used to terminate the simulation loop. The loop is simple, yet provides the control that is necessary to perform a variety of automated tasks. The PBO Lab EDI tool for MATLAB enables access to a large collection of MATLAB and third party tools, including Power Systems, Communications, Control Systems, Signal Processing, Fuzzy Logic and Neural Network toolboxes.

4 SUMMARY

An external data interface tool has been developed for the Particle Beam Optics Laboratory that leverages the popular mathematical environment, MATLAB. The PBO Lab EDI tool for MATLAB supports the import and export of beam line model parameters, as well as diagnostic data generated from the different PBO Lab physics Application Modules, although Data Repository modules have not been completed for all PBO Lab Applications. The MATLAB EDI tool supports an integrated simulation loop that automates the exchange of data and execution of user defined operations with MATLAB MEX or M files.

5 ACKNOWLEDGEMENTS

The assistance of James S. Gillespie in the design of the S.P.A.R.C.-MP framework is gratefully acknowledged.

- The PBO Lab software is available from AccelSoft Inc., San Diego, California, U.S.A., www.ghga.com/accelsoft.
- [2] B. W. Hill, H. Martono, J. M. Moore and J. S. Gillespie, "An Application Framework and Intelligent Graphic User Interface for Multiple Accelerator Codes," to be published in the proceedings of the International Computational Accelerator Physics (ICAP) Conference, Monterey, California, 15-18 September 1998.
- [3] B. W. Hill, H. Martono and J. S. Gillespie, "An Object Model for Beamline Descriptions," AIP Conference Proceedings 391, 361-365 (1996).
- [4] The Matlab software is available from The MathWorks Inc., Natick, MA, U.S.A., www.mathworks.com.
- [5] G. H. Gillespie, B. W. Hill, H. Martono, J. M. Moore, M. C. Lampel and N. Brown, "Using the Particle Beam Optics Laboratory (PBO LabTM) for Beamline Design and Analysis," to be published in the proceedings of the 15th International Conference on Cyclotrons, Caen, France, 15-19 June 1998.
- [6] G. H. Gillespie, B. W. Hill, N. A. Brown, M. C. Lampel, H. Martono, and J. M. Moore, "The Particle Beam Optics Laboratory (PBO LabTM): A New Education and Training Aid," Proceedings of the 6th European Particle Accelerator Conference,1183-1185 (1998).
- [7] G. H. Gillespie and B. W. Hill, "Particle Optics and Accelerator Modeling Software for Industrial and Laboratory Beamline Design," Nucl. Inst. Meth. Phys. B 139, 478-480 (1998).
- [8] The MathWorks Inc., <u>MATLAB Application Program Interface</u> <u>Guide</u>, 1998.
- [9] The MathWorks Inc. Using MATLAB Version 5, 1998.

NEW MATHEMATICAL OPTIMIZATION MODELS FOR RFQ STRUCTURES*

B. I. Bondarev, A. P. Durkin, Moscow Radiotechnical Institute A. D. Ovsyannikov*, St. Petersburg State University

Abstract

Conventional approach to the designing of controlled systems is to start with calculation of program motion and to continue afterwards by examining perturbed motions using equations in deviations. It does not always, however, result in desirable outcomes. Thus, while analysing perturbed motions, which depend significantly on the program motion, it can happen, that dynamical characteristics of obtained perturbed motions are not satisfactory.

This paper suggests new mathematical models, which allow joint optimization of program motion and an ensemble of perturbed motions. These mathematical models include description of controlled dynamical process, choice of control functions or parameters of optimization as well as construction of quality functionals, which allow efficient evaluation of various characteristics of examined control motions.

This optimization problem is considered as the problem of mathematical control theory. The suggested approach allows to develop various methods of directed search and to conduct parallel optimization of program and perturbed motions. Suggested approach is applied to the optimization of RFQ channel. Simple model for description of beam longitudinal motion in the equivalent running wave is suggested. For the estimation of beam dynamics corresponding functionals are suggested.

1 MATHEMATICAL MODELS OF OPTIMIZATION

First we consider following dynamic system:

$$\frac{\mathrm{dx}}{\mathrm{dt}} = \mathbf{f}(\mathbf{t}, \mathbf{x}, \mathbf{u}), \tag{1}$$

$$\frac{\mathrm{d}y}{\mathrm{d}t} = F(t, x, y, u), \qquad (2)$$

with initial conditions:

$$x(0) = x_0, \quad y(0) = y_0 \in M_0;$$
 (3)

Here t is time, x is n-vector, u = u(t) is r-dimensional control vector function, y - m-vector, f(t,x,u) and F(t,x,y,u) are n-dimensional and m-dimensional

vector functions correspondingly. We assume that f, F and $\text{div}_y F = \sum_{i=1}^m \partial F_i/\partial y_i$ are continuous with their partial derivatives. The set M_0 is a given compact set in the phase space of nonzero measure in R^m . We assume that admissible controls u(t) constitute certain class D of functions, that are piecewise continuous on interval [0,T] and have values in a compact set $U \subset R^r$.

Equation (1) describes dynamics of synchronous particle. Here in this paper we will consider this motion as the program one. Equation (2) is the derivations equation describing perturbed motions.

Along with equations (1), (2) we consider changes of density of particles $\rho(t,y)$, along the system (2) trajectory:

$$\frac{\mathrm{d}\rho}{\mathrm{d}t} = -\rho \cdot \mathrm{div}_{y} F(t, \mathbf{x}(t), \mathbf{y}(t), \mathbf{u}(t)), \qquad (4)$$

$$\rho(0,y(0)) = \rho_0(y_0), \quad y_0 \in M_0, \quad (5)$$

where $\rho_0(y_0)$ is density of particles distribution at the set M_0 .

We introduce following functionals:

$$I_1(u) = c_1 \int_0^T \varphi_1(t, x(t), u(t)) dt + c_2 g_1(x(T)), \quad (6)$$

$$I_2(u) = c_3 \int_0^T \Phi(\omega_1(t)) dt + c_4 \cdot G(\omega_2).$$
 (7)

Here C_i (i = 1,2,3,4) are non-negative constant,

$$\omega_{1}(t) = \int_{M_{t,u}} \phi_{2}(t, x(t), y_{t}, \rho(t, y_{t}), u(t)) dy_{t}, \quad (8)$$

$$\omega_2 = \int_{M_{T,u}} g_2(y_T, \rho(T, y_T)) dy_T,$$
 (9)

where set $M_{t,u}$ is the cross-section of trajectories set of system (2) at the moment t, that can be obtained by time shift of the initial set M_0 at corresponding control u=u(t):

$$\mathbf{M}_{t,u} = \{ y_t \mid y_t = y(t, y_0, x(t), u(t)) \\ y_0 \in \mathbf{M}_0, \ x(0) = x_0 \},$$
 (10)

functions $\phi_1, g_1, \phi_2, g_2, \Phi, G$ are continuously differentiable functions, T is fixed.

^{*}Work supported in part by Russian Foundation for Fundamental Researches, project 99-01-00678

[#] Email: ovs@apcp.apmath.spbu.ru

Together with the functional (6), which characterizes dynamics of program motion, and the functional (7), which characterizes beam of particles with taking into account their density of distribution, we introduce following functional:

$$I(u) = I_1(u) + I_2(u)$$
. (11)

The functional (11) estimates dynamics of program and perturbed motions and allows to conduct their optimization.

By using methods of investigation of functionals (6), (7) types presented at the work [1] variation of functional (11) (at admissible variation of control $\Delta u(t) = \widetilde{u}(t) - u(t)$) can be represented in the following form:

$$\delta \mathbf{I} = -\int_{0}^{T} (\chi^* \cdot \Delta_{\mathbf{u}} \mathbf{f} - \mathbf{c}_1 \cdot \Delta_{\mathbf{u}} \phi_1) dt$$

$$-\int_{0}^{T} \int_{\mathbf{M}_{t,\mathbf{u}}} (\mu^* \cdot \Delta_{\mathbf{u}} \mathbf{F} - \mathbf{c}_3 \cdot \Phi'(\omega_1) \cdot \Delta_{\mathbf{u}} \phi_2) dy_t dt \quad (12)$$

$$-\int_{0}^{T} \int_{\mathbf{M}_{t,\mathbf{u}}} (\mathbf{v} \cdot \Delta_{\mathbf{u}} div_y \mathbf{F}) dy_t dt.$$

Here Δ_u denotes increment of a function at only increment of variable u, for example, $\Delta_u f = f(t, x, u + \Delta u) - f(t, x, u)$.

Auxiliary functions $\chi(t)$, $\mu(t,y_t)$, $\nu(t,y_t)$ satisfy the following systems along the trajectories of systems (1), (2), (4):

$$\frac{d\chi}{dt} = -\left(\frac{\partial f}{\partial x}\right)^* \cdot \chi + c_1 \cdot \left(\frac{\partial \phi_1}{\partial x}\right)^* \\
- \int_{M_{t,u}} \left(\left(\frac{\partial F}{\partial x}\right)^* \cdot \mu + \nu \cdot \left(\frac{\partial \operatorname{div}_y F}{\partial x}\right)^*\right) dy_t \\
+ c_3 \cdot \Phi'(\omega_1(t)) \cdot \int_{M_{t,u}} \left(\frac{\partial \phi_2}{\partial x}\right)^* dy_t, \tag{13}$$

$$\frac{d\mu}{dt} = -\left(\frac{\partial F}{\partial y} + E \cdot \operatorname{div}_{y} F\right)^{*} \cdot \mu$$

$$-\nu \cdot \left(\frac{\partial \operatorname{div}_{y} F}{\partial y}\right)^{*} + c_{3} \cdot \Phi'(\omega_{1}(t)) \cdot \left(\frac{\partial \varphi_{2}}{\partial y}\right)^{*}, \qquad (14)$$

$$\frac{d\nu}{dt} = -\nu \cdot \operatorname{div}_{y} F$$

$$+ c_{3} \cdot \Phi'(\omega_{1}(t)) \cdot (\varphi_{2} - \rho \cdot \frac{\partial \varphi_{2}}{\partial \rho}), \qquad (15)$$

and terminal conditions

$$\chi(T) = -c_2 \cdot \frac{\partial g_1(x(T))}{\partial x}^*, \tag{16}$$

$$\mu(T, y_T) = -c_4 \cdot G'(\omega_2) \left(\frac{\partial g_2(y_T, \rho_T)}{\partial y}\right)^*, \quad (17)$$

$$v(T, y_T) = -c_4 \cdot G'(\omega_2) \cdot (g_2(y_T, \rho_T) - \rho_T \frac{\partial g_2(y_T, \rho_T)}{\partial \rho}),$$
(18)

where $\rho_T = \rho(T, y_T)$,, $G'(\omega_2) = dG(\omega_2)/d\omega_2$, $\Phi'(\omega_1) = d\Phi(\omega_1)/d\omega_1$.

The representation (12) of functional variation allows to construct various methods of optimization for functional (11).

2 BEAM DYNAMICS MODELLING

Let us consider charge particle dynamics in RFQ channel. Longitudinal motion in equivalent running wave can be represented in the following form:

$$\frac{\mathrm{d}\beta}{\mathrm{d}t} = \frac{2\mathrm{e}U_{L}\Theta}{W_{0}L} \cdot \cos(\widetilde{\omega} \cdot \tau - \Psi + \varphi_{s}). \quad (19)$$

Here
$$\beta = \dot{z}/c$$
, $\tau = ct$, $\widetilde{\omega} = 2\pi\omega/c$,

$$\Psi = \int_{z}^{z_s} \Omega(\xi) d\xi = \Omega \Delta z$$
, $\Omega = 2\pi/L$, U_L - intervane

voltage, Θ - accelerating efficiency, W_0 - rest mass energy, L - period length, ω - accelerating field frequency, ϕ_s - synchronous phase.

For synchronous particle $\tilde{\omega}\tau = \Omega z_s$ and, hence

$$\frac{\mathrm{d}\beta_{s}}{\mathrm{d}\tau} = \frac{2\mathrm{e}U_{L}\Theta}{W_{0}L}\cos\varphi_{s},\tag{20}$$

$$\frac{d^{2}(z_{s}-z)}{d\tau^{2}} = \frac{2eU_{L}\Theta}{W_{0}L}(\cos\varphi_{s} - \frac{1}{2}\cos(\Omega(z-z_{s})+\varphi_{s})), \tag{21}$$

Let us make notations:

$$\Omega_0^2 = \frac{4\pi e(U_L\Theta)_{max}}{W_0 L_0^2}, \ \eta = \frac{(U_L\Theta)}{(U_L\Theta)_{max}},$$

and use new variables:

$$\Psi = \Omega(z_s - z)$$
, $\tilde{\tau} = \Omega_0 \tau$.

After all transformation equations (20), (21) takes form:

$$\frac{\mathrm{d}}{\mathrm{d}\tilde{\tau}}(\mathrm{L}/\mathrm{L}_0)^2 = 2\mathrm{k} \cdot \eta(\tilde{\tau}) \cdot \cos\varphi_s(\tilde{\tau}), \qquad (22)$$

$$\psi'' + \frac{(L/L_0)^2}{(L/L_0)^2} \psi' + \frac{(L/L_0)''}{(L/L_0)} \psi - \frac{\eta(y)}{(L/L_0)^2} (\cos \varphi_s - \cos(\psi + \varphi_s)) = 0,$$
(23)

where the stroke denotes the derivative with respect to $\tilde{\tau}$ and $k = \Omega_0/\tilde{\omega}$.

Various optimization problems of longitudinal motion can be formulated on the basis of equations (22), (23). Further we will consider the functions $u_1 = \eta(\tilde{\tau})$ and $u_2 = \phi_s(\tilde{\tau})$ as control functions.

It should be noted that all accelerators with the same plots $\phi_s(\widetilde{\tau})$ and $\eta(\widetilde{\tau})$ and with k=const has similar beam behaviour. The relation between unites $\widetilde{\tau}$ and period number N is defined by $kN = \widetilde{\tau}$.

3 OPTIMIZATION CRITERIA

As the aim of RFQ structure optimization we consider the following: obtaining of maximal capture of particles under the acceleration regime; obtaining of required or maximal possible output energy; minimization of defocusing factor effect; obtaining of monotonicity of particles' grouping which reduces Coulomb forces' effect on the dynamics of charged particles, subsequently improves the dynamic process in RFQ channel.

Let
$$x = (L/L_0)^2$$
, $y = (y_1, y_2)^* = (\psi, \psi')^*$,
 $M_0 = \{ y \mid -\pi \le y_1 \le \pi, \theta_1 \le y_2 \le \theta_2 \}$

For the process dynamics assessment we introduce functionals:

$$\begin{split} I_{1}(u) &= c_{1} \int_{0}^{T} \varphi_{1}(A_{def}) d\tilde{\tau} + c_{2}(x(T) - \overline{x})^{2}, \quad (24) \\ A_{def} &= \frac{2k^{2} \eta \left| \sin \varphi_{s} \right|}{(L/L_{0})^{2}} = \frac{2k^{2} u_{1} \left| \sin u_{2} \right|}{x}, \\ I_{2}(u) &= c_{3} \int_{0}^{T} \Phi(w_{1}(t)) d\tilde{\tau}, \quad (25) \\ w_{1}(t) &= \frac{d}{d\tilde{\tau}} \int_{M_{\tilde{\tau},u}} (\psi^{2} \cdot \rho) dy_{\tilde{\tau}} = \int_{M_{\tilde{\tau},u}} 2y_{1} y_{2} \rho dy_{\tilde{\tau}}, \\ I(u) &= I_{1}(u) + I_{2}(u). \quad (26) \end{split}$$

Here ϕ_1 and Φ are penal functions, which can be introduced in following way:

$$\phi_1(A_{def}) = \begin{cases} 0, & A_{def} \leq \overline{A} \\ (A_{def} - \overline{A})^{2p}, & A_{def} > \overline{A} \end{cases}$$

$$\Phi(\mathbf{w}_1) = \begin{cases} 0, & \mathbf{w}_1 \le 0 \\ {\mathbf{w}_1}^{2q}, & \mathbf{w}_1 > 0 \end{cases}$$

where p,q are certain positive integer constants.

 A_{def} is defocusing factor; $\overline{x} = (\overline{L}/L_0)^2 = (\overline{\beta}/\beta_0)^2$ is fixed value, which determines velocity of synchronous particle at the output of accelerator; $\rho = \rho(\overline{\tau}, \psi, \psi')$ is density of particle distribution.

Functional (24) integrally estimates the deviation of defocusing factor from given value and accounts the deviation of synchronous particle velocity from given one at the output of accelerator. Functional (25) characterizes velocity of variation of mean square phase distribution. In this connection, condition $w_1 \le 0$ ensures the monotonicity of grouping and simultaneously ensures the capture of particles into acceleration mode.

On the basis of variation (12) for the functional (26) numerical methods of optimization which allow joint minimization of functionals (24), (25). The realization of these methods shows their effectiveness.

4 CONCLUSION

Under RFQ structure optimization following parameters are considering as controlling: voltage between electrodes, modulation of electrodes, mean value aperture on the period of modulation, synchronous phase, i.e. each cell of developing structure is described by all parameters for each cell ([2]). In this case full-scale modeling of particles dynamics and conducting of optimization require much time and numerous attempts. Such approach seems to be reasonable for improvement of parameters in the vicinity of chosen already variant.

Thus for the practical use of optimization methods it is necessary to use step by step method of choice of RFQ structure parameters. At each stage of this calculation various mathematical models with growing level of complexity should be considered.

In this paper the simple mathematical model which describes beam dynamics in RFQ channel is suggested, that can be used on the initial stage of optimization. Suggested mathematical models of optimization and developed methods and approaches of their analysis allow effective optimization of the RFQ channel.

It should be noted, that developed methods of optimization can be applied to the optimization problem of intense beam dynamics.

5 REFERENCES

[1] Ovsyannikov D.A., "Modeling and Optimization of Charged Particle Beam Dynamics", Leningrad State University, Leningrag, 312p., (1990).

[2] Drivotin O.I., Loukianova A.E., Ovsyannikov D.A., Garvish Yu.N., Svistunov Yu.A., Vorogushin M.F., "The Choice of Acceleration Structure for PET-System", EPAC'96, Proceedings, Barselona, Spain, Vol.1, p.783-785, (1996).

ON THE INVARIANT MOMENTUM HYPOTHESIS AT EXTREMELY LARGE VELOCITIES

V. Baranauskas, Faculdade de Engenharia Elétrica e Computação, Universidade Estadual de Campinas, Av. Albert Einstein N. 400, 13083-970 - Campinas - SP - Brasil

Abstract

Starting from the hypothesis of the invariancy of the subluminal momentum and applying the beyond-Lorentz transformations we derive a new equation for the invariant momentum-velocity of particles which can be applied to subluminal or superluminal particles. The kinetic energy shows a maximum at the velocity of light and falls at subluminal or superluminal velocities. There is good agreement with the Newtonian and relativistic results for particle momentum and energy at subluminal velocities.

1 INTRODUCTION

The Special Theory of Relativity Theory (STR) makes use of the Lorentz transformations, whose real solutions are limited to velocities below the velocity of light (subluminal velocities). One of the STR's main assertions is that the relativistic momentum is conserved regardless of the frame of reference. The mass of a particle assumes an energy content and apparently increases with an increase in its velocity, becoming infinite at the velocity of light (c). Photons or neutrinos are thus considered particles with zero rest-mass since that they can travel with limited energies at the velocity of light. Recent experiments, however, suggest that neutrinos are massive particles [1].

When exploring the extreme limits of bunches of particles, why not to seek more general transformations that can also be applied above c (superluminal velocities), including the Lorentz transformation as a special case? Recently, we demonstrated the existence of such general transformations which also obey the principle of the constancy of c [2].

In the present work, starting from the hypothesis of invariant momentum and applying such general transformations, we demonstrate the existence of a new equation for the momentum that agrees with the STR's predictions for momentum of subluminal phenomena but can also be applied at superluminal velocities. The

This work is dedicated to the memory of my son, V. B. Filho (1987-1997). The author acknowledges the kind help of S. F. Durrant in editing the manuscript and CNPq, CAPES, FAPESP and the PAC-99 organizers for partial financial support.

Email: vitor@dsif.fee.unicamp.br

kinetic energy of the particle, calculated from the integration of this new momentum-velocity equation, shows that all terms depend on the velocity, which contradicts the STR's prediction of the existence of an associated rest energy related only to the mass of the particle. Finally, predictions are made concerning the dependence of the momentum and kinetic energy on the velocity of superluminal particles.

2 BEYOND-LORENTZ TRANSFORMATIONS

Accepting the hypothesis that the velocity of light is constant, i. e., does not depend on the reference system, we can write the following transformation equations between a system reference S and a system S' that moves with a constant speed v in the direction of the axis x, relative to S:

$$x \longrightarrow x' = \beta_B x - \sqrt{\beta_B^2 - 1} ct$$
 (1)

and
$$t \longrightarrow t' = \beta_B t - \sqrt{\beta_B^2 - 1} \frac{x}{c}$$
 (2)

with $\beta_{\rm B} = \sqrt{\sum_{\rm n=0}^{\rm k} \left(\frac{\rm v}{\rm c}\right)^{\rm 2n}} = \sqrt{\frac{\left(\frac{\rm v}{\rm c}\right)^{\rm 2(k+1)} - 1}{\left(\frac{\rm v}{\rm c}\right)^{\rm 2} - 1}}$

These equations can be applied to describe light wave propagation invariance under uniform translation of S' relative to S in the x direction for any value of the order number k (k=1,2,...). It can easily be verified for subluminal velocities that the above equations can be made as close as is wanted to the Lorentz transformations by a convenient choice of k (k large). However, unlike with the Lorentz transformations, the new solutions are always real for any velocity, including superluminal velocities.

3. MOMENTUM-VELOCITY RELATIONSHIP

Through the conservation of the energy-momentum in

particle collisions it was demonstrated that the relativistic momentum can be expressed by [3]:

$$p = m \frac{\Delta x}{\Delta t'}$$
 (3)

which, with application of the beyond-Lorentz transformations can be written as:

$$p = \frac{m v}{\beta_B - \frac{v}{c} \sqrt{\beta_B^2 - 1}} = \gamma_B m v$$
 (4)

where γ_B is the new correction factor. This equation can be applied for any velocity, either subluminal or superluminal. Figure 1 compares the curves of momentum versus velocity calculated from this result (equation (4)) and the STR momentum, respectively. Newtonian momentum is also ploted for reference.

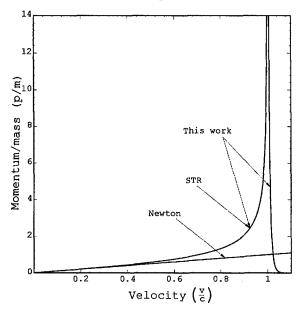


Figure 1: Momentum versus velocity: Comparison of the results of the Newtonian, STR and the present approach.

We observe a good agreement between this new result and the STR momentum for subluminal velocities. Thus, great part of the subluminal experiments that validate the relativistic momentum also confirm the new momentum equation. However, this new equation can also be used to foresee the momentum at superluminal velocities. As we can see, when a particle is passing the light velocity barrier its momentum is strongly attenuated, as in the evanescent transmission of particles-waves in tunneling phenomena. The existence of a very thin spike at v = c, with an upwards divergence at c- and a strong attenuation at c+ suggests a very high momentum for luminal particles, but not a limitless momentum. It should also be observed that in spite of the momentum tending to zero for superluminal velocities, the velocity of the particle is not reduced since its momentum-velocity relationship differs both from Newtonian and the usual relativistic formulas.

4. KINETIC ENERGY

We can calculate the kinetic energy from the usual expression of the integration of a force F continuously acting on a particle along the axis x:

$$K = \int F dx = \int dp \frac{dx}{dt} = p v - \int_{v=0}^{v} p dv$$
 (5)

and applying equation (4), we find

$$K = m c2 \left(\Phi_1(v) - \Phi_2(v)\right)$$
 (6)

with

$$\Phi_1(v) = \gamma_B \frac{v^2}{c^2}$$

and

$$\Phi_2(v) = \int_0^v \gamma_B \frac{v}{c^2} dv$$

We did not find an algebraic solution to solve the integral for $\Phi_2(v)$ but it can easily be numerically integrated. The curve of the kinetic energy versus the velocity of the particle shows a maximum at the velocity of light which decays at subluminal or superluminal velocities (see Figure 2 (a)). Again, there is a good agreement with the STR predictions for subluminal velocities. Besides this good fitting, it should be pointed out that there is a fundamental difference between the kinetic relativistic formula for $(K = m c^2 ((1-v^2/c^2)^{-1/2} - 1))$ and the presented by equation (6) since all terms (Φ_1 and Φ_2) in the latter depend on v. Thus, it is demonstrated that the hypothesis of an energy associated to the mass of the particle in rest in not a necessary condition for obtaining the results foreseen by STR. The mass of the particle can be assumed invariant with the velocity, being just a multiplying parameter of the related energy.

For low velocities (see Figure 2 (b)) the functions Φ_1 and Φ_2 may be approximated respectively by $\Phi_1(v) \cong \frac{v^2}{c^2}$ and $\Phi_2(v) \cong \frac{1}{2} \frac{v^2}{c^2}$. Therefore equation (6) is reduced to $K \cong \frac{1}{2} m v^2$, which coincides with the

Newtonian formula.

For subluminal velocities very close to the velocity of light $(v \cong c^-)$ we have that $\Phi_1 \cong v_B \approx (1-v^2/c^2)^{-1/2}$ and $\Phi_2 \cong 1$ (see Figure 2 (a)). In this case, equation (6) reduces to the usual relativistic formula for kinetic energy: $K \cong m \ c^2 \ ((1-v^2/c^2)^{-1/2}-1)$.

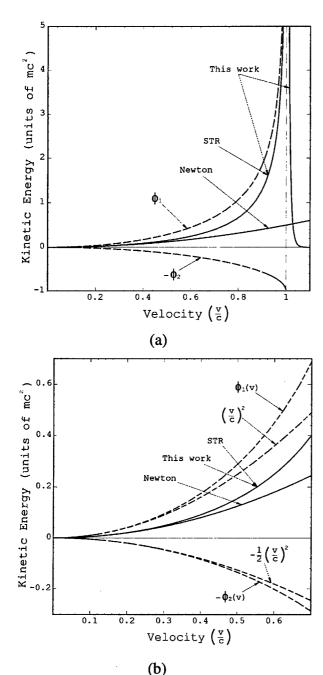


Figure 2: (a) Kinetic energy versus velocity: Comparison of Newtonian, STR, and of this approach. The dependence of the functions Φ_1 and Φ_2 on velocity are also shown. For subluminal velocities there is a good agreement between this work and the STR, however, there are no terms independent of the velocity. (b) For low velocities, Φ_1 and Φ_2 approaches a dependence on $\frac{v^2}{c^2}$ and $\frac{1}{2}\frac{v^2}{c^2}$, respectively.

Surpassing the barrier of the velocity of light the kinetic energy of the particle diminishes, as illustrated in Figure 2 (a). The fall in the kinetic energy with an

increase in the velocity is an interesting effect because it is not necessary to increase the energy of the particle to increases its velocity. On the contrary, the particle needs to lose energy (by radiation?) to increase its velocity. The vacuum for superluminal particles behaves as a superfluid. If the superluminal particle emits light to lose kinetic energy the emitted photons may be luminal, thus, not changing the refractive index of the vacuum. The radiation emitted by the superluminal particle may be similar to the Cerenkov radiation. In fact, the new equations presented here may be rewritten for the propagation of particles in a material medium other than vacuum (refractive index > 1), thus serving as an explanation for the Cerenkov radiation in liquid and solid materials.

Just as in the dynamics of a resonance problem, the value of the energy of the luminal particle should be very high due to the singularity at v=c, but not infinite. Other conditions are necessary to calculate its limit. Equation (6) explicitly shows that the kinetic energy depends directly on the mass of the particle, thus particles with larger mass will have to have larger energies to become luminal particles. We did not find any support in our derivation for the supposition that luminal particles have to have zero mass.

5. CONCLUSIONS

Through the use of the beyond-Lorentz transformations (velocity of light is constant) we derived a new equation for the invariant momentum-velocity of particles that can be applied to subluminal or superluminal particles. Good agreement of this new equation was demonstrated (for subluminal velocities) with the relativistic momentum and with Newtonian momentum, in its respective range of application. For superluminal particles this new equation foresees that the momentum is strongly attenuated with an increase of velocity. The kinetic energy calculated using this new equation for the momentum shows a maximum at the velocity of light and decays at subluminal or superluminal velocities. There is also a good agreement with the relativistic and Newtonian results for subluminal velocities. However, there is no need to consider an energy associated with the rest-mass of the particle to calculate its kinetic energy.

REFERENCES

[1] D. Normile, Science, 280, p. 1689 (1998).

[2] V. Baranauskas in 6th European Particle Accelerator Conference EPAC-98, 1998, edited by S. Myers, L. Liljeby, Ch. Petit-Jean-Genaz, J. Poole, K.-G. Rensfelt, (Institute of Physics Publishing, Bristol, 1998), p. 835.

[3] G. N. Lewis and R. Tolman, Phil. Mag. 18, p. 510 (1909).

TO THE QUANTUM LIMITATIONS IN BEAM PHYSICS*

A. A. Mikhailichenko[†]

Wilson Laboratory, Cornell University, Ithaca, NY 14850

Abstract

The conditions reviewed for degeneration in an electron bunch treated as a Fermi gas. Some comparison made for photoinjectors and storage rings. In some cases a quantum limitations are very close.

1 INTRODUCTION

In recent times some interest is growing to the beams with minimal emittance [1-3]. Schemes proposed which look like they even could reach the quantum limit in beam emittance. However, in some of these publications claimed that the minimal normalized emittance of the beam is defined by uncertainty principle only like $\gamma \varepsilon_{\min} \equiv \lambda_C / 2$, where $\lambda_C = \hbar / mc \cong 3.86 \cdot 10^{-11} \, \text{cm}$ —is a Compton wavelength [2,3]. Meanwhile it is well known that the *Fermi*-particles could not occupy the same states. This fact yields that for the beam with population equals N, the minimal emittance is N times bigger, than indicated above. This fact was illuminated first in [1].

2 CONDITION FOR DEGENERATION

Electron gas has a tendency to generate with lowering its temperature. If gas is fully degenerated, each state occupied by a pair of electrons having different spin orientation. Basically we have definition of degenerated state as one having temperature small compared with Fermi energy E_F [4]. The last is the highest one while states are tightly packed. We will consider the minimal emittance definition from two slightly different approaches. First uses the fact, that there are no free states in a system below E_F . This yields that the number of states equals to the number of the particles in the beam. This definition basically corresponds to assumption that the beam has zero temperature. We will simply calculate the number of allowed states. The second approach, indeed, uses the definition of the beam temperature in a moving system of reference. We compare the emittance restrictions obtained with these two approaches. Ultrarelativistic electron gas becomes more ideal in a Lab frame with increasing its energy due to cancellation of forces between the particles as $\approx 1/\gamma^2$. In principle, some amount of particles with opposite charge can be added to the beam moving along a straight line in a focusing channel [7].

Now let us estimate the minimal emittance from the compact packing approach. For the electrons in a volume V, the number of states with absolute magnitude of momentum in the interval from $p_{x,y,s}$ to $p_{x,y,s} + dp_{x,y,s}$ is

$$dn \cong 2 \frac{dp_x dp_y dp_s \cdot V}{(2\pi\hbar)^3}, \tag{1}$$

where factor 2 reflects two possibilities for spin statement. Let us suggest that all lower states are occupied up to the highest one. Then the number of the states equals to the number of the particles in the volume. The Fermi-momenta p_F defined as

$$N = \int dn \approx 2 \cdot \frac{4\pi}{3} \frac{p_F^3 \cdot V}{(2\pi\hbar)^3} \approx \frac{8\pi}{3} \frac{V}{\lambda_B^3}, \qquad (2)$$

where $\lambda_B \cong 2\pi\hbar/p_F$ is the length of the de-Broigle wave corresponding to the particle with Fermi energy. So the density N/V in degenerated Fermi-gas corresponds to the reverse cube of de-Broigle wavelength, corresponding to the Fermi momenta. In formula (1) for the number of states the variables (momenta and coordinate) are canonically conjugated. The particles in a focusing system behave more likely as a harmonic oscillator. Description of transverse motion with envelope function satisfy the requirements to be a canonically conjugated as

 $p_x p_y S_{\perp} \cong m c_y \sqrt{\varepsilon_x / \beta_x} \cdot m c_y \sqrt{\varepsilon_y / \beta_y} \cdot \sqrt{\varepsilon_x \beta_x} \cdot \sqrt{\varepsilon_y \beta_y}$, (3) where $\beta_{x,y}$ —are the envelope function. The total number of electrons in these states can be estimated for uniform distribution from (1) using (3)

$$N = \int dn \approx \frac{2p_x p_y \Delta p_{\parallel} S_{\perp} l_b}{(2\pi \hbar)^3} \approx \frac{2\gamma \varepsilon_x \gamma \varepsilon_y \gamma l_b (\Delta p_{\parallel} / p_0)}{(2\pi \hbar_c)^3}, (4)$$

or
$$(\gamma \varepsilon_x)(\gamma \varepsilon_y)(\gamma \varepsilon_s) \ge (\frac{1}{2})(2\pi \lambda_C)^3 N$$
, (5)

where $\gamma \varepsilon_s = \gamma l_b (\Delta p_{\parallel} / p_0)$ —is an invariant longitudinal

emittance, l_b -is the bunch length, $(\Delta p_{\parallel} / p_0)$ - the

relative momentum spread in the beam, \mathcal{X}_x and \mathcal{X}_y are the transverse horizontal and vertical emittances. We can also say, that the beam with the number of the particles N cannot have emittances lower than defined by (5) as all lower states are occupied. So in that sense formula (5) corresponds to zero beam temperature and

^{*}Work supported by National Science Foundation

[†] Phone: (607) 255-3785, Fax: (607) 255-8062, e-mail "mikhail@lns62.lns.cornell.edu

cold be treated as absolute lower limit for the beam emittances. The right side in (5) is tremendously small as $(2\pi\lambda_c)^3 \cong 1.4 \cdot 10^{-30} \,\mathrm{cm}^3$. So even for $N \cong 10^{10}$ the right side in (5) will be $\approx 10^{-20} \,\mathrm{cm}^3$.

Now let us estimate the minimal emittance from the requirement that the beam temperature is much less, than the Fermi energy. This condition is weaker, that (5). From (2) one can obtain

$$p_F = (3/8\pi)^{1/3} 2\pi\hbar \rho^{1/3}, \tag{6}$$

were $\rho \approx N/V$ —is a density in the rest frame. From (6) one can obtain, that the Fermi energy is

$$E_F = \frac{p_F^2}{2m} \cong (3\pi^2)^{2/3} \frac{\hbar^2}{2m} \rho^{2/3}$$
 (7)

or
$$E_F = cp_F = (3\pi^2)^{1/3}\hbar c\rho^{1/3}$$
, (8)

if the particles in the rest frame are relativistic. The formulas (7), (8) represent the height of the well.

Using (7) or (8) one can find the condition for degeneration as

$$k_B T \leq \frac{(3\pi^2)^{2/3}}{2} mc^2 (\lambda_C^3 \rho)^{2/3},$$

or
$$k_B T \le (3\pi^2)^{1/3} mc^2 (\lambda_C^3 \rho)^{1/3}$$
,

where $k_B \cong 1.38 \cdot 10^{-23} \text{ J/}^{\circ}\text{K}$ -is Boltzmann's constant. The electron gas temperature T in a moving frame can be calculated using (3). The transverse momenta is invariant and the transverse kinetic energy is

$$\frac{p_x^2}{2m} + \frac{p_y^2}{2m} \cong \frac{1}{2m} m^2 c^2 \gamma^2 \frac{\varepsilon_x}{\beta_x} + \frac{1}{2m} m^2 c^2 \gamma^2 \frac{\varepsilon_y}{\beta_x}.$$

Full energy is a sum of kinetic and potential energy of motion in a focusing system. According to the virial theorem for harmonic oscillator the average potential energy equals to the kinetic one. So the temperature of the beam could be represented as the following

$$\frac{3}{2}Nk_{B}T \cong N \cdot mc^{2}\gamma[\gamma \varepsilon_{x}/\beta_{x} + \gamma \varepsilon_{y}/\beta_{y} + \beta^{2}(\Delta p_{\parallel}/p_{0})^{2}/\gamma], (9)$$

where $\beta^2 \cong 1$ — is a square of normalized speed in the lab frame. Let us consider one example. In damping rings developed as injectors for future linear colliders, typical values are $\beta_{x,y} \cong 10$ m, $l_b \cong 1$ cm, $\Delta p/p \cong 510^4$, $\gamma \mathcal{E}_x \cong 3$ cm, $\gamma \mathcal{E}_x \cong 3 \cdot 10^{-4}$ cm rad, $\gamma \mathcal{E}_y \cong 3 \cdot 10^{-6}$ cm rad. This gives $\frac{3}{2}k_BT \cong mc^2\gamma(3\cdot10^{-7}+3\cdot10^{-9}+4\cdot10^{-11}]$. One can see that despite the longitudinal emittance is the biggest one, the longitudinal temperature is the lowest one. This yields the possibility for redistribution the temperatures. Compare formula (9) with (8) one can obtain for relativistic electron gas

$$mc^2\gamma \left[\frac{\gamma \varepsilon_x}{\beta_x} + \frac{\gamma \varepsilon_y}{\beta_y} + \frac{1}{\gamma} \left(\frac{\Delta p}{p_0}\right)^2\right] << (3\pi^2)^{1/3} mc^2 (\lambda_C \rho)^{1/3},$$

where $\rho = \rho_0 / \gamma$, ρ_0 -is the density in the Laboratory frame. Neglecting the longitudinal temperature and supposing that, $\gamma \mathcal{E}_x \approx \gamma \mathcal{E}_y$ one can obtain the condition

$$(\gamma \varepsilon_x)^4 \le \beta_x^2 \lambda_C^3 N / (\gamma^3 l_b). \tag{10}$$

Substitute here for estimation $\beta_x \approx l_b \approx 1 \, \mathrm{cm}$, $N \approx 10^{10}$, $\gamma \approx 6 \cdot 10^3$, one can obtain $\gamma \epsilon_x \leq 2 \cdot 10^{-8}$ cm rad. This is estimation for the *maximal* possible transverse emittance required for degeneration. One can compare this figure with the one suggested for the Linear Collider. From the other hand this is not drastically lower, than for specially designed coolers, see lower.

3 REDUCTION OF DIMENSIONS

We suggested that the phase space corresponds to 3D motion in real space. So the particle could reach every point in phase space. Defining the speed of motion in the rest frame as $v = \sqrt{3k_BT/m}$, one can find the frequency of collision $f_{x,y}$ with the potential wall as

$$f_{x,y} = \frac{v_{x,y}}{a_{x,y}} = c\sqrt{\gamma(\gamma \varepsilon_{x,y})/\beta_{x,y}}/\sqrt{(\gamma \varepsilon_{x,y})\beta_{x,y}/\gamma} = \frac{c\gamma}{\beta_{x,y}}$$
(11)

like it must be if one transforms the frequency into moving frame. This frequency does not depend on emittance. For longitudinal motion one can estimate $f_s \cong \gamma_\parallel / \mathcal{H}_b \cong c(\Delta p/p)/\mathcal{H}_b$. So one can see that the frequency of longitudinal oscillations is much smaller, than the transverse. In motion along the focusing channel the longitudinal motion is practically absent at all. So for a two-dimensional phase space

$$(\gamma \varepsilon_x)(\gamma \varepsilon_y) \ge (\frac{1}{2})(2\pi \hbar_C)^2 N.$$
 (12)

Considerations [5] show that thermalization due to intrabeam scattering (also through the third agent, such as a resistive wall or parasitic cavity) can happen only when momentum compaction factor is *negative*.

From quantum mechanical consideration of the problem, for N fermions the wave function is fully antisymmetric one. It could be written as a Slater's determinant. As the particles experience the motion in a kind of harmonic oscillator potential, the energy of each particle is proportional

$$E \cong E_{kin} + \frac{1}{2} \sum K_i x_i^2, \quad i = 1, 2, 3,$$
 (14)

where K_i —is the effective rigidity for selected degree of freedom. Using methods of quantum mechanics one can obtain that the energy of ground state is

$$E_0 = \sum_{i=1,3} \hbar \omega_i \cdot (\frac{N}{2} + \sum_{n=1}^{N-1} n), \qquad (15)$$

where *n* counts the states occupied and $\omega_i = \sqrt{K_i/m}$ - is a partial frequency. Expanding (15) one can obtain

(17)

$$E_0 = N^2 \cdot \sum \hbar \omega_i = \vec{J} \cdot \vec{\omega}, \quad i = 1, 2, 3, \quad (16)$$

where $|\vec{J}| = \hbar \cdot N^2$ could be treated as total action. So for one degree of freedom using (3) one can obtain

one degree of freedom using (3) one can obtain $p_{\varepsilon} \cdot \Delta x \cong m_{\varepsilon} N_{v} \sqrt{\varepsilon_{\varepsilon} / \beta_{\varepsilon}} \cdot \sqrt{\varepsilon_{\varepsilon} \beta_{\varepsilon}} \cong m_{\varepsilon} (\gamma \varepsilon) N.$

(17) one can find the minimal emittance as

This could be called the total action for selected degree of freedom. Equaling (16) to the value of action from

$$(\gamma \varepsilon_{\star}) \cong \hbar N^2 / mc \cdot N = \lambda_c N. \tag{18}$$

For a typical bunch population $N \approx 10^{10}$ (18) will be $(\gamma \epsilon_x) \cong 3.8 \cdot 10^{11}.10^0 = 0.38$ cm only. So we are coming to fundamental conclusion that one-dimensional system is always degenerated under real conditions. That means that there is no dynamic aperture for the particles in 1D. In that sense the claim that so called Mobius ring [6] brings particle motion into 1D and, hence, has some advantages, needs to be treated with cautions.

4 COOLERS AND BEAMS

One type of a cooler able to reach extreme emittances considered in [7]. Basically it contains the dipole wigglers and accelerating cavities installed in series so the average energy of the beam kept constant. It gives the emittances obtained after considerations the radiation dynamics for a single electron as

$$(\gamma \varepsilon_x) \cong (\frac{1}{2}) \cdot \lambda_C \overline{\beta}_x (1 + K_x^2 / 2) K_x / \lambda \qquad (19)$$

$$(\gamma \varepsilon_y) \cong (\frac{1}{2}) \cdot \lambda_C \overline{\beta}_y K_x / \lambda,$$
 (20)

where $\overline{\beta}_{x,y}$ -are averaged envelope functions in the wiggler. $K = eH_{\perp}\lambda/2\pi mc^2$, H_{\perp} -is the magnetic field in the wiggler, λ -is the wiggler period. The last formulas together with the cooling time

$$\tau_{cool} \cong (\frac{3}{2}) \cdot (\lambda^2 / cK^2 \gamma), \tag{21}$$

defines the cooling dynamics under SR. One can see that equilibrium invariant emittances do not depend on energy. In addition, quantum equilibrium vertical emittance and the cooling time do not depend on the wiggler period. For successful operation of Laser Linear Collider the only $N \approx 10^6$ particles required [6]. If the $\overline{\beta}_{v}K_{x}/\lambda \approx 1$, then, formally, the emittance could be close to $(\gamma \mathcal{E}_{y}) \approx (\frac{1}{2}) \hat{\lambda}_{C}$. The last means that quantum limitations for the lowest emittance are important here. So one can treat this as emittance occupied by a phase trajectory of a single electron. For radiation in dipole wiggler the electron in a ground state remains radiating the photons. So to damp the transverse emittance any electron must re-radiate its full energy. This brings some final equilibrium emittance like (19), (20). Until this emittance is big compared with (4) there is no

confusion.

In [3] there was considered the radiation effects in a focusing channel. The last might be a sequence of focusing and defocusing lenses (what is basically a quadrupole wiggler). Here the electron in a ground state is not radiating. So there is no formal requirements for re-radiation of particle's full energy. However in this publication was clamed that the energy of the ground state is $E_0 = \hbar \omega (\frac{1}{2} + n)$, n=0 and the minimal emittance for the beam here could be as low as $(\gamma \varepsilon_{\nu}) \approx (\frac{1}{2}) \lambda_{C}$. One can see that the factor associated with the number of the particles is missed here. One can see also that there are no advantages between dipole and quadrupole wiggler from the point of minimal emittance. We can add, that the quantum limitation occurs much earlier. In contrast, the cooling time for a traditional dipole wiggler is much smaller, than for quadrupole one.

In [8] there was considered the radiation of a relativistic electron in a solenoid. It was shown here that radiation here carries out the transverse energy only. In that sense the particle in a ground state is not radiated also. This means that electron can decrease its' emittance without re-radiation of its' full energy.

There was made a comparison of the lowest emittances in the RF photo-injectors and (5) in [9]. In some cases the quantum limitation (5) is close.

- [1] A. Mikhailichenko, On the physical limitation to the lowest emittance (toward colliding electron-positron crystalline beams), 7th Advanced Accelerator Concepts Workshop, 12-18 October 1996, Lake Tahoe, CA, AIP Conference Proceedings 398, p.294. CLNS 96/1437, Cornell, 1996.
- [2] K-J. Kim, Emittance in Particle and Radiation Beam Techniques, ibid., p.243.
- [3] Z. Huang, P. Chen, R.Ruth, Radiation Reaction in a Continuous Focusing Channel, Phys. Rev. Lett., Vol. 74, 10(1995).
- [4] L.D. Landau, E.M. Lifshitz, *Statistical Physics*, Pergamon Press, 1985.
- [5] Ya. S. Derbenev, Collision relaxation of the heavy particles in a damping ring, All-Union Conference, Dubna, 1979, vol.1, p.119-121.
- [6] R. Talman, Phys. Rev. Lett., 74, 1590(1995).
- [7] A. Mikhailichenko, *Injector for a Laser Linear Collider*, CLNS 98/1568, a Talk on 8th Advanced Accelerator Concepts Workshop, Baltimore, Maryland, July 5-11, 1998.
- [8] V.L. Ginzburg, *Theoretical Physics and Astrophysics*, Science, Moscow, 1975.
- [9] L. Serafini, A.D. Yeremian, Summary Report on Particle Beam Sources, Ref. [1], p. 203.

QUANTUM ASPECTS OF ACCELERATOR OPTICS

Sameen A. Khan*, Dipartimento di Fisica Galileo Galilei, Università di Padova, Istituto Nazionale di Fisica Nucleare (INFN), Sezione di Padova Via Marzolo 8, Padova 35131, ITALY

Abstract

Present understanding of accelerator optics is based mainly on classical mechanics and electrodynamics. In recent years quantum theory of charged-particle beam optics has been under development. In this paper the newly developed formalism is outlined.

Charged-particle beam optics, or the theory of transport of charged-particle beams through electromagnetic systems, is traditionally dealt with using classical mechanics. This is the case in ion optics, electron microscopy, accelerator physics etc [1]-[4]. The classical treatment of chargedparticle beam optics has been extremely successful, in the designing and working of numerous optical devices from electron microscopes to very large particle accelerators, including polarized beam accelerators. It is natural to look for a prescription based on the quantum theory, since any physical system is quantum at the fundamental level! Such a prescription is sure to explain the grand success of the classical theories and may also help towards a deeper understanding and designing of certain charged-particle beam devices. To date the curiosity to justify the success of the classical theories as a limit of a quantum theory has been the main motivation to look for a quantum prescription. But, with ever increasing demand for higher luminosities and the need for polarized beam accelerators in basic physics, we strongly believe that the quantum theories, which up till now were an isolated academic curiosity will have a significant role to play in designing and working of such devices.

It is historically very curious that the, quantum approaches to the charged-particle beam optics have been very modest and have a very brief history as pointed out in the third volume of the three-volume encyclopaedic text book of Hawkes and Kasper [5]. In the context of accelerator physics the grand success of the classical theories originates from the fact that the de Broglie wavelength of the (high energy) beam particle is very small compared to the typical apertures of the cavities in accelerators. This and related details have been pointed out in the recent article of Chen [6]. A detailed account of the quantum aspects of beam physics is to be found in the Proceedings of the recently held 15th Advanced ICFA Beam Dynamics Workshop [7].

A beginning of a quantum formalism starting *ab initio* with the Dirac equation was made only recently [8]-[9]. The formalism of Jagannathan *et al* was the first one to use the Dirac equation to derive the focusing theory of electron lenses, in particular for magnetic and electrostatic axially

symmetric and quadrupole lenses respectively. This formalism further outlined the recipe to obtain a quantum theory of aberrations. Details of these and some of the related developments in the quantum theory of charged-particle beam optics can be found in the references [8]-[17]. I shall briefly state the central theme of the quantum formalism.

The starting point to obtain a quantum prescription is to build a theory based on the basic equations of quantum mechanics appropriate to the situation under study. For situations when either there is no spin or spinor effects are believed to be small and ignorable we start with the scalar Klein-Gordon and Schrödinger equations for relativistic and nonrelativistic cases respectively. For electrons, protons and other spin- $\frac{1}{2}$ particles it is natural to start with the Dirac equation, the equation for spin- $\frac{1}{2}$ particles. In practice we do not have to care about the other (higher spin) equations.

In many situations the electromagnetic fields are static or can reasonably assumed to be static. In many such devices one can further ignore the times of flights which are negligible or of not direct interest as the emphasis is more on the profiles of the trajectories. The idea is to analyze the evolution of the beam parameters of the various individual charged-particle beam optical elements (quadrupoles, bending magnets, \cdots) along the optic axis of the system. This in the language of the quantum formalism would require to know the evolution of the wavefunction of the beam particles as a function of 's', the coordinate along the optic axis. Irrespective of the starting basic time-dependent equation (Schrödinger, Klein-Gordon, Dirac, \cdots) the first step is to obtain an equation of the form

$$i\hbar \frac{\partial}{\partial s} \psi(x, y; s) = \hat{\mathcal{H}}(x, y; s) \psi(x, y; s) , \qquad (1)$$

where (x,y;s) constitute a curvilinear coordinate system, adapted to the geometry of the system. For systems with straight optic axis, as it is customary we shall choose the optic axis to lie along the Z-axis and consequently we have s=z and (x,y;z) constitutes a rectilinear coordinate system. Eq. (1) is the basic equation in the quantum formalism and we call it as the beam-optical equation; \mathcal{H} and ψ as the beam-optical Hamiltonian and the beam wavefunction respectively. The second step requires to obtain a relationship for any relevant observable $\{\langle O \rangle(s)\}$ at the transverse plane at s to the observable $\{\langle O \rangle(s_{\rm in})\}$ at the transverse plane at $s_{\rm in}$, where $s_{\rm in}$ is some input reference point. This is achieved by the integration of the beam-optical equation in (1)

$$\psi(x, y; s) = \hat{U}(s, s_{\rm in}) \psi(x, y; s_{\rm in}), \qquad (2)$$

which gives the required transfer maps

$$\begin{split} \left\langle O\right\rangle \left(s_{\mathrm{in}}\right) & \to \left\langle O\right\rangle \left(s\right) \\ & = \left\langle \psi \left(x,y;s\right) \left|O\right| \psi \left(x,y;s\right)\right\rangle \,, \\ & = \left\langle \psi \left(x,y;s_{\mathrm{in}}\right) \left|\hat{U}^{\dagger}O\hat{U}\right| \psi \left(x,y;s_{\mathrm{in}}\right)\right\rangle (3) \end{split}$$

The two-step algorithm stated above may give an oversimplified picture of the quantum formalism than, it actually is. There are several crucial points to be noted. The first-step in the algorithm of obtaining the beam-optical equation is not to be treated as a mere transformation which eliminates t in preference to a variable s along the optic axis. A clever set of transforms are required which not only eliminate the variable t in preference to s but also gives us the s-dependent equation which has a close physical and mathematical analogy with the original t-dependent equation of standard time-dependent quantum mechanics. The imposition of this stringent requirement on the construction of the beam-optical equation ensures the execution of the second-step of the algorithm. The beam-optical equation is such, that all the required rich machinery of quantum mechanics becomes applicable to compute the transfer maps characterizing the optical system. This describes the essential scheme of obtaining the quantum formalism. Rest is mostly a mathematical detail which is built in the powerful algebraic machinery of the algorithm, accompanied with some reasonable assumptions and approximations dictated by the physical considerations. For instance, a straight optic axis is a reasonable assumption and paraxial approximation constitute a justifiable approximation to describe the ideal behaviour.

Before explicitly looking at the execution of the algorithm leading to the quantum formalism in the spinor case, we further make note of certain other features. Step-one of the algorithm is achieved by a set of clever transformations and an exact expression for the beam-optical Hamiltonian is obtained in the case of Schrödinger, Klein-Gordon and Dirac equations respectively, without resorting to any approximations! We expect this to be true even in the case of higher-spin equations. The approximations are made only at step-two of the algorithm, while integrating the beamoptical equation and computing the transfer maps for averages of the beam parameters. Existence of approximations in the description of nonlinear behaviour is not uncommon and should come as no surprise, afterall the beam optics constitutes a nonlinear system. The nature of these approximations can be best summarized in the optical terminology as; a systematic procedure of expanding the beam optical Hamiltonian in a power series of $|\hat{\pi}_{\perp}/p_0|$ where p_0 is the design (or average) momentum of beam particles moving predominantly along the direction of the optic axis and $\hat{\pi}_{\perp}$ is the small transverse kinetic momentum. The leading order approximation along with $|\hat{\pi}_{\perp}/p_0| \ll 1$ constitutes the paraxial or ideal behaviour and higher order terms in the expansion give rise to the nonlinear or aberrating behaviour. It is seen that the paraxial and aberrating behaviour get modified by the quantum contributions which are in powers of the de Broglie wavelength ($\lambda_0 = 2\pi\hbar/p_0$). Lastly, and importantly the question of the classical limit of the quantum formalism; it reproduces the well known Lie algebraic formalism of charged-particle beam optics pioneered by Dragt *et al* [18].

We start with the Dirac equation in the presence of static electromagnetic field with potentials $(\phi(r), A(r))$

$$\hat{\mathbf{H}}_D |\psi_D\rangle = E |\psi_D\rangle , \qquad (4)$$

where $|\psi_D\rangle$ is the time-independent 4-component Dirac spinor, E is the energy of the beam particle and the Hamiltonian \hat{H}_D , including the Pauli term in the usual notation is

$$\hat{\mathbf{H}}_D = \beta m_0 c^2 + c \boldsymbol{\alpha} \cdot \hat{\boldsymbol{p}} - \mu_a \beta \boldsymbol{\Sigma} \cdot \boldsymbol{B}, \qquad (5)$$

where $\hat{\boldsymbol{\pi}} = \hat{\boldsymbol{p}} - q\boldsymbol{A} = -i\hbar\boldsymbol{\nabla} - q\boldsymbol{A}$. After a series of transformations (see [14] for details) we obtain the accelerator optical Hamiltonian to the leading order approximation

$$\begin{split} \mathrm{i}\hbar\frac{\partial}{\partial z}\left|\psi^{(A)}\right\rangle &=& \hat{H}^{(A)}\left|\psi^{(A)}\right\rangle\,,\\ \hat{H}^{(A)} &\approx& \left(-p_0-qA_z+\frac{1}{2p_0}\hat{\pi}_\perp^2\right)\\ &+\frac{\gamma m_0}{p_0}\underline{\Omega}_s\cdot\boldsymbol{S}\,,\\ \mathrm{with}~\underline{\Omega}_s &=& -\frac{1}{\gamma m_0}\left\{q\boldsymbol{B}+\epsilon\left(\boldsymbol{B}_\parallel+\gamma\boldsymbol{B}_\perp\right)\right\}\,(6) \end{split}$$

where $\hat{\pi}_{\perp}^2 = \hat{\pi}_x^2 + \hat{\pi}_y^2$, $\epsilon = 2m_0\mu_a/\hbar$, $\gamma = E/m_0c^2$, and $S = \frac{1}{2}\hbar\sigma$. We can recognize $\hat{H}^{(A)}$ as the *quantum mechanical*, accelerator optical, version of the well known semiclassical Derbenev-Kondratenko Hamiltonian [19] in the leading order approximation. We can obtain corrections to this by going an order beyond the first order calculation.

It is straightforwrd to compute the transfer maps for a specific geometry and the detailed discussion with the quantum corrections can be found in [14]. In the classical limit we recover the Lie algebraic formalism [18].

One practical application of the quantum formalism would be to get a deeper understanding of the polarized beams. A proposal to produce polarized beams using the proposed spin-splitter devices based on the classical Stern-Gerlach kicks has been presented recently [20].

Lastly it is speculated that the quantum theory of charged-particle beam optics will be able to resolve the choice of the position operator in the Dirac theory and the related question of the form of the force experienced by a charged-particle in external electromagnetic fields [19], [21]. This will be possible provided one can do an extremely high precision experiment to detect the small differences arising in the transfer maps from the different choices of the position operators. These differences shall be very small, i.e., proportional to powers of the de Broglie wavelength. It is the extremely small magnitude of these minute differences which makes the exercise so challenging and speculative!

- [1] P.W. Hawkes and E. Kasper, *Principles of Electron Optics*, Vols. I and II (Academic Press, London, 1989).
- [2] M. Conte and W.W. MacKay, An Introduction to the Physics of Particle Accelerators (World Scientific, Singapore, 1991).
- [3] H. Mais, "Some topics in beam dynamics of storage rings", DESY 96-119 (1996).
- [4] H. Wiedemann, Particle Accelerator Physics: Basic Principles and Linear Beam Dynamics (Springer-Verlag, Berlin, Heidelberg, 1993)
 H. Wiedemann, Particle Accelerator Physics II: Nonlinear and Higher-Order Beam Dynamics (Springer-Verlag, Berlin, Heidelberg, 1995)
- [5] P.W. Hawkes and E. Kasper, Principles of Electron Optics Vol.3: Wave Optics (Academic Press, London and San Diego, 1994).
- [6] P. Chen, ICFA Beam Dynamics Newsletter 12, 46 (1996);
- [7] Proceedings of the 15th Advanced ICFA Beam Dynamics Workshop on Quantum Aspects of beam Physics, Ed. P. Chen, (World Scientific, Singapore, 1999).
- [8] R. Jagannathan, R. Simon, E. C. G. Sudarshan and N. Mukunda, *Phys. Lett. A* 134, 457 (1989); R. Jagannathan, in *Dirac and Feynman: Pioneers in Quantum Mechanics, Ed.* R. Dutt and A. K. Ray (Wiley Eastern, New Delhi, 1993).
- [9] R. Jagannathan, Phys. Rev. A 42, 6674 (1990).
- [10] S.A. Khan and R. Jagannathan, "Theory of relativistic electron beam transport based on the Dirac equation", Proc. of the 3rd National Seminar on Physics and Technology of Particle Accelerators and their Applications, (Nov. 1993, Calcutta, India) Ed. S. N. Chintalapudi (IUC-DAEF, Calcutta) 102; S.A. Khan and R. Jagannathan, "Quantum mechanics of charged-particle beam optics: An operator approach", Presented at the JSPS-KEK International Spring School on High Energy Ion Beams-Novel Beam Techniques and their Applications, March 1994, Japan, Preprint: IMSc/94/11 (The Institute of Mathematical Sciences, Madras, March 1994).
- [11] S.A. Khan and R. Jagannathan, Phys. Rev. E 51, 2510 (1995).
- [12] R. Jagannathan and S.A. Khan, Advances in Imaging and Electron Physics, 97, Ed. P. W. Hawkes (Academic Press, San Diego) 257 (1996).
- [13] S.A. Khan, Quantum Theory of Charged-Particle Beam Optics, Ph.D. Thesis (University of Madras) (1997).
- [14] M. Conte, R. Jagannathan, S.A. Khan and M. Pusterla, *Part. Accel.* 56, 99 (1996).
- [15] R. Jagannathan and S.A. Khan ICFA Beam Dynamics Newsletter 13, 21 (1997).
- [16] R. Jagannathan, "The Dirac equation approach to spin-¹/₂ particle beam optics", in: Proceedings of the 15th Advanced ICFA Beam Dynamics Workshop on Quantum Aspects of beam Physics, Ed. P. Chen, (World Scientific, Singapore, 1999).
- [17] S. A. Khan, Quantum theory of magnetic quadrupole lenses for spin-¹/₂ particles, in: Proceedings of the 15th Advanced ICFA Beam Dynamics Workshop on Quantum Aspects of beam Physics, Ed. P. Chen, (World Scientific, Singapore, 1999).

- [18] A.J. Dragt and E. Forest, Adv. Electronics and Electron Phys. 67, 65 (1986); A.J. Dragt, F. Neri, G. Rangarajan, D.R. Douglas, L.M. Healy and R.D. Ryne, Ann. Rev. Nucl. Part. Sci. 38, 455 (1988); G. Rangarajan, A.J. Dragt and F. Neri, Part. Accel. 28, 119 (1990); R.D. Ryne and A.J. Dragt, Part. Accel. 35, 129 (1991); É. Forest and K. Hirata, A Contemporary Guide to Beam Dynamics KEK Report 92-12; É. Forest, M. Berz and J. Irwin, Part. Accel. 24, 91 (1989); K. Yokoya, "Calculation of the equilibrium polarization of stored electron beams using Lie algebra", Preprint KEK 86-90 (1986); Yu.I. Eidelman and V.Ye. Yakimenko, Part. Accel. 45, 17 (1994); and references therein.
- [19] "On Stern-Gerlach forces allowed by special relativity and the special case of the classical spinning particle of Derbenev-Kondratenko", e-print: physics/9611001; D. P. Barber, K. Heinemann and G. Ripken, Z. Phys. C 64 (1994) 117; D. P. Barber, K. Heinemann and G. Ripken, Z. Phys. C 64 (1994) 143.
- [20] M. Conte, A. Penzo and M. Pusterla, Il Nuovo Cimento A 108, 127 (1995); Y. Onel, A. Penzo and R. Rossmanith, AIP Conf. Proc. 150 Ed. R. G. Lernerand and D. F. Geesaman, (AIP, New York, 1986) 1229; M. Conte, and M. Pusterla, Il Nuovo Cimento A, 103, 1087 (1990); M. Conte, Y. Onel, A. Penzo, A. Pisent, M. Pusterla and R. Rossmanith, The spin-splitter concept, Internal Report: INFN/TC-93/04; M. Pusterla, "Polarized beams and Stern-Gerlach forces in classical and quantum mechanics", in: Proceedings of the 15th Advanced ICFA Beam Dynamics Workshop on Quantum Aspects of beam Physics, Ed. P. Chen, (World Scientific, Singapore, 1999),
- [21] A. O. Barut and R. Raczka, Theory of Group Representations and Applications (World Scientific, 1986); J. Anandan, Nature 387, 558 (1997); M. Chaichian. R. G. Felipe and D. L. Martinez, Phys. Lett. A 236, 188 (1997); J. P. Costella and B. H. J. McKellar, Int. J. Mod. Phys. A 9, 461 (1994); and references therein.

ON LANDAU SCENARIO OF CHAOTIZATION FOR BEAM DISTRIBUTION *

Z. Parsa,[†] Brookhaven National Laboratory, 901A, Upton, NY 11973, USA V.Zadorozhny[‡], Institute of Cybernetic National Academy of Sciences of Ukraine.

Abstract

We examine a problem in nonlinear dynamics in which both regular and chaotic motions are possible. Thus we deal with some of the fundamental theoretical problem of accelerator physics, mathematics theory of dynamical systems, and other fields of physics. The focus is on the appearance of chaos in a beam distribution. A study of the problem is based on two observation: First, Using Lyapunov method and its extension we obtain solutions of partial differential equations [1, 2]. Using this approach we discuss the problem of finding a solution of Vlasov-Poisson equation, i.e., some stationary solution where we consider magnetic field as some disturbance with a small parameter. Thus the solution of Vlasov equation yields an asymptotic series such that the solution of Vlasov-Poisson equation is the basis solution for one. The second observation is that physical chaos is weakly limit of, well known, the Landau bifurcation's. This fact we have proved using ideas on the Nature of Turbulence [3].

1 INTRODUCTION

The aim of this paper is to find the solution for Vlasov-Poisson (VP) equation in the attraction region of an integral manifold. As known VP is system which can be written as follows

$$\partial_t f + v \partial_x f + E(tx) \partial_v f = 0 \tag{1}$$

$$\Delta U(tx) = 4\pi\gamma\rho(tx) \tag{2}$$

Where

$$E(tx): = \partial_x U(tx); \tag{3}$$

$$\rho(tx):=\int f(txy)dv. \tag{4}$$

Here we have $\gamma=+$, 1f=f(txy) is the distribution of the particles in phase space depending upon the time $t\geq 0$, the position $x\in R^n$ and the velocity, U=U(tx) is the Newtonian potential. The quantity n indicates the space dimension. If not stated otherwise, we assume n=3. With the opposite sign of γ , i.e. for $\gamma=-1$, the VP system is used as a first

model to describe the evolution of equally charged particles (with repulsive forces) in plasma physics.

As well known, this system is considered to be an approximation to the more involved Vlasov-Maxwell system [1]. Below we shall reduce the quasi linear equation (1,2) to a linear partial differential equation of first order.

2 LANDAU BIFURCATION AND WEAKLY- CONVERGENCE

Using the arguments in [4], we get

$$f(txy) = f_0(xy)e^{-i\omega t}.$$
 (5)

Thus, the function $f_0(xy)$ satisfies equation

$$\partial_x f_0 + \partial_v f_0 E = i\omega f_0 \tag{6}$$

Let

$$\rho_0 = \int f_0(xy) dv \tag{7}$$

then the coefficients of the equation be independent of the time t. A general solution f(txx) may be introduced by a sum of the particular solutions such that the function f depends on the time by the multiplier of the type $e^{-i\omega t}$. Here the frequency ω can't be arbitrary. They be defined completely from the equation (6). The equation (6) is quasi linear equation. Using the well known approach, we reduce it to a linear equation by the way of introducing some function:

$$w = -f_0 + f_0(xy) = 0, (8)$$

then

$$Lw \equiv \partial w_x v + \partial w_v E = \partial w_{f_0}(i\omega f_0) \tag{9}$$

The equation (9) is a linear equation.

In the following, we transform (9) into a Fredholm's equation

$$w = Rf_0. (10)$$

Where R is some kernel operator, i.e.

$$\sum |\lambda_i| < \infty, \lambda_i \in \sigma(R), \tag{11}$$

^{*} Supported by U.S. Department of Energy contract number DE-AC02-98CH10886.

[†] E-mail: parsa@bnl.gov

[‡] E-mail: zvf@umex.istrada.net.ua

here $\sigma(R)$ is spectrum of R (see [1],[4]). Now, by differentiating equation (10) with respect to the given VP system, we obtain

$$f_0 = \mu \tilde{R} f_0 \tag{12}$$

where $\tilde{R}=LR$, and $\mu=-i\omega^{-1}$. Suppose there exists a small bounded set of data (x,v) such that \tilde{R}_0 is a small operator:

$$|\mu| < mes |\Omega_N| ||\tilde{R_1}||^{-1}$$
. (13)

We assume that the measure of the domain Ω_N increases with increasing number N, and $\omega \to 0$. This case yields to some bifurcation sequence. One may be the divergent series or the convergent series. The term "the convergent" may have the various sense.

Theorem: Under the assumption $|f_{0N}| \le 1$ for all N, there is an invariant measure τ_0 such that $\lim_{N\to\infty} d\tau_N \equiv f_{0N} dx = d\tau^0$. This measure be a stochastic measure on the manifold $f_0(x,v)=1$. Thus we have an ergodic motion on this manifold. As opposed to first case, we have a wave motion.

Consequently the Landau chaotisation take place for series bifurcation is not always true.

- [1] Zubov V.I., Integral Equations for the Lyapunov Function. Soviet Math. Dokl. Vol. 42(1991), N 2, p. 535-537.
- [2] Parsa Z., Zadorozhny V.F., On the beam dynamics which has been described by Vlasov Equation. Proceedings of the fifth international workshop: Beam dynamics & optimization. St. Petersburg, Russia,1998.
- [3] Rueller D., Takens F., On the Nature of Turbulence, common. Math. Phys., 20,167-192, Springer- Verlag, 1971.
- [4] Parsa Z., Zadorozhny V.F., On the solution of Vlasov-Poisson equation in some neighborhood of a singular point (to appear).

SCATTERING MATRIX ANALYSIS OF THE NLC ACCELERATING STRUCTURE*

V. Dolgashev, INP, Novosibirsk, Russia K. L. F. Bane, Z. Li, K. Ko, SLAC, Stanford, CA

1 INTRODUCTION

In the Next Linear Collider (NLC)[1], long trains of short, intense bunches are accelerated through the linac on their way to the collision point. One serious problem that needs to be addressed is the multi-bunch, beam break-up instability in the linac. To counteract this instability the accelerating structures are designed so that the dipole mode wakefields are detuned and weakly damped. Detuning is accomplished by gradually varying the dimensions of the 206 cavity cells in each structure, and weak damping by surrounding the structure with four manifolds, which allow the dipole modes to weakly couple out of the cells. In order to design and predict the performance of such a structure in the NLC, it is necessary to be able to calculate accurately the strength of its long-range wakefields.

NLC detuned structures were designed first using an equivalent circuit approach, for example, the double band model of Ref. [2]. With the introduction of weak damping, a more elaborate equivalent circuit approach was required[3]. Other methods that have been used for detuned structures are the open-mode, field expansion method[4], and a finite element calculation employing 206 parallel processors[5]. A scattering matrix method can also be applied to cavities that consist of a series of waveguide sections[6], such as the NLC structure, and such a method has also been applied to the problem of detuned accelerating structures[7],[8]. Among its natural strengths when applied to structure problems are the ability to model the effects of complicated 3 dimensional couplers and to investigate the behavior of higher passband modes. In this report we will employ a computer program that uses such an approach [9], to demonstrate that the scattering matrix method can yield accurate results concerning the wakefields of damped, detuned accelerating structures.

We begin by calculating the dipole mode impedance and wakefield of a slightly simplified version of a detuned (DT) structure, results which we compare with those of the double band circuit model. An important related problem is the wakefield effect caused by internal structure misalignments, a problem which has the special difficulty of no longer being cylindrically symmetric; and we next study the transverse kicks to the beam caused by misaligning just one cell in a DT structure, and compare results with those of a perturbation calculation based on the circuit model. Finally, a future goal is to be able to use the scattering matrix formalism to model the more complicated NLC damped, detuned structure (DDS), and we present some preliminary results toward this goal.

2 CIRCUIT MODEL COMPARISON

In this report we consider cylindrically symmetric, disk-loaded accelerating structures at X-band (with fundamental frequency $f_0=11.424$ GHz), but with the simplification that the irises are rectangular, and not rounded. Let us consider an earlier version of the NLC structure, a DT structure. It consists of 206 cells, with Gaussian detuning of the dipole modes, with a central synchronous frequency $\bar{f}_s=15.07$ GHz, an rms $(f_s)_{rms}=0.025\bar{f}_s$, and a total width $\Delta f_s=0.1\bar{f}_s$. The structure period p=8.75 mm, iris thickness p-g=1.46 mm, cavity radius $b\approx 11$ mm, and iris radius a varying from 5.9 mm at the beginning of the structure to 4.1 mm at the end.

DT structures have been modelled using a double band circuit model computer program[2]. If M is the number of cells in a structure, this program generates 2M coupled mode frequencies f_m and kick factors k_m . The transverse wakefield is then given by

$$W_{\perp}(s) = 2\sum_{m=1}^{2M} k_m \sin(2\pi f_m s/c) e^{-\pi f_m s/Qc} \quad , \quad (1)$$

with s the distance between driving and test particles, c the speed of light, and Q the quality factor due to the wall resistivity.

For the scattering matrix calculations we follow the approach of Ref. [6], implemented in the program described in Ref. [9]. A structure with M cells is modeled by a set of 2M joined waveguide sections of radii a_m or b_m , filled with a number of dipole TE and TM waveguide modes. For each section the S-matrix is obtained, and the S-matrix for the composite chain is constructed by cascading the individual S-matrices. From this the longitudinal dipole impedance for a beam offset at r = 4 mm is calculated, from which, using the Panofsky-Wenzel theorem, the transverse impedance Z_{\perp} is obtained. The real part of the impedance R_{\perp} consists of a series of infinitesimally narrow spikes, and to reduce the calculation time for our problem the peaks have been artifically widened by introducing an imaginary 1.5 MHz frequency shift, corresponding to a Q of 5000 (the width of the peaks is still narrow compared to the minimum mode spacing ~ 7 MHz, however). The number of modes used in the cavity region is 15 TE and 15 TM modes, and in the iris region 8 TE and 8 TM modes.

To compare with the circuit model results, the impedance can be fit, for resonant frequencies and kick factors, to a sum of Lorentzian distributions. Or, the area under $R_{\perp}(f)$, averaged over frequency bins—the average impedance \bar{R}_{\perp} —can be compared to $\frac{1}{2}k\,dn/df$ of the circuit model. Results for all first and second band modes, comparing the kick factors, the density of modes, and \bar{R}_{\perp}

^{*}Work supported by Department of Energy contract DE-AC03-76SF00515.

for the two methods are shown in Fig. 1 (to facilitate comparison, discrete results are connected by straight lines). The agreement is very good. There is disagreement in the k of the (much weaker) second band modes, but for these modes it is not expected that the double—band circuit model be accurate. With the S-matrix approach, to obtain the wakefields, the fitted mode frequencies and kick factors are summed according to Eq. 1. Finally, the envelope of the dipole wake (with Q set to 6500, appropriate for copper wall losses) up to s=80 m (the NLC bunch train length) for the two methods is shown in Fig. 2.

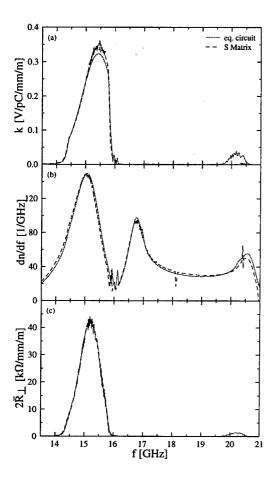


Figure 1: Comparison with the circuit model.

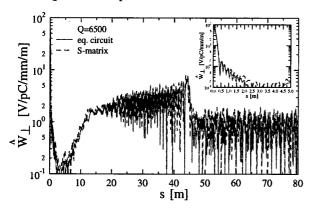


Figure 2: Wakefield envelope comparison.

3 INTERNAL MISALIGNMENTS

If there are internal misalignments in the accelerating structure, due to e.g. fabrication errors, then even if the beam is aligned to the nominal structure axis there will be residual transverse wakefield kicks, both at frequencies near the fundamental mode (11 GHz) and the 1st band dipole modes (15 GHz). In the NLC these kicks can, independent of orbit, increase the beam projected emittance, and destroy the resolution of the structure as a beam position monitor.

Internal misalignments break cylindrical symmetry in geometry, and we study this problem with a 3-dimensional version of the S-matrix program. In the NLC what is normally used to estimate the effects of internal structure misalignments (due to the dipole modes) is a perturbative approach based on the circuit model solution[10]. The method assumes that, for small misalignments, the mode frequencies and eigenfunctions do not change significantly, and the kick factors associated with them can be obtained through an integration of fields along a path described by the misalignments. The result is linear in cell offset, and the effect of a misaligned structure can be decomposed into many single-cell misalignments.

Let us study the effect of modes near 15 GHz on a beam on-axis in a structure with a single cell misaligned. We consider a 21-cell section of the DT structure described above (cells 175-195, with a varying from 4.527-4.343 mm). The structure has been shortened to save computing time, and this particular section was chosen since it contains many trapped dipole modes that do not reach, and therefore are not affected by, the boundary cells. For the simulations, 45 waveguide modes are used in the cavity region (15 each of TM and TE dipole, and TM monopole) and 15 modes in the iris region (5 modes of each type). To avoid fundamental mode standing waves, matching cells were added at the ends (with $a_{in}=6.39$ mm, $b_{in}=11.112$ mm, $a_{out}=5.65$ mm, and $b_{out}=10.815$ mm), and the resulting SWR at 11.4 GHz is below 1.02.

When one cell (of cells 187–192) is misaligned, the Smatrix program finds that only very few modes are excited significantly, and that nearly the total effect is due to just one or two modes. To obtain kick factors the impedance was fitted to a set of Lorentzians, as before. The results for six cases, showing the kick of the one or two dominant modes, are given in Fig 3. Note that here k has been normalized to 1 mm offset of the shifted cell; k has also been scaled to the full 206 cell structure (by multiplying the 21-cell result by 21/206). Also shown in Fig. 3, for comparison, is the results of the perturbation calculation based on the double-band circuit model, but with frequencies all shifted down by 44 MHz. The agreement is remarkably good. It validates the perturbation theory, showing that there is no missing contribution due to having broken cylindrical symmetry. Finally, note that the sum of kick factors due to one misaligned cell is almost the same for all cases, $\sim 0.3 \text{ V/pC/mm/m}$, and that this value is about the same as is found in the peak of the distribution for k of Fig. 1a.

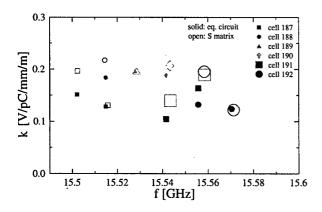


Figure 3: Largest kick factors for dipole modes near 15 GHz, in a DT structure with one cell misaligned. 3.1 Transverse Kick at 11 GHz

When the monopole field interacts with a shifted cell it excites a dipole field that causes a transverse kick independent of the position of a witness bunch. This is true whether the field is external or excited by the beam. The dipole field does not propagate far from the shifted cell because the fundamental frequency is far below the first dipole passband. In Fig. 4 we plot the ratio of transverse to longitudinal voltage V_{\perp}/V_L excited by the beam at the fundamental mode frequency. The integral over the real part is in each case zero. Then the transverse impedance was calculated in the frequency range 11.4–11.5 GHz, and the results were inverse Fourier transformed to yield a wakefield (see Fig. 5). Note that these kicks are much weaker than those of the dipole modes near 15 GHz.

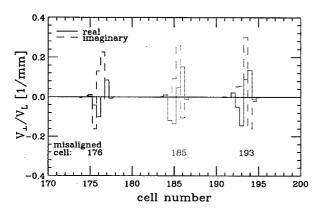


Figure 4: Real and imaginary parts of the ratio of transverse to longitudinal voltage, excited at 11.4 GHz by an on-axis beam, in a DT structure with one cell misaligned.

4 THE DDS STRUCTURE

The S-matrix calculation was performed for the geometry of cell 106 in DDS3, using periodic boundary conditions. DDS3 is a disk-loaded structure, surrounded by 4 manifolds, with rectangular cross-sections that are aligned radially outward, and that couple through a slot to the structure cells. The dimesions are: a=4.783 mm, b=10.757 mm, p-g=1.464 mm; the manifold cross-section

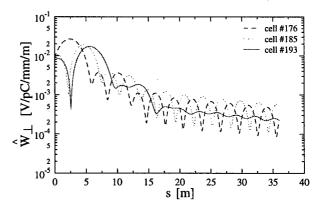


Figure 5: Wakefield envelope of transverse kicks at 11.4 GHz due to one misaligned cell.

is 5.0 mm×10.496mm, and the distance from manifold edge to structure axis is 11.921 mm. Modelled was 1/4 of the cell; in the cavity region 23 waveguide modes (including manifold modes) were used, in the iris region 28 waveguide modes. The waveguide modes were obtained using the 2-d finite element code SLANS[11]. Final results are compared in Fig. 6 with those obtained with MAFIA[12], and we see that agreement is good.

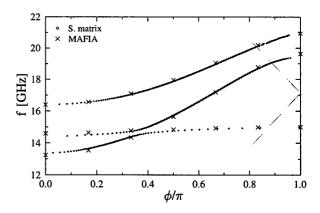


Figure 6: Dispersion curves for the geometry of cell 106 of DDS3, including 2 dipole and 1 manifold mode.

- [1] NLC ZDR Design Report, SLAC Report 474, 589 (1996).
- [2] K. Bane and R. Gluckstern, Part. Accel., 42, 123 (1994).
- [3] R. M. Jones, et al, Proc. of EPAC96, Sitges, Spain, 1996, p. 1292.
 [4] M. Yamamoto, et al, Proc. of LINAC94, Tsukuba, Japan, 1994,
- [5] X. Zhan and K. Ko, Proc. of 1996 Comp. Accel. Phys. Conf. (CAP96), Williamsburg, VA, 1996, p 389.
 [6] J.N. Nelson, et al, IEEE Trans. Microwave Theor. Tech., 37, No.8,
- [6] J.N. Nelson, et al, IEEE Trans. Microwave Theor. Tech., 37, No.8 1165 (1989).
- [7] U. van Rienen, Part. Accel., 41, 173 (1993).
- [8] S. Heifets and S. Kheifets, IEEE Trans. Microwave Theor. Tech., 42, 108 (1994).
- [9] V.A. Dolgashev, "Calculation of Impedance for Multiple Waveguide Junction," presented at ICAP'98, Monterrey, CA, Sept. 1998.
- [10] R.M. Jones, et al, "Emittance Dilution Due to Long Range Wakefields in the NLC." this conference. FRA39.
- [11] D. Myakishev and V. Yakovlev, Proc. of IEEE Part. Accel. Conf., San Francisco, 1991, p. 3002.
- [12] The CST/MAFIA Users Manual.

TUNING POSSIBILITIES OF THE LONGITUDINAL BEAM SHAPE OF A RACETRACK MICROTRON

W.H.C. Theuws, J.I.M. Botman, H.L. Hagedoorn, A.F.J. Hammen, Eindhoven University of Technology, Cyclotron Laboratory, P.O. Box 513, 5600 MB Eindhoven, The Netherlands.

Abstract

The beam shape in the longitudinal phase plane at the extraction point of an RTM strongly depends on the choice of the stable phase of the accelerating cavity. This is due to the fact that the main longitudinal focusing force is the derivative of the accelerating potential with respect to time (or phase). Furthermore, this focusing force is applied to the electron beam each turn, such that the output beam shape in the longitudinal phase plane is significantly affected. This effect can for instance be used in order to minimise the bunch length or the energy spread of the output beam of the RTM. For this paper we have used the lay-out of the Eindhoven RTM for the calculations of the stable-phase variations, which have been studied in linear approximation. The stable phase area for this RTM equals 18 degrees. It will be shown that stable-phase variations in the order of 1 degree already have a significant impact on the longitudinal beam shape. Furthermore, some remarks are made on the consequences of non-linear beam dynamics in relation to stable-phase variations.

1 BUNCH-LENGTH COMPRESSION

In contrast to linear accelerators the shape of an RTM's output beam in the longitudinal phase plane can be modified. This can be done by changing the amplitude and phase of the RTM cavity. The possibility to modify this beam shape makes it possible to either minimise the bunch length or the energy spread of the output beam [1].

The energy gain per turn, E_r , has been chosen 5 MeV for the Eindhoven racetrack microtron. As RF acceleration is being used this energy gain E_r is set as

$$E_{r} = \hat{E}\cos\left(\phi_{c}\right),\tag{1}$$

where \hat{E} is the amplitude and ϕ_s the stable phase of the cavity voltage. The slope of the RF voltage at the stable phase provides the longitudinal focusing force. For that reason it is obvious that the choice of the combination of \hat{E} and ϕ_s has an influence on the longitudinal beam shape of the RTM's output beam. As this focusing force is applied 13 times to the electron beam it can be expected that a slightly different choice of \hat{E} and ϕ_s may have a great impact.

First, this impact has been studied, utilising linear motion only, see section 2. Second, the validity of the linear theory in the RTM is discussed in section 3, where the linearity of the longitudinal phase plane is studied by means of a numerical simulation program of the Eindhoven RTM. All calculations, which are presented in this paper, start just before the first cavity traversal. The beam shape in the longitudinal phase plane just before the first cavity traversal has been estimated from measurements and simulations of the RTM injector [2]. This beam shape can be approximated by an ellipse with Twiss-parameters: $\alpha = 0$, $\beta = 0.185$ m, $\gamma = 5.41$ m⁻¹, and $\varepsilon = 2.10^{\circ}$ m. This ellipse is used as input for the first-order calculations in section 2 and also for some of the numerical calculations in section 3.

2 FIRST-ORDER CALCULATIONS

The effect of the stable phase of the cavity, ϕ_s , on the beam shape in the longitudinal phase plane has been studied in linear approximation. The transfer matrix, \mathbf{M}_n , describing the transport of the n^{th} orbit in the racetrack microtron starting just before the cavity is given by the product of first-order matrices:

$$\begin{aligned} \mathbf{M}_{n} &= \mathbf{D}_{_{\mathcal{V}_{n}(L-Lcav)}} \cdot \mathbf{F}_{\alpha_{1}} \cdot \mathbf{B}_{1,n} \cdot \mathbf{F}_{\alpha_{2}} \cdot \mathbf{B}_{2,n} \cdot \mathbf{F}_{\alpha_{3}} \cdot \mathbf{D}_{L+2L}\tau_{n} \cdot \\ & \mathbf{F}_{\alpha_{3}} \cdot \mathbf{B}_{2,n} \cdot \mathbf{F}_{\alpha_{2}} \cdot \mathbf{B}_{1,n} \cdot \mathbf{F}_{\alpha_{1}} \cdot \mathbf{D}_{_{\mathcal{W}_{n}(L-Lcav)}} \cdot \mathbf{C}_{\hat{\mathcal{E}}, \phi_{5}}. \end{aligned} \tag{2}$$

The transport that is described by all the matrices in this equation is pointed out in figure 1. The matrices **D**, **B**, **F**,

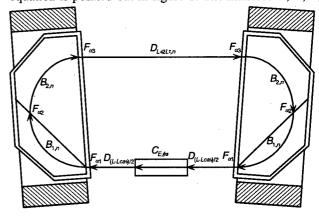


Figure 1: The transport described by the matrices for the linear approximation.

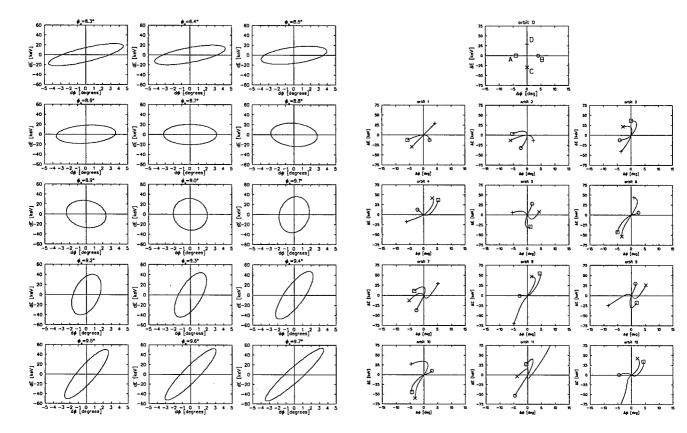


Figure 2: The beam shape in the longitudinal phase space at the extraction point of the RTM for different values of ϕ .

C in eq.(2) describe the effect of a drift space, a sector bending magnet, a non-normal entrance/exit of a magnet and an accelerating cavity, respectively. The subscripts 1 and 2 in $\mathbf{B}_{1,n}$ and $\mathbf{B}_{2,n}$ refer to the sectors 1 and 2 of the main bending magnets, respectively. The subscripts α_1 , α_2 and α_3 denote the entrance/exit angles for the edge focusing. The parameters \hat{E} and ϕ_3 are the amplitude and stable phase of the cavity potential. L_{cav} is the length of the cavity, L the distance between the bending magnets at the central axis of the cavity, and L_{τ} is the extra drift that results from the rotation of the main bending magnet over τ . The subscript n indicates that the concerning matrix is orbit dependent. The matrix that describes the transport of all twelve orbits, denoted by \mathbf{M} is given by the product of

The longitudinal sub-matrix of M together with the longitudinal input beam have been used to calculate the longitudinal output beam of the RTM for different values of ϕ_s . The results are shown in figure 2. From this figure it appears that variations in ϕ_s that are much smaller than the stable phase area of about 18 degrees have a large influence on the beam shape in the longitudinal phase space. This implies that it is possible to use ϕ_s to influence the longitudinal beam shape, such that this beam shape matches the acceptance of the following electron-optical

matrices M₁₂ through M₁.

Figure 3: Two straight lines in the longitudinal phase plane AB and CD are injected just before the first cavity traversal (orbit 0). The stable phase of the cavity has been set to 9 degrees. These lines are given after each full orbit.

system better that it might have done with the nominal settings for \hat{E} and ϕ_s .

3 VALIDITY OF THE LINEAR THEORY

In order to verify the validity of the linear theory, two straight line segments in the longitudinal phase plane, which are a little larger than the main axes of the nominal longitudinal input beam as it is delivered by the RTM injector, have been used as input for numerical tracking through the Eindhoven RTM, see figure 3. From this figure it can be seen that the longitudinal sizes of the linac beam are much larger than the linear regime. Therefore, the longitudinal input beam has also been calculated through the Eindhoven RTM by means of the numerical simulation program for different values of ϕ_{ij} see figure 4. Of course, the longitudinal beam shape still depends on ϕ , but making the bunch length shorter or the energy spread smaller by means of ϕ , is less effective. On the other hand, if the RTM will be used for the acceleration of short bunches [3], another pre-accelerator, which will already produce much shorter bunches, will become necessary. In that case the linear approximation may become valid and useful.

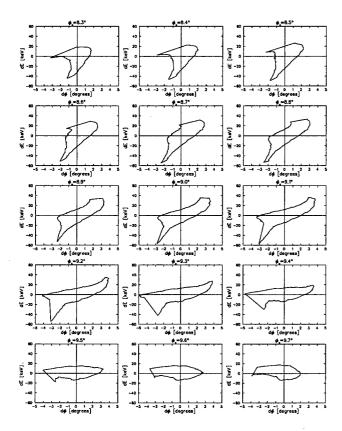


Figure 4: The longitudinal beam shape of the RTM output beam for different values of ϕ .

As an example a beam with the nominal longitudinal beam shape but with a much smaller longitudinal emittance of $\varepsilon=1\cdot10^{-7}\pi$ m has been tracked through the RTM numerically, with $\phi_s=9$ degrees. The longitudinal output beam is shown in figure 5. This longitudinal beam shape is similar to the beam shape shown in figure 2 for $\phi_s=8.3$ degrees. Now, say that it is tried to minimise the energy-spread of the beam. Then it can be seen form figure 2 that this is achieved for $\phi_s=8.7$ degrees, which is 0.4 degrees above the 8.3 degrees representing the situation we have in our experiment for 9.0 degrees. So, adding 0.4 degrees to the 9.0 degrees gives the output beam which is also shown in figure 5. In this figure the energy spread is minimised quite well.

4 CONCLUDING REMARKS

The RTM's output-beam shape in the longitudinal phase plane is very sensitive to small variations of the stable phase of the RTM's accelerating cavity. Therefore, the choice of this stable phase can be used to minimise either the bunch length or the energy spread of the output beam. The principle has been studied in linear approximation, but it has been shown that the linear approximation is only valid for longitudinal beam sizes that are much smaller than the longitudinal beam size that is delivered by the current injector. The non-linear behaviour of the RTM makes this minimisation less effective, but still

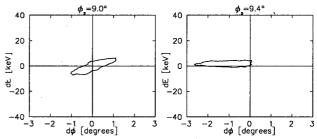


Figure 5: The longitudinal output beam shape for a beam that is injected with a small longitudinal emittance (ε =1·10⁻⁷ π m) for ϕ_s =9.0 degrees and ϕ_s =9.4 degrees.

useful, as has been shown. Furthermore, if short bunches will have to be accelerated with the RTM, another injector will be used for the microtron. This injector will most-probably produce beams with smaller longitudinal emittances, such that the linear approximation might become valid, which makes the minimisation of the bunch length of the energy spread more effective.

If short bunches are to be accelerated in the RTM other problems, which have not been considered in this paper at all, may play an important role. For instance Coherent Synchrotron Radiation, which is important if short bunches are bent by a magnetic field, may destroy the short bunch length and therefore the RTM may not be useful as an accelerator for ultra-short bunches at all [3].

- [1] W.H.C. Theuws, J.I.M. Botman, H.L. Hagedoorn, The Eindhoven linac-racetrack microtron combination, Nucl. Instr. and Meth. B 139 (1998) 522-526.
- [2] A.F.J. Hammen, Particle dynamics in the 10 MeV TUE electron linac, Internal report VDF/NK 97-07, M.Sc. Thesis, Eindhoven University of Technology (1997).
- [3] M.J. van der Wiel, Personal communications (1998).

STRETCHED BUNCH SHAPES IN THE NSLS VUV RING

N. Towne*, National Synchrotron Light Source Brookhaven National Laboratory, Bldg. 725B, Upton, NY 11973-5000[†]

Abstract

For bunches stretched with a higher-harmonic cavity, longitudinal bunch shapes are influenced by small variations in the potential wells of the buckets of the bunch train. This paper discusses three things that perturb the bunch shapes in the NSLS VUV ring: the -90° (non-optimal) phase of the harmonic cavity maintained by the RF controls [1], higher-order modes (HOM) of the main cavity, and the effect of unfilled buckets on the RF fields in the accelerating modes of the two cavities. The suppression of the lowest-lying HOM in an experiment using RF feedback applied to two HOM damping-probe ports is described and results of calculations of the effect of unfilled buckets are given. Measured bunch shapes are shown and discussed.

1 INTRODUCTION

Operation of an RF system with a higher-harmonic cavity (HHC) provides two benefits. The addition of synchrotronfrequency spread provides Landau damping of coupledbunch modes [2] and bunch lengthening increases the Touschek-scattering lifetime. Both are important in the NSLS VUV ring where a near- ϕ^4 potential is used. A consequence of the use of this potential is that bunch shapes are sensitive to perturbations of the potential well on the order the intrinsic energy spread of the ring. A number of such perturbations are present in the VUV ring. First, near the optimum voltage of the HHC, the bunch shape is especially sensitive to the HHC phase. Second, higher-order modes affect the potential wells of the different buckets differently. Third, the use of empty buckets for the control of ion trapping again provides asymmetric distortion of the potential wells. All of these effects can be seen in the VUV bunch shapes (figure 1) and it is the purpose of this paper to describe these influences. Although the first two effects have been reported previously [1], additional information is provided here. The third effect is assessed for the VUV ring for the first time and occupies the majority of this paper. Bunch lengthening through the broad-band impedance is a substantial effect, although it is not discussed here.

Machine parameters are given in table 1.

2 HARMONIC-CAVITY PHASE

Stretching the bunches is, in part, an exercise in the control of the voltages and phases of the main and harmonic cavities. The ideal condition for bunch stretching [3] has, in

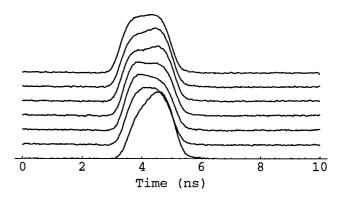


Figure 1: Longitudinal bunch shapes for a 620-mA sevenof-nine bucket fill in the NSLS VUV ring. The first bunch is at the bottom.

Table 1: Values of VUV ring, cavity parameters and symbols used in the text.

Revolution frequency	$\omega_0/2\pi$	
Energy spread	$\sigma_{arepsilon}$	5×10^{-4}
Momentum compaction	α	0.0245
Cavity voltages	V_1/V_2	80/20 kV
Cavity harmonics	h_1/h_2	9/36
Cavity loss factors	k_1/k_2	10/20 GΩ/s

the VUV ring, cavity phase of -94° and voltage ratio near h_1/h_2 , where h_1 and h_2 are the harmonic numbers of the two cavities. Some HHC power is provided by the beam. The RF controls for the HHC do not attempt to meet this condition but instead maintain a relative phase of -90° [1]. The bunch shapes, in spite of this, are nearly optimal (figure 2) because a shift of the cavity phase much smaller than the four degrees is required to meet this condition—a consequence of the near- ϕ^4 potential. Reference [4] explains this more fully.

3 HIGHER-ORDER MODES

Higher-order mode (HOM) losses in the cavities of the VUV ring are not, in most cases, known with any accuracy. The oscillation of bunch shapes visible in figure 1 voltages at non-RF revolution harmonics are at work. In only the case of the lowest monopole HOM of the main cavity at 270 MHz is the Q known and the influence assessable. This mode has center frequency only a few hundred kilohertz above the 46th revolution harmonic, which is once removed from a bucket harmonic, and significant voltage is generated. In an experiment RF feedback centered

^{*}Email: towne@bnl.gov

[†] Work performed under the auspices of the U.S. Department of Energy, under contract DE-AC02-76CH00016.

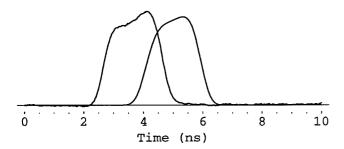


Figure 2: Measured bunch shape in the VUV ring for a symmetric nine-bunch fill (left) and calculated assuming ideal stretching but with the HHC phase set so that the net power transfer between the HHC and the beam is zero $(-90^{\circ}$ condition, right).

on the 270 MHz mode was applied to the cavity through two damping probes fitted with high-pass filters to reject the pickup from the powered accelerating mode. Feedback gain sufficient to reduce the strength of the mode by a factor of two at the revolution harmonic was applied and the result, in figure 3, verifies that there is some voltage in this HOM affecting the bunch shapes. Remaining oscillation of the bunch shapes shows that there is a voltage in the ring at least one other revolution harmonic.

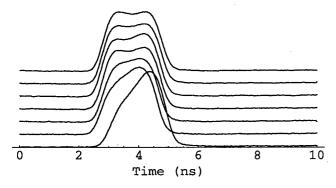


Figure 3: Bunch shapes for a 570-mA seven-bunch fill with 7.2 dB of gain applied to the 270-MHz mode of the main cavity. There is 5.3 dB gain at the 46th revolution harmonic a few hundred kilohertz below the resonance (the revolution harmonic is displaced one from a bucket harmonic).

This result, that the 270 MHz mode is responsible for only part of the distortion of the buckets, and the result that suppressing the impedance of the mode had little effect on the coupled-bunch modes, dictated the conclusion that the mode suppression is of little utility in the VUV ring.

4 THE BUNCH TRAIN [5]

Empty buckets break the periodicity, at the RF frequency, of the beam current. As a result the voltage in the ring induced by the beam current has Fourier components at revolution harmonics other than harmonics of the bucket fre-

quency. This has the effect of introducing non-uniformity, perhaps very small, of the bucket potentials. Ordinarily this non-uniformity is not of concern but, when one considers stretched bunches of electrons in a storage ring where the RF potential may approximate a ϕ^4 potential, small changes become significant. In the NSLS VUV ring the effect of this potential-well distortion is significant. It is the task of this section to give a calculation of the shifts of the bunch shapes, apply the calculation to the VUV ring, and compare the results with measurements.

To begin, consider a ring of b buckets with beam current I_b due to an asymmetric fill of n empty buckets and b-n bunches in a train. Imagine that the beam current I_b is the sum of a part where all buckets are filled \bar{I}_b and a part δI_b where empty buckets are filled with charge opposite the others. Furthermore, assume that the current I_b due to the fictitious charge in the n empty buckets is lumped into the center of the train of empty buckets and that its Fourier component at the RF frequency $\omega_{RF} = h\omega_0$ (h is the harmonic number of the cavity and ω_0 is the revolution frequency) is canceled by another voltage:

$$\delta I_b = eN \sum_{p=-\infty}^{\infty} \delta(t - pT_0) - \kappa \cos(h\omega_0 t), \qquad (1)$$

where $\kappa=2I_{av}/(b/n-1)$, $eN=\kappa T_0/2$, I_{av} is the average beam current, and T_0 is the revolution period. It is assumed that a nominal potential well is generated by the RF cavities driven by a combination of generator current and beam current so that the voltage in the cavities generated by \bar{I}_b is (conceptually) absorbed into the voltage in the cavities for ideal bunch stretching. δI_b is regarded as a perturbation without a Fourier component at $\hbar\omega_0$.

One then models the cavity as a resonator with resonant frequency ω_r , detuning $\Delta = \omega_r - h\omega_0$ from the cavity's harmonic h of ω_0 , quality factor Q, and impedance R. The voltage $V_{\delta I_b}$ induced by δI_b has two terms corresponding to the terms on the right-hand side of equation 1,

$$V_{\delta I_h} = V_1 + V_2. \tag{2}$$

The result of Kramer and Wang [6] gives

$$V_1 = eNke^{-i\Omega\tau}/(e^{-i\Omega T_0} - 1) + \text{c.c.},$$
 (3)

where k is the loss factor (the product of the damping rate $\Gamma = \omega_r/2Q$ and the impedance R) of the cavity, $\Omega = \omega_r - i\Gamma$, and $\tau = t \mod T_0$. The term V_2 is the negative of the wake potential $-W(t) = -2k\cos(\omega_r t)e^{-\Gamma t}$ for the cavity convolved with the second term of equation 1

$$V_2(t) \simeq -\frac{k\kappa}{2} \frac{e^{-h\omega_0 t}}{-i(\Delta - i\Gamma)} + \text{c.c.}$$
 (4)

Summing V_1 and V_2 ,

$$V_{\delta I_b} \simeq k \left(\frac{eNe^{-i\Omega\tau}}{-i(\Delta - i\Gamma)T_0} - \frac{\kappa e^{-i\hbar\omega_0 t}}{-2i(\Delta - i\Gamma)} \right) + \text{c.c.}$$

$$\simeq \frac{\kappa k}{2} e^{-i\hbar\omega_0 t} \frac{e^{-i(\Delta - i\Gamma)\tau} - 1}{-i(\Delta - i\Gamma)} + \text{c.c.}$$

$$\simeq \kappa k \cos(\hbar\omega_0 t)\tau. \tag{5}$$

Note that this is a small quantity, it has a Fourier component at the RF frequency due to the approximations made, and it adds a locally constant voltage to each bucket. We add a term at the RF frequency $h\omega_0$, borrowed from the prescribed RF voltage, to remove this locally constant voltage so $V_{\delta I_b}$ meets the periodic boundary condition $eNk = V_{\delta I_b}(0_+ + pT_0) = -V_{\delta I_b}(0_- + pT_0)$, where $p = \ldots, -1, 0, 1, \ldots$ This gives

$$V_{\delta I_h} \simeq \kappa k \cos(\hbar \omega_0 \tau) (\tau - T_0/2). \tag{6}$$

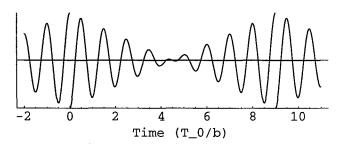


Figure 4: Equation 6 for h = 9 and time in units of the RF period.

The solution is illustrated in figure 4. Bunches are located at the either the minima or maxima on the first half of the train and on the maxima or minima, respectively, on the second half. The RF voltage at a bucket are, to first order in phase, shifted by $V_{\delta I_b}$ evaluated at the time of the bucket. To remind the reader, a shift of the RF voltage upward makes the synchronous phase later while a shift downward has the opposite effect. The first leading and the first lagging bucket with respect to the kick receive the largest shifts and of opposite signs with respect to each other. The signs of the shifts depend on the number of empty buckets. To see this consider the phase of $V_{\delta I_b}$ for the first bunch after the kick.

$$\varphi = 2\pi \frac{n+1}{2} \frac{h}{b}.\tag{7}$$

By inspection one can see that the cases where the shift for this bunch, proportional to $-\cos\varphi$, is positive and negative are:

- negative when n is odd or h is an even multiple of b and
- positive when n is even and h is an odd multiple of the b.

To illustrate with the VUV ring, there are nine RF buckets and, in normal operation, there are two empty buckets (n=2 and b=9). The main cavity has h=9 determining the bucket frequency and the harmonic cavity has h=36 (table 1). The shift in the total RF voltage at the phase of the first bunch following the kick due to the main cavity is positive while the shift due to the harmonic cavity is opposite the shift of the main cavity. Since the loss factor of the harmonic cavity is larger than that of the main cavity, the

effect of the harmonic cavity prevails and the net shift of the RF voltage at the first bunch after the kick is negative (figure 5). When comparing this conclusion with the first bunch in figure 1 we see that it is shifted slightly later in time suggesting that the potential for that bunch is locally high instead of low. Based on this observation we conclude that the actual perturbation of the RF voltage at that bunch is dominated by a higher-order mode(s) pushing the voltage upward.

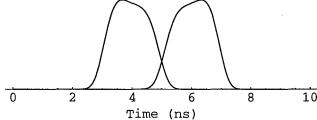


Figure 5: Calculated bunch shapes for the leading (left) and trailing (right) bunches of a seven-bunch train and two empty buckets in the VUV ring given the ideal RF voltages for stretching.

5 CONCLUSION

Bunch shapes in the NSLS VUV ring are influenced uniformly by the harmonic cavity phase, asymmetrically by the HOMs not near bucket harmonics, and the presence of, in normal operation, a gap in the fill. The unusually asymmetric shape of the first bunch (figure 1) is a result of the combination of the voltages from the HOMs and HHC phase; the affect of the empty buckets is a moderating but minor influence. Near ideal bunch shapes are obtained for the other bunches.

- R. Biscardi, S. L. Kramer, and G. Ramirez, Nucl. Instrum. Methods A 366 (1995), p. 26-30.
- [2] H. Frischold et al., in 10th International Conference on High Energy Accelerators, Serpukhov, USSR, 1977.
- [3] A. Hofmann and S. Myers, in Proceedings of the 11th International Conference on High Energy Accelerators, p. 610 (1980).
- [4] N. Towne, "Slow feedback loops for a Landau cavity with high beam loading", in these proceedings.
- [5] The work of this section was made possible by discussions held at ALS with J. Byrd and others.
- [6] S. L. Kramer and J. M. Wang, Nucl. Instrum. Methods A 423 (1999), p. 260, equation 22.

STUDY OF THE BESSY II BEAM LIFETIME *

S. Khan †, BESSY, Berlin, Germany

Abstract

This paper presents beam lifetime measurements at the BESSY II storage ring and their interpretation.

1 INTRODUCTION

The beam lifetime is one of the key parameters of a high-brilliance synchrotron radiation source [1] [2]. Commissioning of the BESSY II storage ring in Berlin-Adlershof started in April 1998 [3]. At the time of writing (February 1999), the vacuum vessel was baked out in 3 of 8 sections at 120°C. During the commissioning period, major parts of the chamber had to be vented several times in order to install new components, and the vacuum is still in a transitory state. It is nevertheless desirable to understand the factors that will ultimately limit the beam lifetime once the vacuum has improved.

Presently, the beam lifetime is clearly dominated by residual gas scattering. Elastic (Coulomb) scattering on the gas nuclei excites betatron oscillations that may exceed the aperture, while inelastic scattering (Bremsstrahlung) on nuclei and electrons leads to momentum loss. Off-momentum electrons can exceed the momentum acceptance given by the rf bucket, or may hit the aperture when displaced by dispersion. In addition, a betatron oscillation is excited if the momentum change happens in a dispersive region.

Table 1: Symbols used in this text and their actual or typical values. The residual gas density n is related to the gas pressure by $n \, [\mathrm{m}^{-3}] = 2.45 \cdot 10^{22} \cdot p \, [\mathrm{hPa}]$.

a	vertical half aperture	8 mm
β_a	beta function at aperture	5 m
$egin{array}{c} eta_a \ ar{eta} \end{array}$	average beta function	12 m
c	velocity of light	$3 \cdot 10^8$ m/s
$\Delta p/p$	momentum acceptance	0.03
γ	Lorentz factor	3327
I	beam current	1-100 mA
n	residual gas density	(s. caption)
N	particles per bunch	$10^9 - 10^{10}$
r_e	classical electron radius	$2.8 \cdot 10^{-15} \text{ m}$
σ_x	rms horizontal beam size	$100\text{-}300\mu\mathrm{m}$
σ_y	rms vertical beam size	10-50 μ m
σ_z	rms bunch length	5-10 mm
$\sigma_{x'}$	rms hor.angular spread	20 - $60~\mu$ rad
Z	residual gas atomic number	7

Once the vacuum has further improved by beam cleaning and bake-out, the Touschek effect will gain importance: when two electrons within a bunch collide, one acquires and the other looses momentum with the same consequences as described above.

The aim of this work was to obtain a consistent picture of the observed beam lifetime under variation of several parameters. As it turns out, the inclusion of other effects (quantum lifetime, ion-related beam loss, etc.) is not required to interpret the data presented below.

2 THEORY

In this section, the relations used in the analysis are reviewed. A list of symbols is given in table 1.

The beam lifetime τ is defined by the current decay rate $1/\tau = -\dot{I}/I$, which is the sum of the Touschek (T) rate and the gas scattering (G) rate

$$\frac{1}{\tau} = \frac{1}{\tau_{\rm T}} + \frac{1}{\tau_{\rm G}} = \frac{1}{\tau_{\rm T}} + cn \left(\sigma_{\rm elast}^{\rm N} + \sigma_{\rm inel}^{\rm N} + \sigma_{\rm elast}^{\rm e} + \sigma_{\rm inel}^{\rm e} \right). \tag{1}$$

The Touschek decay rate can be written as (e.g. [4])

$$\frac{1}{\tau_T} = \frac{Nr_e^2 c}{8\pi\sigma_x \sigma_y \sigma_z \, \gamma^2 \, (\Delta p/p)^3} \cdot D\left(\frac{(\Delta p/p)^2 \sigma_{x'}^2}{\gamma^2}\right), \quad (2)$$

where $D\approx 0.3$ is a slowly varying function that is evaluated numerically. Relativistic effects and beam polarization modify the Touschek rate on the level of 10-20% [5].

The total cross sections for elastic and inelastic scattering on residual gas nuclei (N) and electrons (e) are [4]

$$\sigma_{\text{elast}}^{\text{N}} = \frac{2\pi r_e^2 Z^2}{\gamma^2} \frac{\bar{\beta} \beta_a}{a^2}$$
(3)

$$\sigma_{\text{inel}}^{\text{N}} = \frac{4r_e^2 Z^2}{137} \frac{4}{3} \left(\ln \frac{183}{Z^{1/3}} \right) \left(\ln \frac{1}{\Delta p/p} - \frac{5}{8} \right)$$
(4)

$$\sigma_{\text{elast}}^{\text{e}} = \frac{2\pi r_e^2 Z}{\gamma} \frac{1}{\Delta p/p}$$

$$\sigma_{\text{inel}}^{\text{e}} = \frac{4r_e^2 Z}{137} \frac{4}{3} \left(\ln \frac{2.5\gamma}{\Delta p/p} - 1.4 \right) \left(\ln \frac{1}{\Delta p/p} - \frac{5}{8} \right),$$

The distinctly different dependence of Touschek scattering and inelastic gas scattering on the momentum acceptance $\Delta p/p$ (equations 2 and 4) can be used to distinguish the two effects by changing the rf voltage (which also changes the bunch length). Coulomb scattering is identified by variation of the physical aperture using scrapers.

^{*}This work is funded by the Bundesministerium für Bildung, Wissenschaft, Forschung und Technologie and by the Land Berlin.

[†] Email: khan@bii.bessy.de

3 MEASUREMENTS AND RESULTS

The data shown below were taken in February 1999. The beam lifetime was deduced from the beam current measured by a current transformer. Low currents (~ 1 mA) were measured by monitoring synchrotron light with a photodiode [6].

3.1 Beam Lifetime versus Current

The gas scattering rate increases with beam current due to synchrotron radiation desorption. However, given a finite pumping rate, the correlation is not necessarily linear and depends on the vacuum history.

The linear dependence of the Touschek rate on the number of particles per bunch (equation 2) is modified by turbulent bunch lengthening and transverse emittance growth due to intrabeam scattering or instabilities.

In view of these uncertainties, the dependence of the lifetime on the beam current was not analysed. Instead, the lifetime was measured as function of rf voltage and aperture within short time intervals at nearly constant current, and the experiments were restricted to ≤ 100 mA.

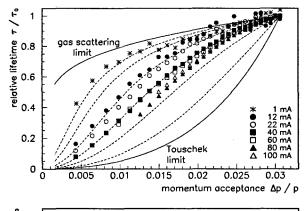
3.2 Beam Lifetime versus Rf Voltage

Under the assumption that the momentum acceptance upto $\Delta p/p=0.03$ is determined by the rf bucket and not by aperture restrictions (which was a design constraint for the vacuum chamber [5]), the curves in figure 1 show the lifetime as function of $\Delta p/p$ in the limits of gas scattering and Touschek scattering (solid lines), and different combinations thereof (dashed lines).

The graphs show the lifetime normalized to τ_0 , the lifetime at $\Delta p/p=0.03$, and do not depend on the actual gas pressure. Some uncertainty remains: (1) The ratio between elastic and inelastic gas scattering depends on $\bar{\beta}$, the average beta function weighted with the local gas pressure. Theoretical pressure profiles suggest values of $\bar{\beta}=10$ -14 m, depending on the beam current. (2) The choice of Z determines the ratio between scattering on gas nuclei and electrons (the latter being of minor importance).

The measured data shown in figure 1 for beam currents between 1 mA and 100 mA are consistent with the theoretical expectation. Figure 2 presents the gas scattering and Touschek decay rates deduced from a fit to the data. In the limit of zero current, the gas scattering rate approaches a finite value, while the Touschek rate vanishes as expected. At 80 mA, the increase of the Touschek rate is apparently halted by instabilities. The respective lifetime contributions are listed in table 2 for 10 mA and 100 mA.

As another confirmation of the Touschek effect, the bottom part of figure 1 shows data for 22 mA in 60 bunches (FWHM of the bunch train) and in 15 bunches. The increased bunch current is indeed reflected by a stronger Touschek contribution.



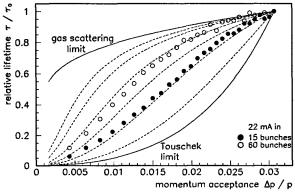


Figure 1: Beam lifetime (normalized to the value τ_0 at $\Delta p/p = 0.03$) as function of the momentum acceptance.

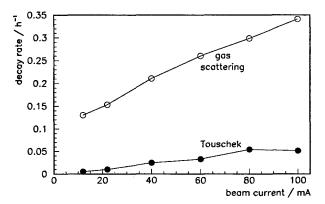


Figure 2: Fitted decay rates versus beam current.

3.3 Beam Lifetime versus Aperture

Moving vertical scrapers towards the beam increases the losses from Coulomb scattering (equation 3). With horizontal oscillations coupling into the vertical plane and the presence of vertical dispersion, a vertical scraper ≤ 1 mm from beam center would also limit the momentum acceptance, but the decay rate from this process is negligible. The quantum lifetime, important below 7-8 σ (≤ 0.1 mm), can be ignored as well.

If dominated by Coulomb scattering, the lifetime would depend quadratically on the scraper position. This is shown in figure 3 (dashed line) together with measured data and fits (solid lines) assuming scraper-independent contributions from Bremsstrahlung and Touschek scattering. The fit parameters were the central position of the beam, the aperture a, and the Touschek rate, while the Bremsstrahlung rate was kept constant. Figure 3 (top) shows measurements at 10 mA and 100 mA. The fact that the fit describes the 10 mA data well confirms the theoretical Bremsstrahlung rate. At larger currents, the inclusion of a small Touschek contribution, increasing with current, clearly improves the fit. As a further confirmation, the Touschek rate was boosted by reducing the rf voltage. Figure 3 (bottom) shows a fit to these data, which agrees well with the expectation. The small deviation at 3-4 mm is not yet understood.

The undulator chambers with 8 mm half-height are presumed to be the limiting apertures, whereas the fits yield a=6.2-6.4 mm at the undulator entrance. A better agreement cannot be expected since equation 3 is based on purely linear beam optics. Furthermore, the beam may be not exactly on the chamber axis, the dynamic aperture may be smaller than the physical aperture, and the beam cross section may be tilted due to coupling.

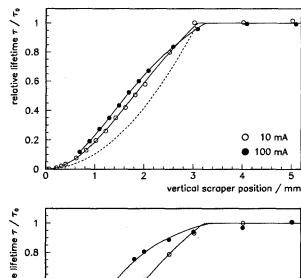
4 CONCLUSIONS AND OUTLOOK

The BESSY II beam lifetime is consistent with the assumption of residual gas scattering and Touschek scattering as limiting effects. At the time of the experiment, the lifetime was 10 h at low current, corresponding to an average N_2 -equivalent pressure of $4\cdot 10^{-9}$ hPa. A further improvement of the vacuum by an order of magnitude can be expected, and the lifetime will be ultimately limited by Touschek scattering. The Touschek lifetime was found to be 20 h at 100 mA in 60 bunches. The measured horizontal-vertical coupling was 1.9%. For this case, calculations using the code ZAP [7] suggest a bunch length of 8 mm and a Touschek lifetime of 15 h.

Larger beam currents, improvement of the coupling to well below 1%, and the operation of feedback systems against longitudinal and transverse multibunch instabilities [8] will certainly increase the Touschek rate. On the other hand, the bunch current can be reduced by filling more buckets (~ 300). Furthermore, the design of passive third-harmonic rf cavities to increase the bunch length is in progress.

Table 2: Contribution of different lifetime limiting effects.

	10 mA	100 mA
elastic scattering on nuclei	18 h	6.8 h
inelastic scattering on nuclei	19 h	7.2 h
elastic scattering on electrons	1100 h	420 h
inelastic scattering on electrons	53 h	20 h
Touschek effect	190 h	20 h
combined lifetime	7.4 h	2.6 h



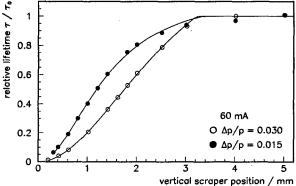


Figure 3: Beam lifetime (normalized to the retracted scraper value τ_0) versus vertical scraper position.

5 ACKNOWLEDGEMENTS

The author would like to thank the BESSY II commissioning team whose combined effort made these measurements possible.

- R.P. Walker et al.: 'Beam Lifetime in ELETTRA', Proceedings of the 4th European Particle Accelerator Conference, London (1994), p.1347.
- [2] J. Byrd, W. Decking, C. Kim, D. Robin: 'Lifetime Studies at the Advanced Light Source', Proceedings of the 6th European Particle Accelerator Conference, Stockholm (1998), p.1347.
- [3] R. Bakker for the BESSY II Project Team: 'Status and Commissioning Results of BESSY II', this conference.
- [4] J. le Duff: 'Current and Current Density Limitations in Existing Electron Storage Rings', NIM A239 (1985), p.83, and references therein.
- [5] S. Khan: 'Simulation of the Touschek Effect for BESSY II -A Monte Carlo Approach', Proceedings of the 4th European Particle Accelerator Conference, London (1994), p.1192.
- [6] The photodiode signal was made available by R. Thornagel et al. (Physikalisch-Technische Bundesanstalt, Berlin).
- [7] M. Zisman, S. Chattopadhyay, J. Bisognano: 'ZAP User's Manual', LBL-21270 (1986).
- [8] S. Khan, T. Knuth: 'BESSY II Feedback Systems', this conference.

EFFECT OF RF PHASE MODULATION NEAR A PARAMETRIC RESONANCE ON THE LONGITUDINAL EMITTANCE

<u>F. Orsini</u>, CEA SACLAY, Gif-sur-Yvette, France A. Mosnier, Projet SOLEIL, Gif-sur-Yvette, France

Abstract

Aiming at increasing the apparent bunchlength and hence the beam life time in electrons storage rings, RF phase modulation near one parametric resonance has been experimentally investigated. Since the eventual benefit of this technique depends greatly on the ring parameters, we studied the effect of such a modulation for different RF parameters on the longitudinal emittance. Theoritical predictions and results of simulations are compared and discussed. It is shown that synchrotron radiation tends to spoil the parametric resonance. In particular, a criterion for islands survival has been found.

1 INTRODUCTION

In order to reach very high brilliance, Synchrotron Radiation Light Sources demand intense bunches with very small transverse and longitudinal emittances. However the high density of electrons increases the Touschek effect and thus reduces the beam lifetime. In order to reduce the electron density, different approaches have been considered: a higher harmonic cavity operating in the bunch lengthening mode or a RF phase modulation which increases the apparent bunchlength but also the energy spread of the beam. This paper focus on the second method near the thirdinteger resonance, because the integer resonance is not an appropriate solution: well developed in [1], it is briefly illustrated here with the example of SOLEIL storage ring with the main ring parameters (see Table 1). Main simulation results proove that the integer resonance is too strong (see figure 1) and leads to distinct bunchlets in phase space and induces a dipole oscillation of the whole bunch as far as the amplitude of the modulation is important, whatever the regime of the modulation frequency is. In order to have an appropriate phase space occupied by the beam, the thirdinteger resonance parameters, frequency ω_m and amplitude A_m , must be first properly chosen. The method of the optimization parameters is discussed in details with some theory and numerical results. Then the synchrotron radiation effect, is studied in opposition with the parametric resonance effect with help of a Fokker-Planck treatment, which leads to the islands formation criterion. Also, further examples are given to illustrate this criterion.

2 THIRD-INTEGER RESONANCE

2.1 Fixed Points and Islands Width

The complete perturbated Hamiltonian in (ϕ, δ) variables is, with ϕ the phase and δ the energy deviation of a particle,

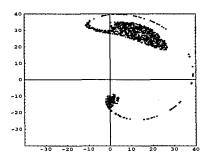


Figure 1: Particles in normalized phase space (ϕ, δ) with modulation at the integer resonance in the regime just before the vanishing of the centered bunchlet.

 $\overline{\phi_s}$ the synchronous angle (in convention $\overline{\phi_s}=\pi-\phi_s$) and ω_s the synchrotron frequency:

$$H(\phi, \delta) = \frac{\omega_s}{2} \delta^2 + \omega_s \tan \overline{\phi_s} (\sin \phi \cos(A_m \sin \omega_m t) + \cos \phi \sin(A_m \sin \omega_m t)) - \omega_s \cos \phi \cos(A_m \sin \omega_m t) + \omega_s \sin \phi \sin(A_m \sin \omega_m t) - \omega_s \phi \tan \overline{\phi_s}$$
(1)

Using action-angle variables $(\tilde{J},\tilde{\psi})$ in a rotating frame: $\delta = -\sqrt{2\,\tilde{J}}\,\cos(\tilde{\psi} + \omega_m\,t/3), \ \phi = -\sqrt{2\,\tilde{J}}\,\sin(\tilde{\psi} + \omega_m\,t/3),$ expanding into Bessel functions and assuming to be close to the third-integer resonance, the Hamiltonian has the much simple form [1]:

$$K(\tilde{J}, \tilde{\psi}) = (\omega_s - \frac{\omega_m}{3})\tilde{J} - \frac{\omega_s \tilde{J}^2}{16} - \frac{\omega_s A_m (2\tilde{J})^{\frac{3}{2}}}{48} \cos 3\tilde{\psi}$$
(2)

In the new phase space $(\tilde{J},\tilde{\psi})$, the stationary trajectories correspond to the H-constant contours. For appropriate modulation parameters, the 3 islands of the third-integer parametric resonance can be well-shaped. The coordinates of the stable fixed points (SFP: $\tilde{\psi}=0,\frac{2\pi}{3},\frac{4\pi}{3}$) $(\frac{\partial K}{\partial \tilde{\psi}}=\frac{\partial K}{\partial \tilde{J}}=0)$ are:

$$\phi_{\sigma} = 0, \frac{\sqrt{3} a_{m}}{4} [1 + R_{FP}], \frac{-\sqrt{3} a_{m}}{4} [1 + R_{FP}]$$

$$\delta_{\sigma} = \frac{a_{m}}{2} [1 + R_{FP}], \frac{-a_{m}}{4} [1 + R_{FP}], \frac{-a_{m}}{4} [1 + R_{FP}]$$
(3)

with the factor $R_{FP} = \sqrt{1 + \frac{64\,Q_s^2}{a_m^2(\sigma_\epsilon h \alpha)^2} \cdot (1 - \frac{\omega_m}{3\omega_s})}$, where a_m is the normalized modulation amplitude $(A_m$ is in units of rms bunchlength), Q_s is the synchrotron tune, σ_ϵ is the natural energy spread, α is the momentum compaction and h is the harmonic number. The fixed points position depends on the ring and the RF modulation parameters. In order to depopulate the bunch center as much

as possible, islands have to be placed close to the bunch core and to be large enough. However, eq. 3 shows that the SFPs can never reach the origin, even for a vanishing distance to the resonance $(\omega_m - 3\,\omega_s)$ and are bounded by a lower limit.

The island width calculation completes the islands structure. The island width is given by the distance between the separatrice, i.e the curve which joins the unstable fixed points, and the SFPs, where the hamiltonian is maximum [2]. The normalized island width (in σ units) and expressed with storage ring parameters (eq. 4) is given by:

$$\Delta \delta_{\sigma} = \pm 16 \sqrt{\frac{2}{3}} \left(\frac{Q_s}{\alpha \sigma_{\epsilon} h}\right)^{\frac{3}{2}} \left(1 - \frac{\omega_m}{3 \omega_s}\right)^{\frac{3}{4}} \frac{1}{\sqrt{a_m} R_{FP}}$$
 (4)

This equation reveals that the more ω_m tends to $3\omega_s$, the more the island width is reduced $(\Delta \delta_\sigma \propto (1 - \frac{\omega_m}{3\omega_s})^{1/4})$. There is then a trade-off between island position $(\omega_m$ very close to $3\omega_s$) and the island width $(\omega_m$ not too close to $3\omega_s$).

2.2 RF phase modulation optimization

Different Synchrotron Light Sources were studied [3]. Table 1 resumes the relevant parameters for Soleil, Bessy I and SuperAco.

Table 1: Synchrotron Light Sources main RF parameters

	Soleil	Bessy I	SuperAco
F_{RF} (MHz)	352.2	499.2	100.0
h	396	104	24
α	4.77 10 ⁻⁴	$1.5 \ 10^{-2}$	$1.48 \ 10^{-2}$
T_{rad} (ms)	4.33	10.0	8.5
σ_{ϵ}	9.24 10-4	5.0 10-4	5.5 10-4

Results of optimization are given in table 2. Both parameters, amplitude and frequency of RF phase modulation, have to be first optimized in such a way that the SFPs are close to the bunch core, while keeping a sufficient island width and the stationary trajectories in phase space are shown in fig.2 for one of the example. It is worth noting that a_m must be not too large (1 or 2 maximum) for preventing any coherent movement of the whole bunch.

Table 2: Final optimization of the RF phase modulation parameters and islands characteristics

	Soleil	Bessy I	SuperAco
ω_m/ω_s	2.9995	2.9850	2.9950
A_m (degrees)	1.48	5.68	3.24
Island width (σ)	2.29	2.71	2.77

When the bunch length is small (ex. Soleil), compared to the RF wave length, the modulation frequency has to be moved very close to $3\omega_s$ in order to draw the SFPs to the

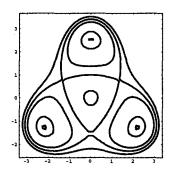


Figure 2: Soleil: separatrices in normalized phase space $(\phi_{\sigma}, \delta_{\sigma})$.

origin. The islands width, table 2, gives the maximum extension trajectory inside one island. For the three machines, particles, located at 1σ , will be drawn out up to nearly 3σ .

3 SYNCHROTRON RADIATION EFFECT

In this section, examples are given with a multi-particle tracking code [4] which simulates the movement of the particles of a bunch faced with RF phase modulation, synchrotron radiation and quantum excitation. The simulation is based on the recurrent equations for each particle:

3.1 Fokker-Planck treatment

In the previous analytical treatment, the synchrotron radiation effect, which includes the synchrotron radiation damping and the quantum excitation, has not been taken into account. Although, this effect has been neglected in previous papers, some strong effects have been observed in multiparticle tracking simulations. The previous Hamiltonian treatment can not be applied with the synchrotron radiation effect because of the non-conservative system properties. Our present analysis is based on the Fokker-Planck equation:

$$\frac{\partial F}{\partial t} + \{H, F\} = R \tag{5}$$

where $F(\phi, \delta, t)$ is the distribution function in the bunch, R is the collision term describing the synchrotron radiation effect, $\{\cdots\}$ denotes the Poisson bracket and H is our peturbated Hamiltonian previously explained.

Expressing eq. 5 in $(\tilde{J}, \tilde{\psi})$ variables and having now a system completely time-independent (details can be found in [4]), the final equation can be written as:

$$\left[\frac{\omega_{\bullet} A_{m} (2\tilde{J})^{3/2}}{32} \sin 3\tilde{\psi} \tan^{2} \tilde{\psi} + \gamma_{d} \tilde{J} + \kappa\right] \frac{\partial S}{\partial \tilde{J}} + \tilde{J} \kappa \frac{\partial^{2} S}{\partial \tilde{J}^{2}} + \gamma_{d} S = 0$$
(6)

and the azimuthal periodicity for the third-integer resonance $F(\tilde{J},\tilde{\psi})=S(\tilde{J})\times e^{j\,3\,\tilde{\psi}}$ has been used. The quantity of interest is the term in bracket, which contains the third-integer resonance perturbation, the damping term with γ_d and the quantum excitation term with κ related to γ_d by the relation $\sigma_\epsilon=\sqrt{\kappa/\gamma_d}$. The RF phase modulation will be still efficient if the magnitude of the first coefficient will be larger than the synchrotron radiation effect $(2^{n\,d})$ and $3^{r\,d}$ coefficients).

3.2 islands formation criterion

Coming back with normalized phase space variables (ϕ, δ) , we express the three coefficients of the bracket term in eq. 6 as follows:

$$c_1 = \frac{\omega_s A_m}{16} \left(\frac{\alpha h \sigma_\epsilon}{Q_s} \right)^3, c_2 = \frac{1}{T_{rad}} \left(\frac{\alpha h \sigma_\epsilon}{Q_s} \right)^2, c_3 = \frac{1}{T_{rad}} \sigma_\epsilon^2.$$

The c_3 term, much smaller than c_1 and c_2 , can be neglected. We find a limit value on the energy spread for the formation of islands, whenever the beam energy spread will be smaller, islands are destroyed by the synchrotron radiation:

$$\sigma_{\epsilon} > \sqrt{\frac{1}{T_{rad}} \times \frac{16 Q_s}{\omega_{RF} \alpha^2 h a_m}}$$
 (7)

3.3 Simulations of formation or absence of islands

We checked the validity of the island survival criterion for the 3 previously cited machines. For each machine, the RF phase modulation parameters (ω_m, a_m) have been first optimized to get well-shaped islands. Multi-particle simulations were performed for island formation or destruction with 2 values of energy spread: the natural one and a fictive one, which gives the reverse situation.

Figure 3 gives the particle distribution in phase space, showing the island destruction for Soleil (upper-left), SuperAco (bottom-left) and the island formation for Bessy I (middle-right) with their natural energy spread. Table 3 resumes the energy spread values, which were tested, as well as the limit value (natural energy spread are in bold characters). The energy spread of SuperAco, larger than the natural one and which was chosen for island creation, corresponds to a real situation, where the beam current is well above the turbulent regime.

Table 3: σ_{ϵ} parameter for island formation or absence.

	Soleil	Bessy I	SuperAco
σ_{\epsilonlim}	11.1310^{-3}	4.1410^{-4}	14.0210^{-4}
σ_{\epsilonisland}	15.010^{-3}	5.010^{-4}	18.3310^{-4}
$\sigma_{\epsilon \ damping}$	9.2410^{-4}	2.310^{-4}	5.510^{-4}

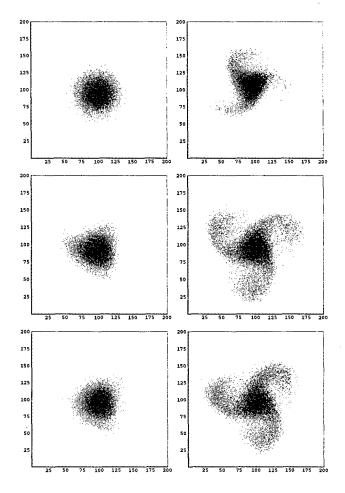


Figure 3: Snapshots (10^5 particles) in normalized phase space (ϕ_{σ} , δ_{σ}) with islands destruction (left) and islands formation (right) for, in order of appearance, Soleil, Bessy I and SuperAco.

4 CONCLUSION

With appropriate modulation parameters, the method can dilute the phase space. However, for some cases, synchrotron radiation effect prevents for the island formation and a criterion on the minimum required energy spread has been found. Anyway, when the $3\omega_s$ excitation is successful, the energy spread is increased, by the same bunch-lengthening factor (islands are rotating in phase space).

- [1] H. Huang and al.,"Experimental determination of the Hamiltonian for Synchrotron motion with rf phase modulation", Physical Review E, Vol.48, N6, Dec.1993.
- [2] R.D. Ruth, "Single-particle dynamics and nonlinear resonances in circular accelerators", Lecture Notes in Physics, Vol.247, Springer Verlag, Proceedinds Sardinia 1985.
- [3] P. Kuske, Yu. Senichev, MP. Level: private communications.
- [4] F. Orsini A. Mosnier," Is RF Phase Modulation a practical method for bunchlengthening?", DAPNIA/SEA 99-03, March 1999.

EXPERIMENT OF RF VOLTAGE MODULATION AT SRRC

M.H. Wang*, Peace Chang, P.J. Chou, K.T. Hsu, C.C. Kuo, J.C. Lee, W.K. Lau, SRRC, Hsinchu, Taiwan

Abstract

The effects of amplitude modulation of RF cavity voltage on the longitudinal beam dynamics were studied experimentally at SRRC by using a streak camera system. The characteristics of parametric resonance in single bunch beam was investigated both by simulation and measurement. The formation of beamlets in the bunch helps to damp the coherent bunch oscillation. This property is employed to provide stable beam in user's shift at SRRC.

1 INTRODUCTION

The modulation of RF system is one of the important beam dynamics topics in accelerator physics. More and more accelerator physicists use the nonlinear property of parametric resonance of RF field modulation intentionly as an advantage to improve the performance of the accelerator[1]. The parametric resonance of RF field modulation resulted in redistribution of particles in the longitudinal plane. The formation of islands within an RF bucket acceptance reducing the density in the bunch core. The beam dynamics property related to the bunch density such as beam life time, beam instability etc. can be improved. At SRRC the effect of the RF phase modulation and the effect of RF voltage modulation were studied. The study of RF phase modulation at SRRC was reported elsewhere[2]. In this paper we discuss the longitudinal beam dynamics with RF voltage modulation. A simulation program was written to track the particle distribution. The characteristics of single bunch under parametric resonance were measured by using streak camera. The application and effects on multibunch is also reported.

2 LONGITUDINAL BEAM DYNAMICS WITH RF VOLTAGE MODULATION

For a charge particle in a circular accelerator, when the amplitude of the RF cavity voltage is modulated by a sinusoidal wave with amplitude ϵ in unit of RF cavity operational voltage and frequency f_m Hz or modulation tune $\nu_m = \frac{2\pi f_m}{\omega_0}$, where ω_0 is the revolution angular frequency, the equation of motion are given by

$$\frac{d\phi}{d\theta} = \nu_s \delta \tag{1}$$

$$\frac{d\delta}{d\theta} = \frac{h\eta}{2\pi E_0 \nu_s} [eV_{RF}(1 + \epsilon \sin(\nu_m \theta + \xi)) \\
\sin(\phi_s + \phi) - U]$$
(2)

Where $\theta=\omega_0 t$ is the revolution angle, ϕ_s the synchronous phase, δ defined by $\frac{h\eta}{\nu_s}\frac{\epsilon}{E_0}$ with η the slip factor, h the harmonic number, and U the radiation energy loss, which

depends on the energy of the particles. The synchrotron mapping equation are given by

$$\phi_{n+1} = \phi_n + 2\pi\nu_s \delta_n \qquad (3)$$

$$\delta_{n+1} = \delta_n - 2\pi\nu_s [1 + \epsilon \sin(\nu_m \theta + \xi)] \cdot$$

$$\sin(\phi_s + \phi_{n+1}) - \frac{4\pi\alpha}{\omega_0} \delta_n \qquad (4)$$

Where α is the radiation damping factor, which is about $200 \ s^{-1}$ of storage ring at SRRC for 1.5 GeV. Comparing to the synchrotron angular frequency ω_s 1.6 \times 10⁵ s^{-1} , it is smaller. Neglecting damping term and the corresponding Hamiltonian is

$$H = \frac{1}{2}\nu_s \delta^2 + \nu_s [1 + \epsilon \sin(\nu_m \theta + \xi)][1 - \cos \phi]$$
 (5)

Analyzing the Hamiltonian we derive island structure in the phase space. The results of applying modulation frequency two times around the synchrotron frequency is summarized[3]. The stable fixed points(SFP's) are located at $J_{SFP} = 8(1 - \frac{f_m}{2f_r}) + 2\epsilon$ for = 0 and $= \pi$, the unstable fixed points (UFP's) located at $J_{UFP} = 8(1 \frac{f_m}{2f_s}$) - 2ϵ for $f_m \leq 2f_s - \frac{1}{2}\epsilon f_s = f_2$, or $J_{UFP} = 0$ for $f_2 \le f_m \le 2f_s + \frac{1}{2}\epsilon f_s = f_1$ for $= \frac{\pi}{2}, \frac{3\pi}{2}$. A tracking program by using Eq.(3) and Eq.(4) is written. Several cases represent the $f_m < f_2$, $f_m = f_2$, $f_2 <$ $f_m < f_1, f_m = f_1$ and $f_m > f_1$ are investigated. The parameters of storage ring at SRRC are used for tracking. The synchrotron frequency of the ring is 25.45 kHz, the damping rate is $200 ext{ s}^{-1}$, and the revolution frequency is 2.5 MHz. The modulation amplitude ϵ is 0.1 and the corresponding f_2 is 49.6275 kHz and f_1 is 52.1725 kHz. The initial particles are uniformly distributed 100×100 in a rectangular box of dimension $\phi \in [-\pi, \pi], \delta \in$ [-2, 2]. The results of tracking of 25000 turns are shown in Fig. 1. As the modulation frequency increases from low frequency to high frequency, the two outer islands move towards the center core, and the population in center core decreases and the two outer islands increases. As modulation frequency equals f_2 the center core disappears. As the modulation increases further the two outer islands come closer, at modulation frequency equals f_1 the two outer islands merge and there exists again single beamlet in a RF bucket. The two outer islands rotate around the center of the RF bucket with angular frequency equals to one half the modulation frequency in all the process.

3 EXPERIMENTAL RESULTS

The experiments of RF amplitude modulation is operated at single bunch mode with beam current about 2 mA. A sinusoidal wave from HP 33120A function generator was split into two to apply to the two gapvoltage feedback loop

^{*} Email:mhwang@srrc.gov.tw

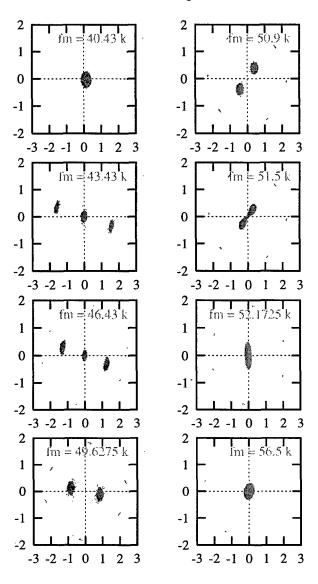
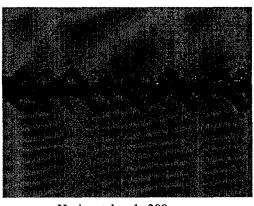


Figure 1: Simulation results of RF amplitude modulation. The modulation frequency is increased from top to down and left to right. The modulation amplitude is 10% of the cavity voltage.

of RF cavity low level system respectively. The operational gapvoltage of each cavity is 400 kV. The modulation frequency is increased step by step from low frequency below 2 f_s to high frequency above 2 f_s . The modulation amplitude ratio is 0.083 and 0.066 respectively. The results were recored by the streak camera. The formation of three beamlets in a RF bucket is shown in Fig. 2. The modulation frequency was 51.08 K Hz with modulation amplitude ratio 0.083. From the upper part of the Fig. 2 it shows that two outer islands rotate with the bucket center at frequency one half the modulation frequency. The lower part of the Fig. 2 shows three beamlets in a single bunch. Which is predicted by the theoretical analysis at modulation frequency below f_2 . The theoretical value of f_2 in this case is 49.84 K Hz. However the observation revealed even at modulation frequency higher than 51.08 kHz there could exit three beamlets in a single bunch. The reason for this discrepancy may be due to the non-coincidence when applied the modulation to the double RF system. The non zero single bunch beam current may affect the results too. It was also found the frequency response was different when modulation frequency was swept from low to high and from high to low. The phenomenon is like the hysteresis of magnetic field.



Horizontal scale 200μsec

Horizontal scale 10µsec

Figure 2: Formation of islands in single bunch beam under RF voltage modulation. The modulation frequency is 51.08 kHz and the amplitude is 8.3% of the RF cavity voltage. The upper plot shows the two outer islands rotate with the bucket center at frequency one half the modulation frequency. The lower part shows the structure in a bunch and the turn by turn motion. The full vertical scale is 1.4 ns.

4 SUPPRESSION OF BEAM INSTABILITY

Longitudinal coupled bunch beam instability is one of the beam instabilities, which deteriorate the beam property. A longitudinal bunch by bunch feed back system is implemented and under commissioning to suppress the instability [4]. Before the completion of the longitudinal feed back system the RF amplitude modulation is used as a temporary solution to suppress the longitudinal coupled bunch beam instability. A modulation frequency slightly below two times of synchrotron frequency with 10% amplitude modulation was applied to the RF system. A

beam spectrum measured from the BPM sum signal from HP4396A before and after the modulation is shown in Fig. 3. The intensity of the beam spectrum is largely reduced after applying the modulation. The suppression of synchrotron side band near revolution harmonics is also shown in Fig. 4. In Fig. 4 the two revolution harmonics is complementary to multiplier of harmonics numbers. The multibunch beam motion under RF amplitude modulation was also recorded by streak camera. The result is shown in Fig. 5. The picture is much like the single bunch event except the amplitude of motion is larger. This indicates that the rotations of beamlets within all the bunches are in phase.

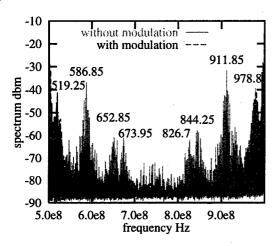


Figure 3: Beam spectrum from BPM sum signal before and after applying RF amplitude modulation. The modulation frequency was 50.155 kHz and the amplitude modulation is 10%. The frequency span of the spectrum is 500 MHz.

In order to further investigate the capability of suppression of beam instability by RF amplitude modulation, the sextupole strength of normal operation was reduced and the vertical betatron side had appeared. The synchrotron photon image pulsing on the screen monitor. When applying the modulation the vertical betatron side band was suppressed and the synchrotron photon image was stabilized again as shown on the screen monitor. From this study it shows the beam can be stabilized by the RF voltage modulation even at lower sextupole strength which is usually to be set to a higher value to provide the head-tail damping.

The application of the RF amplitude modulation close resonance will reduce line charge density, provide larger energy spread. Thus suppresses the coherent motion of beam and increase lifetime. However, because the increase of energy spread the horizontal beam size at dispersion region will increase.

- [1] J.D. Fox, et al., EPAC'92, proceedings, p. 1079, P. Kuske, EPAC'98, proceedings, Yu, Senichev, et al., EPAC'98, proceedings.
- [2] M.H. Wang, et al, EPAC'97, proceedings.

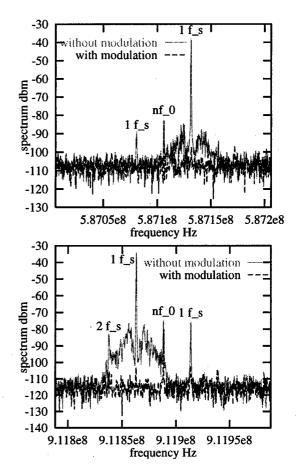


Figure 4: Beam spectrum zoom in from Fig. 3. The revolution harmonic frequency of the upper is 587.106 MHz, and the lower is 911.888 MHz. The frequency span of the spectrum is 200 kHz.



Horizontal scale 100μ sec

Figure 5: Longitudinal motion of multibunch beam under RF amplitude modulation. The modulation frequency is 50.8 kHz and the amplitude is 8.3% of the RF voltage. The full vertical scale is 1.4 ns and $100\mu\text{sec}$ for horizontal.

- [3] D. Li, et al., Phys. Rev. E 48, p. 1638(1993). D. Li, et al., Nucl. Instr. and Meth. A364(1995)205.
- [4] W.K. Lau, et al., these proceedings.

RF MANIPULATIONS IN THE FERMILAB MAIN INJECTOR*

I. Kourbanis, and D. Wildman, FNAL, Batavia, IL 60510 USA

Abstract

The Fermilab Main Injector will have a multifunctional role in the Run II Collider run. It will not only provide beam for antiproton stacking and intense proton and antiproton bunches to the Tevatron collider, but will also decelerate antiprotons for recycling in the new Recycler Ring [1]. To accomplish these goals a series of RF manipulations will be needed.

1 PROTON COALESCING

In order to provide intense proton bunches $(270\times10^9\,\mathrm{ppb})$ for the Tevatron, five to seven 53 MHz proton bunches will be colalesced using a rotation in a 2.5 MHz harmonic RF system [2],[3]. The coalesced bunch is then recaptured with 1 MV of 53 MHz and then the voltage is adiabatically reduced to 440 KV to match the 1 MV Tevatron voltage. Before coalescing each of the proton bunches has a longitudinal emittance of about 0.15 eV-sec and a typical intensity of $40-50\times10^9\,\mathrm{p}$. The coalesced bunch will have a longitudinal emittance of 1.4-2.0 eV-sec depending on the number of coalesced bunches.

The coalescing process has been simulated with ESME [4]. A mountain range of coalescing is shown in Figure 1.

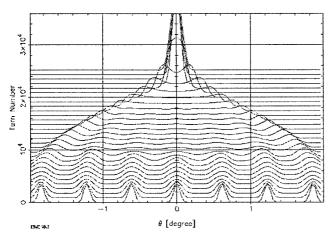


Figure 1: Mountain range picture of the coalescing process. One degree equals 31 nsec.

A total of 36 coalesced proton bunches will be needed in the Tevatron for each store so to avoid repeating the coalescing process 36 times, we plan to eventually inject from the Booster 4 groups of 5-7 bunches each spaced 400 nsec apart accelerate them to 150 GeV, and coalesce them. Then the 4 coalesced bunches will be transferred to the Tevatron and the whole process will be repeated 9 times. In order for the multibatch coalescing to work efficiently we need to apply beam loading compensation to the 53 MHz cavities during the 2.5 MHz rotation.

2 ANTIPROTON ACCELERATION

To provide the 36 antiproton bunches for the Tevatron collider, Main Injector will have to accelerate cooled antiproton bunches provided by the Recycler. No antiproton coalescing is needed. The cooled antiproton bunches from the Recycler will have a longitudinal emittance of 1.5 eV-sec and intensity of 60×10^9 p each. Since we are going to exceed the Main Injector momentum aperture if we try to accelerate these large longitudinal emittance bunches trough transition, the 2.5 MHz coalescing cavities will be used for crossing transition. This will require a 2.5 MHz low level control system with a radial position loop in order to keep the beam in the design radius during the acceleration.

Four antipron bunches at a time will be injected from the Recycler at 8.9 GeV in 2.5 MHz buckets. The 2.5 MHz voltage will be adiabatically raised from 2.0 KV (matching value at injection) to 60 KV. Then the four antiproton bunches will be accelerated through transition to 25 GeV. At 25 GeV a bunch rotation is performed by dropping the 2.5 MHZ voltage to 6 KV for 1/4 of a synchrotron period and then raising it back to 60 KV for another 1/4 period. After bunch shortening, the antiproton bunches are recaptured in the 53 MHz rf buckets, accelerated to 150 GeV, and then transferred into the Tevatron. This entire process is summarized in Fig. 2.

The entire acceleration process of one antiproton bunch has been simulated using ESME. A mountain range of the transfer from 2.5 MHz to 53 MHz at 25 GeV is shown in Fig. 3.

^{*}Operated by Universities Research Association, Inc. under contract with the U.S. Department of Energy.

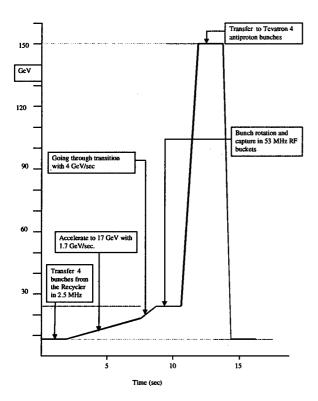


Figure 2: Acceleration of antiproton bunches from the Recycler into the Main Injector.

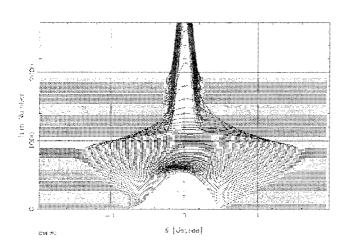


Figure 3: Mountain range picture of the transfer from 2.5 MHz to 53 MHz at 25 GeV during the antiproton acceleration.

No emittance blowup is observed during the transition crossing. The final longitudinal emittance is 1.65 eV-sec with the 10% growth happening during the transfer from the 2.5 to 53 MHz. Beam loading on the 2.5 MHz cavities is a concern that needs to be addressed.

3 ANTIPROTON DECELERATION

The antiproton bunches left at the end of the store in the Tevatron collider will be recycled. For this, after the proton bunches are eliminated at 1000 GeV, the antiproton bunches will be decelerated to 150 GeV. From there they will be transferred to the Main Injector four bunches at a time for a total of nine transfers.

The decelerated antiproton bunches will have a typical longitudinal emittances between 3-4 eV-sec so, as with the antiproton acceleration, we will need to transfer to the 2.5 MHz system before going through transition.

The transfer from 53 MHz to 2.5 MHz is accomplished at a front porch at 25 GeV. First the 53 MHz voltage is reduced until the beam fills the bucket. The 53 MHz is turned off and the bunches are rotated for a quarter of a period in 2.5 MHz buckets with 60 KV of 2.5 MHz and 12.0 KV of 5.0 MHz. The rotated bunches are captured with 300 V of 2.5 MHz and then the voltage is adiabatically raised to 60 KV. Next the bunches are decelerated through transition to 8.9 GeV, the voltage is reduced till the beam fills the bucket and the bunches are transferred to the Recycler. This process is summarized in fig. 4.

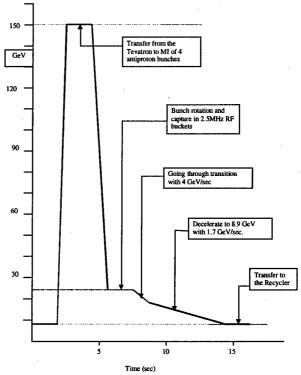


Figure 4: Deceleration process of antiproton bunches in Main Injector.

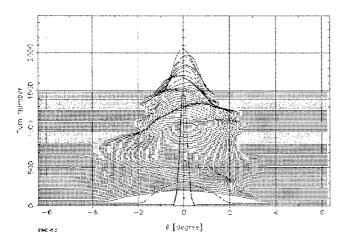


Figure 5: Mountain range picture of the transfer from 53 MHz to 2.5 MHz at 25 GeV during the antiproton deceleration.

The transition crossing with 4 eV-sec bunches results in a 25% emittance growth, mostly due to nonlinearities because of the slow transition crossing (the nonlinear time T_{nl} much longer than the non-adiabatic time).

To reduce the emittance growth during transition crossing, a bipolar γ_t jump was considered in the simulations. The bipolar jump considered maintains a clearance of:

$$[\gamma - \gamma_t] \ge 0.65 \approx 2 \frac{d\gamma}{dt} T_{nl}$$
 except for about 10 msec.

Transition is crossed at about $d(\gamma - \gamma_t)/dt = 130 \sec^{-1}$, almost 30 times faster than without a jump. ESME simulations predict that crossing transition with such a γ_t jump leads to no particle loss and reduces the emittance growth to less than 10%. At present there are no plans for a γ_t jump during deceleration.

4 BUNCH ROTATION FOR ANTIPROTON PRODUCTION

At Fermilab antiprotons are produced by the delivery of trains of 120 GeV proton bunches to a production target from which antiprotons are collected with mean kinetic energy 8 GeV and momentum spread $\Delta p/p \ge 3\%$. The antiproton beam has the same time structure as the incident protons. The proton bunch spacing-to-length ratio is made as large as possible ($\ge 20:1$) so that the resulting antiproton momentum spread may be reduced by bunch rotation in the debuncher ring where time spread is exchanged for momentum spread.

The narrow bunches in the Main Injector are obtained by doing two successive one-quarter period phase rotations within unmatched buckets. At 120 GeV flattop the rf voltage is held at 3.5 MV so the proton bunches with 0.15 eV-sec longitudinal emittance have a full width of

about 1.8 nsec. The rf voltage is then dropped to 350 KV within about 40 $\mu\,\rm sec$ by doing a fast paraphasing. Ideally in one quarter synchrotron period (4msec) the mismatched bunch rotates to span 5.7 nsec within the bucket. At this point the rf voltage is suddenly raised back to 3.5 MV and the bunch rotates another quarter period so that the bunch energy spread becomes 205 MeV and the full bunch length becomes 0.8 nsec.

An ESME picture of the proton bunch narrowing is shown in Fig. 6.

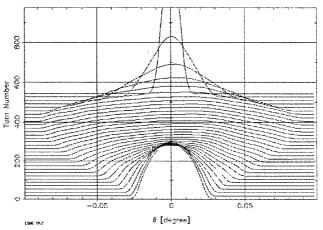


Figure 6: Mountain range picture of the proton bunch narrowing. After two successive bunch rotations the bunch length is reduced by half.

- G. Jackson, "The Fermilab Recycler Ring Technical Design Report", FERMILAB-TM-1991, (1996)
- [2] J. Dey, I. Kourbanis, and D. Wildman "A New RF System For Bunch Coalescing In The Fermilab Main Ring", Proc. of the 1995 Particle Accelerator Conf., Dallas, TX., May 1-5, 1995, pp. 1672-1674.
- [3] J. Dey, I. Kourbanis, and D. Wildman "Improvements in Bunch Coalescing in the Fermilab Main Ring", Proc. of the 1995 Particle Accelerator Conf., Dallas, TX., May 1-5, 1995, pp. 3312-3314.
- [4] J. A. MacLachlan, Jean-Francois Ostiguy "User's Guide to ESME v. 8.2" September 22, 1997, Unpublished.

STUDY OF LONGITUDINAL INJECTION/STACKING IN THE SNS ACCUMULATOR RING*

J. Beebe-Wang, BNL, Upton, NY 11973

Abstract

Various longitudinal distributions, resulting from the specific injection and stacking methods, are considered to minimize longitudinal and transverse instabilities and particle losses in SNS accumulator ring. The longitudinal phase space paintings by linac energy ramping, increased linac energy spread and the use of a random phase RF debunching cavity are reported. Bunch lengthening and beam in gap rate as functions of injection energy spread, RF voltage and injection energy error is summarized. Finally, the energy error tolerance is concluded.

1 INTRODUCTION

At Brookhaven National Laboratory work is in progress for the design and construction of a proton accumulator ring for the spallation neutron source (SNS) [1]. One of the performance requirements of the Spallation Neutron Source (SNS) is to keep the uncontrolled beam loss in the accumulator ring to $< 2x10^4$ /pulse. In order to lower the e-p instability threshold and to reduce the extraction beam loss, it is essential to produce a longitudinal distribution that has broad energy spread, uniform distribution and clean gap. This study is devoted to longitudinal injection/stacking. The study on transverse phase space painting and related issues are reported separately [2].

The investigations are performed by tracking 10⁵ macroparticles in full 6-dimensions through the ring lattice, in the presence of space charge, with the simulation code ACCSIM [3]. The initial longitudinal distribution of injected pulse is Gaussian in energy and uniform in time. All the physical quantities used in the simulations are chosen to be as close as possible to the specifications in the current design [4]. The lattice functions [5] and other salient parameters used in the study are listed in Table 1.

Table 1 Design parameters used in the simulation study.

Beam Kinetic Energy	1 GeV
Beam Average Power	1.0-2.0 MW
Beam Emittance $\varepsilon_{x,y}$	120 πmm-mr
Tunes v_x / v_y	5.82 / 5.80
Max. $β_x$ / max. $β_y$	19.2 / 19.2 m
Dispersion X_n (max/min)	4.1 / 0.0 m
Injection Pulse Length / Gap	546nsec / 295nsec
Extraction Pulse Length / Gap	591nsec / 250nsec
RF Voltage (1 st / 2 nd harmonic)	40 kV / 20 kV

Work performed under the auspices of the U. S. Department of Energy.

2 EFFECTS OF ENERGY RAMPING

One of the easiest ways to increase the energy spread is to paint longitudinal phase space by energy ramping. During the injection, the energy may be ramped in any combinations of linearly/nonlinearly, up/down towards/away from the designed energy as function of We demonstrate, in Fig. 1 and Fig. 2, two longitudinal phase space painting results from the two basic methods of energy ramping shown in Fig.3 (a) and (b), respectively. Other painting schemes are variations of these two. It was found that various undesirable annular structures were developed during the painting depending on the ramping schemes. Because the injection time is comparable to the synchrotron oscillation period, the injected particles do not have enough time to redistribute through synchrotron oscillations. Therefore, energy ramping does not provide a satisfactory longitudinal particle distribution in the SNS accumulator ring.

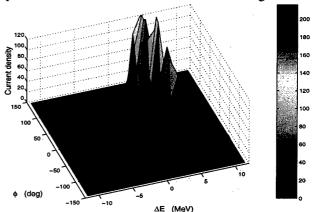


Fig. 1 Current density distribution in longitudinal phase space obtained by energy ramping illustrated by Fig. 3(a).

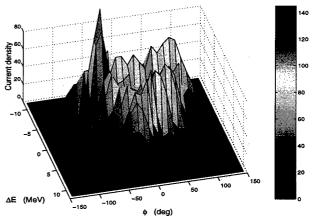


Fig. 2 Current density distribution in longitudinal phase space obtained by energy ramping illustrated by Fig. 3(b).

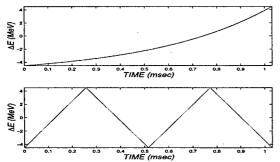


Fig. 3 Two basic energy ramping schemes. (a) Nonlinear monotonic, (b) linear non-monotonic during the injection.

3 EFFECTS OF LINAC ENERGY SPREAD

In order to investigate the effects of increased linac energy spread, the longitudinal phase space distributions for σ_E =1-4MeV in 1MW and 2MW beams were produced by computer simulations. As examples, Fig. 4 and 5 show the current density profiles in longitudinal phase space for the cases of σ_E =1MeV and 2MeV in a 2MW beam. These profiles indicate that increasing linac energy spread is an effective method of broadening beam energy spread. However, the particle leakage to the gap is associated with the broad beam energy spread. Fig. 6 shows the particle in gap rate vs. injection energy spread σ_E . Considering the beam loss requirement of SNS, energy spread σ_E has to be limited to 1.5MeV if injected linac beam has long tails.

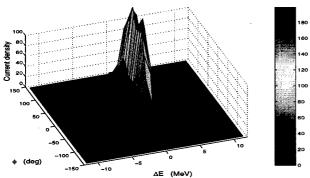


Fig. 4 Current density distribution in longitudinal phase space obtained by 1225 turns of injection/stacking with injection energy spread $\sigma_v=1$ MeV and truncation of $5\sigma_v$.

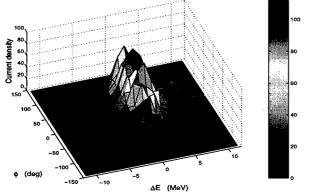


Fig. 5 Current density distribution in longitudinal phase space obtained by 1225 turns of injection/stacking with injection energy spread σ_e =2 MeV and truncation at $5\sigma_e$.

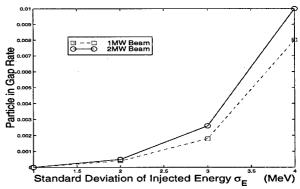


Fig. 6 Particle in gap rate vs. injection energy spread $\sigma_{\!\scriptscriptstyle E}$ in 1MW and 2MW beams.

4 EFFECTS OF DEBUNCHING

A random phase RF debuncher in the pre-injection line for increasing momentum spread was proposed in BNL [6]. By modulating RF frequency to mismatch the beam with RF frequency, the individual micro-bunches effectively get a random energy kick which increases the rms momentum spread of linac beam. Fig. 7 gives a beam profile obtained by computer simulation applying such random phase debuncher. As a result, the injection energy spread is broadened to $\sigma_{\rm E} \approx 5 \, \text{MeV}$ without any tail enhancement. Simulation shows, see Fig. 8, that the injection/stacking with such energy distribution, gives a beam with broad energy spread and maintains a clean gap.

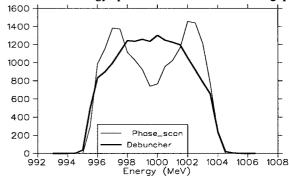


Fig. 7 Beam profile obtained by simulation applying random phase debuncher and conventional debuncher.

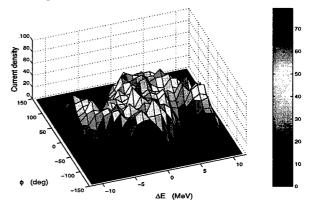


Fig. 8 Current density distribution in longitudinal phase space obtained by injection/stacking with injection energy spread σ_r =5MeV and truncation at 5MeV.

4 BEAM LOSS VS. RF WAVEFORMS

Two major factors leading to longitudinal beam losses are bunch lengthening and particle leakage to the gap. Previous work [7, 8] has established that a dual-frequency RF system has significant advantages over a singlefrequency system on beam handing. In the current dualfrequency RF system design, the 1st and 2nd harmonic has voltage of 40kV and 20kV respectively. In order to make a realistic comparison of dual-frequency and singlefrequency RF system on the effects of longitudinal beam loss, we study single-frequency at 40kV and dualfrequency at 40kV and 20kV, for the 1st and 2nd harmonic, with identical physical conditions. The simulation results of the effects of dual-frequency and single-frequency RF systems on bunch lengthening and particle in gap rate at the end of 1 MW injection/stacking (with tail truncation at $5\sigma_{E}$) are summarized in Table 2 and 3 respectively.

Table 2 Bunch lengthening (nsec) versus RF waveforms and voltages with injection energy spread $\sigma_E = 1, 2, 3 \text{MeV}$.

		Injection Energy Spread σ _E		
		1MeV	2MeV	3MeV
Single-freq. RF 40 kV		19	46	84
Dual-freq. RF	40 / 20	19	23	37
Voltage (kV)	36 / 18	21	30	
(1 st /2 nd harm.)	30 / 15	23	42	
	20 / 10	37	107	

Table 3 Particle in gap rate (10⁴) versus RF waveforms and voltages with injection energy spread $\sigma_E = 1, 2, 3 \text{MeV}$.

		Injection Energy Spread σ _E		
		1MeV	2MeV	3MeV
Single-freq. RF	40 kV	2.9	8.9	28.7
Dual-freq. RF	40 / 20	0	4.5	22.0
Voltage (kV)	36 / 18	0.1	5.1	
(1 st /2 nd harm.)	30 / 15	0.3	5.7	
	20 / 10	1.8	46.4	

5 ENERGY ERROR TOLERANCE

If the injected linac energy is slightly different from the design energy of the accumulator ring, undesirable annular structures may develop in the longitudinal phase space distribution, which may cause instabilities and beam losses. The energy error tolerance is crucially dependent on injection energy spread $\sigma_{\rm p}$ and RF voltages applied. Bunch lengthening and particle in gap rate as functions of injection energy error with various injection energy spread $\sigma_{\rm E}$ (with tail truncation at $5\sigma_{\rm E}$) and RF voltages are show in Fig. 9 and Fig. 10 respectively, which are obtained from simulations of 10⁵ macro-particles during 1225 turns of injection/stacking. The statistical fluctuation is ~10%. From this study we give, in Table 4, the energy error tolerance versus injection energy spread $\sigma_{\rm e}$ and RF voltage for 1MW SNS accumulator ring injection. The tolerance level can be expected to be lower for the 2MW injection.

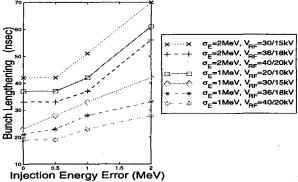


Fig. 9 Bunch lengthening versus injection energy error.

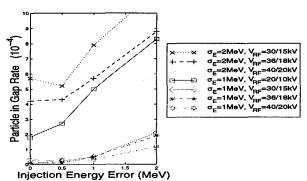


Fig. 10 Particle in gap rate versus injection energy error.

Table 4 Injection energy error tolerance versus injection energy spread σ, and RF voltage.

nijection en	injection chergy spread of and its voltage.					
RF Voltage	Injection Energy Spread σ _E					
(1 st /2 nd harm.)	1 MeV 2 MeV 3 Me					
40kV / 20kV	< 2MeV	N. A.	N. A.			
36kV / 18kV	< 1.5MeV	N. A.	N. A.			
30kV / 15kV	< 1MeV	N. A.	N. A.			
20kV / 10kV	0MeV	N. A.	N. A.			

N. A. = Not Acceptable

6 ACKNOWLEDGEMENT

The author would like to thank Y.Y. Lee for stimulating discussions on longitudinal injection/stacking issues, M. Blaskiewicz for the proposal on random phase preinjection debuncher, and D. Raparia for providing Fig. 7 in this paper. The author also thanks F. Jones and A. Luccio for developing ACCSIM and setting it up at BNL.

- [1] W.T. Weng et al, Proc. of PAC'97, p.972, (1997).
- [2] J. Beebe-Wang et al, "Transverse Phase Space Painting for SNS Accumulator Ring", these proceedings.
- [3] F. W. Jones, "User's Guide to ACCSIM", TRIUMF Design Note TRI-DN-90-17, June 1990 (and later additions).
- [4] SNS Collaboration, "Spallation Neutron Source Design Manual", p.5.12-1, June 1998.
- [5] C.J. Gardner et al, Proc. of PAC'97, p.962, (1997).
- [6] M. Blaskiewicz, private communications, 1998.
- [7] M. Blaskiewicz et al, "RF Options for the NSNS", BNL/NSNS Tech. Note No. 009, December 5, 1996.
- [8] M. Blaskiewicz et al, "The NSNS RF System", BNL/NSNS Tech. Note No. 036, May 12, 1997.

RF FREQUENCY SHIFT DURING BEAM STORAGE IN THE SLC DAMPING RINGS *

R. Akre, F. -J. Decker, M.G. Minty Stanford Linear Accelerator Center (SLAC), Stanford, CA USA

Abstract

A method to reduce the horizontal damping time and equilibrium emittance of the SLC Damping Rings required changing the RF frequency during the beam storage time. The changed frequency causes the beam to pass off center through the quadrupoles effectively stretching the ring. The timing and phasing of the ring is required to be locked to the accelerator for both injection and extraction. The requirement was to change the RF frequency by up to 100kHz after injection transients were damped. Before extraction from the ring, the bunch had to be in the correct bucket and phase locked to the linac. It was necessary that the frequency shift not interfere with the operation of several feedback loops and that any stimulated bunch oscillations be damped to less than 0.1° at 714MHz before extraction, less than 200us after returning to the nominal frequency of 714.000MHz. Several methods were evaluated to perform the task. The modifications made to the ring's RF system and operating parameters to accomplish the intrastore frequency shift are described.

1 QUEST FOR A METHODE TO CHANGE FREQUENCY

During past experiments unlocking of the ring oscillator, changing to a different frequency for a period of time, and then relocking had been done to shift timing of the extracted beam. Frequency shifts on the order of several kilohertz had been successfully accomplished by unlocking the rings phase locked oscillator from is reference source, however locking would take place several milliseconds before extraction. The current requirement of changing the frequency back to the correct phase and relocking to maintain an extraction jitter of less than 0.1° RMS within 200µs did not seem possible using existing hardware.

The ring oscillator used was not able to stabilize after a 100kHz frequency shift in time for extraction. Attempts were made to inject a 100kHz error signal into the feedback loop of the phase-locked oscillator. This method seemed promising although side band noise levels were higher than desired. Use of the ring oscillator to change frequency was set aside as a new method was tested.

Rather than change the frequency of the reference RF to the ring, a phase rotation could be used to cause a frequency change. Adding a phase rotation to a reference frequency results in a new frequency, above or below the reference depending on the direction of the phase rotation. The constant phase change shown in Figure 1 is equal to 360° per 10 cycles of RF. This causes the frequency to increase by 10%.

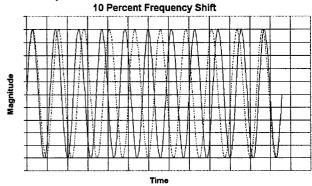


Figure 1. Example of frequency shift due to addition of constant phase change.

An In-phase and Quadrature-phase, I&Q, modulator was built using two RF mixers, two power splitters, two 20dB attenuators, and an amplifier (see Fig. 2). An RF mixer has the property that when the local oscillator, LO, port is biased with RF, the RF port output amplitude is proportional to the intermediate frequency, IF, port input amplitude. As the IF input changes polarity, the RF output changes phase by 180°.

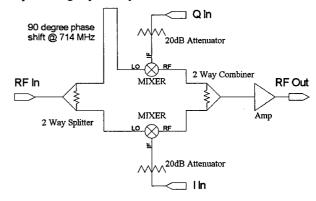


Figure 2. I & Q Modulator.

The power into an I&Q modulator is split with one of the RF paths being 90° longer than the other. The RF is then used to drive the LO ports of the two mixers. The RF output ports of the two mixers are combined, amplified and then sent out. A 20 dB attenuator was placed on the

^{*} Work supported by the U.S. Department of Energy, contract DE-AC03-76SF00515

IF port of each mixer to be able to drive the mixer with a voltage source. With a linear combination of the two orthogonal vectors any vector can be created. The voltage to the I & Q inputs were adjusted to give a constant RF amplitude output for different RF output phases. The I & Q voltages were then recorded (see Fig. 3).

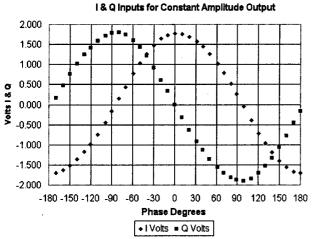


Figure 3. Calibration Data of the I & Q Modulator.

Two arbitrary function generators were programmed to drive the I and Q mixers. Software was written to create waveforms for the I and Q arbitrary function generators. The function generators were triggered using the rings timing system. The predetermined waveform would run for the specified amount of time

2 DAMPING RING FEEDBACKS

The system was installed in the damping ring as shown in Figure 5. There are two phase references for the damping ring. The RF, which drives the ring, is divided down from the 2856 MHz at the injector. This RF is used to drive the ring and set the injection phase. The second phase reference comes from sector 2 where the damping ring bunch is injected. During the store the bunch phase is locked to the 2856 MHz from sector 2 for extraction.

2.1 Cavity Phase Angle

The cavity phase measurement measures the phase between the forward RF into the cavity and the RF in the cavity. The measurement phase error is small since the difference in cable length between the forward RF coupler and the cavity probe to the phase detector is small. With a frequency change of 100kHz at 714MHz (140 ppm) a 40ns difference in cable length would cause a 1.5° error.

A frequency change for a resonant cavity is similar to a tuning angle change for the cavity. The cavity being run off frequency would require more RF power as the frequency changed. From Figure 4 an 80kHz offset in frequency would cause a 7dB drop in cavity power and a -60° change in phase angle. Near resonance the cavity phase angle changes about 1.2° per kHz. In order to minimize the amount of power required the tuning angle

should be set to +36° at 714MHz. A frequency shift of +80kHz would then change the tuning angle to -36°, requiring the same klystron power for the same gap voltage. The RF phase measurement for the loop is sampled-and-held during a time after the beam has stabilized and before any change in frequency.

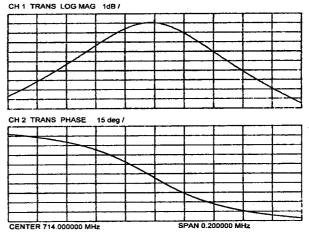


Figure 4. Cavity 591 Probe RF – Cavity Forward RF.

2.2 Klystron Phase Loop

The klystron phase loop measures the phase of the RF coming into the ring and compares it with the amplitude sum of the cavities. The loop is about 900ns in length. A 140ppm frequency change in the ring would cause a phase reading error of 33°. The loop is a slow loop which purpose is to compensate for phase drifts caused by temperature change and maintain the correct injection phase. During operation of the frequency change the feedback was turned off.

2.3 Direct Feedback Loop

The direct feedback loop mixes the vector sum of the cavities with the input drive RF to the klystron to stabilize transients. The length of the loop is about 350ns and in order to be stable, the loop must stay within a limited phase range around 180° (negative feedback). A frequency change of 140ppm will cause a phase change in the feedback loop of 13°. The cavity phase change will dominate this value. Beam intensity changes in the cavities will also change the feedback phase. The gain of the loop was set low enough to allow all combinations of beam/no beam and frequency shift/no frequency shift to be stable.

2.4 Extraction Phase Feedback

Every 360° rotation of the phase causes the bunch to shift a bucket with respect to where it would have been without the phase rotation. In order for the bunch to be extracted the same as if there would be no phase rotation it must precess the ring an integer number of turns. This places the bunch in the exact place it would have been if there were no frequency shift. The bunch passes through the extraction kicker at the exact same time it would have with no frequency shift and is injected into the linac in the same bucket. The phase ramp, which is required to compensate for the difference between the injection and extraction phase, is accomplished by stopping the phase rotation at the correct extraction phase. In order to maintain collisions it is necessary to keep track of the bucket the bunches are in and inject them into the correct accelerator bucket.

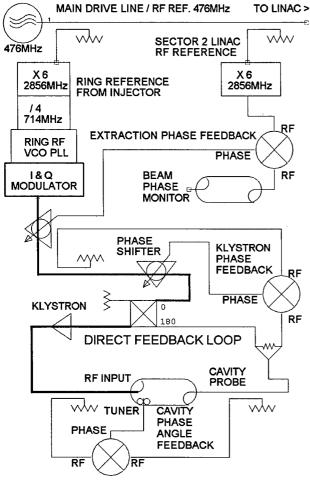


Figure 5. Damping Ring RF - Single Cavity Shown.

As the ring frequency returns to the original value the horizontal damping time and equilibrium emittance change back to their original values. It is desired therefore to stop the phase rotation and return to the original frequency as close to extraction as possible. To keep energy jitter below that which will effect luminosity, the ring extraction phase of the beam with respect to the linac must have an RMS value below 0.1 degree at 714.000MHz. The extraction feedback loop must be given enough time to stabilize from after locking and to before extraction. The extraction feedback loop was closed 200µs before extraction in order to minimize emittance and extraction jitter.

3 OPERATION

The system was installed and operated in the south damping ring initially. Files were set up to run the frequency shift at several different frequencies. Each of the frequencies allowed the modulator to run for a multiple of 84 rotations over 6.8ms. This requirement caused the frequency offset to be an integer multiple of 12.353kHz. The frequency shift was started about 1.33ms into the store. Initial damping of the injection transients and stabilization of the beam occurred during this first 1.33ms. Sampling of the RF for the cavity phase angle loop took place 1.0mS after injection. The frequency shift ended 200µs before extraction.

The instantaneous frequency shift at the start and stop of the phase rotation caused a phase jump that kicked the beam. In order to minimize the effect the phase rotation was ramped up at the start and down at the end over a period of 200µs, see Figure 6.

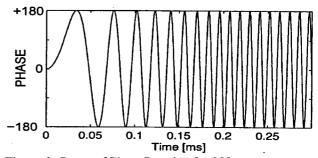


Figure 6. Ramp of Phase Rotation for 200µs.

The tuning angle of one of the cavities was not able to be set to the desired value due to outgassing of a newly installed tuner. The cavities were unable to maintain the voltage during the frequency shift. In order not to saturate the voltage feedback loop, the voltage desired value was ramped to a lower value as the frequency was increased. The south damping ring has been run with the mid-store frequency shift and a reduction in emittance noted, Reference 1.

4 ACKNOWLEDGEMENTS

The authors would like to acknowledge Keith Jobe, Joe Frisch, Marc Ross, and Frank Zimmermann for their ideas, suggestions and encouragement, Doug McCormick for his assistance in tying the I & Q modulator system into the damping ring control system, and R. Siemann.

5 REFERENCES

 M.G. Minty et al., "Emittance Reduction via Dynamic RF Frequency Shift at the SLC Damping Rings," SLAC-PUB-7954, Stanford Linear Accelerator Center, Stanford, CA Sept. 1998; To be published in proc. of 17th Intl Conf on High-Energy Acc., Dubna, Russia (1998).

A HIGH-CURRENT DENSITY CONTACT IONIZATION SOURCE FOR HEAVY-ION FUSION*

S. MacLaren*, D. Beck, A. Faltens, W. Ghiorso, E. Henestroza, P. Seidl, Lawrence Berkeley National Laboratory, Berkeley, CA 94720

Abstract

Heavy ion fusion (HIF) sources will be low-emittance, high current (0.5-1A), and suitable for injection into a multiple beam induction linac, where the diameter of each beam aperture at the beginning of the accelerator is 3-6 cm. Practical transport limits involved in matching the beam to the accelerator aperture in a reasonably-sized structure correspond to several mA/cm² of space charge limited flow with an injector extraction voltage of 1-2.5 MV. We have built a $J \approx 8 \text{ mA/cm}^2 \text{ Cs}^+ \text{ contact}$ ionization source for a 160kV diode; this represents a factor of four increase in the Cs+ current density over previous sources for HIF. The emitter is sintered iridium, operating at 950 < T < 1150 °C. We are experimenting with several methods of alkali feeding capable of maintaining a fraction (<5%) of a monolayer coverage on the iridium surface.

1 BACKGROUND

In developing sources and injectors for a heavy ion fusion driver, high current density is desired because it allows smaller and/or fewer beams and thus a less expensive injector design. Ideally, one desires that the current density be limited by voltage breakdown and beam transport considerations rather than the emission limit of the ion source. Recent designs, which are still evolving, place the desired current density of the ion source at 8 mA/cm2 Cs+ equivalent.

At Lawrence Berkeley National Laboratory, a surface ionization source that achieves > 8 mA/cm2 has been built and tested. This particular type of surface ionizer, in which Cs atoms are first applied to and then evaporated from a refractory metal surface, has routinely produced highly uniform ion beams with low emittance. The resulting transverse emittance for an injector with good optics is slightly above the lower limit established by the temperature of the emitting surface (~0.1 eV), which is difficult to achieve with gas or plasma sources.

Previous surface ionizers designed as ion thrusters have used a sintered W plug as a diffuser to control the flow of Cs atoms from a rear mounted vapor Cs reservoir to the front surface ionizer [1]. For the HIF Cs emitter, the sintered iridium "sponge" is both the contact ionizer and the Cs reservoir; the Cs is stored in an ionized state on the large surface area of the porous Ir. We expect a much slower depletion process that is controlled by surface

diffusion with essentially immeasurably small vapor pressures.

2 DESIGN

2.1 Ion and Neutral Emission Considerations

Previously we have used porous W in the same manner, yielding emission currents of $J \approx 2 \text{ mA/cm}^2$, but changed from W to Ir in the expectation of reduced Cs neutral emission. From the Saha-Langmuir equation, the ion to neutral emission fraction from a clean surface is:

$$\frac{v_i}{v_n} = 2\exp\left[\frac{(\phi - I)}{kT}\right] \tag{1}$$

where ϕ is the work function of the metal and I is the ionization potential of the adsorbed atom. This ratio is 624 for Cs on W, and 2x10⁶ for Cs on Ir. Additionally, the difference in work functions results in overall emission that is somewhat less for iridium than for W. Therefore, the source needs to operate at a higher temperature (+~100°C) to achieve the same ion current density. The duty factor of a HIF injector is $2x10^{-4}$, so neutral emission dominates the depletion of Cs on W. We believe Ir, being a noble metal, is fairly clean at the 1000-1200 °C operating temperatures, and therefore less prone to adverse chemical effects than W. experimentally observed longer emission lifetime (50 hrs vs. 15 hrs) and higher current density (8 mA/cm² vs. 2 mA/cm²) for the Ir compared to the W seem to confirm the above expectations.

In the W sponge, diffusion models developed by Langmuir and Taylor [2] predict a diffusion time of $\tau \approx$ 200 seconds compared to an emission lifetime or Cs depletion time of ~15 hours. For this system, at any instant the surface coverage θ is constant within the volume of sintered material. In the case of Ir, Cs ions are more tightly bound to the surface, and there is some indication that we may have non-uniform concentrations within the sponge. Thus, we are looking for the time dependence of the depletion, essentially a t-1/2 decay instead of $e^{-t/\tau}$, at different temperatures. In the porous W, the initial doping of the Cs is based on achieving a small $(\theta \sim 3\%)$ surface coverage. In the Ir sponges, if diffusion from the volume of the sponge to the emitting surface is the limiting process, we may be able to increase the surface coverage in the interior region and gain additional

email: samaclaren@lbl.gov

^{*} Work supported by the Director, Office of Energy Research, Office of Fusion Energy, U.S. DOE, under contract No. DE-AC03-76SF00098.

2.2 Re-supply of Cs

It is desirable to have some means of closely controlling θ to get high current. By using the large surface areas of porous sintered metals as a reservoir the time over which the emission of ions falls below the space charge limit of interest (8 mA/cm²) can be several days.

Various possible schemes may be used to re-supply Cs atoms to the source, ranging from a continuous Cs vapor feed to a pulsed vapor feed to an infrequent application of a Cs-containing compound. We used a spark source for several years to supply Cs for a 1-Ampere beam on every pulse, and more recently we have used a Cs₂CO₃ solution that we apply every few days onto the porous W emitters with a syringe.

Two methods are currently being considered for resupplying the Ir emitter with Cs under vacuum. One approach uses a liquid reservoir of Cs₂CO₃ solution, a small amount of which would be sprayed at the cold source under vacuum through a retractable nozzle. A short burst could deliver enough cesium atoms to supply a large driver-scale source for a full day. Another method uses a small array of commercially available alkali dispensers that would be remotely positioned in front of the emitter similar to the nozzle. The dispensers are activated by ≈7A of current and emit of Cs atoms; this method has been successfully tested. It is appropriate for small sources for scaled experiments, but the storage capacity of the dispensers could not re-supply a HIF driver scale source more than a few times. We are currently investigating another long-term vapor delivery option using a directed nozzle and a much larger reservoir of Cs compound.

2.3 Effects on High Voltage

One of the main motivations for using the minimum amount of Cs and for using it efficiently is that even a small amount of Cs on insulators and high voltage electrodes tends to lower their breakdown strength. We presently run a 200 kV Cs beam combining experiment [3], a 160 kV scaled final focusing experiment [4] and a 2 MV K injector without noticeable problems from contamination, but have had such problems in previous experiments. This is one of the leading concerns about using contact ionization sources in injectors for heavy ion fusion.

2.4 Source, Filament and Heat Shield

The heat shield assembly was built with an emphasis on achieving higher temperatures (>1150 °C) for higher current densities with an Ir emitter while still maintaining good thermal efficiency. The filament is freestanding in a Mo chamber, in contrast to our previous potted filaments, or filaments in contact with alumina insulators.

Figure 1 shows a CAD cutaway view of the complete source, including the sintered iridium emitter, the filament, the heat shields, and the carbon Pierce electrode.

The conductive heat path from the Mo cup enclosing the filament is via the reentrant path of three concentric thin (0.005") molybdenum cylinders to reach the back plate of the assembly which would act as a thermal sink. Radiation to the sides and rear of the filament encounters many layers of highly reflective shielding.

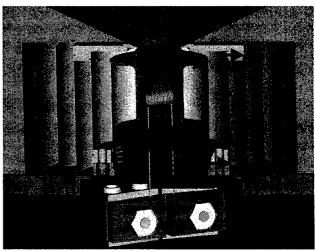


Figure 1: CAD cutaway view of the source, filament, heat shield assembly and the conical Pierce electrode. The Ir emitter diameter is 1.0 cm (black arrows). The red arrows indicate the conductive path from the filament housing to the rear support flange.

The curved (11 cm radius) emitting surface is the end of a sintered iridium cylinder, 1 cm in diameter and 1 cm long. The emitter was then finished to size with a diamond grinder, including grinding the spherical surface. This surface was then etched using electric discharge machining to recover the porous nature of the sintered material near the emitting surface. This allows Cs atoms attached to the internal surfaces of the sintered metal to migrate forward and repopulate the emitting area. Figure 2 shows an electron microscope image of the porous emitting surface.

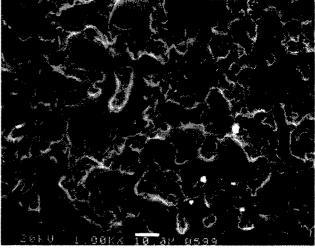


Figure 2: Electron microscope image of the sintered Ir. The line indicates 10µ on the surface.

Another important detail of the design is the molybdenum ring that serves as an intermediate stage between the emitter edge and the edge of the carbon Pierce electrode. It is positioned <0.005" from the emitting surface, but does not make thermal contact. Because the properties of the extracted ion beam are very sensitive to the geometry in the immediate vicinity of the emitting surface, a Mo intermediate piece was used so that the inner surface could be machined to a "knife edge". This positions the Pierce angle of the electrode as close as possible to the emitter edge. The less precise edge of the graphite electrode is then no longer a part of the critical region adjacent to the emitter.

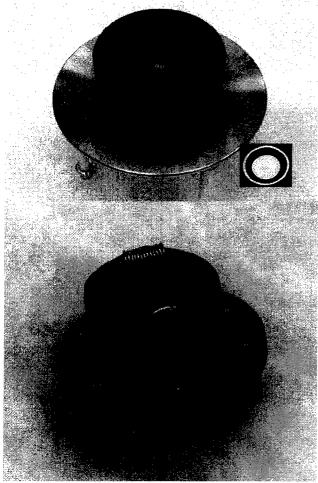


Figure 3: Source and filament after ~100 hours of use.

3 PERFORMANCE AND FUTURE PLANS

The thermal performance of the heat shield assembly is quite good. The emitter surface was raised to a temperature of 1140°C using a filament power of 40 watts, and the source was operated at an emitter temperature as high as 1225 °C using 52 watts. Upon disassembly, there was no visible degradation of the filament or damage to any of the heat shield package components (See fig. 3). The pyrometer used for all

measurements was calibrated against thermocouple measurements made of an identical piece of sintered Ir over a temperature range of 900 to 1150°C.

In fig. 4 we compare our observations to some previous measurements. The data from Wilson [6] are critical-current measurements. It appears that Cs on Ir will give sufficiently high current density for HIF applications at an acceptable operating temperature.

We observed a space charge limited current of 9mA/cm² for >50 hrs of continuous running without need to resupply the Ir with Cs. This represents a significant increase in lifetime over our experience with similar sized porous W emitters [3] where the current density was considerably lower (≈2mA/cm²).

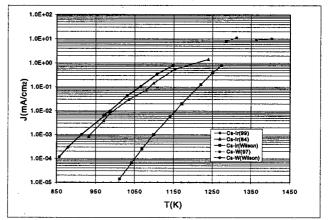


Figure 3: Current density vs. T.

The source will be used in a scaled HIF final focusing experiment [4] where the emittance and beam uniformity will be measured. This design may be implemented in a driver –scale injector [5].

6 ACKNOWLEDGEMENTS

The authors gratefully acknowledge the technical support of Mr. Tak Katayanagi.

- [1] A. Theodore Forrester, "Large Ion Beams", Wiley (1988) 242.
- [2] John B. Taylor and Irving Langmuir, Phys. Rev 44, 6 (1933) 423.
- [3] P. A. Seidl et al., NIM A415 (1988) 243.
- [4] S. MacLaren et al., "Preliminary Results from a Scaled Final Focus Experiment for Heavy Ion Inertial Fusion", these proceedings.
- [5] J. Kwan, "A Multiple-Beam Injector for Heavy Ion Fusion", these proceedings.
- [6] R. G. Wilson, IEEE 9th Ann. Symp. on Electron, Ion, and Laser Beam Technology, IEEE# F-79, (1967) 22

PRELIMINARY RESULTS FROM A SCALED FINAL FOCUS EXPERIMENT FOR HEAVY ION INERTIAL FUSION*

S. MacLaren*, A. Faltens, E. Henestroza, G. Ritchie, P. Seidl, Lawrence Berkeley National Laboratory, Berkeley, CA 94720

Abstract

Vacuum ballistic focusing may be a straightforward method to obtain the heavy ion beam spot size necessary to drive an inertial confinement fusion target. Proper scaling of particle energy, mass, beam current, beam emittance, and magnetic field replicates the dynamics of a full driver beam in a small laboratory experiment. By expanding the beam and then focusing to a very small spot, the effects of aberrations and space charge on this method of final focus can be studied. To date, 200 µA of 120keV K+ has been focused to test the matching and focusing elements. A recently designed high brightness contact ionization source is being tested for upcoming focusing measurements with an 87 µA Cs beam that will duplicate the dynamics of a proposed driver design at onetenth scale. Transverse phase space and beam current density at various stages of the focus will be presented. Follow-on measurements studying electron neutralization of space charge and its effect on the focus will be explored.

1 BACKGROUND AND MOTIVATION

There are several important challenges associated with the final focus system design in a heavy ion fusion (HIF) driver. A combination of target design and the performance of the final focusing section determine the emittance budget for the accelerator. Additionally, for many accelerator designs there is a lower limit of approximately 10 GeV for the ion kinetic energy in an unneutralized vacuum focus scenario [1]. This statement is troublesome when considering the economic expense of achieving high ion kinetic energy in an induction accelerator. Combined with the limitations of current fusion target requirements, this indicates a need for a detailed experimental study of final focus performance.

Proper scaling of the terms in the beam envelope equation that relate particle energy and mass, beam current, emittance, and focusing field replicates the dynamics of a full driver beam in a small laboratory beam. The experiment can be scaled to reproduce the beam conditions in a full-scale driver, including aberrations from the focusing elements and the longitudinal momentum spread. In addition to partial neutralization from the reactor chamber gas and secondary electrons from beam target interactions, current reactor scenarios include deliberate methods for reducing the perveance of the beams

incident on the HIF target. Controlled neutralization of the experimental beam may be used to explore proposed methods to bring higher perveance beams to a small focal spot. These additional effects, which are very difficult to model accurately in simulations, must be studied closely in order to advance a valid design for the final focus subsystem.

2 DESCRIPTION OF THE EXPERIMENT

A Scaled Final Focus Experiment has been built at Lawrence Berkeley National Laboratory to investigate the ballistic focus of a heavy ion beam using a series of pulsed magnetic quadrupoles. The final focus system designed by H. Wollnik for the HIBALL II study [2] used 10 GeV Bi+ and has been experimentally reproduced with 160 keV Cs⁺ at a one-tenth scale. Accordingly, the beam current is scaled from 1.25 kA to 87µA. The beam is apertured and matched to the entrance of the final focus section in a 1.5-meter lattice of ten electrostatic quadrupoles. The magnetic focusing section is 8.2 meters long, including initial and final drifts. The middle drift between the third and fourth magnetic quadrupoles has been shortened with respect to the HIBALL II design as the bending magnets that allow for the neutron dump are not included.

A schematic of the experiment along with the beam envelope is shown in Figure 1. The upper part of the figure contains a to-scale drawing of the vacuum system with electrostatic quadrupoles in pink and magnetic quadrupoles in green. The lower part is a schematic of the horizontal (red) and vertical (blue) beam envelope with the transverse scale exaggerated. The dashed lines represent the locations of the diagnostic probes, and the solid black line represents the aperture location.

The source for the Cs⁺ ion beam is a sintered iridium emitter that can be replenished with Cs atoms using an aqueous Cs₂CO₃ solution. A method for replenishing the emitter under vacuum using a Cs vapor feed is currently being investigated. The emitter sits in a diode with a Pierce cathode geometry that extracts 8 mA/cm² Cs⁺ when pulsed at 160 kV. The design and performance of the source are discussed in detail elsewhere in these proceedings [3].

*email: samaclaren@lbl.gov

_

^{*} Work supported by the Director, Office of Energy Research, Office of Fusion Energy, U.S. DOE, under Contract No. DE-AC03-76SF00098.

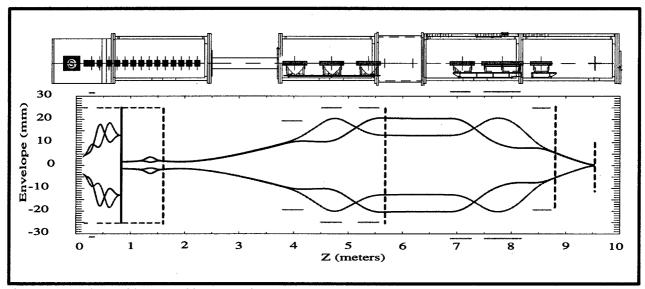


Figure 1: Experimental layout and beam envelopes.

Upon exit from the diode, 6.3 mA of Cs⁺ is transported through the first set of five electrostatic quadrupoles to an aperture plate. A 3-mm diameter aperture passes 87µA of beam into the second set of five quadrupoles, which allow the beam to expand and then give it an overall convergence of a few milliradians in both transverse directions for the drift into the magnetic section. The final focus lattice consists of six pulsed magnetic quadrupoles, each with two layers of copper windings in a cos20 distribution on cylindrical shells. Several of the magnets are pictured in Figure 2, and their properties are summarized in Table 1. The beam leaves the sixth magnetic quadrupole with a converging (-9 mr) envelope angle and reaches its focal point approximately 80 cm from the last magnet.

Magnet	Effective length (cm)	Pole Tip Field (gauss)
QM1	40.0	310
QM2	40.0	596
QM3	40.0	346
QM4	40.0	402
QM5	71.7	440
QM6	35.1	665

Table 1: Magnetic quadrupole properties

The beam is diagnosed in several locations that are indicated by the dashed lines in Figure 1. The slit scanners are arranged in pairs and can be used together to measure the phase space distribution, or to measure the transverse profiles. Orthogonal slits are used together to create transverse, time-resolved current density of the beam. There are also two deep Faraday cups to measure the total ion current: One is after the sixth electrostatic quadrupole. The other is at the focus, where beam profiles are also measured with a moveable single-slit. Data acquisition is automated using LabViewTM software.



Figure 2: Magnetic quadrupoles and winding rig

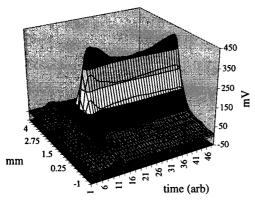
3 RECENT DATA

Thus far, a 0.86-mm radius focal spot has been achieved with a 200- μA beam of 120 keV K⁺ ions from an aluminosilicate source that had been used in experiments several years ago. Figure 3 shows the beam profile measured with a single 50μ slit at the focus as a function of the duration of the pulse. At each time slice, the data are well represented by two Gaussian curves, one broad with low amplitude, and another narrower with larger amplitude. The widths of these Gaussians are plotted in the lower half of the figure.

The size of the focus compares very well with the calculated value (0.88 mm) of for the minimum of the beam envelope. This value was obtained by integrating the envelope equation from the exit of the last magnet to the focus using the measured beam emittance and convergence angle. For the calculation, the beam current corresponding to the core Gaussian (142 μ A) was used.

As the full 10-mA beam from the K⁺ source was highly non-uniform, it was not expected that the apertured beam would be perfectly uniform. In fact, current density and phase space measurements made of the apertured beam 80 cm from the aperture demonstrate this non-uniformity. The lower amplitude Gaussian represents a beam halo most likely resulting from the non uniformity of the current distribution emerging from the aperture. The high degree of uniformity from the newly tested sintered

iridium source will remove this possible aberration from the focal spot measurement [3].



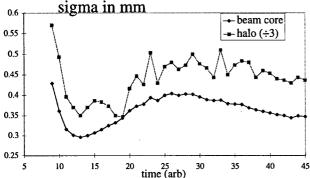


Figure 3: Beam profile dataat focus

The time dependence of the beam pulse shows a monotonic decreaseof the spot radius from the to the end. The measurement was made with a steel diagnostic slit that intercepted the beam just upstream of a Faraday cup. This time dependenteffect is most likely due to secondary electrons produced by the unbiased slit paddle neutralizing the incident beam. The decrease to 0.74-mm radius is consistent with a 42% neutralization of the space charge. A diagnostic probe that includes secondary-electron suppression and is capable of three-axis motion is currently being manufactured.

4 FUTURE PLANS

Once the apertured Cs⁺ beam is brought to a focus, the next step in the evaluation of the HIBALL-IIstudy will be to match the emittance of the experiment to the corresponding scaled value of 3π mm mr. This may be done with the use of an emittance-spoiling grid at the diode exit, or possibly with a poor match in the electrostatic section. A comparison of the measured spot size with the study's results can then be made.

An effort to simulate the experiment with a 3-D PIC code is currently underway. The quadrupole end fields of the magnets will be included in the PIC simulations in order to make comparisons with the measured phase space and the focal spot profiles.

Beyond this, there are two more studies that will be carriedout in the near future. First, there is the question

of chromatic aberrations caused by the magnets due to deviations from the design longitudinal momentum. This effect can be studied by deliberately detuning the magnetic quadrupole fields to alter the forces on the particles, simulating a deviation in their longitudinal momentum from the reference value. Measurements of the resulting effect on the focal spot could then be compared directly with simulation.

Second, the possibility of reducing the focal spot size by partially neutralizing the beam with electrons can be examined. Due to the brightness of the beam, a larger aperture may be used in the electrostatic section to allow approximately 400µA of beam into the final focus lattice. Increasing the beam perveance by a factor of four while only doubling the emittance moves the focus into a regime that is highly space charge dominated with a focal spot radius of several millimeters for a completely unneutralizedbeam. A high transparency grid inserted in the beam path immediately following the last magnet could produce enough secondary electrons to have a considerable and easily measurable effect on the beam spot size. This experimental measurement could then be compared with a separate measurement of the fractional current neutralization as well as the PIC simulation results.

5 ACKNOWLEDGMENTS

The authors gratefully acknowledge the outstanding support of the LBNL technical staff including Mr. R. Beggs, Mr. R. Hipple, Mr. C. Rogers, and Mr. W. Strelo.

- [1] R.O. Bangerter, The US Heavy Ion Fusion Program, Fus. Eng. Des., 32-33 (1996) 27-32.
- [2] HIBALL-II An Improved Conceptual Heavy Ion Beam Driven Fusion Reactor Study", KfK 3840, KernforschungszentrumKarlsruhe (July 1985), pp. 57-71.
- [3] S. MacLaren et. al., "A High Current Density Contact Ionization Source For Heavy-Ion Fusion", these proceedings.

ION BEAM DYNAMICS IN POLYHARMONIC FIELD OF LINAC

E.S. Masunov[#], N.E. Vinogradov, MEPhI, 115409, Moscow, Russia

Abstract

This paper describes the problem of ion RF focusing in the axisymmetric RF field involving one synchronous and several nonsynchronous harmonics. The influence of nonsynchronous harmonics on ion beam dynamics is studied by means of 3D effective potential, which is obtained for smooth approximation. The motion equation is presented in Hamilton's form. The possibility of simultaneous transverse focusing and phase stability for accelerating ion beam in the RF field without the synchronous harmonic is shown.

1 INTRODUCTION

It is known, that in order to achieve simultaneous transverse focusing and phase stability for the accelerating ion beam in linac it is necessary to use external focusing elements or to apply a special configuration of the RF field. The second way is more effective for low energy ion RF accelerators. In papers [1-3] it was shown that the RF system with several traveling waves, one being synchronous with the beam may provide simultaneously acceleration and focusing of ions. The systems with infinite numbers of harmonics were investigated numerically [4]. Besides, it was shown that the required effect can be achieved in the undulator accelerators, where the synchronous harmonic is absent [5]. In this paper the method of analysis of 3-D beam dynamics in the polyharmonic RF field of linac is suggested. For this purpose the averaging method is used. In such approach the motion equation has the Hamilton's form. It allows us to take into account the relationship between transverse and longitudinal oscillations. The shape of the effective potential obtained describes the 3D motion of the particle completely.

2 MOTION EQUATION

The RF field in the periodical structure can be presented in the form

$$E_{z} = \sum_{n=0}^{\infty} E_{n}^{z} \cos(h_{n}z) \cos(\omega t),$$

$$E_{r} = \sum_{n=0}^{\infty} E_{n}^{r} \sin(h_{n}z) \cos(\omega t),$$
(1)

where $E_n^z = E_n I_0(h_n r)$, $E_n^r = E_n I_1(h_n r)$, $h_n = h_0 + 2\pi n / D$, $h_0 D$ —a phase advance per period

of structure D. Trajectories of particles in the field (1) may be expressed by the summation of two different types of motion r_s and \tilde{r} , which are caused by slowly varying field and the rapidly oscillating one respectively. By means of averaging method the motion equation for slow component can be obtained in the form

$$\frac{d^2 \mathbf{R}}{d\tau^2} = -\frac{\partial}{\partial \mathbf{R}} U_{eff} \tag{2}$$

where $U_{\it eff} = U_{\it 0} + U_{\it 1} + U_{\it 2} + U_{\it 3}$ is the effective potential function:

$$U_{0} = \frac{1}{2} e_{s}^{z} \sin \psi;$$

$$U_{1} = \frac{1}{16} \sum_{n \neq s} \frac{e_{n}^{2}}{\Delta_{s,n}^{-s}^{2}} + \frac{1}{16} \sum_{n} \frac{e_{n}^{2}}{\Delta_{s,n}^{+s}^{2}};$$

$$U_{2} = \frac{1}{16} \sum_{\substack{n \neq s \\ n+p=2s}} \frac{e_{n}^{z} e_{p}^{z} - e_{n}^{r} e_{p}^{r}}{\Delta_{s,n}^{-s}^{-s}} \cos(2\psi) \quad (3)$$

$$U_{3} = \frac{1}{16} \sum_{p \neq s} \frac{e_{n} e_{p}}{\Delta_{s,p}^{-2}} \cos(2\psi), |h_{p} - h_{n}| = 2h_{s}.$$

 $e_n = eh_s E_n / m\omega^2$, $e_n^{z,r} = e_n I_{0,l}(h_n r)$, $\mathbf{R} = 2\pi r_s / \lambda \beta_s$, $\tau = \omega t$, $\Delta_{s,n}^{\pm} = (h_n \pm h_s) / h_s$, Ψ and β -are phase and velocity of synchronous particle and s is synchronous harmonic's number. In the following the variable $\chi = z - z_s$ and r will be used as a longitudinal and transverse variable respectively. The effective potential function $U_{\it eff}$ describes particle dynamics in the RF field in smooth approximation completely. The result is that the equation (2) is presented in Hamilton's form. The function $U_{\it eff}$ connects longitudinal and transverse motions of ion and allows us to investigate their influence on each other. The first summand U_o describes the interaction between particle and synchronous wave, the second one U_1 defines the focusing action of nonsynchronous harmonics. The functions $U_{2,3}$ are mixed terms, which are describing the influence of nonsynchronous waves both on transverse and longitudinal dynamics. Simultaneously radial and phase stability takes place when the function $U_{\it eff}$ has an absolute minimum. This is possible when some conditions

on amplitudes and phase of harmonic are satisfied.

[#] E-mail:masunov@dinus.mephi.ru

3 SYNCHRONOUS AND ONE NONSYNCHRONOUS HARMONICS

For two harmonics s and n the item $\boldsymbol{U}_2=\boldsymbol{0}$. Let's define the frequencies of radial and phase oscillations as

$$\omega_r(r) = \frac{1}{r} \frac{\partial U_{eff}}{\partial r}; \qquad \omega_z(\chi) = \frac{1}{\chi} \frac{\partial U_{eff}}{\partial \chi}.$$
 The

conditions of transverse and longitudinal stability are

$$\omega_r^2 > 0, \, \omega_z^2 > 0 \tag{4}$$

Then in the linear approximation $\omega_r^2(0) = \omega_{r0}^2 + \omega_{rl}^2 \cos(2\psi)$,

 $\omega_z^2(0) = \omega_{z0}^2 + \omega_{z1}^2 \cos(2\psi)$, where $\omega_{r,z1}$ are defined by term U_3 :

$$\omega_{r0}^{2} = -\frac{1}{4}e_{s}\sin\psi + \frac{3}{32}\frac{e_{s}^{2}}{\Delta_{s,s}^{+}}^{2} + \frac{3}{32}e_{n}^{2}\left(\frac{1}{\Delta_{s,n}^{+}}^{2} + \frac{1}{\Delta_{s,n}^{-}}^{2}\right)\left(\frac{h_{n}}{h_{s}}\right)^{2}$$

$$\omega_{rl}^{2} = \frac{1}{16}\frac{e_{s}e_{n}}{\Delta_{s,n}^{-}}^{2}\frac{h_{n}^{2} + h_{s}^{2} + h_{n}h_{s}}{h_{s}^{2}}$$

$$\omega_{z0}^{2} = \frac{1}{2}e_{s}\sin\psi; \ \omega_{zl}^{2} = \frac{1}{2}\frac{e_{s}e_{n}}{\Delta_{s,n}^{-}}^{2}$$
(5)

It can be seen from (4), (5) that the larger the ratio e_n/e_s , the more effective transverse focusing is. Besides, this focusing is stronger when s < n, i.e. the acceleration wave is faster than the focusing one. The simple analysis shows that for the case $e_n/e_s >> 1$ impact of the term U_s is unessential and $\omega_{r,z,l}$ can be neglected. In the following we will assume $e_n = e_{max}$, $e_s = ke_{max}$, where k < l and e_{max} is defined by the breakdown voltage. The critical value of k can be found from (4). The overlapping of the phase stability buckets of neighboring harmonics is undesirable. Thus, the parameter e_{max} is also bounded above:

$$\sqrt{2}e_{max}^{1/2}(1+k^{1/2}v_{s}/v_{n})<\left|\Delta_{n,s}^{-}\right|$$
 (6)

The function U_{eff} allows us to take into account the relationship between radial and phase oscillations accurately. In the simplest approach [7], considering the longitudinal oscillations to be in the form $\chi = \Phi \sin(\omega_z \tau)$, we can obtain from (2) the equation of the transverse motion as $d^2r/du^2 + \pi^2(a+2q\sin 2\pi u)r = 0$ with $a = [2\omega_r(0)/\omega_z(0)]^2$, $q = \Phi ctg\psi$; Φ is the amplitude of longitudinal oscillations. Then the condition of resonance is

$$2\omega_r(0)/\omega_r(0) = l$$
, $l = 1, 2, 3, ...$ (7)

The zone of instability corresponds to each l in (7). The conditions (4), (6), (7) formulate the restrictions on amplitudes of harmonics. The diagram of stability including only conditions (4) and (7) is shown in Figure 1. In order to investigate the dependence of transverse frequency and/or transverse emittance on harmonic's numbers one can fix the parameters e_{max} , k, ψ (i.e. fix the ω_z and/or the longitudinal emitance) and calculate the value of ω_r for different s, n and h_o . This analysis was done for the proton acceleration system with $E_{max} = 100$ kV/cm, k=0.15, $\psi = \pi/4$, $\beta_s = 0.015$, $\lambda = 200$ cm. The most effective transverse focusing is provided by the system with s = 2, s = 1 for s = 1

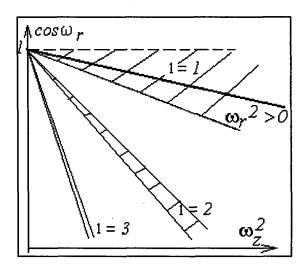


Figure 1: The transverse stability and the zones of parametric resonance

4 SYNCHRONOUS AND TWO NONSYNCHRONOUS HARMONICS

Let's add one more nonsynchronous harmonic with number p to the RF field discussed above. In this case summands U_2 and U_3 can be not equal to 0. These terms render acceleration and defocusing influence on particle motion. Here the items $U_{2,3}$ are of the same order as U_1 so it is necessary to take them into account. The analysis of influence of the summands $U_{2,3}$ shows that these terms deform the shape of $U_{\rm eff}$ significantly. So the phase capture is reduced considerably. At the same time, the contribution of the items $U_{2,3}$ into the acceleration gradient can exceed the contribution of U_0 in several times. It means, that such system may turn out

to be effective for acceleration of the bunched beam. The transverse emittance and/or ω_r is determined by the ratio between terms U_1 and $U_{2,3}$. Figure 2 shows $\omega_r(r)$ for different combinations s, n, p. The parameters of the system are the same as those discussed above; k=0.3, $e_p=e_{max}$. The most effective transverse focusing is provided by the system with s=2, n=1, p=3 and $h_0=0$.

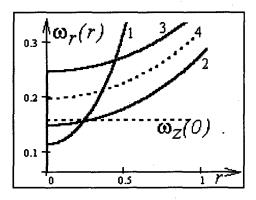


Figure 2: The dependence of transverse frequency on the radius

1—{s=0, n=1, p=2}; 2—{s=1, n=0, p=2}; 3—{s=2, n=1, p=3}; $h_0 = \pi / D$. 4—{s=2, n=1, p=3}; $h_0 = 0$.

5 TWO NONSYNCHRONOUS HARMONICS

The conclusion about the influence of nonsynchronous waves on longitudinal dynamics of the beam becomes even more convincing if in the RF system, discussed in the previous chapter the synchronous harmonic is absent.

Table 1: The comparison of different acceleration systems

		$e_{s,n} \neq 0$	$e_{s,n,p} \neq 0$	$e_{n,p} \neq 0$
	s=1,	$\omega_r = 0.13$	$\omega_r = 0.10$	$\omega_r = 0.16$
] 1	n=2, p=0,	$\omega_z = 0.17$	$\omega_z = 0.24$	$\omega_z = 0.17$
	P 0,	T=0.75	T=1.19	T=1.1
	s=2,	$\omega_r = 0.18$	$\omega_r = 0.16$	$\omega_r = 0.19$
2	n=3, p=1	$\omega_z = 0.17$	$\omega_z = 0.29$	$\omega_z = 0.23$
	P-1	T=0.75	T=2.7	T=1.96

 $T \equiv dW_s / dz_s$, MeV/m; 1: $h_0 = \pi / D$; 2: $h_0 = 0$

In this case the influence of focusing term U_1 and accelerating ones $U_{2,3}$ may turn out to be sufficient to create 3D potential well in which radial and phase oscillations are stable. Besides, the conditions similar to (6) and (7) can be obtained. The comparison of characteristics of different acceleration systems are shown in Table 1. The parameters of the system are the same as those discussed above, $\psi=\pi/3$.

One can see that acceleration and transverse focusing in the RF field without synchronous harmonic is possible. Moreover, such system may be more effective than the standard one with synchronous and one nonsynchronous waves.

6 COMPUTER SIMULATION

In order to test all the results obtained the computer simulation was done. The motion equation in the field (1) was solved numerically for all the acceleration systems discussed. It was shown that the averaging method allows us to describe the behavior of the beam correctly. The range of velocities where the investigation of the beam dynamics by means of effective potential function $U_{\it eff}$ is completely valid is bounded below. For instance, in the case of protons $\beta_s > 0.005$.

7 CONCLUSION

The method of analysis of the ion beam's dynamics in the polyharmonic RF field is suggested. The RF system with synchronous and one nonsynchronous harmonics is investigated completely. The conditions of stability are obtained. The features of the acceleration system with two nonsynchronous waves are shown. The possibility of simultaneous longitudinal and transverse focusing of the beam in the field without synchronous harmonic is exhibited. The comparison of the acceleration system discussed is done. All results are tested by computer simulation of beam dynamics in the RF field.

- [1] V.S. Tkalich, Zh. Ex. and Theor. Fiz. Vol. 32, p. 625, 1957.
- [2] V.K. Baev, N.G. Gavrilov, S.A. Minaev and A.V. Shalnov, Zh. Tekn.Fiz. Vol. 53, p. 1287, 1983.
- [3] V.D. Danilov, A.A. İliin, Y.K. Batygin, Proc. 3 Europ. Part. Accel. Conf., Berlin, vol.1, p. 569, 1992.
- [4] H.Okamoto, Nucl. Instr.and Meth. in. Phys. Res. A 284, p233, 1989.
- [5] E.S. Masunov, Proc. of the 18 Internation. Linac. Confer., Geneva, Switzerland, CERN 96-07, 1996, vol. 2, p. 487-489.
- [6] E.S. Masunov, N.E. Vinogradov, 15 Internation. Linac Workshop, Alushta, Krim, 1997, vol 1, p.184-186.
- [7] I.M. Kapchinsky. Theory of Res.Linear Accelerator, Harwood, 1985.

3D MODELING OF ION RIBBON BEAM FOCUSING AND ACCELERATION IN UNDULATOR LINAC

E.S. Masunov*, S.M. Polozov, A.S. Roshal, MEPHI, RUSSIA

Abstract

One of the possible versions of undulator linear accelerator (UNDULAC-E) using a ribbon beam is discussed. The computer 3D simulation of the beam dynamics is fulfilled. The possibility of simultaneous acceleration of both positive and negative ions in undulator linac is shown. The influence of the fundamental and higher space harmonics of the RF field on ion ribbon beam dynamics in UNDULAC-E is analyzed. The optimal parameters of the accelerator are calculated in order to reach the higher transmission. Simulation results are presented.

1 INTRODUCTION

Earlier the idea to apply a combination of a plane electrostatic undulator and radio frequency fields for acceleration and focusing of intense ion beams with low injection energy was suggested and theoretically investigated in [1]. The current in such undulator linac (UNDULAC-E) can be increased by using a ribbon beam [2]. One of the possible versions of UNDULAC-E with the ribbon beam was discussed in [3]. It was shown that the focusing force is normal to the plane surface of the ribbon beam. The beam focusing in another transverse direction can be created by a nonuniform distribution of the undulator field along the ribbon width (Fig. 1). In [4] there was suggested to change the form of electrodes for two-dimensional transverse beam focusing. Using the smooth approximation method it was found the electrodes shape and the amplitudes of the undulator and RF fields for beam focusing.

The other factor limiting the beam intensity in the undulator linac is a space charge force. The influence of the space charge effects on the ribbon beam focusing was investigated in [4]. The computer simulation of ion dynamics in the undulator, RF and self-consistent Coulomb fields was done by some approximations. The most important of it was the assumption that all ions had the same axial velocity as the synchronous particle and its spread was neglected. The initial transverse velocities was supposed to be normally distributed with relatively small standard deviation. This crude method is good for bunched beam when the coupling resonance is absent. It was shown that the electrostatic shielding of the space charge field decreases Coulomb defocusing of the particles in the narrow accelerating channel. The results of simulation for intense ion beam dynamics demonstrated the possibility to accelerate the high current beam in UNDULAC-E.

The other important way for increasing of the beam intensity is using the space charge compensation [1,5]. In the UNDULAC the accelerating force does not depend on a sign of the particle charge and the averaged motion of the positive and the negative charges are identical. The eZ^- and eZ^+ ions will be inside the same separatrix (bunch) and the current limit of the ion beam can be substantially increased. Space charge compensation effect can be disturbed if the transverse emittance has been changing asymmetrical for eZ^+ and eZ^- and halo phenomenon has been forming. In this paper the behavior of transverse and longitudinal dynamics are investigated in nonlinear RF and undulator fields.

2 SMOOTH APPROXIMATION FOR MOTION EQUATION

At first let us consider the ions 3D dynamics in the RF and the undulator fields using the smooth approximation. In the periodic structure the RF potential U_{ν} and the electrostatic periodic potential U_{o} are delivered to the same electrodes (Fig.1.). The both potentials can be represented as the sum of the space harmonics:

$$U_{v} = -(\Phi_{v}^{(0)}(y) + \sum_{n=1}^{\infty} \Phi_{v}^{(2n)}(x,y)\cos(4\pi n \int dz/D))\sin\omega t,$$

$$U_o = -\sum_{n=1}^{\infty} \Phi_o^{(n)}(x, y) \cos(2\pi n \int dz / D), \qquad (1)$$

where $\Phi_{o,v}^{(n)}(x,y) = \Phi_{o,v}^{(n)} \cosh(nk_x x) \sinh(nk_y y)$,

D is the undulator field z-depended period.

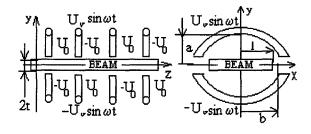


Figure 1: Cross section of the accelerator system.

The fundamental and the higher space harmonics of the RF and the undulator fields are nonsynchronous with the beam. The mechanism of the acceleration and the

^{*} E-mail: masunov@dinus.mephi.ru

focusing is produced by a combined wave field, resulted from a superposition of the first space harmonic of the undulator field and the zero space harmonic of the transverse RF field. The interaction of the accelerated particle with the nonsynchronous harmonics fields can be analyzed by averaging method. In accordance with that, the trajectory of a ion may be represented as a combination of rapidly oscillations r(t) and slow variation R(t). After the procedure of averaging over rapidly oscillations one can derive the expression for effective potential function U_{eff} describing the averaged particle motion [1,4]. Using this effective potential U_{eff} the equation for the synchronous particle velocity $\beta_s = v_s/c$ can be written as

$$\frac{d\beta_s^3}{dz} = \frac{3e^2Z^2}{4\pi} \frac{E_o^{(1)} \cdot E_v^{(0)}}{m^2c^4} \cdot \cos\varphi_s$$
 (2)

where $E_o^{(I)}$ and $E_v^{(0)}$ are the amplitudes of the first undulator field harmonic and the zero RF field harmonic

and
$$\varphi = \frac{2\pi}{\lambda} \int \frac{dz}{\beta_s} - \omega t + \delta$$
 is the particle phase in the

combined wave.

The efficient capture and bunching of the beam can be obtained by the adiabatic growth of the amplitudes E_o and E_v along the longitudinal axis and the corresponding increase of undulator period $D=\beta/\lambda$ to maintain the beam synchronism with the combined wave field. The choice of the function E_o and E_v is not arbitrary because simultaneously with acceleration it is necessary to keep up the transverse focusing of the beam. The analysis of the transverse beam dynamics by means of U_{eff} shows that the focusing along y direction is possible if $2E_o > E_v \sin \varphi$ and the focusing along x direction is possible if $E_o > E_v \sin \varphi$. The accurate analysis of beam 3D dynamics in UNDULAC can be made only by numerical simulation.

3 BEAM DYNAMICS IN UNDULAC

We are discussed UNDULAC design for deuterium ions D^- and D^+ . The UNDULAC consists of the gentle buncher (GB) and acceleration area. The transverse sizes of the channel 2a=0.8 cm, 2b=20 cm. Computer simulation of two component ion beam, consisting of $D^$ and D^+ was carried out by a macroparticle method. The input characteristics of D^- and D^+ are identical. The ribbon beam had the input thickness 2t=0.5 cm and the input width 21=11.5 cm. The input transverse velocity has deviation σ =0.01. The input/output energy are respectively 150 keV/1 MeV and the operating frequency is set at 200 MHz. The amplitude of RF field E_v <240kV/cm. In the buncher the fundamental harmonic amplitudes of RF and undulator fields were gradually grown $\sin[\pi(z+z_0)/2(z_0+L_f)]$ when $0 \le z \le L_f$. The synchronous phase φ_s was linearly decreased from $\pi/2$ to $\pi/4$ when $0 \le$ $z \le L_{\varphi}$. In the acceleration area E_{φ} and φ_s are constant. The dynamics has been calculated by using these parameters to reach the higher transmission. For the basic

variant $E_v=E_o=150$ kV/cm, the length of the accelerator I=2.5 m.

The numerical simulation shows that the beam capture and the transmission depend on the choice of L_{ϕ} and L_{f} . The transmission coefficient K increases from 0.74 to 0.9 when L_{ϕ} and L_{f} are enhanced from 40 to 100 cm but the acceleration gradient decreases. Some results for K and the output energy W are listed in Table 1.

Table 1.

	L_{β} cm	40	50	75	100
L_{φ} cm					
40	K, %	73.8	75.5	76.7	77.6
	W, keV	1070	1058	1030	991
50	K, %	75.7	78.0	78.1	80.0
	W, keV	1056	1050	1020	985
75	K, %	73.8	78.9	81.4	84.0
	W, keV	1027	1018	1005	971
100	K, %	71.5	76.3	80.3	89.9
	W, keV	991	988	973	949

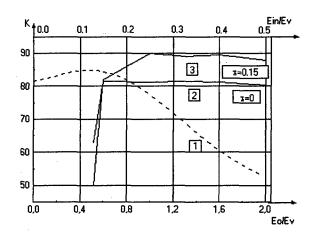


Figure 2: Transmission coefficient K versus field parameters.

The modeling shows that the input transverse RF field amplitude E_{in} must be small (Fig. 2, curve 1). The transmission coefficient K>0.8 if $0<E_{in}/E_{v}<0.22$ and $E_{o}=E_{v}$. Then K rapidly decreases if $E_{in}/E_{max}>0.3$. The most of the ions losses are located at the beginning of the GB section. These losses are due to the longitudinal dynamics The transverse dynamics and the focusing effect depend on the undulator field amplitude. For small E_{o} focusing is absent and K is very small (Fig. 2, curve 2). The beam transmission rapidly increases when $0.46<E_{o}/E_{v}<0.5$. If $E_{o}/E_{v}>0.5$ and the value of $E_{o}\cdot E_{v}$ is given constant the coefficient K has the limit 0.81 for $L_{i}=0.75$ m.

The next figure gives simulation results for two cases:

- a) $E_o = 150 \text{ kV/cm}$, $E_v = 150 \text{ kV/cm}$, $E_o / E_v = 1.0$;
- b) $E_o = 125 \text{ kV/cm}$, $E_v = 180 \text{ kV/cm}$, $E_o / E_v = 0.7$.

All output characteristics of D^+ and D^- are identical and the transverse emittances have been changing symmetric. This fact illustrates that the space charge compensation effect is preserved.

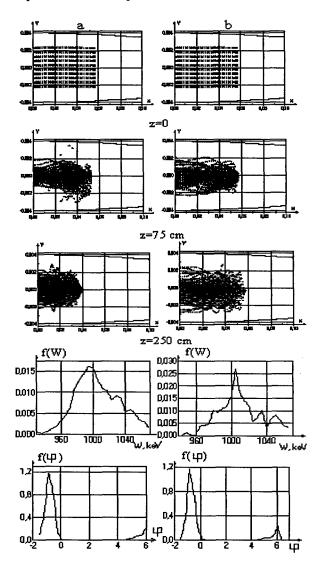


Figure 3: Beam cross-section at different z; density functions of output energy f(W) and output phase $f(\phi)$.

4 INFLUENCE OF SECOND SPACE HARMONIC OF RF FIELD

The higher space harmonics of RF and undulator fields may influence on ion ribbon beam dynamics in UNDULAC. Here we restrict ourselves by the consideration of the second RF harmonic. Using the smooth approximation the new effective potential U_{eff} can be obtained. The shape of this effective potential deforms significantly. The analysis of the U_{eff} shows that the phase capture and the acceleration gradient are increasing in this case. The transmission coefficient K has maximum when $\chi = E_{\nu}^{(2)}/E_{\nu}^{(0)} = 0.15$ (Fig. 4). The

dependence of K on the E_o/E_v for $\chi=0.15$ is been imaged in Fig. 2, curve 3. The limit of K=0.9 if $E_o \ge E_v$ and $L_f=0.75$ m. The transverse emittances for D^+ and D^- are identical too and the space charge compensation effect is preserved.

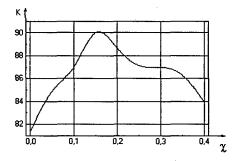


Figure 4: Transmission coefficient K versus χ .

5 CONCLUSION

The computer 3D simulation of the ribbon beam dynamics in the undulator linac is fulfilled. The optimal parameters of the UNDULAC are calculated. A preliminary design leading to the ion beam transmission larger than 90% is presented. The possibility of simultaneous acceleration of D^+ and D^- ions in the UNDULAC is shown. It is proved that space overlapping of the positively and negatively charged ion beams allows to obtain space charge compensation. Simulation results for the design of the undulator linac with two component ion beam are presented.

- [1] E.S. Masunov, Zh. Tekh. Fiz. vol.60, p 152 (1990)
- [2] E.S. Masunov, Proc. of the XVIII International Linac Conf., Geneva, Switzerland, CERN 96-07, 1996, vol.2, p.487-489
- [3] E.S.Masunov, A.P.Novikov, Proc. 1991 Part. Accel. Conf., San Francisco, vol.5, p.3177 (1991)
- [4] E.S. Masunov, A.S. Roshal, Proc. 1997 Part. Accel. Conf., Vancouver, p.2835 (1997)
- [5] E.S. Masunov, A.P. Novicov, Proc. IV Europe Part. Accel. Conf., London, v. 2, p. 1171 (1994)

A Calculation of the Dynamic Aperture of the LHC at Collision * †

Norman M. Gelfand, Fermilab, Batavia, IL

Abstract

The dynamic aperture for version 5.1, with a $300\mu r$ crossing angle at IP1 and IP5, of the Large Hadron Collider (LHC) lattice has been estimated using the tracking code TEVLAT. The dynamic aperture calculated here is due to the magnetic field errors in the high gradient quadrupoles (MQX) in the two low- β interaction regions at IR1 and IR5. No errors were assigned to the magnets in the arc regions of the lattice, nor were beam-beam effects incorporated. The dynamic aperture is expressed in terms of the σ of the beam corresponding to the beam emittance of 3.75mm mr. With only short term tracking, the combined effect of the multipoles and the crossing angle is to yield an average (over multipole coefficients generated with 100 different seeds) dynamic aperture of $\approx 11.7 \pm 1.2\sigma$.

1 INTRODUCTION

It is necessary with any new lattice, to try and calculate the emittance of the beam that can be accepted by the lattice and to verify that the acceptance, the *dynamic aperture*, is large enough for the intended beam. The physical aperture of the magnets, of course, sets the absolute upper limit to the dynamic aperture, but with superconducting magnets the dynamic aperture is typically limited by the high order multipoles (the *magnets errors*) used to describe the field of the magnet.

The methodology for calculating the dynamic aperture is fairly standard:

- Construct a computer model of the lattice;
- Adjust the tunes and chromaticites with the arc quadrupoles and sextupoles to the nominal values;
- Introduce the magnetic field errors;
- Track a series of test particles for a given number of turns;
- Impose an aperture limit of ±30mm; and
- Calculate the emittance of the test particles which survive for the required number of turns.

While well defined, this procedure can only give an upper limit to the dynamic aperture since,

 The model of the lattice is an approximation to the true lattice and all the unknown errors which exist in an actual lattice are not incorporated in to the model.

- The actual magnet errors are not known until the magnets are built and measured.
- A particle can be realistically tracked for a number of turns which is far smaller than the number of turns it will need to survive in the actual lattice.

With these caveats, results are presented on the dynamic aperture for version 5.1 the Large Hadron Collider (LHC) lattice. The lattice has the beams crossing at IR1 and IR5 with a 300μ r full crossing angle. At IR1 the crossing angle is vertical and at IR5 horizontal. Tracking was done using the code TEVLAT [1].

The lattice has regions of very high- β ($\approx 4700m$) in the inner triplet quadrupoles (MQX), in which the beam is off axis, which generate the low- β at the interaction points. The corresponding maximum β in the arcs is only $\approx 180m$. The effect of magnetic field errors increase with β so it is expected that the errors in the MQX will dominate the calculation of the dynamic aperture. For that reason only the magnetic field errors in the MQX will be considered and incorporated into this calculation.

2 MAGNET ERRORS

The low- β insertions at each IR are formed by a quadrupole triplet consisting of four quadrupoles [2]. Two different designs of the coils for the MQX will be used in the LHC, those built at FERMILAB and those built at KEK. In the model the outer members of the triplet are KEK magnets while the two inner magnets are from FERMILAB. The field errors for each are expressed in terms of multipole coefficients given at a reference radius of 17mm. The values for the multipole coefficients are given in Table 1 and Table 2.[3]. One hundred different sets of multipole errors were generated from these tables.

Table 1
FNAL Reference Harmonics at Collision. (Version 2)
Reference radius= 17.0mm

CERN				
n	$\langle b_n \rangle$	$\sigma(b_n)$	$\langle a_n \rangle$	$\sigma(a_n)$
3	.000	.800	.000	.800
4	.000	.800	.000	.800
5	.000	.300	.000	.300
6	.000	.600	.000	.100
7	.000	.060	.000	.060
8	.000	.050	.000	.040
9	.000	.030	.000	.020
10	.000	.030	.000	.030

^{*} Work supported by the U.S. Department of Energy under contract No. DE-AC02-76CHO3000.

[†] Email: gelfand@popgtw.fnal.gov

Table 2
KEK Reference Harmonics at Collision. (Modified.)
Reference radius= 17.0mm

CERN				
n	$\langle b_n \rangle$	$\sigma(b_n)$	$\langle a_n \rangle$	$\sigma(a_n)$
3	.000	1.00	.000	1.00
4	.000	.570	.000	.570
5	.000	.380	.000	.380
6	.000	.190	.000	.190
7	.000	.060	.000	.060
8	.000	.030	.000	.010
9	.000	.010	.000	.010
10	-0.250	.010	.000	.010

3 METHOD AND RESULTS

A particle was launched at a point in phase space (x, x' = 0), (y, y' = 0). For each value of x, which ranged from x = 0 to $x = 20 \cdot \sigma_x$ [4] in steps of σ_x , the maximum value of y was found where the particle completed 1024 turns. The stable points, from the hundred sets of multipole errors, are plotted in Figure 1.

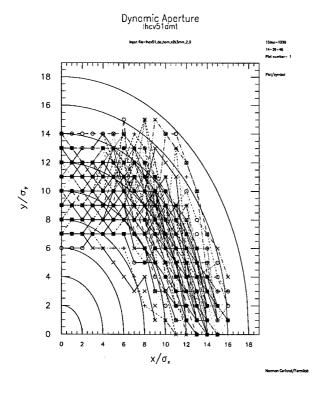


Figure 1: Stable Points for 100 Different Sets of Multipole Errors.

It is apparent that the dynamic aperture depends on the particular values of the multipole coefficients. That is, the size of the random component of the multipoles is large enough that the dynamic aperture can change by a significant factor depending on the value in a given magnet.

In order to provide a more concise representation of the dynamic aperture, (though a less complete one) for each set of the multipoles errors, the average radius of the stable points was computed. The results are histogrammed in Figure 2 [5].

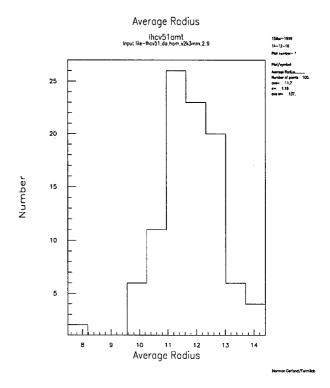


Figure 2: Distribution of the Radius for the Stable Points

The average dynamic aperture, that is the average of the average radius for the 100 distributions is 11.7σ with a width of $\approx 1.2\sigma$. Depending on the set of multipoles found in the actual magnets the dynamic aperture could be as small as $\approx 8\sigma$ or as large as $\approx 14\sigma$.

The dynamic aperture also depends on whether the initial displacement was primarily along x or along y. Figure 3 plots the average dynamic aperture as a function of $\epsilon_x/(\epsilon_x+\epsilon_y)$. It is quite clear that the dynamic aperture, when a particle is launched along the y direction, is smaller than if it were launched along the x direction.

It is helpful to compute the dynamic aperture with only some of the multipoles present. Figure 4 shows the effect on the dynamic aperture when the highest order of the multipoles is changed. The results are summarized in Table 3.

If it were possible to remove the b_{10} and a_{10} multipole errors from the magnets we would gain $\approx 1.6\sigma$ in the dynamic aperture. There are no other significant improvements until we remove the b_6 and a_6 from the magnets.

The variance of the distribution of the dynamic apertures decreases when the octupole contribution to the magnetic field is removed. The octupole moment contributes to an amplitude dependent tune shift. A smaller random octupole moment would reduce the spread in the dynamic aperture

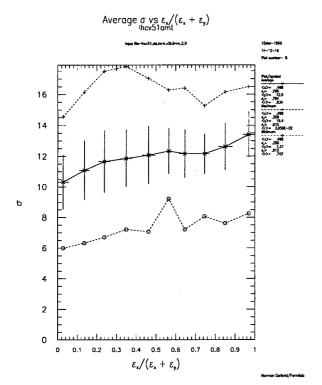


Figure 3: Dynamic Aperture vs. $\epsilon_x/(\epsilon_x + \epsilon_y)$ The upper and lower curves are the maximum and minimum values coming from the different sets of the moments.

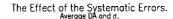
Table 3
The Effect of Removing High Order Multipoles on the
Dynamic Aperture

Min. Order	Max. Order	Average DA	Variance
3	10	11.659	1.181
3	9	13.396	1.551
3	· 8	13.446	1.533
3	7	13.459	1.518
3	6	13.530	1.554
3	5	14.147	1.272
3	4	14.576	1.032
3	3	15.199	.867

seen in Figure 1 and Figure 2.

4 CONCLUSION

This is the first use of TEVLAT for calculations on the LHC lattice, though it has been used extensively with other lattices. The calculations presented here utilize 100 different sets of multipole error coefficients, a factor of 10 more than calculations reported earlier. The large variation in the dynamic aperture, including tails in the distribution, makes it important to do calculations with a large number of sets of multipole coefficients for the MQX. This variance suggests a need to monitor the random component of the magnet er-



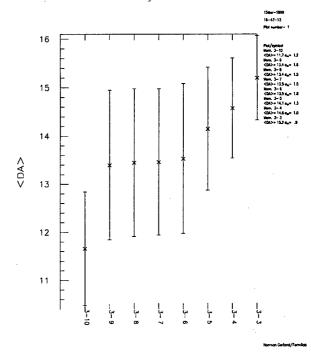


Figure 4: The Variation in the Dynamic Aperture with the Order of the Multipoles

rors, particularly the octupoles, since they make a significant contribution to the computed variance in the dynamic aperture. Non-linear correctors could also be used to reduce the variance.

The dynamic aperture appears sensitive to the highest order multipole specified in the reference tables. Tracking has also been done with errors in all magnets derived from an earlier version of the Fermilab error table. This error table included estimates for the moments up to b_{14} and a_{14} . Those calculations showed a decrease in the dynamic aperture when the moments beyond b_{10} were included. It is important to check that the dynamic aperture is not sensitive to the multipoles which will be present in the magnets, but because they are not specified, are not included in the calculations described here.

- [1] A. Russell, private communication.
- [2] The two middle magnets are used as a single optical element.
- [3] The uncertainty in the average multipoles, db_n and da_n were not included in the calculations.
- [4] σ_x and σ_y are defined by the values of the lattice functions at the launch point and the normalized invariant emittance of the beam. For the LHC $\epsilon_{nx}=\epsilon_{ny}=3.75$ mmmr.
- [5] The radius of a stable point is defined as $r = \sqrt{(x/\sigma_x)^2 + (y/\sigma_y)^2}$

PARTICLE DYNAMICS IN LOW-ENERGY TRAVELLING-WAVE LINACS

J.M.Corstens, A.F.J.Hammen, J.I.M. Botman Eindhoven University of Technology, Cyclotron Laboratory, P.O.Box 513, 5600 MB Eindhoven, The Netherlands.

Abstract

In this paper, we present the particle dynamics in lowenergy travelling-wave linear accelerators, applying analytical theory, based on Hamiltonian mechanics, and numerical simulations, performed by commercially available codes. The paper is an extension on earlier work, presented at EPAC'98. Cylindrical co-ordinates are used and solenoid magnetic fields are incorporated. The Hamiltonian equations of motion are given and examples of calculations are presented and compared to numerical simulations, yielding excellent agreement between both approaches.

1 INTRODUCTION

At the Eindhoven University of Technology, a Hamiltonian theory of particle motion of accelerated electrons in standing-wave RF structures has been developed[1]. However, this theory was only valid in principle under the assumption that the particle velocity equals the phase velocity of the main accelerating wave. This condition is not fulfilled in low-energy linear accelerators. The present, adapted Hamiltonian theory, in which also solenoidal magnetic fields are incorporated does not have this restriction. The set of equations obtained with this Hamiltonian theory is suitable for particle motion calculation. Calculations using this set of equations are compared to the results of a commercially available particle tracking code, yielding excellent agreement.

2 THE EQUATIONS OF MOTION

The vector potential in cilindrical co-ordinates representing electromagnetic waves in the periodic part of the linac is given by [2]:

$$A_{r} = \sum_{n} \frac{k_{n}}{\omega} \frac{a_{n} E_{z}(z)}{\alpha_{n}} I_{1}(\alpha_{n} r) \cos(k_{n} z - \omega t),$$

$$A_{\theta} = \sum_{j=1}^{8} A_{\theta, j},$$

$$A_{z} = -\sum_{n} \frac{a_{n} E_{z}(z)}{\omega} I_{0}(\alpha_{n} r) \sin(k_{n} z - \omega t),$$
(1)

in which $\sum_{n=-\infty}^{\infty} stands$ for $\sum_{n=-\infty}^{\infty} a_n$, a_n for the Fourier coefficients, $k_n = k_f + 2\pi n/d$ with d the cell length and k_f the phase shift per cell, $\alpha_n^2 = k_n^2 - k^2$, $E_z(z)$ the amplitude of the electric field in the z-direction. Note that this amplitude is a

function of the longitudinal co-ordinate z. A_{θ_j} is the vector potential of the static magnetic field j. This vector potential of solenoid j, expanded up to third order in r, reads:

$$A_{\theta,j}(r,z) = \frac{1}{2} r B_z(r=0,z) - \frac{1}{16} r^3 \frac{\partial^2}{\partial z^2} (B_z(r=0,z)),$$
with: $B_z(r=0,z) = -\mu_0 \frac{\partial}{\partial z} V_m(z),$ (2)

in which:

$$V_{m}(z) = -\frac{NI}{2L} \left(\sqrt{\left(z + \frac{L}{2}\right)^{2} + a^{2}} - \sqrt{\left(z - \frac{L}{2}\right)^{2} + a^{2}} \right),$$

with μ_o the magnetic permeability in vacuum, I the current through the solenoid, N the number of turns, L the length and a the radius of the solenoid. z is defined at the axis with respect to the center of the solenoid.

Relativistic motion is described by the Hamiltonian:

$$H = \{E_r^2 + (p_r - eA_r)^2 c^2 + \left(\frac{p_\theta}{r} - eA_\theta\right)^2 c^2 + (p_z - eA_z)^2 c^2\}^{\frac{1}{2}},$$
(3)

where c is the speed of light, E, the particle rest energy, p_{ρ} , p_{θ} , p_z the canonic momenta in cylindrical co-ordinates and A_{ρ} , A_{θ} , A_z the components in cylindrical co-ordinates of the vectorpotential, given by eq. 1. The new Hamiltonian becomes $K_1 = -p_z$, -H and t form a new pair of conjugated canonical variables. On this Hamiltonian K_1 the following scaling transformations is performed:

$$\pi_{r} = \frac{c}{H_{i}} p_{r}, \pi_{\theta} = \frac{c}{H_{i}} p_{\theta}, \pi_{z} = \frac{c}{H_{i}} p_{z}, h = -\frac{H}{H_{i}},$$

$$e_{r} = \frac{E_{r}}{H_{i}}, \varepsilon_{n} = \frac{ea_{n}E_{z}(z)}{H_{i}k}, \varsigma = ct.$$
(4)

in which H_i is the initial energy, yielding Hamiltonian $K_2 = -\pi_i$:

$$K_{2} = -\left\{h^{2} - e_{r}^{2} - \left(\pi_{r} - eA_{r}^{*}\right)^{2} - \left(\frac{\pi_{\theta}}{r} - eA_{\theta}^{*}\right)^{2}\right\}^{\frac{1}{2}} - eA_{z}^{*}, \quad (5)$$

in which:
$$\vec{A}^* = \frac{c}{H} \vec{A}$$
.

In eq. 5 ζ is transformed to $\zeta_2 = \zeta - k_z / k$ (new variables are indicated by higher numerical subscripts), by generating function $G_0 = -h\zeta_2 - hk_z / k$ ($h_2 = h$). Further the signs of h_2 and ζ_2 are changed in h_3 and ζ_3 by generating function

 $G_1 = h_2 \zeta_r$. Now h_3 is a positive quantity and $k\zeta_3$ has the meaning of phase. The final Hamiltonian K_f becomes (in new co-ordinates, numerical subscripts are omitted):

$$K_{f} = K_{2} + \frac{\partial G_{0}}{\partial z} + \frac{\partial G_{1}}{\partial z} = \frac{k_{f}}{k} h - \{h^{2} - e_{r}^{2} - (\pi_{r} - eA_{r}^{*})^{2} - (\frac{\pi_{\theta}}{r} - eA_{\theta}^{*})^{2}\}^{\frac{1}{2}} - eA_{z}^{*},$$
(6)

in which the arguments of the components of the vector potential $(k_n z - \omega t)$ in eq. 1 has been replaced by $(2\pi n z/d + k\zeta)$. The equations of scaled energy and phase are:

$$\frac{dh}{dz} = -\frac{\partial K_f}{\partial \varsigma} = \frac{\pi_{r,kin}}{\pi_{z,kin}} \left(-\sum_n \frac{\varepsilon_n}{\alpha_n} k_n k I_1(\alpha_n r) \sin\left(\frac{2\pi n}{d} z + k\varsigma\right) \right) - \sum_n \varepsilon_n k I_0(\alpha_n r) \cos\left(\frac{2\pi n}{d} z + k\varsigma\right), \tag{7}$$

$$\frac{d\varsigma}{dz} = \frac{\partial K_f}{\partial h} = -\frac{h}{\pi_{z,kin}} + \frac{k_f}{k},$$

in which

$$\pi_{z,kin} = \sqrt{h^2 - e_r^2 - \pi_{r,kin}^2 - \left(\frac{\pi_{\theta,kin}}{r}\right)^2}.$$

The transversal equation of motion for the canonical momentum reads:

$$\frac{d\pi_{r,can}}{dz} = -\frac{\partial K_1}{\partial r} = \frac{\pi_{r,kin}}{\pi_{z,kin}} e^{\frac{\partial A_r^*}{\partial r}} + e^{\frac{\partial A_z^*}{\partial r}} + \frac{\pi_{\theta,kin}^2}{r^3 \pi_{z,kin}} + e^{\frac{\pi_{\theta,kin}}{r^2 \pi_{z,kin}}} \frac{\partial (rA_{\theta}^*)}{\partial r}.$$
(8)

This expression is inconvenient for practical use. Furthermore, $\pi_{r,can}$ is not of interest but $\pi_{r,kin}$, therefore the differential equation for $\pi_{r,kin}$ will be derived in the appendix and is given by:

$$\frac{d\pi_{r,kin}}{dz} = \sum_{n} \varepsilon_{n} \frac{I_{1}(\alpha_{n}r)}{\alpha_{n}} k \left(k - k_{n} \frac{h}{\pi_{z,kin}} \right) \sin \left(\frac{2\pi n}{d} z + k\zeta \right) + \frac{\pi_{\theta,kin}^{2}}{r^{3}\pi_{z,kin}} + e \frac{\pi_{\theta,kin}}{r^{2}\pi_{z,kin}} \frac{\partial (rA_{\theta}^{*})}{\partial r}.$$
(9)

The remaining transversal equations are:

$$\frac{dr}{dz} = \frac{\partial K_f}{\partial \pi_{r,can}} = \frac{\pi_{r,kin}}{\pi_{z,kin}},$$

$$\pi_{\theta,kin} = \pi_{\theta,can}(0) - erA_{\theta}^*(r,z),$$

$$\frac{d\theta}{dz} = \frac{\partial K_f}{\partial \pi_{\theta}} = \frac{\pi_{\theta,kin}}{r^2 \pi_{\theta,kin}}.$$
(10)

It is seen that $\pi_{r,kin}$ is needed in the set of equations and not $\pi_{r,can}$. Furthermore, the expression $d\pi_{r,kin}/dz$ is much simpler than the expression $d\pi_{r,can}/dz$. With this set of equations particle motion calculations can be performed.

The equations of motion for calculations without static external solenoidal magnetic field are obtained by setting A_{θ} equal to zero. Calculations without electromagnetic field are obtained by setting $\mathcal{E}_{n}(z)$ equal to zero. In this case the differential equation for energy changes in h(z)=1 and the differential equation for the phase does not have any meaning anymore, because of the absence of an electromagnetic field.

3 CALCULATIONS COMPARED TO SIMULATIONS

In this section calculations based on the Hamiltonian equations of motion of the previous section are presented and compared to the results of the particle-tracking code General Particle Tracer (GPT) [3]. In this code, the same electric and magnetic field description is specified as is used in the Hamiltonian calculations, however this particle-tracking code uses an entirely different calculation method. Calculations of motion in an electromagnetic field with and without static external magnetic field have been applied to the periodic part of the Eindhoven 10 MeV linac.

The energy and phase have been calculated for the 10 MeV linac using eq. 7 (fig. 1). Because of the small dependence of the particle distance to the z-axis on the calculation of energy and phase, particles with a different initial position and divergence will have similar energy and phase evolution. Calculations are performed at four different injection phases, with an initial energy of 1 MeV. Energy calculations are compared to the results of GPT, showing good agreement between both methods. The particle phase is not provided by GPT, so a comparison of phases is not possible. However, because of the agreement in energy calculations, it is obvious that the Hamiltonian phase calculations must be consistent.

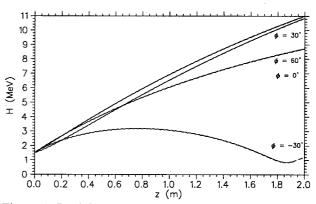


Figure 1: Particle energy H as a function of longitudinal co-ordinate z in the periodic part of the linac, at various injection phases. Hamilton calculations are presented by the dashed line, GPT simulations by the solid line.

Fig. 2 depicts the calculations of the distance of a particle to the z-axis, r, and the divergence r' in the linac, using eqs. 9 and 10. Particles are injected at various phases at 1 MeV parallel to the z-axis with an initial radius r = 3mm. It is shown that there is a good agreement between Hamiltonian calculations and GPT simulations.

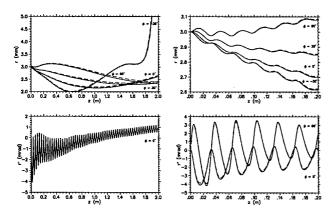


Figure 2: Particle distance to z-axis, r, and divergence, r', calculations as a function of z, for the entire periodic part of the linac (left figs.) and for the first six cells of the periodic part (right figs.) Hamilton calculations are presented by the dashed line, GPT simulations by the solid line.

Fig. 3 shows the azimuthal co-ordinate θ and its derivative θ ' as a function of z in the linac for the same calculations as depicted in fig. 2. Again there is a good agreement between Hamiltonian calculations and GPT simulations.

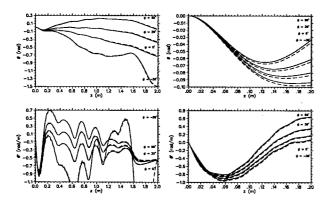


Figure 3: Particle azimuthal co-ordinate, θ , and its derivative, θ' , calculations as a function of z, for the entire periodic part of the linac (left figs.) and for the first six cells of the periodic part (right figs.) Hamilton calculations are presented by the dashed line, GPT simulations by the solid line.

4 CONCLUSIONS

An analytic description of particle motion in linear accelerators has been developed, in an earlier paper restricted to higher energy standing wave structures,

while in the present paper this has been extended to the case of low-energy travelling-wave linacs, in which solenoidal fields may be incorporated. The Hamiltonian calculations yield a remarkable agreement with results of particle-tracking codes but they are much faster performed than simulations by these codes.

5 REFERENCES

- A.F.J. Hammen, J.M. Corstens, J.I.M. Botman, H.L. Hagedoorn, W.H.C. Theuws, "Hamiltonian Calculations on Particle Motion in Linear Electron Accelerators", European Particle Accelerator Conference, Stockholm, Sweden (1998).
- [2] R.W. de Leeuw, "The accelerator injection chain of the electron storage ring EUTERPE", Ph.D. Thesis, Eindhoven University of Technology, Eindhoven, The Netherlands (1996).
- [3] General Particle Tracer, "User Manual", Pulsar Physics, Utrecht, The Netherlands (1997).

APPENDIX

Consider the following equations:

$$\frac{d\pi_{r,kin}}{dz} = \frac{d\pi_{r,can}}{dz} - e\frac{dA_r^*}{dz},$$

$$\frac{dA_r^*}{dz} = \frac{\partial A_r^*}{\partial r}\frac{dr}{dz} + \frac{\partial A_r^*}{\partial z} + \frac{\partial A_r^*}{\partial t}\frac{1}{v_z},$$

$$\frac{dr}{dz} = \frac{\pi_{r,kin}}{\pi_{z,kin}}.$$
(A1)

Thus, using eq. 8:

$$\frac{d\pi_{r,kin}}{dz} = e^{\frac{\partial A_z^*}{\partial r}} - e^{\frac{\partial A_r^*}{\partial z}} - e^{\frac{\partial A_r^*}{\partial t}} \frac{1}{v_z} + \frac{\pi_{\theta,kin}^2}{r^3 \pi_{z,kin}} + \frac{e^{\frac{\pi_{\theta,kin}}{r^2 \pi_{z,kin}}}}{e^{\frac{\pi_{\theta,kin}}{r^2 \pi_{z,kin}}}} \frac{\partial (rA_\theta^*)}{\partial r}.$$
(A2)

Substitution of the vectorpotential given by eq. 1 yields:

$$\frac{d\pi_{r,kin}}{dz} = \sum_{n} \varepsilon_{n} I_{1}(\alpha_{n} r) \left\{ -\alpha_{n} + \frac{k_{n}^{2}}{\alpha_{n}} - \frac{\omega}{v_{z}} \frac{k_{n}}{\alpha_{n}} \right\} \sin(k_{n} z - \omega t) + \frac{\pi_{\theta,kin}^{2}}{r^{3} \pi_{z,kin}} + e \frac{\pi_{\theta,kin}}{r^{2} \pi_{z,kin}} \frac{\partial (r A_{\theta}^{*})}{\partial r}.$$
(A3)

in which the z-dependence of the amplitude in A, has been ignored. After some mathematical manipulation and replacement of the argument $(k_{\mu}z-\omega t)$ by $(2\pi nz/d+k\zeta)$ the following expression holds:

$$\frac{d\pi_{r,kin}}{dz} = \sum_{n} \varepsilon_{n} \frac{I_{1}(\alpha_{n}r)}{\alpha_{n}} k \left(k - k_{n} \frac{h}{\pi_{z,kin}} \right) \sin \left(\frac{2\pi n}{d} z + k\zeta \right) + \frac{\pi_{\theta,kin}^{2}}{r^{3}\pi_{z,kin}} + e \frac{\pi_{\theta,kin}}{r^{2}\pi_{z,kin}} \frac{\partial (rA_{\theta}^{*})}{\partial r}. \tag{A4}$$

BUNCH ENERGY LOSS IN CAVITIES: DEPENDENCE ON BEAM VELOCITY *

Sergey S. Kurennoy, Los Alamos National Laboratory, Los Alamos, NM 87545, USA

Abstract

Proton or H⁻ linacs accelerate particles through the wide range of the particle velocities. For intense beams, and especially when superconducting cavities are used, a detailed knowledge about how the beam energy loss depends on the beam velocity $\beta = v/c$, and what part of the lost energy remains in the cavity, is required to calculate the cavity heat load. Using a frequency-domain approach, we calculate the bunch energy loss as a function of β for a few particular cases. We are mostly concerned about the cavity modes below the beam-pipe cutoff, because they produce most of the cavity heating. While the loss factor due to an individual mode can show peaks at some particular values of β , the total loss for important particular cases was found smoothly decreasing as β decreases. Comparison with time-domain results for the ultra-relativistic case, $\beta \rightarrow 1$, is also presented.

1 INTRODUCTION

Many modern accelerator projects — Accelerator Production of Tritium (APT) [1], Spallation Neutron Source (SNS) [2], and the accelerator-driven transmutation of nuclear waste (ATW) [3] — consider to use linacs to accelerate intense proton or H⁻ beams providing the final beam power in the range 1-200 MW. Most of them will also rely on superconducting (SC) technology for the accelerating cavities, e.g. [1, 3], to reduce operational costs. With the final beam energies around 1-2 GeV, the ion beam during acceleration changes its velocity from a non-relativistic one to $\beta = v/c = 0.9 - 0.95$. At the same time, the number of types of SC cavities is limited to a few due to cost and production reasons. In the APT linac design [1] there are only two types of SC cavities, optimized for $\beta = 0.64$ and $\beta = 0.82$, respectively, but they are to accelerate protons in the velocity range from $\beta = 0.58$ (proton energy 211 MeV) to 0.94 (1.7 GeV). It is important to know how the amount of the beam energy deposited in the cavities depends on the beam velocity.

It is common to believe that loss factors of a bunch moving along an accelerator structure at velocity $v=\beta c$ with $\beta<1$ are lower than those for the same bunch in the ultrarelativistic case, $\beta\to1$. Computations with time-domain codes like MAFIA [4] or ABCI [5] work only for $\beta=1$, because of difficulties in imposing proper boundary conditions at the open ends of the beam pipe in the numerical time-domain approach for $\beta<1$. Often the loss factors computed numerically for the ultra-relativistic bunch are considered the upper estimates for $\beta<1$. We study the

 β -dependence of loss factors using the frequency-domain approach and concentrating primarily on the cavity modes below the beam pipe cutoff frequency, since they contribute the major part of the cavity heat load. In particular, we find that the above assumption on the upper estimate from the ultra-relativistic case may be incorrect, especially when only some individual modes of the cavity are concerned. More details can be found in a recent paper [6].

2 CAVITY LOSS FACTORS

Let \vec{E}_s , \vec{H}_s be a complete set of eigenfunctions (EFs) for the boundary problem in a closed cavity with perfect walls. The longitudinal impedance can be written as (e.g., [7])

$$Z(\beta,\omega) = -i\omega \sum_{s} \frac{1}{\omega_s^2 - \omega^2} \frac{|I_s(\beta,\omega)|^2}{2W_s}, \qquad (1)$$

where $I_s(\beta,\omega) = \int_L dz \exp(-i\omega z/\beta c) E_{sz}(0,z)$ is the overlap integral and W_s is the energy stored in the s-th mode. Here $E_{sz}(0,z)$ is the longitudinal component of the s-th mode electric field taken on the chamber axis.

The loss factor $k=\pi^{-1}\int_0^\infty d\omega \ Re \ Z(\beta,\omega)|\lambda(\omega)|^2$, where $\lambda(\omega)=\int ds \exp\left[i\omega s/(\beta c)\right]\lambda(s)$ is a harmonic of bunch spectrum, can be expressed as a series by assuming all $Q_s>>1$ and integrating formally $Re \ Z(\beta,\omega)$ in Eq. (1). For a Gaussian bunch with rms length 2σ , it gives $k(\beta,\sigma)=\sum_s k_s(\beta,\sigma)$, where the loss factors of individual modes k_s are

$$k_s(\beta, \sigma) = \exp \left[-\left(\omega_s' \sigma/\beta c\right)^2 \right] |I_s(\beta, \omega_s')|^2 / (4W_s)$$
$$= \exp \left[-\left(\omega_s' \sigma/\beta c\right)^2 \right] \omega_s' R_s(\beta) / (2Q_s) . (2)$$

In the last expression the shunt impedance $R_s(\beta)$ and Q-factor for the s-th cavity mode are used.

From a physical viewpoint, the loss factor (2) of a given mode includes two velocity-related effects. The exponent factor shows that the bunch length σ effectively increases to σ/β . The β -dependence of R_s is essentially due to that of the cavity transit-time factor for this resonance mode: the effective cavity length scales as $1/\beta$. Although Eqs. (2) give us the dependence of the loss factor on β , it is only practical when the number of strong resonances is small, since this dependence varies from one resonance to another:

$$\frac{k_s(\beta,\sigma)}{k_s(1,\sigma)} = \exp\left[-\left(\frac{\omega_s'\sigma}{c\beta\gamma}\right)^2\right] \frac{R_s(\beta)}{R_s(1)}, \quad (3)$$

where
$$\gamma = 1/\sqrt{1-\beta^2}$$
.

^{*} Work supported by the U.S. Department of Energy.

It follows from Eq. (3) that for long bunches loss factors will decrease rapidly with β decrease, as $\exp(-\beta^{-2})$. The impedance ratio dependence on β is generally more complicated, and we consider below a few typical examples.

3 EXAMPLES

3.1 Cylindrical Pill-Box

For a cylindrical pill-box cavity of length L and radius d, in the limit of vanishing radius of the beam pipes, the ratio of loss factors (3) for the lowest E_{010} -mode is

$$\frac{k_{010}(\beta,\sigma)}{k_{010}(1,\sigma)} = \exp\left[-\left(\frac{\mu_{01}\sigma}{d\beta\gamma}\right)^2\right] \left(\beta \frac{\sin\frac{\mu_{01}L}{2\beta d}}{\sin\frac{\mu_{01}L}{2d}}\right)^2, \quad (4)$$

where μ_{mn} is the *n*-th zero of the first-kind Bessel function $J_m(x)$. The ratio is almost independent of β when the bunch is short, $\sigma \ll d$, and the cavity is short compared to its radius, $L \ll d$. For longer cavities, however, the ratio oscillates and can exceed 1 many times, see [6]. Obviously, a similar behavior is expected for any other individual resonance mode in this case.

3.2 Small Discontinuity

Consider now the case with a small number of modes below the pipe cutoff. The simplest example is a small discontinuity on a smooth beam pipe, like a small axisymmetric cavity or a hole. Let the area of the longitudinal cross section of the cavity be A, and its length and depth be small compared to the pipe radius b, i.e. $A \ll b^2$. In this case there exists a trapped mode [8] with the frequency slightly below the pipe cutoff frequency $f_c = \mu_{01} c/(2\pi b)$. The on-axis longitudinal electric field of the mode is given by a simple expression $E_z(z) = E_z(0) \exp(-|z|/L)$, where $L = b^3/(\mu_{01}^2 A) \gg b$ is the characteristic length occupied by the trapped mode in the pipe.

The overlap integral is easily calculated analytically, and the ratio of the shunt impedances Eq. (3) is

$$\frac{R_s(\beta)}{R_s(1)} = \beta^4 \left[\frac{(\omega L/c)^2 + 1}{(\omega L/c)^2 + \beta^2} \right]^2 \simeq \beta^4 , \qquad (5)$$

where $\omega \simeq 2\pi f_c = \mu_{01}c/b$ is the resonance frequency. The last expression in the rhs of Eq. (5) is due to the fact that $\omega L/c \gg 1$, since $\omega b/c \simeq \mu_{01}$ and $L \gg b$. The above results hold for a small hole in the pipe wall: one just has to substitute $A = \alpha_m/(4\pi b)$, where α_m is the magnetic susceptibility of the hole, in all expressions, see [8]. For comparison with a small but finite-size cavity, see [6].

3.3 APT 1-cell Cavities

As a more realistic example, consider an APT SC 1-cell cavity, e.g. [9]. Direct time-domain simulations with the codes MAFIA [4] and ABCI [5] show the existence of only 2 longitudinal modes below the cutoff for the $\beta = 0.64$

cavity, and only 1 such mode for $\beta=0.82$, in both cases including the fundamental mode at $f_0=700$ MHz. The contributions from these lowest resonance modes for a Gaussian bunch with $\sigma=3.5$ mm for $\beta=0.64$ and $\sigma=4.5$ mm for $\beta=0.82$ are about 1/3 of the total loss factor.

The on-axis longitudinal field of the fundamental mode is fitted very well by $E_z(z)=E_z(0)\exp{[-(z/a)^2]}$, with a=0.079 m for $\beta=0.64$ and a=0.10 m for $\beta=0.82$. The ratio of the shunt impedances in Eq. (3) is then easy to get analytically: $R_s(\beta)/R_s(1)=\exp{\left[-(\omega a/\beta\gamma c)^2/2\right]}$, where $\omega=2\pi f_0$. The resulting loss factor for the lowest mode for the cavity design value of $\beta=0.64$ is 0.378 times that with $\beta\to 1$, and for $\beta=0.82$ is 0.591 times the corresponding $\beta\to 1$ loss factor.

3.4 APT 5-cell Cavities

For 5-cell APT SC cavities the lowest resonances are split into 5 modes which differ by a phase advance per cell, $\Delta\Phi$, and their frequencies are a few percent apart [9]. The calculated on-axis fields of all five modes in the TM₀₁₀-band, with $\Delta\Phi$ from $\pi/5$ to π — the last one is the accelerating mode of the cavity — are shown for the cavity with $\beta=0.82$ in Fig. 1, left column. Using MAFIA results for the fields of the modes to calculate overlapping integrals in Eq. (2) with an arbitrary β , we find the β -dependencies of the loss factors for the five TM₀₁₀-modes, see the right column of Fig. 1. Obviously, they are strongly influenced by the mode field pattern.

When we sum up all five contributions to the loss factor for this band, the resulting dependence on β is smooth, and the total loss factor decreases monotonically as β decreases, see Fig. 2. As seen in Fig. 2, the loss factor of the accelerating mode is maximal near the design β , while for all other modes it is almost zero in that region. This is not surprising, since the cavity design is optimized for that value of β to provide a strong interaction of the accelerating mode with the beam.

A similar picture holds for the $\beta = 0.64$ APT cavity: loss factors of individual modes in the given band show a rather irregular β -dependence, with peaks at different values of β , but their sum smoothly decreases with the β decrease. It works for both bands below the cutoff frequency of the pipe, TM_{010} and TM_{020} . The total loss factor for all longitudinal modes below the cutoff is shown versus β in Fig. 3, as well as the separate contributions of both bands. The contribution of the TM₀₁₀-band is certainly larger, about 0.5 V/pC for $\beta = 1$, compared to less than 0.1 V/pC from TM₀₂₀-band. These $\beta = 1$ results are in a good agreement with direct time-domain simulations using ABCI [5], see [6]. In the velocity range near the design value of $\beta = 0.64$, TM₀₁₀ contribution dominates, and the total loss factor is mostly due to the accelerating π -mode, cf. Fig. 3. The total loss factors for a given resonance band are lower for the design β than at $\beta = 1$, except the TM_{020} band for the $\beta = 0.82$ cavity. This band, however, includes some propagating modes, and for those the

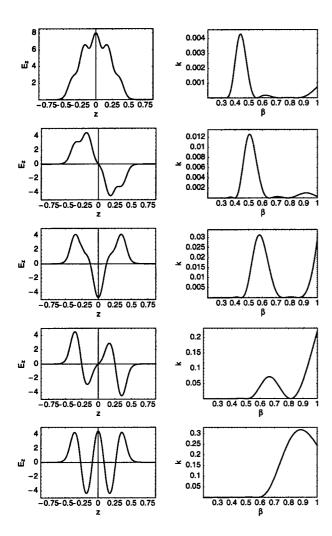


Figure 1: Longitudinal component of the on-axis electric field (arbitrary units) for the TM_{010} -modes in the 5-cell APT $\beta=0.82$ cavity versus z (m) (left column), and their loss factors (V/pC) versus β (right).

frequency-domain results can not be trusted. Its contribution is certainly very small anyway, see [6] for detail.

Of course, the contribution of higher-frequency modes to the bunch loss factor can also be significant. However, the beam energy transferred to the higher modes, which have frequencies above the cutoff and propagate out of the cavity into the beam pipes, will be deposited elsewhere outside the cavity. For the SC cavities, we are mostly concerned about the lowest resonance modes, below the cutoff, since they contribute to the heat load on the cavity itself.

4 DISCUSSION

The bunch loss factors were calculated with the frequency-domain approach as functions of the beam velocity β . The approach is useful when we know the fields of all modes that contribute significantly into the bunch energy loss. Calculating modes above the cutoff presents most difficulties, since there is no well-established numerical method, except for periodic structures. Nevertheless, for many prac-

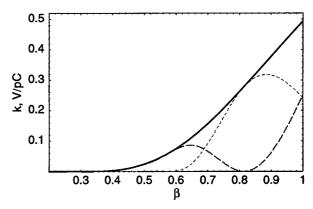


Figure 2: The loss factor for all TM₀₁₀-modes in the 5-cell APT $\beta = 0.82$ cavity versus β (solid). The contribution of the accelerating (π) mode is short-dashed, and that of all others is long-dashed.

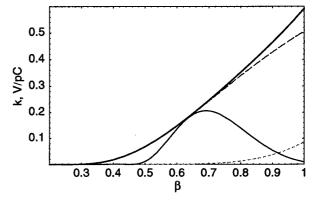


Figure 3: The total loss factor for all modes below the cutoff in the 5-cell APT $\beta=0.64$ cavity versus β . The contribution of the TM₀₁₀-band is long-dashed and that of TM₀₂₀-band is short-dashed. The thin solid line shows the loss factor for the accelerating mode, TM₀₁₀ π -mode.

tical applications, especially in SC cavities, the contribution of the lowest modes is a major concern, because the above-cutoff modes travel out of the cavity and deposit their energy far away from the structure cold parts, where the heat removal is not a big problem.

The author would like to thank Frank Krawczyk for providing MAFIA results for the 5-cell cavities.

- [1] APT CDR, Report LA-UR-97-1329, Los Alamos, 1997.
- [2] SNS CDR, Report NSNS-CDR-2/V1, Oak Ridge, 1997.
- [3] C.D. Bowman et al., NIM A230, 336 (1992).
- [4] MAFIA Release 4.00 (CST, Darmstadt, 1997).
- [5] Y.H. Chin, Report LBL-35258, Berkeley, 1994.
- [6] S.S. Kurennoy, Phys. Rev. ST Accel. Beams 2, 032001 (1999).
- [7] S.S. Kurennoy, Phys. Part. Nucl. 24, 380 (1993).
- [8] G.V. Stupakov and S.S. Kurennoy, Phys. Rev. E 49, 794 (1994); S.S. Kurennoy, Phys. Rev. E 51, 2498 (1995).
- [9] F.L. Krawczyk, Proc. PAC97, Vancouver, BC, 1997, p.3093.

Single-Mode Beam-Cavity Interaction In Relativistic Klystrons*

S.M. Lidia, Lawrence Berkeley National Laboratory, Berkeley, CA 94720 USA

Abstract

The interaction between a modulated, intense electron beam and a single-mode rf cavity is discussed. A formalism is described which accounts for steady-state and transient beam loading, input/output waveguide coupling, and finite Q effects. A circuit equation is analyzed for short-time behavior. Algorithms are presented for designing detuned structures to ensure longitudinal stability in relativistic klystron two-beam accelerators.

1 FUNDAMENTAL ELEMENTS AND DYNAMICS

We are specifically concerned with the interaction of the beam with the fundamental monopole mode (TM_{010}) in a single standing-wave (SW) idler or output cavity. We express the cavity electric field as a product of a time-dependent mode amplitude with a spatial mode profile (indexed by λ),

$$\overrightarrow{E}(\overrightarrow{r},t) = a_{\lambda}(t)\overrightarrow{E_{\lambda}}(\overrightarrow{r}). \tag{1}$$

The spatial profile of the mode is assumed to have the socalled 'Slater' normalization,

$$\int_{cavity} d^3r \overrightarrow{E}_{\lambda}(\overrightarrow{r}) \cdot \overrightarrow{E}_{\lambda}(\overrightarrow{r}) = 1.$$
 (2)

The other dynamical quantity is the current density representing the beam travelling through the cavity structure. We define a modal current density, $J_{\lambda}(t)$, by computing the overlap of the time-dependent current density with the spatial profile of the mode electric field, as in (2).

We may write down an equivalent circuit equation describing the time evolution of the mode amplitude due to excitation by both the external rf current drive and the incoming waveguide mode, and losses from wall heating, beam loading, and coupling to the outgoing waveguide mode [1] [2],

$$\left(\frac{d^2}{dt^2} + \frac{\omega_{\lambda}}{Q_w} \frac{d}{dt} + \omega_{\lambda}^2\right) a_{\lambda}(t) =$$

$$-\frac{1}{\epsilon_0} \frac{d}{dt} J_{\lambda}(t) + \frac{\omega_{\lambda}}{Q_{ext}} \frac{d}{dt} \left(\frac{V_1^+ - V_1^-}{V_{1\lambda}}\right).$$
(3)

For quasi-steady-state harmonic oscillation at the modulation rf frequency, we express the time-dependence of the rf amplitudes as $a_{\lambda}(t) \cong \widehat{a_{\lambda}} \cos(\omega_b t + \varphi_{\lambda})$, $J_{\lambda}(t) \cong \widehat{J_{\lambda}} \cos(\omega_b t)$, $V_1^{\pm}(t) \cong \widehat{v}^{\pm} \cos(\omega_b t + \varphi_{\pm})$.

1.1 Normalization of the Cavity Electric Field

We only consider the *on-axis* longitudinal electric field profile and assume that it is only a function of longitudinal position (z), with a separable time dependence. The values of the field and its derivatives along the axis are used to generate all other electric and magnetic field components (permitted by symmetry) near the axis by construction of the vector potential.

Without the detailed description of the total electric field profile throughout the entire cavity, we are unable to normalize the modes according to the Slater prescription (2). However, this normalization may be done when the modes are initially generated by electromagnetic codes [Superfish, URMEL, MAFIA, GdfidL, et. al.]. This can be performed through a combination of analytical modeling of the onaxis field profile with numerical calculation of the [R/Q]. This relates the on-axis voltage seen by the beam to the total energy stored in the cavity, and introduces a normalization constant, N_{λ} . In terms of the modal fields, the *accelerator* [R/Q] is

$$\left[\frac{R}{Q}\right]_{\lambda} = \frac{2}{\epsilon_0 \omega_{\lambda}} \left| \int_{cavity} dz E_{z\lambda}(z) \exp\left[i\omega_{\lambda} z/\beta_z c\right] \right|^2. \tag{4}$$

For a Gaussian distributed on-axis longitudinal electric field component, with RMS width σ in z, the normalization constant is

$$N_{\lambda} = \left(\frac{1}{2}\epsilon_0 \omega_{\lambda} \left[\frac{R}{Q}\right]_{\lambda}\right)^{1/2} \exp\left[\frac{\omega_{\lambda}^2 \sigma^2}{2\beta_z^2 c^2}\right].$$
 (5)

This defines the connection between the modal fields used in the circuit analogy, and the fields used in determining the beam dynamics. We refer to this definition of the field as the 'line voltage' normalization.

1.2 Periodic Klimontovich Current Distribution

The connection between the discrete particle description employed by the tracking code and the current density used in the circuit equation is made by appealing to the Klimontovich distribution.

Since the amplitude of the modulated current density varies only very slowly on the rf time scale, the charge per bunch and the distribution function appear to be periodic when observed over a few rf periods' duration. We describe the time dependence of the charge density distribution by expanding in a Fourier series basis defined over a

^{*}This work supported under the auspices of the U.S. Department of Energy by LBNL under Contract No. AC03-76SF00098.

single rf period. The relativistic nature of the beam allows us to neglect the transverse current density components.

The modal current density at time t_0 is calculated to be

$$\begin{split} J_{\lambda}(t_{0}) &= I_{b} \left\langle \int_{cavity} dz E_{z\lambda} \left(\overrightarrow{r_{\perp}}, z \right) \right\rangle + \\ &+ 2I_{b} \sum_{l=1}^{\infty} \left\langle \int_{cavity} dz E_{z\lambda} \left(\overrightarrow{r_{\perp}}, z \right) \cos \left[l\omega_{b} \left(t_{0} - t(z) \right) \right] \right\rangle \end{split}$$

For the beams we consider here, only the l=1 term is necessary to retain for the monopole mode. Higher-order azimuthal modes may couple to higher harmonic components in the beam's spectrum.

We have denoted with angular brackets an average over the bunch distribution. Here, t(z) is the arrival time at beamline position z with transverse offset $\overrightarrow{r_{\perp}}$ of an element of the current density. It will be convenient to use the real parts of complex-valued quantities. We will define,

$$\widetilde{w}(\omega, \overrightarrow{r_{\perp}}) = \int_{cavity} dz E_{z\lambda}(\overrightarrow{r_{\perp n}}, z) \exp[-i\omega t(z)].$$
 (6)

The particular function defined by (6) plays an extremely important role in the dynamics of the beam and the evolution of the cavity field amplitude. It serves to define the cavity voltage, and hence the mode [R/Q] and shunt impedance. It contains transit time effects, and when applied to beam particle trajectories in the presence of a background rf field, it will compute beam loading contributions to the shunt impedance and the net energy deposited into the mode. We will refer to it as the *mode transit function*.

2 ANALYSIS OF THE CIRCUIT EQUATION

Two distinct time-scales of interest exist in these problems. A fast time-scale, where variations occur within an rf period, and a slow time-scale. The latter can be the fill time of the cavity (T_F) , the rise time of the driving current, or some other relevant time-scale. The mode amplitude and current density are modulated at the fast time-scale. But the evolution of the amplitude as well as any phase drift occurs on the slow time-scale. As a result, we may re-write the governing circuit equation in terms of these slowly-varying quantities and the slow time-scale.

2.1 Slow Time-Scale Equation of Motion

Introducing slow time variations into the modal amplitudes and phases: $\widehat{a_{\lambda}} = \widehat{a_{\lambda}}(t)$, $\varphi_{\lambda} = \varphi_{\lambda}(t)$, $\widehat{J_{\lambda}} = 2I_b(t)\left\langle \widetilde{w}^{\dagger}\right\rangle$, $\widehat{v^{\pm}} = \widehat{v^{\pm}}(t)$, $\varphi_{\pm} = \varphi_{\pm}(t)$. These functions are required to be slowly varying in time with respect to the rf period. Substituting these into the circuit equation , and neglect second-order time derivatives of slowly-varying quantities to obtain,

$$\left(\omega_{\lambda}^{2} - \omega^{2} - \frac{i\omega\omega_{\lambda}}{Q_{w}}\right)\left(\widehat{a_{\lambda}}e^{-i\varphi_{\lambda}}\right) +$$

$$\left(\frac{\omega_{\lambda}}{Q_{w}} - 2i\omega\right)\frac{d}{dt}\left(\widehat{a_{\lambda}}e^{-i\varphi_{\lambda}}\right) =$$
(7)

$$= \frac{\omega_{\lambda}}{Q_{ext}V_{1\lambda}} \left(\frac{d}{dt} - i\omega \right) \left(\hat{v}^{+}e^{-i\varphi_{+}} - \hat{v}^{-}e^{-i\varphi_{-}} \right) \\ -2\frac{\left\langle \widetilde{w}^{\dagger} \right\rangle}{\epsilon_{0}} \left(\frac{d}{dt}I_{b} - i\omega I_{b} \right).$$

This equation can be simplified by introducing a voltage normalization. We define an on-axis cavity circuit voltage, and forward and reverse port voltages via $\widetilde{V}_c = \left(\widetilde{w_0}\widehat{a_\lambda}e^{-i\varphi_\lambda}\right), \ \widetilde{V}_F = \left(\frac{\widetilde{w_0}\widehat{v^+}e^{-i\varphi_+}}{V_{1\lambda}}\right), \ \text{and} \ \widetilde{V}_R = \left(\frac{\widetilde{w_0}\widehat{v^-}e^{-i\varphi_-}}{V_{1\lambda}}\right), \ \text{where} \ \widetilde{w_0} = \widetilde{w}\left(\overline{r_\perp} = 0, \omega_b\right).$ As defined, these voltages are complex-valued. The bunch-averaged accelerator shunt impedance is defined through $R_b = Q_\lambda \left<[R/Q]\right>$, where

$$\left\langle \left[\frac{R}{Q} \right] \right\rangle = \frac{2\widetilde{w_0} \left\langle \widetilde{w}^{\dagger} \right\rangle}{\epsilon_0 \omega_{\lambda}}.$$
 (8)

The shunt impedance as defined here is a complex-valued quantity, but that it can be expressed as, $\left\langle \left[\frac{R}{Q}\right] \right\rangle =$

 $\left[\frac{R}{Q}\right]_{\lambda}F_{b}$, where $\left[\frac{R}{Q}\right]_{\lambda}=2\frac{\left|\widetilde{w_{0}}\right|^{2}}{\epsilon_{0}\omega_{\lambda}}$ is a manifestly *real*-valued quantity, and F_{b} is a complex-valued bunch distribution-dependent form-factor, with magnitude of order unity. The shunt impedance is given by $R_{\lambda}=Q_{L}\left[\frac{R}{Q}\right]_{\lambda}$.

Using the continuity condition [2], we may express the reverse voltage in terms of the cavity and forward voltages, $\widetilde{V}_R = \widetilde{V}_c - \widetilde{V}_F$. From standard microwave terminology, we recall the definitions of the tuning angle, ψ (tan $\psi = Q_L\left(\frac{\omega_\lambda}{\omega} - \frac{\omega}{\omega_\lambda}\right)$), cavity fill-time, $T_F = \frac{2Q_L}{\omega_\lambda}$, and coupling parameter, $\beta = \frac{Q_{wall}}{Q_{ext}}$. We introduce the phase change in a fill time, $\nu = \omega T_F$, and $\alpha = (1+i\tan\psi)$. Finally, we re-scale the time dependence by the fill time, $\tau = t/T_F$, to obtain

$$\widetilde{V}_{c}' + \alpha \widetilde{V}_{c} = \frac{2\beta}{\beta + 1} \widetilde{V}_{F} \left(1 + \frac{i}{\nu} \widetilde{V}_{F}' / \widetilde{V}_{F} \right)$$

$$- R_{\lambda} F_{b} I_{b} \left(1 + \frac{i}{\nu} I'_{b} / I_{b} \right),$$

$$(9)$$

This is the main result of this section. We do not attempt to find a global solution over time, which requires inclusion of the self-consistent interaction of the cavity back upon the beam. Rather, we will seek a local solution, valid only over a short time duration (though still long compared to the fast time scale), as an approximation to use within the numerical simulation. We will take the form factor, F_b , as approximately constant over the interval.

2.2 Observed Fields and Power Flow

Of interest is the amount of rf power flowing into and out of the cavity. This power flow is derived from the Poynting flux. The net rms power flowing in the waveguide, again assuming a single mode, can then be shown to be

$$\overline{P}_{+} = \frac{\epsilon_{0}\omega_{\lambda}}{2Q_{ext}} \left| \frac{\widetilde{V_{F}}}{\widetilde{w_{0}}} \right|^{2}, \overline{P}_{-} = \frac{\epsilon_{0}\omega_{\lambda}}{2Q_{ext}} \left| \frac{\widetilde{V_{c}} - \widetilde{V_{F}}}{\widetilde{w_{0}}} \right|^{2}$$

denoting the forward and reverse rms power flows in the connecting waveguide, respectively. Note that the reverse

voltage has been expressed in terms of the forward and cavity voltages.

3 INTERNAL BUNCH DYNAMICS AND THE AVERAGED SHUNT IMPEDANCE

In the usual linac formulation, the function \widetilde{w}_0 is calculated by assuming a constant velocity, β_0 , of particles through the cavity. In that case $t(z)=t_0+(z-z_0)/(\beta_0c)$. Here, we allow for intra-bunch particle motion resulting from a finite beam energy spread, and from the influence of rf fields generated from the interaction of previous bunches with the cavity. We determine the value of t from the fiducial orbit.

For a SW monopole mode, we use

$$E_{z\lambda}(\overrightarrow{r_{\perp}},z) = f_0(z) + r_{\perp}^2 f_2(z) + r_{\perp}^4 f_4(z) + \cdots$$
 (10)

and the auxiliary functions are (primes denoting total derivatives with respect to z)

$$f_0(z) = E_{z\lambda}(\overrightarrow{r_{\perp}} = 0, z) = N_{\lambda}e_0(z),$$

$$f_2(z) = -1/4N_{\lambda}(e_0'' + k_0^2e_0),$$

$$f_4(z) = 1/64N_{\lambda}(e_0^{(iv)} + 2k_0^2e_0'' + k_0^4e_0),$$

and $k_0 = \omega_{\lambda}/c$. We re-write the mode transit functions as

$$\widetilde{w} \cong \int_{cavity} dz \left(f_0(z) + r_{\perp}^2 f_2(z) + r_{\perp}^4 f_4(z) \right) \times \exp\left[-i\omega_b t(z) \right].$$

For the beams of interest to us for RK-TBA devices, the longitudinal phase space is characterized by bunches which subtend a significant fraction of the rf wavelength. The bunch-averaged shunt impedance is evaluated by taking averages over the spatial and phase coordinates of the particles in the bunch. This serves to define the bunch-averaged form factor, F_b .

4 DESIGN OF IDLER AND OUTPUT CAVITIES

The collection of idler and output cavities in an RK-TBA requires detailed design so that its rf properties match the demands of the device in terms of beam transport stability and output power production. In particular, the resonant frequency and loaded Q-value of a cavity determine the longitudinal impedance seen by the beam. This impedance is tuned inductively to counteract the (capacitive) effects of space charge debunching and loss of rf current carried by the beam.

4.1 Steady-State Scaling

In this section, we consider the steady-state behavior of the beam-cavity system. We neglect the energy spread of the bunch as it passes through the cavity, and further assume that the individual particle velocities remain constant (the 'linac' approximation). The arrival time at the center of the cavity of a given particle is given by $t(z) = t_0 + (z - t_0)$

 $z_0)/(\beta_0c)+\widehat{s}/c$. The distribution in arrival time (\widehat{s}) is taken to be gaussian. Following the phase convention of (6), we set $t_0=0$. The transverse distribution is also taken to be gaussian, and essentially static. We take the bunch distri-

bution to be
$$g\left(\overrightarrow{r_{\perp}},\widehat{s}\right)=\frac{\exp\left(-\frac{r_{\perp}^2}{2\sigma_r^2}\right)}{2\pi\sigma_r^2}\frac{\exp\left(-\frac{\widehat{s}^2}{2\sigma_s^2}\right)}{\sqrt{2\pi}\sigma_s}$$
, so that $\widetilde{w}=\widetilde{w_0}\exp\left(-ik_b\widehat{s}\right)=N_\lambda\exp\left(-\frac{k_b^2\sigma^2}{2\beta_0^2}\right)\exp\left(-ik_b\widehat{s}\right)$, where $k_b=\omega_b/c$. And, in this case, the bunch-averaged form factor is real-valued, $F_b=\exp\left(-\frac{k_b^2\sigma_s^2}{2}\right)$. We can find the steady-state power flow out of the beam and into the wall and into the reverse waveguide mode,

$$\overline{P}_b = R_\lambda I_b^2 \cos^2 \psi \exp\left(-k_b^2 \sigma_s^2\right),$$

$$\overline{P}_w = \frac{Q_L}{Q_w} R_\lambda I_b^2 \cos^2 \psi \exp\left(-k_b^2 \sigma_s^2\right),$$

$$\overline{P}_- = \frac{Q_L}{Q_{ext}} R_\lambda I_b^2 \cos^2 \psi \exp\left(-k_b^2 \sigma_s^2\right). \quad (11)$$

4.2 Beam Energy Modulation

The beam energy distribution undergoes modulation from this field. The modulation of beam energy (γ) is then

$$\Delta\gamma\left(\widehat{s}\right) = -\frac{R_{\lambda}\left|I_{b}\right|}{m_{e}c^{2}/\left|e\right|} \exp\left(-\frac{k_{b}^{2}\sigma_{s}^{2}}{2}\right) \cos\psi\cos\left(\psi + k_{b}\widehat{s}\right). \tag{12}$$

The cavity interaction thus produces a correlation between arrival time and energy.

4.3 Inductive Detuning for Beam Stability

The energy modulation imposed upon the beam by its interaction with the cavity contains a sinusoidal variation with arrival time and a phase offset determined by the cavity tuning angle. The tuning angle contains two free parameters, ω_b and Q_L . For RK-TBA applications, these parameters are used to adjust the amount of energy loss experienced between the head and tail of the rf bunch. Or, equivalently, the average bunch energy loss and the longitudinal phase-space rotation of the bunch. The average energy loss is determined by the rf power required, while the bunch rotation degree of freedom is used to counterbalance the opposite rotation (and debunching effect) of self-fields. The average energy change for the bunch is then found to be $\overline{\Delta\gamma} = -\frac{\overline{P_b}}{V_0|I_b|} = -\frac{(Q_{ext}/Q_L)\overline{P_-}}{V_0|I_b|}, \text{ where } V_0 = mc^2/e \text{ is the electronic rest mass in voltage units.}$

- [1] J.C. Slater. "Microwave Electronics". D. Van Nostrand Company, Inc., 1950.
- [2] D.H. Whittum. Introduction to electrodynamics for microwave linear accelerators. In *RF Engineering for Particle Accelerators*. World Scientific, 1998.

IMPEDANCE OF A LONG SLOT IN A COAXIAL BEAM PIPE*

S. De Santis[#], LBNL, Berkeley, CA
A. Mostacci, L. Palumbo, Università di Roma "La Sapienza", Rome, Italy
B. Spataro, INFN-LNF, Frascati, Italy

Abstract

We derive an analytical expression for the coupling impedance and loss factor of a long narrow slot in a coaxial beam pipe. The method used differs from the classical Bethe's theory of diffraction since we define differential polarizabilities to take into account the effect of the interference between the fields scattered all along the slot. The expressions obtained are thus valid even for slots longer than the wavelength.

1 INTRODUCTION

Different analytical or semianalytical methods can be used to study the effects, on the beam dynamics, of pumping holes and slots coupling the vacuum chamber to an external antichamber.

When the wavelength is much longer than the aperture dimensions, the problem is treated in terms of static polarizabilities and coupling impedance and loss factor can be calculated by different methods [1,2]. For longer wavelengths this procedure can no longer be followed and frequency dependant polarizabilities have been introduced in [3].

The method we present here is based on the slot subdivision in infinitesimal slices, as suggested in [4], so that it is still possible to use the modified Bethe's theory of diffraction [5].

2 GENERAL THEORY

We consider a long and narrow slot on the inner tube of a coaxial beam pipe (Fig. 1). Subdividing the slot in infinitesimally long elements, which dimensions are much shorter than the wavelength, we can still calculate the equivalent dipole moments for each element according to the modified Bethe's diffraction theory:

$$dM_{\varphi}(z) = \left[H_{0\varphi}(z) - H_{s\varphi}(z)\right] d\alpha_{m}$$

$$dP_{r}(z) = \varepsilon \left[E_{0r}(z) - E_{sr}(z)\right] d\alpha_{e}$$
(1)

where $H_{0\varphi}(z)$ and $E_{0r}(z)$ are the fields radiated by a point charge q, travelling with velocity c along the axis of a perfectly conducting pipe. $H_{s\varphi}(z)$ and $E_{s\varphi}(z)$ are the scattered fields; their amplitude, which is a function of the equivalent dipole moments, can be expressed through the Lorentz reciprocity theorem [2]. The differential

polarizabilities $d\alpha_m$ and $d\alpha_e$ are approximated by averaging the static polarizabilities along the slot length L:

$$d\alpha_m = \alpha_m / L dz$$
 and $d\alpha_e = \alpha_e / L dz$ (2)

Limiting our analysis to frequencies below the inner and outer pipes TE_{11} cutoff, we can rewrite Eqs. (1) as

$$\frac{dM_{\varphi}}{dz} = \frac{\alpha_{m}}{L} \left[H_{0\varphi} - j \frac{\omega \mu h_{0\varphi}^{2}}{2} \int_{-L/2}^{L/2} \frac{dM_{\varphi}}{d\xi} e^{-jk_{0}|z-\xi|} d\xi + \right. \\
+ j \frac{\omega h_{0\varphi} e_{0r}}{2} \int_{-L/2}^{L/2} sign(\xi - z) \frac{dP_{r}}{d\xi} e^{-jk_{0}|z-\xi|} d\xi \right] \\
\frac{dP_{r}}{dz} = \frac{\varepsilon \alpha_{e}}{L} \left[E_{0r} - j \frac{\omega \mu e_{0r}^{2}}{2} \int_{-L/2}^{L/2} \frac{dP_{r}}{d\xi} e^{-jk_{0}|z-\xi|} d\xi + \right. \\
+ j \frac{\omega \mu h_{0\varphi} e_{0r}}{2} \int_{-L/2}^{L/2} sign(\xi - z) \frac{dM_{\varphi}}{d\xi} e^{-jk_{0}|z-\xi|} d\xi \right]$$
(3)

where $h_{0\varphi}$ and e_{0r} are the TEM modal functions [6] and $k_0 = 2\pi/\lambda$.

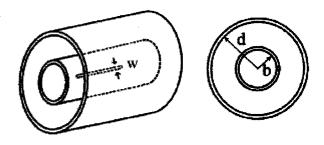


Figure 1: Coaxial beam pipe with slot.

From a physical point of view, Eqs. (3) reveal that the scattered fields depend on the electric and magnetic dipoles all over the aperture, since each infinitesimal slice radiates a forward and a backward wave in the coaxial region [6].

Once Eqs. (3) have been solved, it is straightforward to derive the longitudinal impedance [7]

$$Z(\omega) = -\frac{1}{q} \int_{-\infty}^{+\infty} E_z(r=0) e^{jk_0 z} dz$$
 (4)

^{*}Supported by Department of Energy contract DE-AC03-76SF00098.

[#] Email: sdesantis@lbl.gov

Since only the TM_{0m} modes have a non zero longitudinal electric field along the pipe axis, each element contribution to the impedance is

$$\frac{dZ}{dz} = j \frac{\omega Z_0}{2 \pi q b} \left(\frac{1}{c} \frac{dM_{\varphi}}{dz} + \frac{dP_r}{dz} \right) e^{jk_0 z}$$
 (5)

where Z_0 is the free-space characteristic impedance. Eq. (5) can be regarded as the differential version of the analogous formula derived in [1].

The total impedance is simply obtained integrating Eq. (5) along the slot.

3 ANALYTICAL EXPRESSIONS FOR IMPEDANCE AND LOSS FACTOR

To obtain final expressions in an analytical form, we choose to solve the integral equation system in Eqs. (3) using an iterative procedure. It will be shown that it is sufficient to stop at the first order solution.

The zero-th order solution corresponds to the original Bethe's theory [8], appropriately transformed to fit in the integral equations:

$$\left(\frac{dM_{\varphi}}{d\xi}\right)^{0th} = \frac{\alpha_m}{L} H_{0\varphi} \text{ and } \left(\frac{dP_r}{d\xi}\right)^{0th} = \frac{\varepsilon \alpha_{\varepsilon}}{L} E_{0r} \quad (6)$$

Replacing Eqs. (6) in the right hand side of Eqs. (3) we get the first order solution

$$\left(\frac{dM_{\varphi}}{dz}\right)^{1st} = \left(\frac{dM_{\varphi}}{dz}\right)^{0th} + \\
-j\frac{\omega}{2}\frac{\alpha_{m}}{L^{2}}\mu H_{0\varphi}(0)h_{0\varphi}^{2}(\alpha_{m}I_{1} - \alpha_{e}I_{2}) \\
\left(\frac{dP_{r}}{dz}\right)^{1st} = \left(\frac{dP_{r}}{dz}\right)^{0th} + \\
-j\frac{\omega}{2}\frac{\alpha_{e}}{L^{2}}\frac{\mu}{c}H_{0\varphi}(0)h_{0\varphi}^{2}(\alpha_{e}I_{1} - \alpha_{m}I_{2})$$
(7)

where

$$I_{1} = \int_{-L/2}^{L/2} e^{-jk_{0}\xi} e^{-jk_{0}|z-\xi|} d\xi$$

$$I_{2} = \int_{-L/2}^{L/2} sign(\xi - z)e^{-jk_{0}\xi} e^{-jk_{0}|z-\xi|} d\xi$$
(8)

The second order approximation is obtained replacing the expressions found for the differential dipole moments in Eqs. (7) on the right hand side of Eqs. (3). Thus obtaining

$$\left(\frac{dM_{\varphi}}{dz}\right)^{2nd} = \left(\frac{dM_{\varphi}}{dz}\right)^{1st} + \frac{\omega^{2}}{4}\mu^{2}\frac{\alpha_{m}}{L^{3}}h_{0\varphi}^{4}H_{0\varphi}(0)\left[-\alpha_{m}(\alpha_{m}I_{11} - \alpha_{e}I_{12}) + \alpha_{e}(\alpha_{e}I_{21} - \alpha_{m}I_{22})\right] \\
\left(\frac{dP_{r}}{dz}(z)\right)^{2nd} = \left(\frac{dP_{r}}{dz}(z)\right)^{1st} + \frac{\omega^{2}}{4}\mu^{2}\frac{\alpha_{e}}{cL^{3}}h_{0\varphi}^{4}H_{0\varphi}(0)\left[-\alpha_{e}(\alpha_{e}I_{11} - \alpha_{m}I_{12}) + \alpha_{m}(\alpha_{m}I_{21} - \alpha_{e}I_{22})\right]$$
(9)

The integrals I_{nm} are given by

$$I_{11} = \iint_{slot} e^{-jk_0|z-\xi|} e^{-jk_0\zeta} e^{-jk_0|\xi-\zeta|} d\zeta d\xi$$

$$I_{12} = \iint_{slot} sign(\zeta - \xi) e^{-jk_0|z-\xi|} e^{-jk_0\zeta} e^{-jk_0|\xi-\zeta|} d\zeta d\xi$$

$$I_{21} = \iint_{slot} sign(\xi - z) e^{-jk_0|z-\xi|} e^{-jk_0\zeta} e^{-jk_0|\xi-\zeta|} d\zeta d\xi$$

$$I_{21} = \iint_{slot} sign(\xi - z) e^{-jk_0|z-\xi|} e^{-jk_0\zeta} e^{-jk_0|\xi-\zeta|} d\zeta d\xi$$

$$I_{22} = \iint_{slot} sign(\xi - z) sign(\zeta - \xi)$$

$$\times e^{-jk_0|z-\xi|} e^{-jk_0\zeta} e^{-jk_0|\xi-\zeta|} d\zeta d\xi$$

The complete expression of impedance and loss factor using the second order approximation for the differential dipole moments is quite complex and of no easy readability. From Fig. 2 we can see, though, that the difference from the loss factor for a Gaussian bunch of length σ_z calculated using the first order approximation is minimal.

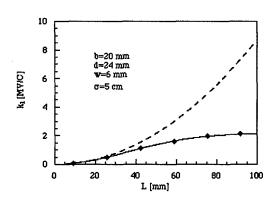


Figure 2: Loss factor vs. length for a rectangular slot. The dashed line is the small aperture approximation [9]; the solid line is the first order solution; the black diamonds are obtained using the second order solution.

In the following analysis, therefore, we will make use of the following analytical expressions for the longitudinal impedance, obtained using the first order solution of Eqs. (3):

$$Z_{RE}(\omega) = \frac{Z_0 k_0^2}{32\pi^3 b^4 \ln(d/b)} \Big[(\alpha_e + \alpha_m)^2 + (\alpha_e - \alpha_m)^2 \frac{1 - \cos(2k_0 L)}{2k_0^2 L^2} \Big]$$

$$Z_{IM}(\omega) = \frac{Z_0 k_0}{4\pi^2 b^2} \Big\{ (\alpha_e + \alpha_m) + \frac{(\alpha_e - \alpha_m)^2}{8\pi b^2 \ln(d/b) L} \Big[1 - \frac{\sin(2k_0 L)}{2k_0 L} \Big] \Big\}$$
(11)

and consequently the loss factor for a Gaussian bunch is

$$k_{l}(\sigma_{z}) = \frac{Z_{0}c\sqrt{\pi}}{128\pi^{4}b^{4}\ln(d/b)\sigma_{z}} \times \left\{ \frac{(\alpha_{e} + \alpha_{m})^{2}}{\sigma_{z}^{2}} + \frac{(\alpha_{e} - \alpha_{m})^{2}}{L^{2}} \left[1 - e^{-(L/\sigma_{z})^{2}} \right] \right\}$$
(12)

4 COMPARISONS WITH NUMERICAL RESULTS

We have performed simulations with the numerical code MAFIA in the case of both rectangular and rounded end slots of different length and width.

To account for the finite wall thickness T that must be used in the simulations, Eqs. (11) and (12) must be slightly modified as shown in [9]. The electric and magnetic polarizabilities change as well and can be represented as a function of the zero-thickness expressions, using the approximation developed by McDonald [10], as:

$$\tilde{\alpha}_e = C_E \alpha_e e^{-\pi T \sqrt{1/L^2 + 1/w^2}}$$

$$\tilde{\alpha}_m = C_M \alpha_m e^{-\pi T/w}$$
(13)

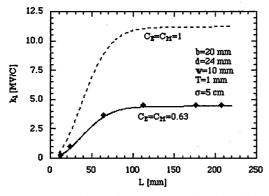


Figure 3: Loss factor for a rectangular slot. The black diamonds are MAFIA points.

Though the C_E and C_M values are known only for a circular aperture, in our case, a comparison of the analytical (Fig. 3, dashed line) and numerical results suggest the following values: $C_E = C_M = 0.63$.

In order to check this result, the loss factor has been computed numerically for a given slot length and different wall thicknesses (Fig. 4), obtaining $C_E = C_M = 0.62$ as best fit.

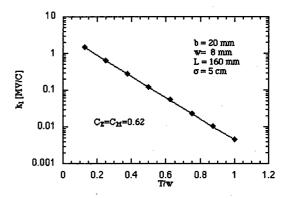


Figure 4: Loss factor for a rectangular slot vs. T/w ratio. The black diamonds are MAFIA points.

5 CONCLUSIONS

We have obtained an approximated analytical expression for longitudinal impedance and loss factor of a long narrow slot in a coaxial beam pipe. When the slot is longer than the wavelength, the real part of the impedance shows a typical resonant behaviour related to the slot length. Our results are in good agreement with those obtained in literature with different methods and with MAFIA simulations.

- [1] S. S. Kurennoy, Part. Accel. 39,1 (1992).
- [2] S. De Santis, et al., Phys. Rev. E 54, 800 (1996).
- [3] A. Fedotov and R. L. Gluckstern, Phys. Rev. E 54, 1930 (1996).
- [4] G. V. Stupakov, Phys. Rev. E 51, 3515(1995).
- [5] R. E. Collin, Field Theory of Guided Waves, 2nd ed. (IEEE, New York, 1991).
- [6] S. De Santis, et al., Phys. Rev. E 56, 5990 (1997).
- [7] L. Palumbo, et al., in CAS Advanced Accelerator School, p. 331 (CERN, Geneva, 1995).
- [8] H. A. Bethe, Phys. Rev. 66, 163 (1944).
- [9] S. De Santis, et al., Phys. Rev. E 58, 6565 (1998).
- [10] N. A. McDonald, IEEE Trans. Microwave Theory Tech. 20, 689 (1972).

THE IMPEDANCE OF RF-SHIELDING WIRES

Tai-Sen F. Wang* and Robert L. Gluckstern**, LANL, Los Alamos, NM

Abstract

We studied the electrostatic fields due to the longitudinal and transverse perturbations of a charged particle beam with a uniform distribution propagating inside an rf-shielding cage constructed from evenly-spaced conducting wires. The beam and the rf-cage are surrounded by a concentric conducting beam pipe. Simple formulae are derived for estimating the space-charge impedances. Numerical examples are given.

1 INTRODUCTION

An rf-shielding cage, or an rf-cage, used in an accelerator or storage ring is a cage-like structure made of conducting wires stretched in parallel to the direction of the circulating charged particle beam.[1] The conducting wires on the cage are arranged to surround the beam to create an electromagnetically shielded environment for the beam. This kind or the similar kinds of devices together with ceramic beam pipes have been implemented[1] and planned[2-4], or is being planned[5] in some high-intensity rapid cycling proton synchrotrons. There are two reasons for using the rf-cage instead of solid beam pipe. The first reason is to avoid excess eddy current that may be induced on the beam pipe by the fast-changing magnetic field. The second reason is that it is easier to vary the crosssection of an rf-cage to reduce the coupling impedance.

Although an rf-cage has been put in service for many years, [1] a serious study of the electromagnetic field of a charged particle beam propagating in an rf-cage has never been documented until recently. [6,7] In Refs. 6 and 7, a rigorous formalism was established to investigate the electrostatic field of a charged particle beam with a uniform distribution inside an rf-shielding cage constructed from evenly-spaced conducting wires. The purpose of the this work is to extend the previous study to include the effect of an external solid beam pipe. Simple formulae will be derived for the longitudinal and transverse coupling impedances in the long wavelength regime. Numerical examples will be given.

2 THE FIELD AND IMPEDANCE

The system considered here is shown in Fig. 1. A beam having a circular cross-section of radius r_b and a uniform charge distribution is propagating inside of an rf-cage composed of N conducting wires extended

in the direction parallel to the beam. The beam and the rf-cage are surrounded by a conducting beam pipe with radius r_t . For simplicity, we shall limit our discussion to the geometry in which wires are evenly distributed over a circle; the surrounding pipe and the rf-cage is positioned concentric with the beam. The radius of the rf-cage, measured from the center of the cage to the centers of wires, is r_c . We assume that the pipe and wires are electrically grounded and all wires have the same circular cross-section of radius ρ_w . The discussions here will be restricted to the regime $\rho_w \ll r_c$ and $N \gg 1$.

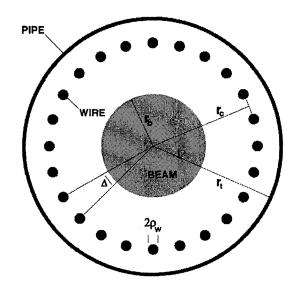


Fig. 1. Cross-sectional view of a beam inside an rfcage and beam pipe. r_t , r_c , and r_b are the radii of the beam pipe, the rf-cage, and the beam, respectively. Δ is the angle subtended by two adjacent wires, and ρ_w is the radius of a wire.

Although one can estimate the impedance in the long wavelength regime by solving the twodimensional electrostatic field using various techniques like the image method etc., we elect to use the threedimensional treatment here. This approach allows one to examine the frequency dependence of the impedance in the low frequency domain, if needed.

We choose a cylindrical coordinate system (r, θ, z) such that the z-axis coincides with the central axis of the beam, and we shall call it the "global coordinate system". In order to conveniently describe the electric field near an individual wire, we shall also use another cylindrical coordinate system, be referred to as the "local coordinate system" in the following, (ρ, ψ, z) in which the z-axis coincides with the central axis of a wire as shown in Fig. 2.

^{*} Email: TWANG@LANL.GOV

^{**} Permanent Address: Univ. of Maryland, College Park, MD

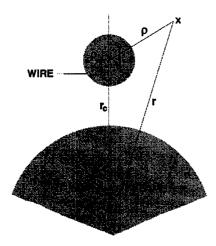


Fig. 2. The local and the global coordinates adopted in this study. The origins of the local and the global coordinates are located at the center of beam and the center of a wire, respectively.

We now consider the electrostatic potential due to the charge-density perturbation that varies in the z-direction according to e^{ikz} , where k is the wave-number of the perturbation. The Poisson equation we want to solve is

$$\frac{1}{r}\frac{\partial}{\partial r}\left(r\frac{\partial\Phi}{\partial r}\right) + \frac{1}{r^2}\frac{\partial^2\Phi}{\partial\theta^2} + \frac{\partial^2\Phi}{\partial z^2} = \begin{cases} 0, & \text{if } r_t > r > r_b, \\ -\sigma e^{ikz}/\epsilon_o, & \text{if } r \leq r_b, \end{cases} \tag{1}$$

where σ is the volume charge density associated with the perturbation, and ϵ_o is the permittivity of free space. To solve Eq. (1) in the presence of wires, we first solve the equation for no wire, i.e., for the boundary condition of $\Phi=0$ at $r=r_t$ only. Then we assume that in the region of $r_t \geq r \geq r_c$ each wire induces a field which has the following multipole expansion in the local coordinate:

$$\phi_w = \sum_{n=-\infty}^{\infty} \left[A_n K_n(k\rho) + B_n I_n(k\rho) \right] e^{in\psi} e^{ikz} , \quad (2)$$

where $I_n(x)$ and $K_n(x)$ are the nth order modified Bessel functions of the first and the second kind, respectively; A_n and B_n are the unknowns to be determined. Applying the addition theorem of Bessel functions [8], ϕ_w can also be expressed in the global coordinate variables. Then applying the boundary condition of $\phi_w = 0$ at $r = r_t$, one can solve B_n in terms of A_n . Because of the symmetry embodied in the system, one can study the field around wires by considering the electric potential around any individual wire. Thus, we call the wire under consideration the 0th wire and number all others by their relative locations with respect to the 0th wire. On the surface of each wire, the potential due to the induced charge should cancel that due to the beam plus that contributed by all other wires. This requirement leads to a complicated equation for A_n which appears to have no closed-form solution. In the regime $kr_t \ll 1$, it is possible to find a solution for A_n expressed in a power series of $h_n(k\rho_w)$. If the coupling among multipoles is neglected, the lowest order solution is

$$\begin{split} A_{n} &\approx -b_{\parallel} h_{n}(k\rho_{w}) \bigg[K_{n}(kr_{c}) - \frac{I_{n}(kr_{c})}{h_{0}(kr_{t})} \bigg] \bigg\{ 1 + (-1)^{n} \\ &\times h_{n}(k\rho_{w}) \sum_{\mu=1}^{N-1} \mathrm{e}^{-in\mu\Delta} K_{0}(kd_{\mu}) - h_{n}(k\rho_{w}) \\ &\times \sum_{j=-\infty}^{\infty} \frac{\big[I_{n+j}(kr_{c}) \big]^{2}}{h_{j}(kr_{t})} \bigg[1 + (-1)^{n} \sum_{\mu=1}^{N-1} \mathrm{e}^{ij\mu\Delta} \bigg] \bigg\}^{-1}, (3) \end{split}$$

where $b_{\parallel} = (\sigma r_b/k\epsilon_o)I_1(kr_b)$, $h_n(x) = I_n(x)/K_n(x)$, $\Delta = 2\pi/N$ is the angular separation between two adjacent wires, and d_{μ} is the distance between the centers of the 0th and the μ th wires.

Using the solution (3) and the addition theorem of Bessel functions, one can derive the total electric potential in the region of $r \leq r_c$. Then taking the approximation by considering n = 0 (the monopole solution) only, we find the total electric potential in the region of $r \leq r_b$ as

$$\Phi = \frac{\sigma}{\epsilon_o k^2} \left\{ 1 - k r_b I_0(kr) \left[\frac{I_1(kr_b)}{h_0(kr_t)} + K_1(kr_b) \right] \right\} e^{ikz}$$

$$+ N \sum_{p=-\infty}^{\infty} \sum_{n=-\infty}^{\infty} A_n \left[K_{n+pN}(kr_c) - (-1)^n \right]$$

$$\times \frac{I_{n+pN}(kr_c)}{h_{nN}(kr_t)} I_{pN}(kr) e^{ipN\theta} e^{ikz}. \tag{4}$$

For $N \gg 1$ and $kr_t \ll 1$, we can apply the small argument expansions of Bessel functions to Eqs. (3) and (4) to yield

$$Z_{\parallel} pprox rac{iLkZ_o}{4eta\gamma^2} \Big[1 + 2\ln\Big(rac{r_t}{r_b}\Big) + C_{\parallel} \Big] \,,$$
 (5)

where

$$C_{\parallel} pprox rac{-2N[\ln(r_t/r_c)]^2}{N\ln(r_t/r_c) - \ln(\pi f_w) + \ln[1 - (r_c/r_t)^{2N}]},$$
 (6)

L is the length or the circumference of the machine, $Z_0 = 377\Omega$, and the wire filling factor f_w is defined as the ratio between the angle subtended by a wire in the global coordinate system θ_w , and Δ , i.e. $f_w = \theta_w/\Delta \approx N\rho_w/(\pi r_c)$. Note that $h_n(kr_t) \to \infty$ when $r_t \to \infty$. Thus, in the absence of the external beam pipe Eqs. (5) and (6) reduce to the previous result.[7]

Next, we consider the electrostatic potential due to a transverse perturbation in a beam. The model of the perturbation to be studied here is a shell with surface charge density varying according to $e^{ikz}\cos\theta$. The Poisson equation is

$$\frac{1}{r}\frac{\partial}{\partial r}\left(r\frac{\partial\Phi}{\partial r}\right) + \frac{1}{r^2}\frac{\partial^2\Phi}{\partial\theta^2} + \frac{\partial^2\Phi}{\partial z^2} = \frac{-\sigma\bar{d}}{\epsilon_o}\delta(r - r_b)e^{ikz}\cos\theta.$$
(7)

We again start the analysis by solving the Poisson equation in the absence of the rf-cage. Then the field due to the induced charge on wires is considered. In contrast to the case of longitudinal perturbation, the system now is not axisymmetric. Therefore, the multipole expansion coefficients of the field due to the induced charges on each wire depend on the angular location of the wire. Other than that, the analysis procedures and the boundary conditions are the same as in treating the longitudinal perturbation.

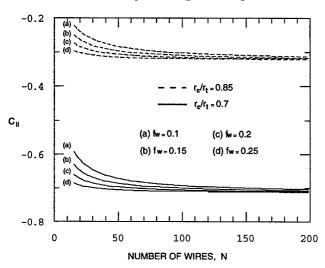


Fig. 3. A numerical example of C_{\parallel} as a function of the total number of wires N. Where C_{\parallel} is calculated using Eq. (6).

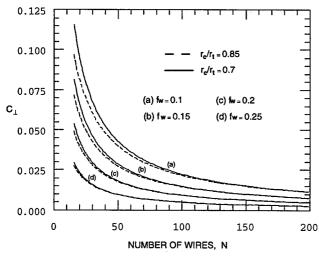


Fig. 4. A numerical example of C_{\perp} as a function of the total number of wires N. Where C_{\perp} is calculated using Eq. (9).

After obtaining the approximate perturbed field by retaining only the contribution from the monopoles due to the wires, all the Bessel functions are expanded to derive the following transverse impedance in the long wavelength regime:

$$Z_{\perp} pprox rac{iLZ_o}{2\pi\beta^2\gamma^2} \left(rac{1}{r_b^2} - rac{1-C_{\perp}}{r_c^2}
ight),$$
 (8)

where

$$C_{\perp} \approx \left[1 - (r_c/r_t)^2\right] \left\{ \left[(r_c/r_t)^2 + (r_t/r_c)^2 \right] \ln[1 - (r_c/r_t)^{2N}] - 2\ln(\pi f_w) \right\} \left\{ N\left[1 - (r_c/r_t)^2\right] - 2\ln(\pi f_w) + \left[(r_c/r_t)^2 + (r_t/r_c)^2 \right] \ln[1 - (r_c/r_t)^{2N}] \right\}^{-1}.$$
(9)

When $r_t \to \infty$, Z_{\perp} reduces to the limits of no external beam pipe obtained before. [7]

3 CONCLUSIONS

For a charged particle beam propagating inside of a beam pipe and an rf-shielding cage made of evenly-spaced conducting wires, the electrostatic fields due to sinusoidal longitudinal and dipole-mode transverse perturbations have been solved analytically for the case that the cage and the wires all have circular cross sections. It was assumed that the beam has a uniform charge distribution and the unperturbed system is azimuthally symmetric. We have derived simple formulae for the coupling impedances in the long wavelength regime. Numerical examples were presented to show the shielding effects of the rf-cage.

4 ACKNOWLEDGEMENTS

TSFW would like to thank the Accelerator Technology Division of Los Alamos National Laboratory and the AUSTRON Project for the support he received during the initial study of this topic. TSFW also likes to extend gratitude to Dr. Phil Bryant for his encouragement, comments, and suggestions, as well as to Drs. B. Zotter and D. Mohl for their comments.

- Dr. G. Rees private communication. An rf-cage has been implemented at ISIS.
- [2] The Physics and Plan for a 45 GeV Facility, Los Alamos National Laboratory Report, LA-10720-MS, May 1986.
- [3] Kaon Factory Study: Accelerator Design Report, TRIUMF-Kaon Project, TRIUMF, 1990.
- [4] AUSTRON Feasibility Study, Eds. P. Bryant, M. Regler, M. Schuster, Im Auftrage des Bundesminis teriums für Wissenschaft und Forschung, Wein, Österreich, Nov. 1994.
- [5] Proposal for Japan Hadron Facility, JHF Project Office, High Energy Accelerator Research Organization, KEK Report 97-3, JHF 97-1, May 1997.
- [6] T. F. Wang, CERN Internal Report, CERN/PS-94-08, April 1994.
- [7] T. F. Wang, AIP Conference Proceedings 448, p. 286, AIP, 1998.
- [8] See, for example, Chapter 9 of Handbook of Mathematical Functions, by M. Abramowitz and I. A. Stegun, US National Bureau of Standards, 1964.

A PROPOSAL FOR THE SURFACE ROUGHNESS WAKE FIELD MEASUREMENT AT THE TESLA TEST FACILITY

A. Novokhatski, M. Timm *, T. Weiland, TEMF, TU-Darmstadt, Schlossgartenstr. 8, D-64289 Darmstadt, Germany H. Schlarb, DESY, Nottkestr. 85, D-22603 Hamburg, Germany

Abstract

The wake fields due to the rough surface of the vacuum chamber have a major influence on the beam dynamics in Linear Colliders and Free Electron Lasers. These wake fields mainly consists of the fundamental tube mode, modified by the rough boundary condition, which decreases its phase velocity to the speed of light. Its wavelength is proportional to the square root of the tube radius and the roughness depth and is comparable to the FEL bunch length, i.e. in the order of 10-30 micron. To study this effect with the beam available at the TESLA Test Facility (TTF) the use of tubes with an artificially increased roughness is suggested. The expected pulse power of these wakes, caused by the 250 micron bunch carrying a charge of 1 nC, can reach up to several MW. In this paper a preliminary design of an installation of a surface roughness wake field experiment at the TESLA Test Facility is presented.

1 INTRODUCTION

The conservation of a small emittance is a major requirement for the feasibility of the experiments in Linear Colliders, especially for the FEL. As the bunch length becomes very short, the contribution of the surface roughness wake fields is not negligible anymore. The longitudinal wake fields increase the energy spread, while the transverse dipole wake fields increase the bunch tails offset from the axis.

But even for longer bunches, in synchrotrons or damping rings, the roughness wake fields might have an influence on beam dynamics. They are suspected to cause sawtooth instabilities [4].

However the model used do describe the surface roughness wake field effect [1, 2, 3] has to be verified by measurements.

2 SURFACE ROUGHNESS WAKE FIELDS

Due to the small corrugations at the beam pipe the fundamental mode in the tube is slightly modified. By this means its phase velocity is decreased to the speed of light at a very high frequency. Its group velocity is very close to the speed of light but does not reach it. No mode with a higher radial dependency experiences the same [3]. The bunch is excit-

ing this mode only. Thus the wake field consists of one single mode running synchronous with the bunch (Fig 1).

The model of a thin dielectric layer can be employed to estimate the wake fields [1].

In the monopole case (m = 0) an estimation for the wave number is

$$k_0^2 = f \cdot \frac{4}{a\delta} \tag{1}$$

where a the tube radius and δ the rms thickness of the surface roughness. The factor f reflects the influence of the roughness shape and its size in comparison to the wave length of the rough tube mode. It is in the order of 1. These parameters mainly influence the frequency. It does not depend on any periodicity of the roughness, if the number of roughness bumps per wavelength of the rough tube mode is sufficiently large. The longitudinal wake function is

$$w_0^{\parallel}(s) = \frac{Z_0 c}{\pi a^2} \cos(k_0 s) \cdot e^{-\alpha(l)s}$$
 (2)

using the impedance of free space $Z_0 = \sqrt{\mu_0/\varepsilon_0}$. c denotes the speed of light. The attenuation α is a function of the tube length l and of the roughness shape. The wake amplitude is inversely proportional to the waveguides cross-section The dipole case can be described similarly. The dipole wake field has the same frequency as the monopole wake field. Its amplitude is twice as large as in the monopole case [2].

2.1 Development of the Wake Field Pulse

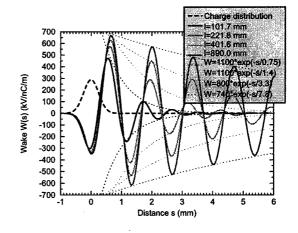


Figure 1: Time development of the the rf-wake field pulse created by a 250μ m bunch in a tube with 5mm radius and an rms roughness depth of 50μ m.

^{*} Email: timm@temf.tu-darmstadt.de

The normalized wake amplitude stays constant inside the Bunch. The rf-pulse length is increasing proportional to the tube length. Accordingly the pulse power of a roughness wake pulse in a given tube is constant too, while its average power is increasing. The attenuation is inversely proportional to the tube length (Fig. 1).

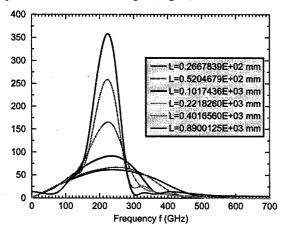


Figure 2: Time development of the spectrum of the rf-wake field pulse created by a $250\mu m$ bunch in a tube with 5mm radius and an rms roughness depth of $50\mu m$.

The bandwidth of the rf-pulse is decreasing with the tube length. Fig 2 shows the development of the frequency spec-

2.2 Normalized Description

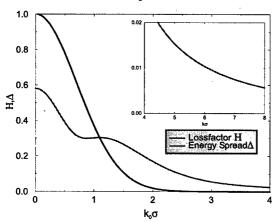


Figure 3: Loss factor H and energy spread Δ due to the rough tube mode in normalized description.

Introducing a normalized description, the loss factor is [3]:

$$H(k_0\sigma_z) = e^{-(k_0\sigma_z)^2}$$
. (3)

It gives the energy transported by the rf-wave traveling along the tube. The normalized energy spread is:

$$\Delta^{2}(k_{0}\sigma_{z}) = \frac{1}{\sqrt{2\pi}} \int_{-\infty}^{\infty} W_{0}^{\parallel 2}(k_{0}\sigma_{z}z) e^{-\frac{z^{2}}{2}} dz - e^{-2(k_{0}\sigma_{z})^{2}}$$

Fig. 3 shows the normalized energy spread and loss factor. The wave number k_0 is a property of the beam pipe only, within the range of validity of the model, i.e. the bunch length has to be larger than the average distance between roughness peaks. For larger values of $k_0\sigma_z$ the loss factor becomes rather small, but the energy spread is still not negligible.

2.3 Wake Fields in Waveguides with Different

The loss factor and the energy spread of a Gaussian bunch in a cylindrical, rough waveguide are

$$k_{loss} = \frac{Z_0 c}{2\pi a^2} H(k_0 \sigma_z)$$
, and $\Delta E = \frac{Z_0 c}{2\pi a^2} \Delta(k_0 \sigma_z)$ (5)

They are inversely proportional to the cross-section of the wave guide. In case of an elliptical waveguide the wave number and the loss factor are

$$k_0^2 = f \frac{2}{\delta} \frac{a+b}{ab}, \qquad k_{loss} = \frac{Z_0 c}{2\pi a b} H(k_0 \sigma_z)$$
 (6)
In case of a rectangular waveguide they are

$$k_0^2 = f \frac{2}{\delta} \frac{a+b}{ab}, \qquad k_{loss} = \frac{Z_0 c}{8ab} H(k_0 \sigma_z)$$
 (7)

a and b are the semi-axes of the elliptical or half the width of the rectangular waveguide respectively.

3D-Wake Field Calculations

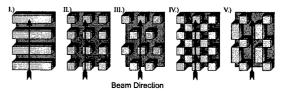


Figure 4: Surface structures of a rectangular waveguide used for 3dimensional wake field calculation. I.) irises, II.) cubes, III.) shifted cubes IV.) chequered and V.) 2 periods.

In order to check the model many 2-dimensional calculations were performed up to this point of time. Now the results of 3-dimensional calculations are presented to show the validity. Common to all computations is the use of a quadratic waveguide with 2mm width, only to verify Eq. 7 waveguides with arbitrary aspect ratio are used. The structure depth as well as the bunch length are $100\mu m$. Schematics for the used surface structures can be seen on Fig. 4. Unless otherwise noted, the width of one gap or one iris is $100\mu m$ too.

The wake fields show the same sine-like behaviour as in the 2-D case. The calculated loss factors and energy spreads (Fig. 5) principally follow the course of the theoretical values (Fig. 3, turquoise curves in Fig. 5). Using the "2 period structure" (Fig. 4.V) the wake field is partly com- $\Delta^{2}(k_{0}\sigma_{z}) = \frac{1}{\sqrt{2\pi}} \int_{0}^{\infty} W_{0}^{\parallel 2}(k_{0}\sigma_{z}z)e^{-\frac{z^{2}}{2}} dz - e^{-2(k_{0}\sigma_{z})^{2}}$ period structure" (Fig. 4.V) the wake field is partly compensated (Diamonds on Fig. 5). But if the period length becomes shorter in comparison to the bunch length the make comes shorter in comparison to the bunch length, the wake follows the curve again.

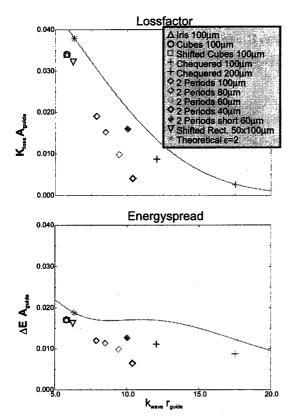


Figure 5: Comparison of loss factor and energy spread of 3D calculations to theoretical values. The star marks the 2D result for irises in a rectangular waveguide. The curves are a sector of Fig. 3

3 THE EXPERIMENT

One possibility to measure the surface roughness wake field effect is the measurement of the energy spread and the energy loss directly with the beam. Another possibility is to guide the rf-fields to an appropriate detector, where the frequency spectrum is measured. However the distinctness of the proof of the surface roughness wake fields does strongly depend on the tube length.

3.1 Proposal for Measurements at the TTF

Table 1: Parameters of the TESLA Test Facility beam

Bunch Length $\sigma_z[\mu m]$	≥ 250
Beam Energy E_0 [MeV]	240-390
Bunch Charge Q [nC]	1
Repetition Rate [Hz]	10
Bunch Spacing [μs]	0.111
Bunches per Bunch Train	1-7200

The parameters of the beam available at the TTF are given in Tab. 1. Behind the TTF-FEL undulator is some space to install a surface roughness experiment. Since it will be small in comparison to an undulator length of 100m or a length of 12km for the TESLA-FEL transfer line, an artificially increased roughness has to be attached to the tubes used for the experiment. The experiment can be set

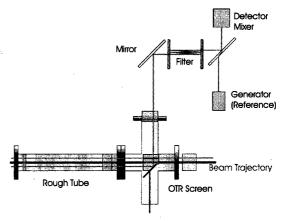


Figure 6: Scheme of the Roughness Wakefield Experiment. The bunch travels through a tube with artificially increased roughness. The rf-pulse, which accompanies the bunch is partially reflected out by an OTR-screen and guide to a detector.

up for a single shot mode. The expected values for the on the beam rf-wake field pulse are given in Tab. 3.

Table 2: Beam Measurements: loss factor and energy spread per 1m rough tube at 240MeV.

Tube	a=4mm,	a=3.3mm,
	$\delta = 50 \mu \text{m}$	$\delta = 75 \mu \text{m}$
$k\sigma_z$	1.118	1.005
Loss Factor $\left[\frac{kV}{m}\right]$	322	602
Rel. Energy spread $\frac{\Delta E}{E_0}$	1.4×10^{-3}	2.05×10^{-3}

Table 3: RF-wake field pulse per 1m rough tube

Tube	a=4mm,	a=3.3mm,
	$\delta = 50 \mu \mathrm{m}$	$\delta=75\mu\mathrm{m}$
Frequency [GHz]	214	192
Pulse Duration $\sigma_e \left[\frac{ps}{m} \right]$	65	65
Pulse Energy $\left[\frac{m\overline{J}}{m}\right]$	0.32	0.6
Pulse Power [kW]	4960	9260

- A. Novokhatski and A. Mosnier, 'Wakefields of Short Bunches in the Canal Covered with thin dielectric layer', PAC'97,p. 1444, Vancouver, Canada, May 1997.
- [2] A. Novokhatski, M. Timm, and T. Weiland, "The Transverse Wake Fields in the TESLA-FEL Transfer Line," *Proceedings* of the EPAC-98, pp. 515-517, 1998.
- [3] A. Novokhatski, M. Timm, and T. Weiland, "The Surface Roughness Wake Field Effect," *Proceedings of the ICAP'98*, to be published, 1998.
- [4] A. Novokhatski and T. Weiland, "Self-consistent model for the beams in accelerators," *Proceedings of the ICAP'98*, to be published, 1998.

HYBRID COMPUTATION OF NORMAL MODE TUNE SHIFTS IN ROUNDED-RECTANGULAR PIPES*

V. Galdi, D.I.I.I.E. - Univ. of Salerno, I-84084 Fisciano (SA), Italy S. Petracca^{†‡}, and I. M. Pinto, Univ. of Sannio at Benevento, I-82100 Benevento, Italy

Abstract

A fast and accurate hybrid (analytical-numerical) technique for computing the normal mode tune-shifts in rounded-rectangular (stadium) pipes is introduced based on Galerkin method together with a smart representation of Poisson's equation Green's function in a rectangular domain. Comparison with standard finite-elements and finite difference methods shows that our method is faster and more accurate, requiring no numerical differentiation.

1 THE PROBLEM

Many beam-pipe cross-section geometries of potential interest for accelerators, including the stadium-shaped one recently proposed for LHC [3], differ from the rectangle only by the rounding of corners, or the substitution of straight sides with circular arcs. Computing the related betatron tune-shifts, resulting from collective (space-charge and image) effects is a key problem to prevent resonant betatron excitations leading to potentially harmful beam instabilities. The normal mode coherent and incoherent tune-shifts can be written in terms of the normal mode Laslett coefficients ϵ as follows [2]:

$$\Delta \nu = -\frac{NRr_0}{\pi \nu \beta_0^2 \gamma_0 L^2} \, \epsilon,\tag{1}$$

where2:

$$\epsilon_{1,2} = \frac{L^2}{4\Lambda} \left\{ -\frac{\delta_x \partial_x \Phi^{(im)} + \delta_y \partial_y \Phi^{(im)}}{2} + \left[\left(\frac{\delta_y \partial_y \Phi^{(im)} - \delta_x \partial_x \Phi^{(im)}}{2} \right)^2 + \left. + \delta_x \partial_x \Phi^{(im)} \delta_y \partial_y \Phi^{(im)} \right]^{1/2} \right\},$$
 (2)

 $\Phi^{(im)}$ is the image-potential produced in the beam pipe by a linear charge density Λ going through the beam center of charge \underline{r}_b , N is the number of particles in the beam, R is

the machine radius, r_0 is the classical particle radius, L is a scaling length (usually, the maximum pipe diameter), ν is the nominal tune, and

$$\begin{cases} \delta_{x,y} = \partial_{x,y}|_{\underline{r}=\underline{r}_b}, \text{ incoherent regime,} \\ \delta_{x,y} = (\partial_{x,y} + \partial_{x_b,y_b})|_{\underline{r}=\underline{r}_b}, \text{ coherent regime.} \end{cases}$$
(3)

2 THE METHOD

For computing the image potential $\Phi^{(im)}$ in rounded rectangular geometries, it is convenient to use the rectangular-domain Green's function g_R (henceforth RDGF), viz. :

$$\Phi^{(im)}(\underline{r},\underline{r}_b) = \Phi(\underline{r},\underline{r}_b) - \Lambda g_0(\underline{r},\underline{r}_b),$$

$$\Phi(\underline{r},\underline{r}_b) = \Lambda \left[\sum_{k} \int_{\sigma_k} g_R(\underline{r},l_k) \rho_{\sigma_k}(l_k) dl_k + g_R(\underline{r},\underline{r}_b) \right], \quad (4)$$

where g_0 is the free-space Green's function, the unknown ρ_{σ_l} are obviously nonzero *only* on the rounded portion of ∂S_0 , i.e., the arcs σ_k , and l_k is the arc-length on σ_k .

We seek a hybrid (analytical-numerical) solution of eq. (4) by using Galerkin (moments) method [6], whereby we first expand the unknown ρ_s :

$$\rho_{\sigma_k}(l_k) = \sum_{n=1}^{N} b_n^{(k)} w_n^{(k)}(l_k), \tag{5}$$

into a suitable (finite) set of basis functions $\{w_1^{(k)}(l_k),\ldots,w_N^{(k)}(l_k)\}$, defined on σ_k , where $\{b_1^{(k)},\ldots,b_N^{(k)}\}$, are N-dimensional vectors of unknown coefficients, and then enforce the (Dirichlet) boundary conditions on the arcs σ_k , whence:

$$\int_{\sigma_k} \Phi(l_k, \underline{r}_b) w_n^{(k)}(l_k) dl_k = 0,$$

$$n = 1, 2, \dots, N; \ k = 1, 2, \dots, P,$$
(6)

thus obtaining a block-matrix linear system:

$$[\mathbf{L}] \mathbf{b} = \mathbf{c}. \tag{7}$$

The matrix [L] is readily shown to be symmetrical, positive definite and hence non-singular. The components of b, c and L are explicitly given by (5),

$$c_i^{(k)} = -\int_{\sigma_k} w_i^{(k)}(l_k)g(l_k,\underline{r}_b)dl_k,$$

^{*} Work supported in part by INFN.

[†] On leave of absence from KEK, Tsukuba, JPN.

[‡] e-mail stefania@kekvax.ac.jp

¹The *incoherent* and *coherent* regimes correspond to $\underline{r} \neq \underline{r}_b = \underline{r}_{eq}$ and $\underline{r} = \underline{r}_b \neq \underline{r}_{eq}$, respectively, \underline{r}_{eq} denoting the beam center of charge equilibrium position [2].

²The pipe-shape independent space-charge contribution to the tuneshift is neglected here for simplicity.

$$i = 1, 2, \dots, N; \quad k = 1, 2, \dots, P,$$
 (8)

and:

$$[L_M^{(p,q)}]_{ij} = \int_{\sigma_p} \int_{\sigma_q} g(l_p, l_q) w_i^{(p)}(l_p) w_j^{(q)}(l_q) \ dl_p \ dl_q,$$

$$i, j = 1, 2, \dots, N, p, q = 1, 2, \dots, P,$$
 (9)

where the upper indexes identify the block sub-matrix, and the lower ones the element in each sub-matrix.

Using eq.s (2)-(5), once (7) has been solved, the Laslett coefficients can be computed *without* resorting to numerical differentiation. This makes the proposed method definitely more accurate than both finite-differences and finite-elements.

3 IMPLEMENTATION AND COMPUTATIONAL BUDGET

Fast and accurate numerical solution of (7) follows from a skillful choice of the RDGF representation in (4) and the basis functions in (5).

A rapidly converging series expansion of the RDGF [5], which explicitly contains the (logarithmic) singular term is ³:

$$g_R(\underline{r}, \underline{r}_b) = -\sum_{m = -\infty}^{\infty} \log \frac{T_m^{10}(\underline{r}, \underline{r}_b) T_m^{01}(\underline{r}, \underline{r}_b)}{T_m^{00}(\underline{r}, \underline{r}_b) T_m^{11}(\underline{r}, \underline{r}_b)}, \quad (10)$$

where:

$$T_{m}^{pq}(\underline{r},\underline{r}_{b}) = 1 + \exp\left[-2|y-(-)^{p}y_{b} + 2bm|\frac{\pi}{a}\right] +$$

$$-2\exp\left[|y-(-)^{p}y_{b}+2bm|\frac{\pi}{a}\right]\cos\left[\frac{\pi}{a}\left(x-(-)^{q}x_{b}\right)\right], \quad (11)$$

a, b being the rectangle side lengths.

A convenient set of (partially overlapping) piece-wise parabolic *subdomain* basis functions, can be defined in terms of the local angles ϕ (we drop the suffix k for simplicity) as follows:

$$w_i(\phi) = \frac{\Delta \phi^2 - (\phi - \phi_i)^2}{\Delta \phi^2},$$

$$\phi_i - \Delta\phi(1 - \delta_{i1}) \le \phi < \phi_i + \Delta\phi(1 - \delta_{iN}),$$

$$i = 1, 2, \dots, N,$$
(12)

where $\Delta \phi$ is the angular discretization step (assumed the same for all arcs), ϕ is related to the local arc-length l by $l=R\phi$, R being the local curvature radius, and δ_{rs} is the Kronecker symbol⁴. The relevant local coordinate systems are sketched in Fig. 1. Note that: i) the choice of subdomain basis functions, rather than full-domain ones, results

into fewer singular integrals in [L]; ii) no polygonal approximation of the arcs is implied, resulting into fewer functions being needed for a given accuracy.

Letting P the number of arcs in the rounded portion of ∂S_0 , the system (7) has rank NP. Computing the matrix elements requires evaluating up to PN(PN-1)/2 double-integrals⁵. These latter can be either evaluated numerically using standard routines appropriate for regular [7] and singular integrands [8], or analytically [4]. Matrix inversion for solving (7) is not the most demanding task, in view of the typically small $(NP \approx 20)$ L matrix size. In all numerical simulations below we truncated (10) at $|m| \leq 3$ and took $\Delta \phi = \pi/10$, corresponding to a matrix size NP = 20.

4 NUMERICAL RESULTS AND CONCLUSIONS

The circular pipe, for which the tune-shifts are known exactly, is the hardest conceivable test case for the proposed method (largest departure from rectangular geometry). It is seen from Fig. 2 that the obtained accuracy is very good.

Our method was subsequently applied [4] to a number of different proposed geometries relevant to LHC [3].

As an example the contour-level plots for the incoherent and coherent (both normal modes) Laslett coefficients for a stadium-shaped pipe, sketched in Fig. 3, are shown in Fig.s 4-6.

As a conclusion, we found that the above hybrid approach is comparatively faster and more accurate than available finite-element and/or finite-difference techniques.

- [1] L.J. Laslett, Proc. of the 1963 Summer Study BNL 7534.
- [2] S. Petracca, Particle Accel., 48, 81, 1994.
- [3] The LHC study group, CERN/AC/95-05 (LHC), 1995.
- [4] V. Galdi, S. Petracca, I. Pinto, Particle Accel., PA(R)-85, 1999, in print.
- [5] M. Bressan and G. Conciauro, Alta Frequenza, LII, 188, 1983, ibidem LVII, 217, 1988.
- [6] R.F. Harrington, Field Computation by Moment Methods, McMillan, New York, 1961.
- [7] W.H. Press et al., Numerical Recipes, the Art of Scientific Computing, 2nd Ed., Cambridge Un. Press, 1992.
- [8] SLATEC Pub. Dom. Math. Lib., NETLIB, http://www.netlib.org

 $^{^3\}mathrm{It}$ is easily recognized that the (logarithmic) singularity of g_R appears in the T_0^{10} term.

⁴For i=1,N, eq. (12) yields the correct behaviour at the points where the circular arcs join the straight portions of ∂S_0 , where ρ_s can be different from zero, but its derivative should vanish.

⁵Due to geometrical (specular) symmetries, the effective number of elements to compute is usually smaller.

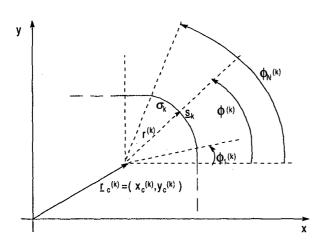


Fig. 1 - Local coordinate system relevant to eq. (12).

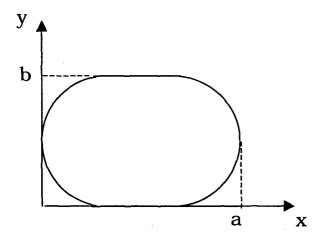


Fig. 3 - Stadium-shaped pipe (a=1, b=0.7).

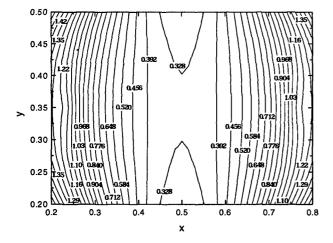


Fig. 5 - Stadium-shaped pipe. Coherent Laslett coefficient (1st normal mode).

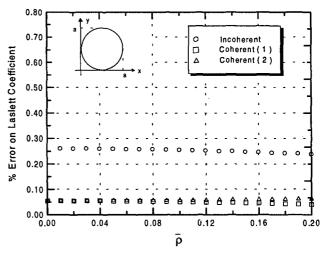


Fig. 2 - Circular pipe. Errors on Laslett coefficients vs. scaled radial distance, $\bar{\rho} = \frac{2}{a} \left[(x - a/2)^2 + (y - a/2)^2 \right]^{1/2}$.

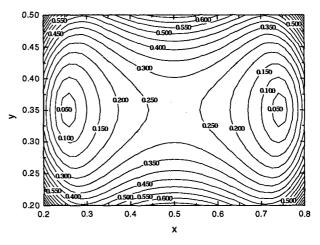


Fig. 4 - Stadium-shaped pipe. Incoherent Laslett coefficients (both normal modes).

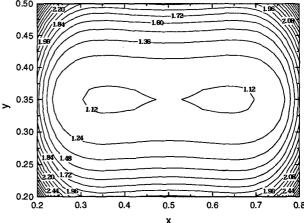


Fig. 6 - Stadium-shaped pipe. Coherent Laslett coefficient $(2^{nd}$ normal mode).

MEASUREMENTS OF TUNE SHIFTS WITH AMPLITUDE AT LEP

A.-S. Müller*, J. Wenninger, CERN, Geneva, Switzerland

Abstract

The beam orbit system of the LEP electron-positron collider is able to store the beam position over 1000 turns following a deflection by a horizontal kicker. A precise analysis of such 1000-turn data for many beam position monitors was used to study the dependence of the tune on the horizontal amplitude. The horizontal tune shift with amplitude was determined from the decay of the beam oscillation for various LEP optics. This parameter turned out to be an important issue for the LEP high energy optics.

1 MOTIVATION

During the last years stronger focusing lattices have been developed to improve the LEP performance at high energy [1]. This search for a good high energy optics has revealed the importance of the horizontal detuning with amplitude (anharmonicity) to guarantee a sufficient aperture for the beam. This is due to the fact that with the regular tune working point at LEP (the fractional part of Q_H is about 0.28) a large detuning with amplitude drives particles on the third order resonance.

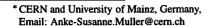
2 DAMPED COHERENT OSCILLATIONS

The detuning with amplitude can be determined from an analysis of "1000-turn" measurements. A coherent horizontal oscillation is excited by a single kick and the centre-of-charge position of the bunch is observed over 1024 consecutive turns. Figure 1 shows such a 1000-turn measurement for one BPM. The moment of the kick is clearly visible. A phase space representation of the same dataset is shown in figure 2 where the horizontal centre-of-charge position of a bunch at two BPMs with a distance of $\approx 90^{\circ}$ in phase is plotted. The Courant-Snyder invariant

$$W \sim x_A^2 + x_B^2$$

can be calculated from the measured positions at the two BPMs. A Fourier spectrum ("Lomb periodogram", [2]) of the time dependence of W shows the tune components (fig. 2). The third order components as well as the change in the horizontal tune Q_x are clearly visible.

A"global" fit to the single BPM 1000-turn data using a damped oscillation with amplitude dependent frequency yields the coherent damping time τ . The coherent damping



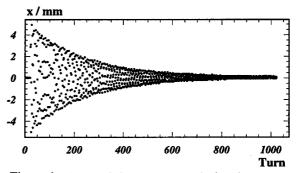


Figure 1: Centre-of-charge position of a bunch versus turn number at an arc monitor. The kick and the subsequent damped oscillation are clearly visible.

at LEP is composed of radiation and head-tail damping:

$$1/ au_{ ext{coh}} = 1/ au_{ ext{o}} + 1/ au_{ ext{head-tail}} ext{ with } 1/ au_{ ext{head-tail}} \sim rac{Q'}{E_{ ext{o}}} I_{ ext{b}}$$

where Q' is the chromaticity, I_b the bunch current and E_0 the beam energy.

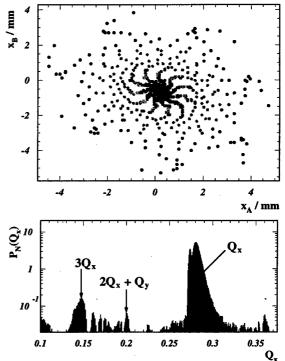


Figure 2: Upper plot: Centre-of-charge position of a bunch after a kick at two BPMS with a distance of 90° in phase. Lower plot: Fourier spectrum ("Lomb periodogram") of the Courant-Snyder invariant W. The detuning with amplitude is clearly seen on Q_x and Q_x and Q_x and Q_x and Q_x are present.

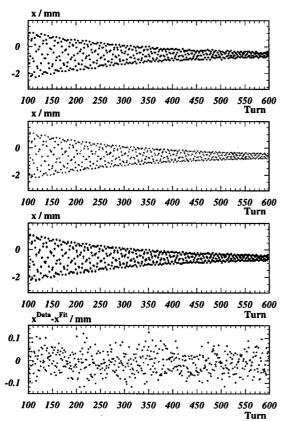


Figure 3: Centre-of-charge position of a bunch versus turn number at an arc monitor. The upper two plots show data and the results of a "global" fit to the oscillation. The third plot is an overlay of data and fit results and the fourth shows the difference.

This relation holds down to very low bunch currents. No filamentation effect is observed down to the smallest measurable currents. In general the head-tail effect is the dominating damping mechanism. Figure 3 shows such a global fit. The first plot shows the measured data, the second one the results of the fit and the third an overlay of measurement and fit results. The last plot of fig. 3 shows the fit residuals. Obviously the damping behaviour is very well reproduced by the fit model.

3 EXTRACTING THE HORIZONTAL DETUNING WITH AMPLITUDE

A series of fits is used to extract the horizontal detuning with amplitude from the 1000-turn measurements. Using the damping time from the previously mentioned "global" fit, the tune evolution with time is extracted by fitting damped harmonic oscillations to subsamples of several turns. The results of such fits to the data of fig. 1 are shown in fig. 4 where the resulting tune is plotted as a function of the turn number. The horizontal detuning with amplitude $(\partial Q_x/\partial W_x)$ is given by the dependence of the tune Q on the Courant-Snyder invariant W. The latter is easily

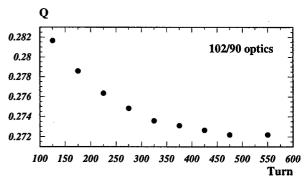


Figure 4: Tune evolution corresponding to the damped bunch oscillation shown in figure 1.

calculated from

$$W = \frac{1 + \alpha^2}{\beta} x^2 + 2\alpha x x' + \beta x'^2 \approx A^2/\beta$$

with

$$A = A_0 e^{-t/\tau}$$

where τ is the damping time and A_0 the zero turn amplitude. x stands for a single particle position and A denotes the measured amplitude of the centre-of-charge oscillation of a bunch. Figure 5 shows the relation between tune Q and Courant-Snyder invariant W for one BPM. The detuning is given by the slope using:

$$Q = Q_0 + \frac{\partial Q_x}{\partial W_x} W$$

This analysis is applied to all 240 beam position monitors of the arcs in order to improve the statistics for a reliable measurement. Averaging over all arcs also cancels periodic perturbations like β -beating. The statistical error is given by the standard deviation of all single measurements

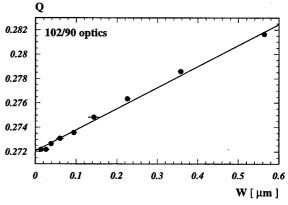


Figure 5: Tune as function of Courant-Snyder invariant for the data sample shown in fig. 1 and fig. 4 (the straight line is a fit to the data).

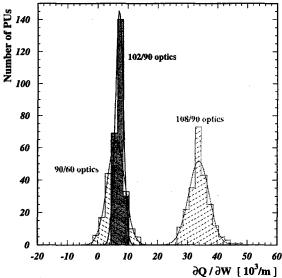


Figure 6: Horizontal detuning with amplitude for the LEP physics optics with horizontal/vertical phase advance in the arcs of 90/60, 102/90 and 108/90 degrees.

 (σ/\sqrt{N}) . Simulation studies of the systematic error with the MAD simulation program [3] show that the method is reliable.

Datasets for several optics have been analysed. The results are shown in tab. 1 and fig. 6. The histograms of fig. 6 represent the distributions of measurements for all arc monitors. The distributions are consistent with a Gaussian shape and are clearly separated. Although the measured detuning is usually larger than the predictions for a perfect machine there is a reasonable agreement between measurements and predictions. A more detailed description of this topic can be found in [4].

4 DETUNING OPTIMISATION

Three horizontal sextupole families are used to optimise the chromaticity and tune shifts with amplitude. The detuning can be trimmed around its nominal value by changing the strength K of sextupole families in opposite directions while keeping the chromaticity constant $(n_1 K_1^s + n_3 K_3^s =$ const where n_1 and n_3 are the number of sextupoles in

0-4:	$\partial Q_x/\partial W_x \ [10^3/\mathrm{m}]$		
Optics	MAD	Measured	
90/60	1.7	6.2 ± 0.8	
102/90	7.0	7.2 ± 1.0	
108/90	25.0	34.0 ± 1.0	

Table 1: Measured and predicted horizontal detuning with amplitude for three LEP physics optics. The errors include statistical and systematic uncertainties.

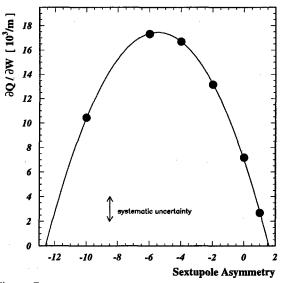


Figure 7: Measured horizontal detuning with amplitude for different sextupole settings. Measurement errors are drawn. The size of the systematic error is given.

the families). The horizontal detuning with amplitude has been measured for several such settings of the sextupoles. Figure 7 shows that the detuning can be changed in a controlled way. The measurement errors are drawn and the systematic uncertainty is shown.

5 SUMMARY

Measurements of damped coherent oscillations following a horizontal kick have been used to study the horizontal tune shift with amplitude. The horizontal detuning can be extracted in a precise and robust way and the measured tune shifts with amplitude confirm predictions of the LEP model.

6 ACKNOWLEDGEMENTS

Many thanks to all who have contributed to the results presented above and in particular to A. Hofmann, A. Verdier and J.M. Jowett for helpful and instructive discussions.

- [1] Y. Alexahin et al. Low emittances lattices for LEP2. In Proceedings of the 17th Particle Accelerator Conference, 1997.
- [2] N.R. Lomb. In Astrophysics and Space Science, volume 39, pages 447–462. 1976.
- [3] H. Grote and F. C. Iselin. The MAD Program, User's Reference Manual. SL Note 90-13 (AP) (Rev. 4), CERN, March 1995.
- [4] A.-S. Müller and J. Wenninger. Measurements of Coherent Damping and Tune Shifts with Amplitude at LEP. In Proceedings of the 6th European Particle Accelerator Conference, pages 1377-1379, 1998.

GENERAL MOMENT MODEL OF BEAM TRANSPORT*

B. A. Shadwick[†] and J. S. Wurtele, Department of Physics, UC Berkeley and Center for Beam Physics, LBNL, Berkeley CA, USA

Abstract

Using the Hamiltonian structure of the Vlasov equation, we develop a general, relativistic, three-dimensional model of beam transport based on phase space moments of the beam particle distribution. Evolution equations for these moments are derived from the non-canonical Poisson bracket for the Vlasov equation. In this model, the beam centroid experiences the full non-linear forces in the system while the higher order moments are coupled to both the centroid and to various spatial derivatives of the applied fields. For example, when moments up to second order are retained, the physics content is similar to considering linearized forces. Given the large number of equations (there are 27 equations when all second order moments are kept) and their algebraic complexity, the use of symbolic computation in the derivation was critical to ensuring the correctness of the equations. This approach also allows for analytical verification of conservation laws associated with the model. The initial investigations [1] have considered only externally applied fields, however in principle spacecharge forces can also be included. We discuss the necessary extensions to the basic theory needed to model ionization cooling for the muon collider[2].

1 INTRODUCTION

Using moments to construct reduced models of phase space dynamics is not a new idea; for example, see Refs. [3, 4] for a linac application and Ref. [5] for general approach to Hamiltonian field theories. The desire such models is clear. Tracking individual particles is computationally very intensive (if reasonable statistics are to be obtained) and in many instances the detailed information that tracking produces is not of great interest. Furthermore, often the beam dynamics is largely linear so representing the bulk of the beam by particles is inefficient. One-dimensional moment equations are of significant pedagogical interest as they provide a simple means for understanding a variety of elementary beam dynamics. While such models are of little use in detailed studies of beam transport, there still exists the possibility of extracting much of the beam behaviour without resorting to tracking individual particles.

Here we present a formalism for a general, fully relativistic, three-dimensional moment description of beam transport based upon the noncanonical Hamiltonian structure of the Vlasov-Poisson equation [6]. This approach has many attractive features. By using a formulation based

on Poisson brackets, derivation of the equations of motion for the moments is purely mechanical and is ideally suited to the application of symbolic manipulation. In this approach, one approximates the Hamiltonian and bracket in terms of moments and then uses Hamilton's equations to obtain equations of motion. Not only is this procedure less cumbersome than directly averaging the single particle equations, it also eliminates the difficulty of determining (in a more less ad hoc fashion) a consistent ordering of the moment expansion. As is common in this type of reduction, one finds that even when the external forces are linearized, for the model to conserve energy (and typically other invariants also, if they exist) it is necessary that the evolution equations retain various terms that are nonlinear in the moments. When the equations are derived from a Poisson bracket and Hamiltonian these nonlinear terms automatically appear as needed. Moment representations are intrinsically statistical in nature and are not susceptible to (nor sensitive to) noise associated with finite particle affects. Terms in the moments equations have two origins: kinematic terms (i.e., those terms associated with the free-streaming of phase space) and terms associated with electromagnetic forces. It turns out the that the kinematic terms have the form of an expansion in the reciprocal of the centroid γ -factor while the electromagnetic forces are essentially Taylor expanded about the centroid location to an order that depends on the order of the moments being retained. Typically one finds that the moment equations do not close, i.e., the equations of motion for a set of moments of a particular order tend to include couplings to moments of higher order. There are numerous methods for imposing a closure. The observation that the moment model is a combination of an asymptotic expansion in γ^{-1} and a Taylor expansion of the applied forces means that for even mildly relativistic beams ($\gamma \sim 2$) and for forces that do not vary to drastically over the extent of the beam, simple truncation is a reasonably accurate closure. It is also the case that imposing a closure may well destroy the Hamiltonian structure of the moment system (in the sense that the bracket typically no longer satisfies the Jacobi identity). While philosophically one might prefer an approximation that fully retains the Hamiltonian character of the underlying dynamics, this loss does not lessen the power of the bracket approach to deriving equations of motion.

2 HAMILTONIAN FORMULATION OF THE VLASOV EQUATION

We examine the simplest case where we ignore the selfinteractions of the beam (i.e. we ignore space charge ef-

^{*} Supported by the U. S. DoE Division of High Energy Physics under grant No. DEFG-03-95ER-40936.

[†]email: shadwick@beams.lbl.gov

fects), although more general models are possible. In this case, the beam dynamics are governed by the relativistic Vlasov equation with *external* fields:

$$\frac{\partial f}{\partial t} + \mathbf{v} \cdot \nabla f + \frac{q}{m} \left(\mathbf{E} + \frac{\mathbf{v}}{c} \times \mathbf{B} \right) \cdot \nabla_{p} f = 0, \quad (1)$$

where f is the phase-space particle density, q and m are the particle mass and charge, respectively and $\nabla_p = \partial/\partial p$. Writing the particle phase-space distribution function in terms of the *canonical* momentum, p, the relativistic Vlasov equation can be written as [6]:

$$\frac{\partial f}{\partial t} = \{f, H\} \tag{2}$$

where the Hamiltonian H is given by:

$$H = \int d^3 \mathbf{r} \, d^3 \mathbf{p} \left(\gamma \, m \, c^2 + \phi \right) f(\mathbf{r}, \mathbf{p}) \,. \tag{3}$$

The (noncanonical) Poisson bracket $\{\cdot, \cdot\}$ of any functionals F and G of f is given by

$$\{F,G\} = \int d^3 \mathbf{r} \, d^3 \mathbf{p} \, f \left[\frac{\delta F}{\delta f}, \frac{\delta G}{\delta f} \right]$$
 (4)

where $[\,\cdot\,,\,\cdot\,]$ is the usual phase-space Poisson bracket:

$$[F,G] = \nabla F \cdot \nabla_{\!p} G - \nabla G \cdot \nabla_{\!p} F. \qquad (5)$$

For the purposes of studying charged-particle optics, it is more convenient to express f in terms of the mechanical momentum, $\mathbf{p} = \mathbf{p} - q/c\mathbf{A}$, where \mathbf{A} is the vector potential. Under this coordinate transformation

$$\frac{\partial}{\partial t} \longrightarrow \frac{\partial}{\partial t} - \frac{q}{c} \frac{\partial \mathbf{A}}{\partial t} \cdot \nabla_{p},$$
 (6)

$$\nabla_{\!\mathfrak{p}} \longrightarrow \nabla_{\!p}, \qquad (7)$$

$$\nabla \longrightarrow \nabla - \frac{q}{c} \nabla A_k \frac{\partial}{\partial n_k}.$$
 (8)

Applying this change of variables to the brackets gives,

$$\{F,G\} = \int d^{3}\mathbf{r} \, d^{3}\mathbf{p} \, f \left[\frac{\delta F}{\delta f}, \frac{\delta G}{\delta f} \right]_{xp} + \frac{q}{c} \int d^{3}\mathbf{r} \, d^{3}\mathbf{p} \, f \, \mathbf{B} \cdot \nabla_{p} \, \frac{\delta F}{\delta f} \times \nabla_{p} \, \frac{\delta G}{\delta f}, \quad (9)$$

where $[\cdot,\cdot]_{xp}$ is given by (5) with **p** replaced by **p** and we will subsequently suppress this subscript. The Vlasov equation now reads

$$\frac{\partial f}{\partial t} - \frac{q}{c} \frac{\partial \mathbf{A}}{\partial t} \cdot \nabla_{p} f = \{ f, H \}$$
 (10)

Upon close examination of (10), we see that $-(1/c)\partial \mathbf{A}/\partial t$ enters the expression for $\partial f/\partial t$ in exactly the same way as does $\nabla \phi$. The following trick is useful (but not necessary):

make the formal identification $\nabla \varphi = \nabla \phi + (1/c)\partial \mathbf{A}/\partial t$, and write (10) as

$$\frac{\partial f}{\partial t} = \left\{ f, \widetilde{H} \right\},\tag{11}$$

where \widetilde{H} is obtained from H by the replacement $\phi \to \varphi$. The chain rule can then be used to obtain the time derivative of any functional of f:

$$\frac{dF}{dt} = \int d^{3}\mathbf{r} \, d^{3}\mathbf{p} \, \frac{\delta F}{\delta f} \left\{ f, \widetilde{H} \right\} + \frac{\partial F}{\partial t} \\
= \left\{ F, \widetilde{H} \right\} + \frac{\partial F}{\partial t}. \tag{12}$$

3 MOMENT EQUATIONS

Our moment models are based on an expansion of the phase space coordinates about the location of the beam centroid:

$$\mathfrak{z}_i = \langle \mathfrak{z}_i \rangle + \delta \mathfrak{z}_i, \tag{13}$$

where $\{\mathfrak{z}_j\}_{j=1}^6 = \{x,y,z,p_x,p_y,p_z\}$ and $\langle \cdot \rangle$ is the normalized phase-space average. To simplify the presentation, we keep moments only up to second order, but it is clear that these procedures can be carried out to arbitrary order. We define

$$M_i \equiv \langle \mathfrak{z}_i \rangle$$
 and $M_{ij} \equiv \langle \delta \mathfrak{z}_i \, \delta \mathfrak{z}_j \rangle$. (14)

The first order moments, M_i , represent the beam centroid, while the second-order moments, M_{ij} , represent the phase-space extent of the beam.

Substituting (13) into the expression for H and keeping terms through second order in $\delta_{\mathfrak{F}_i}$, we obtain a Hamiltonian for the moment system:

$$\widehat{H} = f_0 \left(\gamma_0 m c^2 + q \varphi \right) - f_0 \frac{m c^2}{2\gamma_0^3} \left(\langle \delta p_x^2 \rangle \langle p_x \rangle^2 + \langle \delta p_y^2 \rangle \langle p_y \rangle^2 + \langle \delta p_z^2 \rangle \langle p_z \rangle^2 + 2 \langle \delta p_x \delta p_y \rangle \langle p_x \rangle \langle p_y \rangle \right)$$

$$+ 2 \langle \delta p_x \delta p_z \rangle \langle p_x \rangle \langle p_z \rangle + 2 \langle \delta p_y \delta p_z \rangle \langle p_y \rangle \langle p_z \rangle$$

$$+ f_0 \frac{m c^2}{2\gamma_0} \left(\langle \delta p_x^2 \rangle + \langle \delta p_y^2 \rangle + \langle \delta p_z^2 \rangle \right)$$

$$- f_0 q \left(\frac{\langle \delta x^2 \rangle}{2} \frac{\partial E_x}{\partial x} + \frac{\langle \delta y^2 \rangle}{2} \frac{\partial E_y}{\partial y} + \frac{\langle \delta z^2 \rangle}{2} \frac{\partial E_z}{\partial z} \right)$$

$$+ \langle \delta x \delta y \rangle \frac{\partial E_x}{\partial y} + \langle \delta x \delta z \rangle \frac{\partial E_x}{\partial z} + \langle \delta y \delta z \rangle \frac{\partial E_y}{\partial z} , \quad (15)$$

where $\gamma_0 = \left[1 + (\langle p_x \rangle^2 + \langle p_y \rangle^2 + \langle p_z \rangle^2)/(m^2 c^2)\right]^{1/2}$, $f_0 = \int d^3 \mathbf{r} d^3 \mathbf{p} f$, and all external fields are evaluated at the centroid position.

Since moments are clearly functionals of f, (12) and (9) give the necessary equations of motion. In evaluating (9),

 $^{^{\}rm I}$ In general this is equation is not solvable for φ ; the solvability condition is $\partial {\bf B}/\partial t=0.$

note that for a functional of f that can be written as a function of the moments alone, i.e., $F[f] = \widehat{F}(M_i, M_{ij})$, we have

$$\frac{\delta F}{\delta f} = \frac{\partial \widehat{F}}{\partial M_i} \frac{\delta M_i}{\delta f} + \frac{\partial \widehat{F}}{\partial M_{ij}} \frac{\delta M_{ij}}{\delta f}$$

$$= \frac{\partial \widehat{F}}{\partial M_i} \frac{1}{f_0} \mathfrak{z}_i + \frac{\partial \widehat{F}}{\partial M_{ij}} \frac{1}{f_0} \mathfrak{z}_i \mathfrak{z}_j. \tag{16}$$

Combining the above we can write the equations of motion for the moments:

$$\dot{M}_{i} = \left\{ M_{i}, \widehat{H} \right\} \quad \text{and} \quad \dot{M}_{ij} = \left\{ M_{ij}, \widehat{H} \right\}. \quad (17)$$

While evaluating (17) is conceptually straightforward, these equations are both numerous (there a total of 27 moments through second order) and algebraically very complex. To overcome this complexity and to ensure the correctness of the resulting equations, we have implemented (9), (12), and (16) using symbolic algebra. In addition to deriving the equations, our symbolic algebra program also produces the necessary source code for the numerical implementation of these equations. This approach not only increases our confidence that the final simulation code is correct but also enables symbolic identification and verification of a variety of conserved quantities (which are then used as diagnostics in the simulation). Examples of such invariants include, energy, six-dimensional emittance ($\det M_{ij}$), angular momentum (in axially symmetric systems), and longitudinal and transverse emittance separately, in systems where the dynamics decouples.

Note that, exactly one expects, the first two terms in \widehat{H} are the Hamiltonian for a single particle, whose trajectory is that of the beam centroid. As higher order moments are added to the model, this "particle" acquires internal structure (in 6-d phase space) which results in additional terms in the equations of motion of the first order moments.

4 APPLICATION TO MUON COOLING

To study the ionization cooling of muons we must extend our formulation to include the non-Hamiltonian interaction of the beam with material absorbers. This interaction can be divided into inelastic (ionization energy loss) and elastic ("multiple scattering") parts. The inelastic part can be viewed as a frictional force in the direction of the beam momentum and the contributions to the moment equations can be found by taking appropriate averages of this force term. The elastic piece is due to small angle scattering in random directions, and thus can only be included in a statistically averaged sense. We have developed a simulation code that takes these effects into account for studying a section of the transverse cooling channel [7] of the muon collider. Our preliminary results [2] show that the moment model is in very good agreement with particle tracking studies and the simulation promises to be a useful design tool.

5 CONCLUSIONS

We have presented a formalism for constructing models of beam dynamics based upon moments of arbitrary order. It is also possible to construct "semi-discrete" models; for example, by averaging only over the transverse phase space, one obtains a system where the transverse dynamics are determined by moments while a full kinetic description is retained longitudinally. One can also envision constructing a δf method using a moment formalism to represent the core of a beam. Such a method could yield important kinetic information (say for studies of halo formation) without the computational burden of using particles to model the beam core. As an application of moment methods, we have studied an ionization cooling channel for the muon collider and have found close agreement between our simulation and full particle tracking, verifying the utility of moments models as design tools. Here we have closed the system by discarding higher-order moments, however, other closures are equally justified: for example, one can, by ignoring correlations, approximate the higher moments using products of lower order moments. Understanding how the choice of closure affects the accuracy of the model will be the subject of future work.

6 ACKNOWLEDGEMENTS

This work was motivated by interest in the problem of muon cooling and has benefited from discussions with various member of the Muon Collider Collaboration, in particular C. M. Celata and A. M. Sessler. In addition, BAS would like thank P. J. Morrison for a long series of conversations on Hamiltonian structure.

- [1] C. M. Celata, A. M. Sessler, P. B. Lee, B. A. Shadwick, and J. S. Wurtele, "A Moment Equation Approach to a Muon Collider Cooling Lattice," in *Proceedings of the Sixth Euro*pean Particle Accelerator Conference, Stockholm (IOP, Bristol, 1998), pp. 1058–1060.
- [2] B. A. Shadwick, J. S. Wurtele, A. M. Sessler, C. M. Celata, and P. B. Lee, "Modeling the Muon Cooling Channel Using Moments," paper #TUP101, this proceedings.
- [3] P. J. Channell, "The Moment Approach to Charged Particle Beam Dynamics," IEEE Trans. Nucl. Sci. NS-30, 2607 (1983).
- [4] P. J. Channell, L. M. Healy, and W. P. Lysenko, "The Moment Code BEDLAM," IEEE Trans. Nucl. Sci. NS-32, 2565 (1985).
- [5] B. A. Shadwick and P. J. Morrison, "Hamiltonian Cell Dynamics," in *Proceedings of International Sherwood Fusion Theory Conference*, Dallas TX (University of Texas, Austin, 1994), p. 250.
- [6] P. J. Morrison, "The Maxwell-Vlasov Equations as a Continuous Hamiltonian System," Phys. Lett. 80A, 383 (1980).
- [7] C. M. Ankenbrandt *et al.*, "Status of Muon Collider Research," submitted to PRST-AB.

CALIBRATION OF THE UVX LNLS STORAGE RING OPTICS USING A LINEAR RESPONSE MATRIX THEORY

Liu Lin and A. L. Xavier Jr⁺, LNLS, Campinas, Brazil.

Abstract

We present initial results of the optics calibration project of the LNLS UVX electron storage ring by the use of the response matrix formalism.

1 INTRODUCTION

Motivated by recent works in the literature [1], the Accelerator Physics Group of the LNLS is currently developing a plan for the UVX optics calibration through a linear response formalism known as response matrix theory. The response matrix is a well-behaved function of the machine parameters. Besides optics parameters, the procedure is used to obtain values for the calibration of the orbit correction system, that is, BPM and steering magnet gains.

The response matrix $M_{i,j}^{k,m}$ is defined by the relation

$$\Delta x_i^m = M_{i,j}^{k,m} \Delta \theta_i^k,$$

where Δx_j^m is the orbit change in the j-th BPM in the m plane after a small kick $\Delta \theta_i^k$ in the i-th steering magnet in the k plane. In the linear approximation, one assumes small coupling between the planes such that the matrix is close to zero for $k \neq m$. An optics calculation program is used to determine the machine optics functions and the response matrix model. For most practical purposes, the MAD program [2] is a convenient tool. A figure of merit function is then defined

$$\chi^{2}([p]) = \sum_{k,m} \sum_{i,j} \frac{[M_{i,j}^{k,m}([p]) - \overline{M}_{i,j}^{k,m}]^{2}}{\sigma_{ij}^{2}},$$

where [p] represents all parameters entering in the calibration, \overline{M} is the experimental matrix and σ_{ij}^{2} is the error associated to the matrix elements. From the numerical point of view, the essence of this work is summarized in the following way: given the experimental matrix, find all the corrections, $[\Delta p]$, to all relevant parameters in such a way that the model matrix is as close as possible to the experimental one. As one approaches the minimum, the chi-squared function ideally gets close to the actual number of degrees of freedom of the system.

2 ASSOCIATED ERRORS

In previous works the matrix error is taken as the noise level at each BPM [1]. Given the definition of the experimental response matrix, the error associated to each of its elements is given by the function

$$\sigma_{ij}^2 = \frac{1}{\Delta\theta_i^2} \left[\sigma_{BPM}^2 + M_{i,j}^2 \sigma_{\theta(j)}^2 \right]$$

where σ_{RMP} is the noise level of the monitors (admitted the same for all monitors) and σ_{θ} the standard deviation associated to the corrector system (also assumed the same to all steering magnets). This last equation means that, even if the noise level of the BPM were zero (ideal monitors), the experimental matrix would suffer from the uncertainty associated to each corrector strength. However, the noise level of the steering magnets is understandably energy-dependent. The matrix error can be easily measured by taking several measurements of the matrix elements for a given steering magnet and then finding the standard deviation from the average value. For the UVX ring of the LNLS machine, at the energy 1.37 GeV, the corrector system has little effect upon the matrix elements. The same is not true at lower energies. e. g., 300 MeV, where we could find a significant effect of the steering magnet errors (see Figure 1).

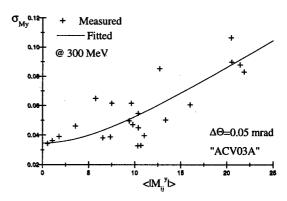


Figure 1: Measured standard deviation of the vertical response matrix for the corrector ACV03A at 300 MeV in terms of the module of the matrix element (effect of the corrector noise for large element values).

^{*}E-mail: xavier@lnls.br

In this report we will present results in the high-energy range. Therefore, the response matrix error is given by

$$\sigma_{ij} \approx \frac{\sigma_{BPM}}{\Delta \theta}$$
.

For the LNLS machine, this standard deviation is around 7mm/rad, given initial corrector kicks of 0.2 mrad. For a certain obtained calibration, therefore, the chi-squared value increases as the intensity of the corrector kickers decreases. Beyond a certain level, however, other systematic errors may perturb the minimum of χ^2 such as non-linear effects in the BPM system.

3 CHOOSING THE PARAMETERS

Due to numerical limitations, the list of parameters entering in the optics calibration can not include all possible elements. Moreover, the number of parameters should be smaller than the number of available data, if the calibration process is to have statistical value. The LNLS machine has a system of 36 quadrupoles divided into 14 independent families, 23 monitors, 24 and 18 steering magnets for vertical and horizontal correction respectively. We have chosen to calibrate for quadrupole and dipole gradient errors (there are 12 dipoles), steering magnets and corrector gains and eventually the energy-shift [1] associated to the correctors in the horizontal plane. The energy-shift correction at each corrector $\Delta \zeta$ is easily included since it is given by the simple formula

$$\Delta \zeta_j = -\frac{\eta_j^x}{\alpha L},$$

where η_j^x is the dispersion function at the j-th corrector, α is the momentum compaction factor and L the machine circumference. We said above 'eventually' because this energy-shift factor is a function of the model lattice and, therefore, should consistently be accounted for in the model horizontal matrix by the optics calculation program. We report that the inclusion of the corrector energy-shifts as fitting parameters showed little effect upon the final value of the minimum. The final total number of parameters used in the fitting was 131 while the number of data points (elements of the matrix) is 966.

4 SEARCHING FOR THE MINIMUM

Compared to other works [1], we have used a slightly different numerical procedure in order to determine the characteristic linear system of equations for the parameter calibration [3]. The set of parameter corrections is obtained by solving the linear system of equations

$$C_{n,r}\Delta p_r = B_n,$$

with

$$C_{n,r} = \sum_{k,m} \sum_{i,j} \frac{1}{\sigma_{ij}^{2}} \frac{\partial M_{i,j}^{k,m}}{\partial p_{n}} \frac{\partial M_{i,j}^{k,m}}{\partial p_{r}},$$

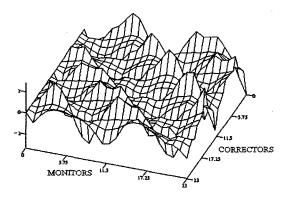
and

$$B_n = \sum_{k,m} \sum_{i,j} \frac{(M_{i,j}^{k,m} - \overline{M}_{i,j}^{k,m})}{\sigma_{ij}^2} \frac{\partial M_{i,j}^{k,m}}{\partial p_n},$$

where the index n runs over all possible parameters. Convergence is attained by singular decomposition methods.[3]. The matrix C may present singular value as a result of physical or numerical degeneracies. A well known example is the fact that multiplying all monitor gains by a certain factor while dividing corrector gains by the same factor leaves the matrix unchanged. The calibration of gains produces therefore relative values, the above mentioned factor should be later adjusted, for instance, by suitably matching the experimental and model dispersion functions.

5 SOME INITIAL RESULTS

The response matrix of the UVX-LNLS storage ring was measured several times during the machine study sessions in 1998 at the highest energy of 1.37 GeV and average current of 100 mA. Some of the measurements were performed with sextupoles turned off in order to avoid non-linear quadrupole components in the model lattice. Moreover, coupling effects were also minimized. Initially, we have imagined that quadrupole fitting would be straightforward. Such impressions proved itself naïve in face of the average distance between the experimental and model matrices. 980mm/rad in the vertical plane and 450 mm/rad in the horizontal one. This was far above the expected value of the matrix standard deviation even accounting for kick standard deviations and indicated that the inclusion of BPM and corrector gains was mandatory before quadrupole fitting [4]. The fitting was therefore performed in two stages, BPM and corrector gains first and then quadrupole and energy-shifts. We observed an asymmetry in the value of the response matrix elements as produced by either positive or negative corrector strengths. Further, in order to minimize hysteresis effects, we had conveniently cycled each steering magnet before measuring the matrix elements. This has significantly enhanced measurement repeatability. In Figure 2 we show surface graphics of the difference between the measured and model vertical matrices before and after calibration for the complete set of parameters. After calibration for BPM and corrector gains, the average distance between the model and experiment became 150 mm/rad in the horizontal plane and 400 mm/rad in the vertical plane.



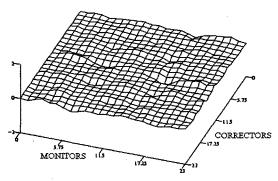


Figure 2: Difference between the experimental and model vertical matrices before (above) and after (below) calibration (seen in the same scale).

Inclusion of quadrupole coefficient further decreased this distance to 60 mm/rad in the horizontal plane and 61 mm/rad in the vertical one.

The LNLS orbit correcting system underwent an upgrade in the end of 1998, which enabled us to check out improvements in the gains of BPM and correctors [5]. In fact we were able to find (via calibration of gains) an improvement of up to 10% in BPM calibration compared to the situation before the upgrade. Also, before the upgrade, using solely calibration of the gains, we could explain the large asymmetry found in the horizontal dispersion by deviations in the BPM calibration. As seen in Figure 3, the calibration could fit well large values of the dispersion function, while the small discrepancies found in the low values are caused mainly by quadrupole errors (not included in this fit). This figure also show the value of a parameter (K) which gives the absolute calibration of BPM gains.

6 CONCLUSIONS

So far the LNLS machine study group has succeeded in establishing a systematic optics calibration process by using the information contained in the response matrix of the ring. The calibration includes the fitting of BPM and corrector gains, energy-shift corrections and quadrupole forces in straight quadrupole and dipoles. In this first period, we have written down the main codes, performed some measurements and debugged

the whole processes. The chi-squared minimum value has not been attained yet, indicating the existence of unknown parameters (possibly hidden quadrupole components) not yet included.

Of particular importance is the error analysis of the response matrix. The response matrix error is composed of two different contributions determined by BPM and corrector noises. The influence of correctors is strong in the low energy range (around 300 MeV) while, at high energy, the corrector system has shown little effect. This is important since we intend to map quadrupole field deviations from nominal values for the entire energy range covered by the LNLS machine (from the injection energy, 120 MeV up to 1.37 GeV), and the matrix error has to be dealt appropriately. Results in this direction will be published in the future.

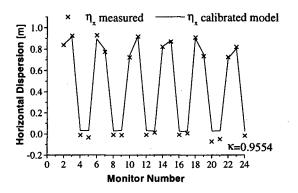


Figure 3: Measured horizontal dispersion function (crosses) and fitted (lines) obtained via BPM and corrector gain calibrations.

ACKNOWLEDGMENTS

Authors would like to thank P. Tavares for interesting discussions. This work is supported by FAPESP under the grand number 97/12948-4.

- J. Safranek, "Experimental determination of storage ring optics using response matrix measurement", Nucl. Instr. And Meth. In Phys. A, 388 (1997) 27;
- [2] F. Christoph Iselin, J. Niederer, "The MAD Program", version 7.2, CERN 88-38 (1998).
- [3] W. H. Press, S. A. Tukolsky, W. T. Vetterling and B. P. Flannery, "Numerical Recipes", Cambridge University Press (1992).
- [4] C. M. Chu et al,"First test of orbit response matrix in proton storage ring", Proc. of the Part. Acc. Phys. 1997.
- [5] J.G.S.Franco et al, "Orbit Correction in the LNLS UVX Electron Storage Ring". These Proceedings.

FIRST RESULTS OF QUASI-ISOCHRONOUS OPERATION AT LNLS

Liu Lin* and P.F. Tavares, LNLS, Campinas, Brazil

Abstract

We have started a program at LNLS to implement a quasi-isochronous operation mode at the 1.37 GeV electron storage ring. The aim is to explore non-linear longitudinal beam dynamics along with the reduction in the electron bunch length. To characterize the modes we have set up an electron bunch length measurement system which uses the visible light emitted from a bending magnet and a commercial fast photodiode with a sampling oscilloscope. The synchrotron oscillation frequency and the orbit displacement were also measured as a mean to assess the momentum compaction factor α . Up until the moment a reduction of a factor of 13 in α was obtained.

1 INTRODUCTION

We describe the first experiments performed at the LNLS synchrotron light source where the momentum compaction factor is reduced in order to reduce the electron bunch length. Similar experiments were carried out at other laboratories [1]. The equilibrium bunch length in a storage ring is proportional to the square root of the linear momentum compaction factor, α_i . Since α_i is proportional to the integral of the dispersion function in the dipoles, we can reduce it by focusing the dispersion in the dipoles so that a negative contribution to the integral is created canceling out part of the positive contribution. In principle, by shaping the dispersion function through the dipoles, the momentum compaction factor can be made as small as desired and even negative. In practice, however, several problems related to higher order longitudinal resonances and beam instabilities limit the value of α_1 and require control on other parameters such as higher order terms of the momentum compaction factor and rf parameters. We present in this report the preliminary results of our efforts to operate the LNLS UVX electron storage ring in a quasi-isochronous (QI) configuration.

2 THE QI OPTICAL CONFIGURATION AND MIGRATION FROM STANDARD OPTICS

The LNLS storage ring lattice is composed of six doublebend arcs connected by six long straight sections. The lattice is flexible enough to be tuned to various optical configurations. In the standard configuration, which is used both for regular user operation and for injection, the arcs are made achromatic, which leaves the long straight sections dispersion free. In this case the dispersion function is always positive and corresponds to a momentum compaction factor of 8.3 x 10³. To reduce this value, we overfocus the dispersion function at the dispersive sections creating a negative contribution to the dispersion integral in the dipoles. A six fold symmetric quasi-isochronous model, QI6, is calculated for UVX in which the linear momentum compaction factor is reduced by a factor of 100 with respect to the standard mode. The bunch length should then be reduced by a factor of 10, changing from approximately 40 ps rms to 4 ps rms.

The betatron tunes were adjusted in the QI6 mode to the same value as the standard mode. In this way, it is possible to transfer the optical configuration from the standard mode to the quasi-isochronous mode with the tunes fixed along the whole migration route. This operation scheme avoids the difficulties related to setting up injection conditions in the quasi-isochronous mode and also allows the opportunity to observe the beam behavior as the momentum compaction is slowly reduced.

We define the parameter χ as the ratio of the dispersion function at the BPMs in the long straight section to the dispersion function at the BPMs in the short section, as shown in Figure 1:

$$\chi = \frac{\eta_{BPM_Long}}{\eta_{BPM_Short}}$$

This parameter can be used to characterize the isochronicity of a configuration since the momentum compaction factor is uniquely determined by the value of the dispersion function at these BPMs for a 6-fold symmetric mode in UVX. As defined above, χ depends only on the orbit change at the BPMs for a given variation in the rf frequency. We have established a migration route with 18 intermediate configurations were χ varies monotonically from zero in the standard mode to -0.78 in the QI6 mode (Figure 2). Figure 3 shows α_1 and the synchrotron oscillation frequency along the migration route.

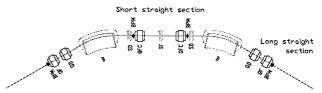


Figure 1: One basic cell of the UVX storage ring.

^{*} E-mail: liu@lnls.br

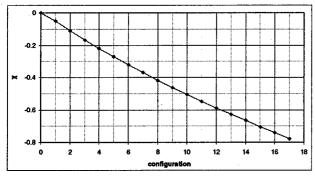


Figure 2: Calculated χ for the configurations in the migration route from the standard mode to the QI6 mode.

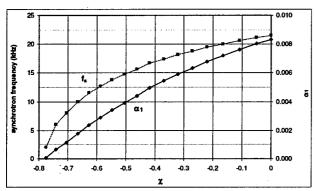


Figure 3: Calculated α_1 and synchrotron oscillation frequency (for $V_n = 340 \text{ kV}$) as a function of χ .

3 EXPERIMENTAL RESULTS

The experiments were carried out at the electron energy of 1.37 GeV with a few bunches filled (15 to 25 instead of the usual 100) to minimize longitudinal coupled bunch effects. The number of filled bunches cannot be controlled very precisely with the present hardware. An upgrade for the injection system is being developed to allow for operation with programmed filling patterns.

The electron beam is injected into the storage ring at 120 MeV and ramped to the standard optical configuration at 1.37 GeV. The 18 configurations of the migration route are then implemented one by one. In the first attempts, the tunes and the orbits had to be corrected at each step. As the momentum compaction is reduced, beam stability becomes more critical: orbit correction becomes more and more difficult, variations in parameters such as the rf frequency or the betatron tunes can cause larger changes in the beam lifetime and cause greater current drops. Up until the moment we have succeed to implement up to the 17th configuration (E17) in the migration route. To characterize the modes, we have measured the bunch length, the synchrotron frequency and the horizontal orbit displacement as a function of the rf frequency.

3.1 x Measurement

We have measured the isochronicity parameter χ for some configurations in the migration route from the

standard to the QI6 mode. For a given change in the rf frequency, the isochronicity parameter is given by $\chi = \Delta x_{BPM_Long}/\Delta x_{BPM_Short}$. Since there is a spread in the measured orbit displacements at the BPMs of the same group, we take the average displacement in each group. The results show that we have reduced χ to -0.74. This value corresponds to a theoretical momentum compaction factor of 6.5×10^4 , a factor of 12.8 smaller than the value for the standard mode. In Figure 4 we show the measured synchrotron tune as a function of the measured parameter χ as well as the theoretical curve.

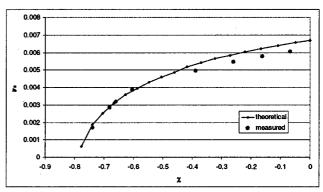


Figure 4: Theoretical and measured values of the synchrotron tune as a function of the isochronicity parameter χ during migration from the standard to the OI6 mode.

3.2 Synchrotron Oscillation Frequency Measurement

If the rf gap voltage is maintained at a constant value, changes in optical configurations can only modify the momentum compaction factor. We can thus derive the reduction in α in going from the standard mode to the QI6 mode from the measured synchrotron oscillation frequency. The measured values are 19.5 kHz and 5.5 kHz respectively for the standard and QI6 modes for $V_{\rm gap}\!\!=\!\!316$ kV. This corresponds to a reduction of a factor of 12.6 in α and agrees with the value measured in the previous section.

3.3 Bunch-Length Measurement

The bunch length is measured by an optical system that couples the visible light emitted by the electron bunch into an ultra-fast photodetector (7 ps FWHM). The signal is captured by a 20 GHz sampling oscilloscope triggered by the zero-bunch signal generated from the storage ring master clock. The bunch length is obtained by fitting a gaussian to the data.

To estimate the time resolution of the system we have measured the bunch length as a function of the rf gap voltage in the standard operation mode with a few bunch configuration. The measured bunch length is about twice the expected value from theoretical calculations. Qualitatively, the expected increase in bunch length (and

decrease in synchrotron oscillation frequency) produced by the reduction of the rf gap voltage is observed. The apparent very poor time resolution of this measurement system may have many contributions, which can be separated essentially into two types: (i) intrinsic resolution of the measurement system and (ii) coherent longitudinal oscillations of the bunches. The intrinsic resolution of the measurement system can be affected by the jitter of the trigger signal, the frequency bandpass of the measuring equipment and imperfections in cables and connectors. The jitter of trigger signal has been reduced to 2.5 ps rms and is thus negligible but the overall bandwidth of the system may be limited in our system. One indication is the fact that we have observed a narrow harmonic composition of the fast photodiode signal on a spectrum analyser. Nevertheless, the intrinsic overall resolution of the system could be subtracted from the measured bunch length data (if we assume that this is given by the quadratic sum of the actual bunch length and the resolution of the system). The other kind of contribution to the enlargement of the measured bunch duration, the coherent longitudinal oscillation of the beam, is more difficult to eliminate and there are indications that it occurred during the measurements. One evidence is the correlation between bunch lengthening and the increase in the observed number and intensity of the synchrotron frequency harmonics. We also observed a trembling of the beam image taken from a dispersive point in the dipole. Furthermore, the operation with few bunches is essential to get repetitive results. The bunch length measured when we operate in the 100 filled bunches mode has a large noise. The contribution of beam longitudinal oscillations to the measured length depends on many parameters and cannot be subtracted from the measured value. In this case, changes in the hardware must be implemented to overcome the limitations. One solution is to use a technique to measure the bunch in a single pass (e.g., streak camera, autocorrelation). Another solution is to implement the single bunch operation mode with a trigger signal generated by the bunch itself. Yet another solution is to eliminate the longitudinal oscillations via a feedback system. All these solutions require a substantial effort (technical and/or financial) to be implemented and we are presently analysing the various alternatives. The single bunch operation and a streak camera may be available in a near future. The present system, however, can be used to observe the qualitative behavior of the bunch length in these configurations.

In Figure 5 we show the measured bunch length (one sigma) as a function of the synchrotron oscillation frequency during migration from the standard mode (f_s=20 kHz) to the mode E17 (f_s=6 kHz). Initially the measured bunch length and the synchrotron frequency decrease with the reduction of the momentum compaction factor. From the configuration which corresponds to

f_s=8.5 kHz on, further reduction of the momentum compaction factor still decreases the synchrotron frequency but not the measured bunch length, which starts fluctuating at larger values. This may be caused by the excitation of longitudinal instabilities in low alpha configurations.

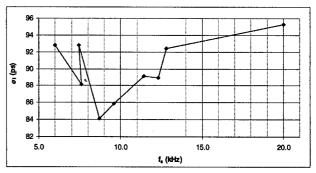


Figure 5: Bunch length (one sigma) as a function of the synchrotron oscillation frequency during migration from the standard mode (f_s =20 kHz) to the quasi-isochronous mode (f_s =6 kHz). Initially the measured bunch length and the synchrotron frequency decrease with the reduction of the momentum compaction factor. From the configuration which corresponds to f_s =8.5 kHz on, further reduction of the momentum compaction factor still decreases the synchrotron frequency but not the measured bunch length, which starts fluctuating at larger values.

4 CONCLUSIONS

We have reduced the momentum compaction factor of the LNLS UVX storage ring by a factor of approximately 13. The isochronicity parameter χ has been reduced from 0 to -0.74. Measurements of bunch length, synchrotron oscillation frequency and orbit displacement have been carried out. Thus far the obtained results were analysed using linear theory only. It is clear, however, that higher order longitudinal terms must be considered. To proceed in the migration route to the QI6 mode we need to consider the effects of the second order momentum compaction factor α_2 by adding configurations to the migration route where the setting of the sextupoles is considered. The steps in the configurations should be reduced as well.

The experience gained from these initial tests has helped us to determine the limitations of the present measurement system and to prepare an upgrade program to perform future experiments, which includes implementation of the single bunch operation mode and of a single pass bunch length measurement system.

5 REFERENCES

[1] H.Hama, S.Takano and G.Isoyama, NIM A329 (1993); P.Tran et al, 1993 PAC; A.Nadji et al, 1994 EPAC; D.Robin et al, Micro Bunches Workshop (1995).

BEAM OPTICS STUDIES FOR THE CEBAF ACCELERATOR

S.A. Bogacz* and V.A. Lebedev, Thomas Jefferson National Accelerator Facility, Newport News, VA

Abstract

Measurements of differential orbits excited by two pairs of horizontal and vertical correctors, and by a change of the energy gain for the first one of two superconducting linacs allowed us to perform on-line control of the machine optics, which provided valuable information for studying optics discrepancies. Off-line analysis of the data has uncovered a number of malfunctioning hardware pieces, e.g. improperly functioning BPMs and incorrectly focusing quadrupoles. It also indicated that our dipoles have significant focusing terms, which have to be taken into account to build a predictable optics. The analysis resulted in a significantly improved optics model for the CEBAF recirculator. The new optics preserved desired lattice architecture and orthogonal tunability. The presented approach was proven very successful in minimizing required tuning time and in building a more accurate theoretical model of beam transport for the CEBAF accelerator.

1 INTRODUCTION

The CEBAF accelerator [1] is a five-pass CW recirculator with beam power up to 800 kW. It consists of a 56 MeV injector, two superconducting linacs of 500 MeV energy gain, and nine arcs, which connect the linacs for beam recirculation for total beam energy of 5.056 GeV. Logically, the machine is separated into the following regions [2]: injector, North and South linacs, nine 180° bend recirculation arcs with associated entrance and exit matching regions, and the spreader and recombiner regions at the ends of each linac, which separate particles of different energies or merge them for reinjection into the succeeding linac. After acceleration to the desired energy, the beam can be split and directed to three experimental halls for nuclear physics experiments. The path traversed to full energy is more than 6 km in length, over which the beam is focused by about 700 quadrupoles. Each quadrupole is independently powered, which on one hand creates many possibilities for machine optics, but on the other hand complicates machine tuning and operation processes.

The large scale of the accelerator requires high field accuracy of the magnets. The design reproducibility specifications for the quadrupoles (~2×10⁴) have not been met in the real machine, which caused significant optics changes during the machine commissioning [3]. The main

motivation for optics redesign was to reduce error sensitivity of the machine optics and to create a set of orthogonal knobs for machine tuning.

We identified three major sources of machine irreproducibility. The first one is adjustments of the accelerating profile, which is always non-uniform and is frequently changed when one or a few cavities cannot support the required accelerating gradient. In this case the focusing for the first pass is corrected, while the higher passes are subject to a significant betatron mismatch. The second source is a path-length adjustment. To keep higher passes on the 'crest' of the accelerating wave the path-length has to be stabilized at the level of $0.25 \text{ mm} (\sim 0.5^{\circ})$. That calls for frequent path-length adjustments to account for seasonal and weather variations. These adjustments cause the vertical beta function mismatch due to significant changes of the vertical focusing in the correction chicane. The third source is an overall deficiency in machine reproducibility, due to substantial temporal drifts of the quadrupole gradients, over a period of a few days or occasionally of a few hours. The first two sources were addressed at the commissioning time, which brought the machine to a reasonable state enabling initial beam delivery for physics. Although we could deliver acceptable quality beam to the experiments at that time, the machine optics was not understood sufficiently, which significantly hampered machine operation and beam optics software tools.

To build an adequate model of the machine optics and to gain some insight into sources of machine irreproducibility, systematic optics studies were initiated. Most of their findings are reported in this article.

2 DIFFERENTIAL ORBIT ANALYSIS

Two efforts to correct accelerator optics were undertaken. The first one is an envelope match in the injector. It is performed by measuring the vertical and horizontal beam sizes with beam profile monitors at four locations in the injector. Then adjustments of four upstream quads are made to match beam sizes to the injector Twiss functions. The second step involves tracking of machine optics with the differential orbit measurements, which serves as our main instrument for optics studies. The beam position measurement system includes approximately 800 BPMs. This large number of BPMs allows us to perform optics measurements, which are much more detailed than those done by any other available method.

To get complete measurements of linear optics one needs to use at least five sources of the beam orbit excitation: two horizontal correctors, two vertical correctors and an energy corrector. The best resolution for betatron motion is achieved when the effects of kicks excited by each

^{*} This work was supported by U.S. D.O.E. contract #DE-AC05-84ER40150.

^{*} bogacz@jlab.org

corrector pair are orthogonal. That implies that correctors have to be shifted in betatron phase by $(1+2n)\pi/4$ [3]. Fast data acquisition for differential measurements was the key to the success of the project. Special data acquisition software was written to make measurements as fast as possible. The measurements are fully automated and it now takes about three minutes to perform measurements for the entire machine. This has allowed us to get the measurements routinely, every day at system checks or by a request from the Beam Transport Team.

To optimize the amplitude of excited betatron perturbation with respect to adiabatic damping, the exciting correctors were chosen at the beginning of Arc 1 (in the 556 MeV region). The energy perturbation was created by changing the accelerating gradient of eight RF cavities at the end of the first superconducting linac. The strengths of the above excitations were adjusted so that the resulting beam motion had initial transverse amplitude of about 3 mm, which after acceleration (by a factor of ten) died down to about 1 mm due to the adiabatic damping.

A complete differential measurement, as illustrated in Figure 1, results in six independent differential orbits: two horizontal and two vertical differential orbits excited by

correctors, and the horizontal and vertical dispersive orbits excited by the energy change. To reach a better clarity Figure 1 shows only the measurement restricted to Arc 2 and the downstream second pass in the North linac. Markers indicate actual measurement data, while continuous lines represent differential orbits predicted by the updated model of the machine optics.

Early post-commissioning experience [3] revealed serious discrepancies between predictions of the optics model and actual beam displacements in the machine. To 'pin down' possible sources of discrepancies, careful analysis of differential orbits through the entire machine was performed. We found out that the major sources of optics irreproducibility were linked to focusing effects of bending dipoles and several quads exhibiting few-percent focusing errors. The effect was particularly large for vertical dipoles of spreaders and recombiners, which were not measured with sufficient accuracy before installation. Simultaneous fitting of six independent difference orbits by varying the focusing terms of each dipole in the spreaders and recombiners allowed us to find a unique set of body gradients for all dipole magnets. A similar process was performed for the horizontal dipoles of nine arcs, but in

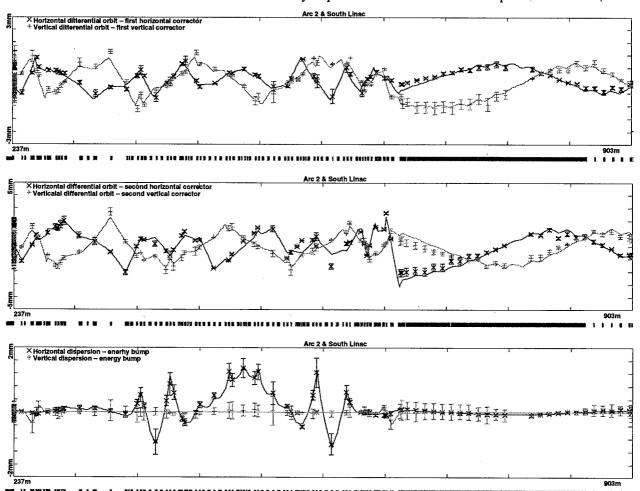


Figure 1: Example of differential orbit analysis for Arc 2 - complete set of six orbits - optics model vs measurement

this case we were able to achieve a reasonable fit assuming that all dipoles of a single arc have identical focusing properties.

Extracted this way body gradients were used to update the optics mode. Improved status of the machine optics did not require betatron correction in the spreaders and the 'orthogonal knobs' for betatron match were left in the recombiners only. Another benefit of the improved optics model was reliable operation of an automated steering program, AutoSteer [5], which would not function properly without updating our initial 'crude' optics.

Careful testing and recalibration of power supplies for quads were performed in parallel with optics studies. After this process was complete the focusing of practically all quads corresponded to the design values. Currently, we are left with only four quadrupoles for which values are fudged by about 10% to fix the machine optics.

Another useful spin-off of optics studies was a test of the BPMs. The study indicated four BPMs, which exhibited incorrect (up to 50%) differential displacement. Further improvements of the optics model are limited by the finite accuracy of the BPMs and long term machine reproducibility.

3 OPTICS UPGRADES

A few recently performed optics upgrades were motivated by improving both beam quality and machine diagnostics:

3.1 Bunch Compression at Injection

Longitudinal bunching in the injector was originally configured in the 5 MeV region. With the polarized source coming into operation we experienced difficulties transporting the beam, because of small tails in the longitudinal beam profile. Particles in these tails were not on the crest of the accelerating wave and were ultimately lost preventing machine operation at high beam current. To alleviate this problem we redesigned the optics in the injector chicane (56 MeV) to create additional bunch compression. A significant advantage of high energy bunching is that the bunching is not affected by the beam space charge. To facilitate that, a new non-isochronous optics with a negative momentum compaction factor of about -30 cm was designed and installed in the injection chicane. To perform the bunch compression one needs to shift the RF phase of the main injector linac by about 6°. To avoid problems with focusing changes at the beginning of the linac only the second of two injector cryomodules is shifted in phase. The new configuration significantly improves machine reliability for high current operation.

3.2 Medium Dispersion Optics in Lower Arcs

Responding to current instrumentation needs (installation of synchrotron light monitors to resolve the beam energy spread with high resolution) the optics of arcs 1 and 2 was redesigned. The goal was to increase (by a factor of three)

the horizontal dispersion and to decrease the horizontal beta function at the middle of both arcs, where the new monitors were supposed to be installed. The new arc optics, with a mirror-symmetric horizontal dispersion pattern, was designed so that it greatly enhances resolution of the beam energy spread and it still does not limit our energy aperture. To preserve tunability of the new optics one needs to allow for independent correction of both the horizontal dispersion and M_{ss}. This was accomplished by appropriate tailoring of the horizontal betatron phase advance inside the arc, to provide two pairs of orthogonal knobs (quadrupoles): for dispersion and momentum compaction adjustments. Furthermore, a betatron wave excited by the first tuning quad, which propagates with twice the betatron frequency, is cancelled by the second wave launched by the remaining quad in the pair, so the net betatron wave is confined to the tuning region and subsequently the tuning process does not affect the betatron match outside the arc.

4 CONCLUSIONS

The presented off-line analysis of routinely measured data has uncovered a number of malfunctioning hardware pieces, e.g. improperly functioning BPMs and quadrupoles. Our analysis resulted in a significantly improved optics model of beam transport for the CEBAF accelerator. The new optics preserves the desired lattice architecture and tunability (betatron match, dispersion and momentum compaction adjustment orthogonality).

Furthermore, motivated by improving beam transport quality and machine diagnostics two major optics upgrades were made. They can be summarized as longitudinal bunch compression at injection and installation of medium dispersion optics in lower arcs.

Finally, the presented approach was proven very successful in scaling optics with energy (frequent energy changes are the standard part of our present operation) and in minimizing required machine tuning.

ACKNOWLEDGEMENTS

We would like to thank M. Tiefenback for fruitful discussions, which resulted in better understanding of magnet reproducibility. Useful discussions and valuable input from all members of the Beam Transport Team are gratefully acknowledged.

- [1] D. Douglas, et al., Proceedings of the 1989 Particle Accelerator Conference, 557-559
- [2] B. Bowling, et al., Proceedings of the 1991 Particle Accelerator Conference, 446-448
- [3] V. Lebedev, et al., Nuclear Instruments and Methods in Physics Research A, 408 (1998) 373-379
- [4] M. Tiefenback, private communication.
- [5] Y. Chao, this proceedings.

NONLINEAR ACCELERATOR PROBLEMS VIA WAVELETS: 2. ORBITAL DYNAMICS IN GENERAL MULTIPOLAR FIELD

A. Fedorova, M. Zeitlin, IPME, RAS, St. Petersburg, Russia * †

Abstract

In this series of eight papers we present the applications of methods from wavelet analysis to polynomial approximations for a number of accelerator physics problems. In this part we consider orbital motion in transverse plane for a single particle in a circular magnetic lattice in case when we take into account multipolar expansion up to an arbitrary finite number. We reduce initial dynamical problem to the finite number (equal to the number of n-poles) of standard algebraical problem and represent all dynamical variables via an expansion in the base of periodical wavelets.

1 INTRODUCTION

This is the second part of our eight presentations in which we consider applications of methods from wavelet analysis to nonlinear accelerator physics problems. This is a continuation of our results from [1]-[8], which is based on our approach to investigation of nonlinear problems - general, with additional structures (Hamiltonian, symplectic or quasicomplex), chaotic, quasiclassical, quantum, which are considered in the framework of local (nonlinear) Fourier analysis, or wavelet analysis. Wavelet analysis is a relatively novel set of mathematical methods, which gives us a possibility to work with well-localized bases in functional spaces and with the general type of operators (differential, integral, pseudodifferential) in such bases. In this part we consider orbital motion in transverse plane for a single particle in a circular magnetic lattice in case when we take into account multipolar expansion up to an arbitrary finite number. We reduce initial dynamical problem to the finite number (equal to the number of n-poles) of standard algebraical problem and represent all dynamical variables as expansion in the base of periodical wavelet functions. Our consideration is based on generalization of variational wavelet approach from part 1. After introducing our starting points related to multiresolution in section 3, we consider methods which allow us to construct wavelet representation for solution in periodic case in section 4.

2 PARTICLE IN THE MULTIPOLAR FIELD

The magnetic vector potential of a magnet with 2n poles in Cartesian coordinates is

$$A = \sum_{n} K_n f_n(x, y), \tag{1}$$

where f_n is a homogeneous function of x and y of order n. The real and imaginary parts of binomial expansion of

$$f_n(x,y) = (x+iy)^n (2)$$

correspond to regular and skew multipoles. The cases n=2 to n=5 correspond to low-order multipoles: quadrupole, sextupole, octupole, decapole. Then we have in particular case the following equations of motion for single particle in a circular magnetic lattice in the transverse plane (x, y) ([9] for designation):

$$\frac{\mathrm{d}^2 x}{\mathrm{d}s^2} + \left(\frac{1}{\rho(s)^2} - k_1(s)\right) x =$$

$$\mathcal{R}e\left[\sum_{n\geq 2} \frac{k_n(s) + ij_n(s)}{n!} \cdot (x + iy)^n\right], \qquad (3)$$

$$\frac{\mathrm{d}^2 y}{\mathrm{d}s^2} + k_1(s)y =$$

$$-\mathcal{I}m\left[\sum_{n\geq 1} \frac{k_n(s) + ij_n(s)}{n!} \cdot (x + iy)^n\right]$$

and the corresponding Hamiltonian:

$$H(x, p_x, y, p_y, s) = \frac{p_x^2 + p_y^2}{2} + \left(\frac{1}{\rho(s)^2} - k_1(s)\right) \cdot \frac{x^2}{2} + k_1(s)\frac{y^2}{2}$$

$$-\mathcal{R}e\left[\sum_{n\geq 2} \frac{k_n(s) + ij_n(s)}{(n+1)!} \cdot (x+iy)^{(n+1)}\right]$$
(4)

Then we may take into account arbitrary but finite number in expansion of RHS of Hamiltonian (4) and from our point of view the corresponding Hamiltonian equations of motions are not more than nonlinear ordinary differential equations with polynomial nonlinearities and variable coefficients.

^{*}e-mail: zeitlin@math.ipme.ru

[†] http://www.ipme.ru/zeitlin.html; http://www.ipme.nw.ru/zeitlin.html

3 WAVELET FRAMEWORK

Our constructions are based on multiresolution approach. Because affine group of translation and dilations is inside the approach, this method resembles the action of a microscope. We have contribution to final result from each scale of resolution from the whole infinite scale of spaces. More exactly, the closed subspace $V_j (j \in \mathbf{Z})$ corresponds to level j of resolution, or to scale j. We consider a r-regular multiresolution analysis (MRA) of $L^2(\mathbf{R}^n)$ (of course, we may consider any different functional space) which is a sequence of increasing closed subspaces V_j :

...
$$V_{-2} \subset V_{-1} \subset V_0 \subset V_1 \subset V_2 \subset ...$$
 (5)

satisfying the following properties:

$$\bigcap_{j \in \mathbf{Z}} V_j = 0, \quad \overline{\bigcup_{j \in \mathbf{Z}}} V_j = L^2(\mathbf{R}^n),$$

$$f(x) \in V_j <=> f(2x) \in V_{j+1},$$

$$f(x) \in V_0 <=> f(x-k) \in V_0, \forall k \in \mathbf{Z}^n.$$
(6)

There exists a function $\varphi \in V_0$ such that $\{\varphi_{0,k}(x) = \varphi(x-k), k \in \mathbf{Z}^n\}$ forms a Riesz basis for V_0 . The function φ is regular and localized: φ is C^{r-1} , $\varphi^{(r-1)}$ is almost everywhere differentiable and for almost every $x \in \mathbf{R}^n$, for every integer $\alpha \leq r$ and for all integer p there exists constant C_p such that

$$|\partial^{\alpha}\varphi(x)| \le C_p(1+|x|)^{-p} \tag{7}$$

Let $\varphi(x)$ be a scaling function, $\psi(x)$ is a wavelet function and $\varphi_i(x) = \varphi(x-i)$. Scaling relations that define φ, ψ are

$$\varphi(x) = \sum_{k=0}^{N-1} a_k \varphi(2x-k) = \sum_{k=0}^{N-1} a_k \varphi_k(2x),$$
 (8)

$$\psi(x) = \sum_{k=-1}^{N-2} (-1)^k a_{k+1} \varphi(2x+k). \tag{9}$$

Let indices ℓ, j represent translation and scaling, respectively and

$$\varphi_{jl}(x) = 2^{j/2} \varphi(2^j x - \ell) \tag{10}$$

then the set $\{\varphi_{j,k}\}, k \in \mathbf{Z}^n$ forms a Riesz basis for V_j . The wavelet function ψ is used to encode the details between two successive levels of approximation. Let W_j be the orthonormal complement of V_j with respect to V_{j+1} :

$$V_{j+1} = V_j \bigoplus W_j. \tag{11}$$

Then just as V_j is spanned by dilation and translations of the scaling function, so are W_j spanned by translations and dilation of the mother wavelet $\psi_{jk}(x)$, where

$$\psi_{jk}(x) = 2^{j/2}\psi(2^{j}x - k). \tag{12}$$

All expansions which we used are based on the following properties:

$$\begin{split} \{\psi_{jk}\}, \quad j,k \in \mathbf{Z} \quad \text{is a Hilbertian basis of } L^2(\mathbf{R}) \\ \{\varphi_{jk}\}_{j \geq 0, k \in \mathbf{Z}} \quad \text{is an orthonormal basis for } L^2(\mathbf{R}), \end{split}$$

$$L^{2}(\mathbf{R}) = V_{0} \bigoplus_{j=0}^{\infty} W_{j}, \tag{13}$$

or
$$\{\varphi_{0,k}, \psi_{j,k}\}_{j\geq 0, k\in \mathbb{Z}}$$
 is an orthonormal basis for $L^2(\mathbb{R})$.

Fig.1 and Fig.2 give the representation of some function and corresponding MRA on each level of resolution.

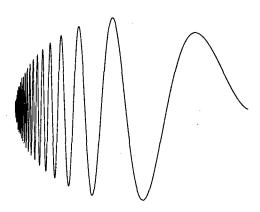


Figure 1: Analyzed function.

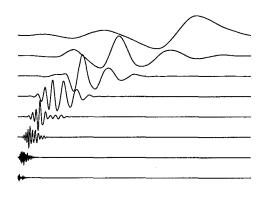


Figure 2: MRA representation.

4 VARIATIONAL WAVELET APPROACH FOR PERIODIC TRAJECTORIES

We start with extension of our approach from part 1 to the case of periodic trajectories. The equations of motion corresponding to Hamiltonian (4) may also be formulated as a particular case of the general system of ordinary differential equations $dx_i/dt = f_i(x_j, t)$, (i, j = 1, ..., n), $0 \le t \le 1$, where f_i are not more than polynomial func-

tions of dynamical variables x_j and have arbitrary dependence of time but with periodic boundary conditions. According to our variational approach from part 1 we have the solution in the following form

$$x_i(t) = x_i(0) + \sum_k \lambda_i^k \varphi_k(t), \qquad x_i(0) = x_i(1), \quad (14)$$

where λ_i^k are again the roots of reduced algebraical systems of equations with the same degree of nonlinearity and $\varphi_k(t)$ corresponds to useful type of wavelet bases (frames). It should be noted that coefficients of reduced algebraical system are the solutions of additional linear problem and also depend on particular type of wavelet construction and type of bases. This linear problem is our second reduced algebraical problem. We need to find in general situation objects

$$\Lambda_{\ell_1\ell_2...\ell_n}^{d_1d_2...d_n} = \int_{-\infty}^{\infty} \prod \varphi_{\ell_i}^{d_i}(x) \mathrm{d}x, \tag{15}$$

but now in the case of periodic boundary conditions. Now we consider the procedure of their calculations in case of periodic boundary conditions in the base of periodic wavelet functions on the interval [0,1] and corresponding expansion (14) inside our variational approach. Periodization procedure gives us

$$\hat{\varphi}_{j,k}(x) \equiv \sum_{\ell \in \mathbb{Z}} \varphi_{j,k}(x-\ell)$$

$$\hat{\psi}_{j,k}(x) = \sum_{\ell \in \mathbb{Z}} \psi_{j,k}(x-\ell)$$
(16)

So, $\hat{\varphi}, \hat{\psi}$ are periodic functions on the interval [0,1]. Because $\varphi_{j,k} = \varphi_{j,k'}$ if $k = k' \operatorname{mod}(2^j)$, we may consider only $0 \le k \le 2^j$ and as consequence our multiresolution has the form $\bigcup_{j>0} \hat{V}_j = L^2[0,1]$ with $\hat{V}_j = \operatorname{span}\{\hat{\varphi}_{j,k}\}_{k=0}^{2j-1}$

[10]. Integration by parts and periodicity gives useful relations between objects (15) in particular quadratic case $(d = d_1 + d_2)$:

$$\Lambda_{k_1,k_2}^{d_1,d_2} = (-1)^{d_1} \Lambda_{k_1,k_2}^{0,d_2+d_1}, \; \Lambda_{k_1,k_2}^{0,d} = \Lambda_{0,k_2-k_1}^{0,d} \equiv \Lambda_{k_2-k_1}^d$$

So, any 2-tuple can be represent by Λ_k^d . Then our second additional linear problem is reduced to the eigenvalue problem for $\{\Lambda_k^d\}_{0 \leq k \leq 2^j}$ by creating a system of 2^j homogeneous relations in Λ_k^d and inhomogeneous equations. So, if we have dilation equation in the form $\varphi(x) = \sqrt{2} \sum_{k \in \mathbb{Z}} h_k \varphi(2x-k)$, then we have the following homogeneous relations

$$\Lambda_k^d = 2^d \sum_{m=0}^{N-1} \sum_{\ell=0}^{N-1} h_m h_\ell \Lambda_{\ell+2k-m}^d, \tag{17}$$

or in such form $A\lambda^d=2^d\lambda^d$, where $\lambda^d=\{\Lambda_k^d\}_{0\leq k\leq 2^j}$. Inhomogeneous equations are:

$$\sum_{\ell} M_{\ell}^{d} \Lambda_{\ell}^{d} = d! 2^{-j/2}, \tag{18}$$

where objects $M_\ell^d(|\ell| \leq N-2)$ can be computed by recursive procedure

$$M_{\ell}^{d} = 2^{-j(2d+1)/2} \tilde{M}_{\ell}^{d}, \tag{19}$$

$$\tilde{M}_{\ell}^{k} = \langle x^{k}, \varphi_{0,\ell} \rangle = \sum_{j=0}^{k} {k \choose j} n^{k-j} M_{0}^{j}, \quad \tilde{M}_{0}^{\ell} = 1.$$

So, we reduced our last problem to standard linear algebraical problem. Then we use the same methods as in part 1. As a result we obtained for closed trajectories of orbital dynamics described by Hamiltonian (4) the explicit time solution (14) in the base of periodized wavelets (16).

We are very grateful to M. Cornacchia (SLAC), W. Herrmannsfeldt (SLAC), Mrs. J. Kono (LBL) and M. Laraneta (UCLA) for their permanent encouragement

- [1] Fedorova, A.N., Zeitlin, M.G. 'Wavelets in Optimization and Approximations', *Math. and Comp. in Simulation*, **46**, 527-534 (1998).
- [2] Fedorova, A.N., Zeitlin, M.G., 'Wavelet Approach to Polynomial Mechanical Problems', New Applications of Nonlinear and Chaotic Dynamics in Mechanics, Kluwer, 101-108, 1998.
- [3] Fedorova, A.N., Zeitlin, M.G., 'Wavelet Approach to Mechanical Problems. Symplectic Group, Symplectic Topology and Symplectic Scales', New Applications of Nonlinear and Chaotic Dynamics in Mechanics, Kluwer, 31-40, 1998.
- [4] Fedorova, A.N., Zeitlin, M.G 'Nonlinear Dynamics of Accelerator via Wavelet Approach', AIP Conf. Proc., vol. 405, 87-102, 1997, Los Alamos preprint, physics/9710035.
- [5] Fedorova, A.N., Zeitlin, M.G, Parsa, Z., 'Wavelet Approach to Accelerator Problems', parts 1-3, Proc. PAC97, vol. 2, 1502-1504, 1505-1507, 1508-1510, IEEE, 1998.
- [6] Fedorova, A.N., Zeitlin, M.G, Parsa, Z., 'Nonlinear Effects in Accelerator Physics: from Scale to Scale via Wavelets', 'Wavelet Approach to Hamiltonian, Chaotic and Quantum Calculations in Accelerator Physics', Proc. EPAC'98, 930-932, 933-935, Institute of Physics, 1998.
- [7] Fedorova, A.N., Zeitlin, M.G., Parsa, Z., 'Variational Approach in Wavelet Framework to Polynomial Approximations of Nonlinear Accelerator Problems', AIP Conf. Proc., vol. 468, 48-68, 1999.
 Los Alamos preprint, physics/9902062.
- [8] Fedorova, A.N., Zeitlin, M.G., Parsa, Z., 'Symmetry, Hamiltonian Problems and Wavelets in Accelerator Physics', AIP Conf. Proc., vol. 468, 69-93, 1999.
 Los Alamos preprint, physics/9902063.
- [9] Bazzarini, A., e.a., CERN 94-02.
- [10] Schlossnagle, G., Restrepo, J.M., Leaf, G.K., Technical Report ANL-93/34.

NONLINEAR ACCELERATOR PROBLEMS VIA WAVELETS: 3. EFFECTS OF INSERTION DEVICES ON BEAM DYNAMICS

A. Fedorova, M. Zeitlin, IPME, RAS, St. Petersburg, Russia * †

Abstract

In this series of eight papers we present the applications of methods from wavelet analysis to polynomial approximations for a number of accelerator physics problems. In this part, assuming a sinusoidal field variation, we consider the analytical treatment of the effects of insertion devices on beam dynamics. We investigate via wavelet approach a dynamical model which has polynomial nonlinearities and variable coefficients. We construct the corresponding wavelet representation. As examples we consider wigglers and undulator magnets. We consider the further modification of our variational approach which may be applied in each scale.

1 INTRODUCTION

This is the third part of our eight presentations in which we consider applications of methods from wavelet analysis to nonlinear accelerator physics problems. This is a continuation of our results from [1]-[8], which is based on our approach to investigation of nonlinear problems - general, with additional structures (Hamiltonian, symplectic or quasicomplex), chaotic, quasiclassical, quantum, which are considered in the framework of local (nonlinear) Fourier analysis, or wavelet analysis. Wavelet analysis is a relatively novel set of mathematical methods, which gives us a possibility to work with well-localized bases in functional spaces and with the general type of operators (differential, integral, pseudodifferential) in such bases. In this part we consider effects of insertion devices (section 2) on beam dynamics. In section 3 we consider generalization of our variational approach for the case of variable coefficients. In section 4 we consider more powerful variational approach which is based on ideas of para-products and approximation for multiresolution approach, which gives us possibility for computations in each scale separately.

2 EFFECTS OF INSERTION DEVICES ON BEAM DYNAMICS

Assuming a sinusoidal field variation, we may consider according to [9] the analytical treatment of the effects of insertion devices on beam dynamics. One of the major detri-

mental aspects of the installation of insertion devices is the resulting reduction of dynamic aperture. Introduction of non-linearities leads to enhancement of the amplitudedependent tune shifts and distortion of phase space. The nonlinear fields will produce significant effects at large betatron amplitudes. The components of the insertion device magnetic field used for the derivation of equations of motion are as follows:

$$B_{x} = \frac{k_{x}}{k_{y}} \cdot B_{0} \sinh(k_{x}x) \sinh(k_{y}y) \cos(kz)$$

$$B_{y} = B_{0} \cosh(k_{x}x) \cosh(k_{y}y) \cos(kz) \qquad (1)$$

$$B_{z} = -\frac{k}{k_{y}} B_{0} \cosh(k_{x}x) \sinh(k_{y}y) \sin(kz),$$

with $k_x^2 + k_y^2 = k^2 = (2\pi/\lambda)^2$, where λ is the period length of the insertion device, B_0 is its magnetic field, ρ is the radius of the curvature in the field B_0 . After a canonical transformation to change to betatron variables, the Hamiltonian is averaged over the period of the insertion device and hyperbolic functions are expanded to the fourth order in x and y (or arbitrary order). Then we have the following Hamiltonian:

$$H = \frac{1}{2}[p_x^2 + p_y^2] + \frac{1}{4k^2\rho^2}[k_x^2x^2 + k_y^2y^2] + \frac{1}{12k^2\rho^2}[k_x^4x^4 + k_y^4y^4 + 3k_x^2k^2x^2y^2] - \frac{\sin(ks)}{2k\rho}[p_x(k_x^2x^2 + k_y^2y^2) - 2k_xp_yxy]$$
(2)

We have in this case also nonlinear (polynomial with degree 3) dynamical system with variable (periodic) coefficients. As related cases we may consider wiggler and undulator magnets. We have in horizontal x-s plane the following equations

$$\ddot{x} = -\dot{s} \frac{e}{m\gamma} B_z(s)$$

$$\ddot{s} = \dot{x} \frac{e}{m\gamma} B_z(s),$$
(3)

where magnetic field has periodic dependence on s and hyperbolic on z.

3 VARIABLE COEFFICIENTS

In the case when we have situation when our problem is described by a system of nonlinear (polynomial)differential

^{*}e-mail: zeitlin@math.ipme.ru

[†] http://www.ipme.ru/zeitlin.html; http://www.ipme.nw.ru/zeitlin.html

equations, we need to consider extension of our previous approach which can take into account any type of variable coefficients (periodic, regular or singular). We can produce such approach if we add in our construction additional refinement equation, which encoded all information about variable coefficients [10]. According to our variational approach we need to compute integrals of the form

$$\int_{D} b_{ij}(t)(\varphi_1)^{d_1}(2^m t - k_1)(\varphi_2)^{d_2}(2^m t - k_2) dx, \quad (4)$$

where now $b_{ij}(t)$ are arbitrary functions of time, where trial functions φ_1, φ_2 satisfy a refinement equations:

$$\varphi_i(t) = \sum_{k \in \mathbb{Z}} a_{ik} \varphi_i(2t - k) \tag{5}$$

If we consider all computations in the class of compactly supported wavelets then only a finite number of coefficients do not vanish. To approximate the non-constant coefficients, we need choose a different refinable function φ_3 along with some local approximation scheme

$$(B_{\ell}f)(x) := \sum_{\alpha \in \mathbf{Z}} F_{\ell,k}(f)\varphi_3(2^{\ell}t - k), \tag{6}$$

where $F_{\ell,k}$ are suitable functionals supported in a small neighborhood of $2^{-\ell}k$ and then replace b_{ij} in (4) by $B_\ell b_{ij}(t)$. In particular case one can take a characteristic function and can thus approximate non-smooth coefficients locally. To guarantee sufficient accuracy of the resulting approximation to (4) it is important to have the flexibility of choosing φ_3 different from φ_1, φ_2 . In the case when D is some domain, we can write

$$b_{ij}(t) \mid_D = \sum_{0 \le k \le 2^{\ell}} b_{ij}(t) \chi_D(2^{\ell}t - k),$$
 (7)

where χ_D is characteristic function of D. So, if we take $\varphi_4 = \chi_D$, which is again a refinable function, then the problem of computation of (4) is reduced to the problem of calculation of integral

$$H(k_1, k_2, k_3, k_4) = H(k) =$$

$$\int_{\mathbf{R}^s} \varphi_4(2^j t - k_1) \varphi_3(2^\ell t - k_2) \times$$

$$\varphi_1^{d_1}(2^r t - k_3) \varphi_2^{d_2}(2^s t - k_4) dx$$
(8)

The key point is that these integrals also satisfy some sort of refinement equation:

$$2^{-|\mu|}H(k) = \sum_{\ell \in \mathbf{Z}} b_{2k-\ell}H(\ell), \qquad \mu = d_1 + d_2.$$
 (9)

This equation can be interpreted as the problem of computing an eigenvector. Thus, we reduced the problem of extension of our method to the case of variable coefficients to the same standard algebraical problem as in the preceding sections.

So, the general scheme is the same one and we have only one more additional linear algebraic problem by which we in the same way can parameterize the solutions of corresponding problem. As example we demonstrate on Fig. 1 a simple model of (local) intersection and the corresponding multiresolution representation (MRA).

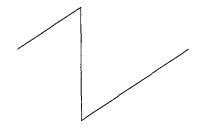


Figure 1: Simple insertion.

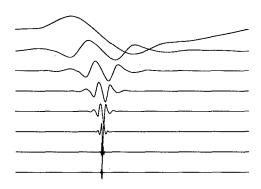


Figure 2: MRA representations.

4 EVALUATION OF NONLINEARITIES SCALE BY SCALE

We consider scheme of modification of our variational approach in the case when we consider different scales separately. For this reason we need to compute errors of approximations. The main problems come of course from nonlinear terms. We follow the approach from [11].

Let P_j be projection operators on the subspaces V_j , $j \in \mathbb{Z}$:

$$P_j$$
 : $L^2(\mathbf{R}) \to V_j$ (10)
 $(P_j f)(x) = \sum_k \langle f, \varphi_{j,k} \rangle \varphi_{j,k}(x)$

and Q_j are projection operators on the subspaces W_j :

$$Q_j = P_{j-1} - P_j (11)$$

So, for $u \in L^2(\mathbf{R})$ we have $u_j = P_j u$ and $u_j \in V_j$, where $\{V_j\}, j \in \mathbf{Z}$ is a multiresolution analysis of $L^2(\mathbf{R})$.

It is obviously that we can represent u_0^2 in the following form:

$$u_0^2 = 2\sum_{j=1}^n (P_j u)(Q_j u) + \sum_{j=1}^n (Q_j u)(Q_j u) + u_n^2 \quad (12)$$

In this formula there is no interaction between different scales. We may consider each term of (12) as a bilinear mappings:

$$M_{VW}^j: V_j \times W_j \to L^2(\mathbf{R}) = V_j \oplus_{j' \ge j} W_{j'}$$
 (13)

$$M_{WW}^{j}: W_{j} \times W_{j} \to L^{2}(\mathbf{R}) = V_{j} \oplus_{j' > j} W_{j'}$$
 (14)

For numerical purposes we need formula (12) with a finite number of scales, but when we consider limits $j\to\infty$ we have

$$u^{2} = \sum_{j \in \mathbf{Z}} (2P_{j}u + Q_{j}u)(Q_{j}u), \tag{15}$$

which is para-product of Bony, Coifman and Meyer.

Now we need to expand (12) into the wavelet bases. To expand each term in (12) into wavelet basis, we need to consider the integrals of the products of the basis functions, e.g.

$$M_{WWW}^{j,j'}(k,k',\ell) = \int_{-\infty}^{\infty} \psi_k^j(x) \psi_{k'}^{j}(x) \psi_{\ell}^{j'}(x) dx,$$
 (16)

where j' > j and

$$\psi_k^j(x) = 2^{-j/2}\psi(2^{-j}x - k) \tag{17}$$

are the basis functions. If we consider compactly supported wavelets then

$$M_{WWW}^{j,j'}(k,k',\ell) \equiv 0 \quad \text{for} \quad |k-k'| > k_0,$$
 (18)

where k_0 depends on the overlap of the supports of the basis functions and

$$|M_{WWW}^r(k-k', 2^rk-\ell)| \le C \cdot 2^{-r\lambda M}$$
 (19)

Let us define j_0 as the distance between scales such that for a given ε all the coefficients in (19) with labels r=j-j', $r>j_0$ have absolute values less than ε . For the purposes of computing with accuracy ε we replace the mappings in (13), (14) by

$$M_{VW}^j: V_j \times W_j \to V_j \oplus_{j \le j' \le j_0} W_{j'}$$
 (20)

$$M_{WW}^j: W_j \times W_j \to V_j \oplus_{J \le j' \le j_0} W_{j'} \qquad (21)$$

Since

$$V_i \oplus_{i < i' < j_0} W_{i'} = V_{j_0 - 1} \tag{22}$$

and

$$V_j \subset V_{j_0-1}, \qquad W_j \subset V_{j_0-1} \tag{23}$$

we may consider bilinear mappings (20), (21) on $V_{j_0-1} \times V_{j_0-1}$. For the evaluation of (20), (21) as mappings $V_{j_0-1} \times$

 $V_{j_0-1} \rightarrow V_{j_0-1}$ we need significantly fewer coefficients than for mappings (20), (21). It is enough to consider only coefficients

$$M(k, k', \ell) = 2^{-j/2} \int_{\infty}^{\infty} \varphi(x - k) \varphi(x - k') \varphi(x - \ell) dx,$$
(24)

where $\varphi(x)$ is scale function. Also we have

$$M(k, k', \ell) = 2^{-j/2} M_0(k - \ell, k' - \ell),$$
 (25)

where

$$M_0(p,q) = \int \varphi(x-p)\varphi(x-q)\varphi(x)\mathrm{d}x \qquad (26)$$

Now as in section (3) we may derive and solve a system of linear equations to find $M_0(p,q)$ and obtain explicit representation for solution.

We are very grateful to M. Cornacchia (SLAC), W. Herrmannsfeldt (SLAC), Mrs. M. Laraneta (UCLA), J. Kono (LBL) for their permanent encouragement.

- Fedorova, A.N., Zeitlin, M.G. 'Wavelets in Optimization and Approximations', *Math. and Comp. in Simulation*, 46, 527-534 (1998).
- [2] Fedorova, A.N., Zeitlin, M.G., 'Wavelet Approach to Polynomial Mechanical Problems', New Applications of Nonlinear and Chaotic Dynamics in Mechanics, Kluwer, 101-108, 1998.
- [3] Fedorova, A.N., Zeitlin, M.G., 'Wavelet Approach to Mechanical Problems. Symplectic Group, Symplectic Topology and Symplectic Scales', New Applications of Nonlinear and Chaotic Dynamics in Mechanics, Kluwer, 31-40, 1998.
- [4] Fedorova, A.N., Zeitlin, M.G 'Nonlinear Dynamics of Accelerator via Wavelet Approach', AIP Conf. Proc., vol. 405, 87-102, 1997, Los Alamos preprint, physics/9710035.
- [5] Fedorova, A.N., Zeitlin, M.G, Parsa, Z., 'Wavelet Approach to Accelerator Problems', parts 1-3, Proc. PAC97, vol. 2, 1502-1504, 1505-1507, 1508-1510, IEEE, 1998.
- [6] Fedorova, A.N., Zeitlin, M.G, Parsa, Z., 'Nonlinear Effects in Accelerator Physics: from Scale to Scale via Wavelets', 'Wavelet Approach to Hamiltonian, Chaotic and Quantum Calculations in Accelerator Physics', Proc. EPAC'98, 930-932, 933-935, Institute of Physics, 1998.
- [7] Fedorova, A.N., Zeitlin, M.G., Parsa, Z., 'Variational Approach in Wavelet Framework to Polynomial Approximations of Nonlinear Accelerator Problems', AIP Conf. Proc., vol. 468, 48-68, 1999.
 Los Alamos preprint, physics/9902062.
- [8] Fedorova, A.N., Zeitlin, M.G., Parsa, Z., 'Symmetry, Hamiltonian Problems and Wavelets in Accelerator Physics', AIP Conf. Proc., vol. 468, 69-93, 1999.
 Los Alamos preprint, physics/9902063.
- [9] Ropert, A., CERN 98-04.
- [10] Dahmen, W., Micchelli, C., SIAM J. Numer. Anal., 30, no. 2, 507-537 (1993).
- [11] Beylkin, G., Colorado preprint, 1992.

NONLINEAR ACCELERATOR PROBLEMS VIA WAVELETS: 4. SPIN-ORBITAL MOTION

A. Fedorova, M. Zeitlin, IPME, RAS, St. Petersburg, Russia * †

Abstract

In this series of eight papers we present the applications of methods from wavelet analysis to polynomial approximations for a number of accelerator physics problems. In this part we consider a model for spin-orbital motion: orbital dynamics and Thomas-BMT equations for classical spin vector. We represent the solution of this dynamical system in framework of biorthogonal wavelets via variational approach. We consider a different variational approach, which is applied to each scale.

1 INTRODUCTION

This is the fourth part of our eight presentations in which we consider applications of methods from wavelet analysis to nonlinear accelerator physics problems. This is a continuation of our results from [1]-[8], which is based on our approach to investigation of nonlinear problems - general, with additional structures (Hamiltonian, symplectic or quasicomplex), chaotic, quasiclassical, quantum, which are considered in the framework of local (nonlinear) Fourier analysis, or wavelet analysis. Wavelet analysis is a relatively novel set of mathematical methods, which gives us a possibility to work with well-localized bases in functional spaces and with the general type of operators (differential, integral, pseudodifferential) in such bases. In this part we consider spin orbital motion. In section 3 we consider generalization of our approach from part 1 to variational formulation in the biorthogonal bases of compactly supported wavelets. In section 4 we consider the different variational multiresolution approach which gives us possibility for computations in each scale separately.

2 SPIN-ORBITAL MOTION

Let us consider the system of equations for orbital motion and Thomas-BMT equation for classical spin vector [9]: $dq/dt = \partial H_{orb}/\partial p$, $dp/dt = -\partial H_{orb}/\partial q$, $ds/dt = w \times s$, where

$$H_{orb} = c\sqrt{\pi^2 + m_0 c^2} + e\Phi,$$

$$w = -\frac{e}{m_0 c\gamma} (1 + \gamma G) \vec{B}$$
 (1)

$$\begin{array}{ll} + & \frac{e}{m_0^3 c^3 \gamma} \frac{G(\vec{\pi} \cdot \vec{B}) \vec{\pi}}{(1 + \gamma)} \\ + & \frac{e}{m_0^2 c^2 \gamma} \frac{G + \gamma G + 1}{(1 + \gamma)} [\pi \times E], \end{array}$$

 $q=(q_1,q_2,q_3), p=(p_1,p_2,p_3)$ are canonical position and momentum, $s=(s_1,s_2,s_3)$ is the classical spin vector of length $\hbar/2$, $\pi=(\pi_1,\pi_2,\pi_3)$ is kinetic momentum vector. We may introduce in 9-dimensional phase space z=(q,p,s) the Poisson brackets $\{f(z),g(z)\}=f_qg_p-f_pg_q+[f_s\times g_s]\cdot s$ and the Hamiltonian equations are $\mathrm{d}z/\mathrm{d}t=\{z,H\}$ with Hamiltonian

$$H = H_{orb}(q, p, t) + w(q, p, t) \cdot s. \tag{2}$$

More explicitly we have

$$\frac{\mathrm{d}q}{\mathrm{d}t} = \frac{\partial H_{orb}}{\partial p} + \frac{\partial (w \cdot s)}{\partial p}
\frac{\mathrm{d}p}{\mathrm{d}t} = -\frac{\partial H_{orb}}{\partial q} - \frac{\partial (w \cdot s)}{\partial q}
\frac{\mathrm{d}s}{\mathrm{d}t} = [w \times s]$$
(3)

We will consider this dynamical system also in another paper via invariant approach, based on consideration of Lie-Poison structures on semidirect products. But from the point of view which we used in this paper we may consider the similar approximations as in the preceding parts and then we also arrive to some type of polynomial dynamics.

3 VARIATIONAL APPROACH IN BIORTHOGONAL WAVELET BASES

Because integrand of variational functionals is represented by bilinear form (scalar product) it seems more reasonable to consider wavelet constructions [10] which take into account all advantages of this structure. The action functional for loops in the phase space is [11]

$$F(\gamma) = \int_{\gamma} p dq - \int_{0}^{1} H(t, \gamma(t)) dt \tag{4}$$

The critical points of F are those loops γ , which solve the Hamiltonian equations associated with the Hamiltonian

^{*} e-mail: zeitlin@math.ipme.ru

[†] http://www.ipme.ru/zeitlin.html; http://www.ipme.nw.ru/zeitlin.html

H and hence are periodic orbits. By the way, all critical points of F are the saddle points of infinite Morse index, but surprisingly this approach is very effective. This will be demonstrated using several variational techniques starting from minimax due to Rabinowitz and ending with Floer homology. So, (M,ω) is symplectic manifolds, $H:M\to R$, H is Hamiltonian, X_H is unique Hamiltonian vector field defined by $\omega(X_H(x),v)=-dH(x)(v), \quad v\in T_xM, \quad x\in M$, where ω is the symplectic structure. A T-periodic solution x(t) of the Hamiltonian equations $\dot{x}=X_H(x)$ on M is a solution, satisfying the boundary conditions x(T)=x(0), T>0. Let us consider the loop space $\Omega=C^\infty(S^1,R^{2n})$, where $S^1=R/\mathbf{Z}$, of smooth loops in R^{2n} . Let us define a function $\Phi:\Omega\to R$ by setting

$$\Phi(x) = \int_0^1 \frac{1}{2} < -J\dot{x}, x > dt - \int_0^1 H(x(t))dt, \quad x \in \Omega$$
(5)

The critical points of Φ are the periodic solutions of $\dot{x} = X_H(x)$. Computing the derivative at $x \in \Omega$ in the direction of $y \in \Omega$, we find

$$\Phi'(x)(y) = \frac{d}{d\epsilon}\Phi(x+\epsilon y)|_{\epsilon=0} =$$

$$\int_0^1 \langle -J\dot{x} - \nabla H(x), y \rangle dt$$
(6)

Consequently, $\Phi'(x)(y) = 0$ for all $y \in \Omega$ iff the loop x satisfies the equation

$$-J\dot{x}(t) - \nabla H(x(t)) = 0, \tag{7}$$

i.e. x(t) is a solution of the Hamiltonian equations, which also satisfies x(0)=x(1), i.e. periodic of period 1. Periodic loops may be represented by their Fourier series: $x(t)=\sum e^{k2\pi Jt}x_k,\ x_k\in R^{2k}$, where J is quasicomplex structure. We give relations between quasicomplex structure and wavelets in our other paper. But now we need to take into account underlying bilinear structure via wavelets. We started with two hierarchical sequences of approximations spaces [10]:

$$\dots V_{-2} \subset V_{-1} \subset V_0 \subset V_1 \subset V_2 \dots,$$

$$\dots \widetilde{V}_{-2} \subset \widetilde{V}_{-1} \subset \widetilde{V}_0 \subset \widetilde{V}_1 \subset \widetilde{V}_2 \dots,$$

$$(8)$$

and as usually, W_0 is complement to V_0 in V_1 , but now not necessarily orthogonal complement. New orthogonality conditions have now the following form:

$$\widetilde{W}_0 \perp V_0, \quad W_0 \perp \widetilde{V}_0, \quad V_j \perp \widetilde{W}_j, \quad \widetilde{V}_j \perp W_j$$
 (9)

translates of ψ span W_0 , translates of $\tilde{\psi}$ span \widetilde{W}_0 . Biorthogonality conditions are

$$\langle \psi_{jk}, \tilde{\psi}_{j'k'} \rangle = \int_{-\infty}^{\infty} \psi_{jk}(x) \tilde{\psi}_{j'k'}(x) \mathrm{d}x = \delta_{kk'} \delta_{jj'},$$
(10)

where $\psi_{jk}(x)=2^{j/2}\psi(2^jx-k)$. Functions $\varphi(x),\tilde{\varphi}(x-k)$ form dual pair: $<\varphi(x-k),\tilde{\varphi}(x-\ell)>=\delta_{kl},<\varphi(x-k),\tilde{\psi}(x-\ell)>=0$. Functions $\varphi,\tilde{\varphi}$ generate a multiresolution analysis. $\varphi(x-k),\psi(x-k)$ are synthesis functions, $\tilde{\varphi}(x-\ell),\tilde{\psi}(x-\ell)$ are analysis functions. Synthesis functions are biorthogonal to analysis functions. Scaling spaces are orthogonal to dual wavelet spaces. Two multiresolutions are intertwining $V_j+W_j=V_{j+1}, \quad \widetilde{V}_j+\widetilde{W}_j=\widetilde{V}_{j+1}$. These are direct sums but not orthogonal sums.

So, our representation for solution has now the form

$$f(t) = \sum_{j,k} \tilde{b}_{jk} \psi_{jk}(t), \tag{11}$$

where synthesis wavelets are used to synthesize the function. But \tilde{b}_{jk} come from inner products with analysis wavelets. Biorthogonality yields

$$\tilde{b}_{\ell m} = \int f(t)\tilde{\psi}_{\ell m}(t)\mathrm{d}t. \tag{12}$$

So, now we can introduce this more complicated construction into our variational approach. We have modification only on the level of computing coefficients of reduced nonlinear algebraical system. This new construction is more flexible. Biorthogonal point of view is more stable under the action of large class of operators while orthogonal (one scale for multiresolution) is fragile, all computations are much more simpler and we accelerate the rate of convergence. In all types of Hamiltonian calculation, which are based on some bilinear structures (symplectic or Poissonian structures, bilinear form of integrand in variational integral) this framework leads to greater success. In particular cases we may use very useful wavelet packets from Fig. 1.

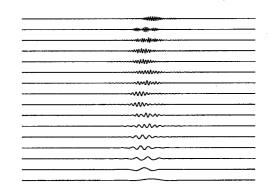


Figure 1: Wavelet packets.

4 EVALUATION OF NONLINEARITIES SCALE BY SCALE.NON-REGULAR APPROXIMATION.

We use wavelet function $\psi(x)$, which has k vanishing moments $\int x^k \psi(x) dx = 0$, or equivalently $x^k = \sum c_\ell \varphi_\ell(x)$

for each k, $0 \le k \le K$. Let P_j be orthogonal projector on space V_j . By tree algorithm we have for any $u \in L^2(\mathbf{R})$ and $\ell \in \mathbf{Z}$, that the wavelet coefficients of $P_\ell(u)$, i.e. the set $\{< u, \psi_{j,k} >, j \le \ell - 1, k \in \mathbf{Z}\}$ can be compute using hierarchic algorithms from the set of scaling coefficients in V_ℓ , i.e. the set $\{< u, \varphi_{\ell,k} >, k \in \mathbf{Z}\}$ [12]. Because for scaling function φ we have in general only $\int \varphi(x) \mathrm{d}x = 1$, therefore we have for any function $u \in L^2(\mathbf{R})$:

$$\lim_{j \to \infty, k2^{-j} \to x} |2^{j/2} < u, \varphi_{j,k} > -u(x)| = 0$$
 (13)

If the integer $n(\varphi)$ is the largest one such that

$$\int x^{\alpha} \varphi(x) dx = 0 \quad \text{for} \quad 1 \le \alpha \le n \quad (14)$$

then if $u \in C^{(n+1)}$ with $u^{(n+1)}$ bounded we have for $j \to \infty$ uniformly in k:

$$|2^{j/2} < u, \varphi_{j,k} > -u(k2^{-j})| = O(2^{-j(n+1)}).$$
 (15)

Such scaling functions with zero moments are very useful for us from the point of view of time-frequency localization, because we have for Fourier component $\hat{\Phi}(\omega)$ of them, that exists some $C(\varphi) \in \mathbf{R}$, such that for $\omega \to 0$ $\hat{\Phi}(\omega) = 1 + C(\varphi) \mid \omega \mid^{2r+2}$ (remember, that we consider r-regular multiresolution analysis). Using such type of scaling functions lead to superconvergence properties for general Galerkin approximation [12]. Now we need some estimates in each scale for non-linear terms of type $u \mapsto f(u) = f \circ u$, where f is C^{∞} (in previous and future parts we consider only truncated Taylor series action). Let us consider non regular space of approximation V of the form

$$\widetilde{V} = V_q \oplus \sum_{q \le j \le p-1} \widetilde{W}_j, \tag{16}$$

with $\widetilde{W_j} \subset W_j$. We need efficient and precise estimate of $f \circ u$ on \widetilde{V} . Let us set for $q \in \mathbf{Z}$ and $u \in L^2(\mathbf{R})$

$$\prod f_q(u) = 2^{-q/2} \sum_{k \in \mathbb{Z}} f(2^{q/2} < u, \varphi_{q,k} >) \cdot \varphi_{q,k} \quad (17)$$

We have the following important for us estimation (uniformly in q) for $u, f(u) \in H^{(n+1)}$ [12]:

$$||P_q(f(u)) - \prod f_q(u)||_{L^2} = O\left(2^{-(n+1)q}\right)$$
 (18)

For non regular spaces (16) we set

$$\prod f_{\widetilde{V}}(u) = \prod f_q(u) + \sum_{\ell=q, p-1} P_{\widetilde{W}_j} \prod f_{\ell+1}(u) \quad (19)$$

Then we have the following estimate:

$$||P_{\widetilde{V}}(f(u)) - \prod f_{\widetilde{V}}(u)||_{L^2} = O(2^{-(n+1)q})$$
 (20)

uniformly in q and \widetilde{V} (16). This estimate depends on q, not p, i.e. on the scale of the coarse grid, not on the finest grid used in definition of \widetilde{V} . We have for total error

$$||f(u) - \prod f_{\widetilde{V}}(u)|| = ||f(u) - P_{\widetilde{V}}(f(u))||_{L^{2}} + ||P_{\widetilde{V}}(f(u) - \prod f_{\widetilde{V}}(u))||_{L^{2}}$$
(21)

and since the projection error in \widetilde{V} : $||f(u) - P_{\widetilde{V}}(f(u))||_{L^2}$ is much smaller than the projection error in V_q we have the improvement (20) of (18). In concrete calculations and estimates it is very useful to consider approximations in the particular case of c-structured space:

$$\widetilde{V} = V_q + \sum_{j=q}^{p-1} span\{\psi_{j,k},$$

$$k \in [2^{(j-1)} - c, 2^{(j-1)} + c] \mod 2^j\}$$
(22)

We are very grateful to M. Cornacchia (SLAC), W. Herrmannsfeldt (SLAC), Mrs. J. Kono (LBL) and M. Laraneta (UCLA) for their permanent encouragement.

- Fedorova, A.N., Zeitlin, M.G. 'Wavelets in Optimization and Approximations', *Math. and Comp. in Simulation*, 46, 527-534 (1998).
- [2] Fedorova, A.N., Zeitlin, M.G., 'Wavelet Approach to Polynomial Mechanical Problems', New Applications of Nonlinear and Chaotic Dynamics in Mechanics, Kluwer, 101-108, 1998.
- [3] Fedorova, A.N., Zeitlin, M.G., 'Wavelet Approach to Mechanical Problems. Symplectic Group, Symplectic Topology and Symplectic Scales', New Applications of Nonlinear and Chaotic Dynamics in Mechanics, Kluwer, 31-40, 1998.
- [4] Fedorova, A.N., Zeitlin, M.G 'Nonlinear Dynamics of Accelerator via Wavelet Approach', AIP Conf. Proc., vol. 405, 87-102, 1997, Los Alamos preprint, physics/9710035.
- [5] Fedorova, A.N., Zeitlin, M.G, Parsa, Z., 'Wavelet Approach to Accelerator Problems', parts 1-3, Proc. PAC97, vol. 2, 1502-1504, 1505-1507, 1508-1510, IEEE, 1998.
- [6] Fedorova, A.N., Zeitlin, M.G, Parsa, Z., 'Nonlinear Effects in Accelerator Physics: from Scale to Scale via Wavelets', 'Wavelet Approach to Hamiltonian, Chaotic and Quantum Calculations in Accelerator Physics', Proc. EPAC'98, 930-932, 933-935, Institute of Physics, 1998.
- [7] Fedorova, A.N., Zeitlin, M.G., Parsa, Z., 'Variational Approach in Wavelet Framework to Polynomial Approximations of Nonlinear Accelerator Problems', AIP Conf. Proc., vol. 468, 48-68, 1999.
 Los Alamos preprint, physics/9902062.
- [8] Fedorova, A.N., Zeitlin, M.G., Parsa, Z., 'Symmetry, Hamiltonian Problems and Wavelets in Accelerator Physics', AIP Conf. Proc., vol. 468, 69-93, 1999.
 Los Alamos preprint, physics/9902063.
- [9] Balandin, V., NSF-ITP-96-155i.
- [10] Cohen, A., Daubechies, I., Feauveau, J.C., Comm. Pure. Appl. Math., XLV, 485-560, (1992).
- [11] Hofer, E., Zehnder, E., Symplectic Topology: Birkhauser, 1994.
- [12] Liandrat, J., Tchamitchian, Ph., Advances in Comput. Math., (1996).

NONLINEAR ACCELERATOR PROBLEMS VIA WAVELETS: 5. MAPS AND DISCRETIZATION VIA WAVELETS

A. Fedorova, M. Zeitlin, IPME, RAS, St. Petersburg, Russia * †

Abstract

In this series of eight papers we present the applications of methods from wavelet analysis to polynomial approximations for a number of accelerator physics problems. In this part we consider the applications of discrete wavelet analysis technique to maps which come from discretization of continuous nonlinear polynomial problems in accelerator physics. Our main point is generalization of wavelet analysis which can be applied for both discrete and continuous cases. We give explicit multiresolution representation for solutions of discrete problems, which is correct discretization of our representation of solutions of the corresponding continuous cases.

1 INTRODUCTION

This is the fifth part of our eight presentations in which we consider applications of methods from wavelet analysis to nonlinear accelerator physics problems. This is a continuation of our results from [1]-[8], in which we considered the applications of a number of analytical methods from nonlinear (local) Fourier analysis, or wavelet analysis, to nonlinear accelerator physics problems both general and with additional structures (Hamiltonian, symplectic or quasicomplex), chaotic, quasiclassical, quantum. Wavelet analysis is a relatively novel set of mathematical methods, which gives us a possibility to work with well-localized bases in functional spaces and with the general type of operators (differential, integral, pseudodifferential) in such bases. In contrast with parts 1-4 in parts 5-8 we try to take into account before using power analytical approaches underlying algebraical, geometrical, topological structures related to kinematical, dynamical and hidden symmetry of physical problems.

In this paper we consider the applications of discrete wavelet analysis technique to maps which come from discretization of continuous nonlinear polynomial problems in accelerator physics. Our main point is generalization of wavelet analysis which can be applied for both discrete and continuous cases. We give explicit multiresolution representation for solutions of discrete problems, which is correct discretization of our representation of solutions of the corresponding continuous cases.

In part 2 we consider symplectic and Lagrangian structures for the case of discretization of flows by corresponding maps and in part 3 construction of corresponding solutions by applications of generalized wavelet approach which is based on generalization of multiresolution analysis for the case of maps.

2 VESELOV-MARSDEN DISCRETIZATION

Discrete variational principles lead to evolution dynamics analogous to the Euler-Lagrange equations [9]. Let Q be a configuration space, then a discrete Lagrangian is a map $L: Q \times Q \to \mathbf{R}$. usually L is obtained by approximating the given Lagrangian. For $N \in N_+$ the action sum is the map $S: Q^{N+1} \to \mathbf{R}$ defined by

$$S = \sum_{k=0}^{N-1} L(q_{k+1}, q_k), \tag{1}$$

where $q_k \in Q$, $k \ge 0$. The action sum is the discrete analog of the action integral in continuous case. Extremizing S over $q_1, ..., q_{N-1}$ with fixing q_0, q_N we have the discrete Euler-Lagrange equations (DEL):

$$D_2L(q_{k+1}, q_k) + D_1(q_k, q_{q-1}) = 0, (2)$$

for k = 1, ..., N - 1.

Let

$$\Phi: Q \times Q \to Q \times Q \tag{3}$$

and

$$\Phi(q_k, q_{k-1}) = (q_{k+1}, q_k) \tag{4}$$

is a discrete function (map), then we have for DEL:

$$D_2L \circ \Phi + D_1L = 0 \tag{5}$$

or in coordinates q^i on Q we have DEL

$$\frac{\partial L}{\partial q_k^i} \circ \Phi(q_{k+1}, q_k) + \frac{\partial L}{\partial q_{k+1}^i}(q_{k+1}, q_k) = 0.$$
 (6)

It is very important that the map Φ exactly preserves the symplectic form ω :

$$\omega = \frac{\partial^2 L}{\partial q_k^i \partial q_{k+1}^j} (q_{k+1}, q_k) \mathrm{d}q_k^i \wedge \mathrm{d}q_{k+1}^j \tag{7}$$

^{*} e-mail: zeitlin@math.ipme.ru

[†] http://www.ipme.ru/zeitlin.html; http://www.ipme.nw.ru/zeitlin.html

3 GENERALIZED WAVELET APPROACH

Our approach to solutions of equations (6) is based on applications of general and very efficient methods developed by A. Harten [10], who produced a "General Framework" for multiresolution representation of discrete data.

It is based on consideration of basic operators, decimation and prediction, which connect adjacent resolution levels. These operators are constructed from two basic blocks: the discretization and reconstruction operators. The former obtains discrete information from a given continuous functions (flows), and the latter produces an approximation to those functions, from discrete values, in the same function space to which the original function belongs.

A "new scale" is defined as the information on a given resolution level which cannot be predicted from discrete information at lower levels. If the discretization and reconstruction are local operators, the concept of "new scale" is also local.

The scale coefficients are directly related to the prediction errors, and thus to the reconstruction procedure. If scale coefficients are small at a certain location on a given scale, it means that the reconstruction procedure on that scale gives a proper approximation of the original function at that particular location.

This approach may be considered as some generalization of standard wavelet analysis approach. It allows to consider multiresolution decomposition when usual approach is impossible (δ -functions case). We demonstrated the discretization of Dirac function by wavelet packets on Fig. 1 and Fig. 2.

Let F be a linear space of mappings

$$F \subset \{f | f : X \to Y\},\tag{8}$$

where X, Y are linear spaces. Let also D_k be a linear operator

$$D_{k}: f \to \{v^{k}\}, \quad v^{k} = D_{k}f, v^{k} = \{v_{i}^{k}\}, \quad v_{i}^{k} \in Y.$$
 (9)

This sequence corresponds to k level discretization of X. Let

$$D_k(F) = V^k = \operatorname{span}\{\eta_i^k\} \tag{10}$$

and the coordinates of $v^k \in V^k$ in this basis are $\hat{v}^k = \{\hat{v}^k_i\}$, $\hat{v}^k \in S^k$:

$$v^k = \sum_i \hat{v}_i^k \eta_i^k, \tag{11}$$

 D_k is a discretization operator. Main goal is to design a multiresolution scheme (MR) [10] that applies to all sequences $s \in S^L$, but corresponds for those sequences $\hat{v}^L \in S^L$, which are obtained by the discretization (8).

Since D_k maps F onto V^k then for any $v^k \subset V^k$ there is at least one f in F such that $D_k f = v^k$. Such correspondence from $f \in F$ to $v^k \in V^k$ is reconstruction and the corresponding operator is the reconstruction operator R_k :

$$R_k: V_k \to F, \qquad D_k R_k = I_k, \tag{12}$$

where I_k is the identity operator in V^k (R^k is right inverse of D^k in V^k).

Given a sequence of discretization $\{D_k\}$ and sequence of the corresponding reconstruction operators $\{R_k\}$, we define the operators D_k^{k-1} and P_{k-1}^k

$$D_k^{k-1} = D_{k-1}R_k : V_k \to V_{k-1}$$

$$P_{k-1}^k = D_k R_{k-1} : V_{k-1} \to V_k$$
(13)

If the set D_k in nested [10], then

$$D_k^{k-1} P_{k-1}^k = I_{k-1} (14)$$

and we have for any $f \in F$ and any $p \in F$ for which the reconstruction R_{k-1} is exact:

$$D_k^{k-1}(D_k f) = D_{k-1} f$$

$$P_{k-1}^k(D_{k-1} p) = D_k p$$
(15)

Let us consider any $v^L \in V^L$, Then there is $f \in F$ such that

$$v^L = D_L f, (16)$$

and it follows from (15) that the process of successive decimation [10]

$$v^{k-1} = D_k^{k-1} v^k, \qquad k = L, ..., 1$$
 (17)

yields for all k

$$v^k = D_k f (18)$$

Thus the problem of prediction, which is associated with the corresponding MR scheme, can be stated as a problem of approximation: knowing $D_{k-1}f$, $f \in F$, find a "good approximation" for D_kf . It is very important that each space V^L has a multiresolution basis

$$\bar{B}_M = \{\bar{\phi}_i^{0,L}\}_i, \{\{\bar{\psi}_j^{k,L}\}_j\}_{k=1}^L \tag{19}$$

and that any $v^L \in V^L$ can be written as

$$v^{L} = \sum_{i} \hat{v}_{i}^{0} \bar{\phi}_{i}^{0,L} + \sum_{k=1}^{L} \sum_{j} d_{j}^{k} \bar{\psi}_{j}^{k,L}, \qquad (20)$$

where $\{d_j^k\}$ are the k scale coefficients of the associated MR, $\{\hat{v}_i^0\}$ is defined by (11) with k=0. If $\{D_k\}$ is a nested sequence of discretization [10] and $\{R_k\}$ is any corresponding sequence of linear reconstruction operators, then we have from (20) for $v^L=D_L f$ applying R_L :

$$R_L D_L f = \sum_{i} \hat{f}_i^0 \phi_i^{0,L} + \sum_{k=1}^{L} \sum_{i} d_j^k \psi_j^{k,L}, \qquad (21)$$

where

$$\phi_{i}^{0,L} = R_{L}\bar{\phi}_{i}^{0,L} \in F, \quad \psi_{j}^{k,L} = R_{L}\bar{\psi}_{j}^{k,L} \in F,$$

$$D_{0}f = \sum_{i} \hat{f}_{i}^{0} \eta_{i}^{0}. \tag{22}$$

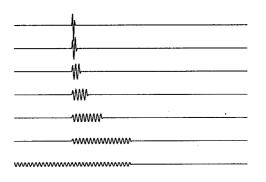


Figure 1: Wavelet packets.

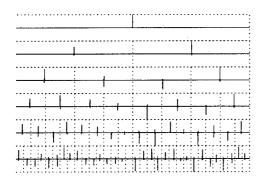


Figure 2: The discretization of Dirac function.

When $L \to \infty$ we have sufficient conditions which ensure that the limiting process $L \to \infty$ in (21, 22) yields a multiresolution basis for F. Then, according to (19), (20) we have very useful representation for solutions of equations (6) or for different maps construction in the form which are a counterparts for discrete (difference) cases of constructions from parts 1-4.

We are very grateful to M. Cornacchia (SLAC), W. Herrmannsfeldt (SLAC) Mrs. J. Kono (LBL) and M. Laraneta (UCLA) for their permanent encouragement.

- Fedorova, A.N., Zeitlin, M.G. 'Wavelets in Optimization and Approximations', *Math. and Comp. in Simulation*, 46, 527-534 (1998).
- [2] Fedorova, A.N., Zeitlin, M.G., 'Wavelet Approach to Polynomial Mechanical Problems', New Applications of Nonlinear and Chaotic Dynamics in Mechanics, Kluwer, 101-108, 1998.
- [3] Fedorova, A.N., Zeitlin, M.G., 'Wavelet Approach to Mechanical Problems. Symplectic Group, Symplectic Topology and Symplectic Scales', New Applications of Nonlinear and Chaotic Dynamics in Mechanics, Kluwer, 31-40, 1998.
- [4] Fedorova, A.N., Zeitlin, M.G 'Nonlinear Dynamics of Ac-

- celerator via Wavelet Approach', AIP Conf. Proc., vol. 405, 87-102, 1997, Los Alamos preprint, physics/9710035.
- [5] Fedorova, A.N., Zeitlin, M.G, Parsa, Z., 'Wavelet Approach to Accelerator Problems', parts 1-3, Proc. PAC97, vol. 2, 1502-1504, 1505-1507, 1508-1510, IEEE, 1998.
- [6] Fedorova, A.N., Zeitlin, M.G, Parsa, Z., 'Nonlinear Effects in Accelerator Physics: from Scale to Scale via Wavelets', 'Wavelet Approach to Hamiltonian, Chaotic and Quantum Calculations in Accelerator Physics', Proc. EPAC'98, 930-932, 933-935, Institute of Physics, 1998.
- [7] Fedorova, A.N., Zeitlin, M.G., Parsa, Z., 'Variational Approach in Wavelet Framework to Polynomial Approximations of Nonlinear Accelerator Problems', AIP Conf. Proc., vol. 468, 48-68, 1999.
 Los Alamos preprint, physics/9902062.
- [8] Fedorova, A.N., Zeitlin, M.G., Parsa, Z., 'Symmetry, Hamiltonian Problems and Wavelets in Accelerator Physics', AIP Conf. Proc., vol. 468, 69-93, 1999.
 Los Alamos preprint, physics/9902063.
- [9] Marsden, J.E., Park City Lectures on Mechanics, Dynamics and Symmetry, CALTECH, 1998.
- [10] Harten, A., SIAM J. Numer. Anal., 31, 1191-1218, 1994.

NONLINEAR ACCELERATOR PROBLEMS VIA WAVELETS: 8. INVARIANT BASES, LOOPS AND KAM

A. Fedorova, M. Zeitlin, IPME, RAS, St. Petersburg, Russia * †

Abstract

In this series of eight papers we present the applications of methods from wavelet analysis to polynomial approximations for a number of accelerator physics problems. In this part we consider variational wavelet approach for loops, invariant bases on semidirect product, KAM calculation via FWT.

1 INTRODUCTION

This is the eighth part of our eight presentations in which we consider applications of methods from wavelet analysis to nonlinear accelerator physics problems. This is a continuation of our results from [1]-[8], in which we considered the applications of a number of analytical methods from nonlinear (local) Fourier analysis, or wavelet analysis, to nonlinear accelerator physics problems both general and with additional structures (Hamiltonian, symplectic or quasicomplex), chaotic, quasiclassical, quantum. Wavelet analysis is a relatively novel set of mathematical methods, which gives us a possibility to work with well-localized bases in functional spaces and with the general type of operators (differential, integral, pseudodifferential) in such bases. In contrast with parts 1-4 in parts 5-8 we try to take into account before using power analytical approaches underlying algebraical, geometrical, topological structures related to kinematical, dynamical and hidden symmetry of physical problems. In section 2 we consider wavelet approach for calculation of Arnold-Weinstein curves (closed loops) in Floer variational approach. In section 3 we consider the applications of orbit technique for constructing different types of invariant wavelet bases in the particular case of affine Galilei group with the semiproduct structure. In section 4 we consider applications of very useful fast wavelet transform (FWT) technique (part 6) to calculations in KAM theory (symplectic scale of spaces). This method gives maximally sparse representation of (differential) operator that allows us to take into account contribution from each level of resolution.

2 FLOER APPROACH FOR CLOSED LOOPS

Now we consider the generalization of wavelet variational approach to the symplectic invariant calculation of closed loops in Hamiltonian systems [9]. As we demonstrated in [3]-[4] we have the parametrization of our solution by some reduced algebraical problem but in contrast to the cases from parts 1-4, where the solution is parametrized by construction based on scalar refinement equation, in symplectic case we have parametrization of the solution by matrix problems - Quadratic Mirror Filters equations. Now we consider a different approach. Let (M, ω) be a compact symplectic manifold of dimension 2n, ω is a closed 2-form (nondegenerate) on M which induces an isomorphism $T^*M \to TM$. Thus every smooth time-dependent Hamiltonian $H: \mathbf{R} \times M \to \mathbf{R}$ corresponds to a time-dependent Hamiltonian vector field $X_H : \mathbf{R} \times M \to TM$ defined by $\omega(X_H(t,x),\xi) = -d_x H(t,x)\xi$ for $\xi \in T_x M$. Let H(and X_H) is periodic in time: H(t+T,x)=H(t,x) and consider corresponding Hamiltonian differential equation on M: $\dot{x}(t) = X_H(t, x(t))$ The solutions x(t) determine a 1-parameter family of diffeomorphisms $\psi_t \in \text{Diff}(M)$ satisfying $\psi_t(x(0)) = x(t)$. These diffeomorphisms are symplectic: $\omega = \psi_t^* \omega$. Let $L = L_T M$ be the space of contractible loops in M which are represented by smooth curves $\gamma: \mathbf{R} \to M$ satisfying $\gamma(t+T) = \gamma(t)$. Then the contractible T-periodic solutions can be characterized as the critical points of the functional $S = S_T : L \to \mathbf{R}$:

$$S_T(\gamma) = -\int_D u^* \omega + \int_0^T H(t, \gamma(t)) dt, \qquad (1)$$

where $D \subset \mathbf{C}$ be a closed unit disc and $u:D \to M$ is a smooth function, which on boundary agrees with γ , i.e. $u(\exp\{2\pi i\Theta\}) = \gamma(\Theta T)$. Because $[\omega]$, the cohomology class of ω , vanishes then $S_T(\gamma)$ is independent of choice of u. Tangent space $T_\gamma L$ is the space of vector fields $\xi \in C^\infty(\gamma^*TM)$ along γ satisfying $\xi(t+T) = \xi(t)$. Then we have for the 1-form $\mathrm{d}f:TL \to \mathbf{R}$

$$dS_T(\gamma)\xi = \int_0^T (\omega(\dot{\gamma}, \xi) + dH(t, \gamma)\xi)dt$$
 (2)

and the critical points of S are contractible loops in L which satisfy the Hamiltonian equations. Thus the critical points are precisely the required T-periodic solutions.

^{*}e-mail: zeitlin@math.ipme.ru

[†] http://www.ipme.ru/zeitlin.html; http://www.ipme.nw.ru/zeitlin.html

To describe the gradient of S we choose a on almost complex structure on M which is compatible with ω . This is an endomorphism $J \in C^{\infty}(\operatorname{End}(TM))$ satisfying $J^2 = -I$ such that $g(\xi, \eta) = \omega(\xi, J(x)\eta), \ \xi, \eta \in T_xM$ defines a Riemannian metric on M. The Hamiltonian vector field is then represented by $X_H(t,x) = J(x)\nabla H(t,x)$, where ∇ denotes the gradient w.r.t. the x-variable using the metric. Moreover the gradient of S w.r.t. the induced metric on L is given by $\operatorname{grad} S(\gamma) = J(\gamma)\dot{\gamma} + \nabla H(t,\gamma), \ \gamma \in L$. Studying the critical points of S is confronted with the well-known difficulty that the variational integral is neither bounded from below nor from above. Moreover, at every possible critical point the Hessian of f has an infinite dimensional positive and an infinite dimensional negative subspaces, so the standard Morse theory is not applicable. The additional problem is that the gradient vector field on the loop space L: $d\gamma/ds = -gradf(\gamma)$ does not define a well posed Cauchy problem. But Floer [9] found a way to analyse the space \mathcal{M} of bounded solutions consisting of the critical points together with their connecting orbits. He used a combination of variational approach and Gromov's elliptic technique. A gradient flow line of f is a smooth solution $u: \mathbf{R} \to M$ of the partial differential equation

$$\frac{\partial u}{\partial s} + J(u)\frac{\partial u}{\partial t} + \nabla H(t, u) = 0, \tag{3}$$

which satisfies u(s,t+T)=u(s,t). The key point is to consider (3) not as the flow on the loop space but as an elliptic boundary value problem. It should be noted that (3) is a generalization of equation for Gromov's pseudoholomorphic curves (correspond to the case $\nabla H=0$ in (3)). Let $\mathcal{M}_T=\mathcal{M}_T(H,J)$ the space of bounded solutions of (3), i.e. the space of smooth functions $u: \mathbf{C}/iT\mathbf{Z} \to M$, which are contractible, solve equation (3) and have finite energy flow:

$$\Phi_T(u) = \frac{1}{2} \int \int_0^T \left(\left| \frac{\partial u}{\partial s} \right|^2 + \left| \frac{\partial u}{\partial t} - X_H(t, u) \right|^2 \right) dt ds. \tag{4}$$

For every $u \in M_T$ there exists a pair x, y of contractible T-periodic solutions, such that u is a connecting orbit from y to x: $\lim_{s \to -\infty} u(s,t) = y(t)$, $\lim_{s \to +\infty} = x(t)$. Then our approach from preceding parts, which we may apply or on the level of standard boundary problem or on the level of variational approach and representation of operators (in our case, J and ∇) according to part 6(FWT technique) lead us to wavelet representation of closed loops.

3 CONTINUOUS WAVELET TRANSFORM. BASES FOR SOLUTIONS.

When we take into account the Hamiltonian or Lagrangian structures from part 7 we need to consider generalized wavelets, which allow us to consider the corresponding structures instead of compactly supported wavelet representation from parts 1—4. We consider an important particular case of constructions from part 7: affine relativity

group (relativity group combined with dilations) - affine Galilei group in n-dimensions. So, we have combination of Galilei group with independent space and time dilations: $G_{aff} = G_m \bowtie D_2$, where $D_2 = (\mathbb{R}_*^+)^2 \simeq \mathbb{R}^2$, G_m is extended Galilei group corresponding to mass parameter m > 0 (G_{aff} is noncentral extension of $G \bowtie D_2$ by R, where G is usual Galilei group). Generic element of G_{aff} is $g = (\Phi, b_0, b; v; R, a_0, a)$, where $\Phi \in \mathbf{R}$ is the extension parameter in G_m , $b_0 \in \mathbb{R}$, $b \in \mathbb{R}^n$ are the time and space translations, $v \in \mathbf{R}^n$ is the boost parameter, $R \in SO(n)$ is a rotation and $a_0, a \in \mathbf{R}^+_*$ are time and space dilations. The actions of g on space-time is then $x \mapsto aRx + a_0vt + b$, $t \mapsto a_0t + b_0$, where $x = (x_1, x_2, ..., x_n)$. It should be noted that D_2 acts nontrivially on G_m . Space-time wavelets associated to G_{aff} corresponds to unitary irreducible representation of spin zero. It may be obtained via orbit method. The Hilbert space is $\mathcal{H} = L^2(\mathbf{R}^n \times \mathbf{R}, \mathrm{d}k\mathrm{d}\omega), k = (k_1, ..., k_n),$ where $\mathbf{R}^n \times \mathbf{R}$ may be identified with usual Minkowski space and we have for representation:

 $(U(g)\Psi)(k,\omega)=\sqrt{a_0a^n}\exp{i(m\Phi+kb-\omega b_0)}\Psi(k',\omega'),$ (5) with $k'=aR^{-1}(k+mv),\ \omega'=a_0(\omega-kv-\frac{1}{2}mv^2),$ $m'=(a^2/a_0)m.$ Mass m is a coordinate in the dual of the Lie algebra and these relations are a part of coadjoint action of G_{aff} . This representation is unitary and irreducible but not square integrable. So, we need to consider reduction to the corresponding quotients X=G/H. We consider the case in which H={phase changes Φ and space dilations a}. Then the space X=G/H is parametrized by points $\bar{x}=(b_0,b;v;R;a_0)$. There is a dense set of vectors $\eta\in\mathcal{H}$ admissible $\operatorname{mod}(H,\sigma_\beta)$, where σ_β is the corresponding section. We have a two-parameter family of functions $\beta(\operatorname{dilations})$: $\beta(\bar{x})=(\mu_0+\lambda_0a_0)^{1/2},\ \lambda_0,\mu_0\in\mathbf{R}$. Then any admissible vector η generates a tight frame of Galilean wavelets

$$\eta_{\beta(\vec{x})}(k,\omega) = \sqrt{a_0(\mu_0 + \lambda_0 a_0)^{n/2}} e^{i(kb - \omega b_0)} \eta(k',\omega'),$$
(6)

with $k' = (\mu_0 + \lambda_0 a)^{1/2} R^{-1} (k + mv), \ \omega' = a_0 (\omega - mv)$ $kv - mv^2/2$). The simplest examples of admissible vectors (corresponding to usual Galilei case) are Gaussian vector: $\eta(k) \sim \exp(-k^2/2mu)$ and binomial vector: $\eta(k) \sim (1 + k^2/2mu)^{-\alpha/2}, \alpha > 1/2$, where u is a kind of internal energy. When we impose the relation $a_0 = a^2$ then we have the restriction to the Galilei-Schrödinger group $G_s = G_m \bowtie D_s$, where D_s is the one-dimensional subgroup of D_2 . G_s is a natural invariance group of both the Schrödinger equation and the heat equation. The restriction to G_s of the representation (29) splits into the direct sum of two irreducible ones $U = U_+ \oplus U_-$ corresponding to the decomposition $L^2(\mathbf{R}^n \times \mathbf{R}, \mathrm{d}k\mathrm{d}\omega) = \mathcal{H}_+ \oplus \mathcal{H}_-$, where $\mathcal{H}_\pm =$ $L^{2}(D_{\pm}, dkd\omega) = \{\psi \in L^{2}(\mathbf{R}^{n} \times \mathbf{R}, dkd\omega), \psi(k, \omega) = 0\}$ 0 for $\omega + k^2/2m = 0$. These two subspaces are the analogues of usual Hardy spaces on R, i.e. the subspaces of (anti)progressive wavelets (see also below, part III A). The

two representation U_{\pm} are square integrable modulo the center. There is a dense set of admissible vectors η , and each of them generates a set of CS of Gilmore-Perelomov type. Typical wavelets of this kind are: the Schrödinger-Marr wavelet: $\eta(x,t)=(i\partial_t+\triangle/2m)\mathrm{e}^{-(x^2+t^2)/2}$, the Schrödinger-Cauchy wavelet: $\psi(x,t)=(i\partial_t+\triangle/2m)\times(t+i)\prod_{j=1}^n(x_j+i)^{-1}$. So, in the same way we can construct different invariant bases with explicit manifestation of underlying symmetry for solving Hamiltonian or Lagrangian equations.

4 SYMPLECTIC HILBERT SCALES VIA WAVELETS

We can solve many important dynamical problems such that KAM perturbations, spread of energy to higher modes, weak turbulence, growths of solutions of Hamiltonian equations only if we consider scales of spaces instead of one functional space. For Hamiltonian system and their perturbations for which we need take into account underlying symplectic structure we need to consider symplectic scales of spaces. So, if $\dot{u}(t) = J\nabla K(u(t))$ is Hamiltonian equation we need wavelet description of symplectic or quasicomplex structure on the level of functional spaces. It is very important that according to [12] Hilbert basis is in the same time a Darboux basis to corresponding symplectic structure. We need to provide Hilbert scale $\{Z_s\}$ with symplectic structure [12]. All what we need is the following. J is a linear operator, $J: Z_{\infty} \to Z_{\infty}$, $J(Z_{\infty}) = Z_{\infty}$, where $Z_{\infty} = \cap Z_s$. J determines an isomorphism of scale $\{Z_s\}$ of order $d_J \geq 0$. The operator J with domain of definition Z_{∞} is antisymmetric in $Z: \langle Jz_1, z_2 \rangle_Z = -\langle$ $z_1,Jz_2>_Z,z_1,z_2\in Z_\infty$. Then the triple $\{Z,\{Z_s|s\in Z_\infty\}\}$ R, $\alpha = \langle \bar{J}dz, dz \rangle$ is symplectic Hilbert scale. So, we may consider any dynamical Hamiltonian problem on functional level. As an example, for KdV equation we have $Z_s = \{u(x) \in H^s(T^1) | \int_0^{2\pi} u(x) dx = 0\}, s \in R,$ $J = \partial/\partial x$, is isomorphism of the scale of order one, $\bar{J} = -(J)^{-1}$ is isomorphism of order -1. According to [13] general functional spaces and scales of spaces such as Holder-Zygmund, Triebel-Lizorkin and Sobolev can be characterized through wavelet coefficients or wavelet transforms. As a rule, the faster the wavelet coefficients decay. the more the analyzed function is regular [13]. Most important for us example is the scale of Sobolev spaces. Let $H_k(\mathbb{R}^n)$ is the Hilbert space of all distributions with finite norm $||\hat{s}||_{H_k(\mathbb{R}^n)}^2 = \int d\xi (1+|\xi|^2)^{k/2} |\hat{s}(\xi)|^2$. Let us consider wavelet transform

$$W_g f(b, a) = \int_{\mathbb{R}^n} dx \frac{1}{a^n} \bar{g}\left(\frac{x-b}{a}\right) f(x),$$

 $b\in R^n, \quad a>0$, w.r.t. analyzing wavelet g, which is strictly admissible, i.e. $C_{g,g}=\int_0^\infty (\mathrm{d}a/a)|\hat{g}(\bar{a}k)|^2<\infty.$ Then there is a $c\geq 1$ such that

$$c^{-1} ||s||_{H_k(\mathbb{R}^n)}^2 \le \int_{H^n} \frac{\mathrm{d} b \mathrm{d} a}{a} (1 + a^{-2\gamma})| \times$$

$$|W_g s(b,a)|^2 \le c ||s||^2_{H_k(\mathbb{R}^n)}.$$

This shows that localization of the wavelet coefficients at small scale is linked to local regularity. So, we need representation for differential operator (J in our case) in wavelet basis. We consider it by means of the methods from part 6.

We are very grateful to M. Cornacchia (SLAC), W. Herrmannsfeldt (SLAC) Mrs. J. Kono (LBL) and M. Laraneta (UCLA) for their permanent encouragement.

- Fedorova, A.N., Zeitlin, M.G. 'Wavelets in Optimization and Approximations', *Math. and Comp. in Simulation*, 46, 527-534 (1998).
- [2] Fedorova, A.N., Zeitlin, M.G., 'Wavelet Approach to Polynomial Mechanical Problems', New Applications of Nonlinear and Chaotic Dynamics in Mechanics, Kluwer, 101-108, 1998.
- [3] Fedorova, A.N., Zeitlin, M.G., 'Wavelet Approach to Mechanical Problems. Symplectic Group, Symplectic Topology and Symplectic Scales', New Applications of Nonlinear and Chaotic Dynamics in Mechanics, Kluwer, 31-40, 1998.
- [4] Fedorova, A.N., Zeitlin, M.G 'Nonlinear Dynamics of Accelerator via Wavelet Approach', AIP Conf. Proc., vol. 405, 87-102, 1997, Los Alamos preprint, physics/9710035.
- [5] Fedorova, A.N., Zeitlin, M.G, Parsa, Z., 'Wavelet Approach to Accelerator Problems', parts 1-3, Proc. PAC97, vol. 2, 1502-1504, 1505-1507, 1508-1510, IEEE, 1998.
- [6] Fedorova, A.N., Zeitlin, M.G, Parsa, Z., 'Nonlinear Effects in Accelerator Physics: from Scale to Scale via Wavelets', 'Wavelet Approach to Hamiltonian, Chaotic and Quantum Calculations in Accelerator Physics', Proc. EPAC'98, 930-932, 933-935, Institute of Physics, 1998.
- [7] Fedorova, A.N., Zeitlin, M.G., Parsa, Z., 'Variational Approach in Wavelet Framework to Polynomial Approximations of Nonlinear Accelerator Problems', AIP Conf. Proc., vol. 468, 48-68, 1999.
 Los Alamos preprint, physics/9902062.
- [8] Fedorova, A.N., Zeitlin, M.G., Parsa, Z., 'Symmetry, Hamiltonian Problems and Wavelets in Accelerator Physics', AIP Conf. Proc., vol. 468, 69-93, 1999.
 Los Alamos preprint, physics/9902063.
- [9] Antoine, J.-P., UCL, 96-08, 95-02.
- [10] G.B. Folland, 'Harmonic Analysis in Phase Space', Princeton, 1989.
- [11] Hofer, E., Zehnder, E., Symplectic Topology: Birkhauser, 1994.
- [12] S. Kuksin, Nearly integrable Hamiltonian systems, Springer, 1993.
- [13] M. Holschneider, CPT-96/P3344, Marseille.

EMITTANCE GROWTH BY SYNCHROTRON RADIATION IN A DOUBLE-SIDED MICROTRON*

J. Herrmann, <u>K.-H. Kaiser*</u>, S. Ratschow Institut fuer Kernphysik, J.-Gutenberg Universitaet, D-55099 Mainz, Germany V.I. Shvedunov

Institute of Nuclear Physics, Moscow State University, R-119899 Moscow, Russia

Abstract

Here we present results of calculations of emittance growth caused by quantum fluctuations of synchrotron radiation (QFSR) for a 1.5GeV Double-Sided Microtron (DSM) [1]. We did both semi-analytical estimations, employing known twiss parameters for the DSM orbits, and a computer simulation of these stochastical effects using the program SYTRACE [2]. This showed that the normalized emittance growth was within reasonable limits, by a factor of about 1.5, thus permitting e.g. the installation of small aperture linacs on the DSM axes.

1 INTRODUCTION

A Double-Sided Microtron (DSM) is being planned to upgrade the three-staged cw racetrack microtron (RTM) cascade MAMI from 0.855GeV to 1.5GeV. The DSM consists of two rf linacs interconnected by symmetrical pairs of 90° segment magnets (s. fig.1). The scheme of the RTM is unpractical in this energy range because of the excessive weight of its end magnets. The relatively strong vertical defocusing by the 45°-pole face inclination at both the beam entrance and the exit of the segment magnets is compensated in the whole energy range by an appropriate field gradient normal to the pole edge [3]. Since the parallel-to-parallel optics in the horizontal plane is not affected by this two-dimensional field gradient, a pair of end magnets acts as energy-dependent effective drift spaces which are specific for the horizontal and vertical planes. Beam focusing is provided by four quadrupole doublets (two of which, Q,&Q, and Q,&Q,, are shown in Fig. 1), installed between linacs and 90° end magnets (M₁, M₂). The main parameters of the DSM are given in Table

As a consequence of the field gradient, the coherent energy gain per turn is no longer constant, leading to a shift of the central bunch phase during the acceleration process. Investigations of the longitudinal beam dynamics have shown that the stability with respect to small deviations of the accelerator parameters can be improved significantly by operating one of the linacs at the first subharmonic of the DSM frequency. This is possible

because at our subharmonic injection (the MAMI-RTMs are operating at half the DSM-frequency), only every second wave crest is occupied in one of the two DSM linacs.

For both the design of the DSM and the use of its beam in nuclear and particle physics experiments it is extremely important to make reliable predictions about the emittance of the beam. Horizontal emittance growth by QFSR was calculated and confirmed by measurements [4] for the third microtron (RTM3). QFSR induced longitudinal and horizontal emittance growth for general polytron scheme has been estimated in [5].

We used a simplified semi-analytical approach to obtain horizontal emittance dependence on the beam energy and to estimate beam losses. Computer simulation with particle tracking code SYTRACE takes into account the bending magnets field gradient, the possible beam mismatch, the change of beam ellipse parameters under synchrotron radiation and the nonlinear distortions of longitudinal phase space.

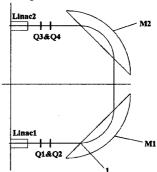


Figure 1. Half of DSM.

Table I. DSM main parameters.

Injection energy	0.855 GeV
Maximum output energy	1.5 GeV
Number of orbits	43
Energy gain per turn	16.58-13.66 MeV
Linac 1 frequency	2.4495 GHz
Linac 2 frequency	4.899 GHz
Field induction	1.53-0.95 T

^{*}Work supported in part by DFG (SFB 201)

^{*} kaiser@kph.uni-mainz.de

2 HORIZONTAL EMITTANCE

2.1 Semi-analytical estimations

Supposing strict mirror symmetry of the DSM optical scheme in canonical coordinates, uniform end magnet field and following [6], [7] we obtain the next estimate for the average emittance growth after passage of one pair of end magnets at the i-th half-turn:

$$\Delta \langle \varepsilon \rangle_{i} = \frac{\langle \Delta E^{2} \rangle_{i}}{E^{2}_{i}} \left[\frac{\pi}{2} \beta_{1i} - 2r_{i} \alpha_{1i} + \left(\frac{3\pi}{2} - 4 \right) r^{2}_{i} \gamma_{1i} \right], \tag{1}$$

where: $\langle \Delta E^2 \rangle_i$ is the mean square beam energy spread due to synchrotron radiation per unit of bending angle, E_i beam energy and β_{ii} , α_{ii} , γ_{ii} - horizontal plane twiss parameters at point 1 (Fig. 1), i=1,2,...2N, N - total number of turns.

$$\frac{\left\langle \Delta E^2 \right\rangle_i}{E_i^2} = \frac{55}{96\sqrt{3}} \frac{e^4 \hbar}{\pi \varepsilon_0 c (m_0 c)^4} B^2 \gamma_i^3 \approx 4.96 \times 10^{-22} B^2 \gamma_i^3 \qquad (2)$$

where B is field in T and γ_i - relative beam energy.

Formula (1) takes into account that pairs of DSM end magnets are achromatic. Twiss parameters at point 1 are obtained from the known twiss parameters at the linac1 center (see Fig. 2) through matrix transformations involving matrices for the half linac, the drift spaces, the quadrupole singlets and the 45° pole face rotation at the entrance of M_i .

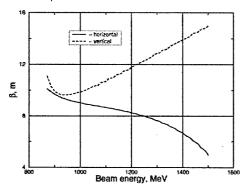


Figure 2. Energy dependence of the horizontal and vertical DSM β -functions at linac centers.

Taking into account the pseudo-damping due to acceleration while neglecting other sources of emittance growth, the average emittance after n turns is:

$$\langle \varepsilon \rangle_n \approx \langle \varepsilon \rangle_0 \frac{\gamma_0}{\gamma_{2n}} + \frac{1}{\gamma_{2n}} \sum_{i=1}^{2n} \Delta \langle \varepsilon \rangle_i \gamma_i ,$$
 (3)

where $\langle \varepsilon \rangle_0$ and γ_0 are emittance and relative energy at injection.

In Fig. 3 the dependence of DSM horizontal emittance on energy is shown, calculated with formulas (1)-(3). The initial value of average emittance at 0.855 GeV was taken to be 0.0107 π mm×mrad [4]. Thus total growth of the

normalized horizontal emittance is by a factor of about 1.5.

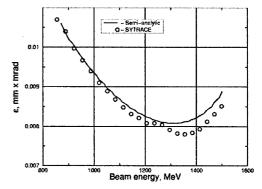


Figure 3: Horizontal emittance behaviour in DSM.

For "clean" DSM operation, relative particle losses during acceleration must be of less than 10^5 . To obtain estimations of the aperture radius $b_n(\eta)$, providing the transmission of a certain fraction η of the beam current at some specific point along the accelerator at the *n*-th turn, we use:

$$b_n(\eta) = \sqrt{\langle \varepsilon \rangle_n \beta_n^*} \Phi^{-1}(\eta) , \qquad (5)$$

here β_n^* - horizontal beta function at a considered point and $\Phi^{-1}(\eta)$ - inverse error function.

The most dangerous positions in DSM from the point of view of beam losses are the linac ends, where β -function β_{le} is close to maximum and is connected with that at linac center, shown at Fig. 2 by $\beta_{le} \approx \beta + L_{1/2}^2/\beta$, where $L_{1/2}$ is half linac length. Beam aperture radii for transmission of a certain beam current fraction, calculated with formula (5), are shown in Fig. 4. In spite of emittance growth, starting from about 1300 MeV, beam limiting aperture steadily decreased with energy because of the horizontal β -function β_{le} decrease. The estimated minimum beam aperture radius for beam losses at the level of 10^5 is less than 1.2 mm, while the beam hole radius for the 4.9 GHz linac will be 5 mm.

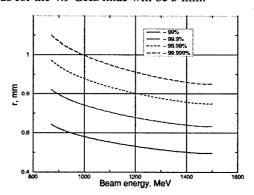


Figure 4. Beam aperture radius for transmission of different fractions of beam current.

2.2 Results of SYTRACE simulation

SYTRACE [2] is an extension of the well-proven PTRACE [8] code, used for the design of the MAMI RTMs. It includes the option to simulate a particle ensemble behaviour with QFSR taken into account. A precise integration of the beam dynamics equations is performed for each DSM element.

When integrating the equations of motion in the end magnets field, particle energy losses due to the emission of photons are taken into account. At each step for each particle, a photon can be emitted with a probability defined by the particle energy, local trajectory curvature and value of step size. Subsequently to each emitted photon an energy is prescribed, according to the probability function produced from the photon number Because the photon number spectrum is divergent for relative photon energy $\xi = \mu / \mu_c \rightarrow 0 \ (\mu_c - \mu_c)$ critical photon energy), it is truncated at $\xi_{tr} \approx 0.002$, producing an increase of 14% of the average energy $\langle \mu \rangle$ of emitted photons. The specific value of ξ_n is defined by limitations of the memory used to store the uniform step probability function. To have an average electron energy loss per turn $U = 2\pi \langle \mu \rangle \langle n \rangle$, in accordance with the theory, the average number of photons $\langle n \rangle$ emitted per unit angle is decreased by the same value. Because of $\langle \Delta E^2 \rangle = \frac{275}{64} \langle \mu \rangle^2 \langle n \rangle$ this procedure, according to (1), can lead to an emittance growth over-estimated by about 14%.

Dependence on energy of the horizontal plane rms emittance, calculated with SYTRACE is shown in Fig. 3 by open circles. For the same values of initial emittance, the semi-analytical value at 1.5 GeV is about 4% higher than the numerical one. Combined with overestimation described above this means a difference of about 18%. This difference can qualitatively be explained by the fact that for the semi-analytical calculations constant field magnets are used, whereas in the SYTRACE simulations the exact field decay could be taken into account. As can be seen from formula (2) the resulting decrease of the mean magnet field at high energies leads to smaller values for $\langle \Delta E^2 \rangle$, consequently, to a smaller emittance growth.

3 LONGITUDINAL EMITTANCE

The energy spread caused by QFSR after the passage of the beam through a pair end magnets increases from about 2.2 keV at the first DSM orbit to 8.8 keV (rms) at the last. Total QFSR energy spread at N-th orbit is defined by:

$$\delta E_N = \sqrt{\pi \sum_{i=1}^{2N} \left\langle \Delta E^2 \right\rangle_i} \tag{6}$$

where $\langle \Delta E^2 \rangle$ is given by (2), π is bending angle of magnet pair, and for N=43, $\delta E_{43} \approx 50$ keV. This energy spread is transformed to the phase spread with resulting longitudinal emittance growth. We estimate this growth supposing that the induced emittance is filling phase space eigenellipse. From numerical simulations a semi-axes ratio of $\delta E_{43} / \delta \varphi_{43} \approx 35$ keV/deg is obtained for the eigenellipse in the middle of the bending systems. This leads to an estimated total emittance growth of about 35 keV×deg, which is in good agreement with the result of SYTRACE simulations shown in Fig. 5.

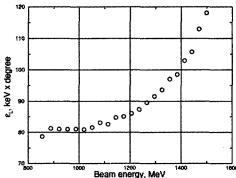


Fig. 5. Longitudinal emittance from SYTRACE. (The phase unit is related to 4.9GHz.)

4 CONCLUSION

We presented results of semi-analytical and numerical calculations of emittance growth caused by QFSR in a 1.5 GeV double sided microtron. Estimated normalised rms horizontal emittance at maximum energy is about 25 π mm×mrad, while longitudinal emittance is about 120 keV×degree.

- H.Herminghaus K.-H. Kaiser, U. Ludwig-Mertin, "The Design of Double-Sided Microtron"; Proc. of the 1981 Linear Acc. Conf., Santa Fe, N.M., LA-9234-c, p.260.
- J.Herrmann, S.Ratschow; development based on PTRACE K.-H. Kaiser, "A Possible Magnet Field Configuration for a C.W. Electron Accelerator in the GeV Region", Proc. of the Conf. On Future Possibilities for Electron Accelerators, Charlottesville, VA, 1979, p. V-1
- H. Euteneuer, F. Hagenbuck, R. Herr, J. Hermann, K. Herter, M.O. Ihm, K.H. Kaiser, Ch. Klumper, H.-P. Krahn, H.-J. Kreidel, U. Ludwig-Mertin, G. Stephan, Th. Weiss, "Beam Measurements and Operating Experience at MAMI", Proc. of the 1994 European Particle Acc. Conf., London, 1994, p.. 506.

 H. Herminghaus, "The Polytron as a CW Electron Accelerator in the 10 GeV Range", NIM A305(1991)1
- Crosbie "Synchrotron Radiation Effects in the Argonne Hexatron", Argonne, 1983, ANL-GEM-40-83
- M. Sands, "The Physics of Electron Storage Rings", SLAC-121, 1970
- K.-H. Kaiser, PTRACE (written on the base of RAYTRACE from S.A. Enge and S. Kowalski), private communication

EDDY CURRENT EFFECT OF THE BNL-AGS VACUUM CHAMBER ON THE OPTICS OF THE BNL-AGS SYNCHROTRON*

N. Tsoupas⁴, L. Ahrens, K.A. Brown, J. W. Glenn, C. J. Gardner Brookhaven National Laboratory, Upton, NY 11973 USA

Abstract

During the acceleration cycle of the AGS synchrotron, eddy currents are generated within the walls of the vacuum chambers of the AGS main magnets. The vacuum chambers have elliptical cross section, are made of inconel material with a wall thickness of 2 mm and are placed within the gap of the combined-function main magnets of the AGS synchrotron. The generation of the eddy currents in the walls of the vacuum chambers, create various magnetic multipoles, which affect the optics of the AGS machine. In this report these magnetic multipoles are calculated for various time interval starting at the acceleration cycle, where the magnetic field of the main magnet is ~0.1 T, and ending before the beam extraction process, where the magnetic field of the main magnet is almost constant at ~1.1 T. The calculations show that the magnetic multipoles generated by the eddy-currents affect the optics of the AGS synchrotron during the acceleration cycle and in particular at low magnetic fields of the main magnet. Their effect is too weak to affect the optics of the AGS machine during beam extraction at the nominal energies.

1 INTRODUCTION

The AGS synchrotron has twelve super-periods with 20 combined-function magnets[1] per super-period. Every two consecutive combined function magnets are paired to form either a horizontally focusing or defocusing quadrupole. The cross section of a horizontally focusing combined-function magnets used in the AGS synchrotron is shown in Figures 1a(C-type), and Figure 1b(B-type). The horizontally defocusing magnets are made of the same magnets (B, and C type) but with the magnets rotated 180° about the vertical axis. The cross section of the elliptical in shape vacuum chamber is also shown in the figure 1a.

Simulations of the beam optics of the AGS synchrotron are normally done using the MAD computer code[2], the BEAM code[3] or a modified version of the RAYTRACE code[4]. In these simulations the quadrupole strength (K1) and sextupole strength (K2) of the combined function magnets is used, and their values are obtained from static magnetic field calculations[5] or from the experimental magnetic field maps of the AGS magnets[6]. In either case, both the quadrupole

and sextupole strengths of the combined function magnets were obtained from static calculations, and did not include any contributions from eddy-currents generated in the vacuum chamber during the acceleration cycle. Measurements on the chromaticity of the AGS synchrotron have shown[7,8,9,10,11] that the chromaticity of the AGS synchrotron is affected by the ramp rate of the AGS main magnets. These measurements were used to generate a momentum dependent magnetic sextupole strength to be used as input data in the MAD computer code for beam optics simulations of the AGS synchrotron.

It is the purpose of this report to calculate the magnetic sextupole produced by the eddy-currents formed in the AGS vacuum chamber, during the ramping of the main magnets. Subsequently to use these magnetic sextupole strengths to calculated the chromaticy of the AGS synchrotron and make comparison with experimental measurments.

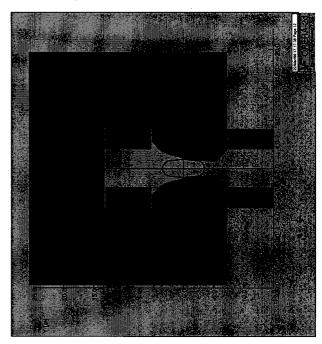


Figure 1a. Cross section of a C-type combined function AGS main magnet. The vacuum chamber is shown between the gap of the magnet. The magnet shown in this orientation is horizontally focusing. By rotating the magnet 180⁰ about the y-axis which passes through the vacuum chamber, the magnet becomes horizontally defocusing.

^{*} Work supported by the U.S. Department of Energy

⁻ email tsoupas@bnl.gov

2 MAGNETIC SEXTUPOLE OF THE AGS MAIN MAGNETS

The magnetic sextupole component of the AGS main magnetic field will affect the chromaticity ξ of the synchrotron according to the formulae:

$$\xi_x \propto -\frac{1}{Q_x} \oint \beta_x(s) b_2(s) \eta_x(s) ds \qquad (1a)$$

$$\xi_y \propto -\frac{1}{Q_y} \oint \beta_y(s) b_2(s) \eta_x(s) ds$$
 (1b)

Where $\beta_x(s)$ and $\beta_y(s)$ are the horizontal and vertical beta functions, Q_x and Q_y are the betatron tunes, $\eta_x(s)$ is the dispersion function, and $b_2(s)$ is a quantity proportional to the sextupole strength, along the synchrotron.

The quantity b2 which is the sextupole component of the magnetic field generated by the AGS main magnet, is calculated as a function of the B₀ dipole field of the main AGS main magnet in two ways:

- a) Static 2-dimentional calculations
- b) Transient 2-dimentional calculations

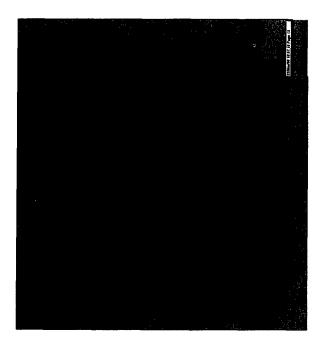


Figure 1b. Cross section of a B-type AGS main magnet. The magnet shown in this orientation is horizontally focusing. By rotating the magnet 180° about the y-axis, passing through the vacuum chamber, the magnet becomes horizontally defocusing.

2.1 Static Calculations

The static calculations were performed using a 2-D computer code[12] for electromagnetic calculations. The C and B type AGS main magnets were modeled based on the cross sections shown in Figures 1a and 1b. In the calculations, the default nonlinear material, which is provided by the code, was used for the permiability of the iron. The quantity $b_2(s)$ appearing in the equations 1a and 1b is the coefficient of the quadratic term in the expansion (as function of x) of the vertical component (B_y) of the magnetic field at the median plane of the magnet.

$$B_{v}(x)=B_{0}(1+b_{1}x+b_{2}x^{2}+b_{3}x^{3}+....)$$
 (2)

In equation (2) the variable x is the distance from the longitudinal axis of the magnet, on the horizontal plane. Figure 2 (dashed line) shows a plot of the quantity $K2 = 2b_2/(B\rho)$ (as defined in the computer code MAD[2]) as a function of the excitation field $B_y(x=0,y=0)$. The calculated values of the sextupole strength K2 for the C-type magnet (see Fig.1a) are almost the same with those of the B-type magnet². This is due to the fact that both type of magnets have the same geometrical shape of the pole tip, therefore the magnetic field within the gap is iron dominated at these excitation currents.

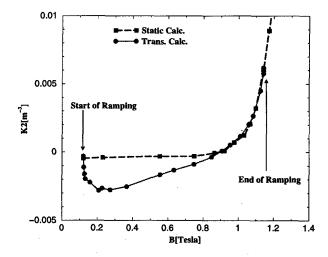


Figure 2: The magnetic sextupole strength K2 of the main magnetic field as a function of the $B_y(x=0,y=0)$ (main magnetic field). The dashed line which connects the filled squares, corresponds to the K2 values from the static case. The solid line connecting the filled circles, corresponds to the calculations of K2, obtained from the transient case.

 $^{^{1}}$ The difference is ~1%. This value is within the error of the calculations.

² The sextupole strength K2 has the same value for both focusing and defocusing magnets.

2.2 Transient Calculations

The transient magnetic field calculations were performed using the same computer code[12] as in the static calculations, but the transient 2-D version. The excitation current I(t) is required as input data in the transient calculations. The function I(t)/Imax is plotted in Figure 3 as a function of time. In the same Figure 3 the derivative dI(t)/dt is also plotted. The input data allow the generation of eddy currents in the coils of the magnet which are made of copper, and the wall of the vacuum chamber which is made of inconel. The magnet iron was assumed to have zero conductivity. This was a reasonable assumption since the iron core is made of electrically isolated laminations 0.031" thick. These laminations are held together by two iron plates 1" thick, each placed at the of the magnets to keep the laminations together.

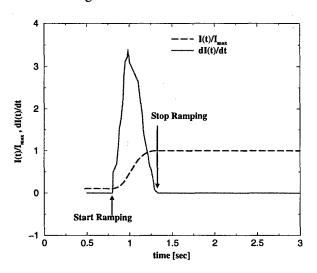


Figure 3: Excitation current $I(t)/I_{max}$ of the main AGS magnets as a function of time (dased curve). The solid curve is the dI(t)/dt curve.

As in the static case, the sextupole strength K2 of the magnetic field was calculated as a function of the magnet excitation and is plotted in Figure 2. A comparison of the sextupole strength K2 between the static and transient cases, shows that the eddy currents of the vacuum chamber affect the sextupole component of the main magnetic field but only at low excitations of the magnet.

At higher excitations of the magnet the K2 values for both static and transient, coincide even before the end of the ramping (see Fig. 2).

The calculated quadrupole strength K1 of the magnetic field yields the same values for both, the static and the transient case, at any excitation level of the magnet.

3 FUTURE STUDIES

The 2-D calculations discussed above provide enough information to calculate the chromaticity of the AGS synchrotron during the acceleration cycle. The chromaticity chalculations can be done by using the MAD computer code. A more rigorous study calls for 3-D transient calculations which will take into account the eddy-currents induced in each of the 1" thick plates which are placed at each end of the magnet to hold the laminations together. These 3-D calculations will be performed, in the near future as an ongoing effort of this task, using the computer code[12] which computes magnetic fields in 3-dimensions. Such calculations will provide a more accurate value of the sextupole strength K2, which can be used to calculate the chromaticity of the AGS synchrotron.

Experimental measurements of the chromaticity of the AGS synchrotron will also be performed as a function of the magnetic field of the main magnet while the main magnet is ramping up, at various rates dI(t)/dt.

4 REFERENCES

- [1] E. Bleser "The Optimum Central Orbit in the AGS"
 ADT Note No. 217
 E. Bleser "Where are the AGS Magnets" ADT Note No. 215
- [2] Hans Grote, and F.Christoph Iselin "The MAD Program" CERN/SL/90-13(AP)
- [3] N. Tsoupas et. al. "Closed Orbit Calculations at AGS and Extraction

Beam Parameters at H13" BNL AD/RHIC/RD-75

- [4] N. Tsoupas et. al. "Stable Spin Direction of a Polarized Proton Beam at the Injection Poin of RHIC" BNL AGS/RHIC/SN No. 021
- [5] W. Meng "Three Dimensional Field Analysis for the AGS Combined Function Magnets" PAC93 May 17-20 1993
- [6] R. Thern "experimental Magnetic Field Maps of the AGS magnets" (private comunication)
- -
- [7] E. Auerbach et. al. "Comments on the AGS Chromaticity" BNL AGS/AD/Tech. Note No. 276
- [8] E. Bleser "Comments on the AGS Chromaticity: II" BNL AGS/AD/Tech. Note No. 288
- [9] C.J. Gardner and L. Ahrens BNL 36490, 1985 Particle Accelerator Conference, 5/13/85
- [10] L. Ahrens, and W. K. van Asselt AGS SR-206, 6/26/86.
- [11] K. Gardner et. al. AGS SR-226, 6/7/87.
- [12] Vector Fields Inc.

INTERACTION REGION LOCAL CORRECTION FOR THE LARGE HADRON COLLIDER*

J. Wei[†], W. Fischer, V. Ptitsin, BNL, USA; R. Ostojic, CERN, Switzerland; J. Strait, FNAL, USA

Abstract

The performance of the Large Hadron Collider (LHC) at collision energy is limited by the field quality of the interaction region (IR) quadrupoles and dipoles. In this paper we study the impact of the expected field errors of these magnets on the dynamic aperture (DA). Since the betatron phase advance is well defined for magnets that are located in regions of large beta functions, local corrections can be very effective and robust. We compare possible compensation schemes and propose a corrector layout to meet the required DA performance.

1 INTRODUCTION

The LHC interaction region consists of a low- β^* quadrupole triplet (Q1-Q3) and a separation dipole (D1) on either side of the interaction point (IP), Fig. 1. The superconducting triplet quadrupoles are built by FNAL and KEK, and assembled in cryostats at FNAL. The separation dipoles in the high luminosity interactions points IP1 (ATLAS) and IP5 (CMS) are room-temperature magnets supplied by IPN-Novosibirsk. In IP2 (ALICE) and IP8 (LHC-B), where the beams are also injected into the two rings, the D1 is a superconducting magnet built by BNL. This magnet has the same coil design as the RHIC arc dipoles, and its field quality is well established. The field quality of the warm D1 is expected to be satisfactory.

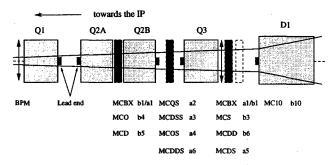


Figure 1: Schematic layout of the LHC inner triplet region.

The target DA for magnet field quality is set at 12 times the transverse rms beam size $(12\sigma_{xy})$ for both injection and collision. During injection and ramping, the impact of IR magnet is small compared with that of the arc magnets. On the other hand, during p-p collision (Tab. 1) the reduction of beam size at IP1 and 5 results in a large beam size $(\sigma_{xy} = 1.5 \text{ mm})$ at the corresponding triplets. Furthermore, beam-beam interaction requires a crossing angle of $\pm 150~\mu r$ corresponding to a closed orbit up to $\pm 7.3 \text{ mm}$. The target $12\sigma_{xy}$ thus corresponds to about 71% of mag-

Table 1: LHC parameters for protons at collision (7 TeV).

tunes H/V/L	63.31/59.32/0.00212
β* IP1,5,2,8 H/V [m]	0.5/0.5, 0.5/0.5, 15/10, 13/15
$\Phi/2 \text{ IP1,5,2,8 H/V } [\mu \text{rad}]$	0/150, 150/0, 0/-150, 0/-150
max rms beam size [mm]	1.5
max orbit offset H/V [mm]	±7.3/±7.3

net coil radius. Similarly, during ion collision [1] when the beam size is squeezed at IP2, the impact from cold D1 is also noticeable. Compensation of field errors of these cold IR magnets is of primary importance in improving the performance of the LHC at collision [2].

The leading source of DA reduction are the field errors of the FNAL and KEK triplet quadrupoles. The expected errors of the FNAL quadrupole (ver. 2.0) are given in Tab. 2. With the experience of model construction and measurements, and design iterations that occurred through close interaction between the magnet and accelerator physics groups, knowledge and confidence in the expected body and end-field errors has substantially improved. The KEK quadrupole errors are shown in Tab. 3; the coil cross-section of this quadrupole has been recently redesigned in order to substantially reduce the geometric b_{10} error.

In Section 2, we evaluate the DA under nominal collision conditions and explore the optimum quadrupole arrangement to minimize the error impact. In Sections 3 and 4, we review the local IR correction principle and propose a corrector layout.

Table 2: Expected field errors of FNAL low- β^* quadrupole at collision (version 2.0, $R_{ref} = 17$ mm). $\langle . \rangle$, d(.) and $\sigma(.)$ denote the mean, mean uncertainty and rms of the harmonics, respectively.

\overline{n}	<u>.</u>	Normal			Skew	
	$\langle b_n \rangle$	$d(b_n)$	$\sigma(b_n)$	$\langle a_n \rangle$	$d(a_n)$	$\sigma(a_n)$
body	[unit]					
3	-	0.3	0.8	-	0.3	0.8
4		0.2	0.8	_	0.2	0.8
5	~	0.2	0.3	_	0.2	0.3
6	-	0.6	0.6	_	0.05	0.1
7		0.05	0.06	_	0.04	0.06
8	-	0.03	0.05	_	0.03	0.04
9	-	0.02	0.03	_	0.02	0.02
10	-	0.02	0.03	_	0.02	0.03
LE	[unit·n	n]	(length:	=0.41 m)	
2	_	_	_	16.4	_	_
6	0.82	0.82	0.31	_	0.21	0.06
10	-0.08	0.08	0.04	_	0.04	0.04
RE	[unit·n	n]	(length	=0.33 m)	
6	_	0.41	0.31	_	_	_
10	-0.08	0.08	0.04	_	_	

^{*} Work performed under the auspices of the US Department of Energy.
† Email: weil@bnl.gov

Table 3: Expected field errors of KEK low- β^* quadrupole at collision (version 2.0, $R_{ref} = 17$ mm).

\overline{n}		Normal			Skew	
	$\langle b_n angle$	$d(b_n)$	$\sigma(b_n)$	$\langle a_n \rangle$	$d(a_n)$	$\sigma(a_n)$
body	[unit]					
3	-	0.51	1.0		0.51	1.0
4	_	0.29	0.57	_	0.29	0.57
5	_	0.19	0.38	_	0.19	0.38
6	_	0.5	0.19	_	0.10	0.19
7	_	0.05	0.06	_	0.05	0.06
8	_	0.02	0.03	_	0.02	0.03
9	_	0.01	0.01	_	0.01	0.01
10	0.25	0.03	0.01	_	0.01	0.01
LE	[unit·n	n]	(length	$=0.45 \mathrm{m}$)	
2	_	_	_	13.4	_	_
6	2.28	_	_	0.07	_	_
10	-0.17	_		-0.02	_	-

2 DA TRACKING ANALYSIS

The leading errors of the IR quadrupoles are the systematic b_6 and b_{10} , which are allowed by the quadrupole symmetry. We assess the effect of magnetic errors by the tune spread of particles with amplitudes of up to 6 times the transverse rms beam size $(6\sigma_{xy})$, and by the DA determined by 6D TEAPOT [3] tracking after either 10^3 or 10^5 turns, averaged over 10 random sets of magnetic errors at 5 emittance ratios ϵ_x/ϵ_y . Tracked particles have 2.5 times the rms momentum deviation $(2.5\sigma_p)$ [2]. Uncertainties in the mean are set at their full amount with either plus or minus sign.

The tune spread due to multipole errors scales as $(x_c + \beta_{xy}\epsilon_{xy})^{n/2}/\epsilon_{xy}$, where x_c is the closed orbit, β_{xy} the lattice β -function and ϵ_{xy} the emittance. The b_{10} error of the KEK magnets alone produces a tune spread of 0.61×10^{-3} at $6\sigma_{xy}$ thereby reducing the DA by $2\sigma_{xy}$ (Tab. 4).

A possibility for reducing the impact of the KEK geometric b_{10} could be to adopt a "mixed" triplet scheme where Q1 and Q3 are KEK quadrupoles and Q2 FNAL quadrupoles. This arrangement would lead to a 30% reduction of the tune spread, and an 18% increase of the DA, as shown in Tab. 4.

The mixed arrangement increases the possibility for magnet sorting [4, 5] and helps randomizing the uncertainty. It may also reduce the number of needed spare magnets and simplifies the engineering process. However, combining quadrupoles of different transfer functions implies a more complicated powering scheme. While a common bus is still possible, retaining the natural compensation of ripple in a triplet, dynamic behaviour at injection related to snap back and eddy-current effects need to be verified [6].

In order to estimate the b_6 impact, we assume that FNAL magnets are placed at IP1 and 5 and gradually decrease the total b_6 to 30% of its original value assuming a positive $d(b_6)$. Tab. 4 shows a steady increase of the DA from $9.3\sigma_{xy}$ to $12.1\sigma_{xy}$.

The orientation of the quadrupoles was chosen to minimize the lead end b_6 impact [2]. With the mixed quadrupole

Table 4: Comparison of DA for various triplet arrangements (10³-turn DA in units of σ_{xy} with $1\sigma_{xy}$ step size).

Case	DA mean	DA rms	DA min			
FNAL IP5, 8; KEK IP1, 2:						
	8.5	1.4	7			
without b_{10}	10.3	1.5	7			
FNAL as Q2; K	EK as Q1, ((mixed)				
	10.0	1.5	8			
reversed Q3 LE	9.6	2.0	6			
FNAL IP1, 5; I	KEK IP2, 8:					
	9.3	2.1	6			
$80\%~b_6$	9.9	2.0	6			
$50\% \ b_6$	11.0	1.8	8			
$30\% \ b_6$	12.1	1.7 .	9			

scheme, the minimization is less effective however. In order to reduce the number of electric buses through Q3, it was further suggested to reverse the orientation of Q3. This leads to a reduction of the average DA of 0.4 sigma, and to an increase of b_6 corrector strength. As the random b_6 is large, this effect could be alleviated by sorting.[4, 5]

3 IR COMPENSATION SCHEMES

3.1 Two-Element Correction Principle

The error compensation is based on the minimization of action-angle kicks [2] produced by each multipole error b_n (or a_n) over a pair of inner triplets. Using two correction elements of each multipole order c_n (either a_n or b_n), we minimize the sum

$$\int_{L} dl C_{z} B_{0} c_{n} + (-)^{n} \int_{R} dl C_{z} B_{0} c_{n}, \quad z = x, y \quad (1)$$

taking advantage of the negligible betatron phase advance within each triplet and D1, and approximate the phase advance between the triplets by 180° . The integral is over the entire left-hand-side (L) or right-hand-side (R) MQX triplet and D1. In dipoles B_0 is simply the main field, in quadrupoles it is the field at the reference radius R_{ref} . In general, the weights C_z in Eq. 1 are chosen according to the multipoles as:

	even b_n	$\operatorname{odd} b_n$	even a _n	$\operatorname{odd} a_n$
C_x	$\beta_x^{n/2}$	$eta_x^{n/2}$		$eta_x^{(n-1)/2}eta_y^{1/2}$
C_y	$\beta_y^{n/2}$	$\beta_x^{1/2}\beta_y^{(n-1)/2}$	$\beta_x^{1/2}\beta_y^{(n-1)/2}$	$eta_y^{n/2}$

The compensation is equally effective for both intersecting beams, since the optics of the interaction region is antisymmetric. However, it does not take into account the closed-orbit deviation due to the crossing angle, and the fact that the crossing planes are respectively vertical and horizontal in the two high luminosity interaction points. On the other hand, the effect of this closed orbit feeddown is partially compensated by the feeddown from the correctors.

3.2 Correction Scheme Comparison

There are three corrector packages (MCX1, MCX2, MCX3) in each triplet, Fig. 1. Each MCX1 and MCX3 contains two dipole layers, and each MCX2 contains

Table 5: Comparison of local IR corrector effectiveness assuming that IR quadrupole errors are measured to a 5% rms accuracy. The DA is given in units of σ_{xy} . The physical aperture of 60 mm corresponds to about $14\sigma_{xy}$.

Case	DA mean	DA rms	DA min
UNMIXED:			
no correction	8.5	1.4	7
scheme 1	11.8	2.4	8
scheme 2	12.1	2.2	9
scheme 3	15.4	1.8	12
scheme 4	15.9	1.7	13
MIXED:			
no correction	10.0	1.5	8
scheme 1	12.8	1.1	10
scheme 2	13.2	1.3	11
scheme 3	16.1	1.8	13
scheme 4	17.6	1.6	14

scheme 1: b_3 , b_4 , b_5 , b_6 , a_3 , a_4 , a_6

scheme 2: b_3 , b_4 , b_5 , b_6 , a_3 , a_4 , a_5 , a_6

scheme 3: b_3 , b_4 , b_5 , b_6 , b_{10} , a_3 , a_4 , a_6

scheme 4: b_3 , b_4 , b_5 , b_6 , b_{10} , a_3 , a_4 , a_5 , a_6

a skew quadrupole layer. A straightforward approach (scheme 1) is to have 3 additional layers of nonlinear skew multipoles (a_3, a_4, a_6) for MCX2, and two additional layers of nonlinear multipoles for MCX1 and MCX3. These layers could be a combination of any of b_3 , b_4 , b_5 and b_6 layers. For each multipole, two correction elements, located symmetrically at both sides of the IP, can be activated to minimize the kick in both the x and y directions (compare Eq. 1). Due to the lattice symmetry both beams are corrected.

Scheme 1 increases the DA by 38% in the unmixed and 28% in the mixed case. With an additional a_5 corrector (scheme 2) the improvement is 42% and 32% respectively. A further improvement can be achieved using a b_{10} corrector, as shown in Tab. 5 and Fig. 2. We also investigated the effect of misalignment of the corrector layers. With an rms misalignment of 0.5 mm in the horizontal and vertical planes we find no degradation of the DA.

The required strength of the multipole correctors, Tab. 6,

Table 6: Needed and available corrector strength.

Order	Available	Needed strength		
	strength	$(mean \pm SD)$	(mean + 6 SD)	
	[T]	[T]	[T]	
b_3	0.100	0.0023 ± 0.0027	0.018	
b_4	0.066	0.0057 ± 0.0043	0.032	
b_5	0.037	0.0015 ± 0.0018	0.012	
b_6	0.020	0.0075 ± 0.0016	0.017	
b_{10}	0.0030	0.0011 ± 0.0002	0.0023	
a_3	0.155	0.012 ± 0.009	0.066	
a_4	0.086	0.014 ± 0.008	0.062	
a_6	0.020	0.0021 ± 0.0016	0.012	
a_5	0.044	0.014 ± 0.008	0.062	

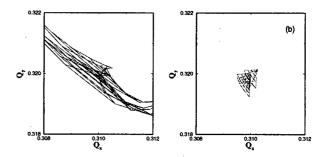


Figure 2: Effect of IR multipole correction on the covered tune space. (a) shows the uncorrected machine and (b) the corrected machine with scheme 4.

can be provided by 50 cm long spool pieces wound using the LHC sextupole corrector wire and operating at less than 50% margin at 600 A [7]. At IP2, the IR correctors are also designed to reduce the effect of the D1 errors during low- β^* heavy ion operations [1].

3.3 Short versus long term tracking

Finally we re-confirmed [2] the difference between the DA determined after 10^3 and 10^5 turns for two selected cases, an uncorrected machine and a corrected machine. The difference (Tab. 7) is $0.7\sigma_{xy}$ or 7% for the uncorrected case, and $0.9\sigma_{xy}$ or 5% for the corrected case.

Table 7: Comparison of 1,000-turn and 100,000-turn DA.

Case	DA mean	DA rms	DA min
no correction (10 ³)	10.0	1.5	8
no correction (10 ⁵)	9.3	1.4	7
scheme 4 (10 ³)	17.6	1.6	14
scheme 4 (10 ⁵)	16.7	1.5	13
target (10 ⁵)	12	_	10

4 SUMMARY

Local nonlinear IR correctors, up to multipole order 6, are proposed for compensating the IR quadrupole errors. These correctors can improve the DA by $2\text{-}3\sigma_{xy}$. Mixing magnets of different origin can help reach the target DA as its improvement is about $1.5\sigma_{xy}$. This would be equivalent to a reduction of the systematic b_{10} and uncertainty of b_6 errors of about 50%. Further benefit of mixing could be expected through randomizing the uncertainties and broader selection of the magnets.

We thank J. Gareyte, J.-P. Koutchouk, O. Brüning and J. Miles for lattice assistance and discussions, and many others, including M. Harrison, A. Ijspeert, J. Kerby, M.J. Lamm, S. Peggs, T. Sen, R. Talman, T. Taylor and A.V. Zlobin.

- [1] V. Ptitsin, W. Fischer, J. Wei, PAC99 (1999).
- [2] J. Wei et al., "US-LHC IR magnet error analysis and compensation", EPAC 1998 proceedings (1998) p. 380.
- [3] L. Schachinger, R. Talman, Part. Accel. 22, 35 (1987).
- [4] J. Wei, R. Gupta, M. Harrison, A. Jain, et al, PAC99 (1999).
- [5] J. Shi, Nuclear Instruments and Methods A (1999).
- [6] J-P. Koutchouk, private communications.
- [7] M. Karppinen, private communications.

THE BEAM LIFETIME FROM ELASTIC SCATTERING ON NUCLEI OF RESIDUAL GAS IN ELECTRON STORAGE RING WITH THE VARIOUS SHAPE OF THE VACUUM CHAMBER.

N. Mocheshnikov, A. Zelinsky, NSC KIPT, Kharkov, Ukraine

Abstract

In report the process of elastic scattering of the stored beam on nuclei of residual gas with take into account of size and shape of the vacuum chamber of a storage ring is considered. The expressions permitting to calculate a cross section of elastic scattering of electrons on nuclei of residual gas and partial lifetime of a beam, stipulated by this process for the various shape of a cross of the vacuum chamber (ellipse, cylinder, rectangle) are obtained.

1 INTRODUCTION

The total lifetime of an electron beam in storage ring τ_{Σ} is determined as the sum of inverse partial lifetimes stipulated by various processes. As main processes, defining lifetime of a beam in a storage ring it is possible to consider the following: elastic scattering of electrons on nucleuses of residual gas, bremsstrahlung on nucleuses of residual gas, inelastic scattering of electrons on nucleuses of residual gas, quantum fluctuations of a radiation, collective effects. Experimentally theoretically is shown [1,2] that for small beam currents the lifetime is determined by elastic scattering of electrons on nuclei of residual gas. There is a number of diagnostic techniques [3], based on a measurement of lifetime of a beam for "zero currents" and definition through it of other parameters of a beam in particular of dynamic aperture. In the present work the technique of deriving of dependence of lifetime of a beam stipulated by process of the elastic scattering for various shapes of the vacuum chamber from characteristic geometric sizes of the chamber is indicated and the expressions obtained for the elliptic, round and rectangular chamber are indicated.

2 LIFETIME OF ELECTRONS STIPULATED BY SCATTERING ON RESIDUAL GAS.

The loss rate of electron beam in storage ring is given by:

$$\frac{1}{\tau} = -\frac{1}{n_0} \frac{\mathrm{d}n}{\mathrm{d}t},\tag{1}$$

where n_0 - the number of electrons, dn/dt - velocity of the lost.

In case, when the main channel of losses of electrons is the scattering on residual gas, electron beam, after passing through a volume with residual gas with number of atoms N and thickness dx loses dn of particles:

$$dn = -n_0 \sigma N dx, \qquad (2)$$

where σ - the cross section of scattering of electrons causing to it to loss.

Then the time of loss of electrons by a relativistic beam will make:

$$\frac{1}{\tau} = -\frac{1}{n_0} \frac{\mathrm{d}n}{\mathrm{d}t} = c \sigma N,\tag{3}$$

where c – velocity of a light.

Defining the lifetime as the time it takes for the initial particle intensity to be reduced by I/e and considering residual gas distributed is uniform in the chamber of a storage and number of atoms N_o in unit of volume to constants, the lifetime is determined by the equation [4]:

$$\frac{1}{\tau_{SC}} = c\sigma N_0. \tag{4}$$

Thus for definition of lifetime of a beam stipulated by elastic scattering of electrons on atoms of residual gas, it is necessary to determine a cross section of scattering of an electron causing to it to loss. Obviously, that the magnitude of this cross section will depend on the shape and sizes of the vacuum chamber.

3 CROSS SECTION OF ELASTIC SCATTERING.

Differential cross section of elastic scattering on nuclei of residual gas has the form [4]:

$$\frac{d\sigma}{d\Omega} = \frac{Z^2}{4} r_0^2 \left(\frac{m_e c}{\beta p}\right)^2 \frac{\left(1 - \beta^2 \sin^2 \frac{\theta}{2}\right)}{\sin^4 \frac{\theta}{2}},\tag{5}$$

where $d\Omega = \sin\theta \ d\theta \ d\phi$ - the solid angle in which electron is scattered,

 φ , θ - axial and polar angle of scattering,

Z-charge of nuclei of residual gas,

 r_0 - radius of an electron,

 βc – velocity of an electron,

p – momentum of an electron,

It can rewrite as:

$$d\sigma(\theta,\varphi) = \frac{Z^2}{4} r_0^2 \left(\frac{m_e c}{\beta p}\right)^2 \frac{\left(1 - \beta^2 \sin^2 \frac{\theta}{2}\right)}{\sin^4 \frac{\theta}{2}} \sin\theta \, d\theta \, d\varphi . (6)$$

For small angle of scattering θ <<1 and relativistic electrons γ >>1 the equation (6) we can write in the form:

$$d\sigma(\theta, \varphi) = \frac{Z^2}{2} r_0^2 \frac{1}{\gamma^2} \frac{\cos^3(\theta/2)}{\sin^3(\theta/2)} d\theta d\varphi$$

$$= \frac{Z^2}{2} r_0^2 \frac{1}{\gamma^2} \frac{8d\theta d\varphi}{\theta^3}$$
(7)

Thus the cross section of elastic scattering in (4) is possible to receive by an integration of expression (6) on θ from θ_{\min} – minimum angle, the scattering on which results in loss of an electron up to π and on φ from 0 up to 2π . After an integration on θ we find:

$$d\sigma(\varphi) = \frac{2Z^2 r_0^2}{\gamma^2} \frac{d\varphi}{\theta_{\min}^2} . \tag{8}$$

For the various shape of the vacuum chamber expression for θ_{\min} will differ, besides for case is axial of the asymmetrical chamber θ_{\min} will be function from φ .

The cross section of elastic scattering, causing to loss of an electron is possible to note as:

$$\sigma = \frac{2Z^{2}r_{0}^{2}}{\gamma^{2}} \int_{0}^{2\pi} \frac{d\varphi}{\theta_{\min}^{2}(\varphi)} = \frac{2Z^{2}r_{0}^{2}}{\gamma^{2}} F(b, a, \beta_{x}, \langle \beta_{x} \rangle, \beta_{z}, \langle \beta_{z} \rangle)$$
(9)

where a and b geometric parameters of the vacuum chamber on a vertical and horizontal plane,

 β_x , $<\beta_x>$, β_z , $<\beta_z>$ - maximum and average value of amplitude functions on a horizontal and vertical plane. After collision with atom of residual gas on azimuth s_0 the particle deviates on angles $\dot{x} = \sin\theta\cos\varphi$ and $\dot{z} = \sin\theta\sin\varphi$. Then on some azimuth s_0 , this particle will have coordinates:

$$\dot{x} = x\sqrt{\beta_x(s_0)\beta_x(s_1)}\sin\left(\int_{s_0}^{s_1}\frac{\mathrm{d}\,s}{\beta_x(s)}\right) =$$

$$\sin\theta\cos\phi\sqrt{\beta_x(s_0)\beta_x(s_1)}\sin\left(\int_{s_0}^{s_1}\frac{\mathrm{d}\,s}{\beta_x(s)}\right)$$

$$\dot{z} = z\sqrt{\beta_z(s_0)\beta_z(s_1)}\sin\left(\int_{s_0}^{s_1}\frac{\mathrm{d}\,s}{\beta_z(s)}\right) =$$

$$\sin\theta\sin\phi\sqrt{\beta_z(s_0)\beta_z(s_1)}\sin\left(\int_{s_0}^{s_1}\frac{\mathrm{d}\,s}{\beta_z(s)}\right)$$

The radius vector of this particle will be noted as $r^2 = x^2 + z^2$.

Considering, that on azimuth s_i the particle reaches the boundary of the vacuum chamber $r=\rho$ and that phase

advance
$$\int_{s_0}^{s_1} \frac{ds}{\beta_x(s)} = \int_{s_0}^{s_1} \frac{ds}{\beta_z(s)} = 0$$
 On this azimuth, we can

write expression for a determination θ_{min} . For it we need only to make out a radius vector ρ of the boundary of the vacuum chamber. For example, for the elliptic vacuum chamber:

$$\frac{z^2}{a^2} + \frac{x^2}{b^2} = 1, z = \rho \sin \varphi, x = \rho \cos \varphi,$$

from here

$$\rho^2 = \frac{1}{\left(\frac{\sin^2 \varphi}{a^2} + \frac{\cos^2 \varphi}{b^2}\right)}.$$

Then we get:

$$\frac{1}{\theta_{\min}^2} = \left(\frac{\sin^2 \varphi}{a^2} + \frac{\cos^2 \varphi}{b^2}\right)$$

$$\left[\beta_z(s_0)\beta_z(s_1)\sin^2 \varphi + \beta_x(s_0)\beta_x(s_1)\cos^2 \varphi\right]$$
(10)

Integrating (10) from θ up to 2π and averaging on all azimuths is received expression for function F for case of the elliptic vacuum chamber. Substituting it in (9), and then (9) substituting in (3), we receive lifetime stipulated by elastic scattering on atoms of residual gas in the chamber of a storage ring the elliptic vacuum chamber.

4 LIFETIME FOR CASES OF THE VARIOUS SHAPE OF THE VACUUM CHAMBER.

We obtained expressions for function F for several most typical variants of the vacuum chamber and disposition in it of the diagnostic equipment bounding the geometric aperture of the chamber. For a simplicity all devices bounding the aperture of the vacuum chamber, we shall name as "shutters". Is clear, that from expression for the vacuum chamber with a shutter it is easy to proceed to expression for the vacuum chamber without a shutter.

1. The rectangular vacuum chamber, rectangular shutter.

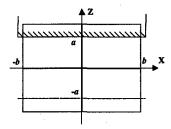


Figure 1.

$$F = \left\{ \beta_z \langle \beta_z \rangle \left[\frac{3 \pi}{4 a^2} + \frac{a^2 - 3b^2}{2 a^2 b^2} \operatorname{arctg} \frac{a}{b} + \frac{a^2 - b^2}{2 a b (a^2 + b^2)} + \frac{2b}{a (a^2 + b^2)} \right] + \beta_x \langle \beta_x \rangle \left[\frac{1 \pi}{4 a^2} - \frac{b^2 - 3a^2}{2 a^2 b^2} \operatorname{arctg} \frac{a}{b} + \frac{b^2 - a^2}{2 a b (a^2 + b^2)} + \frac{2a}{b (a^2 + b^2)} \right] \right\}$$

2. The elliptic vacuum chamber, elliptic shutter.

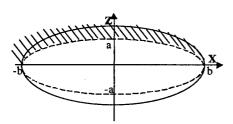


Figure 2.

$$F = \left\{ \beta_z \langle \beta_z \rangle \left[\frac{3}{4} \frac{\pi}{a^2} \left(1 + \frac{a^2}{3b^2} \right) \right] + \beta_x \langle \beta_x \rangle \left[\frac{3}{4} \frac{\pi}{a^2} \left(1 + \frac{b^2}{3a^2} \right) \right] \right\}$$

3. The elliptic vacuum chamber, rectangular shutter...

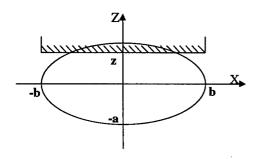


Figure 3.

$$F = \left\{ \beta_z \langle \beta_z \rangle \left[\frac{3 \pi}{4 z^2} + \frac{1}{2} \left(\frac{3}{a^2} + \frac{1}{b^2} - \frac{3}{z^2} \right) \operatorname{arctg} \frac{az}{b\sqrt{a^2 - z^2}} + \left(1 - \frac{z^2}{a^2} \right) \left[\frac{2ab\sqrt{a^2 - z^2}}{z \left[b^2 (a^2 - z^2) + a^2 z^2 \right]} + \left(\frac{3}{a^2} - \frac{1}{b^2} - \frac{1}{z^2} \right) \left[\frac{abz\sqrt{a^2 - z^2}}{2 \left[b^2 (a^2 - z^2) + a^2 z^2 \right]} + \left(\frac{1}{a^2} - \frac{1}{z^2} \right) \left[\frac{1}{4} \frac{\pi}{z^2} + \frac{1}{2} \left(\frac{3}{b^2} + \frac{1}{a^2} - \frac{1}{z^2} \right) \operatorname{arctg} \frac{az}{b\sqrt{a^2 - z^2}} + \left(\frac{2az\sqrt{a^2 - z^2}}{b \left[b^2 (a^2 - z^2) + a^2 z^2 \right]} + \left(\frac{1}{b^2} - \frac{1}{a^2} + \frac{1}{z^2} \right) \left[\frac{abz\sqrt{a^2 - z^2}}{2 \left[b^2 (a^2 - z^2) - a^2 z^2 \right]} \right] \right\}$$

4. The round vacuum chamber, rectangular shutter.

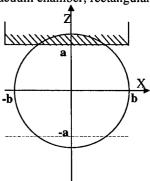


Figure 4.

$$F = \left\{ \frac{\beta_z \langle \beta_z \rangle}{a^2} \left[\frac{3\pi}{4} + \frac{4a^2 - 3b^2}{2b^2} \arcsin\frac{a}{b} + \frac{a\sqrt{b^2 - a^2}}{b^4} \left(3b^2 - 2a^2 \right) \right] + \frac{\beta_x \langle \beta_x \rangle}{b^2} \left[\frac{\pi b^2}{4a^2} + \frac{4a^2 - b^2}{2a^2} \arcsin\frac{a}{b} + \frac{\sqrt{b^2 - a^2}}{2ab^2} \left(2a^2 - b^2 \right) \right] \right\}$$

5 CONCLUSION

The obtained expressions allow analytically to connect lifetime of a beam stipulated by elastic scattering on residual gas, to amplitude functions of a storage ring and geometric sizes of transversal area of circulation of a beam. Besides that it allows to evaluate influence of the shape of the vacuum chamber to lifetime of a beam, the installation of such relation allows by a measurement of lifetime for "zero currents" to determine sizes of area of stable motion of a beam (dynamic aperture).

- P.I.Gladkikh, A.Yu. Zelinsky, S.G. Kononenko et all "Collective effects in intensive electron beam of storage ring N-100", JTPh, 1991, v. 61, is.4, pp. 118-122.(In Russ)
- [2] V. Nemoshkalenko, V. Molodkin, A. Shpak et. all., "Synchrotron radiation complex ISI-800", Journal de Physique, Vol.4, november 1994, pp. C9-341 – C9-348.
- [3] A.Yu. Zelinsky, N.I. Mocheshnikov, L.V.Reprincev, A.A.Shcherbakov "Measurement of dynamic aperture of Kharkov electron storage ring N-100", XIII symposium at accelerators of charge particles, UINI, Dubna, 13-15 oct. 1992, D-9-92-380, pp.101.(In Russ)
- [4] CAS CERN accelerator school. Fifth general accelerator physics course. Geneva, 1994, v.1, p.421.

MULTITURN INJECTION OF AN ELECTRON BEAM IN A STORAGE RING

Grigor'ev Yu., Zvonaryova O., Zelinsky A, NSC KIPT, Kharkov, Ukraine

Abstract

In report the radial-phase motion of electrons in a storage ring is investigated. The expression for Hamiltonian, connecting amplitudes of two modes of oscillations is received in view of nonlinear magnetic fields of the third order. Received Hamiltonian has a stationary point of a type "limiting cycle", which in coordinate space defines an equilibrium orbit. The existence "of a limiting cycle" allows to carry out multiturn injection of electron beam with final phase volume in a storage ring. The conditions of realization of multiturn injection are received.

The results of researches can be used and for stores of particles with large weight.

1 INTRODUCTION

Much attention (see, for example, [1-2]) were given to the study of a problem of a multiturn injection in storage rings. Researches of the particle injection in systems with stable motion round an equilibrium orbit is carried out in most cases. In the condition of a steady motion about closed orbit the "reflexive" Poincare theorem [3-4] is fulfilled which hampers a realization of multiturn injection of a charged particles beam.

In the this report the multiturn injection in a storage ring, in which there is no stable motion about closed orbit during injection, is investigated. In this case in the space of dynamic variables there can be a stationary point with the type of a "limiting cycle". A closed orbit becomes a limiting set for other trajectory. Particles can be injected in a storage ring along this trajectory unlimitedly long, and at small deviations from it - quite long. The "limit cycle" in a storage ring carry out with the help of impulse sextupole and octupole magnets. After realization of the injection the impulse elements switch off.

We obtained expressions for a Hamiltonian of a set of equations describing motion of electrons in a horizontal plane of a storage ring taking into account nonlinear magnetic fields. The task was solved in the first approximation by the Krylov-Bogolyubov method [5]. At deriving the short equations for guadrates of an oscillation amplitudes the representation of solutions in the Floquet form is used. The oscillations were not divided into fast "betatron" and slow "synchrotron" oscillations, and it allowed to define a Hamiltonian connecting amplitudes of these modes of oscillations.

2 THE EQUATIONS OF MOTION AND THEIR SOLUTION

The differential equations of motion of a charged particle in a horizontal plane of a storage ring look like [6]:

$$\frac{dx_l}{d\theta} - \sum_{m=1}^4 A_{lm} x_m = F_l(x,\theta)$$

$$F_1(x,\theta) = -gx_2x_3 + sx_2^2 - sx_2^2x_3 + Qx_3^3$$
(1)

$$F_2(x_l,\theta) = F_3(x_l,\theta) = F_4(x_l,\theta) = 0$$
,

where

 $x_1 = dx/d\theta$

 x_2 - a deviation of an electron from equilibrium orbit, x_3 - a relative deviation of an energy from an equilibrium value,

 x_4 - a deviation of a phase of oscillations from an equilibrium value,

 θ - azimuth coordinate.

Matrix (A) describe effect of electromagnetic fiels of storage ring in linear approximation without taken into account radiation $A(\theta + \theta) = A(\theta)$,

$$g = -\frac{eK_0^{-2}}{p_0c} \frac{dH_z}{dx_2}, s = -\frac{1}{2} \frac{eK_0^{-2}}{p_0c} \frac{d^2H_z}{dx_2^2},$$

$$Q = -\frac{1}{6} \frac{eK_0^{-2}}{p_0c} \frac{d^3H_z}{dx_2^3},$$

where

e - charge of an electron,

c - velocity of a light,

 p_0 - impulse of an equilibrium orbit,

 $K_o = 2\pi/\Pi$,

 Π - perimeter of equilibrium orbit,

 θ_i - period,

 H_{\star} – axial component of a magnetic field.

In the equation (1) the most important nonlinear terms up to the 3d order inclusive are left. For the solution of this equation the method of average of Krylov-Bogolyubov [5] is applied, using representation of a solution of the homogeneous equation (1) $(F_I=0)$ in the Floquet form:

$$x_l = C_1 f_l^{(1)} e^{i\psi_1 \theta} + C_2 f_l^{(2)} e^{i\psi_2 \theta} + c.c.$$
 (2)

where $f_l^{(l)}$, $f_l^{(2)}$ (l = 1,2,3,4) periodic Floquet functions, $C_p C_2$, constants.

In case of a piecewise constant dependence of the elements of a matrix (A) from ϑ , Floquet functions $f_i^{(l)}$, $f_i^{(2)}$ (l = 1,2,3,4) and the magnitudes of Floquet indexes ψ_p , ψ_2 can be calculated.

Assuming that C_1 and C_2 are slowly varying functions of ϑ and substituting (2) in (1) and after the averaging it is possible to obtain a short differential equations for quadrates of an oscillation amplitude $I_1 = |C_1|^2$ and $I_2 = |C_2|^2$:

$$\frac{dI_{1}}{d\theta} = (L_{1}^{s} + L_{1}^{Q})I_{1}^{2} + (L_{12}^{s} + L_{12}^{Q})I_{1}I_{2}
\frac{dI_{2}}{d\theta} = (M_{1}^{s} + M_{2}^{Q})I_{2}^{2} + (M_{12}^{s} + M_{12}^{Q})I_{1}I_{2}
\text{where}
L_{1}^{s} = \frac{1}{4} \left\langle \left\{ s\Delta_{1} f_{x_{2}}^{(1)} \left[2 f_{x_{2}}^{*(1)} f_{x_{3}}^{(1)} + f_{x_{2}}^{(1)} f_{x_{3}}^{*(1)} \right] + c.c. \right\rangle,
M_{1}^{s} = \frac{1}{4} \left\langle \left\{ s\Delta_{2} f_{x_{2}}^{(2)} \left[2 f_{x_{2}}^{*(2)} f_{x_{3}}^{(2)} + f_{x_{2}}^{(2)} f_{x_{3}}^{*(2)} \right] + c.c. \right\rangle,
L_{12}^{s} = \frac{1}{2} \left\langle \left\{ s\Delta_{1} \left[\left| f_{x_{2}}^{*(2)} \right|^{2} f_{x_{3}}^{(1)} + f_{x_{2}}^{(1)} f_{x_{2}}^{*(2)} f_{x_{3}}^{(2)} + f_{x_{2}}^{(1)} f_{x_{3}}^{*(2)} f_{x_{3}}^{*(2)} \right] \right\} \right\} \right\}$$
(3)

, $M_{12}^{s} = \frac{1}{2} \left\langle \left\{ s \Delta_{2} \left[\left| f_{x_{2}}^{*(1)} \right|^{2} f_{x_{3}}^{(2)} + f_{x_{2}}^{*(1)} f_{x_{2}}^{(2)} f_{x_{3}}^{(1)} + f_{x_{2}}^{(1)} f_{x_{2}}^{(2)} f_{x_{3}}^{*(2)} \right] \right\},$ $+ c.c. \right\}.$ $L_{1}^{Q} = -\frac{3}{4} \left\langle Q \left| f_{x_{2}}^{(1)} \right|^{2} \left\langle \Delta_{1} f_{x_{2}}^{(1)} + c.c. \right\rangle \right\rangle,$ $M_{1}^{Q} = -\frac{3}{4} \left\langle Q \left| f_{x_{2}}^{(2)} \right|^{2} \left\langle \Delta_{2} f_{x_{2}}^{(2)} + c.c. \right\rangle \right\rangle,$ $L_{12}^{Q} = -\frac{3}{2} \left\langle Q \left| f_{x_{2}}^{(2)} \right|^{2} \left\langle \Delta_{1} f_{x_{2}}^{(1)} + c.c. \right\rangle \right\rangle,$ $M_{12}^{Q} = -\frac{3}{2} \left\langle Q \left| f_{x_{2}}^{(1)} \right|^{2} \left\langle \Delta_{2} f_{x_{2}}^{(1)} + c.c. \right\rangle \right\rangle,$ $\left\langle F(\theta) \right\rangle \text{ stands for } \lim_{T \to \infty} \frac{1}{T} \int_{T}^{T} F(\tau) d\tau.$

At a normalization of the Floquet function the value of a wronskian Δ is put equal to "-4":

$$\Delta = \begin{vmatrix} f_{x_1}^{(1)} & f_{x_1}^{*(1)} & f_{x_1}^{(2)} & f_{x_1}^{*(2)} \\ f_{x_1}^{(1)} & f_{x_1}^{*(1)} & f_{x_2}^{(2)} & f_{x_2}^{*(2)} \\ f_{x_2}^{(1)} & f_{x_2}^{(1)} & f_{x_2}^{(2)} & f_{x_2}^{*(2)} \\ f_{x_3}^{(1)} & f_{x_3}^{(1)} & f_{x_3}^{(2)} & f_{x_3}^{*(2)} \\ f_{x_4}^{(1)} & f_{x_4}^{*(1)} & f_{x_4}^{(2)} & f_{x_4}^{*(2)} \end{vmatrix} = -4$$

$$(4)$$

 Δ_1 , Δ_2 - cofactors of a matrix Δ . Δ_1 - first column and first line, Δ_2 - third column and first line. At an averaging it was supposed that $\psi_1 \neq \psi_2$, $\psi_1 \neq K$, $\psi_2 = K$, and also that none of the resonance conditions is fulfilled: $n\psi_1 + j\psi_2 \neq q, n, j, k, q = (0,\pm 1,\pm 2,...)$. It is possible to show, that:

$$\begin{pmatrix} L_1^s + L_1^Q \end{pmatrix} = - \left(M_{12}^s + M_{12}^Q \right) / 2;$$

$$\left(M_2^s + M_2^Q \right) = - \left(L_{12}^s + L_{12}^Q \right) / 2$$
(5)

In consequence the expression (5), the equations (3) has the following Hamiltonian:

$$H = I_2^2 I_1(M_2^s + M_2^Q) - I_1^2 I_2(L_1^s + L_1^Q) = I_2^2(0)I_1(0)(M_2^s + M_2^Q) - I_1^2(0)I_2(0)(L_1^s + L_1^Q),$$
 (6)

where $I_1(0)$ and $I_2(0)$ - initial values of quadrates of amplitudes.

The connection between I_1 and I_2 is stipulated by an unresonance interaction of azimuth harmonics of sextupole and octupole components of a magnetic field of a storage ring with modulation of oscillation amplitudes of a particle in a periodic lattice of a storage ring.

 $I_1(0)$ and $I_2(0)$ are expressed through initial values x_i and value of Floquet functions $f_i^{(1)}$, $f_i^{(2)}$ on an azimuth of injection by the following formulas:

$$I_1(0) = a_1^2 + b_1^2$$

$$a_{1} = \frac{\sum_{l=1}^{4} \overline{x}_{l} \varphi_{l1}}{\Phi}, \quad b_{1} = \frac{\sum_{l=1}^{4} \overline{x}_{l} \varphi_{l2}}{\Phi}$$
 (7)

$$I_2(0) = a_2^2 + b_2^2$$

$$a_{2} = \frac{\sum_{l=1}^{4} \overline{x}_{l} \varphi_{l3}}{\Phi}, \quad b_{2} = \frac{\sum_{l=1}^{4} \overline{x}_{l} \varphi_{l4}}{\Phi}$$
 (8)

where Φ - determinant of a matrix (Φ)

$$(\Phi) = \begin{pmatrix} 2\operatorname{Re}\,\bar{f}_{x}^{(1)} & -2\operatorname{Im}\,\bar{f}_{x_{1}}^{(1)} & 2\operatorname{Re}\,\bar{f}_{x_{1}}^{(2)} & -2\operatorname{Im}\,\bar{f}_{x_{1}}^{(2)} \\ 2\operatorname{Re}\,\bar{f}_{x_{2}}^{(1)} & -2\operatorname{Im}\,\bar{f}_{x_{2}}^{(1)} & 2\operatorname{Re}\,\bar{f}_{x_{2}}^{(2)} & -2\operatorname{Im}\,\bar{f}_{x_{2}}^{(2)} \\ 2\operatorname{Re}\,\bar{f}_{x_{3}}^{(1)} & -2\operatorname{Im}\,\bar{f}_{x_{3}}^{(1)} & 2\operatorname{Re}\,\bar{f}_{x_{3}}^{(2)} & -2\operatorname{Im}\,\bar{f}_{x_{3}}^{(2)} \\ 2\operatorname{Re}\,\bar{f}_{x_{4}}^{(1)} & -2\operatorname{Im}\,\bar{f}_{x_{4}}^{(1)} & 2\operatorname{Re}\,\bar{f}_{x_{4}}^{(2)} & -2\operatorname{Im}\,\bar{f}_{x_{4}}^{(2)} \end{pmatrix},$$

 φ_{ii} - cofactors of 1st column of a matrix (Φ).

The line above \bar{X}_l , $\bar{f}_{x_l}^{(1)}$ and $\bar{f}_{x_l}^{(2)}$ stands for initial

values of coordinates and Floquet functions on an azimuth of injection.

At H=0 equations (6) have two solutions:

1.
$$I_1(0) = I_2(0) = 0$$
 and according (3) $\left(\frac{dI_1}{d\theta}\right)_0 = 0$

and
$$\left(\frac{dI_2}{d\theta}\right)_0 = 0$$
. The point in a phase space, which

is taken by a particle moving about equilibrium orbit corresponds to this solution.

2.
$$I_1(0) \neq 0, I_2(0) = 0$$
;

$$I_2(0) = I_1(0) \frac{\left(L_1^s + L_1^Q\right)}{\left(M_2^s + M_2^q\right)} \tag{9}$$

If the condition (9) is fulfilled, and further at a modification of ϑ will be fulfilled the following relation:

$$I_2 = I_1 \frac{\left(L_1^s + L_1^Q\right)}{\left(M_2^s + M_2^q\right)} \tag{10}$$

Substituting (5) and (10) in (3) we shall receive:

$$\frac{dI_1}{d\theta} = -\left(L_1^s + L_1^Q\right)I_1^2 \tag{11a}$$

$$\frac{dI_2}{d\theta} = -\left(M_1^s + M_1^Q\right)I_2^2 \tag{11b}$$

Integrating (11a) and (11b) we shall receive:

$$I_{1} = \frac{1}{1/I_{1}(\theta) + (L_{1}^{s} + L_{1}^{Q})\theta};$$

$$I_{2} = \frac{1}{1/I_{2}(\theta) - (M_{2}^{s} + M_{2}^{Q})\theta}$$
(12)

It is made out from the relation (6) that for H=0 it is necessary that the magnitudes $(L_1^s + L_1^o)$ and $(M_2^s + M_2^o)$ were should be with identical signs. And it is clear from (12) that for I_1 and I_2 being aimed to zero at $\theta \rightarrow \infty$ it is necessary that the conditions $(L_1^s + L_1^o) > 0$ and $(M_2^s + M_2^o) > 0$ were fulfilled.

On account of relations (12) and (11a) and (11b) at $(L_1^s + L_1^\varrho) > 0$ and $(M_2^s + M_2^\varrho) > 0$ at $\theta \to \infty$ the particles, initial conditions of which satisfy the condition (10), will be indefinitely long coming close to a fixed point with

parameters
$$\left(\frac{dI_1}{d\theta}\right) = 0$$
, $\left(\frac{dI_2}{d\theta}\right) = 0$, $I_1 = I_2 = 0$, that is to an

equilibrium orbit. Thus, for a realisation of multiturn injection the realisation of two conditions $(L_i^s + L_i^\varrho) > 0$, $(M_2^s + M_2^\varrho) > 0$ and H=0 is necessary and sufficient. In common case:

$$I_2 = \frac{1}{2} \frac{L_1}{M_2} I_1 \pm \sqrt{\frac{1}{4} \frac{I_1^2 L_1^2}{M_2^2} + \frac{H}{I_1 M_2}},$$
 (13)

Where I_i is a solution of the differential equation:

$$\frac{dI_{1}}{\pm 2(M_{2}^{S} + M_{2}^{Q})\sqrt{\frac{1}{4}\frac{I_{1}^{2}L_{1}^{2}}{M_{2}^{2}} + \frac{H}{I_{1}M_{2}}}} = d\theta.$$
 (14)

For short here and below it is necessary: $(L_1^s + L_1^\varrho) = L_1$ e $(M_2^s + M_2^\varrho) = M_2$.

Assuming H = -H, H > 0, $M_2 > 0$ and by integrate (14) we shall receive expressions:

$$-\frac{2}{3}\frac{1}{L_{1}}\ln\frac{1-\sqrt{1-\left(I_{1}\min/I_{1}(0)\right)^{3}}}{1+\sqrt{1-\left(I_{1}\min/I_{1}(0)\right)^{3}}}=\theta,$$
(15)

where $I_{1\text{min}} = \left(\frac{4\overline{H}M_2}{H_1^2}\right)^{1/3}$ - minimum value, which will

take I_1 during the injection. At $I_1=I_{min}$ $dI/d\theta=0$ and after reaching this value the increase of I_1 will begin. From (15) follows, that number of turns during which it is possible to carry out the injection is equal to:

(10)
$$n = -\frac{2}{3\pi} \frac{1}{L_1} \ln \frac{1 - \sqrt{1 - (I_{1min}/I_1(0))^3}}{1 + \sqrt{1 - (I_{1min}/I_1(0))^3}}.$$
 (16)

Assuming $I_{lmin}/I_1(0) << 1$ we shall receive the approximate formula for an estimation of number of turns - n.

$$n = -\frac{2}{3\pi} \frac{1}{L_1} \ln \left(\frac{(I_{1 \min}/I_1(0))^3}{4} \right). \tag{17}$$

From (17) follows, that less is L_i , the more turns it is possible to inject, but L_i should be great enough to ensure the separation of a beam from a septum for one turn. Integrating (14) and assuming $\theta=2\pi$ we shall receive:

$$L_{1} = \frac{1}{\pi} \frac{I_{1}(0) - I_{1}(2\pi)}{I_{1}(0)}.$$
 (18)

Substituting L_i , from (18) to (17) we shall receive:

$$n = -\frac{2}{3} \left(\frac{I_1(0)}{I_1(0) - I_1(2\pi)} \right) \ln \left(\frac{(I_{1min}/I_1(0))^3}{4} \right).$$
 (19)

Magnitude of a phase volume of a beam in space of x_p which can be injected in a storage ring during n turns (17) is equal to the volume limited by the surface, the parameters of which can be obtained at a substitution in the equation (6) expressions for $I_1(0)$ and $I_2(0)$ from (7) and (8).

3 CONCLUSION

The method of an average applied in the work for a research of radial-phase motion of electrons in a storage ring, is approximate. The obtained formulas will be describe dynamics of particles well at realization of the condition $2\pi/\theta$,>>1.

For a realization of conditions for existence of "limit cycle" it is necessary to select a storage system with close values ψ_1 and ψ_2 . In common case sextupole and octupole fields result to the mutual transmission of an energy of synchrotron and betatron oscillations.

Multiturn injection can be used for the injection of heavy particles.

REFERENCES

[1] V.A. Titov, I.A.Shshukeylo, "Resonance injection with two dimension of freedom in synchrotron with strong focucsng", J.T.Ph., v. XXXVIII, is. 10. pp. 1752-1755, 1968 y.

[2] C.R. Prior, "Multiturn Injection for Heavy ion Fusion", Proc. Symposium on Accelerator Aspects of HIF, GSI-82-8, 1982, p.290
[3] H. Poincare,, "Acte math.",1890, v.13, pp. 1-270

[4] N.G. Chetaev, C.R. Acad. Sci., 1928, v.187, pp. 637-

[5] N.N. Bogolubov, Yu. A. Mitropolsky"The assymptotic methods in theory of nonlinear oscillations", PhysMathGis, 1958, p. 445

[6] A.A. Kolomensky, A.N. Lebedev, "Theory of cyclic accelerator", Moskow, 1962, p 345

COMPENSATION OF THE INSERTION DEVICES EFFECT IN ELECTRON STORAGE RINGS

AYu. Zelinsky, I.M. Karnaukhov, NSC KIPT, Kharkov, Ukraine

Abstract

The method of designing of the local compensation schemes for suppression of wigglers and undulators affects on lattice functions of low emittance storage rings is described. The method is based on the analysis and optimization of a transport matrix of the insertion device section. The features of magnetic lattices permitting to compensate effects of various wiggler and undulator types are discussed.

The effects of the insertion devices to lattice functions and parameters of storage ring UNK Kharkov are discussed. The schemes of compensation are presented.

1 INTRODUCTION

Nowadays, the beams of photons obtained from insertion devices (wiggler, undulator) (ID), installed on storage rings - sources of a synchrotron radiation (SR), became the necessary tool for realization of researches in science and technology. Owing to this reason SR sources of the third generation are oriented on magnetic lattices with the great amount of ID [1]. As the ID installed in a storage ring affects on the electron beam, there is a problem of suppression of ID effect on a beam dynamics in a ring. The methods of compensation of ID effect on particles dynamics in a ring should be universal and effective.

In this report the technique of designing of the schemes of compensation based on use of a matrix formalism and optimization of elements of a transport matrix is offered. Compensation is carry out on a section of "insertion", where ID is disposed, in such a manner on a remaining ring of a focusing function are not changed, thus the effect of ID is localized on a section of "insertion" [2].

With use of this technique we have designed variants of the scheme of local compensation of effect of flat wiggler for UNK Kharkov storage ring [3]. In this report we consider effects, to which the installation of flat wiggler on an UNK Kharkov are resulted and we reduce outcomes of application of the schemes of compensation.

2 EFFECT OF ID ON PARAMETERS OF STORAGE RINGS LATTICES

The ideal ID in electron storage ring bring a modification of a focussing functions, frequencies of oscillations and increase of emittance and energy spread, emerging of a horizontal dispersion on a ID space. The field of spiral ID call coupling of horizontal and vertical oscillations, that changes focusing properties of a lattice and results in

increase of vertical phase volume in a ring. This coupling of oscillations should be localized on a space of an insertion.

When in ID there are only transverse fields the changes of focussing functions and tunes of betatron oscillations are caused by a edge-focussing effects of coils of these devices. The tune shifts and change β -functions can be calculated by a method of transport matrixes. The field of a ideal flat wiggler is well describe by a matrix of a rectangular magnet. The matrix models of other types of devices also can be created.

In a lattice of UNK Kharkov the installation of superconducting horizontal three-polar wiggler with a maximum field up to 7 T and length 0.62 m is stipulated [4]. We evaluated a tune shift of vertical oscillations, change of horizontal emittance ε_x , distortion β - functions of UNK Kharkov depending on a field value in wiggler B_W by use of the application package DeCA [5]. The field in wiggler was changed from 0 up to 7 T. Results of calculations are indicated in table 1 and on fig.1.

Table 1.

Number in fig.1	В _w [Т]	Emittance ε_x [m*rad]	Q_z
1	0.00	2.480*10 ⁻⁸	4.25739
2	5.00	2.850*10-8	4.35516
3	5.50	3.130*10 ⁻⁸	4.38047
4	6.00	3.534*10 ⁻⁸	4.41436
5	6.25	3.706*10 ⁻⁸	4.42998
6	6.50	4.090*10 ⁻⁸	4.51322
	7.00	Motion unstable	e

Obviously, that for providing of normal work of a ring when the magnetic field in wiggler is big it is necessary to localize effect of ID on a space of "insertion" or to suppress it by anyone methods. The scheme of compensation should ensure normal work of a ring for any modification of magnitude of a field in ID.

3 DESIGN OF THE SCHEMES OF LOCAL COMPENSATION

It is possible to describe the focusing properties of the ID by a transport matrix M_{wU} by a size 6*6 [6,7]. By making a combination from matrixes M_{wU} , M_{wU} , ..., M_{wU} of ID sections and matrixes M_{comp1} , M_{comp2} ... M_{comp_i} of groups of compensatory elements we should receive a resulting matrix of an insertion ID. It will be noted as follows:

$$M_{comp_i}^* M_{w_{II}} \dots M_{comp2}^* M_{w_{II}} M_{comp1} = M_{ip}$$
 (1)

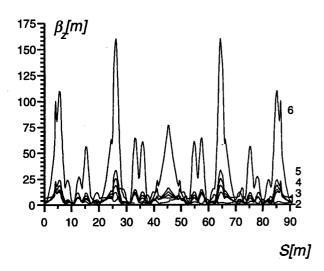


Figure 1. β -function of UNK Kharkov with ID without compensation.

(1) represents a system from 20 equations. When taking into account conditions of stability of particles motion in a storage ring [8]:

$$Det M_{1D}|_{x} = 1, \ Det M_{1D}|_{z} = 1,$$
 (2)

we receive a system of 18 independent equations, for sufficing of that is necessary to have 18 independent parameters. Such parameters can be forces of quadrupole lenses, lengths of drift spaces, turn angles in dipole magnets, rotation angles of quadrupole lenses. In depending from kind of resulting matrix of a section of an insertion that we want to receive and what type ID we use, the number of the equations can be reduce.

The transport matrix of flat wiggler with n poles is the matrix of n rectangular magnets. Combining this matrix with matrixes of compensatory sections, when considering a condition (2) received a system of 10 equations. Thus, for suppression of flat wiggler effect it is necessary to make a magnetic lattice with 10 varied parameters, to impose requests on focusing properties of a transport matrix of an insertion M_{ID} and to decide this system. If requests to compensation of dispersion function are not to impose then amount of the equations and elements, required for compensation, is reduced up to 6.

Most simple configuration of insertion lattice permitting to compensate focusing properties of flat wiggler, receive, if to surround wiggler by a system from quadrupole lenses. In this case (1) has a kind:

$$M_{\text{comp2}}$$
, M_{wu} , M_{comp1} , M_{lb} , (3)

The requests to focusing properties of M_{ID} can be arbitrary and are determined by real conditions of a storage ring lattice and soluble problems. However most natural are the variants, when the transport matrix of an insertion is represented as a matrix of drift space or the matrixes of a focusing section, where ID is disposed. In these cases all properties of lattices of storage rings in a

linear approximation will be saved, and the effects of ID will be localized on a section of an insertion.

4 COMPENSATION SHEMES FOR UNK KHARKOV STORAGE RING

In a fig. 2 the layout of an insertion consisting from wiggler and compensatory a structures permitting to receive arbitrary matrix of a focusing is shown.

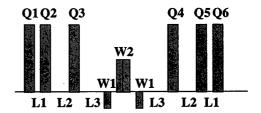


Figure 2: Layout of compensatory insertion.

We designed two variants of compensatory structures for UNK Kharkov. First variant (I) realized a transport matrix of an insertion appropriate to length of drift space, where it is disposed, and uses 6 additional quadrupole lenses. Second variant (II) realized a transport matrix appropriate to a focusing matrix of long straight section of a storage ring, in which wiggler is situated. In table 2 the parameters of elements of an insertion for two variants of a transport matrix are indicated.

Table 2. K1 [T/m], B [T] L[M]II II 0.2 K1 = -44.616K1=2.8997 0.2 Q1 Q2 K1=100.152 K1 = -1.94050.2 0.2 0.2 K1=14.8653 0.2 K1 = -160.76Q3 K1=14.8653 0.2 0.2 04 K1 = -132.98Q5 K1=98.909 K1 = -1.94050.2 0.2 K1=2.8997 0.2 Q6 K1 = -54.5390.2 W₁ B=-3.5, B = -3.50.2067 0.2067 B=7.0B=7.0W2 0.2067 0.2067 0.3 L1 0.4614 L2 0.1204 0.2 0.2682 3.34953

where $K1 = \frac{1}{B\rho} \frac{\partial B}{\partial x}$, B – magnetic field, L – elements

length.

For keeping of a kind of transport matrix when value of a field in wiggler is vary gradients of quadrupole lenses are changing directly as a field in wiggler.

The amplitude functions of UNK Kharkov without ID and with taken into lattice of compensatory insertion and ID are shown in a fig. 3. In a result of an operation of an insertion the horizontal tune of betatron oscillations is not changed, and the vertical tune is increased on 1 and they are $Q_x = 7.21114$, $Q_z = 5.25832$. In a result of magnification of energy losses on a SR the energy spread

has increased from $1.085*10^{-3}$ up to $1.258*10^{-3}$, and emittance from $2.48*10^{-8}$ m*rad up to $3.76*10^{-8}$ m*rad. At the same time, horizontal β_x - function at centre of wiggler has decreased almost twice (from 11.123 m up to 6.842 m), that allows to compensate effect of growth of emittance and energy spread on a horizontal size of a beam.

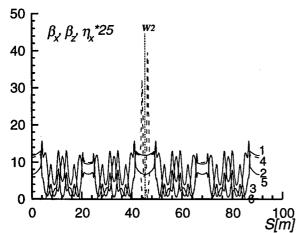


Figure 3:. 1 - β_x - B_w =0 T, 2 - β_z - B_w =0 T, 3 - η_x - B_w =0 T, 4 - β_x - B_w =7 T insertion I switch on, 5 - β_z - B_w =7 T insertion I switch on, 6 - η_x - B_w =7 T insertion I switch on, W2 - centre of wiggler magnet.

We also calculated the dynamic aperture (DA) of a UNK Kharkov. The calculations of the DA with and without of insertion with taken into account only transverse motion and longitudinal motion with chromatic aberration too were conducted. The DA in a vertical plane not was changed, as the tune of betatron oscillations was not actually changed, and the amplitude functions in a vertical plane also was changed a little (fig. 4). The minor diminution of area of stability in a horizontal plane is caused by an amplification of sextupole lenses in bending sections of lattice that compensate the natural chromaticity. The taking into account of longitudinal motion of particles and chromatic aberrations show that without insertion they do not have essential influence on area of stable motion of particles. However, when magnetic elements of the insertion switch on influence of chromatic aberrations are increased and DA decrease on \pm 5 mm. Despite of it, the DA at center of wiggler remain rather large (± 12 mm), that it is quite enough for realization of injection in a ring.

The amplitude functions of a storage ring with taking into account of an insertion and without it and for normal mode of quadrupole lenses of straight section for variant II of insertion are shown on fig.4. The effect of an insertion to amplitude functions in a ring is unsignificant. On a section of an insertion β_z will increase up to 55,9 ì, and β_x up to 13 m is increased. The tune of horizontal and vertical betatron oscillations practically is not changed and they are $Q_x = 7.22598$, $Q_z = 4.18371$. In a result of increase of energy losses on a SR the energy spread has

increased up to 1.258*10⁻³, and emittance up to 4.407*10⁻⁸ m*rad.

The calculations of the DA with taking into account only transverse motion and also longitudinal motion and chromatic aberrations were conducted. As the tune of betatron oscillations after including of insertion in lattice was provided were not actually changed, the DA not was changed. The minor magnification of area of stability in a vertical direction is caused by slack of sextupole lenses in bending section of a lattice, and remove of tune of vertical oscillations from a resonance Qz/4. The effect of chromatic aberrations on particles motion less essential, than in case of an insertion as drift space and the magnitude of the DA is changed unsignificantly.

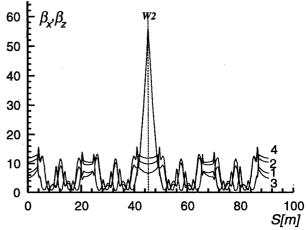


Figure 4:. $1 - \beta_x - B_w = 0$ T, $2 - \beta_z - B_w = 0$ T, $3 - \beta_x - B_w = 7$ T insertion II switch on, $4 - \beta_z - B_w = 7$ T insertion II switch on, W2 – center of wiggler magnet.

5 CONCLUSION

The results of calculations of a compensatory insertion show that the theory of transport matrixes allows calculating parameters of structures compensatory the ID effects in storage rings. The designed compensatory schemes will be used in a storage ring UNK Kharkov.

REFERENCES

[1] SPRING-8 Project, Facility Design 1991, August 1991.

[2] A. Ando, S.Date, K. Soutome et all. "A local compensation scheme for insertion devices in the 8 GeV storage ring SPRING-8", EPAC 94, v.1, pp. 660-662

[3] E.Bulyak, A.Dovbnya, P.Gladkikh, "A multipurpose accelerator facility for Kharkov national scientific center", Conference SR-98 Novosibirsk, July, 1998, to be published.

[4] P. Gladkikh, I. Karnaukhov, A. Mytsykov, "The effect of superconducting wiggler on the DA ISI-800", EPAC 96, v.1, pp.656-658, 1996

[5] A.Zelinsky, P.Gladkikh, M. Strelkov, New version 3.3 of the DeCA code, Proceeding of the 3 EPAC, 1992, v.1, pp. 685-687.

[6] A Zelinsky, I.. Karnaukhov, A. Shcherbakov, "Compensation of coupling caused by solenoid", Preprint KPTI 88-47, Moskow-CNIIatominform-1988, pp. 12.(In Russ) [7]V. Kartashev, V.I. Kotov, "The base of magnetic optic of charge particles", Paris, 1966.(In Russ)

[8] A. Bruck, "Accelerateurs Circulaitares de Particules", Moskow: Atomizdat, 1970.(In Russ)

New Space-Charge Methods in Accsim and Their Application to Injection in the CERN PS Booster

F.W. Jones, TRIUMF, 4004 Wesbrook Mall, Vancouver, V6T 2A3, Canada H.O. Schönauer, CERN, CH-1211 Geneva 23, Switzerland

Abstract

The tracking and simulation code Accsim has recently been upgraded with new treatments of transverse space charge, one based on a conventional multiple-Fourier-transform technique and another using a new hybrid-fast-multipole (HFM) method. We present the application of the code to the study of multiturn injection in the CERN PS Booster in its LHC-injector-chain operation scenario. In particular, the ability of the HFM method to accurately model the turn-by-turn stacking and subsequent development of the beam is evaluated, especially its development near the sharp cut-off produced by beam loss on the injection septum. Results are compared with measured injection efficiencies and betatron amplitude distributions.

1 INTRODUCTION

As part of a TRIUMF/CERN collaboration agreement, the tracking and simulation code Accsim is being developed to support the study of injection and collimation in the CERN PS Booster, in its role as part of the LHC injector chain. The code contains many useful simulation features for injection and collimation scenarios, including phase-space painting, programmed orbit bumps, rf harmonics, barrier buckets, and Monte Carlo treatments of particle interactions with stripping foils and collimator materials. These features are built on top of a 3D (6 phase-space variables) symplectic tracking engine.

Longitudinal space charge effects are included in the conventional manner by binning, smoothing, and differentation of the line density. Until recently, a complete model of transverse space-charge effects was lacking, but early-on a package a package "DQ" was added, which utilitizes amplitude binning and averaging over betatron phases to derive the effective beam potential, and thence a "fast parameterization" of the distribution of tune-shifts in the beam.

With improvements in computing resources, the desire has arisen to develop a more general, self-consistent treatment of transverse space charge, while keeping in mind the mandate of the code to run on conventional desktop computers rather than supercomputers. The present paper describes the upgrading of the code to achieve this, via new routines using field-solve/kick methods which are integrated with Accsim's matrix/thin-lens tracking. This will be followed by initial test results and some simulation results for the PS Booster.

2 TRANSVERSE SPACE-CHARGE MODEL

To satisfy the computing-time constraints, a $2\frac{1}{2}D$ transverse space-charge model was chosen for Accsim, where the term " $2\frac{1}{2}D$ " refers to mixed 2D and 3D aspects: the model is 2D in the sense that the nominal transverse space-charge field is evaluated by viewing all macroparticles as 2-dimensional (line) charges; whereas the model is 3D in the sense that the space-charge force on a given macroparticle is scaled according to the longitudinal charge density at its position in the bunch, thus coupling the longitudinal motion into the transverse tune space.

We consider that the bunch length is much larger than the transverse beam size, and that there is no significant correlation between transverse and longitudinal distributions. In typical Accsim applications, this holds because any such correlations in the injected linac beam will be masked in the ring by the multiturn injection and phase-space painting process. Under these circumstances, the projected 2D distribution of transverse macroparticle coordinates can be condsidered representative of the local transverse beam distribution at a given location in the ring. In fact, Accsim's transfer-matrix/kick formalism already lends itself this model because it tracks in distance steps rather than time steps: each macroparticle carries a time-difference (rf phase) coordinate locating it in the bunch, and the stored transverse coordinates are a "snapshot" in space rather than in time.

As in other codes, tracking with space-charge is done a successive "field-solve/particle-push" integration, where the "push" operation consists of applying angular kicks representing the force integral over the integration step, followed by matrix/thin-lens transport over the step.

3 FIELD SOLUTION METHODS

The rapid and accurate evaluation of the 2D space-charge field is the key to usability of the model in Accsim, and here two methods have been implemented, both founded on the usual Particle-In-Cell (PIC) scheme where the field is solved on a set of discrete mesh points, using bilinear weighting to assign macroparticle charges to the mesh and to derive the resultant forces on the macroparticles. The first field-solution method uses the Multiple-Fourier-Transform (MFT) technique, via routines contributed by Accsim users at BNL and ORNL[5]. The second field-solution method uses a new Hybrid Fast-Multipole (HFM) technique that was developed for Accsim in order to ad-

dress beam-distribution and halo issues that may arise in short-term or long-term injection simulations.

The HFM technique utilizes the DAPIP2 package of routines developed by L. Greengard[1]. They are a robust 2D implementation of his Fast-Multipole Method (FMM) field solver, which is designed to solve the field for an arbitrary collection of discrete charges. The FMM method does not use a grid, but rather subdivides the solution domain into a heirarchical tree of square or cubic regions, in which multipole expansions of the field are computed. The regions and the multipole orders are chosen to satisfy the desired field accuracy while minimizing the computing time. This method is nominally slower than FFT-based methods, but it is superior in dealing with heterogeneous mixtures of charges and distance scales.

From FMM, it is a simple step to Accsim's HFM method: namely choosing a PIC grid on the solution domain, assigning charges to it, and giving the PIC grid charges to the FMM routine to solve, rather than giving it the set of discrete macroparticle charges. What does this achieve? Since there are usually much fewer PIC grid points that actual macroparticles, this obviously speeds up FMM so that it can compete with an FFT-based solution. The use of a PIC grid also achieves an intrinsic smoothing of the charge distribution, which greatly eases the noise problem found in FMM and direct-sum field solutions, usually dealt with by incorporating a smoothing parameter in distance reckonings.

The MFT and HFM techniques both do the same job, but there are some important differences:

- MFT must solve the field at all PIC grid points, even though many of them may have no nearby macroparticles. HFM solves the field only at the grid points that have charges on them.
- In MFT the PIC grid must be made somewhat larger than the charge ensemble, in order to provide a "guard band" against the (non-physical) implicit periodic boundary conditions. When a beam halo develops, and the PIC grid is augmented to accommodate it, there is a large uplift in computation time. HFM does not have this penalty and therefore becomes faster than MFT, at the same spatial resolution, when a significant halo is present.
- MFT normally uses a regular grid, whereas in HFM there are no restrictions on the grid: it can be irregular in spacing and of arbitrary size and shape. Where needed, additional grid points can be added to resolve fine details in the charge distribution. Particles that grow to large amplitudes and fall outside the grid are no problem: they are simply added as discrete charges to the list of charges presented to the FMM solver.

The charge-assignment and force-interpolation processes are identical for MFT and HFM, although some additional bookkeeping is required for HFM to handle possible mixtures of gridded and single-particle charges. The computational details and some comparison tests can be found in Reference [2].

4 CODE AND LATTICE VALIDATION

The CERN PS Booster is a period 16 triplet lattice of circumference 157.08 meters. In order to best resolve the quadrupole spacing in the triplet structure, a nominal space-charge integration step size of 0.70125m, or 14 steps per period, was chosen. Since the code had formerly only been tested with regular FODO lattices, where the step subdivision is much simpler, some validation runs were performed on the PSB lattice subdivision by tracking a slightly mismatched K-V beam of 10000 macroparticles (representing $\sim 10^{13}$ protons and yielding tune shifts of ~ 0.2) for 100 turns. The nominal single-particle tune, and envelope eigenfrequencies were measured by FFT's on the tracking data, as shown in Table 1.

Table 1: Comparison of predicted and measured singleparticle tunes and envelope eigenfrequencies

Frequency	Q_x	Q_y	$Q_{ m env}^-$	$Q_{ m env}^+$
Analytical result	4.077	5.371	8.323	10.920
Accsim FFT	4.09	5.38	8.32	10.87

The results are in excellent accord with analytical predictions of the single-particle tunes by the generalized Laslett formula

$$\Delta Q_{x,y} = \frac{r_p N_I(q^2/A) F_{x,y} G_{x,y} \bar{H}_{x,y}}{\pi \varepsilon_{x,y} \beta^2 \gamma^3 B_f}$$
(1)

and of the envelope eigenfrequencies[3]

$$Q_{\text{env}}^2 = 2Q_{0x}^2 + 2Q_{0y}^2 - 5Q_{0x}\Delta Q_x$$
$$\pm \sqrt{(2Q_{0x}^2 - 2Q_{0y}^2)^2 + (Q_{0x}\Delta Q_x)^2}, (2)$$

where Q_{0x} and Q_{0y} are the bare tunes (4.28 and 5.55). We also observed good tune uniformity over the K-V distribution, with 99% tune spreads of \sim 0.01 in each plane.

5 CERN PS BOOSTER SIMULATION PARAMETERS

The CERN PS Booster is one of the few proton machines using classical multiturn injection. A falling sawtooth-shaped orbit bump of 49 mm initial horizontal amplitude and 50 μ s fall time approaches a magnetic septum at 45 mm. The linac beam is injected at 53.7 mm and mismatched such that its ellipse in phase space osculates the ellipse of the final circulating beam. By varying the length of the linac pulse and time-shifting the bump with respect to it, emittance and intensity can be controlled—within limits. At present the linac current is about 160 mA or 2.2×10^{12} protons/turn, at an emittance of 16π mm mrad. There are two particularly interesting injection schemes:

Table 2: Results of Accsim and Measurements after Injection at 50 MeV with BeamScope.

	Accsim	BeamScope	Unit
Injected beam	1.77×10 ¹²	1.07×10^{12}	Protons
ϵ_h (95%)	40.0	37.5	π mm mr
ϵ_v (95%)	36.0	44.8	π mm mr
ϵ_h proj. (2σ)	21.1	23.5	π mm mr
ϵ_v proj. (2 σ)	18.5	19.4	π mm mr

One for highest intensity (typically 13 turns injected, filling horizontal emittances of up to 300π mm mrad), and a low intensity, high brilliance beam for future LHC filling (3 turns and about 30π mm mrad). In this paper we concentrate on the high brilliance beam, mainly because there are less unknown factors like stopbands to be simulated, and because the shorter tracking duration allows comparison with the Agile code [4] featuring direct interaction between macroparticles.

6 SIMULATION RESULTS

The amplitude profiles after removal of the circulating beam from the septum are compared with profiles measured with BeamScope, the PS Booster emittance measurement device. Characteristic beam parameters are compared in Table 2 and example profiles are shown in Figure 1.

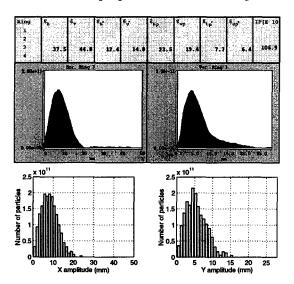


Figure 1: Comparison of BeamScope (top) and Accsim profiles

Another, already mentioned test consists in comparing phase space distributions after a few turns between Acc-sim and the Agile interactive lattice design code, featuring also tracking of macroparticle distributions with direct electrostatic interaction. Based on a PC under Windows95, these computations take time and are thus limited to few-turn tracking. The phase-space plots are shown in Figure 2. Real space plots, less instructive, are almost identical.

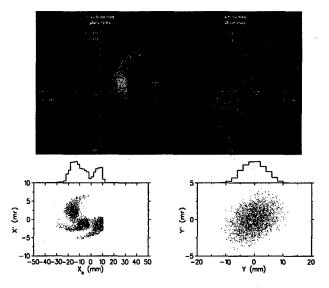


Figure 2: Comparison of Agile (top) and Accsim phasespace plots (the closed orbit deviation is removed in the Accsim plot).

7 DISCUSSION OF RESULTS

The BeamScope profiles show a halo in the vertical plane, which is not present in the simulation. It should be noted that BeamScope measurements take some time and cannot be performed immediately, which means that the circulating beam is subject to the machine nonlinearities during 2-3 ms. The halo is probably due to growth on one of or both the stopbands $4Q_v=25$ or $2Q_v=10$, which are not simulated. Apart from the halo, emittances compare rather well and the agreement is satisfactory.

The comparison between Agile and Accsim is even more convincing, taking into account that, due to different algorithms of the two codes, the distribution of the injected beam is only approximately the same: a truncated (at 3σ) Gaussian in Agile and a binomial distribution (m=3.5) in Accsim, both matched to have the same variance and the same finite radii.

- Leslie F. Greengard, The Rapid Evaluation of Potential Fields in Particle Systems, Cambridge, Mass: MIT Press, 1988.
- [2] F.W. Jones, "A Hybrid Fast-Multipole Technique for Space-Charge Tracking With Halos," Workshop on Space Charge Physics in High Intensity Hadron Rings, Shelter Island NY, May 1998, AIP Conf. Proc. 448, p. 359.
- [3] R. Baartman, "Betatron Resonances with Space Charge," ibid, p. 56.
- [4] P. Bryant, personal communication and Agile WWW Page, http://nicewww.cern.ch/~bryant.
- [5] J.A. Holmes et al., "A Particle-In-Cell Model for Space-Charge Dynamics in Rings," Proc. European Particle Accelerator Conference, Stockholm, 1998.
- [6] Accsim home page, http://www.triumf.ca/compserv/accsim.html.

OPTIMIZATION OF BLOCK-COIL DIPOLES FOR HADRON COLLIDERS'

C. Battle, N. Diaczenko, T. Elliott, D. Gross, E. Hill, W. Henchel, M. Johnson, P. McIntyre[#], A. Ravello, A. Sattarov, R. Soika, D. Wind, Texas A&M University, College Station, TX R. Gaedke, Trinity University, San Antonio, TX

Abstract

A first model dipole is being built for a 16 Tesla blockcoil dipole for future hadron colliders. The design uses stress management: a support matrix that intercepts Lorentz stress between successive sections of the coil and bypasses it to prevent strain degradation of the superconductors and insulation. The block-coil methodology has also been used to design dipoles for 12 Tesla and 15 Tesla, in which the amount of superconductor is minimized by cabling copper stabilizer strands with superconductor strands. The 12 Tesla block-coil dipole requires only one-fifth as much superconductor as does a 12 Tesla $\cos \theta$ dipole that is being developed elsewhere.

1 INTRODUCTION

The technology of superconducting dipoles determines the cost and performance of future hadron colliders. The field strength determines the relation between energy and circumference; the field quality and provisions for beam stability and synchrotron radiation determine the luminosity and lifetime of the colliding beams. Over the past several years much work has been done to relate the several requirements of a high-luminosity collider to the parameters of its magnets. A first example is synchrotron radiation. It was once thought that field strength beyond ~10 Tesla would create a problem from the heat deposited by synchrotron radiation in the cryogenic magnet. it is now realized that synchrotron radiation damping at high field strength can damp beam size and improve luminosity, and schema have been conceived (one presented below) whereby the synchrotron radiation can be absorbed at a higher temperature within the dipoles so that its refrigeration impact is reduced.

A second example is aperture. It was once thought that an aperture radius of at least 2.5 cm was necessary to have acceptable growth times for single-beam and mode coupling instabilities. Several schema have been developed recently whereby such instabilities can be damped within a single turn, so that apertures as small as 1 cm can support stable beams. With presently available superconductors, the coil for a high-field dipole is thick compared to its inner radius, so that reducing aperture has the potential to dramatically reduce magnet cost.

A third example is the impact of various multipoles upon beam growth mechanisms in a high-luminosity collider.

With NbTi superconductor, it was possible to make strands with extremely small filament diameter (few µm) so that multipoles produced by persistent currents at injection energy were suppressed. NbTi cannot support fields higher than ~9 Tesla, and the superconductors that are used at higher fields (today Nb₃Sn, in the future Bi-2212) currently have very large filament diameter (>50 µm) if fabrication is optimized for high current density.

2 **BLOCK COIL DESIGN STRATEGY**

We are developing a new approach to dipole design, in which the coils are configured in rectangular blocks instead of the $\cos \theta$ geometry used in most superconducting dipoles to date. We are currently building a 16 Tesla dual dipole embodying this approach. We report here the results of recent work to optimize the block coil approach in the placement and composition of superconducting coil elements for 12 Tesla and 15 Tesla versions of the same design. The 12 Tesla design is shown in Figure 1.

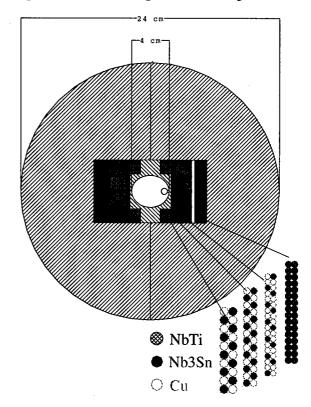


Figure 1. 12 Tesla block-coil dipole: optimized Nb₃Sn, NbTi.

Work supported in part by U.S. Dept. of Energy grant ##DE-FG03-95ER40924.

[#] Email: p-mcintyre@physics.tamu.edu

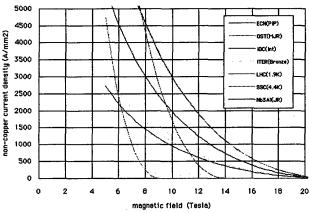


Figure 2. j_c vs. B for various superconductors.

The aperture can be optimized to the application. The block-coil geometry is intrinsically scalable: the coil structure can be scaled to optimum for the aperture that is required for collider application, and also for the cable current that is best for quench protection (typically ~10 kA). This feature is distinct from $\cos\theta$ coil geometry, in which the arch configuration of high-current cables makes it problematic to optimize with less than a 2.5 cm aperture radius. The design in Figure 1 has an aperture of 3.5 cm horizontal, 3 cm vertical.

Block-coils enable stress management. For field strength beyond ~12 Tesla, the stress in the coils of a superconducting dipole exceeds 100 MPa, at which point superconductors like Nb₃Sn and Bi-2212 experience degradation of critical current capability. We devised a strategy [1] in which the stresses from the magnetic field acting upon the inner portions of a coil are intercepted by a support matrix that is distributed within the block-coil assembly. In this way the stress on superconducting elements can be limited to <70 MPa everywhere in the coil, even for fields as great as 20 Tesla.

Block-coil geometry suppresses persistent-current multipoles. The steel flux return in a block-coil dipole forms a planar boundary above and below the coil region. At injection field strength the steel is unsaturated, and this planar boundary condition suppresses multipoles arising from persistent current magnetization within the coil. For the 16 Tesla design of Ref. 1, the sextupole is suppressed by a factor 10 at injection.

Block-coil assemblies are easy to build. Each coil is a racetrack pancake coil. The coils are wound with simple fixturing and tight dimensional control can be achieved. While the center pancake coils must be bent out-of-plane to accommodate the beam tube, we have succeeded in winding them as planar coils and bending the completed coils in as a unit.

3 CONDUCTOR OPTIMIZATION

Figure 2 shows the magnetic field dependence of the critical current density j_c in various superconductors. In a high-field dipole the coil is arranged in several segment: the inner segments are immersed in higher field

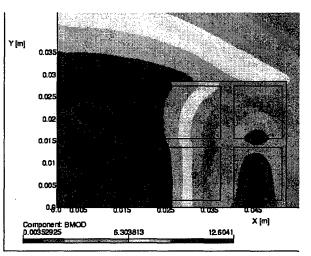


Figure 3. Field strength (modulus) in 12 T dipole.

and so can carry less current density than the outer segments. At the same time the magnet must be stable against quench. There must be sufficient copper within each cable that a quench can safely propagate throughout the coil without creating a damaging "hot spot" where it began. Current-day quench protection strategies for high-field dipoles typically require that the copper/superconductor ratio be sufficient that the current density j_{Cu} in the copper during quench not exceed ~1,500 A/mm².

Figure 3 shows the field distribution in the block-coil dipole of Figure 1. The contours of constant field strength are arranged in nearly vertical planes, so that the conductor in successive coil segments can be graded in Cu:SC ratio to maintain this stability requirement. The conventional way to grade conductor in a high-field magnet is to incorporate the required fraction of copper into the billet with the superconductor so that it is drawn together with the superconducting filaments to form strands. There are two reasons why this approach is problematic at high field. First, it is expensive: the main cost in making superconducting strand is the complex processing to stack, draw, and heat treat the multi-filament strands. Adding copper proportionally increases the amount of this expensive commodity that is needed. The second reason is that the copper is actually degraded in its cold conductivity by the strand processing. The residual resistivity ratio RRR = ρ_{300K}/ρ_{4K} of pure copper is ~500, that of the copper in superconducting strand is typically ~50.

We choose instead to provide most of the copper in the form of pure Cu strands that are cabled along with the superconducting strands into the Rutherford cable for each coil. In this way the Cu strands add very little cost, and the material cost arises mainly from that of the superconducting strands.

Indeed we take this approach one step further in the 12 Tesla design. The outermost coil segment has a maximum field of 6 Tesla. We use NbTi cable for this coil. As seen from Figure 2, its current density at this field is equal to that of Nb₃Sn and it is much less expensive.

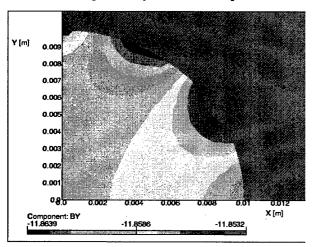
Magnet, coil	superconductor	B _{max} Tesla	jsc A/mm²	Cu:SC	SC strand area (cm ²)	Total Nb ₃ Sn strand area in dipole (cm ²)
12 Tesla block-coil						
sextupole, inner	Nb ₃ Sn	12.5, 12.2	2,000	1.4	1.25, 2.36	5.6
middle	Nb ₃ Sn	9	3,600	2.4	1.97	
outer	NbTi	6			3.94	
12 Tesla cos θ	Nb₃Sn					28

Table 1. Optimized conductors for the coil segments of the 12 T and 15 T block-coil dipoles.

The impact of this approach is evident in Table 1, which summarizes the maximum field, the Cu:SC ratio required for stability, and the cross-sectional area of superconducting strand required for the 12 Tesla design of Figure 1 and a 12 Tesla (5 cm aperture) $\cos\theta$ dipole being developed at Fermilab[2]. It had once been thought that block-coil designs were intrinsically less current-efficient than $\cos\theta$ designs. This is demonstrably not the case.

4 FIELD QUALITY

The field quality in a block-coil dipole is dominated at injection field by the boundary condition of the steel flux return, and at high field by the conductor placement. We



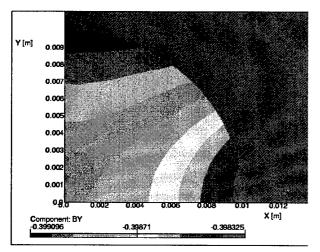


Figure 4. Field distribution at center of 12 T dipole: a) injection; b) max field.

provide for correction of the multipoles that arise from saturation by placing a sextupole correction winding above and below the beam tube region, as shown in Figure 1. The correction winding is designed to be off at injection, and carries the same current as the main windings at maximum field. Figure 4 shows the calculated field distribution within a radius of 1 cm, at injection and maximum field. In each case the sextupole is about 10^4 cm⁻². This current programming enables us to suppress the dominant multipoles over the entire range of operation.

5 SYNCHROTRON RADIATION AND CRYOGENICS

The synchrotron radiation in a high-field dipole can be a pacing consideration, both for effective cooling of the dipoles and for the overall refrigeration budget in a collider. We contemplate the incorporation of a cooling channel within the beam tube, internally cooled by either liquid neon (~30° K) or liquid nitrogen (80° K). The tube is shown in Figure 1, located in the mid-plane to the radial outside in the collider so that it forms the first wall upon which synchrotron radiation is absorbed. By taking the heat of the synchrotron radiation at such elevated temperature, the refrigeration needed to remove it to ambient is dramatically reduced. We have simulated such a conductor geometry in TBCI and SUPERFISH; no problematic higher-order modes are driven. Gas molecules that are desorbed from the tube walls by the synchrotron radiation should be trapped on the (4° K) walls of the beam tube after a traversal of the vacuum space.

6 CONCLUSIONS

The block-coil dipole provides an effective basis for optimizing the design of a high-field dipole to make most effective use of superconductor. The separation of stabilizing copper into separate strands within each cable offers a dramatic reduction in conductor cost. The impact of this separation upon stability against micro-quenches and upon AC losses must be studied to determine whether it is consistent with all of the many requirements upon the dipoles of a hadron collider.

^[1] N. Diaczenko, Stress management in high-field dipoles, Proc. 1997 Particle Accel. Conf. Vancouver, 1997.

^[2] T. Arcan et al., "Conceptural design of the Fermilab Nb $_3$ Sn high-field dipole model", this proceedings.

ANALYTICAL STUDIES OF TOP-UP SAFETY FOR THE ADVANCED PHOTON SOURCE *

L. Emery, M. Borland, ANL, Argonne, IL

Abstract

The Advanced Photon Source (APS) is a 7 GeV, third-generation synchrotron radiation source. To provide more stable beam for users, we are pursuing a new operating mode called "top-up." In this mode, the beam current is not allowed to decay as it normally would, but instead is maintained at a high level through frequent injection. A safety question with top-up mode is, during injection with photon shutters open, can injected beam ever exit a photon beamline? This might happen, for example, due to a full or partial short of a dipole coil. We discuss a number of analytical calculations that can be used to quickly assess top-up safety for a general ring. We also apply these results to the specific case of the APS. A companion paper in this conference discusses detailed tracking procedures for assessing safety.

1 INTRODUCTION

Injection into a storage ring is usually done with all photon safety shutters closed to protect against radiation accidents. As one can easily picture, injecting into a ring with shorted dipole will transport the injected beam down a photon beamline. If the safety shutter of the beamline is open, then the injected beam can exit the accelerator enclosure and potentially produce a large radation dose.

A sufficient condition for safe injection with shutters open ("top-up" injection) is to ensure that no dipoles are shorted. This could be done directly by interlocking on the voltage across each dipole. An indirect way is to detect the absence of stored beam, which indicates the possibility of a shorted dipole. Since a shorted dipole will presumably preclude the storing of beam, one could inhibit injection with shutters open when no beam is stored in the ring. Injection could only proceed in an empty ring when the shutters are closed. This simple idea becomes more complicated when one includes the possibity of a partially shorted dipole.

It may not be obvious at first but the possibility of extracting beam into a photon beamline under normal circumstances is severely restricted by the internal apertures of the storage ring, in particular the dipole crotch absorbers. The extraction of injected beam can only occur from a short (full or partial) of a directly upstream dipole magnet. Accompanying magnet faults or lattice configuration errors may enhance the possibility of extraction, but they alone cannot extract the injected beam. A full proof of this statement as applied to the APS storage ring has been done using detailed tracking simulations and is given in an accom-

panying paper [1]. The stored beam detection safety interlock has been adopted for top-up operation at APS (for other details on top-up operation see [2]).

This paper will illustrate some of the principles of the tracking simulations. The discussion will refer to the field strength error (FSE) of a dipole as a variable quantity. A normal dipole has an FSE value of 0, while a completely shorted dipole has an FSE value of -1. These two limiting values of FSE correspond to two situations of definite character. We shall show that when FSE = 0 (i.e., the ring is normal), stored beam is possible but extraction of injected beam into a photon line is impossible. When FSE = -1, stored beam is impossible but extraction of injected beam into a photon beamline is possible.

For intermediate values of FSE, one has to estimate separately the possibility of stored beam or of the extraction of injected beam. If there are some values of FSE that allow both a stored beam and extraction of injected beam, then top-up injection is not safe. We shall show that in the case of APS and its apertures, there are no unsafe values of FSE.

At APS there are two X-ray beamline types of slightly different geometry: ID beamlines with photons exiting the first (AM) dipole photon port, and BM beamlines (bending magnet radiation) with photons collected from a point 1/8 th the distance downstream of the second (BM) dipole entrance. They will be treated separately where possible.

2 NORMALLY OPERATING DIPOLES

If all dipoles are operating normally, extraction of injected beam is impossible, no matter what other magnet faults or lattice configurations might be used. Illustration of this point involves tracking a hypothetical extracted injected beam backwards in the photon beamline.

To begin, assume that the photon beamline acceptance is very small, so that the backtracked beam is a single ray through the center of the acceptance-defining apertures. Using the simple geometry in Figure 1, the particle beam trajectory (going backwards) crosses the entrance of the dipole at the corner of the pole. In APS, the effective pole width is 112 mm and the vacuum chamber is 43 mm. Therefore, the hypothetical beam must have originated non-physically from the vacuum chamber, from which we conclude that extraction of beam is impossible. Note that since the backtracked beam is "lost" before leaving the dipole, no other magnet fault or configuration, including extreme injection kicker settings, can affect the result and produce an extracted beam.

The picture gets more complicated if one allows for the rather large acceptance of the photon beamlines. There is an increased chance for a particle to backtrack successfully

^{*} Work supported by U.S. Department of Energy, Office of Basic Energy Sciences, under Contract No. W-31-109-ENG-38.

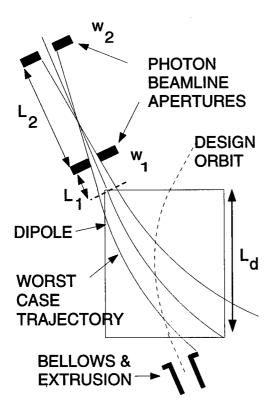


Figure 1: Schematic layout of dipole and hypothetical trajectories. Curvature is highly exaggerated for clarity.

through the dipole and disprove our case. The backwards trajectory that might best make it through the dipole is the one that starts out with negative coordinate (negative means inboard) at the last aperture and has a positive divergence angle (outboard direction) such that it just makes it through the first aperture. The dipole, of radius $\rho=39$ m and length $L_{\rm d}=3.06$ m, is a distance L_1 (see Figure 1) from the first aperture. The apertures have widths w_1 and w_2 , and are separated by distance L_2 . The coordinate of the trajectory at the entrance of the dipole is $x_{\rm traj}=-w_2+(L_{\rm d}+L_1+L_2)(w_2+w_1)/L_2-L_{\rm d}^2/(2\rho)$. In both beamlines, whose aperture dimensions are shown in Table 1, the endpoint of the trajectory coordinate is beyond the -43 mm vacuum chamber limit.

Table 1: Photon aperture dimensions

Beamline	L_1	L_2	w_1	w_2	$x_{ m traj}$
	m	m	mm	mm	mm
ID	0.765	11.331	22	36	-78
BM	0.865	16.300	13	66	-88

3 SINGLE DIPOLE COMPLETELY SHORTING OUT

When a dipole is completely off, the injected beam can easily be extracted. The phase space of the injected beam with a typical betatron oscillation can easily fit inside the photon acceptance. When a dipole is off, a beam cannot be stored. Though this may seem obvious, the extreme closed orbit created by such a perturbation on the dipole can be calculated from the standard formula $x(s) = \Delta x' \frac{\beta_x(s)\beta_{x,d}}{2\cos(\pi\nu_x)}\cos\{|\phi(s)-\phi_{\rm d}|-\pi\nu_x\}$. $\Delta x'$ is the same as the dipole bend angle $\pi/40=79$ mrad. A small value for $\beta_{x,\rm d}$ of 2 m is a conservative choice, making the effect of the dipole perturbation small. Using a typical value of $\beta_x(s)=20$ m for apertures around the ring and maximizing the cos term (since there are apertures at all phases), we obtain a closed orbit distortion of about 250 mm, compared to a horizontal aperture of 43 mm.

4 SINGLE DIPOLE PARTIALLY SHORTING OUT

From the above, we have explored only the two limiting values of field strength error for a dipole. We expect that stored beam will be possible for an FSE range of FSE_{stored} to 0, and extraction of the injected beam will be possible for an FSE range of -1 to FSE_{extr} . It is important for topup safety that the ranges do not overlap, i.e., $FSE_{gap} = FSE_{stored} - FSE_{extr} > 0$.

The FSE limit for a stored beam, FSE_{stored}, can be estimated from the formula for a closed orbit of a linear lattice due to a point orbit kick, as used above. One obtains an expression for the maximum orbit kick allowed for a uniform aperture $x_{\rm ap}$ around the ring $\delta x'_{\rm lim} = \frac{2x_{\rm ap}}{\sqrt{\beta_x\beta_{x,\rm d}}}$. Using the aperture of the vacuum chamber extrusion of 43 mm (the other smaller apertures around the ring are ignored for simplicity), then one gets a limiting kick angle of $\delta x' = 14$ mrad, which gives FSE_{stored} = -0.17.

The FSE limit for an injected beam is estimated approximately as follows. We consider only the trajectory centered on the photon beam axis and assume a parabolic negative trajectory through the whole length of the dipole. One equates the backtracked trajectory using the limiting FSE with the aperture of the dipole: $x_{\rm ap} = -(1+{\rm FSE})\frac{L_{\rm d}^2}{2\rho}$. For an aperture of 43 mm, we get ${\rm FSE}_{\rm extr} = -0.61$.

Comparing the two results above we see that $FSE_{gap} = FSE_{stored} - FSE_{extr} > 0.47$, and therefore the ranges of FSE for stored beam and extracted injected beam do not overlap. To the extent that the assumptions of these computations are correct, top-up injection is safe.

A better estimate of the FSE limit for an injected beam involves detailed tracking [1]. The full acceptance of the photon beamline and the unusual edge focusing due to the beam exiting the side of the dipole are included, both of which will weaken our case. However, particle tracking includes magnets and apertures upstream of the faulty dipole, which strengthen our case. These effects roughly cancel out, giving a value of $FSE_{extr} = -0.60$, which doesn't change the conclusion.

4.1 Effect of Orbit Correction

Steering magnets between the injection point and the shorted dipole will displace both the injected beam and the

stored beam within the same apertures, without changing the separation in phase space of the two beams. Though the FSE limits for the extracted injected beam and the stored beam may vary in an actual ring with arbitrary steering between the injection point and the shorted dipole, the quantity $FSE_{gap} = FSE_{stored} - FSE_{extr}$ is not expected to change, and any conclusions obtained for an unsteered beam are unchanged.

However, a steering magnet placed downstream of a shorted dipole may partially compensate the error on the dipole while leaving the extracted injected beam unchanged, since the injected beam never sees the steering magnet. This possibility will change FSE_{stored} for the worse while leaving FSE_{extr} unchanged.

A possible source of steering is a regular horizontal corector magnet, with a maximum kick for a 7-GeV beam of 1.2 mrad, which is small compared to the FSE_{stored} angle equivalent of 14 mrad. The other possible sources of such steering are quadrupole and sextupole magnets shorted in such a way that a strong dipole field is produced. To be conservative, we use the peak field value the multipole can produce when operating at maximum current of the power supply. The maximum kick for a 6-GeV beam produced by the sextupoles and quadrupoles ranges from 24 to 71 mrad. This at first appears to be a serious problem since the dipole field error could apparently be compensated to maintain a stored beam while the injected beam gets extracted out of the dipole.

However, the betatron phase difference between the dipole and the multipoles works in our favor to impede the ability of these shorted multipole elements to reduce the orbit distortion. The length of the dipole itself serves to provide some phase advance separation that reduces the ability of outside kicks to correct the orbit distortion produced by the dipole. An approximate expression for the maximum possible relative increase in FSE_{stored} aided by a steering element can be derived as follows. We start with the closed orbit formula and simplify the expression by making $\beta_x(s)$ constant and introducing one oscillatory term for the shorted multipole dipole kick, $\delta x'_{\rm M}$. Dropping common factors, we get two oscillatory terms,

$$-FSE(\pi/40)\cos\psi(s) + \delta x'_{M}\cos\{\psi(s) - \Delta\phi\},\$$

where $\psi(s) = \phi(s) - \phi_{\rm d} - \pi \nu_x$ and $\Delta \phi$ is the phase separation between the shorted dipole and the multipole steering element. The idea is to choose a value of $\delta x_{\rm M}'$ to minimize the effect of the FSE term. Solving graphically with phasors, the orbit oscillation for a given FSE can be reduced by a factor $\sin \Delta \phi$, and the corresponding correction angle is ${\rm FSE}(\pi/40)\cos \Delta \phi$. Thus for a given aperture, the FSE limit is increased in magnitude by factor $1/\sin \Delta \phi$ which is always greater than one.

Table 2 shows the estimated increased magnitude FSE_{stored} values, which range from the original -0.17 to -0.29. Since $FSE_{stored} = -0.61$, then we are still safe for top-up injection. Different lattices may have different

original FSE_{stored} and $\Delta \phi$'s, in which case the possible FSE_{stored} will have to be re-evaluated.

Table 2: Estimated increase of FSE_{stored}

Dipole	Location	$\Delta \phi/2\pi$	FSE _{stored}	$\Delta x'$
	,		 	mrad
AM	end of dipole	0.16	-0.20	7
AM	A:S3	0.18	-0.19	6
AM	A:Q4	0.23	-0.17	2
AM	A:Q5	0.25	-0.17	0
BM	end of dipole	0.10	-0.29	11
BM	B:S2	0.11	-0.27	10
BM	B:Q3	0.13	-0.23	9
BM	B:Q2	0.14	-0.22	9

5 INJECTION ENERGY ERROR

A higher energy beam injected into the SR will be deflected less by the dipoles, making it easier to extract down a photon beamline. A positive relative energy error, $\Delta p/p$, in an injected beam will change the FSE_{extr} to $(1 + \text{FSE}_{\text{extr}}) * (1 + \Delta p/p) - 1$.

The maximum energy output of the booster is 7.7 GeV. In addition, we installed an interlock for the storage ring main dipole current circuit that prevents top-up operation below 6 GeV. Therefore, the largest possible energy error is about 28%. Apertures also limit the energy error. There are one and a half sectors between the injection beamline and the first photon beamline, which ensures that an off-energy beam will experience a dispersion trajectory through apertures. The dispersion in the standard lattice is 188 mm at the 31-mm crotch absorber aperture, giving a realistic limit to the energy error of 16%.

The maximum $\Delta p/p$ of 16% reduces the magnitude of FSE_{extr} from -0.60 to -0.536, but does not change the conclusion that top-up is safe. Using the 28% value for $\Delta p/p$ results in FSE_{extr} = -0.488, which again does not change the conclusion.

6 ACKNOWLEDGEMENT

The authors wish to acknowledge the suggestions and advice of John Galayda (ANL), Jeff Corbett (SLAC), Al Garren (LBL), and James Safranek (SLAC).

7 REFERENCES

- [1] M. Borland, L. Emery, "Tracking Studies of Top-Up Safety at the Advanced Photon Source," these proceedings.
- [2] L. Emery, M. Borland, "Top-Up Operation Experience at the Advanced Photon Source," these proceedings.

DIAGNOSTICS AND CORRECTION OF THE ELECTRON BEAM TRAJECTORY IN THE CORNELL WIGGLER AT THE ACCELERATOR TEST FACILITY

V. Sajaev, ANL, Argonne, IL, Li-Hua Yu, A. Douryan, R. Malone, X. Wang, V. Yakimenko, BNL, Upton, NY

Abstract

High-Gain Harmonic Generation experiment is underway at the ATF. This experiment utilizes 41 MeV electron beam produced by photocathode electron gun and s-band linac. The strict requirements on electron beam trajectory in a 2-m long, 60 period undulator are essential for the success of the experiment. The simulation demands that trajectory errors should be less than 100 μm in the wiggler. Five pop-in monitors are used to measure the electron beam trajectory along the wiggler. HeNe laser defines reference line. We present our results and experience concerning different aspects of the electron beam alignment.

1 INTRODUCTION

Currently, a high gain harmonic generation experiment is being commissioned at the Accelerator Test Facility at BNL. This experiment is based on collaboration between BNL and the APS. A brief description and status of the experiment can be found in these proceedings [1].

One of the important requirements of the experiment is the electron beam trajectory tolerance inside the radiator - Cornell wiggler. Using multi-particle simulations with the TDA-3D code the gain as a function of the transverse rms displacement of the trajectory was studied [2]. Based on these simulations it was concluded that the displacement of the trajectory in the wiggler should be less than $100~\mu m$. In this paper we present the details of the beam trajectory measurement and correction in the Cornell wiggler.

2 BEAM LINE DESCRIPTION

The experiment layout consists of two wiggler magnets separated by dispersive section. First wiggler in combining with CO₂ laser radiation provides energy modulation of the electron beam. Dispersive section transforms the energy modulation to spatial bunching. Upon passing through the third wiggler (the Cornell wiggler) the prebunched electron beam radiates coherently. Main parameters of the Cornell wiggler are presented in the table below.

Undulator Period	3.3 cm
Number of Periods	60
Peak Magnetic Field	0.467 T

The horizontal trajectory of the beam calculated using measured magnetic field is shown on Figure 1. The averaged electron trajectory in the Cornell wiggler has offset of about 800 μ m relative to the axis of the beam line.

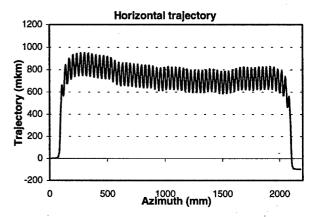


Figure 1 Horizontal trajectory in the Cornell wiggler calculated using measured magnetic field.

The gain of FEL depends on maintaining a precise phase relationship between the wiggle motion and the electric field of the radiation. It is necessary to effectively control the transverse betatron oscillations to satisfy this relationship. In a wiggler of conventional design there is no focusing in horizontal plane so external focusing is required. This focusing is provided by four-wire correctors mounted on the vacuum chamber inside the magnetic gap of the Cornell wiggler. Four separate corrector sections are distributed over the wiggler. These correctors can provide both dipole and quadrupole fields. The strength of the quadrupole correctors is adjusted to horizontal and vertical beta functions approximately constant along the wiggler and equal to 0.6 m. Lattice functions of the beam line are shown on Figure 2.

3 ELECTRON BEAM DIAGNOSTICS

Electron beam diagnostics are provided by pop-in monitors. There are 8 pop-in monitors along the beam line. Five of them are in the Cornell wiggler. These use coaxial actuators because access to the vacuum chamber is limited to only one side. Fluorescent screens are used for imaging. Each pop-in monitor is equipped with own CCD camera and can be connected to a frame grabber.

The CCD cameras and optics provide resolution of $10\mu m$.

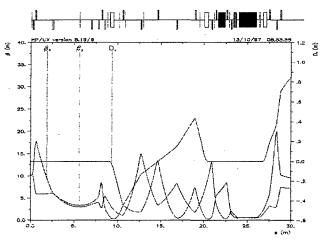


Figure 2 Beta functions of the beam line. First and third wigglers are black boxes.

A HeNe laser, which is aligned using two irises, defines the reference straight line. The HeNe laser beam position strongly depends on the temperature of the laser. For our case 1 degree C approximately corresponds to $20\mu m$ displacement at the pop-in monitor locations. There is no temperature stabilization for the HeNe laser so this dependence should be always kept in mind.

The HeNe laser is also used for calibration of the pop-in monitors. The laser beam is deviated with rotating thick glass, and frame grabber readings are compared with known laser displacement. It was found that the calibration is not constant along the monitor area, so we suppose that aluminium mirrors inside the vacuum chamber are not flat.

The HeNe laser beam is focused to have a wedge on 3^d monitor of the Cornell wiggler. The distance between focusing telescope and the 3^d monitor is about 10 m so the minimum possible beam size at that point is about 1 mm. On other pop-in monitors the laser spot a bit larger. Such big laser beam size places high demands on laser beam and pop-in monitor optics quality because it is necessary to determine the position of the centroid of the 1 mm spot with accuracy of order of ten microns.

3 TRAJECTORY CORRECTION

Magnetic measurements of the Cornell wiggler has demonstrated that the real magnetic field of the wiggler does not have considerable distortions and corresponds well to the designed values. So one can expect that the trajectory of the electron beam with initial coordinates corresponding to the focusing axis of the wiggler should be straight line. Therefore the problem of the trajectory correction in the Cornell wiggler is to find the initial conditions for the electron beam corresponding to the focusing axis. The HeNe beam, which design position should coincide with the focusing axis, defines this axis.

Despite the precise positioning of the irises used for the HeNe laser alignment, it turned out that the electron beam trajectory with the same initial conditions as the laser beam is not straight but has betatron oscillations. This means the HeNe laser beam position is not coincident with the focusing axis of the Cornell wiggler. In such situation, to correct the trajectory it is necessary first to determine the position of the HeNe laser beam relative to the focusing axis. To find this we assume that the HeNe laser beam is a straight line but with unknown position at the entrance of the wiggler. Then we measure difference between the electron beam trajectory and the HeNe laser beam for each pop-in monitor in the wiggler. After that we use calculated beam transfer matrices to fit the betatron oscillations of the electron beam. The variables for this fit are position and angle of the HeNe beam and angle of the electron beam at the entrance of the wiggler. The initial position of the electron beam can be found as sum of the HeNe beam position and measured distance between laser and electron beam at the first pop-in monitor. A least square fit procedure is used to determine the HeNe offset and the electron beam entrance coordinates. The examples of the measured and fitted vertical trajectories are presented on Figure 3. The vertical offset between the HeNe laser beam and the focusing axis is about 400 µm.

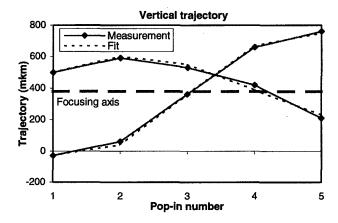


Figure 3 Examples of measured and fitted vertical trajectories. Focusing axis is also shown. The offset between the HeNe laser and the focusing axis is about 400µm.

After the HeNe offset is determined, the electron beam can be moved to the focusing axis using only correctors outside the wiggler. This procedure is implemented on Labview, and results of correction of the vertical trajectory are shown on Figure 4. Maximum errors for the corrected trajectory are $\pm 50\mu m$, which satisfies the requirements.

Same technique can be applied to horizontal trajectory but there are few obstacles that make it more difficult. According to Figure 1 the trajectory on first and fifth pop-in monitors (which are situated right before and after the wiggler) lies on a beam line axis, while on other three monitors it lies in the wiggle motion region with $800~\mu m$ average offset. Longitudinal positions of these three monitors with respect to the wiggle motion are also known with moderate accuracy. That's why it is useful to have trajectory measurement not relying on the HeNe laser.

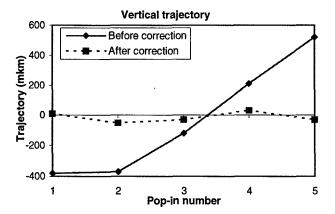


Figure 4 Vertical trajectory before and after correction.

The main purpose of the HeNe laser in our case is to define zeros of the pop-in monitors. Without the laser another definition of zeros is necessary. In the magnetic field of the wiggler there is no natural focusing in the horizontal plane so the only candidate for the zeros definition is the focusing axis of the 4-wire correctors.

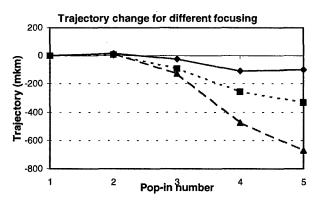


Figure 5 Relative trajectory change due to focusing variation.

To find the trajectory without the HeNe laser we vary the focusing in the Cornell wiggler and measure the corresponding beam position changes. Example of these measurements for different focusing is presented on Figure 5. The difference in beam trajectories for various focusing in the wiggler depends on the focusing properties of the wiggler and initial coordinates of the electron beam. Comparing measured beam behaviour with calculated one the unknown beam position at the entrance of the wiggler can be found.

Least squares are used to fit measured data and to find position and angle of the electron beam at the entrance of the wiggler. A singular value decomposition method is used to find inverse matrix in the least squares. The results of the trajectory correction are shown on Figure 6. The maximum errors of the corrected trajectory in this method are $\pm 30\mu m$ in both horizontal and vertical planes.

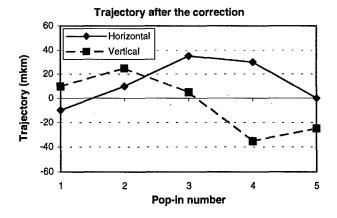


Figure 6 Results of the correction using the focusing variation for horizontal and vertical planes.

4 CONCLUSION

We present the electron beam diagnostics and the trajectory correction schemes for the HGHG experiments. The experiment requires the beam trajectory in the wiggler magnets to be straight line within 100 μm , and our correction schemes allow achieving such accuracy. However using HeNe laser as a reference line demands surprisingly high quality optical elements in pop-in monitors to achieve same accuracy as in methods using focusing variation in the wiggler.

In our case the focusing variation method demonstrates better accuracy of correction than the first method relying on the HeNe laser. The main problem of the first method seems to be in the determination of the HeNe beam positions. Due to long distance between telescope, which focus the HeNe beam, and pop-in monitors the minimum possible laser beam size on the monitors is about 1mm. To get good correction it is necessary to determine the HeNe beam position with accuracy of order of 10 μ m. But non-ideal optical elements (telescope, mirrors, filters, etc.) cause small laser image distortions which result in the errors in measuring of the positions of the HeNe beam centroid. Therefore the laser beam trajectory is not a straight line any more, and this defines limitation for correction scheme.

5 REFERENCES

[1] L.-H. Yu at al, "The status of the high gain harmonic generation free electron laser experiment...", these proceedings.

[2] L.-H. Yu, "Design parameters of the high gain harmonic generation experiment using Cornell undulator A at the ATF", BNL-65983, informal report.

THE NEW INJECTOR AND STORAGE RING FOR THE MAX-LABORATORY

Sverker Werin*, Åke Andersson, Mikael Eriksson, Mattias Georgsson, Greg LeBlanc, Lars-Johan Lindgren, Erik Wallén MAX-lab, P.O. Box 118, S-221 00 Lund, Sweden

Sandra Biedron

Advanced Photon Source, Argonne National Laboratory, Argonne, IL 60439

Abstract

In December 1998 the FRN - The Swedish Council for Planning and Coordination of Research - decided to fund a new injector and storage ring for the MAX-laboratory. The system will consist of a 50-MeV linac, a 600-MeV booster synchrotron, and a 600-MeV storage ring for VUV undulator beamlines. The system will replace an old 100-MeV racetrack microtron and will inject the two existing storage rings: the 550-MeV MAX I and the 1.5-GeV MAX II, as well as the new 600-MeV-storage ring. The linac injector will also be designed with intentions to provide electrons for a future infrared free-electron laser (IR-FEL) facility. The detailed design of the system began in January 1999 with a planned first beam in the summer of 2001.

1 OVERVIEW

The current MAX-lab accelerator system [1] consists of a 100-MeV racetrack microtron used as injector for the 550-MeV storage ring, MAX I. MAX I is able to store electrons for synchrotron radiation production, stretch

Table 1. Pre-injector system

GUN	Thermionic rf gun	
	Energy	~ 2MeV
	Micropulse length	≤ 10 ps
	rf frequency	3 GHz
	Charge/micropulse	0.2 nC
	Normalised emittance	15 mm mrad
LINAC	Energy range	25-50 MeV
	Macropulse current	10-100 mA
	Rep. rate	1-50 Hz
	rf frequency	3 GHz
	Max. rf power	35 MW
	Normalised emittance	15 mm mrad

Most values are preliminary

them in pulse-stretcher mode for nuclear physics research, or serve as an injector supplying a 500-MeV beam to MAX II. MAX II, used exclusively for synchrotron radiation production, accepts beam from MAX I and is able to further accelerate it to 1.5 GeV.

Although the injector system provides a quality beam, the aging, twenty-year old, radiation damaged racetrack microtron needs replacement to ensure reliable operation in the future.

A new injector system is being designed but has a number of constraints for the various modes of operation. These include,

- ♦ Injection into the MAX II storage ring without entering MAX I.
- ♦ Full energy injection into MAX I (550 MeV).
- ◆ Increased energy of MAX I in pulse-stretcher mode (from 100 to 250 MeV).

Also, additional desires arose, including

- ♦ Additional space for VUV-beamlines.
- Drive beam for an IR-FEL.
- ♦ Capabilities for a storage ring (SR) UV-FEL.

The injector upgrade concept, presented to the FRN - The Swedish Council for Planning and Coordination of Research, consists of a thermionic electron gun, a normal-conducting 50-MeV linac, a 600-MeV booster and, *on top of* the booster, a 700-MeV storage ring. The rings both have a 33-m circumference and will be placed in an available area, between the two existing storage rings. The linac system, however, will be placed in a presently unoccupied space in the basement.

^{*} E-mail: sverker.werin@maxlab.lu.se

2 THE GUN AND LINAC-SYSTEM

The gun and linac parameters can be found in Table 1. The linac will consist of a 3-GHz accelerating structure identical to the ones for the Swiss Light Source (SLS) injector and the normal-conducting TESLA alternative [2]. A 35-MW klystron will feed the linac with sufficient rf power to accelerate 200 mA to 50 MeV. Until recently, it was assumed that a standard thermionic dc gun with a 500-MHz pre-buncher and a 3-GHz buncher would be used. Now, however, a thermionic rf gun with a magnetic compressor is under examination, since this would eliminate the need for a pre-buncher and buncher. This pathway seems most promising, since both SSRL [3] and APS [4] routinely operate with such guns.

3 THE BOOSTER

The booster concept was chosen as a convenient and reliable way to provide 500-MeV electrons for the storage rings at the laboratory.

3.1 Lattice

A combined function four-fold structure, as illustrated in Figures 1 and 2, will be used. The quadrupoles are focussing in the horizontal direction and the dipole magnets have a gradient for vertical focussing. Sextupole components are included in the quadrupole and dipole magnets to provide a positive chromaticity. The booster lattice parameters are given in Table 2.

Table 2. Booster parameters

Max energy	600 MeV	
Injection energy	50 MeV	
Circulating current	40 mA	
Circumference	≈30 m	
Straight section length	3.1 m	
Mom comp factor	0.045	
Nat hor emittance	31 nmrad (@600MeV)	
Quadrupoles	L=0.25/0.4 m; K:3.998;	
	R=2 cm	
Dipoles	L=1.3333 m; n:1.8836;	
	g/2=1 cm	
Hor admittance	26 mm mrad	
Vertical admittance	5 mm mrad	
Momentum acceptance	1%	
Rep rate	10 Hz / 1 Hz	

Most values are preliminary

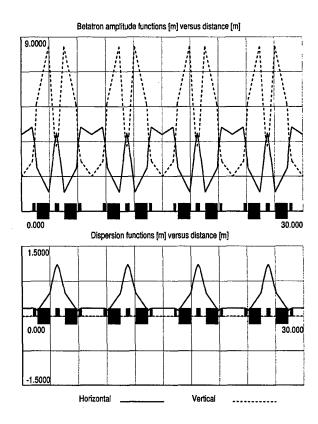


Figure 1. The lattice for both booster and storage ring.

4 THE STORAGE RING

The storage ring is designed to provide a simple and inexpensive way to provide additional VUV beamlines. Here, a lattice combining compactness and low emittance, also applicable to the booster, was created by allowing dispersion in the straight sections and a gradient in the bending magnets thus enhancing synchrotron radiation damping. The storage ring parameters are given in Table 3.

Since this ring has a lattice similar to the booster, it will be conveniently placed on top of and injected by the booster. Using the same girders will save space and make survey and alignment less time consuming. Also, producing a "double set" of magnets will minimize the production cost. To avoid crosstalk between the magnetic fields of the two rings, however, a separation distance of approximately 40 cm is necessary.

5 OPERATION MODES

5.1 Injector for MAX II

The quality of an injector for MAX II is defined by its emittance. The booster will operate at 1 Hz and 500 MeV, providing significant improvement regarding both

Table 3. Storage ring parameters

Operating energy	700 MeV
Circulating current	200 mA
rf frequency	100 MHz
rf voltage	0.21 MV
Half bucket height	1%
Energy spread (natural)	0.4*10-3
Bunch length (natural)	0.75 cm
Lifetime: Touschek	0.27 Ah @ 10% coupling
Vacuum	8 h @ 1 nTorr CO
Emittance	26 nm rad (@700 MeV)
Beam size in SS	0.35*0.07 mm2

Most values are preliminary

the repetition rate of the injection and the injected current.

5.2 Injector for MAX I

The MAX I storage ring will be injected at the full design energy of 500 MeV instead of the present 100 MeV. Given the low emittance injector design, more reliable operation is predicted, even at increasingly higher currents.

5.3 Storage ring mode

The storage ring was designed to have the same qualities as MAX II, a full third generation light source, implying excellent stability, low coupling, long lifetimes and a low emittance. To provide painless operation, injection will be made at almost full energy.

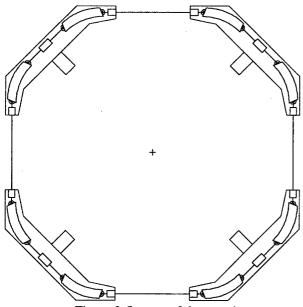


Figure 2. Layout of the two rings.

5.4 Nuclear physics operation

In pulse-stretcher mode, the operating energy of MAX I will be extended up to 250 MeV, at a repetition rate of 10 Hz. Since the new injector will be able to deliver higher peak currents, new nuclear physics experiments have been proposed.

5.5 FEL laser prospects

The linac will allow for a future IR-FEL facility. In order to supply the 10-µs rf pulse necessary for FEL operation, however, modifications to the klystrons and/or the gun may be required. The main demands placed on an FEL injector are the low energy spread and high peak current beams.

The storage ring will also be well tuned for a UV SR-FEL. This concept is presently being researched by an EU-sponsored collaboration at ELETTRA, in which MAX-lab is participating.

Neither of these two FEL concepts are included in the present funding.

6 RADIATION SHIELDING

The issue of radiation shielding is currently under investigation and may cause construction and/or design changes. This is due to possible structural limitations in the building intended to house the new injector system.

REFERENCES

- [1] Å. Andersson et al, Nucl. Instr. And Meth. A 343 (1994) 644
- [2] R. Brinkman et al, (eds) "Conceptual design of a 500 GeV e+e- Linear Collider with Integrated X-ray Laser facility", DESY 1997-048
- [3] M. Borland et al, "Performance of the 2 MeV Microwave Gun for the SSRL 150 MeV Linac", SLAC-PUB-5333, 1990
- [4] J.W. Lewellen, S. Biedron, A. Lumpkin, S.V. Milton, A. Nassiri, S. Pasky, G.Travish, M. White, "Operation of the APS RF Gun," Proceedings of the XX International Linear Accelerator Conference, Chicago, Illinois, August 23-28, 1998, to be published.

PERFORMANCE OF A RADIO-FREQUENCY-BASED STREAK CAMERA

A.V. Aleksandrov¹⁾, N.S. Dikansky¹⁾, V. Guidi²⁾, G.V. Lamanna³⁾, P.V. Logatchov¹⁾, S.V. Shiyankov¹⁾, L. Tecchio⁴⁾

¹⁾Institute of Nuclear Physics, 630090 Novosibirsk, Russia.

²⁾Dipartimento di Fisica dell'Università and INFN, I-44100 Ferrara, Italy.

³⁾Dipartimento di Fisica dell'Università and INFN, I-70125 Bari, Italy.

⁴⁾Laboratori Nazionali di Legnaro INFN, I-35020 Legnaro, Italy.

Abstract

We have experimented with a streak camera based on radio-frequency deflection of the electron beam. The time resolution was measured to lie in the sub-ps domain. The method also allowed considerable simplification of triggering, weaker dependence on space-charge within the electron beam, high modularity, and ease of implementation. We discuss experimental results and future prospects.

1 INTRODUCTION

This paper is devoted to illustrate the setting up of a RFbased streak Camera (RFC). Beam deflection was accomplished by replacing the standard deflecting plates of a conventional streak camera (SC) by a RF cavity located just after the accelerating optics.

The magnetic field in the cavity imparts a transverse force to incoming electrons, whose direction depends on the time at which each individual electron enters the cavity, i.e. on the RF-phase experienced by an incoming electron (circular scanning) [1]. The high sweep speed, which is possible by the method, envisaged sub-ps resolution [2]. The other components of a streak camera keep unchanged.

The circular deflection of an electron beam can be performed by transverse magnetic field of TM_{110} mode with circular polarization in a cylindrical cavity. Circular polarization is provided by exciting two orthogonal modes shifted by $\pi/2$ rad in phase.

A complete treatment on theoretical basis for the RFC can be found in Ref. [3].

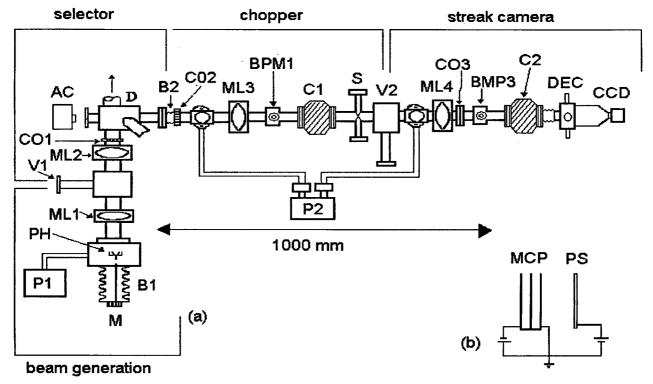


Figure 1 Schematic drawing of the experimental apparatus

2 EXPERIMENTAL

The setup of the experiment is sketched in Fig. 1. It basically consisted of three parts: electron gun, chopper-system, and RFC.

In order to test the time resolution of the RFC, one had to provide a sub-picosecond electron bunch. Since the existing GaAs photo-gun operated at 40 kV [4] was unable to deliver electron bunches shorter than 60 ps, a system to form a sub-ps electron bunch was implemented. This was a chopper consisting of deflecting cavity CI, drift tube, and slit S (see Fig.1(a)). An iris with 400 μ m aperture was installed to reduce transverse beam size at the entrance. The slit width of the chopper could be varied through micrometric control.

The deflecting cavity was axially symmetric and made of OFHC copper. The electromagnetic field of the TM_{110} mode inside the cavity was excited through magnetic loop. The bunch outcoming the cavity was swept on the horizontal plane and hit onto a vertical slit. In our case a minimum beam size of about 200 μ m provided a minimum bunch length of 0.7 ps at the exit of the chopper system. This way the electron bunch passing through the chopper cavity was sufficiently short to calibrate the RFC.

The measuring part of the experimental apparatus—strictly speaking—the RFC consisted of deflecting cavity C2, drift tube, detector DEC and magnetic lens ML4. Cavity C2 had the same design as the chopper cavity (C1) but was fed by two orthogonal TM_{110} modes, resulting in a rotating magnetic field orthogonal to the cavity axis. Each mode was excited by separate magnetic loop. The two loops were geometrically at right angle and fed by two RF amplifiers, reciprocally shifted by $\pi/2$ rad in phase. The resonant frequency of each mode could be separately adjusted by means of two piston tuners.

Deflected electrons passed through the drift tube and were collected by position sensitive detector. This was a two-stage MCP coupled to a circular phosphor screen 28 mm in diameter (see Fig.1(b)). High voltage of 4 kV was applied between the backside of the MCP and the screen. The image on the screen was read out by a charge coupled device (CCD) camera and acquired by computer. The overall resolution of the detector was about 60 μ m (rms) mainly limited by the MCP.

A pulsed RF-power amplifier with three separate channels was used to feed both the chopper and the measuring cavities. Output power up to 800 W could be independently controlled on each channel. Phase difference between the two channels could be varied by coaxial phaseshifter. The signal of the mode-locking RF generator of the laser was multiplied by 64 in frequency and used as an input for the amplifier. This scheme provided synchronization between electron bunch and chopper phase.

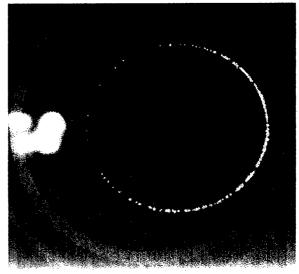


Figure 2. Image of a circularly scanned beam on the phosphor screen. The chopper cavity is switched off.

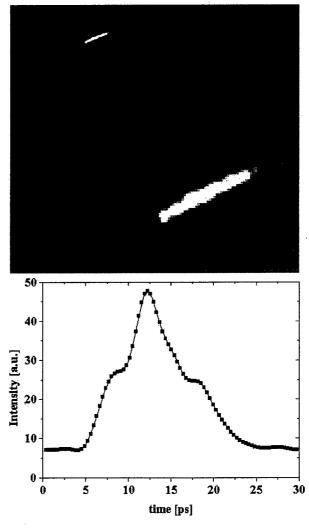


Figure 3. Image of the electron beam on the phosphor screen (magnified in the inset) and its cross-section when the chopper cavity is switched on.

3 RESULTS

We firstly adjusted the optics to focalize the beam as much as possible onto the screen. It was measured that the profile of the spot exhibited an rms size of 1.7 pixels, i.e. about 100 µm—limited by beam emittance.

Then the RF power was fed on the cavity and phase shift between the two modes was optimized to achieve an arc of a circumference for the beam trace as shown in Fig. 2. The arc was not a complete circumference because the laser pulse was shorter than one RF period. The radius of deflection drawn by electrons on the screen is an important parameter since it is bounded up to the resolution of the instrument. Measuring the radius allowed one to calibrate the RFC: here a diameter of 314 pixels was measured, corresponding to 18.5 mm.

The response of the RFC to a short electron bunch was tested using the chopper system and the adjustable slit. As the RF power on the chopper cavity was supplied, short electron bunches entered the RFC and were analyzed as shown in Fig. 3, where a beam-trace image and its crosssection are shown. The resolution of the instrument was sufficiently high to follow the profile of the electron bunch.

The ultimate capability of the RFC in terms of resolution can be determined by probing through even shorter electron bunches. As the RF power on the chopper cavity was raised, the outcoming electron bunch became shorter, like illustrated in Fig. 4. Error bars are rms values of the distribution obtained after a large number of measurements. The dashed line represents the resolution limit achievable by the instrument in the present configuration, i.e. 700 fs (rms).

4 DISCUSSION

On the basis of the experience we gained during execution of measurements, the RFC exhibits the following advantages:

1) Microsecond accuracy for triggering is needed in contrast with normal SCs where triggering may often be a serious problem. In addition the position of the trace on the screen may provide information on the phase of the incoming bunch with respect to the RF field.

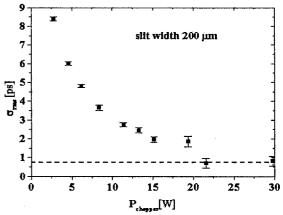


Figure 4. Dependence of bunch length on RF power

- 2) The accelerating voltage of conventional SC is usually no higher than 20 kV. This means that space charge may have non-negligible effect and limit the performance of a SC. On the contrary, since electron deflection is driven by magnetic field for the RFC, a bending force proportional to the bunch velocity is exerted. Operation up to 60 kV was proven, leading to significantly weaker dependence on space charge.
- 3) The RFC consists of separate modules: electron source, electron gun, deflecting system and detector. Each module can be conceived to be a part of a general-purpose instrument.
- 4) The RFC was shown to feature a resolution no worse than 700 fs (rms). However it is far from any physical limitation and further improvement should be obtained by increasing the angle of deflection or the screen size. Alternatively one may resort to higher frequency cavities.

A newly designed compact RFC based on the same RF cavity as we used is currently under test (Fig. 5). Expected resolution should be lower than that we measured due to better beam quality.

5 REFERENCES

- [1] A.V. Aleksandrov et al., Rev. Sci. Instrum. 66 (1995) 3363
- [2] V. Guidi et al., Meas. Sci. Tech. 6 (1995) 1555
- [3] A.V. Aleksandrov et al., submitted
- [4] A.V. Aleksandrov et al., Phys. Rev. E. 51 (1995) 1449.

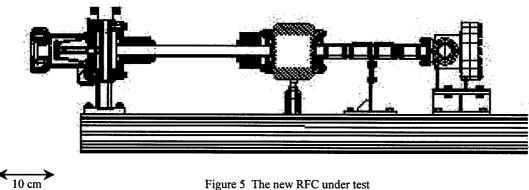


Figure 5 The new RFC under test

NEW SIMULATION RESULTS FOR THE S-DALINAC ELECTRON SOURCE*

U. Becker, <u>P. Schütt</u>, S. Setzer, A. Skocic, T. Weiland,
Theorie elektromagnetischer Felder, TU-Darmstadt
R. Eichhorn, H.-D. Gräf, S. Kostial, A. Richter, Institut für Kernphysik, TU-Darmstadt

Abstract

For the operation of its mid-infrared FEL the superconducting electron accelerator S-DALINAC has to produce bunches with a charge of 6 pC and a duration of 2 ps FWHM. In order to achieve these figures a subharmonic injection scheme was added to the 3 GHz cw accelerator. The electron gun consists of a grid controlled thermionic cathode on a 250 kV terminal. It produces electron pulses with a charge of 20 pC and a width of 800 ps FWHM at a repetition rate of 10 MHz. For a reliable simulation of the subsequent parts of the injector (600 MHz chopper/prebuncher section and a superconducting linac consisting of 2- and 5-cell capture cavities and two 20-cell accelerating structures) the beam parameters at its input have to be known as exactly as possible.

Since we expect that due to the pulsed operation of the gun, longitudinal space charge effects might be important, the electron gun and the 250 kV electrostatic acceleration have been studied using the 2 1/2 dimensional PIC code MAFIA-TS2, and the tracking code GPT.

This calculation takes into account the time structure of the beam and yields results like bunch shape at the gun exit, correlated and uncorrelated energy spread, as well as the transverse emittance.

The results of the simulation as well as a comparison with measurements of the transverse emittance and the electron pulse length at the exit of the electrostatic acceleration will be presented in this paper.

1 MOTIVATION

The generation of an electron beam with a peak current of 2.7 A for the operation of the FEL is a big challenge for the S-DALINAC, originally designed for a cw beam with low bunch charge. The necessary bunching in the injector was calculated before[1] using beam parameters at the exit of the gun resulting from a time independent simulation (DC emission). While transverse beam parameters were determined earlier, the longitudinal phase space was not known.

However, these longitudinal parameters are essential for the achievable peak current and therefore for the laser operation. The simulation results presented in this paper, which include energy spread and bunch length, are crucial for understanding particle dynamics in the buncher section and injector linac. Therefore extensive tracking calculations for these sections already have been started.

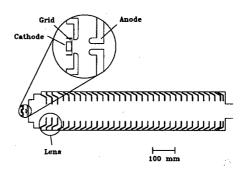


Figure 1: The S-DALINAC electron source.

The layout of the electron gun is shown in Fig. 1. The time structure of the emission from the thermionic gun is controlled by a grid in a distance of 150 μ m. The pulse length is $\sigma_t = 300$ ps. Downstream of the anode, the beam is focused by an electrostatic lens and then accelerated to 250 keV in an 80 cm long electrostatic cascade.

2 SIMULATION METHODS

For the simulation of this electron gun, it is necessary to include space-charge forces. Since we are interested in longitudinal phase space, we must choose a program, that works in time domain. Two different computer codes were used for the calculation:

2.1 The PIC Codes MAFIA-TS2 and -TS3

TS2 and TS3 are the names of the Particle in Cell (PIC) modules in MAFIA[2]. They have been used successfully for the computer aided design of klystrons and other RF sources[3]. The PIC programs solve Maxwell's equations in the time domain with a FDTD algorithm and in parallel, selfconsistently, integrate the equations of motion of the charged particles. These particles, in turn, are the source of the electromagnetic fields.

TS2 is the axisymmetric, two dimensional version, TS3 works with three dimensional cartesian coordinates. Both are fully relativistic and due to their basic physics algorithm a priori include all interaction of the charged particles and electromagnetic fields. Therefore, space charge, self magnetic fields, wake fields etc. are all included. Furthermore,

^{*} Supported by DFG under Contract Nos. Ri 242/12-1, SCHU 1241/1-1 and through the Graduiertenkolleg "Physik und Technik von Beschleunigern".

[†] Email: schuett@temf.tu-darmstadt.de

both codes can use precalculated fields, which are provided by other solvers in the MAFIA package.

However, these PIC codes are very expensive to use. Especially, for very low particle energies close to the cathode, a fine resolution of the calculation grid is necessary and many particles must be used. Therefore, we also used a faster tracking code and compared the results.

2.2 The Tracking Code GPT

The General Particle Tracer (GPT)[4] code is a well established 3D tracking program. It includes the calculation of space-charge forces in a point-to-point model. Its integration method is based on a fifth order embedded Runge-Kutta method with adaptive step size control.

The field pattern in the gun was calculated in MAFIA-S and read into GPT via our own interface.

3 RESULTS OF THE SIMULATION

3.1 Initial Conditions

The thermionic cathode is operated at a temperature of 1100° C. Therefore the mean energy of the electrons at emission is $k_BT = 0.1$ eV. The normalized transverse rms emittance at the cathode surface (radius R) is[5]:

$$\tilde{\varepsilon}_{n,th} = \frac{R}{2} \left(\frac{k_B T}{mc^2} \right)^{1/2}$$

in our case $\tilde{\varepsilon}_{n,th} = 0.33$ mm mrad.

The control grid in front of the cathode also has a defocusing effect on the beam. In order to reduce the calculation cost, this effect was calculated in a separate simulation in TS3, whereas the complete gun was calculated in TS2, exploiting the rotational symmetry.

Although the TS3 calculation includes space charge effects, it is in good agreement with an analytical expression for the normalized rms emittance acquired by a beam after passing the wire mesh, which is given by Reiser[5]:

$$ilde{arepsilon}_{n,g} = rac{Ra}{4} \left(rac{2eV_g}{mc^2}
ight)^{1/2} rac{|E_2 - E_1|}{4V_q},$$

where 2a is the distance between mesh wires, V_g the grid voltage, and E_1 and E_2 the electric field on either side of the mesh. In our case $\tilde{\varepsilon}_{n,g} = 0.35$ mm mrad.

If the intrinsic thermal emittance is included, one obtains for the normalized rms emittance at the cathode grid the result

$$\tilde{\varepsilon}_n = \left(\tilde{\varepsilon}_{n,th}^2 + \tilde{\varepsilon}_{n,g}^2\right)^{1/2}.$$

3.2 Simulation with MAFIA-TS2

The TS2 simulation may use the result of the TS3 calculation as initial condition. However, in order to reduce the number of macro particles in the calculation, the beam was initialized with zero emittance. Nevertheless, we used more than 70000 macro particles and the mesh step for the

FDTD grid was 250 μ m. Since this is larger than the distance of the control grid from the cathode, the initial energy of the electrons was set to 10 eV, which corresponds to the grid voltage at the center of the bunch. Fig. 2 shows the results of this calculation.

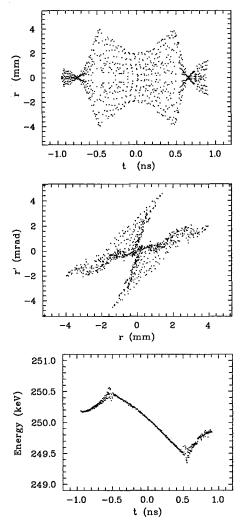


Figure 2: Distributions as calculated by MAFIA-TS2 at the exit of the gun. From top to bottom the figures show the radius as a function of time, the transverse phase space and the longitudinal phase space.

All plots show the influence of the space charge. Especially, a correlated energy spread is acquired by the bunched beam: particles in the head of the bunch are accelerated by space charge forces, while particles in the tail are decelerated. This effect is much larger than the uncorrelated energy spread. Another space charge effect can be observed in the transverse plane: particles in the head and tail of the bunch are focused more strongly than those in the center. This increases the projected emittance; however, those particles will be discarded at the chopper and therefore do not contribute to the beam quality in the FEL. The numerical results are summarized in table 1. When the initial emittance is included, the transverse emittance increases to 0.86 mm mrad. Since the axisymmetric cal-

culation in TS2 excludes any misalignment effects, these values give a lower limit for the actual emittance.

normalized transverse rms emittance	0.7 mm mrad
normalized longitudinal rms emittance	51.3 eV ns
beam radius σ_x	1.5 mm
beam divergence $\sigma_{x'}$	0.8 mrad
pulse length σ_t	332 ps
energy spread σ_E	155 eV

Table 1: Beam parameters at the end of the electrostatic cascade according to the simulation with MAFIA-TS2.

3.3 Simulation with GPT

The calculation with GPT was started with the parameters given above for the thermionic cathode. The influence of the control grid was neglected. 1000 particles were used.

Table 2 shows the numerical results. GPT yields the same space charge effects discussed above with a tendency to higher uncorrelated momentum and energy spread. An additional calculation starting with 10 eV particle energy and zero emittance yielded similar results, confirming that this is not a physical effect in the low energy part, which was neglected in TS2.

normalized transverse rms emittance	1.55 mm mrad
normalized longitudinal rms emittance	248 eV ns
beam radius σ_x	1.1 mm
beam divergence $\sigma_{x'}$	1.4 mrad
pulse length σ_t	294 ps
energy spread σ_E	228 eV

Table 2: Results of the simulation with GPT.

4 MEASUREMENT OF BEAM PARAMETERS

In order to check the predictions of the simulations and to verify the validity of the assumptions made therein, beam parameters were measured in the front section of the injector beamline of the S-DALINAC.

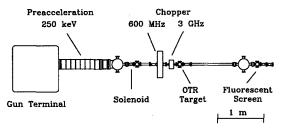


Figure 3: Setup for the measurement of the beam parameters.

The transverse parameters were determined a short distance downstream of the electrostatic acceleration tube (see fig. 3). The two-dimensional intensity distribution of the beam on a thin aluminum foil was measured as a function of the focal strength of the solenoidal lens located upstream, by detecting and recording the visible part of the

emitted transition radiation (OTR) by a standard CCD camera, framegrabber board, and a PC. Fitting a parabola to the measured beam sizes (see fig. 4) yields the complete set of transverse beam parameters at the location of the lens. The resulting figures for normalized emittance, beam radius, divergence, and correlation are given in the inset in fig. 4.

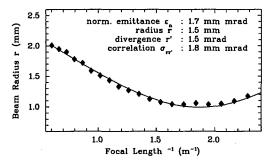


Figure 4: Beam size as a function of the inverse focal length of the solenoid lens. From the fitted curve, the transverse beam parameters were obtained.

In the front end of the injector beamline of the S-DALINAC diagnostics for the energy spread of the 250 keV beam is not available. The pulse length however could be determined by deflecting the beam vertically by a 600 MHz and horizontally by a 3 GHz chopper cavity. From the resulting Lissajous figures observed on a fluorescent screen further downstream (right edge of fig. 3) a pulse duration of 600–700 ps (FWHM) was deduced.

5 CONCLUSION

We used two different programs to simulate beam dynamics in the S-DALINAC electron gun. Both yield similar results on space charge effects. The measured values for the transverse phase space and the pulse length are in remarkably good agreement with the simulation results. For the first time, longitudinal phase space was considered in the gun of the S-DALINAC.

We are therefore convinced that the results obtained here can be used successfully in simulations of the fairly complex beam dynamics in the remaining sections of the S-DALINAC injector.

6 REFERENCES

- K.Alrutz-Ziemssen et.al., Nucl. Instr. Meth. A304 (1991), p.300.
- [2] The MAFIA collaboration, User's Guide MAFIA Version 4.00, CST GmbH, Lauteschlägerstr. 8, D-64289 Darmstadt, Germany.
- [3] U.Becker, M.Dohlus, T.Weiland, Three Dimensional Klystron Simulation, Particle Accelerators, 1995, Vol. 51, pp. 135-154.
- [4] GPT User Manual, Pulsar Physics, Flamingostraat 24, 3582 SX Utrecht, The Netherlands.
- [5] M.Reiser, Theory and Design of Charged Particle Beams, John Wiley & Sons, New York, 1994.

THE APT SCRF CRYOMODULE: PRESENT STATUS AND POTENTIAL FUTURE PLANS

R. Bourque[#], J. Gioia, W. Homeyer, J. Kuzminski, D. Richied, P. Smith, and J. Tooker, General Atomics, San Diego, CA
B. Campbell and K. C. D. Chan, LANL, Los Alamos, NM

Abstract*

A prototype cryomodule for the $\beta=0.64$ superconducting rf linac is being developed at Los Alamos National Laboratory (LANL) for the Accelerator Production of Tritium (APT) program. This design is aimed toward proof-of-principle testing and forms the starting point for the large-scale APT plant. Several alternate design options are also being explored to improve manufacturability and maintainability, reduce cost, increase reliability, and increase availability of qualified commercial suppliers. Progress to date on the prototype cryomodule is summarized in this paper, as are some interesting possible design improvements.

1 THE ENGINEERING DEVELOPMENT AND DEMONSTRATION PROGRAM

The APT high-energy proton linac uses superconducting radio frequency (SCRF) technology [1]. It has two sections of cryomodules designed to accelerate proton beams with betas of 0.64 in the first section and 0.82 in the second. Each cryomodule contains two, three or four solid niobium cavities. Each cavity has two rf power couplers.

The scope of work for the SCRF High Energy Linac Engineering Development and Demonstration (ED&D) program includes the design, fabrication, and testing of prototypes of the cavities, power couplers, and cryostats. The goal is to provide integrated design and performance data for very high rf power and beam currents.

The APT superconducting cavities, which will be fabricated by industry, are made of solid sheet niobium having a residual-resistance-ratio (RRR) value of ≥250. They are contoured five-cell cavities with elliptical irises, optimized to operate reliably at an accelerating field ranging between 4–6 MV/m. They will be housed in individual liquid helium vessels and operated at 2.15 K. Each power coupler is required to transmit 210 kW of rf power to the cavity. Each coupler has a dual room-temperature alumina RF window followed by a 50-ohm coaxial line. Because of the high power, it is important to optimize cooling and RF matching of the couplers.

The cavities, helium vessels and couplers are housed in a cryostat that supplies insulating vacuum and structural support, and provides the access required for a prototype. Fig. 1 shows a cutaway view of the cryomodule assembly.

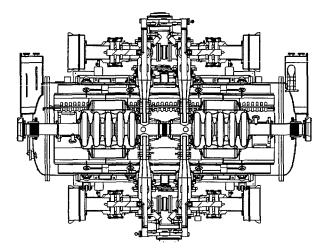


Figure 1: The assembled ED&D cryomodule seen from above with a section cut at the beamline. Clearly seen are the 5-cell cavities and the 4 power couplers.

2 CURRENT STATUS AND HIGHLIGHTS

In general, we plan to fabricate and test power couplers and cavities through March, 2000. They will be installed into the cryostat and be ready for integrated testing by October, 2000. Each item is briefly described below.

2.1 Five-Cell Cavity Fabrication

Four five-cell β =0.64 solid niobium cavities are being been fabricated at *Centre de Recherche en Calcul Appliqué* (CERCA). The cavities will be installed in titanium helium vessels. The vessel bulkhead assemblies with bellows have been completed and sent to CERCA. Edged-welded titanium bellows used in these assemblies are being lifetime tested at *Thomas Jefferson National Accelerator Facility*.

^{*} Work supported by DOE contract DE-AC04-96AL89607

[#] Email: robert.bourque@gat.com

2.2 Power Coupler

To evaluate the developing designs of the power coupler and rf windows, a room-temperature test bed (RTTB) has been completed including data acquisition programming and instrumentation [2]. Parameters to be tested are coupler matching, peak power levels, rf losses, window-coupler power matching, and coupler adjusting. Tests on the first coupler will begin in early April.

2.3 Cryostat

Fabrication drawings for the two-cavity cryostat are nearing completion. Shown in Fig. 1, it is based on the CERN design and provides the necessary access and flexibility needed for an experimental facility. A full-size cryostat mockup has been built complete with mockups of the cavity/helium vessel, thermal shields, and power couplers. Procurement packages are expected to be released in October.

3 OPTIONS BEING CONSIDERED FOR THE APT PLANT

The primary objective of the ED&D program is to test high-level rf power couplers and the associated cavity assemblies integrated into a cryostat. The objective of the APT plant is to build these SCRF systems at minimum cost and operate them at very high availability for 40 year lifetime. Consequently, there are incentives to improve upon the ED&D design to meet these more demanding goals of fabricability, inspectability, reliability, and maintainability. Design alternatives are therefore being considered for the cavity, helium vessel, cryostat, power coupler window material and shape, window changeout schemes, and power coupler vacuum system. Each are briefly discussed below. They will be explored contingent on funding.

3.1 Cavity Fabrication

The cavity represents a large cost item in the cryomodule and every effort must be made to reduce cost consistent with achieving the desired Q at the expected MV/m. The solid niobium option was chosen as the most conservative with the most predictable performance. The sputtered niobium coating on copper may be worth revisiting to explore recent technology advances.

However, another possibility is vacuum deposition on copper of niobium supplied by pulsed laser ablation of a high-purity articulating niobium source. This would provide a middle ground between low-energy thermal vapor deposition and high-energy magnetron sputtering. Niobium ion energy levels would be 1-2 eV. With normal losses, a 10 micron layer could be deposited on

the inside of a 5-cell copper cavity in about four hours with a 5 J laser pulsed at 10 Hz. Use of high-expansivity copper rather than niobium for cavity structure eliminates the differential expansion issue if steel is used for the helium vessel.

3.2 Helium Vessel

An alternate, lower cost, helium vessel and cavity tuning structure is also being explored. Figure 2 shows the concept, which consists of 12-inch and 18-inch diameter pipes with elliptical heads and joined with two 8-inch pipe sections. The lower pipe contains the SCRF cavity. The liquid level is in the upper pipe, about 4-inches inches above the cavity.

The tuning structure consists of titanium rods and AISI 310S rings that connect the flange on the left with the tuner. The ED&D tuner design is used, which could be made from AISI 310S rather than titanium.

This vessel has about half the liquid helium and about one-third less metal volume than the ED&D design, but more ullage to allow helium expansion. The total weld length is reduced by about 20%, and all welds are simple pipe-to-pipe or pipe-to-head with no difficult weld intersections.

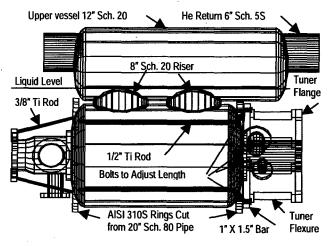


Figure 2: Alternate helium vessel that could be made of stainless steel pipe sections.

Rather than titanium, the vessel could be made of less expensive 310S austenitic stainless steel, which prevents martensite domains from forming due to cold-work, welding, or thermal cycling to liquid helium temperature. This alloy is much stronger than Grade 2 titanium used in the present vessel and eliminates titanium-to-stainless joints in the helium piping. An even stronger Inconel alloy could replace the titanium in the tuning bellows, allowing more flexibility and a greater fabrication base. The simpler shape and lower material and welding costs are expected to lead to significant cost reductions.

Thermal and fluid analyses, including the response to a sudden loss of beam tube vacuum, have shown the response of this vessel to be similar to that of the ED&D design. Stress analyses have shown acceptable stresses in the stainless-steel-to-niobium transition joint after cooling to 4 K, and low stresses due to a 45-psi helium pressure in the vessel.

3.3 All-Welded Cryostat

In order to obtain the required high availability for the APT plant, scheduled downtimes must be minimized. The elastomer seals used in the ED&D prototype are not expected to last the full plant life. Therefore, the option of welded, but accessible, seals is being explored for the cryostat and other joints. These seals, shown schematically in Fig. 3, are commonly used in vacuum applications. The seal material is only 1-2 mm thick and the seal weld can be cut and remade several times.

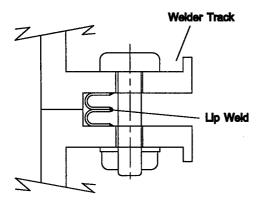


Figure 3: Typical lip-welded flange. This can be used on the cryostat covers and on cryogenic penetrations.

In the cryostat, these seals would be mounted on horizontal rigid flanges above and below the beamline, as seen in Fig. 4. Provision can also be made for elastomer seal grooves to be used during system checkout. Coated metal seal rings are also a possibility which, unlike elatomers, do not have to be removed prior to seal welding.

The upper and lower covers, which look like auto engine oil pans, can be removed allowing considerable access to the interior. Space must be allowed for the automatic welder/cutter, which results in a bowing out of the support structure. The rf waveguides are not in place when the lip seal is welded. The cryogenic bayonets can be placed on the upper cover in the middle of the cryomodule where there is space both inside and out. This facilitates disassembly and maintenance functions.

3.4 Power Coupler Components

Replacement of failed power coupler windows could severely reduce plant availability. Therefore a program has been established to explore windows with very long design life along with procedures for quickly replacing those that do fail. Being examined are other window materials, such as aluminum nitride, surface treatments and coatings, other shapes, e.g., planar, and waveguide valves that maintain cavity vacuum during replacement.

There are two other options for the power coupler vacuum pumps besides ion and turbo pumps: (1) cryogenic pumps with a specifically designed gettering arrays, or (2) a system of non-evaporating getters (NEG). The cryopumps would not use built-in compressors and expanders but would take a small portion of the main

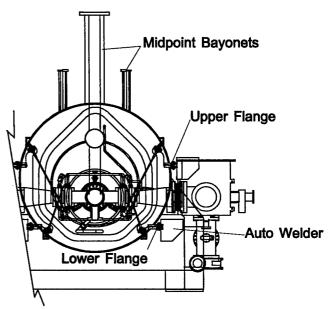


Figure 4. End view of optional cryomodule showing horizontal flanges containing lip welds.

cryomodule cryogen supply. Either option would consist of pumps capable of regeneration during operation. Since neither option has moving parts, they should meet the requirements of long life with low maintenance.

4 REFERENCES

- [1] G.P. Lawrence, "High-Power Proton Linac for APT; Status of Design and Development", presented at the International Conference LINAC '98, Chicago, IL, August 23-28, 1998.
- [2] J. Gioia et al, "A Room-Temperature test bed for Evaluating 700 MHz RF Windows and Power Couplers for the Superconducting Portion of the APT Linac", presented at this conference.

A 0.5 MW / 10 Hz OPTION OF THE SPALLATION SOURCE AUSTRON

Ph. Bryant¹⁾, E. Griesmayer²⁾, E. Jericha³⁾, H. Rauch⁴⁾, M. Regler⁵⁾, H. Schönauer¹⁾

¹⁾ CERN, PS Division, Geneva, Switzerland, ²⁾ Fachhochschule Wiener Neustadt, Austria, ³⁾ Institut für Kernphysik, Technische Universität Wien, Austria, ⁴⁾ Atominstitut der Österreichischen Universitäten, Wien, Austria, ⁵⁾ Institut für Hochenergiephysik der Österreichischen Akademie der Wissenschaften, Wien, Austria

Abstract

In 1993-94 a feasibility study for AUSTRON, a neutron spallation source, was made on behalf of the Austrian Ministry of Science and Research. At that time, the machine was a synchrotron cycling at 25 Hz and delivering an average beam power of 205 kW at 1.6 GeV. An option to double the power by doubling the frequency was foreseen. Now a more ambitious development of the original concept is proposed that aims at 0.5 MW at 1.6 GeV, pulsed at either 50 Hz or 10 Hz. The slow repetition rate is achieved by the addition of a storage ring holding four consecutive (single bunch) pulses from the 50 Hz synchrotron until a fifth pulse is accelerated and transferred to the target with the four stored ones. In this way, an energy per pulse of 50 kJ (one half of the pulse energy of the 5 MW ESS) is obtained, yielding about 3.5×10¹⁶ thermal neutrons /(s cm²). This peak flux matches well a number of innovative instruments and allows unprecedented resolution for some more conventional ones.

On August 20, 1998, the Austrian Government has unanimously decided to contribute one third of the total cost of the facility and invites international partners to participate.

1 HISTORY OF THE PROJECT

The history of AUSTRON begins in the years 1991 - 92, where a number of politicians and scientists contemplated the creation of a large-scale research facility in the eastern part of Austria that would radiate into and attract scientific potential from the now accessible East European Countries. In 1991, Prof. C. Rubbia advised the government that a pulsed spallation neutron source would be the most attractive and useful 'centre of excellence' (at that time the concept proposed for 'Pentagonale' - a loose collaboration of Italy, Austria and its three eastern neighbours). The basic parameters and the scenario were fixed in a meeting gathering nuclear, material structure, instrumentation and accelerator physicists at CERN, and proposed to the Austrian government [1],[2],[3] which subsequently financed a feasibility study [4],[5] for the project. Target and infrastructure was studied at the Atominstitut of the Austrian Universities while the accelerator study group was based at CERN. From the beginning, the machine was designed to be realised in stages (I - III).

2 AUSTRON I, II, III

In view of the philosophy of building the accelerator with conventional technology and to fully profit from existing experience, in particular at ISIS [6], the scenario of a low-energy linac injecting in a Rapid Cycling Synchrotron (RCS) was adopted. Based on considerations on target optimisation the top energy of the RCS was chosen to 1.6 GeV. The basic machine (I) aimed at a beam power of 100 kW onto a single target, the first upgrade (II) would double the the beam intensity and hence the delivered power by augmenting the linac energy, and the second upgrade (III) doubles the repetition rate from 25 Hz to 50 Hz so that two target stations can be served.

Table 1: The Stages of AUSTRON

	Pulse	Inject.	Nr. of	Av. Beam
AUSTRON	rate	energy	protons	power
Stage	[Hz]	[MeV]	p / pulse	[kW]
I	25	70	1.6×10 ¹³	102
II	25	130	3.2×10 ¹³	205
III	50	130	3.2×10 ¹³	410
0.5 MW	50	130	0.4×10^{13}	500
0.5 MW	10	130	2.0×10^{13}	500

The feasibility study deals in most details with stages I and II, while stage III was anticipated by rating the hardware components to meet its specifications.

The lattice of the 213 m circumference RCS uses FDF triplets and a superperiodicity of three like the ESS reference design. H⁻ Injection is taking place at the end of the fall of the magnet field in a finite-dispersion section with the foil on the inside of the circulating beam, which is traversed by the H⁻ beam in the combining bending. The RF accelerating system operates at harmonic number h=2 and requires a peak voltage of 160 kV (Stage I, II) and 246 kV (III), respectively.

¹⁾ Email: Horst.Schonauer@cern.ch

3 AUSTRON 0.5 MW

Some smaller complementary studies have been made after the Feasibility Study, such as the optimisation of the RF voltage program for trapping and acceleration [7]. It turned out that the longitudinal losses of the 50 Hz-cycling AUSTRON III could not be reduced to below ≤10% while the 25 Hz stages lost far less than 1%. As a consequence, the magnet cycle had to be modified to a dual-frequency (33 Hz rise / 100 Hz fall) cycle with short flat bottom clamping in order to match the loss figures of the 25 Hz cycle, at 0.41 and also at 0.5 MW. The augmented power entails a more marked peak space-charge tune shift of -0.42 at 1.5 ms in the cycle [8]. This means that particles will cross a third-order stopband for 2 ms. The best way to cope with possible adverse effects depends on details of the real machine and should be studied there. A secondharmonic RF system and/or an advanced collimator system are part of the options. Simulation of an advanced loss collimator in the AUSTRON lattice yielded a collimation efficiency of injection and RF trapping losses of 97.2% to be compared with 94.7% for a three-stage graphite collimator array [9].

4 AUSTRON 0.5 MW AT 10 HZ

In order to reduce the pulse frequency from 50 to 10 Hz. while maintaining the average beam power, the only economic issue is the addition of a storage ring (SR). The latter must be able to hold four consecutive pulses from the RCS along its circumference until a fifth pulse is accelerated and all the five can be sent to the target. Holding four RCS pulses side by side in a ring of comparable size is only possible if a single bunch is accelerated there (harmonic number h=1). Its length at extraction must be short enough to leave comfortable gaps for rise and fall of the injection kicker of the storage ring. This is possible indeed with a RF voltage of the h=1system of the RCS raised to 250 kV at the end of the cycle, shortening the bunch to a length of 76 ns or 36 RF degrees. In the storage ring the four bucket centres are separated by 191 ns, leaving a gap of 115 ns between neighbouring bunches. In the h=4 system of the SR bunches are 144 degrees long. To match the bucket to the bunch shape only 65 kV RF voltage are needed at 5.23 MHz.

Fig. 1 shows a SR of the same shape as but mirror symmetric to the RCS of the Feasibility Study [3]. This geometry allows the probably shortest possible transfer beam line between the two rings. The original extraction outward from the RCS is just turned inward. Note that the lattice structure of the SR is slightly different from the RCS: The quadrupole triplets of the long straight sections of the RCS have been replaced by quadruplets in the SR, in order to free the centre for the symmetric injection/extraction/direct-pass array of two septum magnets plus a kicker. Every fifth RCS cycle the

accelerated bunch is sent straight to the target before or after the row of the four bunches extracted from the SR. This configuration allows these bunches coming directly from the RCS to pass straight through the septa to the extraction line, the kicker being deactivated during their pass. A further simplification requiring a modification of the RCS lattice would be to make both rings intersecting in the same plane.

Dipoles and quadrupoles of the SR are smaller than those of the RCS as the beam dimensions at 1.6 GeV are less than half those at injection, and the fields of the d.c. magnets can be raised to 1.5 T. The very long free straight section of the SR appears well suited for accommodation of an efficient loss collimation system capable to cope with residual loss at 1.6 GeV.

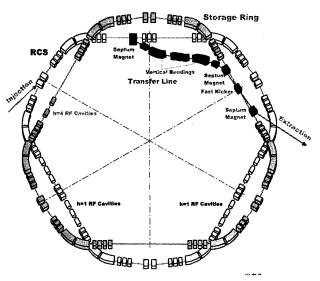


Figure 1: The Storage Ring above the RCS with the transfer line.

5 TARGET AND INSTRUMENTATION

According to the present concept of AUSTRON it is planned to start with one single target station. The target station houses the spallation target, the moderators and several beam tailoring elements like in-pile collimators or background suppression and bandwidth choppers, accessible via separate access hatches for the various beam lines. The proposed spallation target in flat target geometry [10, 11] consists of one block of solid tungstenrhenium (W-5%Re). The target temperature at 0.5 MW -10 Hz operation is expected to reach some 1300 °C which can be controlled by an advantageous edge-cooling technique. In the current design, the target is surrounded by 4 moderators. Following the requirements for the proposed neutron instrumentation, one moderator at ambient or intermediate temperature and 3 cold moderators are needed. This clearly reflects the increasing importance of cold neutrons for condensed matter research. In 1998 a suite of 21 instruments was proposed

for AUSTRON [12, 13]. The corresponding layout is shown in fig. 2.

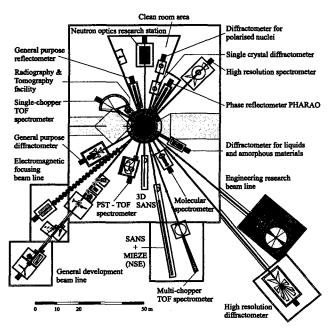


Figure 2: Schematic layout of the proposed AUSTRON instrumentation.

Most of these instruments will highly gain from the slow repetition rate of the neutron source. With total flight path distances ranging from 12 m to more than 100 m, the AUSTRON instruments aim at high resolution by TOF analysis. Owing to the repetition rate of the source a large wavelength band (up to 30 Å) can be used in one frame of the source without having to deal with overlapping neutron from subsequent pulses. This is of particular importance for the proposed diffractometers which cover momentum transfer regions for the investigation of liquids and amorphous substances, powder crystallography, and single crystal studies under special environmental conditions, for the reflectometers and the small-angle scattering instruments. This also holds for the crystal analyser spectrometers, especially the high resolution spectrometer.

Advanced environmental control is one of the unique features of the AUSTRON facility. A part of the experimental hall will be covered by a special vibration-isolated area under clean room conditions. This has become an issue since neutron research has reached a level of sensitivity where environmental effects can influence the results of an experiment considerably. The reflectometers, single crystal diffractometers and the neutron optics research station will profit from these conditions, unprecedented at any other neutron source.

Several instruments are based on experimental methods which are still under development and will be unique at AUSTRON. These innovative instrument concepts are the neutron spin echo instrument for pulsed sources, the phase reflectometer, the spin echo small-angle scattering

instrument, the diffractometer for polarised nuclei, the phase space transformation spectrometer and the pulsed neutron optics instruments.

6 CONCLUSIONS

By modifying the magnet cycle, the beam power of AUSTRON III can be raised to 0.5 MW (one tenth of the ESS goal of 5 MW). By integrating a storage ring capable of holding four consecutive 50 Hz pulses, a repetition frequency of 10 Hz without loss of average power can be achieved. In this way, an energy per pulse of 50 kJ (one half of the pulse energy of the ESS) is obtained, yielding a peak flux of 3.5×10^{16} thermal neutrons per sec and cm².

7 ACKNOWLEDGEMENTS

The authors would like to thank the Austrian Ministry of Science and Transport and in particular Dr A. Stoklaska for their continuing support and faith in the project. The help and encouragement of the CERN Directorate, and especially from K. Hübner, and the hospitality extended to the study team by the PS Division and its Leader D. J. Simon over several years are all gratefully acknowledged. The authors would also like to thank the International Scientific Council of the AUSTRON Project under Prof. A. Furrer whose advice and wisdom has always been very much appreciated. Finally to mention Dr H. Weber who has recently agreed to take on the difficult, but vital, task of Project Management.

8 REFERENCES

- [1] H. Aiginger et al. (editors), "AUSTRON, an Interdisciplinary Research Centre", Vienna, January 1992.
- [2] AUSTRON Machine Study Team: "A Pulsed Spallation Source in Central Europe", Proc. of the 3rd EPAC, Berlin, March 1992, p. 432.
- [3] P. Bryant, M. Regler, M. Schuster (editors), "The AUSTRON Feasibility Study", Austrian Ministry for Science and Research, Vienna, Nov. 1994.
- [4] F. Baumann et al., "The Accelerator Complex for the AUSTRON Neutron Spallation Source and Light-Ion Cancer Therapy Facility", Int. Rept. CERN/PS 95-48 (DI), December 1995.
- [5] P. Bryant et al., "The Accelerators for the AUSTRON Spallation Source", Proc. of the 4th EPAC, London, June 1994, p. 2677.
- [6] C.W. Planner, "Reaching 200 μA at ISIS", Proc. of the ICANS-XII Meeting, Abingdon, May 1993, RAL Report 94-025, Vol.2, p. A-4 .
- [7] E. Griesmayer, "RF Trapping and Acceleration in AUSTRON", Int. Rept. CERN/PS 95-10 (DI), May 1995.
- [8] E.Griesmayer, "RF Trapping and Acceleration in the 500 kW AUSTRON Rapid-Cycling Synchrotron", Int. Note CERN PS/CA 98-18, July 1998.
- [9] H. Schönauer, "Loss Concentration and Evacuation by Mini-Wire-Septa", Proc. of the 1995 PAC, Dallas, May 1995, p.1894.
- [10] M. Schuster, "Status of the AUSTRON-Project", ICANS XIII, PSI-Proc. 95-02, Villigen, October 1995, p. 831.
- [11] M. Schuster et al, "Material and geometry studies for the AUSTRON target", Physica B 234-236 (1997) 1224
- [12] E. Jericha et al, "AUSTRON progress report", ICANS XIV, Starved Rock Lodge, Utica, Illinois, June 1998 (in print)
- [13] AUSTRON Project Team, "AUSTRON project study 1998" (Part 2), Vienna, September 1998

DESIGN, DEVELOPMENT AND OPERATIONAL EXPERIENCES OF THE POWER CONVERTERS USED ON THE SRS *

S. A. Griffiths, CLRC Daresbury Laboratory, Warrington WA4 4AD, UK

Abstract

This report provides an overview of the past and present developments in power converter technology used on the CLRC Daresbury Laboratory Synchrotron Radiation Source (SRS). These converters have ratings which range from hundreds of watts to 750kW and supply both conventional inductive loads and super-conducting magnets. The paper summaries the impact of advances in semi-conductor component specification on the design and operation of these power converters and indicates the recent developments which have occurred.

1 SUPER CONDUCTING MAGNET POWER CONVERTERS

There are two super conducting Wiggler magnets in the SRS, which are supplied by commercially available switch-mode power converters. These supplies have a rated long-term stability of 1 part in 10³ which is insufficient for the duty required. A combined external current and voltage stabiliser is incorporated using a DCCT to measure the load current and potential divider to feedback the voltage. The switch-mode units serve only as a high power amplifier and long term stability of 1 part in 10⁴ is easily achieved.

1.1 Energy Storage

The dissipation of the stored energy of the smaller 5 Tesla magnet is provided by freewheel diodes connected to the four individual main coils of the magnet; full discharge is achieved in approximately 7 minutes.

The second magnet rated at 6 Tesla consists of a main and auxiliary winding shown in Fig.1. It is not possible to power the coils separately as the connection from the interlink is only rated to conduct 10% of the nominal current. A freewheel diode on the main magnet would provide discharge in approximately 30 minutes and prolong refill times.

To improve the discharge rate, high power MOSFETs are used to control the operation of a dumping circuit. The design utilises the main current feedback system to adjust the switching time of the MOSFETs and track the reference as it ramps to zero in 6 minutes.

To avoid a possible quench, the discharge rate must be controlled particularly at maximum field. If an interlock trip should occur the supply must remains 'on' until zero current.

The auxiliary winding is connected with anti parallel schottky diodes to provide a path for the discharging main current. This limits the voltage, which is generated across the auxiliary coil because of the current difference in the main and auxiliary windings. The low forward voltage drop of the schottky rectifiers is insufficient to meet the need for high impedance during the ramp. As a compromise the trim power supply is overrated and the DCCT for the auxiliary current is positioned close to the magnet terminals to prevent inaccuracies resulting from diode conduction.

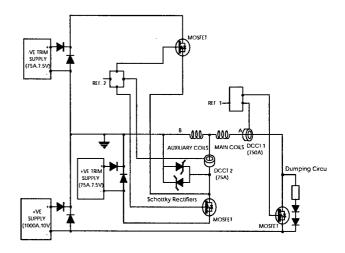


Fig.1 Schematic diagram of the 6 Tesla Superconducting Wiggler Power Converter

2 QUADRUPOLE SHUNTS

A significant vertical tune shift can arise from the focussing effects of the insertion devices. (wigglers and undulators) This can be compensated by local correction on a quadrupole adjacent to the wiggler. The main magnet families of the storage ring are series connected and to adjust current to individual quadrupoles a controllable active current shunt is required.

2.1 Design Changes

The initial shunt design was a transistor bank containing 32 parallel bipolar transistors. Their base drive was generated by a transformer-coupled chopper and rectifier to amplify the current and provide electrical isolation.

This system has since been simplified and the new design is shown in Fig.2. It consists of two parallel high

power MOSFETs with an isolation amplifier providing the interface to the control circuit. The high input impedance and large power gain of the MOSFET is ideally suited to this type of application.

The main contactor is used for electrical isolation as part of the personnel safety system. The on/off switching is achieved by clamping the base drive.

The capacitor and zener diodes on the magnet side of the contactor ease the breaking of the dc arc in the contactor and prevent high voltages being generated.

2.2 Control Electronics

The control circuitry for the quadrupole shunts was designed multi-functional and provides a site standard for all power converter applications. Its features include a ramp generator, voltage feedback conditioning and isolated analogue output drive. The system also houses a QtecQ Macc plus DCCT burden card, providing a simple and compact feedback interface. The electronics are housed in a Euro-crate with a PCB backplane providing an interface to external control electronics. This makes the control crate portable and easy to replace.

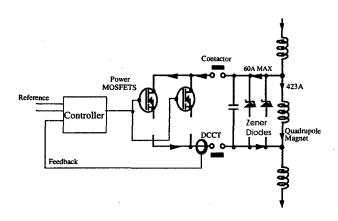


Fig.2 Schematic Diagram of Quadrupole Shunt Circuit

3 MAIN STORAGE RING POWER CONVERTERS

The main magnets of the storage ring were initially powered by roller regulator, transistor trimmer type power converters. This type of supply is expensive to maintain and has poor efficiency compared to modern design. Their reliability had become unacceptable due to age for an accelerator expected to deliver 6000 scheduled beam hours per year. It was decided to replace these supplies with a 50Hz line commutated thyristor technology, designed to the CERN, LEP specifications [1,2,3].

There are five converters in this power range, two at 750kW, one at 250kW and two at 90kW. These power the SRS storage ring dipoles, quadrupoles and sextupoles.

3.1 Design Benefits

The improved performance of the new converters reduced the ramp time from 14 minutes, with the old regulator type design, to just 70 seconds. The hysteresis cycling before each refill is also faster, now being 30 seconds instead of 4 minutes.

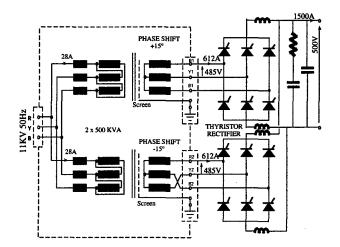


Fig.3 Electrical Circuit of 750kW Power Converter

All of the new converters are naturally air cooled, thus making it possible to dispense completely with the closed circuit de-mineralised water cooling system used by the old equipment. This, together with the high efficiency of the converter, yields a reduction in power of about 30kW.

The inclusion of two DCCTs, one for control and the other for monitoring, allows direct on-line calibration checks at the nominal output current. This can then be used to identify drifts in the DAC, ADC and loop parameters. The extensive range of command protocol and monitoring facilities provides a comprehensive diagnostic system for troubleshooting.

Since the installation of the new converters, downtime due to failures has reduced by a factor of 10 on the old design.

4 BEAM STEERER POWER CONVERTERS

The present system consists of two 24 volt switch-mode power converters providing a dual dc distribution network to support 224 steering modules as shown in Fig.4. The load regulation is generated by individual current control of the transistorised modules with a stability of 1 part in 10⁴. The DC supply from the switch-mode units is over specified for this application, but due to its complex switch-mode design and 10 years operating period the reliability is poor.

4.1 Proposed Replacement

It is now proposed to replace the switch-mode supplies with a transformer rectifier set; the design simplicity and generously rated components would guarantee a high mean time between failures and provide a low cost solution. Before the power supplies are replaced the modules must be assessed for bandwidth and attenuation of the 300Hz ripple produced from the three-phase rectifier.

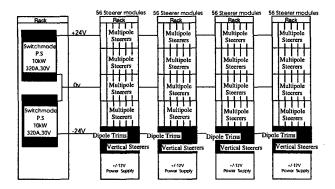


Fig.4 Electrical Distribution of the Steerer Magnet Power Converters.

The major problem with this type of dc distribution systems is the large amount of stored energy, which can result from the combined magnet loads. When redesigning the system all possible fault conditions must be assessed; for example:

- module fuse failure, each unit must be capable of discharging the magnet energy, preventing further damage to module.
- power converter failure, this would not cause damage as the control circuit would remain operational and the energy discharged normally.
- A loss of control reference to the modules, this can result in the stored energy being discharged into the output capacitors of the power converter causing an over voltage; the supply must have built in over voltage protection to prevents damage.

5. FUTURE DEVELOPMENTS

5.1 Booster Power Converter

The ac power converter for the 10Hz Booster White circuit used on the SRS has been operational for 20 years. The design consists of a thyristor rectifier, which controls the dc voltage to the 10Hz thyristor inverter circuit. The inverter then supplies the losses to the white circuit using an auxiliary winding on the energy storage choke. The ideal solution to improve the power converter would be to specify and procure an entire new unit. This is not

possible and it is now proposed to upgrade the control electronics, providing a low cost alternative.

5.2 Crowbarless Klystron Power Converter

The power converter for the existing storage ring RF klystron is a 6-pulse transformer rectifier, with roller regulator output voltage control. Advances in power electronics components now make possible the production of switch-mode power converters exceeding 100kW. The use of high frequency inverters means that the stored energy at the high voltage end is greatly reduced compared to a line commutated rectifier. This makes it possible to eliminate fast protection by electronic crowbar. This is an expensive device, which requires high quality design and manufacture. A liaison with an industrial company, to jointly produce such a converter, is currently being explored.

6. REFERENCES

- [1] D.E.Poole, S.A.Griffiths and M Heron, "New Magnet Power Converter for the SRS at Daresbury", Proceedings of European Particle Accelerator Conference, 1994, vol. 3, pp 2333-2334.
- [2] H.W.Isch, J.G.Pett and P.Proundlock, "An Overview of the LEP Power Converter System", Proceedings of the IEEE Particle Accelerator Conference, Washington, 1987, vol.3, pp. 1399-1401.
- [3] H.W.Isch, "Realisation of LEP Power Converters",1st European Particle Accelerator Conference, Rome, 1988, vol.2, pp 1166-1186.

Author Index

Abe, Hiroshi 2015, 2749 Aberle, Oliver 949 Abo-Bakr, Michael 2385 Acharya, R. 1393 Adachi, Toshikazu 2271, 3348, 3752 Adamenko, Stanislav V. 3269, 3271 Adams, D.J. 2199 Adderley, P. 1991 Adolphsen, Christopher D. 253, 777, 3411, 3423, 3477 Afonin, A.G. 53 Agafonov, Alexey V. 1731, 1734 Agematsu, Takashi 2259 Ahle, Larry 1937, 3248 Ahn, Hyo-Eun 875, 1255 Ahrens, Leif A. 614, 1276, 1746, 2063, 2286, 2918, 3291, 3294 Akagi, Hirofumi 3749 Akai, Kazunori 440, 1132, 2731 Akaoka, Nobuo 3546 Akasaka, Nobumasa 1132, 2238, 2731, 3411 Akemoto, Mitsuo 3414 Akiyama, Atsuyoshi 343, 3158 Akre, Ronald A. 2846 Alai Tafti, A. 2722 Alba, Rosa 2578 Aleksandrov, A. 237, 3321 Aleksandrov, Aleksander V. 78, 2948 Aleksandrov, Vladimir S. 3501 Alekseev, Nicolay N. 1479 Aleshaev, Alexander N. 750 Alessi, James G. 106, 614, 1297, 1902, 1964, 3300 Alexahin, Yuri 1527 Alford, Owen J. 2590, 3251 Alimov, Andrey S. 2301, 2555 Alonso, Jose 574 Alton, Gerald D. 1878, 1881 Alton, William J. 845 Altuna, Xavier 2617 Amano, Daizo 2403, 2689 Amatuni, Andrey Ts. 3657, 3660 Ambrosio, G. 174 Ames, Friedhelm 1955 Anderegg, Jim 1402 Anders, W. 197, 2385 Anderson, David E. 3390 Anderson, Edwin B. 1686 Anderson, James L. 571 Anderson, Oscar 1908, 1937 Anderson, Scott 217, 2006, 2039, 2042, 2045 Andersson, Ake 2945 Andreev, N. 174, 3194, 3197 Andreev, Nikolai 154 Andreev, V.A. 2256 Andrianov, Serge N. 1866, 2701 Anerella, Michael D. 185, 3161, 3170 Anferov, Vladimir A 392 Anguelov, Vladimir 2289 Anthouard, Philippe 3260

Antoine, Claire 919

Antonello, M. 1324

Antonsen Jr., Thomas M. 360

Aoki, Yasushi 2018, 2036

Apel, Ruediger 812, 818

Arakawa, Dai 1141, 1653, 1821 Arakawa, Kazuo 2259 Araki, Sakae 343 Arapov, L. 237 Arcan, T. 174, 3197 Archambault, L. 325, 3705 Arduini, Gianluigi 1282, 1285, 2617, 2996 Argan, Andrea 1599 Arimatea, Claudio 2617 Arkan, T. 3194 Arkan, Tug T. 3242 Arnett, Don 1390 Arnold, Ned D. 2024 Aronson, A 548 Artoos, Kurt 154 Arutunian, Suren G. 1468, 2105, 3657 Arvin, Adrian H. 1444, 1447, 1929, 1946 Arvin, Andy 349 Asaka, Takao 2015, 2749, 3507 Asano, K. 777, 3417, 3423 Asaoka, Seiji 667, 670 Aspenleiter, Jeffrey 1390, 2698 Assadi, Saeed 711, 720, 1082, 1085, 2719 Assmann, Ralph 330, 2996, 2999, 3002 Aston, David 2990 Atencio, Samuel J. 965 Aune, Bernard 432 Autin, Bruno 3071 Autrey, Daryl 3248 Avilov, Alexandr M. 2549 Ayers, James J. 1961 Baartman, Richard A. 128, 3534, 3537 Babayan, Ruben A. 2424 Baboi, N. 922 Babzien, Marcus 2024, 2158, 2471, 2480, 3722 Bach, H. 2427 Backe, H. 165 Badan, L. 1324 Badea, V. 3767 Bae, Young-Soon 3525 Bai, Mei 387, 471, 2725, 3336 Bailey, Roger 2617, 2996 Bak, J. S. 1384 Bak, Peter A. 2167 Bakker, Rene J. 197, 726, 2078, 2379, 2382 Baklakov, Boris 1387 Balakin, Vladimir 461 Balbekov, Valeri I. 315, 3062, 3146 Baldis, Hector A. 2000 Ball, M. 498, 1545, 1548 Ball, Millicent J. 3245 Ballarino, Amalia 1405 Balleyguier, Pascal P. 1444, 1447, 1946 Baltadoros, D. 1037 Bane, Karl F. 3432, 3486 Bane, Karl L.F. 1725, 1728, 2822, 3423, 3453, 3474, 3477 Bangerter, Roger O. 3215 Banks, Thomas I. 1686 Banna, S. 3600, 3606, 3609 Bannon, M. 3767 Baptiste, Ken 1471, 3131 Baranauskas, V. 2811 Barber, D. P. 2635 Bardy, Jacques 3260

Barklow, Timothy L. 307, 3489 Barlow, D. 3576 Barnard, John J. 1761, 1803, 1830, 3248 Barnes, C. 321 Barnes, Michael J. 1509, 3378 Barnes, Peter D. 2590 Barnes, Phil 980 Barnett, Ian 3743 Barone Tonghi, L. 2578 Barov, N. 2027 Barr, Dean S. 2214, 2241 Barraza, Juan 2090 Barry, Walter C. 636, 1207 Barsotti, E.L. 2146, 2211 Bartolini, R. 1557 Barzi, E. 174, 3330 Bassalleck, B. 471 Batchelor, Kenneth 75 Batskikh, Gennady I. 2564 Battle, Chris 2936 Batygin, Yuri K. 1737, 1740 Bauda, B. 197 Bauer, P. 3194 Baumann, C. A. 2659 Bayanov, Boris F. 3086 Bazhan, Anatoli 461 Bazzani, Armando 1773 Bechstedt, Ulf 1701, 2292 Bechtold, Alexander 530 Beck, David 1937, 2849 Beck, U. 206 Becker, R. 1899 Becker, T. 197 Becker, Ulrich 2951 Beczek, Kevin J. 1378 Beebe, E. 1902 Beebe-Wang, Joanne J. 1743, 2843, 3143, 3185 Beetham, C.Gary 765 Behne, Dan 1333 Beinhauer, Wolfgang 1647 Bellavia, S. 1902 Bellomo, Giovanni 1776 Bellomo, Paul 206, 3429 Belomestnykh, Sergey A. 272, 980, 1112 Belousov, Ilja V. 750 Belov, Victor P. 3086 Ben-Zvi, Ilan 75, 2018, 2158, 2471, 2480, 2552, 3495, 3722 Benabed, Karim 2990 Benjamin, John 2277 Benjegerdes, R. 3233 Benson, S.V. 212, 2456 Bent, Bruce 931 Berg, Georg P. A. 2519 Berg, J. Scott 3152 Berg, Jeff 1333 Berg, William J. 2024, 2134 Berger, Christoph 2172 Bergstrom, Paul M. 1827 Bernal, Santiago 234, 1749, 1758, 1970, 2102, 3372 Bernard, Michel 922 Bertolini, Louis R. 2477, 3251 Besnier, Gilbert 1192, 1195 Besson, Jean-Claude 1569, 2686

Bharadwaj, Vinod K. 3429, 3447, 3450 Boriskin, V.N. 753 Buerkmann, Klaus 2385 Borland, Michael D. 200, 1587, 1644, 1979, 2319, Bugrov, Vladimir P. 1312 Bhat, Chandra M. 114, 717, 3155 Bhatia, Tarlochan S. 3585 Bulfone, Daniele 1120 Borne, Jean-Luc 919 Bullard, D. 3309 Biagini, Maria E. 1536 Biallas, George 2456, 3306, 3312 Borodich, Andrei, I. 1869, 1872 Bullard, Donald 3306 Bultman, Nathan K. 3591, 3594 Bibber, Karl V. 2480 Borovina, Dan L. 786, 2772 Bickley, Matthew H. 732, 735, 741 Borunov, Ivan E. 750 Bulyak, Eugene V. 1770, 3122, 3269, 3271 Biedron, Sandra G. 2024, 2471, 2483, 2486, 2945 Bosch, Robert A. 2388, 2394, 2397, 2659 Bunce, G. 471 Bieler, Michael 554 Boscolo, Ilario 1982, 1985 Burgess, Edward L. 617, 3257 Burke, D.L. 3423 Boscolo, M. 1536 Bielicki, J. 1249 Burke, Jason 1952 Bieniosek, F. M. 1249, 1937 Bossart, R. 250 Bienvenu, Gerard 913 Bosser, Jacques 465 Burkhardt, Helmut 2996, 3011 Billen, James H. 3570, 3585 Bossert, R. 3194, 3197 Burla, Paolo A. 762 Botman, J.I.M. 759, 1539, 2825, 2864, 3266 Billen, Ronald 2617 Burn, Kenneth W. 2531 Billing, Michael G. 410, 1112, 1115, 2975, 2978, Bottura, Luca 154, 3179 Burns, Michael J. 617 3221, 3501 Boucham, Abdel 2990 Burov, Alexey V. 521, 1088, 1201, 1608, 1707, Bourdon, Jean-Claude 2012 1710 Birke, Thomas 197, 726, 2382 Birx, D. 3257 Bourque, Robert F. 2954 Bushuev, Alexander A. 2033 Boussard, Daniel 946, 949 Busse-Grawitz, Max Erick 986 Biryukov, Valery M. 53, 1234, 1237, 1240, 3050 Biscari, Caterina 131, 1536 Bousson, Sebastien 919 Butenko, Andrey V. 2262 Buth, Gernot 2424 Boutigny, D. 2990 Bish, P. 3233 Bovet, Claude 465 Butterworth, Andy 2996 Bishofberger, Kip 2006 Bisoffi, Giovanni 1324 Bowden, Gordon B. 206, 824, 1390, 3423, 3426 Buxton, W. 2128 Bower, Gary 307 Bychenkov, Valery Yu. 3716 Blank, M. 1016 Byer, Robert.L 321 Bowles, Edward 3755 Blas, Alfred 143 Bowling, Bruce A. 732 Byers, B. 2990 Blasche, K. 527, 1704, 1788 Bylinsky, Yuri V. 450, 893 Blaskiewicz, Michael M. 109, 614, 857, 1611, Bowman, Jim 1333 Byrd, John M. 382, 495, 1207, 1806, 2370, 3131 Boyce, Richard M. 206, 1363 2280, 3185 Boyd, John K. 3513 Cai, Y. 296 Blazhevich, Sergey V. 2584 Blind, B. 611, 3582 Calabretta, Luciano 2578, 3288 Brabson, B. 1548 Bracco, Roberto 2680 Calame, J. 1016 Blinov, Boris B. 392 Bradley III, Joseph T. 1010 Calatroni, Sergio 949 Bliss, Neil 2656 Callin, Richard S. 783 Bradshaw, David J. 2656 Blokland, Wim 1085, 2211 Braeutigam, Werner 957, 959, 3549 Cameron, Peter R. 2114, 2117, 2146, 2250, 3185 Blondel, Alain 2999 Brandt, Daniel 304, 3005 Campbell, B. 965 Blosser, H. 1318 Campbell, Billy M. 971, 1327, 2954 Brandt, J. 3194, 3197 Bluem, Hans 3570 Campbell, Lora P. 3722 Braun, Hans H. 250, 3402 Blum, Eric B. 2304 Bocchetta, Carlo J. 2060, 2313 Brautti, Giulio 1905 Campbell, Richard 1515 Breese, Mark 53 Campisi, Isidoro E. 937, 1177, 1180, 2456 Boege, Michael 1129, 1542, 2430 Boehnke, Michael 851 Breidenbach, Martin 3384 Cao, Jianshe 2140 Brennan, Joseph M. 614, 857, 1746, 2280 Capista, David P. 714 Bogacz, S. Alex 738, 2897 Caporaso, George J. 617, 622, 625, 1204, 1303, Bogart, S. Locke 603 Brennan, Michale 1258 1824, 1827, 3254, 3381 Bogdanovitch, Boris Yu. 1291, 1932, 2570, 2573 Bressanutti, Raffaele 1120 Boggia, Antonio 1905 Bricault, P. 100, 450, 3540 Carathers, Jeremy R. 1447 Briggs, R. 3257 Carlier, Etienne 1509 Bogomolov, Guenrikh. D. 592 Bohl, Thomas 2617 Brinkmann, Reinhard 16 Carlson, Charles 2277 Bromberek, David J. 3095 Carlsten, Bruce E. 477, 617 Bohlen, Heinz P. 445 Bohn, Courtlandt L. 2450, 2456 Brooksby, Craig A. 625 Carneiro, Jean-Paul 992, 2027 Bohne, D. 2513 Brouet, Michel 562 Carr, G. Lawrence 134 Carr, Roger 1390, 2477, 2698 Brovko, Oleg I. 2262 Boine-Frankenheim, B. 1788 Browman, Andrew A. 518, 998, 2790, 3582 Boine-Frankenheim, O. 1785 Carrigan, R.A. 2027 Brown, Bruce C. 714, 717, 3315, 3318 Carron, Georges 250 Boisvert, Veronique 2217 Brown, C.N. 3324 Carter, Anthony 3101 Boivinet, Raynald 3260 Brown, Kevin A. 614, 1258, 1267, 1270, 2123, Carwardine, John A. 2093 Bollen, Georg 1955 Bolme, Gerald O. 1444, 1447, 1946 2722, 2725, 2728, 2918, 3291 Cary, John R. 369, 377, 2784 Brown, Terence F. 3381 Casas-Cubillos, Juan 3203 Bolotin, Igor M. 1482 Bolshakov, Timophei 1387 Brown, Winthrop J. 81, 833 Casey, Jeffrey A. 568, 1491 Bruenger, W.H. 2575 Caspers, Fritz 1408, 2629 Bolt, A. Scott 349, 1444, 1447, 1929, 1946 Caspi, Shlomo 174, 2793, 3194, 3197, 3233, 3236 Bruhwiler, David L. 369 Bonati, R. 3767 Cassel, Richard L. 1494, 1500, 3429 Bondarev, Boris I. 1764, 2808 Brumwell, Franklin R. 2274 Brunelle, Pascale 1569, 2686 Cassinari, Lodovico 1168, 1569 Bongardt, Klaus 1767 Castellano, Michele 1985, 2193, 2196, 2695 Brunet, Jean-Claude 1330, 1339 Bongers, Henning 3516 Bruning, Oliver 40, 2629 Castillo, Vincent 490 Boni, Roberto 866 Bruno, Donald 3734 Castle, Mike 1040, 1046 Bonnafond, Christophe 1381, 3260 Bruns, Warner 2767 Castro, Maurizio 97 Bonthond, J. 1228 Bryan, David A. 732, 735 Castro, Pedro 456 Booch, Rex 1506 Bryant, Phil 2957 Catani, Luciano 1985, 2196 Bopp, Markus 795 Buckles, Robert 1303 Catravas, Palmyra 325, 330, 2111, 3705 Borak, Thomas 2990 Borburgh, Jan C. 2283 Budnick, J. 1545, 1548 Caussyn, D.D. 1548 Bordry, Frederick 3203, 3740 Buerkmann, K. 197 Celata, Christine M. 1716, 1803, 1830

Celona, Luigi 97, 2578 Cerny III, Joseph 533 Chae, Yong-Chul 1644, 2486 Chai, Jongseo 2265, 3137 Chai, Xuedong 1453 Champion, Mark S. 992, 2027 Chan, C. F. 1937 Chan, K.C.D. 1327, 2954, 3582 Chan, Kwok-Chi D. 965, 968, 971 Chang, Cheng-Hsiang 2671 Chang, H.P. 2409 Chang, J. H. 2593 Chang, Lung Hai 1159 Chang, Peace 2837 Chang, S. S. 2009 Chang, S.S. 679, 2205, 2501 Chang, Shi-Horng 1375 Chang, Suk S. 2418 Channell, Paul J. 1629 Chao, Yu-Chiu 738 Chapelle, Sonja 3758 Chapman-Hatchett, Arthur 2202, 2223 Chargin, Anthony (Tony) K. 2590 Charrier, Jean-Pierre 432, 919 Chattopadhyay, Swapan 330, 2370 Chavanne, Joel 2662, 2665 Cheever, Dan 3101 Chel, Stéphane 916 Chen Y .- J. 617 Chen, C.S. 682, 685, 2412 Chen, Chien-Rong 1150 Chen, Chiping 1875, 2752 Chen, H.H. 2671 Chen, J. 682, 2021 Chen, J.R. 1605, 2409, 2415 Chen, J.S. 682, 1450 Chen, Jenny 685, 2069, 2072, 2412, 2671 Chen, Jie 741, 747 Chen, June-Rong 1150, 1375 Chen, Longkang 2184 Chen, Pisin 224, 330, 3648 Chen, Senyu 209 Chen, Szu-Yuan 3666, 3716 Chen, W. 3345 Chen, Y. J. 1824 Chen, Yu Ju (Judy) 617, 622, 2235, 3254, 3381 Chen, Yu-Jiuan 1204, 1210, 1303, 1827, 3254, 3257, 3513 Chen, Zukun 3591, 3594 Cheng, Daniel W. 1911, 1914, 1958, 1961 Cheng, Hung-Ming 1150 Cheng, W.H. 382 Chepegin, V.N. 53 Chepurnov, Alexander S. 2584 Cherbak, Ernest E. 1019 Cherenshchikov, S. A. 1973, 1976 Cherepakhin, A. 1249 Cherix, Jacques 418 Cherniakin, Alexander D. 3086 Chernin, David P. 360 Cherwinka, Jeffrey J. 3221 Chesnokov, Yury A. 53, 1237 Chesworth, Andrew A. 2433 Chiaveri, Enrico 946, 949 Chichili, Deepak R. 174, 3194, 3197, 3242

Chin, Y.H. 1058

Chines, Franco 97

Chin, Yongho 633, 3414

Chiou, J.P. 1450, 2009

Chin, Paul 234, 1970, 2102, 3369, 3372

Chishiro, Etsuji 3546 Chitose, Norihisa 2602 Chiurlotto, F. 1324 Cho, M.H. 2593 Cho, Yong-Sub 875, 1255, 3525 Chohan, Vinod 2202 Choi, B. H. 206 Choi, Byung-Ho 875, 1255, 3525 Choi, J. 1016 Choi, Jae-Young 2205, 2501, 2593 Choi, Jinhyuk 2418 Chojnacki, Eric 845, 980, 2635 Chong, Henry 2370, 2498 Chou, Ping-Jung 1159, 2415, 2837 Chou, W. 565, 3285 Chow, Ken P. 171, 3233, 3236 Christiansen, David W 3573 Christina, Vincent 780, 3306 Chu, C.M. 392, 1545, 1548, 2286 Chu, Chunjie 1940 Chu, W. 2537 Chung, Kie-Hyung 2558, 2561 Chung, Sukmin 1357 Chupyra, Andrei 1387 Church, Michael D. 56 Church, Roy A. 1013 Cianchi, Alessandro 2193, 2196 Ciavola, Giovanni 97, 2578 Cimabue, Anthony G. 965 Cinabro, David 3221 Citver, G. 1420 Clark, George S. 3378 Clark, J. 1991 Clark, John C. 3513 Clark, Robert E. 2746 Clark, William L. 965 Clarke, James A. 2433, 2653, 2656 Clauser, Tarcisio 1779 Claverie, Joseph 2686 Clayton, Christopher E. 330, 2006, 3651, 3654, 3708 Clendenin, James E. 1988, 3384, 3447, 3450 Clifft, Ben E. 524 Cline, D. B. 2552, 3639, 3722 Codner, Gerald W. 1115, 1441, 3221, 3224 Cola, Mark J. 962 Colby, E. 321 Cole, M. 780 Cole, Michael D. 3570 Colestock, Patrick L. 114, 2027, 2181, 3155 Collier, Michael 3594 Collier, Paul 2617, 2996 Collins, Ian R 2629 Collins, J.C. 673, 1548 Comins, J.D. 3257 Comunian, Michele 1773 Conde, Manoel E. 2030, 3621 Conkling Jr., Charles R. 699 Connolly, Roger C. 2114, 2117, 2250 Cooke, Simon J. 360 Coosemans, W. 250 Corbett, Jeff 206, 2355, 2358, 2364 Corlett, John N. 296, 800, 896, 1207, 3149, 3429 Corlier, Muriel 2686 Cornacchia, Max 267, 2480 Cornelis, Karel 1189, 2617, 2996 Cornelius, W. D. 1884, 1887 Cornuelle, J. 3423 Corredoura, Paul L. 435, 800, 3429

Corsini, Roberto 250, 3396

Corstens, J.M. 2864 Counsell, Joseph 1025 Coupal, David 2990 Cours, Alexander 1022 Cousin, J.M. 1569 Coutrakon, George 11 Cozzolino, John 185, 3230 Craddock, Michael 2620, 2623 Craievich, P. 1123 Craig, George D. 1830, 3248 Crandall, K.R. 611, 3582 Crandell, D.A. 392 Crawford, A.C. 521 Crawford, Curtis 237, 3321 Crisp, J. L. 2164 Crisp, Jim 2146, 2211 Crist, Charles 1303 Crockford, Guy 2617 Crosbie, Edwin A. 1587, 2325 Cruikshank, Paul 1330, 3203 Ctcherbakov, Anatoliy M. 1482 Cullen, J.R. 1267, 1270 Cummings, Karen A. 881, 1396 Cundiff, Tim 2090 Cupola, J. 2117 Cuttone, Giacomo 2578 Czarnaski, Mark 360 d'Amico, Tommaso E. 250, 1638, 2202, 3399 D'Olando, Stefano 1120 D'Ottavio, Theodore W. 693 D'Yachkov, Mikhail 128, 1408 DaCosta, Tony 1333 Dahlerup-Petersen, Knud 3200, 3203 Dai, Jianping 1453 Dalesio, Leo R. 349, 652, 655 Daly, E. T. 206, 1363 Dambach, S. 165 Danared, Håkan 1698 Danby, Gordon T. 3185, 3333 Danilov, Vyacheslav V. 109, 641, 1198, 1201, 1608, 1710, 3140, 3143, 3303, 3728 Danly, B. 1016 Danowski, G. 3767 Darpentigny, Jacques 1168, 1569 Date, Schin 2346 Dattoli, Giuseppe 1219 Datz, Sheldon 1671 Davidson, Ronald C. 1518, 1623, 1626, 1629, 1875 Davis, Brent 1506 Davis, Jerry L. 1001 Davis, Roger 557 Day, T. 1991 de Hoon, Michiel J.L. 1803, 1830 de Loos, Marieke 2462, 3266 De Monte, R. 2253 De Ryck, C. 3212 De Santis, Stefano 2075, 2873 De Wit, F.F. 759 Debeling A. 3248 Debiak, Ted, W. 587 Debus, J. 2513 Decker, Franz-Josef 307, 330, 771, 774, 1252, 1728, 2846, 2987, 3384, 3648 Decker, Glenn A. 2051, 2093, 3092 Decking, Winfried 1581 Decyk, V. K. 3672 Degasperi, Francisco T. 1366 Degtyarev, I.I. 1321 DeHart, Terrance E. 2668

Dehler, Micha 1129, 2087 Dehning, Bernd 2999 Dejus, Roger J. 2486, 2489, 2492 Dekin, W. D. 2590 Delahaye, J.P. 250 DeLamare, Jeffery E. 1494 Delayen, Jean R. 925, 928, 934, 937, 940, 955, 1462, 3498 Dell'Orco, D. 206, 2355 Den Hartog, P.K. 1369, 2483, 2489 Deng, Jianjun 3263 Denker, A. 3519 Denz, Reiner 3200 Derbenev, Yaroslav S. 392 Derenchuk, V. 1548 Derrick, M. 2635 Deruyter, H. 590, 3423 Deryuga, Vyacheslav A. 2546, 2549 DeSantis, Stefano 382 Desforges, Bernard 2617 Desmons, Michel 916 Despas, Claude 2617 Despe. Oscar 3773 DeStaebler, Herbert 2990 Detweiler, Gerald 2468 DeVan, W.R. 355 Devin, André 3260 Devmal, S. 2990 DeVries, Jan 162 Dewa, Hideki 3690, 3702 Dey, Joseph E. 869 Di Bartolo, Gaetano 2578 Diaczenko, Nick 2936 Dias, Joao M. 3725 Dickson, R. 646 Dietderich, D.R. 171, 3233, 3236 Diete, W. 957 Dietrich, J., 2054 Dietrich, Jürgen 1701, 2292 Dikansky, Nikolay S. 78, 2167, 2948 Dimaggio, S. 325 DiMaggio, S. 3705 DiMarco, Joseph 3194, 3197, 3318, 3327 Ding, Bainan 3263 Ding, X 2504 Ding, X. 2003, 2021, 2039, 2042, 2045 Ding, Xiaodong 2006 Dinkel, J. 1249

Dittmann, B. 197 Diviacco, Bruno 2680 Divin, Yuri Y. 2178 Diwan, Milind V. 3023 Dix, Brendon 1390

Dobbing, Gavin S. 2433, 2653 Dobrovolski, Nikolaj M. 1468, 2105

Dohlus, Martin 1650 Dolgashev, Valery 2822 Doll, D.W. 1393 Dombsky, M. 100 Dome, George 1408 Domer, Gregory A. 649 Donald, Martin H. 296, 1584

Dong, Xiaoli 1596

Donohue, John T. 1797, 3387 Dooling, Jeffrey C. 2274

Doolittle, Lawrence R. 768, 928, 934, 937, 940,

1462

Doose, Charles L. 2024, 2093

Dormiani, M. 206

Dortwegt, Robert J. 1414, 2024

Doskow, J. 471 Doss, J. Daniel 426

Douglas, David 1177, 1180, 2456, 3306, 3312

Douryan, Adnan 2471 Dovbnya, A. 3122 Doyle, Stephen 2424 Doyuran, Adnan 2480, 2942 Drago, Alessandro 131, 636 Dragt, Alex J. 1551, 1593, 2761 Drees, K. Angelika 2117 Dressler, Olaf 1279

Drivotin, Oleg I. 1857 Drozhdin, Alexandr I. 56, 1231, 1234, 2614, 3050

Drury, Michael 931

Ducimetière, Laurent 1228, 1509

Duda, Brian J. 3669 Duerr, Volker 2385 Duffau, Michael J. 2096 Duffy, Patrick 1390, 2477

Dugan, Gerald F. 48, 2057, 2632, 3221, 3224

Duke, Jonathan P. 2208 Dunbar, Ann 1100 Dunham, B. 1991 Dupaquier, Andre 3740 Dur, V. 197

Durkin, Alexander P. 1764, 2808 Dutto, Gerardo 106, 893 Dykes, Michael D. 1025, 2096

Eardley, Matthew 1943

East, G. 1548

Ecklund, Stan D. 296, 3450 Economou, A. 1037 Edamenko, N. S. 1866 Edgell, Dana 1043, 1890 Edwards, Helen T. 992, 2027 Egawa, Kazumi 3351, 3354, 3357 Egiazarian, Suren L. 1468

Ehrlich, Richard 980 Eichhorn, Ralf 2951 Eichner, John 1512

Eickhoff, Hartmut 527, 1704, 2513

Eilerts, S. 471

Einfeld, Dieter 806, 809, 1360, 2424, 2427, 3375

Eisert, D. E. 2659 El-Shazly, M.N. 1896 Elbakian, Sergey S. 3657, 3663

Elioff, T. 206

Elleaume, Pascal 2662, 2665, 3119

Elliott, T. 780 Elliott, Tim 2936 Ellis, Gretchen G. 965 Ellison, M. 1548 Elmer, John 777 Elzhov, Artem V. 3393 Emamian, Mark 221, 2468

Emery, Louis 200, 401, 1644, 2137, 2319, 2939

Emhofer, Stephan 3516

Emma, Paul 3429, 3438, 3447, 3456

Emmerling, M. 1788 Endo, Akira 2018, 2036, 2552

Endo, M. 600 Engels, Oliver 3519 Enomoto, A. 1132, 2731 Eppley, Kenneth R. 2778 Erdmann, M. 1369, 2489 Erickson, John L. 3594 Eriksson, L. 3462 Eriksson, Mikael 2945 Ermakov, Dimitry I. 2555 Erokhin, Alexander 1387

Esarey, E. 330, 2111 Esarey, Eric 325, 3696, 3699 Escallier, John 3161 Eschenko, Viktor N. 3086 Esin, Sergei K. 3561 Etzkorn, Franz-Josef 851 Evans, I. 206

Evans, Jr., Kenneth 352, 744 Evans, Lyndon R. 21 Evans, R. 2456 Eyl, Patrick 3260

Eylon, Shmuel 1934, 3248, 3390

Eyssa, Y. 3227 Ezura, Eiji 413, 440 Faatz, B. 2486

Fabris, Alessandro 809, 1120, 1123

Fagan, M.J. 1327 Fahmie, Michael P. 756 Falabella, Steve 1303 Falkenstern, F. 2078 Fallmann, W. 2575

Faltens, Andris 1503, 1830, 1937, 2849, 2852,

3215, 3339

Fan, Kuanjun 1315, 1596 Fan, Mingwu 1940 Fan, T.C. 2671 Fang, J.M. 3627 Fang, Lei 2125 Fang, Shouxian 1695 Fang, Shuyao 890 Fang, Si 3761 Fang, Zhigao 2125 Fann, C.S. 1450 Fant, Karen 1435

Farkas, Zoltan David 771, 774, 3423

Farrell, J. Paul 75 Fartoukh, Stéphane 922 Farvacque, Laurent 3119 Faugier, Andre 2617, 2996

Faulbaum, D. 197

Fawley, William M. 1204, 1210, 1934, 3254, 3257

Fedorov, Vacheslav 1479, 1485 Fedorov, Vladimir M. 1734

Fedorova, Antonina 1614, 1617, 1620, 2900,

2903, 2906, 2909, 2912

Fedotov, Alexei V. 606, 1752, 1755

Fedotov, M. G. 2167 Fedotov, Yu.S. 53

Feher, Sandor 1420, 1426, 3191, 3194, 3197

Feigenbaum, Irv 2277 Feikes, Joerg 197, 1279, 2376 Feldl, Erich 928, 934 Fellenz, Brian 2146, 2211 Feng, Z.Q. 3345 Ferianis, Mario 1120

Fernow, Richard C. 3020, 3032 Ferracin, Paolo 3206

Ferrari, Antoin 2617

Ferrario, Massimo 1985, 1997, 2734

Fessenden, Tom 2235 Fieguth, Theodore 296, 2990 Field, R. Clive 296, 307

Fields, D. 471

Figueira, Goncalo 3725 Figueroa, Terry L. 1929

Filhol, Jean-Marc 2331, 2334, 3119

Filippas, A. V. 1037 Finkelstein, Ken D. 2217 Finley, David A. 3728

Finocchiaro, Paolo 2578 Futami, Y. 600 Godlove, Terry F. 234, 1758, 1970, 3369 Fiorito, Ralph B. 487, 3722 Gaedke, Rudolph 2936 Godot, J.C. 250 Firebaugh, J. 1246 Gahl, John M. 786, 2772 Goeppner, George A. 2024 Firjahn-Andersch, Arne 530 Gai, Wei 2030, 3618, 3621 Goergen, R. 2078 Gaillard, Michel 2012 Fisch, Nathaniel J. 3675 Goerz, D. 625 Fischer, Claude 465 Gaiser, H. 3552 Goethe, J.W. 3516 Fischer, Wolfram 702, 1261, 2716, 2725, 2921 Galambos, John D. 109, 1198, 1201, 3140, 3143, Gold, Saul 1512 Fisher, Alan S. 296 Gold, Steven H. 1049, 1474 Fisher, M. V. 2659 Galayda, John N. 2024, 2471 Goldberg, J. D. 1043 Fitch, Michael J. 2027, 2181 Galdi, Vincenzo 2882 Goldenberg, Constantin A. 1055 Fitze, Hansruedi 418, 795 Galimberti, Andrea 2060 Golkowski, Cz. 3600, 3603 Fitzgerald, Daniel H. 518, 1198, 1201 Gallardo, Juan C. 3032, 3722 Gomez-Costa, Jose Louis 3200 Fitzgerald, Jim 2211 Gallo, Alessandro 131, 866, 1147 Gonzalez, Carlota 474, 1408 Galstjan, Eugene A. 1477 Goodenough, C. 2990 Flanagan, John W. 1132, 2120, 2731 Flechtner, D. 3600, 3606 Galvin, J. 2537 Goodzeit, Carl L. 3245 Fliflet, Ame W. 1049 Gamba, Claudio 1120 Gorbachev, A.M. 1474 Flippo, Kirk 3716 Gambitta, A. 2060 Gorchenko, V.M. 2256 Gammino, Santo 97, 2578 Gordon, Daniel 3684 Floersch, D. 652 Ganetis, George L. 3161, 3170, 3734 Gorev, V. V. 3711 Floersch, Richard H. 649 Gorski, Anthony J. 1411, 2635, 3342 Gao, Jie 1216, 1809, 1812, 1815, 3017 Flora, R. H. 714 Flottman, K. 3450 Gardelle, Jacques 1797, 3387 Goto, Akira 2268 Gardner, Christopher J. 614, 1276, 2063, 3182, Goto, Y. 471 Flynn, G. 1533, 1569 Fong, Ken 450, 890 3185 Gottschalk, Stephen C. 2668, 2674, 2677, 3722 Gouard, P. 1797 Gardner, K. 2918 Foose, R. 590 Forest, Etienne 404 Garnett, Robert 518 Gough, Richard A. 884, 1911, 1914, 1917, 1920, Garren, A. 206 1952, 1958 Foster, G. William 182, 3324, 3327, 3330 Fouaidy, Mohammed 913, 919 Garren, Alper A. 2364, 2439, 3050, 3065, 3068, Gourlay, S. A. 171, 3236 3152 Govorov, A.I. 2256 Fournier, P. 103 Graef, Hans-Dieter 2951 Fowkes, W.B. 3423 Garven, M. 1016 Fowkes, William R. 783, 1432, 3426 Garvey, Terrence 916, 2012 Grafstrom, Per 1671 Fox, John D. 131, 636, 1207, 1213 Gassner, D. M. 2123 Granatstein, Victor 1040, 1046 Graves, Bill 2471 Franchetti, Giuliano 1782, 1785 Gassot, Huimin 919 Gaudreau, Marcel P.J. 568, 1491 Graves, Rossie M. 2388 Franco, Jose G.S. 2421 Gautier, Cort 977, 1396 Graves, Williams S. 1949 Franczak, B. 527, 1704 Green, Michael A. (LBL) 2439, 3149, 3227 Gavrilov, Nikolay M. 1932 Franks, R. Mark 800, 803 Gebel, Ralf 2292 Green, Michael A. (SRC) 2391, 2659 Franzcak, B. 1788 Gebre-Amlak, K. 3681 Greenler, Lee 2388 Franzke, B. 527, 1704 Freedman, Stuart J. 1952 Geer, S. 3062 Greenwald, Shlomo 3221 Greenwald, Zipora 1300, 3221 Geitz, Marc 2172, 2175, 2178, 2507 Frei, Hans 418, 795 Fresquez, M.G. 426 Geld, T. 2990 Greer, James B. 1961 Gelfand, Norman M. 1677, 2861 Gregoire, Guillaume 103 Freund, Henry P. 2486 Geller, Joseph M. 2247 Grelick, A. 2024 Friedman, Alex 1830, 2758, 3248 Geng, Rong-Li 429, 980, 983 Greninger, Paul 878, 3570, 3573 Friedsam, Horst 2051, 2635 Gentzlinger, Robert C. 962, 965, 968 Griep, B. 957 Friesel, Dennis L. 498, 1548 Georgsson, Mattias 2945 Grieser, Manfred 1955, 3543 Frigola, Pedro 217, 2480 Frisch, Josef C. 253, 3447, 3450 Gericke, W. 197 Griesmayer, Erich 2957 Ghebremedhin, Abiel 11 Griffin, James E. 1201, 3152 Fritz, A. 3248 Frommberger, Frank 3098 Ghigo, Andrea 131, 1536 Griffiths, Stephen A. 2960 Grigorev, Yu. 2927, 3122 Ghiorso, William 2849 Fromowitz, Daniel B. 1632 Grimm, Terry L. 3719 Ghosh, Arup K. 185, 3161, 3188, 3197, 3230 Fuerst, Joel D. 992, 2027 Ghosh, Subhendu 952 Grippo, A. 2229 Fugita, H. 3110 Grishin, Vladislav K. 2581, 2584, 2587 Fujieda, Miho 413, 798, 857, 860, 863, 1007, Giachino, Rossano 2617 Giannessi, L. 1985 Grishiu, V.N. 392 1653, 2271, 2280 Grobner, Oswald 1339 Gibbins, Peter E. 1025 Fujikawa, Brian 1952 Fujioka, M. 3348 Gies, Albert 2424 Groening, L. 527, 1704 Gromov, Roman G. 78, 750 Gillespie, George H. 1551, 2805 Fujiwara, Chikara 842 Fukuda, Mitsuhiro 2259 Gilpatrick, John D. 2152, 2214, 2241, 3528, 3582 Gross, Dan 2936 Grossberg, Phyllis 338 Ginzburg, Naum S. 1055 Fukuda, Shigeki 3414 Fukui, Yasuo 3032 Gioia, Jack G. 977, 1396, 2954 Grote, David P. 1761, 1830, 1833, 1937, 2758, 3248 Giovannozzi, M. 1282 Fukuma, H. 633, 1132, 2731 Funahashi, Y. 777, 3423 Girault, F. 1569 Groöbner, Oswald 2629 Gladkikh, P. 3122 Gu, Shaoting 3716 Funahashi, Yoshisato 2731, 3417 Glass, Henry D. 3318 Gu, Sunhee 1357 Funakoshi, Yoshihiro 1132, 2108 Glazov, Alim A. 2262 Gubin, Konstantin V. 750, 1456, 2167 Fung, K.M. 1545, 1548, 2286 Glenn, Joseph W. 614, 702, 1258, 1270, 1746, Guerra, Al 3306 Funk, L.W. 3582 2918, 3291 Guharav, S.K. 234, 1306 Furman, Miguel A. 1674, 1791, 1794 Glover, Ernie 2370, 2498 Guidi, Vincenzo 2948 Furst, Mitchell L. 2388 Gluckstern, Robert L. 606, 1752, 1755, 2876 Guiducci, Susanna 277, 1536 Furukawa, Kazuro 1132, 2238, 2731 Guignard, Gilbert F. 250, 1635, 1638, 3399 Furuya, Takaaki 440 Gluskin, Efim 2489

Godefroy, Jean-Marie 2686

Fuss, Brian 1390

Guler, Hulya 3026

Guo, Fanqing 533 Guo, Zhiyuan 633

Gupta, Ramesh C. 171, 185, 3161, 3176, 3236,

3239

Gurd, David P. 355, 3528 Guthrie, Arthur 3594 Guy, F.W. 3531 Göettert, Jost 2424 Ha, Jangho 2265, 3137 Haagenstad, Harvey 965

Haber, Irving 234, 1749, 1758, 1830, 1970

Haberer, Th. 2513 Habib, Salman 366, 1845 Habs, Dietrich 3516 Haebel, Ernst 946, 949 Haeuser, Juergen 3519

Hafizi, Bahman 3687, 3693 Haga, Kaiichi 2310 Hagedoom, H.L. 1539, 2825 Hagedorn, Dieter 3200 Hagel, Johannes 250, 1635 Hagelstein, Michael 2424 Hagenbuck, F. 165 Hagestedt, Andre 2424

Hahn, Alan A. 468, 1085, 2066, 2164

Hahn, Harald 1100, 1103 Hahn, Robert von 1955 Hahn, Ulrich 1369 Hairapetian, G. 3708 Halaxa, Ernie 1937, 3248 Halbach, K. 2301 Haldemann, Paul 234, 1970 Hama, Hiroyuki 592 Hambikov, Valeriy D. 1456 Hamilton, Andrew 2388 Hamilton, B. 498, 1545, 1548 Hammen, A.F.J. 759, 2825, 2864

Hammon, Duncan L. 965 Hammonds, J.P. 355 Han, Bum-Soo 3525 Han, D. H. 1079 Han, Jang-Min 875, 3525 Han, Qian 1228

Han, Y.J. 3345, 3504 Hanaki, Hirofumi 2015, 2749, 3507

Hancock, Steven 143, 2226 Hanke, K. 2178

Hanke, Klaus 1282, 1285, 2617

Hanks, Roy L. 625 Hanna, S. 3423 Hanna, Samy M. 2516 Hannaford, R. 3233 Hanni, Raymond 949

Hansborough, Lash D. 1444, 1447, 1929, 1946

Hansen, Gene 1336 Hansen, Jan 562 Hansen, Robert 1049 Hansknecht, J. 1991 Hanuska, S. 2635 Harada, Hisashi 848 Harada, Kentaro 2436 Harano, Hideki 2605

Hardek, Thomas W. 1444, 1447, 1946

Hardekopf, Robert A. 3597 Harding, David J. 3318 Hardy, L. 2331, 2334 Hargenrater, Thomas 1396

Harkay, Katherine C. 123, 1641, 1644

Harnden, W. 171, 3233 Harper, Mark 1333

Harrington, Margye P. 349, 1929

Harriott, Lloyd 595 Harris, Guy 1342 Harris, Neville 2656

Harrison, Michael A. 6, 3176, 3230 Hartemann, Frederic V. 2000, 2003 Hartill, Don 980, 2975, 2978

Hartman, N. 3149 Hartmann, H. 696 Hartmann, P. 1991 Hartouni, Edward P. 2590 Hartung, Walter H. 992, 2027 Harvey, A. 3576, 3579 Harwood, Leigh 3306, 3309

Hasan, A. 2990 Hasegawa, Kazuo 3546 Hasegawa, N. 3690 Haseroth, Helmut 103 Hashimoto, Yoshinori 860 Hassanein, A. 3062 Haustein, Peter 533 Hawkey, Timothy P. 568, 1491

Hawkins, Alonzo 1037, 1515 Hayano, H. 1994 Hayano, Hitoshi 256, 2143

Hayano, Hiyoshi 3432 Hayashi, K. 3330 Hayashi, Y. 3600, 3606

Haynes, W. Brian 965, 977, 1396

Hayoshi, N. 471 He, P. 2552, 3639, 3722 He, Xiaoye 1315 Heese, Richard H. 2304 Heidenreich, G. 1360 Heifets, Samuel 1118, 1665 Heimann, Philip 2370, 2498

Helm, D. 259 Hemker, Roy G. 330, 3672 Hemmer, Michael 37 Henchel, Bill 2936 Henderson L. 296

Henderson, Stuart D. 410, 1351, 2217, 3221

Henderson, Tom 803

Hendrickson, Linda J. 307, 338, 3456 Henestroza, Enrique 1934, 1937, 2849, 2852,

Henke, Heino 812, 815, 818, 1034

Henn, Kurt 1701, 2292 Henrist, Bernard 2629 Herbeaux, Christian 2686 Hermle, Stefan 1360, 2424 Hernandez, Kenneth 803 Heron, Mark T. 661 Herr, Werner F. 304, 3005 Herrmann, J. 2915 Herrmannsfeldt, William 1937 Herrup, David A. 1091 Hershcovitch, Ady I. 584, 1902

Hertel, N. 2427 Hess, Mark 2752 Hettel, R. 206 Hezel, T. 165

Hiatt, Thomas 1462, 3306, 3309

Hickman, Bradley C. 625 Hidaka, S. 1821

Hig 3423

Higashi, Yasuo 777, 3417, 3423

Higley, H. 3233

Higo, Toshiyasu 777, 3417, 3420, 3435, 3468,

Hilaire, Alain 40 Hildreth, Mike 2999 Hill, Barrey W. 1551, 2805 Hill. Ed 2936 Hill, Jeremy M. 2480 Hill, M.E. 3612 Hill, Marc E. 545 Hill, R. 2456 Hilleret, Noel 2629

Himel, Thomas M. 293, 296, 338 Hinson, William M. 3212

Hiramatsu, Shigenori 492, 633, 1132, 2120, 2731

Hiramoto, Kazuo 2528, 3366 Hirata, Kohji 1689

Hiraya, A. 2689

Hirose, Tachishige 256, 2552

Hirota, Jun'ichi 3366

Hirshfield, Jay L. 1049, 1052, 1474, 3627, 3630

Hitomi, Nobuteru 777, 3417 Ho, C.H. 1450, 2000, 2009 Ho, Darwin D.-M. 1827 Hoag, Harry 777, 3423 Hoberg, H. G. 197 Hockman, Jeffrey N. 2590

Hodgkins, David J. 349, 1444, 1447, 1946

Hodgkinson, Chervl L. 2656 Hoellering, Frank 3519 Hoeltermann, H. 1899 Hoff, Lawrence T. 693, 1261 Hoff, Matthew D. 884, 1958, 1961

Hoffman, J.R. 3651 Hoffmann, Markus 3098 Hoffstaetter, George H. 407 Hofmann, A. 296

Hofmann, Ingo 137, 1782, 1785, 1788

Hogan, Bart 1046 Hogan, G. E. 579 Hogan, J. 1462, 1991 Hogan, John 934 Hogan, M. 217

Hogan, Mark J. 330, 1997, 2111

Holden, Travis 2006 Holder, David J. 2433 Holmes, Clifford 2235

Holmes, Jeffrey A. 109, 1198, 1201, 3140, 3143,

3303

Holmes, Stephen D. 43 Holstein, Friedrich 2424

Holtkamp, Norbert 896, 3062, 3149

Holtzapple, Robert L. 410, 2057, 2972, 2975, 2978

Homeyer, H. 3519 Homeyer, William G. 2954 Homma, T. 600 Homscheidt, M. 165 Honda, Tohru 2310

Horan, Douglas 1019, 1022

Hori, H. 3507

Hori, Toshitada 2298, 2400, 2403, 3702

Horioka, Kazuhiko 3690

Horny, M.J. 2000, 2009 Hosaka, Masahito 592 Hosokai, Tomonao 3690, 3702

Hosoyama, Kenji 440, 1132, 2731 Houck, Timothy L. 1210, 1303, 2755, 3257, 3390

Hourican, Michael D 2283 Hovater, Curt 768, 1177 Howell, Joseph W. 3095 Hower, Nelson L. 221, 2099, 2468

Hoyer, Egon H. 162

Hseuh, Hsiao-Chaun 557, 1345 Ivers, J.D. 3600, 3603, 3606 Julian, R.A. 2394 Hsi, W.C. 1548, 2286 Iverson, R. 2111 Jung, Roland 465 Jungmann, K. 1488 Hsiao, Ko-Ming 1375 Iverson, Richard H. 330, 1252, 2987, 3648 Hsiung, Gao-Yu 1375, 1605 Iwasaki, H. 492 Junquera, Tomas 919 Hsu, Ian C. 2220 Iwashita, Y. 2280 Juras, M. 658 Iwashita, Yasuhisa 3110 Hsu, Kuo Tung 682, 685, 1153, 1156, 1159, 1162, Kabel, Andreas 1650, 2507 1450, 1605, 2009, 2069, 2072, 2220, 2409, Iwashita, Yoshihisa 857, 1294, 2528, 3645 Kabeya, Zenzaburo 842 2412, 2671, 2837 Izawa, Masaaki 633, 904 Kadantsev, S. 106 Hsu, S.Y. 1450, 2009, 2072 Jablonka, Marcel 922 Kaganovich, Dmitri 3693 Hsu, Shen-Nung 1375 Jackson, Alan 2641 Kageya, Tsuneo 392 Hsu, Yao-Jane 1375 Jackson, G.P. 3324 Kahn, S. 185 Hu, Hongliang 1596 Jackson, John W. 3185, 3333 Kahn, Stephen A. 3023, 3026 Hu, Kuo Hwa 2412 Jackson, Leslie T. 3257 Kai, Satoru 1309 Hu, Kwo Hwa 682, 1153, 1156, 2069, 2072 Jacob, Jorn 1647 Kaiser, Hartwig 2385 Hu, Shouming 1596 Jacobs, Kenneth D. 3101 Kaiser, K.-H. 165, 2915 Huan, N. 1132 Jaekel, Markus 2424 Kaji, M. 343 Huang, H. 471, 1548, 2128 Jaeschke, E. 197 Kako, Eiji 432 Jagger, Jack M. 1378, 1979, 2635 Huang, Hong 633 Kalinichenko, Alexandr I. 2546 Huang, Jung-Yun 1076, 2131, 2418 Huang, M.H. 2671 Jaggi, Andreas 2087 Kaltchev, Dobrin 2620, 2623 Jahnel, Lucia 2421 Kamada, Susumu 256, 2155, 3432 Huang, N. 2731 Jain, Animesh 185, 3161, 3170, 3173, 3176, 3179, Kaminsky, Alexander A. 1055, 3393 Huang, Nan 2963 3188, 3336 Kaminsky, Alim K. 1055, 3393 Jaitly, Ray 1010 Huang, Yen-Chieh 321 Kamitani, T. 1132, 2731 Jakob, Ansgar 1288, 1836 Huang, Zhirong 262, 1644, 2495 Kamitsubo, Hiromichi 188 Hubbard, E. 3576, 3579 Jander, Donald R. 2668 Kamiya, Yukihide 904, 1174, 2436, 3363 Janssen, Dietmar 2033 Hubbard, Richard F. 3687, 3693 Kamperschroer, James H. 1444, 1447, 1929, Jansson, Andreas 2223, 2226 1946, 2214 Huelsmann, Peter 3405 Jeanneret, Jean-Bernard 40, 2620, 2623 Kamps, T. 2075 Hughes, Thomas P. 2746 Jensen, C. 2164 Kamykowski, Edward 587 Hughey, Lanny R. 2388 Jensen, Erk 250, 1408 Kanai, T. 600 Huhtinen, Mika . 1231 Humpert, Michael 806 Jeon, D. 1545 Kanai, Y. 1653 Jeon, Dong-o 109, 1198, 1201, 3140, 3143, 3303 Humphries Jr., Stanley 2737, 2772, 2778 Kanai, Yasumori 3348 Hundzinger, Denis 3743 Jeong, S. C. 1893 Kanaya, Noriichi 664, 667, 670 Hunt, W. A. 676 Jeram, B. 658 Kanazawa, Mitsutaka 413, 600, 798, 863, 2271 Hunter, W. Ted 3576, 3594 Jericha, Erwin 2957 Kando, Masaki 3690, 3702 Hurh, Patrick G. 1423 Jett, Nelson D. 649 Kaneda, T. 592 Kang, H.S. 2205, 2501, 2593 Husmann, Dirk 3098 Jia, Qika 2406 Jiang, Daoman 1315 Jin, Yuming 2184, 2406 Hutchins, S. 250 Kang, X. 1545 Kang, Yoon W. 168, 3092 Huttel, Erhard 1360, 2424 Hwang, C.S. 1450, 2671 Job, P.K. 2090 Kaplan, Danniel M. 3032 Hwang, J.Y. 2000, 2009 Jobe, R. Keith 253, 3411, 3429, 3447, 3453 Kaplan, Roger 980 Johnson, D. 1318 lazzourene, Fatma 2707 Karabarbounis, A. 1037 Ichihara, Masahiro 3546 Johnson, David 518 Karantzoulis, Emanuel 1126, 2316 Ieiri, Takao 1132, 1135, 2731 Johnson, David E. 714, 717, 1243, 2647 Karasuk, V. 3086 Igarashi, Susumu 1141 Johnson, Erik D. 584, 2471, 2480 Karliner, Marlen M. 2033 Igolkin, Alexsandr G. 1456 Johnson, Kenneth F. 1929, 3528 Karn, Jeff 3306, 3309, 3312 lida, Naoko 1132, 2108, 2731 Johnson, Mark 2936 Karnaukhov, I.M. 2930, 3122 lino, Youshuke 842 Johnson, Marty 2468 Karyotakis, Yannis 2990 Johnson, Neil G. 3764 Kashikhin, Vladimir 174, 182, 3327 Ikegami, Kiyoshi 1653 Ikegami, Masanori 62, 1818, 1821, 3546 Johnstone, Carol J. 1677, 3050, 3065, 3068, 3071, Kashiwagi, Shigeru 256, 2143, 3432 3152 Kaspar, Klaus 3552 Ikezawa, Mikihiko 2187 Ilg, Thomas 3594 Johnstone, John A. 1082 Kasuga, Toshio 633, 2310 Imai, K. 471 Joly, Jean-marc 922 Katane, Mamoru 2528 Jones, Frederick W. 128, 2933 Ingalls, William B. 1917, 1923 Katayama, Takeshi 404, 1719, 1722, 1737, 3164 Inoue, Makoto 1294, 2528, 3110 Jones, Justin 2051, 3095 Kato, S. 1132, 2731 Jones, Kevin H. 518, 3528 Irwin, John 259, 363, 3423, 3453, 3480 Katoh, Masahiro 664, 2307 Isaev, V.A. 1474 Jones, Roger M. 777, 3423, 3468, 3471, 3474, Katoh, Tdahiko 343 Ishchanov, Boris S. 2584 3477 Katonak, David J. 974 Ishi. Kimihiro 2187 Jones, W.P. 1548, 2519 Katsouleas, Thomas C. 330, 3651, 3654, 3672, Jongewaard, Erik N. 783 Ishi, Sadahiro 2271 3708, 3713 Ishi, Yoshihi 1653 Jonker, Michel 2617, 2996 Katsumata, Tadasu 1309 Ishibori, Ikuo 2259 Joosten, Rainer 533 Katsumura, Yosuke 2602 Jordan, Kevin 2229, 2456 Kawachi, K. 600 Ishihara, M. 471 Joshi, Chad 931 Ishkhanov, Boris S. 2555 Kawamoto, Takashi 343, 2108 Issinsky, Igor B. 2262, 2289 Joshi, Chan 330, 2006, 3651, 3654, 3684, 3705, Kaye, Robert A. 524 Ito, Takashi 3546 3708 Kazacha, Vladimir I. 3393 Ivanov, Alexander P. 3501 Jowett, John M. 1680 Kazakov, S. 1058

Judkins, J. 206

Juillard, Michel 432

Julian, James 1471, 3131

Kazakov, Serguei 3414

Kazanskiy, Lev N. 1477

Kazarinov, Nikolai Yu. 3501

Ivanov, G. M. 1973, 1976

Ivanov, O.A. 1474

Ivanov, Yu.M. 53

Kazimi, R. 1991 Keane. John 1028 Kedzie, Mark 524, 955 Keesee, Marie 747 Keffeler, David R. 1444, 1447 Kehne, David M. 234, 1970 Keil, Eberhard 1408 Keil, J. 2054, 3098 Keller, L. 2990 Keller, Roderich 87, 884, 1911, 1914, 1917, 1923, 1926, 1943, 1958 Kelley, John P. 965 Kelly, Eugene 185, 3161 Kempkes, Michael A. 568, 1491 Kenda, K. 658 Kennedy, K. 206 Kennedy, Kurt D. 884 Kenney, S. 3227 Kerby, J. 3194, 3197 Kernel, Philippe 1192, 1195 Kerner, Thomas M. 696, 699 Kerstiens, Debora M. 349, 652, 655, 1929, 1946 Kesselman, Martin 2250 Kester, Oliver 3516 Kewisch, Jorg 705, 708 Kezerashvili, Guram Ya. 2232 Khachatryan, Arsen G. 3663 Khan, Sameen A. 2817, 3280 Khan, Shaukat 197, 1144, 1147, 2831 Khodvachikh, A. 3122 Khodzhibagiyan, Gamlet G. 2262 Khomenko, S. 103 Kiang, L.L. 1545 Kikuchi, Mitsuo 1132, 2108, 2731

Kikutani, Eiji 633, 1132, 1138, 2731

Kikuzawa, Nobuhiro 2459 Kim, Eun-San 3053, 3056 Kim, G.N. 2593

Kim, Han-Sung 2558, 2561 Kim, Jin-Soo 1043, 1890 Kim, Jong-Won 2268 Kim, K.R. 3504 Kim, Kwang W. 1384 Kim, Kwang-Je 2495 Kim, Mun-Gyung 2418 Kim, Sang-Ho 2558, 2561

Kim, Y.C. 3504

Kim, Yong-Hwan 2558, 2561 Kim, Young-Hwan 2558, 2561 Kim, Yujong 1076, 1079 Kim, Yuseok 3137 Kimura, Wayne D. 487, 3722

Kincaid, Brian 162

Kindermann, Hans-Peter 946 King, Bruce J. 318, 3035, 3038, 3041 King, Quentin 762, 3743

Kinkead, Allen K. 1049 Kinoshita, Kenichi 2605 Kinsho, Michikazu 3128, 3546

Kirbie, Hugh C. 625 Kirichenko, A.E. 2256

Kirk, Harold G. 896, 3029, 3032, 3149 Kishek, Rami A. 234, 1656, 1749, 1758, 1761, 1830, 1970, 3274, 3369, 3372

Kishiro, Jun'ich 1141

Kishiyama, Keith 1333, 1336, 1396

Kitabayashi, Teruyuki 343 Kitagawa, A. 600 Kitazawa, Yasuji 592 Klaffky, Roger 2304

Klaisner, L. 206 Kleev, Andrey I. 592 Kleimenov, Victor 1339 Klein, Horst 1288, 1836, 3405

Klein, John 551 Kleinod, M. 1899 Klenov, V. 106 Klette, Hallgeir 562 Klingmann, Jeffrey 777 Knapp, Edward A. 2301, 2555 Kneisel, Peter 937, 943 Kniegl, Gregor 3740 Knobloch, Jens 980 Knoch, Herbert 2424 Knudsen, Helge 1671

Knuth, Thomas 197, 1144, 1147 Ko, In-Soo 1076, 1079, 2131, 2593, 3525

Ko, Kwok 2822, 3423, 3480 Koba, Kiyomi 1653, 2271 Kobayashi, T. 3507

Kobayashi, Yukinori 633, 2436, 3113, 3363

Koehler, G. 800 Koepke, Karl P. 992, 2027 Koeth, Tim 995 Koganeya, M. 3330 Kohaupt, Rolf Dieter 1171 Koiso, H. 1132, 2731 Koizumi, Nozomi 343

Kolbe, J. 197 Kolysko, A.L. 1474 Komada, Ichitaka 343 Kondo, Shuji 3690, 3702 Kondo, Yasuhiro 2187 Kondrashev, S. 103 Kondratenko, Anatoly 2289

Konecny, Richard 2030, 3618, 3621

Kononenko, S. 3122

Konstantinov, Sergey G. 2033 Koontz, Roland 1512 Korabelnikov, Maxim B. 2167 Korenev, Igor L. 1764 Kornilova, Alla A. 1312 Korolev, Aleksey 2567 Koroliov, Alexander N. 2570 Koscielniak, Shane R. 143, 1839

Koseki, Shoichiro 3770 Koseki, Tadashi 592, 2436, 3363

Koseki, Takashi 904 Kostas, Chris 360 Kostial, Stephan 2740, 2951 Kostin, Denis V. 910, 2301 Kotaki, Hideyuki 3690, 3702 Kotov, V.I. 53, 1237 Kotseroglou, T. 3432, 3447 Kotseroglou, Theofilos 3450

Koupsidis, J. 2385 Kourbanis, Ioanis 2840 Koutchouk, Jean-Pierre 372 Koutin, S.V. 392

Kovalenko, Alexander D. 2256, 2289

Kowalski, Ludwik 490 Koyama-Itou, H. 600 Kozanecki, W. 2990 Kozanecki, Withold 296 Kozawa, Takahiro 2018, 2596 Koziol, Heribert 465 Kozyrev, Evgeny V. 1049 Kponou, A. 1902 Kraemer, Dieter 197, 2379 Krafczyk, George 3761

Krafft, Geoffrey A. 1177, 2229, 2448, 2456

Kraft, G. 2513 Krakauer, D. 2635

Kramer, Stephen L. 134, 140 Krasnopolsky, Vsevolod A. 1479 Krasnykh, Anatoly 1512

Kraus, David E. 490 Krause, Herbert F. 1671

Kravchuk, Leonid V. 2799, 3282, 3561 Krawczyk, Frank L. 965, 977, 1396, 3588

Kreischer, Kenneth E. 81

Kreicik, Patrick 296, 3429, 3447, 3450

Kresnin, Yuri A. 2546 Krienen, Frank 3134 Krietenstein, Bernd 3552 Krinsky, Samuel 2304, 2471 Krisch, Alan D. 392 Krishnagopal, Srinivas 1674

Krishnan, Mohan 3666 Kriznar, I. 658

Kroc, T. 521

Krogh, Michael L. 1303, 2611

Kroll, Norman M. 777, 830, 1432, 1435, 3423, 3468, 3471, 3474, 3477, 3612

Kruchkov, Jaroslav G. 2033 Kruessel, Alois 2424, 3375

Krylov, Stanislav Y. 1479, 1485, 2567

Krämer, D. 2078 Kubantseva, Natalia 1423 Kube, G. 165

Kubo, Hiroshi 3770 Kubo, Kiyoshi 256, 2143, 3432, 3435

Kubo, Ta. 3158 Kubota, Chikashi 1653 Kuchnir, Moyses 992, 2027 Kudinov, Valery V. 1291 Kudo, Hirofumi 3363 Kudo, Kikuo 343 Kugler, Hartmut 103 Kuhler, S. 197

Kulikov, Artem V. 3447, 3450

Kulikov, I.I. 2256

Kumada, Masayuki 600, 2510 Kumagai, Keiko 2337, 2343, 2346

Kumagai, Noritaka 188, 2337, 2340, 2343, 2346,

2349, 2352 Kuner, B. 197 Kuno, Kazuo 3363 Kuo, C.C. 2409, 2412, 2837

Kuo, Chang Hor 685, 1153, 1156, 1159, 1162,

1165, 2069, 2409, 2412

Kurennoy, Sergey S. 1399, 2867, 3588

Kurita, Nadine R. 206, 1363 Kurnaev, O. 1249 Kuroda, Ryunosuke 2298 Kuroda, T. 1306 Kurokawa, S. 633 Kurz, Stefan 2796 Kusano, Joichi 3128, 3546

Kusche, Karl P. 2552, 3722 Kushin, Victor V. 3564 Kusikov, S.V. 1474

Kuske, Bettina 197, 2379, 2382 Kuske, Peter 197, 2078, 2379, 2385 Kustom, Robert L. 168, 518, 998

Kuszynski, J. 2078 Kuzay, Tuncer M. 2090 Kuzminski, Joze 965 Kuzminski, Jozef 968, 2954 Kuznetsov, G. 237, 1902

Kuznetsov, Yu. 106 Lee, Peter J. 177 Lin, Ke Kang 682, 1450, 2009, 2409, 2412, 2415 Kvasha, Adolf I. 893, 3561 Lee, Roger C. 557, 1348, 2146 Lin, Tsai-Fu 1375 Kwan, Joe 1937, 1943, 2537 Lee, S. 3672 Lin, Xintian E. 75, 1429, 3612 Kwan, Thomas J.T. 617, 1842 Lee, S.H. 682 Lindgren, Lars-Johan 2945 Kwiatkowski, K. 471 Lee, S.Y. 109, 392, 1545, 1548, 1854, 2286 Lindroos, Mats 143, 2226 Kwon, Hyeok-Jung 2558, 2561 Lee, Seung 330 Linnecar, T. 2617 Kwon, Myeun 899, 902, 1076, 1079, 1357 Lee, Seung C. 1384 Lira, Antonio C. 3125 Kwon, Sung-il 1064, 1067, 1070 Lee, T. 2021 Lisi, Nicola 103 Lee, Tae-Yeon 679, 1384, 2131, 2418 Kwon, Y. K. 1893 Lisitsyn, A. 461 Kühnel, K.U. 3516 Littauer, Raphael M. 410, 2057 Lee, W. Wei-Li 1623, 1626 Lach, Joseph 1387 Lee, Yong Y. 1297, 1488, 1743, 3182, 3185, 3300 Litvak, A.G. 1474 Laclare, Jean-Louis 1533 Lee, Yvette 2540, 2575 Litvinenko, Vladimir N. 221, 2099, 2468 Leemans, Wim P. 325, 330, 2111, 3696, 3699, Ladran, A. S. 2590 Liu, Chen-Yao 3776 Lager, Darrel L. 3513 Liu, Dekang 633, 2140 Lakatos, Andreas 1288, 1836 Lefebvre, Daniel 2686 Liu, G. 2337 Lalot, Michel 922 Lefevre, Thibaud 1797, 3387 Liu, Guangjun 2125 Lamanna, Giuseppe V. 2948, 3522 Legan, Al. 56 Liu, H.C. 2671 Lamarre, J.F. 1569 Lehrach, A. 1578 Liu, James 3450 Lambertson, Glen R. 1225 Lehrach, Andreas 1701, 2292 Liu, Jinhong 2048 Lambiase, Robert F. 3734 Lei, Ge 747 Liu, Kuo-Bin 3776 Lamm, Michael J. 3191, 3194, 3197 Leissner, Boris 2172 Liu, Lin 2421, 2891, 2894, 3125 Lamont, Michael 304, 2996, 3008 Leitner, Matthaeus A. 1911, 1914, 1958 Liu, Y. 2552, 3639, 3722 Landahl, Eric C. 2000, 2003 Lekston, J.M. 3387 Liu, Yuan 1878, 1881 Lange, M. 2424 Len L. K 70 Liu, Zuping 2048, 2406 Lange, R. 197 Leng, Yongbin 1315, 2125 Lo, C.C. 1471, 3131 Lobo, Ricardo P.S.M. 134 Lange, Ralph 2382 Lenkszus, Frank R. 333, 2093 Lanting, T. 2990 Leon, Asunción 2531, 2534 Lockey, R. 1902 Lanza, Richard C. 584 Lepercq, Pierre 916 Loew, G.A. 3423 Lapik, Roman M. 2170 Lepeule, Patrick 1339 Loewen, Roderick J. 3420, 3423, 3426, 3480 LaPointe, Mike A. 3627 Lesjak, B. 658 Logan, B. Grant 3248 Lapostolle, Pierre 1860 Lesrel, Jean 919 Logatchov, Pavel V. 78, 237, 2167, 2948 Lapshin, V. 3122 Lessner, Eliane S. 1644, 1967, 2325 Loh, M. 3708 Larbalestier, David C. 177 Letchford, Alan P. 1767, 2208 Lohrmann, Erich 554 Larimer, Ruth-Mary 533 Lettry, J. 92 Lombardi, Alessandra M. 103, 1860 Lombardi, Augusto 1324, 3522 Larrieu, Christopher A. 741, 747 Leung, Ka-Ngo 1911, 1914, 1917, 1920, 1923, 1943, 1958, 2540, 2575 Larsen, Ray 636 Lonza, Marco 1120 Leunissen, Leonardus H.A. 1557, 1683 Larsen, Richard C. 490 Lopes, Nelson 3725 Latypov, Tomas A. 1485, 2567 Level, Marie-Paule 1533 Lorenz, Ronald 2075 Lau, Wai Keung 1153, 1159, 1162, 1165, 2000, Levush, Baruch 360, 1016 Lorenzon, Wolfgan 392 Levy, C.D. Philip 106, 1964 Loschner, H. 2575 Laurent, Jean-Michel 2629 Lewellen, John W. 1979, 2024, 2134, 2483 Losito, Roberto 946, 949 Lauth, W. 165 Lou, G.H. 2220 Lewis, B. 471 LaVeigne, Joseph 134 Lewis, S.A. 355 Lou, Weiran 1441, 3221, 3224 Laverty, Michael 890 Li, C.D. 2671 Loulergue, Alexandre 1530 Lawrence, George P. 3567, 3582 Li, Derun 382, 800, 896, 907, 1207, 1548, 3149 Low, Raymond 1920 Lawson, Wesley 1040, 1046 Li, Guangyeng 2125 Lozowski, B. 471 Li, Jingyi 2048 Lawton, Don 234 Lu, Chang-guo 3026 Laxdal, Robert E. 893, 3534, 3537 Li, Nanyang 3339 Lu, Ping 2184 Lazarus, Donald M. 490 Li, Rui 118, 2456 Lucas, Peter W. 1246, 2614 Laziev, Eduard M. 3393 Li, Shaopeng 633 Luccio, Alfredo U. 1578, 3143 Le Duff, Joel 913, 2012 Li, Weimin 2406 Ludewig, Hans 548, 3185 Le Sage, G.P. 2480 Li, Yongjun 2406 Ludewigt, B. 2537 Lebedev, Pavel 1387 Li, Yulin 3221 Luft, P. A. 1914 Lebedev, Valeri A. 646, 738, 1183, 2897 Li, Yun 234, 1656, 1758, 1970, 2102, 3369 Luhmann, Jr., Neville C. 2000 Leblanc, G. 206 Li, Zenghai 2822, 3423, 3447, 3468, 3480, 3483, Luiten, O.J. 3266 LeBlanc, Greg 2945 3486 Lujan, Richard E. 977 Liaw, Chong-Jer 1345, 3300 LeBon, Douglas J. 3758 Lumpkin, Alex H. 1644, 2134, 2137, 2161 Lebrun, Paul 3032, 3062 Libkind, Marcus A. 1390, 2477, 2590 Lund, Steven M. 1785, 1788, 3248, 3381 Lidia, Steven M. 1797, 1800, 2698, 2870, 3387, LeCocq, C. 1390 Lundah, Eric W. 3480 Lee, Y.Y. 1267 3390 Lunev, Pavel 461 Lee, Bryan S. 625 Liebermann, Holger 530 Luo, Xiaoan 2963 Lee, Chun Sik 1893 Lietzke, A. 171, 3233 Luo, Xuefang 1596 Lee, Edward P. 1830, 3254 Likhachev, Sergey P. 2587 Luo, Yun 633 Luong, Michel 250, 821 Lee, Hyeyoung 3137 Liljeby, Leif 1955 Lee, J.C. 1602, 1605, 2837 Lill, Robert M. 1411 Lyles, John T. M. 998, 1001 Lee, J.W. 679 Lima, Roberto R. 1366 Lynch, Don 2244 Lee, Jan Fung 1162 Limberg, Torsten 1650 Lynch, Michael T. 453, 1061 Lee, Jinhyung 2784 Limborg, Cecile G. 206, 2361, 3104, 3107 Lyneis, Claude M. 533, 1952 Lee, Kang-ok 2558, 2561 Limon, Peter J. 174, 1420, 2644, 3194, 3197 Lyons, Mike B. 962 Lee, P. B. 1716 Lin, F.Y. 2671 Lysenko, Walter P. 3528

Ma, Li 633, 2140 Ma, Qing 1342 Macek, Robert J. 518, 1198, 1201 MacGill, R.A. 3149 MacGill, Robert 884 Machida, Shinji 62, 1653, 1818, 1821, 2271 Machie, D. 1991 MacKay, William W. 693, 702 MacLachlan, J. 521, 1707 MacLaren, Stephan A. 1937, 2849, 2852 Madden, Robert P. 2388 Madrid, Mike 1396 Maeng, AeHee 1384 Maerki, Max 418 Maezawa, Hideki 667, 670 Magerski, Andy W. 3573 Magne, Christian 922 Magurno, Benjamin 490 Mahler, G. 2128 Maier, Rudolf 851, 1701, 2292 Mailian, M.R. 1468, 2105, 3657 Majka, Richard 1258 Makarov, A. 3327 Makarov, K. 103 Makdisi, Y. 471 Makhnenko, L. A. 1973, 1976 Makita, Yo 848 Mako, Frederick M 70 Maksimchuk, Anatoly 3666, 3716 Malamud, E. 3330 Malchow, Russell 2990 Malitsky, Nikolay 2713, 3185 Malone, Robert G. 2158, 2471, 2942 Mamaev, Gennady L. 1479, 1482, 1485, 2564, Mamaev, Sergey L. 1479, 1482, 1485, 2567 Mamaev, Yuri A. 1988 Mammosser, John 925, 934, 937, 955, 1462 Manglunki, D. 1282 Mangra, Danny 1967, 1979 Manni, Mario 2277 Mant, Geoff 3248 Manwaring, Wm. 498, 673 Manzo, Mario P. 965 Mao, Stan 3429 Mapes, M. 1345 Marcellini, Fabio 131, 866, 1147 Marchand, Patrick 986, 989 Marcouille, Olivier 2686 Marhauser, Frank 3405 Marini, J. 919 Markiewicz, Thomas W. 307, 3462, 3489

Manzo, Mario P. 965
Mao, Stan 3429
Mapes, M. 1345
Marcellini, Fabio 131, 866, 1147
Marchand, Patrick 986, 989
Marcouille, Olivier 2686
Marhauser, Frank 3405
Marini, J. 919
Markiewicz, Thomas W. 307, 3462, 3489
Markovich, G. M. 2024
Marks, Steve 162, 3429
Marl, Ron 2656
Marlats, Jean-Louis 2686
Marletta, Salvo 97
Marneris, Ioannis 2543, 3767
Marone, Andrew 3161, 3170
Marque, Sébastien 946, 949
Marriner, John 641, 1707, 2638
Marsh, Kenneth A. 330, 2006, 3651, 3705
Marshall, Thomas C. 3627

Marlats, Jean-Louis 2686
Marletta, Salvo 97
Marneris, Ioannis 2543, 3767
Marone, Andrew 3161, 3170
Marque, Sébastien 946, 949
Marriner, John 641, 1707, 2638
Marsh, Kenneth A. 330, 2006, 3651,
Marshall, Thomas C. 3627
Marteau, Fabrice 2686
Marti, F. 1318
Martin, D. 206
Martin, Edward 3309
Martin, K. S. 714
Martin, Michael C. 495
Martin, Philip S. 31, 1082, 3318

Martin, Siegfried A. 959, 3549 Martinez, D. 2214 Martinez, Derwin G. 2241 Martinez, Felix A. 965 Martinez, Horace J. 965 Martini, M. 1282 Martins, Marcos N. 1366 Martlew, Brian G. 661 Martono, Hendy 1551, 2805 Martyshkin, Pavel V. 1456, 2170 Marusic, A. 2128 Marutsuka, Katumi 3360 Maruyama, T. 3447 Maruyama, Takahashi 3450 Maruyama, Takashi 1988 Marx, Michaela 2385

Masahiro, Kaji 343 Masaki, Mitsuhiro 2346 Masi, M. 1324 Masullo, Maria R. 1599 Masunov, E. 2855, 2858 Masuzawa, Mika 1132, 2731, 3351, 3354, 3357

Matheisen, A. 2033

Matheisen, John 2999

Mathie Vice Legent 2424

Mathis, Yves-Laurent 2424 Matoba, Suguru 2271 Matsufuji, N. 600 Matsurpato, Hipobi 536, 84

Matsumoto, Hiroshi 536, 842, 3411

Matsumoto, Shuji 3414 Mattison, Thomas 2990 Matuk, Charles 1920 May, Michael P. 1423 May, T.E. 2394 Maymon, Jean-Noel 1168 Mazaheri, G. 296

Mazur, Peter O. 182, 3318, 3330 Mazzitelli, Giovanni 1536 McAllister, Brian 3101 McAshan, M.S. 182 McCandless, Brian 3480

McCarrick, James F. 1303, 1827, 2755 McCarthy, Michael P. 1061, 1402 McChesney, David D. 3179, 3188 McClellan, Jonathan T. 965

McCormick, Douglas J. 253, 307, 1994, 3411,

3453, 3477 McDaniel, Boyce 410 McDonald, Kirk T. 310, 3026 McGehee, Peregrine M. 652, 3528 McGehee, Robert 688 McGinnis, David 59, 854, 1713 McGuire, David 1402 McIntosh, Peter A. 1025

McInturff, Alfred D. 171, 3197, 3233, 3236

McIntyre, Gary T 3336 McIntyre, Peter 2936 McKee, B.D. 3429, 3447 McKemey, Adrian 2990 McKinney, W. 495 McMahan, Margaret A. 533 McMichael, Gerald E. 2274 McNerney, A.J. 1267, 1270 Mead, William C. 2790 Meadow, B. 2990 Meads, Phillip, F. 3549

Meddahi, Malika 304, 2996, 3005

Meier, Wayne R. 1503 Meilunas, Ray 2599

Meinke, Rainer B. 3212, 3215, 3245

Mele, K. 658

Melissinos, Adrian C. 2027, 2181

Meller, Robert E. 1115

Melnychuk, Stephan T. 587, 2599

Mendonca, Jose T. 3725 Menefee, Tina 3306 Menegat, Al 824, 3420 Menna, Mariano 2578 Menshov, Alexander A. 893

Menzel, Jan 2178 Meot, Francois 2445 Merl, Robert 2093 Merle, Eric 3260

Merminga, Lia 768, 1177, 1180, 2456

Merrill, Frank 518
Merte, Rolf 815, 818
Mertens, Volker 40
Meseck, Atoosa 554
Meth, Marvin 3336
Metral, G. 1282
Meurdesoif, Y. 3387
Meusel, Oliver 1288, 1836
Mexner, Wolfgang 2424
Meyer, Christophe 103
Meyer, Dirk 1917
Meyer, Earl 1946
Meyer, H.O. 471
Meyer, Ross K. 3594
Meyer-ter-Vehn, Jurgen 3675

Mezi, Luca 1219 Mi, J-L. 1488 Michaut, Jean 2686 Michelato, P. 2027

Michizono, Shin-ichiro 1132, 2731, 3414 Michnoff, Robert J. 693, 2114, 2247

Michta, Richard J. 2081 Middendorf, Mark E. 2274 Miera, D.A. 426 Miertusova, Jana 2316 Migliorati, M. 131 Migliorati, Mauro 1219 Mikawa, Katsuhiko 3360

Mikhailichenko, Alexander A. 2814, 3218, 3633,

3636

Mikhailov, Vladimir A. 2256, 2262, 2289

Miki, Miyako 2596 Mikkelsen, Ulrik 1671 Milardi, Catia 1536 Milharcic, T. 658

Millage, Kyle K. 3429, 3447, 3450

Miller, J.R. 3227 Miller, Roger H. 777, 3423, 3426, 3468, 3471;

3474, 3477, 3480, 3483, 3486 Millich, Antonio 250, 1863 Millo, Daniele 2680 Millos, Gabriel 171, 3236 Mills, Frederick E. 3152 Milton, Bruce 587

Milton, Stephen V. 1644, 1979, 2024, 2134, 2325,

2483, 2486

Mimashi, T. 1132, 2731 Minaev, Sergey A. 1291, 3552 Minaev, Serguei 3555 Mincer, Allen 1258

Minehara, Eisuke J. 2459, 3546

Minohara, S. 600

Minty, Michiko G. 256, 296, 307, 338, 771, 800,

1207, 2846, 3384, 3432 Mirabal, J.S. 426 Mirochnik, E. 2567 Mirzojan, Alexandr N. 3561

Mischenko, Aleksandr V. 2564 Mishin, Andrey V. 590 Mishney, V. M. 2167 Mishra, C. Shekhar 31, 2641, 2644, 2647, 2719, 3318 Mistry, Nariman B. 3221 Mitchell, John C. 965 Mitchell, Russell R. 965 Mitra, Amiya K. 450, 839, 893 Mitsuhashi, Toshiyuki 492, 2120, 2143, 2307 Mitsumoto, Toshinori 2268 Mitsunobu, Shinji 440 Miyade, Hiroki 2403 Miyahara, N. 600 Miyahara, Tsuneaki 2155 Mizumoto, Motoharu 513, 3128, 3546 Mizuno, Akihiko 2015, 2749, 3507 Mizuno, Hajime 3414 Mizutani, Yasuhiro 2596 Moallem, M. 2099 Mocheshchnikov, N.I. 2924 Mochihashi, Akira 1821 Moeller, Soeren Pape 2295, 2427 Mohos, I., 2054 Moir, David C. 617, 1842 Moir, Ralph W. 1503 Mokhov, Nikolai V. 56, 1231, 1234, 2525, 2614, 3041, 3047, 3050, 3074 Molodkin, V. 3122 Mojodozhentsev, Alexander 2522 Molvik, Arthur W. 1503, 3248 Monard, H. 2012 Monchinsky, V.A. 2256 Mondelli, Alfred A. 360 Montag, Christoph 1566 Montoya, Debbie I. 965 Montoya, Dennis R. 965 Moog, Elizabeth R. 2483, 2489 Moore, Christopher I. 3687, 3693 Moore, Craig D. 1246, 2614 Moore, D. 652 Moore, John M. 1551, 2805 Moore, T. L. 2590 Morcombe, Peter H. 221, 688 Moretti, Alfred 896, 3032, 3149, 3152 Morgan, Gerry H. 185, 3161, 3170 Mori, Warren B. 330, 3669, 3672, 3684 Mori, Yoshiharu 106, 413, 565, 798, 857, 860, 863, 1007, 1653, 1821, 1964, 2271, 2280, 3348, Morita, Akio 1294, 2528 Morpurgo, Giulio 2996 Morrison, L. 171, 3233

Morrison, M. 171, 3233 Morse, W.M. 1488 Mortazavi, Payman 1028 Morvillo, Michele 1408, 2629 Moser, Herbert O. 165, 2424 Moser, S. Scott 3041 Mosnier, Alban 628, 1533, 1662, 2834 Moss, Andrew J. 1025 Moss, James D. 965 Mostacci, Andrea 2873

Mouton, Bernard 2012 Muchnoi, Nickolay Yu. 2232 Mueller, Roland M. 726, 2078, 2379, 2382, 2385 Mugge, Marshall 777

Muggli, Patrick 330, 2006, 3651, 3654, 3708

Mugnai, G. 2999

Mouillet, Marc 3260

Mukherjee, Sam K. 1911, 1914

Mukugi, Ken 3546

Mulhollan, Gregory A. 1988, 3447, 3450

Mullacrane, I. D. 2656

Muller, Anke-Susanne 2885, 3011

Muller, Ralph 197

Mulvaney, J. Michael 568, 1491

Muneyoshi, T. 2689 Munoz, Marc 1542

Munro, Morrison H. 3429, 3447

Munson, D.V. 3257 Murakami, T. 600 Muramatsu, M. 600

Muramatsu, Ryosaku 413, 798, 860, 863, 1007,

2271

Murata, Hirohiko 2403

Muratore, Joseph F. 185, 3161, 3170 Murokh, Alex 217, 2006, 2480

Murova, Yusa 2602

Murphy, James B. 134, 140, 1106

Musameci, Pietro 2480 Musson, John 768, 1183 Muto, Masayuki 565, 3348, 3770 Myakishev, Dmitry G. 2775 Myers, Stephen 299 Myskin, O. 2033

Mytsykov, A. 3122 Nadji, Amor 1168, 1533, 1569

Nagai, Ryoji 2459

Nagaitsev, Sergei 521, 1088, 1707 Nagaoka, Ryutaro 1192, 1195, 3119

Nagayama, Takahisa 848

Nahon, Laurent 2686 Naito, Takashi 256, 343, 1994, 2143, 2155, 3432

Naitoh, Takashi 492

Nakajima, Kazuhisa 2510, 3690, 3702

Nakajima, Mitsuo 3690 Nakajima, Tsukasa 3360 Nakamura, Eiji 1141

Nakamura, M. 471

Nakamura, Norio 1174, 2436, 3363

Nakamura, Shinsuke 3098 Nakamura, T. 1132, 2731, 3158 Nakamura, Takeshi 2346 Nakamura, Tatsuro 343 Nakamura, Yoshiteru 2259

Nakanishi, T. 3098

Nakayama, Hitoshi 413, 798, 1007 Nam, S.H. 2205, 2501, 3504 Namito, Yoshihito 3450 Namkung, W. 2593

Nantista, Christopher D. 1432

Napoly, Olivier 922 Nara, Takayuki 2259

Narang, R. 3708

Nasonov, Nikolay N. 2584, 2587 Nassiri, Alireza 1073, 1979, 2024, 2483 Nath, Subrata 611, 1929, 3528, 3582

Nation, J.A. 3600, 3603, 3606, 3609 Naumann, Olaf 1647 Navarro, G. 1324

Nawrath, Guenther 554 Nawrocky, Roman J. 2081 Neil, G. R. 2456

Nelson, Eric M. 360, 2778 Nelson, Scott D. 1824, 2235 Nelson, W. Ralph 253, 2990, 3450

Nemoshkalenko, V. 3122

Nesterovitch, Alexandre V. 1291, 1932, 2573 Neuffer, David V. 3062, 3080, 3083, 3152

Neugebauer, F. 2764 Neuman, Charles P. 1949 Neurath, R. 2611 Nevada, Bechtel 1506 Newman, Ernest W. 971 Newsham, D. 2003, 2021

Nezhevenko, Oleg A. 1049, 1052, 1474, 3492 Ng, Cho-Kuen 206, 800, 3423, 3426 Ng, King Y. 872, 1545, 1548, 1854, 3077

Nghiem, Phi 1533 Nguyen, Dinh C. 217, 2480

Nguyen, K. 1016

Nguyen, Minh N. 1494, 1497 Nguyen, Viet 780, 928, 931, 934, 1459 Niederer, James A. 1270, 1578, 2722

Nief, J.-Y. 2990 Niell, Fred M. 237, 1004 Nielsen, B.R. 2427 Niki, Kazuaki 3770 Nikiforov, Alexej A. 750 Nikitine, Iouri 1339 Ninomiya, Shiro 1821 Niquille, C. 2617 Nishi, Masatsugu 2528 Nishimori, Nobuvuki 2459 Nishimura, Hiroshi 203, 234 Nishiura, M. 1306

Nobrega, A. 3194, 3197

Noda, Akira 857, 1294, 2280, 2528, 3110

Noda, Fumiaki 3128, 3546

Noda, Koji 413, 600, 798, 863, 1309, 1821, 2271

Noda, Takashi 2352 Nogiec, Jerzy M. 1426, 3191 Noguchi, Shuichi 432 Nordberg, Emery 980, 3221 Norem, J. 1417, 2635, 3062 Norman, Eric B. 533 Normann, L. 2617 North, William 1037, 1515 Norum, W. Eric 3764

Nosochkov, Yuri 206, 2355, 2358, 2364, 3465

Novikov, Gleb A. 2301 Novikov, Vladimir N. 3716 Novikova, Tat'ana A. 2581 Novitski, I. 3194, 3197

Novokhatski, Alexander 2743, 2879

Nuhn, H. D. 2486 Nurushev, S. 471 Nusinovich, G. 1040 Nyman, M. 3257 O'Hara, James F. 2214 O'Neil, James 533 O'Shea, Patrick G. 234, 1949

Oakeley, Owen 221, 2099 Oakley, Owen 2468 Obina, Takashi 1135, 2310 Oerter, Brian R. 699 Ogata, Atsushi 3713 Ogawa, Y. 2731 Ogawa, Yujiro 1132, 2984

Ogitsu, T. 174, 3158, 3194 Oguri, Hidetomo 3546 Oguri, Yoshiyuki 3525 Oh, Saewoong 2265, 3137

Ohkuma, Haruo 2337, 2340, 2343, 2346, 2349,

Ohmi, Kazuhito 633, 1132, 2731, 3113

Ohmori, Chihiro 413, 798, 857, 860, 863, 1007, 1653, 2271, 2280

Ohnishi, Y. 1132, 2731, 2981

Ohnuma, S. 2590 Park, Chongdo 1357 Ohsawa, S. 2731 Ohsawa, Satoshi 1132, 2238 Ohshima, Takashi 2346 Ohtomo, Kiyotaka 1722 Ohuchi, N. 1132, 2731, 3158 Oide, Katsunobu 288, 1132, 2238, 2731, 3432 Oishi, Masaya 2352 Okada, Yasuhiro 2018, 2036 Okamura, M. 3161 Okamura, Masahiro 106, 471, 1964, 3164 Oki, Toshiyuki 1821 Okita, Shunsuke 2605 Okugi, Toshiyuki 256, 2143, 2155, 3432 Okumura, Susumu 2259 Oliveira e Silva, Luis 3725 Olsen, David K. 109, 1198, 1201, 3140, 3143, 3303 Omori, Tsunehiko 2552 Onda, Takashi 842 Ongaro, Carla 2531, 2534 Onillon, Emmanuel 1109 Ono, Masaaki 432 Op de Beeck, W.J. 3212 Opanasenko, Anatoly N. 1976 Oragiri, Jun-ichi 343 Oren. Will 3309 Orlandi, Gianluca 2193, 2196 Ormond, Kern W. 1354 Orris, Darryl F. 1420, 1426, 3191, 3194, 3197, 3318 Orsini, Fabienne 2834 Ostiguy, Jean-Francois 2710 Ostojic, R. 1330, 2921 Ostrikov, Sergey V. 1932 Ostroumov, Petr N. 103, 893, 3282, 3561 Otboyev, Alexey 1524 Ott, Klaus 197, 2385, 2608 Otting, Donnie 803 Ouchi, Nobuo 3546 Overett, Trevor 1061, 3755 Ovsvannikov, Alexander D. 2808 Ovsyannikov, Dmitri A. 1857 Owen, Hywel L. 2433 Oyaizu, M. 1893 Ozaki, K. 592 Ozaki, T. 3158 Ozelis, J.P. 174, 3194, 3197 Pabst, Michael 1767 Padamsee, Hasan S. 429, 980, 983 Pagani, Carlo 1776, 2027 Pagano, Oreste 3209 Pai, Chien-Ih 1100, 1488 Pakter, Renato 1875, 2752 Palmer, Dennis T. 545, 1997, 3612 Palmer, Robert B. 3023, 3032, 3062, 3149, 3152 Palmieri, Vincenzo 541, 943 Palumbo, Luigi 1219, 1599, 2873 Pantell, R. H. 3722 Panvier, Roger 916 Paolicelli, Guido 2060 Paolucci, Giorgio 2060 Papaleo, R. 2578 Papanicolas, N. 1037

Papaphilippou, Yannis 1554, 1557, 1560

Pappas, Chris 1494, 1500, 3429

Paramonov, Valentin V. 893, 2799

Pappas, G.C. 1488

Pardo, R. C. 1890

Parietti, L. 3591

Park, E.S. 2418 Park, H. J. 899 Park, I. S. 899, 902 Park, S. 206, 2367 Park, Seong Hee 221, 2468 Parker, Brett L 3336 Parkhomchuk, Vasily V. 1387, 1704 Parodi, Renzo 913 Parsa, Zohreh 2820, 3044 Pasky, Stanley J. 1414, 2024 Pasotti, Cristina 809, 1123 Pasquinelli, Ralph J. 1094 Pastrnak, J. W. 2590 Pate, David 557, 1348 Paterson, J.M. 3423 Patterson, Janet L. 2468 Paul, Arthur C. 1204, 3251, 3254, 3513 Pavlovic, M. 2513 Pavlovskii, V. V. 2178 Payet, Jacques 1530 Pearce, P. 250 Pearson, Chris 777, 3423, 3426 Pearsons, R. 3579 Peaupardin, Philippe 2686 Peck, Stuart B. 285, 980 Pedeau, Dominique 1168 Pedersen, Flemming 143, 474 Pedrozzi, Marco 81 Peggs, Stephen G. 705, 1572, 3176, 3179, 3336 Pei, A. 1545 Pei, X. 1548 Pei, Yuanji 1315, 1596 Peikert, Martin 815 Peiniger, M. 957, 3510 Pekeler, M. 245, 2033 Pelaia, Thomas A. 1115 Pellegrin, Eric 2424 Pellegrini, Claudio 217, 2006, 2021, 2045, 2480, 2504, 3708 Pellico, William A. 1097 Pelzer, Wolfgang 3519 Penn, Gregg 3059 Peraire, Serge 40 Perelstein, Elkuno A. 3393, 3501 Perera, Lalith 3221 Perevedentsev, Eugene 1521, 1524 Perez, Francisco 806, 809, 2424 Perko, M. 658 Pershing, D. 1016 Peskov, Nickolay Yu. 1055 Pestrikov, D. 1132, 2731 Petelin, M.I. 1474 Peternel, M. 658 Peters, Craig 3257 Peterson, Edward 551 Peterson, T. 1420, 3194, 3197 Petillo, John J. 360, 2737, 2778 Petit, Annie 2686 Petitpas, Patrick 2990 Petracca, Stefania 1689, 2882 Petrak, Sibylle 2990 Petree, Mark 2990 Petrichenkov, Michael V. 3086 Petrossian, Marzik L. 3657 Petrov, Viktor M. 2033 Pett, John G. 762, 3743 Petukhov, Vladimir P. 2584 Pfeffer, Howie 3761 Pflüger, Joachim 157, 1369

Phelps, R.A. 392 Phillips, H.L. 1459 Phillips, Lawrence 780, 934, 937, 1462 Phinney, Nan 307, 338, 3384, 3447, 3456 Piaszczyk, Christopher 1465 Pichoff, Nicolas 1860, 3277 Pickard, D. 1943 Pico, Randolph E. 2590 Picon, Jean-Claude 3260 Pieck, M. 652 Piekarz, Henryk 182, 3330 Piel, C. 3510 Pierini, Paolo 1776 Pierret, Olivier 3260 Pikin, A. 1902 Pilat, Fulvia 37, 2716, 2728, 3179 Pile, P.H. 1267 Pile, Geoffery 1022 Pilipenko, Yuri 2289 Pillai, Chandra 518 Piller, C. 955 Pinayev, Igor V. 221, 2468 Pincosy, Philip A. 1827 Pinto, Innocenzo 2882 Piot, Philip 2229, 2456 Pipersky, Paul 162 Piquemal, Alain C. 1851 Pirkl, Werner 103 Pirozhenko, A. 2567 Pirozhenko, Vitaly M. 2564 Pisent, Andrea 1773, 3522 Pitts, Cliff 3342 Pivarc, J. 1896 Pivarc, J., Jr. 1896 Pivi, Mauro 2629 Placidi, Massimo 296, 2999 Plate, David 162, 803 Platise, U. 658 Plawski, Eugeniusz 3408 Plesko, M. 658, 2424, 2424 Plettner, Tomas 321 Plotnikov, Sergey V. 3564 Plum, Michael A. 518, 1198, 1201 Podlech, Holger 1955, 3543 Podlevskih, Vitaly V. 2802 Podobedov, Boris 146, 1665, 2978 Poelker, B.M. 1991 Pogorelsky, Igor V. 2471, 2552, 3722 Poirier, Roger L. 450, 839, 893, 3540 Pollet, Patrick 2087 Polozov, S. 2858 Pomazan, Yu. V. 1291 Poncet, A. 1330 Pont, Montse 2424, 3375 Poole, Brian R. 1824, 3381 Poole, Michael W. 2433, 2656 Pope, Rodd 777 Popov, Gennadiy F. 2546, 2549 Poppe, Uli 2178 Porcellato, A.M. 1324 Portante, Luciano 1366 Portmann, Gregory, J 2373 Potier, J.P. 250 Potukuchi, Prakash N. 952 Poutchkov, Sergey N. 1479, 1482, 1485, 2567 Powell, James 533 Power, John F. 1399, 2214, 2241 Power, John G. 1967, 2024, 2030, 3621 Pozimski, Jürgen 1288, 1836 Prabhakar, Shayam 131, 636

Prabhaker, Shyam 1207 Pradal, Franco 2316 Praestegaard, L. 2427 Prange, H. 197 Prasuhn, Dieter 1701, 2292 Preble, Joseph P. 780, 931, 934, 1459, 1462, 2456 Prebys, Eric J. 3026 Preger, Miro A. 131, 1536 Prelec, K. 1902 Prestemon, S. 3227 Price, J.S. 1991 Prichard, Benjamin A. 1917, 1923 Prieto, Peter S. 1246 Pritzkau, David P. 824 Prodell, Albert 185, 3161, 3170 Pronin, Oleg D. 3561 Prono, Daniel S. 617 Proudlock, Paul I. 1330, 3200, 3203, 3746 Pruessner, Marcel 234 Przeklasa, Roy 1010 Przewos, B. 471 Ptitsin, Vadim I. 37, 702, 1575, 2716, 2921 Puggli, P. 3705 Pugh, M. J. 2656 Pukhov, Alexander 3675 Puntus, Vladimir A. 3561 Pusterla, Modesto 3280 Péerez, José 2531 Oian, Zubao 872 Qiang, Ji 137, 366, 1845 Qin, Hong 1623, 1626, 1629 Qin, Qing 633 Qinggui, Lai 3263 Quigley, Peter 980 Quimby, David C. 2668, 2674, 2677, 3722 Quintana, Bobby 349 Quintana, Stephen W. 965 Rabedeau, T. 206 Radecke, F. 197 Radeka, Veljko 2114 Rago, C. E. 3447 Raia, Guido 2578 Raimondi, Pantaleo 307, 338, 2996, 3384 Raino', Antonio 1905 Ramanathan, Mohan 2051

Rakowsky, George 1390, 2471, 2477, 2698 Ramamoorthy, Susila 690 Rambo, Peter W. 1827 Ramos, H.J. 1306 Ramsell, Christopher T. 3719 Raparia, Deepak 1297, 1743, 1964, 3185 Rasson, J. 800 Rathjen, Eric 2424 Rathke, J. 780 Rathke, John 551 Ratner, Lary G. 392 Ratschow, S. 2915 Ratti, Alessandro 884, 1961 Ratzinger, Ulrich 1788, 1955, 3552, 3555 Raubenheimer, Tor O. 240, 250, 253, 338, 800, 3423, 3429, 3438, 3441, 3444, 3447, 3453, 3456, 3462, 3465, 3474, 3483, 3486, 3489 Rauch, Helmut 2957

3456, 3462, 3465, 3474, 3 Rauch, Helmut 2957 Ravello Alberto 2936 Reass, William A. 426, 453 Redin, Sergei I. 3167 Redler, K. 1393 Reece, C.E. 940 Reed, C. 3062 Reed, C.A. 1881

Rees, Daniel E. 786, 881, 1010, 1061, 1402, 2772, Regan, Amy H. 1061, 1064, 1067, 1070, 3528, 3582 Reginato, Louis L. 2537, 3257 Regler, Meinhard 2957 Reiche, S. 2486 Reichel, I. 296 Reid, Ron J. 2656 Reijonen, Jani 1943 Reilly, John 980 Reilly, Robert E. 56 Reiman, Sergei I. 1312 Reiser, Martin 234, 1040, 1046, 1656, 1659, 1749, 1758, 1970, 2102, 3274, 3369, 3372 Reitze, David H. 134 Rendon, Armando M. 965 Rensfelt, K.G. 1955 Repnow, Roland 1955, 3543 Revol, Jean-Luc 1192, 1195 Reymermier, Christian 1339 Reyzl, Ingrid 1171 Riabko, A. 1548 Ribes, Jean-Bernard 765 Rice, David H. 410, 2217, 2972, 3221 Rice, John A. 3242 Richards, Mitchell C. 349, 655, 1444, 1447, 1929, 1946 Richardson, Roger A. 1303, 2149 Riche, A.J. 250, 1863 Richied, Donald, E. 2954 Richter, Achim 2740, 2951 Richter, D. 197 Riddone, Germana 3203 Ries, T. 3540 Rieul, B. 1569 Rifkin, Jeff 777, 3423 Rifuggiato, Danilo 2578, 3288 Rimmer, Robert A. 800, 803, 896, 907, 3131, 3429 Rindfleisch, Ulrich 851 Ringwall, A. 3462 Rinkel, Tomas 392 Rinolfi, I. 250 Ristau, U. 2424, 2427 Ritchie, Gary 2852, 3339 Rizawa, Takahito 1722 Roberts, L. 1488

Roberts, Scott E. 1351, 3221 Robin, David 203, 1581 Robin, G. 2617 Robinson, Kem E. 2668, 2674, 2677, 3722 Robinson, Theodore G. 702 Robl, Phil 2388 Rodarte, Henry J. 3573 Rode, Claus 3309 Rodenas, Jose 2534 Rodier, Jacques 2012 Rodriguez-Mateos, Felix 154, 3200, 3203 Roerich, V. 103 Rogers, G. C. 2659 Rogers, Joseph T. 1354, 1686 Rohmig, P. 1330 Rokni, Sayed 253, 330, 3429 Romanov, G.V. 2799, 3561 Romanov, S.V. 2256

Roncarolo, Frederico 2999

Root, Larry 3534

Ropert, Annick 2328

Roper, R. 3540

Rosenberg, Richard A. 1641 Rosenzweig, James B. 217, 2003, 2006, 2021, 2027, 2039, 2042, 2045, 2480, 2504, 3624, 3708 Roser, Thomas 26, 614, 857, 1267, 1270, 1276, 1578, 1746, 1964, 2128, 2280, 2725, 3291, 3336 Roshal, A. 2858 Ross, Marc C. 253, 307, 800, 1994, 3411, 3429, 3432, 3447, 3453, 3477 Rossmanith, R. 165, 2424, 2427 Rotela, E. 2635 Rothemund, Karsten 2787 Rothman, Jeffrey L. 2081 Roudskov, I. 103 Rovelli, Alberto 482, 2578 Rowe, Michael 533 Roy, Ghislain 2617, 2996 Roybal, William 1396, 1402 Roódenas, José 2531 Rubin, David L. 285, 410, 980, 1300, 3221 Rudiger, H. 197 Rudolph, Klaus 3516 Rudychev, Vladimir G. 2549 Ruegg, Roman 587 Rueter, M. 1369 Ruggiero, Alessandro G. 2590, 3731 Ruggiero, Francesco 1408, 2626, 2629 Ruland, Robert 1390, 2698 Rule, Donald W. 487, 3722 Rullier, Jean-Luc 1797, 3387 Rusnak, Brian 965, 974, 977, 1396 Russell, Steven J. 477 Russenschuck, Stephan 154, 2796 Ruth, Ronald D. 250, 262, 423, 777, 3423, 3468, 3480 Rutkowski, Henry L. 617, 3257 Rutt, P.M. 1991 Ryan, K. 1991 Ryan, W. 2114, 2117 Rybalchenko, G.V. 2689 Rybarcyk, Lawrence J. 881, 3528, 3582 Ryne, Robert D. 137, 366, 611, 1845 Rödel, Volker 946 Saban, Roberto 3203 Sabbi, Gianluca 3179, 3194, 3197 Sabjan, R. 658 Sachleben, W. 928 Saeki, Akinori 2596 Saeki, Hiroshi 2352 Saethre, Robert B. 625 Saewert G. 237 Safa, Henri 432, 919, 1396 Safranek, James 206, 1584, 2244, 2304, 2364, Sagan, David C. 410, 2966, 2969 Sah, R.C. 2409, 2415 Saito, Kenji 432 Sajaev, Vadim V. 2471, 2942 Saka, K. 592 Sakai, Fumio 2036, 2298, 3702 Sakai, I. 2271 Sakai, Y. 592 Sakaki, Horonao 3507 Sakanaka, Shogo 904, 2310 Sala-Ferrari, Paola 40 Salakhutdinov, A.S. 2555 Salazar, Gilbert A. 655 Sampayan, Stephen E. 617, 1303, 2611

Sampson, William B. 185, 3230

Sander, Oscar R. 518, 1917, 1923

Sandberg, J. 3767

Sanders, David M. 1303, 2611 Sanders, Ralph T. 1100, 1261, 1264, 1488, 3336 Sandner, Wolfgang 2033 Sandweiss, J. 3722 Sangster, T. Craig 1937, 3248 Sannibale, Fernando 131, 1536 Santucci, James K. 237, 2027 Sapp, W. 590 Sarkisov, Gennady S. 3716 Sasao, M. 1306 Sassowsky, Manfred 3378 Sato, H. 3098 Sato, Hikaru 392, 2650, 3360, 3749, 3752 Sato, Shigeru 664 Sato, Yasuo 413, 600, 633, 798, 857, 860, 863, 1007, 2271, 2280

Satogata, Todd J. 693, 705, 2722, 2728
Satoh, Kotaro 1132, 2084, 2108, 2731
Satoh, Masanori 1174
Satov, Y. 103
Satpute, Sharad 1402
Sattarov, Dior 2936
Savchenko, A.N. 753
Sawada, Junichi 3546
Sawamura, Masaru 2459
Sazonov, Michael N. 3501

Scanlan, Ronald M. 171, 3194, 3197, 3233, 3236

Schachter, L. 3600, 3603, 3606, 3609

Scandale, Walter 53, 3206, 3209

Schaffner, Sally K. 729 Scheer, Michael 2385 Scheidenberger, Christoph 1671

Schempp, Alwin 530, 1955, 3516, 3519

Schep, T.J. 1539 Schieler, H. 658, 2424 Schilcher, Thomas 1129 Schill, J. 75

Schlabach, Phillip 3194, 3197, 3327

Schlarb, Holger 2879
Schleuter, Ross 3429
Schlicher, Thomas 2087
Schlitt, Bernhard 3555
Schlott, Volker 1129, 2087
Schlueter, Ross 162
Schmalzle, Jesse D. 3170
Schmickler, Hermann 465
Schmidt, C.W. 521

Schmidt, Frank 1557, 1560, 1563 Schmidt, Gerald 2172, 2175, 2507 Schmidt, Rüdiger 3200, 3203 Schmierer, Eric N. 977, 1396 Schmolke, Michael 1034 Schmor. Paul W. 100, 106, 508 Schmueser, Peter 2172, 2175, 2178 Schnase. Alexander 851, 1701, 2292

Schneegans, T. 197 Schneider, Gerhard 1339 Schneider, Herbert 1701

Schneider, J. David 503, 1946, 3528

Schneider, Th. 165

Schneider, William J. 934, 1462, 1991 Schnuriger, Jean-Claude 103 Schoenlein, Robert 2370, 2498

Schoessow, Paul 1967, 2030, 3621, 3624

Scholfield, George 1010 Schonauer, Horst O. 2933, 2957

Schonberg, R.G. 590

Schrage, Dale L. 965, 1333, 1399 Schreiber, Siegfried 84, 922

Schröder, Gerhard H. 1228, 1408, 1509

Schuch, Reinhold H. 1671 Schuett, Petra 2951 Schug, Gebhard 3549

Schulte, Daniel 250, 259, 1668, 1863, 3441

Schultheiss, Carl M. 3737 Schultheiss, Thomas 780, 3306 Schultz, David C. 1252, 3447, 3450

Schultz, Sheldon 830

Schulze, Martin E. 3528, 3576, 3579, 3582, 3758

Schwalm, Dirk 1955, 3543 Schwandt, Peter 392 Schwartz, Charles 1073 Schwarzkopf, S. 545 Schwarz, Heinz 206, 800, 3429 Scorzato, Carlos 2421 Scott, Benjamin 206, 1363 Scott, Mike 1010 Scott, Paul K. 1911, 1926

Scrivens, Richard 103 Sears, James 980

Sebek, James J. 206, 2361, 3104, 3107

Sedlyarov, Igor K. 2033 Sedykh, Sergey N. 1055, 3393 Seeman, John T. 1, 296 Seidel, Mike 34, 554 Seidl, Peter 1937, 2849, 2852 Selchow, Nicholas 2235 Seleznev, Igor B. 2567 Sellyey, W. C. 2152, 2214 Semenov, P.A. 392

Semertzidis, Yannis K. 490, 1488

Sen, T. 1677, 2635 Senichev, Yurij V. 2442, 3549 Senioukov, Victor A. 2570

Senti, M. 3212 Seon, Dong K. 2131 Serafini, Luca 1997, 2039, 2734

Sereno, Nicholas S. 1587, 1644, 2322 Sergeev, Anatoly P. 1055, 3393 Serio, Luigi 1405, 3203 Serio, Mario 131, 636, 1536 Serov, Valeri L. 3561 Sertore, D. 2027 Servranckx, Roger 2620 Sery, Andrey 237, 3321, 3728 Sessler, Andrew M. 1716, 3053, 3056

Shabunov, Alexey V. 2262 Shadwick, Bradley A. 1716, 2888 Shafer, Robert E. 3758 Shang, Clifford C. 3251 Shang, Lei 1315, 1596 Shank, Charles 2370

Setzer, Stefan 2951

Shapiro, Michael A. 81, 833, 836

Shapiro, Stephen 2990 Sharamentov, S.I. 3561 Sharapa, Anatoly 237 Sharkov, B. 103

Sharma, Sushil K. 2635, 3095, 3342

Sharonov, S. 3191

Sharp, William M. 1830, 1833, 3248 Shasharina, Svetlana G. 369, 377

Shatilov, Dmitry 1536 Shchepounov, V. 3288 Shcherbakov, A. 3122

Shea, Thomas J. 2114, 2117, 2146, 2250

Sheehan, J. 3495 Sheffield, Richard L. 217 Shemyakin, Alexander 237, 521 Shen, Stewart S. 1333, 1336, 1372, 1396 Shepard, Kenneth W. 524, 952, 955 Sheppard, John C. 3429, 3447, 3450, 3486 Sherman, Joseph D. 349, 655, 1444, 1447, 1929, 1946, 3528

Sheu, Jeng-Tzong 1450, 3776 Shevchenko, Oleg A. 2492 Sheynin, S. 3576, 3579 Shibata, Yukio 2187 Shibuya, S. 1653 Shibuya, Takashi 3363

Shiltsev, Vladimir 237, 641, 1387, 1608, 1692,

2638, 3321, 3728 Shimbo, M. 600 Shinn, M. 2456 Shinoe, Kenji 3363 Shintake, Tsumoru 3411 Shinto, Katsuhiro 1653 Shioya, Tatsuro 2683

Shirai, Toshiyuki 1294, 2528, 3110

Shirakabe, Y. 565
Shirakata, Masashi 3360
Shirasawa, K. 2689
Shirotov, V. V. 2178
Shishido, Toshio 432
Shiyankov, Sergei V. 2948
Shoaee, Hamid 338
Shoaff, Phillip V. 1336
Shpak, A. 3122
Shu, Deming 2051, 2090
Shumakov Igor V. 1764
Shuman, Derek 3339

Shumshurov, A. 103 Shurter, Robert B. 2214, 2241

Shvedunov, Vasiliy I. 910, 2301, 2555, 2584,

2915 Shvets, Gennady 3675 Sibley, Coles 3101 Sidorov, Aleksey 1479, 1485 Sidorov, Guennady 2522 Sieber, Thomas 3516 Siedling, Rolf 2172 Siegel, Norbert 154

Siemann, Robert H. 146, 321, 330, 545, 824,

3612, 3648 Siemko, Andrzej 154 Sigg, Peter K. 418 Siggins, T. 2456 Sikora, John P. 1115 Sikora, Robert E. 2114, 2117 Silbar, Richard R. 2790 Silvestri, M. 2578

Silvestrov, Gregory I. 3062, 3086, 3089

Sim, James W. 1426, 3318 Simmering, D. 197 Simon, Rolf 2424

Simonov, Karlo G. 2567, 2570

Simos, Nikolaos 548 Simrock, Stefan 922 Sinclair, Charles K. 65, 1991 Sinenko, Irina G. 1468, 2105 Singatulin, Shavkat 1387 Singh, Om 2051, 2093, 2244 Sinjavski, A.V. 1468 Sivers, Dennis W. 392 Skarbo, Boris 237, 3321 Skarita, John 2552

Skaritka, John 1390, 2471, 2477, 2480, 3722

Skarpass, Knut VIII 3384 Skocic, Ante 2951 Skoczen, Blazej 1339

Skowbo, D. 590 Skozen, Blazej 1330 Skrinsky, Alexander N. 3089 Slater, James 11 Slaton, Timothy 3411, 3477 Sloan, T. 498, 1545, 1548 Smart, Loralie A. 557, 1348 Smedley, John 75, 75 Smirnov, Alexei V. 3615 Smith, Brian G. 977, 1396 Smith, David R. 830 Smith, Frank M. 965, 968 Smith, G. 2128, 2286 Smith, H. Vernon 1444, 1447, 1929, 3528 Smith, Howard 2987 Smith, John D. 355, 690, 2713 Smith, Jr., H. Vernon 1946 Smith, Kevin 2280 Smith, Kevin S. 614, 857, 2725 Smith, Peter D. 2954, 3573 Smith, Robert J. 2096 Smith, Susan L. 2433 Smith, Terry L. 3755, 3758 Smith, Todd I. 321 Smithwick, J. 3233 Smolej, M. 658 Smolyakov, M. N. 2692 Smolyakov, N.V. 2689 Snell, Charles M. 1842 Snodgrass, N. Leon 3594 Snyder, Arthur 2990 Sobenin, Nicolay P. 910, 2301 Soga, F. 600 Soika, Rainer 2936 Sokoloff, M. 2990 Solheim, Larry 1515 Solomon, Lorraine 2244, 2471, 2698 Solyak, Nikolay 461 Solvga, Steffen 1034 Someya, Hirohiko 3348, 3752 Sommer, M. 1569, 2686 Song, Jinhu 2229 Song, Joshua J. 168, 789, 3092 Sonnemann, Florian 154, 2999, 3200 Sonnendrucker, Eric 1830, 2758 Soukas, A. 1264, 1267, 1270, 3767 Sourkont, Konstantin V. 392 Soutome, Kouichi 2337, 2340, 2343, 2346, 2349, 2352 Souza, R. J. 2590 Spalek, George 3573 Spataro, Bruno 1147, 2873 Spataro, Charles 3333 Spence, William 1043 Spencer, Cherrill M. 1252, 3429, 3447 Spencer, James E. 321 Spentzouris, Linda K. 114, 2027, 3155 Spentzouris, Panagiotis 3062, 3083 Sperisen, Franz 392 Spiller, P. 1785, 1788

Spinos, Frank 1333

Spitz, Richard 857, 2280

Spyropoulos, Basile 2543

Sredniawski, Joseph 587

Stagno, Vincenzo 1779 Stanford, G. 100, 3540

Sprangle, Phillip A. 3687, 3693

Srinivasan-Rao, Triveni 75, 490 Staats, Joachim 2740

Staples, John W. 884, 1958, 1961

Starling, W.J. 3531 Starostenko, Alexander A. 2167 Stassen, Rolf 1701, 2292 Steck, M. 527, 1704 Stedinger, M. 2978 Stefani, Giovanni 2060 Steier, Christoph 3098 Steigerwald, M. 1991 Steinhauer, Loren C. 3722 Steinhof, A. 165 Steininger, Ralph 2424 Stella, A. 131 Stelzer, James E. 1923 Stengl, G. 2575 Stepanov, A. 103 Stepanov, Anatoli A. 3561 Stepanov, Sergey S. 1932, 2573 Stephani, Dmitri 2114 Steski, Dannie B. 2277 Stettler, Mathew W. 349, 652, 1946, 2214, 2241 Stevens, Alan F. 1013 Stevens, Alan J. 1237 Stevens, Jr., Ralph R. 1444, 1447, 1917, 1923, 1929, 1946 Stiliaris, E. 1037 Stirbet, Mircea 946 Stockhorst, Hans 851, 1701, 2292 Stoner, J. M. 2590 Stout, Daniel S. 3597 Stover, Greg D. 636, 1213 Strait, J. 2921, 3194, 3197 Strasburg, Sean 1518 Stratienko, Vladimir A. 3269, 3271 Street, Richard W. 3755 Streun, Andreas 1542, 2430 Striganov, Sergei I. 2614 Stroman, Charles R. 1115 Stronisch, U. 197 Strubin, Pierre M. 346, 562 Stupakov, Gennady V. 382, 3444, 3453, 3474 Subashiev, Arsen V. 1988 Suberlucq G. 250 Suda, M. 600 Suemine, Shouji 2596 Sueno, Takeshi 3360 Suetake, M. 1132, 2731 Suetsugu, Y. 633, 1132, 2731 Sugahara, Jun 2187, 2602 Sugimoto, Masayoshi 2459 Sugimura, Takashi 1294, 3110 Suk. H. 1659 Suk, Hyyong 2006, 3708 Sukhanova, Asiya K. 2262 Sukhina, Boris 237, 3321 Suller, Victor P. 2433 Sullivan, Kevin 3306, 3309 Sullivan, Michael K. 296, 2990 Summers, Don 3149, 3152 Sun, Baogen 2048, 2184, 2406 Sun, Ding 854 Sun, H. 913 Sun, Yong 3480 Sutton, Terry D. 3597 Suwada, T. 1132 Suwada, Tsuyoshi 2108, 2238, 2731 Suzuki, Shinsuke 2015, 2749, 3507 Suzuki, Shoji 664 Suzuki, Toshikazu 777, 3417 Suzuki, Yasuaki 2352 Svandrlik, Michele 809, 1120, 1123

Sveshnikov, B.N. 2256 Swenson, Donald A. 3531 Swent, Richard L. 321 Swift, Gary 221, 2099, 2468 Sylvester, C. 1420 Sylvestor, C. 3194 Syphers, Michael J. 1578, 2128, 2632 Syphers, Mike 2641 Syratchev, I. 250 Tadokoro, Masahiro 2528, 3366 Taffarello, L. 1324 Tafti, A. Alai 2728 Tagawa, Seiichi 2018, 2596 Tajima, Tsuyoshi 440 Takada, Ei-ichi 600, 1309 Takado, Hiroshi 3546 Takagi, Akira 413, 565, 798, 860, 863, 1007, 1653 Takagi, Makoto 343 Takahashi, Hiroshi 1273 Takahashi, Jiro 1366 Takahashi, Takeshi 904 Takaki, Hiroyuki 592, 2436, 3363 Takanaka, Masao 1719 Takano, M. 256, 3432 Takano, Siro 2346 Takao, Masaru 2337, 2340, 2343, 2346, 2349, Takata, Koji 3414, 3417 Takatomi, Toshikazu 777, 3417 Takayama, Ken 1141 Takayama, T. 592 Takayama, Takeshi 2403, 2689 Takayama, Yasuhiro 256, 2155 Takeda, Harunori 3585 Takeda, Osamu 3546 Takeda, S. 3447 Takeichi, N. 592 Takeuchi, Takeshi 106, 1964 Takiyama, Youichi 3363 Tallerico, Paul J. 426, 453 Talman, Richard 410, 2713 Tamura, Hiroyuki 2259 Tamura, Kazuhiro 2346 Tanabe, J. 206, 2355 Tanabe, Toshiya 1722 Tanaka, Hitoshi 2337, 2340, 2343, 2346, 2349, 2352 Tang, Ch. 2769 Taniguchi, Yoshiki 1007 Taniuchi, Tsutomu 2015, 2749, 3507 Taniuchi, Yukiko 2352 Tanke, E. 1860 Tanner, David B. 134 Tantawi, S.G. 3423 Tantawi, Sami G. 423, 783, 1432, 1435 Tao, Xiaoping 2125 Tarakanov, Vladimir P. 1734 Tarasov, Sergej G. 2799 Tartaglia, Michael A. 1420, 1426, 3191, 3194, 3197 Tassotto, Gianni 2211 Tatanov, V.I. 753 Tavares, Pedro F. 2421, 2894, 3125 Tavian, L. 1330 Tawada, M. 1132, 2731 Taylor, Brian 1471 Taylor, C. 3233 Tazzari, Sergio 2313 Tazzioli, Franco 1985, 2734

Tecchio, Luigi B. 2948, 3558 Tecker, Frank A. 711, 720, 1082, 2719 Tejima, M. 1132, 2731 Telegin, Yu. 3122 Telfer, S. 2021 Temkin, Richard J. 81, 833, 836 Temnykh, Alexander B. 410, 3221 Tenenbaum, Peter G. 253, 338, 3453, 3456, 3459, 3462 Teng, Lee C. 2635 Tenishev, Vladimir 103 Tenyakov, Igor E. 1479, 1485, 2567 Tepes, Frank 3306 Tepikian, Steven 37, 1575, 2114, 2728 Terechkine, Iouri 174, 3242 Terekhov, V.I. 53 Terunuma, Nobuhiro 2143, 3432 Teter, Dave F. 962 Teytelman, Dmitry 131, 636, 1207, 1213 Theuws, W.H.C. 759, 2825 Thibus, Jan 530 Thieberger, Peter 548, 2277 Thiery, Yves 2012 Thikim, M. 2659 Thivent, Michel U. 2283 Thomae, Rainer 1917, 1920, 1943 Thomas, Catherine 913 Thomas, Manfred 1028 Thomas, Richard A. 3170, 3188 Thompson, K. 3465 Thompson, Kathleen A. 259, 307, 3423, 3489 Thompson, Kenneth 1979, 2635 Thompson, Pat 185, 3176 Thorndahl, L. 250 Thorson, I. 100 Thuot, Michael E. 349, 1929, 1946 Tichonchuk, Vladimir T. 3716 Tiefenback, Michael G. 1183 Tighe, Richard C. 800, 1438, 3429 Tilley, K. 2199 Timm, Martin 2879 Ting, Antonio C. 3687, 3693 Tisserand, Vincent 2990 Tiunov, M. 1902 Tkacik, G. 658 Tobiyama, Makoto 633, 1132, 1138, 2731 Toda, Makoto 413, 1007 Todd, Robert 557 Todesco, Ezio 3206, 3209 Todosow, M. 548 Toelle, Raimund 2292 Toge, Nobukazu 777, 2143, 3414, 3417, 3432 Tohyama, I. 592 Tojyo, E. 1893 Toki, Walter 2990 Tokumoto, Shuichi 3414 Tollestrup, Alvin V. 3032, 3062 Tolmachev, Nikolay G. 3269, 3271 Tolstun, Nickolay 603 Tominaka, Toshiharu 3164 Tomisawa, Tetsuo 3546 Tommasini, Davide 154 Tompkins, John C. 174, 3191, 3194, 3197, 3318 Tonguu, Hiromu 1294, 3110 Tonutti, Manfred 2172, 2178 Tooker, Joseph F. 1061, 2954, 3567 Toole, Loren 1402, 2772 Torikoshi, Masami 600, 1309

Toriyama, Minoru 3770

Torrence, Eric 2999

Tosi, Lidia 1120, 1126, 2316 Tosin, Giancarlo 3125 Tovo, E. 1324 Towne, Nathan A. 1028, 1031, 2828 Toyama, Takeshi 1141, 1653, 1821, 3098 Trakhtenberg, Emil 1369, 2489 Trautwein, T. Ann 206, 1363 Travier, Christian 916 Travish, Gil 2024, 2045, 2483 Trbojevic, Dejan 37, 1237, 2117, 3176, 3336 Tremaine, Aaron 217, 2006, 2021, 2480 Tremblay, Kelly 3306, 3312 Treps 2990 Tribendis, Alexey G. 2033 Trines, D. 245 Trines, R.M.G.M. 1539 Trofimov, A.V. 2704 Trofimov, Nikolai 346 Troha, Anthony L. 2000 Tromba, G. 2316 Trombly-Freytag, Kelley 3318 Tron, Alexander 2190 Tron, Wolfgang 986 Tropea, Paola 3206 Trower, W. Peter 910, 2301, 2555 Troyanov, E. 53 True, Richard 1049 Trujillo, Marcos C. 965 Trzeciak, Walter S. 2388, 2391, 2659 Tsai, H.J. 1162, 2409 Tsai, Y.L. 2000, 2009 Tsai, Zone-Da 1150 Tsang, Thomas 490 Tsarenkov, A.P. 2256 Tsoupas, Nicholaos 702, 1100, 1267, 1270, 1578, 2114, 2117, 2722, 2725, 2918, 3182, 3185, 3291 Tsubuku, Hideo 1309 Tsuchidate, Hiroyuki 848 Tsuchiya, Kimichika 2683, 3158 Tsukamoto, K. 633 Tsukishima, Chihiro 848 Tsunemi, Akira 2036, 2552 Tsung, F. S. 3672 Tsutsui, Hiroshi 1058, 3414 Tuckmantel, Joachim 949 Tung, Louann S. 1372 Tuozzolo, Joseph E. 1100, 1264, 1267, 1270, Tupikov, Vitaliy S. 2167 Turner, James 256, 774, 1252, 3432, 3450 Turner, William C. 1674, 3149 Tölle, Reimund 1701 Ueda, Toru 2187, 2602, 2605 Ueng, Tzong-Shyan 1375, 1450, 2069, 2072, 2412 Ueno, Ryuichi 2271 Uesaka, Mitsuru 2187, 2602, 2605 Uesugi, Tomonori 62, 413, 798, 860, 863, 1007, 1653, 1818, 1821, 2271 Umezawa, K. 2271 Umezawa, Masumi 2528, 3366 Umstadter, Donald 3666 Urabe, Osamu 2602 Urakabe, E. 600 Urakawa, Junji 256, 2143, 2155, 2552, 3432 Urbanus, W.H. 2462 Urita, K.K 471 Ursic, Rok 1120, 1129, 2087, 2253 Usack, Victor 490 Usher, Tracy 307, 3384

Uythoven, Jan 1228, 2996, 2999 Uzat, H. W. 450 Uzunoglou, N. 1037 v. Drachenfels, Wolther 3098 Vaccaro, Vittorio G. 1599 Vahsen, Sven E. 3026 Vaillancourt, Kurt W. 3423, 3480 Valdiviez, Robert 1333 Valentini, Marco 250, 3402 Valentino, Vincenzo 1905 Valero, Saby 1860 Valicenti, Raymond A. 971, 1327 Valla, Arthur S. 2668 van Asselt, Willem K. 1746 van Bibber, Karl A. 777, 3447, 3450 van der Geer, Bas 2462, 3266 van der Wiel, M.J. 3266 van Duppen, Piet 1955 Van Eijndhoven, S.J.L. 1539 Van Ginneken, Andy 2525, 3074, 3080 Van Hagan, T. 1393 Van Rienen, U. 2764, 2787 van Steenbergen, Arie 3722 Van Vaerenbergh, Pierre 2662, 2665 van Zeijts, Johannes 705, 732, 2146, 2722, 2725, 2728 VanAsselt, W. 614, 3291 VanBrocklin, Henry 533 Vane, C. Randy 1671 Vanecek, David L. 3390 Vanenkov, Iouri 154 Varela-Rodriguez, F. 103 Variale, Vincenzo 1779, 1905 Vascotto, Alessandro 2316 Vasilishin, Bogdan V. 2256, 2262 Vasiniuk, Ivan E. 1468, 2105 Vasserman, Isaac B. 2471, 2489 Vasyuchenko, Alexandr V. 3561 Vella, Michael C. 3257 Veness, Raymond J. 1339 Vengrov, R. M. 3561 Venturini, Marco 234, 1590, 1593, 1752, 1758, 1970, 3274, 3369, 3372 Ver Planck, Peter 1491 Verbeke, Jerome M. 1926, 2540 Verdier, Andre 304, 398, 1557, 1563, 2623, 3005 Verdu, Gumersindo 2534 Verhoeven, A.G.A. 2462 Vermare, C. 3387 Vernon, W. 2021 VerPlanck, Peter 568 Verstovsek, I. 658 Verzilov, Viktor A. 2193, 2196 Veshcherevich, Vadim 980 Vest, Robert E. 2388 Veteran, J. 2686 Vetter, Arthur M. 1186 Vetter, Paul 1952 Vier, David C. 830, 3612 Vignola, Gaetano 131, 866, 1536 Vikharev, A.L. 1474 Vilakazi, Zeblon Z. 1671 Villate, Denis 1381 Vinciguerra, Domenico 2578 Vinogradov, N. 2855 Vinogradov, Stanislav V. 1764 Vinokurov, Nikolai A. 2492 Virostek, Steve 884 Vlieks, Arnold E. 3420, 3423, 3447 Voevodin, M.A. 2256

Vogel, Greg 2211 Vogel, Hans 957, 2033, 3510 Vogel, Vladimir 461 Vogt, S. 197 Voigt, Siegfried 806, 809, 2424 Volfbeyn, Paul 325, 330, 3696, 3705 Volk, J.T. 182, 3324 Volkov, Igor A. 1872 Volkov, O. Y. 2178 Volkov, V.I. 2256 Volkov, Vladimir N. 2033 vom Stein, Peter 957, 2033, 3510 von Hahn, R. 3543 von Hartrott, M. 197 von Holtey, Georg 3008 von Przewoski, Barbara 392 Vondrasek, R. 1890 Vorobiev, Leonid G. 234, 2781, 3116 Vos, Lucien 304, 465 Voss, Gustav A. 2385 Vossenberg, Eugene B. 1228, 1509 Vsevolozhskaya, Tatiana A. 3062, 3086, 3089 Vujic, Jasmina 2540 Vysotskii, Vladimir I. 1312, 3642 Wada, M. 1306 Wagner, Stephen 2990 Wahl, Dan 2388 Wait, Gary D. 1509 Wake, M. 174, 3330 Walbridge, Dana G.C. 3318 Walcher, Th 165 Waldron, William L. 3257 Walker, J. 548 Walker, R. 182, 2456 Walker, Richard P. 2313, 2680 Wallen, Erik 2945 Walters, Dean R. 1342, 1378 Walther, R. 2424 Walz, Dieter R. 253, 330, 2111, 3453 Wan, Weishi 395, 1677, 2465, 3065, 3068, 3152 Wan, Xiang 81 Wanderer, Peter J. 185, 3161, 3170, 3173, 3176, 3230 Wang, C.J. 682, 685 Wang, Ch. 2409, 2671 Wang, Changbiao 1052, 3630 Wang, Chunxi 363 Wang, D. X. 934 Wang, Fuhua 3101 Wang, Guicheng 1315, 1596, 2048, 2125, 2184 Wang, Huacen 3263 Wang, J.G. 1659, 1970 Wang, J.M. 1106 Wang, J.Q. 1058 Wang, J.W. 3423, 3468 Wang, Jian-Guang 234, 1656, 2102, 3369, 3372 Wang, Jihong 2125 Wang, Jiuqing 633, 3414 Wang, Ju 3773 Wang, Junhua 2048, 2184 Wang, Juwen 777, 3420, 3426, 3477, 3480 Wang, Lanfa 633 Wang, Li-Fang 3381 Wang, Lin 1315, 1596, 2140 Wang, M.H. 1159, 1602, 1605, 2837 Wang, P. 3600, 3603, 3606, 3609 Wang, Ping 221, 2099 Wang, S. 330, 1695, 3705 Wang, S.T. 3227 Wang, Sho Qin 3651

Wang, Shuhong 633 Wilson, Ian 250, 821 Wilson, J. H. 2590 Wang, Shumei 2140 Wang, Tai-Sen F. 1623, 1848, 2876 Wilson, P. 2003 Wang, X. 2018 Wilson, Perry B. 423, 3423 Wang, X.J. 229, 2024, 3495, 3627 Wind, D. 2936 Wang, Xiangqi 1315, 1596 Wines, Robin 3309 Wang, Xijie 2158, 2471, 2480, 2942 Winick, Herman 2385 Wang, Yi-Ming 1064, 1067, 1070 Winkler, Martin 2578 Wangler, Thomas P. 611, 1061, 1848, 3582 Winkler, T. 527, 1704 Winschuh, Erich 530 Warburton, D. 1488 Warner, A. 521 Winter, W. R. 2659 Warren, David S. 349, 655 Wiseman, Mark 934, 3309 Warsop, C.M. 2199 Wisnivesky, Daniel 792 Washio, Masakazu 2018, 2298, 2552 Wissmann, Mark 768 Watanabe, Kowashi 2352 Witherspoon, R. 545 Watanabe, Takahiro 2187, 2602, 2605 Witherspoon, Sue D. 732 Watanabe, Tamaki 1653 Witkover, Richard L. 2128, 2247, 2250 Wolcott, Chip 1037, 1515 Watanabe, Yuichi 777, 3417 Wolf, Z. 1390 Watson, Scott A. 617 Waynert, J.A. 977, 1327 Wolff, Dan 3761 Webber, Robert C. 1097 Wolfley, Rick 3306 Weber, Robert 3740 Wollnik, Hermann 2578 Weggel, Robert J. 3041, 3047 Wolski, Andrzej 2433 Wong, Seung 1043, 1890 Wei, Jie 548, 1575, 1743, 2713, 2921, 3176, Wong, Tom 3618 3179, 3182, 3185 Wei, Wen-His 1375 Wong, Victor K. 392 Weihreter, Ernst 197, 2385 Woodle, Martin 1028, 2471 Weijers, S.R. 759 Woodley, Mark D. 256, 307, 3384, 3429, 3432, Weiland, Thomas 2740, 2743, 2879, 2951 3447, 3456 Weindl, A. 658 Woods, Mike 3465 Weinrich, U. 2331, 2334 Woodworth, Lee 2114 Weir, John T. 622, 1303, 3513 Wright, R. 652 Wright, Robert 3342 Weise, Hans 922, 2507 Weiss, Daniel 557, 1348 Wrulich, Albin F. 192 Weiss, M. 759 Wu, G. 714, 717, 1462 Weisse, Eberhard 40 Wu, Guozhong 2602 Welch, James J. 1441, 3221, 3224 Wu, Lydia K. 1926, 2540 Welsch, C. 3516 Wu, Xiaoyu 1318, 3116 Welz, J. 100 Wu, Ying 221, 688, 2099, 2468 Wen, Long 3263 Wu, Yingzhi 282 Weng, Wu-Tsung W. 1297, 3185 Wuensch, Walter 250, 821, 827, 3387 Wenninger, Joerg 2885, 2996, 2999, 3011, 3014 Wuestefeld, Godehard 197, 2376, 2385 Werin, Sverker 2945 Wurtele, Jonathan S. 1716, 2888, 3053, 3056, Wermelskirchen, C. 206 3059 Westenskow, Glen A. 617, 1303, 3251, 3254, Wutte, Daniela 533, 1952 3387, 3390 Wyss, Carlo 149, 3203 Westphal, T. 197 Xavier, Jr., Ademir L. 2891 White, Jeff 2217 Xiao, Meigin 404 White, Karen S. 729, 732, 735 Xie, Ming 3678 Xie, Zu Qui 533, 1952 White, Marion M. 1414, 1967 Whittum, David H. 330, 2111, 3612 Xu, Hongjie 209 Wiedemann, Helmut 206, 321 Xu, Hongliang 1315 Wiemerslage, G. 1369 Xu, Jingwei 633 Xu, S. 1369 Wienands, Hans-Ulrich 296, 1252, 2993 Wieting, James 1923 Xu, X.J. 533 Wight, Geoff .W. 106 Xu, Z. 3600 Wilcox, Marc 1926 Xue, K. 2140 Wilde, Stephen 1920 Yadav, S. 174, 3194, 3197 Wildman, David W. 237, 869, 2840 Yakimenko, Vitaly 461, 2158, 2471, 2552, 2942, Will, Ingo 2033 3495, 3722 Wille, K. 206 Yakovlev, Vyacheslav P. 1049, 2775, 3492 Willeke, Ferdinand 407, 554 Yamada, Hironari 592 Willen, Erich 185, 3161, 3173 Yamada, R. 174 Williams, C. 1881 Yamada, S. 600, 2271 Williams, David J. 2223 Yamaguchi, Seiya 1058, 3414 Williams, Malcom D. 1911, 1914, 1917, 1920, Yamamoto, Masanobu 413, 798, 860, 863, 1007, 1923, 1943, 1958, 2540, 2575 1653 Williams, Neville W. 2063, 2128, 2286 Yamamoto, N. 2731 Williams, Robert A. 2790 Yamamoto, Nobor 1132 Williams, Ronald L. 3681 Yamamoto, Noboru 343

Yamamoto, Tamotsu 2596 Yamamoto, Y. 492, 2271 Yamashita, H. 600 Yamauchi, Toshihiko 2459 Yamazaki, Junichiro 592 Yamazaki, Yoshishige 513

Yan, Yiton T. 363

Yanagida, Kenichi 2015, 2749, 3507

Yanaoka, Eiichi 3348

Yang, Bingxin 1644, 2024, 2134, 2137, 2161

Yang, J. S. 902

Yang, Jinfeng 2018, 2036, 2298, 3702

Yang, Ming-Jen 711, 720, 723, 1082, 1085, 2719

Yang, Tz Te 1159, 2000
Yang, W.Y. 2265
Yano, Yasushige 2268
Yao, Chenggui 1596
Yarba, V. 174
Yashin, Yuri P. 1988
Yazynin, Igor A. 1321
Ye, Kairong 633

Yeh, Meng Shu 1153, 1159, 1162, 2000

Yen, Boris 1506 Yeremian, A. D. 1994 Yin, B.G. 3345 Yin, Yan 2048 Yip, Harry H. 1402 Yokoi, Takeichiro 1653

Yokomizo, Hideaki 3128, 3507, 3546

Yokota, Watalu 2259 Yokoya, Kaoru 633, 1725, 3435 Yoon, Byung-Ju 3525

Yoon, J.C. 679

Yoon, Moohyun 2265, 3137

York, Richard C. 234, 1318, 2781, 3116, 3719

Yorozu, Masafumi 2018, 2036

Yosh 2731

Yoshida, H. 2689

Yoshida, Katsuhisa 848, 848 Yoshida, Mitsuhiro 3158, 3411 Yoshida, Susumu 343

Yoshida, Yoichi 2596 Yoshida, Youichi 2018 Yoshii, Jean 3654 Yoshii, Kenji 343

Yoshii, Koji 2187, 2602, 2605

Yoshii, Masahito 413, 798, 857, 860, 863, 1007,

1653, 2280 Yoshii, Masato 2271 Yoshikawa, H. 3507 Yotam, R. 206

Young, Andrew 131, 636, 1213

Young, Anthony 162

Young, Lloyd M. 881, 1444, 1447, 1929, 1946,

3528, 3570, 3582 Yourd, Roland 884 Youssof, S.S. 392 Yovchev, I. 1040, 1046

Yu, D. 2042

Yu, David 815, 2003, 2021

Yu, H. 2140

Yu, Li Hua 2471, 2474, 2942

Yu, Simon S. 1800, 1934, 2746, 3257, 3390

Yudin, Ivan P. 2704 Yun, V. 3372

Yunn, Byung C. 1177, 1180, 2453, 2456

Zachariadou, Katerina 2990 Zadorozhny, Vladimir 2820

Zagar, K. 658

Zagel, James R. 468, 2164, 2211

Zahir, Nastaran 1926, 2540

Zalateu, M. 2680

Zaltsman, Alexander 857, 2280 Zalyubovskiy, Ilya I. 2549 Zangrando, Dino 2680

Zanini, Alba 2531 Zapasek, R. 1488

Zaplatine, Evguenii N. 887, 959, 3549

Zaugg, Thomas J. 349, 655, 1444, 1447, 1923, 1929, 1946

Zavialov, V. 592

Zeitlin, Michael 1614, 1617, 1620, 2900, 2903,

2906, 2909, 2912 Zelazny, Michael S. 2987 Zelenski, Anatoli N. 106, 1964

Zelinsky, A.Yu. 2924, 2927, 2930, 3122

Zeng, J. 2003, 2021 Zeno, Keith L. 1276

Zhabitsky, Vyacheslav M. 1222 Zhang, Chuang 633, 1695 Zhang, F.Q. 3348, 3752 Zhang, Jinguo 1315 Zhang, Jun 1273 Zhang, Kaizhi 3263

Zhang, Min 2769 Zhang, S.Y. 614, 3185, 3294, 3297

Zhang, T-B. 3627 Zhang, T. 1881 Zhang, Tiejue 1940

Zhang, Wenwei 234, 1970, 3263, 3372

Zhang, Wu 1261, 1264, 2406 Zhang, Xiaolong 2629 Zhao, Feng 1315, 2125 Zhao, G.Y. 3345 Zhao, Yongxiang 3149 Zhao, Zheng 2140

Zhao, Zhentang 209, 1453 Zhogelev, Pavel 461

Zholents, Alexander A. 1794, 2370, 2465, 2498

Zhou, Anqi 2406 Zhou, Feng 633, 2963 Zigler, Arie 3687, 3693 Zigrosser, Douglas 557, 1348 Zimmerman, Robert 1396 Zimmermann, F. 1560, 2626

Zimmermann, Frank 206, 256, 307, 382, 1728,

3432

Zimmermann, Holger 530
Zinchenko, Alexander 1692
Ziomek, Chris D. 1064, 1070
Zisman, Michael S. 293, 296
Zlobin, Alexander V. 174, 3194, 3197
Zobov, Mikhail 131, 1147, 1536
Zolecki, Robert A. 2274
Zolfaghari, Abbi 1037, 1515
Zolotorev, Max S. 2111, 2370, 2498

Zorko, B. 658

Zotter, Bruno 1118, 1408

Zou, Peng 3618

Zou, Yong 3263

Zou, Yun 234, 1659, 1970, 2102, 3369

Zoubets, V. 106 Zubovsky, Victor P. 1932 Zumdieck, John F. 2668

Zuo, K. 206

Zvonaryova, O. 2927



1999 Particle Accelerator Conference

Brookhaven National Laboratory, Bldg. 911B, P.O.Box 5000, Upton, New York USA 11973-5000 http://pac99.bnl.gov/

AT THE NEW YORK MARRIOTT MAROUS March 29 - April 2, 1999

Conference Chairman W.T. Weng, BNL Telephone: 516-344-2135 Fax: 516-344-5954 E-mail: weng@bnl.gov

Program Chairman I. Ben-Zvi, BNL Telephone: 516-344-5143 Fax: 516-344-3029 E-mail: ilan@bnl.gov

Organizing Committee M. Allen, SLAC (NPSS) J. Ball, ORNL W. Barletta, LBNL

I. Ben-Zvi, BNL Y. Cho, ANL L. Costrell, NIST

M. K. Craddock, UBC & Triumf W.K. Dawson, TRIUMF (IEEE) D. Finley, FNAL

D. Friesel, IUCF

D. Hartill, Cornell U.

C. Joshi, UCLA

M. Kihara, KEK (APAC)

S. Krinsky, BNL

C. Leemann, TJNAF

Peoples, FNAL (DPB) M. Reiser, U. Maryland

B. Ripin, APS

C. Roberson, ONR

Schriber, LANL

R. Siemann, SLAC

D. Sutter, DOE

S. Tazzari, U. Roma & INFN-LNF (EPAC)

W.T. Weng, BNL, Chairman

G. Westenkow, LLNL

R. York, NSCL

Conference Secretary M. Campbell, BNL Telephone: 516-344-5458 Fax: 516-344-5954 E-mail: pac99@bnl.gov

Local Committee, BNL

J. Becker, Treasurer

J. Laurie, Printing

E. Lowenstein, BNL Tour

P. Lucas, Publishing (FNAL)

A. Luccio, Editor

W. MacKay, Editor

C. Ronick, Hotel Coordinator

J. Smith, Electronic Publishing

P. Yamin, Social & Spouse Activities

February 23, 2000

DTIC 8725 John J Kingman Road Ste. 0944 Ft. Belvoir, VA 22060-6218

Dear Sir.

The 1999 Particle Accelerator Conference (PAC'99) took place on March 29 -April 2, 1999 at the New York Marriott Marquis. We had approximately 1,195 registrants, 76 invited speakers and 1,528 abstracts covering all aspects of accelerator science, technology and applications. Among the registrants. approximately 2/3 were from the United States, 1/3 from abroad - truly an international conference in its scope and participation. Concurrent with the conference, there were 40 industrial firms participating in the exhibition.

The proceedings of PAC'99 were published and distributed in November 1999. Total published papers are 1,223 which are published in a 5 volume set with the total pages numbering 3,779.

The total amount of the ONR grant of \$10,000.00 was all used in the support of the expense of junior staff, graduate students, and scientists from the developing nations and former Soviet Union.

As requested form SF298 is enclosed, and shipped separately is one set of the PAC '99 proceedings.

I would like to express my sincere thanks to ONR for its support to PAC'99 which is a very effective vehicle for the development and communication in H. Kirk, Coordinator, Poster & Exhibits the accelerator profession.

Sincerely yours,

Wu-Tsung Weng Chair, PAC'99

attachment: Form SF298

The American Physical Society



K. Galuchie, IEEE CC:

Grant Administrator - ONR

BROOKHAVEN NATIONAL LABORATORY BROOKHAVEN SCIENCE ASSOCIATES

WTW:mc

